M.Y.H. Bangash
Y. F. Al-Obaid
F. N. Bangash
T. Bangash

Trauma

An Engineering Analysis

With
Medical Case Studies
Investigation

Springer

Trauma – An Engineering Analysis

M.Y.H. Bangash · Y.F. Al-Obaid
F.N. Bangash · T. Bangash

Trauma – An Engineering Analysis

With Medical Case Studies Investigation

With 504 Figures, 38 in Color and 63 Tables

Springer

Authors
M.Y.H. Bangash
Emeritus Professor
Aerospace and Nuclear Engineering Structures
London, UK

Y.F. Al-Obaid
Professor of Mechanical Engineering
Fracture, Impact/Structure
Kuwait City, State of Kuwait

F.N. Bangash
Senior Medical Doctor
London, UK

T. Bangash
Consultant Structure Engineering
London, UK

Library of Congress Control Number: 2006931129

ISBN-10 3-540-36305-X Springer Berlin Heidelberg New York
ISBN-13 978-3-540-36305-7 Springer Berlin Heidelberg New York

© Bangash, Alobaid, Bangash, Bangash

This work is subject to copyright. All rights are reserved, whether the whole or part of the material is concerned, specifically the rights of translation, reprinting, reuse of illustrations, recitation, broadcasting, reproduction on microfilm or in any other way, and storage in data banks. Duplication of this publication or parts thereof is permitted only under the provisions of the German Copyright Law of September 9, 1965, in its current version, and permission for use must always be obtained from Springer, Violations are liable for prosecution under the German Copyright Law.

Springer is a part of Springer Science+Business Media
springer.com

The use of general descriptive names, registered names, trademarks, etc. in this publication does not imply, even in the absence of a specific statement, that such names are exempt from the relevant protective laws and regulations and therefore free for general use.

Typesetting by SPi using a Springer LaTeX macro package

Cover design: de´blik, Berlin

Printed on acid-free paper SPIN: 11319344 62/3100/SPi 5 4 3 2 1 0

Preface

A number of books and research papers have been published on trauma and biomechanics. They have so far not been realistically integrated. The basic aim of this book is to present a unified approach between the engineering and medical professions. The available engineering analyses and mathematical models can be interlinked and glued together with the medical findings by means of surgeries and X-rays/scans. They can be translated into vastly developed computer programs predicting effects of plasticity, temperature, cracking, and crushing with and without muscles and other interlocking phenomenon.

The available mathematical-cum-engineering model on trauma and bone mechanics are then linked to the finite element analysis and to a computer program in which provisions are made to cater for all possible eventualities and medical parameters. The problem encountered by surgeries can be easily be incorporated into hybrid finite element computer programs such as PROGRAM ISOPAR used in this book. In all case studies the surgical influences have been considered together with the bone material data for both the operational, nonoperational and overloading behaviour of the human body structure. In all circumstances the human body structure and its important elements were treated as composite. The bone–blood interaction has been incorporated in order to obtain realistic solutions. Material properties in three-dimension have always been considered in throughout in various investigations.

Engineering analysis of trauma is being continuously developed taking into consideration the ever increasing changes in analytical, design, safety, and manufacturing techniques. The engineering advances in that direction are steadily gaining international acceptance in the wide sense of the medical profession.

The purpose of this book is to bring together experts from the medical and engineering fields in which trauma acts as a fulcrum of understanding the engineering approach to medical cases. The emphasis of this book is on the retrospective study of medical scenarios as seen from the engineering perspective. An in-depth study is required to ensure the accuracy of both medical and engineering data. Where static, dynamic, temperature and impact loads, and

velocities/accelerations are unknown they are evaluated using the material properties and fracture geometry of case studies.

From the analytical techniques, a prospective study would assist in predicting the outcome of post-trauma damage. Generally, the book covers a wide spectrum of trauma case studies and could be used in medico-legal test cases. The medical opinion can be translated into the engineering analysis there by validating or invalidating the total medical decisions. Hence the engineering profession in many simple and complicate medical test cases would assist the medical profession in providing results, thereby, cementing the bond between them on a common platform.

Chapter 1 gives a comprehensive literature survey on trauma and traumatic injuries caused by mechanical and physical factors. The human structure and its component and element have been functionally explained with charts for the reader. The function of the trauma engineers has been carefully examined. The responsibilities towards assisting the medical profession in the trauma scenario has been established.

Chapter 2 is devoted to the mechanics of fracture and dislocation. The basic ideas leading to the start of modern fracture mechanics have been established. In the light of the medical requirement, the engineering approach to *fracture* in this chapter has plausible conclusions. It is essential at this stage to inform the reader on bone tissues and their material properties. A vast research is documented in this regard.

Chapter 3 for assessing numerical modeling and collaborating results.

Chapter 4 dilates upon material properties, clinical data and tolerance thresholds. This chapter has also covers materials properties from existing clinical data, surgical tests and design threshold from various researchers. They are to be earmarked for surface modeling and meshing associated with specific medical-cum-engineering requirements. Results as part of the finite element in output data form a main fulcrum. A valuable data on tolerance thresholds have been included for major human body parts so as to assess and correlate results obtained from numerical and finite element techniques. The main advantage is the choice of material properties actually used for overcoming traumatic injuries.

Chapter 5 deals with medical case studies on traumatic surgeries. Various X-rays are included for present and future exercises using engineering analysis presented in this book. Some of these test cases have been analysed already, leaving some of the readers to carry out in-depth study of medical devices and surgical equipment. Methodologies are given exclusively in order to assist the reader on the legal, technical and medical aspects.

Chapter 6 covers the medical devices, surgical equipment, and their methodologies. Emphasis is placed on the fixation devices, orthopedic devices, hardware, and methodologies of reinforcing and stabilizing the human parts.

Chapter 7 is exclusively devoted to the engineering analysis of medical case studies. More emphasis is placed on most common surgical procedures.

Various implants are highlighted. Results obtained are fully collaborated, thus they bring about a close cooperation between the medical and engineering professions.

Chapter 8 denoted for traumatic injuries, complications and management. The diagnosis of each traumatic case and complication associated with it is distinctly given. The methodology of managing it is then explained especially in post-traumatic conditions.

Chapter 9 covers the engineering aspects of trauma management, safety and health. The objective of this chapter is to deal with the subject of trauma and safe systems of work. As far as possible the risk assessment have been identified and quantified. Health and Safety issues have been discussed. They are followed by systematic training and processes for pre- and postmanagement trauma.

The book is supported by ten appendices covering three-dimensional cracking and fracture criteria, program ISOPAR and its subroutines used in the finite element investigation, threshold limits, injuries and protection criteria, knee–systems and instrumentations, surgical techniques, total hip system, Nailing systems, small bone external fixation systems, and polyethylene products, and usage, and surgical protocol. These appendices are included to assist the reader for further in depth of studies on different case studies. A vast amount of references exist to assist the researchers to evaluate the engineering methodology behind the main case studies in the medical profession.

The book can be used by engineer and medical doctors actively involved in trauma and traumatic injuries, technologists, manufacturers, mathematicians, and specialists in computer-aided techniques and lawyers and experts in medico-legal cases involved in areas of validation and verifications.

This book is also relevant to postgraduate courses in trauma, biomechanics, medical equipments manufacture, and for engineers, in particular, in the fields of impact, dynamics and medical management, and trauma psychology.

Prof. Dr. MYH BANGASH
Prof. Dr. Y.F. AL-OBAID
Dr. F.N. BANGASH
Dr. T. BANGASH

Acknowledgement

The authors wish to express their appreciation and gratitude to many civil, structural, and biomedical engineers and medical doctors whose name are mentioned in the text for helpful discussions, criticisms, and guidance. The authors are indebted to all authors of the research papers and reports mentioned in the bibliography for generous help in the acquisition of data, graphs, X-rays, photographs and computer outputs. Special thanks to the medical organisation, specialist manufacturer of various equipment and hospital providing comprehensive data on surgical procedures without which it would have not been possible to prepare the book of this magnitude.

It will not be out of place to mention the help of many students who spent hours and days in the initial stages of the artwork and the successful running of computer programs.

The authors are indebted to the following:

- Mr. Mike Chrimes and his staff, the library of the Institution of Civil Engineers London, UK
- The staff of the library of the institution of mechanical Engineers, London, UK
- The Librarian British Medical Association(BMA), London, UK
- The Director of Information ASME, New York, USA
- The Director of Information American Medical Associations (AMA) New York and Washington D.C, USA
- Diana Analysis Delft, The Netherlands
- ABASCUS, Manchester, UK
- Faculty of Technological Studies-PAAET, State of the Kuwait
- ENS Elisabeth. A. Pimental, Uniform Service University, USA
- J.E Simirniotopaulos, M.D Uniform Services University, USA
- A.H. Martin, M.D. National Naval Medical Center, USA
- Philip A. Dinauer, M.D. Walter Reed Army Medical Center, USA
- Stryker Howmedica Osteonics, NJ, USA
- Cardiovascular Associates, NJ, USA
- St. Georges Hospital, Tooting, London, UK

Dedication

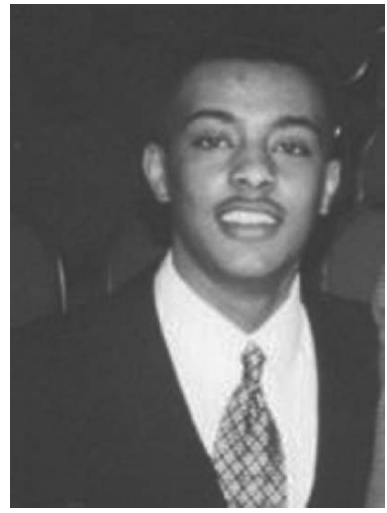

In memory of

AMMAR Y.F. AL-OBAID
1981–2003

Ammar Yaqoob Alobaid, entered into eternal rest on April 25, 2003, surrounded by his loving father, mother, grandmothers, brothers, sister, family members, and numerous friends. Born on May 11, 1981 in Manchester, United Kingdom. Ammar received his early education in Kuwait schools. Then he joined King Fahed Academy in London, UK, in 1989. In 1990, he joined AL Qattara school in Al Ein, UAE. After that, he pursued his studies in USA from 1998 to 2001. Owing to the events witnessed then, his study programme abroad was suspended. He, therefore joined the College of Technological Studies in Kuwait and was about to graduate from it when he passed away as a result of a grievous accident and traumatic injuries.

His ambition could not be realised in time, when a contract was signed for this book. We decided, then, to dedicate this book in his name.

Prof. Dr. MYH BANGASH
Prof. Dr. Y.F. AL-OBAID
Dr. F.N. BANGASH
Dr. T. BANGASH

– Agha Khan Hospital, Karachi, Pakistan
– St. Thomas's Hospital, Westminister, London, UK
– Mrs. Nourah Saad Al-Nukhailan, State of the Kuwait
– Dr. Shehab. A. Al-Shehab, State of the Kuwait
– Dr. Tamer Elnady, Egypt
– Mr. Abbas Al-Mawsawi, Kuwait

The authors are grateful for typing the manuscript under a special contract

This acknowledgement would be incomplete without praising the enormous help given by The Accident Bureau of the City of London Police, The UK Highway Agency, the Computer Bureau STRUCOM Ltd., London, and the FEA, Kingston, Survey, UK.

The authors acknowledge the enormous sufferings that their families were subjected to during many years of research and preparations for this book.

Cynthia Rodrigues, Kuwait
Harry Rodrigues, Kuwait
Eldon D'souza, Kuwait

The Whitaker Foundation and Department of Orthopaedic Surgery, Massachusetts General Hospital/Harvard Medical School.

Solid modeling and static finite element analysis of the human tibia
2003 Summer Bioengineering Conference, June 25–29,
Sonesta Beach Resort in Key Biscayne, Florida
Irina lonescu, Ted Conway, Alexandra Schonning,
Mutlaq Almutairi, David W. Nicholson.
Mechanical, Material and Aerospace Engineering Department
College of Engineering, University of Central Florida, Orlando, Florida

Coversion Table

Units		
Imperials units	SI units	Additional
1 in.	= 25.4 mm	
1 in^3	= 0.003785 m^3	
1 ft.	= 30.48 cm	
1 ft^2	= 0.09290 m^2	1 ft^3 = 0.02832 (m^3)
10 ga	= 3.57 mm	1 cu yard = 0.765 (m^3)
18 ga	= 1.27 mm	
1 lb	= 0.454 kg	
1 ton	= 9.964 kN	
1 sq ft	= 929 cm^2	
1 cubic ft	= 16.4 cm^3	
1 psi	= 6.89 kPa	= 6895 Pascal (Pa)

$20\,\mathrm{T\,ft^{-2}}$	$= 1915.2\,\mathrm{kN\,m^{-2}}$	
$1\,\mathrm{lb/sq\,ft}$	$= 992.16\,\mathrm{kPa}$	= 47.88 Pascal (Pa)
$1\,\mathrm{lb\,ft^{-3}}$	$= 16.02\,\mathrm{kg\,m^{-3}}$	
$1\,\mathrm{ft\,lb}$	$= 1.356\,\mathrm{N\,m}$	
$1\,\mathrm{ft\,sec^{-1}}$	$= 0.3048\,\mathrm{M\,s^{-1}}$	
1 slug	$= 14.59\,\mathrm{kg}$	
$1\,\mathrm{in\,lb}$	$= 0.1129848\,\mathrm{Nm}$	
$1\,\mathrm{kip/in}$	$= 1.75.1268\,\mathrm{kN\,m^{-1}}$	
1 bar	$= 100\,\mathrm{kN\,m^{-2}}$	
1 kip	$= 1,000\,\mathrm{lb}$	$= 4.448\,\mathrm{kN}$
1 short ton (2000 lb)	= 0.9072 megagram (Mg)	

MKS units	SI units	
1 Pascal (Pa)	$=\ \mathrm{kN\,m^{-1}}$	
$1\,\mathrm{kg\,m}$	$= 9.807\,\mathrm{N\,m}$	
$1\,\mathrm{kg\,f}$	$= 99.807\,\mathrm{N}$	
Temperature in °C (Celsius)		
1 °F	$-t_\mathrm{f} = 5/9\,\mathrm{K}$	$t_\mathrm{c} = (t_\mathrm{f} - 32)/118$
1 °C		$t_\mathrm{f} = 1.8\,t_\mathrm{c} 1.32$

Contents

1 Trauma and Traumatic Injuries: General Introduction 1
1.1 Trauma Types and Management 1
1.1.1 Human Body Systems 1
1.2 Definitions 5
1.3 Human Body Regions and Organs 16
1.3.1 Body Regions 16
1.3.2 Body Organs Under Trauma 16
1.4 Brain Structure and Trauma 20
1.4.1 Head/Neck 28
1.5 Thorax, Chest, and Shoulder 40
1.5.1 Thorax and Chest 40
1.5.2 Shoulder 42
1.6 Traumatic Injuries of the Upper Extremities 43
1.7 Trauma and Abdominal Injuries 47
1.7.1 General Introduction 47
1.7.2 Anatomy of the Abdomen 47
1.8 Trauma, Lower Limb, and Pelvis 49
1.8.1 Anatomy of the Lower Limb 50
1.8.2 Traumatic Injury Mechanism 51
1.9 Anthropomorphic Test Devices (ATD) 53
1.9.1 Introduction 53
1.9.2 Fields of Application 54

2 Mechanics of Fracture and Dislocation 77
2.1 Introduction 77
2.2 Fractures and Dislocations 80
2.2.1 Phalangeal Fractures and Forces 80
2.2.2 Metacarpal Fractures 82
2.2.3 Boxer's Fracture 84
2.2.4 Carpal Fractures 84
2.2.5 Pediatric Fractures 85

2.2.6 Radial and Ulnar Fractures 86
2.2.7 Elbow Fractures 88
2.2.8 Radial Head Fractures 88
2.2.9 Distal Humeral Fractures 89
2.2.10 Fractures of the Proximal Humerus 90
2.2.11 Fractures of the Clavicle 91
2.2.12 Scapular Fractures 91
2.2.13 Fractures of Hip 92
2.2.14 Skull Fractures 95
2.2.15 Depressed Fractures 96
2.2.16 Basilar Fractures 97
2.2.17 Open Fractures 97
2.2.18 Contusions 98
2.2.19 Epidural Hematoma 98
2.2.20 Subdural Hematoma 99
2.2.21 Traumatic Subarachnoid Hemorrhage 99
2.2.22 Intracerebral Hematoma 100
2.3 Dislocations 100
2.3.1 Knee Fractures in Adolescent Athletes 101
2.3.2 Tibial Intercondylar Eminence Fractures 101
2.4 Instability 102
2.5 Initial Theory of Elasticity in Three Dimensions: A Step-by-Step Analysis 102
2.6 Strength Theories and Design 105
2.7 Initiation of Fracture 106
2.7.1 Bone Fracture: Material Analysis 107
2.8 Four-Parameter Model 107
2.9 Finite Element Analysis for Traumatic Injury and Fracture 124
2.9.1 Finite Element Formulation 124
2.9.2 Reduced Linear Transient Dynamic Analysis 127
2.9.3 Solution Procedures: Acceleration and Convergence Criteria 128
2.9.4 Intermediate Problems Associated with the Finite Element Analysis 131
2.10 Hallquist et al. Method as Gap and Contact Element 131

3 Bones: Tissues and Material Properties 135
3.1 Introduction 135
3.2 The Cells of Bone and the Structure of Tissues 138
3.2.1 Woven and Lamellar Bone/Tissue 139
3.2.2 Fibrolamellar and Haversian Bone 140
3.2.3 Primary and Secondary Bone 142
3.2.4 Compact and Cancellous Bone 142
3.3 Summary 144

3.4 Material Properties as Input in Numerical Models 145
3.4.1 Material Properties use in the Numerical Models . . . 147
3.5 Fatigue Strength of Cancellous Bone 148
3.6 Additional Material Properties of Cortical Bone 150

4 Material Properties, Clinical Data on Tolerance Thresholds 153
4.1 General Information 153
4.2 Carbon Fibers-High Modulus Fibers 153
4.2.1 Production of the Composite 155
4.2.2 Mechanical Properties 155
4.2.3 Dimensional Stability 161
4.2.4 Mechanics of Composite 163
4.3 Biomedical Materials 165
4.3.1 Glass Fiber Reinforced Composite 165
4.3.2 Constitutive Properties of Bone Anisotropy and Cementless Removal Implants 168
4.4 Human Body Geometry: Nonlinear Material Properties 173
4.4.1 Optimization of the Shape for the Numerical Model 173
4.4.2 Modeling and Load/Material Data 173
4.4.3 Finite Element Model 174
4.4.4 Surface Meshing for Human Structure 175
4.5 Material Properties and Stress Analysis Material Identification Symbols 176
4.5.1 Stress Analysis for Finding Material Properties 176
4.6 Experimental Materials and Data for Finite Element Analysis 177
4.6.1 Introduction 177
4.6.2 UHMWPE 178
4.6.3 Titanium Nitride, TiN 179
4.6.4 Oriented HDPE 180
4.6.5 Stainless Steel and Coated Materials 181
4.6.6 Diamond-Like Carbon, DLC 181
4.6.7 Micronite 182
4.6.8 Tribology of Coated Materials: a Comparative Study 182
4.6.9 Characterization of Wear Debris 183
4.7 Material Data on Cortical and Cancellous Bone for the Finite Element and Experimental Test Results 184
4.8 Solid Modeling Using of the Human Tibia Using Finite Element 185
4.9 Material Properties for Lumbar Intervertebral Joint 186
4.10 Modeling of Bones and Finite Element Input 187
4.11 Finite Element Knee Models 187

4.12 Traumatic Injury Tolerance Thresholder 189
4.12.1 Head Injury Criterion (HIC) 190
4.13 Thoracic Trauma Index (TTI) 194
4.14 Plasters as Clinical Materials for Trauma Patients 197
4.14.1 Introduction 197
4.14.2 Plaster Management 197
4.14.3 Plaster of Paris Slab 197
4.14.4 Above Elbow Back Slab Plaster 199
4.14.5 Above Knee Back Slab Plaster 200
4.14.6 Plaster for Colles' Fracture 201
4.14.7 Plaster for a Fracture of the Scaphoid Bone 204
4.14.8 Additional Zones of Plastering and Bandaging 205

5 Medical Test Case Studies on Traumatic Surgeries 207
5.1 General Introduction 207
5.2 Elbow X-Ray Plain Film: Case Study 208
5.2.1 Nondisplaced Radial Neck Fracture: Types I–IV by E.N.S. Elizabeth, A Perimental (Uniform Services University) 208
5.2.2 Elbow Fat Pad Sign: Case Study 2 by William Hwang Civil Medical Center, USA 208
5.2.3 Fractures of the Proximal Radius in Children: Case Study 3 by Chad Holmes 211
5.3 Anterior Dislocation Right Shoulder 213
5.4 Psoriatic Arthritis 217
5.5 Salter–Harris Fractures 221
5.6 Hand Fracture 221
5.7 Foot/Ankle Traumatic Injury 223
5.7.1 Septic Arthritis/Cellulitis 223
5.7.2 Enchondroma as a Trauma 226
5.8 Leg X-Rays Traumatic Injuries 228
5.8.1 Contributor: Patricia McKay, USU Ewing Sarcoma 229
5.8.2 Contributor: Chun W. Chen Segond Fracture and Pellegrini–Stieda 234
5.9 Lumber: Flexion–Distraction, Osseous–Ligamentous Fracture 234
5.10 Skull 235
5.10.1 Skull Fracture with Small Epidural Hemorrhage by Jason Rexroad 238
5.10.2 Skull Fractures in Tension Contributor: James G. Smirniotopoulos, MD 238
5.11 Ankle 240
5.11.1 Distal Fibular Fx by Mathew J. Hoffman 240
5.11.2 Toddler's Fracture by Richard P. Moser III (Plate 5.41) 242

5.11.3 Intraosseous Ganglion by Fred R. Brandon (Plate 5.42) . . . 243
5.12 Segond Fracture with Associated ACL Tear . . . 244
5.13 Rib Fracture: Stages of Healing . . . 245
5.13.1 Left Lower Lobe Collapse . . . 248
5.14 Knee: ACL Tear . . . 249
5.14.1 Anterior Cruciate Ligament Injury (Plate 5.49) . . . 250
5.14.2 Osteochondritis Dissecans (OCD) (Plate 5.50) . . . 252
5.14.3 Cemented Enchondroma with Appearance of Bone Island (Plate 5.51) . . . 253

6 Medical Devices, Surgical Equipment and Methodologies . . . 255
6.1 General Introduction . . . 255
6.2 Spine: Lumbosacral Axial Fixation Device . . . 255
6.2.1 Results . . . 256
6.3 Hand Mechanism with High Degrees of Freedom . . . 258
6.4 Prosthetic Sockets . . . 261
6.4.1 Method . . . 262
6.4.2 Design of Spiral Slot Compliant Features . . . 263
6.5 Shoulder Prosthesis and Reconstruction . . . 265
6.5.1 Features . . . 267
6.6 3D Knee and Foundation Total Knee System . . . 267
6.6.1 A reference is made to Plate 6.3 . . . 267
6.6.2 Foundation® Modular Revision System . . . 269
6.6.3 3D Matrix Porous Coating . . . 269
6.7 Total Hip System . . . 270
6.7.1 Revelation Total Hip System . . . 270
6.7.2 The Ilio-Tibial Band Model . . . 270
6.7.3 Bone Preservation and Regeneration . . . 271
6.7.4 Primary Stability . . . 271
6.7.5 Subsidence (Stability) . . . 271
6.7.6 Foundation Total Hip System . . . 271
6.7.7 Keystone Revision Hip System . . . 271
6.7.8 Proximal Femur Load Transfer . . . 272
6.7.9 Minimised Distal Stem . . . 272
6.7.10 Standard and Lateralised Offset Options . . . 272
6.7.11 Proven Design . . . 272
6.7.12 Linear Total Hip Series . . . 272
6.7.13 R120 Modular Stem Series . . . 273
6.7.14 Intraoperative Versatility . . . 273
6.7.15 R120 System Modular Necks . . . 273
6.7.16 3D Macro-Interlock . . . 273
6.7.17 Foundation Total Hip System: Cemented Options . . . 273

6.7.18 Three Degree Tapered Geometry . . . 273
6.7.19 Distal Stem Tape (Plate 6.4) . . . 273
6.7.20 Cemented Foundation 460 Hip Series . . . 274
6.7.21 Cemented Foundation 450 Hip Series . . . 274
6.7.22 Keramos Acetabular System . . . 274
6.7.23 Metal/Metal CoCr . . . 274
6.7.24 Superior Surface Quality . . . 274
6.7.25 Homogenous Structure . . . 275
6.7.26 Carbide vs. Fine Grain . . . 275
6.7.27 Comparison . . . 275
6.7.28 VariGrip (Plate 6.4) . . . 275
6.7.29 Cyclone (Plate 6.4) . . . 275
6.8 Traumatic Injuries and Orthopedic Devices/Hardware . . . 276
6.8.1 Classification of Orthopedic Fixation Devices . . . 277
6.8.2 Screws . . . 277
6.8.3 Plates . . . 279
6.8.4 Wires . . . 292
6.8.5 Rods and Nails . . . 293
6.8.6 Spinal Fixation Devices . . . 294
6.8.7 External Fixation . . . 294
6.8.8 Indications for External Fixation . . . 294
6.9 A Device for Assessment of Hand and Wrist Coronal Plane Strength . . . 295
6.9.1 Methods . . . 295
6.9.2 Results . . . 296
6.10 Cranial Stabilization and Retractor Systems . . . 298
6.10.1 DORO Adjustable base Unit . . . 298
6.10.2 DORO Skull Clamp . . . 299
6.10.3 DORO Skull Pins . . . 300
6.10.4 DORO Swivel Adaptor . . . 301
6.10.5 DORO Ball Pivot Adaptor . . . 301
6.10.6 Multipurpose Skull Clamp for Children Complete . . . 303

7 The Engineering Analysis of Medical Case Studies . . . 305
7.1 Femur with Hip Endoprosthesis . . . 305
7.1.1 Fibrous Dysplasia . . . 305
7.1.2 Comminuted Femur Fracture . . . 308
7.1.3 Transient Osteoporosis of the Hip . . . 308
7.1.4 Case Study – Engineering Analysis . . . 309
7.1.5 Input Data for the Finite Element Analysis . . . 311
7.1.6 Finite Element Discretisation . . . 313
7.1.7 Calculation of the Inner Boundary of the Bone . . . 319
7.1.8 Elasto-Plastic Finite Element Analysis Behind Program ISOPAR-II . . . 320

7.1.9 Sample Cases . . . 324
7.1.10 Dynamic Analysis . . . 325
7.1.11 Criteria for Convergence and Acceleration . . . 332
7.1.12 Data on Modeling Failure Criteria on Implant . . . 335
7.1.13 General Steps of Crack Flow and Crack Calculations . . . 335
7.1.14 Computer Program ISOPAR-II: Three-Dimensional Finite Element Analysis . . . 338
7.2 The Human Skull: An Engineering Analysis . . . 343
7.2.1 General Introduction to Human Skull Structure . . . 343
7.2.2 The Bones of the Neurocranium . . . 344
7.2.3 The bones of the Viscerocranium . . . 346
7.2.4 International Mechanisms of Brain Injury Due to Impactive Forces . . . 352
7.2.5 Dynamic Model of the Human Head: Neck Complex . . . 362
7.3 A Relevant Engineering Analysis of the Traumatic Knee Injuries . . . 366
7.3.1 Experimental Studies of Individual Ligaments . . . 367
7.3.2 Force Measurement of Ligaments . . . 367
7.3.3 Strain Measurement of Ligaments . . . 368
7.3.4 Finite Element Model of the Knee Joint . . . 369
7.4 Traumatic Injury Analysis of Spine/Vertebra (Plate 7.28) . . . 376
7.4.1 Introduction . . . 376
7.4.2 Extraction of the Curve Parameters . . . 378
7.4.3 Study of the Spine Curve in Three Dimensions . . . 379
7.5 Hand and Wrist Trauma Under Impact Loading Using Three-Dimensional Finite Element Analysis . . . 384
7.5.1 Introduction . . . 384
7.5.2 Extrinsic Muscles . . . 384
7.5.3 Innervation . . . 386
7.5.4 Wrist Injuries from Impact Loading . . . 386
7.5.5 Free Vibration of a Finger Tip: Finite Element Analysis . . . 389
7.5.6 Three-Dimensional Dynamic Analysis of Impacted Fingers . . . 390
7.6 Simulation of Lower Extremity Traumatic Injuries in Sport . . . 390
7.6.1 Introduction . . . 390
7.6.2 Car Impact and Explosion Analysis . . . 393
7.7 The Solid Modeling of the Human Leg in a Car Accident . . . 397
7.7.1 Introduction . . . 397
7.8 Traumatic Damages to Achilles Tendon . . . 400
7.8.1 Introduction . . . 400

7.8.2 Finite Element Analysis of a Foot with Traumatic Injuries . . . 401
7.9 Fractures about Shoulder, Arm and Elbow Joint Fracture . . . 404
7.9.1 Fractures of Scapula . . . 404
7.9.2 Fractures and Fracture-Dislocations of Shoulder . . . 405
7.9.3 Arm and Elbow Joint Fracture . . . 406
7.10 Trauma of a Female Bladder Due to Dynamic Loads Caused by a Short Cough and Other Impacts . . . 408
7.10.1 Introduction . . . 408
7.10.2 The Geometry . . . 409
7.10.3 Input Data . . . 411
7.10.4 Dynamic Analysis . . . 412
7.10.5 Traumatic Injuries in a Network of Blood Vessels . . . 417
7.10.6 Analysis of Rubber-Like Tissue and Artery Material Model . . . 419
7.10.7 Fluid-Dynamics Analysis . . . 421
7.11 Posterior Rib Fractures from Side Airbag Deployment . . . 425

8 Traumatic Injuries, Complications, and Management . . . 429
8.1 Head Traumatic Injury Complications and Management . . . 429
8.2 Diagnostic Strategies and Management . . . 434
8.3 Radiology . . . 434
8.3.1 Skull Films . . . 434
8.3.2 Computed Tomography of the Head . . . 435
8.4 Trauma Types vs. Management . . . 435
8.4.1 Severe Head Trauma . . . 435
8.4.2 Out-of-Hospital Care . . . 436
8.4.3 Emergency Department . . . 436
8.4.4 Hypotension . . . 437
8.4.5 Hyperventilation . . . 438
8.4.6 Osmotic Agents: Mannitol . . . 438
8.4.7 Barbiturates . . . 438
8.4.8 Steroids . . . 439
8.4.9 Disposition . . . 442
8.4.10 Cranial Decompression . . . 443
8.4.11 Moderate Head Trauma . . . 445
8.4.12 Minor Head Trauma . . . 447
8.4.13 Pathological Appearances . . . 448
8.4.14 Temporal Bone Fractures . . . 449
8.5 Fractures of Capitellum and Trochlea . . . 449
8.5.1 Introduction . . . 449
8.6 Epidemiology . . . 450
8.7 Functional Anatomy . . . 450

8.8 Fracture Classification 451
8.9 Clinical Evaluation and Radiography 452
8.10 Treatment Approach and Management 453
8.11 Results: Based on Management cum Surgical Techniques . . . 456
8.11.1 Two Groups Have Reported Good Results After Immediate Excision of the Capitellar Fracture Fragments 456
8.12 Cervical Spine Injury 457
8.12.1 Principles of Disease 457
8.12.2 Clinical Features 457
8.12.3 Diagnostic Strategies 458
8.12.4 Management 459
8.13 Abdominal Injury 460
8.13.1 Perspective 460
8.13.2 Principles of Disease 461
8.13.3 Clinical Features 461
8.13.4 Diagnostic Strategies and Management 462
8.13.5 Diaphragmatic Herniation 462
8.13.6 Splenic Injury 462
8.13.7 Liver Injury 463
8.13.8 Renal Injury 463
8.13.9 Penetrating Injury 463
8.13.10 Radiology 463
8.14 Management of Traumatic Injuries: Head, Scalp, Cranium, and Brain 464
8.14.1 Brain and Cerebrospinal Fluid 465
8.15 Fractures of Hip 465
8.15.1 Hip Fractures 466
8.15.2 Intertrochanteric Femoral Fractures 467
8.15.3 After Treatment 468
8.15.4 Prosthetic Arthroplasty 468
8.15.5 Implant Selection 474
8.15.6 Fixation with Sliding Compression Hip Screw Devices 475
8.16 The Dislocated Knee 486
8.16.1 High-Velocity Knee Dislocation Vascular Injury Treatment: Principles and Management 486
8.16.2 Origins of High-Velocity Knee Dislocation and Injury Mechanism 486
8.16.3 Medical Examination 487
8.16.4 Initial Treatment 489
8.16.5 Treatment of Knee Ligaments 490
8.16.6 Emergency Department Evaluation and Treatment of Knee and Leg Injuries 491

8.17 Leg Emergencies . . . 502
8.17.1 Anatomy of the Leg . . . 502
8.17.2 Tibial Diaphyseal Fracture . . . 503
8.17.3 Fibular Fractures . . . 504
8.18 Traumatic Fracture of Distal Humerus . . . 505
8.18.1 General Introduction . . . 505
8.18.2 Acute Trauma . . . 506
8.18.3 Nonunion . . . 506
8.18.4 Traumatic Arthrosis . . . 506
8.18.5 Technique . . . 506
8.18.6 Results . . . 507

9 Trauma Management, Safety, and Health . . . 511
9.1 General Introduction . . . 511
9.2 Trauma and Safe Systems of Work . . . 511
9.2.1 Components of Safe System of Work . . . 511
9.3 Principle of Accident Prevention Related to Trauma . . . 519
9.3.1 What is an Accident . . . 519
9.3.2 Health and Safety: A Multiple Approach Related to Trauma . . . 519
9.4 Major Incidents and Emergency Procedures Causing Trauma and Traumatic Injuries . . . 522

APPENDICES

APPENDICES I-IV RELATED TO TRAUMA ENGINEERING ANALYSES AND COMPUTATIONS

I Three-Dimensional Cracking Phenomenon and Crack Calculations . . . 527
I.1 General Steps of Crack Flow and Crack Calculations . . . 527
I.1.1 Flow Chart on Cracking Phenomenon . . . 527

II Finite Element Program ISOPAR-Major Subroutines . . . 533

III Threshold Limits . . . 577
III.1 . . . 577
III.2 Pedestrian Injuries . . . 577
III.2.1 Injury Distribution by Body Segments . . . 577
III.2.2 Overall Pedestrian Impact Responses . . . 578
III.3 Threshold and Tolerances . . . 579
III.3.1 Thorax . . . 579

III.3.2 Pelvis 579
III.3.3 The Knee Joint 580
III.3.4 Body Segments: A Summary 583

IV Injury and Protection Criteria 585
IV.1 Neck Injury Criterion NIC 585
IV.2 N_{ij} Neck Injury Criterion 586
IV.3 Neck Protection Criterion $\boldsymbol{N}_{km}$ 587
IV.4 Intervertebral Neck Injury Criterion (IV-NIC) 589
IV.5 Lower Neck Load Index (LNL) 590
IV.6 Neck Displacement Criterion (NDC) 590
IV.7 Compression Criterion (C) 591
IV.8 Viscous Criterion (VC) 591
IV.9 Acceleration and Force 592
IV.10 Lateral Impact Tolerances of the Thorax 592
IV.11 Thoracic Trauma Index (TTI) 592
IV.12 Combined Thoracic Index (CTI) 593

APPENDICES V-X
RELATED TO MEDICAL EQUIPMENT USED IN TRAUMATIC SURGERIES AND CASE STUDIES

V Knee Systems and Instrumentation 597

VI Surgical Technique 623
VI.1 Meridian® ST Femoral Component* Meridian® PA Femoral Component* Meridian® TMZF® Femoral Component* 624
VI.2 STARTING† 625
VI.3 BROACHING 629
VI.4 COMPLETION 631
VI.5 Starting Options 633
VI.6 Reaming Options 636

VII Total Hip System 645

VIII Recon Nailing System 679

IX Small Bone External Fixation System 707

X Polyethylene Products, Usage and Surgical Protocol 735

REFERENCES/BIBLIOGRAPHY

References/Bibliography 763

Index 837

1

Trauma and Traumatic Injuries: General Introduction

1.1 Trauma Types and Management

Trauma is a wound or injury caused by mechanical or physical factors. It can also occur due to a negative psychological effect such as an emotional shock caused by a stressful event eventually leading to neurosis or psychosis. Flowchart 1.1 gives a full picture of types and the assessment of the trauma. Doctors and clinicians assess patients after traumatic injuries and further treatments are arranged and finally carried out. The function of the trauma engineers is to carry out analytical-cum-numerical analyses fully backed-up by computer softwares to assess injuries and fractures. In addition, the trauma engineers evaluate the causes and effects of traumatic injuries and fractures, and finally assist the medical profession in medico-legal cases if ever arise. The computer-aided results will also give a clear picture of the trauma scenario. In order to understand this subject fully, it is important to grasp a minimum knowledge of the components constituted in the human body. The major ones related to trauma are fully illustrated in Sect. 1.1.1.

1.1.1 Human Body Systems

The plates offer in parts a detailed description of various human systems. They can be looked at specifically for any kind of trauma affecting within the entire system related to a specific field of interest. Every area of interest is labeled thus giving a clear and vivid view of the body component under each system. It will be easier to isolate and identify areas in each system under trauma for major analytical and numerical study, yet it can be viewed as an element operating in the global environment. For the engineering system analyst, both elemental and global modelings are needed so that the results can be processed for localized and global case studies having sophisticated and nonrigorous finite element meshes. Even in medico-legal arguments both refined and nonrefined mesh schemes will be needed to impress upon the legal system, the kind of results derived from the finite element techniques.

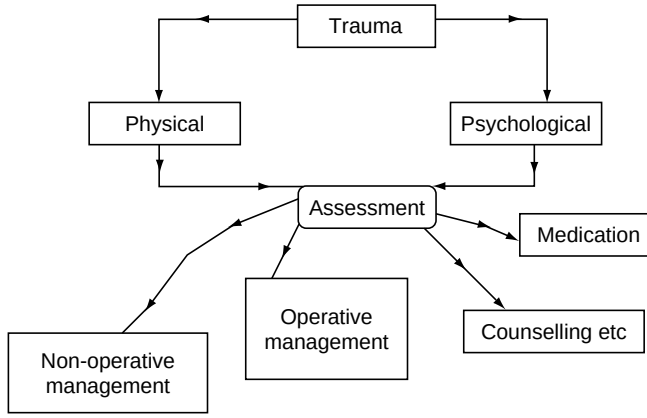

Flowchart 1.1. Trauma and trauma management

They also give a clear overall vision to a clinician upon whom he/she will plan medical assessment and provide a clear cut report on short- and long-term management criteria and management execution. The psychologist or psychiatrist will frame an objective opinion on medication and/or counseling. The engineering results will offer a basis of interaction between a surgeon and a psychologist.

For this purpose the text incorporates smaller case studies such as *hand and wrist, hand and neck, hip and knee, and foot and ankle.* They are the highest pressure areas which most likely take a higher percentage of traumatic injuries in the human system. They are fully dealt within the text. In order to assist the analyst, many X-rays and photographs are included which have been examined using well-established numerical techniques and computer softwares, thus paving the way in applying the principles of applied mechanics successfully to human biological system. Therefore the engineering trauma approach is related in this text.

The analysis of the effects caused by impact to the body. This is then known as biomechanical response of the body. The *Engineering Analysis of Trauma* addresses injuries due to mechanical impact and can be treated as a multidisciplinary research field uniting engineering sciences and medicine. The engineering analysis of trauma is extremely useful in the field of epidemiology. Epidemiology is a fundamental science for studying the occurrence, causes, and prevention of injury. The term includes the tools to identify the injury risk, analyze positive possible causative factors with respect to possible intervention, and develop methodology and its effectiveness of counter measures. In the field of "Engineering Analyses of Trauma," the accident data are definitely a pre-requisite. Although major limitation exists on the applicability of statistics, field studies and data bases, one should be aware of the problems associated with the collection, classification and interpretation techniques. The engineering analysis requires a sound statistical evaluation and can simply

fail owing to the insufficient number of cases available at the time. It is, therefore, essential to have input a complete data base inclusive of experimental and site monitoring. Injury criteria are important tools to assess the severity of mechanical impact occurring from all sources. The injury criterion correlates a function of the engineering parameters such as force, velocity, acceleration, etc., with a probability of certain body regions to be on the receiving end of trauma. The trauma as a result of injury can be understood and generally must be evaluated and thus finally validated on the basis of experimental and site monitoring studies. Since the advent of advanced computers, numerical methods and computer programs have been developed to evaluate and to examine the trauma meted out in the human infrastructure. Depending on the type of analysis, it is now easy to differentiate between injury criterion, damage criterion with and without living tissues. In such circumstances, a threshold value is established in order to detect anatomical or physiological human structures as and when the limit is exceeded. A damage criterion is then postulated, using human cadavers as surrogates for the live human beings. The analytical methods such as hybrid finite element and finite/discrete element analyses can also become valid, as described later on in this text for a protection criterion. A comparative study can be carried out using these numerical techniques and anthropomorphic test devices (dummies) for establishing protection criterion. In such cases, the relation to human trauma and injury tolerance levels is derived from these investigations. It is, therefore, taken that level to be a bottom line for an adult of not sustaining injuries of the kind addressed by this particular criterion when exposed to loading conditions defined in this protection criterion. Hence the actual risk of this traumatic injury can then be estimated with a risk function which relates the probability to be injured to the criterion underlying mechanical properties measured. A threshold value in this case will be defined such that given a certain loading scenario, represented by a certain value for the criterion, the risk of sustaining injury does not exceed a chosen percentage. The medical profession considers this to be not more than 50%. It is to be noted that scales to classify the type of injury are generally based on medical diagnosis. In trauma research, the most widely used injury scale is the Abbreviated Injury Scale (AIS) which is a system to define the severity of injuries through out the body, regularly being revised and updated (AAAM 2004). The AIS classification is given in Table 1.1. Each category represents a certain threat-to-life associated with an injury.

Table 1.1 is a standardized system and is an anatomically based, global severity scoring system that classified each injury in every body region by assigning a code (AISO-AIS6). The AIS severity code is a single time-dependent value for each injury and every body region. As stated, the severity is clearly defined in Table 1.1. It must be remembered that blindness or life-threatening complication, including infections occurring after certain period are not generally coded as severe injury. Thus resulting trauma since they do not represent an initial threat. Generally the AIS is not a linear scale. For example the differences between AIS1 and AIS2 is the same as between

Table 1.1. The AIS classification

AIS code	injury
0	noninjured
1	minor injury
2	moderate injury
3	serious injury
4	severe injury
5	critical injury
6	untreatable injury

AIS5 and AIS6. Hence, mean value calculation becomes senseless. It is recommended that for one person the overall trauma severity shall be treated maximum AIS known as MASI; the highest ASI code sustained by one occupant on any part of the body, even if the same occupant sustained several injuries of the same severity level at different body parts. This means that for an occupant with an injury AIS2 on head and legs with no injuries classified higher, MAIS will still be MAIS2.

People with multiple injuries producing trauma of unusual nature, the Injury Severity Score (ISS) can easily be updated and the latest version serialized as AAAM (2001). For each region, the highest code is determined. As a result the ISS is calculated as the sum of the $\sum^3 (\text{AIS})^2$, i.e., the squares of AIS codes of at least three severely body regions. The minimum ISS = 0 to the maximum ISS = 75 = 3 AIS injuries. For AIS6, the ISS shall be 75. The major trauma is when the ISS value is >15. This assessment is related to mortality (Baker and O'Neil 1976) and long-term impairment (Campbell et al. 1994). Other scales are also recommended such as involving scaling scheme for categorizing soft tissue and neck injuries. This work is noted in detail later in many areas in the text. This is noted against QTF, the Quebec Task force (Spitzer et al. 1995). There are other scales which are cost scales addressing impairment, disability and societal loss throughout the ratings of long-term consequences by assigning an economic value. Some of the major ones are given below have been adopted by the US government.

- Injury Cost Scale (ICS) (Zeidler et al. 1989)
- Injury Priority Rating (IPR) (Carsten and Day 1988)
- Harm (Malliaris 1985)

One of the most crucial problems in "Trauma Engineering" is the assessment of the relationship between injury severity and mechanical load including impact loading which causes this injury. It is therefore necessary to find a relationship that allows the probabilities that a certain load will cause a particular injury. Such correlations are vital without which it will become useless to interpret or to carry out a comparative study of any results obtained from experimental tests or existing patients monitoring data. This theme in the text

will be highlighted in detail using computerized analyses based on well-known numerical techniques.

Hence it becomes necessary for the trauma to be assessed to

- Develop a comprehensive analytical tool
- Perform well equipped laboratory experiments using human surrogates for determining the biomechanical response and corresponding injury tolerance levels
- Establish injury risk functions and risk curves, perhaps, statistical methods, cumulative frequency distribution, and the Weibull distribution methods

Despite certain limitations, decades of trauma engineering research have provided a sufficiently large number of sources that allow to establish several well-founded relationships thus linking mechanical loads to injury probability and injury mechanisms. The latest research has been utilized to extend this kind of relationship.

1.2 Definitions

Abrasion. Wearing away of tissue by sustained or heavy friction between surfaces.
Acetasulum. The socket in the side of the bony pelvis into which the spherical head of the thigh bone (femur) fits.
Acoustic trauma. The often damaging effect of loud nose on the inner ear.
Acomioclaviclar joint. The joint between the outer end of the collar bone and the acromion process on the shoulder blade.
Acromion. The outer most extremely of the spine of the shoulder blade.
Adduction. Movement towards the center line of the body.
Adrenal Glands. The small internally secreting organs that sit on top of each kidney producing various steroid hormones.
Alveolus. One of the many million tiny thin-walled, air sacs in the lungs.
Amnesia. Loss of memory as a result of physical or mental disease or injury.
Anatomy. The structure of the body or the study of the structure.
Aneurysm. A berry-like or diffuse swelling or an artery, usually at or near a branch, and caused by localized damage or weakness to the vessel wall.
Anterior. In front of anus short terminal portion of the alimentary canal which contains two sphincters by means of which the contents of the section are retained until they can be discharged as faeces.
Aorta. The main and largest artery in the body originating from the left side of the heart and gives off branches to the heart and rest of the body.
Apex. The tip of an organ with a painted end.

Aphasia. An acquired speech disorder resulting from brain damage which affects the understanding and production of language rather than the mechanical aspects of articulation.
Appendix. A worm-like structure attached to the caecum (start of the large intestine).
Apraxia. Disorder of the cerebral cortex leading to loss of the ability to perform skilled movements with control and accuracy.
Arachnoid. Middle layer of the three meninges covering the spinal cord and brain.
Arrythmia. Any abnormality in the regularly of the heart beat.
Ataxia. Unsteadiness in standing and walking from a disorder of the control mechanisms in the brain or from inadequate information input to the brain from the skin, muscles, and joints.
Atrial fibrillation. Irregularity of heart rate due to a defect in upper chambers in the heart.
Atrium. One of the thin-walled upper chambers of the heart that receives blood from the veins and passes it down to the lower powerful pumping chambers (ventricles).
Auditory. Pertaining to hearing or to the organs of hearing.
Avascular. Lacking blood vessels.
Avascular necrosis. Death of a tissue due to lack of blood supply.
Axial skeleton. The skull and spine.
Axilla. Armed Biceps Prominent and powerful muscles on the front of the upper arm allowing the elbow to bend and the forearm to rotate outwards.
Bile. Fluid provided by liver and stored in gall bladder and secreted into the duodenum to aid fat absorption.
Bile duct. Narrow tube carrying bile from the liver to the bowel.
Biomechanical engineering. The application of the principles of mechanical engineering to improve the results of surgical treatment, e.g., design of prosthetic parts.
Biomedical Engineering. Principles of both engineering and medicine are used to broaden the scope of medicine.
Bionic. Relating to a living or life-like system enhanced by or constructed from electronic or mechanical components.
Bone. The main structural material of the body consisting of protein scaffolding (collagen) and calcium phosphorous salts.
Bowel. The intestine.
Bradycardia. Slow heart rate.
Bronchiole. One of the many thin-walled, tubular branches of the bronchi which extend the airway to the alveoli.
Bronchus. A breathing tube which is a branch of the wind pipe (Trachea).
Burns. Damage respire of the skin and underlying tissues to high temperatures from any source.
Bursa. Small fibrous sacs lined with a membrane that secretes lubricating fluid which occur around joints and in areas where tendons pass over bone.

Caecum. Beginning of the large intestine (colon).
Calcaneus. Heel bone.
Callus. A collection of partly calcified tissue formed in the blood clot around the site of a healing fracture.
Capitellum/capitulum. Any small round prominence or ending on a bone.
Carpal. Pertaining to the wrist or wrist bones.
Cartilage. A dense form of connective tissue performing various functions in the body, e.g., Bearing surfaces in joints.
Cauda equina. Collection of spinal nerves hanging down in the spinal canal below the termination of the spinal cord.
Caudal. Pertaining to the tail end of the body.
Cephalad. Situated towards the head.
Cephalic. Relating to the head or in the direction of the head.
Cerebellum. Small part of the brain lying below and behind the cerebrum which aids coordination of information concerned with posture, balance and fire voluntary movement.
Cerebral cortex. Grey outer layer of the cerebral hemisphere.
Cerebrospinal fluid. Fluid that bathes the brain and spinal cord and also circulates within the ventricles of the brain and central canal of the cord.
Cerebrum. Largest and most highly developed part of the brain containing several structures for various functions, e.g., memory, vision, etc.
Cervical. Pertaining to the neck.
Cervix. The neck of the womb (uterus).
Choroid. Densely pigmented layer of blood vessels lying just under the retina of the eye supplying nutrition.
Ciliary body. Thickened ring of muscular and blood vascular tissue that forms the root of the Iris and contains the focusing muscle of the eye.
Clavicle. Collar bone.
Clot. Thick, coagulated viscous mass especially of blood elements.
Coccyx. Rudimentary tail bone beneath sacrum.
Cochlea. The structure of the inner ear containing the coiled transducer that converts sound energy into nerve impulse information.
Coeliac. Pertaining to the abdominal cavity.
Colon. Large intestine.
Concussion. "Shaking up" of the brain from violent acceleration or deceleration of the head causing unconsciousness lasting for seconds to hours.
Conjunctiva. Transparent membrane attached around the cornea.
Connective tissue. Loose or dense collections of collagen fibres and many cells in a liquid, gelatinous, or solid medium.
Contralateral. Pertaining to the opposite side.
Contrecoup. Damage occurring at a point opposite the point of impact especially injury to the brain against the inside of the skull.
Confusion. Bruise.
Convulsion. Fit or seizure.
Cornea. Outer and principal, lens of the eye helping to focus latter.

Coronal. Relating to the crown of the head.
Coronal plane. An anatomical plane lying vertically and dividing the body into front and rear halves.
Coronary arteries. Two important branches of the aorta that supplies the heat muscle.
Cranium. Skeleton of the head without the jaw bone.
Cricoid. Ring shaped.
CT scanning. Computer-assisted tomography.
Cuboid. One of the bones of the foot lying on the outer size immediately in front of the heel bone.
Cuneiform. Wedge-shaped bone of the foot.
Cutaneous. Pertaining to the skin.
Cuticle. Outer layer of the skin.
Decerebellate. Suffering the effects of loss of cerebellar function.
Decerebrate. Suffering from the effects of loss of cerebral activity.
Deformity. State of being misshape or distorted in body.
Deltoid muscle. Large, triangular "shoulder-pad" muscle which raises arm sideways.
Dental. Pertaining to the teeth.
Dentine. The hard tissue that makes up the bulk of the tooth.
Dermis. Layer of skin deep to epidermis.
Diaphragm. Dome-shaped muscular and tendinous partition that separates the cavity of the chest from that of the abdomen.
Doppler effect. Change in the frequency of waves, e.g., sound/light, received by doserver when the source is moving relative to the doserver.
Duodenum. The C-shaped first part of the small intestine into which the stomach empties.
Dura mater. Tough fibrous membrane, the outer of the three layers of meninges that cover the brain.
Ear drum. Lympanic membrane that separates the inner end of the external auditory canal from the middle ear.
Ecchymosis. Bleeding or bruising in the skin or a mucous membrane in the form of small, round spots or purplish discoloration.
Electrocardiography. Recording of the rapidly varying electric currents which can be detected as varying voltage differences between different points on the body surface, as a result of heat muscle contraction.
Embolism. Sudden blocking of an artery by solid, semisolid or gaseous material brought to the site of the destruction in the blood stream.
Enamel. Hard outer covering of the crown of a tooth.
Endocrine system. A group of hormone-producing glands, controlled by different parts of the brain, consisting of pituitary, pineal, thyroid, parathyroid, pancreas, adrenal, testes/ovaries, and placenta glands during pregnancy.
Enzyme. A biochemical catalyst that accelerates a chemical reaction.
Epicardium. Outer layer of the heart.

Epidermis. Structurally the outer most layer of the skin containing no nerves, blood vessels or hair follicles.
Epididymis. Long, coiled tube that lies behind the testicle and connects it to the vas deferens.
Epigastrium. The central upper region of the abdomen.
Epiglottis. Leaf-like cartilaginous structure behind the back of the tongue which acts as a "lid" to cover the entrance to the voice box (larynx) preventing food/liquid entering it during swallowing.
Epiphysis. Growing part at the end of a long bone.
Ethmoid bone. Delicate T-shaped sponge-like bone forming the roof and upper sides of the nose and the inner walls of the eye sockets.
Euryon. One of the two most widely separated points in the transverse diameter of the skull.
Eustachian tube. A short passage leading backwards from the back of the nose, on either side, to the cavity of the middle ear allowing a balance of pressure on either side of the ear drum.
Exsanguination. Loss of a large amount of blood.
External carotid artery. Major artery that springs from the common carotid artery in the neck and supplies blood to the front of the face, neck, scalp, ear and sides of the head.
Extracellular. Space surrounding a cell/collection of cells.
Extradural haemorrhage. Bleeding between the skull and the outer layer of the brain lining (dura mater).
Facet. Small flat surface on a bone or tooth.
Facial index. Ratio of the length of the face to its width multiplied by 100.
Fallopian tube. Open-ended tube along which eggs travel from the ovaries to the womb.
Fascia. Tendon-like connective tissue arranged in sheets or layers under the skin between the muscles and around organs, blood vessels and nerves.
Femur. Thigh bone.
Fetal distress. Observable changes in the fetus during pregnancy/labour caused by an insufficient oxygen supply via the placenta.
Fever. Temperature of the body elevated above 37°C.
Fibula. Slender bone on the outer side of the main bone of the lower leg (tibia).
Flexion. Act of bending a joint.
Flexor. Muscle causing flexion of a joint.
Flexure. A bend/curve/angle or fold.
Fontanelles. Gaps between the bones of the vault of the growing skull of the body/young infant which can be felt.
Fourth ventricle. The centrally places, rear most of the four fluid-filled spaces in the brain.
Forea. Any shallow cup-like depression.
Fracture. Break, usually of a bone.
Frontal lobe. Large foremost part of the brain.

Frozen shoulder. Painful, persistent, stiffness of the shoulder joint restricting normal movement.
Gait. The particular way in which a person walks.
Gall bladder. Small fig-shaped bag, lying under the liver which stores and concentrates bile.
Gastronemius. Main muscle forming the bulge of the calf.
Glomerulus. Microscopic spherical tuft of blood capillaries in the kidney through which urine is filtered.
Gonads. The sex glands.
Gracilis. Long, slender muscle lying on the inner side of the thigh.
Granulation tissue. Tissue which forms on a raw surface or open wound in the process of healing.
Glanuloma. A localized mass of granulation tissue forming a nodule.
Haematoma. Accumulation of free blood anywhere in the body.
Haemptysis. Coughing of blood.
Haemoptysis. Abnormal escape of blood from a blood vessel.
Hallux. Big toe.
Hamstrings. The tendons of three long spindle-shaped muscles at the back of the thigh.
Hemiplegia. Paralysis of one half of the body.
Hernia. Abnormal protrusion of an organ/tissue through a natural or abnormal opening.
Humerus. Long upper arm bone that articulates at its upper end with a shallow cup in the side process of the shoulder blade (scapula) and, at its lower end, with the radius and ulnar bones of the lower arm.
Hypertension. Abnormally high blood pressure.
Hypotension. Low blood pressure.
Hypotonia. A condition in which the muscles offer reduced resistance to passive movement.
Hypoxaemia. Deficiency of oxygen in the blood.
Hypoxia. Deficiency of oxygen in the tissues.
Ileum. The third part of the small intestine.
Iliopsoas. Large muscle group arising from the inside of the back wall of the pelvis and the lower abdomen and insert in front of the thigh bone.
Ilium. Uppermost of the three bones into which the in nominate bone of the pelvis is arbitrarily divided.
Interlobar. Situated between lobes.
Iris. Colored diaphragm of the eye forming the real wall of the front, water-filled chamber and lying immediately in front of the crystalline lens.
Ischium. Lowest of three hip bones in which the nominate bones are divided.
Jejunum. The length of small intestine between Duodenum and ileum where most of the enzymatic digestion of food occurs.
Kyphosis. Abnormal degree of backward curvature of the dorsal spine.

Labyrinth. Group of communicating anatomical cavities especially in the inner ear.
Lacrimal. Pertaining to the tears.
Lacrimal gland. Tear secreting gland.
Larynx. "Adams" Apple or voice box.
Lateral. At or towards the side of the body.
Lateral ventricles. Fluid filled cavities in each half of the brain that communicate with the third ventricle.
Latissimus dorsi. Broadest muscle of the back.
Ligaments. Bundles of tough, fibrous, elastic protein called collagen that act as binding and supporting materials in the body.
Lordosis. Abnormal degree of forward curvature of the lower part of the spine.
Lunate bone. One of the bones of the wrist (carpal bones).
Lymph. Tissue fluids drained by the lymph vessels and returned to the large veins.
Lymph nodes. Small, oval or bean-shaped bodies up to 2 cm in length, situated in groups along the course of the lymph drainage vessels.
Malleolus. Either of the two bony prominence on either side of the ankle.
Malleus. Outermost and larger of the three small bones of the middle ear.
Mandible. Lower jaw bone.
Manubrium. The shield-shaped upper part of the breastbone.
*Massetes**.* Short, thick, paired muscle in each cheek running down from the cheekbone to the outer corner of the jaw bone.
Mastoid bone. Prominent bony process which can be felt behind the lower part of the ear.
Maxilla. One of a pair of joined facial bones that form the upper jaw, the hard palate, part of the wall of the cavity of the nose and part of the floor of each eye socket.
Maxillary sinus. Mucous membrane-lined air space within each half of the maxillary bone.
Medial. Situated towards midline of the body.
Medulla oblongata. Part of the brainstem beneath pons and above spinal cord in front of the cerebellum containing nerves to spinal cord and centers for respiration and heart beat control.
Meningitis. Inflammation of the meninges.
Meninges. The three layers of membrane that surround the brain and spinal cord.
Metacarpal bone. One of the five long bones situated in palmar part of the hard immediately beyond the carpal bones of the wrist and articulating with bones of the fingers.
Metatarsal. One of the five long bones of the foot lying behind the TACSAl bones and articulating with the bones of the toes.
Middle ear. The narrow cleft within the temporal bone lying between the inside of the ear drum and the outer wall of the inner ear.
Molar. One of the 12 back grinding teeth.

Mucous membrane. The lining of most of the body cavities and hollow internal organs, e.g., mouth/nose
Mucus. Slimy, jelly-like material provided by globlet cells of mucous membranes.
Muscle. Tissue containing large numbers of parallel elongated cells with the power of shortening and thickening so as to approximate their ends and effect movement.
Nail. A protective and functional plate of a hard tough (Keratin) lying on the back surface of the end part of fingers/toes.
Nasal. Pertaining to the nose.
Neuralgia. Pain experienced in an area supplied by a sensory nerve as a result of nerve disorder that results in the production of pain impulses in the nerve.
Neuron. Functional unit of the nervous system.
Occipital lobe. Rear lobe of the main brain (cerebral hemisphere) concerned with vision.
Oesophagus. The gullet of a muscular tube of 24 cm length from the throat to the stomach.
Olecranon. Hook-shaped upper end of one of the forearm bones (ulna) that projects behind the elbow joint.
Olfactory. Pertaining to the sense of smell.
Opthalm-, Opthalma-. Pertaining to the eye.
Optic chiasma. The junction of the two optic nerves lying under the brain.
Optic disc. Small circular area at the back of the eye at which all the nerve fibres from the retina meet to form the optic nerve.
Orbit. The bony cavern in the skull that contains the eyeball and optic nerve, eye muscles, tear glands and blood vessels.
Ossicle. Small bone in middle ear.
Ossification. Process of conversion of other tissues into bone.
Osteoporosis. A form of bone atrophy involving both collagen scaffolding and the mineralization.
Ovary. One of paired female gonads situated in the pelvis.
Pancreas. A gland situated behind the stomach which has a duct, that secretes digestive enzyme into duodenum and hormones for glucose control.
Paraplegia. Paralysis of both lower limbs.
Parathyroid glands. Four yellow bean-shaped bodies lying behind the thyroid gland that secretes a hormone into the blood for maintenance of calcium levels.
Porotid gland. The largest of the three pairs of salivary glands.
Patella. Knee-cap.
Pelvis. The basin-like bony girdle at the lower end of the spine with which the legs articulate. It consists of the sacrum, coccyx and in nominate bones.
Periosteum. The tissue that surrounds bone.
Peritoneum. Double-layered serum secreting membrane that lines the inner wall of the abdomen and covers/supports abdominal organs.
Phalanges (S. Phalanx). Small bones of the fingers/toes.

Pharynx. The common passage to the gullet and wind pipe from the back of the mouth and nose.
Pia mater. Delicate, innermost layer of the meninges.
Pineal gland. Tiny, cone-shaped structure within the brain which appears to secretes a hormone called melatonin.
Pinna. Visible external ear.
Pituitary gland. The central controlling gland in the endocrine system which is situated on the underside of the brain that produces and stores many hormones of different functions.
Plantar. Pertaining to the sole of the foot.
Pleura. Tin, double-layered membrane that separates the lungs from the inside of the chest wall.
Pons. Middle part of the brainstem.
Prostate gland. Solid, chestnut-like organ situated under the bladder surrounding the first part of the urine tube (urethra) in the male that secretes seminal fluid.
Pulmonary. Pertaining to the lungs.
Pylorus. Narrowed outlet of the stomach.
Quadriceps muscles. The bulky muscle group on the front of the thigh, consisting of four muscles arising from the femur.
Quadriplegia. Paralysis of the muscles of both arms/legs and trunk.
Radial. Pertaining to the radius or its associated nerves or artery.
Radius. One of the two forearm bones on the thumb side.
Rectum. A 12.5 cm long, distensible terminal segment of the large intestine situated above the anal canal.
Rectus. Any of the several straight muscles, e.g., Abdomen – recks abdominis.
Reflex. Automatic, involuntary and predictable response to a stimulus applied to the body or arising within it.
Renal. Pertaining to the kidneys.
Retina. Complex membranes network of nerve cells, fibers and photoreceptors that lines the inside of the back of the eye and converts optical images formed by the lens system of the eye into nerve impulses.
Rib. Any of the flat, curved bones that form a protective cage for the chest organs and provides the means of varying the volume of the chest aiding respiration.
Sacral. Pertaining to the sacrum.
Sagittal. Pertaining to the lens that joins the Z parietal bones of the skull.
Sagittal plane. The front-to-back longitudinal vertical plane that divides the upright body into right and left halves.
Scapula. Shoulder blade.
Sclera. The white of the eye.
Seizure. An episode in which uncoordinated electrical activity in the brain causes sudden muscle contraction, either local or widespread.

Sigmoid colon. The S-shaped lower end of the colon extending down from the brim of the pelvis to the rectum.
Spasm. Involuntary muscular contraction.
Spinal cord. Downward cartrivation of the brainstem that lies within a canal in the spine, 45 cm long containing bundles of nerve-fibres tracts running up and down, to and from the brain.
Spleen. Large collection of lymph tissue acting as an organ to filter blood.
Stapes. The innermost of the three tiny linking bones of the middle ear.
Sternum. Breastbone.
Subarachnoid hemorrhage. Bleeding over and into the substance of the brain from a ruptured artery lying under the arachnoid layer of the meninges.
Subdural haematoma. A dangerous complication of head injury in which bleeding occurs from tearing of one of the blood vessels under the dura mater.
Sublingual. Under the tongue.
Supine. Lying on the back with the face upwards.
Symphysis. A joint on which the component bones are immovably hold together by strong, fibrous cartilage.
Talus. The second largest bone of the foot that rests on top of the heel bone.
Tarsal. Pertaining to the tarsal bones of the foot.
Tendon. A strong bond of collagen fibres that joins muscles to bone or cartilage and transmits force of muscle contraction to cause movement.
Testis. One of male gonad.
Thalamus. One of the two masses of grey matter lying on either side of the midline in the lower part of the brain. It collects, coordinates and selects information received by the body.
Thorax. Part of the trunk between neck and abdomen.
Thymus. Small, flat organ of the lymphatic system situated immediately behind the breastbone.
Thyroid gland. Gland situated in back of the neck across the wind pipe that secretes hormones affecting rate of metabolism.
Tibia. The shin bone of the lower leg.
Tonsil. Oval mass of lymphoid tissue situated in the back of the throat on either side of the soft palate.
Trachea. Wind pipe.
Tragus. Small projection of skin-covered cartilage lying in front of the external ear opening.
Transverse colon. The middle third of the colon.
Trapezius muscle. A large triangular back muscle extending from the lower part of the back of skull almost to the lumbar region of the spine on each side.
Trauma. An injury caused by a mechanical, physical, psychological agent.
Triceps muscle. A 3-headed muscle attached to the back of the upper arm bone (humerus) and to the outeredge of the shoulder blade and running down the back of the arm to be inserted by a strong tendon into the curved process on the back of the ulna, it allows the elbow to strengthen out.

Trochanter. One of the two major bony processes, the greater and lesser trochanters on the upper part of the femur.
Ulna. One of the pair of forearm long bones on the little finger side.
Umbilicus. The scar formed by the healing at the exit site of the umbilical cord after this has been tied and cut and the tissues have died and dropped off.
Uncus. Hook-shaped part near the front of the temporal lobe of the brain that is concerned with the senses of small and taste.
Ungual. Pertaining to a finger or toe nail.
Unilateral. On or affected one side only.
Ureter. Tube that carries urine from each kidney to the urinary bladder for temporary storage.
Urethra. Tube that carries urine from the bladder to the exterior.
Urinary bladder. Muscular bag for the temporary storage of urine situated in the midline of the pelvis at the lowest point in the abdomen, immediately behind the pubic bone.
Uterus. The female organ in which the fetus grows and is nourished until birth and is a hollow, muscular organ 8 cm long in non pregnant state.
Urea. The coat of the eye lying immediately under the outer sclera containing many blood vessels and a variable quantity of pigment.
Vagina. Fibromuscular tube of $\approx$ 8–10cm length lying behind the bladder and urethra and in front of the rectum in females.
Valgus. Abnormal displacement of a part in a direction away from the midline of the body.
Valve. A structure allowing movement in a predetermined direction only.
Varum/varus. Displaced or angulated towards the midline of the body.
Vas deferens. Fine tube that runs up in the spermatic cord on each side from the epididymis of the testicle, over the pubic bone and alongside the bladder to end by joining the seminal vesicle near its entry to the prostate gland. It conveys spermatozoa from the testicle to the seminal vesicle.
Vasospasm. Tightening or spasm of blood vessels.
Vena cavae. Largest veins in the body joined to right atrium of the heart.
Ventral. Pertaining to the front of the body.
Ventricle. A cavity or chamber filled with fluid, especially the Z lower pumping chambers of the heart.
Vertebra. One of the 24 bones of the vertebral column.
Vertebral Column. The bony spine.
Vitreous body. The transparent gel that occupies the main cavity of the eye between the back of the crystalline lens and the retina.
Volar. Pertaining to the palm of the hand or sole of foot.
Vulva. Female external genitalia.
Wind pipe. Trachea.
X-ray. A form of electromagnetic radiation produced when a beam of high speed electrons, accelerated by a high voltage, strikes a metal, e.g., copper.
Zygoma. Cheek bone.

Zygomatic arch. A bony arch extending below and to the outer side of the eye socket and forming the prominence of the cheek.

1.3 Human Body Regions and Organs

1.3.1 Body Regions

For trauma related engineering analysis, the ISS distinguishes different human body regions encompassing the limbs, organs, head, etc. Flowchart 1.2 shows identifying upper and lower extremities with respective organs as shown in Plates 1.1–1.5.

1.3.2 Body Organs Under Trauma

History of the Mechanism of Injury (MOI)

In the event of any level of trauma, there is a chance that any one or all relevant organs would be affected as shown in Plates 1.1–1.12. The mechanism of trauma and injury associated could be due to anyone of the following:

- Fall
- Road traffic accident (RTA)

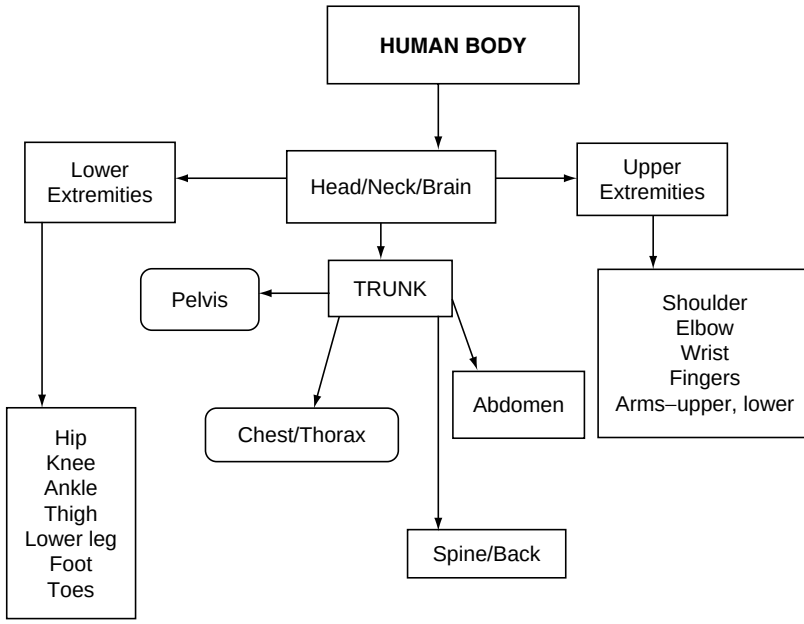

Flowchart 1.2. Human body regions

- Assault
- Blunt and penetrating objects
- Motor/aircraft accidents
- Alcohol
- Occupational hazards/accidents

Post Medical History Related to Trauma

It is extremely important to take into consideration the past medical history. For example:

- Previous head injury trauma
- Existing medical conditions, e.g., epilepsy
- Medication, e.g., aspirin, warfarin
- Alcohol/illicit drug use
- Social history
- Allergies

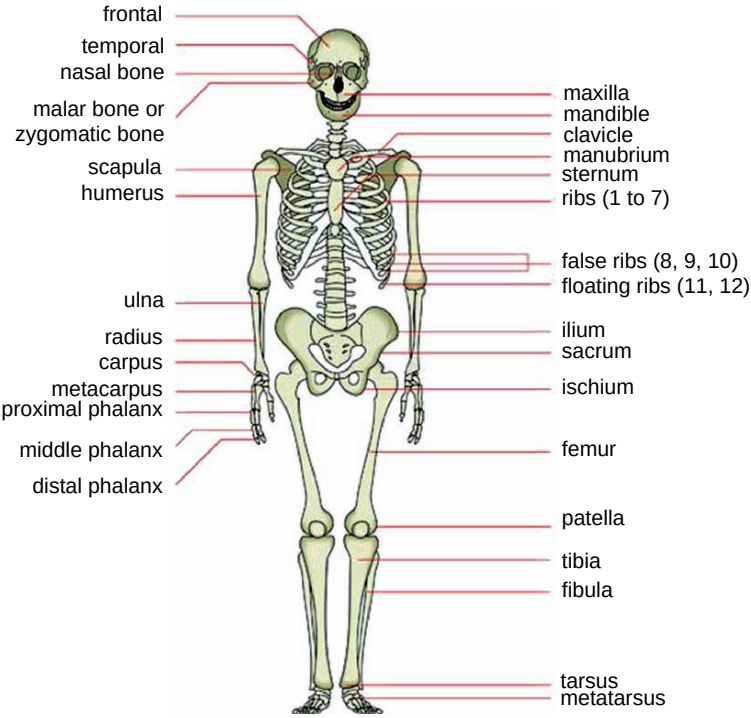

Skeletal-Anterion View
(Courtesy of info.Visual.org)

Plate 1.1. The skeletal system

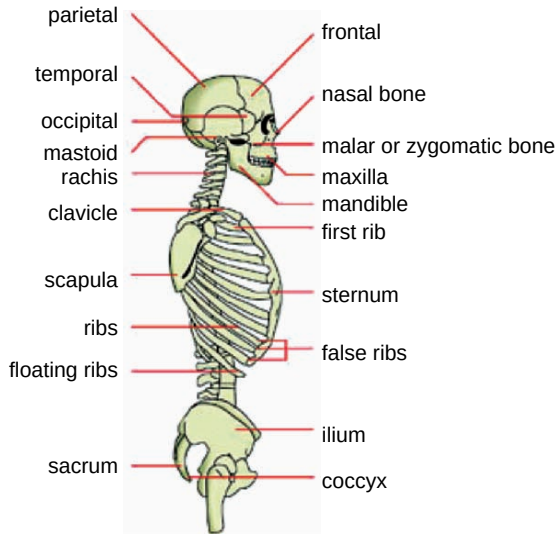

Skeletal-Lateral View
(Courtesy of info.Visual.org)

Plate 1.1. *Continued*

Treatment Priorities

This helps to assess patients based on their injuries and vital signs. Sensible and logical approach is needed to assess and treat trauma patients. Initially, this can be divided into:

1. Primary assessment
2. Secondary assessment
3. Begin definitive care

1. *Primary assessment*
   Airway maintenance with cervical spine protection
   Breathing and ventilation
   Circulation with hemorrhage control
   Disability (assessment of Neurological status)
   Exposure (undress patient with core to prevent hypothermia)
2. *Secondary assessment.* This involves obtaining a quick history of events and patients individual history from either patient, family or emergency service personnel.
   It also comprises a thorough assessment of the patient from head to toe for injuries, signs, causes and further care.
   Investigations can be carried out at this stage which initially includes: blood tests and standard trauma X-rays (chest, neck, pelvis). Subsequent

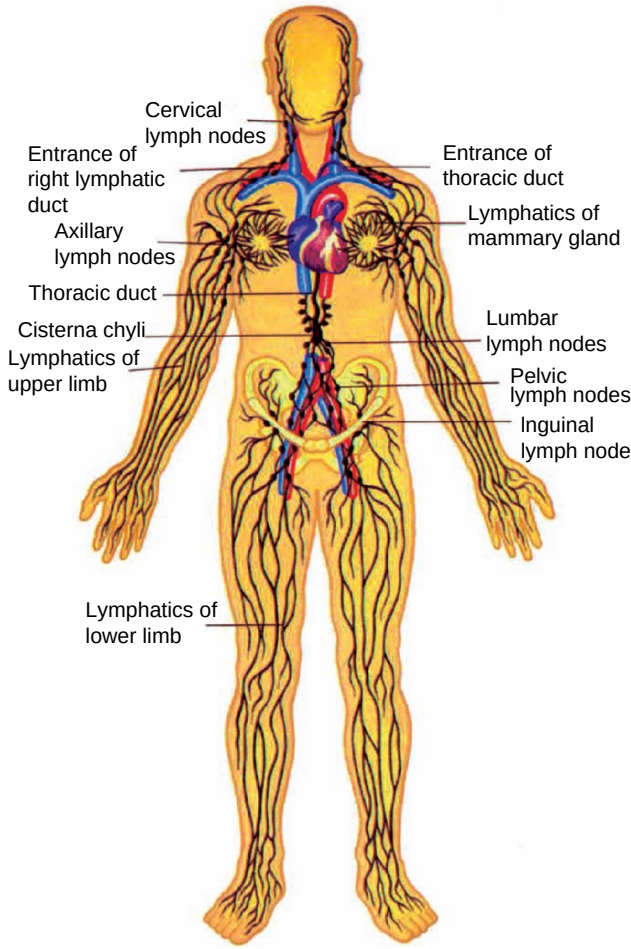

(Courtesy of lymphomation.org)

Plate 1.2. The lymphatic system

tests may be needed including specialized radiological scans like computer tomography (CT) or magnetic resonance imaging (MRI), to determine cause, need for transferring patient for specialized treatment/care or emergency operative intervention.

3. *Definitive care.* After assessment and stabilization of patient, the concept of definitive care arises. If latter is not possible at the local hospital then transfer to a center with appropriate facilities and trained staff is needed. This decision is judged as an individual basis by the trauma team.
   Prior to transfer, the patient must be stabilized and contact made with the receiving team and transferring personnel. Results from investigations and

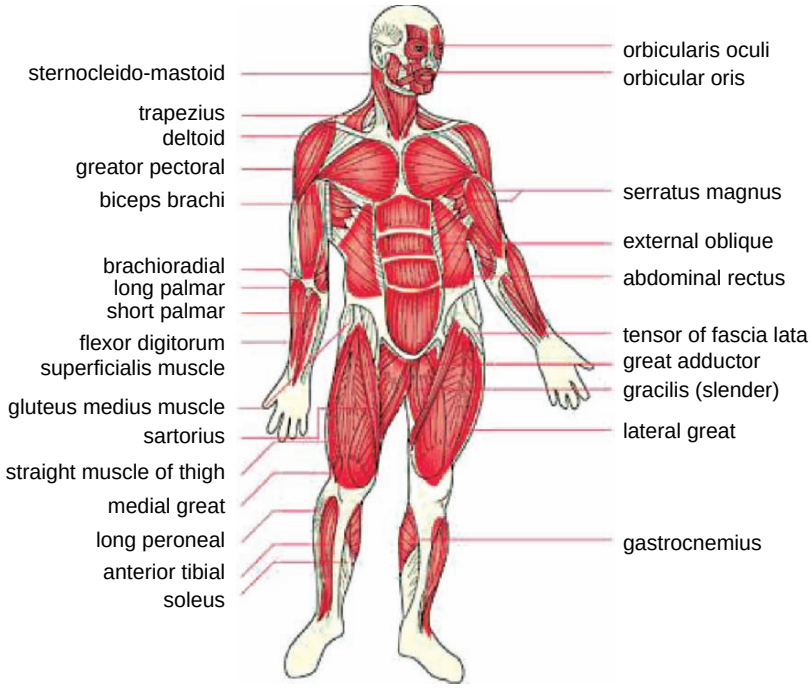

Plate 1.3. The muscular system

appropriate written documents should accompany the patient. The main purpose of caring for these individuals is to prevent further deterioration post trauma and optimizing their conditions for recovery.

1.4 Brain Structure and Trauma

The brain is one of the most essential yet complex organs of the body. It has influence on maintenance, supply, protection and transport to the remainder structures of the body. But this approximately three pound mass of pink grey tissue is what makes it distinctly human (Plate 1.6 and Flowchart 1.3).

It controls basic bodily functions as well giving anyone consciousness, self awareness, imagination and creativity. It contains more than 100 billion nerve cells and each of these electrically active units which can be connected with up to 10,000 others – creating a structure of mind-bogging complexity. If one counts the nerve connections of just the cortex, it would take 32 million years to finish the task. It seems to everyone that there are more nerve connections

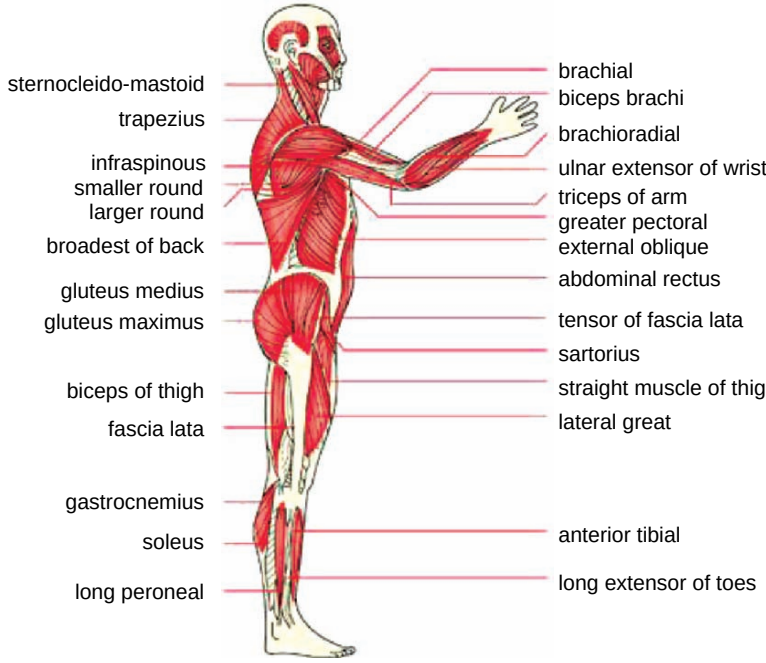

Muscular System-Lateral View
(Courtesy of info.Visual.org)

Plate 1.3. *Continued*

in the brain than there are start in the sky, millions of electrical and chemical messages handled by the brain each second of anyone's life are carried at a speed of 200 miles per hour. In addition, although the brain represents about 2% of a person's body weight, it consumes about one-fourth oxygen requirements – a substantial amount of human daily energy intake. It is vital to know that about half of the 30,000 or so human genes are dedicated to brain functions such as the nonstop of the 50 or so known chemical neurotransmitters that are critical to every conscious thought and feeling.

One of the most enigmatic functions of the brain is to store memories of events that have taken place either in the recent or distant past. This ability of long-term preservation when one gets older is a subject of intensive research. The childhood memory appear to be stored in the hippo campus before eventually being itched into the cortex as long-term memories. The frontal cortex plays a critical role in retrieving memories of the past events. About 100,000 tests on dementia around 35% in cortex is shown to be heavily affected by mechanical impact, particularly in short-term cases. Paul Broca,

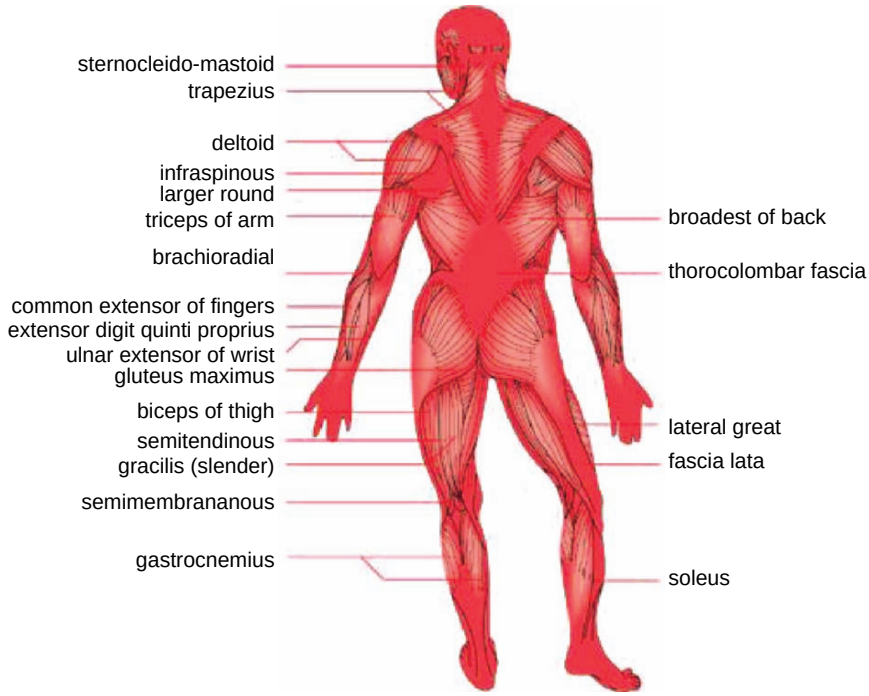

Muscular System-Posterior View
(Courtesy of info.Visual.org)

Plate 1.3. *Continued*

a French doctor described a patient in 1861 who could say one word and yet understand everything that was said. He has suffered a damage on the left-hand side of the cortex due to mechanical impact. Unfortunately, he has received pressure caused by impact on Wernicke, located in the temporal lobe. Both speech and language were affected. It is interesting to note that heavy impactive loads alter the sense of smell which has a direct connection to the brain via the olfactory nerves in the nasal cavity. Normally stimulating these nerves triggers activity in the brain smell center. On the question of psychological consequences, severe injuries to brain due to fall or impact can certainly alter basic emotions terminating into angry outbursts or loss of an overall control, by damaging frontal lobes and orbito-frontal cortex.

The brain controls essential biological functions of the body such as breathing, hormone (production/storage/release) and blood pressure. The control stems at the top of the healthy spinal cord. Another part of the brain called the hypothalamus controls other basic elements such as hunger or thirst due to trauma of any kind, there are huge changes occurring in secreting body

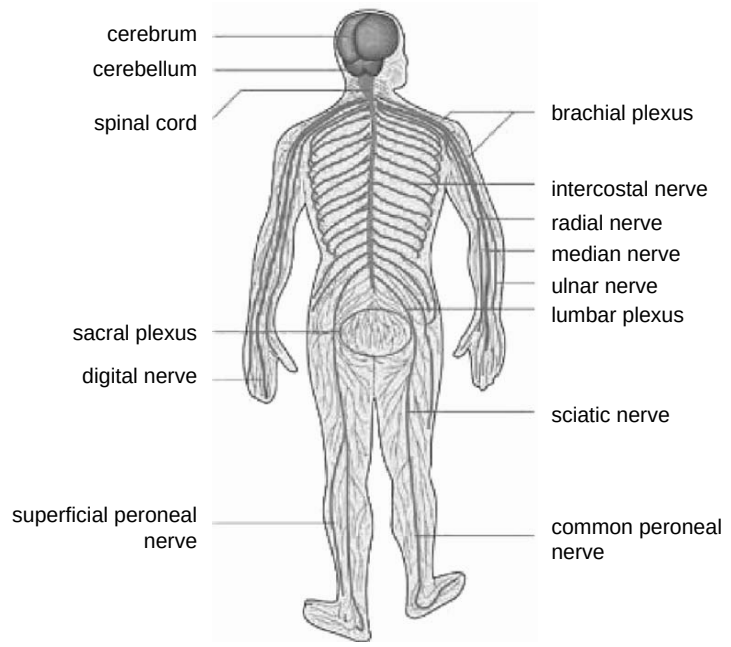

(Courtesy of info.Visual.org)

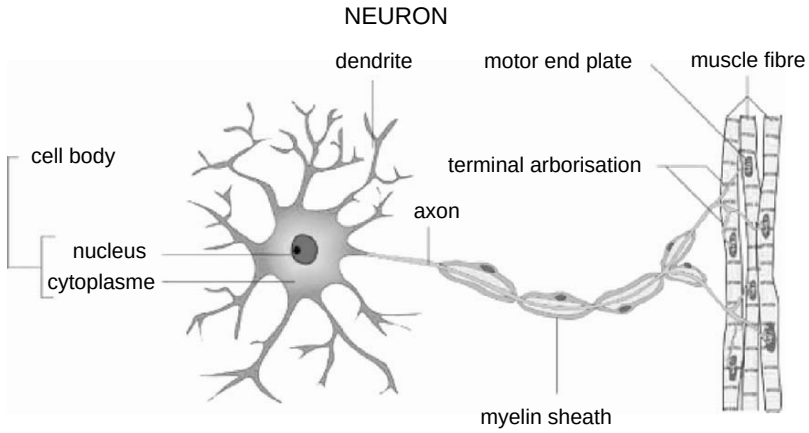

(Courtesy of info.Visual.org)

Plate 1.4. The nervous system

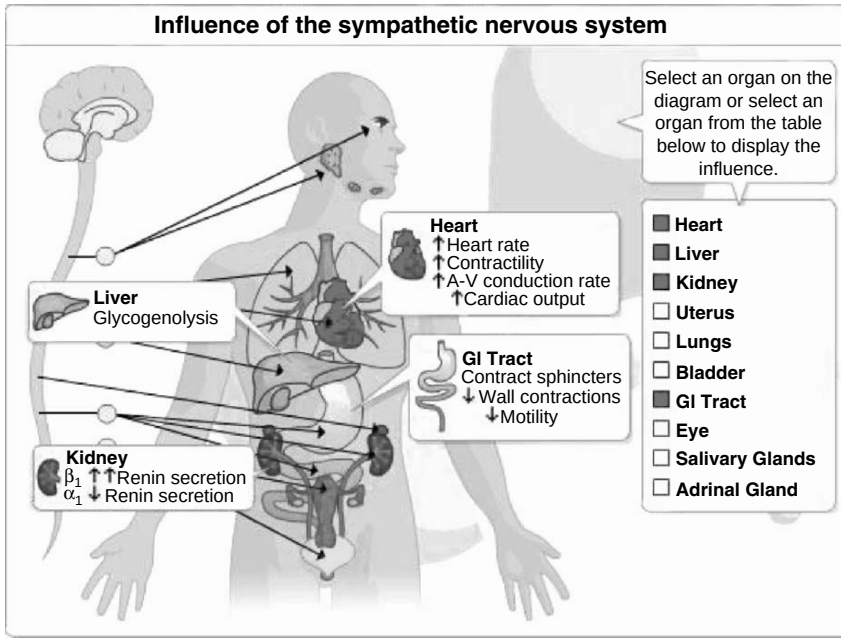

(Courtesy of vudat.msu.edu)

Plate 1.4. *Continued*

chemicals or hormones, thus not keeping constant temperature control for vital body mechanisms. Some case studies show the temporary loss of breathing and blood pressure and some times appetite.

The mechanical impact on head immediately causes vibrations in the air which are detected by sensory nerve cells in the ear and transmitted to the brain via two known auditory nerves. The temporal lobe containing the hearing center of the brain which determines tone and loudness will not focus on a particular source of sound after heavy impact. The sound among cacophony of background noises will, according to medical history be altered. The chances are that hearing can also be affected after severe trauma. The type of which determines whether or not is temporary.

There are hundreds of muscles in the body. The motor cortex at the back of the frontal lobes, allows the person to move his/her muscles consciously controlling the nerve impulses sent from the central nervous system to the face, limbs and torso. In case of trauma, the facial muscles affect the speech and other muscles will be slacked or loosened, some fractured, will affect fingers and hands. In such circumstances extreme dexterity would involve the motor cortex will ever be working efficiently.

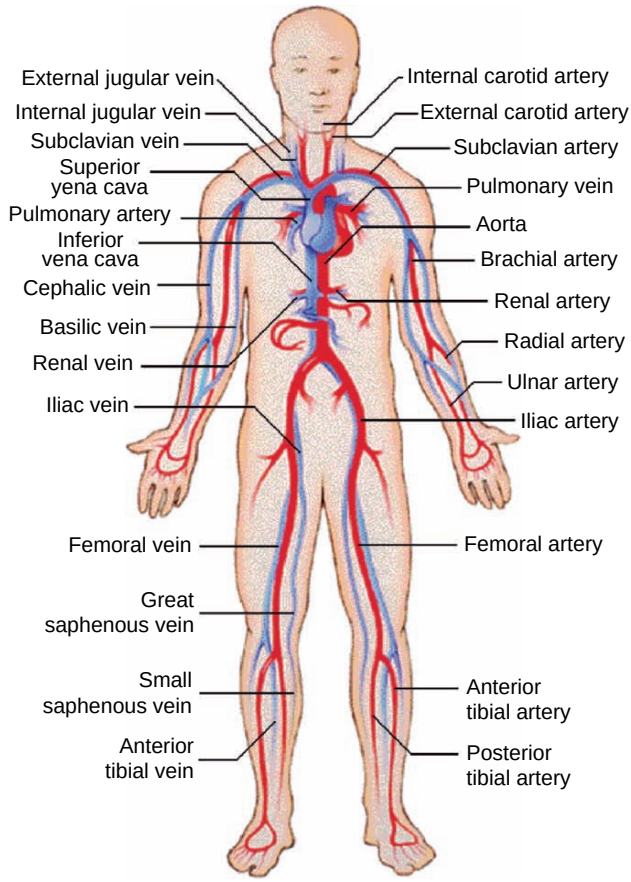

Plate 1.5. The vascular system and viscera

The skin is loaded with sensory receptors that send information about "touch," "pain," and other sensations to the brain. In case of trauma these messages are not easily handled and processed by sensory cortex, which just lies behind the motor cortex. The lips, finger tips and genitals will in some cases of trauma loose responsibility for generating much of this sensory information. The "no touch" sense will not keep human being in contact with immediate environment when a trauma occurs.

The cerebellum is a cauliflower-like appendage and the second largest structure of the brain after the cerebrum. It is known by the scientists as the brains "auto pilot," since it controls and coordinates complex muscle movements such as lifting, although one can walk easily. Owing to trauma of one

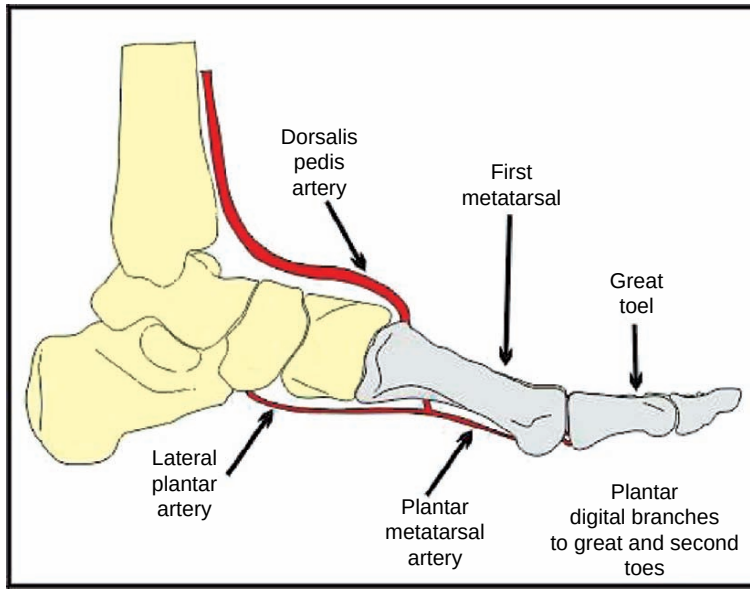

Vascular System with Grea
(Courtesy of microsurgeon.org)

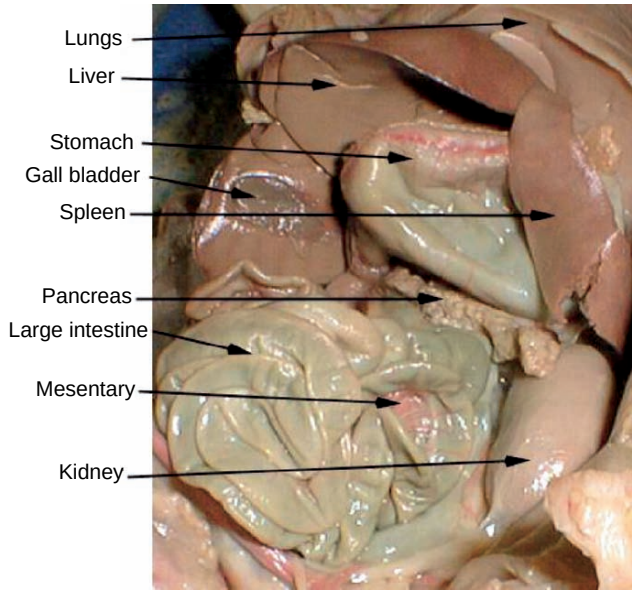

Viscera Close
(Courtesy of dravin.bruch.cuny.edu.)

Plate 1.5. *Continued*

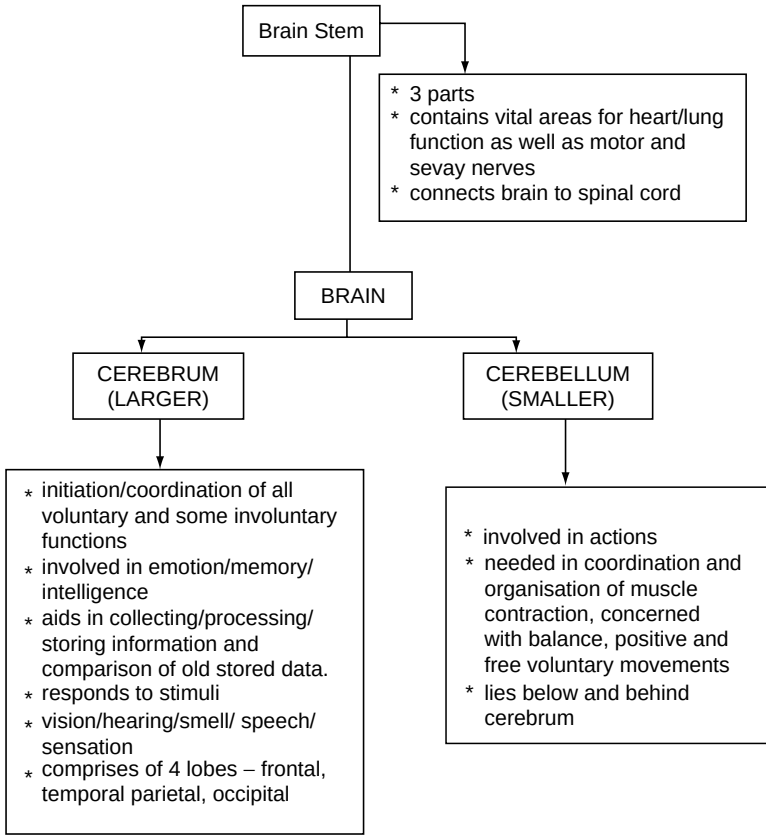

Plate 1.6. Composition of the brain

kind or the other, cerebellum shows clumsiness and can be tempered with it. The occipital lobes at the back of the brain are entirely devoted to the information process from the eyes. Color, light and movement can consume large resources of the brain. Due to impact, the damage to the vision centers of the brain causes a variety of disorders, from color blindness to the inability to recognise close relatives. The trauma would then seriously affect vision, memory and consciousness.

It is interesting to note from the case studies examined that anger, sadness, fear, disgust and other unhappy feelings can largely be out of control during or after specified period of trauma.

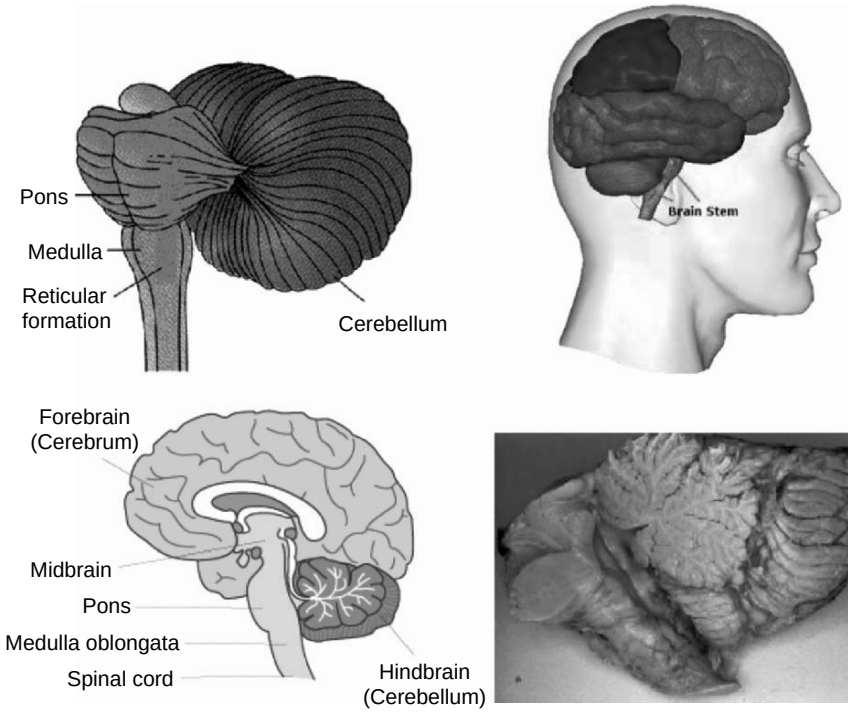

Plate 1.6. *Continued*

1.4.1 Head/Neck

(a) Head injury sustained in car accidents continues to be a leading cause of death and disability. Around 30% of all vehicular injuries, according to Kramer (1998) and Allsop and Kennett (2002), are head and face injuries. The human head (cranium) meaning skull is regarded as a multilayered structure with the scalp being (5 mm–7 m) the outer most layer followed by the skull, the meninges and eventually the central nervous system that represents the innermost tissue. The skull is a complex structure consisting of several bones fused together with associated suture lines as indicated in Plate 1.7. The only facial bone connected to the skull by free movable joints is the mandible. The thickness and the curvature of such bones may vary substantially. The inner surface of the cranial vault is concave with irregular plate type bone forming the base which contains several holes for arteries, veins and nerves. It has also a large hole which is known as "foramen magnum" through which the brain stem passes through the spinal cord. This spinal cord is supported by three membranes, known as "meninges" which protect this and the brain and separate them from the surrounding bones from outside to inside there is an

"arachnoid" mater and the "dura mater" and the "pia mater." Out of these two the dura mater is a tough fibrous membrane while the arachnoid mater resembles a spider web.

Both membranes are separated by a narrow space – the "subdural space." The arachnoid mater is separated from the pia mater by this subarachnoid space. The surface of the brain, in turn, is covered by pia mater. Cerebrospinal fluid (CSF) between subarachnoid space and the ventricles of the brain act as a lubricant also for the spinal cord as and when shock and impact exist and they are subjected to them. The fluid now known as CSF constantly circulates and surrounds the brain as a buffer. It helps to support the brain. The meninges have several blood vessels which supply blood to the brain and the scalp. When trauma due to impact occurs, the subdural space can

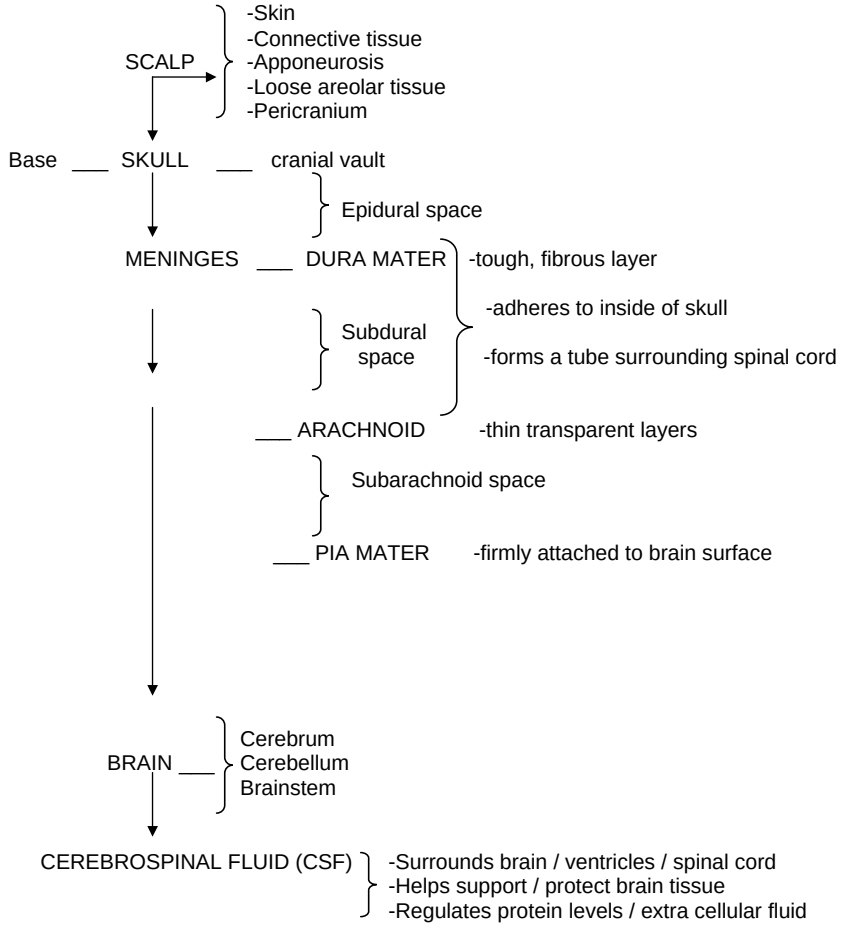

Flowchart 1.3. Anatomy Of The cranium (head)

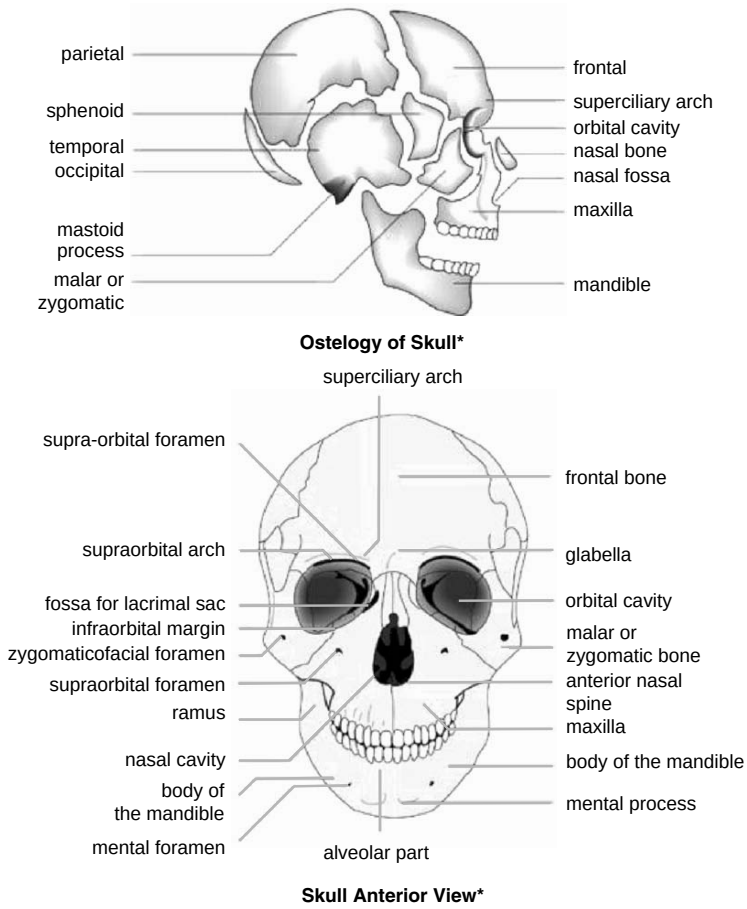

Plate 1.7. Skull structure

be subjected to injury through tearing. Due to severe head injury, brain which having five parts, namely cerebrum, cerebellum, mid brain, pons and medulla oblongata could easily be affected which in turns, include contusion (bruises) and laceration (cut) likewise facial injuries to the eyes and ears and fracture of nasal bone may cause a severe trauma to central nervous system. Such injuries are given AIS codes which are given in Table 1.2 Le Fort classification (adapted from Vetter (2000)) with facial fractures and head injuries is shown in Plate 1.8 More severe head injuries where fracture occurs, resulting "hematoma," can cause unending trauma. Three sources are identified for subdural hematoma which are:

(a) Laceration of cortical veins and arteries by penetrating wounds
(b) Confusion bleeding into subdural space
(c) Tearing of veins between the brain's surface and dural sinuses

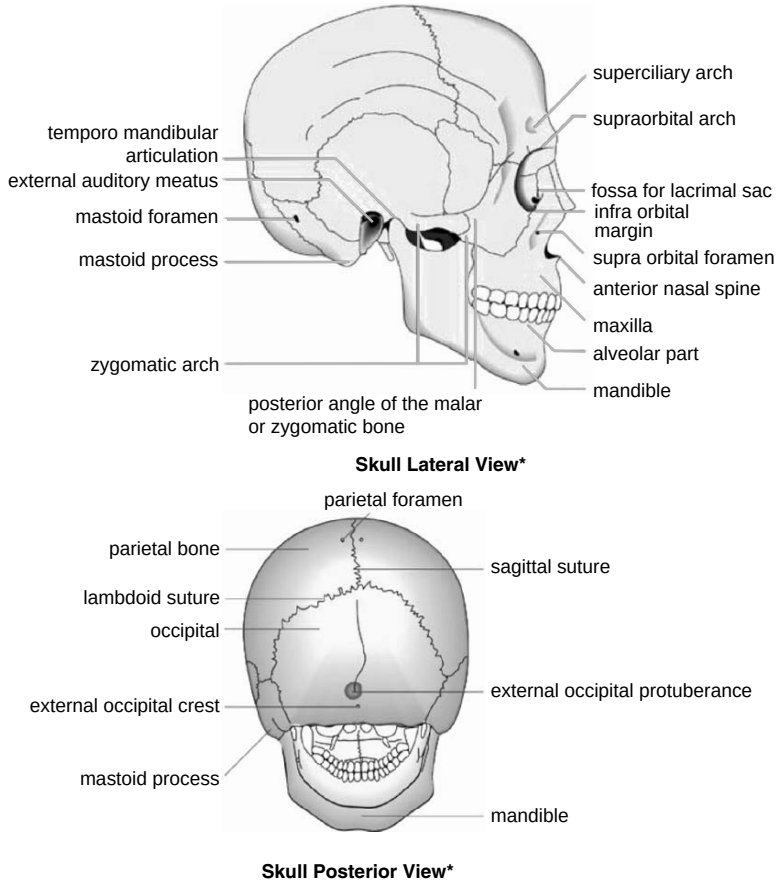

Plate 1.7. *Continued*

During impact and under impulsive loading, Melvin and Lighthall (2002) investigated the mortality rate of 30%. In such a trauma situation, when the brain accumulates blood, in contrast to contusion intracerebral haematoma occurs and a standard computer tomography can distinguish this type of hematoma. The injury mechanism will be dealt with in detail in a separate chapter.

(b) Neck Injury Criterion (NIC): In addition to the tolerance values for neck loading, a number of neck injury criteria are established. Simple load limits to more complex criteria are proposed, particularly the pseudo name such as whiplash or neck sprain injury. The type of impact can easily lead to type of injuries sustained. Different criteria have also been established which relate to different phases of crash and related occupant kinematics. The neck injury has to be assessed on the basis of impact direction. Researchers Bostrom et al.

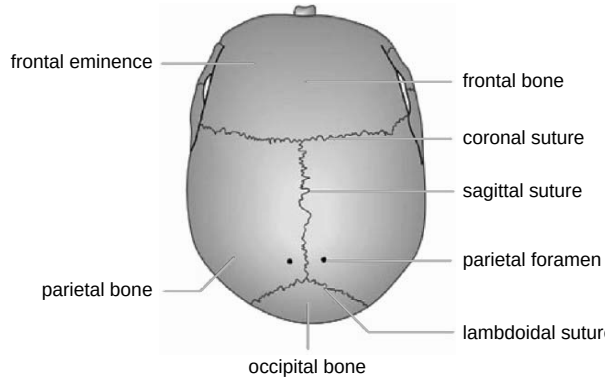

Plate 1.7. *Continued*

(1996), Klinch et al. (1996), Schmitt (2001), Schmitt et al. (2002a), Kullgren et al. (2003) and Muser et al. (2003) have put forward their assessments on neck injuries based on rear end injuries of the neck with and without soft tissues. The AIS code for neck injuries are sustained in rear end collisions Table 1.3. Sometimes it is difficult to take neck trauma in isolation from cervical spine. It has been well-established that a sudden change of flow inside the fluid compartments of the cervical spine are related to neck injury. The neck injury criterion by US Natural Highway Traffic Society Administration (NHTSA) (Klinch et al. 1996 and Kleinberger et al. 1998) has been well-established including the neck protection criterion. Panjabi et al. (1999) proposed intervertebral neck injury criterion. The neck displacement criterion proposed (Viano and Davidsson 2001b) to assess the risk of soft tissue neck injury. Recently Heitplatz et al. (2003) neck injury criterion to assess the risk of soft tissue neck injury Table 1.4. Threshold values for neck load included in (FMVSS 208) will be discussed in the text under a separate section. However, one cannot ignore the data based on GDV Institute of Vehicle Safety, Munich which serves as a basis to determine the neck injury in real world accidents.

Spinal Anatomy

The vertebral or spinal column, known to most as the spine, is the principal load bearing structure of the head and torso. It is divided as follows:

A/7 cervical (C1–C7)	natural lordosis on lateral view flexible movement C1 (atlas) is a large bony ring with large articulated surfaces that forms the atlanto-occiptal joint with the skull (to allow nodding movements) and the atlanto-axial joint with C2 (axis) via its adontoid peg (allowing rotational head movement)
B/12 Thoracic (T1–T12)	natural kyphosis on lateral view restricted movement provides extra support to ribcage
C/5 Lumbar (L1–L5)	kyphosis on lateral view
D/ Sacrum	5 fused vertebrae
Coccyx	lower tip of sacrum

Table 1.2. AID classified head injury (AAAM 2004)

AIS	code description
AIS 1	skin/scalp – abrasion – super facial laceration face – nose fracture
AIS 2	skin – major avulsion – vault fracture (simple, undisplated) – mandible fracture (open and displaced) – maxilla fracture (LEFORT I and II)
AIS 3	basilar fracture – maxilla fracture LEFORT III – total scalp loss – single contrusion cerebellum
AIS 4	vault fracture – complex, open and torn – exposed and loss of tissues – small epidural or subdural hematoma
AIS 5	major penetrating injury – brain step compression – large subdural or epidural hematoma – diffuse axonal injury (DAI)
AIS 6	massive destruction – cranium – brain

Note: DAI describes the disruption to axons in the cerebral hemisphere and subcortical white matter

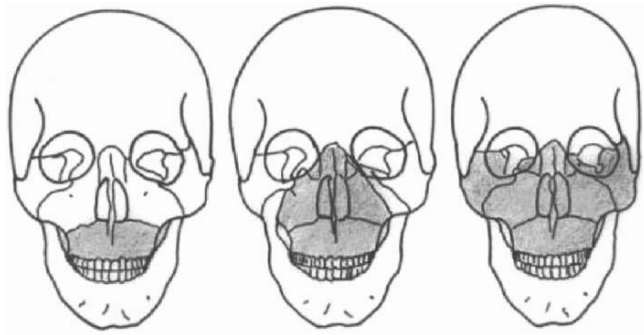

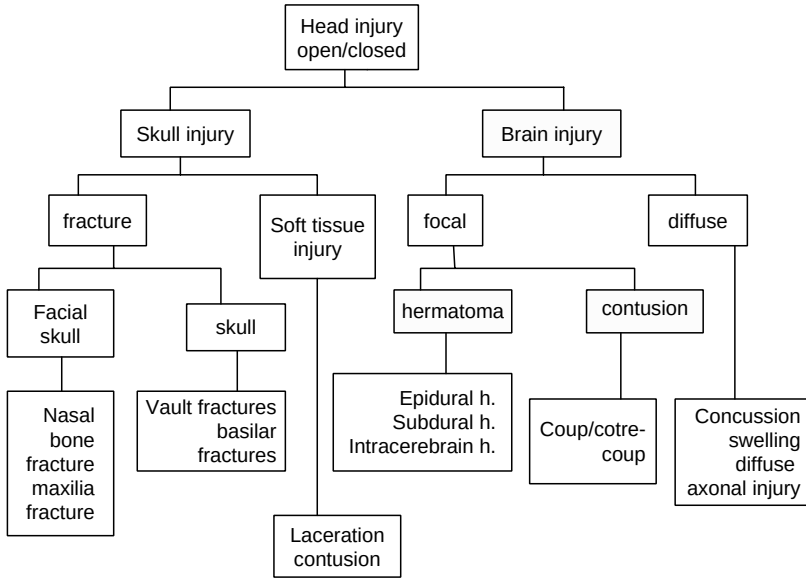

Plate 1.8. Head injuries

(c) Spinal Anatomy and Trauma

They consist of roughly the same shape but vertebral size appears to increase caudally. The vertebrae mainly have a vertebral body (anterior) which are separated from each other by intervertebral discs and are further stabilized by anterior and posterior longitudinal ligaments.

Behind the body lies an arch which encloses a space that carries the spinal cord. The arch also bears bony projections that aid in the further stabilization of column and ligament/muscle attachments, e.g., transverse or dorsal spines processes or facet joints. Note that in the cervical spine C1 (atlas) and C2 (axis) are designed differently from other vertebrae and also there is no intervertebral discs between C1 and C2.

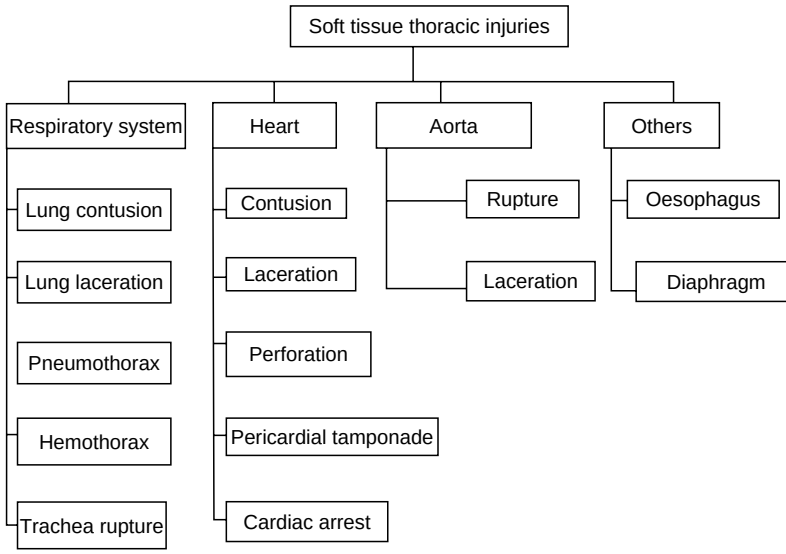

Plate 1.8. *Continued*

Table 1.3. Examples of spinal injuries according to AIS scale (AAAM 2004)

AIS code	description
1	skin, muscle: abrasion, contusion (hematoma), minor laceration
2	vertebral artery: minor laceration cervical/thoracic spine: dislocation without fracture thoracic/lumbar spine: disc herniation
3	vertebral artery: major laceration cervical/thoracic spine: multiple nerve root laceration
4	cervical/thoracic spine: spinal cord contusion incomplete
5	cervical/thoracic spine: spinal cord laceration without fracture
6	decapitation cervical spine: spinal cord laceration at C3 or higher with fracture

Reproduced from AAAM (2004) with compliments

The spinal cord begins at the medulla oblongata of the brainstem and exits the skull via the opening called the foramen magnum. It terminates around the L1 bony level where it becomes known as the conus medullaris and beneath this level as cauda equina.

As mentioned before the spinal cord lies within the spinal canal surrounded by cerebrospinal fluid. The cervical part of the canal is widest between the foramen magnum and C2. Injuries below level of C3 are associated with higher rate of neurological deficits. The dimensions of thoracic canal are narrow and hence any fracture dislocation will almost always lead to complete neurological deficit. A significant proportion of all spinal injuries occurs at the level of

Table 1.4. Neck injury criterion

AIS skeletal injury	AIS soft tissue injury
1. one rib fracture	1. contusion of bronchus
2. 2–3 rib fractures, sternum fracture	2. partial thickness bronchus tear
3. 4 or more rib fractures on one side, 2–3 rib fractures with hemothorax or pneumothorax	3. lung contusion, minor heart contusion
4. flail chest, four or more rib fractures on each of two sides, four or more rib fractures with hemo- or pneumothorax	4. bilateral lung laceration, minor aortic laceration, major heart contusion
5. bilateral flail chest	5. major aortic laceration, lung laceration with tension pneumothorax
	6. aortic laceration with hemorrhage not confined to mediastinum

thoracolumbar junction. The latter acts as a pivot between the rigid thoracic spine and strong lumbar area.

The spinal cord carries many nerve tracts in pairs as follows:

(1) Corticospinal tract	lies in posterolateral segment of cord responsible for ipsilateral motor power
(2) Spinothalamic tract	lies in anterolateral segment of cord conveys contralateral pain and temperature sensation
(3) Posterior columns	transmits ipsilateral position sense (proprioception) vibration sense and some light touch sensation

It is possible to test these nerve tracts clinically to assess any damage post injury.

Trauma Mechanism

Most spinal injuries can be classified into four main types:

– Burst Fractures	axial loading to the spine. Bone fragment may protrude into the spinal canal causing neurological deficit.
– Compression Fractures	hyperflexion of spine around a mid-disc space axis compromising bone integrity. This usually affects the anterior part of the vertebral body.
– Seat belt-related injuries	sudden deceleration injuries usually associated with lap-type seat belts, produces tensile forces on a flexed spine.

– Fracture Dislocations associated with different tensile forces that lead to loss of spinal stability via dislocation and subluxation of bone and joints.

This gives us a good idea as to the mechanism of injury.

Of all spinal segments, the cervical spine is most frequently injured. In the trauma analysis, the vast majority of cervical spine injuries are minor tissue, neck injuries usually graded as AISI, generally not exhibiting a morphological manifestation. These injuries are not associated with over structural types not causing damage to cervical spine or the central nervous system, are potentially treated as debilitating injury since they frequently occur in road accidents. Head, neck and spine injuries according to Morris and Thomas (1996). In a car accident as pointed by Byland and Bjornstig (1998), soft tissue injuries developed prolonged medical disability, resulting in long sick leave leading to granting disability pension. Hence for the accurate analysis, using finite element or other methods a greater understanding of the vehicle, occupants, and collision parameters are needed to assess soft tissue injuries. Murer et al. (2002) cannot regard the soft tissue injury mechanism whether in the head, neck or spine as conclusive. A greater data can be obtained from various sources. Soft tissue injuries require data base on epidemiology, injury assessments, medical diagnosis/treatment, and development of "whiplash" counter measures have been dealt with extensively by Ferrari (1999), Yoganandan and Pintar (2000), and McElhaney et al. (2002). Although in the last century "whiplash" was introduced (whiplash associated disorder – WAD) as a type of injury, the term "whiplash" is misleading and incorrect since it invokes a forward backward movement of the injury mechanism during the development of the "crack of the whip." The clinical presentation of the WAD is classified by the Quebec Task Force which is adapted from Spitzer et al. (1995) is given in Table 1.5. Regarding the injury mechanism whatever hypotheses do exist.

They have to rely on experimental, symptomatic clinical observations, and numerical-cum-computer aided analysis. This is due to the fact that the anatomy of the cervical variable structures are assembled in quite a small area

Table 1.5. Classification of WAD as proposed by the Quebec Task Force

grade	clinical presentation
0	no complaint about the neck no physical sign(s)
1	neck complaint of pain, stiffness or tenderness only no physical sign(s)
2	neck complaint and musculoskeletal sign(s)
3	neck complaint and neurologic sign(s)
4	neck complaint and fracture or dislocation

Courtesy Spitzer et al. (1995)

with complex anatomy. The neck injury is highly dependent on the injured tissues.

(d) Tissues and Trauma

Different tissues are proposed to the cause for neck injuries. Current studies suggest that ligaments and muscles are injured. The zygapophysial joint can also be injured or for that matter nerve tissues in the vicinity of "spinal ganglia" can be abnormally injured. Other hypothetical consideration presented by Ferrari (1999) identifying other tissues such as vertebral arteries and inter vertebral discs cannot be discounted by offering tissue injuries. The statistics shows that the movement of the neck (rear end and frontal collision) can result soft tissue neck injuries since kinematic sequences inclusive of mechanical loading conditions. During accident the contact and force transmission occurs in the "shoulder area." Since inertia force is developed, the head is not in contact with any part of the occupants car, the head will be accelerated forward and the head behind lags behind the torso. It moves back without rotation about the internal axis. The upper cervical spine is forced into flexion (bending) mode and as a result the lower cervical spine goes into extension. The deformation of the neck can also be in "S" shaped formation which is crucial for injury mechanism. This "S" shaped mechanism is fully supported by the research work carried out by Ono and Kaneoka (1997), Ono et al. (1998), Eichberger et al. (1998), Grauer et al. (1997), Svensson et al. (1993), Wheeler et al. (1998), and Yoganandan and Pintar (2000).

The entire cervical spine is extended maximum as soon as the head starts rotating backward. This phenomenon causes severe tissue injuries, however depending upon impact severity. During the forward movement the head, neck and torso causes tissue injuries depending upon how this phase strongly influenced by the elasticity of the seat and corresponding rebound effect. This phenomenon is fully examined by Muser et al. (2000). The occupants dynamics is further discussed in detail by Walz and Muser (1995). More innovative work is done for shear movement of vertebrae related to lesions of the facets of the intervertebral joints (Yang et al. 1997), the hyper extension of the neck and head movement and excursion angles (Mertz and Patrick 1971) and pressure gradient developing various and cerebrospinal fluid of the spinal and canal causing cellular injuries (Aldman 1986, Svensson et al. 1993, Schmitt 2001) and tissue neck injuries. However the literature indicates that tissue injuries have never been biomechanically understood. Since the S-shape deformation plays a crucial role when elucidating and explaining injury mechanism, especially relative motion between the head and torso, the finite element analysis and solution procedures can be the only answer to the problem. Here the engineering analysis can offer a greater assistance to the medical profession (Plate 1.9).

Injuries to the thoracolumbar spine injuries sustained are negligible to cervical spine injuries, back pain, and severe injuries to the spinal cord have been identified during and after vehicle crashes (King 2002) by anterior wedge fractures of the vertebral bodies burst fracture of vertebral bodies,

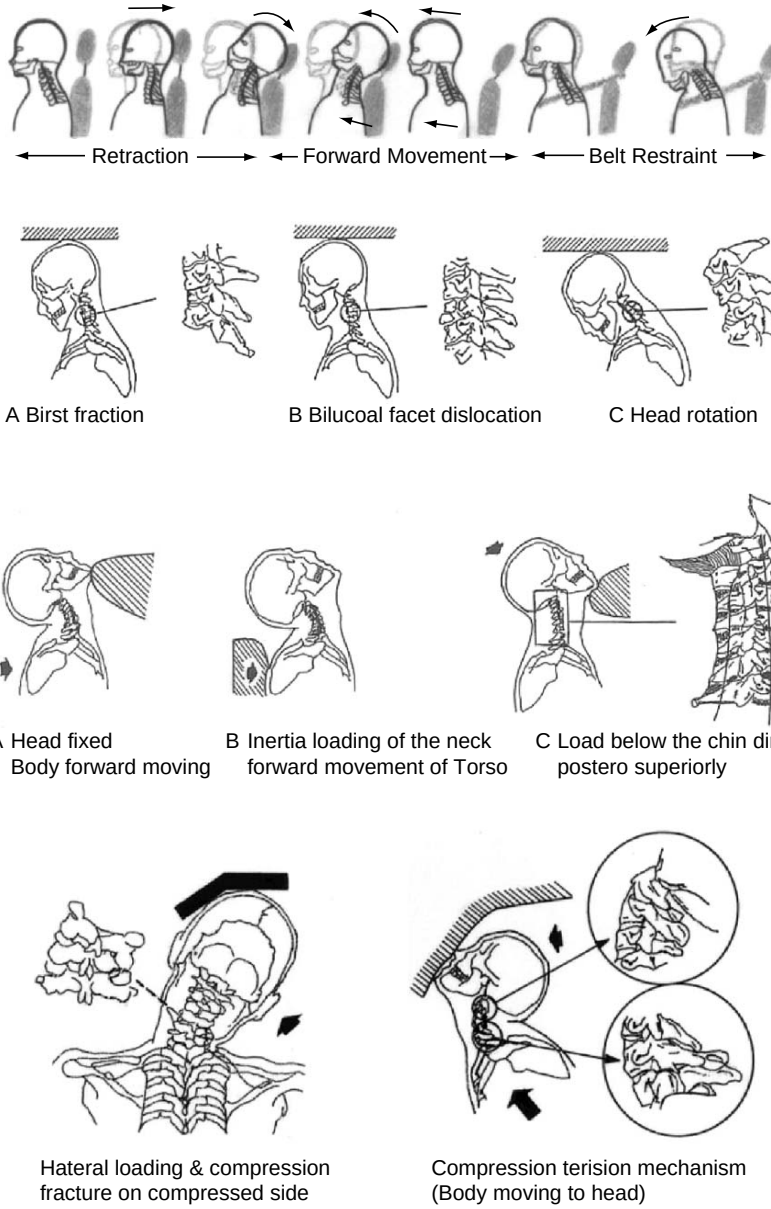

Plate 1.9. Neck and head movement mechanism. Reference: Library St. George Hospital and Medical School, London, UK (2004)

fracture/dislocation, rotational injuries, chance fracture, hyperextension injuries, and soft tissue injuries. Wedge fractures have been further examined by Begeman et al. (1973). Chance fractures are due to improper wearing of the lap belt in case of frontal collision. If the lap belt angle is too flat to the horizontal plane, the belt can ride over the iliac crest leading to compression produced in the abdominal organs. The lumbar spine flexion occurs which can separate posterior elements of spine stretch. The spine cord leading to subsequent injury. The soft tissue, as a result of the thoracolumbar spine, can certainly be injured. The rupture of the supra and interspinous ligaments can also occur. If suitable tools are devised, the engineering analysis can provide a comparative study with known experimental results.

1.5 Thorax, Chest, and Shoulder

1.5.1 Thorax and Chest

The thorax consists of the rib cage and the underlying soft tissue organs. It extends from the base of the neck to the diaphragm which inferiorly bounds the thorax and separates the thoracic cavity from the abdominal cavity. Twelve pairs of ribs from the rib cage: They are posterior connected to the thoracic vertebrae of the vertebral column. At the anterior side of the thorax the sternum fixes the upper seven ribs. However, the lower ribs are either connected indirectly to the sternum or attached to the muscles and the abdominal wall. They are called *floating ribs*. The ribs are inter-connected by means of intercostal muscles. These connections between ribs, vertebrae, and sternum are flexible as are intercostal muscles, however, the rib cage is quite rigid with movable cover of internal organs. This cover facilitates respiration. The trauma of the thorax is the direct result of injuries commonly occurring due to frontal and side impact and, in some cases, occur in between. Normally, the impact to the thorax occurs at the contact between the occupant and the vehicle interior such as the steering assembly, the door, the dash board and other restraint systems. In the engineering analysis, it becomes essential to represent restraints as contact or the gap elements in the global analysis using finite element or any other numerical techniques. The procedure is explained in the separate chapter. Based on AAAM (2004), the AIS codes for skeletal and soft tissue thoracic injuries are given in Table 1.4. According to the AIS code, a single rib fracture can be graded as AISI. If fractures occur in 2–3 ribs or multiple, life threatening complications may arise. When the skin and the soft tissue overlying in the fracture are intact, the fracture is known as *closed fracture*. The skin and soft tissue can be treated in the analysis as membrane spanning over a rib crack. This analysis is essential for the assessment of fracture by the medical professionals. If on the other hand, ribs perforate the chest wall, the impact analysis must take into consideration sharp edges of the broken ribs. These open fractures are of great concern they can eventually lead

to pneumothorax, lung collapse and infections. The correct size of a fracture to evaluate is the main responsibility of the engineer, since the size factor can generate time-dependent spread of the above-mentioned scenario and that of visceral or parietal pleura causing especially respiratory problems.

The question arises what triggers a single rib collapse and for that matter the creation of multirib fracture. The answer is that sagittal loading of the thorax may cause single rib fracture and lateral impact or impulsive force is generally responsible for multiple fracture. In both cases maximum curvature at the level of the impactive force will occur prior to the rib cracking or fracturing. In order to assess all those cases the medical profession relies on the engineering analysis of developing or checking the requisite fractures in three dimensions. The description of the thoracic injuries then focuses on the impact in accidents where objects strike the chest with and without penetration. If the thorax is suddenly decelerated due to impact from blunt objects, three different injury mechanisms can be identified, namely, compression, viscous loading, and inertia loading of the internal organs.

In case of multirib fracture, the thorax wall may lose its overall stability or the disrupted thorax wall is sucked in, thus reduces the volume of the lung. On expiration the thorax wall moves outwards making it difficult to expel the air out of the lungs. The research of Stalnaker and Mohan (1974) and Melvin et al. (1975) shows that the greater the area of thorax wall damaged, the lesser the amount of air which can be exchanged. In some cases thorax wall moves outwards, making it difficult to expel air. The area of this condition is known as a *flail chest* which eventually results in *hypoxaemia*. The research concludes that the time-dependent force is directly related to the number of rib fractures which in turn depends on the magnitude rather than the rate of rib deflection. It is also noted that a lung contusion can occur due to thorax compression. The lung contusion is, unlike rib fractures, very much rate dependent as concluded by Fung and Yen (1984). At high velocity of impactive object, a pressure wave is transmitted through thorax wall to the lung tissue which can damage the capillary bed of the *alveoli*. In case of a serious complication, lung contusion may increase thus risking an inflammation of the lung tissue. Due to impactive force, laceration, and perforation of the lung tissue can occur. Various numerical methods and high level computer programs exist for the lung perforation, especially in areas where rib fracture exists. In such circumstances, laceration-cum-perforation may cause *pneumothorax* (Pleural cavity filled with air) and *hemothorax* (filled with blood). Where a combined situation exists, i.e., pleural cavity filled with air and blood, the case is termed as *hemo-pneumothorax*. When the impactive force is applied, a perforation of the pleura, i.e., a hole is created in the pleural sac between lung and the rib cage in case of broken rib, pneumothorax is resulted. When the lung leaks, the inter pleural pressure is reduced. However during expiration, the laceration in the lung tissue is compressed and the air in the pleural cavity is not able to be expelled. The more air comes from breathing, the size of the pleural cavity increases leading eventually to *a compressed lung*.

A time dependent finite element analysis under successfully reducing inter pleural pressure could be a great eye opener to the medical professionals, especially where a case study is examined. The same engineering analysis can be applied in case of a hemothorax which reduces the lung volume with the blood in pleural cavity. The laceration of the blood vessels can cause blood to accumulate in the pleural cavity.

Under large impactive or other impulsive forces, the *heart* can be subjected to several traumatic injuries including contusion and laceration. At a high rate of loading the heart may undergo *arrhythmias*, (e.g., Fibrillation) or arrest. High speed blunt impact such as occurring in the car accident, may interrupt electromechanical transduction of the heart wall. In such circumstances, there is a possibility thoracic blood vessels like the aorta, may be injured (Cavanaugh 2002; Smith and Chang 1986; Oschsner et al. 1989). Aortic rupture may occur from traction and shear forces as a result of loading rates (Viano 1983). The most vulnerable case is the thoracic aortic structures. These areas are dealt with later on in the modes and responses in the text under specific chapters.

1.5.2 Shoulder

The views are given in Plates 1.10 and 1.11 which vividly describe various areas of the shoulder.

Some important elements are:

– Bones – humerus, scapular, clavicle		
– Shoulder joint (glenohumeral)	ball and socket type	
	wide range of movement	
	involves head and humerus articulating with smaller glenoid fossa of the scapula	
– Articular capsule	fibrous	
	forms loose sleeve around joint	
– Muscles	subscapularis	tendonsfusewith
	infraspinatus	capsuletoformthe
	supraspinatus	rotatoroff
	teres minor	
– Ligaments	glenohumeral	
	coraco clavicular acromioclavicular	
– Blood vessels/nerves/lymphatic vessels		

They are reproduced in Plate 1.11 as areas related to shoulders when judging impact involving skeletal, muscular and nervous systems leading to severe trauma. It is important to note that head and neck trauma can lead to possible shoulder trauma. For example, if subjected to tension–extension loading, tension–tension and tension–compression loading conditions. Shoulder injury can also result from impacts in vehicles. When a person is restrained by seat belts. Subsequent stresses and strains may lead to torsional effects. Direct

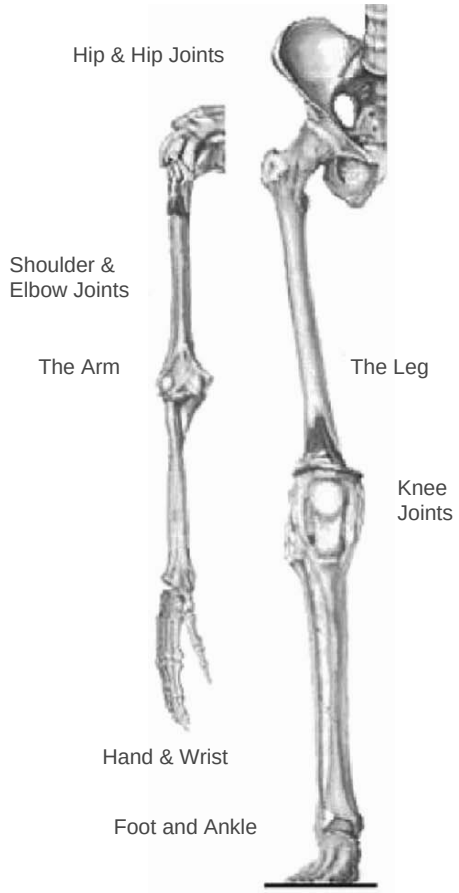

Plate 1.10. Bones and joints – skeletal

injury, e.g., falling into shoulder can lead to a damaged shoulder. Trauma to arms can have an effect on shoulders. A shoulder or shoulder girdle is also treated as part of four different areas of the upper limbs. They can be dealt with in a separate section.

1.6 Traumatic Injuries of the Upper Extremities

The upper extremities can be divided into four different parts and they are:

- shoulder or shoulder girdle
- the arm — humerus bone
- the fore arm — ulnar and radius bones
- the hand — phalanges metacarpal and carpal bones

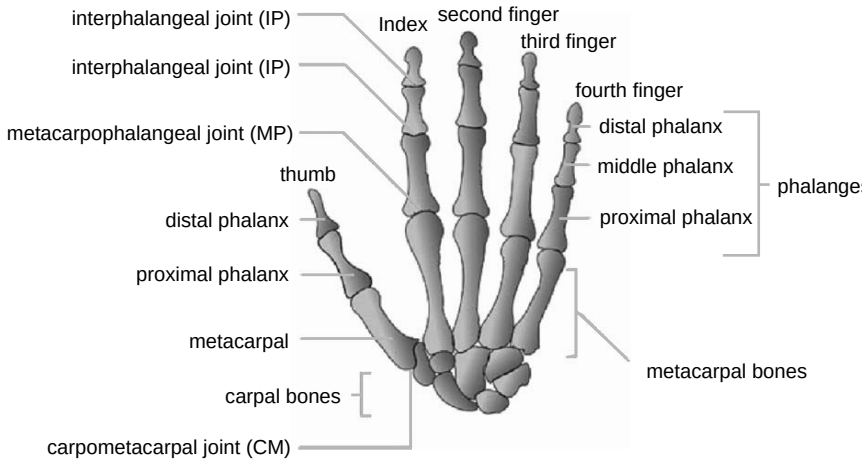

Bones of the Hand-Dorsal View*

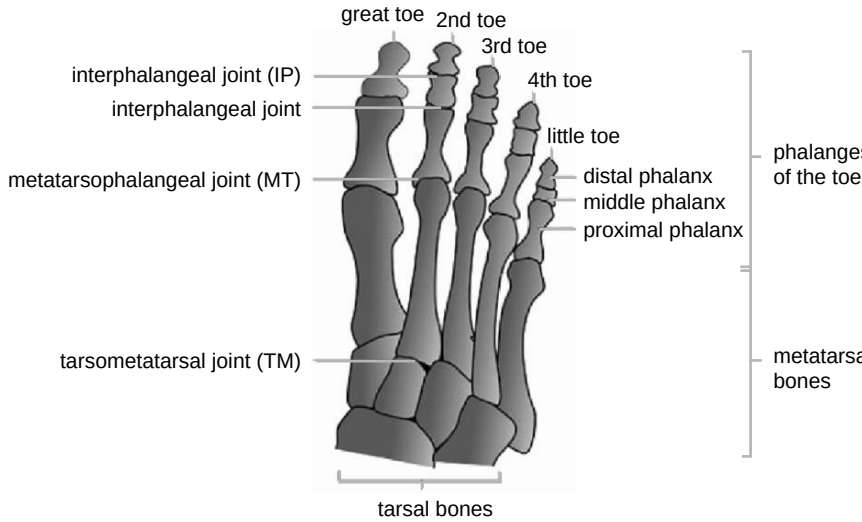

Bones of the Foot-Dorsal View*

(Courtesy of info.Visual.org)*

Plate 1.10. *Continued*

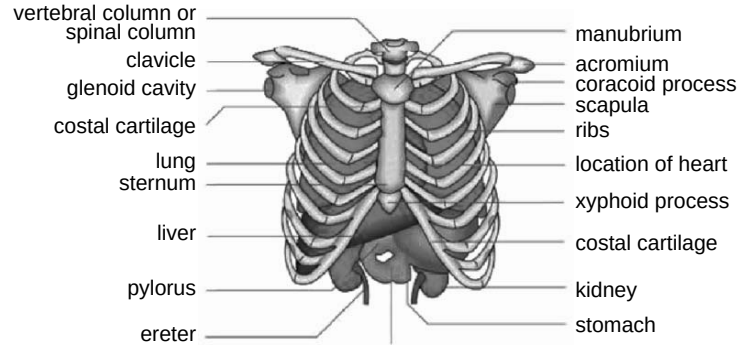

Ribcage-Anterior View*

Ribcage–cross section*

Muscles-Anterior View*

Muscles-cross section*

Plate 1.11. Skeletal, muscular- and nervous-cross section

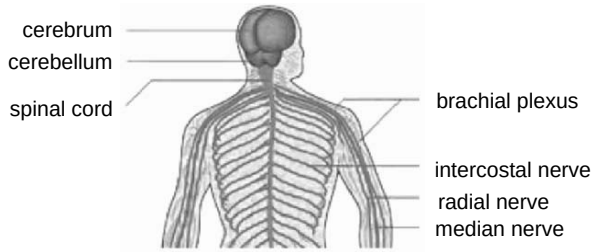

Nervous System*

Nervous System-cross section*

(Courtery of info.Visual.org)

Plate 1.11. *Continued*

Plate 1.10 shows bones and joints of the upper extremities and the skeleton of the hand. Hand injuries are recorded during boxing and in some frontal collisions. In general, the following are some of the major upper extremity injuries investigated by Huelke et al. (1997), Segui-Gomez and Baker (2002), Atkinson et al. (2002), and Schneider et al. (1998):

(a) Direct contact to air bag.
(b) Contact of the arm with the interior part of the vehicle when arms are being flange by the airbag.
(c) Contact to the interior involving intrusions and side impacts.
(d) Inboard limb injuries owing mutual contacts among the occupants.
(e) clavicular fractures caused by seat belt diagonal section lying across the out board shoulder thereby transmitting the belt loads transversely across clavicula.

The early work by Weber (1859) and Messerer (1880) which determined load and moment to produces failure or fracture. The bones of the human upper extremities have to form the basis for the engineering analysis of Trauma. Since the advent of the computers and advanced numerical analyses and techniques, forearm fractures in which ulna night stick fractures and multiple fractures can be assessed. The engineering results will suggest that the humerus position, the forearm pronation angle and air bag module affecting the risk injuries.

Table 1.6. Failure tolerances for the humerus

humerus bending moment male (N m)	female (N m)	shear force male (k N)	female (k N)	reference
115	73			Weber (1859)
151	85			Messerer (1880)
157	84	1.96 (overall)		Kirkish et al. (1996)
230	130	2.5	1.7	Kirkish et al. (1996), scaled to 50% male and 5% female
138				Kallieris et al. (1997)
	154			Duma et al. (1998a)
217	128			Duma et al. (1998b), scaled to 50% male and 5% female

Like Pintar et al. (1998), these analyses can predict the dynamic bending mode. As a reference the failure tolerances given in Table 1.6 can be highly correlated to bone mineral density.

1.7 Trauma and Abdominal Injuries

1.7.1 General Introduction

The abdominal cavity is a sensitive and vulnerable region of the human body. Owing to any kind of impact, whether sharp or blunt, trauma to the abdomen is caused. It becomes worsened if any penetration occurs. Blunt impact in car accidents is frequently observed although not visible initially. Where penetration due to impact occurs, the injury can be life threatening. If it happens to be a side impact, according to Rouhana and Foster (1985), more than one-fifth of severe injuries (AIS ≥ 4) is abdominal. It is the one area where experimental studies are difficult to be performed and the results obtained are not quite meaningful. There is a lack of sufficient knowledge of injury mechanisms and injury predictors.

1.7.2 Anatomy of the Abdomen

The abdominal cavity is bounded by the diaphragm and caudally by the pelvic bones with attached muscles. The posterior boundary of the abdomen, in fact is formed by the lumbar vertebral column, sacrum and pelvis. Anteriorly and laterally the upper abdomen is defined as the lower rib cage. Sometimes the upper abdominal region is known as *hard thorax*.

The lower abdomen is surrounded anteriorly and laterally by musculature (Eppinger et al. 1982) gives an exhaustive analysis of Impactive load on

the behavior of upper abdomen and found its impact response and tolerance are different from the lower abdomen. According to them the side impact is critical to lower ribs and organs directly in front of the vertebral column are at great risk of, when subject to frontal impact, receiving heavy compression.

The abdominal cavity hosts several organs that are generally divided into "solid" and "hollow" organs. The main characteristic to divide the organs into these two groups is the gross density of an organ (not the tissue density). Solid organs like the liver, spleen, pancreas, kidneys, ovaries, and adrenal glands have a higher density than hollow organs such as the stomach, large and small intestines, bladder, and uterus. The lesser density of the hollow organs is due to the presence of a relatively large cavity within the organ itself. Those cavities are, for example, filled with "air" or digestive matter. The solid organs, in contrast, contain fluid-filled vessels and therefore exhibit a higher density.

Major blood vessels are the abdominal, aorta, the inferior vena cava the iliac chip artery and hip or iliac vein. The geometry indicates that abdominal aorta and vena cava enter the abdomen from cranial through separate openings in diaphragm. Plate 1.12 shows various element of abdomen. Since organs inside in abdomen cavity has a relatively high.

Degree of mobility, the biomechanical response of nonrigidly fixed organs to the abdominal wall on traumatic impact needs a careful analysis. Partly these organs embedded in fat, particularly kidney, and partly the complicated nature of the performance of these organs, inside abdomen. The abdominal injury is extremely important. Under impact load, particularly blunt to the abdomen, Rouhana et al. (1986) , Rouhana (1987), Rouhana (2002), Miller (1989), and Stalnaker and Ulman (1985) have carried out comprehensive studies. One must keep in mind that solid organs of the abdomen are "fluid filled," the engineering analysis must consider a rate dependent behavior.

In case of low loading (under seat belt loading) maximum compression is a better predictor of the abdominal injury for high loading, the maximum velocity is a better injury predictor. The abdominal compression can correlate well with the probability of AIS ≥ 4 injury.

As far as the injury criteria is considered (ECER 95) – The European regulations for side impact loading, the abdominal peak force (ADF) can easily be evaluated using Euro SID Dummy, properly collaborated with engineering analysis. It is important not to ignore in the analysis of the "seat belt syndrome" owing to submarining as well as belt misplacement. In any case force displacement relationship of lower abdomen due to frontal impact (Nusholtz et al. 1988) must always be analyzed. The laceration hemorrhage to liver, laceration disrupture to spleen and contusion laceration to kidney must also be clinically assessed.

It is worth mentioning that correct placement of the belt is crucial for pregnant women to ensure that the fetus is not exposed to high loading. If the belt is placed above pelvis, it loads the abdomen instead of more stable pelvis. The structure of the seat also influences the probability of submarining.

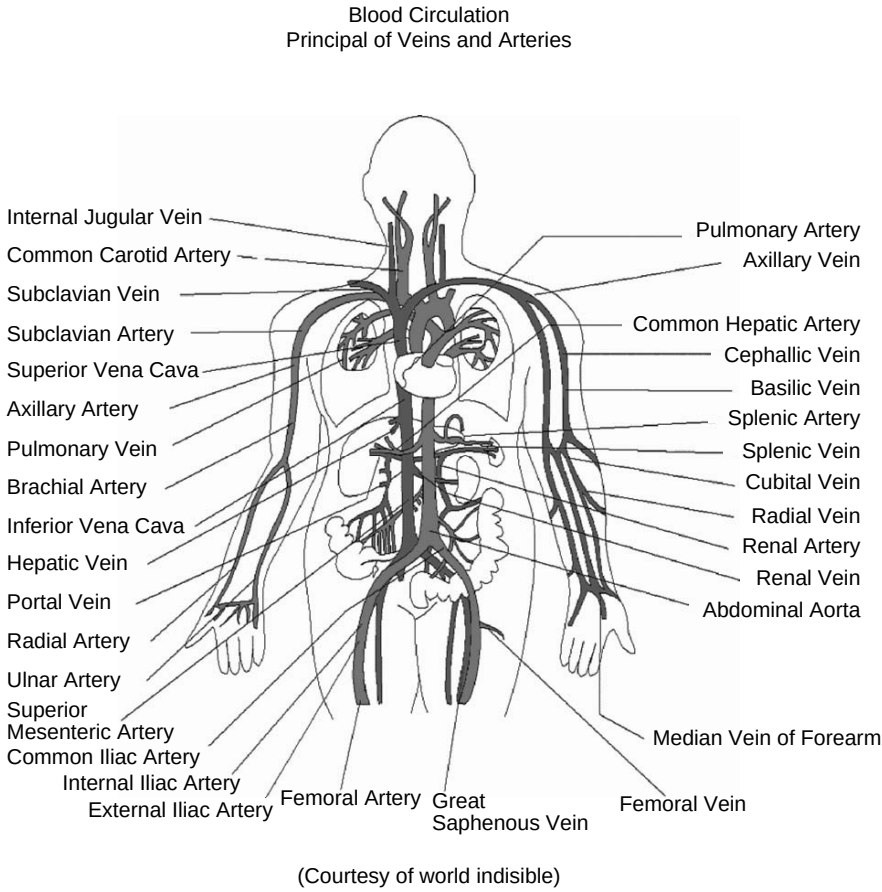

Plate 1.12. Blood circulation: Principle of veins and arteries

Lane (1994), and Rouhana (2002) carried out research and many studies indicate that unbetted occupants are twice as likely to sustain fatal injuries than betted occupants. At the same time, it must be clearly established that belt effectively reduces head, neck, and thorax injury.

1.8 Trauma, Lower Limb, and Pelvis

Crandall et al. (1996), Haland et al. (1998), and Parenteau et al. (1998) reported that air bag restraint system have reduced incidents of fatalities, thoracic and head trauma in automotive frontal collisions. Injuries to pelvis and lower extremities have emerged as the most frequent injuries resulting frontal crashes. In this section a short review of the anatomy is given which is

followed by a brief description of failure mechanisms and resulting in injuries. The trauma response shall be analyzed on the basis of the criteria developed in this section to predict injuries of the lower limbs.

1.8.1 Anatomy of the Lower Limb

The lower limbs are divided into pelvis, thigh, knee, lower leg ankle, and foot. The pelvis which links the lower extremities to the spine is a ring of bones, four in number: two hip bones forming the side and front of the wall while the other two, namely sacrum and coccyx, form the rear wall. The pelvis mechanically identifying the only load path to transmit the torso weight to the ground. The hip bones consist of three fused bones (ilium, ischium, pubis) and host also a cup-shaped articular cavity forming one part of the hip joint, known as a cetabulum. The frontal part of the pelvis known as symphsis – a joint connecting the right and left pubic bone. The thinner parts of frame-like of pubic bones are called "superior" and "inferior" "pubic rami" which are vulnerable to traumic injury. The sacrum is a fusion of several vertebral sacral nerves called "siatic nerves" which arise from the spinal cord passing the sacrum. Both sacrum and coccyx are near to major blood vessels.

The femur is the long bone of the thigh and is proximally connected by the hip joint to the pelvis and also distally linked to the knee. Two bones, tibia and fibula, form the lower leg between the knee and the ankle. It is interesting to see the knee as a joint connecting the femur and the lower leg. Here the reader must know that it is anatomically dense area consisting of several muscles, tendons, and ligaments. The patella in the knee is often as a vulnerable structure is the recipient of the direct impact. A strong musculature which can create huge forces and hence may influence the injury mechanisms surrounding the legs. The foot is adjoined to the lower leg. As can be seen in Plate 1.10, the foot has a number of bones and they are:

- calcaneus
- talus

} proximal end

- metastarsal
- phalanx
- tarsal

} distal end

This engineering analysis of forearm for static and dynamic loads can easily be correlated, provided the right data are available with experimental tests carried out by Begeman et al. (1999) who had used a drop weight with a velocity of $3\,\mathrm{m\,s^{-1}}$ fracture of the ulna can be assessed. Despite the possibilities offered by the different arm test devices, the inconsistencies between test objects can be easily corrected by these advanced analyses such as a finite element technique or any other hybrid analyses. The differences in the results of interaction ofthe shoulder arm region recognized by Kallieris et al. (1997) can

certainly be solved using the hybrid analyses, thus solving the most intricate problem in the medical profession.

Fractures to these delicate zones of the hard skeleton have been fully dealt with by Sobotta (1997). There are differences between females and males are the mass and bone mineral density. Fingers and wrist, in general, are subject to unusual fractures under minimal loads. In order to assist the medical profession, a comprehensive analysis can be carried out in order to develop a relationship between static/dynamic loads developed from various sources and the wrist fractures inclusive of ligament fractures in fingers.

1.8.2 Traumatic Injury Mechanism

Fractures in pelvis and the lower extremities occur more from sports accidents or falls rather than from automotive accidents (around 1%). Hip fractures are common from falls as per data base from various researchers such as Hubacher and Wettstein (2000), Kannus et al. (1999), King (2002), Kramer (1998), and Nass data base. The leg and foot injury are very common. The analysis of the lower extremities showed that the feet and the ankles are at high risk for AIS ≥ 2. The researchers mentioned that the traumatic injuries as twice high of the lower limb than the head injuries, even when occupants are belted and the vehicle is equipped with air bags. The best assessment is always based on AIS – the abbreviated injury scale. It must be noted that the pelvis and the proximal femur are simultaneously injured and such injuries are commonly referred to as a hip injury. A hip is, if the reader is reminded, the bony structure (femur head, pelvis, acetabulum). Table 1.7 gives the AIS rated injuries for pelvis and lower extremities.

Table 1.7. AIS rated injuries AAAM (2004) for pelvis and lower extremities

AIS code	description
1.	ankle, hip: sprain, contusion
2.	patella, tibia, fibula, calcaneus, metatarsal: fracture pelvis: fracture (closed, undisplaced) toe: amputation, crush hip, knee dislocation muscles, tendons: laceration (rupture, tear, avulsion)
3.	femur: fracture pelvis: fracture (open, displaced) traumatic amputation below knee
4.	pelvis: “open book” fracture traumatic amputation above knee
5.	pelvis: substantial deformation with associated vascular disruption and blood loss $> 20\%$ by volume

Reproduced with courtesy of AAAM (2004)

Classification of Fractures

In medical and engineering professions, various methodologies can be invoked to classify fractures. In medical profession fractures are assessed and examined while in engineering profession. They are developed and produced using analytical and numerical logistic approaches.

In this section classification based on medical aspects can be listed as below based on Levine (2002):

(a) Fractures open and closed.
(b) Closed fractures when intact soft tissues and skin are overlying the fracture.
(c) The position of the fractured segments displaced or undisplaced.
(d) Fracture location along the bone (Intra articular, Metaphyseal, disphyseal).
(e) Long bones of legs with fracture based on loose conditions such as,
   - Fracture due to direct loading – common in motor accidents.
   - Fracture due to indirect loading – common in motor accidents.
   - Fracture due to repetitive loading.
   - Fracture due to penetration.

For Injuries of pelvis and lower extremities, the AIS tables are considered for classification and categorization.

Traumatic Injuries to Pelvis and the Proximat Femur

In case of pelvis injury, it is categorized as an isolated single fracture of the pelvioting. In case of multiple fractures, the pelvic ring becomes unstable causing large displacement of the fractured segments. They can be with urogenital injuries. Sacrum fracture occurs in extensive pelvic injuries fracturing usually across the foramina or in the vicinity of the holes through which sacral nerves pass which are in danger in case of such injuries, especially hemorrhage. Excessive bleeding occurs from large blood vessels in the pelvic wall as well as from the fractured surfaces themselves. The pelvic fracture has been dealt by Otte (2002) in much greater detail. Femoral fractures can cause excessive bleeding due to its rich blood supply as well as obvious deformity sometimes post injury fractures involves neck of femur (hip) are commonly seen in elderly as a result of direct impact.

Leg, Knee, and Foot

Crandall (2000) has carried out investigation on the injury mechanism for femur fracture and has given the following details:

- Axial compression 62%
- Bending 24%
- Torsion and shear 5% each

He stated that fracture pattern femur, being bowed anteriorly, with convex side forward, plays a role especially in indirect loading.

Levine (2002) discovers that impact on knee, can under direct loading, cause patella to fracture. Patella fracture can also occur from strong muscles contraction (quadriceps) on partially fixed knee. In reality the bone anatomy of the knee gives very little support to the joints stability which in turn, makes the knee ligaments prone to injury. Assuming on some occasion, the knee becomes bent and an object hits the tibia backwards the posterior cruciate ligament can tear and the injury is termed *dash board injury.* When the pedestrian impact (lateral impact) occurs, the lateral ligament then ruptures. The knee joint is completely dislocated when all four knee joint ligaments rupture.

Tibia fractures can be caused by direct and indirect loading and are common in the lowest limb. Crandall (2001) states that tibia lies subcutaneously and the bone is covered by the skin and if breached deeply it will result such fractures are called *open fractures.* Most fractures occur between the mid shaft region and the distal third of the tibia Crandall (2001) reports that for tibia as well as for fibula injuries, the fracture is dependent on numerous things. Both tibia and fibula fractures when occurred will depend on stability that is the fracture is more unstable if both bones are broken on the same shaft level. A severe fracture of tibia involves the tibia plateau. The injury mechanisms of ankle and foot injuries are according to Crandall (2001), closely related to the possible motion range of the ankle and the hind foot. From the axial load in frontal collisions, injuries are 58%, inversion with 15% and eversion with 11%. Metatarsal injuries are solely caused by direct impact and 100% of all calcaneus injuries are due to axial loading Crandall (2001) indicates that pure axial loading can result talus fracture known as Pylon fracture. Inversion and eversion account for the vast majority of malleolar injuries especially ankle fractures, making the ankle most frequently injured major joint of the human body.

A number of tests have been carried out to determine factual data and some of them are known for basic work. Among them are Kitagawa et al. (1998a), Kitagawa et al. (1998a), Petit et al. (1996), in order to match with the list. Please check. Crandall et al. (1995) and Cappon et al. (1999) are known per experiments on injury mechanism of the lower limb injuries and studies addressing the role of muscles force.

1.9 Anthropomorphic Test Devices (ATD)

1.9.1 Introduction

The ATD is a mechanical model of the human body which is normally used as a human surrogate in crash testing. It offers also a possibility to measured static, dynamic and impact loading. Different types are used as crash – test

dummies. The dummy is generally made of steel, aluminum (for skeleton), polymers (for joints and skin) and foam (for flesh). The dummies are equipped with accelerometers for measuring accelerations and load cells for recording force and deformation or displacement. The ATDs are used in the automotive engineering for new vehicles and occupant protection potential. Dummies can also be used in aircraft industry for testing and protection of individuals against aviation hazards, parachutes structure failure and ejection of seats. From the experimental purposes, crash test dummies should be sensitive to various parameters and injury mechanism. The ATDs should on one hand represent human in terms of size, mass and mass distribution and sitting posture and finally must have a human-like response that is biomechanical response impact and impulsive load. Hence the ATDs must have the following requirements:

(a) Anthropometry: Data on standing height 1.751 m, weight = 78.2 kg.
(b) Biofidelity: Data based on cadaver (dead body).
(c) Test repeatability: Data on test capability and calibration regularly.
(d) Model durability: To withstand a high number of tests and over loading up to 1.3 times, i.e., 102 kg.

1.9.2 Fields of Application

The following family of dummies are given as test models

Hybrid III Frontal Impact Loading

This dummy types consists of three, six and ten year old small adult female (fifth percentile), midsize adult male (50th percentile) and large size adult male (95th percentile). This family is designed for frontal impact test. The 50th percentile male dummy is a regulated test device in the European ECE regulations and in the US safety standards. The skull and skull cap of Hybrid III 50th percentile male dummy and it consists of the following:

- One piece cast in aluminium parts.
- Removable Vinyl skins.
- The neck is segmental rubber with aluminium attached a center cable.
- The rib cage has 6NO H.S. ribs with polymer based damping material to stimulate human chest force-displacement relations. Each rib consists of right and left anatomical contains again ribs in one continuous part while open with upper part (Sternum) and anchored to the back of thoracic spine. The sternum assembly includes a slider for the chest deflection/displacement rotary potentiometer.
- The angle between the neck and the upper torso has a neck bracket in corporated with a six axis neck transducer. A two piece clavicle (Collar Bone) and clevical link assemblies have integral *scapulae* to interface with shoulder belts.

- A curved cylindrical rubber lumbar spin (lower part) mount has been provided human like touch of a seated person and stuck to the pelvis through a three axis lumbar load cell. The pelvis constructed is of a vinyl skin/urethane foam molded on an aluminium casting in a seated position. The ball-jointed femur attachments offer hip moment-rotation characteristics.
- An allowance can be made to predict bone fracture by instrumenting femur, tibia and ankle. A typical ligament injury, heel compression and ankle rotations can be determined.

Thor Frontal Impact Loading

Thor (Test Device for Human Occupant Restraint) is a further impact dummy and is based on the anthropometry of the 50th percentile male. While comparing the design for Hybrid III family, here all dummy components have been improved except the arms which are identical to those of Hybrid III. In order to assess the facial fracture the facial region is instrumented with uni-directional load cells. It is interesting to know that the biofidelity and the geometry, the ribcage is made up of elliptical ribs and by improving instrumentation a SD dynamic compression can now be evaluated at four distinct points. A new abdominal assembly had been devised to measure directly belt intrusion and upper abdomen displacement due to air bag compression. Here changes are brought about in pelvis, lower limbs and ankle joint.

Dummies for Lateral Impact (SID)

Various types of dummies are available for lateral and sick impact and they are:

(a) EUROSID: This a European side impact dummy with different versions.
(b) EUROSID2: This is the European side impact dummy. This is an updated version of EUROSID. It is 50th percentile adult male. It consists of metal and plastic skeleton covered by flesh simulating material. Generally the sitting height is 0.904 m with mass 72 kg. It has no lower arms while the rest is the same as Hybrid III.
(c) SID: Is based on Hybrid III with an adapted Thorax but without arms and shoulder structures. It is the official US impact testing of new cars (FMVSS2140) and the size corresponds to the 50th percentile male. It measures injury to the head, chest and pelvis.
(d) SID HIII: To account for better head–neck biofidelity, this SID is equipped with a Hybrid III head and neck.
(e) SID IIS: This is a side impact dummy representing a 5th percentile female.
(f) BIOSID: This is a dummy of biofidelity side impact type.

(g) WORLD SID: The International Standardization Organization (ISO) has developed a harmonized side impact dummy of a mid size. This dummy is used through out the world. This is used for improved assessment of injury risk to car occupants in lateral collision. Besides an improved biofidelity, it leads to a harmonization in safety regulations.

Biofidelic Rear-End Dummy (BIO RID) or RID2

Injuries and trauma developed in low speed rear end collision, the need is emerged to modify anthropomorphic test device that allowed the investigation of such impact condition. Two different dummy types exist, namely Bio RID and RID2. Both are middle sized male dummies developed in Europe for assessing for so-called "Whiplash" injuries under low speed rear and impacts.

(a) Biofidelic Rear-End Dummy (BIO RID). The main feature is full segmented spine consisting of 24 segments. Each human spinal pivot point is reproduced. Due to such a detailed representation, a high biofidelic spinal is generally observed.
(b) The Rear Impact Dummy (RID2). This is based on the Hybrid III 50th percentile male. However, several modifications have been made of which new design of the neck. The most acceptable one is made up of seven aluminium discs with flexible thorax and lumbar spine.
Some difficulties in handling arise with specially designed rear-end dummies. Because of increased flexibility the positioning of dummies compared with Hybrid III becomes more difficult.

Polar Dummy

The polar dummy has been designed to simulate kinematics of the human body during car-pedestrian collisions. The dummy stands 175 cm tall and weighs 75 kg. It is intended to gather more accurate date on the pedestrians injuries. The instrumentations suggests, it is entirely meant for the car-pedestrian interacting and producing necessary answers.

Dummies Representing Children Trauma and Injuries

The following symbols adopted for dummies with instrumentations pertaining children injuries:

(a) PO – Newborn child.
(b) P3/4 – Nine month old child.
(c) P3 – Three year old child.
(d) P6 –
(e) P10 –
(f) Q-Dummies – Infant dummy types.

(g) CRABI – Child Restraint Air Bag Dummy. It is used to evaluate air bag exposure to infant restrainer in child safety seats. They come in three sizes

6 month old	Hybrid III family
12 month old	
18 month old	

TNO – 10

It is a loading device for testing safety belts in a simulated crash condition. It represents 50th percentile male dummy with size and weight distribution. The dummy has no lower arm and only one lower leg.

Impactors

The most common Impactors are

- Head Impactors
- Headship Impactors
- Pedestrian Impactors

Plate 1.13 gives test conditions and threshold values for vehicles tested under FMVSS208 and FMVSS214 and ECER94 and R.95. Plate 1.14 gives data on wind generated missiles and objects might cause impact to human body. Plate 1.15 indicates data for other vehicles as impactors or involved in trauma injury factors and data which effect the impact parameters and influence the evaluation of traumatic injuries.

Plate 1.13. Test conditions for lateral impact threshold values frontal impact threshold values

	FMVSS 208	ECE R94
dummies	2 hybrid III	2 hybrid III
head	HIC < 1,000	HPC < 1,000 a3ms < 80 g
neck	N_{ij}, 1.0	next, 57 Nm not exceeding defined force corridor
thorax	deflection < 76.2 mm a3ms < 60 g	deflection < 50 mm VC < 1.0
femur	axial force < 10 kN	not exceeding defined force corridor
knee		deflection < 15 mm
tibia		axial force < 8 kN TI < 1.3

Plate 1.13. *Continued*

side impact threshold values		
	FMVSS 214	ECE R95
dummies	2 SID	1 EuroSID
head		HPC $< 1,000$
thorax	TTI < 85 g	VC < 1.0
abdomen		internal force < 2.5 kN
pelvis	A (peak) < 130 g	pubic force < 6 kN

test conditions applied by the Euro-NCAP (http>//www.euroncap.com)	
impact	test conditions
frontal impact	64 km/h, deformable barrier, 40% overlap
side impact	50 km/h, trolley fitted with a deformable front is towed into the driver's side of the car

Plate 1.14. Wind generated elements in accidents with human beings

missile type	geometry				
	diameter (mm)	length (m)	impact area (m^2)	velocity (m/s)	weight (kg)
wooden plank	–	3.67	0.03	41.5	56.7
wooden pole	200	3.67	0.03	5.73	94.8
circular hollow sections in steel (average)	168.3	4.00	0.000026	70.2	60
sign boards (average)	–	–	6.0	57.0	56
steel I-beam light sections (average)	–	4.0	0.000032	40.5	100
steel members channel sections (average)	–	3.0	0.000013	50.5	30

Plate 1.14. *Continued*

missile type	geometry				
	diameter (mm)	length (m)	impact area (m^2)	velocity (m/s)	weight (kg)
steel members L-sections (average)	–	3.0	0.000015	45.5	36
steel rafters T-sections (average)	–	3.0	0.000018	45.5	42
steel rod	25	0.92	0.00049	75.6	3.63
concrete lintels	–	3.0	0.025	60.5	1.80
concrete sleepers	–	2.70	0.0031	75.0	0.20
precast concrete beams or piles at delivery stage	–	9.0	0.09	60.5	19.44
precast concrete wall panels	–	5.0	11.5	2.5	1,380
prestressed concrete pipes	400	–	–	–	1.100
	500	–	–	–	1.375
	600	–	–	–	1.650
	700	–	–	–	1.920
	800	–	–	–	2.200
	900	–	–	–	2.474
	1,676	6.0	0.032	–	4.608
prestressed concrete poles	–	17.0	0.0019	30.5	65.7
		12.0	0.00080	50.1	14.46
		9.0	0.000025	65.2	9.65

Reproduced from
Bangash M.Y.H. Impact and Expulsion – Analysis and Design
Blackwell, Oxford (1993)

Plate 1.15. Data on Cars as Missiles for Traumatic Injuries

manufacturer vehicle	length (m)	width (m)	height (m)	wheel base (m)	laden weight (kg)	max. speed (miles h^{-1})
Alfa Romeo						
33 1.7 Sport Wagon Veloce	4.142	1.612	1.345	2.465	925	115
75 2.0i Veloce	4.330	1.630	1.350	2.510	1,147	124
164 3.0 V6	4.555	1.760	1.4	2.660	1,300	142
American Motors (USA)						
Jeep Wagoner limited	4.198	1.790	1.615	2.576	2,074	90
Aston Martin						
Lagonda	5.820	1.790	1.3	2.91	2,023	143
V8 Vantage Volante	4.39	1.86	0.1295	2.610	1,650	160
Vantage Zagato	4.39	1.86	0.1295	2.610	1,650	186
Audi (D)						
80 1.85	4.393	1.695	1.397	2.544	1,020	113
90 Quattro	4.393	1.695	1.397	2.546	1,270	125
100	4.792	1.814	1.422	2.687	1,250	118
100 Turbo Diesel	4.793	1.814	1.422	2.687	1,250	108
200 Avant Quattro	4.793	1.814	1.422	2.687	1,410	139
Austin						
Maestro 1.60 Mayfair	4.049	1.687	1.429	2.507	946	102
Metro 1.0 Mayfair 3-door	3.405	1.549	1.361	2.251	771	86
Montego Vanden Plas EFi Estate	4.468	1.710	1.445	2.570	1,111	110
Bentley (GB)						
Mulsanne	5.268	1.887	1.485	3.061	2,245	119
Mulsanne Turbo R	5.268	1.887	1.486	3.061	2,221	143
Bitler (D)						
Type III	4.450	1.765	1.395	–	1,300	140
BMW (D)						
320i Convertible	4.325	1.645	1.380	2.57	1,125	123
325i Touring	4.325	1.645	1.380	2.57	1,270	132
M 3	4.325	1.645	1.380	2.57	1,150	139
520i	4.72	1.751	1.412	2.761	1,400	126
735i	4.91	1.845	1.411	2.832	1,590	145
750i L	5.024	1.845	1.401	2.832	–	155
Z 1	3.921	–	–	2.45	110	140
Bristol (GB)						
Brigand Turbo	4.902	0.1765	1.4535	2.895	1,746	150
Buick (USA)						
Lesabre T-type Coupe	4.991	1.838	1.389	2.814	1,458	115

Plate 1.15. *Continued*

Cadillac (USA)						
Allante Convertible	4.537	1.864	1.325	2.525	1,585	110
Cadillac (USA)						
Allante Convertible	4.537	1.864	1.325	2.525	1,585	110
Chevrolet (USA)						
Camaro IROC-2	4.775	1.850	1.270	2.565	1,525	130
Corvette Convertible	4.483	1.805	1.185	2.438	1,414	142
Chrysler (USA)						
le Baron Convertible	4.697	1.738	1.326	2.546	1,474	110
GS Turbo 2	4.555	1.76	1.302	2.465	1,194	125
Portofino	–	–	–	–	–	150
Citroen (F)						
Ax 14 TRS	3.495	1.56	1.35	2.285	695	99
Bx 19 GTi 16v	4.229	1.657	1.365	2.655	1,093	130
Bx 25 GTi Turbo	4.660	1.77	1.36	2.845	1,385	126
Coleman Milne (GB)						
Grosvenor limousine	5.563	1.964	1.575	3.661	2,100	115
Dacia (R)						
Duster 4 × 4 GLX	3.777	1.6	1.74	2.4	1,180	70
Daihatsu (J)						
Charade LX Diesel Turbo	3.61	1.615	1.385	2.34	810	87
Charade GT ti	3.61	1.615	1.385	2.34	816	114
Fourtrak Estate EL TD	4.065	1.580	1.915	2.53	1,660	83
Daimler						
3.6	4.988	2.005	1.358	2.87	1,770	137
Dodge (USA)						
Daytonna Shelby 2	4.545	1.76	1.279	2.464	1,220	120
Ferrari						
F40	4.43	1.981	1.13	2.451	1,100	201
Mondial 3.2 Quattro valvole	4.58	1.79	1.26	2.65	1,430	143
Fiat						
Croma Turbo ie	4.495	1.76	1.433	2.66	1,180	131
Panda 4 × 4	3.378	1.485	1.46	2.159	761	83
Ford						
AC (GB)	3.962	1.816	1.168	2.477	907	140
Ford (D)						
Escort RS Turbo	4.046	1.588	1.348	2.4	1,017	124
Granada 2.4i GL	4.669	1.76	1.41	2.761	1,265	120
Scorpio 4 × 4 2.9i	4.669	1.766	1.453	2.765	1,385	126
XR3i Cabriolet	4.049	1.64	1.336	2.398	925	115

Plate 1.15. *Continued*

manufacturer vehicle	length (m)	width (m)	height (m)	wheel base	laden weight (kg)	max. speed (miles h^{-1})
Ford (GB, B)						
Sierra Sapphire GLS 2.0EFi	4.468	1.699	1.359	2.609	1060	115
Ford (B)						
Sierra Ghia 4 × 4 Estate	4.511	1.694	1.359	2.612	1315	119
Ford (USA)						
Taurus	4.785	1.796	1.795	2.692	1299	105
Ginetta (GB)						
G32	3.758	1.651	1.168	2.21	753	135
Honda (J)						
Accord Aerodeck 2.0 EXL	4.335	1.651	1.335	2.6	1147	110
Legend Coupe	4.755	1.745	1.37	2.705	1395	132
Prelude 2.0L-16	4.460	1.695	1.295	2.565	1145	128
Hyundai (J)						
Pony 1.5 GLS	3.985	1.595	1.38	2.38	890	96
Stellar 1.6 GSL	4.427	1.72	1.372	2.579	1034	98
Isuzu (J)						
Trooper Turbo Diesel	4.38	1.65	1.8	2.3	1655	78
Jaguar (GB)						
Sovereign 3.6	4.988	2.005	1.358	2.87	1770	137
XJ6 2.9	4.988	2.005	1.38	3.87	1720	117
Lada (Su)						
Riva Cossack	3.708	1.676	1.638	2.197	1150	77
Samara 1300 SL	4.006	1.62	1.335	2.46	900	92
Lamborghini (I)						
Countach 5000s Quattro valvole	4.14	2.0	1.07	2.45	1446	178
Lancia (I)						
Delta 1.6 GTie	3.895	1.62	1.38	2.475	995	115
Delta HF vitegrade	3.9	1.7	1.38	1.38	1200	134
Thema 2.0ie Turbo Estate	4.59	1.755	1.433	2.66	1150	139
Thema 8.32	4.59	1.755	1.433	2.66	1400	139
Y10 Turbo	3.392	1.507	1.425	2.159	790	111
Land Rover (GB)						
One Ten Diesel Turbo	4.445	1.79	2.035	2.795	1931	73
Range Rover Vogue Turbo D	4.47	1.718	1.778	2.591	2061	90
Lincoln (USA)						
Continental	5.21	1.847	1.412	2.769	1645	112

Plate 1.15. Continued

Lotus (GB)						
Esprit Turbo	4.331	1.859	1.138	2.459	1,268	152
Maserati (I)						
Bi Turbo 228	4.46	1.865	1.33	2.6	1,240	151
Mazda (J)						
121 1.3LX Sun Top	3.475	1.605	1.565	2.295	775	99
626 2.0 GLX Hatchback	4.515	1.69	1.375	2.575	1,196	111
626 2.0i GT Coupe	4.45	1.69	1.36	2.515	1,230	130
RX7	4.29	1.69	1.265	2.43	1,221	134
Mercedes Benz (D)						
190E 2.6	4.427	1.678	1.39	2.665	1,209	130
300CE	4.655	1.682	1.41	2.715	1,390	126
560 SEL	5.16	2.006	1.446	1.555	1,780	147
Mercury (USA)						
Topa 3 XR5	4.468	1.747	1.339	2.537	1,135	92
MG (GB)						
Maestro 2.0 EFi	4.05	1.69	1.42	2.51	975	114
Metro Turbo	3.403	1.563	1.359	2.251	840	110
Montego Turbo	4.468	1.71	1.42	2.565	1,079	125
Mitsubishi (J)						
Galant Sapporo	4.66	1.695	1.375	2.6	1,230	114
Starion 2000 Turbo	4.43	1.745	1.315	2.435	1,308	133
Mitsubishi Colt (J)						
Lancer 1500 GLX Estate	4.135	1.635	1.42	2.38	950	95
Morgan (GB)						
Plus 8	3.96	1.575	1.32	2.49	830	122
Nissan (J)						
Bluebird 1.6 LS	4.405	4.365	1.69	1.395	1,120	103
Praire Anniversary II	4.09	1.655	1.6	2.51	1,070	95
Silvia Turbo ZX	4.351	1.661	1.33	2.425	1,136	124
Oldsmobile (USA)						
Trofeo	4.763	1.798	1.346	2.741	1,526	115
Panther (GB)						
Kallista 2.9i	3.905	1.712	1.245	2.549	1,020	112
Solo 2	4.344	1.78	2.18	2.53	1,100	150
Peugeot (F)						
205 GTi Cabriolet	3.706	1.572	1.354	2.421	884	116
205 GRD	3.706	1.572	1.369	2.421	895	96
Peugeot (GB)						
309 SRD	4.051	1.628	1.379	2.469	950	99
Plymouth (USA)						
Sundance	2.463	1.71	1.339	2.463	1,131	105
Pontiac (USA)						
Bonneville SSE	5.046	2.838	1.409	2.814	1,504	112

Plate 1.15. *Continued*

manufacturer vehicle	length (m)	width (m)	height (m)	wheel base	laden weight (kg)	max. speed (miles h^{-1})
Porsche (D)						
911 Speedster	4.291	1.65	1.283	2.273	1,140	152
944 S	4.2	1.735	1.275	2.4	1,280	140
Reliant (GB)						
Scimitar 1800 Ti	3.886	1.582	1.24	2.133	889	124
Renault (F)						
Espace 2000 – 1	4.25	1.277	1.66	2.58	1,177	105
5 GTD	3.65	1.585	1.397	2.466	830	94
21 GTS	4.46	1.714	1.415	2.659	976	113
21 Turbo	4.498	1.714	1.375	2.597	1,095	141
Rolls-Royce (GB)						
Silver Spirit	5.27	1.887	1.495	3.06	2,245	119
Rover (GB)						
216 Vanden Plas	4.16	1.62	1.39	2.45	945	107
820i	4.694	1.946	1.398	2.759	1,270	126
Saab (S)						
900 Turbo 16S Convertible	4.739	1.69	1.42	2.525	1,185	124
9000i	4.62	1.765	1.43	2.672	1,311	118
Seat (E)						
Ibiza 1.5 GLX 5-door	3.638	1.609	1.394	2.448	928	107
Malaga 1.5 GLX	4.273	1.65	1.4	2.448	975	103
Skoda (CS)						
130 Cabriolet LUX	4.2	1.61	1.4	2.4	890	95
Subaru (J)						
Justy 4 × 4	3.535	1.535	1.42	2.85	770	90
XT Turbo Coupe	4.49	1.69	1.335 1.370	2.465	1,139	119
Suzuki (J)						
Santana	3.43	1.46	1.69	2.03	830	68
Swoft 1.3 GTi	3.67	1.545	1.35	2.245	750	109
Toyota (J)						
Celica 2.0 GTi Convertible	4.365	1.71	1.29	2.525	1,195	125
Corolla GTi	4.215	1.655	1.365	2.43	945	122
Space Cruiser	4.285	1.67	1.815	2.235	1,320	87
Supra 3.0i	4.62	1.745	1.31	2.595	1,550	135
TVR						
S Convertible	4	1.45	1.117	2.286	900	128
TVR (GB)						
9205 EAC Convertible	4.051	1.628	1.379	2.469	950	99
Vauxhall						
Astra Cabriolet	2.463	1.71	1.339	2.463	1,131	105
Astra GTE 2.0ie 16v	5.046	2.838	1.409	2.814	1,504	112
Carlton CD 2.0i	4.291	1.65	1.283	2.273	1,140	152
Carlton GSi 3000	4.2	1.735	1.275	2.4	1,280	140
Senator 3.0i CD	3.886	1.582	1.24	2.133	889	124

Plate 1.15. *Continued*

Volkswagon (D)						
Golf GTi 16v	4.25	1.277	1.66	2.58	1,177	105
Jetta GTi 16v	3.65	1.585	1.397	2.466	830	94
Scirocco GTX	4.46	1.714	1.415	2.659	976	113
Volvo (NL)						
360 GLY	4.498	1.714	1.375	2.597	1,095	141
480 ES	5.27	1.887	1.495	3.06	2,245	119
Volvo (S)						
760 GLE	4.16	1.62	1.39	2.45	945	107
Yugo (YU)						
65A GLX	4.694	1.946	1.398	2.759	1,270	126

type of missile	weight (kg)	impact area (cm^2)	impact velocity ($m\,s^{-1}$)
control rod	53	15.5	91.5
mechanism or fuel rod			
disc 90° sector	1,288	4,975	125
disc 120° sector	1,600	6,573	156
hexagon head bolts			
1.4 cm diameter	0.20	1.54	250
2.0 cm diameter	0.30	2.30	230
2.4 cm diameter	0.37	2.84	189
3.3 cm diameter	0.42	3.22	150
6.8 cm diameter	0.97	7.44	100
turbine rotor fragments			
high trajectory			
heavy	3,649	5,805	198
moderate	1,825	3,638	235
light	89	420	300
low trajectory			
heavy	3,649	5,805	128
moderate	1,825	3,638	235
light	89	420	244
valve bonnets			
heavy	445	851	79
moderate	178	181	43
light	33	129	37
valve stems			
heavy	23	25.0	27.5
moderate	14	9.7	20.0
other			
30 cm pipe	337.0	260.00	68
12 cm hard steel disc	1.6	113.0	140
steel washers	0.0005	3.0	250
Winfrith Test missile	15.6	176.0	240

Plate 1.16. Data on Impacting Two Vehicles and Missile Shapes

KEY Two vehicles Impacting

1. FMVSS – USA

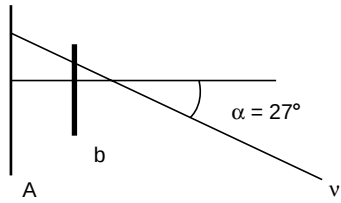

Data FMVSS 214

Width $b = 1,676\,\mathrm{mm}$

Mass $m = 1,368\,\mathrm{kg}$

Speed $v = 33.5\,\mathrm{m\,h^{-1}} = 54\,\mathrm{km\,h^{-1}}$

A one vehicle 90°

B other vehicle Impact angle $a = 27°$

2. ECE-R95 Europe

$b = 1,500\,\mathrm{mm}$
$m = 950\,\mathrm{kg}$
$v = 50\,\mathrm{km\,h^{-1}}$

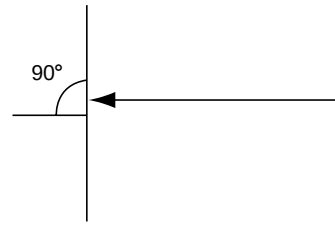

A one vehicle 90°

B other vehicle $a = 0$

i.e., at right angle to each other

For unit weight all expressions are multiplied by p

(1) Rectangular cross section of a missile

$$I_{xx} = bh^3/12,$$
$$I_{yy} = hb^3/12.$$

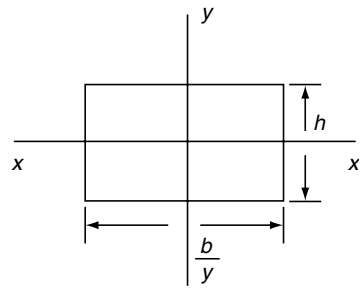

(2) Solid circular cross section of diameter D

$$I_{xx} = I_{yy} = \pi d^4/64.$$

(3) Hollow circular cross section of outer diameter D and inner diameter d

$$I_{xx} = I_{yy} = \pi(D^4 - d^4).$$

(4) Thin-walled tubular cross section of outer diameter D and thickness t.

$$I_{xx} = 1_{yy} = \pi t D^3/8.$$

(5) Elliptical type

$$I_{xx} = \pi D d^3/64,$$
$$I_{yy} = \pi D^3 d/64.$$

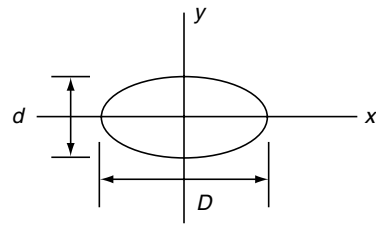

(6) Triangular cross section with base b and height h

$$I_{xx}\,(\text{parallel to } b) = bh^3/36$$

(7) Right circular cylindrical type missile

$$I_{zz} = \pi h R^4/2,$$
$$M = p\pi R^2\text{h}.$$

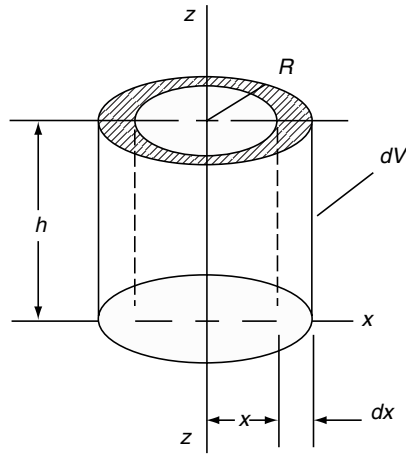

(8) Cone-shaped missile

$$I_{xx} = R^4 h/10,$$
$$P = m/(\pi R^2 h/3).$$

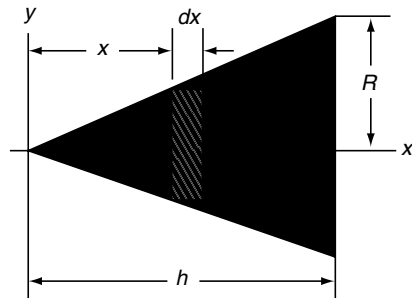

(9) Solid spherical missile

$$I_{xx} = 8/15\pi r^5,$$
$$x = \sqrt{(r^2 - y^2)},$$
$$y = \sqrt{(r^2 - x^2)},$$

where $p = m/4/3\pi r^3$

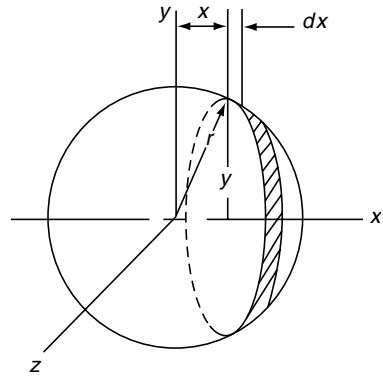

(10) Hollow spherical missile

$$I_{xx} = I_{yy} = I_{zz} = 2/3\, Wr^2,$$
$$W = 4p\pi r^2.$$

(11) Wedge-shaped semicylindrical missile

$$I_{zz} = ph\pi R4/4,$$
Where $p = m/\pi^2 h$.

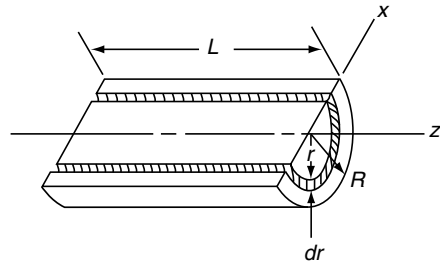

(12) Pyramid-shaped missile
(a) Right rectangular pyramid

$$I_{xx} = W/20(b^2 + 3h^2/4),$$
$$I_{x1x1} = W/20(b^2 + 2h^2),$$
$$I_{yy} = W/20(a^2 + 3/4h^2),$$
$$I_{y1y1} = W/20(a^2 + 2h^2),$$
$$I_{zz} = W/20(a^2 + b^2),$$
$$W = pabh/2.$$

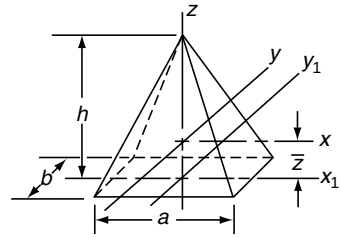

(i) Right rectangular pyramid–type missile.

(b) Regular triangular prism

$$I_{xx} = I_{yy} = W/24(a^2 + 2h^2),$$
$$I_{zz} = Wa^2/12,$$
$$W = \sqrt{3/4a^2h}.$$

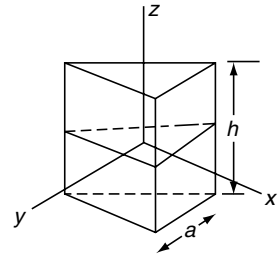

(ii) Regular triangular prism–type missile.

(13) Rod-shaped missile

(1) Segment of a circular rod

$$I_{xx} = WR^2[1/2 - (\sin\theta_1 \cos\theta_1)/2\theta_1)$$
$$I_{x1x1} = WR^2[1/2 - (\sin\theta_1 \cos\theta_1)/2\theta_1) + \sin^2\theta],$$
$$I_{yy} = WR^2[1/2 + (\sin\theta_1 \cos\theta_1/2\theta_1) - \sin^2\theta/\pi^2),$$
$$I_{y1y1} = WR^2(1/2 + \sin\theta_1 \cos\theta_1/2\theta_1)X$$
$$X = R\sin\theta_1/\theta_1$$
$$I_c = WR^2(1 - \sin^2\theta_1/\theta_1^2),$$
$$Y = R\sin\theta_1,$$
$$W = (\text{density})(\text{volume}).$$

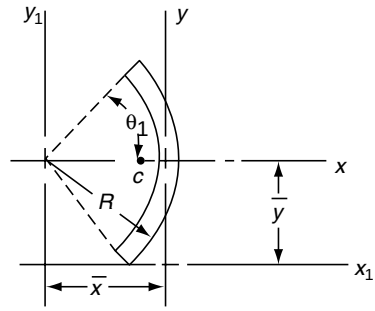

Rod (segment–shaped) missile.

(2) Elliptical rod

$$I_{xx} = Wb^2(55a^4 + 10a^2b^2 - b^4)/2(45a^4 + 22a^2b^2 - 3b^4),$$
$$I_{yy} = Wa^2(35a^4 + 34a^2b^2 - 5b^4)/2(45a^4 + 22a^2b^2 - 3b^4),$$
$$I_c = I_{xx} + I_{yy}.$$

(3) U-rod shaped missile

$$X = L_2^2/(L_1 + 2L_2);\ y = A_1/2,$$
$$I_{xx} = WA_1^2(A_1 + 6B_2)12(A_1 = 2B_2),$$
$$I_{yy} = WB^3/_2(2A_1 + B_2/3(A_1 + 2B_2)^2,$$
$$I_c = I_{xx} + I_{yy}.$$

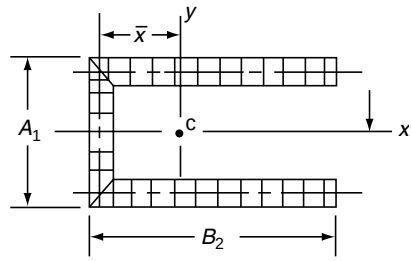

(4) V-rod shaped missile

$$X = {}^1\!/_2 L\sin\theta_1;\ y = L\cos\theta_1$$
$$I_{xx} = {}^1\!/_3 WL^2\cos^2\theta_1$$

$$I_{x1x1} = 4/3WL^2 \cos^2 \theta_1,$$
$$Iyy = \frac{WL^2}{12} \sin^2 \theta_1,$$
$$Iy_1y_1 = 1/3WL^2 \sin^2 \theta_1,$$
$$I_c = I_{xx} + I_{yy},$$
$$I_c = I_{x1x1} + I_{y1y1}.$$

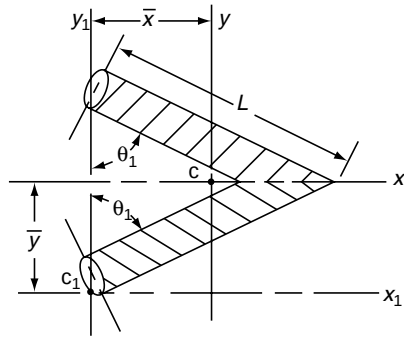

V–rod–shaped missile.

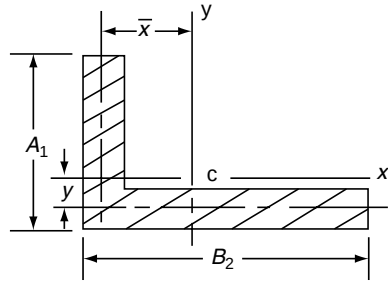

L–rod–shaped missile.

(5) L-rod shaped missile

$$x = 1/2B_2;\ y = 1/2A_1$$
$$I_{xx} = WA_1^2(A_1 + 3B_2)/12(A_1 + B_2),$$
$$I_{yy} = WB_2^2(3A_1 + B_2)/12(A_1 + B_2),$$
$$I_c = I_{xx} + I_{yy}.$$

(6) Hollow rectangular missile

$$
\begin{aligned}
I_{xx-} &= \frac{WA^2}{12}\ /_1(A_1 + 3B_2)/A_1 + B_2)^2, \\
I_{yy} &= WB_2^2(3A_1 + B_2)/(A_1 + B_2)^2, \\
I_c &= I_{xx} + I_{yy}.
\end{aligned}
$$

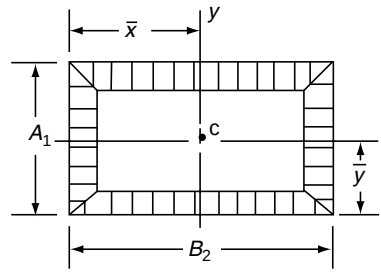

Hollow rectangular missile.

(7) Inclined rod-shaped missile flight (not through centroidal axis)

$$
\begin{aligned}
I_{xx} &= {}^1\!/_3 W\sin^2\theta_1(Ax^2 - A_1B_2 + B_2^2), \\
I_{yy} &= {}^1\!/_3 \mathrm{W}\cos^2\theta_1(Ax^2 - A_1B_2 + B_2^2), \\
I_c &= I_{xx} + I_{yy}.
\end{aligned}
$$

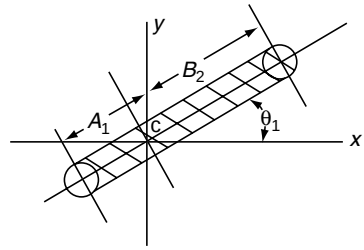

Rod-shaped missile at an inclination.

(8) Ogive-shaped missile

$$
\begin{aligned}
A_s x &= \text{surface area developed}; x = \text{centroid}, \\
A_s x &= 2\pi f_0^h\ xyds, \\
&= 2\pi R\{h^2 - br + bh_1[\sin^{-1}(h + h_1)/R - \sin^{-1} h_1/R]\}, \\
y &= [(R^2 - h_1^2) - 2h_1x - x^2]^{1/2} - b,
\end{aligned}
$$

$A_s =$ surface area developed; $x =$ centroid,

$$A_s = 2\pi R(h - b[\sin^{-1}(h + h_1)/R - \sin^{-1} h_1/R]\}.$$

I_{xx} and I_{yy} can thus be easily calculated for a typical curve of radius R.

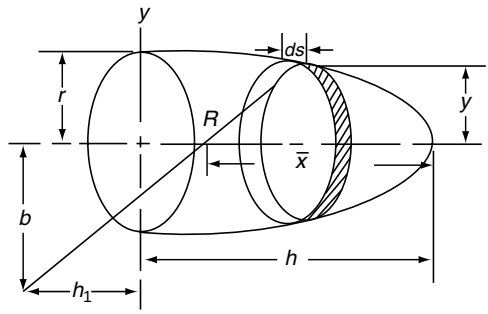

Ogive–shaped missile.

(9) Torus and spherical sector missiles

(a) Torus

$$I_{xx} = I_{zz} = \frac{\mathrm{W}}{8}(4R^2 + 5r^2),$$

$$Iyy = \frac{\mathrm{W}}{4}(4R^2 + 3r^2),$$

$$W = 2\pi^2 r^2 p,$$

$$X = z = R + r,$$

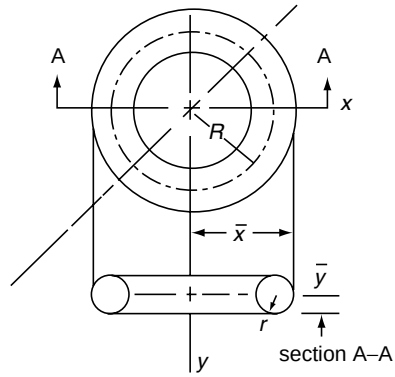

Torus–shaped missile.

(b) Spherical sector

$$I_{zz} = \frac{\mathrm{Wh}}{5}(3R - h),$$
$$W = {}^{2}/_{3}\pi p R^2 h$$

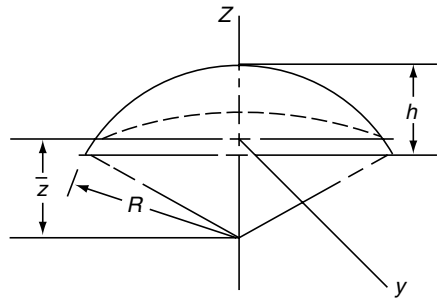

Spherical sector type missile.

2

Mechanics of Fracture and Dislocation

2.1 Introduction

Several structural failures can be associated with the fracture of one or more of the materials making that structure. When such events occur, they are mostly unexpected, sudden, and unfortunate, and it is natural for any one to focus attention on minimizing the undesired consequences when designing equipment and analyzing human body structures. The study of crack behavior, prevention and analysis of fracture of materials is known as *fracture mechanics*.

In every discipline, including fracture mechanics, it is of critical importance to examine the historical antecedents. Progress not only depends on revolutionary ideas, but a significant part of it depends on retentiveness as well. People who tend to ignore the past are more prone to repeat mistakes. Although developments in fracture mechanics concepts are quite new, assessing human body to avoid fracture is not a new idea.

By the end of the nineteenth century, the influence of crack on the structural strength was widely appreciated, but its nature and influence was still unknown. Inglis (1913) published the first significant work in the development of fracture mechanics. The work was an analytical formulation of stresses in a plate in the vicinity of a two-dimensional elliptical hole. The plate was pulled at both ends perpendicular to the ellipse as shown in Fig. 2.1. Inglis observed that the corner of the ellipse (point A) was feeling the most pressure and as the ellipse gets longer and thinner the stresses at A become larger. He examined local stresses at the tip of the ellipse and estimated that the stress concentration is approximately

$$2\left(\frac{a}{b}\right) \quad \text{or} \quad 2\sqrt{\frac{a}{p}}, \tag{2.1}$$

where a and b are the semimajor and semiminor axes, respectively, and r is the root radius at the tip of the ellipse. Inglis evaluated various hole geometries

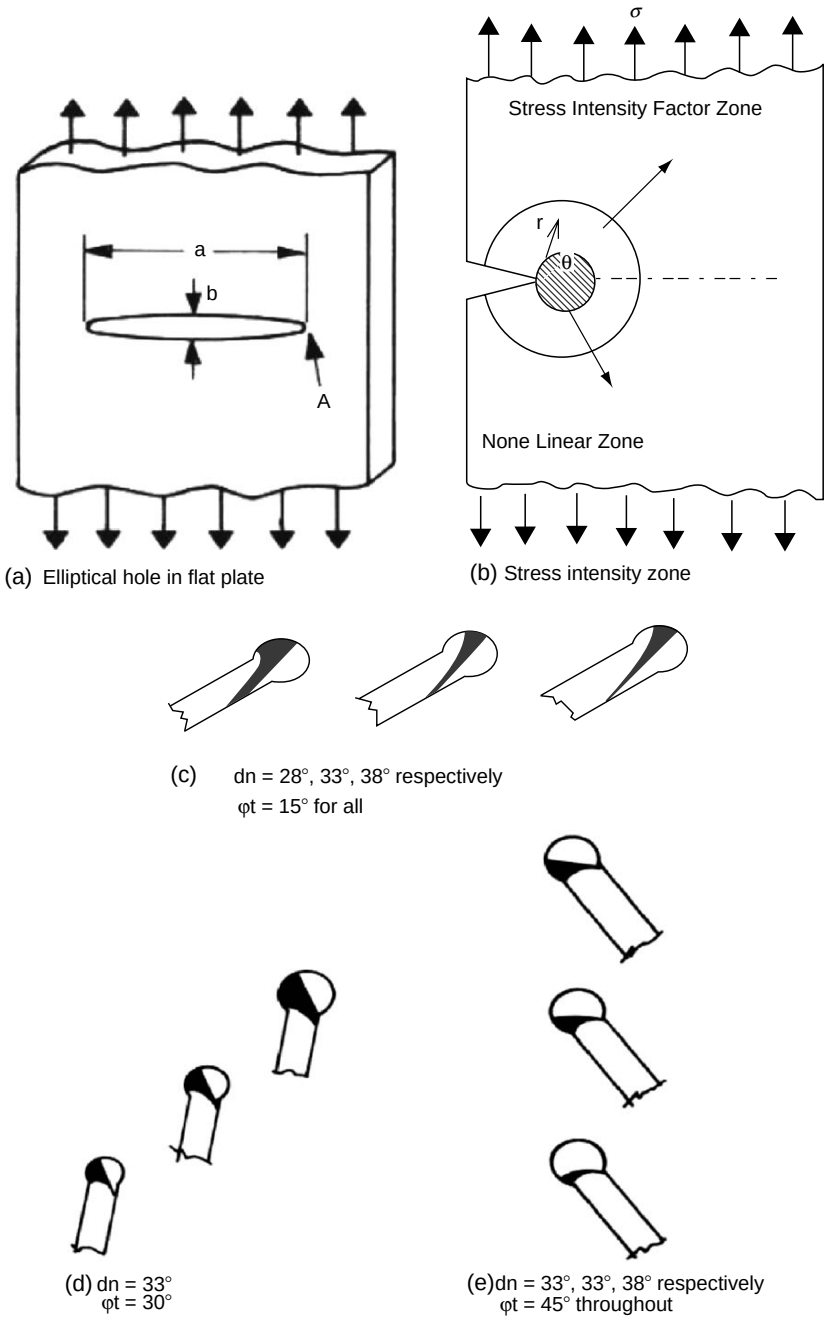

Fig. 2.1. Stresses in a plate in the vicinity of a two-dimensional elliptical hole

and realized it is not really the shape of the hole that matters but the length of hole perpendicular to the load and the curvature at the end of the hole that matters in cracking. He also notice that pulling in a direction parallel to the hole does not produce a great effect.

The basic ideas leading to the start of modern fracture mechanics can be attributed to a theory of fracture strength of glass, which was published by Griffith (1921) Using Inglis' work as a foundation, Griffith proposed an energy balance approach to study the fracture phenomenon in cracked bodies. A great contribution to the ideas about breaking strength of materials emerged when Griffith suggested that the weakening of material by a crack could be treated as an equilibrium problem. He proposed that the reduction in strain energy of a body when the crack propagates could be equated to the increase in surface energy due to the increase in the surface area. The Griffith theory assumed that the fracture strength was limited by the existence of initial cracks and that brittle materials contain elliptical microcracks, which introduce high stress concentrations near their tips. He developed a relationship between crack length (a), surface energy connected with traction-free crack surfaces (2γ), and applied stress, which is given by

$$\sigma^2 = \frac{2\gamma \mathrm{E}}{\pi\alpha}. \tag{2.2}$$

Plasticity effects in metals limited the theorem and it was not until Irwin's work in 1948 that a modification was made to Griffith's model to make it applicable to metals. Irwin's first major contribution was to extend the Griffith approach to metals by including the energy dissipated by local plastic flow. Orowan independently proposed a similar modification to Griffith's theory in 1949. Orowan limited practical use to brittle materials while Irwin made no such restrictions.

Contemporary research and development in fracture mechanics focus on several interesting areas, such as dynamic fracture mechanics, interface fracture mechanics, shear ruptures in earthquakes, stress corrosion cracking, environmental effects on fatigue crack propagation, and fracture of novel materials such as nanocomposites and graded materials. Extremely powerful numerical codes that are able to investigate fracture due to separation of atoms are being developed. Also, experimental techniques have progressed enough to investigate fracture in materials at nanometer length scales and nanosecond time resolution. However, experimental techniques that could provide spatial and temporal resolution simultaneously at the nanolevel are still scares.

In biomedical cases fractures and dislocation in bones are common occurrences. More sophisticated analyses are to be developed to evaluate three-dimensional fractures in bones. Similarly, partial or complete dislocation after fracture in bones is to be assessed as well. The analyses include three-dimensional hybrid finite element techniques, finite difference techniques, and finite/discrete element techniques with and without gaper contact elements. These are the most popular ones normally adopted for such

traumatic conditions in order to evaluate bone fracture and dislocation. Both static and dynamic loading cases can be associated with these techniques, for linear and nonlinear solution procedures. A vast literature exists on the crack propagation and fracture developments in other materials. Since both bone and concrete are brittle materials, the Young's modulus and Poisson's ratios will be identical and crack and fracture processes can easily be postulated. It is vital that a comparable material properties shall be established. Crack arrest and crack closure and reopening of cracks can be modeled easily. Obviously the bovine materials do not have aggregates and the analysis would be comparatively simple. In this chapter they have explained in detail. Numerous formulations and solution procedures are given to devise and check the damage scenarios.

2.2 Fractures and Dislocations

Fractures of bones are categorized according to their bony anatomic location. The fracture may occur in the head, diaphysis, or base of the bone and be palmarly or dorsally located. Epiphyseal fractures in children may result in growth disturbances. Fractures can be further described by the nature of the fracture, including transverse, spiral, oblique, comminuted, condylar, extraarticular, and intraarticular. Fractures associated with soft tissue injury are called *open fractures*. Axial forces produce comminuted and transverse fractures. Twisting or rotatory forces give rise to spiral and oblique fractures. Angular deformities are named based on the apex of the fracture. Intraarticular fracture–dislocations of small joints require precise articular surface realignment for prevention of traumatic arthritis.

2.2.1 Phalangeal Fractures and Forces

Distal phalangeal fractures are the most commonly encountered fractures in the hand. Distal phalangeal tuft fractures are frequently associated with nail bed injuries. Often comminuted, they are reduced at the time of nail bed repair and are protected with a splint for 3–4 weeks. A displaced, unstable transverse fracture may require fixation with a 0.035-in. (0.375 mm) diameter pin. In three-dimensional finite element analysis the three-dimensional dowel/pin matrices given later on would be used for overall fracture behavior.

Mallet Finger

Dorsal fractures at the base of the distal phalanx may involve the terminal extensor tendon insertion. A mallet deformity results from the unopposed flexor force on the DIP joint in extension, provided that the injury involves less than 30% of the joint surface and less than 2 mm of displacement. Mallet

finger deformities require 8 weeks of DIP joint extension splinting. Any flexion of the joint during this time interrupts healing. For larger or displaced joint fractures, open reduction and internal fixation are necessary. Restoration of joint congruency may minimize late arthritic changes of the joint.

Research into the problem of fractures initiated at square-hatched corners where local stress concentration and the sharp corners acting like starter cracks had prompted to the development and definition of what one now refers as lineal elastic fracture mechanics (LEFM). A major breakthrough occurred in the early 1950s when Irwin and Kies provided the extension of Griffith theory for an arbitrary crack and proposed the criteria for the growth of this crack. The criterion was that the strain energy release rate (G) must be larger than the critical work (G_c), which is required to create a new unit crack area. Irwin also related strain energy release rate to the stress field at the crack tip using Westergaard's work. Westergaard had developed a semi-inverse technique for analyzing stresses and displacements ahead of a crack tip. Using Westergaard's method, Irwin showed that the stress field in the area of the crack tip is completely determined by a quantity K called the *stress intensity factor*. Using the method of virtual work, Irwin presented a relationship between the energy release rate and the stress intensity factor as

$$\sigma_{\iota jj} = \frac{K f_{\iota jj}(\theta)}{\sqrt{2\tau r}}, \tag{2.3}$$

$$K^2 = EG, \tag{2.4}$$

where E is Young's modulus.

Fracture toughness had not been large enough to prevent crack propagation in the failure cases mentioned above.

Williams (1957) developed an infinite series that defined stress around a crack for any geometry. The use of the optical method "photoelasticity" to examine the stress fields around the tip of a running crack was published by Wells and Post (1958), and Irwin observed that the photoelastic fringes not only formed closed loops at the crack tip as predicted by singular stress field equations, but also showed a tilt as a result of the hear specimen boundaries. In 1960, a significant contribution to the development of LEFM was put forth when Paris and his coworkers advanced an idea to apply fracture mechanics principles to fatigue crack growth. Although they provided convincing experimental and theoretical arguments for their approach, the initial resistance to their work was intense and they could not find a peer-reviewed technical journal to publish their manuscript. They finally opted to publish their work in a University of Washington periodical entitled *The Trend in Engineering*. The work by Paris and colleagues was a landmark in the fatigue aspects of fracture mechanics, and yielded the equation

$$\frac{\mathrm{d}a}{\mathrm{d}N} = c(\Delta K)^n, \tag{2.5}$$

where c and n are the curve-fitting parameters of experimentally obtained fatigue data.

Linear elastic fracture mechanics is not valid when significant plastic deformation precedes failure. Although earlier theoretical developments were aimed at understanding brittle crack behavior, it became apparent from experiments that except for a few, most materials are ductile and therefore linear elastic analysis should be modified accordingly. Dugdale (1960) made the first attempts to include cohesive forces in the crack tip region by developing an elaborate model within the limits of elasticity. Later, Rice (1968) conducted a simplified analysis of complete plastic zone formation, approximated by a circular region ahead of the crack tip. The results derived from the energy–momentum tensor concept and applied to elastic cracks were extended to include plastic cracks by defining a path-independent integral termed the J integral. The plastic zone size and the crack opening displacement were found to correlate with the elastic stress intensity factor criterion. The successful experiments by Begley and Landes (1971), who were the research engineers at Westinghouse, led to the publication of a standard procedure for J testing of metals in 1981. Sih (1976) introduced the strain–energy density concept, which was a departure from classical fracture mechanics. He was able to characterize mixed-mode extension problems with this method, which also provided the direction of the crack propagation in addition to the amplitude of the stress field.

Middle phalangeal fractures may be intraarticular with proximal and distal fragments or shaft fractures. Displacements are a result of forces exerted by FDS tendon insertion and the extensor mechanism. Transverse fractures distal to the insertion of the FDS result in palmar angulation. Fractures proximal to the FDS tendon result in dorsal angulation secondary to the intact extensor tendon insertion.

Line element described in this chapter can be used with finite element analysis. Most proximal phalangeal shaft fracture angelate palmarly which is produced by forces of the interosse's muscle. These fractures when in transverse direction are usually unstable after reduction. Instability analysis would be required and stability established with pins, wires, plates, and screws can be assessed using three-dimensional dynamic finite element analysis. Complications do occur in fracture analysis when malrotation, malunion, and nonunion conditions exist. Ordinary fracture analysis cannot handle such cases, the finite element or similar advanced methods shall be executed.

2.2.2 Metacarpal Fractures

Fractures of the metacarpals are the second most commonly seen fractures in the primary care setting. Metacarpal fractures are classified according to their location: head, neck, shaft, or base. Because most fractures of the metacarpal head are comminuted, they should be referred to an orthopedic surgeon for definitive treatment. Acute management includes immobilization in an ulnar

or radial gutter splint, ice, elevation, and analgesia. The patient should be evaluated within 1 week of injury.

Fractures of the metacarpal neck often result from a direct impact, as occurs with punching with a closed fist. Although it is often referred to as a "boxer's fracture," true boxers rarely experience this injury. This fracture most frequently involves the fourth and fifth metacarpal. Because of the action of the interosseous muscles, the head of the metacarpal is displaced volarly (apex dorsal angulation).

Physical examination reveals tenderness and swelling over the dorsum of the hand. The MCP joint may appear depressed because of the volar displacement of the metacarpal head. The examiner should be aware of the appearance of pseudoclawing. When pseudoclawing is present, there is hyperextension at the MCP joint and flexion at the PIP joint as the patient attempts to extend the finger. This occurs when there is dorsal angulation greater than 40°. The displaced metacarpal head interferes with the extensor apparatus. As mentioned earlier, assessment for rotational displacement should be done.

Radiographs include AP, lateral, and oblique views. The degree of apex dorsal angulation may be measured on the lateral view. The expected metacarpal neck angle is 15°, so a measurement of 45° is actually only 30° of angulation. The more distal the fracture, the greater amount of acceptable dorsal angulation. Greater loss of dorsal knuckle contour and greater volar prominence of the metacarpal head in the palm occur with more proximally located fractures of equivalent angulation. Deformity is better tolerated in the fourth and fifth digits because of the arc of motion at their respective carpometacarpal (CMC) joints. Apex dorsal angulation of up to 50° can be tolerated if the fracture is close to the joint. In contrast, lack of CMC motion at the second and third metacarpals makes angulation greater than 15° unacceptable.

Although the most stable position for immobilization is with the MCP joint complete extension, the MCP joint should be splinted in approximately 70°–90° of flexion using an ulnar or radial gutter splint. Flexion is important because the MCP joint is apt to develop significant stiffness if held in extension for more than 7–10 days. The PIP and DIP joints may remain in slight flexion.

Reduction is limited to injuries in which pseudoclawing is present or angulation is significant (fourth metacarpal $> 30°$, fifth metacarpal $> 40°$) without pseudoclawing. Although these patients may benefit from closed reduction, they may achieve good clinical healing from immobilization without reduction. Therefore, patients should be informed that residual angulation and deformity are likely despite closed reduction. Such angulation and deformity are usually cosmetic and cause no functional impairment.

Reduction may be accomplished after administering a hematoma block or an ulnar nerve block. Once anesthesia is obtained, the fracture may be reduced using the 90–90 method. The MCP, PIP, and DIP joints are all flexed to 90°. Dorsally directed pressure is applied over the PIP joint while a volar-directed force is simultaneously applied over the fracture site. Using an ulnar gutter

splint, the wrist should be immobilized in 30° of extension with the MCP joint flexed to 90° and the interphalangeal (IP) joints in extension. A short-arm cast extended to the PIP joints may also be used.

2.2.3 Boxer's Fracture

The most common metacarpal fracture is the boxer's fracture, produced by a direct blow to the fifth metacarpal head with axial loading, resulting in a fractured metacarpal head or neck. Angular deformities from palmar protrusion of the metacarpal head may lead to pain in the palm when gripping. An angular deformity may also lead to extensor lag deformity. Acceptable degrees of angulation are 15° in the index and long finger metacarpal and 20°–40° in the ring and small finger metacarpals. Boxer's fractures can be reduced by flexing the proximal phalanx at the MCP joint and applying palmar pressure on the distal fragment while maintaining dorsal pressure on the proximal segment. Pin fixation can be applied as indicated. A plaster splint is applied for 3–4 weeks, followed by buddy tapes.

Metacarpal shaft fractures can be oblique, spiral, and transverse. Up to 3 mm of shortening and angulation can be tolerated. Metacarpal shortening and angular deformities result in changes in the mechanical efficiency of the tendons. Complications arising are similar to phalangeal type of fracture. An intraarticular comminuted fracture of the base of the thumb metacarpal is known as *Rolando's fracture*.

2.2.4 Carpal Fractures

Scaphoid Fractures

The scaphoid is the most commonly fractured carpal bone, accounting for 70–80% of all carpal bone injuries and 8% of all sports-related fractures. The scaphoid is unique in that it spans both carpal rows and is firmly anchored by ligaments on the volar surface. Because of its position, it is susceptible to injury when stress is applied to the dorsiflexed wrist, as occurs with a fall on an outstretched hand. The patient will complain of wrist pain, particularly over the anatomic snuffbox. There is often swelling and tenderness over the area as well. Motion is commonly limited.

Radiographs are essential in the evaluation of suspected scaphoid fractures. Routine series should include scaphoid views. These views elongate the scaphoid along its long axis. In 85% of scaphoid fractures, the navicular fat stripe (a radiolucent line parallel to the radial surface of the scaphoid bone on AP and oblique views) is laterally displaced or obliterated. A negative radiograph does not rule out a fracture.

If the clinical picture suggests a scaphoid fracture but initial radiographs are nonconfirmatory, the patient should be placed in a short-arm thumb spica cast for 10–14 days, and radiographs should be repeated out of the cast at that

time. If more expedient evaluation is necessary, a bone scan may be obtained at 72 h after the injury. A negative scan at that time virtually eliminates the possibility of the fracture.

Nondisplaced fractures of the distal third or scaphoid tubercle heal well and may be easily handled by the family practitioner. The patient may be placed in a short-arm thumb spica cast for approximately 10–12 weeks. It has been recommended that follow-up radiographs be obtained every 2–3 weeks until radiographic healing is demonstrated.

In contrast with the independent blood supply of the distal scaphoid, the proximal two thirds of the scaphoid relies on an intraosseous retrograde blood flow. Therefore, fractures through the waist and proximal portion of the scaphoid are prone to ischemia, resulting in prolonged healing and complications such as nonunion or avascular necrosis (AVN). In general, orthopedic consultation should be obtained for these proximal fractures because of the high risk of complications. The patient may be placed in a long-arm thumb spica splint until consultation is obtained.

Other indications for referral include a displaced or angulated fracture, development of nonunion after treatment, or suspicion of AVN or scapholunate dissociation. The primary care physician should also refer the patient for orthopedic consultation if he or she is uncomfortable managing nondisplaced scaphoid fractures.

Hook of the Hamate Fracture

An often overlooked carpal fracture is the hook of the hamate fracture, which produces hypothenar pain and tenderness. Patients with persistent ulnar-sided wrist pain after a fall on the palm should be evaluated with radiographs. Long-standing hook of the hamate fractures are usually treated with resection of the hook.

2.2.5 Pediatric Fractures

Pediatric fractures alter bone growth by affecting the epiphyseal plate. Phalangeal epiphyses are located in the proximal aspect of the bone. The metacarpal growth centers are located at the distal aspect of the bone, with the exception of the thumb, which has its growth center at the metacarpal base. The Salter–Harris epiphyseal classification describes five types of fractures. Type I is associated with complete separation of the epiphysis from the metaphysic, usually the result of shearing forces. These are usually reduced easily, produce no sequelae, and heal in 4–6 weeks of splinting. Type II is a fracture through the metaphysic but not into the epiphysis. The growth center is therefore not affected. This group is also treated with reductions and 4–6 weeks of immobilization. Type III is an intraarticular fracture involving the epiphysis. Accurate reduction and immobilization produce good results. Type IV is an intraarticular fracture that extends through the epiphysis and

the metaphysic. Type V is a compression fracture to the epiphyseal plate with no fracture to the metaphysic or epiphysis. These are the most severe and often result in early closure of the epiphyseal plate. Parents should be warned of the possibility of loss of growth of the bone in types IV and V fractures.

Deformities, such as angular, rotational, and lateral angulation, can also occur in children. Only angulation in the anteroposterior plane remodels. Rotational and lateral angular deformities do not remodel and should be accurately reduced. The physical performance of the fracture model in medical environment necessitates that three-dimensional hybrid fracture computation rather that simple fracture analysis would handle angular, rotational, and lateral angulation.

Triquetral Fractures

The triquetrum is the second most commonly fractured carpal bone. Unlike scaphoid fractures, a triquetral fracture seldom results in long-term problems. The typical mechanism of injury is a fall on the outstretched hand with the wrist in dorsiflexion and ulnar deviation. Most of these fractures are chip or avulsion fractures. Though uncommon, fracture of the body of the triquetrum may occur with blunt trauma and is associated with other wrist injuries.

Clinical examination may detect swelling and tenderness over the dorsal ulnar aspect of the wrist. Oblique radiographs are best for visualizing fractures of the triquetrum. Treatment entails short-arm cast immobilization for 4 weeks. If a fracture is not significantly displaced, a removable wrist splint may be used.

Hamate Fractures

The next most frequently fractured carpal bone is the hamate. This fracture is an unusual injury in the general population but is fairly common in athletes. Fracture of the hook is a significant injury and may be initially diagnosed as tendonitis or a simple sprain. The mechanism of injury may involve a fall on the outstretched hand or from compressive forces exerted by the handle of a club, racquet, or bat. The patient complains of pain over the hypothenar eminence or the dorsal ulnar aspect of the wrist. The pain is exacerbated with gripping and swinging movements.

2.2.6 Radial and Ulnar Fractures

In general, radial and ulnar fractures are usually displaced and unstable; therefore, most should be referred for surgical intervention and care. Acutely, the patient should be immobilized in a double sugar-tong splint and referred within 24–48 h to an orthopedic surgeon (Table 2.1).

Isolated distal radius fractures are frequently encountered. The most common distal radius fracture is the Colles' fracture. Resulting from a fall

Table 2.1. Guidelines for management of phalangeal fractures

	metacarpal neck fractures[a]	scaphoid fractures[a]	radial and ulnar fractures[a]
Radiographic view	AP, lateral, oblique	PA, lateral, scaphoid views	AP, lateral, oblique
Cast/splint type and position	Radial/ulnar gutter splint or cast; MCP flexed to 90° and PIP/DIP in slight flexion	Short-arm thumb spica cast or long-arm thumb spica cast for initial 6 weeks, then short-arm thumb spica cast	Double sugar-tong sp acutely
Length of immobilization	3–4 weeks	Distal and waist fractures 10–12 weeks	Average 6–8 weeks
Follow-up	7 days initial, then every 2 weeks	Every 2–3 weeks until radiographic union	Nondisplaced 3–5 days displaced, reduced 2 days
Repeat radiograph	At initial follow-up to assess for angulation and rotation	Every 2–3 weeks until radiographic union	
Orthopedic referral	Angulated or displaced fractures of the second or third metacarpal, malrotation, unable to maintain reduction	Proximal fractures, displaced or angulated fractures, nonunion, or evidence of AVN	Most require orthopedic care

AP, anterior–posterior; PA, posterior–anterior; MCP, metacarpophalangeal joint; PIP, proximal into distal interphalangeal joint

[a]The analyses must be considered the periods established with aspect time ratio Δt

on an outstretched hand, Colles' fractures may be evident by dorsal swelling, ecchymosis, and the typical "silver fork" deformity of the hand and wrist. Radiographs of the wrist (AP, lateral, and oblique) reveal an apex volar fracture with dorsal comminution and shortening of the radius. A Colles' fracture typically occurs within 2 cm of the distal radial articular surface. Definitive care may be provided by a family physician who is comfortable with reduction techniques. With short-arm casting, the family physician may also treat minimally displaced fractures in older individuals who may not tolerate operative fixation.

A less common fracture of the distal radius is the Smith's fracture. Unlike the Colles' fracture, the Smith's fracture results in an unstable fracture in

which the distal fragment is displaced volarly and proximally (apex dorsal). The mechanism of injury is often a direct blow to the dorsum of the wrist. These injuries should be referred to an orthopedic surgeon for care.

Two additional injuries that must be promptly identified and referred for definitive care are Galeazzi's fracture and Monteggia's fracture. Galeazzi's fracture involves a radial shaft fracture at the junction of the middle and distal thirds with disruption of the distal radioulnar joint. This injury is often the result of a fall on the extended, pronated wrist. It should be suspected if tenderness at the distal radius and distal radioulnar joint (DRUJ) is present. Radiographic findings include a transverse or oblique fracture at the junction of the middle and distal thirds seen on the AP view. Widening of the DRUJ on the AP view, fracture of the base of the ulnar styloid, radial shortening of more than 5 mm, and dislocation of the radius relative to the ulna on the lateral view suggest disruption of the DRUJ.

Monteggia's fracture includes a fracture of the ulnar shaft with dislocation of the radial head. A fall on the outstretched, extended, and pronated elbow is the usual mechanism. The radial head may be palpated in the antecubital fossa, and radial nerve neuropraxia may be present. Radiographs reveal an ulnar fracture and dislocation of the radial head. Because radial head dislocations are often missed, a high index of suspicion is required to diagnose this complicated injury.

2.2.7 Elbow Fractures

Most elbow fractures are complex and are often associated with a high rate of complications. The demand for near anatomic reduction of these injuries necessitates orthopedic referral in most cases. However, the skillful family physician may be able to manage certain types of fractures. The key is the ability to identify injuries that require referral.

2.2.8 Radial Head Fractures

Fractures of the radial head and neck often result from a fall on an outstretched hand or from a valgus compressive force. They may occur in association with an elbow dislocation. Swelling is often present on the lateral aspect of the elbow. Range of motion, especially forearm rotation and extension, is limited. Maximal tenderness over the radial head is invariably present. Severe crepitation or blockage of motion through flexion and extension may indicate the presence of displaced fragments. If the patient has significant wrist pain or central forearm pain, longitudinal radioulnar dissociation with disruption of the DRUJ (Essex–Lopresti fracture) should be suspected.

Anterior–posterior and lateral views of the elbow should be obtained. The fat pad sign may be the only clue to the existence of a radial head fracture. The fat pad sign occurs as the result of distension of the capsule by an intraarticular hemarthrosis. A small anterior fat pad may be present normally, but a large

sail-shaped lucency anterior to the joint suggests an effusion. A posterior fat pad is always abnormal.

Initial treatment of a nondisplaced fracture of the radial head or neck consists of immobilizing the patient in a long-arm posterior splint with the elbow at 90° (Table 2.1). The patient should be instructed on proper icing and elevation for the first 48 h. Significant pain relief may be obtained by aspirating blood from the joint and instilling a local anesthetic. This analgesia may also allow the patient to begin earlier range-of-motion exercises. The patient may begin forearm rotation out of the splint as soon as pain allows, usually within 3–5 days.

At 1 week, the patient may be transitioned to a sling used for comfort only. Repeat radiographs should be obtained to assess any displacement of the fracture fragments. Active range-of-motion exercises are initiated and include forearm pronation and supination and elbow flexion and extension. These exercises should be performed at least three or four times per day. The patient should be advised that pain and stiffness may continue for several weeks, but more patients can expect good to excellent results after 2–3 months of rehabilitation. Formal physical therapy may be indicated if adequate progress is not obtained.

The most common complication of these fractures is limited motion. Some loss of extension, 10°–15°, is common but generally does not affect function. If there is an associated osteochondral fracture of the capitellum that was not detected on initial radiographs, the patient may develop osteoarthritis, stiffness, and pain.

Orthopedic referral should be emergently obtained with any fracture–dislocation or any evidence of brachial artery or median or ulnar nerve injury. Other criteria for referral include fractures that are displaced more than 2 mm, involve more than one-third of the articular surface, are angulated more than 30°, are depressed more than 3 mm, or are severely comminuted. Mechanical block also requires referral.

2.2.9 Distal Humeral Fractures

Fractures of the distal humerus may be described as supracondylar, transcondylar, or intercondylar. The typical mechanism of injury involves hyperextension of the elbow during a fall on an outstretched hand, and, less commonly, a direct blow to the elbow. Anterior–posterior and lateral views are sufficient to confirm the diagnosis of fracture. One helpful landmark on the lateral view is an extension of the anterior humeral line through the capitellum. This line should transect the middle third of the capitellum; however, it may transect the anterior third or fall completely anterior to the capitellum in supracondylar injuries.

The most important aspect in acutely assessing these injuries is the neurovascular examination. All three major nerves of the arm and the brachial

artery may be injured in distal humeral fracture. Examination should proceed in a systematic fashion. First, distal pulses and capillary refill should be checked for diminished amplitude or cyanosis of the nail bed. Next, integrity of the radial nerve should be checked by observing extension of the fingers and sensation of the dorsal surface of the thumb. Median nerve function is evidenced by flexion of the fingers and wrist and sensation to the thumb and index fingers. Inability to adduct and abduct the fingers or decreased sensation of the fifth digit suggests ulnar nerve injury. Volkmann's ischemia, or acute volar compartment syndrome, should be suspected if there is marked swelling or palpable induration of the forearm flexors with pain on passive extension of the fingers.

2.2.10 Fractures of the Proximal Humerus

Proximal humeral fractures may occur at any age, but they increase in incidence with age, perhaps because osteoporosis is more prevalent in older adults. These injuries often result from a fall onto an outstretched hand or from a direct blow to the shoulder. Because most proximal humeral fractures are nondisplaced, relatively few complications occur, therefore, they may be managed comfortably by the family physician.

Several critical structures surround the humeral neck. They include the axillary nerve and artery, posterior brachial plexus, and radial nerve. Fortunately, injury to these structures is unusual unless significantly displaced fractures are present. Blood supply to the humeral head is similar to that of the scaphoid. It is supplied by branches of the axillary artery and enters distal to the anatomic neck of the humerus. As a consequence, fractures through the anatomic neck are at increased risk for avascular necrosis of the humeral head.

The patient with a proximal humeral fracture often presents with the typical mechanism of injury and complaints of diffuse shoulder pain. The upper arm is usually held against the body in an attempt to minimize movement. Swelling and large ecchymosis may also be present. If gross deformity or drooping of the arm is noted, shoulder dislocation should be suspected, because isolated fractures rarely present with these findings. Physical examination may detect well-localized tenderness over the site of injury. Integrity of the axillary nerve may be demonstrated by testing sensation over the middle third of the deltoid. Distal neurovascular status should be assessed as previously described. Radiographic evaluation should include a true AP view, a Y view, and an axillary view. A large proportion of proximal humeral fractures will appear impacted and occurs at the surgical neck or greater tuberosity. An understanding of the Neer classification system for proximal humeral fractures provides the family physician with criteria to differentiate between fractures that he or she may comfortably manage and those that need orthopedic referral. The system is based on the identification of the four major fragments of the proximal humeral – the greater tuberosity, the lesser tuberosity, the humeral head, and the shaft – and the number of these that are displaced. A fragment

is considered displaced if it is separated by more than 1 cm or angulated more than 45°. For example, if all the fracture fragments are nondisplaced, the injury is referred to as a Neer one-part fracture. If one fragment is displaced or angulated, it is classified as a Neer two-part fracture. The primary care physician may comfortably manage nondisplaced or Neer one-part fractures.

2.2.11 Fractures of the Clavicle

Fractures of the clavicle account for approximately 5% of all fractures seen by family physicians. Most clavicular fractures occur in the middle one-third of the bone, followed by the distal third, and then the proximal third.

Typical mechanisms of injury for fracture of the clavicle include a fall onto an outstretched hand, a fall onto the shoulder, or direct trauma to the clavicle. No correlation between the mechanism of injury and fracture pattern exists.

Fractures of the middle third of the clavicle are often easily diagnosed because of obvious downward and inward deformity of the shoulder. The patient complains of pain with any movement of the shoulder and holds the arm against the chest to prevent motion. Physical examination reveals edema and point tenderness over the fracture site. Crepitance and even motion of the fracture fragments may also be noted. If the fragments are widely displaced, ecchymosis or tenting of the skin may be present. Careful, passive range-of-motion assessment should demonstrate full range-of-motion, and motor strength should remain intact. If either of these is limited, a humeral fracture, shoulder dislocation, or muscle tear might be present.

Anterior–posterior and 45° cephalic tilt views should be obtained to confirm the diagnosis of clavicular fracture. The medial portion of the fractured clavicle is often displaced upward by the pull of the sternocleidomastoid muscle, and the distal fragment is displaced downward and medially, in children, greenstick fractures and plastic bowing may be seen.

2.2.12 Scapular Fractures

Fractures of the scapula are uncommon and often require significant force. Trauma from a direct blow or fall is the usual mechanism of injury. Fractures of the scapula may occur at several locations: the body, coracoid process, acromion, glenoid fossa, spine, or glenoid neck.

Because of the force necessary to fracture the scapula, these fractures are often associated with other traumatic injuries. The clinician must evaluate the patient for associated pheumothorax, fractured ribs, pulmonary contusion, clavicle fractures, and brachial plexus injury. Fractures of the body have the highest incidence of associated injury.

The patient often holds the injured extremity in adduction and resists any motion of the shoulder. Swelling, pain, and localized tenderness are present. Ecchymosis is variably present and is often minimal. If the shoulder appears flattened, a displaced glenoid neck or acromion fracture may be present.

Radiographic evaluation should include a true AP view, an axillary view, and a lateral view of the scapula. Fractures most commonly occur through the neck and body of the scapula.

Initial management of scapular fractures includes the use of ice, analgesics, and a sling or sling and swathe for comfort. Fortunately, most scapular fractures heal well without operative treatment. Certain fractures require orthopedic referral: a displaced glenoid neck fracture with an associated clavicular fracture, glenoid fractures involving more than 25% of the articular surface or associated with a subluxed humeral head, significantly displaced coracoid fractures, especially combined with complete acromioclavicular separation, and displaced acromion fractures.

In general, nondisplaced types I and II fractures may be cared for by the family physician. Type I fractures with displacement of the epiphysis, displaced type II fractures, or type II fractures involving a large proportion of the physis should be referred to an orthopedist. Because of the potential for growth complications, type II injuries in a younger child or involving the femur or tibia should also be referred for definitive care. All types III–V injuries require orthopedic intervention.

Distal radius fractures are the most common type of childhood fracture. They often result from a fall on an outstretched hand. They are often types I or II injuries. Most metaphyseal fractures are torus or buckle fractures. They may also take the form of a greenstick fracture. Clinical examination reveals point tenderness over the distal radius within 2.5 cm of the distal articular surface. Examination should include assessment of the elbow and shoulder for associated injuries. Anterior–posterior and lateral radiographs are used to confirm and classify the injury.

Treatment of nondisplaced torus fractures involves immobilization in a short-arm cast for 2–4 weeks. These fractures heal well without complications. If there is no clinical healing after 4 weeks of immobilization, radiographs should be repeated. Use of a volar splint with activity for an additional 2 weeks is advisable to reduce the risk for reinjury.

Nondisplaced greenstick fractures are treated like torus fractures. If both cortices are disrupted, however, rigid immobilization becomes more important to minimize the risk of angulation. Angulation of more than 15° should be corrected by closed reduction and may be referred for orthopedic care if the primary car physician is uncomfortable with reduction procedure.

2.2.13 Fractures of Hip

Fractures of the proximal femur, generally referred to as fractures of the hip, are classified first according to their anatomical location. Isolated fractures of the lesser or greater trochanter are not common and rarely require surgery; they can be associated with pathological disease. Avulsions of the lesser trochanter occur in immature children from the pull of the iliopsoas muscle

and can be treated nonoperatively. Fractures of the greater trochanter often result from direct trauma to the trochanter, usually are minimally displaced, and can be treated nonoperatively with protected weight-bearing on crutches until the symptoms subside. If a fracture of the greater trochanter is obvious on routine roentgenograms, then computed tomography (CT) or magnetic resonance imaging (MRI) should be performed to rule out an intertrochanteric element before the decision is made for nonoperative treatment. An unsuspected intertrochanteric fracture can drift into varus without open reduction and internal fixation.

Most proximal femoral fractures occur in elderly individuals as a result of only moderate or minimal trauma. In younger patients these fractures usually result from high-energy trauma. Despite similar locations of the fracture, the differences in low- and high-velocity injuries in older vs. younger patients outweigh the similarities. Most often than not, high-velocity injuries are more difficult to treat and are associated with more complications than low-velocity injuries, intertrochanteric and subtrochanteric femoral fractures.

The prognosis for each of the three major categories of hip fractures is entirely different. Intertrochanteric fractures usually unite if reduction and fixation are properly done, and, although malunions may be a problem, late complications are rare. A wide area of bone is involved, most of which is cancellous, and both fragments are well supplied with blood. Fractures of the neck of the femur are intracapsular and involve a constricted area with comparatively little cancellous bone and a periosteum that is thin or absent. Intertrochanteric femoral fractures have been estimated to occur in more than 200,000 patients each year only in the United States with reported mortality rates ranging from 15 to 20%. Boyd and Griffin (1949) classified fractures in the peritrochanteric area of the femur into four types.

Their classification, which follows, included all fractures from the extracapsular part of the neck to a point 5 cm distal to the lesser trochanter.

Type 1. Fractures that extend along the intertrochanteric line from the greater to the lesser trochanter. Reduction usually is simple and is maintained with little difficulty. Results generally are satisfactory.

Type 2. Comminuted fractures, the main fracture being along the intertrochanteric line but with multiple fractures in the cortex. Reduction of these fractures is more difficult because the comminution can vary from slight to extreme. A particularly deceptive form is the fracture in which an anteroposterior linear intertrochanteric fracture occurs, as in type 1, but with an additional fracture in the coronal plane, which can be seen on the lateral roentgenogram.

Type 3. Fractures that are basically subtrochanteric with at least one fracture passing across the proximal end of the shaft just distal to or at the lesser trochanter. Varying degrees of comminution are associated. These fractures usually are more difficult to reduce and result in more complications, both at operation and during convalescence.

Type 4. Fractures of the trochanteric region and the proximal shaft, with fracture in at least two planes, one of which usually is the sagittal plane and many be difficult to see on routine.

Fortunately, the most difficult types to manage, types 3 and 4, accounted for only about one-third of the trochanteric fractures in Boyd and Griffin's series.

Evans devised a widely used classification system based on the division of fractures into stable and unstable groups.

He divided the unstable fractures further into those in which stability could be restored by anatomical or near anatomical reduction and those in which anatomical reduction would not create stability. In an Evans type I fracture, the fracture line extends upward and outward from the lesser trochanter. In type II, the reversed obliquity fracture, the major fracture line extends outward and downward from the lesser trochanter. Type II fractures have a tendency toward medial displacement of the femoral shaft because of the pull of the adductor muscles.

Closed methods of treatment of intertrochanteric fractures have largely been abandoned. In the 1960s, Horowitz reported a mortality rate of 34.6% for trochanteric fractures treated by traction and 17.5% for those treated by internal fixation. Rigid internal fixation of intertrochanteric fractures with early mobilization of the patient should be considered standard treatment. Medical complications after internal fixation are fewer and less serious than those after nonoperative treatment. The rare exception to this is a medically unstable patient who is an extremely poor anesthetic and surgical risk.

One goal of operative treatment is strong stable fixation of fracture fragments. In this, the assessment of fixation process can easily be handled using the line element of the finite element analysis in which fragments can be meshed out. The following variables are listed to determine the strength of the fracture fragment implant assembly (1) bone quality, (2) fragment geometry, (3) reduction, (4) implant design, and (5) implant placement. The surgeon can control only the quality of the reduction and the choice of implant and its placement.

Open reduction and internal fixation of hip fractures should be done with the aim of obtaining rigid and stable internal fixation that will permit patients to be ambulatory within a short period. Most patients are allowed to sit in a chair the day after surgery. Mobilization is advantageous in preventing pulmonary complications, venous thrombosis, pressure sores, and generalized deconditioning. Protected weight-bearing may be permitted within 24 h after surgery, provided the fracture is well reduced and securely and rigidly fixed with stable internal fixation. Bony continuity should be reestablished so that the bone itself assumes a significant portion of the load.

It is important before treatment to distinguish by roentgenograms whether the intertrochanteric fracture is stable or unstable based on fracture geometry and whether reduction can restore cortical contact medially and posteriorly. The status of the lesser trochanter is important determining the stability

of reduction. If the lesser the trochanter is displaced with a large fragment, a significant cortical defect is present and the fracture geometry indicates a potentially unstable reduction. The surgeon should carefully inspect the roentgenograms for this defect or palpate this region to feel for a defect.

Reduction can be carried out by either open or closed means; with either, the objective is a stable reduction, whether anatomical or nonanatomical. Usually, closed reduction by manipulation should be attempted initially. After the anesthetized patient has been placed on the fracture table and the extremity has been secured in the traction foot piece, traction is exerted longitudinally on the abducted extremity.

2.2.14 Skull Fractures

Clinical Assessment and Significance

Skull fractures are local injuries caused by direct impact to the skull. The presence of a skull fracture does not always indicate underlying brain injury. However, the force required to fracture the skull is substantial, and all cases of skull fracture must be carefully evaluated to ensure that no additional injury is present. With increasing severity of head injury the likelihood of skull fracture increases, and the presence of a skull fracture by clinical examination, and if this can be done, it is highly likely that substantial underlying brain injury is also present. The pattern, extent, and type of skull fracture depend on the force of impact applied and the ratio of the impact force to the impact area. The fracture usually starts at the point of maximum impact.

Clinically significant skull fractures (1) result in intracranial air and pass through an air-filled space (e.g., sinus), (2) are associated with an overlying scalp laceration (open skull fracture), (3) are depressed below the level of the skull's inner table, or (4) overlie a major dural venous sinus or the middle meningeal artery.

The best way to assess for skull fractures is by plain skull radiographs; however, these X-ray films are expensive and time-consuming and should be ordered selectively. The most useful plain radiographs are those that help demonstrate a depressed skull fracture, the depth and extent of a penetrating injury, or the presence of an intracranial foreign body. A CT scan with bone windows also demonstrates these findings, and therefore patients undergoing CT do not require skull radiographs. If the patient is not likely to undergo CT and is at high risk for skull fracture, especially depressed fracture, skull radiographs may prove useful to detect clinically significant fractures, MRI is not as useful for detecting skull fractures.

Linear Fractures

A linear skull fracture is a single fracture that goes through the entire thickness of the skull. Linear skull fractures are clinically important if they cross the middle meningeal groove or major venous dural sinuses; they can disrupt

these vascular structures and cause the formation of epidural hematomas. Most other linear skull fractures are not clinically significant.

It is sometimes difficult to distinguish linear skull fractures demonstrated on radiographs from cranial sutures. In general, fractures are more lucent than vascular grooves and sutures. Sutures are usually less than 2 mm wide in adults; fractures are often 3 mm or greater in overall width and tend to be widest in the midportion and narrow at each end. Linear fractures are most common in the temporoparietal, frontal, and occipital regions of the skull and can usually be visualized on more than one radiographic view. In children, skull fractures heal within 3–6 months; in adults, complete healing may take up to 3 years.

Sutural diastase is the traumatic disruption of a cranial suture. In adults, sutural diastasis often involves the coronal or lambdoid sutures. Sutural diastasis usually occurs when a linear fracture extends into the suture line, and it is rare after sutures have undergone bony fusion.

Comminuted skull fractures are multiple linear fractures that radiate from the impact site. Usually this injury suggests a more sever blow to the head than that producing a single linear fracture.

A linear vault fracture substantially increases the risk of intracranial injury. If a skull fracture is detected, CT scan should be obtained, and the patient should be carefully observed for delayed complications of head trauma.

2.2.15 Depressed Fractures

Depressed skull fractures are clinically important because they predispose to significant underlying brain injury and to complications of head trauma, such as infection and seizures. When a depressed fracture occurs, traumatic impact drives the bony piece below the plane of the skull. The edges of the depressed portion of skull may become locked underneath the adjacent intact bone and fail to rebound into their previous position. As a result, the depressed piece of bone can penetrate tissue and lacerate the dura. Depressed skull fractures are usually caused by direct impact injury with small blunt objects, such as a hammer or a baseball bat. Most depressed skull fractures occur over the parietal or temporal regions. If the free piece of bone is depressed deeper than the adjacent inner table of the skull, most neurosurgeons consider this injury significant enough to require elevation.

On skull radiographs, depressed fractures may be difficult to visualize. The free piece of bone will demonstrate increased or double density, because it often overlaps the nonfractured bone or it is viewed relatively rotated from the rest of the adjacent cranium. Tangential views of the skull may increase the ability to visualize the fracture.

Depressed skull fractures can often be felt with palpation of the skull beneath a scalp laceration. This examination should be done cautiously to avoid driving a depressed bone fragment deeper into the cranial tissue. The clinical examination for a depressed skull fracture may be misleading. The

mobility of the scalp can result in nonalignment of the fracture with an overlying scalp laceration. As a result, the skull underlying the laceration may be normal, with the depressed area several centimeters away. Scalp swelling also may interfere with physical examination findings and hide any palpable bony defects. The signs and symptoms of a depressed skull fracture depend on the depth of depression of the free bone piece.

Depressed skull fractures may increase the risk for developing seizures. ED patients suspected of having a depressed skull fracture warrant prophylaxis for posttraumatic seizures, especially if they have altered level of consciousness or require chemical paralysis. Depressed skull fractures may also increase the risk for meningitis, and some consultants advocate the use of antibiotics in these patients.

2.2.16 Basilar Fractures

Basilar fractures are linear fractures at the base of the skull. The fracture usually occurs through the temporal bone, with bleeding into the middle ear producing hemotympanum. Often the fracture has caused a dural tear, which produces a communication between the subarachnoid space, the paranasal sinuses, and the middle ear. This offers a route for the introduction of infection into the cranial cavity and is suggested by a CSF leak. As with linear skull fractures, a basilar fracture is not always associated with significant underlying brain injury; these fractures are the result of considerable impact force, however, and TBI must be ruled out.

Basilar fractures can compress and entrap the cranial nerves that pass through the basal foramina, can dislocate the bones of the auricular chain, and can disrupt the otic canal or cavernous sinuses, with subsequent injury to cranial nerves 3–5. Fractures of the sphenoid bone can disrupt the intracavernous internal carotid artery, creating the potential for the formation of pseudoaneurysms or carotid venous fistulas. The diagnosis of a basilar skull fracture is based on associated clinical signs and symptoms.

Skull radiographs do not detect basilar fractures well. All patients with clinical evidence suggesting a basilar skull fracture should have a CT scan, to define the fracture and to rule out concurrent intracranial pathology, and should be admitted for observation. Because the basilar skull fracture may afford an entrance for bacteria, antibiotics are often considered. Most CSF leaks spontaneously resolve with no complications in 1 week. Therefore, in general, antibiotics are not given prophylactically during the first week of CSF rhinorrhea. If a patient with a previously diagnosed CSF leak returns to the ED later with fever, the diagnosis of meningitis should be strongly suspected and appropriate workup and antibiotic treatment initiated immediately.

2.2.17 Open Fractures

A skull fracture is open when a scalp laceration overlies a fracture. If the fracture has disrupted the dura, a communication exists between the external

environment and the brain. A fracture that disrupts the paranasal sinuses or the middle ear structures is also considered open. An open skull fracture requires careful irrigation and debridement. Blind probing of the wound should be avoided because this can introduce contaminants into the wound and can further depress comminuted fracture pieces.

2.2.18 Contusions

Contusions are bruises on the surface of the brain, usually caused by impact injury. Most often, contusions occur at the poles and the inferior surfaces of the frontal and temporal lobes where the brain comes into contact with bony protuberances in the base of the skull. If the contusion occurs on the same side as the impact injury, it is a coup injury; if it occurs on the opposite side, the contusion is a contrecoup injury. Contusions also develop often in the brain tissue that underlies a depressed skull fracture. Multiple areas of contused tissue may be produced with a single impact, often in association with other intracranial injuries.

Contusions are produced when parenchymal blood vessels are damaged, resulting in scattered areas of petechial hemorrhage and subsequent edema. Contusions develop in the gray matter on the surface of the brain and taper into the white matter. Often, subarachnoid blood is found overlying the involved gyrus. With time the associated hemorrhages and edema of a contusion can become widespread and serve as a nidus for hemorrhage or swelling, thus producing a local mass effect. Compression of the underlying tissue can cause local areas of ischemia, and tissue infarction is possible if the compression is significant and unrelieved. Eventually these ischemic areas become necrotic, and cystic cavities form within them.

Patients with contusions frequently are delayed in their clinical presentation. They may have sustained only a brief LOC, but the duration of posttraumatic confusion and obtundation may be prolonged. If contusions occur near the sensorimotor cortex, focal neurologic deficits may be present. Many patients with significant contusions make uneventful recoveries, but contusions may cause significant neurologic problems, including increased ICP, posttraumatic seizures, and focal deficits.

Noncontrast-enhanced CT is the best diagnostic test to discover contusions in the early posttraumatic period. These appear heterogenous and irregular because of mixed regions of hemorrhage, necrosis, and infarction. Often the surrounding edematous tissue appears hypodense. By posttrauma days 3 and 4, the blood located within the contusions has begun to degrade, and MRI becomes more useful.

2.2.19 Epidural Hematoma

Epidural hematomas (EDHs) are blood clots that form between the inner table of the skull and the dura. Most EDHs are caused by direct impact injury that

causes a forceful deformity of the skull. Eighty percent are associated with skull fractures across the middle meningeal artery or across a dural sinus and are therefore located in the temporoparietal region. The high arterial pressure of the bleeding vessel dissects the dura away from the skull, permitting the formation of the hematoma. The incidence of skull fractures in children with EDH is lower than in adults because the elasticity of the skull during childhood permits it to spring back to its original position instead of breaking after a significant impact.

2.2.20 Subdural Hematoma

Subdural hematomas (SDHs) are blood clots that form between the dura and the brain. Usually they are caused by the movement of the brain relative to the skull, as is seen in acceleration–deceleration injuries. These hematomas are common in patients with brain atrophy, such as alcoholic or elderly patients. In these patients the superficial bridging vessels traverse greater distances than in patients with no atrophy. As a result, the vessels are more prone to rupture with rapid movement of the head. Once ruptured, blood can fill the potential space between the dura and arachnoid.

2.2.21 Traumatic Subarachnoid Hemorrhage

Traumatic subarachnoid hemorrhage (TSAH) is defined as blood within the CSF and meningeal intima and probably results from tears of small subarachnoid vessels. TSAH is detected on the first CT scan in up to 33% of patients with severe traumatic brain injury and has an incidence of 44% in all cases of severe head trauma. It is therefore the most common CT scan abnormality seen after head injury. Data from the National Traumatic Coma Data Bank demonstrate a 60% unfavorable outcome in severely brain-injured patients in the presence of TSAH, compared with a 30% unfavorable outcome if no TSAH occurs. And increased incidence of skull fractures and contusions is found in patients with TSAH compared with patients with no TSAH. The amount of blood within the TSAH correlates directly with the outcome and inversely with the presenting GCS.

Patients may complain of headache and photophobia. The diagnosis is made by CT scan, with increased density noted within the basilar cisterns. Blood can also be seen within the interhemispheric fissures and sulci.

TSAH with no other brain injury does not generally carry a poor prognosis. The most serious complication of TSAH is aggravation of cerebral vasospasm, which may be severe enough to induce cerebral ischemia. Posttraumatic vasospasm is common, occurring about 48 h after injury and persisting for up to 2 weeks. Calcium channel blockers (e.g., nimodipine, nicardipine) have been used to prevent vasospasm after TSAH. Although a radiographic reduction of vasospasm is not consistently seen, the overall outcome of patients treated with these agents seems to be improved compared with no treatment.

2.2.22 Intracerebral Hematoma

Intracerebral hematomas (ICHs) are formed deep within the brain tissue and are usually caused by shearing or tensile forces that mechanically stretch and tear deep small-caliber arterioles as the brain is propelled against irregular surfaces in the cranial vault. Resulting small petechial hemorrhages subsequently coalesce to form ICHs. Almost 85% are in the frontal and temporal lobes. They are often found in the presence of extraaxial hematomas, and in many patients, multiple ICHs are present. Isolated ICHs may be detected in as many as 12% of all severe head trauma patients.

2.3 Dislocations

Dislocation can occur at any hand joint but is more frequently seen in the PIP joint. Dislocation is described based on the distal side in reference to the proximal articular surface. In dorsal dislocation, the base of the middle phalanx is dorsal in relation to the head of the proximal phalanx. Dorsal dislocation is classified into three groups. Type I is hyperextension of the joint with avulsion of the palmar plate. These injuries are usually stable after reduction and can be treated by a dorsal blocking splint for 3 weeks. Type II is a dorsal dislocation with rupture of the palmar plate with no contact present between the two articular surfaces. After reduction, if the joint is stable, a dorsal blocking splint prevents recurrence of the dislocation.

Large fragments or unstable dislocations require fragments stabilization with wires and pins. The analysis must include as fracture cracks with dowel elements.

Palmar dislocation occurs from longitudinal forces and results in the base of the middle phalanx positioned palmarly to the proximal phalangeal head. In this dislocation, the condyle of the proximal phalanx often becomes trapped between the central slip and the lateral bands of the finger extensor mechanism. If this trapping occurs, open reduction is necessary. After surgery, palmar dislocations should be placed in an extended position, particularly if the central slip is repaired. A separate analytical formulation is required for dislocation technique.

Acute patella dislocation in athletes usually occurs during the second decade, with the average age being 19–21 years. Lateral dislocation of the patella is the most common direction, although superior dislocation has been reported. Traumatic dislocations can occur with athletes of both normal and abnormal patellofemoral mechanics. The latter can dislocate with less trauma and soft tissue injury. Predisposing factors for dislocation include hypoplastic lateral femoral condyle, dysplastic vastus medialis oblique (VMO), patella alta, contracted iliotibial band, tight lateral retinaculum, valgus knee deformity, increased Q angle, generalized ligament laxity, lateral insertion patella tendon on tibia, and excess internal rotation of femur and external rotation of

tibia. There are two proposed mechanisms of injury for acute patella dislocation during athletic participation, indirect and direct. The indirect mechanism involves a powerful quadriceps contraction with an internally rotated femur. A direct blow mechanism to the medial side of the patella can also produce lateral dislocation. The combination of these two mechanisms can also occur.

Acute dislocations are mostly found with cutting sport activities. Many studies report no gender difference in outcome with acute dislocation. Only Hughston reported a higher incidence with males for acute patellar dislocations, which may reflect few competitive female athletic participants during the study period.

During field evaluations and diagnosis of acute patella dislocation can become challenging if spontaneous reduction of the patella has occurred. A large hemarthrosis may be present as well as tenderness of the medial retinaculum, medial facet of the patella, and along the lateral femoral condyle. Aspiration of the knee joint can be performed to allow for a better physical exam. The presence of fat droplets from the aspirate may be associated with an osteochondral fracture.

Standing anteroposterior and lateral radiographs are useful in assessing patella alta and baja. Tangential views of the patella are used to evaluate patellofemoral articulation and the presence of osteochondral fractures. However, studies have shown these fractures missed on initial radiographs. One study revealed 40% cases with osteochondral fractures not seen on X-ray. MRI may be useful to detect smaller osteochondral fractures, status of patellofemoral ligament, and bone contusions on the patella or femoral condyle. Radiographs of the noninjured knee to assess patella and trochlea morphology and patella tilt angle can be beneficial to determine predisposing factors for acute dislocations.

Osteochondral fractures can arise from the lateral femoral condyle or medial facet of the patella. During dislocation, the lateral edge of the patella can lever off the lateral femoral condyle, producing a chondral or osteochondral lesion from the condyle. During relocation, the medial patella facet can be sheared off by the condyle. Avulsion fracture off the medial retinaculum from the patella's medial edge can also occur.

2.3.1 Knee Fractures in Adolescent Athletes

Skeletally immature athletes have different bone characteristics than adults, predisposing them to unique fracture types sustained during sports trauma. Tibial intercondylar eminence fractures and physeal fractures of the adolescent knee will be discussed.

2.3.2 Tibial Intercondylar Eminence Fractures

Tibial intercondylar eminence fractures can occur in adolescents, and infrequently in adults. They are seen with sports trauma, including cycling

and motorized accidents. The mechanism of injury most commonly involves a strong valgus and external rotation of the tibia and can also occur with hyperflexion, hyperextension, or tibial internal rotation.

Distal femoral physeal fractures account for 1–5% of all physeal fractures. They occur in sports – related injuries – and motor vehicle accidents. The physis of the distal femur is the largest and fastest-growing physis of the body (70% growth of femur, and 37% growth of lower extremity) and is therefore at risk of angular deformities and leg-length discrepancy. Distal femoral physeal fractures most commonly occur during growth spurt of early adolescence where the physis is the weakest and competitive sports increase.

2.4 Instability

The joints of the fingers have capsular support for function and stability. This is provided by collateral ligaments on the radial and ulnar side, the palmar plate on the palmar side, and the balancing forces, can cause instability. Hence in fractural and dislocation analysis, instability shall be included.

2.5 Initial Theory of Elasticity in Three Dimensions: A Step-by-Step Analysis

Stresses in a three-dimensional system can be defined by constructing a Cartesian coordinate system at a point and considering the average forces acting on the faces of an infinitesimal cube surrounding that point. The stresses on each face of an infinitesimal cube around a point in a Cartesian coordinate system are shown in Fig. 2.2. As a general convention, the tensile stresses are considered positive normal stresses and they are presented as arrows pointing outward and along the surface normal for that face and are denoted with the corresponding coordinate as subscript, i.e., σ_x, σ_y, σ_z. Shear forces require two subscripts. The first subscript denotes the face on which the shear forces act and the second subscript indicates the direction in which the resultant shear is resolved. All the stresses shown in Fig. 2.2 are positive stresses.

Since the cube is infinitesimally small and the stresses are slowly varying across the cube, the moment equilibrium about the centroid of the cube gives the stress components represented in an array form as

$$\sigma_{ij} = \begin{pmatrix} \sigma_x & \tau_{xy} & \tau_{xz} \\ \tau_{xy} & \sigma_y & \tau_{yz} \\ \tau_{xz} & \tau_{yz} & \sigma_z \end{pmatrix}. \tag{2.6}$$

The above array has the transformation properties of a symmetric second-order tensor and is called the *stress tensor*. If we rotate the infinitesimal element, all the shear stresses vanish at one particular orientation of

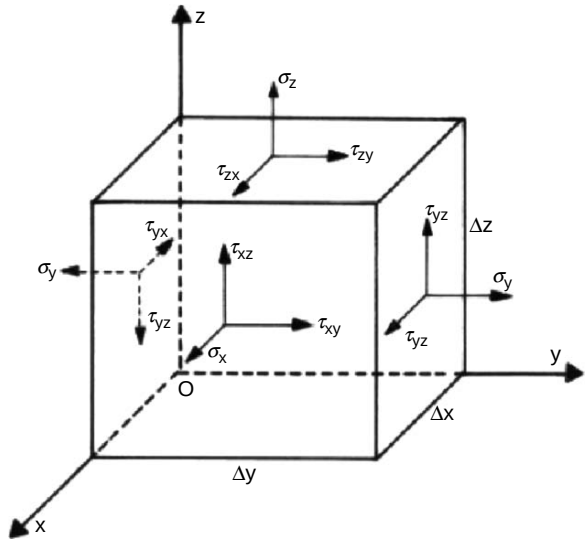

Fig. 2.2. Stress components in a three-dimensional Cartesian coordinate system

that element. In essence, in a three-dimensional stress system one can find three mutually perpendicular directions in which only normal stresses σ_1, σ_2, σ_3 are acting. Under these conditions where no shearing stresses are present, σ_1, σ_2, σ_3 are defined as principal stresses.

The stress tensor when the coordinate system is oriented in principal stress directions will be

$$\sigma_{ij} = \begin{pmatrix} \sigma_1 & 0 & 0 \\ 0 & \sigma_2 & 0 \\ 0 & 0 & \sigma_3 \end{pmatrix}, \tag{2.7}$$

where by convention, $\sigma_1 > \sigma_2 > \sigma_3$.

The strains are defined in terms of displacements of a point from its undistorted position and its derivatives. In the Cartesian system we can define the displacements in the x, y, and z directions as u, v, and w, respectively. For small displacements in a continuous body, the normal strains (also known as *dilatational strain*) in terms of displacement are given by

$$\varepsilon_x = \frac{\partial u}{\partial x}, \quad \varepsilon_y = \frac{\partial v}{\partial y}, \quad \varepsilon_z = \frac{\partial w}{\partial z}. \tag{2.8}$$

The engineering shear strains (measure of angular distortion) are given by

$$Y_{xy} = \frac{\partial v}{\partial x} + \frac{\partial u}{\partial y}, \quad Y_{xz} = \frac{\partial w}{\partial x} + \frac{\partial u}{\partial z}, \quad Y_{yz} = \frac{\partial w}{\partial y} + \frac{\partial v}{\partial z}. \tag{2.9}$$

An array that defines a complete state of strain and turns out to be symmetric is

$$\varepsilon_{ij} = \begin{pmatrix} \varepsilon_x & \frac{Y_{XY}}{2} & \frac{Y_{XZ}}{2} \\ \frac{Y_{XY}}{2} & \varepsilon_Y & \frac{Y_{YZ}}{2} \\ \frac{Y_{XZ}}{2} & \frac{Y_{YZ}}{2} & \varepsilon_Z \end{pmatrix}. \tag{2.10}$$

When defining stresses, it is assumed that a material medium exists for the stress to act against some resistance and the medium is continuous so that the derivatives defining strain in (2.8) and (2.9) are meaningful. The equations relating the state of stress with the state of strain are called the *constitutive equations*. While introducing the basic theory of elasticity, we will assume isotropic, homogenous, and elastic material medium. In addition, strains are assumed to be sufficiently small and it is also assumed that the normal and shear modes of deformation are uncoupled. A set of constitutive equation that can be applied to linear, elastic, and isotropic materials are referred to as "generalized Hook's law." In a three-dimensional Cartesian coordinate system, the strain is related to stress by the following relations:

$$\begin{aligned} \varepsilon_X &= \frac{1}{E}\left[\sigma_X - v\left(\sigma_y + \sigma_z\right)\right], \\ \varepsilon_y &= \frac{1}{E}\left[\sigma_y - v\left(\sigma_x + \sigma_z\right)\right], \\ \varepsilon_z &= \frac{1}{E}\left[\sigma_z - v\left(\sigma_x + \sigma_y\right)\right], \\ \Upsilon_{xy} &= \frac{1}{E_\mathrm{s}}\tau_{xy}, \\ \Upsilon_{xz} &= \frac{1}{E_\mathrm{s}}\tau_{xz}, \\ \Upsilon_{yz} &= \frac{1}{E_\mathrm{s}}\tau_{yz}, \end{aligned} \tag{2.11}$$

where E is the elastic modulus, v is Poisson's ratio, and E_s is the shear modulus.

If $\nu \neq 1/2$ then (2.11) can be inverted to express stress in terms of strain components

$$\begin{aligned} \sigma_x &= \frac{E}{1+v}\varepsilon_x + \frac{vE}{(1+v)(1-2v)}\left(\varepsilon_x + \varepsilon_y + \varepsilon_z\right), \\ \sigma_y &= \frac{E}{1+v}\varepsilon_y + \frac{vE}{(1+v)(1-2v)}\left(\varepsilon_x + \varepsilon_y + \varepsilon_z\right), \\ \sigma_z &= \frac{E}{1+v}\varepsilon_z + \frac{vE}{(1+v)(1-2v)}\left(\varepsilon_x + \varepsilon_y + \varepsilon_z\right), \\ \tau_{xy} &= E_\mathrm{s}\gamma_{xy}, \\ \tau_{xz} &= E_\mathrm{s}\gamma_{xz}, \\ \tau_{yz} &= E_\mathrm{s}\gamma_{yz}. \end{aligned} \tag{2.12}$$

The governing equations of elasticity can be simplified and formulated in two dimensions for the two special cases of plain strain and plain stress. If a body is in a state of plain strain such that all its strain components in the z direction are zero, then

$$\varepsilon_z = 0, \quad \gamma_{xz} = 0, \quad \gamma_{yz} = 0, \tag{2.13}$$

and we obtain the plane-strain form of Hook's law as

$$\begin{aligned}
\varepsilon_x &= \frac{1+v}{E}\left[(1-v)\,\sigma_x - v\sigma_y\right], \\
\varepsilon_y &= \frac{1+v}{E}\left[(1-v)\,\sigma_y - v\sigma_x\right], \\
\sigma_x &= \frac{vE}{(1+v)\,(1-2v)}\left[(1-v)\,\varepsilon_x + v\varepsilon_y\right], \\
\sigma_y &= \frac{vE}{(1+v)\,(1-2v)}\left[(1-v)\,\varepsilon_y + v\varepsilon_x\right], \\
\sigma_z &= v\,(\sigma_x + \sigma_y), \\
\tau_{xy} &= E_{\mathrm{s}}\gamma_{xy}.
\end{aligned} \tag{2.14}$$

If a body is in a state of plane stress such that all the stresses in the z direction are zero, then

$$\sigma_z = 0, \qquad \tau_{xz} = 0, \qquad \tau_{yz} = 0, \tag{2.15}$$

and

$$\begin{aligned}
\varepsilon_x &= \frac{1}{E}\,(\sigma_x - v\sigma_y), \\
\varepsilon_y &= \frac{1}{E}\,(\sigma_x - v\sigma_x), \\
\varepsilon_z &= -\frac{v}{E}\,(\sigma_x - v\sigma_y), \\
\sigma_x &= \frac{E}{1-v^2}\,(\varepsilon_x + v\varepsilon_y), \\
\sigma_y &= \frac{E}{1-v^2}\,(\varepsilon_y + v\varepsilon_x), \\
\tau_{xy} &= E_{\mathrm{s}}\gamma_{xy}.
\end{aligned} \tag{2.16}$$

The above section summarizes some of the basic equations that are required in the theory of linear elastic fracture mechanics. A textbook on the theory of elasticity should be referred to for a detailed study of this section.

2.6 Strength Theories and Design

The first half of this century exhibited considerable interest in developing practical techniques for dealing with more classical behavior of ductile and brittle materials and the justification of the various strength theories in design.

Ductile material, where the plastic deformation region on the stress–strain curve is well defined, was considered to have failed when the last point on the elastic portion of the curve was reached, i.e., plastic deformation began. A brittle material, on the other hand, was not considered completely failed until it had broken through a tensile fracture at ultimate strength. In compression the failure of a brittle material appears to be a shear fracture. The elongation of 5% was used as the arbitrary dividing line between ductile and brittle materials. However, under special circumstances involving low temperature, high strain rate, combined loading, residual stress, stress raisers, large size, or hydrogen absorption, ductile steel may show a brittle response.

The following four theories of elastic failure received probably the widest acceptance:

Maximum stress theory. Elastic failure occurs when the maximum working stress equals the yield value σ_y.

Maximum strain theory. Elastic failure occurs when the maximum tensile strain reaches (σ_y/E).

Maximum shear theory. Elastic failure occurs when the maximum shear stress becomes equal to $(0.5\sigma_y)$.

Distortion energy theory. Elastic failure occurs when the principal stresses $\sigma_1, \sigma_2, \sigma_3$ satisfy the following relation:

$$(\sigma_1 - \sigma_2)^2 + (\sigma_2 - \sigma_3)^2 + (\sigma_3 - \sigma_1)^2 = 2\sigma_y^2, \tag{2.17}$$

where

E	Modulus of elasticity, psi ($\mathrm{N\,mm^{-2}}$)
E_b	Bulk modulus, psi ($\mathrm{N\,mm^{-2}}$)
E_s	Shearing modulus of elasticity, psi ($\mathrm{N\,mm^{-2}}$)
ε	Engineering strain, $\mathrm{in.\,in.^{-1}}$ ($\mathrm{mm\,mm^{-1}}$)
ν	Poisson's ratio
σ	General symbol for normal stress, psi ($\mathrm{N\,mm^{-2}}$)
σ_y	Yield strength, psi ($\mathrm{N\,mm^{-2}}$)
$\sigma_1, \sigma_2, \sigma_3$	Principal stresses, psi ($\mathrm{N\,mm^{-2}}$)
τ	General symbol for shear stress, psi ($\mathrm{N\,mm^{-2}}$)

2.7 Initiation of Fracture

It is assumed that incipient fracture in ideally brittle materials takes place when the elastic energy supplied at the crack tip is equal to or greater than the energy required to create new crack surfaces. His analysis was based on a model in the form of an elliptical cutout of length $2h$, where for a very small dimension b (minor half-axis) and sharp corner radius, the cutout resembles a typical crack geometry. At this point the symbol h, standing for major half-axis of the ellipse, is changed to α, denoting crack length. This is a wide belief and cannot be universally accepted because of the elliptical shape. Additional conditions required in analyzing crack extension include:

– The stresses ahead of the crack tip must reach a critical magnitude.
– The total energy of the system must be reduced during crack extension.

The collapse stress can be the combined effect when the length of a through thickness crack (or notch depth) is greater than one-half of the width of the bone under examination. If $2W$ is the total width and a is the crack length, for a single edge crack widths, $a/w > 1.0$ is realistic for certain crack lengths, the stress in the net ligament might be sufficiently high to cause yielding. The process of ligament yielding in the collapse process and the stress that causes this is known as *the collapse stress*. It is extremely difficult to assess the initiation, development, and propagation of fracture (crack) in a bone in three dimensions. However, an attempt has been made to produce a three-dimensional cracking phenomenon in bones on the lines suggested in Appendix I. This criterion is extremely valuable in the three-dimensional finite element analysis in which variations can be accommodated for elastic, inelastic, and cracking phenomena in bone materials and in human bones, tissues, etc.

2.7.1 Bone Fracture: Material Analysis

The bone can be isotropic and orthotropic. If the material property of the both with and without tissues can be represented by $[D]$, then Tables 2.2–2.4 give these matrices as described. The four-parameter model given by Ottoson which is shown. Table 2.3 will form the basis of bone fractures such that the values of Y and E can have an input for bone materials. This concept in three dimensions was originally developed for unreinforced concrete. Since concrete like bones is also a brittle material, this approach has been validated by experiments developed for the medical environment. Material matrix for reinforcement in Appendix II can be used for INSERT for damaged parts of the bones. The same algorithm can also be adopted for dislocated parts need to be joined together. The strength of the INSERT can certainly be evaluated using the given finite element program in Appendix II. The material and cracking matrices based on OTTOSON'S MODEL can easily be associated with any computer package. The CRACK D is given as an algorithm on Appendix II.

2.8 Four-Parameter Model

An analytical failure model in which four parameters are included has been developed by Ottoson. The same chain rule of partial differentiation is applied. The gradient $\{\partial f/\partial\sigma\}$ is given by Bangash

$$C = \frac{\partial f}{\partial(\sigma)} = \frac{\partial f}{\partial I_1}\frac{\partial I_1}{\partial \sigma} + \frac{\partial f}{\partial J_2}\frac{\partial J_2}{\partial \sigma} + \frac{\partial f}{\partial \cos 3\theta}\frac{\partial \cos 3\theta}{\partial \sigma} \tag{2.18}$$

$$= a_1c_1 + a_2c_2 + a_3c_3,$$

Table 2.2. $[D]$: variable Young's modulus and Poisson's ratio

$$
\begin{array}{lllllll}
D_{11}=\frac{E_1\left(E'\right)^3-E_{\mathrm{cr}}}{v''} & D_{12}=\frac{vE_1E_2\left(E'\right)^2+E_{\mathrm{cr}}}{v''} & D_{13}=\frac{vE_1E_3\left(E'\right)^2+E_{\mathrm{cr}}}{v''} & D_{14}=0 & D_{15}=0 & D_{16}=0 \\
 & D_{22}=\frac{E_2E_3\left(E'\right)^2+E_{\mathrm{cr}}}{v''} & D_{23}=\frac{vE_2E_3\left(E'\right)^2+E_{\mathrm{cr}}}{v''} & D_{24}=0 & D_{25}=0 & D_{26}=0 \\
 & & D_{33}=\frac{E_3\left(E'\right)^3-E_{\mathrm{cr}}}{v''} & D_{34}=0 & D_{35}=0 & D_{36}=0 \\
 & & & D_{44}=G_{12} & D_{45}=0 & D_{46}=0 \\
 & & & & D_{55}=G_{23} & D_{56}=0 \\
 & & & & & D_{66}=G_{31}
\end{array}
$$

$$
\begin{aligned}
E_{\mathrm{cr}} &= v^2E_1E_2E_3E', \\
E' &= \left(E_1+E_2+E_3\right)/3, \\
v'' &= \left(E'\right)^3-2E_1E_2E_3v^2-E'v^2\left(E_1E_2+E_1E_3+E_2E_3\right), \\
G_{12} &= E_{12}/2\left(1+v\right), \\
E_{12} &= \left(E_1+E_2\right)/2, \\
G_{23} &= E_{23}/2\left(1+v\right), \\
E_{23} &= \left(E_2+E_3\right)/2, \\
G_{31} &= E_{31}/2\left(1+v\right), \\
E_{31} &= \left(E_3+E_1\right)/2,
\end{aligned}
$$

$$
\left[\begin{array}{lllllll}
D_{11}=\frac{\left(1-v_{23}v_{32}\right)}{\bar{v}}E_1 & D_{12}=\frac{\left(v_{12}+v_{12}v_{32}\right)}{\bar{v}}E_2 & D_{13}=\frac{\left(v_{13}+v_{12}v_{23}\right)}{\bar{v}}E_3 & D_{14}=0 & D_{15}=0 & D_{16}=0 \\
D_{21}=\frac{\left(v_{21}+v_{23}v_{31}\right)}{\bar{v}}E_1 & D_{22}=\frac{\left(1-v_{13}v_{31}\right)}{\bar{v}}E_2 & D_{23}=\frac{\left(v_{23}+v_{13}v_{21}\right)}{\bar{v}}E_3 & D_{24}=0 & D_{25}=0 & D_{26}=0 \\
D_{31}=\frac{\left(v_{31}+v_{21}v_{32}\right)}{\bar{v}}E_1 & D_{32}=\frac{\left(v_{32}+v_{12}v_{31}\right)}{\bar{v}}E_2 & D_{33}=\frac{\left(1-v_{12}v_{21}\right)}{\bar{v}}E_3 & D_{34}=0 & D_{35}=0 & D_{36}=0 \\
D_{41}=0 & D_{24}=0 & D_{43}=0 & D_{44} & D_{45}=0 & D_{46}=0 \\
D_{51}=0 & D_{52}=0 & D_{53}=0 & D_{54}=0 & D_{55} & D_{56}=0 \\
D_{61}=0 & D_{62}=0 & D_{63}=0 & D_{64}=0 & D_{65}=0 & D_{66}
\end{array}\right],
$$

$$
\bar{v}=1-v_{12}v_{21}-v_{13}v_{31}-v_{23}v_{32}-v_{12}v_{23}v_{31}-v_{21}v_{13}v_{32}.
$$

Due to symmetry of compliances, the following relations can be written:

$$\begin{aligned} E_1 v_{21} &= E_2 v_{12}, \qquad & D_{55} &= G_{23}, \\ E_2 v_{32} &= E_3 v_{23}, \qquad & D_{66} &= G_{13}, \\ E_3 v_{13} &= E_1 v_{31}. \end{aligned}$$

The values of G_{12}, G_{23}, and G_{13} are calculated in terms of modulus of elasticity and Poisson's ratio as follows:

$$G_{12} = \frac{1}{2}\left[\frac{E_1}{2(1+v_{12})} + \frac{E_2}{2(1+v_{21})}\right] = \frac{1}{2}\left[\frac{E_1}{2(1+v_{12})} + \frac{E_1}{2\left(\frac{E_1}{E_2}+v_{12}\right)}\right],$$

$$G_{23} = \frac{1}{2}\left[\frac{E_2}{2(1+v_{23})} + \frac{E_3}{2(1+v_{32})}\right] = \frac{1}{2}\left[\frac{E_2}{2(1+v_{23})} + \frac{E_2}{2\left(\frac{E_2}{E_3}+v_{23}\right)}\right],$$

$$G_{13} = \frac{1}{2}\left[\frac{E_3}{2(1+v_{31})} + \frac{E_1}{2(1+v_{13})}\right] = \left[\frac{E_3}{2(1+v_{31})} + \frac{E_2}{2\left(\frac{E_3}{E_1}+v_{31}\right)}\right].$$

For isotropic cases

$$E_1 = E_2 = E_3 = E,$$

$$\nu_{12} = \nu_{13} = \nu_{23} = \nu_{21} = \nu_{31} = \nu_{32} = \nu.$$

[$\boldsymbol{D}$]: **constant Young's modulus and Poisson's ratio**

$$[D] = \frac{E}{(1+v)(1-2v)} \begin{bmatrix} 1-v & v & v & 0 & 0 & 0 \\ v & 1-v & v & 0 & 0 & 0 \\ v & v & 1-v & 0 & 0 & 0 \\ 0 & 0 & 0 & \frac{1-2v}{2} & 0 & 0 \\ 0 & 0 & 0 & 0 & \frac{1-2v}{2} & 0 \\ 0 & 0 & 0 & 0 & 0 & \frac{1-2v}{2} \end{bmatrix}.$$

Table 2.2. *Continued*

Bulk and shear moduli

$$[D] = \begin{bmatrix} K+\frac{4}{3}G & K-\frac{2}{3}G & K-\frac{2}{3}G & 0 & 0 & 0 \\ K-\frac{2}{3}G & K+\frac{4}{3}G & K-\frac{2}{3}G & 0 & 0 & 0 \\ K-\frac{2}{3}G & K-\frac{2}{3}G & K+\frac{4}{3}G & 0 & 0 & 0 \\ 0 & 0 & 0 & G & 0 & 0 \\ 0 & 0 & 0 & 0 & G & 0 \\ 0 & 0 & 0 & 0 & 0 & G \end{bmatrix}.$$

For plane stress

$$[D] = \frac{E}{1-v_2} \begin{bmatrix} 1 & v & 0 \\ v & 1 & 0 \\ 0 & 0 & \frac{1-v}{2} \end{bmatrix}.$$

For plane strain

$$[D] = \frac{E(1-v)}{(1+v)(1-2v)} \begin{bmatrix} 1 & \frac{v}{1-v} & 0 \\ \frac{v}{1-v} & 1 & 0 \\ 0 & 0 & \frac{1-2v}{2(1-v)} \end{bmatrix}.$$

For axisymmetric cases

$$[D] = \frac{E}{(1+v))(1-2v)} \begin{bmatrix} 1-v & v & v & 0 \\ v & 1-v & v & 0 \\ v & v & 1-v & 0 \\ 0 & 0 & 0 & \frac{1-2v}{2} \end{bmatrix}.$$

Table 2.3. Material matrices $[D]$ and $[D^*]$ cracking matrices

Uncracked material matrix $[D]$

$$[D] = \begin{bmatrix} D_{11} & D_{12} & D_{13} & 0 & 0 & 0 \\ D_{21} & D_{22} & D_{23} & 0 & 0 & 0 \\ D_{31} & D_{32} & D_{33} & 0 & 0 & 0 \\ 0 & 0 & 0 & D_{44} & 0 & 0 \\ 0 & 0 & 0 & 0 & D_{55} & 0 \\ 0 & 0 & 0 & 0 & 0 & D_{66} \end{bmatrix}.$$

Cracked material matrices $[D^*]$:

Cracks in principal direction "1"

$D^*_{11} = D^*_{12} = D^*_{13} = D^*_{21} = D^*_{31} = 0,$
$D^*_{22} = D_{22} - D_{12}D_{12}/D_{11},$
$D^*_{33} = D_{33} - D_{13}D_{13}/D_{11},$
$D^*_{23} = D_{23} - D_{12}D_{13}/D_{11},$
$D^*_{44} = \beta' D_{44},$
$D^*_{55} = D_{55},$
$D^*_{66} = \beta' D_{66}.$

Cracks in principal direction "3"

$D^*_{33} = D^*_{13} = D^*_{31} = D^*_{23} = D^*_{31} = 0,$
$D^*_{11} = D_{11} - D_{13}D_{13}/D_{33},$
$D^*_{22} = D_{22} - D_{23}D_{23}/D_{33},$
$D^*_{12} = D_{12} - D_{13}D_{23}/D_{33},$
$D^*_{21} = D^*_{12},$
$D^*_{44} = \mathrm{D}_{44},$
$D^*_{55} = \beta' D_{55},$
$D^*_{66} = \beta' D_{66}.$

Cracks in principal direction "2"

$D^*_{22} = D^*_{12} = D^*_{21} = D^*_{23} = D^*_{32} = 0,$
$D^*_{11} = D_{11} - D_{21}D_{21}/D_{22},$
$D^*_{33} = D_{33} - D_{23}D_{23}/D_{22},$
$D^*_{13} = D_{13} - D_{12}D_{23}/D_{22},$
$D^*_{31} = D^*_{13},$
$D^*_{44} = \beta' D_{44},$
$D^*_{55} = \beta' D_{55},$
$D^*_{66} = D_{66}.$

Cracks in principal directions "1" and "2"

$D^*_{11} = D^*_{22} = D^*_{12} = D^*_{21} = 0,$
$D^*_{13} = D^*_{31} = D^*_{23} = D^*_{32} = 0,$
$D^*_{33} = D_{33} - D_{13}D_{13}/D_{11} - D_{23}D_{23}/D_{22},$
$D^*_{44} = \beta' D_{44},$
$D^*_{55} = \beta' D_{55},$
$D^*_{66} = \beta' D_{66}.$

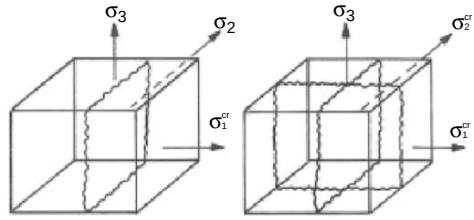

(a) One crack (b) Two cracks

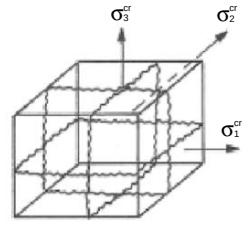

(c) Three cracks

Table 2.3. *Continued*

Cracks in principal directions "2" and "3"	Cracks in principal directions "3" and "1"
$D^*_{22} = D^*_{33} = D^*_{23} = D^*_{32} = 0,$	$D^*_{11} = D^*_{33} = D^*_{12} = D^*_{21} = 0,$
$D^*_{13} = D^*_{31} = D^*_{12} = D^*_{21} = 0,$	$D^*_{13} = D^*_{31} = D^*_{23} = D^*_{31} = 0,$
$D^*_{11} = D_{11} - D_{21}D_{21}/D_{22} - D_{13}D_{13}/D_{33},$	$D^*_{22} = D_{22} - D_{12}D_{12}/D_{11} - D_{23}D_{23}/D_{33},$
$D^*_{44} = \beta' D_{44},$	$D^*_{44} = \beta' D_{44},$
$D^*_{55} = \beta' D_{55},$	$D^*_{55} = \beta' D_{55},$
$D^*_{66} = \beta' D_{66}.$	$D^*_{66} = \beta' D_{66}.$
Cracks in all three principal directions	
$[D^*] = [0].$	

$$
\begin{aligned}
a_1 &= \frac{\partial f}{\partial I_1} = \frac{B}{f_c^1}, \\
a_2 &= \frac{\partial f}{\partial J_2} = \frac{\partial}{\partial J_2}\frac{AJ_2}{f_c^{12}} + \frac{\partial}{\partial J_2}\frac{\lambda J_2^{1/2}}{f_c^{12}} = \frac{A}{f_c^{12}} + \frac{\partial}{\partial J_2}\frac{\lambda J_2^{1/2}}{f_c^{12}}, \qquad (2.19)\\
\frac{\partial}{\partial J_2}\frac{\lambda J_2^{1/2}}{f_c^{12}} &= \frac{\lambda_{1/2} J^{1/2}}{f_c^1} + \frac{J^{1/2}}{f_c^1}\frac{\partial(\lambda)}{\partial J_2}, \\
\frac{\partial(\lambda)}{\partial J_2} &= \frac{\partial}{\partial J_2}\left\{K_1 \cos\left[1/3\cos^{-1}\left[K\frac{3\sqrt{3}}{2}\frac{\sqrt{3}}{J_2^{3/2}}\right]\right]\right\},
\end{aligned}
$$

where

$$
\begin{aligned}
\cos 3\theta \geq 0 = -K_1 \sin(P)\frac{1}{3}\frac{(-1)}{\sqrt{1-t^2}}K_2\left[\frac{3}{2}\right]\sqrt{3}J_3\left[-\frac{3}{2}\right]J_2^{-6/2} \\
= -K_1 \sin(P)\frac{1}{3J}\left[K_2\frac{3\sqrt{3}}{2}\frac{\sqrt{3}}{J_2^{3/2}}\right]\left[\frac{1}{\sqrt{1-t^2}} + \frac{3}{2}\right] \\
= -K_1\frac{t}{\sqrt{1-t^2}}\sin(P)\frac{1}{2J} = \frac{-K_1}{2J}\frac{t}{\sqrt{1-t^2}}\sin(P), \\
t = K_2\frac{3\sqrt{3}}{2}\frac{J_3}{J_2^{3/2}},
\end{aligned}
$$

$$
\begin{aligned}
\frac{\partial(\lambda)}{\partial J_2} = \frac{\partial}{\partial J_2} \quad \left\{K_1\cos\left[\frac{\pi}{3} - \frac{1}{3^{\cos -1}}\left[K\frac{3\sqrt{3}}{2}\frac{J_3}{J_2^{3/2}}\right]\right]\right\}, \quad \cos\theta \leq 0 \qquad (2.20)\\
= K_1(-\sin P)\left[-\frac{1}{3}\frac{(-1)}{\sqrt{1-t^2}}\left[-K_2\frac{3\sqrt{3}}{2}J_3\right]\left[-\frac{3}{2}\right]J^{-6/2}\right] \\
= \frac{K_1}{T}(-\sin P)\left[-\frac{1}{3}\frac{t}{\sqrt{1-t^2}}\left[-\frac{3}{2}\right]\right] = -\frac{K}{2J}(\sin P)\frac{t}{\sqrt{1-t^2}}.
\end{aligned}
$$

Table 2.4. Stress and strain transformation matrices $\{T''\}\{T''\}$

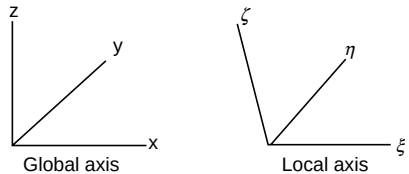

	x	y	z
ξ	l_1	m_1	n_1
η	l_2	m_2	n_2
ξ	l_3	m_3	n_3

Direction cosines of the two axes are given by

$$
\begin{aligned}
l_1 &= \cos(\xi, x) m_1 = \cos(\xi, y) n_1 = \cos(\xi, z), \\
l_2 &= \cos(\eta, x) m_1 = \cos(\eta, y) n_1 = \cos(\eta, z), \\
l_3 &= \cos(\zeta, x) m_1 = \cos(\zeta, y) n_1 = \cos(\zeta, z).
\end{aligned}
$$

The following relationships can be written for local and global strain and stress vectors

$$
\left\{\varepsilon'_x\right\} = [T\,]\{\varepsilon_x\}, \quad \{\sigma_x\} = [T\,]^T \left\{\sigma'_x\right\}
$$

and also

$$
\left\{\sigma'_x\right\} = [T\,]\{\sigma_x\}, \quad \{\varepsilon_x\} = [T\,]^T \left\{\varepsilon'_x\right\},
$$

$$
\left[T''\right] = \begin{bmatrix}
l_1^2 & m_1^2 & n_1^2 & l_1 m_1 & m_1 n_1 & l_1 n_1 \\
l_2^2 & m_2^2 & n_2^2 & l_2 m_2 & m_2 n_2 & l_2 n_2 \\
l_3^2 & m_3^2 & n_3^2 & l_3 m_3 & m_3 n_3 & l_3 n_3 \\
2l_1 l_2 & 2m_1 m_2 & 2n_1 n_2 & l_1 m_2 + l_2 m_1 & m_1 n_2 + m_2 n_1 & l_1 n_2 + l_2 n_1 \\
2l_2 l_3 & 2m_2 m_3 & 2n_2 n_3 & l_2 m_3 + l_3 m_2 & m_2 n_3 + n_2 m_3 & l_2 n_3 + l_3 n_2 \\
2l_1 l_3 & 2m_1 m_3 & 2n_1 n_3 & l_1 m_3 + m_1 l_3 & m_1 n_3 + m_3 n_1 & l_1 n_3 + n_1 l_3
\end{bmatrix},
$$

Table 2.4. *Continued*

$$\left[T''\right] = \begin{bmatrix} l_1^2 & m_1^2 & n_1^2 & 2l_1m_1 & 2m_1n_1 & 2l_1n_1 \\ l_2^2 & m_2^2 & n_2^2 & 2l_2m_2 & 2m_2n_2 & 2l_2n_2 \\ l_3^2 & m_3^2 & n_3^2 & 2l_3m_3 & 2m_3n_3 & 2l_3n_3 \\ l_1l_2 & m_1m_2 & n_1n_2 & l_1m_2 + l_2m_1 & m_1n_2 + n_1m_2 & l_1n_2 + l_2n_1 \\ l_2l_3 & m_2m_3 & n_2n_3 & l_2m_3 + l_3m_2 & m_2n_3 + n_2m_3 & l_2n_3 + l_3n_2 \\ l_1l_3 & m_1m_3 & n_1n_3 & l_1m_3 + l_3m_1 & m_1n_3 + m_3n_1 & l_1n_3 + n_1l_3 \end{bmatrix},$$

where $\{u_1\}$ is the vector of displacements in element Cartesian coordinated and $\{u\}$ the vector of displacements in global Cartesian coordinates.

$$[T_R] = \begin{bmatrix} T & 0 & 0 & 0 \\ 0 & T & 0 & 0 \\ 0 & 0 & T & 0 \\ 0 & 0 & 0 & T \end{bmatrix},$$

$[T]$ is defined by:

$$C_2 = \frac{L_{xy}}{L}, \quad [T] = \begin{bmatrix} C_1C_2 & S_1C_2 & S_2 \\ (-C_1S_2 - S_1S_3) & (C_1C_3 - S_1S_2S_3) & S_3C_2 \\ (S_1S_3 - C_1S_2C_3) & (-S_1S_2C_3 - C_1S_3) & C_3S_2 \end{bmatrix},$$

$$C_3 = \cos(\theta).$$

X_1, etc. $= x$ coordinate of node 1, etc.,
$L_{xy} =$ projection of length onto X–Y plane,
$d = 0.0001L$,
$\theta =$ input.

If a third node is given, θ is not used. Rather C_3 and S_3 are defined using

$\{V_1\} =$ vector from origin to node 1,
$\{V_2\} =$ vector from origin to node 2,
$\{V_3\} =$ vector from origin to node 3,
$\{V_4\} =$ unit vector parallel to global Z-axis, in which case it is parallel to the X-axis,

Then,

$\{V_5\} = \{V_3\} - \{V_1\} =$ vector between nodes I and K,
$\{V_6\} = \{V_2\} - \{V_1\} =$ vector along element X-axis,
$\{V_7\} = \{V_6\} \times \{V_4\}$,
$\{V_8\} = \{V_6\} \times \{V_5\}$,
$\{V_9\} = \{V_7\} \times \{V_8\}$.

$$S_1 = \left\{ \begin{array}{ll} \frac{Y_2 - Y_1}{L_{XY}} & \text{if } L_{xy} > d \\ 0.0 & \text{if } L_{xy} < d \end{array} \right\},$$

$$S_2 = \frac{Z_2 - Z_1}{L},$$

$$S_3 = \sin(\theta),$$

and

$$C_3 = \frac{\{V_7\} \cdot \{V_8\}}{|\{V_7\}|\,|\{V_8\}|},$$

$$C_1 = \left\{ \begin{array}{ll} \frac{X_2 - X_1}{L_{XY}} & \text{if } L_{xy} > d \\ 1.0 & \text{if } L_{xy} < d \end{array} \right\},$$

$$S_3 = \frac{\{V_6\} \cdot \{V_9\}}{|\{V_6\}|\,|\{V_9\}|}.$$

The $\times$ and $\cdot$ refer to vector cross and dot products, respectively. Thus, the element stiffness matrix in global coordinated becomes

$$\begin{aligned} [K_{\mathrm{e}}] &= [T_R]^T [K_1] [T_R], \\ [M_{\mathrm{e}}] &= [T_R]^T [M_1] [T_R], \\ [S_{\mathrm{e}}] &= [T_R]^T [S_1] [T_R], \\ [F_{\mathrm{e}}] &= [T_R]^T [F_1]. \end{aligned}$$

Table 2.4. *Continued*

Orders of degrees of freedom for bone element

The order of degrees (DOFs) is shown in the figure below. The stiffness matrix in element coordinates (Przemieniecki) is

$$
\begin{bmatrix}
AE/L & & & & & & & & & & & \\
0 & a_z & & & & & & & & & & \\
0 & 0 & a_y & & & & & & & & & \\
0 & 0 & 0 & GJ/L & & & & & \text{Symmetric} & & & \\
0 & 0 & d_y & 0 & e_y & & & & & & & \\
0 & c_z & 0 & 0 & 0 & e_z & & & & & & \\
-AE/L & 0 & 0 & 0 & 0 & 0 & AE/L & & & & & \\
0 & b_z & 0 & 0 & 0 & d_z & 0 & a_z & & & & \\
0 & 0 & b_y & 0 & c_y & 0 & 0 & 0 & a_y & & & \\
0 & 0 & 0 & -GJ/L & 0 & 0 & 0 & 0 & 0 & GJ/L & & \\
0 & 0 & d_y & 0 & f_y & 0 & 0 & 0 & c_z & 0 & e_y & \\
0 & c_z & 0 & 0 & 0 & f_z & 0 & d_y & 0 & 0 & 0 & e_z
\end{bmatrix},
$$

where

$A =$ cross-sectional area,
$E =$ Young's modulus,
$L =$ element length,
$G =$ shear modulus 8,
$r_y = \sqrt{I_{YY}/A} =$ radius of gyration 12,
$r_z = \sqrt{I_{zz}/A} =$ radius of gyration,
$[M_l] = M_t$,
$r_z = \sqrt{I_{zz}/A} =$ radius of gyration, and
$[M_l] = M_t$.

$$
\begin{bmatrix}
1/3 & & & & & & & & & & & \\
0 & A_z & & & & & & & & & & \\
0 & 0 & A_y & & & & & & & & & \\
0 & 0 & 0 & J_x/3A & & & & & \text{Symmetric} & & & \\
0 & 0 & -C_y & 0 & E_y & & & & & & & \\
0 & C_z & 0 & 0 & 0 & E_z & & & & & & \\
1/6 & 0 & 0 & 0 & 0 & 0 & 1/3 & & & & & \\
0 & B_z & 0 & 0 & 0 & D_z & 0 & A_z & & & & \\
0 & 0 & B_y & 0 & -D_y & 0 & 0 & 0 & A_y & & & \\
0 & 0 & 0 & J_x/6A & 0 & 0 & 0 & 0 & 0 & J_x/3A & & \\
0 & 0 & D_y & 0 & F_y & 0 & 0 & 0 & C_Y & 0 & E_y & \\
0 & -D_z & 0 & 0 & 0 & F_z & 0 & -C_z & 0 & 0 & 0 & E_z
\end{bmatrix},
$$

Table 2.4. *Continued*

where

$M_t = (pA + m)L(1 - \varepsilon^{\text{in}})$,
$p =$ density,
$m =$ added mass,
$\varepsilon^{\text{in}} =$ prestrain,
$A_z = A(r_z, \phi'_y)$,

$A_y = A(r_y, \phi'_z)$,
$B_z = B(r_z, \phi'_y)$,
$\vdots$
$F_z = F(r_z, \phi'_y)$,
$F_y = F(r, \phi'_z)$,

and where

$$A(r, \phi') = \frac{13/35 + 7/10\phi' + 1/3\phi'^2 = 6/5(r/L)^2}{(1 + \phi')^2},$$

$$B(r, \phi') = \frac{9/70 + 3/10\phi' + 1/6\phi'^2 - 6/5(r/L)^2}{(1 + \phi')^2},$$

$$C(r, \phi') = \frac{11/210 + 11/120\phi' + 1/24\phi'^2 + (1/10 - 1/2(r/L)^2)}{(1 + \phi')^2},$$

$$D(r, \phi') = \frac{13/420 + 3/40\phi' + 1/24\phi'^2 - (1/10 - 1/2\phi'(r/L)^2)L}{(1 + \phi')^2},$$

$$E(r, \phi') = \frac{1/105 + 1/60\phi' + 1/120\phi'^2 + (2/15 + 1/6\phi' + 1/3\phi'^2(r/L)^2)L^2}{(1 + \phi')^2},$$

$$F(r, \phi') = -\frac{1/140 + 1/60\phi' + 1/120\phi'^2 + (1/30 + 1/6\phi' - 1/6\phi'^2(r/L)^2)L^2}{(1 + \phi')^2},$$

$$J = \text{torsional moment of inertia} = \left\{ \begin{matrix} J_x \text{ if } I_x = 0 \\ I_x \text{ if } I_x \neq 0 \end{matrix} \right\},$$

where

$I_x =$ input as IXX,
$J_x =$ polar moment of inertia $= I_y + I_z$,
$a_z = a(I_z, \phi'_y)$,
$a_y = a(I_y, \phi'_z)$,
$b_z = b(I_z, \phi'_y)$,
$\vdots$
$f_z = f(I_z, \phi'_y)$,
$f_y = f(I_y, \phi'_z)$,
$A_i^{\mathrm{s}} =$ shear area normal to direction $i = A/F_i^{\mathrm{s}}$,
$F_i^{\mathrm{s}} =$ shear coefficient,
$I_i =$ moment of inertia normal to direction i,
$a(I, \phi') = \frac{12EI}{L^3(1+\ ')}$,
$b(I, \phi') = \frac{-12EI}{L^3(1+\ ')}$,
$c(I, \phi') = \frac{6EI}{L^2(1+\ ')}$,
$d(I, \phi') = \frac{-6EI}{L^2(1+\ ')}$,
$e(I, \phi') = \frac{(4+\ ')EI}{L(1+\ ')}$,
$f(I, \phi') = \frac{(2-\ ')EI}{L(1+\ ')}$.

$$\phi'_y = \frac{12EI_z}{GA_z^{\mathrm{s}}L^2},$$

$$\phi'_z = \frac{12EI_y}{GA_y^{\mathrm{s}}L^2}.$$

Local to global conversion (ANSYS User's Manual, courtesy STRUCOM, London)
The element coordinates are related to the global coordinated by

$$\{u_1\} = [T_R]\{u\}.$$

Two-dimensional elastic beam (courtesy STRUCOM, London)

Table 2.4. *Continued*

Element matrices and load vectors

The element stiffness matrix in element coordinates is

$$[K_1] = \begin{bmatrix} \frac{AE}{L} & 0 & 0 & \frac{AE}{L} & 0 & 0 \\ 0 & \frac{12EI}{L^3(1+\Phi')} & \frac{6EI}{L^2(1+\Phi')} & 0 & \frac{12EI}{L^3(1+\Phi')} & \frac{6EI}{L(1+\Phi')} \\ 0 & \frac{6EI}{L^2(1+\Phi')} & \frac{EI\left(4+\Phi'\right)}{L(1+\Phi')} & 0 & \frac{6EI}{L^2(1+\Phi')} & \frac{EI\left(2-\Phi'\right)}{L(1+\Phi')} \\ \frac{AE}{L} & 0 & 0 & \frac{AE}{L} & 0 & 0 \\ 0 & \frac{12EI}{L^3(1+\Phi')} & \frac{6EI}{L^2(1+\Phi')} & 0 & \frac{12EI}{L^3(1+\Phi')} & \frac{6EI}{L^2(1+\Phi')} \\ 0 & \frac{6EI}{L^2(1+\Phi')} & \frac{EI\left(2-\Phi'\right)}{L(1+\Phi')} & 0 & \frac{6EI}{L^2(1+\Phi')} & \frac{EI\left(4+\Phi'\right)}{L(1+\Phi')} \end{bmatrix} ,$$

where $[K]$ is the shear and torsion included for line element.

$$[D] = \begin{bmatrix} \frac{EA}{L} & & & & & & & & & & & \\ 0 & \frac{12EI_\varepsilon}{L^3(1+\bar{\tau}_\eta)} & & & & & & & & & & \\ 0 & 0 & \frac{12EI_\varepsilon}{L^3(1+\bar{\tau}_\eta)} & & & & & & & & & \\ 0 & 0 & 0 & \frac{GJ}{L} & & & & & & & & \\ 0 & 0 & \frac{-6EI_\eta}{L^2(1+\tau_\varepsilon)} & 0 & \frac{(4+\bar{\tau}_\eta EI_\eta)}{L(1+\bar{\tau}_\eta)} & & & & & & & \\ 0 & \frac{6EI_\varepsilon}{L^2(1+\tau_\eta)} & 0 & 0 & 0 & \frac{(4+\bar{\tau}_\eta EI_\varepsilon)}{L(1+\bar{\tau}_\eta)} & & & & & & \\ \frac{-EA}{L} & 0 & 0 & 0 & 0 & 0 & \frac{AE}{L} & & & & & \\ 0 & \frac{-12EI_\varepsilon}{L^3(1+\bar{\tau}_\eta)} & 0 & 0 & 0 & \frac{-6EI_\varepsilon}{L^2(1+\tau_\eta)} & 0 & \frac{12EI_\varepsilon}{L^3(1+\bar{\tau}_\eta)} & & & & \\ 0 & 0 & \frac{-12EI_\eta}{L^3(1+\bar{\tau}_\varepsilon)} & 0 & \frac{6EI_\eta}{L^2(1+\bar{\tau}_\varepsilon)} & 0 & 0 & 0 & \frac{12EI_\eta}{L^3(1+\bar{\tau}_\varepsilon)} & & & \\ 0 & 0 & 0 & \frac{-GJ}{L} & 0 & 0 & 0 & 0 & 0 & \frac{GJ}{L} & & \\ 0 & 0 & \frac{-6EI_\eta}{L^2(1+\bar{\tau}_\varepsilon)} & 0 & \frac{(2-\bar{\tau}_\varepsilon)EI_\eta}{L(1+\bar{\tau}_\varepsilon)} & 0 & 0 & 0 & \frac{6EI_\eta}{L^2(1+\bar{\tau}_\varepsilon)} & 0 & (4+) & \\ 0 & \frac{6EI_\varepsilon}{L^2(1+\tau_\eta)} & 0 & 0 & 0 & \frac{(2-\bar{\tau}_\eta)EI_\varepsilon}{L(1+\bar{\tau}_\mu)} & 0 & \frac{-6EI_\varepsilon}{L^2(1+\tau_\eta)} & 0 & 0 & & \end{bmatrix} \quad \frac{(2-\bar{}_\varepsilon)\,EI_\eta}{L\,(1+\bar{}_\varepsilon)} \quad \frac{-6EI_\eta}{L^2\,(1+\bar{}_\varepsilon)} ,$$

where

$$\bar{}_\eta = \frac{12EI_\varepsilon}{GA_{\mathrm{S}\eta}L^2} = 24\,(1+v)\,\frac{A}{A_{\mathrm{S}\eta}}\left(\frac{T_\varepsilon}{L}\right)^2 , \quad \bar{}_\varepsilon = \frac{12EI_\eta}{GA_{\mathrm{S}\varepsilon}L^2} = 24\,(1+v)\,\frac{A}{A_{\mathrm{S}\varepsilon}}\left(\frac{T_\eta}{L}\right)^2 ,$$

A_{S} is the shear area, T the torsional moment of inertia, the density, and local axes are parallel to Z- and Y-axes.

From this equation

$$a_2 = \frac{A}{f_c^{12}} + \frac{1}{2J_2^{1\lhd 2} f_c^1}\left\{\lambda - K_1 \sin\left[\frac{1}{3^{\cos -1}}\left[K_2 \frac{3\sqrt{3}}{2}\frac{J_3}{J_2^{3\lhd 2}}\right]\right]\frac{t}{\sqrt{1-t^2}}\right\}, \quad (2.21)$$

$$\cos 3\theta \geq 0$$

$$= \frac{A}{f_c^{12}} + \frac{1}{2J_2^{1\lhd 2} f_c^1}\left\{\lambda - K_1 \sin\left[\frac{\pi}{3}\frac{1}{3^{\cos -1}}\left[-K_2 \frac{3\sqrt{3}}{2}\frac{\sqrt{3}}{J_2^{3\lhd 2}}\right]\frac{t}{\sqrt{1-t^2}}\right]\right\}$$

$$a_3 = \frac{\partial}{\partial \cos 3\theta}\left[\lambda \frac{J_2^{1\lhd 2}}{f_c^1}\right], \quad \cos 3\theta \geq 0$$

$$= \frac{J_2^{1\lhd 2}}{f_c^1}\frac{1}{3}K_1 \sin\left[\frac{1}{3^{\cos -1}}\left(K_2 \cos 3\theta\right)\right]\frac{K_2}{\sqrt{1-t^2}}$$

$$= \frac{1}{3}\frac{K_1 K_2 J_2^{1\lhd 2}}{3 f_c' \sqrt{1-t^2}} \sin\left[\frac{1}{3}\cos^{-1}\left(K_2 \cos 3\theta\right)\right], \quad \cos\theta \geq 0,$$

$$a_3 = \frac{K_1 K_2 J_2^{1\lhd 2}}{3\sqrt{1-t^2} f_c'} \sin\left[\frac{\pi}{3} - \frac{1}{3}\cos^{-1}\left(-K_2 \cos 3\theta\right)\right], \quad \cos 3\theta \geq 0,$$

where $t = K_2 \cos 3\theta$

$$J_2 = \left[\frac{1}{2}\left(S_x^2 + S_y^2 + S_z^2\right) + \tau_{xy}^2 + \tau_{yz}^2 + \tau_{zx}^2\right]. \quad (2.22)$$

The values of C_1, C_2, C_3 are

$$C_1 = \frac{\partial I_1}{\partial \{\sigma\}} = \begin{Bmatrix} 1 \\ 1 \\ 1 \\ 0 \\ 0 \\ 0 \end{Bmatrix}, \quad (2.23)$$

$$C_2 = \frac{\partial J_2}{\partial \{\sigma\}} = \frac{\partial J_2}{\partial S_x}\frac{\partial S_x}{\partial \{\sigma\}} + \frac{\partial J_2}{\partial S_y}\frac{\partial S_y}{\partial \{\sigma\}} + \frac{\partial J_2}{\partial S_z}\frac{\partial S_z}{\partial \{\sigma\}} \quad (2.24)$$

$$+ \frac{\partial J_2}{\partial \tau_{xy}}\frac{\partial \tau_{xy}}{\partial \{\sigma\}} + \frac{\partial J_2}{\partial \tau_{yz}}\frac{\partial \tau_{yz}}{\partial \{\sigma\}} + \frac{\partial J_2}{\partial \tau_{zx}}\frac{\partial \tau_{zx}}{\partial \{\sigma\}}$$

$$= S_x \begin{Bmatrix} \frac{2}{3} \\ -\frac{1}{3} \\ -\frac{1}{3} \\ 0 \\ 0 \\ 0 \end{Bmatrix} + S_y \begin{Bmatrix} -\frac{1}{3} \\ \frac{2}{3} \\ -\frac{1}{3} \\ 0 \\ 0 \\ 0 \end{Bmatrix} + S_z \begin{Bmatrix} -\frac{1}{3} \\ -\frac{1}{3} \\ \frac{2}{3} \\ 0 \\ 0 \\ 0 \end{Bmatrix} + 2 \begin{Bmatrix} 0 \\ 0 \\ 0 \\ \tau_{xy} \\ \tau_{yz} \\ \tau_{zx} \end{Bmatrix} \quad (2.25)$$

or

$$C_2 = \begin{Bmatrix} \frac{1}{3}(2S_x - S_y - S_z) \\ \frac{1}{3}(2S_y - S_x - S_z) \\ \frac{1}{3}(2S_z - S_x - S_y) \\ 2\tau_{xy} \\ 2\tau_{yz} \\ 2\tau_{zx} \end{Bmatrix} = \begin{Bmatrix} S_x \\ S_y \\ S_z \\ 2\tau_{xy} \\ 2\tau_{yz} \\ 2\tau_{zx} \end{Bmatrix}, \tag{2.26}$$

$$\cos 3\theta = \frac{3\sqrt{3}}{2} \times \frac{J_3}{J_2^{3/2}}, \tag{2.27}$$

$$C_3 = \frac{\partial \cos 3\theta}{\partial J_3} = \frac{\partial \cos 3\theta}{\partial J_3}\frac{\partial J_3}{\partial \{\sigma\}} + \frac{\partial \cos 3\theta}{\partial J_2}\frac{\partial J_2}{\partial \{\sigma\}}. \tag{2.28}$$

From equation

$$\frac{\partial \cos 3\theta}{\partial J_3} = \frac{3\sqrt{3}}{2J_2^{3/2}}\frac{\partial \cos 3\theta}{\partial J_2} = \left(\frac{3\sqrt{3}}{2}J_3\right)\left(\frac{-\frac{3}{2}}{J_2^{5/2}}\right) = -\frac{9}{4}\sqrt{3}\frac{J_3}{J_2^{5/2}}. \tag{2.29}$$

Hence

$$C_3 = \frac{3}{2}\frac{\sqrt{3}}{J_2^{3/2}}\frac{\partial J_3}{\partial \{\sigma\}} - \frac{9}{4}\sqrt{3}\frac{J_3}{J_2^{5/2}}\frac{\partial J_2}{\partial \{\sigma\}} = \frac{3}{2}\frac{\sqrt{3}}{J_2^{3/2}}\left[\frac{\partial J_3}{\partial \{\sigma\}} - \frac{3}{2}\frac{J_3}{J_2}\frac{\partial J_2}{\partial \{\sigma\}}\right]. \tag{2.30}$$

Now

$$J_3 = \left[S_x S_y S_z + 2\tau_{xy}\tau_{yz}\tau_{zx} - S_x\tau_{yz}^2 - S_y\tau_{xz}^2 - S_z\tau_{xy}^2\right],$$

$$\frac{\partial J_3}{\partial \{\sigma\}} = \frac{\partial J_3}{\partial S_x}\frac{\partial S_x}{\partial \{\sigma\}} + \frac{\partial J_3}{\partial S_y}\frac{\partial S_y}{\partial \{\sigma\}} + \frac{\partial J_3}{\partial S_z}\frac{\partial S_z}{\partial \{\sigma\}} + \frac{\partial J_3}{\partial \tau_{yx}}\frac{\partial \tau_{xy}}{\partial \{\sigma\}} + \frac{\partial J_3}{\partial \tau_{yz}}\frac{\partial \tau_{yz}}{\partial \{\sigma\}} + \frac{\partial J_3}{\partial \tau_{zx}}\frac{\partial \tau_{zx}}{\partial \{\sigma\}},$$

$$\frac{\partial J_3}{\partial S_x} = S_y S_z - \tau_{yz}^2, \quad \frac{\partial J_3}{\partial S_y} = S_x S_z - \tau_{xz}^2, \quad \frac{\partial J_3}{\partial S_z} = S_x S_y - \tau_{xy}^2, \tag{2.31}$$

$$S_x = \frac{1}{3}(2\sigma_x - \sigma_y - \sigma_z), \tag{2.32}$$

$$\frac{\partial S_x}{\partial \{\sigma\}} = \frac{1}{3}\begin{Bmatrix} 2 \\ -1 \\ -1 \\ 0 \\ 0 \\ 0 \end{Bmatrix}, \quad \frac{\partial S_y}{\partial \{\sigma\}} = \frac{1}{3}\begin{Bmatrix} -1 \\ 2 \\ -1 \\ 0 \\ 0 \\ 0 \end{Bmatrix}, \quad \frac{\partial S_y}{\partial \{\sigma\}} = \frac{1}{3}\begin{Bmatrix} -1 \\ -1 \\ 2 \\ 0 \\ 0 \\ 0 \end{Bmatrix}, \tag{2.33}$$

$$\frac{\partial J_3}{\partial \tau_{xy}} = 2\tau_{yz}\tau_{zx} - 2S_z\tau_{xy}, \quad \frac{\partial J_3}{\partial \tau_{yz}} = 2\tau_{xy}\tau_{zx} - 2S_x\tau_{yz},$$

$$\frac{\partial J_3}{\partial \tau_{xz}} = 2\tau_{xy}\tau_{yz} - 2S_y\tau_{xz}, \tag{2.34}$$

$$\frac{\partial \tau_{xy}}{\partial \{\sigma\}} = \begin{Bmatrix} 0 \\ 0 \\ 0 \\ 1 \\ 0 \\ 0 \end{Bmatrix}, \quad \frac{\partial \tau_{yz}}{\partial \{\sigma\}} = \begin{Bmatrix} 0 \\ 0 \\ 0 \\ 0 \\ 1 \\ 0 \end{Bmatrix}, \quad \frac{\partial \tau_{xz}}{\partial \{\sigma\}} = \begin{Bmatrix} 0 \\ 0 \\ 0 \\ 0 \\ 0 \\ 1 \end{Bmatrix}, \tag{2.35}$$

$$\frac{\partial J_3}{\partial \{\sigma\}} = \begin{Bmatrix} \frac{1}{3}\left[2\left(S_y S_z - \tau_{yz}^2\right) - \left(S_x S_z - \tau_{xz}^2\right) - \left(S_x S_y - \tau_{xy}^2\right)\right] \\ \frac{1}{3}\left[-\left(S_y S_z - \tau_{yz}^2\right) + 2\left(S_x S_z - \tau_{xz}^2\right) - \left(S_x S_y - \tau_{xy}^2\right)\right] \\ \frac{1}{3}\left[-\left(S_y S_z - \tau_{yz}^2\right) - 2\left(S_x S_z - \tau_{xz}^2\right) + 2\left(S_x S_y - \tau_{xy}^2\right)\right] \\ 2\left(\tau_{yz}\tau_{zx} - S_z \tau_{xy}\right) \\ 2\left(\tau_{xy}\tau_{zx} - S_x \tau_{yz}\right) \\ 2\left(\tau_{xy}\tau_{yz} - S_y \tau_{xz}\right) \end{Bmatrix}. \tag{2.36}$$

Equation (2.36) is further simplified as

$$\frac{\partial J_3}{\partial \{\sigma\}} = \begin{Bmatrix} \frac{1}{3}\left[2S_y S_z - S_x S_z - S_x S_y - 2\tau_{yz}^2 + \tau_{xz}^2 + \tau_{yz}^2\right] \\ \frac{1}{3}\left[2S_x S_z - S_y S_z - S_x S_y - 2\tau_{xz}^2 + \tau_{yz}^2 + \tau_{xy}^2\right] \\ \frac{1}{3}\left[2S_x S_y - S_y S_z - S_x S_z - 2\tau_{xy}^2 + \tau_{yz}^2 + \tau_{zx}^2\right] \\ 2\left(\tau_{yz}\tau_{zx} - S_z \tau_{xy}\right) \\ 2\left(\tau_{xy}\tau_{zx} - S_x \tau_{yz}\right) \\ 2\left(\tau_{xy}\tau_{yz} - S_y \tau_{xz}\right) \end{Bmatrix}. \tag{2.37}$$

From the flow rule of the normality principle, the following relationship exists between the plastic strain increment and the plastic stress increment

$$\mathrm{d}\{\varepsilon\} = \lambda \frac{\partial f}{\partial \{\sigma\}}. \tag{2.38}$$

This equation can be interpreted as requiring the normality of the plastic strain increment vector to yield the surface in the hyperspace of n stress dimensions. As before $\mathrm{d}\lambda$ is the proportionality constant.

For stress increments of infinitesimal size, the change of strain can be divided into elastic and plastic parts, thus (as before)

$$\mathrm{d}\{\varepsilon\} = \mathrm{d}\{\varepsilon\}_{\mathrm{e}} + \mathrm{d}\{\varepsilon\}_{\mathrm{p}}. \tag{2.39}$$

The elastic increment of stress and strain is related to an isotropic material property matrix $[D]$ by

$$\mathrm{d}\{\varepsilon\}_{\mathrm{e}} = [D]^{-1}\,\mathrm{d}\{\sigma\}. \tag{2.40}$$

From (2.38)–(2.40) the following equation is established

$$\mathrm{d}\{\varepsilon\} = [D]^{-1}\,\mathrm{d}\{\sigma\} + \mathrm{d}\lambda \left\{\frac{\partial f}{\partial \sigma}\right\}. \tag{2.41}$$

The function stresses, on differentiation, can be written as

$$\mathrm{d}f = \frac{\partial f}{\partial \sigma_1}\mathrm{d}\sigma_1 + \frac{\partial f}{\partial \sigma_2}\mathrm{d}\sigma_2 + \cdots + 0 = \left\{\frac{\partial f}{\partial \sigma}\right\}^{T''} \mathrm{d}\{\sigma\}. \tag{2.42}$$

Equation together with equation can be written in matrix form as

$$\mathrm{d}\{\varepsilon\} = [D]_{\mathrm{ep}}^{-1}\,\mathrm{d}\{\sigma\} \tag{2.43}$$

or

$$\begin{Bmatrix} \mathrm{d}\varepsilon_x \\ \mathrm{d}\varepsilon_y \\ \mathrm{d}\varepsilon_z \\ \mathrm{d}\gamma_{xy} \\ \mathrm{d}\gamma_{yz} \\ \mathrm{d}\gamma_{zx} \\ 0 \end{Bmatrix} = \begin{bmatrix} & & & & & & \frac{\partial f}{\partial \sigma_x} \\ & [D]^{-1} & & & & & \frac{\partial f}{\partial \sigma_y} \\ & & & & & & \frac{\partial f}{\partial \sigma_z} \\ & & & & & & \frac{\partial f}{\partial \tau_{xy}} \\ & & & & & & \frac{\partial f}{\partial \tau_{yz}} \\ & & & & & & \frac{\partial f}{\partial \tau_{zx}} \\ \frac{\partial f}{\partial \sigma_x} & \frac{\partial f}{\partial \sigma_y} & \frac{\partial f}{\partial \sigma_z} & \frac{\partial f}{\partial \tau_{xy}} & \frac{\partial f}{\partial \tau_{yz}} & \frac{\partial f}{\partial \tau_{zx}} & 0 \end{bmatrix}. \tag{2.44}$$

Inversion of the above matrix $[D]^{-1}$ will give stresses

$$\mathrm{d}\{\sigma\} = [D]_{\mathrm{ep}}\,\mathrm{d}\{\varepsilon\}. \tag{2.45}$$

The explicit form of the elastoplastic material matrix $[D]_{\mathrm{ep}}$ is given by

$$[D]_{\mathrm{ep}} = [D] - [D]\left\{\frac{\partial f}{\partial \sigma}\right\}\left\{\frac{\partial f}{\partial \sigma}\right\}^{T}[D]\left[\left\{\frac{\partial f}{\partial \sigma}\right\}^{T}[D]\left\{\frac{\partial f}{\partial \sigma}\right\}\right]^{-1}. \tag{2.46}$$

The value of $\{\partial f/\partial\sigma\}$ has been evaluated above.

The rest of the procedure using finite elements is described in this chapter and elsewhere.

2.9 Finite Element Analysis for Traumatic Injury and Fracture

2.9.1 Finite Element Formulation

In general terms, such formulations are described by the following

$$\left[\begin{array}{c|c} K & K_R \\ \hline K_R^{T''} & K_{RR} \end{array}\right]\left\{\begin{array}{c} U \\ \hline U_R \end{array}\right\} = \left\{\begin{array}{c} F \\ \hline F_R \end{array}\right\}, \tag{2.47}$$

where B is the width of the human element perpendicular to the direction of horizontal excitation, L is the length of the human element in the direction of horizontal excitation, and β_x, β_ψ, β_z are constants that are functions of the dimensional ratio L/B.

The subscript R represents reaction forces under impact. The top half of (2.47) is used to solve for $\{U\}$

$$\{U\} = -[K]^{-1}[K_R]\{U_R\} + [K]^{-1}\{F\}. \tag{2.48}$$

The reaction forces $\{F_R\}$ are computed from the bottom half of the equation as

$$\{F_R\} = [K_R]^{T''}\{U\} + \{K_{RR}\}\{U_R\}. \tag{2.49}$$

Equation (2.48) must be in equilibrium with (2.49).

The Superelement and Substructuring

For large human skeleton with complicated features, a substructure (superelement) may be adopted on the lines suggested in (2.47). This superelement may then be used as a reduced element from the collection of body elements. If subscripts γ and γ' represent the retained and removed degrees of freedom of the equations partitioned into two groups, then the expressions in (2.47) can be written as

$$\left[\begin{array}{c|c} K_{\gamma\gamma} & K_{\gamma\gamma'} \\ \hline K_{\gamma'\gamma} & K_{\gamma'\gamma'} \end{array}\right] \left\{\begin{array}{c} U_\gamma \\ \hline U \end{array}\right\} = \left\{\begin{array}{c} F_\gamma \\ \hline F_{\gamma'} \end{array}\right\}. \tag{2.50}$$

Equation (2.50) when expanded assumes the following form:

$$\{F_\gamma\} = [K_{\gamma\gamma}]\{U_\gamma\} + [K_{\gamma\gamma}]\{U_{\gamma'}\}, \tag{2.51}$$

$$\{F_{\gamma'}\} = [K_{\gamma'\gamma}]\{U_\gamma\} + [K_{\gamma'\gamma}]\{U_{\gamma'}\}. \tag{2.52}$$

When a dynamic analysis is carried out, the subscript γ (retained) represents the dynamic degrees of freedom.

When (2.52) is solved, the value of $U_{\gamma'}$ is then written, similarly to (2.51)

$$\{U_{\gamma'}\} = [K_{\gamma'\gamma'}]^{-1}\{F_{\gamma'}\} - [K_{\lambda'\gamma'}]^{-1}[K_{\gamma'\gamma}]\{U_\gamma\}. \tag{2.53}$$

Substituting $\{U_{\gamma'}\}$ into (2.51) gives

$$\Big[[K_{\gamma\gamma}] - [K_{\gamma'\gamma}][K_{\gamma\gamma'}]^{-1}[K_{\gamma'\gamma}]\Big]\{U_\gamma\} = \Big[\{F_\gamma\} - [K_{\gamma\gamma'}][K_{\gamma\gamma'}]^{-1}\{F\gamma'\}\Big] \tag{2.54}$$

or

$$\big[\overline{K}\big]\big\{\overline{U}\big\} = \big\{\overline{F}\big\}, \tag{2.55}$$

where

$$\big[\overline{K}\big] = [K_{\gamma\gamma}] - [K_{\gamma\gamma'}][K_{\gamma'\gamma'}]^{-1}[K_{\gamma'\gamma}], \tag{2.56a}$$

$$\big\{\overline{F}\big\} = \{F_\gamma\} - [K_{\gamma\gamma'}][K_{\gamma'\gamma'}]^{-1}[F_{\gamma'}], \tag{2.56b}$$

$$\big\{\overline{U}\big\} = \{U_\gamma\}, \tag{2.56c}$$

and $\boxed{K}$ and $\left\{\overline{F}\right\}$ are generally known as the substructure stiffness matrix and load vector, respectively.

In the above equations, the load vector for the substructure is taken as a total load vector. The same derivation may be applied to any number of independent load vectors. For example, one may wish to apply thermal, pressure, gravity and other loading conditions in varying proportions. Expanding the right-hand sides of (2.51) and (2.52) gives

$$\{F_\gamma\} = \sum_{i=1}^{n} \{F_{\gamma i}\}, \tag{2.57}$$

$$\{F_{\gamma'}\} = \sum_{i=1}^{n} \{F_{\gamma' i}\}, \tag{2.58}$$

where n is the number of independent load vectors.

Substituting into (2.56c)

$$\left\{\overline{F}\right\} = \sum_{i=1}^{n} \{F_{\gamma\gamma'}\} - [K_{\gamma\gamma'}]\,[K_{\gamma''\gamma'}]^{-1} \sum_{i=1}^{n} \{F_{\gamma' i}\}, \tag{2.59}$$

where the initial load $\{P_t\}$ is specified by

$$\{P_t\} = -\,[\Delta C_{0\to t}]\left\{\dot{U}_t\right\} - \{\Delta K_{0\to t}\}\,\{\delta_t\}\,. \tag{2.60}$$

To obtain the solution at time $t + \Delta t$, the equation is stated as

$$[M]\left\{\ddot{U}_{t+\Delta t}\right\} + [C_0]\left\{\dot{U}_{t+\Delta t}\right\} + [K_0]\,\{U_{t+\Delta t}\} = \{R_{t+\Delta t}\} + \{P_t\} + \{\Delta P_{t\to t+\Delta t}\}\,, \tag{2.61}$$

$\{\Delta P_{t\to t+\Delta t}\}$ represents the influence of the nonlinearity during the time increment t and is determined by iteration and satisfied for $t + \tau$, where $\tau = \theta\Delta t$ ($\theta > 1.37$ for an unconditionally stable method) when applied to a linear problem. $[\Delta C_{0\to t}]$ and $[\Delta K_{0\to t}]$ represent the change $[C]$ and $[K]$, respectively, from $t = 0$ to t.

To obtain the solution at time $t + \Delta t$, (2.54) can be written as

$$[M]\left\{\ddot{U}_{t+\Delta t}\right\} + [C_0]\left\{\dot{U}_{t+\Delta t}\right\} + [K_0]\,\{U_{t+\Delta t}\} = \{R_{t+\Delta t}\} + \{F_t\} + \{\Delta F_{t\to t+\Delta t}\}\,, \tag{2.62}$$

$\{\Delta P_{t\to t+\Delta t}\}$ represents the influence of the nonlinearity during the time increment t and is determined by iteration

$$\begin{aligned}\{\Delta P_{t\to t+\Delta t}\} = &-[\Delta C_{0\to t}]\left\{\Delta\dot{U}_{t\to t+\Delta t}\right\} - [\Delta C_{t\to t+\Delta t}] \\ &\times\left(\left\{\dot{U}\right\} + \left\{\Delta\dot{U}_{t\to t+\Delta t}\right\}\right) - [\Delta K_{0\to t}]\,\{\Delta U_{t\to t+\Delta t}\} \\ &-[\Delta K_{t\to t+\Delta t}]\,(\{U_t\} + \{\Delta U_{t\to t+\Delta t}\})\,,\end{aligned} \tag{2.63}$$

$(\Delta P_{t\to t+\Delta t})$ is calculated using the initial stress approach.

A modified Newton–Raphson or initial stress approach is adopted for solving these nonlinear equations. A step-by-step integration method is given. Using these methods along with acceleration and convergence procedures described in this chapter allows successful solution of finite element-based problems.

2.9.2 Reduced Linear Transient Dynamic Analysis

This is a reduced form of nonlinear transient dynamic analysis. This analysis is carried out faster than the nonlinear analysis since the matrix requires to be inverted once, and the analysis is reduced to a series of matrix multiplications and essential degrees of freedom (dynamic or master of freedoms) to characterize the response of the system. The analysis generally has restrictions such as constant $[M]$, $[C_t]$, $[K_t]$, and time interval for all iterations and nodal forces applied at dynamic or master degrees of freedom.

Quadratic integration

$$\begin{aligned}&\left(\frac{1}{\Delta t^2}[M]_R + \frac{3}{2\Delta_t}\left[\hat{C}_t\right]_R + [K_t]_R\right)\{U_t\}_R \\ &\quad = \{F(t)\}_R + [M]_R \frac{1}{\Delta t^2}\left(2\{U_{t-1}\}_R - \{U_{t-2}\}_R\right) \\ &\qquad + \frac{1}{\Delta_t}\left(2\{U_{t-1}\}_R - \frac{1}{2}\{U_{t-2}\}_R\right). \end{aligned} \tag{2.64}$$

The symbol R represents reduced matrices and vectors.

Cubic integration

$$\begin{aligned}&\left(\frac{2}{\Delta t^2}[M]_R + \frac{11}{6\Delta t}[C_t]_R + [K_t]_R\right)\{U_t\}_R \\ &= \{F(t)\} + [M]_R \frac{1}{\Delta t^2}\left(5\{U_{t-1}\}_R - 4\{U_{t-3}\}\right) \\ &\quad + [C_t]_R \frac{1}{\Delta t^2}\left(3\{U_{t-1}\}_R - \frac{3}{2}\{U_{t-2}\}_R + \frac{1}{3}\{U_{t-3}\}_R\right). \end{aligned} \tag{2.65}$$

Mode frequency analysis

The equation of motion for an undamped structure with no applied forces is written as

$$[M]\left\{\ddot{U}_t\right\} + [K_t']\{U_t\} = \{0\}, \tag{2.66}$$

$[K_t']$ is the structure stiffness matrix, may include stress-stiffening effects.

The system of equations is initially condensed down to those involved with the master (dynamic) degrees of freedom.

The number of dynamic degrees of freedom would at least be equal to two times the selected frequencies. The reduced form of (2.66) can be written as

$$[M]_R\left\{\ddot{U}_t\right\}_R + [K_t']_R\{U\}_R = \{0\}. \tag{2.67}$$

For a linear system, free vibrations of harmonic type are written as

$$\{U_t\}_R = \{\psi_i\}_R \cos \omega_i t, \tag{2.68}$$

where $\{\psi_i\}_R$ is the eigenvector representing the shape of the ith frequency, ω_i the ith frequency (radians/unit time), and t the time.

Equation (2.66) assumes the form

$$-\omega_i^2 [M]_R + [K_t']_R \{\psi_i\}_R = \{0\}. \tag{2.69}$$

2.9.3 Solution Procedures: Acceleration and Convergence Criteria

Convergence criteria

To ensure convergence to the correct solution by finer subdivision of the mesh, the assumed displacement function must satisfy the convergence criteria are:

(a) Displacements must be continuous over element boundaries.
(b) Rigid body movements should be possible without straining.
(c) A state of constant strain should be reproducible.

Euclidean norm is given by $\psi_i/R_i \leq C$. The term ψ_i represents the unbalanced forces and the norm of the residuals. With the aid of the iterative scheme described above, the unbalanced forces due to the initial stresses $\{\sigma_0\}$ become negligibly small. As a measure of their magnitude, the norm of the vector $||\psi_i||$ is used. The Euclidean norm and the absolute value of the largest component of the vector are written as

$$||\psi_i|| = \left(|\psi_1|^2 + \cdots + |\psi_n|^2\right)^{1/2}, \tag{2.70}$$

$$||R_i|| = \left(|\{R_i\}^T \{R^i\}|\right)^{1/2},$$

the convergence criterion adopted is

$$||\psi|| = \max_i |\psi_i| < C = 0.001. \tag{2.71}$$

Uniform acceleration

Various procedures are available for accelerating the convergence of the modified Newton–Raphson iterations. Figure 2.3 shows the technique of computing individual acceleration factors when δ_1 and δ_2 are known. Then, assuming a constant slop of the response curve, and from similar triangles, the value of δ_3 is computed

$$\frac{\delta_1}{\delta_2} = \frac{\delta_2}{\delta_3}, \quad \delta_3 = \delta_2 \frac{\delta_2}{\delta_1}. \tag{2.72}$$

When δ_3 is added δ_2, then the accelerated displacement $\delta_2{}'$ is expressed as

$$\delta_2' = \delta_2 + \delta_3 = \delta_2 \left(1 + \frac{\delta_2}{\delta_1}\right) = \alpha \delta_2, \tag{2.73}$$

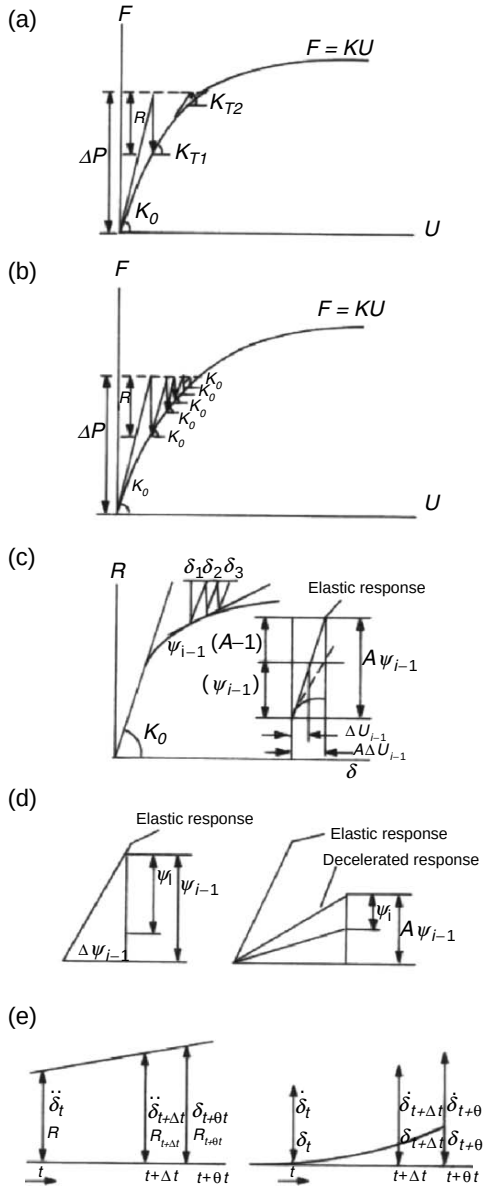

Fig. 2.3. Modified Newton–Raphson iterations techniques

where the acceleration factor α is

$$\alpha = 1 + \frac{\delta_2}{\delta_1}. \tag{2.74}$$

Generally the range of α is between 1 and 2. The value of $\alpha = 1$ for zero acceleration, and the value of α reaches the maximum value of 2 when the slope of the δ–R curve approaches zero.

The acceleration factor α is computed individually for every degree of freedom of the system. The displacement vector obtained from the linear stiffness matrix $[k_0]$ is then multiplied by the $[\alpha]$ matrix having the above constants on its diagonals. The remaining components of $[\alpha]$ are zero. The accelerated displacement vector is then expressed as follows:

$$\{\Delta u_i'\} = [a_{i-1}]\,\{\Delta u_i\}\,. \tag{2.75}$$

From these accelerated displacements $\{\Delta u_i'\}$, the initial stresses $\{\sigma_0\}$ are found and they are equilibrated with the forces $\{\psi_i\}$. They are then used for the next solution

$$\{\Delta \hat{u}_i\} = [k_0]^{-1}\,\{\psi_i\}\,, \tag{2.76}$$

which results in a new set of acceleration factors. Now an estimate for the displacement increment is made in order to find the incremental stresses and total stresses.

A new displacement now results from

$$\{\Delta u_{i+1}\} = -\,[k_0]^{-1}\left\{\hat{\psi}_i\right\}. \tag{2.77}$$

In order to carry out these iterative steps, numerical integration is required. First of all the evaluation of $\left\{\hat{\psi}_i\right\}$ from the initial stresses is required, and this requires integration over the elastic–plastic region only. The value of $\left\{\hat{\psi}_i\right\}$ is computed by carrying out the integration over the entire domain of the analysis. Since these kinds of accelerated steps unbalance the equilibrium, it therefore has to be reestablished by finding the residual forces $\left\{\hat{\psi}_i\right\}$. Since the state of stress produced by the accelerated displacements is not in balance with the residual forces of the previous iteration, the new residual forces $\left\{\hat{\psi}_i\right\}$ of (2.77) must balance $\{\sigma_\gamma\}$ and $\{R_i\}$. Here the acceleration scheme is needed to preserve equilibrium, which will eventually make the equivalent forces over the whole region unnecessary. This is achieved by applying a uniform acceleration, i.e., the same acceleration factor $\bar{A}$ to all displacements, found by averaging the individual factors α_i

$$\overline{A} = \frac{1}{n}\sum_{i=1}^{n} \alpha_i. \tag{2.78}$$

The force–displacement equation is then written by multiplying both sides with the scalar quantity $\bar{A}$ without disturbing the equilibrium

$$\overline{A}\{\Delta u_i\} = [k_0]^{-1}\overline{A}\{\varphi_I\}. \tag{2.79}$$

The residual forces needed to reestablish equilibrium can now easily be evaluated.

$$\left\{\hat{\psi}_I\right\} = \int_v [B]^T \{\sigma_{0\gamma}\}\,\mathrm{d}V - \{R_I\}, \tag{2.80}$$

where $[R_i]$ represents the total external loads and $\mathrm{d}V$ is the volume.

Now to evaluate $\{\psi_{I+1}\}$, the previous values of ψ_i must be multiplied by $\bar{A}$, and the previously accelerated forces from the initial stresses σ_0 must be included such that

$$\{\psi_{I+1}\} = \int_V [B]^T \{\sigma_0\}\,\mathrm{d}V - (A-1)\{\psi_{i-1}\}. \tag{2.81}$$

2.9.4 Intermediate Problems Associated with the Finite Element Analysis

There are a number of associated problems. They are given as subroutines to be linked to any computer program package:

(a) Stress–strain principal stresses and fracture criteria
(b) Shear and torsion on the bone element
(c) The influence of dowel/pin or insert in bone connection and repair
(d) The order of the degree of freedom of the bone, as an element
(e) Where the bones are not in specific direction, the necessity of the transformation matrices
(f) Stiffness matrix for the insert mass matrix
(g) Displacements, velocities, and acceleration linked to specific FE programs (Appendix II)

2.10 Hallquist et al. Method as Gap and Contact Element

Hallquist et al. developed a useful concept of master and slave nodes sliding on each other. As shows in Fig. 2.4 slave nodes are constrained to slide on master segments after impact occurs and must remain on a master segment until a tensile interface force develops. The zone in which a slave segment exists is called a *slave zone*. A separation between the slave and the master line is known as *void*. The following basic principles apply at the interface:

(a) Update the location of each slave node by finding its closest master node or the one on which it lies.
(b) For each master segment, find out the first slave zone that overlaps.
(c) Show the existence of the tensile interface force.

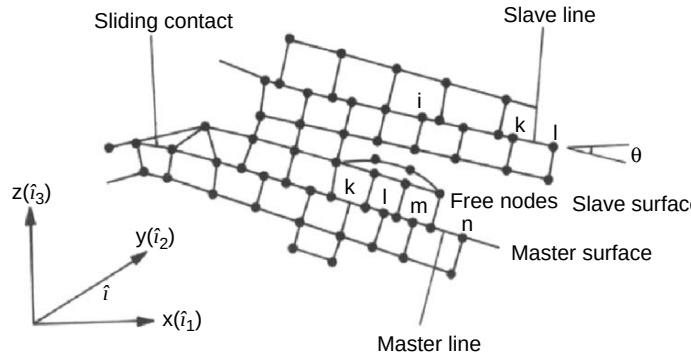

Fig. 2.4. Slave nodes on master segment

Constraints are imposed on global equations by a transformation of the nodal displacement components of the slave nodes along the contact interface. Such a transformation of the displacement components of the slave nodes will eliminate their normal degrees of freedom and distribute their normal force components to the nearby master nodes. This is done using explicit time integration, as describe in the finite element solution procedures. Thereafter impact and release conditions are imposed. The slave and master nodes are shown in Fig. 2.4. Hallquist et al. gave a useful demonstration of the identification of the contact point which is the point on the master segment to the slave node n_{s} and which finally becomes nontrivial during the execution of the analyses. When the master segment t is given the parametric representation and t is the position vector drawn to the slave node n_{s} the contact point coordinate must satisfy the following equations:

$$\begin{aligned} \frac{\partial \hat{r}}{\partial \zeta}\left(\zeta_{\mathrm{c}}, \eta_{\mathrm{c}}\right) x\left[\hat{t}-\hat{r}\left(\zeta_{\mathrm{c}}, \eta_{\mathrm{c}}\right)\right]=0, \\ \frac{\partial \hat{r}}{\partial \eta}\left(\zeta_{\mathrm{c}}, \eta_{\mathrm{c}}\right) x\left[\hat{t}-\hat{r}\left(\zeta_{\mathrm{c}}, \eta_{\mathrm{c}}\right)\right]=0, \end{aligned} \tag{2.82}$$

where $(\varepsilon_{\mathrm{c}}, \eta_{\mathrm{c}})$ are the coordinates on the master surface segment S_i. Where penetration through the master segment S_i occurs, the slave node n_{s} (containing its contact point) can be identified using the interface vector f_{s}

$$f_{\mathrm{s}}=-l k_i n_i, \quad \text{if } l<0 \tag{2.83}$$

to the degree of freedom corresponding to n_{s}, and

$$f_m^i=N_i\left(\zeta_{\mathrm{c}} \eta_{\mathrm{c}}\right) f_{\mathrm{s}}, \quad \text{if } l<0, \tag{2.84}$$

where

$$l=\hat{n}_i \cdot\left[\hat{t}-\hat{r}\left(\zeta_{\mathrm{c}}, \eta_{\mathrm{c}}\right)\right]<0. \tag{2.85}$$

A unit normal

$$\hat{n}_i = \hat{n}_i\left(\zeta_{\mathrm{c}}, \eta_{\mathrm{c}}\right), \quad \hat{t}_i = \hat{n}_i \sum_{j=1}^{n} N_j \left(F_1\right)^j (t), \tag{2.86}$$

$$k_i = f_{si} K_I A_I^2 / V_I, \tag{2.87}$$

where

$(F_1)^j(t)$ = impact at the jth node,
K = stiffness factor,
K_i, V_i, A_i = bulk modulus, volume, and face area, respectively,
f_{si} = scale factor normally defaulted to 0.10,
$N_i = \frac{1}{4}(1+\zeta\zeta_i)(1+\eta\eta_i)$ for a four-node linear surface.

Bangash extended this useful analysis for other shape functions, such as Ni for eight-noded and twelve-noded elements. On the basis of this theory and owing to the nonavailability of the original computer source, a new subprogram CONTACT was written in association with the program ISOPAR. The subprogram CONTACT is in three dimensions.

$$\begin{aligned}\left\{\overrightarrow{\hat{F}_{\mathrm{N}}}\right\} &= \left[K_{\gamma\gamma}\right]_i \left\{U_\gamma\right\}_i = \left[\sum k\right]\left\{\sum \Delta_i, \Delta_j, \ldots\right\} \\ &= \left\{\hat{\vec{F}}_{i,j}, \ldots\right\} + \left\{\pm\mu\hat{\vec{F}}_n \cdots \pm k\Delta_i \cdots\right\},\end{aligned} \tag{2.88}$$

$$\begin{aligned}\Delta_{\mathrm{s1}} &= \text{distance of sliding} \\ &= (\Delta_j - \Delta_i) - \frac{\mu|\hat{\vec{F}}_n|}{[K_{\gamma\gamma}]},\end{aligned} \tag{2.89}$$

$$\begin{aligned}\mu &= \text{friction}, \\ \left\{\hat{F}_{\mathrm{SN}}\right\} &\le \mu\left\{\hat{\mathrm{F}}_{\mathrm{N}}\right\} \text{ no sliding} \\ &\ge \mu\left\{\hat{F}_{\mathrm{N}}\right\} \text{ sliding} \\ &= 0 \text{ contact broken}, \\ \theta &= \cos^{-1} -\frac{X}{\gamma} \quad \text{or} \quad \sin^{-1}\frac{Y}{\gamma}.\end{aligned} \tag{2.90}$$

3

Bones: Tissues and Material Properties

3.1 Introduction

Tissues are the coherent collections of specialized cells of which human beings and animals are made. The most important of them are bone tissues, muscular tissues, brain tissues, and nervous tissues. Huiskes et al. (2000) suggests the structure of the bone tissue, and of the whole bone makes sense only if its mechanical function is known. The mechanical properties of bones are determined by their structure in order to understand its function. Human bone is a stiff skeletal material made principally of the fibrous protein collagen, impregnated with a mineral closely resembling calcium phosphate. It contains water which is mechanically important. Most bones inside a body is covered with cells throughout life. It has living cells and blood vessels within it. Bone is generally hard and cannot swell or shrink. In fact, all changes in shape must take place at the surfaces. Most bones are hollow and contain hematopoietic or furry marrow which has little mechanical significance. Tendons and ligaments inserted into the bone substance such that the ends of bones are covered by a thin layer of cartilage for lubrication. Some tissues such as antler and dentine are not called bones but extremely like them. Although in antler bone the cells are all dead by the time the antler comes to be used. Dentine is a collagen mineralized with calcium phosphate but it contains cell bodies. The other significant tissue mineralized with calcium phosphate as opposed to calcium carbonate is enamel and this is very different in that it has virtually no cells or cell processes or indeed, much organic matrix. In the human being, unlike small mammals, the situation is complex. This chapter contains a list of mechanical properties which eventually will be used as material properties for input data in numerical analysis and computer aided results.

At the lowest level bone can be considered to be a composite material consisting of a fibrous protein, collage, stiffened by an extremely dense filling and surrounding of calcium phosphate crystals. There are other constituents, notably water, some ill-understood proteins and polysaccharides living cells and blood vessels. The mechanical property or behavior can be determined

having the amount of water present in the bone. The bone biologists who are focused entirely on cells of bone, use often the word *MATRIX* which means the *BONE TISSUE*. Since bone is found only in vertebrates, the range of scales of different forms, would give a complete spectrum of categorization. The question mark is the mechanical properties of scales since very little is known about them.

Collagen is a structural protein found in probably all metazoan animal phyla. It is the most abundant protein found in animals, but only in the vertebrates does it undergo a whole hearted transformation into a mineralized skeletal structure.

Unmineralized collagen is also found in the vertebrates, and in many invertebrates, in skin, tendon, ligament, blood vessel walls, cartilage, basement membrane, and in connective tissue generally, in those circumstances where the material is required to be flexible but no very extensible. Collagen makes up more than half the protein in the human body (Dusty et al 1984). Collagen from different sites often has different amino acid compositions; in the mid-1990s 19 types of collagen were known throughout the animal kingdom, and the known number increases relentlessly (Prockop and Kivirikko 1995). The collagens of skin, tendon, dentin, and bone share the same type of composition, and are called type 1 collagen. The protein molecule tropocollalgen, which aggregates to form the microfibrils of collagen, consists of three polypeptides of the same length – two have the same amino acid composition, one a different one. These form on ribosomes, are connected by means of disulfide cysteine links, and leave the cell. Outside the cell the ends of the joined polypeptides are snipped off, the lost part containing the disulfide bonds. The three chains are by now held together by hydrogen bonds in a characteristic left-handed triple helix.

The primary structure of the polypeptides in the tropocollagen molecule is unusual, great stretches of it being repeats of glycine–X-Y, with X often being proline and Y sometimes hydroxyproline. The imino acids proline and hydroxyproline are unlike amino acids in that the nitrogen atom is included in the side chain as part of a five-membered ring. The effect of this is to reduce the amount of rotation possible between units of the polypeptide. It also prevents α

broad. However, they do not seem to grow in the depth direction, remaining about 5 nm.

Reports of the visualization of the crystals directly overwhelmingly supports this view that the crystals in all bone examined are platelet-shaped. Weiner and Price (1986) examined the size of bone mineral crystals, extracting them from the bone by a gentle procedure, and proposed value of about $50 \times 20 \times 2$ nm.

Kim et al. (1995) did not measure the thickness but suggested it was about 2 nm.

3.2 The Cells of Bone and the Structure of Tissues

Bone is permeated by and lined by various kinds of specialized cells.

Bone-lining cells cover all surfaces of bones, including the blood channels, forming a thin continuous sheet that controls the movement of ions between the body and the bone. The layer of cells on the outside of the bone is called the periosteum, although this word is often used to include the strong collagenous sheet covering the outer surface. The layer of cells on the inside of the bone is called the endosteum. The bone-lining cells, which are often considered to be quiescent osteoblasts, are derived, via complex series of changes, from osteoprogenitor cells. These stages are described by (Stein et al. 1996).

Osteoblasts derive from bone-lining cells and are responsible for the formation of bone. They initially lay down the collagenous matrix, osteoid, in which mineral is later deposited, and they probably also have a role in its mineralization.

Osteocytes are the cells in the body of the bone. In cancellous bone the density of osteocytes varies from about 90,000 mm^{-3} in rats to about 30,000 mm^{-3} in cows. In general, the larger the animal the lower the density of osteocytes (Mullender et al. 1996). They derive from osteoblasts. They are imprisoned in the hard bone tissue and connect with neighboring osteocytes and with bone-lining cells by means of processes that are housed in little channels (canaliculi), of about 0.2–0.3 μm diameter. The actual connections with neighboring cells are by means of gap junctions that allow small molecules through easily.

Osteoclasts are bone-destroying cells. They are large, multinucleated cells derived from precursor cells circulating in the blood. In time-lapse photography they give the appearance of being extremely aggressive, clamping themselves to the bone's surface and leaving a space underneath a ruffled border that is very mobile and beneath which the bone can be seen dissolving. Debris, both organic and mineral, are packed into little vesicles and pass through the cell body of the osteoclast and are dumped into the space above (Salo et al. 1997). When osteoclasts have done their job they disappear and presumably die.

3.2.1 Woven and Lamellar Bone/Tissue

Above the level of the collagen fibril and its associated mineral, mammalian bone exists in two usually fairly distinct forms: woven bone and lamellar bone. Parallel-fibered bone is intermediate.

Woven bone is usually laid down very quickly, more than 4 μm a day and often much more, most characteristically in the fetus and in the callus that is produced during fracture repair. The collagen in woven bone is variable, the fibrils being 0.1–3 μm or so in diameter and oriented almost randomly, so it is difficult to make out any preferred direction over distances greater than about a millimeter (Boyde 1980; Boyde and Jones 1998). The mineralization process involves roughly spherical centers, impregnating both the collagen and ground substance at the same time, in which the crystals seem to be randomly arranged. As these mineralization centers spread they abut and often leave mineral-free spaces (Boyde 1980). As a result, woven bone, though highly mineralized, is often quite porous at the micron level. As in most bone, woven bone contains cells (osteocytes) and blood vessels. Rather frequently, the spaces surrounding the osteocytes are extensive and differ in this way from those in lamellar bone. There are of the order of 60 canaliculi per osteocyte (Boyde 1972), though no doubt this number varies greatly between osteocytes and between species. "Woven" bone is a misnomer, because there are very few examples of weaving, that is, true interlacing, in biology. (It would be a trick almost impossible to bring off, though, surprisingly, the enamel of some rodents has something almost as good – structures arranged in three orthogonal directions.)

Lamellar bone is more precisely arranged, and is laid down much more slowly than woven bone, less than 1 μm a day (Boyde 1980). The collagen fibrils and their associated mineral are arranged in sheets (lamellae), which often appear to alternate in thickness. The final degree of mineralization of lamellar bone is less than that of woven bone. The classical view is that the fibrils lie within the plane of the lamella, rarely passing from one to the next and that the fibrils tend to be oriented in one direction within the lamella. Indeed, some workers suggest that the collagen fibrils in a particular lamella are all oriented in the same direction (Ascenzi et al. 1978). However, this is probably not the case; in many lamellae the fibrils are in small domains about 30–100 μm across. With a domain the fibril orientation is constant, but it changes, within one lamella, from one domain to the next (Boyde and Hobdel 1969; Frasca et al. 1977). The collagen fibrils in lamellar bone form branching bundles, 2–3 μm in diameter (Boyde 1980), thicker than in most woven bone. The osteocyte lacunae in lamellar bone are oblate spheroids, the equatorial diameters being about five times longer than the polar axis. The shorter axis of each lacuna is oriented parallel to the direction of the thickness of the lamella. Frequently, lamellae seem to come in alternating thickness. There is a relatively thick one, about 5 μm thick, and has mineral

plates oriented in the plane of the circumferential extension of the lamellae, with their smallest dimension normal to the long axis of the bone.

The model of Weiner and his co-workers suggests that collagen fibrils, only 80 nm or so in diameter, are the basic unit. These may lie parallel to each other through the thickness of the lamella, or be at an angle, usually about 30°, to their neighbors. Helicoidal arrangements of fibers are found frequently in biological tissues, and (Neville 1993) has written a whole book about them. They occur in all sorts of structures, such as insect cuticle and plant cell walls, and are a prime example of the ability of organisms to produce complex structures by self-assembly, that is to say, without cells being involved directly in the placing of the succeeding layers. Helicoidal structures give rise to a confusing artifact it cut and examined at an angle to the plane of the sheets: The structure appears to consist of a series of arcs (Kingsmill et al. 1998) but, in fact, there are no arcs.

Parallel-fibered bone described by (Ascenzi et al. 1977) and by (Enlow 1969) is structurally intermediate between woven home and lamellar bone. It is quite highly calcified, but the collagen fiber bundles are much more parallel than those in woven bone.

3.2.2 Fibrolamellar and Haversian Bone

In mammals there are, at higher levels of structure, four main types of bone. Woven bone can extend uniformly for many millimeters in all directions. Such a large block is found only in very young bone (of rather large mammals) and in large fracture calluses. Lamellar bone may also occupy quite large volumes. Usually, in mammals it does so in circumferential lamellae, initially wrapped around the outside or the inner cavity of bones. There are blood channels in such bone, but they do not much disturb the general arrangement of the lamellae.

Lamellar bone also exists in a quite separate form: Harversian systems, or secondary osteons. The British and other Europeans are inclined to use "Harversian" systems,: whereas Americans prefer "secondary osteons." It does not matter which is used, except that it is critical to distinguish primary osteons, which I shall describe in a moment, from secondary osteons. Haversian systems form like this: many bone-destroying cells, called osteoclasts, move forward in a concerted attack on the bone tissue. They form a so-called cutting cone, shaped, as (Martin and Burr 1989) say in an excellent account of the process, like "half an eggshell which is about 200 μm in diameter 300 μm long." Osteoclasts are not derived from cells that occur locally, but instead come from cells circulating in the blood. As the cutting cone advances it leaves a cylindrical cavity.

The Harversian system is the classic result of the process of remodeling. There are two ways in which new bone may appear. In modeling the gross shape of the bone may be altered; that is, bone may be added to the periosteal or endosteal surfaces or it may be taken away from these surfaces.

In remodeling all surfaces of the bone may be affected, including the internal body of the bone, by the formation of Haversian systems. In remodeling the bone involved is usually a small individual packer called a basic multicellular unit (BMU), and typically the amount of bone remaining after the remodeling cycle is little changed; new bone has more or less replaced old bone.

There is a type of secondary osteon that is different from the type described above; this is called the drifting osteon. It is found in younger animals, in general. After the cavity is formed by the cutting cone, it is not filled in at once; instead, one side continues to be eroded by osteoclasts, while the opposite side is filled in by osteoblasts. As a result the cylinder of the osteon drifts sideways through the tissue, and in so doing erodes and replaces a great deal of preexisting bony tissue (Robling and Stout 1999). Nothing is known about the mechanical consequences of the presence of such secondary osteons.

There is an outer sheath to the Haversian system, called the cement sheath (or line, because it is usually viewed in cross-section). This is formed when the cutting cone stops its erosional activity and just before new lamellar bone is laid down on the raw surface so formed. The composition of the cement sheath is still controversial. Some, for instance Frasca (1981), propose that it is more highly mineralized than surrounding bone; others, for instance, Schaffler et al. (1987), propose that it is less highly mineralized. There is agreement that there is very little collagen in it. Schaffler et al. produce evidence that it has more sulfur and less calcium and phosphorus than the neighboring bone lamellae, and is therefore probably less mineralized then them. It may be that the cement line is simply a very thin layer of osteoid that remains when the process of bone erosion is replaced by bone deposition (Martin and Burr 1989), Zhou et al. (1994) suggest that there are globular accretions (of unknown composition) on the ends of the degraded collagen fibrils that have partially eroded away, and that these accretions act as a bridge between the old degraded collagen fibrils, and the newly deposited ones. The cement line is also the site of a concentration of osteopontin, a bone protein that probably has some role in bone remodeling (Barnes et al 1999; McKee and Nanci 1996; Terai et al. 1999).

Woven bone is almost certainly inferior to lamellar bone in its mechanical properties. The undesirable mechanical results of having a bone made from woven bone are partially obviated by the production of fibrolamellar bone. Essentially, an insubstantial scaffolding of woven or parallel-fibered bone is laid down quickly to be filled in more leisurely with lamellar bone.

In bovine bone, each lamina is about 200 μm thick. In the middle a two-dimensional network of blood vessels is sandwiched between layers of lamellar bone. Beyond these layers, on each side, is a layer of parallel-fibered or woven bone, which is more heavily mineralized than the lamellar bone (Fig. 3.1). In particular, there is a line in the middle, which is exceptionally heavily mineralized. This is the line at which growth stops for a short while before the next later is initiated. The way fibrolamellar bone is laid down means that there are, in effect, alternating layers of parallel-fibered or woven bone

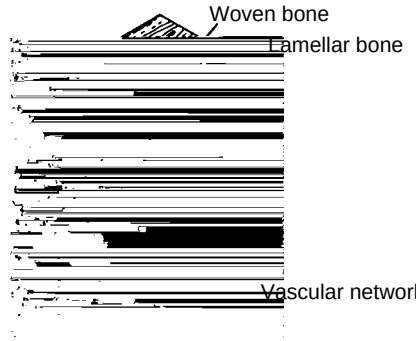

Fig. 3.1. Block diagram of fibrolamellar bone: with compliments of Whitehouse and Dyson (1974), with compliments of Shaffler et al. (1987), with compliments of Martin and Burr (1989)

and lamellar bone tissue extending, quite often, for many millimeters, or even centimeters, in the radial direction. Fibrolamellar bone can be laid down very rapidly. For instance (Castanet et al. 2000) report that the femur of a young emu Dromaius novaehollandiae can be added up to 80 µm per day on the subperiosteal surface.

3.2.3 Primary and Secondary Bone

Primary bone is replaced by secondary bone in two ways: The bone can be eroded away at its surface, and then new bone can be laid down, or else Haversian systems can be formed. Enlow (1963, 1969) gives very clear descriptions of these processes. It is often quite difficult to tell when the former has happened, and the effects, if any, of such replacement on mechanical properties are uncertain.

Human bone is like that of many primates and carnivores in that primary fibrolamellar bone is laid down initially, but this bone type is soon replaced by Haversian bone. However, this is not the case in many other mammalian groups. In most bovids (cattle) and cervids (deer), for example, the long bones keep their primary, fibrolamellar structure all through life, with only small regions, usually under the insertion of strong muscles, becoming Haversian. Many smaller mammals show no remodeling at all (Enlow and Brown 1958), the bone being fibrolamellar or, often, mainly composed of circumferential lamellae.

3.2.4 Compact and Cancellous Bone

At the next higher order of structure there is the mechanically important distinction between compact and cancellous bone. Compact bone is solid, with the only spaces in it being for osteocytes, canaliculi, blood vessels, and erosion

cavities. In cancellous bone there are large spaces. The difference between the two types of bone is visible to the naked eye. The material making up cancellous bone of adults is usually primary lamellar bone or fragments of Haversian bone. In young mammals it may be made of woven or parallel-fibered bone.

The structure of cancellous bone varies in three ways: in its fine-scale structure, in its large-scale structure, and in its porosity. At the lowest level, cancellous bone is usually made of lamellar, not woven bone. However, the lamellae usually do not usually run precisely parallel with the external surfaces of the trabecular struts and so they come out to the surface, rather like rocky strata coming to the surface of the earth, at odd angles. Singh (1978) has a convenient description of cancellous bone morphology at the next level. The simplest kind of cancellous bone consists of randomly oriented cylindrical struts, about 0.1 mm in diameter, each extending for about 1 mm before making a connection with one or more other struts (Fig. 3.2), usually roughly at right angles. In a variation of this pattern the cylindrical struts are replaced by little plates. The amount of variation ranges from cancellous bone in which there is just the occasional plate among the struts to

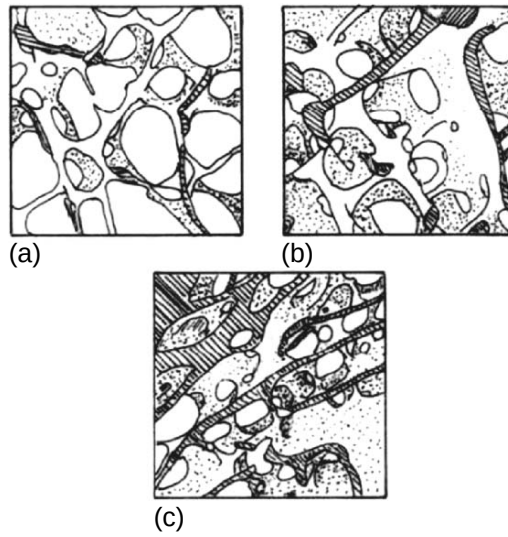

Fig. 3.2. Drawings of cancellous bone, seen by SEM. In each, the hatched parts are at the level of the top of the section. (**A**) Middle of the human sternum. Rather fine, nearly candom network of mainly cylindrical struts. Width of picture 3.4 mm (**B**) Human greater trochanter. Many of the elements are plates. Width of picture 3.4 mm. (**C**) Human femoral neck. The longitudinal plates are very obvious. There are many plates and struts lying orthogonal to them. Width of picture 8 mm (note smaller scale). (**A**) Derived from Whitehouse (1975); (**B**, **C**) derived from Whitehouse and Dyson (1974)

cancellous bone in which there is just the occasional strut among the plates. In other cancellous bone the plates may be considerably longer, up to several millimeters. When this happens there is a higher level of anisotropy: these longer plates are not randomly oriented but are preferentially aligned in one direction. The final form of such cancellous bone is shown in Fig. 3.2c, where there are parallel sheets of bone with fine struts joining them. Another type of cancellous bone consists almost wholly of sheets, forming long tubular cavities that interconnect by means of fenestrae in the walls. Gibson (1985) produced a somewhat idealized classification, which, through not grounded so firmly in the messy reality of life, is nevertheless convenient for mechanical modeling.

These different versions of cancellous bone as classified by Singh are found in characteristically different places. The type make of cylindrical struts, with no preferred orientation, is usually found deep in bones, well away from any loaded surface, while the more oriented types, made of many sheets, are found just underneath loaded surfaces, particularly where the pattern of stress is reasonably constant. If the trabeculae are more than about 300 μm thick, they often contain blood vessels, usually within secondary osteons (Lozupone and Favia 1990). The porosity of cancellous bone is the proportion of the total volume that is not occupied by bone tissue. Usually it is filled with marrow, but in birds there may be gas. The porosity varies from being effectively complete, where there is only the occasional tentative strut sticking into the marrow cavity, down to about 50%. If the porosity is less than about 50%, then cancellous bone becomes difficult to distinguish from compact bone with many holes in it. However, the change from compact to cancellous bone is usually clear and takes place over a small distance, and bone with a porosity of between 50% and 15% is uncommon.

3.3 Summary

- Tropocollagen molecules (wrapped in a triple helix) lined up in files, and bonding side to side to form:
- Microfibrils, which aggregate to form:
- Fibrils, which are impregnated by and surrounded by the mineral hydroxyapatite or, somewhat more accurately, dahllite.

These fibrils appear in three different forms:

woven bone	parallel-fibered bone	lamellar bone
fibrils 0.1–3 μm in diameter, arranged fairly randomly	intermediate	fibrils 2–3 μm in diameter, arranged in sheets (lamellae) 2–6 μm in thickness

Bone has bone cells, enclosed in lacunae:

roughly isodiametric	oblate spheroids, 5:1 ratio of
∼20 µm in diameter	major and minor axes. major axes 20 µm

Canaliculi, about 0.2–0.3 µm in diameter, are channels containing cell processes that connect the cells with each other and with the nearest blood channel. Each osteocyte has about 60 canaliculi.

The bone is organized, at the next higher level, in four different ways:

lamellar bone	woven bone	fibrolamellar bone	secondary osteons (Haversian systems)
often found in large lumps in reptiles. found as circumferential lamellae in mammals and birds. primary and secondary	found in large lumps in young animals and in fracture callus. primary	alternating sheets of lamellar and woven bone/ parallel-fibered bone, with 2-dimensional nets of blood vessels. Ca. 200 µm between blood vessel nets. primary	cylinders of lamellar bone, solid except for a tube in the middle for blood vessels. Ca. 200 µm in diameter. secondary

3.4 Material Properties as Input in Numerical Models

Cortical bone was modeled as a homogeneous isotropic material. The thick cortical bone of the tibial and fibular shaft was assigned a Young's modulus of $E = 17,960$ MPa representing diaphyseal cortical bone as in the work of Lewis and Austin. This corresponded well with experiments performed by Reilly and Burstein (see Table 3.1). Observations of architecture of cancellous bone in the talus indicated that the plates of trabeculae in the head of the talus were running vertically and parallel to the applied load. This implied that the thin cortical shell was oriented longitudinally with respect to our applied load. For this reason, a longitudinal Young's modulus of metaphyseal bone $E = 9,650$ MPa was chosen based on measurement by Lotz et al. This material property was assigned to the volume 1 mm thick and 3 mm wide surrounding the resected areas of the talus dome (Fig. 3.3). The two 3-mm-wide volumes immediately below the talar component meshed with cancellous and cortical bone elements contained 44,870 nodes. To save computational time, the size of cortical bone (and cancellous as well) elements increased distally. To compensate for the increased thickness of the cortical bone, a reduced zone with decreased Young's modulus of metaphyseal bone in the distal section of the talus was created in a manner similar to Lotz et al. The Young's modulus of metaphyseal bone in this reduced zone was one-fifth

Table 3.1. Material properties used in the model

material	E (MPa)	ν	yield criteria	failure criteria
cortical diaphyseal bone[6]	17,580	0.3	NA[a]	NA[a]
cortical metaphyseal bone[109]	9,650	0.3	$\sigma_y = 100\,\text{MPa}$	$\varepsilon_u = 3\%$[108]
cortical reduced	9,650/5	0.3	$\sigma_y = 100/5\,\text{MPa}$	$\varepsilon_u = 3\%$[108]
cancellous homogeneous[6]	280	0.3	NA[a]	NA[a]
cancellous heterogeneous[100]	500–850	0.3	$\varepsilon_y = 0.8\%$[86,91,92,97]	$\varepsilon_u = 1.5\%$[86,91,97]
cobalt–chrome alloy[6]	193,000	0.29	NA[a]	NA[a]
titanium alloy[6]	110,000	0.33	NA[a]	NA[a]
polyethylene[157]	557[b]	0.46	$\sigma_y = 10.86\,\text{MPa}$	

[a] Not part of the current study
[b] Nonlinear material properties

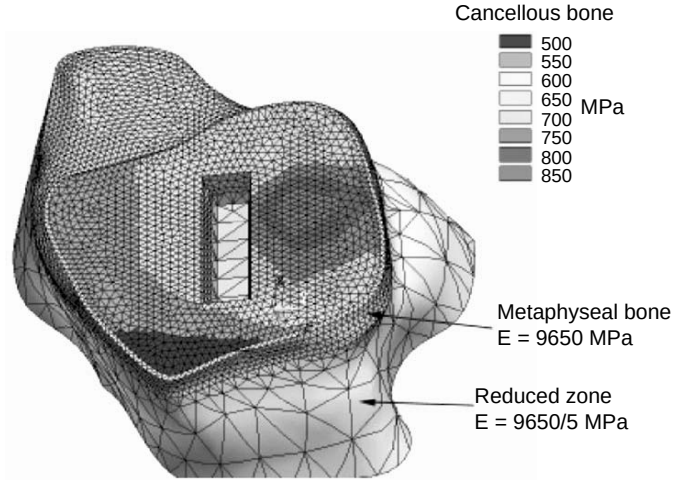

Fig. 3.3. Heterogeneous material properties of talus

of the original value. The talar bone in generaly loaded in compression. The cortical bone behaves when loaded as elastoplastic material. Cancellous bone under compression behaves like a damaging material with strain softening. Talar stresses can be computed as a plastic material model for both cancellous and cortical bones. Table 3.1 gives the material properties for various bones. The Evalue for the metaphyseal bone is generally taken as 9,650 MPa. The stress–strain curve is defined for cancellous bone in Fig. 3.4.

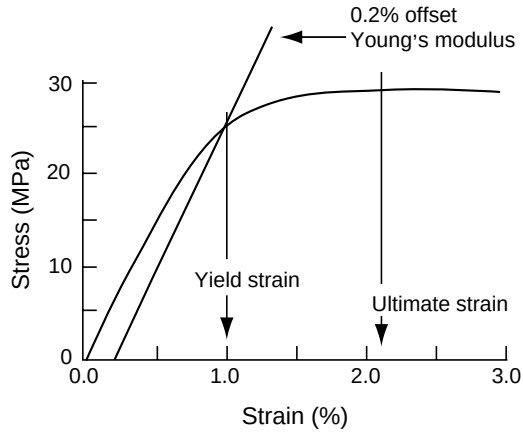

Fig. 3.4. Definition of the cancellous bone failure parameters as used in Keaveny's experiments. The ultimate strain was calculated as the lowest strain that occurred for the maximum stress

Shear failure tests of cancellous bovine bone by Ford and Keaveny showed that the ultimate and yield stresses depended on apparent densities while the ultimate and yield strain were constant. Based on these results, they suggested that the mean failure strain values might be extrapolated to low density human bone.

Table 3.2 shows the yield and ultimate strains vs. Young's modeling obtained by various researchers for various bones.

3.4.1 Material Properties use in the Numerical Models

The latest study on dependence of yield strain of human cancellous bone on anatomic location by Morgan and Keavany showed that the yield strain in both compression and tension differed between the anatomic locations but could be considered uniform within each location. The differences of yield strain across the location were small, almost 20% (Table 3.2), while the yield stress and modulus differed by a factor of 8 and 10, respectively. They concluded that interlocation differences are not due to testing or anisotropy artifacts as previously thought. They recommended using yield criteria, whether based on stress or strain, that would be specific to the anatomic location. It should be pointed out that all the tests by Keavany et al. were performed along the direction of the principal axis of cancellous bone and therefore, the results provided no information for different loading directions.

French and Keaveny showed that for uniaxial tensile or compressive load coupled with torsional loading around the same direction, minimum principal strain criterion accurately predicted failure in tension, but was less accurate in compression. In addition, experimental and finite element studies by Lotz et al.

Table 3.2. A Comparative Study of E and E-values for Various Bones

reference	bone	$\varepsilon_y(\%)$	$\varepsilon_u(\%)$	E (MPa)*
compression				
Keaveny[62]	bovine tibia	1.08	1.86	2380
Morgan[92]	human tibia	0.73	NR	1091
Morgan[92]	great. trochanter	0.70	NR	622
Morgan[92]	human vertebra	0.77	NR	344
Morgan[92]	femoral neck	0.83	NR	3230
Fyhrie[97]	human vertebra	0.67	1.5	500
Kopperdahl[91]	human vertebra	0.81	1.45	219
Linde[81]	knee	NR	2.0	408
tension				
Keaveny[62]	bovine tibia	0.78	1.37	2630
Morgan[92]	human tibia	0.65	NR	1068
Morgan[92]	great. trochanter	0.61	NR	597
Morgan[92]	human vertebra	0.70	NR	349
Kopperdahl[91]	human vertebra	0.78	1.59	301
Shear				
Ford[79]	bovina tibia	1.35	4.24	$G = 349$

*Average Young's modulus

and Silva et al. found cancellous bone failure criteria based on strains to be more successful than failure criteria based on stress. In contrast, a study by Keyak et al. without experimental confirmation showed that strain-based failure theories performed more poorly.

In summary, the mechanical properties of cancellous bone show:

- The same tensile and compressive Young's moduli
- Asymmetric yield strengths and strongly dependency on density
- Asymmetric yield strains with no dependency on density and loading direction
- Yield strains constant between anatomic locations
- Asymmetric post-yield behavior with brittle fracture in tension and strain softening in compression
- The poisson's ratio in one to three-dimensional cases with constant and variable cases are given in Appendix I.

3.5 Fatigue Strength of Cancellous Bone

Fatigue failure can occur at stress levels considerably lower than the static strength. Even though the fatigue failure of bone is not well understood, it is known to resemble the fatigue of composite materials, in which a gradual loss of stiffness and strength occur over the loading period. It is also well

knows that fatigue creates microfractures in cancellous bone and it has been hypothesized that these microfractures trigger a remodeling response. If the damage by microfracture exceeds the repair by remodeling, the bone will fracture, or as in case of implants, the implant will subside into cancellous bone.

While there have been many studies of the fatigue behavior of cortical bone (see, for example (Caler and Carter) only a few studies examined fatigue behavior of cancellous bone. Experiments by Choi and Goldstein suggested that the fatigue strength of trabecular tissue (the intrinsic property of cancellous bone) was lower than the fatigue strength of cortical bone tissue. For our macroscopic level FEM study, the fatigue strength of cancellous bone is more important. Kempson estimated, without experimental evidence, that the fatigue strength of cancellous bone was one third of the ultimate compressive strength. Since then, some studies used it as a "rule of thumb" for predicting implant subsidence. Similarity in fatigue behavior between cancellous and cortical bone was reported by Michel et al. The results showed that the fatigue life was strongly dependent on the magnitude of the maximum strain applied in first cycle (Fig. 3.5). Bovine cancellous bone failed in cyclic loading at loads below the yield strength. For a lifetime of one million cycles, one can estimate a failure strain of 1% which is approximately 40% of the original ultimate compressive yield of the study. It was hypothesized that cancellous bone at low cycle, high initial stress, will fail by creep and at high cycle, low initial strain, will fail by microcracking. In any in vitro study in general, the remodeling process that would accompany damage accumulation in vivo is not present. Moreover, all studies of fatigue properties of cancellous bone have been conducted with bovine bone which is more dense and structurally different than human cancellous bone.

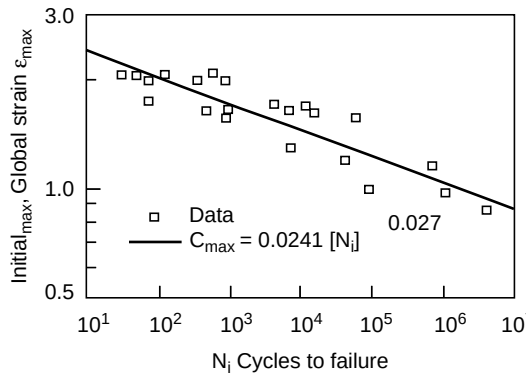

Fig. 3.5. Fatigue curve for bovine cancellous bone

3.6 Additional Material Properties of Cortical Bone

The study of static mechanical properties of human cortical bone by Reilly and Burstein has been used as a reference in many papers. The experiments were carried out on diaphyseal cortical bone. As with cancellous bone, the tensile and compressive Young's moduli were shown to be the same while ultimate strengths were asymmetric. The mechanical properties are listed in Table 3.3.

The post-yield behavior of cortical bone (Fig. 3.6) is also asymmetric. In tension, the behavior can be modeled as bilinear with a post-yield modulus

Table 3.3. Mechanical properties of diaphyseal cortical bone from experiments by Reilly and Burstein

mechanical property	longitudinal	transverse
E(MPa)	17,000	11,500
ultimate strength (MPa)	133^{t}, 193^{c}	$51^{t}, 133^{c}$
ultimate strain	3.1%	0.7%

t-tension c-compression

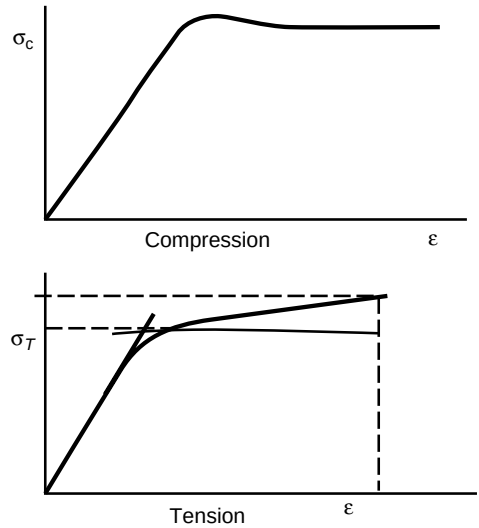

Fig. 3.6. Stress–strain curve in tension and compression for cortical bone

Table 3.4. Mechanical properties of metaphyseal cortical bone from experiments by Lotz et al

mechanical property	longitudinal	transverse
E(MPa)	9,650	5,470
ultimate strength (MPa)	100	50

of approximately $E = 0.8\,\text{GPa}$. In compression, cortical bone behaves like an elasto-perfectly plastic material. The material properties of thin metaphyseal cortical shells were investigated by Lotz et al. who found a moderate decrease in mechanical properties compared to cortical diaphyseal bone. The difference between the metaphyseal and the diaphyseal bone was attributed to lower density of the metaphyseal bone. The material properties are listed in Table 3.4.

4

Material Properties, Clinical Data on Tolerance Thresholds Used for Assessing Numerical Modeling

4.1 General Information

This chapter covers material properties from existing clinical data and tests and manufacturers designs of artificial parts. Material properties are chosen in areas of traumatic injuries – some materials are earmarked and their technical properties have been discussed in relation to various finite element modelings. A brief discussion is given on surface modeling, meshing associated with specific medical-cum-engineering requirements. Some results are included on the behavior of materials.

A valuable data on tolerance thresholds have been included on major human body parts so as to assess and correlate results obtained from numerical and finite element techniques.

4.2 Carbon Fibers-High Modulus Fibers

Carbon fibers consists of rows, each made up of numerous filaments (10,000). The filaments are 7–15 cm in diameter, and they consist of small crystallites of "turbostatic" graphite, which is one of the allotrophic forms of carbon. In the graphic crystal, carbon atoms are arranged in an hexagonal array in a plane (Fig. 4.1) and the planes are stacked together, with covalent bonds acting within the planes and weaker Van der Waals forces holding the planes together. To obtain a high modulus and strength, the layered planes of graphics must be weaker Van der Waals forces holding the planes together. "To obtain a high modulus and strength, the layered planes of graphic must be aligned parallel to the fiber axis. However, the structure of the stacked planes is not ideally regular as can be seen from the schematic representation in (Fig. 4.2). Therefore, the properties of carbon fibers can vary over a wide range, depending upon the degree of perfection, which is a function of the production process.

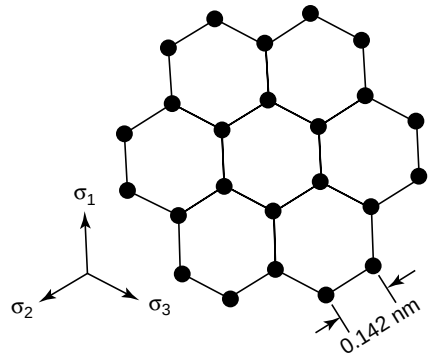

Fig. 4.1. Structures of carbon atoms in graphite layer

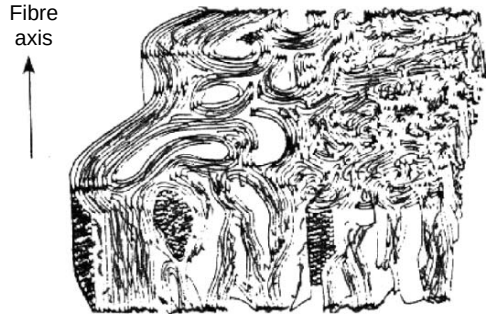

Fig. 4.2. Carbon fibers – schematic description of the structure using X-ray diffraction and electron microscopy

The two main processes for making carbon fibers are based on different starting materials, either polyacrylonitrile (PAN carbon fibers) or petroleum and coal tar pitch (pitch carbon fibers). Both processes involve heat treatments, and various grades of carbon fibers can be obtained with each, depending on the combination of heat treatment, stretching, and oxidation. Typical properties are presented in Table. The PAN carbon fibers are of higher quality, and are sometimes classified into two types, I and II, with type I having a higher modulus of elasticity and strength. The pitch carbon fibers have a much lower modulus of elasticity and strength, but their price is much lower than that of one of the PAN fibers. The pitch fibers still have superior properties to many other synthetic fibers, and their modulus of elasticity is equal to or greater than that of the cement matrix. This, combined with their lover price, has made them more attractive for cement reinforcement. The pitch fibers were developed in Japan, and much of the work on reinforcing cement with these fibers has been carried out there.

4.2.1 Production of the Composite

Carbon reinforced cement composites can be produced by hand lay-up of continuous fibers or mats, filament winding, spraying, and conventional mixing. The maximum fiber content that can be incorporated in a cement matrix, based on the assumption that the diameter ($\sim$10 μm) is of the same order of magnitude as the size of a cement particle. For cement particles to be able to penetrate between the individual filaments, i.e., if the spacing between the filaments is about the same size as the cement grain, the maximum fiber content is about 12% by volume for unidirectional orientation, and less than 4–5% for random orientation.

Another method has been used carbon tow impregnated with polyvinyl acetate (PVA) to obtain a good fiber–matrix bond, and to avoid the difficulty of opening up the spaces between filaments to allow penetration of cement particles. The PVA served as an intermediate medium for achieving effective stress transfer. Other attempts to improve bond and to compensate for potentially poor dispersion has also been based on polymer impregnation of the composite.

The dispersion of the carbon fibers into individual filaments is controlled when preparing composites with short fibers by the mixing technique. The methods used have included fiber separation by a dispenser or a hammermill, mixing with the Omni mixer, or mixing with an ordinary mortar mixer but replacing 40% of the protland cement with silica fume. In these applications, the mortar mix also contained various combinations of water reducing and air entraining agents. Using such methods, it was possible to incorporate up to 3–5% by volume of short fibers (3–10 mm) with effective dispersion. Although the flow properties tended to decrease with an increase in fiber content (Fig. 4.3), mixes containing up to 5% short fibers were found to possess suitable flow characteristics for casting, and their moldability and finishability were similar to those of the unreinforced matrix.

Curing of the carbon composites was carried out either by normal room temperature procedures or by autoclaving. The carbon fiber is sufficiently stable to endure the height pressure and temperature conditions in the autoclave.

4.2.2 Mechanical Properties

The mechanical properties have generally been evaluated for two types of composites, prepared either by hand laying of continuous fibers and mats, or by mixing of short fibers. Most of the work with continuous, hand lay-up reinforcement was carried out with the high quality PAN carbon fibers, while random short fiber reinforced composites have generally been studied using the lower quality pitch carbon fibers.

(a) Continuous hand laid reinforcement. Stress–strain curves of continuous and aligned carbon FRC are shown in Fig. 4.4. They clearly demonstrate the effect of the increase in fiber content on the increase in modulus of

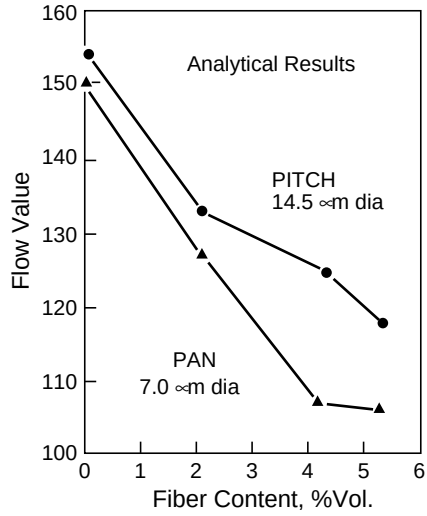

Fig. 4.3. Effect of fiber content and type on the flow of mortar mixes

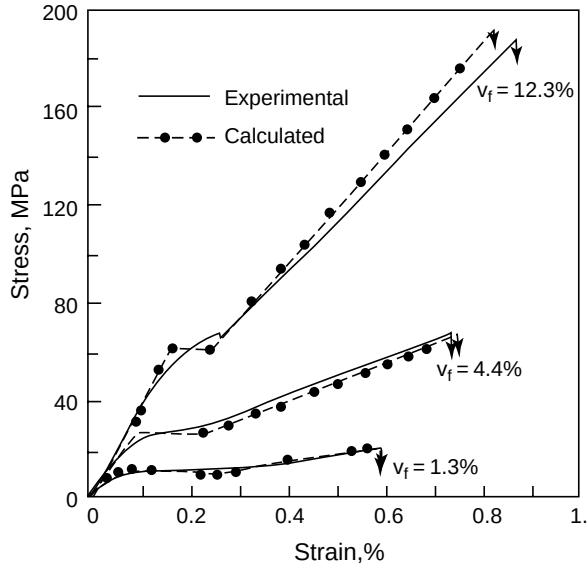

Fig. 4.4. Effect of reinforcement with continuous carbon fiber on stress–strain curve of cementatious composites

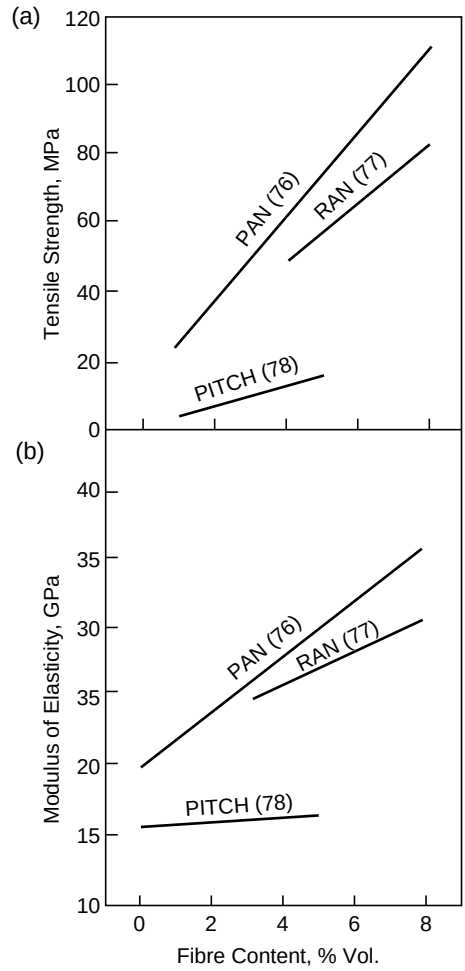

Fig. 4.5. Carbon fiber contents vs. tensile strength and E of cementitious composites

elasticity, first crack stress, and strain, and ultimate tensile strength. Similar curves have been reported for continuous reinforcement. However, for random mat fibers, with 3% fiber content by volume, the composite failed at the limit of proportionality, without exhibiting the marked postcracking behavior typical of the continuous and aligned fibers.

These results show that although a linear strength and fiber content may be established as of composite materials theory, the slope of these curves can be quite different. Tensile strength is plotted in (Fig. 4.5a).

Similar effects have been found in the modulus of elasticity results (Fig. 4.5b). It should be noted that here, no improvement was obtained

Table 4.1. Properties of PAN carbon fiber

property	PAN		pitch
	type(I)	type(II)	
diameter (μm)	7.0 to 9.7	7.6 to 8.6	18
density ($\mathrm{kg\,m^3}$)	1,950	1,750	1,600
modulus of elasticity (GPa)	390	250	30–32
tensile strength (MPa)	2,200	2,700	600–750
elongation at break (%)	0.5	1.0	2.0–2.4
	−0.5–1.2 (parallel)	−0.1–0.5 (parallel)	
coefficient of thermal expansion ($\times 10^{-60}\mathrm{C}^{-1}$)	7–12 (radial)	7–12 (radial)	–

with the pitch fibers, reflecting the fact that their modulus of elasticity is similar to that of the matrix, whereas the PAN fibers have been a modulus which is much greater (Table 4.1).

(b) Short and randomly mixed fibers. The effect of mixing short carbon fibers, mainly of the pitch type, has been studies primarily in Japan using fibers up to 10 mm in length. The aspect ratio or such fibers is quite high more than 100, since the diameter of the individual filaments is about 10 μm. The SEM micrographs suggest dispersion of the tow into individual filaments. Thus, the reinforcing effect of these short fibers is quite high, even the volume contents of less than 4%. The load–deflection curves presented in Fig. 4.6 clearly indicate the marked improvement in the flexural strength and postcracking behavior achieved with such fibers.

It is interesting to note the effect of strengthening the matrix by reducing its w/c ratio (compare Figs. 4.6a and 4.5b) which leads to a marked change in the shape of the load–deflection curve, reducing its postcracking portion in the low w/c ratio matrix, without much changing its peak load. The matrix composition has a greater effect on toughness than on the flexural strength. It is worth noting, in the later case, the particularly low toughness values of the low w/c ratio mix of 0.298.

The influence of pressure on the load–deflection curve is shown in Fig. 4.7 of the carbon fiber reinforced paste with 1.7% fibers by volume. In the actual composite many of the fibers would be in this length range, because the longer, 10 mm fibers, introduced during mixing tend to break, and the average fiber length is ½ to ¼ of the original value. The length distribution of the fibers after mixing (Fig. 4.8) is quite different from the uniform original 10 mm in length. The reduction in the average length and the resulting distribution apparently depends on the strength of the fibers, with the weaker ones (A in Fig. 4.8) breaking up more than the stronger ones (F in Fig. 4.8). This change in fiber length results in a shortening of many of the fibers to the critical length of 0.8–1.4 mm, thus accounting for the mixed mode of fiber fracture and fiber pull out.

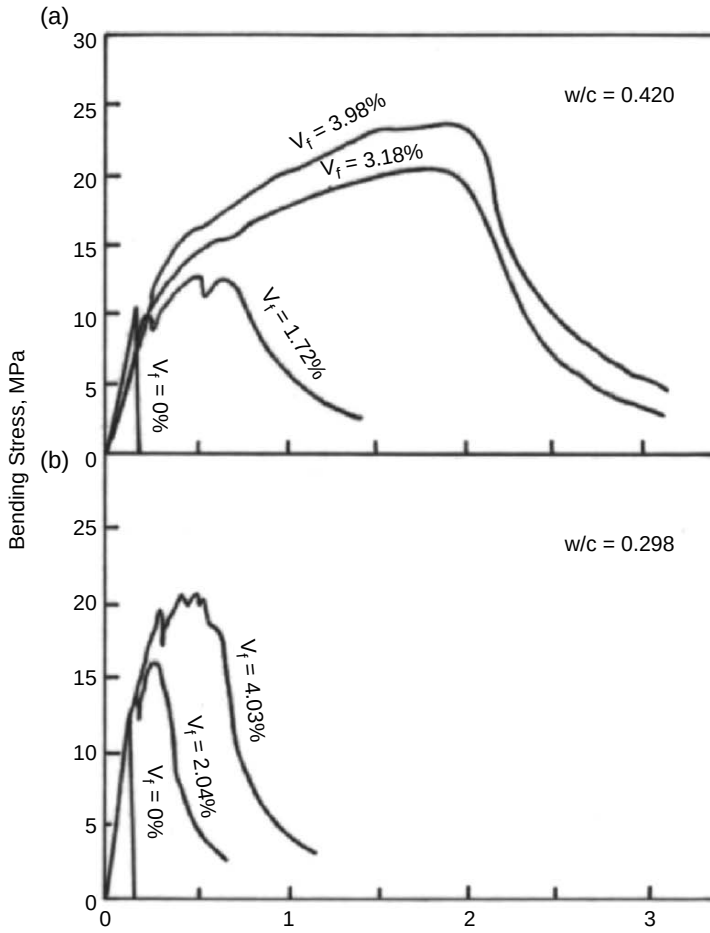

Fig. 4.6. Load–deflection curves in bending of mixes with paste matrix fiber 10 mm long and 14.5 μm

The effect of the quality of the carbon fibers on the properties of the composite was evaluated by Nishioka et al. using pitch fibers with tensile strength in the range 440–764 MPa, and elastic moduli in the range 26.6–32.4 GPa. An increase in fiber strength was associated with an increase in flexural strength and toughness (Fig. 4.9). On this basis it was suggested that for effective reinforcement, the fiber should have a strength greater than 640 MPa. Apparently, part of the poor performance of the lower strength fibers is associated with their breakdown into shorter lengths during mixing (Fig. 4.8). For the data in Fig. 4.9 a better correlation can be established when the composite property is plotted against the average fiber length after mixing (Fig. 4.10). This emphasizes

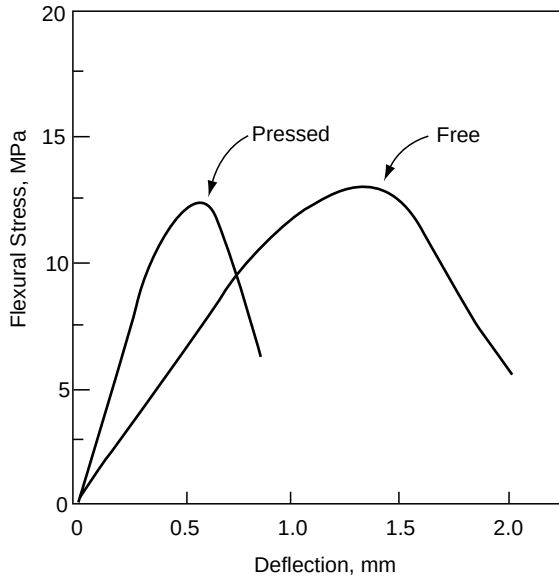

Fig. 4.7. Load–deflection curve of carbon fiber reinforced past with 1.7% fibers by volume. Compaction pressure after casting

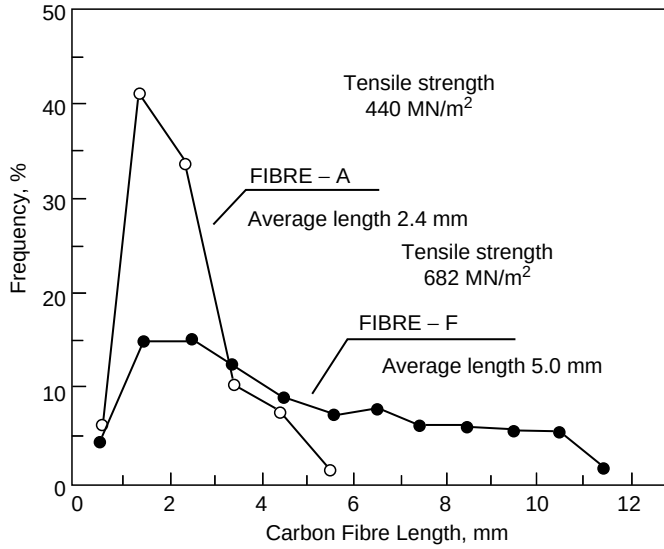

Fig. 4.8. Percentage frequency vs. carbon fiber lengths

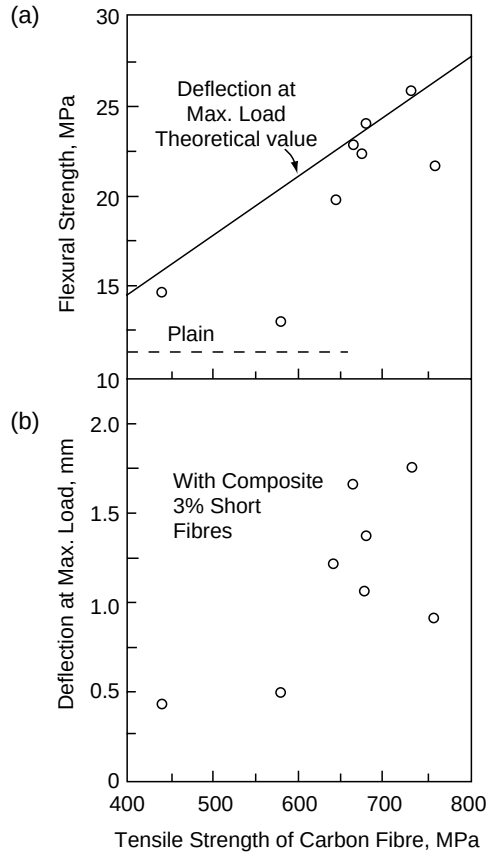

Fig. 4.9. Load–depletion curve. The effect of pitch carbon fiber strength on the flexural strength (10 mm long and 18 μm dia.)

the importance of accounting for the composite properties on the basis of the length of the fibers after mixing, rather than the original length.

The modules of elasticity of a pitch carbon composite, produced with short fibers, tended to decrease slightly with an increase in fiber content. This is because the modulus of elasticity of the type of fiber (Table 4.1) is not much greater than that of the matrix, combined with the reduced density of the matrix at higher fiber content. The latter effect is the result of the greater difficulty in the compaction of the fresh composite containing fibers.

4.2.3 Dimensional Stability

The presence of carbon fibers has been found to be effective in decreasing strains due to swelling and shrinkage, both for PAN fibers and pitch fibers

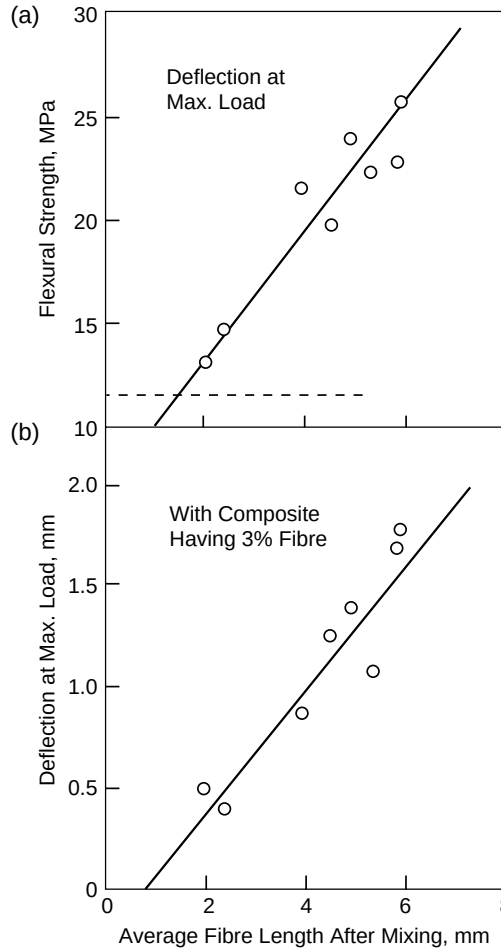

Fig. 4.10. The fire of 10 mm long effect of pitch carbon fiber length after mixing on the flexural strength 3%

(Fig. 4.11). The reduction was by about a factor to 2–3 for 3% of short fibers, and considerably greater for higher fiber contents. Briggs et al. reported a decrease in shrinkage by a factor of 10 with a 5.6% fiber volume, and a reduction in creep by a factor of 6 with 2% fibers. The shrinkage values can be lowered further by autoclave curing of the composite. As a result of the reduced shrinkage and improved toughness, this composite is both dimensionally stable and less sensitive to cracking. This stability, combined with the high strength, was utilized in the construction of lightweight tiles and curtain walls.

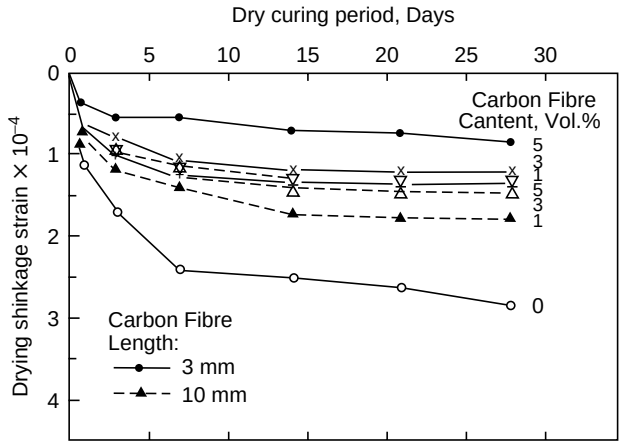

Fig. 4.11. The effect of pitch carbon fiber content on the shrinkage of autoclaved composites

The alkali resistivity of carbon FRC was tested using an accelerated procedure (immersion in water at 50°–75°C). Similar to the test applied for GRC. Most of the strength and toughness were retained after prolonged testing, up to 3 months or 1 year (Fig. 4.12a). Exposure of the composites to freeze-thaw cycles and alternating wetting and drying cycles also did not lead to any reduction in strength or modulus of elasticity (Fig. 4.12b). Such results indicate that carbon FRC would not be expected to exhibit long-term performance problems.

4.2.4 Mechanics of Composite

A number of investigators applied the ACK model to account for the stress–strain curves of continuous carbon fibers composites. The average bond strength:

$$B_{\mathrm{T}} = 0.8\,\mathrm{MN\,m^{-2}} \rightarrow \text{fibers } 9.2\,\mathrm{m} \text{ diameter}$$
$$= 2.5\,\mathrm{MN\,m^{-2}} \rightarrow \text{fibers } 9.2\,\mathrm{m} \text{ diameter}$$

A typical pitch will carbon fiber strength of $600\,\mathrm{MN\,m^{-2}}$–$750\,\mathrm{MN\,m^{-2}}$ for 10–20 μm diameter with a bond strength ranging from 0.8 to $2.5\,\mathrm{MN\,m^{-2}}$ with a critical fiber length of 0.6–2.0 mm.

The rule of mixtures can also be applied to account for the tensile strength of composites with short and randomly dispersed pitch carbon fibers. For a fiber length of 10 mm, which exceeds the critical length, the overall coefficient was found to be in the range of 20–40%, with the value decreasing with an increase in fiber volume. Since, during mixing, some of the fibers do break and become shorter. This should also be taken into account. The actual length

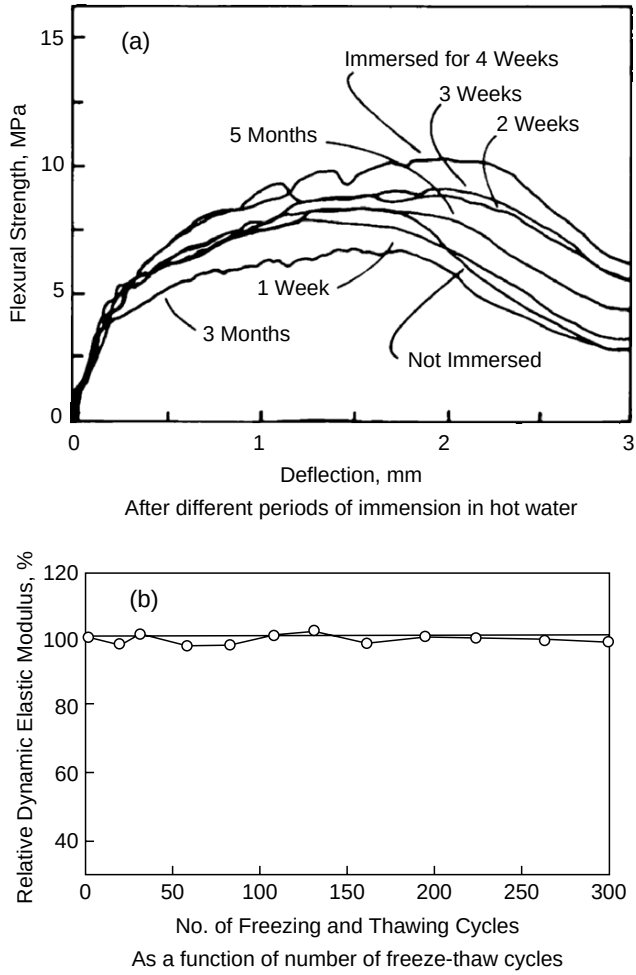

Fig. 4.12. Durability of pitch carbon fiber reinforced cement with 2% fibers and autoclaved matrix

distribution of the fibers after mixing (Fig. 4.8) and calculated the strength by summing the contributions of fibers with lengths shorter than the critical length, and those with lengths greater than the critical length:

$$\sigma_{\mathrm{cu}} = \eta_1 \left(1 - \frac{1}{2}\frac{l_{\mathrm{c}}}{l_1}\right) \sigma_{\mathrm{f}} \nu_{\mathrm{f1}} + \eta_1 \left(\frac{1}{2}\frac{l_2}{l_{\mathrm{c}}}\right) \sigma_{\mathrm{f}} \nu_{\mathrm{f2}} \tag{4.1}$$

where

η_1 = orientation efficiency factor
l_1 = average length of fibers shorter than the critical length

l_2 = average length of fibers longer than the critical length
$V_{f1} V_{f2}$ = volume contents of fibers shorter and longer than critical length, respectively.

4.3 Biomedical Materials

4.3.1 Glass Fiber Reinforced Composite

Since the composite materials have a high strength and low weight, they are useful for all biomedical structures. The use of these materials in the biomedical structures and in others such as aeronautic, marine vehicles, cars and the likes, is ever increasing and has found its place in other fields of industry. Further information on destruction and rupture of these materials has a special importance, particularly in biomechanics.

The rupture of a composite material, because of the variety of the mechanisms used in the destruction of structure, is very complicated. Figure 4.13 shows a variety of possibilities of destruction.

In multilayer composites another phenomenon is added to the mechanisms of failure, which is delamination of the layers. In the mechanism of delamination which is analogous to the crack growth in the isotropic materials, all the possibilities of rupture shown in Fig. 4.13 exist.

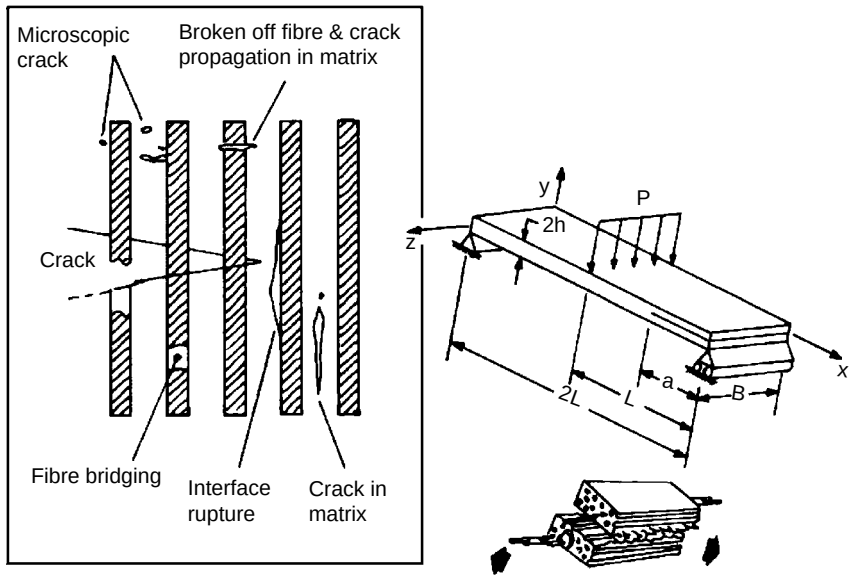

Fig. 4.13. The type of rupture in composite structure

The mechanical behavior of thermoset matrix composite materials is similar to the brittle materials. So the plastic zone at the tip of crack is very small and in analyses using finite element method, the plasticity of that zone is not generally considered in the field of biomechanics and biomedical engineering. The material properties are used in the finite element analysis are as follows:

$$\begin{aligned} E_x &= 40\,\text{GPa} \\ E_y &= E = 10.5\,\text{GPa} \\ V_{xy} &= 0.3 \\ V_{xz} &= V_{yz} = 0.078 \end{aligned} \tag{4.1a}$$

Data for Engineering Analysis

For two-dimensional (2D) modeling, we have used the element of four corners with 8 nodes and element of three corners with 6 nodes. As the width of specimen is higher than its thickness, the problem is studied in plane strain state. As the dimension of the zone of stress concentration is lower than the dimensions of the rest of specimen, only a small zone around the tip of the crack is grid generated with a high concentration. The type of element and the type of mesh generation lead to the singularity of stress and strain at the tip of the crack.

In the three-dimensional (3D) specimen, we have used an element of 6 faces with 20 nodes and an element of 5 faces with 15 nodes.

The type of grids and boundary conditions are also taken as a 2D specimen. Any other elements from the appendices of the text can be selected depending upon the suitability of the complexity of the problem.

Analyzing the specimen by using the finite element method, different stresses are calculated at the end of crack. Using one of the rupture criteria in composite materials and the obtained stresses at the end of the crack, the strain energy release rate of the specimen for delamination is evaluated. As the plastic zone at the end of the crack is very little, we consider only an elastic rupture at the end of the crack. The procedure of finding crack sizes and directions are fully dealt with in the appendices.

Theory of the Tsai–Hill

$$\left(\frac{\sigma_x}{X}\right)^2 - \frac{\sigma_x \sigma_y}{X^2} + \left(\frac{\sigma_y}{Y}\right)^2 + \left(\frac{\tau_{xy}}{S}\right)^2 = 1. \tag{4.2}$$

This criterion is obtained from development of the von Mises theory. If the stresses in a test satisfy the relation (4.1a), the test bar will be at the beginning

of rupture. X, Y, are the yield stresses in directions x, y and S is the shear yield stress on the xy plane.

Theory of Tsai–Wu

According to this theory, if the stresses increase to the extent that the relation (4.3) becomes true, the test bar will be at the beginning of rupture.

$$\frac{\sigma_x^2}{X_\mathrm{t} X_\mathrm{c}} + \frac{C_{xy}\sigma_x\sigma_y}{\sqrt{X_\mathrm{t} X_\mathrm{c} Y_\mathrm{c} Y_\mathrm{t}}} + \frac{\sigma_y^2}{Y_\mathrm{t} Y_\mathrm{c}} + \frac{\tau_{xy}^2}{S^2} + \left(\frac{1}{X_\mathrm{t}} - \frac{1}{X_\mathrm{c}}\right)\sigma_x + \left(\frac{1}{Y_\mathrm{t}} - \frac{1}{Y_\mathrm{c}}\right)\sigma_y = 1. \tag{4.3}$$

The index t means tension, and index c means compression. C_{xy} is the coefficient in then plane xy, which is equal to (-1) for a unidirectional composite.

In the finite element method using the above theory, the critical load (P_c) and deflection (δ_c), for which the stresses at the tip of the crack reach their critical values (limit of rupture), are computed. Repeating this analysis for different initial crack lengths, we obtain the compliance as a function of the crack length. Using the general relation of strain energy release rate, the value of G_II as a function of crack length is obtained.

The effect of fiber bridging from the matrix between the two faces of the crack should be taken into account in the analysis of delamination. The area in which one observes this phenomenon, is a small zone in the left-hand part of the crack. During the crack growth, this zone follows the delamination. The existence of this zone increases the strain energy release rate, because after rupture occurring at the end of the crack, a part of energy is used to pull out the fiber from the matrix. This effect (fiber bridging) operates like the plastic zone at the end of the crack in isotropic materials. Thus, the total strain energy release rate is the sum of strain energy release rate of crack growth. G_m and the strain energy release rate, resulting from fiber bridging of the matrix, G_p.

$$G_\mathrm{t} = G_\mathrm{p} + G_m \tag{4.4}$$

The strain energy release rate G_{11} can be easily derived as

$$G_{11}^{\mathrm{CBT}} = \frac{9Pa^2\delta}{2B\left(2L^3 + 3a^3\right)}, \tag{4.5}$$

$$G_{11}^{\mathrm{CBT}} = \frac{9Pa^2}{16EB^2h^3} \tag{4.6}$$

where δ is the deflection of the specimen (BT: Beam Theory, CBT: Compliance Beam Theory).

Physical properties of materials (such as the Young modulus: E), are known with some percent of error, so (4.5) in which physical indicators of the material do not appear explicitly, has higher precision than (4.6).

4.3.2 Constitutive Properties of Bone Anisotropy and Cementless Removal Implants

General Introduction

Implant separation from bone tissue, resulting in the necessity for revision surgery, is a serious drawback of cementless total joint replacement. Unnatural stress distribution around the implant is considered the main reason for the failure. Optimization of the implant properties, especially its geometric parameters, is believed to be the right way to improve reliability of joint prosthetics. Numerical models of femur-implant system enabling approximate analysis of stress distribution and shape optimization of implants suffer from numerous simplifications as, e.g., the assumption of bone isotropy, which may put in question reliability of the results obtained. In this section a numerical model including orthotropic properties of both cancellous and cortical bone is presented and influence of this assumption on results of the analysis and optimization is investigated.

Total joint replacement is a standard surgical technique employed in treatment of various types of joint diseases and damages, especially in hips and knees. The surgery consists in removal of femoral head and acetabular surface and placement of a pair of implants, being elements of an artificial joint, in cavities of appropriately drilled bones. Implants can either be directly forced (press-fitted) into the cavity or fixed to its walls by an interfacing layer of flexible polymeric cement (like PMMA).

The precise mechanism of the failure is not clear, however, mechanical rather than medical factors are reported to play the major role. In cementless implants, load transfer between a stiff implant and relatively flexible bone results in extremely unnatural stress distribution in the latter, i.e., excessive stress concentrations near to the implant ends, and stress shielding followed by bone resorption in other areas of the bone–implant interface. The reason for short-term loosening are relative micromotions resulting, e.g., from improper implant fitting in the bone cavity. These may affect bone ingrowth into the porous implant surface and, consequently, lead to permanent debonding of implant from bone.

Stressed and motions in bone and implant depend mainly on loading conditions and on the implant design, i.e., its mechanical properties and geometry. As the latter is easy to be modified in quite a wide range, design optimization of the implant shape appears to be a promising way to improve the reliability of joint prosthetics.

Numerical simulations of mechanical behavior of bone–implant systems are mainly based on the finite element method of over 200 contributions in this field. The method is criticized for limited reliability of results due to effects of mesh size and distortion, simplified constitutive models and loading conditions. Yet, it still remains the fundamental noninvasive tool in effective analyzing of deformation and stress distribution in both intact and implanted bones.

Design optimization of implants requires, apart from the numerical analysis tool, the computation of design gradients (sensitivity) of implants appeared in the literature but it is only in recent years that comprehensive finite-element sensitivity and optimization studies have become of major interest of researchers. In these studies, one and two-dimensional models of bone–implant interaction were analyzed with optimization of the implant shape or mechanical properties. Such models enable efficient analysis, but they fail to include fully 3-D effects which is serious drawback. An example of a 3-D analysis and optimization of the femoral implant shape can be found. However, even in the latter paper, bone is assumed to be isotropically elastic which again raises a question of reliability of the results. It should always be assured that plant surface is generally porous coated in order to induce tissue growth and better adhesion between bone and implant.

In computation low friction contact is assumed on the smooth bone implant interface while the porous coated interface is modeled as the high friction interface. The contact or gap element will have a much bigger part to play in the computational analysis.

Loading and Material Properties

Load conditions have strong influence on the stress distribution and, consequently, on the results of shape optimization. The hip joint is subjected to various types of loads in the patient's everyday life activities (walking, running, standing, etc). Appendices I and II gives various material to be linked to the finite element analysis. Where the information is not available from the given case study, it is recommended that the load values and angles for both joint head and abductor forces are to be considered as shown in Table 4.2.

Data on the Constitutive Properties of Material

In the biomechanical research, the lack of comprehensive and reliable material data is one of the fundamental difficulties. Experimental studies, especially for cancellous bone, give results that are fragmentary and prone to various types of errors. They do not provide sufficient information necessary to perform computations, i.e., in the general case, nine orthotropic elastic constants

Table 4.2. Numerical data for loads. Angle is measure from the horizontal axis

load case	joint force		abductor force	
	value (N)	angle (°)	value (N)	angle (°)
1	2,317	−104	702	62
2	1,158	−75	351	98
3	1,548	−146	469	55

plus three angles describing orientation of principal directions of orthotropy (in the case of transverse isotropy this reduces to five elastic constants and two angles). Additionally, due to the material inhomogeneity, all these constitutive parameters must be understood as function of spatial location. The following elastic constants and the other relevant data as:

Data

$E_1 = E_2 = 14.33\,\mathrm{GNm}^{-2}$ $E_3 = 21.5\,\mathrm{GNm}^{-2}$

$v_{12} = 0.43,$ $v_{31} = v_{32} = 0.367,$

$G_{12} = 5.0\,\mathrm{GNm}^{-2}$ $G_{31} = G_{32} = 5.95\,\mathrm{GNm}^{-2}$

$v = 0.3$

$E = E_1$ Trabecular tissue assumed isotropic

Within the range of volume fraction between 0.1 and 0.3
The ratio $E_3/E_1 \rightarrow$ varies from 2.5 to 1.5
γ_{canc} (cancellous bone density in the proximal femur excluding head corresponding to volume fraction 0.1–0.15 = 200–300 $\mathrm{g\,cm}^{-2}$

For an isotropic materials, the values of coefficients of stiffness matrix

$$K_{11}, K_{33}, K_{12}, K_{13} \textit{ and } K_{66}$$

will have the isotropic values as

$$\overline{K}_{11} = \overline{K}_{33} = \frac{E\,(1-v)}{(1+v)\,(1-2v)} \rightarrow \overline{K}_{11} = \overline{K}_{13} = \frac{Ev}{(1+v)\,(1-2v)} \qquad (4.7)$$

$$\overline{K}_{66} \frac{E}{2\,(1+v)}$$

Results. Figures in Plate 4.1 show the stress distribution σ_x, τ_{xy} and σ_y in crack zones. For different initial crack lengths, the type of the stress distribution in crack zone will preserve its shape. In figure (Plate 4.2) the curve of strain energy release rate obtained by means of the beam theory classical plates theory of the shear deformation theory and numerical results using the finite element method, are shown. The values of critical load $\mathrm{P_c}$ and maximum deflection Δ_m are obtained from the experimental result used in different theories A 2D finite element analysis was carried out and using 4 noded Isoparametric elements, the energy release in the xy directions were computed. They are shown in Plate 4.2. The numerical results of finite element analysis for the strain energy release rate are shown for two states, the existence and nonexistence of the effect of fiber bridging and also the results of the calibration test bar introduced.

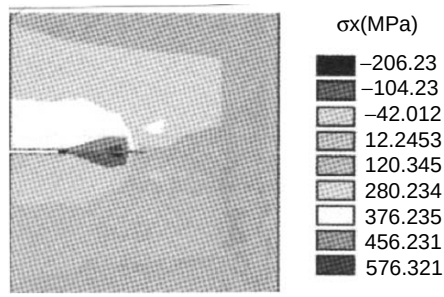

σ_x distribution in the crack tip of a bone

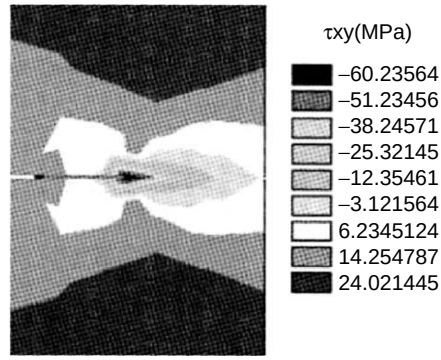

τ_{xy} distribution in the crack tip of a bone

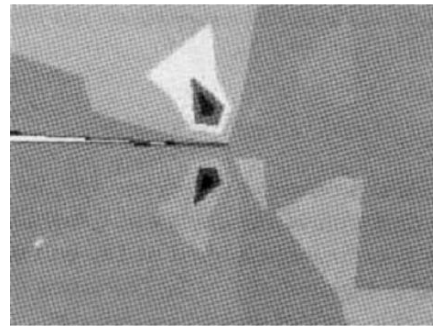

σ_y distribution in the crack tip of u bone

Plate 4.1. Needle penetration stresses

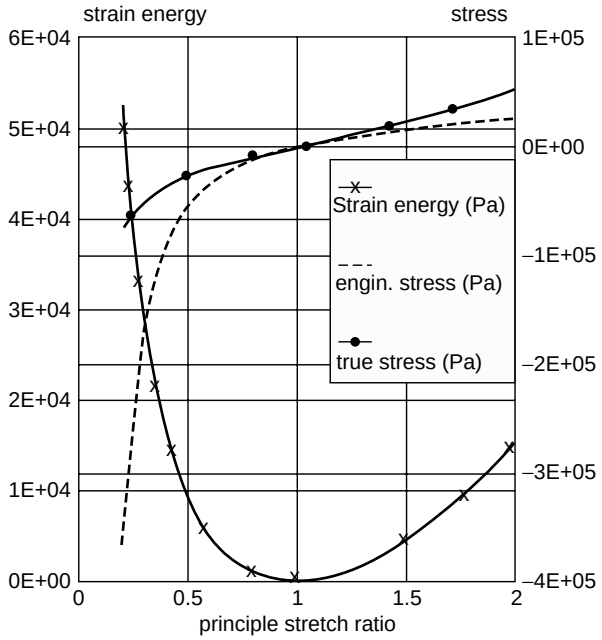

(a) The strain energy, the engineering stress and the Cauchy stress functions

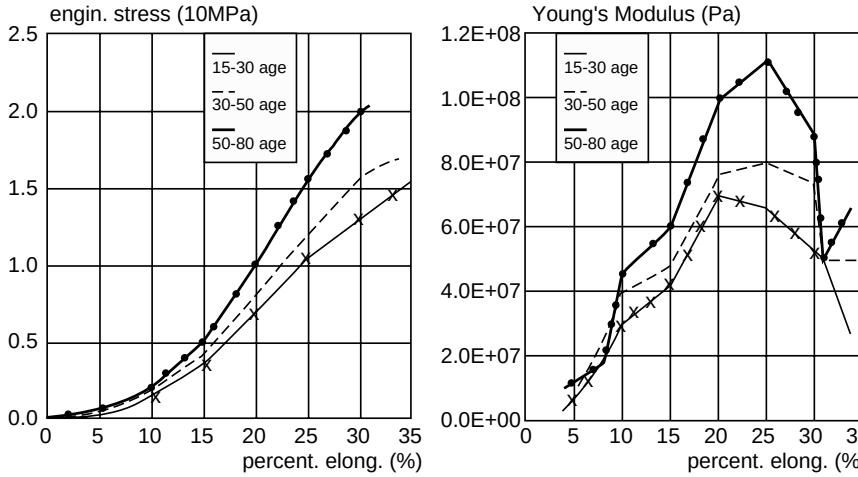

(b) The stress-strain relationships of the skin for different age groups (Rollhauser,1950)

Plate 4.2. Computed energy released

4.4 Human Body Geometry: Nonlinear Material Properties

4.4.1 Optimization of the Shape for the Numerical Model

To optimize the shape of the interface between the skin and a sitting support a finite elements model is needed. The geometry of the model is based on (i) in vivo measured sking shape data of the upper leg and the buttock area, and the position of a set of bony landmarks, or in vitro measured bone shape data on the visible human dataset, (ii) auxillary surfaces to bridge the skin and the bone data. First a closed surface FE model is constructed followed by hexmeshing to obtain the sold model. The boundary and the contact conditions are derived from the spatial, the continuum and the force application boundaries. To quantify the material properties, a one parameter version of the Mooney model is generally adopted. The actual coefficient was estimated by reference with predicted values of the maximum pressure.

Many consumer products are physically handled by the user. For such products the shape of the contact area is among the most important aspects of product design. To generate the optimal shape specific ergonomics requirements are needed. Such requirements usually relate to the pressure distribution during the expected product usage. Often such requirements are available in the form of specific measures, guidelines or rules that are applicable for a specific product group, type of usage, or user group (Bullinger and Solf, 1979; Sanders and McCormick, 1993). The development of an engine that generates suggestions for the shape of the contact area for a large range of products needs a fundamental approach, based on fundamental, including medical and physiological criteria.

The physical body of the initial configuration to be optimized is represented as a valid FE model. If a pressure distribution is applied to the FE model, the model will deform. Now two situations can be compared. First, the physical body is supported by a given shape, which results in a pressure distribution, II. Second, the FE model is loaded by the same II, which results in a deformed model, outwardly represented as a set of geometric points coinciding with the surface nodes of the contact area. The assumption was made that the shape of the support is not significantly different from the shape that is derived from the mentioned surface points.

The goal of this part of the research is the construction of the FE model, including (i) the geometric definition of anatomical components the model, (ii) the scaling and the assembly of the components, (iii) the generation of the surface elements, (iv) the generation of the solid mesh, and (v) the validation of the model for material characteristics.

4.4.2 Modeling and Load/Material Data

Earlier attempts to build an FE model of the human buttock area were reported by, among others (Chow and Odell, 1978). They constructed a

axisymmetric linearly elastic model. Young's modulus to $15\,\mathrm{KN\,m^{-2}}$ calculate the internal stress distribution for several types of load. But to elaborate the last, high deforming part of the analysis, the value of the Young's modulus is increased to $300\,\mathrm{KN\,m^{-2}}$. The material was considered almost incompressible (Poisson's ration 0.49). They found for a 300 N flat frictionless sitting load that the maximum pressure at the interface was ca. $200\,\mathrm{KN\,m^{-2}}$ and von Mises stress contours up to 400. The hydrostatic pressure caused minimal deformation, while the pressure gradient caused von Mises stress.

Another linear analysis was carried out by Todd and Tacker (1994), who tried to relate the interface pressure with the internal pressures at the ischium. They constructed the geometry from MRI images. The support was a model of a cushion, which was intimately integrated with the buttock model. The linear Young's modulus for the male and the female subjects were 64.8 and $47.5\,\mathrm{KN\,m^{-2}}$. The pressure values at the interface and the element just beneath the ischial tuberosity were 17 and $74\,\mathrm{KN\,m^{-2}}$ for the male subject, and 15 and $205\,\mathrm{KN\,m^{-2}}$ for the female subject.

The procedures were elaborated and implemented for sitting support. The initial, not optimized support was a horizontal, flat and hard surface, without support for the arms and the back. This configuration is also used to check the validity of the FE model. So far only the areas of the upper leg and the buttock area are, included in the generally model of the body, and the arm rests and the back-rest omitted.

4.4.3 Finite Element Model

The actual calculation of the deformation of the continuum, the deformation of the shape of the contact area, and the internal pressure distribution for the progressively varying external pressure distribution, PE, within the contact area, is done by FEA. A complete, perfect FE model includes all tissues that possibly participate in the continuum mechanical behavior of the body, such as skin, muscles, tendons, ligaments and fat, and it describes the morphological properties. In addition each tissue is defined by geometry, material properties (anisotropic, nonlinear, time-dependent), and contact conditions or boundary conditions. In the current research a much simpler model is constructed for several reasons.

- No data are available that describe the shape of the involved tissues.
- A perfect FE model would require an unacceptable amount of CPU-time with hardware currently available.
- The construction of a simpler model is already a very complex job, that
- Requires much modeling to be done by hand.

The FE model that developed for this research consists of three tissues: skin, bone, and soft tissue. The soft tissue replaces all deformable tissues between the skin and the bony part of the model. The mobility of the joints between the different bones is reduced to zero.

For detailed solutions of the FE model, it is necessary to measure the actual shape of the bones which requires CT-scanning showing medical tissues.

The surface geometry was used to create the FE surface meshes of the four components (skin, three bony parts). These surface meshes were combined to one surface model, and processed further to a solid mesh.

4.4.4 Surface Meshing for Human Structure

In order to apply solid meshing, the surface mesh of the overall model must enclose a volume, while showing no defects such as holes, free edges, or crossing elements. The actual continuum, where the internal pressure values will be evaluated for the E, and Ergonomics Goodness Index, is the soft tissue enclosed by the femur and the skin. At the distal end (knee) the continuum is closed by a cross-sectioning surface. At the caudal boundary the skin surface ends in the end curve (b), which is closed curve along the iliac crest, the inguinal ligament, the pubic symphysis, the buttock fold, and via the SIPS back to the iliac crest. The boundary between the soft tissue of the pelvis and the abdominal region is a surface coinciding with the pelvic inlet surface (C). The medial boundary is the intersection with the medio-sagittal surface $x = 0$ (D).

Since the bodies originate from different subjects, the surfaces will probably not fit exactly. Therefore auxillary surfaces must be generated finalize the closing operation.

Solid Meshing for Human Structure

The solid meshing of the continuum will be done using a hexahedral element mesh. The HEXMESH option of the FE modeler applies a hexmesh within the volume, leaving after the first pass a gap with the inner aspect of the surface mesh. This gap is then filled with elements in a final meshing operation. The parameters that are used to create the hexmesh will be discussed in Sect. 4.7.

When the solid mesh is generated, due to the properties of the FE modeler all information about the surface elements has been lost, including the sets definitions, the morphological structure and the original tissues the elements belong to. Therefore, to apply the boundary conditions for the FEA, a number of sets of elements have to be generated.

The set of the skin elements, the skin set is needed to apply the mechanical properties of the skin. A subset of the skin set is needed to apply for contact conditions. The set of the elements enclosing the volume, that was formerly occupied by the bony parts will be used to apply the fixation in space (geometric boundary condition). Actually the surface nodes of the bone set will be fixed in space. This set is called bone set. The medial closing plane is used to inhibit transversal translation (symmetry condition for the left and right body parts). The distal closing plane is used to inhibit translation along the longitudinal axis of the femur.

4.5 Material Properties and Stress Analysis Material Identification Symbols

$\{C_{10,}C_{01}\}$	money coefficients
ect	ectomorphic index
E	ergonomics goodness index
F	permanent force
F_{n}	maximum nodal force
G^1	neo-Hookean elasticity constant
$\{I_1, I_2, I_3\}$	deformation invariants
M	body mass
MCS	measuring coordinate system
SE_{f}	strain energy function
WCS	working coordinate system
	principal stretch ratio
P	pressure value
Pac	physiologically acceptable pressure
Pd	pressure distribution
PE	externally applied pressure distribution
	stress
	strain

4.5.1 Stress Analysis for Finding Material Properties

Material properties were considered for soft tissue and skin. In the current model the bony parts are fixed in space and only used as part of the boundary of the soft tissue; thus its material properties are irrelevant. Since the soft tissue is subject to large deformation, the elastic behavior is necessarily nonlinear. The simplest nonlinear approach is the neo-Hookean elastic behavior.

$$\sigma = G\left((1+\varepsilon) - (1+\varepsilon)^{-2}\right) \tag{4.8}$$

which is a special case of the Mooney–Rivline definition for incompressible ($I_3 = 1$) rubber materials

$$SE_f = C_{10}(I_1 - 3) + C_{01}(I_2 - 3) \tag{4.9}$$

where I_1, I_2 and I_3 are the invariants $I_1 = \sum_{i=1,2,3} \lambda_i^2, I_2 = \lambda_1\lambda_2 + \lambda_2\lambda_3 + \lambda_3\lambda_1$, and $I_3 = \lambda_1^2\lambda_2^2\lambda_3^2$ is the strain energy function and $\lambda_{1,2,3}$ are the principle stretch ratios.

If this is elaborated for the elements below the ischial tuberosity, assuming uniaxial compression and λ_3 the principle stretch ratio in the Z-direction, then $\lambda_3 = \lambda$, and $\lambda_1 = \lambda_2 = 1\sqrt{\lambda}$. The strain energy function can then be written as

$$\mathrm{SE}_f = C_{10}\left(\lambda_1^2 + \lambda_2^2 + \lambda_3^2\right) = C_{10}\left(\lambda_1^2\right) + 2/\lambda - 3. \tag{4.10}$$

The coefficient $C_{10} = G'/2$, where G' is the shear modulus, for $\lambda \approx 1$. The engineering stress function σ is

$$\sigma = \mathrm{d}W/\mathrm{d}\lambda = G\,(\lambda - 1/\lambda)\,, \tag{4.11}$$

The true stress is (Cauchy stress)

$$\tau = \sigma/\,(1/\lambda) = G\left(\lambda^2 - 1/\lambda\right). \tag{4.12}$$

In figure the function W, σ, and τ are shown for $G' = 15\,\mathrm{kN\,m^{-2}}$ and $0.2 \leq \lambda \leq 2$

Rolhauser (1950) reported the elongation of the skin without dermis constituents for several age groups. In figure the stress–strain curves and the derived Young's modulus (σ / ε) are shown, as they were derived from the graphs of the original paper.

Todd and Tacker (1994) describe a method to obtain an estimation of the effective normal Young's Modulus for the sitting load of the tissues below the ischial tuberosities while the buttock were unsupported. The lowest value was found for the supine position: $11.9\,\mathrm{KN\,m^{-2}}$ for a female and $15.2\,\mathrm{KN\,m^{-2}}$ for a male subject. The largest value was found for the normal seated position: 47.5 and 64.8, respectively.

The mechanical properties of the human skin vary with the relative humidity of the environment, the wetness of the skin, the direction of the applied load, age, and even the season of the year. Moreover, the layers of the skin vary strongly in this respect. The elastic behavior is nonlinear: the skin stiffness increases with the applied tension by a factor of 50(!); a mathematical formulation for the coefficient of elasticity was derived by Manschot and Brakkee (1987a,b). They found that the elastic characteristics of the skin depend on the direction of the strain (anisotropic), and that many other variables have a significant influence, such as the season of the year. The characteristics of the underlying soft tissues were not investigated. The strain energy and Cauchy stress functions are given in figures in Plate 4.2.

4.6 Experimental Materials and Data for Finite Element Analysis

4.6.1 Introduction

The corrosive environment and the body's low tolerance to some chemicals limit the choice of possible materials for an implant. Stainless steels, CoCr alloys titanium alloys are the most common metallic biomaterials used in artificial joints. These metallic materials have typical metallic advantages such as high tensile and fatigue strength but also disadvantages such as chemical and mechanical wear.

Ceramics materials like alumina and zirconia are used in artificial joints as femoral heads because of their high damage resistance. Their high strength (could cause stress shielding) and their brittle nature however make these ceramics less suitable as bulk material for artificial joints. Stress shielding occurs when the harder and stiffer implant materials (with a higher Young's modulus) carry the entire load, and shield the natural bone from stress. Without continuous loading, the bone does not thrive and this may lead to osteoporosis which may cause loosening of the implant.

The suitability of the ceramic material strongly depends on the type of load that is applied and therefore on the application. A ceramic material like alumina can withstand ten times higher stresses in compression (4,500 MPa) than in tension (450 MPa). When used in femoral heads, the material experiences mostly compressional loads, and a ceramic material could therefore be a good choice in this situation.

The most commonly used material combination for an artificial hip joint consists of a femoral component made of a metal stem with a polished metallic or ceramic ball which articulates against a metal shell with a plastic inner socket. Different bearing materials such as metal-on-metal or ceramic-on-ceramic have been investigated but the original Charnley like prosthesis is still the most common.

4.6.2 UHMWPE

The UHMWPE grade used in this study was GUR 1020 provided by PolyHi Solidur, Germany. In all cases the material used from compression-molded blocks. The compression-molding process was identical to that used for commercially available UHMWPE materials. Y-irradiation of materials was performed at Nordisk Sterilisering AB Skarham, Sweden, at a dose of 56–60 kGy at room temperature. The material was annealing air either at 60°C for 4 days or at 150°C for 2 hours. After the annealing, the materials were allowed to cool slowly to room temperature in the oven at an estimated rate of 40°C per hour. Cylindrical pins, length 20 mm and diameter 8 mm, were machined from a block of UHMWPE. One end of each pin was tapered to form a truncated cone with an angle of 60° and a contact surface of 3 mm in diameter.

Accelerated aging is necessary in order to assess the long-term properties of UHMWPE. The aging was performed at a raised temperature and in the presence of oxygen. Oxygen diffuses into the polymer and causes oxidation, which may change the mechanical properties of the polymer.

The machining and the artificial aging of the samples were performed at SP, Boras, Sweden. The test samples were aged for 23 days at 80°C and atmosphere pressure. The air humidity during the aging was not controlled. Circulation in the heat chamber was set at a rate of six air changes per hour.

Addition of Vitamin E to Y-irradiated UHMWPE

Yannick Luisetto at Lund University, Sweden, added vitamin E to the UHMWPE material. The vitamin E was provided by Merck, Germany. It consisted of a mixture of tocopherol enantiomers, but mostly $\vec{\alpha}$-tocopherol (99%). The VE was blended with the UHMWPE powder prior to the compression molding by adding a certain weight percentage to the powder. Different weight percentages (0, 0.1, 0.2 and 0.5 w%) of VE were added to 500 g UHMWPE in a one-liter glass bottle. The bottles were placed in an oven at 60°C and biodegradation, surgical aspects and the size and shape of wear debris. Coating a material is one way to control the biological reactions and the functional properties (wear, load bearing properties, corrosion etc) of the implant, and to optimize it separately for the work piece (bulk material) and the surface.

A disadvantage of using a coated material is the unknown long-term properties and the risk for coating breakthrough and failure. If that happens, the wear of UHMWPE would increase extensively as a result of a damage of the surface (high roughness) and third body abrasive wear.

The mechanical properties of the coating depend on its chemical composition and structure. Harder materials with extreme properties are particularly sensitive to defects (cracks, pores etc.) important processing factors that influence the quality of the coatings are, for example, temperature of substrate, degree of ion-bombardment, gas composition, and distribution of electrical fields.

Studies of retrieved implants have shown damaged femoral heads with a high surface roughness. Hard particles like bone cement, damaged coating or metal can damage the femoral head and significantly increase the wear rate (third-body abrasive wear). A hard ceramic or metallic femoral head that articulates on an UHMWPE cup is a combination that provides low friction and that remains undamaged and thus improves long-term properties. To use smooth surfaces that remain smooth is a very important way to reduce wear.

Stainless steel was the original stem and femoral head material for the Charnley prostheses. Nowadays it is however often replaced because of the improved corrosion resistance with CoCr-alloys. Stainless steel is also alloyed with nickel, which may lead to allergic reactions. The stainless steel 316L used here contains several different elements, where the L indicates low carbon. (316L: Fe bal, 17–19% Cr, 12–14% Ni, 2–3% Mo, <2% Mn, <0.03%C).

4.6.3 Titanium Nitride, TiN

Titanium nitride (TiN) is the most common coating material applied by PVD (physical vapor deposition) today. In industry, TiN coating is used to improve tribological, corrosive and high temperature properties. The gold colored coating can also be used for esthetic applications.

Raimondi et al., have studied TiN-coated femoral heads and some of the coatings had distinct surface scratches. These are believed to be a result of third-body abrasive wear from cement particles. Other coated femoral heads from the same study showed coating breakthrough. One reason for coating breakthrough is the high stresses that arise from microcontact of hard particles that are trapped between two articulating surfaces (acetabular and femoral head). If the coating is locally damaged, this will accelerate the failure mechanism, extensive breakthrough, of the coating is possible even at low loads.

From impact studies of TiN-coated titanium have shown that coating failure often depends on the substrate properties. When plastic deformation of the substrate takes places, the coating itself cannot carry the entire load and failure may occur rotated at 60 rpm for 24 hours. At room temperature, VE is an amber viscous liquid, but at 60°C its viscosity is considerably reduced and it could then be homogeneously mixed with the UHMWPE powder. A small beaker containing VE was also placed in the oven and NMR measurements were before and after the 24 hours at 60° in order to study the stability of the VE. No changes could be detected.

Once the mixing was done, the powder was sent to PolvHi Solidur and pressed into 200×200×10 mm sheets according the same procedure as for commercially available UHMWPE for orthopaedic applications. The sheets were then cut into four smaller sheets of the same size. Tow small sheets of each material were sent to Nordisk Sterlisering Ab, Skarhamn, Sweden for y-irradiation at 60 kGy. Samples were machined out of each Y-irradiated sheets and also out of two nonirradiated, non-VE-containing sheets. Y-irradiated materials are referred as GammaX %VE where X is the concentration of VE, and the nonirradiated, non-VE-containing material was used a reference. All the samples were then sent to Paper Pak Sweden AB, Aneby, Sweden for ethylene oxide (ErO) sterilization and the samples were finally aged at SP, Boras, Sweden.

4.6.4 Oriented HDPE

The wear resistance of cold roll-drawn HDPE materials was evaluated (paper I) in order to clarify to what extent the wear properties depend on the degree and direction of orientation. As control, a clinical grade UHMWPE material was used under the same test conditions. The oriented HDPE materials were supplied by the Industrial Materials Institute, Quebec, Canada. The materials were processed into sheets via a double orientation process, which consisted of a series of four oil-heated rolling stations held at 110°C. The draw ratio, λ, is defined as the ratio of the length after to the length before the roll-drawing process and this is an important parameter in the solid-state orientation of polymers. The higher the value of λ, the better will be the mechanical properties (the strength and modulus) in the draw direction. HDPE materials with two relatively low draw ratios, $\lambda = 2$ and $\lambda = 4$, were investigated.

4.6.5 Stainless Steel and Coated Materials

The disc used in the tribological investigations had a diameter of 80 mm and a thickness of 4 mm. The stainless steel 316L (hard counter-face) was used as a reference and also as a substrate for the coating. The stainless steel discs were delivered by Vattenfall Ringhals AB. All coatings were manufactured at Micromy (Täby, Stockholm) using magnetic sputtering PVD (physical vapor deposition) at 300°C, and a coating thickness of about 3 µm.

All discs were ground with abrasive papers that gave a surface roughness of 0.03–0.3 µm. The discs were washed with a soap solution to remove most of the dirt, followed by an ultrasonic bath in ethanol for five minutes. After the ethanol bath, the discs were rinsed in distilled water and dried with acetone and air.

Load-demanding applications are mainly met by the bulk properties, whereas the interaction with the surrounding tissue is controlled by the surface properties. The body's reactions to the implant depend mostly on its surface composition, texture, micromotions.

4.6.6 Diamond-Like Carbon, DLC

DLC, diamond-like carbon, is an amorphous metastable network consisting of carbon an hydrogen. Carbon can exist in three different hybridizations, sp3 (diamond-like), sp1 (graphite-like) and sp1, and it is therefore able to form a great variety of crystalline and disorders structures. The DLC coating used in this study was based on amorphous carbon with a titanium content of 15%, with mostly sp3 hybridization.

The properties of DLC depend on the content of hydrogen and the ratio of sp3/sp2 bonds, which in turn depends on the deposition process. DLC can exhibit some extreme properties similar to diamond, such as hardness, elastic modulus, and chemical inertness.

A was carried out static corrosive experiment in 10 wt% HCl for 45 days and found dramatic decrease in corrosion of stainless steel coated with DLC. The rate of corrosion was about 400 times less for a DLC-coated than for an uncoated stainless steel. Experiments to investigate the biocompatibility of DLC have shown good results in both in vivo and in vitro studies.

Normally the softer material becomes worn when sliding against a harder material, but the DLC layer has an interesting property. DLC is a two-phase material (graphite and diamond-like) and a thin transfer layer of graphite forms on the opposite counter-face with which it is in contact. Therefore, DLC articulates against itself and the result is low friction and a low wear rate. It is not clear whether this is an ideal case in the body, because body fluids may clean out wear debris.

In vitro experiments on the tribology of coated DLC components have given contradictory results. Some experiments show an improvement and

Table 4.3. Differences in wear rate between coated and uncoated samples gliding against UHMWPE

% change in wear rate for DLC coated relative uncoated steel	
steel	DLC coated
0	−32.4
1	−24.2

lower wear with DLC coating and others do not. These differences probably depend on differences in the experimental arrangement (machine, load, lubricant, geometry, etc). Results of experiments with DLC-coating are summarized in Table 4.3 where an attempt was made to limit the interlaboratory differences by evaluating the difference between DLC coated sample and the reference used in the experiments (stainless steel).

Today there are two major tentative application areas for DLC-coated materials in blood contacting (hear valves) and tribological applications (artificial joints). Blood-contracting implants are commercially available, but no DLC coated hip or knee joint is year available. There are no in vivo studies of DLC components that show an improvement of tribological properties. In 2001, implant design AG sold joints with the femur partially coated, but the company did not complete all the required tests prior commercialization. Within a short time, some implants showed increased wear and coating delamination and had to be replaced.

4.6.7 Micronite

Micronite (Patent pending) is manufactured by introducing a high molecular material into the substrate that consists of a specially treated PVD-coated titanium nitride or diamond-like carbon. This material combination gives a low coefficient of friction and low wear. In the present study, titanium nitride is the substrate that is modified. A previous tribological study has been made (in accordance with ASTM G99-9a (2000) el with Micronite-treated titanium coating with oil as lubricant, and a significant reduction was noted in the coefficient of friction.

4.6.8 Tribology of Coated Materials: a Comparative Study

(a) Surface analysis

The AFM analysis revealed differences in the R_a – value of the disc when the same surface roughness of substrate was used before the coating, see Table 4.4. clearly, the thin coating (few μm) increased the surface roughness of all the coated discs. The highest surface roughness were noted for DLC and Micronite followed by TiN.

Table 4.4. Surface roughness results from the study with uniform substrate roughness

material	R_a(μm)	R_{max}(μm)
316L (substrate)	0.025	0.180
TiN	0.052	0.362
Micronite	0.228	1.028
DLC	0.243	1.592

Table 4.5. Surface roughness results, before and after the wear test

	before the wear test	
material	R_a(μm)	R_{max}(μm)
316L	0.104 ± 0.033	0.689 ± 0.205
Tin	0.169 ± 0.041	0.895 ± 0.179
Micronite	$0.176 + 0.046$	$1.133 + 0.322$
	after the wear test (on wear track)	
316L	0.134 ± 0.086	$0.880 + 0.537$
TiN	0.155 ± 0.026	$0.877 + 0.233$
Micronite	$0.175 + 0.038$	$1.035 + 0.290$

Some results obtained for discs with a similar roughness after coating are shown in Table 4.5. Here, the surface roughness was measured before and after the wear tests. As expected, the differences in surface roughness between the substrate (3136L) and the coated discs were in this case smaller. An increase of the surface roughness was observed for 316L after the wear test (in the wear track area), and a number of distinct surface scratches were the AFM analysis indicated that the surface roughness of the coated materials does not change during the wear test. This may be due to the higher hardness of the PVD-coated material.

4.6.9 Characterization of Wear Debris

The results of the study of wear debris with the same surface roughness on the substrate before the coating are summarized in Table 4.6, which shows the mean size of particles and the amounts of wear debris below 1 μm. The mean size is calculated as the average value of the dimensions in the longest and shortest directions. The wear debris of UHMWPE1316L was in general spherical in shape, with occasional flakes and elongated particles. The mean size of the debris was larger for the coated surfaces, and more flakes and elongated debris were found among the larger sized debris. Wear debris generated using stainless steel typically exhibited a distribution with a mean size of 0.46 μm (98%). The debris exhibited the typical morphology and also the

Table 4.6. Mean particle size and amount of debris below 1 µm in size, from the study with the same surface roughness on the substrate before coating

material	mean size µm	< 1 µm [%]
316L	0.46	98.7
TiN	0.72	70.6
micronite	1.15	51.8
DLC	2.34	56.4

typical size and shape of wear debris reported from numerous hip simulator studies, indicating that the modified pin-on-disc method may be regarded as a reliable method for studying the wear properties of material used in artificial joints.

Both the amount of large debris and the specific wear wee higher for the TiN, Micronite, and DLC surfaces. The amount of debris from the DLC sample was significantly higher than that from the other counter-surfaces, which corresponds to the higher total wear rate. The amounts of wear debris below 1 µm in size for TiN, Micronite, and DLC were about 70%, 51%, and 56%, respectively, see Table 4.6. The smaller debris wasMostly spherical in shape, whereas the larger debris contained more flakes and elongated particles.

The higher surface roughness is believed to be the main reason for the higher specific wear on the coated counter-surfaces. Results of the study with the same surface roughness after the coating confirmed this hypothesis. The specific wear of 316L increased more than 15 times when the R_a-value was increased from 0.03 µm to almost the same level as that of the coated material. Although there was no significant difference in the R_a-value between Micronite and TiN, specific wear and μ for TiN were more than 30% and 10%, respectively, higher than for Micronite.

4.7 Material Data on Cortical and Cancellous Bone for the Finite Element and Experimental Test Results

It is shown that in young subjects, before the age of 40 years, the stiffness modulus of cancellous bone increases at approximately constant volume fraction (which indicates tissue strengthening associated with increase of the microscopic stiffness modulus) while later, after the age of 50, both the stiffness modulus and the volume fraction decrease (which indicates that trabeculae get thinner at approximately constant tissue modulus). In order to evaluate how the phenomena affect the optimized implant shape, additional two numerical tests are performed. In one of them, all orthotropic elastic moduli of both trabecular and cortical tissue are diminished by 10%. In the other – density distribution is modified such that in most parts of cancellous bone the trabecular thickness is lower by about 5% (so that the overall macroscopic

stiffness decreases by about 10%) and the thickness of cortical wall in the bone shaft is also diminished by 5%.

Material data taken for implant (titanium) in all numerical tests are: $E = 100\,\mathrm{GN\,m^{-2}}$ and $\nu = 0.33$.

4.8 Solid Modeling Using of the Human Tibia Using Finite Element

Currently many finite element (FE) models of human bones and joints exist. Computer Tomography (CT) Scans or Magnetic Resonance Imaging (MRI) constitute the input data for a variety of software that will produce a solid model of the object. A finite element model of the (FEM) is superimposed on the geometrical one; material properties are assigned and loading conditions are prescribed. The needed analysis is then performed. Depending on the level of sophistication of the software used and the requirements of the specific research, the geometry and the FE mesh are more or less detailed and accurate.

Most FE analyses performed up to the present date for the human tibia consider the bone as an isotropic homogenous medium. A reasonable approximation of bone is to consider it an orthotropic linear elastic solid governed by Hooke's law.

Three orthotropic FE models of the whole tibia have been created constitute the object of an ongoing research. The effect of the fibula was neglected. Table 4.7 contains the sets of material properties assigned to the cortical and cancellous bone partitions. As bone marrow is mostly fat and does not have a support function the material properties assigned to it are the properties of air.

The cortical bone layer was considerd homogenous for all the models, as the properties vary only slightly through thickness. Three sets of properties for

Table 4.7. Material properties for human tibia

material property (MPa)	cortical bone	cancellous bone		
		1	2	3
E_1	6.91	4.48	–98–1.52p	$0.06p^{1\flat 51}$
E_2	8.51	4.48	–124–1.81p	$0.06p^{1\flat 55}$
E_3	18.4	9.64	–326–5.54p	$0.51p^{1\flat 37}$
G_{12}	2.41	1.41	931p	931p
G_{13}	3.56	1.28	775p – 158	775p – 158
G_{23}	4.91	1.28	775p – 158	775p – 158
v_{12}	0.49	0.35	0.35	0.35
v_{13}	0.12	0.12	0.12	0.12
v_{23}	0.14	0.12	0.12	0.12

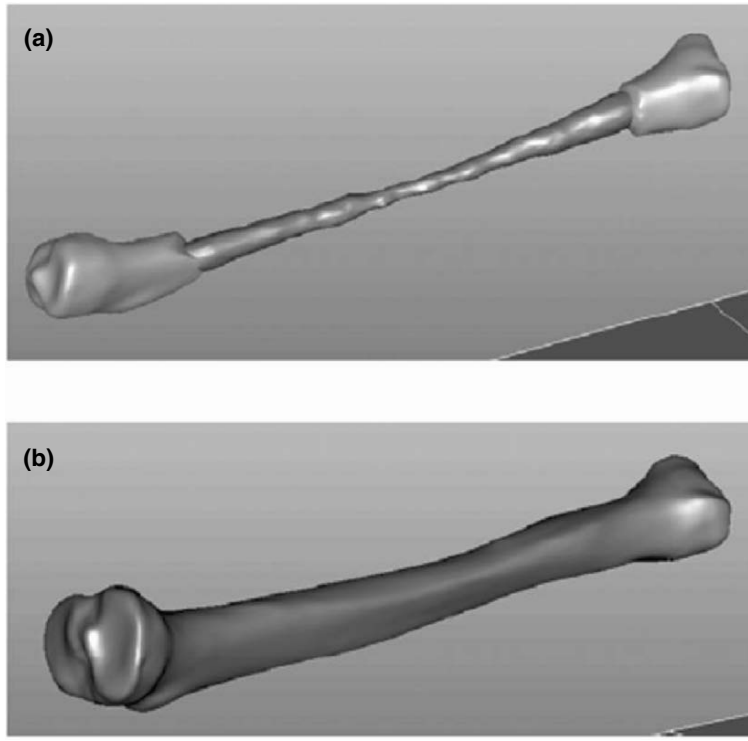

NURBS surfaces: (**a**) the epiphysical cancellous bone and the bone marrow cavity, (**b**) the outer critical surface

Plate 4.3. cancellous bone and bone marrow

the cancellous bone layer were considered. The numerical material properties included in Table 4.7 are averaged.

4.9 Material Properties for Lumbar Intervertebral Joint

Disk rupture is caused generally if an axial torsion occurs on lumbar intervertebral joint and is normally resisted by the facet joint which could be in compression and which in turn, can produce highly nonlinear load–displacement curves. The only realistic finite element model must replicate this nonlinearity. Both geometrical and material nonlinearities are to be considered. This concept requires A3-D model of this type of joint will be adequate in simulating compression, flexion, and tension of the joint. The model consisted of 10 different materials. The material properties were all linear. Table 4.8 lists the material properties for all the elements of the model. Nonlinear behavior of the soft tissue was produced not from material

Table 4.8. Material properties

material property	value	source
elastic modulus of cortical bone	15,000 MPa	Hart (1992)
elastic modulus of cancellous bone	456 MPa	Hart (1992)
elastic modulus of disc	1.8 MPa	Fonte not (1985)
Poisson's ratio of cortical bone	0.31	Hart (1992)
Poisson's ratio of cancellous bone	0.21	Hart (1992)
Poisson's ratio of disc	0.40	Chen (1991)

nonlinearity but from the geometrical nonlineraity of the meshed fibers embedded in the ground substances modulus of elasticity E and Poisons ratio, ν, of annular fibers and ground substances can easily simulate a whole range of nonlinear load deformation curves normally obtained from the tests. Since the material of the vertebral body consists of a stiff cortical shell, it has a softer cancellous core. Both materials are transversely isotropic. All ligaments are treated in compression with small tensile stresses. Torsion generally increases both compressive stresses in the ground substance and the nucleus pressure.

4.10 Modeling of Bones and Finite Element Input

The temporal bone, mandibular condyle, and articular disc were all modeled as deformable bodies using four-nodel brick elements. The material properties that are to be used in the 3-D model are shown in the above table:

Attachments to the disc are to modeled using spring elements. The nodes of the cut edges of the temporal bone are to be fixed in place. Motion is to induced into the model by specifying the position of the lower left corner of the modeled part of the mandible and applying a constant vertical force to the lower right corner. The disc moved only passively due to its geometric relationship with the mandibular condyle and the temporal bone. During normal opening of the mouth, the mandibular condyle initially rotates some degrees and then translates along the temporal bone until it is just anterior to the articular eminence. This motion is then simulated in the model by defining 20 different steps and doing a static analysis for each step.

4.11 Finite Element Knee Models

Here generally the contacts stress is more sensitive to thinning rather than thickening of the cartilage. The finite element model shall be constructed from MR images and can be treated as reliable for the stress analysis. Around 10% variations do exist in results due to digitization procedure. The Whitaker foundation (Harvard Medical Centre) finally produces relations between maximal

Table 4.9. Maximal surface contact pressure, von Mises Stress and hydrostatic pressure (MPa) in the cartilage

FE model	surface pressure	von Mises stress	hydrostatic pressure
−10%	1.895	1.081	1.335
−5%	1.783	1.031	1.262
0%	1.7	0.9796	1.199
5%	1.622	0.9461	1.142
10%	1.555	0.9177	1.092

surface contact pressure, von Mises stress and Hydrostatic pressure in $\mathrm{MN\,m^{-2}}$ in the cartilage. This relationship is given in Table 4.9.

Modeling

A CT scan of a cadaveric human tibia was used as the basis of this present research. A total of 201 CT scan slices of the tibia were taken, the distances between the scans varying along the length of the bone with a higher density at the proximal and distal ends, as those were the regions of interest.

The data was imported into MIMICS (materialize), and the threshold method was used to differentiate between the cortical bone region, cancellous bone region and the bone marrow cavity. The individual elements of a CT image are called voxels and each has a value referred to in Hounsfield units based on the density of the structure (the value for water is 0). The threshold used in the present work for cortical bone was: 1990–3127 (upper limit of the scanned date), and for cancellous bone: 1100–1990 (both coarse and fine trabecular bone, as the trabeculae of tibial cancellous bone are almost longitudinal). The epiphyseal line was considered as part of the cancellous bone since the Hounsfield values associated did not pass the cortical bone threshold, most probably due to the age of the specimen. The values lower than 1,100 were used to construct the bone marrow cavity Table 4.10.

Each slice was manually edited: the external and internal contours were smoothed out and internal cortical bone cavities removed. The density numbers throughout the cortical and cancellous regions were recorded in separate files to be used in determining the numerical values of the elastic and shear moduli.

The geometry data for the cortical and cancellous bone regions were imported individually into GeoMagic Studio (Raindrop Geomagic, Inc.) as point clouds. GeoMagic Studio was used to process the data in order to create Nonuniform Rational B-Splines (NURBS) surfaces, which are easily handled by FE software. After editing the data (denoising, smoothing, filling of gaps), the curves or points were wrapped as closed manifold surfaces. A manifold surface is a triangle based surface in which all the triangles are continuously connected by their edges, the closed kind bounds volumes.

Table 4.10. Material properties used in the model

material	material properties		comments
vertebral body shell	$E_x = 700.0$	MPa	transversely isotropic
	$E_y = 700.0$		
	$E_z = 1000.0$		
	$v_{xy} = 0.45$		
	$v_{xz} = 0.315$		
	$v_{yz} = 0.315$		
	$G_{xy} = 241.4$		
	$G_{xz} = 241.4$		
	$G_{yz} = 241.4$		
vertebral body core	$E_x = 140.0$	MPa	transversely isotropic
	$E_y = 140.0$		references are the same as above
	$E_z = 200.0$		
	$v_{xy} = 0.45$		
	$v_{xz} = 0.315$		
	$v_{yz} = 0.315$		
	$G_{xy} = 48.3$		
	$G_{xz} = 48.3$		
	$G_{yz} = 48.3$		
bone of the posterior element	$E = 1000.0$		isotropic
	$v = 0.45$		references are the same as above.
cartilage	$E = 23.8$		isotropic
endplate	$v = 0.40$		
annulus ground substance	$E = 1.0$		isotropic
	$v = 0.48$		
annulus fiber	$E = 500.0$		isotropic
nucleus pulposus	$x = 1666$		x (bulk modulus of nucleus pulposus)
ligaments	$E = 200.0$		isotropic
facet cartilage	$k = 1000.0\,\mathrm{N\,mm^{-1}}$		k (stiffness)

4.12 Traumatic Injury Tolerance Thresholder

For the finite element analysis, it is necessary to identify certain thresholds for the output. Here the engineering analysis would receive help from the medical experimental results since various researchers in biomechanics and biomedical engineering have established certain thresholds for injuries. The results of computer program would terminate as soon as these thresholds would reach. For example Table 4.11 gives a tolerance thresholds for rotational acceleration and velocity of the brain. The injury is related to impact.

Table 4.11. Tolerance thresholds for rotational acceleration and velocity of the brain

tolerance threshold	type of brain injury
50% probability:	cerebral concussion
$\ddot{x} = 1,800\,\mathrm{rad\,s^{-2}}$ for $\mathrm{t} < 20\,\mathrm{ms}$	
$\ddot{x} = 30\,\mathrm{rad\,s^{-2}}$ for $\mathrm{t} \geq 20\,\mathrm{ms}$	
$\ddot{x} < 4,500\,\mathrm{rad\,s^{-2}}$ and/or $\dot{\alpha} < 70\,\mathrm{rad\,s}$	rupture of bridging vein
$2,000 < \ddot{x} < 3,000\,\mathrm{rad\,s^{-2}}$	brain surface shearing
$\ddot{x} < 30\,\mathrm{rad\,s^{-1}}$:	(general)
safe: $\ddot{\alpha} < 4,500\,\mathrm{rad\,s^{-2}}$	
AIS 5: $\ddot{\alpha} > 4,500\,\mathrm{rad\,s^{-2}}$	
$\ddot{x} > 30\,\mathrm{rad\,s^{-1}}$:	
AIS 2: $\ddot{\alpha} = 1,700\,\mathrm{rad\,s^{-2}}$	
AIS 3: $\ddot{\alpha} = 3,000\,\mathrm{rad\,s^{-2}}$	
AIS 4: $\ddot{\alpha} = 3,900\,\mathrm{rad\,s^{-2}}$	
AIS 5: $\ddot{\alpha} = 4,500\,\mathrm{rad\,s^{-2}}$	

4.12.1 Head Injury Criterion (HIC)

Kramer (1998) has created a generalized acceleration model for brain injury (GAMBIT). This criterion is based on acceleration response only and the traumatic injuries are related with impact force.

The curve for a GAMBIT of 1.0 was determined to represent a probability of 50% for irreversible head injury. Noncontact head impact accounted for a GAMBIT values below 0.62.

Assuming that translational and rotational accelerations contribute equally to the probability of head injury and assuming that the tolerances derived in experiments with either translational or rotational acceleration are also valid in a combined loading scenario, (4.13) has been derived.

$$\mathrm{GAMBIT} = \frac{\ddot{x}_m}{250} + \frac{\ddot{\varphi}_m}{10} \tag{4.13}$$

The US National Highway Traffic Safety Administration (NHTSA) included in FMVSS No. 208, computes HIC as:

$$\mathrm{HIC} = \max \left[\frac{1}{t_2 - t_2} \int_{t_1}^{t_2} a\,(t)\,\mathrm{d}t \right]^{-2,5} (t_2 - t_1)\,, \tag{4.14}$$

where t_2 and t_1 are any two arbitrary times during the acceleration pulse. Acceleration is measured in multiples of the acceleration of gravity (g) and time is measured in seconds. FMVSS 208 requires the HIC time interval to be 36 ms (thus called HIC_{36}) and the maximum HIC_{36} not to exceed a value of 1,000 for the 50th percentile male. In 1998 NHTSA also introduced the HIC_{15}, i.e., the HIC evaluated over a time interval of 15 ms (Kleinberger et al. 1998).

As for the according threshold value, a maximum of 700 was suggested for the 50th percentile male.

The probability of skull fracture (AIS ≥ 2) is given by the formula

$$p(\text{fracture}) = N\left(\frac{\text{In}(\text{HIC} - \mu)}{\sigma}\right), \tag{4.15}$$

where $N(\,)$ is the cumulative normal distribution, $\mu = 6.96352$ and $\sigma = 0.84664$.

Since the data used to establish this risk analysis consists of short duration impacts of typically less than 12 ms, the HIC curve is applicable to both HIC_{15} and HIC_{36}.

Goldsmith and Ommaya (1984) had conducted tests for the dynamic effects when loading the neck. The results are shown in Fig. 4.14.

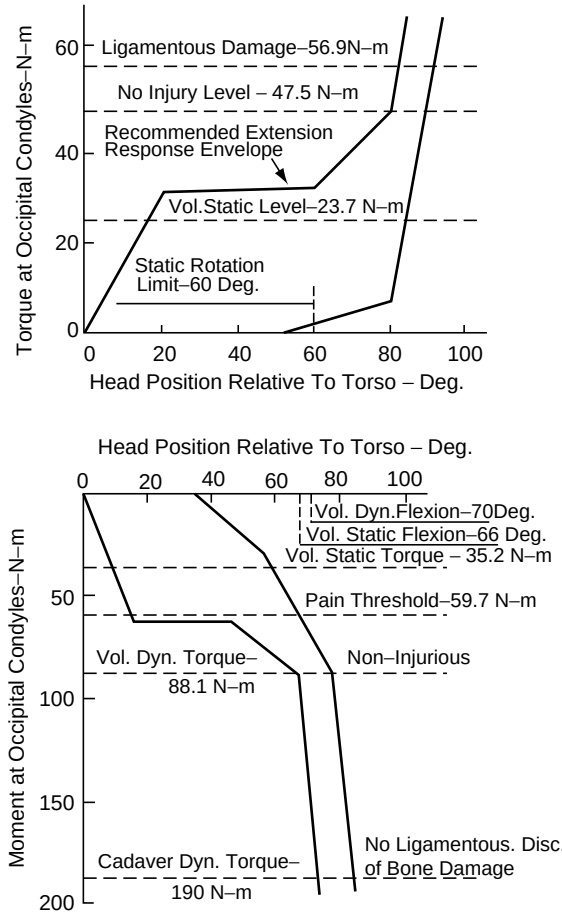

Fig. 4.14. Head–neck response envelope for extension (*top*) and flexion (*bottom*) as determined by Goldsmith and Ommaya (1984)

For the lumbar spine, limits for frontal, rear-end and downward acceleration were proposed such that for impact durations of less than 100 ms, a 40 g threshold shall not be exceeded for well-restraint seated passengers (Viano 2001a).

Table 4.11 summarized tolerance values of the cervical spine derived from the various experiments reported in the literature; however, due to differences in experimental techniques and test conditions, the data show a considerable spread.

Hence, it is not surprising that Nightingale et al. (1997) report significant differences for male and female tolerance when testing compressive failure. Similarly, differences between the adult and the pediatric spine were found (cf. e.g., Yoganandan and Pintar 2000; Yoganandan et al. 2002). For compression tolerance, McElhaney et al. (2002) conclude that for the cervical spine average forces of 1.68 and 3.03 kN result for females and males, respectively, and that tolerance values for the young human male range from 3.64 to 3.94 kN.

With respect to neck injury, the neck injury criteria NIC (Bostrom et al. 1996) N_{ij} (Klinich et al. 1996, Kleinberger et al. 1998) and N_{km} (Schmitt 2001, 2002a) are often used. While N_{ij} was designed to detect severe neck injuries in frontal impact, the other two developed with regard to soft tissue neck injuries in rear-end impacts. Recent work by Kullgren et al. (2003) and Muser et al. (2003) show that both NIC and N_{km} correlate well with the risk of AISI neck injury sustained in rear-end collisions. Table 4.12 and 4.13 shows the intercept values for calculating N_{ij} as included in FMVSS208. Hence, evaluating the criterion for all possible load cases, four different values are obtained: N_{te} for tension and extension, N_{tf} compression. An injury threshold value of 1.0 applies for each load case.

Adopting the N_{ij} to analyze the effect of deploying side airbags, Duma et al. (1999) replaced the sagittal bending moment by the total bending moment.

To assess AISI neck injury, reduced threshold values of 0.2 and 0.16 for long-term and short-term injury, respectively, were proposed (Bostrom et al. 2000; Bohmann et al. 2000).

However, evaluating N_{ij} in its original form for rear-end collisions (for which it was not designed) produced difficulties in the interpretation of the results obtained (Linder et al. 2000). Therefore, a modification of the N_{ij} criterion – called the N_{km}–which is suitable for the assessment of low-speed rear-end collisions was developed.

The neck protection criterion N_{km} was proposed by Schmitt (2001), 2002a. It is based on the hypothesis that such a criterion should take into account a linear combination of loads and moments. A similar approach lead to the definition of the N_{ij} criterion for frontal impacts (Kleinberger et al. 1998) and thus the newly proposed N_{km} can be regarded as a modification thereof.

Table 4.12. Tolerance of the cervical spine to injury

response measured	test objects	threshold criterion	threshold value	reference
extension	volunteers	noninjury (static)	23.7 N m	Goldsmith and Ommaya (1984)
		pain	47.3 N m	Mertz and Patrick (1971)
		no-injury	47.5 N m	Goldsmith and Ommaya (1984)
	cadavers	AIS2, ligamentous injury	56.7 N m	Goldsmith and Ommaya (1984)
flexion (bending) or	volunteers	pain	59.4 N m	Mertz and Patrick (1971)
			59.7 N m	Goldsmith and Ommaya (1984)
(flexure)		maximum	87.8 N m	Mertz and Patrick (1971)
		voluntary loading	88.1 N m	Goldsmith and Ommaya (1984)
	cadavers	AIS2	189 N m	Mertz and Patrick (1971)
		(no fractures)	190 N m	Goldsmith and Ommaya (1984)
compression	cadavers	bilateral facet dislocation	1.72 kN	Myers et al. (1991)
		compression injuries	4.8–5.9 kN	Maiman et al. (1983)
tension	volunteers	no-injury (static)	1.1 kN	Mertz and Patrick (1971)
	cadavers	failure	3.1 kN	Shea et al. (1991)
shear (a-p)	volunteers	no-injury	845 N	Mertz and Patrick (1971)
	cadavers	irreversible damage	2 kN	Goldsmith and Ommaya (1984)
	functional unit	(odontoid) fractures	1.5 kN	Doherty et al. (1993)
	functional unit	ligament rupture	824 N	Fielding et al. (1974)

Table 4.13. Intercept values for calculating N_{ij} as included in FMVSS 208

Dummy	M_y (flexion) (N m)	M_y (extension) (N m)	F_z (compression/ tension) (N)
50th%	310	125	4,500
5th%	155	62	3,370
6 year	93	39	2,800
3 year	68	27	2,120

However, with respect to possible injury mechanisms in rear-end collisions, sagittal shear forces rather than axial forces are regarded as the critical load case. A combination of shear and the sagital bending moment accounts for a constellation often found in cervical spine also during S-shape formation (e.g., Deng et al. 2001). To date, the S-shape formation is mainly associated

with retraction phase but looking at the kinematics an opposite S-Shape, i.e., the torso lags behind the head, could result in a similar deformation and therefore also incorporate an injury risk (Bostrom et al. 2001). This opposite S-shape which can for instance be observed during the rebound phase is not assessed by the maximum NIC due to its time limitation.

Furthermore, it is assumed that shear forces could potentially be harmful for the facet joints, in particular in the upper neck region (Yang et al. 1997; Deng et al. 2000; Winkelstein et al. 2000).

> For neck injuries, the relevant load combination is shear + extension/bending or flexion.

Hence N_{km} values are for combination of loads and moments. Inaccuracy of measuring shear forces is possible since in human axial compression/tension forces do influence the magnitude of shear (Yang et al. 1997). Various reasons for the inaccuracy are given and are identified as:

- The centripetal force from rotation of the dummy around the pelvis is measured as an axial force.
- Due to the fact that most dummies of today (except the BioRID dummy) do not represent the thoracic kyphosis, they consequently do not account for compression forces resulting from the straightening (ramping) effect.
- Recent dummy designs do not allow physiological backward movement of the head during the retraction phase i.e., when the torso is pushed forward by the seat back, the head is expected to lag behind due to its inertia. However, as the neck is connected with joints to the head and to the torso, a rotation of the head is originated which creates axial forces (although the head is intended to move relative to the torso without any rotation in the sagittal plane).

4.13 Thoracic Trauma Index (TTI)

The Thorax Trauma Index (TTI) is an injury criterion for the thorax in the case of a side impact. It assumes that the occurrence of injuries is related to the mean of the maximum lateral acceleration experienced by the struck side rib cage and the lower thoracic spine. Furthermore, the TTI takes into account the weight and the age of the test subject and thus combines information on the kinematics with parameters of the subject's individual physique. The TTI (dimension g) is defined as follows:

$$\mathrm{TTI} = 1,4\mathrm{age} + 0,5(\mathrm{RIB}_y + T12_y)(M/M_{\mathrm{std}}) \tag{4.16}$$

with AGE being the age of the test subject (in years); RIB_y (g) represents the maximum of the absolute value of the lateral acceleration of the fourth and eighth rib on the struck side; $\mathrm{T12}_y$ (g) gives the maximum of the absolute value of the lateral acceleration of the 12th thoracic vertebra; M denotes the subject's mass (kg) and M_{std} refers to a standard mass of 7.5 kg.

When using a 50th percentile Hybrid III dummy to perform crash tests, a different version of the TTI (d), can be calculated. To obtain TTI (d) values, the age related term in 5.1 is omitted and the mass ration becomes 1.0. It is important to note that the acceleration signals needed to determine the TTi and TTI (d), respectively, have to be preprocessed, i.e., filtered and sampled, according to a prescribed procedure.

Early attempts to quantify thoracic loading focused on acceleration. As of today, the human tolerance for severe thorax injuries is considered as peak spinal acceleration sustained for 3 ms or longer not to exceed 60 g in a frontal impact. This value is also embodied in FMVSS 208 to assess frontal impact crash worthiness. For lateral impact, different thresholds are proposed.

Closely related to acceleration is the definition of force tolerance values. Assuming an effective thorax mass of 30 kg, a force limit of 17.6 kN corresponds to the $60g$ acceleration level. However, cadaver tests by Patrick et al. (1969) observed a minor skeletal injuries already at 3.3 kN for impacts to the sternum and 8.0 kN for distributed loads to the shoulders and the thorax. These results show that the reliability of a single acceleration or force criterion as a general injury parameter for thoraco injuries is rather limited. Neither of the two criteria takes the viscous nature of the thorax into account. Consequently, more complex criteria need to be developed to obtain a better correlation with experimental results.

Loads and moments are required to produce failure in the bone of human upper extreme ties. Table 4.14 summarized tolerance values for the humans.

Concerning forearm fractures, Bass et al. (1997) performed cadaver tests in which ulna nightstick fractures and multiple fractures were observed. The results suggest that the humerus position, the forearm pronation angle and the forearm position relative to the airbag module affect the risk of injury from airbag deployment. Furthermore, it was concluded that there is a forearm strength above which the risk of injury is low, even if the forearm is positioned in front of the airbag module. These findings support the hypotheses that women are at higher risk of sustaining upper extremity injuries.

Investigating the human forearm under a dynamic bending mode, Pintar et al. (1998) determined that the mean failure bending moment for all (male and female) specimen was 94 N m. However, the bending tolerance of the forearm was found to be highly correlated to bone mineral density.

Table 4.14. Lateral impact tolerances of the thorax

tolerance level	inury level	reference
force:		
7.4 kN	AIS0	Tarriere et al. (1979)
10.2 kN	AIS3	Tarriere et al. (1979)
5.5 kN	25% probability of AIS ≥ 4	Viano (1989)
acceleration:		
T8-Y 45.2g	25% probability of AIS ≥ 4	Viano (1989)
T12-Y 31.6g	25% probability of AIS ≥ 4	Viano (1989)
60 g	25% probability of AIS ≥ 4	Cavanaugh et al. (1993)
TTI (d):		
TTI (d) 85g	max. in SID dummy for 4 door cars	FMVSS 214
TTI (d) 90g	max. in SID dummy for 2 door cars	FMVSS 214
TTI 145g	25% probability of AIS ≥ 4	Cavanaugh et al. (1993)
TTI 151g	25% probability of AIS ≥ 4	Pintar et al. (1997)
compression to half thorax:		
35%	AIS3	Stalnaker et al. (1979) Tarriere et al. (1979)
33%	25% probability of AIS ≥ 4	Cavanaugh et al. (1993)
compression to whole thorax:		
38.4%	25% probability of AIS ≥ 4	Viano (1989)
VC_{max} to half thorax:		
0.85 m s^{-1}	25% probability of AIS ≥ 4	Cavanaugh et al. (1993)
VC_{max} to whole thorax:		
1.0 m s^{-1}	50% probability of AIS ≥ 3	Viano (1989)
1.47 m s^{-1}	25% probability of AIS ≥ 4	Viano (1989)

humerus bending male (N m)	moment female (N m)	shear	force	reference
115	73			Weber (1859)
151	85			Messerer (1880)
157	84	1.96	(overall)	Kirkish et al. (1996)
230	130	2.5	1.7	Kirkish et al. (1996), scaled to 50%ile male and 5%ile female
138				Kallieris et al. (1997)
	154			Duma et al. (1998a)
217	128			Duma et al. (1998b) scaled to 50%ile male and 5%ile female

4.14 Plasters as Clinical Materials for Trauma Patients

4.14.1 Introduction

Plasters are well known in the management fractures and/or immobilization of joints or limbs during the receipt of traumatic injuries. Two basic types are available:
(a) Plaster of Paris
(b) Synthetic casts

4.14.2 Plaster Management

- Application of cotton tubular bandage. Cotton tubular bandage can be pulled onto the limb. This is an optional layer, which often makes the cast tidier and more comfortable
- Application of orthopedic wool
  Orthopedic wool must be wrapped around the limb smoothly and evenly, avoiding wrinkles. Orthopedic wool is designed to be eased and stretched round the body contours and over bony prominences. Very swollen areas and bony prominences should be protected by a double layer of orthopedic wool.

4.14.3 Plaster of Paris Slab

- Prepare a plaster of Paris slab of about ten layers of plaster of Paris bandage. The slab should be long enough to extend from the base of the neck, along the lateral aspect of the upper arm, under the elbow, and up to the axilla. Add 5 cm to allow for shrinkage.
- Immerse the slab in warm water, holding the ends together to ensure the layers do not separate.
- Apply the slab from the axilla down to the elbow, round the elbow, up the lateral aspect of the upper arm and over the shoulder. Fan the slab over the shoulder padding, molding it into position to ensure a snug fit (Plate 4.4)
- Smooth out all wrinkles, taking care not to indent the plaster with your fingers. At the shoulder and elbow, turn back the cotton tubular bandage and excess orthopedic wool over the plaster slab. Ensue that there is no restriction to the circulation at the axilla or elbow.
- apply wet cotton conforming bandage in a spiral fashion to anchor the slab in position.
- cut a double layer of plaster of Paris bandage, 7.5×5 cm; immerse it in warm water and use it to anchor the cotton conforming bandage. Apply it over the plaster slab, not over the orthopedic wool, in order to avoid completing the plaster and thus compromising the circulation.
- apply a collar-and-cuff (procedure ii). Allowing the arm to hand and thus bringing the humeral fragment into alignment.

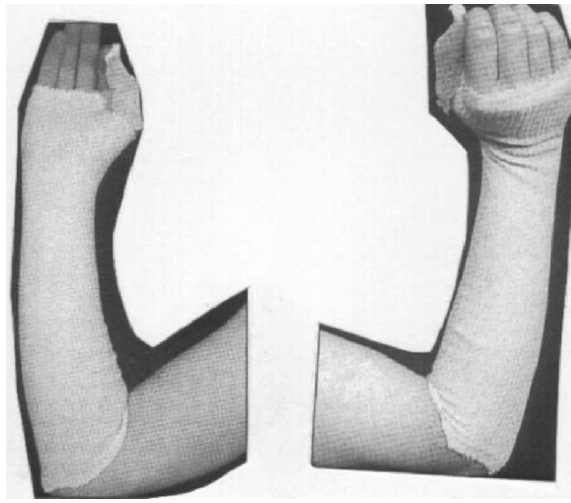

(a) Plaster for a fracture of the scaptroid bone

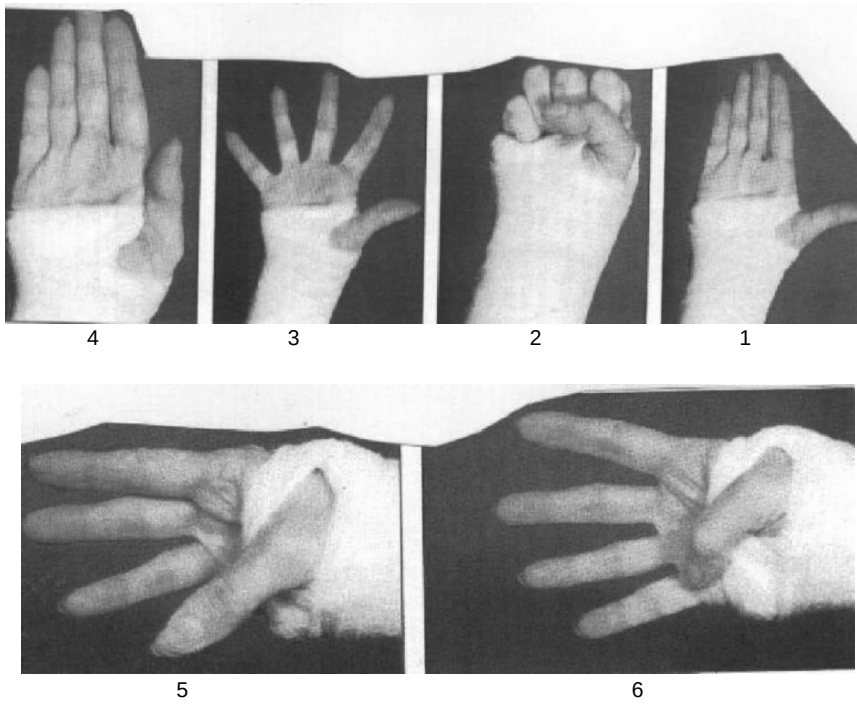

(b) Finger and Thumbs in Plaster-sequence of plastering

Plate 4.4. Bandages and plasters: (1) fully straightened out the finger and thumb; (2) make a good fist and bend the thumb; spread fingers wide apart; (5) then close them together, touch the tip of the thumb to the tip of the little finger; (6) slide it down the little finger

4.14.4 Above Elbow Back Slab Plaster

Uses

- Supracondylar fracture of the humerus
- After reduction of dislocated elbow
- Fracture of the head of the radius
- Fractures of the radius and ulna

Equipment

- Cotton tubular bandage, 10 cm wide
- Orthopedic wool, 7.5 cm and 10 cm wide
- Plaster of Paris bandage, 10 cm and 15 cm wide
- Cotton conforming bandage, 10 cm wide
- Scissors
- Plastic sheet
- Bucket of warm water

Procedure

1. Make sure the patient is comfortable on a chair or trolley and expose the injured arm up to the shoulder
2. Protect the patient's clothes with the plastic sheet
3. Position the arm with the elbow at a right angle and the hand in a neutral position
4. Make a plaster of Paris slab by folding the 15 cm wide plaster of Paris bandage five times, so that the final slab extends from the knuckles to the axilla and consists of six layer of plaster of Paris bandage.
5. Cut a semicircle from one corner of the plaster slab to accommodate the thumb.
6. Using the 10 cm wide plaster of Paris bandage, make two slabs about 20 cm in length and five layers thick; these will form the reinforcing supports at the elbow.
7. Snip a 1 cm hole about 5 cm from one end of the cotton tubular bandage. Slide the cotton tubular bandage up the arm to the axilla, putting the patient's thumb through the hole. If the elbow is very swollen or is likely to become increasingly swollen, either omit the cotton tubular bandage or snip a 2 cm piece out of it at the elbow crease.
8. Apply 7.5 cm wide orthopedic wool from the knuckles to the elbow and 10 cm wide orthopedic wool from the elbow to the axilla.
9. Immerse the plaster slab in warm water holding the ends together to ensure that the layers do not separate.
10. Apply the plaster slab along the posterior surface of the forearm, elbow, and upper arm, from the knuckles to just below the axilla.

11. Immerse the first 20 cm reinforcing slab in the warm water and apply it to the medical aspect of the arm, from the proximal forearm to the mid-humerus. Similarly, apply the second 20 cm reinforcing slab to the lateral aspect of the arm in an equivalent position. Take care not to allow the slabs to meet at the elbow crease, as this would complete the plaster and thus compromise the circulation.
12. Smooth out all wrinkles, molding the slab gently to the arm and taking care not to indent the slab with your fingers.
13. Turn back the cotton tubular bandage and excess orthopedic wool over the plaster slab, ensuring that the knuckles are exposed and that the axilla is free, a couple of small (1 cm) snips in the orthopedic wool may aid this process.

4.14.5 Above Knee Back Slab Plaster

Uses

- Fracture of the tibia and fibula, above the lower quarter.
- A plaster of Paris back slab is applied in order to provide temporary splintage in the presence of swelling or before or after manipulation of a fracture.

Equipment

- Cotton tubular bandage, 10 cm wide
- Orthopedic wool, 15 cm wide
- Plaster of Paris bandage slab, 20 cm wide
- Cotton conforming bandage, 10 cm wide
- Scissors
- Plastic sheet
- Bucket of warm water
- Plaster bridge

Procedure

1. Make sure the patient is comfortable on a plaster table and expose the injured leg to the groin with the knee supported by the plaster bridge when necessary, at an angle of about 10° of flexion.
2. Protect the patient's clothes with the plastic sheet.
3. One person holds the foot at a right angle throughout the procedure.
4. Apply the cotton tubular bandage from the toes to the groin.
5. Apply the orthopedic wool from the toes to the groin.
6. Cut a plaster of Paris bandage slab to extend from the base of the toes, along the back of the lower leg and knee, and along the back of the thigh almost to the buttock.
7. Immerse the plaster of Paris bandage slab in warm water, holding the ends together to ensure that he layers do not separate.

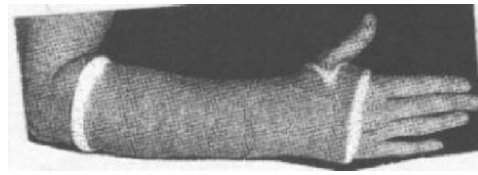

(a) Synthetic Cast

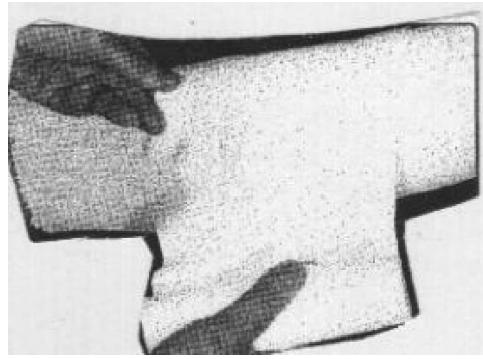

(b) Orthopedic Wool

Plate 4.5. Bandages and plasters

With the knee at an angle of about 10° degrees of flexion, apply the plaster of Paris bandage slab from the base of the toes, underneath the heel, along the posterior surface of the lower leg and the knee, and as high up the posterior surface of the thigh as is comfortable for the patient (Plate 4.5).

4.14.6 Plaster for Colles' Fracture

Uses

- Colles' fracture (a fracture of the distal end of the radius in which the distal fragment is angulated posteriorly, displaced posteriorly, and deviated to the radial side, resulting in a 'dinner fork' deformity).

Equipment

- Cotton tubular bandage, 5 cm wide
- Orthopedic wool, 7.5 cm wide
- Plaster of Paris bandage, 7.5 cm wide
- Scissors
- Plastic sheet
- Bucket of warm water

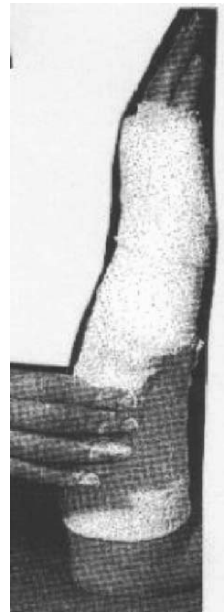

(c) Bandage around Limb

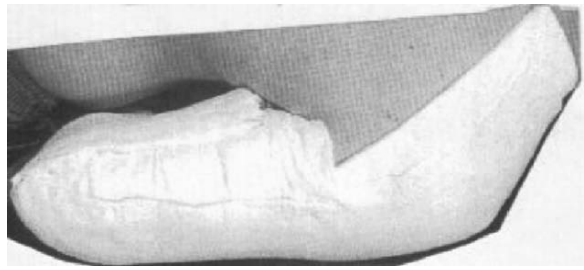

(d) U-Slab Plaster from the Axilla down to the Elbow

(e) U-Slab: Collar-and-cuff

Plate 4.5. *Continued*

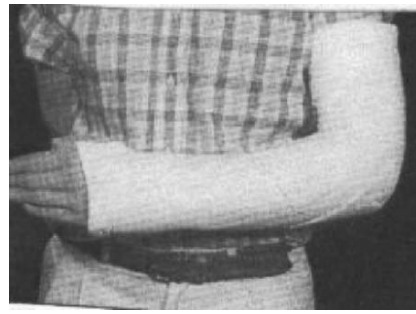

(f) Above-Elbow Back Slab plaster

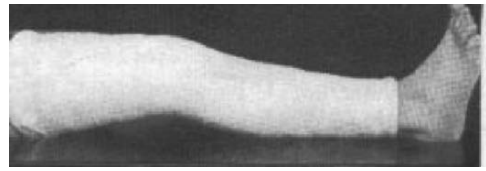

(g) Plaster Cylinders

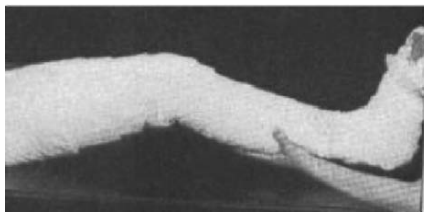

(h) Above-knee Back slab plaster

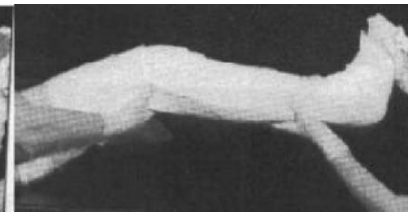

(i) Bellow-Knee back slab plaster

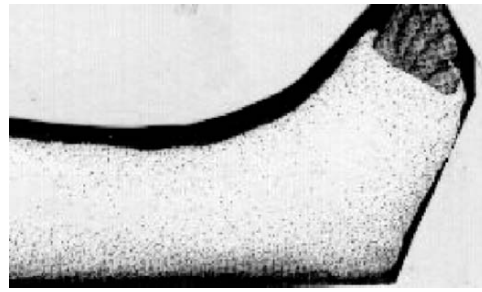

(j) Below-knee back slab plaster

Plate 4.5. *Continued*

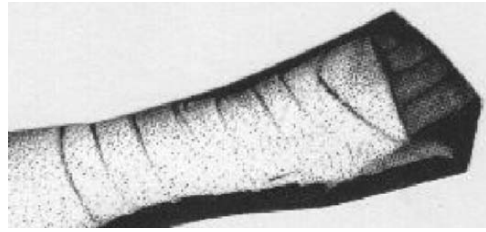

(k) Plaster for Colles Fracture

Plate 4.5. *Continued*

Procedure

1. Make sure the patient is comfortable on a chair or trolley, and expose the injured arm to above the elbow.
2. Protect the patient's clothes with the plastic sheet.
3. Position the arm according to the surgeon's instructions, usually the wrist is flexed and in ulnar deviation. The fracture may have been manipulated under Bier's block (intravenous regional anesthesia)
   [Procedure 79] or hematoma block
   (Procedure 80). The surgeon may have to hold the limb in position while the assistant applies the plaster/
4. Snip a small (1 cm) hole about 5 cm from one end of the cotton tubular bandage. Slide the cotton tubular bandage up the arm to the elbow, putting the patient's thumb through the hole.
5. Apply orthopedic wool from the knuckles to the elbow (Plate 4.5)
6. Immerse one roll of plaster of Paris in warm water.
7. Anchor the plaster of Paris bandage around the wrist with two fixing turns. Continue around the hand in a figure-of-eight fashion. Continuing up the forearm in a spiral fashion, covering two-thirds of the width of the bandage with each turn, up to the elbow. This usually requires two plaster of Paris bandages.
8. Smooth out all wrinkles and mold the plaster firmly, taking care not to indent the plaster with your fingers.
9. Turn back the cotton tubular bandage and excess orthopedic wool over the plaster, ensuring that the knuckles and the palmar creases remain exposed and that full movement of the elbow is possible.

4.14.7 Plaster for a Fracture of the Scaphoid Bone

Equipment

- Cotton tubular bandage, 1.5 cm and 5 cm wide
- Orthopedic wool, 7.5 cm wide
- Plaster of Paris bandage, 7.5 cm wide

- Scissors
- Plastic sheet
- Bucket of warm water

Procedure

1. Make sure the patient is comfortable, and expose the injured arm to above the elbow with the elbow resting on a table.
2. Protect the patient's clothes with the plastic sheet.
3. Snip a small (1 cm) hole about 5 cm from one end of the 5 cm wide cotton tubular bandage. Slide the 5 cm wide cotton tubular bandage up the arm to the elbow, putting the patient's thumb through the hole.
4. Apply a length of 1.5 cm wide cotton tubular bandage to the thumb.
5. The arm is positioned according o local policy, as surgeons have different opinions. The position described and illustrated here is the most common position selected. Ask the patient to cock back the wrist and to hold an imaginary roll of bandage in the palm of the hand, with the tip of the index finger touching the tip of the thumb. This position must be maintained until the plaster is completed (Plate 4.4).
6. Apply orthopedic wool from the knuckles to the elbow and around the thumb, snipping the orthopedic wool in order to ease the fit (Plate 4.4).
7. Immerse one roll of plaster of Paris bandage in warm water and apply this from just below the elbow, working in a spiral fashion towards the wrist. Two-Thirds of the width of the bandage should be covered with each turn. Aim to include the wrist and the thumb with this first roll, so that the plaster of Paris bandage is applied around the thumb to the interphalangeal joint, and around the hand to the knuckles and the palmar crease. The bandage may be snipped around the web space of the thumb in order to minimize the thickness around this area.

4.14.8 Additional Zones of Plastering and Bandaging

Similar procedures are adopted for other types of fractures such as:

- Smith fracture: a fracture of a distal end or the radius in which the distal fragment is angulated anteriorly, displaced anteriorly and deviated to the radial side.
- Benneth's fracture: a fracture-dislocation of the first carpometacarpal joint at the base of the thumb.

5

Medical Test Case Studies on Traumatic Surgeries

5.1 General Introduction

This chapter deals with the medical case studies on traumatic surgeries. Various X-rays are included for present and future exercise using engineering analyses presented in the text. The main purpose of this chapter, for the reader, is to test engineering analysis in order to provide collaborative result for the medical profession. Some of these test cases will be analyzed in Chap. 6 and to assist surgeons and physicians to get evidence and to prove and disprove their reasonable findings. The following areas are supported by tentative X-rays provided by famous surgeons, physicians' establishments to whom due acknowledgment are given. The following areas have been selected and the X-rays reproduced with the authors' acknowledgments:

- Elbow
- Shoulder
- Arm
- Fingers, wrists, and joints
- Hand
- Foot
- Leg
- Lumber
- Spine
- Chest/rib
- Knee
- Skull
- Ankle

Medical assessments provided by engineering analysis results, when fully collaborated, can provide test certificates for overcoming medico-legal problems.

5.2 Elbow X-Ray Plain Film: Case Study

5.2.1 Nondisplaced Radial Neck Fracture: Types I–IV by E.N.S. Elizabeth, A Perimental (Uniform Services University)

This patient is a young healthy active duty male with a recent injury that corresponds with the fracture seen on X-ray. This makes a fracture due to underlying pathology much less likely although the diagnosis must not be overlooked entirely. Radial head/neck fractures account for about 30% of all elbow fractures and often result from a fall on an outstretched hand as seen in this patient. Typically associated with the fracture in a effusion of the elbow is often seen anteriorly as a "sail sign," a large triangular-shaped lucency anterior to the joint. The posterior fat pad sign is always abnormal and is due to the distension of the capsule by intraarticular hemarthrosis. Radial fractures can be classified using the Mason classification system in which a type I fracture is nondisplaced, a type II fracture is displaced with more than 30% of the radial head involved, a type III fracture is comminuted, and a type IV fracture is associated with elbow dislocation. Initial treatment in the clinic can consist of aspirating blood from the joint. This usually relieves some of the pain, the patient is experiencing. Treatment for a type I fracture is as described above, immobilization with elbow at 90° for approximately 1 week, followed by repeat radiographs to ensure no displacement has occurred, transition to a sling and initiation of range of motion exercises three or four times per day. The nondisplaced fracture almost always has a good result. Some patients can experience a minimal loss of elbow extension and forearm rotation, however arm function is rarely limited. Nonunion rarely occurs. If the patient follows the above treatment plan there is every reason to expect that he will recover fully without any loss of function.

5.2.2 Elbow Fat Pad Sign: Case Study 2 by William Hwang Civil Medical Center, USA

Trauma to the elbow is common in all age groups. Fracture in the region may remain occult if not carefully looked for. A clue to fracture in the elbow is the pat pad sign. The elbow has three fat pads which are located inside the joint capsule but outside the synovial sheath. Two of them are useful in diagnosing elbow injuries on a lateral radiograph of the elbow. The anterior fat pad is located in the anterior coronoid and radial fossae and is normally visualized as a flat strip lying on the anterior cortex of the humerus. The posterior fat pad lies in the olecranon fossa and is not normally seen. When blood or other fluid fills the joint cavity (joint effusion), as occurs with an intraarticular fracture, the fat pads are displaced. The anterior fat pad tents out. Becoming triangular in shape, and the posterior fat pad becomes visible. This is the positive fat sign. Either a triangular anterior fat pad or a visible

posterior fat pad constitutes a positive sign. It is also known as a "sail" sign since the fat pad now resembles the sails of a ship. With history of elbow trauma and a positive fat pad sign there is a high likelihood of intraarticular fracture (Plates 5.1–5.3).

Sinus tracts due to infected, dead bone after surgery, trauma

Active and passive forms of disease. Passive chronic osteomyelitis is generally asymptomatic; bacteria may be inactive for long periods of time (even up to 50 years) before evolving to an active infection.

Pathogenesis. The original content contributors and/or by H. Irvine and J.G. Smirniotopoulos, MD.

Osteomyelitis that is untreated or insufficiently treated forms sequestra – areas where necrotic bone, bacteria, and granulation tissue have been walled off by an involucrum (new reactive bone) or fibrous tissue. Antibiotics and host defenses penetrate poorly, if at all, into sequestra. Over time, reactive bone changes and the further formation of sequestra may deform and weaken the bone giving rise to pathologic fracture. A 0.5% develop squamous cell carcinoma at the drainage site. Most common organism is *Pseudomonas aeruginosa.*

Elbow

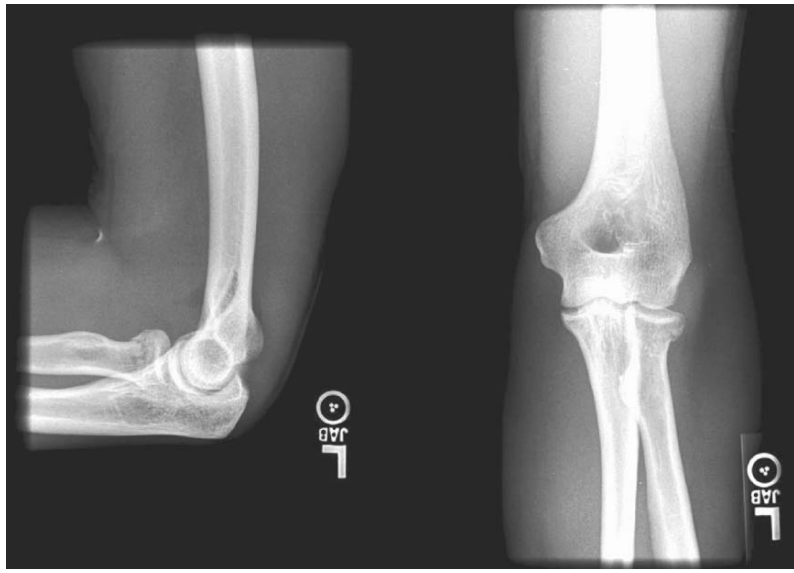

Contributor: ENS Elisabeth A. Pimentel
Nondisplaced (Type I) radial neck fracture

Plate 5.1.

Elbow-Humerus Fracture

Contributor: ENS Elisabeth A. Pimentel
Uniform Services University

Plate 5.2.

Elbow-Chronic Osteomyelitis

Contributor: Jefferson Jex

Plate 5.3.

5.2.3 Fractures of the Proximal Radius in Children: Case Study 3 by Chad Holmes

The most common fracture of the elbow in children occurs in the supracondylar region of the distal humerus. Adults usually fracture the radial head. Fractures of the proximal radius comprise approximately only 8% of elbow fractures in children. Typically, pediatric fractures involve the neck of the radius and the physis. If the fracture involves the physis of the proximal radius, any of the Salter–Harris types may be seen.

There are two typical mechanisms of injury. The child may fall on the outstretched hand with the elbow extended, transmitting a valgus force to the neck of the radius. Otherwise, the fracture may occur as a consequence of posterior elbow dislocation. If so, the injury is usually a fracture through the physis with displacement of the epiphysis posteriorly. The radial injury occurs when the elbow dislocation spontaneously reduces; the capitellum fractures the radial epiphysis as the elbow reduces, pushing the epiphysis posteriorly. The epiphysis may also be fractured through the physis at the time of the posterior elbow dislocation. In this case, the epiphysis is displaced anteriorly (Plates 5.4–5.7).

Fractures of the Proximal Radiusin Children–X-rays I

Plate 5.4.

Fractures of the Proximal Radius in Children–X-rays II

Plate 5.5.

Fractures of the Proximal Radius in Children–X-rays III

Plate 5.6.

Fractures of the Proximal Radius in Children–X-rays IV

Plate 5.7.

5.3 Anterior Dislocation Right Shoulder

Jeremy Eager contributed effectively on the anterior dislocation of right shoulder. Plate 5.8 demonstrates this type of dislocation. Plates 5.9–5.12 give the additional noted information.

Of the two principle types of shoulder dislocations, anterior and posterior, the former is by far the most common and accounts for approximately 95–97% of cases of glenohumeral dislocation. This type of injury usually results from a combination of indirect forces–abduction, extension, and external rotation applied to the arm. The humeral head becomes displaced forward, anterior to the glenoid, and comes to rest beneath the coracoid process of the scapula. Although anterior dislocation is usually obvious both clinically and radiographically, there can be associated lesions that may escape the untrained eye.

One such defect is the Hill-Sachs lesion, which is best demonstrated on the anteroposterior view with the arm internally rotated. It appears as a "hatchet" defect on the posterolateral aspect of the humeral head at the junction of the neck. The lesion is an impaction fracture that is associated with recurrent

Contributor : Jeremy Eager

Plate 5.8.

anterior dislocations. The finding of it in the patient presented would be consistent with her history of a previous dislocation.

Another finding sometimes associated with an anterior shoulder dislocation, though less common than the Hill-Sacks lesion, is the Bankart lesion. This is a fracture of the anterior aspect of the inferior rim of the glenoid caused by the anterior movement of the humeral head, and is best seen on the anteroposterior projection with the arm in the neutral position. When dislocation of the humeral head is not demonstrated, the presence of either of these abnormalities is virtually diagnostic of previous anterior dislocation.

Dislocation of right Shoulder-I

Plate 5.9.

Dislocation of right Shoulder-II

Plate 5.10.

Dislocation of right Shoulder-III

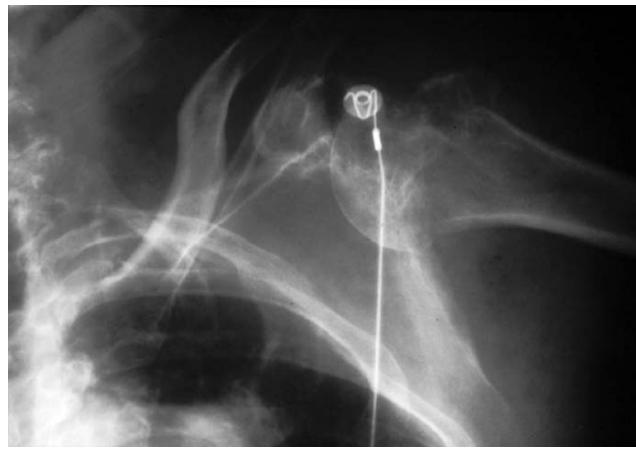

Plate 5.11.

Dislocation of right Shoulder- IV

Plate 5.12.

Anterior Dislocation Right Shoulder
Prepared by: MS-4 Teaching File
Affiliation: Uniformed Services University-II
Peer review/approval: Wait Carpenter
Affiliation: Civilian Medical Center-II

5.4 Psoriatic Arthritis

Contributor: Amy H. Martin, MD
Prepared by: Amy H. Martin, MD
Affiliation: National Naval Medical Center, Bethesda-II, USA
Peer review/approval: James G. Smirniotopoulos, MD
Affiliation: Uniformed Services University

A reference is made to Plates 5.13–5.17.

Psoriatic arthritis is considered a seronegative spondyloarthropathy and shares may of its features with Reiter's, ankylosing spondylitis, and inflammatory bowel disease. Of the 5% of patients with psoriasis who develop arthritis, 80% of these will be HLA-B27 positive.

Psoriatic arthritis can involve almost any synovial joint, cartilaginous joint, or entheseophyte of psoriatic arthritis; however, it is most commonly characterized by asymmetric proliferative erosions, distal predominance, periosteal reaction, and soft-tissue swelling. The more severe forms can result in ankylosis of the joint and arthritis mutilans.

Psoriatic Arthritis-I

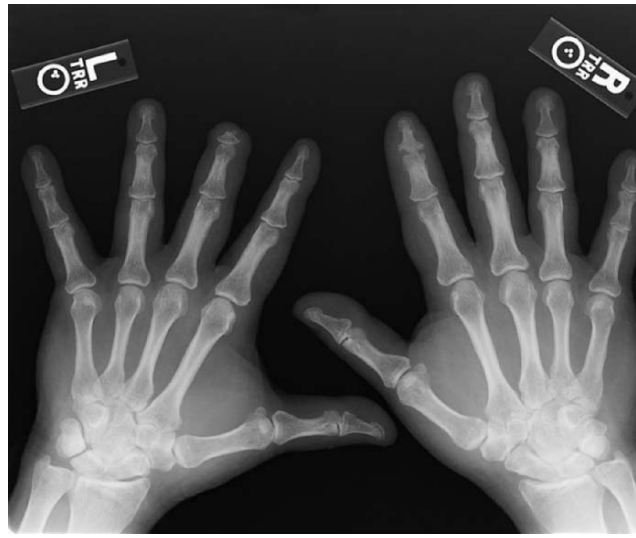

Plate 5.13.

Psoriatic Arthritis-II

Plate 5.14.

Psoriatic Arthritis-III

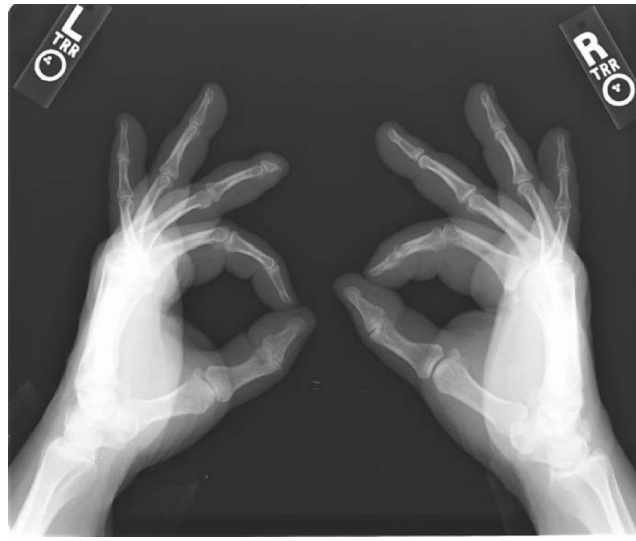

Plate 5.15.

Psoriatic Arthritis-IV

Plate 5.16.

Psoriatic Arthritis-V

Plate 5.17.

The hands are involved in approximately 50–75% of patients with the DIP, PIP, MCP commonly involved. Asymmetric erosions with ill-defined margins and adjacent periosteal reaction can produce a classic "pencil-in-cup" deformity. Bone production near erosions is often referred to as "mouse-ears." Sclerosis or acroosteolysis of the distal phalanx is not uncommon and ankylosis occurs in up to 10% of patients. There is often fusiform soft-tissue swelling involving one or several digits. The absence of juxtaarticular osteoporosis and presence erosive changes with bone production helps differentiate it from rheumatoid arthritis (RA). The feet are less commonly involved which help differentiate it from Reiter's.

Spondyloarthropathy of the sacroiliac joints and the spine occurs in 50% of patients with psoriasis. Spine findings include no marginal, asymmetric osteophyte formation which appears as large vertically oriented paravertebral ossification involving the disk annulus, not the disk endplates. There is often squaring of the vertebrae and ankylosis. Sacroiliitis is not uncommon and is usually bilateral.

Contributor: 2LT Shahin Nassirkhani

RA is a chronic, systemic, inflammatory disorder of unknown etiology that primarily involves joints. The arthritis is symmetrical, may be remitting, but if uncontrolled may lead to deformity and destruction of joints due to erosion of cartilage and bone. The disease usually progresses from the periphery to more proximal joints, and in the majority of patient's results in significant locomotor disability within 10–20 years.

RA affects women two to three times as often as men. The incidence of RA has been reported to be around 30–100,000 population and it may affect any age group from children to elderly. The disease prevalence is about 1% in Caucasians, but varies between 0.1% (in rural Africans) and 5% (in Pima and Chppewa Indians). The peak onset is between the ages of 30 and 55, and because of the consistently higher rates in females, the prevalence of RA in females over 65 years is up to 5%.

1. Erosion of cartilage and none are one of the cardinal features of RA although they occasionally occur in SLE and some overlap syndromes. To be seen radiographically, they have to be sufficiently advanced to have eroded through the cortex of the bone around the margins of the joint. Erosions, typically in the MCP and PIP Joints, are present in 15–30% of patients in the first year of the disease. There is a subsequent cumulative increase in frequency of joint erosions over time (greater that 90% after the first 2 years).
2. In some patients, erosions occur first in the ulnar styloid or metatarsophalangeal joints. It is therefore worth evaluation for both the hands (including the wrists) and the feet in all patients in whom a diagnosis of RA is suspected. Thus, as with other features of RA, the presence of erosions becomes more useful diagnostically with increasing duration of

disease. However, with extreme destruction, the severity of erosions may reach a level beyond which further progression cannot be assessed radiographically, despite continued joint damage.

3. Other classic finding includes ankylosis, soft-tissue swelling, osteopenia, narrowing of the joint spaces due to destruction of articular cartilage, and malalignments, all of which are seen in our patient. Magnetic resonance imaging (MRI) is a more sensitive technique than plain radiography for identifying bony erosions. When radiography and MRI were compared in a group of 55 patients with early arthritis, MRI identified sevenfold more erosions in the metacarpophalangeal and proximal interphalangeal joints of the hand than did plain radiographs.
4. MRI may detect bon erosions even earlier in the course of the disease than is possible with plain films. In one study, approximately 45% of patients with symptoms for only 4 months were found to have erosions detected by this method.
5. It is also possible to identify and estimate the quantity of hypertrophic synovial tissue using MRI. The presence of such MRI-detected synovial proliferation correlates with the later development of bone erosion.
6. Use of this imaging technique for joints of the hands and wrists of patients with RA outside the research setting may be hastened by the development of MRI scanners that are designed specifically for imaging the extremities.

5.5 Salter–Harris Fractures

Contributor: Fred R. Brandon
Affiliation: National Capital Consortium
Peer review/approval: Philip A. Dinauer
Affiliation: Walter Reed Army Medical Center

Salter–Harris fractures are fractures through the epiphyseal plate and happen in children prior to growth plate fusion. The common sites are the wrist and the ankle. At least five types of Salter–Harris injury have been described: type 1 slipped, type 2 above (metaphyseal), type 3 lower (epiphyseal), type 4 together (fracture through epiphysis and metaphysic), and type 5 ruined (crushed growth plate), which has the greatest growth disturbance.

5.6 Hand Fracture

Plate 5.18 shows hand fracture called *Moore's fracture*. In fact the fracture is of distal radius and ulna with posterior displacement. The following are the contributor and the reviewer:

Prepared by: William Hwang
Affiliation: Civilian Medical Center

Hand Fracture-Moore's Fracture

Plate 5.18.

Peer review/approval: James G. Smirniotopoulos, MD
Affiliation: Uniformed Services University

Plate 5.19 is zygomatic arch fracture. The contributor and reviewer to which the contribution is attributed to are:

Written by: Jason Bothwell
Prepared by: Joshua S. Ritenour
Affiliation: Uniformed Services University
Peer review/approval: James G. Smirniotopoulos, MD
Affiliation: Uniformed Services University

This case demonstrates, in the context of a common injury, the importance of multiple views. Both the AP and lateral were read as normal at the time of injury, and the patient would have been discharged from the ER if the physical exam had not been so convincing for a fracture that (several hours after the initial imaging) the SMV view was ordered. The old craniotomy scar is also an interesting additional feature in this patient.

Zygomatic Arch Fracture

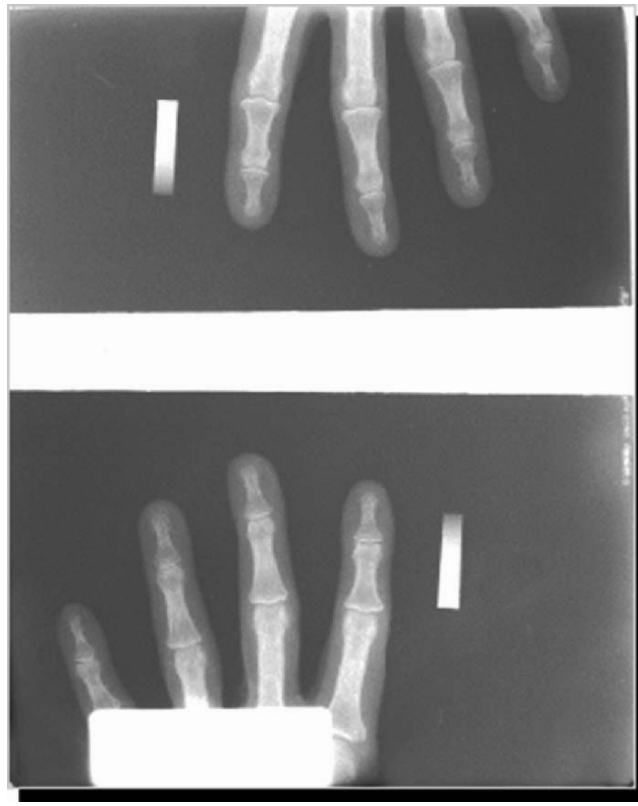

Plate 5.19.

5.7 Foot/Ankle Traumatic Injury (Reference Plates 5.20–5.24)

5.7.1 Septic Arthritis/Cellulitis

Contributors Jason Regoles: A Reference Plates 5.20 and 5.21

Acute onset of erythema, warmth, swelling, and pain on passive movement of the joint suggests septic arthritis with manifestations of cellulitis. Patients often present with systemic symptoms such as fever, malaise, and irritability. The most common cause of septic arthritis is hematogenous seeding, but it may also occur via spread from a contiguous infection or traumatic injury. Septic arthritis most commonly occurs in knee, followed by the hip, ankle, elbow, and then shoulder. Overall, *S. aureus* is the most common infecting organism in all age groups, followed by group A streptococci, and then

Foot-X-rays I

By : Jason Regoles

Plate 5.20.

S. pneumoniae. *N. gonorrhea* should be considered a possibility in neonates and sexually active individuals. IV drug users tend to get Pseudomonal and Candidal septic arthritis. Patients with sickle cell disease tend to get infections with Salmonella.

If septic arthritis is suspected, joint fluid should be aspirated and sent for gram stain, cultures, and cell count. However, the yield of organisms from culture is only about 50–60%, and it is fairly common for no microorganisms to be identified at all. If no organisms are identified, empiric therapy should be based upon most common organisms for the patient's age group and clinical picture. If the infection (1) presents in the hip, (2) is associated with a large amount of debris/pus/fibrin in the joint, or (3) does not improve within 3 days of antibiotic treatment, surgical drainage should be considered.

The fatality rate is only 1% in treated cases, compared to a 50% fatality rate in untreated cases.

Plain radiography is not an effective tool for the early evaluation of septic arthritis. They may be normal, show periarticular edema, and/or joint space widening. Bone erosions and sclerosis may be seen later in the course of infection. MRI is currently the best method of visualizing bones, cartilage, and soft-tissue structures without ionizing radiation. T2-weighted images will show enhanced signals of early inflammation.

Plate 5.21.

A reference is made to Plate 5.20 indicating X-ray for the foot.

Prepared by: MS-4 Teaching File
Affiliation: Uniformed Services University
Peer review/approval: James G. Smirniotopoulos, MD
Affiliation: Uniformed Services University

Note: Images and Text© 1999–2003 by the Original Contributors and/or others.

Some Portions of this Program and the Content Images and Text are Copyright © 1999–2003

By the Original Content Contributors and/or by H. Irvine and J.G. Smirniotopoulos, MD

Copyrighted material is reproduced by permission.

Enchondroma-X-rays I

Contributor: Jason Rexroad

Plate 5.22.

5.7.2 Enchondroma as a Trauma

Prepared by: Jason Rexroad
Peer review/approval: Donald J. Flemming
Affiliation: National Naval Medical Center, Bethesda, USA
A reference is made to Plates 5.22 and 5.23.

An enchondroma is a benign neoplasm of bone composed of hyaline cartilage lobules, localized to the medullary cavity (1, 2). They most commonly occur in patients aged 10–30 years old, with equal frequency in men and women (1, 2). Generally, the patient is asymptomatic and enchondromas are located in the diaphysis of tubular bones of the hand and foot about half of the time (1, 2). These lesions also present in the metaphyseal portion of long bones of the upper and lower extremities – femur, tibia, and humerus (1, 2). If pain is referable to the site of the lesion, a pathologic fracture should be excluded. If no fracture is seen, the diagnosis of chondrosarcoma is frequently considered. However, pain is not an uncommon presenting complaint when enchondromas are visualized radiographically. In this situation, pain is

Enchondroma-X-rays II

Plate 5.23.

Plate 5.24.

typically referable to another source (e.g., arthritis, rotator cuff tear, soft-tissue injury, etc.). Chondrosarcoma is very rare in the small tubular bones of the feet and hands. Cortical disruption, soft-tissue mass, and other aggressive features are usually present to allow an accurate diagnosis to be rendered.

Peer review/approval: Donald J. Flemming
Affiliation: National Naval Medical Center, Bethesda

5.8 Leg X-Rays Traumatic Injuries (Reference: Plates 5.25–5.31)

Contributors for this section:

- Patricia McKay, USU
  Donald J. Flemming, Naval Medical Center, Bethesda, USA
- Peer review/approval: James G. Smirniotopoulos, MD, USU
- Original Contributors: H. Irvine and J.G. Smirniolopoulos

Leg-X-rays I

Contributor: Patricia McKay, USU

Plate 5.25.

Leg X-ray II

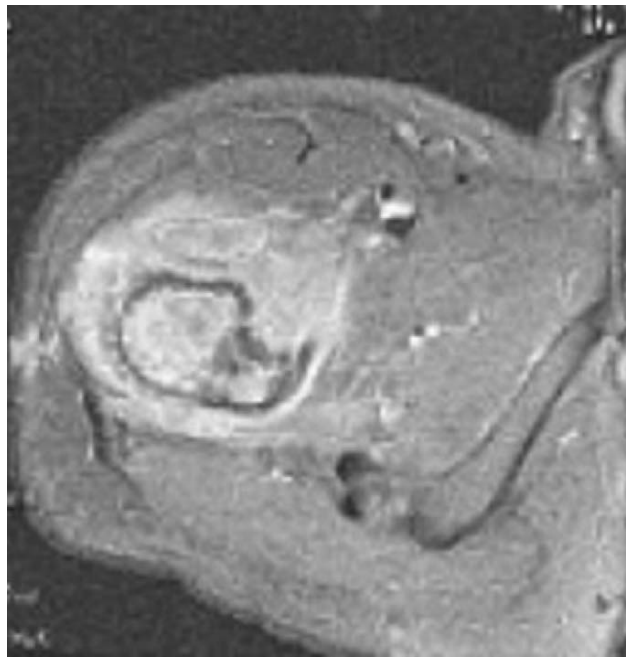

By the Original Content Contributors and / or by H Irvine and JG Smirniotopoulos, M.D.

Plate 5.26.

5.8.1 Contributor: Patricia McKay, USU Ewing Sarcoma

- Etiology: unclear but thought to be derived from either reticuloendothelial cells or undifferentiated mesenchymal cells of the bone marrow.
- Age of onset: 75% are under the age of 20 years; 90% are under the age of 30 years.
- Epidemiology: male > female (3:2); 95% are Caucasian.
- Location: younger patients tend to have the tumor arise in tubular bones whereas older patients tend to have tumor arise in axial skeleton, pelvis, and shoulder girdle.
- Signs/symptoms: localized pain and swelling, pyrexia and elevated ESR, weight loss, anemia; usually involves a single bone with extensive involvement of the diaphysis, as exemplified in this case. However, 25% arise primarily in the metaphysic. Bones commonly involved are the femur (most common), tibia, and humerus, as well as marrow-rich sites such as the pelvis and ribs.
- Radiologic features: destructive bone lesion with extensive periosteal reaction. Tumor rapidly traverses the cortex and expands in the subperiosteal

Leg X-ray IV

Proximal Tibia Fracture

Plate 5.27.

region. Erosion of the outer cortex occurs, producing so-called "saucerization" as mentioned in the findings in this case. Also classic is the "onion-peel" appearance that is formed from episodic growth and repaired by the tumor. This feature was not readily apparent in these films. The permeative pattern is produced by infiltration of cortical bone as the tumor spreads through the haversian canals.

- Differential diagnosis: in the early stages it includes osteomyelitis or trauma. Both of which produce a periosteal reaction with little bone destruction. Other tumors in the differential include lytic osteosarcoma, primary lymphoma, secondary neuroblastoma, and eosinophilic granuloma.
- Prognosis: 15–30% have metastasis at time of presentation (most commonly to lung). Current treatment protocols report up to a 79% disease-free survival. For patients with recurrence, survival is half of that number. Nonresectable central lesions, particularly those in the pelvis, have a worse prognosis, large lesions exceeding 8 cm are also more likely to present with metastasis and/or recur. Other adverse prognostic

Plate 5.28.

indicators include older age, elevated ESR, and elevated leukocyte count at the time of presentation.
– Treatment: multiagent chemotherapy (vincristine, dactinomycin, and cyclophosphamide) is used prior to radiation or surgical therapy. In this case, the patient will receive all three treatments (chemotherapy, radiation, and surgery).

Prepared by: Donald J. Flemming
Affiliation: National Naval Medical Center, Bethesda, USA
Peer review/approval: James G. Smirniotopoulos, MD, USU
Affiliation: Uniformed Services University

There is a comminuted and impacted fracture of the proximal tibia. This injury was sustained in an MVA with the patient bracing his foot against the brake pedal.

Leg X-ray VI

Seagond Fracture and Pellergrini- Stieda

Plate 5.29.

Leg X-ray VII

Plate 5.30.

Leg X-ray VIII

Seagond Fracture and Pellergrini-Stieda

Plate 5.31.

Prepared by: Chun W. Chen
Affiliation: National Capital Consortium
Peer review/approval: Philip A. Dinauer
Affiliation: Walter Reed Army Medical Center

Prepared by: Chun W. Chen
Affiliation: National Capital Consortium
Peer review/approval: Philip A. Dinauer
Affiliation: Walter Reed Army Medical Center

Prepared by: Chun W. Chen
Affiliation: National Capital Consortium
Peer review/approval: Philip A. Dinauer
Affiliation: Walter Reed Army Medical Center

5.8.2 Contributor: Chun W. Chen Segond Fracture and Pellegrini–Stieda

Segond fracture of the knee is a avulsion fracture at the lateral aspects of the proximal tibia at the insertion of the middle third of the lateral capsular ligament. Preceding studies show a high association with anterior cruciate ligament tear (75–100%). It is also associated with meniscal tears (66–75%). The fracture is a result of internal rotation and varus stress on a flexed knee.

Treatment: multiagent chemotherapy (vincristine, dactinomycin, and cyclophosphamide) is used prior to radiation or surgical therapy. In this case, the patient will receive all three treatments (chemotherapy, radiation, and surgery).

5.9 Lumber: Flexion–Distraction, Osseous–Ligamentous Fracture

A reference is made (Plate 5.32) to the contribution made by C. Carison of Uniform Services University with a peer review and approved by James G. Smirniotopoulos, MD of the same University.

A chance fracture is a flexion–distraction injury of the lumbar spine sustained when there is an acute, severe forward flexion of the spine across a restraining device, such a seat-belt, during sudden deceleration. Because of the frequency of its occurrence in motor vehicle accidents, it is often called a "seat-belt" fracture, and is associated with wearing a lap belt only, in the absence of a shoulder/chest belt. The spine above the restraining device is pushed forward and distracted from the lower, fixed portion of the spine.

The flexion–distraction mechanism of injury results in a fracture through the midportion of the L1 vertebral body with extension through the pedicle and lamina. Specifically, a chance fracture involves the horizontal splitting of the vertebra, beginning in the spinous process or lamina and extending through the pedicles and vertebral body. Significantly, there is no damage to ligamentous structures in a true Chance fracture; however, chance variants have been described which involve varying degrees of ligament and intervertebral disk disruption, as seen with this patient. The hallmark of a chance fracture is a transverse fracture without dislocation type fracture–dislocation, which resembles a Chance fracture, but is unstable because the entire annulus fibrosis is torn, allowing the vertebra above and below to dislocate or sublux. Chance fractures, on the other hand, are usually stable because the upper and lower halves of the neural arch remain firmly attached to the vertebrae above and below, respectively. The result is a separation between the upper and lower portions of the vertebrae. The transverse processes may also be horizontally fractured and there is often associated compression of the ventral aspect of the vertebral body. Chance fractures are also associated with

Osseous Ligamentous Fracture

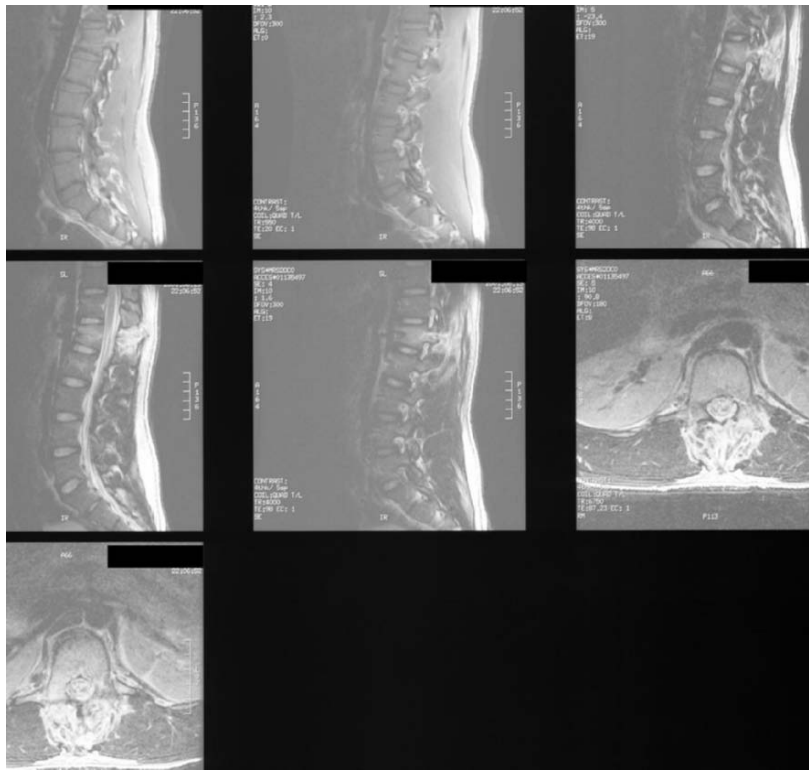

Contributor: Christian Carlson

Plate 5.32.

soft-tissue injury as manifest by edema with increased signal intensity on MR images.

Flexion–distraction, osseous–ligamentous (chance variant) fracture of L1
Peer review/approval: James G. Smirniotopoulos, MD
Affiliation: Uniformed Services University

5.10 Skull

Basilar skull fractures are the result of external forces transmitted through surrounding tissues. Areas commonly involved include the orbital surface of the frontal bone, the petrous portion of the temporal bone, the sphenoid body and wings, and the base of the occipital bone. If surrounding structures are intact these fractures may be missed without the presence of symptoms such as CSF otorrhea/rhinorrhea, hemotympanum, mastoid

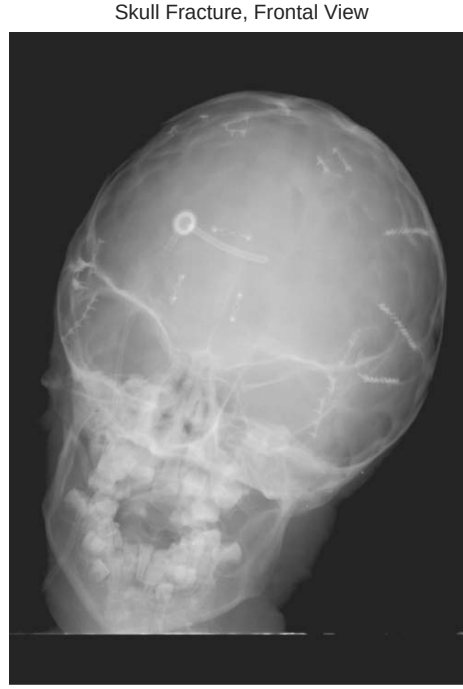

Plate 5.33.

ecchymosis (aka Battle's sign), periorbital ecchymoses ("Raccoon eyes"), or cranial nerve deficits (Plates 5.33–5.36).

Basilar skull fractures are often occult on plain film radiographs and are best imaged initially with axial CT with contrast. If CSF leak is suspected, intrathecal contrast can be administered prior to CT study to delineate the extent of the leak. Unresolving CSF leak may warrant surgical repair as there is a substantial risk of infection and chronic headache from intracranial hypotension.

This is a crosstable lateral view of the skull. A fluid level is seen in sphenoid sinus. This is another example of a patient with a basilar skull fracture.

Frontal radiograph of the skull demonstrates the presence of extensive surgical hardware as a result of prior surgeries performed to correct the coronal suture synostosis seen in these individuals.

This is a lateral view of the skull. However, the exam is not a crosstable lateral so a fluid level would not be visualized. There is a linear fracture demonstrated. This fracture is in the temporal parietal area and crosses the middle meningeal groove.

There is a shift of the pineal glad (calcified) to the left with fractures over the groove for the middle meningeal artery. This suggests the possibility of an epidural hematoma. The pineal shift is secondary to the epidural hematoma in this patient.

Linear skull fracture, lateral View

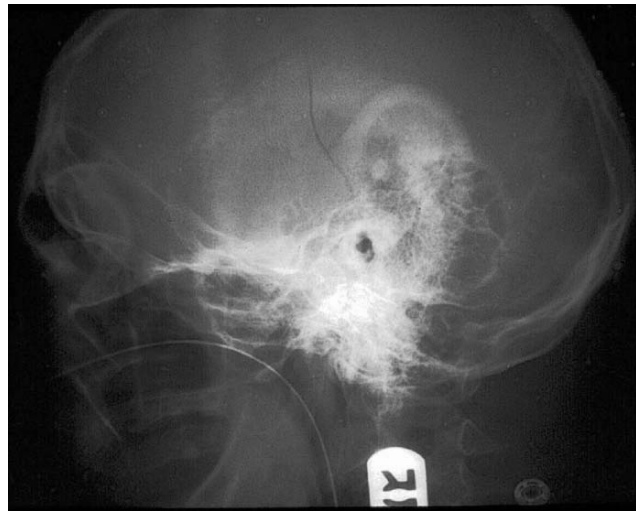

Plate 5.34.

Skull fracture with shift of pineal gland
Frontal View

Plate 5.35.

Skull fracture with shift of pineal gland
Lateral View

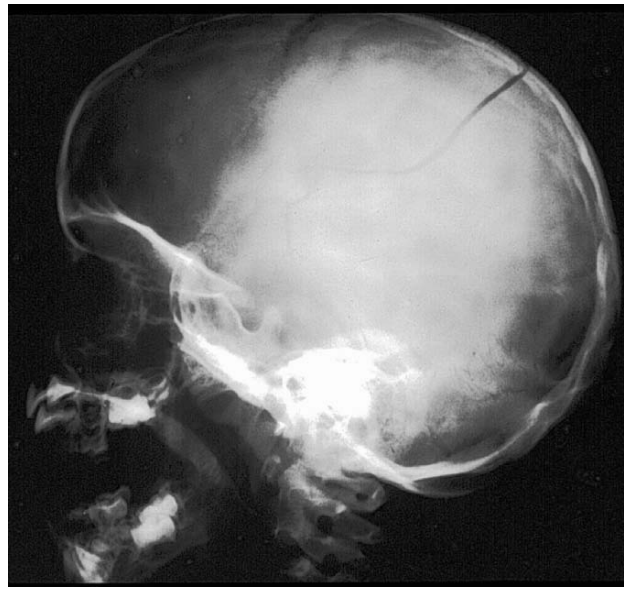

Plate 5.36.

5.10.1 Skull Fracture with Small Epidural Hemorrhage by Jason Rexroad

A fracture which tears the middle meningeal artery or a dural venous sinus is present in 85–95% of cases of epidural hemorrhage (EDH). The vast majority of EDHs (>95%) are supratentorial (frontotemporal and frontoparietal) and unilateral. A diploic EDH occurs when the inner table of the skull is fractured and venous oozing occurs without arterial laceration.

Because an EDH is located between the skull and the dura, separation of the dura from the skull by the space-occupying blood results in the focal biconvex or lentiform appearance which is characteristic of EDH. However, only rarely, crescentic configuration is also possible. The gray–white matter interface is displaced away from the inner table of the skull.

EDHs cross dural reflections (such as the falx), but they do not cross suture lines. Two thirds of the cases of EDH are hyperdense on CT and one-third are mixed hyper- or hypodense and indicate active bleeding. Herniations as a result of an EDH are common.

5.10.2 Skull Fractures in Tension Contributor: James G. Smirniotopoulos, MD

The calvarium (skull) fractures are in tension, not under compression. Skull fractures usually occur from external forces that produce inbending. The

dense cortical inner table fractures first, and the crack propagates through the diploic space (spongy marrow) to break the cortical outer table. Fractures are classified by shape and pattern. If bone fragments have been driven into the skull chamber, the fracture is "depressed" (Plates 5.37 and 5.38).

Skull Fracture with Small Epidural Hemorrhage

Plate 5.37.

Skull Fracture-Dipressed

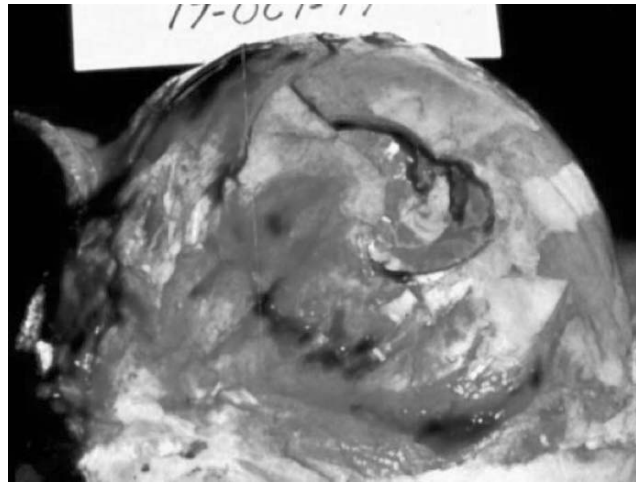

Contributor: James G. Smirniotopoulos, MD

Plate 5.38.

Contributor: Jason Rexroad
Peer review/approval: James G. Smirniotopoulos, MD
Affiliation: Uniformed Services University

5.11 Ankle

5.11.1 Distal Fibular Fx by Mathew J. Hoffman

Pronation–lateral (external) rotation injuries of ankle (subtype of Lauge–Hanses classification):

Stage I. Rupture of the deltoid ligament or transverse Fx of medial malleolus
Stage II. Disruption of the anterior tibiofibular ligament and interosseous membrane
Stage III. Fracture of the fibula usually 6 cm or more above the level of the joint
Stage IV. Chip fracture of the posterior tibia or rupture of the posterior tibiofibular ligament

Plate 5.39.

Frontal and Oblique Right Ankle Radiographs

Plate 5.40.

Examples of fractures caused by Eversion-type injury:

Dupuytren fracture. Fracture of the fibula occurring 2–7 cm above the distal tibiofibular syndesmosis, including disruption of the medal collateral ligament and with associated tear of the syndesmosis.

Maisonneuve fracture. Fracture in proximal half of the fibula (most commonly at junction of proximal and middle thirds) with disruption of syndesmosis and either a tear of the medial collateral ligament or Fx of medal malleolus. Associated disruption of the interosseous membrane is always up to Fx point.

Other key points. Fractures of the fibula above the anterior tubercle strongly suggest that the tibiofibular syndesmosis is completely disrupted. Fractures of the fibula above the level of the ankle joint without accompanied Fx of the medial malleolus indicate rupture of the deltoid ligament.

Frontal: XR – Plain Film (Plates 5.39 and 5.40).

Affiliation: National Capital Consortium
Peer review/approval: Philip A. Dinauer
Affiliation: Water Reed Army Medical Center

There is a short oblique fracture through the distal fibula and a nondisplaced fracture of the posterior aspect (posterior malleolus) of the tibia. These fractures are visualized to best advantage on the lateral radiograph. There is soft-tissue swelling about the ankle. The mortise is intact.

5.11.2 Toddler's Fracture by Richard P. Moser III (Plate 5.41)

The toddler's fracture, so-called because of its tendency to occur in young infants, is a spiral, hairline tibial shaft fracture that is often invisible of nearly so on the initial radiographs. It behaves like a stress fracture and is frequently more apparent on one projection than the others. Patients typically present

Contributor: Richard P. Moser III

Plate 5.41.

with a limp or stop walking. If present, soft-tissue swelling involving the muscles about the tibia may be a clue to the diagnosis. In cases in which the fracture is radiographically occult, the diagnosis can be cinched if there is reproduction of the patient's pain with application of a torque stress across the fracture site: one hand is placed on the knee and one hand is placed on the ankle, and the leg is twisted in opposite directions.

Caveat: always look for associated plastic bending fractures of fibula

Prepared by: Richard P. Moser III
Affiliation: National Capital Consortium
Peer review/approval: Philip A. Dinauer
Affiliation: Walter Reed Army Medical Center

5.11.3 Intraosseous Ganglion by Fred R. Brandon (Plate 5.42)

Intraosseous Ganglion is typically seen in adults between the ages of 20 and 60 years. It is typically seen within the articular ends of long bones along the nonweight bearing side. It is usually seen as an eccentric lucent lesion with sclerotic margin that does not communicate with the joint cavity. They may look similar to chondroblastoma, osteoblastoma, enchondroma, or bone abscesses.

Intraosseous Ganglion

Plate 5.42.

Prepared by: Fred R. Brandon
Affiliation: National Capital Consortium
Peer review/approval: James G. Smirniotopoulos, MD
Affiliation: Uniformed Services University

5.12 Segond Fracture with Associated ACL Tear (Plate 5.43)

First described by Segond (1879), internal rotation and varus stress on a flexed knee results in tension at the lateral capsule of the knee. The lateral capsular ligament can then pull free of its insertion site at the lateral tibial plateau,

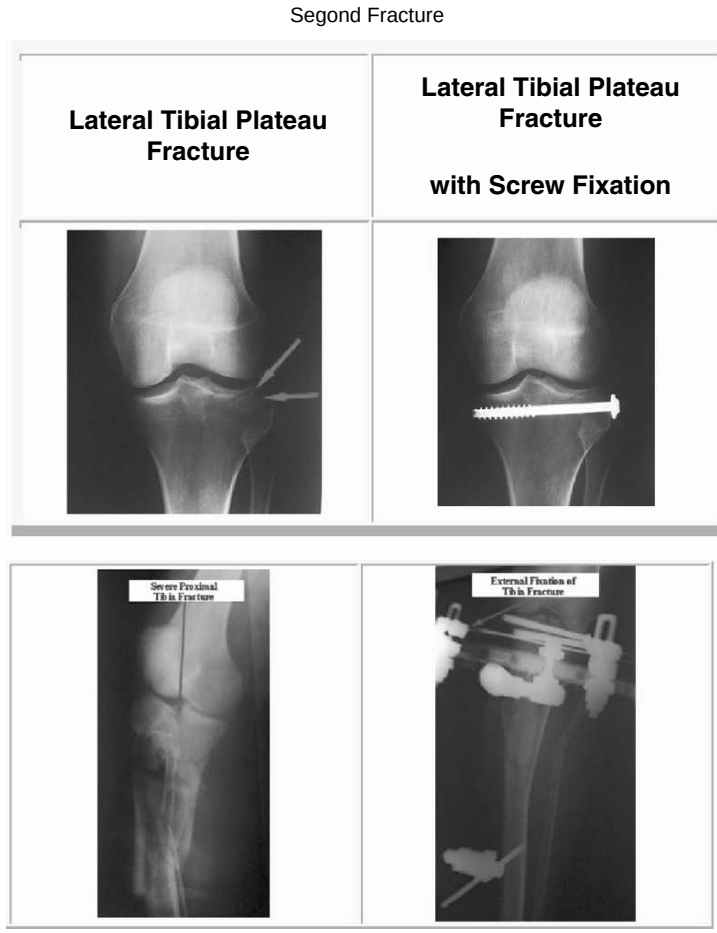

Contributor: Jason Rexroad

Plate 5.43.

causing an avulsive injury at this location. A key feature of this fracture is its association with anterior cruciate ligament tear. One source cites that 75–100% of patients with a Segond fracture will also have an ACL tear. Thirty-five percent will have an associated lateral meniscal tear. Interestingly, a "reverse Segond"-type fracture has been described. As the name implies, this injury is caused by external rotation and valgus stress on a flexed knee and results in an avulsion off the medial tibial plateau with associated tears of the posterior cruciate ligament and medial meniscus.

Peer review/approval: Philip A. Dinauer
Affiliation: Walter Reed Army Medical Center

5.13 Rib Fracture: Stages of Healing

A reference is made to Plates 5.44–5.47.

Lindsell et al. (1982) described a study in St. George's Hospital and Medical School in London, England, where the CXRs of pts with liver disease who

Rib Fractures, stages of healing I

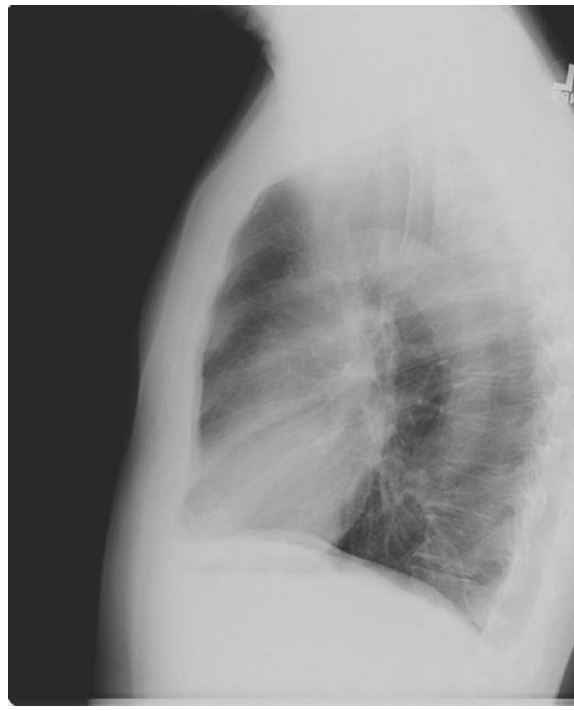

Plate 5.44.

Rib Fractures, stages of healing II

Plate 5.45.

Rib Fractures, stages of healing III
Left Lower Collapse

Contributor: Hayden O Jack

Plate 5.46.

Rib Fractures, stages of healing IV

Prepared by: Hayden O Jack

Plate 5.47.

were about to under liver biopsy were examined. There were 149 total, 72 with prolonged alcohol use as the etiology of their liver disease, while 77 had other nonalcoholic etiologies.

Fractures in general were much more common in the alcohol group vs. the patients with other etiologies for their liver disease (28 vs. 1.3%) or age- and sex-matched controls (6.7%). Of the fractures, rib fractures were predominantly found on the CXRs. In the alcoholic liver disease group, rib fractures were more likely to be bilateral or multiple or both ($p < 0.01$). They have found that bilateral and/or multiple (>2) rib fractures had a sensitivity of 16.7% but a specificity of 100% for the presence of alcoholic liver disease.

Differential diagnosis of multiple rib fractures includes cough-induced rib fractures, especially in patients with COPD. However, vast majority (93%) of cough-induced rib fractures are axillary, while only 40% of rib fractures seen with patients with alcoholic liver disease were axillary. Only 15.2% of cough-induced rib fractures were multiple (i.e., >2), and only 9.7% of cough-induced rib fractures were bilateral; little over 60% of rib fractures seen in patients with alcoholic liver disease are multiple, and close to 40% of them are bilateral.

Although bilateral/multiple rib fractures seen on routine CXR are lousy screening tool for alcoholic liver disease, the specificity shown on this study is so high that when found, clinicians should be notified of this finding and its meaning. Clinicians themselves also should raise the index of suspicion of

Peer review/approval: David S. Feigin, MD, COL, USA
Affiliation: Uniformed Services University

Prepared by: Hayden O. Jack
Affiliation: National Capital Consortium
Peer review/approval: David S. Feigin, MD, COL, USA
Affiliation: Uniformed Services University

Affiliation: National Capital Consortium
Peer review/Approval: David S. Feigin, MD, COL, USA
Affiliation: Uniformed Services University

5.14 Knee: ACL Tear (Plate 5.48)

The cruciate ligaments serve as stabilizers for posterior and anterior "displacement of the tibia on the femur." It is the most commonly injured ligament of the knee as 200,000 tears occur in the US annually. The ACL can be injured via

Contributor: Brain Johnston

Plate 5.48.

numerous mechanisms. ACL injuries occur most often in noncontact, planting, pivoting, and cutting sports such as basketball, volleyball, and soccer. Direct Impact blows to a flexed knee can as in an automobile accident or as in the case of a football player falling to the turf can often cause ACL injury. History is an important element in diagnosing ACL injury as 70% of patients note a "pop" at the time of injury, 15–65% of patients report their knee gives out in the case of a tear, most report the pain as immediate.

Clinical evaluation often reveals obvious tenderness to palpation along the joint lines and femoral and tibial physis. A positive anterior drawer's sign and positive Lachman's test are classic tests used to determine the presence of an anterior cruciate ligament injury.

MRI with T1- and T2-weighted images is highly sensitive in identifying ACL injury documented at 90–98%. On MRI of the knee, findings of abnormal ligamentous signal and morphology are indicative of ACL tear, and one should always look for concurrent meniscal, PCL and LCL tears.

Treatment can involve nonoperative therapy which includes the initial use of antiinflammatory meds and potentially draining the knee to enhance recovery. After the initial pain and swelling are over, a rehabilitation program concentrating on strengthening quadriceps and hamstrings is beneficial. Also the wearing of a brace during activity is beneficial.

Surgical therapy for ACL injuries is recommended for those wishing to return to cutting/pivoting styles of sports or who cannot perform regular ADLs with their injury. Reconstruction of the ligament in surgery is often achieved using hamstring autografts, bone–patellar tendon–bone autograft, or allograft tissue often from patellar tendon and Achilles tendon after which hardware is used to secure graft placement in the knee. Rehabilitation follows the surgery and patients can often return to full activity in about 6 months.

5.14.1 Anterior Cruciate Ligament Injury (Plate 5.49)

There are several plain film findings in the distal femur and proximal tibia that imply that an anterior cruciate injury is present:

1. Avulsion fracture of the anterior tibial eminence. These occur at the site of attachment of the ACL. They are more common in children and adolescents than in adults, who tend to injure the ligament itself rather than avulse its attachment. If present in an adult, the likelihood of accompanying medial ligamentous or meniscal injury is higher. Rarely does the ACL avulse from the femoral origin.
2. Lateral tibial rim fracture (Segond fracture). A fracture fragment arising at the site of tibial attachment of the lateral capsular ligament has a high association with ACL injury. On frontal projections, the fragment is usually located inferior and lateral to the joint space.

Plate 5.49.

3. Posterolateral fracture of the tibial plateau. This injury is seen on the lateral radiograph, and may represent avulsion at the insertion of the posterior portion of the joint capsule. Compression fractures of the posterior tibial plateau or fractures at the insertion of the semimembranosus tendon may also occur. This is demonstrated on the lateral film as an irregular contour of the lateral tibial plateau.
4. Osteochondral fracture of the lateral femoral condyle. This is thought to result from impaction of the condyle on the tibial plateau. The lateral notch sign consists of the lateral condylopatellar sulcus being deeper than 1.5 cm on the lateral film. The sign is specific for ACL injury, but it is insensitive, occurring in only 5% of patients with torn anterior cruciate ligaments. There is some question of whether this finding results from ACL injury, or whether is an anatomic variant that predisposes to the ligamentous injury.

Prepared by: Aaron M. Taylor
Affiliation: National Capital Consortium
Peer review/approval: James G. Smirniotopoulos, MD
Affiliation: Uniformed Services University

5.14.2 Osteochondritis Dissecans (OCD) (Plate 5.50)

OCD lesions are defects or fragmentation of subchondral bone, thought to be caused by trauma or ischemic necrosis. Intercondylar aspect of medial femoral condyle is most common location. MRI is necessary to determine firm or partial attachment of fragments, with 92% sensitivity and 90% specificity. The presence of interface fluid between the fragment and its parent bone on a T2-weighted image is a reliable sign of loosening. Loose fragments require surgical removal, while conservative management can be pursued with firm fragments.

Written by: Paul Lewis
Prepared by: MS-4 Teaching File
Affiliation: Uniformed Services University
Peer review/Approval: James G. Smirniotopoulos, MD
Affiliation: Uniformed Services University

Plate 5.50.

5.14.3 Cemented Enchondroma with Appearance of Bone Island (Plate 5.51)

A bone island is an area of mature cortical bone within cancellous bone. It is considered to be a benign lesion that is discovered incidentally, although it may resemble malignant processes such as an osteoblastic metastasis from prostate or breast cancer. Enostoses are composed of normal cortical bone with the aversion canals and have spicules or "thorny" radiations that coalesce with the surrounding cancellous bone. They are distinguished by characteristic radiographic findings: typically round or avoid intramedullary sclerotic densities that remain subcortical. They may express radiating spicules of sclerosis into the trabecular environment. Bone islands greater than 2 cm in size are considered "giant," and are more commonly found in the pelvis, although they can occur in any osseous site (commonly the long bones). Characteristic radiographic findings provide accurate diagnosis, but follow-up may be appropriate if an enostosis is unusually large, grows rapidly, is symptomatic or is found in a patient with a history of cancer. This lesion does not meet the characteristic appearance of an enchondroma. An enchondroma is also a benign and asymptomatic lesion. A cartilaginous tumor most commonly seen in young adults, and representing a failure of normal ossification, is characteristically located in the central metaphysic. It is seen most often in the bones of

Cemented Enchondroma (Post-Surgery) with Appearance of Bone Island

Plate 5.51.

the hands or feet, but may occur in the humerus or femur. The lesion is noted for its propensity to cause pathologic fracture, and does have the potential for malignant transformation to chondrosarcoma. They are radiographically identified as having a central radiolucent area with a thickened bony margin. Plain, destructive changes on X-ray, increased radioisotope uptake on scintigraphy, growth may indicate need for biopsy to rule out malignancy.

Written by: E.N.S. Lindsey Steele
Prepared by: MS-4 Teaching File
Affiliation: Uniformed Services University
Peer review/approval: Philip A. Dinauer
Affiliation: Walter Reed Army Medical Center

6

Medical Devices, Surgical Equipment and Methodologies

6.1 General Introduction

Brief details are included for medical devices, surgical equipment and their methodologies. A vast literature exists on surgical devices and methods of repair of various organs. They need volumes to adopt their usages and at present, they are beyond the scope of this book. In this chapter more emphasis is placed on the fixation devices, hand mechanisms, prosthetic sockets, shoulder prosthetic and construction knee system, total hip system, orthopedic devices, hardware and methodologies of reinforcing and stabilizing the human parts, and muscle stabilization, hand and wrist coronal plane strength and cranial stabilization and retracting systems. A reference is made to selected medical devices and instrumentations given in Appendices V–X. As far as possible various plates are included to visualize how various repair system in surgery have been adopted. References are given to researchers to proceed with in-depth study of any specific case study related to this chapter.

6.2 Spine: Lumbosacral Axial Fixation Device

Background: Interbody arthrodesis is employed in the lumbar spine to eliminate painful motion and achieve stability through bony fusion. Bone grafts, metal cages, composite spacers, and growth factors are available and can be placed through traditional open techniques or minimally invasively. Whether placed anteriorly, posteriorly, or laterally, insertion of these implants necessitates compromise of the annulus – an inherently destabilizing procedure. A new axial percutaneous approach to the lumbosarcal spine has been described. Using this technique, vertical access to the lumbosacral spine is achieved percutaneously via the presacral space. An implant that can be placed across a motion segment without compromise to the annulus avoids surgical destabilization and may be advantageous for interbody arthrodesis. The purpose of this study was to evaluate the in vitro biomechanical

performance of the axial fixation rod, an annulus sparing, centrally placed interbody fusion implant for motion segment stabilization.

Method of Approach: Twenty-four bovine lumbar motion segments were mechanically tested using an unconstrained flexibility protocol in sagittal and lateral bending, and torsion. Motion segments were also tested in axial compression. Each specimen was tested in an intact state, and then drilled (simulating a transaxial approach to the lumbosacral spine). Then with one of the two axial fixation rods placed in the spine for stabilization. The range of motion, bending stiffness, and axial compressive stiffness were determined for each test condition. Results were compared to those previously reported for femoral ring allograft, bone dowels, BAK and BAK Proximity cages. Ray TFC, Brantigan ALIF and TALIF implants, the InFix Device, Danek TIBFD, single and double Harms cages, and Kaneda, Isola, and University plating systems.

Results: While axial drilling of specimens hand little effect on stiffness and range of motion, specimens implanted with axial fixation rod exhibited significant increases in stiffness and decreases in range of motion relative to intact state. When compared to existing anterior, posterior, and interbody instrumentation, lateral and sagittal bending stiffness of the axial fixation rod exceeded that of all other interbody devices, while stiffness in extension and axial compression were comparable to plate and rod constructs. Torsional stiffness was comparable to other interbody constructs and slightly lower than plate and rod constructs. Torsional stiffness was comparable to other interbody constructs and slightly lower than plate and rod constructs.

Conclusion: For stabilization of the L5–S1 motion segment, axial placement of implants offers potential benefits relative to traditional exposures. The preliminary biomechanical data from this study indicate that the axial fixation rod compares favorably to other devices and may be suitable to reduce pathologic motion at L5–S1, thus promoting bony fusion.

6.2.1 Results

There were no failures or fracture of implants or motion segments during testing. All implants were placed centrally through the disc space. During drilling, there was a distinct "pop" when the drill penetrated through the endplate into the disk space. A substantial amount of torques was necessary to drive the threaded rods through the motion segments using the hand held instrumentation for both the tapered the nontapered rods. By direct visualization, the disk space in many specimens was distracted several millimeters during placement of the rods. Although not measured, this distraction appeared to be maintained during mechanical testing.

Drilling of the axial tunnel through the motion segment had little effect on the stability of the segment. The effects of drilling alone were only significant in axial compression, where the stiffness was reduced to 88% of intact, and torsion, where range of motion was increased by up to 50% of intact.

Table 6.1. Mean range of motion (ROM) and axial compressive stiffness data for specimens in the low load groups

mean data (% of intact)	ROM at 5 N m flexion (°)	ROM at 5 N m extension (°)	ROM at 3 N m right LB (°)	ROM 3 N m left LB (°)	ROM 3 N m CW (°)	ROM 3 N m CCW (°)	axial stiffness ($N\,mm^{-1}$)
taper							
Intact	4.5	1.8	2.9	3.0	0.4	0.3	2708.5
specimen	(100%)	(100%)	(100%)	(100%)	(100%)	(100%)	(100%)
Drilled	4.3	2.3	2.9	2.9	0.3	0.4[a]	2409.3[a]
specimen	(91.7%)	(137.6%)	(104.1%)	(95.1%)	(107.8%)	(147.3%)	(88.6%)
Implant	0.9[a]	0.4[a]	0.8[a,b]	0.9[a]	0.2	0.2[a]	3537.0[a]
placed	(20.8%)	(40.1%)	(34.3%)	(29.1%)	(72.6%)	(77.7%)	(131.7%)
nontaper							
Intact	4.3	1.8	3.9	4.1	0.4	0.4	2489.8
specimen	(100%)	(100%)	(100%)	(100%)	(100%)	(100%)	(100%)
Drilled	4.6	2.2	4.0	3.5	0.4	0.5[a]	2146.3[a]
specimen	(105.6%)	(124.7%)	(101.0%)	(91.1%)	(96.4%)	(151.2%)	(87.6%)
Implant	0.6[a]	0.5	0.4[a,b]	0.5[a]	0.2	0.3[a]	3442.5[a]
placed	(14.7%)	(32.5%)	(11.1%)	(18.9%)	(51.7%)	(98.8%)	(143.8%)

LB = lateral bending, CW = clockwise, CCW = counter clockwise
[a] Statistically significant difference ($p < 0.05$) relative to intact condition
[b] Statistically significant difference between tapered and nontapered treatments

Figure 6.1. The axial fixation rod is a cannulated, with U-shaped thread and self-tapping section

Results in the low load group, as shown in Table 6.1, indicate that specimens tested with the axial fixation rod (Fig. 6.1 tapered or nontapered) exhibited an increase in axial compressive stiffness to 131.7% and 143.8% of their intact values, respectively. An increase in angular stiffness of the nontaper group was indicated by the marked reduction in ROM in flexion

Table 6.2. Mean ROM data for specimens in the high load groups

mean data (% of intact)	ROM at 10 N m flexion (°)	ROM at 10 N m extension (°)	ROM at 10 N m right LB (°)	ROM at 10 N m left LB (°)	ROM at 10 N m CW (°)	ROM at 10 N m CCW (°)
taper						
Intact	5.1	2.5	7.1	7.1	1.2	1.3
specimen	(100%)	(100%)	(100%)	(100%)	(100%)	(100%)
Drilled	5.5	2.8	7.2	7.1	1.3	1.3
specimen	(107.0%)	(111.5%)	(100.6%)	(98.8%)	(100.9%)	(102.6%)
Implant	1.9[a]	1.4[a,b]	3.7[a]	3.3[a]	1.0	1.0[a]
placed	(39.0%)	(56.6%)	(53.6%)	(47.3%)	(82.5%)	(76.8%)
nontaper						
Intact	4.5	2.9	5.2	5.5	1.0	1.0
specimen	(100%)	(100%)	(100%)	(100%)	(100%)	(100%)
Drilled	4.9	2.9	4.9	5.7	1.0	1.0
specimen	(107.4%)	(101.7%)	(97.0%)	(103.9%)	(101.4%)	(93.6%)
Implant	1.2[a]	1.2[a,b]	1.9[a]	2.0[a]	1.0	0.9
placed	(29.3%)	(41.1%)	(40.2%)	(38.9%)	(96.0%)	(83.9%)

LB = lateral bending, CW = clockwise, CCW = counter clockwise
[a] Statistically significant difference ($p < 0.05$) relative to intact condition
[b] Statistically significant difference between tapered and nontapered treatments

to 14.7%, extension to 32.5%, right lateral bending to 11.1%, and left lateral bending to 18.9% when compared to intact specimens. Similar reductions in ROM were observed in the taper group, with greatest reduction in motion observed in flexion (20.8% of intact). A decrease in torsional ROM was observed with both implants but not to the extent of the other motions.

In the high load groups, there were increases in the stiffness of the tapered and nontapered groups, resulting in a reduced range of motion in all loading directions. As shown in Table 6.2, range of motion was reduced to 39% of intact flexion in the tapered group and 29% in the nontapered group, with similar reductions in other ranges of motion.

6.3 Hand Mechanism with High Degrees of Freedom

This paper presents the design and prototyping of an inherently compliant light weight hand mechanism. The hand mechanism itself has 15 degrees of freedomand five fingers (Plate 6.1). Although the degrees of freedom in each finger are coupled, reducing the number of independent degrees of freedom to five, the 15 degrees of freedom of the hand could potentially be individually actuated. Each joint consists of a novel flexing mechanism that is based on the loading of a compression spring in the axial and transverse direction via a cable and conduct system. Currently, a bench top version of the prototype is being developed; the three joints of each finger are coupled together to simplify the control system. The current control scheme under investigation simulates

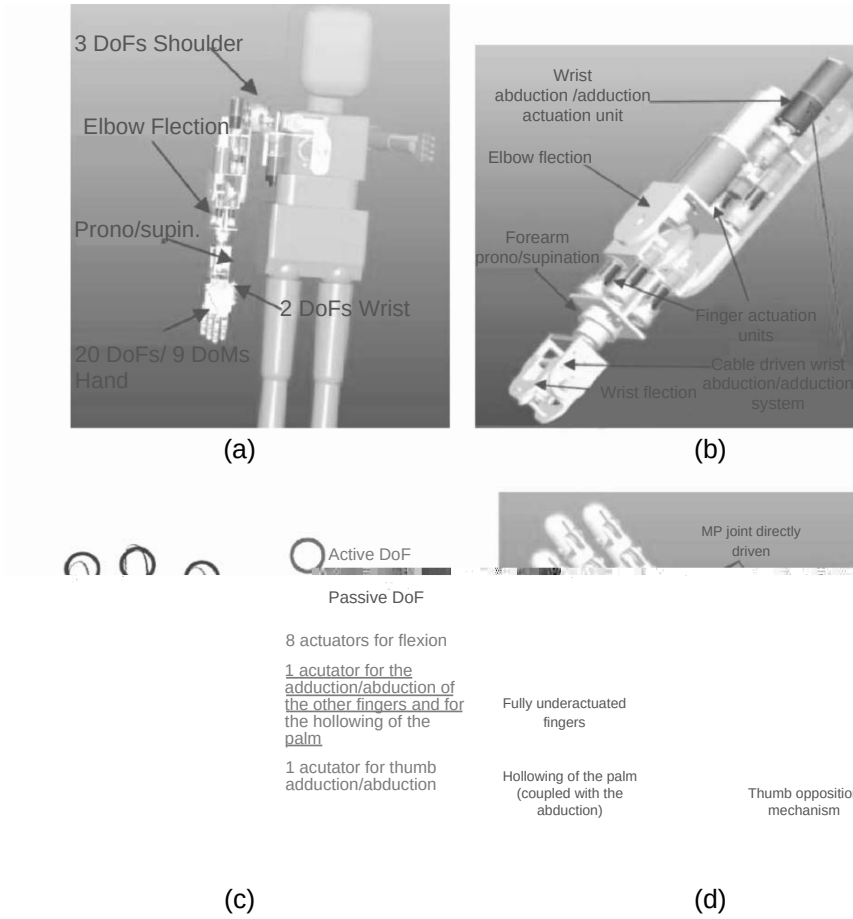

(a) The upper limb integrated drawing of the arm and forearm
(b) The CAD drawing of the arm and forearm
(c) The selection DoFs/DoMs in the Cub Hand
(d) The CAD drawing of the Cub Hand

Prepared by
Giovanni Stellin, Giovanni et al.
Cappiello, Stefano Roccella, Maria
Chiara Carrozza,
ARTS Lab, v.le Piaggio 34, 56025 Pontedera, Italy

Plate 6.1. Design and protoyping of the hand mechanism: (**a**) the upper limb integrated drawing of the arm and forearm; (**b**) the CAD drawing of the arm and forearm; (**c**) The selection DoFs/DoMs in the cub hand; (**d**) The CAD drawing of the cub hand.

a control scheme where myoelectric signal in the wring flexor and extensor muscles are converted in to x and y coordinates on a control schemed chart. Static load–deformation analysis of finger segments is studied based on a 3D model without taking the stiffener into account, and the experiment validates the simulation. (DOI: 10.1115/1.2052805)

In this work we developed a five-fingered hand with 15 DOFs that mimics a human hand in terms of appearance, motion, and grasping ability. One key feature that makes this hand more advanced than any other multifingered hands is the mechanism used for the joints that are similar to the elastic manipulation. This newly developed mechanism is based on the loading of a compression spring in both the axial and transverse direction and offers several advantages over a hand mechanism based on rigid links and revolute joints. Since the structure of each finger is primarily made up of compression spring, the majority of the volume of each finger is occupied by empty space. Thus, the potential for constructing a very light hand exists if the proper materials are used along with an efficient design. A lightweight design is critical aspect of a comfortable, wearable prosthetic devise and offers obvious advantages for robotics applications, such as smaller actuators and less power consumption. The unique mechanism also allows the hand to be inherently compliant. Tables 6.3 and 6.4 gives spring properties and joint range of motion respectively.

Table 6.3. Spring properties

spring properties					
joint	outside spring diameter, o.d. (mm)	wire diameter, d (mm)	length, L (mm)	number of active coils, n	spring constant, k ($\mathrm{N\,mm^{-1}}$)
1–1	18.0	0.965	22	2	6.9
1–2	22.0	0.927	19	3	3.9
1–3	22.0	1.016	21	2.1	9.1
2–1	13.6	0.610	21	4	0.3
2–2	17.7	0.737	20	5	0.6
2–3	21.0	0.914	32	5	2.5
3–1	12.7	0.762	19	5	1.2
3–2	13.6	0.622	20	4.5	0.4
3–3	17.7	0.724	33	9.5	0.1
4–1	12.7	0.699	21	5	1.7
4–2	13.6	0.610	23	4.5	0.6
4–3	17.7	0.699	25	5.5	0.1
5–1	10.6	0.622	19	6	0.4
5–2	12.7	0.737	21	5.25	0.8
5–3	15.8	0.838	20	3.3	2.7

Table 6.4. Joint range of motion

finger	joint	minimum joint angle (°)	maximum joint angle (°)	range of motion (°)	rotation (°)
thumb	1–1, Interphangeal	22	49	27	
	1–2, Metacarpophalangeal	12	44	32	
	1–3, Carpometacarpal	18	49	31	200
	total range of motion			90	
index	2–1, Distal interphangeal	12	83	71	
	2–2, Proximal interphalangeal	12	62	50	
	2–3, Metacarpophalangeal	9	66	57	170
	total range of motion			178	
middle	3–1, Distal interphangeal	4	76	72	
	3–2, Proximal interphalangeal	12	72	60	
	3–3, Metacarpophalangeal	10	84	74	170
	total range of motion			206	
ring	4–1, Distal interphangeal	13	75	62	
	4–2, Proximal interphalangeal	19	87	68	
	4–3, Metacarpophalangeal	0	56	56	200
	total range of motion			186	
little	5–1, Distal interphangeal	17	76	59	
	5–2, Proximal interphalangeal	17	77	60	
	5–3, Metacarpophalangeal	15	63	48	130
	total range of motion			167	

6.4 Prosthetic Sockets

A very attractive advantage of manufacturing prosthetic sockets using solid freeform fabrications the freeform to introduce design solutions that would be difficult to implement using traditional manufacturing techniques. Such is the case with complaint feature embedded in amputee prosthetic socket to relieve contact pressure at the residual limb-socket interface. The purpose of this study was to present a framework for designing complaint features to be incorporated into transtibial sockets and manufacturing proto-types using selective laser sinering (SLS) AND Durafor TM material. The design process included identifying optimal compliant features using topology optimisation algorithms and integrating these features within the geometry of the socket model. Using this process a compliant feature consisting of spiral beams and a supporting external structure was identified. To assess its effectiveness in reducing residual limb-socket interface pressure, a case study was conducted using SLS manufactured prototype to quantify the difference in interface pressure while a patient walked at his self selected pace with one noncompliant and two different compliant sockets. The pressure measurements were performed using thin pressure transducers located at the distal tibia and

Table 6.5. Peak and average interface contact pressure at the distal tibia and fibula head during single leg support averaged over 40 step cycles

pressure measurement results from case study			
	noncompliant socket	compliant socket A	compliant socket B
average pressure at distal tibia during single support	67.51 ± 17.23 kPa	58.47 ± 6.13 kPa	52.67 ± 3.28 kPa
average peak pressure at distal tibia	103.35 ± 15.59 kPa	67.83 ± 8.11 kPa	57.01 ± 1.87 kPa
average pressure at fibula head during single support	73.85 ± 9.03 kPa	62.86 ± 5.37 kPa	59.50 ± 4.06 kPa
average peak pressure at fibula head	82.74 ± 1.84 kPa	70.59 ± 1.56 kPa	63.60 ± 2.63 kPa

Socket B was 25% more compliant than socket A

fibula head (Table 6.5). The measurements revealed that the socket with the greatest compliance reduced the average and peak pressure by 22% and 45% at the anterior side distal tibia, respectively, and 19% and 23% at the lateral side of the fibula head, respectively. These results indicate that the integration of compliant features within the socket structure is an effective way to reduce potentially harmful contact pressure and increase patient comfort.

6.4.1 Method

Overview. The method used for designing and implementing orthogonally compliant features for prosthetic sockets initial involved identifying the design constraints and boundary conditions and the material characteristic used in the SLS fabrication process. A preliminary study identified several variants of compliant features that were analyzed and tested through experimentation to identify those that provided the greatest compliance. These features were combined with structures developed using a topology optimization algorithm to precisely control the compliance. The resulting compliant features were then incorporated into a nominal PTB socket design and fabricated using SLS. To assess the effectiveness of the design, a case study was performed on a patient using three SLS fabricated sockets (all were topologically similar, two with different levels of compliance and one without) and quantifying the resulting and changes in interface pressure at the compliant sites using this pressures sensor. Below, details of the design and analysis are described.

6.4.2 Design of Spiral Slot Compliant Features

A preliminary study showed that compliant features including concentric spiral slots was the best approach for relieving interface pressure at the residual limb–socket interface based on its capacity to provide orthogonal compliance in a relatively small area while satisfying the overall design constraints. However, through finite element method (FEM) analysis and experimental validation, the preliminary study also demonstrated that the optimum number of concentric slots (four) that provide a smooth deformation of the inner surface while preserving the structural integrity also led to an overshot of the target compliance. The compliant feature was shown to provide little reaction force for a given displacement, which could potentially lead to a concentration of limb–socket contact pressures in the area around the compliant feature and result in poor socket fit. To remedy this situation, a stiffening structure was deemed necessary in order to provide increased stiffness and control compliance, such a structure could be placed between the outer protective wall and the complaint feature (Figs. 6.2–6.5). However, it was unclear what form the stiffening structure should take. To identify potential structure designs, topology optimization was used, which is an ideal technique given the well defined design domain and the freedom of design provided by the SLS fabrication process.

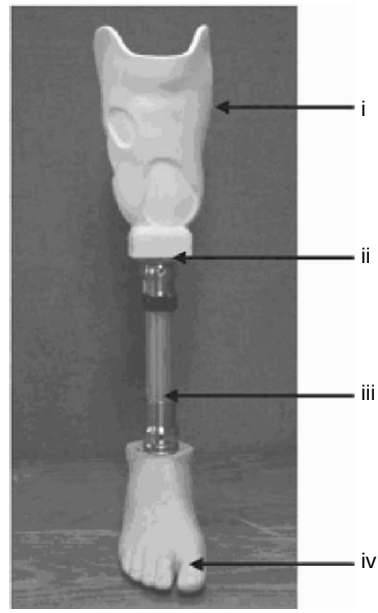

Fig. 6.2. A patient using an SLS fabricated socket; description of the parts of a prosthesis for below-the-knee amputees (i) socket, (ii) attachment fitting, (iii) pylon, and (iv) prosthetic foot

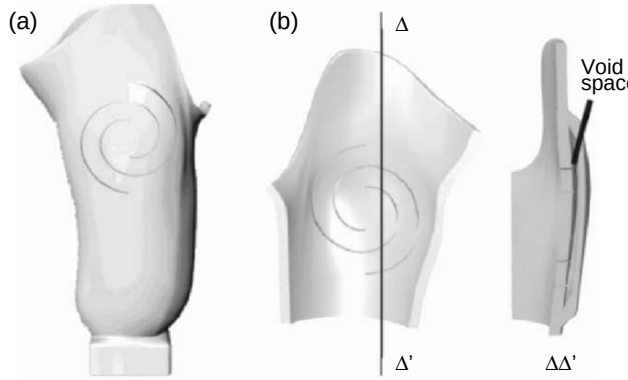

Fig. 6.3. (**a**) Example of orthogonally compliant spiral-slotted features incorporated in a socket; (**b**) a detailed view of spiral slot compliant feature and a section view showing the void space between the slotted wall and the back protective wall

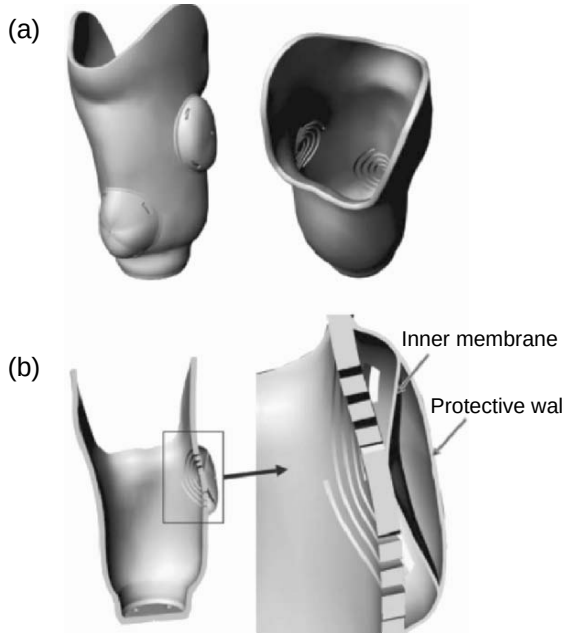

Fig. 6.4. (**a**) Views of a prosthetic socket with complete compliant features incorporated; (**b**) section view of socket exposing the compliant feature and detailed view of compliant feature

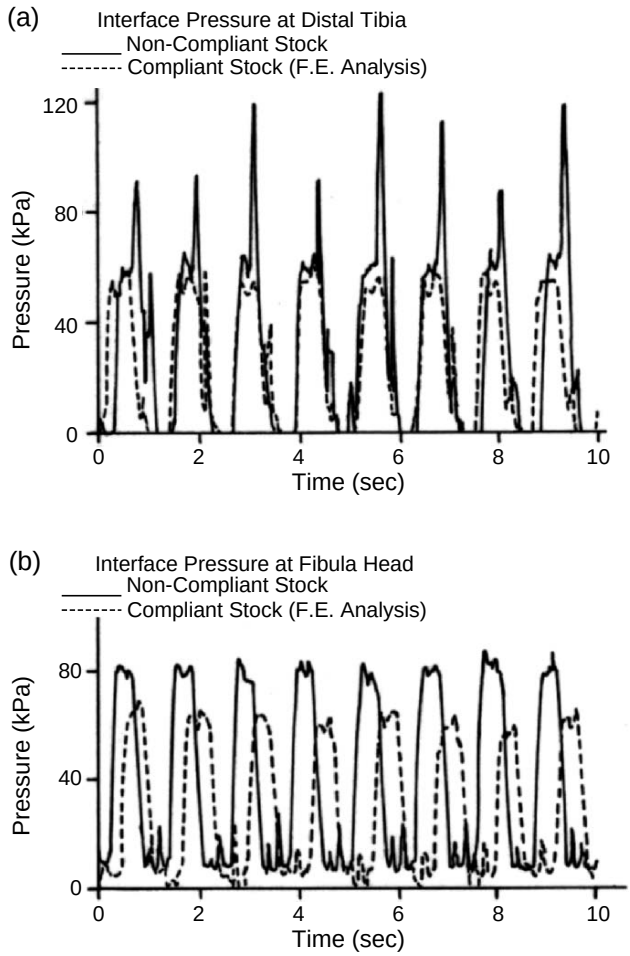

Fig. 6.5. (**a**) Interface contact pressure measured at the distal tibia for both the noncompliant and most compliant sockets; (**b**) interface contact pressures at the fibula head (only the first 10 s of data are shown)

6.5 Shoulder Prosthesis and Reconstruction

Plate 6.2a Reverse Shoulder Reconstruction

The reverse ball and socket design has had early success in restoring shoulder function and relieving pain in patients with a rotator cuff deficient shoulder. Shoulder prostheses which were derived directly from hip replacements, with a constrained ball and socket.

In the reversed design, the forces in the joint are directed through the center of the glenosphere, converting the centrifugal (outward) forces

Plate 6.2. Shoulder Replacements

into centripetal (inward) forces. This in turn creates inherent stability in the reversed design because of the congruency of the humeral socket and glenosphere.

Plate 6.2b Foundation Shoulder System

Developed in conjunction with Richard J. Friedman, MD FRCS (C) and Mark A. Frankle, MD, world-renowned authorities in shoulder reconstruction, the Foundation Shoulder System offers the latest advances in shoulder technology.

The Foundation Shoulder Fracture System's modular trials as in Plate 6.2b establish a stable trial reduction without the use of an external jig simultaneously determining canal size, stem height, and stem version all in one simple step.

Establishing proper head height in relation to the glenoid is critical to the outcome of arthroplasty for fractures of the proximal humerus. A prosthesis placed too high or too low will cause excessive forces on the glenoid and rotator cuff. The challenge has been how to determine the proper height when the final implant is cemented. The Foundation® Shoulder Fracture System provides an easy answer for this challenge.

(C) Modular Trial Instrumentation

Plate 6.2 *Continued*

6.5.1 Features

- Markings are present on the trial bodies so that height can be reproduced independent to the stem sizing.
- Prosthesis holes for suture attachment are available anterior, posterior, medial and lateral.
- Anterior fin allows for anatomical reconstruction of the tuberosities.
- A guide to ensure proper restoration of head to tuberosity height.

6.6 3D Knee and Foundation Total Knee System

6.6.1 A reference is made to Plate 6.3

The result of more than a decade of research. The 3D Knee is the first knee implant specifically engineered to accommodate the important changes in contact, movement and pressure that occur in the knee joint after total knee

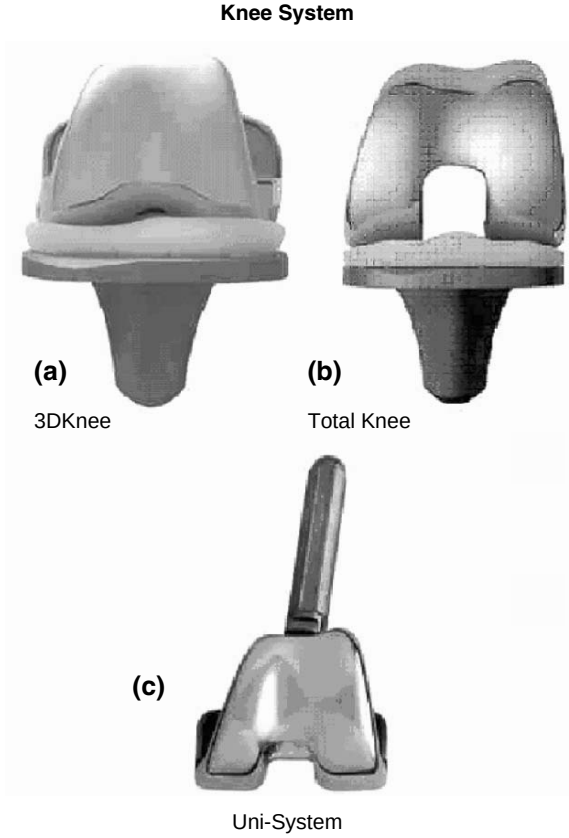

Plate 6.3. Knee System

replacement. Not only is the 3D Knee designed to provide a wider range of motion and greater stability than other knee prostheses, its revolutionary design is also intended to minimise the stresses that have traditionally led to the premature deterioration of most available implants. As a result, the 3D Knee should have longer life expectancy than other devices, making it ideal for younger patients.

Encore® offers a variety of implants for applications in one comprehensive knee system. The knee market is basically divided by the type of procedure the surgeon will perform, based primarily on the surgical indications of each patient. The Foundation® System provides a large array of options for the surgeon. The Foundation® System was designed to replicate normal knee kinematics. The precise simplicity of the Foundation® Knee Instrumentation was designed to provide accurate cuts for reproducible results.

MIKA Encore's Minimally Invasive Knee Arthroplasty Instrumentation allows the surgeon to make an incision that is optimal to the patient. The

system features sleek guides, cut blocks, and handles that encourage a smooth, reproducible surgery for all patients.

6.6.2 Foundation® Modular Revision System

The Foundation® Modular Revision System offers a femoral option and tibial insert which provides a specially designed cam action that engages at 60° of flexion to induce a smooth stable femoral roll-back motion and allow for 130° of flexion. The constrained tibial insert in conjunction with the femur is designed to maximise "in-plane" joint motion while minimizing "out-of-plane" translation and rotation.

Femoral and tibial components in six sizes for right and left:

- Augments can be easily added in the management of bone deficiencies, distal (5 and 10 mm), posterior (5 and 10 mm)
- Mechanical attachment
- No cement required
- Milly-bolt design
- Femoral and Tibial Stem extensions 100 and 150 mm overall lengths
- Tibial Inserts in five thicknesses (11–19 mm)
- Constrained PS Insert up to 25 mm thick
- Multiple patella options available

Unicompartmental knee arthroplasty has proven to be successful alternative to high tibial osteotomy and total knee arthroplasty with proper indications. The EPIK® Uni is minimally invasive (Plate 6.3c). Unicompartmental knee system developed to streamline hemi-knee arthroplasty surgery. Using the latest conservation surgical techniques with the EPIK® system will reduce hospital stay, shorten recovery time, restore normal kinematics, and maximise ROM. In addition, bone stock is preserved to facilitate future conversion to tricompartment replacement as long as conservative operative techniques have been used.

6.6.3 3D Matrix Porous Coating

Encore has chosen an innovative approach to an industry standard for porous coating on their implants. This coating consists of small, 3D (nonspherical) beads. The porous material is either commercially pure titanium or CoCr alloy, depending on the base substrate. The nonspherical shape of the beads provides more points of contact and a much rougher surface area.

The 3D Matrix porous coating is much rougher and aggressive than spherical beads, providing for more bone apposition. In a canine study for bone ingrowth (Data on file at Encore), 3D Matrix porous coating outperformed spherical beads.

The 3D Matrix has a thickness of 0.5 mm (a minimum of tow bead layers), bead size 180–850 microns, and pore size of 250–450 microns. The porosity volume represents 61%. The pore size of 100–500 microns has been shown to be optimal for bone in growth.

Mont MA, Hungerfors DS: Proximally Coated Ingrowth Prosthesis. A Review. ClinArthop 344: 139–149, 1997

6.7 Total Hip System

6.7.1 Revelation Total Hip System

The Revelation Total Hip System designed based on a more complete understanding of hip joint biomechanics and bone morphology (Plate 6.4).

6.7.2 The Ilio-Tibial Band Model

The ilio-tibial band model as presented by Dr. Fetto et al. extends Koch's model by adding the ilio-tibial band as a lateral tension band. As a result, the lateral femur is shown to be under compression rather than tension during

Plate 6.4. Total Hip System

the unilateral stance phase gait. The lateral femur thus becomes a potential base of support for femoral components.

6.7.3 Bone Preservation and Regeneration

By respecting Wolff's law, which states that bone is formed in response to the loading it experiences, the Revelation® femoral component has been shown not only to preserve up to 95% of bone stock in primary surgeries, but to contribute to bone regeneration in revision surgeries with prior bone loss. Because of this feature, the Revelation Total Hip System is suitable for younger, more active patients, in whom implant longevity is particularly important.

6.7.4 Primary Stability

By engaging the lateral femoral cortex as an additional base of support, the Revelation® femoral component prevents stem subsidence and provides secure primary stability, which is a prerequisite for a long-term biological fixation. Compared to a straight stem, the Revelation® stem has been shown to significantly less likely to migrate. In addition, the trapezoidal cross-section of the stem resists rotational forces. Due to its inherent stability, the Revelation stem allows for full postoperative weight bearing.

6.7.5 Subsidence (Stability)

0.32 ± 0.24 mm @ 2 years 0.51 ± 0.31 @ 3 years
(< 0.5 mm @ 2 years and < 1 mm @ 4 years)

6.7.6 Foundation Total Hip System

The Foundation Total Hip System has been developed by enhancing proven design features and utilizing simplified instrumentation, thus providing a state-of-the-art system. The Foundation System offers a range of options to best match the individual patient's needs, all with one standard set of instrumentation. The system offers cemented stems with the 450 and 460 series, porous stems with the 470 and 480 series and a press-fit 440 series stem.

6.7.7 Keystone Revision Hip System

The Keystone® Revision Hip System will allow quick restoration of those challenges facing the surgeon in revision cases. Keystone provides the culmination of design principles for an optimised clinical outcome.

– Providing fit-and-fill in the proximal portion of the femur while independently fitting the distal portion of the femur.

- Matching the Foundation® primary system with reduced medial bodies and distal proximal mismatch.
- Six proximal bodies.
- Eight distal stems at 210 and 250 mm

6.7.8 Proximal Femur Load Transfer

By loading the lateral femoral, the Revelation Hip System reproduces normal physiologic loading patterns, reduces potential for subsidence, and avoids diaphyseal overloading which has been sited as a cause of thigh pain.

6.7.9 Minimised Distal Stem

The gradual change in stiffness of the wedge design is less likely to cause thigh pain. In a study of 297 primary hips of a competitive design. 12% of the patients reported thigh pain at one year follow-up. A direct correlation was found between stem size and thigh pain. In general, thigh pain increased with stem size due to increasing bending stiffness. This creates abnormally high femoral stresses at the distal tip of the component. The Linear hip stem has a more tapered distal stem to decrease this stiffness and reduce the incidence of thigh pain.

6.7.10 Standard and Lateralised Offset Options

The Linear hip stem is offered in two offsets, standard and lateralised. If the hip is unstable with a standard offset, the lateralised version improves soft tissue tension to increase stability. The improved abductor mechanics may also decrease limp.

6.7.11 Proven Design

The Linear hip stem is a titanium flat wedge stem designed for metaphyseal fit. The wedge shape allows the stem to subside to stability and the flat edge provides enhanced rotational stability. Reported results of 145 hips of similar stem design at a mean of ten years followup showed only 1% rate of revision for aseptic loosening.

6.7.12 Linear Total Hip Series

- Ti alloy material.
- Six standard femoral stem sizes.
- Three special sizes.
- Tapered geometry.
- 135° neck angle.

6.7.13 R120 Modular Stem Series

The R120™ and R120PC™ are modular stems with a patented star-shaped mechanism that is designed to give the surgeon a greater ability adjust offset, anteversion and leg length. This allows greater accuracy in correcting biomechanical alignment to ensure minimal joint reaction force and correct stress transfer. The R120 series gives the surgeon intraoperative versatility by offering cemented and cementless options in one instrument system. This implant configuration is proven successful through 20 years of clinical data.

6.7.14 Intraoperative Versatility

The R120 series gives the surgeon intraoperative versatility by offering cemented and cementless options in one instrument system.

6.7.15 R120 System Modular Necks

Modular necks available in 32 mm, 35 mm, and 38 mm lengths, each length offered in both 8 and 12° angles.

6.7.16 3D Macro-Interlock

Three dimensional porous coating allows 3D macro-interlock of bone into the depths of the porous coating down to the substrate.

6.7.17 Foundation Total Hip System: Cemented Options

Enhanced Cement Fixation

- The proximal PMMA Centralisers assure a cement mantle of two millimeters around the entire femoral stem.
- The cobra flange and normalization arches contribute to medial cement compression while improving the resistance to lateral tensile forces.

6.7.18 Three Degree Tapered Geometry

Three degree tapered geometry provides continuous compression to cement mantle.

6.7.19 Distal Stem Tape (Plate 6.4)

The gradual taper of the distal stem geometry allows cement to flow over the stem and reduce the likelihood of air bubbles being introduced in to the implant cement interface. The taper allows thicker cement at distal tip resulting in lower cement stresses.

6.7.20 Cemented Foundation 460 Hip Series

- Forged CoCr material
- Six femoral stem sizes
- Tapered geometry
- Cobra Flange
- Normalization arches
- Proximal textured surfaces
- PMMA proximal cement spacers
- Modular PMMA distal centraliser
- 132° neck angle
- Ceramic head capability
- Size Options: 8, 9, 10.5, 12, 13.5, 15 and 16.5 mm

6.7.21 Cemented Foundation 450 Hip Series

- Forged CoCr material
- Six femoral stem sizes
- Tapered geometry
- Cobra Flange
- 132° neck angle
- Size Options: 9, 10.5, 12, 13.5, 15 and 16.5 mm

6.7.22 Keramos Acetabular System

The Keramos^{TM} Acetabular System utilises alumina ceramic to provide extreme strength, smoothness and wear resistant properties that allow you to meet the needs of younger patients for greater mobility and longevity. Our new acetabular system offers the qualities you demand and the quality of life your patients desire.

6.7.23 Metal/Metal CoCr

The Encore® Metal/Metal CoCr acetabular liners and femoral heads utilise new production technology, which includes removal of large block carbides, resulting in a smooth, groove-free surface.

6.7.24 Superior Surface Quality

A unique process is used to remove large block carbides within the material. The presence of large block carbides can elevate wear-in periods for metal-on-metal bearings.

6.7.25 Homogenous Structure

The removal of block carbides gives the encore metal/metal components a homogenous, fine-grained structure.

6.7.26 Carbide vs. Fine Grain

Removal of block carbides results in favorable wear properties by improving corrosion resistance.

6.7.27 Comparison

In a wear–rate test of metal on metal vs. alumina on polyethylene, the wear of the metal-on-metal articulation was significantly decreased; this reduction was even more substantial when compared to the wear rate of the current standard of metal on polyethylene.

6.7.28 VariGrip (Plate 6.4)

VariGrip technology offers a strong, stable hold for added security for the surgeon and patient alike. Designed like no other fixation product, VariGrip® hooks onto the lamina of the vertebral for a tight, secure grip without involving pedicles or facets. It also allows for additional bone at the lateral graft sites and leaves other structures intact, thereby maximising vertebral strength. Surgeons benefit from superior axial and rotational stability from this low-profile attachment and patients may experience less post-operative pain due to reduced muscle retraction.

6.7.29 Cyclone (Plate 6.4)

Profile

The Cyclone anterior cervical plate is made of industry standard Titanium alloy and offers surgeons an extremely low profile plate (1.9 mm) with both variable and fixed screw options.

Plates

The Cyclone System features a comprehensive offering of plates ranging in length from 14–88 mm in 1–4 level configurations.

Plate Features

- Temporary fixation pin hole.
- Easy one step locking mechanism.
- Excellent graft visualization.
- Cephalad/caudad stabilization spikes.
- Fixed or variable screw hole design.

6.8 Traumatic Injuries and Orthopedic Devices/Hardware (Screws, Plates, Wires, and Pins)

The radiologists add some real value to the examination of traumatic surgeries; however, they are not going to know the history, physical findings surgical findings and post operative course as the orthopaedists does. The orthopedists does a superb job of interpreting plain radiographs on trauma patients, they tend to do less when it comes to other disorders such as metabolic bone disease, infection, neoplasms or arthritis. The radiologists certainly do look closely for these entities. They are likewise on much shaker ground when it comes to understanding the underlying physics, indications and the interpretation of a radio nuclide bone scan, fluoroscopy, ultrasound, CT, and MRI. Hence it must be the radiologists who monitors the imaging work up and suggests the most efficacious and cost-effective follow up in aging studies for each patient. Another important role of the radiologists is the film quality role. The following points should be kept in mind when performing radiographs of the orthopedic fixation hardware:

- Expose a minimum of two orthogonal views of each body part.
- Place the entire limb on the film, including the joint above and the joint below.
- If orthopedic hardware is present, the entire device should be included on the film, preferably with several centimeters of normal bone on either end.
- A slight overexposure may be helpful for looking at metal fixation devices.
- Comparison with old films is mandatory.

Indications for operative fixation:

- Closed methods have failed.
- Closed methods will probably fail.
- Displaced intraarticular fractures.
- Pathological fracture.
- Associated neurovascular injury.
- Polytrauma.
- When it will minimise confinement to bed.
- When it will substantially reduce cost of treatment.

It is hard to say anything intelligent about orthopedic hardware unless one knows the general names and function of the various orthopedic devices. One is not proposing that one learns the specific manufacturer or model number of each device. This is as hard for anyone to keep up with as it is for orthopedists to keep up with the latest MR pulse sequences. However, one would expect to learn the general name and function of each device. Fortunately, this is not too difficult.

6.8.1 Classification of Orthopedic Fixation Devices

- Internal Fixation Devices
  - Screws
  - Plates
  - Wires and pins
  - Intramedullary rods and nails
  - Spinal fixation devices
- External Fixation Devices
  - Fracture fixation
    - radius
    - tibia
    - pelvis
  - Bone lengthening
    - Illizarov device

6.8.2 Screws

One of the current tenets of orthopedic fixation is that bone heals better if the fracture fragments are pressed firmly together. Many orthopedic devices are designed to do just that, we well as their primary function of stabilising the fracture in anatomic alignment. Fracture compression increases the contact area across the fracture and increases stability of the fracture. It also decreases the fracture gap and decreases stress on the orthopedic implant. This compression can be static, where the compression is produced by the fixation device alone, or dynamic, where body weight or muscle forces are used to produce additional compression.

Screws are one of the most ubiquitous hardware devices. They may be used by themselves to provide fixation or in conjunction with other devices. Any screw that is used to achieve interfragmental compression is termed lag screw. Such screws do not protect fractures from bending, rotation or axial loading forces, and other devices should be used to provide these functions.

The two most common types of screws are cortical and cancellous screws, as shown (Fig. 6.6):

Cortical screws tend to have fine threads all along their shaft, and are designed to anchor in cortical bone. Cancellous screws tend to have coarser

Fig. 6.6. Cortical and Cancellous Screws

Fig. 6.7. Cannulated Screws

threads, and usually have a smooth, unthreaded portion, which allows it to act as a lag screw. These coarser threads are designed to anchor in the softer medullary bone.

Another commonly used screw is the cannulated screw, so called because of its hollow shaft. Although these screws have somewhat diminished pull-out strength compared to conventional screws, cannulated screws have many advantages over other screws, especially the precision with which they can be placed. To place these screws, the orthopedist first drills a small Kirschner wire across the area of interest under C-arm fluoroscopic control. These "K" wires can be placed and replaced with minimal trauma to the bone until they are in optimal position. The cannulated screw (Fig. 6.7) is then placed over the wire and slid down to the bone surface. A special driving tool then allows the screw to be driven into the bone along the shaft of the K-wire, in a manner very similar to the way radiologists pass angiographic catheters over guide wires using the Seldinger technique. The K-wire is then withdrawn. One major complication of these screws is perforation of the articular surface when these screws are placed into a bone with their tips close to the subchondral bone. If an orthopedist is concerned about this possibility during surgery, contrast material may be injected through the hollow center of the screw in question–spillage into the joint cavity under fluoroscopy will be inequivocal evidence of perforation.

Certain specialty screws are also often seen. The Herbert screw is designed for use in fractures of small articular bones such as the carpals. It is cannulated and threaded at both ends. These threads run in the same direction, but the proximal portion has a wider pitch to its thread. Thus, when the proximal threads engage in the bone, they tend to move through the bone faster than the treads at the distal end, causing the two ends of the bone to compress together. This screw is used where a standard screw would impinge on adjacent tissues, such as in the treatment of scaphoid or osteoarticular fractures.

Orthopaedists at our institution are not using the Acutrak screw for the treatment of most scaphoid fractures. This screw, like the Herbert screw, is cannulated. It is also headless, which allows it to be implanted below the surface of the bone. It uses the same concept of variable thread pitch as Herbert screw, but unlike the Herbert screw, is fully threaded. This feature may improve internal holding power, as well as allow a fracture or osteotomy site to lie anywhere along the length of the screw.

Another specialty screw occasionally seen is the interference screw. This screw is sometimes used in the repair of the anterior cruciate ligament (ACL). In this type of repair, the surgeon employs a cadaveric allograft ligament which has a block of bone still attached at both ends. A tunnel is drilled through the distal femur and the screws are placed alongside the bone blocks so that they tightly wedge them into the side of the tunnel and prevent them from moving.

One final word on screws: in order to use them, one have to make a screw hole in the bone or in the hardware that used them. This is of note because screw holes weaken whatever material they pass through. I have read biomechanical estimates that one screw hole passing through both cortices of a femoral shaft will weaken that femur by 90% to some type of stress! There are several ramifications to this for the orthopedist and radiologist. First, since these holes weaken bones and orthopedic hardware, we should look closely at these areas on the films since the bones and metal will tend to fracture at these sites. Second, orthopedic hardware is generally removed as soon as possible so that these holes can fill with new bone formation and bring the bone strength back up to normal.

Washers are generally used in two situations. They are used to distribute the stresses under a screw head so as to prevent thin cortical bone from splitting.

Serrated washers are used to affix avulsed ligaments, small avulsion fractures or comminuted fractures to the remainder of the bone.

6.8.3 Plates

A references is made to Plates from Plate 6.5 to Plate 6.12.

Plates come in several flavors, and are named for their function. In general, there are compression, neutralization and buttress plates.

Compression plates are used for fractures that are stable in compression. They may be used in combination with lag screw, and they may provide dynamic compression when used on the tension side of bone. The dynamic compression plate is one of the most common types of plates, and can be recognised by its special oval screw holes. These holes have a special beveled floor to them with an inclined surface. If desired, this inclined surface can be used to pull the ends of the bone together as the screws are tightened.

A new variety of dynamic compression plate is currently undergoing trials at UW. This variant is called a low contact dynamic compression plate

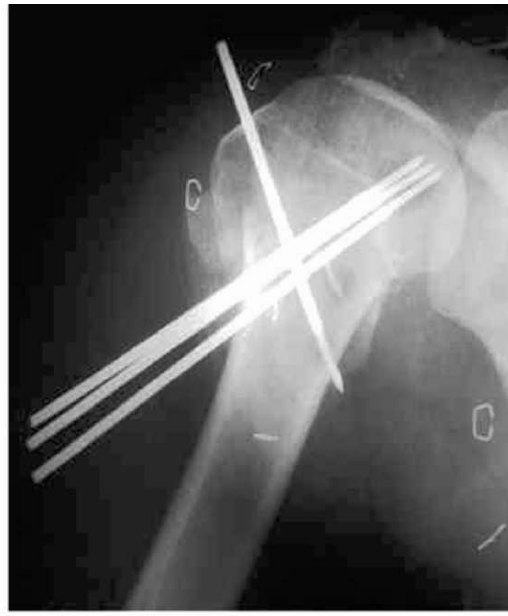

Comminuted fracture of the surgical neck of the humerus bridged by four percutaneous

Olecranon fracture bridged by cancellous

Plate 6.5.

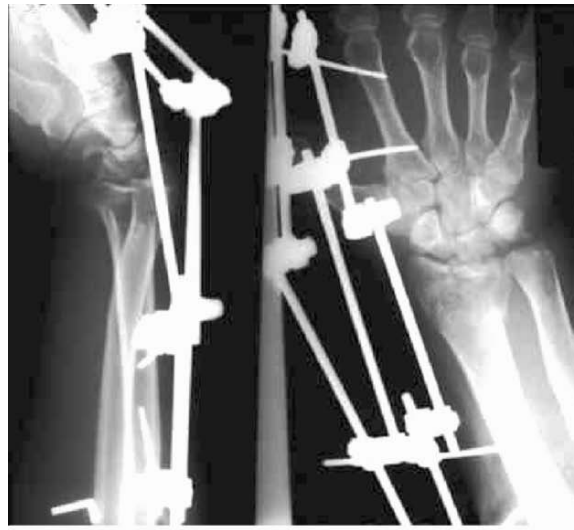

External fixator bridging an unstable
Radial fracture

Kirschner wires used to stabilizer
A distal radial fracture

Plate 6.5. *Continued*

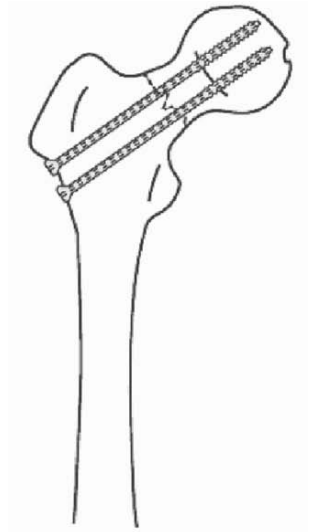

Parallel screw fixation of a femoral neck Fracture with cannulated screw

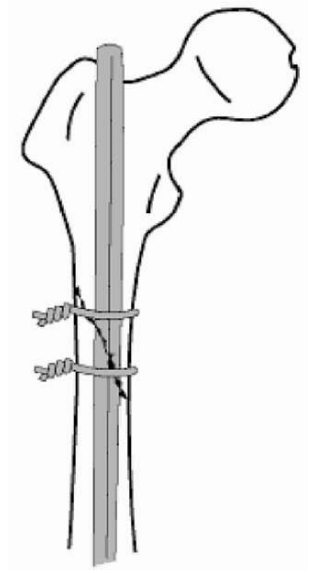

Femoral fracture bridged by an Intramedullary nail and two cerclage wires

Plate 6.6.

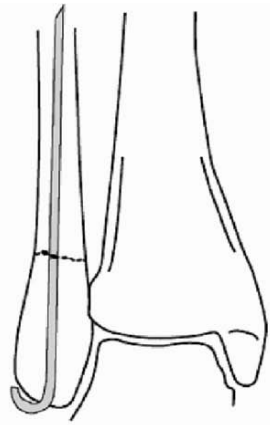

Rush rod bridging a distal fibular Fracture

Knowles ins bridging the right physeal Line in patient with a slipped femoral Capital epiphysis

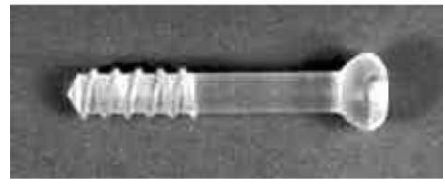

The medial malleolar fracture above is held together by one of these screws, made of a radiolucent polycarbonate material, which is designed to eventually be absorbed by the body—this type of screw is known locally as “stealth hardware”

Plate 6.6. *Continued*

A comminuted intertrochanteric fracture of the proximal left femur bridged by a dynamic hip screw

Low contact dynamic compression(LCDC) plate bridging a humeral shaft fracture — note the undercutting between each screw hole also noted is a humeral fracture through the distalmost screw hole

Plate 6.7.

Blade plate bridging a distal femoral fracture note that the distalmost screw is broken, and the plate itself is broken just above the fracture line at a screw hole—a channel is also noted distal to the current blade plate secondary to a previous failed blade plate

Plate 6.7. *Continued*

(LCDC plate). This plate is distinguished from the conventional DCP by the way it is undercut under each screw hole and between adjacent screw holes. The rationale for this design is as follows. Whenever one clamps a plate down against the surface of a bone, one markedly diminishes the periosteal blood supply to that area. Theoretically, one would expect this to slow healing of the fracture beneath that place. The undercutting of the plate decreases the amount of contact that the plate makes with the bone surface, and hopefully will increase the periosteal blood supply and, it is hoped, fracture healing as well.

Another type of plate seen commonly at UW is the reconstruction plate, which is widely used for the repair of the pelvic and calcaneal fractures. This plate is fairly malleable, and can be readily shaped and trimmed to length for support of fractures through complex bony surfaces. These are also occasionally used to posterior fusion of the cervical spine.

Neutralization plates are designed to protect fracture surfaces from normal bending, rotation and axial loading forces. They are often used in combination with lag screws.

Buttress plate bridging a humeral neck Fracture–note that 2 of 3 most proximal Screws have backed out (they are loose) and That 2 of tem may penetrate into the joint Space

Dynamic compression plate (DCP) bridging a fibular fracture–the arrow is pointing to a syndesmosis screw which is bridging the tibiofibular syndesmosis whose ligaments have been torn during the injury– also noted is a medial malleolar fracture bridged by a screw channel, but apparently little else. What is holding the parts of this fracture together

Plate 6.8.

Reconstruction plate

Plate 6.8. *Continued*

Ender nails bridging a femoral shaft fracture
with subsequent callus formation

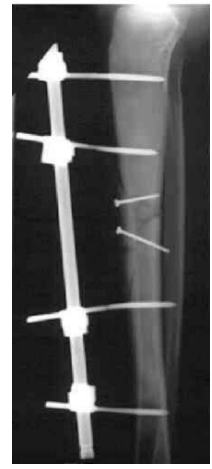

External fixator bridging a tibial fracture

Plate 6.9.

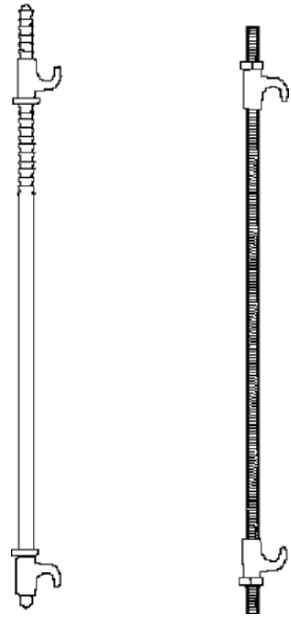

Harrington distraction rod
and compression rod

Plate 6.9. *Continued*

Buttress plates are used to support bone that is unstable in compression or axial loading. These plates are often used in the distal radius and tibial plateau to hold impacted and depressed fragments in position once they have been elevated. Yet another type of plate commonly seen on postoperative films is the blade plate. This plate is usually shaped at an oblique or right angle and is designed to be used with subtrochanteric femoral fractures or supracondylar fractures of the femur. It is also occasionally used to bridge a femoral osteotomy. One arm of this device has a chisel-shaped end that is driven into bone, bridging the fracture. The other arm is used as a side plate and anchored to the bone with multiple screws.

There are a variety of devices used to treat femoral fractures. The blade plate above and the Jewett nail below are not used so commonly these days but patients still walk into orthopedic clinic wearing these devices every day. The most common device used nowadays is the dynamic hip screw, also shown below. Its main design goals are to resist angular deformation while permitting early fracture impaction by allowing shortening along the axis of the lag screw. This device is specifically designed to treat intertrochanteric fractures, but is occasionally used to treat subtrochanteric fractures as well. Like the blade plate, it has a side plate that is attached to the distal femur with several

Segmental fracture of the tibia, bridged by
an intramedullary nail with a proxma
interlocking screw–the distal interlocking
screws have been removed

Patient with thoracic scoliosis, convex
To the right, bridged by a Harrington
Rod and bone graft along the concave side of the spine

Plate 6.10.

The images above are anteroposterior (AP) and lateral views of Bilateral posterior sinal rods bridgingL4, and L5 and SI. This Patient underwent spinal fusion following a laminectomy done For spinal stenosis. The small metal cage seen in the L5-SI disk Space contains bone graft material which will hopefully promote Osseous fusion at this site

Plate 6.11.

cortical screws. Rather than a blade, this plate has a hollow metal barrel through which a large lag screw is placed. This large lag screw is placed so that it bridges the femoral fracture. Ideally, this lag screw should go right down the center of the femoral neck on every radiographic view, and its tip should be in the subchondral bone of the femoral head. The hollow barrel of the side plate holds the lag screw, and hence the femoral neck and head a an anatomic angle for healing. It also allows the lag screw to slide distally as the ends of the fracture impact and the fracture fragments move closer together. When followed over time, is quite common to see evidence of this impaction as the lag screw telescopes down into the barrel of the side plate. The average amount of impaction seen with these devices is about 7 mm.

These devices can fail just like any other device. The cortical screws holding the side plate to the bone may come loose. The side plate may fracture at a

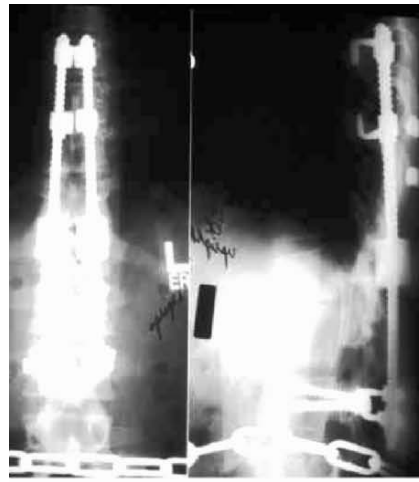

Bilateral Edwards rods bridging a spinal facture

Harrington and Edwards rods have been largely superseded by other newer devices. The most common spinal fixator that I see these days is some form of posterior spinal rod. These rods are usually used in pairs, and are attached to pedicular screws which are anchored in multiple vertebral bodied above and below the site of treatment

Zickel nail bridging a subtrochanteric fracture

Plate 6.12.

screw hole. The lag screw may perforate the articular surface of the femur. These complications and many more await the eagle-eyed radiologist.

Dynamic hip screws (DHS) are a popular device used to bridge fractures of the well-vascularized intertrochanteric area. However, when the fracture occurs a bit more proximally in the femoral neck, parallel screw fixation is often used instead. The rationale here is that the parallel screws will cause less trauma to the tenuously supplied proximal head and neck fragment than a larger screw such as the DHS. If the screws are placed parallel to each other, they can allow the fragments of bone to impact together, much as a DHS will, Knowles pins (shown later) were once commonly used for this purpose, although other types of screws are more commonly used today.

Another type of pin used currently at Harborview is the percutaneous pin. They are commonly used to treat humeral neck fractures. These pins have a self-threading screw tip and are placed under C-arm fluoroscopy.

6.8.4 Wires

A variety of wires are used by orthopedic surgeons. One common type is the cerclage wire, in which the wire is placed around the circumference of the bone to pull various fracture fragments together. In the example below, two cerclage wires are used in conjunction with a intramedullary nail to provide support for the comminuted fragments above the transverse fracture.

Yet another type of wiring seen in orthopedic surgery is called tension band wiring. This type of wiring may be placed either by itself, as shown in the patellar fracture below, or in conjunction with a screw or Kirschner wire. These tension band wires perform a sort of "biomechanical judo," in that they take the normal muscular pull that is trying to pull the fracture fragments apart, and use it in a clever way to force the bony fragments together in compression. In the example below, one can see that the actual location of the tension band wire is important. If the wire is placed too far posteriorly (left drawing), the muscular pull on the wire will cause the fracture to gape open anteriorly (distraction). When the wires are placed far enough anteriorly (right drawing), the muscular pull now causes the patellar fragments to be pushed firmly together in compression, patellar fracture bridged by tension band wire.

This same sort of biomechanical judo is employed when the tension band wire is used with a wire or screw. In the example below, a fracture is seen through the olecranon process. In a situation like this, the triceps muscle group will exert a large force tending to pull the proximal fragment far away from the rest of the ulna. Even when the fracture has been bridged by one or more screws, there is a tendency for these screws to be pulled out by the triceps. The addition of a tension band wire as shown below will convert some of the triceps traction into compression of the ends of the bone together and prevent the screw from pulling out.

As I have already alluded, the Kirscher or "K" wires are a very handy device in the hands of the orthopedist. Besides their usage with cannulated screws, they are used in many other ways to help reduce and stabilize fractures. A K-wire is essentially an unthreaded segment of extruded wire which is drilled into bone like a drill bit. The major advantage of a K-wire is that it is very small and relatively noninvasive as hardware goes. It can be placed through an articular surface or even across an open physeal plate without injury. K-wires can be used for either temporary or final stabilization. They can be placed between bones as shown below, or they can be used as an intramedullary device to bridge a fracture of a small tubular bone. They are commonly used to help piece all of the fragments of a comminuted fracture prior to placement of the final fixation device, especially with an intraarticular fracture.

6.8.5 Rods and Nails

A large variety or devices are placed down the intramedullary canal of bones, ranging from Kirschner wires up to large femoral nails. One can generally classify these devices by whether intramedullary reaming is necessary prior to placement of the device. With the first nails placed down the femoral shaft, the medullary space first had to be reamed out so that the large nail would not shatter the bone as it was hammered down the shaft. However, reaming is an invasive procedure, and can compromise the already tenuous blood supply of the medullary space. Reaming can also lead to thermal osteonecrosis, especially if the medullary canal is small, a tourniquet is used during reaming, fat emboli to the lungs are possible. For these reasons, a variety of unreamed devices have been developed. The rush rod, shown below, has a chisel-like tip, and is commonly used for fibular shaft fractures, and occasionally in other tubular bones as well.

Another type of unreamed nail is the Ender nail. These nails also have a chisel-like end. These nails are usually used three or four at a time, and pushed through a cortical hole up or down the shaft of the bone and across the fracture under fluoroscopic control.

The odds-on favorite nowadays for fixation of fractures of the femoral or tibial shaft is a reamed or undreamed nail like the ones shown below. These nails permit early weight-bearing and can be placed with closed technique, which avoids damage to soft tissue and to the periosteal and muscular blood supply. If the fracture is transverse and otherwise uncomplicated (not comminuted, rotated or too near the end of the bone), the nail may be placed by itself. However, interlocking screws are very commonly added both proximally and distally to provide stability in cases of comminution, and to prevent shortening of the bone or rotation of the fracture fragments. When these screws are used, the nail is commonly referred to as an "interlocking" nail.

Subtrochanteric fractures are a particularly difficult type of fracture to treat, and they behave very differently from a garden variety intertrochanteric

fracture. In the latter fracture type, a dynamic hip screw (DHS) can be used to merely provide angular support. Longitudinal support by the DHS is not as important in this fracture type, since the ends of the bone tend to impact against each other in a stable manner. Subtrochanteric fractures, on the other hand, put a huge stress on a DHS, especially along the side plate. For this reason, special nails such as the Zickel nail shown below and the gamma nail have been developed. These devices are much stronger devices than the DHS, and offer a much shorter moment arm for rotational forces to act upon than the DHS. On the minus side, these nails are also more invasive.

6.8.6 Spinal Fixation Devices

The prototypical spinal fixation device is the venerable Harrington rod. These tend to come in two flavors: distraction and compression. The hooks are designed to be placed under the lamina or transverse processes, and the device is either extended or compressed to the desired position. Sometimes both types of rods will be used in the same spine.

6.8.7 External Fixation

All things being equal, orthopedists generally prefer to treat fractures in a closed fashion. Failing that, they would prefer to treat them with internal fixation. However, sometimes there are extenuating circumstances that preclude the use of internal fixation. External fixators can be very helpful in these circumstances.

6.8.8 Indications for External Fixation

- Open fracture with massive soft tissue damage.
- To provide instant fixation in cases of polytrauma.
- May be the only way to treat fractures with deficient bone stock or infection (external fixation allows easy access to wounds).

The weak link in the external fixation system are the threaded pins that are anchored in the bone. These pins should pass through the cortex on either side of the medullary space, and only a few millimeters of the pin tip should ideally protrude through the distal cortex. The usual complications of this fixation system are loosening or infection (or both) of the pins. Lucency developing about a pin as it travels through the cortex is evident of loosening of that pin. Infection is a much harder diagnosis to make radiographically. Long before signs of radiographic infection develop, the orthopedist will make the diagnosis by seeing pus oozing up along the pins as they exit the skin. Even the presence of periosteal new bone formation about the pin tracts is unhelpful, since these

drilled holes are after all fractures of a sort, and fractures do produce callus, even without infection.

There is one late finding which is said to be pathognomonic of pin tract infection. This has been termed the *ring sequestrum sign*, although the sequester thus formed actually are shaped like cylinders, rather than rings. The appearance of this finding is due to the particular geometry of a pin and pin tract, which are cylindrical in shape. As a pin tract becomes infected, the bone immediately adjacent to the pin becomes infected first, and a certain amount of it dies. The viable bone adjacent to this infected dead bone then becomes hyperemic and becomes relatively osteopenic. The infected dead bone remains at its original density. Once the pin has been removed, if one looks directly down the pin tract with a radiograph, this cylinder of dead bone looks like a "ring." Occasionally, such a cylinder will be dense enough to also be seen when viewed at 90° to the pin tract, and it presents as two parallel dense lines surrounded by lucent zones.

6.9 A Device for Assessment of Hand and Wrist Coronal Plane Strength

Diagnostic and rehabilitative assessments of hand function commonly omit measurement of twisting strength even though many activities of daily living require turning handles, lids and object of many sizes. A simple device to quantify twisting strength was designed and constructed to establish normative data and test hypotheses about hand function. The instrument is easy to use and includes an electronic torsion load cell and disks of several sizes. Tests were conducted on the dominant and nondominant hand of 64 normal subject and 13 arthritic patients with arthritis of the thumb carpometacarpal joint. Hands were tested with disks ranging in diameter from 2.5 to 12.5 cm. A three-way repeated measures analysis showed that gender ($p < 0.001$). Handedness ($p < 0.001$) and disk size ($p < 0.001$) hand significant effects. There was no difference between radial and ulnar deviation strengths ($p < 0.365$). The arthritic group had significantly reduced strength ($p < 0.02$). Nine subjects were tested twice, with one day between tests: no differences occurred between the first and second testing ($= 0.930$). The ability to distinguish the test groups with reproducible results proves that the device fulfills all basis requirements: continued testing and development are warranted.

6.9.1 Methods

Description of the Instruments

A scientific device was designed and constructed (Fig. 6.8). A custom-fitted, flanged aluminum shaft was bolted to a torques-sensing load cell (17 N m maximum, model TRT50, Transducer Techniques, Ins., Temecula, CA) and

Mark Carl Miller
Allegheny General Hospital, Pittsburg, PA 15212
University of Pittsburg, Pittsburg, PA 15261

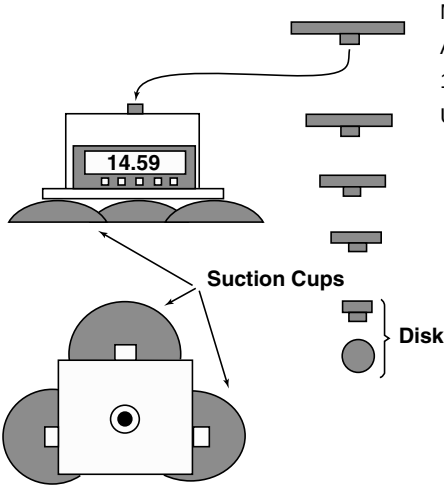

Fig. 6.8. The scientific version of the device with the five disks

the load cell was rigidly fixed to a stiff platform fitted with suction cups for anchoring. A modified conditioning amplifier was mounted with the load cell on the platform. Disks of 8 mm thickness and diameters of 2.5, 5, 7.5, 10 and 12.5 cm were fabricated from plastic, the edges were rounded and smoothed and each disk was rubber coated. Each disk could be firmly fixed to the load cell shaft by a simple key.

Functional testing was accomplished by gripping and simultaneously twisting a disk while the device was fixed to a surface. The meter recorded the applied torque and the peak value was displayed. The device was able to test both maximal and sustained voluntary isometric strength and could record torques with radial or ulnar deviation. With the suction cups attached to a wall, supination–pronation strength was also tested, although only the radial–ulnar deviation results are presented here.

6.9.2 Results

Figures 6.9 and 6.10 show the results for the normal population grouped by dominant and nondominant hand. The independent variable of gender was statistically significant ($p = 0.005$). Two repeated measures were statistically significant: hand dominance ($p < 0.001$) and disk size ($p < 0.001$); radial and unlar deviation strength were not statistically different ($p = 0.365$). The post-hoc comparison of disk size showed that each size proved to be different from all other ($p < 0.001$) except disk diameters of 10 and 12.5 cm ($p = 0.059$).

Figure 6.11 shows all normal subjects compared to all subjects diagnosed with thumb carpometacarpal arthritis. The independent variable of the

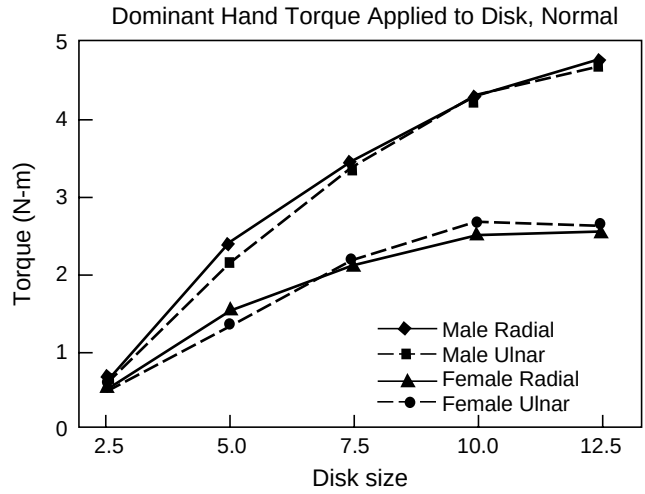

Fig. 6.9. Torque applied by normal male ($n = 18$) and female ($n = 46$) subjected to the disks in ulnar and radial deviation using the dominant hand

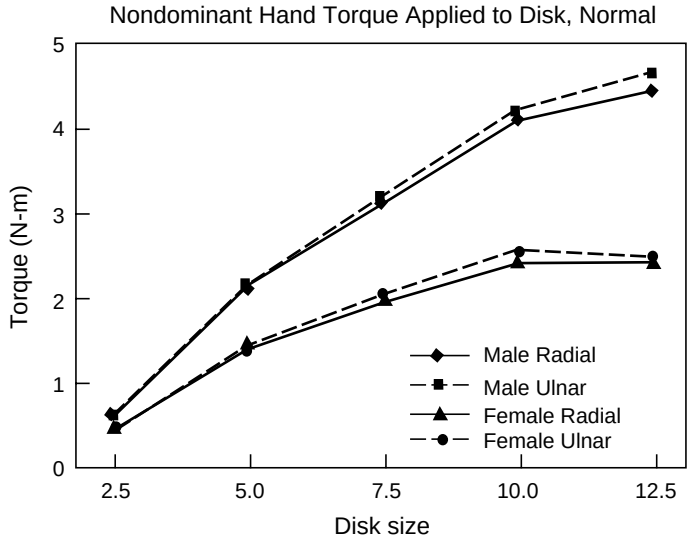

Fig. 6.10. Torque applied by normal male ($n = 18$) and female ($n = 46$) subjected to the disks in ulnar and radial deviation using the nondominant hand

subject type was statistically significant in the repeated measure analysis ($p < 0.01$).

The test–retest comparison found no statistical difference between the first day and the second day results ($p = 0.930$).

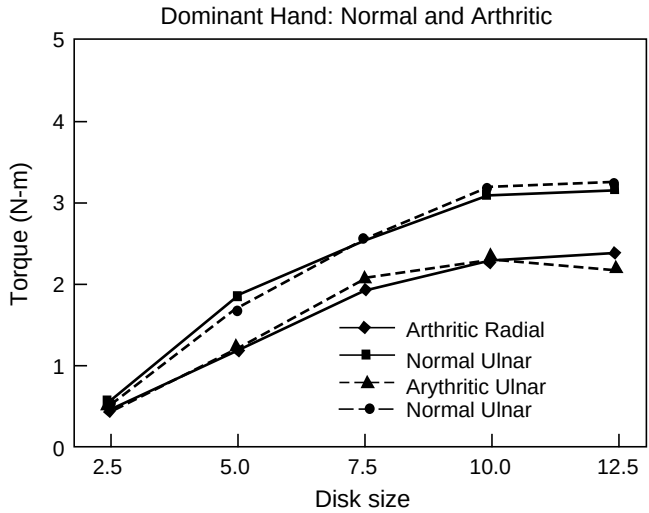

Fig. 6.11. Torque applied by normal subjects ($n = 64$) and arthritic patients ($n = 13$) in ulnar and radial deviation using the dominant hand

6.10 Cranial Stabilization and Retractor Systems

Equipments have been devised and manufactured by the pro med instruments GmbH under DORO System. Adjustable base Units, Skull Clamp, Skull Pins, Swivel Adapter, Ball Pivot Adapter and Retractor System for increased stability for the benefit of the patients. The details are given in Plates 6.13–6.16.

6.10.1 DORO Adjustable base Unit

- Easy and stable mounting to all standard operating tables.
- Newly designed base handle assembly.
- Improved clamping function for increased stability.
- Prevents inadvertent opening of the mechanical system during surgery. Flexibly adjustable joints, particularly for lateral fixation of patient's head.
- Double clamping function allows simultaneous fixation of the lateral and vertical positions.
- Particularly suitable for lateral positioning due to longer table rod.
- A crossbar adaptor (item no. 3007-00) can be connected to the side rails of standard operating tables for fixation in the sitting position.
- Isolation prevents stray currents between operating table and Base Unit.

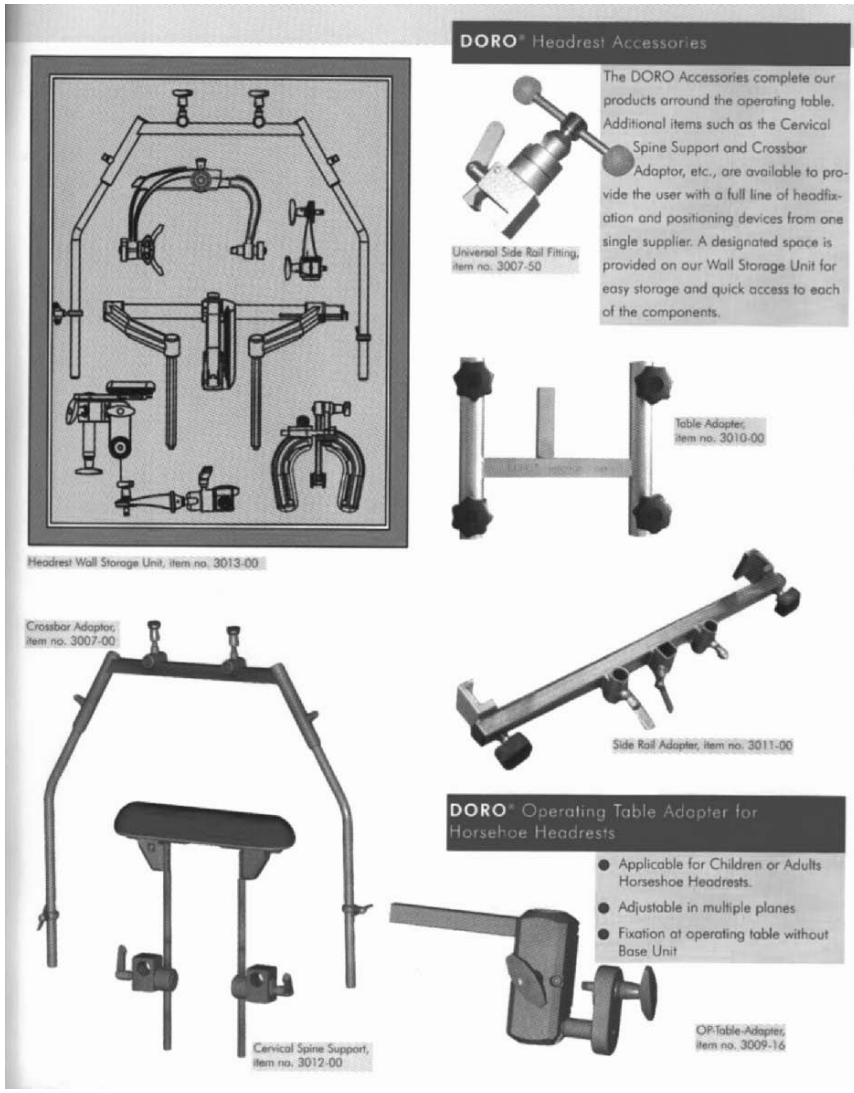

Plate 6.13.

6.10.2 DORO Skull Clamp

- Suitable for children and adults.
- New mechanical design of the skull pin holder and the clamp base ensures improved rigid skull fixation.
- Stable, high-precision three-point fixation of the head during surgery.
- Fixation of patient in prone, supine, lateral and sitting position.
- Particularly suitable for applications requiring maximum precision.

Plate 6.14.

- Head support (item no. 3020-03). Supports the head in addition to the three-point skull clamp fixation. Suitable for application with all standard models.
- Available with elastic head ring (item no. 3020-61), twin elastic pad, (item no. 3020-54) or a skull pin holder.

6.10.3 DORO Skull Pins

- Reusable skull pins are available in two versions; for children (item no 3004-00) and for adults (item no 3005-00) with three Skull Pins per pack.
- Sterile, disposable Skull Pins, 36 pins per pack (item no. 3006-00).

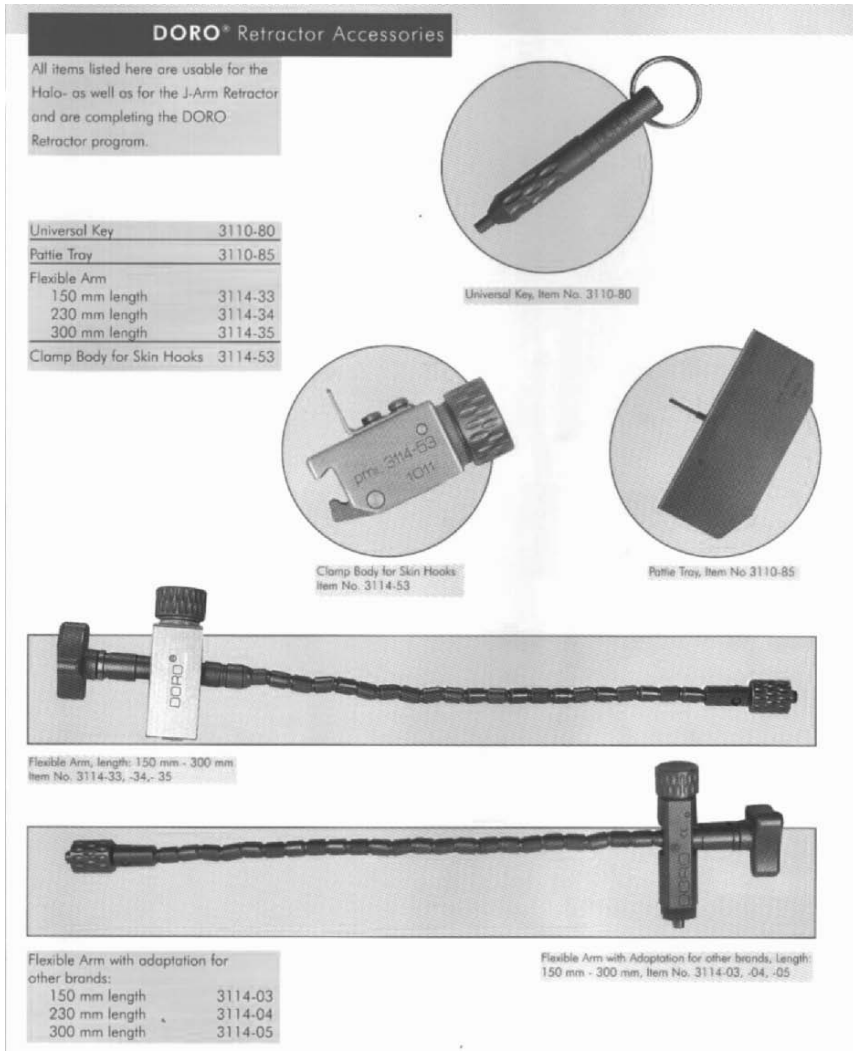

Plate 6.15.

6.10.4 DORO Swivel Adaptor

- Connects the skull clamp to the base unit.
- 360° rotation.
- Sturdy, advanced design.

6.10.5 DORO Ball Pivot Adaptor

- Connects the skull clamp to the base unit.
- 360° freedom of rotation.
- Horizontal inclination up to 90°.
- Sturdy, advanced design.

Also available in radiolucent!
Cranial Stabilization
Easy and stable mounting to all standard operating tables.
Improved clamping function for increased stability.
Prevents inadvertent opening of the mechanical system during surgery.
Rapid mounting and dismantling before, during and after surgery. Flexibly adjustable joints improve positioning, particularly for lateral fixation of patient's head.
Double clamping function allows for simultaneous fixation of the lateral and vertical positions.
For further information please ask for our brochure "DORO Cranial Stabilization"

Plate 6.16.

6.10.6 Multipurpose Skull Clamp for Children Complete

3020-00

MP-skull clamp	3020-50
Head support	3020-03
Pin holder	3020-01
Pin holder, adjustable	3020-62
Reusable skull pins (2 Pack)	3004-00
Gel head ring 90 mm With base (3 packs)	3020-61
Adjustment key	3020-65

Additional accessories for adults

Pin holder	3020-56
Single pin holder	3020-55
Gel head ring 140 mm	3020-63
Reusable skull pins (3 packs)	3005-00

The head support is a useful accessory for supporting and fixating the patient's head in skull clamps with three point fixation. The advantages of this additional support element comprise:

- Adjustable in all planes for optimum fixation.
- Modular system with replaceable pin holder and elastic pads.
- Safe positioning of patient's head before, during and after surgery.
- No holding of the patient's head required during fixating and opening the skull clamp.
- Increased safety, for example in operations involving the skull base or patients with bone defects. Can also be used for third-party systems.
- Noninvasive head support.
- Protects the head, face, neck and ears during all types of surgery and is suitable for use in many surgical procedures.
- Gel pads perfectly match all head shapes.
- Gel head rings, open (diameter; 90, 140 and 200 mm).
- Gel head rings, closed (diameter: 90, 140 and 200 mm).
- Gel head rest (Adults, Children), rectangular.

7

The Engineering Analysis of Medical Case Studies

7.1 Femur with Hip Endoprosthesis

A reference is made to selected X-rays given in Plates 7.1–7.3. The femur is the largest and strongest bone in the body, and also one of the more difficult to break. However, in frontal automobile collisions, the impact loading on the femur can be sufficient to induce a fracture. The most common surgical procedure is to insert proximally, an intramedullary rod (IMR) through the femoral shaft, that is secured by interlocking screws inserted both distal and proximal to the break. Though healing times vary, nearly all patients recover well from their surgery and are able to return to normal activity with little or no residual pain or discomfort. Those who do suffer from consequent side-effects can elect to have the IMR removed. This surgery is commonly practiced, and is deemed safe and is often the best choice for patients. However, because of the extensive surgery required for IMR removal, many surgeons recommend the patient leave the IMR in for life. Research is being conducted currently to examine the advantages and disadvantages of removing the IMR.

Prior to the analysis leading to the fracture and collapse, it is essential that hip implants need to be discussed in advance. This approach will make the researcher familiar with the problems associated with typical positioning and direction of fracture and how it reflects on the hip implant, (McCarthy 2002 (Google)) organized substance on fibrous dysplasias while referring to the following reference:

7.1.1 Fibrous Dysplasia

Fibrous dysplasia is a benign skeletal developmental anomaly of the mesenchymal precursor of born in which osteoblasts fail to properly differentiate and mature. Seventy-five percentage of cases present before the age of 30. Two forms of the disease are classically described: polyostotic (20–30%), monostotic (70–80%) and craniofacial (10–15% of monostotic and 50% of polyostotic).

(a) Two fractures at the upper part

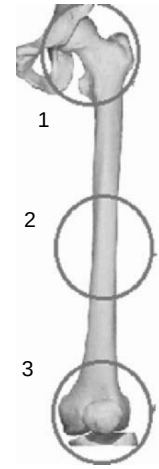

(b) Three zones of fracture for a full length

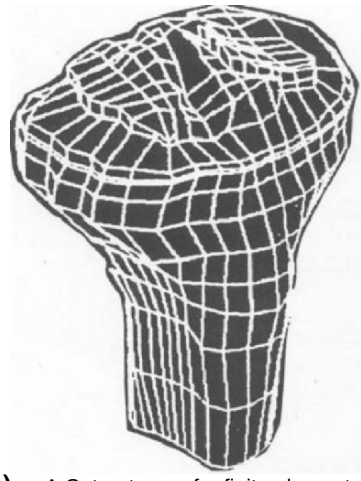

(c) A Cut-out zone for finite element analysis (three major areas)

Plate 7.1. Common fracture location

The craniofacial form is also knows as *Leontiasis ossea*. Common loci of involvement include the frontal, sphenoid, maxillary, and ethmoid bones. Patients are often asymptomatic but asymmetry and deformity of the head and face lead to a variety of neurologic complications. Distortion of a particular bone may lead to displacement of any adjacent cranial nerve, brain parenchyma, or organ resulting in corresponding cranial nerve or neurologic deficits (blindness, tinnitus, hearing loss, vestibular dysfunction, insomnia).

Plate 7.2. Comminuted femur fracture

Plate 7.3. Transient osteoporosis of the hip

An unusual but important association is the occasional marked hypervascularity of fibrous dysplasia in the skull. Recurrent hemorrhage has been a well-documented complication.

7.1.2 Comminuted Femur Fracture

A reference is made to Plate 7.2 which shows an X-ray for the fractures of femoral neck.

The review was prepared by Kevin F. McCarthy
Affiliation: National Capital Consortium
Peer Review/Approval: Philip A Dinauer
Affiliation: Walter Reed Army Medical Center

Fractures of the femoral neck and intertrochanteric fractures are most common in elderly women who have anything from minor twisting motion of the leg to high impact trauma. The risk factors, besides trauma, include osteoporosis, malnutrition, decreased physical activity, impaired vision, neurologic disease, poor balance, altered reflexes, and muscle atrophy. Patients with intratrochanteric fractures are slightly older and have higher morbidity and morality rates than those with femoral neck fractures. Avascular necrosis of the femoral head is very rare in cases on intertrochanteric and subtrochanteric fractures as opposed to the high rate in femoral neck fractures as the more distal fractures have less compromise to the lateral epiphyseal artery than femoral neck fractures.

7.1.3 Transient Osteoporosis of the Hip

The text is prepared and reviewed by the following:
Prepared by: Glenn Richard
Affiliation: National Naval Medical Center Bethesda
Peer Review/Approval: Donal J Flemming
Affiliation: National Naval Medical Center Bethesda
A reference is made for which an extract has been prepared:

Transient osteoporosis of the hip is a rare entity that may occur in the third trimester of pregnancy. Clinical symptoms include antalgic gait, reduced range of motion, and joint pain. Curiously, the left side is nearly always the involved side. Radiographs demonstrate osteoporosis in the femoral head that spares the acetabulum.

No definitive cause has been identified, although possible factors such as vitamin D, calcium deficiencies and secondary hyperparathyroidism have been suggested. Additionally, factors affecting pregnant women, such as endocrine alterations and local compression of vessels or nerves by the enlarging fetus, have been implicated, yet less likely as the condition also occurs in nonpregnant women and in men.

7.1.4 Case Study – Engineering Analysis

A Femur With Hip Endoprosthesis

The hip is the largest load-bearing joint in the body. The hip joint is located where the thigh bone (femur) meets the pelvic bone. It is a "ball and socket" joint, when the upper end of the femur is formed into a round ball (the "head" of the femur) and a cavity in the pelvic bone forms the socket (acetabulum). The ball is normally held in the socket by strong ligaments that form a complete sleeve around the joint (the joint capsule). The capsule has a delicate lining (the synovium). The head of the femur is covered with a layer of smooth cartilage, which is a fairly soft, white substance about 3 mm thick. The socket is also lined with cartilage (also about 3 mm thick). The cartilage cushions the joint, and allows the bones to move against one another with very little friction. The hip joint is triaxial permitting movement in three planes:

Flexion–extension
Abduction–adduction
Rotation

Implant separation from bone tissue, resulting in the necessity for revision surgery, is a serious drawback of cementless total joint replacement. Unnatural stress distribution around the implant is considered the main reason for the failure. Optimization of the implant properties, especially its geometric parameters, is believed to be the right way to improve reliability of joint prosthetics. Numerical models of femur-implant system enabling approximate analysis of stress distribution and shape optimization of implants suffer from numerous simplifications as, e.g., the assumption of bone isotropy, which may put in question reliability of the results obtained. In this section, a numerical model including orthotropic properties of both cancellous and cortical bone is included and influence of this assumption on results of the analysis and optimization is investigated.

The most common material combination used for an artificial hip joint consists of a femoral component made of a metal stem with a polished metallic or ceramic ball which articulates against a metal shell with a plastic inner socket, (Plate 7.1). Ultra high molecular weight polyethylene (UHMWPE) has been widely and successfully used as a bearing material in orthopaedic prostheses. Despite the recognized success and worldwide acceptance of a total joint replacement, the number of failures increases after 15–20 years. Complications of total hip replacement can be thrombophlebitis, infection, dislocation, and loosening of the joint. Loosening of the joint is still one of the major causes of failure in total hip replacements.

Total hip replacement (THR) attempts to mimic the design of a natural hip joint. THR is usually composed of a stem, inserted into the femoral canal, with a head articulating in a cup, inserted in the pelvic acetabulum, (Plate 7.1). Different acetabular–femoral material combinations have been

used in hip prostheses, including metal–metal, polymer–polymer, ceramic–metal and polymer–metal.

Most widely used and perhaps also the most successfully designed hip joint (judging from clinical experience) is the Charnley hip joint prosthesis, consisting of a one piece stainless steel femoral component and an acetabular cup. The cup consists of a metal backing which is fitted into the pelvic acetabulum, internally covered with UHMWPE. The femoral stem and the cup can be attached to the bone by using a type of bone cement (usually PMMA bone cement) or by using a porous contact surface area which allows the bone to grow into the material. The femoral head slides against the inside of the cup with relatively low friction, μ between 0.03 and 0.1.

The geometry and loading conditions of the model are assumed identical and it displays the frontal cross-section of the three-dimensional model of a femur with the hip endoprosthesis. The geometry of bone is simplified in the sense that the planar symmetry with respect to the frontal mid-plane is assumed, for both bone and implant. This simplification is not expected to significantly affect the stress distribution in bone; on the other hand, it enables easy automatic generation of finite element meshes of the system for different values of implant shape parameters.

A standard implant with oval cross-section, bent shape and a vertical stabilizing "winglet," on the lateral side is considered (see Chap. 5 for more details of the bone and implant transversal cross-sections). The upper part of the implant surface (Plates 7.1 and 7.2) is taken to be porous-coated to induce the tissue in growth and better adhesion between bone and implant. The porous coated interface is modeled as the high friction interface thus having perfect bonding contact condition. Here the GAPELEMENT or CONTACT ELEMENT formulation, given in the appendix, can act with the main Algorithm (as an interface between implant and porous coated area), analyzing bone implant composite structure.

UHMWPE exhibits a very high strain to failure and a greater wear resistance than many other polymers. Nevertheless, the polymer wears. The normal wear rate is acetabular cups can be as low as 50–100 μm year^{-1}, but a large number of submicron particles can still be generated ($>10^{10}$), and these can have negative biological effects.

UHMWPE is a tough material and can undergo substantial plastic deformation before rupture, but in artificial joints continuous deformation leads to embrittlement and finally rapture, also called fatigue wear. Oxidative wear is related to environmental factors, like oxidation from artificial aging that changes the mechanical properties of the polymer and may increase the wear rate.

Polymer wear depends strongly on the roughness and texture of the counterface. In general, the wear rate is largely independent of the apparent area of contact, as long as the change in this area does not introduce new factors into the wear mechanism.

Four distinct wear mechanisms can be identified for polymers.

- Fatigue wear through cyclic deformation from blunt micro-asperities. Wear against smooth surfaces is likely to involve a significant contribution from fatigue.
- Adhesive wear caused by adhesive forces tearing material from the polymer surface. Only a thin surface layer is involved in this process. Adhesive wear resistance depends on the cohesive strength of the material. It plays a significant role during sliding against metal.
- Abrasive wear is the result of rough surfaces or surfaces with a sharp texture deforming the polymer to a significant depth. Material loss can occur through cutting or shearing. Abrasion can also occur if hard particles are introduced into the system, so-called third body abrasive wear.
- Roll formation at the interface, a fourth and in our case less important wear mechanism, occurs when highly elastic materials slide against a smooth base surface. The rolled material is eventually removed from the worn surface.

To reduce friction and/or wear, a viscous medium is placed between the articulating surfaces in a tribo-system i.e., three lubrication mechanisms:

Boundary lubrication involves the presence of a thin lubrication film coating the sliding surfaces. The lubrication film helps by reducing both friction and the real area of contact. The pressure from the lubricant is, however, insufficient to separate the two surfaces and part of the load is transferred through direct surface contact. The coefficient of friction in boundary lubrication is usually relatively independent of sliding velocity (v), lubricant viscosity (η) and contact pressure (P).
Mixed lubrication is the regime between boundary lubrication and full film lubrication. Gradually the asperities lose contact and the pressurized lubricant carries more of the load. In this regime, the film is not thicker than the height of the asperities and some solid–solid contact occurs.

Full film lubrication is the most efficient form of lubrication for reducing friction and wear since the articulating surfaces are never in contact and all the load is carried by the lubricant becomes greater than the reduction in surface-to-surface friction, illustrates the three stages of lubrication.

7.1.5 Input Data for the Finite Element Analysis

Loading Cases and Methods of Application

Type I Case Study

$$\left.\begin{array}{l}\mathrm{F1} = \text{Loading during stance of gait} \rightarrow \text{variable} \\ \mathrm{F2, F3} = \text{Normal loads : activities} \rightarrow \text{variable}\end{array}\right\} \quad \begin{array}{c}\text{Loads are to be} \\ \text{equilibrated by} \\ \text{forces in the knee joints}\end{array}$$

In Extreme situation: the load values and angles of both joint head and abductor forces are given:

loading cases	$R =$ joint force/angle		F_M abductor force/angle muscles	
	joint force (KN)	$\alpha =$ degrees	joint force (KN)	$\alpha =$ degrees
1	2.238	−103.5	0.704	+61.5
2	1.156	−74.9	0.355	+97.5
3	1.550	−147.0	0.470	+55.0

Note: The hip joint is subjected to loads from walking, running, standing, etc.
The angle is measured from the horizontal axis.
The data has been obtained from St. James Hospital, London.

It is recommended that the analysis and optimization procedure are performed for an equivalent load, being a weighted average of different load patterns. Through out the finite element analysis the medical profession recommended that the same weight for each load should be taken and which must correspond to equal number of cycles occurring for each load case during the activities of a patient.

Type II Case Study

This case study is the *stance phase of walking*, the femoral loading now consists of the following.

The stance phase of walking W_B, represents the body weight less the weight of the supporting leg. It acts medially, giving rise to the muscles force F_M of the abductors which act laterally. Force F_T acting on the greater trochanter, stimulates the tension banding effect of the iliotibial tract of the fascia lata on the femoral shaft. Its magnitude cannot be determined from static force analysis. From in vivo experimental determinations on three subjects, it was found that this force approaches a value close to partial body weight W_B in walking. It acts simultaneously with the vastus lateralis muscle which lies between the iliotibial tract and the demur. Force F_T was varied from zero to two times partial body weight W_B.

Constitutive Properties

Cortical Bone

Cortical bone is treated as orthotropic material with E's varies along the three principal axes with constant Poisson ratio. The material matrix $[D]$ given in the appendix. The direction 3 is treated as the principal axis of the higher stiffness modulus E_3 oriented longitudinally and tangentially to the bone axis, for this type of bone tissue, the following values obtained from medical tests and data bank:

$$
\begin{aligned}
E_1 &= 13.5 \times 10^3\,\mathrm{MN\,m^{-2}},\\
E_2 &= 14.34x10^3\,\mathrm{MN\,m^2},\\
E_3 &= 21.75 \times 10^3\,\mathrm{MN\,m^{-2}},\\
\nu_{12} &= 0.38, \quad \nu_{31} = 0.353 = \nu_{32},\\
G_{12} &= 5.0 \times 10^3\,\mathrm{MN\,m^{-2}}\\
G_{31} &= 5.785 \times 10^3\,\mathrm{MN\,m^{-2}},\\
G_{32} &= 5.94 \times 10^3\,\mathrm{MN\,m^{-2}} = G_{13},\\
E^1 &= (E_1 + E_2 + E_3)/3
\end{aligned}
$$

for bone model, endochronic theory is adopted with three-dimensional cracking criteria defined in the appendix, where $[D]$ is zero, cracks are generated and the critical load sustained by the bone at the time of failure is evaluated. This critical load divided by the pre-implant failure load of the bone shall provide a factor of safety.

Cancellous Bone

For cancellous bones, a great deal of discrepancy exists in results. Data are required at only few locations and are not complete in the sense of number of the measured constants. Great deal of difficulties occur for this bone to know initially the directions of principal axes and how they are related to the directions of measured module.

It is assumed that cancellous bone in femur is built of interconnecting bars only, and forms a microstructure of "prismatic cells," i.e., each microstructural node is a 5-bar node. This yields microstructures with the macroscopic properties of transverse isotropy with remarkably higher stiffness in the principal direction. Within the range of volume fraction between 0.1 and 0.3 the ratio E_3/E_1 varies from about 2.5 to 1.5. Since this microstructure is parameterized by only one parameter (bar thickness), we can as well parameterize it by volume fraction instead. Thus, to define material properties of cancellous bone, it is necessary to provide distribution of volume from another design so that FE meshes with identical topology can be created from different design parametric sets.

Implant Material Properties

For steel implant material properties, the value of $E = 200\,\mathrm{GN\,m^{-2}}$ is chosen through out and the poisons ratio $V_\mathrm{s} = 0.3$ is maintained for the finite element analysis. For using implant material as titanium which now-a-days in general use, the value of $F = 110\,\mathrm{GN\,m^{-2}}$ with $V = 0.33$.

7.1.6 Finite Element Discretisation

Plates 7.4 and 7.5 indicate the finite element discretisation. The mesh scheme basically consists of 20-noded isoparametric solid elements with 8-noded

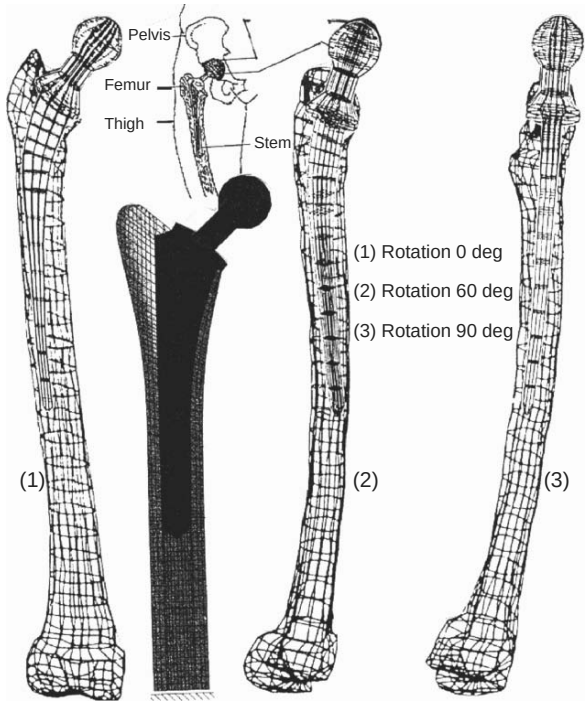

Plate 7.4. Finite element global model of femur with hip endoprosthesis

implant elements. The contact cement layer is modeled as Hallquist Gap Elements as the mesh is obtained from a structured mesh generator written for this purpose. It allows for generation of meshes for different sets of implant shape parameters. The mesh topology (number of rows, circumferential segments, radial layers in each segment, etc.) is determined depending on the geometric proportions of implant and bone in the particular design, but it can as well be adopted. The stress distribution in a human femur with an endoprosthesis is evaluated, using three-dimensional finite element Analysis with more than 18000 degrees of freedom. A brief relevant analysis by other researchers are discussed. As a result this analysis has been adopted. Geometrical and material data have been taken from various researchers who had previously tackled femur with an endoprosthesis. The medical data provided have been thoroughly examined and then taken as an input data for Program Isopar II as a three-dimensional finite element algorithm for the analysis of this specific case study. The relevant X-rays have been examined as test cases for the analytical evaluation of damage scenario. Various loading cases and modes of loading have been investigated. One mode of loading that brings about the damage scenario exhibited by the X-ray(s) will be treated as the correct one. A perfect bond at the interface between materials of different

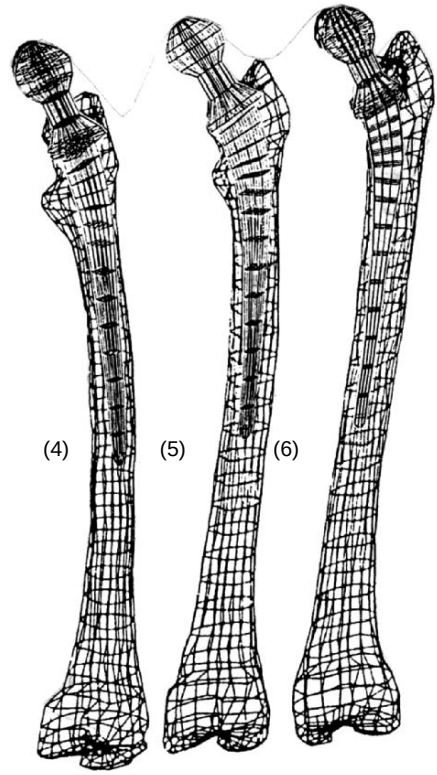

Plate 7.5. Finite element global model of femur with hip endoprosthesis

elastic module was initially assumed. The results are validated for this endoprosthesis with those structural stem surfaces as to allow transfer of tensile and shear stresses.

Numerical optimization of a mechanical system, like that consisting of bone and implant, requires the parameterized physical model of the system, a numerical code for static analysis, and an appropriate optimization scheme. The computational code must be capable of computing strains, stresses and all other variables needed to determine the objective function and, since most efficient optimization procedures are gradient-based, also design derivatives (sensitivities) of these quantities. A finite analysis code with the design sensitivity gradient computation routines implemented has been used. Mathematical details of computational sensitivity analysis are included.

Optimization Objective

The goal of optimization is to minimize the mechanical phenomena that are believed to result in the implant loosening. In this paper, short-term (postoperative) factors will be focused on. This failure type consists in improper bone ingrowth into the porous-coated implant surface which results in formation of permanent gaps filled with loose fibrous tissue. The reason for this may be either initial improper fitting of the implant into the medullary canal or excessive micromotions occurring at the bone-implant interface. Such micromotions can prevent osseointegration and a permanent layer of fibrous tissue is formed instead of the desired stiff bonding. Such a layer, even if mechanically stable, may lead in the long run to inflammatory reactions and bone resorption. It is taken that the minimization of micromotion more or less corresponds to minimization of tangential stresses on the implant surface. The maximum tangential stresses $\sigma'_{\max}$ are computed at nodal points as well which are based on the porous-coated part of the implant surface which in turn are based on stress tensor components σ_{ij} in a specific bone computed at these points using Program ISOPAR-II. In the program sequence the following equation for $\sigma'_{\max}$ is simulated

$$\sigma'_{\max} = \sqrt{(\sigma_{n1}^2 + \sigma_{n2}^2 + \sigma_{n3}^2 + \sigma_1^2) - \text{Parallel}} \tag{7.1}$$

$$\sigma_1 \text{ in perpendicular direction} = \sigma_{ni} \cdot n_i. \tag{7.2}$$

To create smooth function, (7.1) can be written as

$$\hat{\eta} = \left[\frac{1}{N} \sum_{i=1}^{N} \left(\sigma'^{(i)}_{\max} \right)^m \right]^{1/m}, \tag{7.3}$$

where N denotes number of nodded on the internal surface $m =$ exponent; Log $N/(\log 1.02)$, where m is large

$$\bar{\eta}_{\max} = \sigma'^{i}_{\max_{v1toN}}. \tag{7.4}$$

Basis of Finite Element Modeling

Bone mineral density (BMD) measurements using dual X-ray absorptiometry (DEXA) scanners are the principal means for diagnosis and clinical management of osteoporosis. While BMD is firmly entrenched in the medical lexicon, the measured quantity and its relationship to bone strength are poorly understood. The quantity measured in a BMD measurement has meaning in terms of the physical principles used to derive it but no intrinsic meaning in a biological or mechanical sense.[1] Volume averaged BMD measurements from complex, variably shaped regions are difficult to model for investigation of strength relationships. To address this problem, a formalism for automated mapping

is devised three-dimensional DEXA data to a pseudo three-dimensional finite element model. Presented here, is an automated process using DEXA data that can quickly generate a thin shell, three-dimensional finite element model representing cortical bone for proximal femurs. The model has been applied to DEXA scan data from several large international epidemiological studies. This process has the potential to provide insights into the mechanical consequences of lost bone mass with age and why hip fracture rates and bone mass values differ between the sexes and among different ethnic groups. This method is very similar to the one adopted by John Hopkin University.

The model is derived as a stack of isoparometric elements with elliptical inner and outer boundaries. The technique begins with a bone mass image from a DEXA hip scan (Plates 7.2 and 7.3). A hyperbolically curved axis is superimposed, asymptotic to the axes of the femoral neck and shaft. Bone mass profiles are extracted orthogonal to the curved axis at regular intervals along its length. For each profile, the cortical equivalent cross-sectional area, subperiosteal width, and centroid in the image plane are measured. In-plane widths for each cross-section correspond to the outer major axis. The outer minor axis is assumed to be constant for all sections through the base of the femoral head and equal to the image plane width at the proximal shaft. Inner ellipses of the hollow structure are derived to yield the measured centroid location. The program also interactively derives the locus of the center of the femoral head as well as its average radius. The data for the femoral head, as well as coordinates of centroids, centers of inner and outer ellipses, and angles of section tilts are exported to a text file.

The model is created from DEXA input data using *FEMVIEW* Software, which provides the option to automate tasks by executing scripts (Program files) written in Program ISOPAR-II. A Fortran program is used to read DEXA data test profile and to generate the corresponding program file.

A series of eight individual program files are used which are then executed by a main file which calls them sequentially. The final program, which creates the finite element model, iterates if more than one model is desired as in testing of strain energy convergence.

The DEXA-derived variables are stored within program ISOPAR AS since all parametric dimensions disappear from the model when it is lofted into a solid part. With dimensional information lost, listing variables is the only way to review the model. Individual coordinate systems for each section are located with respect to a global coordinate system, then tilted in the scan plane to correspond to the orthogonal to the hyperbolic reference axis in the DEXA image. Coordinate systems for the femoral head are derived within the Fortran program, based on the center and radius of the head. A single point is added above the final coordinate system, corresponding to the apex of the femoral head. With median cortical ellipses, midway between inner and outer ellipse at each section, sketched onto coordinate system planes (Plate 7.6), lofting completes the solid model. After partitioning the model with extruded

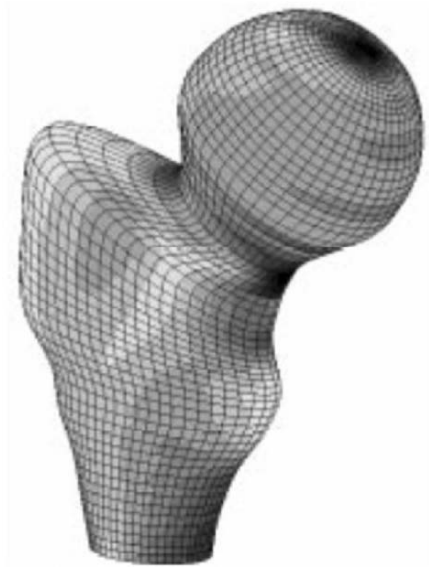

Plate 7.6. Stress contour for one legged stance load condition. The finite element model includes 3,120 thin shell elements (48 columns by 3 rows per section)

planes between the section locations and about the frontal plane,[3] the outer surface is prepared for meshing.

The finite element mesh is mapped onto the outer surfaces with eight-noded, thin-shell elements over all but parts of the femoral head where six-noded elements are used. Frontal plane symmetry of the elliptical cross-sections allows element thickness. All elements are assigned orthotropic material properties consistent with cortical bone. The final automated step is the definition of material directions normal to the plane of a given section. Boundary conditions and loading configurations are then created manually by the user for each finite element model generated. The time between executing the Fortran Program to the creation of three-dimensional finite element models measures approximately 30 min up to 5,000 elements. The test figure used 13 DEXA data sections, however, a DEXA scan often contains in excess of 90 sections. The Fortran program is designed to operate regardless of the section count. In addition to the versatility designed within the process, options exist prior to execution of the Fortran program to allow users a more custom result. Even though the user is only prompted for desired mesh densities, several other variables can be modified in the Fortran code itself. These variables include all aspects of the orthotropic material property, the number of sections defining the femoral head, their spacing, and the thickness assigned to elements of the femoral head.

Since a DEXA image is a projection of the three-dimensional femur into a two-dimensional plane, only mechanical loading in the frontal plane is appropriate. Plate 7.6 depicts the stress contour for a one-legged stance loading condition: a restrained shaft with a load applied to the femoral head in the frontal plane, 30° to the shaft axis. While the model allows the application of muscle forces.

The main purpose of this project is to generate a reasonably realistic model of the hip that is dimensionally and bone mass consistent with DEXA image data acquired on adult human subjects. The model will be adaptable to mimic measured changes in bone mass and geometry that accompany the aging process. The intent will be to use the automated modeling process together with DEXA data from an aging population to examine the structural consequences of altered bone mass and geometry in the aging hip as well as sex and ethnic differences in those consequences.

7.1.7 Calculation of the Inner Boundary of the Bone

In order to create a mechanically equivalent parametric model of the femur, the moment of inertia and the mass of the bone and the model must be equal for each cross-section of the bone. We calculated the cortical/cancellous and cortical/marrow boundary such that the cross-sectional moment of inertia (CSMI) and cross-sectional area (CSA) of the model and the original bone remained equal (note that both are calculated from the mass of the cross-section based on one voxel thickness). We used the density map data for each cross-section plus the CSMI and CSA equations to calculate the appropriate elliptical fit for the cortical/cancellous or cortical/marrow boundaries. This enabled us to define the bone geometry and its material distribution with a finite number of control points for each cross-section. Thus, a full parametric model of the femur was created.

The algorithm accounted for the cortical thickness variations within a cross-section of the bone by allowing eccentric inner contours with respect to their corresponding outer contours. The coordinates of the center of inner ellipses, x_{ij} was found by manipulating the equations for the first moment of inertia as follows:

$$x_1 = \frac{A_\mathrm{o} \cdot x_\mathrm{o} - CSA \cdot x_\mathrm{cg}}{A_\mathrm{i}}, \tag{7.5}$$

where x_o is the coordinates of the outer ellipse, x_cg is the coordinates of the centrorid of the density map, A_o is the area under the outer elliptical ellipse, and A_i is the area under the inner ellipse.

The tissue porosity, μ for the trabecular volume enclosed by the cortex varies with each cross-section. The value of the trabecular porosity was defined and adjusted for each cross-section using the following equation:

$$\mu = 1 - \frac{\sum_{j=1}^{N} d_j}{N \cdot \rho} \tag{7.6}$$

where N is the number of pixels in the inner cortex, d_j is the density value for each pixel, and ρ is the average tissue density.

7.1.8 Elasto-Plastic Finite Element Analysis Behind Program ISOPAR-II

Plastic Flow Rule and Stresses During Elastoplastic Straining

Many materials have been examined, including concrete. They behave elastically up to a certain stage of the loading beyond which plastic deformation takes place. During this plastic deformation the state of strain is not uniquely determined by the state of stress, as stated previously. In a uniaxial state of stress a simple rule is required to initiate yielding at any Gaussian point of the isoparametric element. In the multiaxial state of stress, there are an infinite number of possible combinations of stresses at which yielding starts. These can be examined by the flow rule. Moreover, the flow rule supplements the elastic constitutive relationship; and the plastic strain increments are related to the plastic stress increments during the occurrence of plastic flow in steel or titanium.

The yield criterion described by a failure surface in a multidimensional stress space is given by Bangash

$$L_{\mathrm{F}}\left(\sigma_{ij}^{s}, \varepsilon^{\mathrm{p}}, S_{\mathrm{H}}\right) = 0 \tag{7.7}$$

where L_{F} is the the yield function; σ_{ij}^{s} the multidimensional stress state; ε^{p} the accumulated plastic strain and S_{H} is the strain hardening or softening parameter.

The general form of the yield surface given by (7.7) allows either isotropic or kinematic hardening of the material. For a given previous history, $L_{\mathrm{F}}(\sigma_{ij})$ is always considered as a function of the current state of stress for which S_H is variable.

To give added generality, the plastic potential to which the normality principle is applicable is assumed as

$$L_Q\left(\sigma_{ij}^{\mathrm{s}}, \varepsilon^{\mathrm{p}}, SH_0\right) = 0. \tag{7.8}$$

This allows nonassociated plasticity to be dealt with and associated rules to be obtained as a special case by making

$$L_{\mathrm{F}} = L_Q. \tag{7.9}$$

For a perfectly plastic material the yield surface of (7.7) remains constant. For a strain hardening material the yield surface must change with continued straining beyond the initial yield.

This phenomenon is included in (7.7) by allowing both L_{F} and S_{H} to be functions of the state of stress and the plastic deformation history. This means

S_{H} will have a new value for every time dependent yielding. Further, if the material is unloaded and then loaded again, additional yielding cannot take place, unless the current value of S_{H} has been exceeded.

A unified approach for arriving at the incremental stress–strain equation based on (7.8) can be written in a combined tensor form in three dimensions as

$$f\left(\sigma, \varepsilon, \dot{\sigma}, \dot{\varepsilon}, S_{\mathrm{H}}\right) = 0, \tag{7.10}$$

where f is a definite representation of L_{F} and is a stress function. The only change is in the value of S_{H}, accounting for isotropic and anisotropic hardening, and allowing the function f to be dependent not only on the present state of stress or strain, but also on the hardening history according to previous states of stress and strain. The value of $(\sigma, \dot{\sigma})$ and $(\varepsilon, \dot{\varepsilon})$ must be in the plastic range, having total values of σ_{ij}^{p} and $\varepsilon_{ij}^{\mathrm{p}}$, respectively.

When (7.10) is satisfied then the total differential of f is written as

$$\mathrm{d}f = \frac{\partial f}{\partial \sigma_{ij}^{\mathrm{p}}} \mathrm{d}\sigma_{ij}^{\mathrm{p}} + \frac{\partial f}{\partial \varepsilon_{ij}^{\mathrm{p}}} \mathrm{d}\varepsilon^{\mathrm{p}} + \frac{\partial f}{\partial S_{\mathrm{H}}} \mathrm{d}S_{\mathrm{H}}. \tag{7.11}$$

The yield condition with $\varepsilon_{ij}^{\mathrm{p}}$ and SH held constant can be interpreted as a yield surface in the multidimensional stress space, and is in conformity with (7.7). When $f < 0$ the condition indicates a purely elastic change towards the inside of the yield surface. In cases where plastic flow does not occur, the increments of plastic strain $\mathrm{d}\varepsilon_{ij}^{\mathrm{p}}$ and the change of hardening parameter $\mathrm{d}S_{\mathrm{H}}$ will be automatically zero, and hence, in the case of the unloading, (7.11) is reduced to

$$\mathrm{d}f = \frac{\partial f}{\partial \sigma_{ij}^{\mathrm{p}}} \mathrm{d}\left\{\sigma_{ij}^{\mathrm{p}}\right\} < 0. \tag{7.12}$$

When $\mathrm{d}f = 0$, which is the case for neutral loading, no plastic strain changes occur and the hardening factor remains unchanged, then

$$\mathrm{d}f = \frac{\partial f}{\partial \sigma_{ij}} \mathrm{d}\left\{\sigma_{ij}^{\mathrm{p}}\right\} = 0, \quad \mathrm{d}\left\{\varepsilon_{ij}^{\mathrm{p}}\right\} = 0. \tag{7.12a}$$

The quantity $\mathrm{d}\sigma_{ij}$ is tangent to the surface for neutral loading. For the vector products to be zero, $\partial f / \partial \sigma_{ij}$ will be normal to the surface. When $\mathrm{d}\sigma_{\mathrm{ij}}$ is pointing to the outside of the surface the vector product will be positive; and this constitutes loading, with plastic flow taking place such that

$$\mathrm{d}f = \frac{\partial f}{\partial \sigma_{ij}} \mathrm{d}\left\{\sigma_{ij}^{\mathrm{p}}\right\} > 0. \tag{7.13}$$

The definition for the structural material stability postulates that during a load cycle that includes loading and unloading, the work performed has to be greater than material stability postulates that during a load cycle that

includes loading and unloading, the work performed has to be greater than zero, i.e.

$$\mathrm{d}\varepsilon_{ij}^{\mathrm{p}}\mathrm{d}\sigma_{ij}^{\mathrm{p}} \geq 0. \tag{7.14}$$

From (7.13) and (7.14) for ideally plastic material the plastic strain increment $\mathrm{d}\,\varepsilon_{ij}^{\mathrm{p}}$ is proportional to the stress gradient of the yield surface

$$\mathrm{d}\varepsilon_{ij}^{\mathrm{p}} = \frac{\partial f}{\partial \sigma_{ij}^{\mathrm{p}}}\mathrm{d}\lambda, \tag{7.15}$$

where $\mathrm{d}\lambda$ is the constant of proportionality.

The normality rule given by (7.14) shows that the plastic strain increment has the same direction as the normal surface f in the stress space. At this stage both isotropic and kinematic hardening cases can be included in (7.15).

In order to perform the plastic analysis, the loading path is discretised into several linear load steps. The increments in stresses and strains for each step are than related by the rate constitutive laws mentioned earlier. The assumption is that the extension in the linearised step can be regarded as infinitesimal, and (7.15), which is true for all infinitesimal increments of stresses and strains can be employed for small increments. Bone structures or implants of steel and titanium require small increments. The total strain increment $\mathrm{d}\varepsilon'_{ii}$ is the algebraic sum of the increments in elastic and plastic strains $\mathrm{d}\bar{\varepsilon}_{ij}$ and $\mathrm{d}\varepsilon_{ij}^{\mathrm{p}}$, respectively. The equation for $\mathrm{d}\varepsilon'_{ij}$ can be written as

$$\mathrm{d}\,\varepsilon_{ij} = \mathrm{d}\bar{\varepsilon}_{ij} + \mathrm{d}\,\varepsilon_{ij}^{\mathrm{p}} + \mathrm{d}\,\varepsilon_{ij}^{\mathrm{e}} + \mathrm{d}\,\varepsilon_{ij}^{\mathrm{T}} + \mathrm{d}\,\varepsilon_{ij}^{\mathrm{p}}. \tag{7.16}$$

The stresses can be written as

$$\mathrm{d}\sigma'_{ij} = [D]\,\mathrm{d}\,\varepsilon_{kl}, \tag{7.17}$$

$$\mathrm{d}\sigma_{ij} = [D]\,\mathrm{d}\,\varepsilon_{kl} - \mathrm{d}\lambda\,[D]^{-1}\,\frac{\partial f}{\partial \sigma_{kl}}. \tag{7.18}$$

The plastic strain relationship is given as

$$\mathrm{d}\,\varepsilon = [D^*]^{-1}\,d\,\{\sigma\}\,. \tag{7.19}$$

The total strain increment $\{\Delta\varepsilon\}_{\mathrm{TOT}}$ becomes

$$\{\Delta\varepsilon\}_{\mathrm{TOT}} = [D^*]^{-1}\,\{\Delta\sigma\} + \frac{\partial f}{\partial \sigma}\mathrm{d}\lambda. \tag{7.20}$$

When (7.11) is written in a compressed form as

$$\mathrm{d}f = \frac{\partial f}{\partial\,\{\sigma\}}\mathrm{d}\,\{\sigma\} + \frac{\partial f}{\partial S_{\mathrm{H}}} = 0. \tag{7.21}$$

Replacing the second term for the hardening characteristics by $\mathrm{d}\lambda$, the following equations are obtained:

$$\left\{\frac{\partial f}{\partial \sigma}\right\}^{\mathrm{T}} \mathrm{d}\{\sigma\} - C\mathrm{d}\lambda = 0, \tag{7.22}$$

$$\mathrm{d}\,\varepsilon_{\mathrm{TOT}} = [D^*]^{-1}\,\mathrm{d}\{\sigma\} + \left\{\frac{\partial f}{\partial \sigma}\right\}\mathrm{d}\lambda, \tag{7.23}$$

$$0 = \left\{\frac{\partial f}{\partial \sigma}\right\}^{\mathrm{T}} \mathrm{d}\{\sigma\} - C\mathrm{d}\lambda. \tag{7.24}$$

Multiplying (7.23) with [D*] throughout, (7.23) can be expressed as

$$\mathrm{d}\{\sigma\} = [D^*]\{\mathrm{d}\,\varepsilon\}_{\mathrm{TOT}} - [D^*]\left\{\frac{\partial f}{\partial \sigma}\right\}\mathrm{d}\lambda. \tag{7.25}$$

Equation (7.25) is then substituted into (7.24), and (7.26) is obtained

$$0 = \frac{\partial f^{\mathrm{T}}}{\partial \sigma}[D^*]\{\mathrm{d}\,\varepsilon\}_{\mathrm{TOT}} - \left\{\frac{\partial f}{\partial \sigma}\right\}^{\mathrm{T}}[D^*]\left\{\frac{\partial f}{\partial \sigma}\right\}\mathrm{d}\lambda - C\mathrm{d}\lambda. \tag{7.26}$$

Equation (7.15) is then combined with (7.14), (7.22) and (7.11) to give the final value of

$$\mathrm{d}\lambda = \frac{\left\{\frac{\partial f}{\partial \sigma}\right\}^{\mathrm{T}}[D^*]\{\mathrm{d}\,\varepsilon\}_{\mathrm{TOT}}}{C + \left\{\frac{\partial f}{\partial \sigma}\right\}^{\mathrm{T}}[D^*]\left\{\frac{\partial f}{\partial \sigma}\right\}}. \tag{7.27}$$

The factor C in (7.27) is an unknown factor defining the state of elasto-plasticity. When C = 0, (7.27) gives a value of dλ for a perfectly plastic situation with no hardening. The stress increments are given by

$$\{\mathrm{d}\sigma\}_{\mathrm{TOT}} = [D^*] - \frac{[D^*]\left\{\frac{\partial f}{\partial \sigma}\right\}\left\{\frac{\partial f}{\partial \sigma}\right\}^{\mathrm{T}}[D*]}{C + \left\{\frac{\partial f}{\partial \sigma}\right\}^{\mathrm{T}}[D^*]\left\{\frac{\partial f}{\partial \sigma}\right\}}\{\mathrm{d}\,\varepsilon\}_{\mathrm{TOT}}\,. \tag{7.28}$$

For the elasto-plastic case

$$\{\mathrm{d}\sigma\}_{\mathrm{TOT}} = [D^*] - [D_P]\{d_\varepsilon\}_{\mathrm{TOT}}\,, \tag{7.29}$$

$$[D_p] = \frac{[D^*]\left\{\frac{\partial f}{\partial \sigma}\right\}\left\{\frac{\partial f}{\partial \sigma}\right\}^{\mathrm{T}}[D]}{C + \left\{\frac{\partial f}{\partial \sigma}\right\}^{\mathrm{T}}[D]\left\{\frac{\partial f}{\partial \sigma}\right\}}. \tag{7.30}$$

The true stress increment in (7.30) is the difference between the stress increment $[D_P]\{\mathrm{d}\bar{\varepsilon}\}_{\mathrm{TOT}}$ and the algebraic sum of stresses $[D]\{D\varepsilon\}$ due to elastic, creep, shrinkage, temperature, fatigue, and other effects.

The matrix $[D]$ has the flexibility to include any bone or implant failure models described elsewhere in this book.

The parameter C is given by Hill as

$$C = 4/9\sigma_{\text{eq}}^2 S_{\text{H}} \tag{7.31}$$

where S_{H} is the slope of the curve and represents hardening. Where the influence of the contact elements or gap elements are to be included in the finite element analysis, the steps given in Table 7.1 are considered together with solid, panel, and line elements, as and when required.

7.1.9 Sample Cases

Plastic Potential of the Same Form as the Yield Surface

$$f(J_2) = f(\sigma_{ij}) = 3/2 = \frac{3}{2} S_{ij} S_{ij}, \tag{7.32}$$

where

$$s_{ij} = \sigma_{ij} - \frac{1}{3}\sigma_{kk}\delta_{ij}, \quad \delta_{\text{ij}} = \text{the Kronecker delta}$$

Differentiating

$$\begin{aligned} \frac{\partial f}{\partial \sigma_{ij}} &= \frac{3}{2}\partial\left(S_{kl}S_{kl}\right)/\partial\sigma_{ij} \\ &= \frac{3}{2} S_{kl}\partial S_{mn}/\partial\sigma_{ij} = 3S_{ij}. \end{aligned} \tag{7.33}$$

The plastic strain increment is stated as

$$\mathrm{d}\lambda\varepsilon_{ij}^{\text{p}} = \lambda S_{ij}. \tag{7.34}$$

The equivalent plastic strain $\lambda\bar{\varepsilon}^{\text{p}}$ can be obtained as

$$\mathrm{d}\lambda\bar{\varepsilon}^{\text{p}} = \left(\frac{2}{3}\mathrm{d}\,\varepsilon_{ij}^{\text{p}}\mathrm{d}\,\varepsilon_{ij}^{\text{p}}\right)^{1/2}, \tag{7.35}$$

where

$$\mathrm{d}\lambda = \frac{3}{2}\frac{\mathrm{d}\bar{\varepsilon}^{\text{p}}}{\sigma_{\text{eq}}}.$$

Van Mises Yield Surface Associated with Isotropic Hardening

The yield function f is written as

$$f = \frac{T}{2}(\sigma_{ij}) - \frac{1}{3}\sigma_{\text{eq}}^2. \tag{7.36}$$

By differentiating, (7.36) becomes

$$\mathrm{d}f = (S_{ij}\mathrm{d}\sigma_{ij}) - \frac{2}{3}\sigma_{\mathrm{eq}}\left(\partial\sigma_{\mathrm{eq}}\right)/\left(\partial\bar{\varepsilon}^{\mathrm{p}}\right)\left\{\mathrm{d}\bar{\varepsilon}^{\mathrm{p}}\right\}. \tag{7.37}$$

Using (7.12) onwards, the values of $\mathrm{d}\lambda$ and $\mathrm{d}\sigma$ given in (7.27) and (7.28) are given by

$$\mathrm{d}\lambda = \left([D^*]_{i.l.k.l} - \frac{[D^*]\, S_{mn} S pq\, [D^*]_{pqkl}}{\sigma_{ij}\, [D^*]_{i,j,k,l}\, S_{kl} + \left(\frac{2}{3}\sigma_{\mathrm{eq}}\right)^2 S_{\mathrm{H}}} \right) \{\mathrm{d}\,\varepsilon\}_{kl}\,. \tag{7.38}$$

7.1.10 Dynamic Analysis

Dynamic analysis is subject by itself. In this text a specific approach to the dynamic analysis of concrete structures is discussed. The equations of motion are discretized in time. The direct integration technique and the Wilson $-\theta$ method are summarized. Where dynamic problems are tackled, the nonlinear equations of motion (coupled or uncoupled), have been solved using these methods.

Nonlinear Transient Dynamic Analysis

The dynamic equilibrium at the nodes of a system of structural elements is formulated at a given time t as

$$[M]\left\{\ddot{U}_t\right\} + [C_t]\left\{\dot{U}_t\right\} + K'_t\,\{U_t\} = \{R_t\}\,, \tag{7.39}$$

where $\{U_t\}$ and $\{R_t\}$ are the vectors of displacement and specified load, respectively. $[M]$ represents the mass matrix which is regarded as constant; $[C_t]$ and $[K'_t]$ are the damping and stiffness matrices, respectively. The subscript t is used for quantities at time t and a dot denotes a derivative with respect to time.

To formulate (7.39), discretisation with respect to time, using isoparametric finite elements, is performed. The simple applicable method is the numerical step-by-step integration of the coupled equations of motion, such as (7.39). The response history is divided into time increments Δt, which are of equal length. The system is calculated for Δt, with properties determined at the beginning of the interval. Only one matrix based on M, is excited. In addition, the direct integration technique allows a general damping matrix $[C_t]$ (which has to be specified explicitly), to be used without resorting to complex eigenvalues.

Discretisation in the Time Domain

The equation of motion formulated at time $t = 0$, is written in the form

$$[M]\left\{\ddot{U}_0\right\} + [C_0]\left\{\dot{U}_0\right\} + [K_0]\,\{U_0\} = \{R_0\}\,, \tag{7.40}$$

where the subscript zero has been introduced. At time t, all quantities are known.

Equation (7.39) is specified as

$$[M]\left\{\ddot{U}_t\right\} + ([C_o] + [\Delta C_{o\to t}])\left\{\dot{U}_t\right\} + ([K'_o] + [\Delta K_{o\to t}])\{U_t\} = \{R_t\} \quad (7.41)$$

or as

$$[M]\left\{\ddot{U}_t\right\} + [C_0]\left\{\dot{U}_t\right\} + [K_0]\{U_t\} = \{R_t\} + \{P_t\} = \{F\}_t\,, \quad (7.42)$$

where the initial load $\{P_t\}$ is specified by

$$\{P_t\} = -[\Delta C_{0\to t}]\left\{\dot{U}_t\right\} - \{\Delta K_{0\to t}\}\{\delta_t\} \quad (7.43)$$

To obtain the solution at time $t + \Delta t$, stated as

$$[M]\left\{\ddot{U}_{t+\Delta t}\right\} + [C_0]\left\{\dot{U}_{t+\Delta t}\right\} + [K_0]\{U_{t+\Delta t}\} = \{R_{t+\Delta t}\} + \{P_t\} + \{\Delta P_{t\to t+\Delta t}\}\,, \quad (7.44)$$

$\{\Delta P_{t\to t+\Delta t}\}$ represents the influence of the nonlinearity during the time increment t and is determined by iteration and satisfied for $t+\tau$, where $\tau = \theta\Delta t$ ($\theta > 1.37$ for an unconditionally stable method) applied to a linear problem. $[\Delta C_{0\to t}]$ and $[\Delta K_{0\to t}]$ represent the change of $[C]$ and $[K]$, respectively, from $t = 0$ to t.

To obtain the solution at time $t + \Delta t$, (7.43) can be written as

$$[M]\left\{\ddot{U}_{t+\Delta t}\right\} + [C_0]\left\{\dot{U}_{t+\Delta t}\right\} + [K_0]\{U_{t+\Delta t}\} = \{R_{t+\Delta t}\} + \{F_t\} + \{\Delta F_{t\to t+\Delta t}\}\,, \quad (7.45)$$

$\{\Delta P_{t\to t+\Delta t}\}$ represents the influence of the nonlinearity during the time increment t and is determined by iteration:

$$\begin{aligned}\{\Delta P_{t\to t+\Delta t}\} = &-[\Delta C_{0\to t}]\left\{\Delta\dot{U}_{t\to t+\Delta t}\right\} \\ &-[\Delta C_{t\to t+\Delta t}]\left(\left\{\dot{U}\right\} + \left\{\Delta\dot{U}_{t\to t+\Delta t}\right\}\right) \\ &-[\Delta K_{0\to t}]\{\Delta U_{t\to t+\Delta t}\} - [\Delta K_{t\to t+\Delta t}](\{U_t\} + \{\Delta U_{t\to t+\Delta t}\})\end{aligned} \quad (7.46)$$

$(\Delta P_{t\to t+\Delta t})$ is calculated using the initial stress approach.

A modified Newton–Raphson or initial stress approach is adopted for solving these nonlinear equations. A step-by-step integration method is given in Table 7.2. Using these methods along with acceleration and convergence procedures described in this chapter can allow successful solution of finite element-based problems.

Reduced Linear Transient Dynamic Analysis

This is a reduced form of nonlinear transient dynamic analysis. This analysis is carried out faster than the nonlinear analysis since the matrix in (7.39) requires to be inverted once, and the analysis is reduced to a series of matrix multiplications and essential degrees of freedom (dynamic or master of freedoms) to characterize the response of the system. The analysis generally has restrictions such as constant $[M]$, $[C_t]$, $[K_t]$ and time interval for all iterations and nodal forces applied at dynamic or master degrees of freedom.

Equations (I) and (J) of Table 7.2 are written in a different form by considering the above-mentioned restraints.

Quadratic Integration

$$\left(\frac{1}{\Delta t^2}[M]_R + \frac{3}{2\Delta_t}\left[\hat{C}_t\right]_R + [K_t]_R\right)\{U_t\}_R = \{F(t)\}_R + [M]_R \frac{1}{\Delta t^2}\left(2\{U_{t-1}\}_R - \{U_{t-2}\}_R\right) + \frac{1}{\Delta_t}\left(2\{U_{t-1}\}_R - \frac{1}{2}\{U_{t-2}\}_R\right). \tag{7.47}$$

The symbol R represents reduced matrices and vectors.

Cubic Integration

$$\left(\frac{2}{\Delta t^2}[M]_R + \frac{11}{6\Delta t}[C_t]_R + [K_t]_R\right)\{U_t\}_R = \{F(t)\} + [M]_R \frac{1}{\Delta t^2}\left(5\{U_{t-1}\}_R - 4\{U_{t-2}\}_R + \{U_{t-3}\}\right) + [C_t]_R \frac{1}{\Delta t^2}\left(3\{U_{t-1}\}_R - \frac{3}{2}\{U_{t-2}\}_R + \frac{1}{3}\{U_{t-3}\}_R\right). \tag{7.48}$$

Mode Frequency Analysis

The equation of motion for an undamped structure with no applied forces is written as

$$[M]\left\{\ddot{U}_t\right\} + [K_t']\{U_t\} = \{0\}, \tag{7.49}$$

where $[K_t']$, the structure stiffness matrix, may include stress-stiffening effects.

The system of equations is initially condensed down to those involved with the master (dynamic) degrees of freedom.

The number of dynamic degrees of freedom should at least be equal to two times the selected frequencies. The reduced form of (7.49) can be written as

$$[M]_R \left\{\ddot{U}_t\right\}_R + [K_t']_R \{U\}_R = \{0\}. \tag{7.50}$$

For a linear system, free vibrations of harmonic type are written as

$$\{U_t\}_R = \{\psi_i\}_R \cos \omega_i t, \tag{7.51}$$

where $\{\psi_i\}_R$ = the eigenvector representing the shape of the ith frequency; ω_i = the ith frequency (radians/unit time); and t = time.

Equation (7.49) assumes the form

$$-\omega_i^2 [M]_R + [K_t']_R \left\{\vec{\psi}_i\right\}_R = \{0\}, \tag{7.52}$$

which is an eigenvalue problem with n values of ω^2 and n eigenvectors $\{\psi_i\}_R$ which satisfy (7.55), where n is the number of dynamic degrees of freedom. Using standard iteration procedures, (7.55) will yield a complete set of eigenvalues and eigenvectors.

Each eigenvector $\left\{\vec{\psi}_i\right\}_R$ is then normalized such that

$$\left\{\vec{\psi}_i\right\}_R^{\mathrm{T}''} [M]_R \left\{\vec{\psi}_i\right\}_R = 1. \tag{7.53}$$

These n eigenvectors are now expanded to the full set of structure modal displacement degrees of freedom. Hence

$$\left\{\vec{\psi}_{\gamma' i}\right\}_R = [K_{\gamma'\gamma'}]^{-1} [K_{\gamma'\gamma}] \left\{\vec{\psi}_i\right\}_R, \tag{7.54}$$

where $\left\{\vec{\psi}_i\right\}_R$ is the salve degree of freedom vector of mode I; and $[K_{\gamma'\gamma'}], [K_{\gamma'\gamma}]$ is the submatrix parts.

The above dynamic analysis approach is generally adopted for structures subjected to normal dynamic loads. The above analysis, with modifications, is also applied to vehicular, missile, and aircraft explosions/impact problems, where traumatic injuries could certainly cause.

Table 7.1. Analytical formulation of the steel/titanium implant

$$[K_{\mathrm{TOT}}]\{\delta\}^{*} + \{F_{\mathrm{T}}\} - \{R_{\mathrm{T}}\} = 0, \tag{7.55}$$

where

$$[K_{\mathrm{TOT}}] = [K_{\mathrm{l}}] + [K_a], \tag{7.56}$$

$$\{\delta\}^{*} = \begin{Bmatrix} \delta_{\mathrm{un}} \\ \delta_{\mathrm{b}} \end{Bmatrix} \quad \{F_{\mathrm{T}}\} = \begin{Bmatrix} F_{\mathrm{un}} \\ F_{\mathrm{b}} \end{Bmatrix}, \quad \{R_{\mathrm{T}}\} = \begin{Bmatrix} R_{\mathrm{un}} \\ R_{\mathrm{b}} \end{Bmatrix}, \tag{7.57a}$$

where $[K_{\mathrm{TOT}}]$ is the total stiffness matrix; $[K_e]$, the steel/titanium stiffness matrix; $[K_a]$, the contact stiffness matrix; $\{F_{\mathrm{T}}\}$, the total initial load vector and $\{R_T\}$ is the total external load vector. The subscripts "un" is the quantities corresponding to unknown displacement and "b" is the quantities corresponding to restrained boundaries.

$$[k_1]\{\delta_{\mathrm{un}}\} + \{F_{\mathrm{un}}\} = 0, \tag{7.58}$$

$$\{\varepsilon\} = [B]\{\delta\}, \tag{7.59}$$

$$\{\sigma\} = [D](\{\varepsilon\} - \{\varepsilon_0\}), \tag{7.60}$$

$$\begin{aligned} \{\bar{S}\} &= \text{anchor shear forces} \\ &= [K_a]\{\delta_{\mathrm{un}}\}, \end{aligned} \tag{7.61}$$

$$\{F_{\mathrm{un}}\} = \int_v [B]^{\mathrm{T}}[D]\{\varepsilon_0\}\,\mathrm{d}v = \int_v [B]^{\mathrm{T}}[D]\{\varepsilon_0\}\det[J]\,\mathrm{d}\xi\mathrm{d}\eta\,\mathrm{d}\zeta. \tag{7.62}$$

The plastic buckling matrix is given for the implant by

$$(K + \lambda K_{\mathrm{G}})F_{\mathrm{T}} = 0, \tag{7.63}$$

where K is the elastoplastic stiffness matrix as a function of the current state of plastic deformation and K_{G} is the initial stress geometric stiffness matrix for implant.

The determinant

$$|K + \lambda_{\mathrm{c}} K_{\mathrm{G}}| = 0. \tag{7.64}$$

The essential equation is characteristically triangularized for the ith loading step as

$$\begin{gathered} \left(K^i + \lambda_{\mathrm{c}} K_{\mathrm{G}}^i\right) F_{\mathrm{T}}^i = 0, \\ \lambda_{\mathrm{c}} = 1 + E_{\mathrm{ps}}, \end{gathered} \tag{7.65}$$

E_{ps} is an accuracy parameter.

Table 7.2. Summary of step-by-step integration method

Initialization

(1) Effective stiffness matrix

$$[K_0^*] = \left(6/\tau^2\right)[M] + (3/\tau)[C_0] + [K_0] \tag{A}$$

(2) Triangularize $[K_0^*]$

For each time step:
Calculation of displacement $(\{U_t + \tau\})$

(1) Constant part of the effective load vector

$$\begin{aligned}\{R_{t+}^*\ \} = \{R_t\} + \theta\left(\{R_{t+\Delta t}\} - \{R_t\}\right) + \{F_t\} = [M] \\ \times\left(\left(\frac{6}{\tau^2}\right)\{U_t\} + \frac{6}{\tau}\left\{\dot{U}_t\right\} + 2\left\{\ddot{U}_t\right\}\right) \\ + [C_0]\left(\frac{3}{\tau}\{U_t\} + 2\left\{\dot{U}_t\right\} + \frac{\tau}{2}\{U_t\}\right)\end{aligned} \tag{B}$$

(2) Initialization $i = 0$,

$$\left\{\Delta P_{t\to t+}^i\ \right\} = 0$$

(3) Iteration
(a) $i \to i + 1$
(b) Effective load vector

$$\left\{R_{t+\ \mathrm{TOT}}^*\right\} = \{R_{t+}^*\ \} + \left\{\Delta P_{t\to t+}^{i-1}\ \right\} \tag{C}$$

(c) Displacement

$$\left\{U_{t+}^i\ \right\}[K_0^*]\left\{U_{t+}^i\ \right\} = \left\{R_{t+\ \mathrm{TOT}}^{*i}\right\} \tag{D}$$

(d) Velocity

$$\left\{\dot{U}_{t+}^i\ \right\} + (3/\tau)\left(\left\{U_{t+}^i\ \right\} - \{U_t\}\right) - 2\left\{\dot{U}_t\right\} - (\tau/2)\left\{\ddot{U}_t\right\}$$

(e) Change of initial load vector caused by the nonlinear behavior of the material

$$\left\{\Delta P_{t\to t+}^i\ \right\}$$

$$\begin{aligned}\left\{\Delta P_{t\to t+}^i\ \right\} = -\left[\Delta C_{0\to t}\right]\left(\left\{\dot{U}_{t+r}^i\right\} - \left\{\dot{U}_t\right\}\right) - \left[\Delta C_{t\to t+r}^i\right]\left\{\dot{U}_{t+r}^i\right\} \\ \times\left[\Delta K_{0\to t}\right]\left(\left\{U_{t+r}^i\right\} - \{U_t\}\right) \\ - \left[\Delta K_{t\to t+r}^i\right]\left\{U_{t+r}^i\right\}\end{aligned} \tag{E}$$

In fact, $\left\{\Delta P_{t\to t+}^i\ \right\}$ is calculated using the initial-stress method.

(f) Iteration convergence

$$\left\|\left\{\Delta P_{t\to t+}^i\ \right\} - \left\{\Delta P_{t\to t+}^{i-1}\ \right\}\right\| / \left\|\left\{\Delta P_{t\to t+}^i\ \right\}\right\| < tol \tag{F}$$

or analogously, on stresses.

Note: $\{P\}$ could be any value of $\{F\}$.

Calculation of velocity, acceleration

Calculate new acceleration $\left\{\ddot{U}_{t+\Delta t}\right\}$ velocity $\left\{\dot{U}_{t+\Delta t}\right\}$, displacement $\{U_{t+\Delta t}\}$ and initial load $\{P_{t+\Delta t}\}$:

$$\begin{aligned}
\left\{\ddot{U}_{t+\Delta t}\right\} &= \left(6/\theta r^2\right)\left(\{U_{t+}\ \} - \{U_t\}\right) - (6/\tau\theta)\left\{\dot{U}_t\right\} + \left(1 - \frac{3}{\theta}\right)\left\{\ddot{U}_t\right\} \\
\left\{\dot{U}_{t+\Delta t}\right\} &= \left\{\dot{U}_t\right\} + \frac{\tau}{2\theta}\left\{\ddot{U}_t\right\} + \left\{\ddot{U}_{t+\Delta t}\right\} \\
\{U_{t+\Delta t}\} &= \{U_t\} + \frac{\tau}{\theta}\left\{\dot{U}_t\right\} + \left(r^2/6\theta^2\right)\left(2\left\{\ddot{U}_t\right\} + \left\{\ddot{U}_{t+\Delta t}\right\}\right) \\
\{P_{t+\Delta t}\} &= \{P_t\} + \left\{\Delta P^i_{t\to t+r}\right\}
\end{aligned} \tag{G}$$

Calculation by quadratic integration

When the velocity varies linearly and the acceleration is constant across the time interval, appropriate substitutions are made into (6.39) giving

$$\left[f_1\,[M] + f_2\,[C_t] + \left[K'_t\right]\right]\{U_t\} = \{F\,(t)\} + \{f_3\,([C_t]\,,[M]\,,U_t,U_{t2},\ldots)\} \tag{H}$$

where f_1, f_2, f_3 = functions of time.

This results in an implicit time integration procedure. The only unknown is $\{U_t\}$ at each time point and this is calculated in the same way as in static analysis. Equation (H) is then written as:

$$\begin{aligned}
&\left(\frac{2}{\Delta t_0 \Delta t_{01}}\,[M] + \frac{2\Delta t_0 \Delta t_1}{\Delta t_0 \Delta t_{01}}\,[C] + \left[K'_t\right]\right)\{U_t\} \\
&\quad = \{F\,(t)\} + [M]\left(-\frac{2}{\Delta t_0 \Delta t_1}\,\{U_{t-1}\} - \frac{2}{\Delta t_0 \Delta t_{01}}\,\{U_{t-2}\}\right) \\
&\qquad + [C_t]\left(\frac{\Delta t_{01}}{\Delta t_0 \Delta t_1}\,\{U_{t-1}\} - \frac{\Delta t_0}{\Delta t_{01} \Delta t_1}\,\{U_{t-2}\}\right)
\end{aligned} \tag{I}$$

where

$$\begin{aligned}
&\Delta t_0 = t_0 - t_1 && t_0 = \text{time of current iteration} \\
&\Delta t_1 = t_1 - t_2 && t_1 = \text{time of previous iteration} \\
&\Delta t_2 = t_2 - t_3 && t_2 = \text{time before previous iteration} \\
& && t_3 = \text{time before } t_2 \\
&\Delta t_2 = \Delta t_0 + \Delta t_1 = t_0 - t_2 &&
\end{aligned}$$

Calculation by cubic integration

Equation (H) becomes cubic and hence is written as

$$\begin{aligned}
&\left(a_1\,[M] + a_2\,[C_t] + \left[K'_t\right]\right)\{U_t\} \\
&= \{F\,(t)\} + [M]\,(a_3\,\{U_{t-1}\} - a_4\,\{U_{t-2}\} + a_5\,\{U_{t-3}\}) \\
&+ [C]\,(a_6\,\{U_{t-1}\} - a_7\,\{U_{t-2}\} + a_8\,\{U_{t-3}\})
\end{aligned} \tag{J}$$

where a_1 to a_8 are functions of the time increments; these functions are derived by inverting a four by four matrix.

For clear-cut solutions, the size of the time step between adjacent iterations should not be more than a factor of 10 in nonlinear cases and should not be reduced by more than a factor of 2 where plasticity exists.

7.1.11 Criteria for Convergence and Acceleration

Convergence Criteria

To ensure convergence to the correct solution by finer subdivision of the mesh, the assumed displacement function must satisfy the convergence criteria are:

(a) Displacements must be continuous over element boundaries.
(b) Rigid body movements should be possible without straining.
(c) A state of constant strain should be reproducible.

Euclidean norm is given by $\psi_i/R_i \leq C$. The term ψ_i represents the unbalanced forces and the norm of the residuals. With the aid of the iterative scheme described above, the unbalanced forces due to the initial stresses $\{\sigma_0\}$ become negligibly small. As a measure of their magnitude, the norm of the vector $\parallel \psi_i \parallel$ is used. The Euclidean norm and the absolute value of the largest component of the vector are written as

$$\parallel \vec{\psi}_i \parallel = \left(|\vec{\psi}_1|^2 + \cdots + |\vec{\psi}_n|^2\right)^{1/2}, \tag{7.66}$$

$$\parallel R_i \parallel = \left(|\{R_i\}^{\mathrm{T}} \left\{R^i\right\}|\right)^{1/2}$$

the convergence criterion adopted is

$$\parallel \vec{\psi} \parallel = \max_i |\vec{\psi}_i| < C = 0.001. \tag{7.67}$$

Uniform Acceleration

Various procedures are available for accelerating the convergence of the modified Newton–Raphson iterations. Fig. 7.1 shows the technique of computing individual acceleration factors, δ_1 and δ_2 are known. Then, assuming a constant slop of the response curve, and from similar triangles, the value of δ_3 is computed

$$\frac{\delta_1}{\delta_2} = \frac{\delta_2}{\delta_3}, \tag{7.68}$$

$$\delta_3 = \delta_2 \frac{\delta_2}{\delta_1}.$$

When δ_3 is added δ_2, then the accelerated displacement $\delta_2{}'$ is expressed as

$$\delta_2' = \delta_2 + \delta_3 = \delta_2 \left(1 + \frac{\delta_2}{\delta_1}\right) = \alpha\delta_2, \tag{7.69}$$

where the acceleration factor α is

$$\alpha = 1 + \frac{\delta_2}{\delta_1}. \tag{7.70}$$

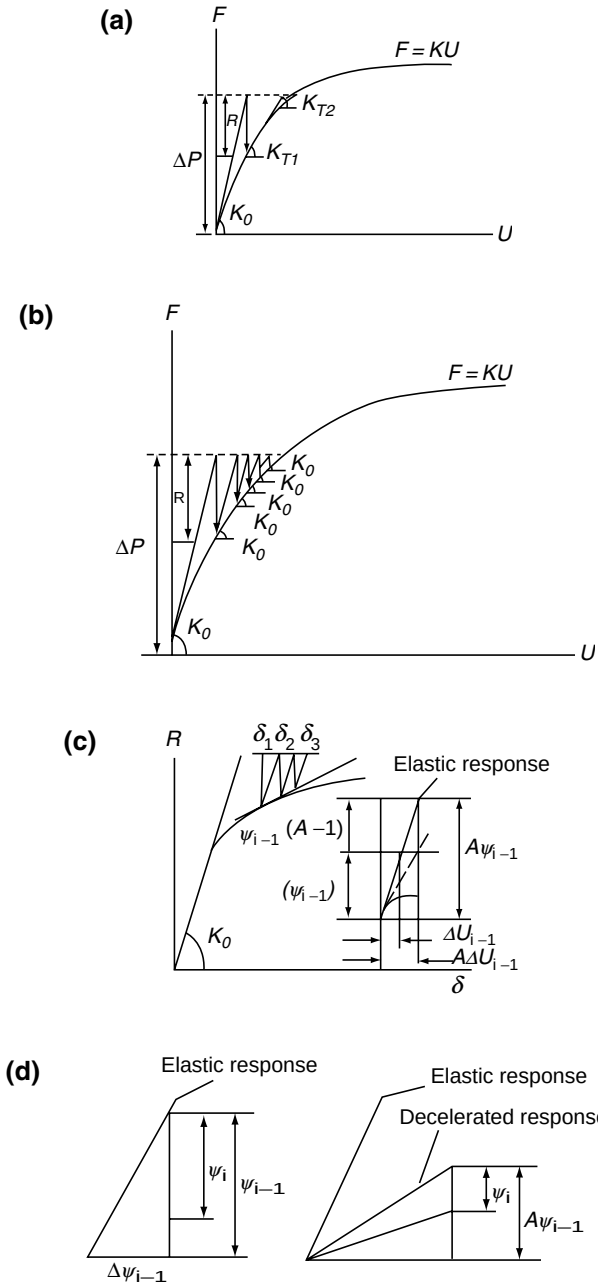

Fig. 7.1. (**a**) Newton–Raphson method; (**b**) initial stress method. *Note*: ΔP is a specific value of F; (**c**) technique of computing acceleration factors; (**d**) graphical representation; (**e**) linear acceleration and load assumptions of the Wilson θ method (**f**) quadratic and cubic variation of velocity and displacement assumptions of the Wilson θ method

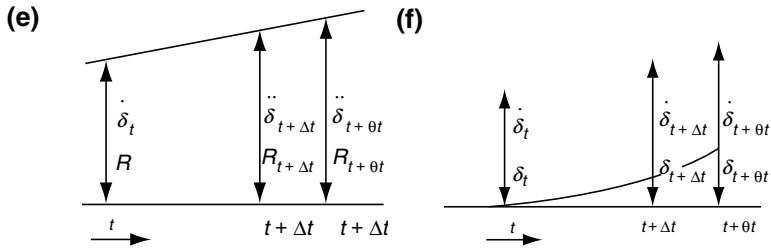

Fig. 7.1. *Continued*

Generally the range of α is between 1 and 2. The value of $\alpha = 1$ for zero acceleration, and the value of α reaches the maximum value of 2 when the slope of the $\delta - R$ curve approaches zero.

The acceleration factor α is computed individually for every degree of freedom of the system. The displacement vector obtained from the linear stiffness matrix $[k_0]$ is then multiplied by the $[\alpha]$ matrix having the above constants on its diagonals. The remaining components of $[\alpha]$ are zero. The accelerated displacement vector is then expressed as follows:

$$\{\Delta u_i'\} = [a_{i-1}]\,\{\Delta u_i\}\,. \tag{7.71}$$

From these accelerated displacements $\{\Delta u_i'\}$, the initial stresses $\{\sigma_0\}$ are found and they are equilibrated with the forces $\{\vec{\psi}_i\}$. They are then used for the next solution

$$\{\Delta \bar{u}_i\} = [k_0]^{-1} \left\{\vec{\psi}_i\right\}, \tag{7.72}$$

which results in a new set of acceleration factors. Now an estimate for the displacement increment is made in order to find the incremental stresses and total stresses.

The residual forces needed to re-establish equilibrium can now easily be evaluated.

$$\left\{\hat{\vec{\psi}}_i\right\} = \int_v [B]^{\mathrm{T}}\,\{\sigma_{0_{\mathrm{T}}}\}\,\mathrm{d}V - \{R_i\}, \tag{7.73}$$

where $\{R_i\}$ represents the total external load and $\mathrm{d}V$ is the volume.

A new displacement now results from

$$\{\Delta u_{i+1}\} = -\,[k_0]^{-1} \left\{\hat{\vec{\psi}}_i\right\}.$$

In order to carry out these iterative steps, numerical integration is required. First of all the evaluation of $\left\{\hat{\vec{\psi}}_i\right\}$ from the initial stresses is required, and this

requires integration over the elastic–plastic region only. The value of $\left\{\hat{\vec{\psi}}_i\right\}$ is computed by carrying out the integration over the entire domain of the analysis. Since these kinds of accelerated steps unbalance the equilibrium, therefore it has to be re-established by finding the residual forces $\left\{\hat{\vec{\psi}}_i\right\}$. Since the state of stress produced by the accelerated displacements is not in balance with the residual forces of the previous iteration, the new residual forces $\left\{\hat{\vec{\psi}}_i\right\}$ of (7.74) must balance $\{\sigma_T\}$ and $\{R_i\}$. Here the acceleration scheme is needed to preserve equilibrium, which will eventually make the equivalent forces over the whole region unnecessary. This is achieved by applying a uniform acceleration, i.e., the same acceleration factor $\bar{A}$ to all displacements, found by averaging the individual factors α_{i}

$$\bar{A} = \frac{1}{n} \sum_{i=1}^{n} \alpha_i \tag{7.74}$$

The force–displacement equation is then written by multiplying both sides with the scalar quantity $\bar{\mathrm{A}}$ without disturbing the equilibrium

$$\bar{A} \{\Delta u_i\} = [k_0]^{-1} \bar{A} \{\varphi_I\} . \tag{7.75}$$

Now to evaluate $\left\{\vec{\psi}_{I+1}\right\}$, the previous values of $\left\{\vec{\psi}_i\right\}$ must be multiplied by $\bar{\mathrm{A}}$, and the previously accelerated forces from the initial stresses $\{\sigma_0\}$ must be included such that

$$\left\{\vec{\psi}_{i+1}\right\} = \int_V [B]^{\mathrm{T}} \{\sigma_0\} \, \mathrm{d}V - (A-1) \left\{\vec{\psi}_{i-1}\right\} \tag{7.76}$$

7.1.12 Data on Modeling Failure Criteria on Implant

Where isoparametric solid elements are employed, Fig. 7.2 indicates whether in the mesh scheme the part of the implant or reinforcing steel lies in the body of this element or lying on the surface on any side of the brick or on any other element. Figs. 7.3 and 7.4 show the concept of stress–strain and failure surface modeling.

7.1.13 General Steps of Crack Flow and Crack Calculations

(1) The load increment $\{\Delta P_n\}$ applied where n is the load increment.
(2) The total is accumulated as

$$\{P_n\} = \{P_{n-1}\} + \{\Delta P_n\}, \tag{7.77}$$

and $\{R\} = \{\Delta P_n\}$, where $\{R\}$ is the residual load vector.

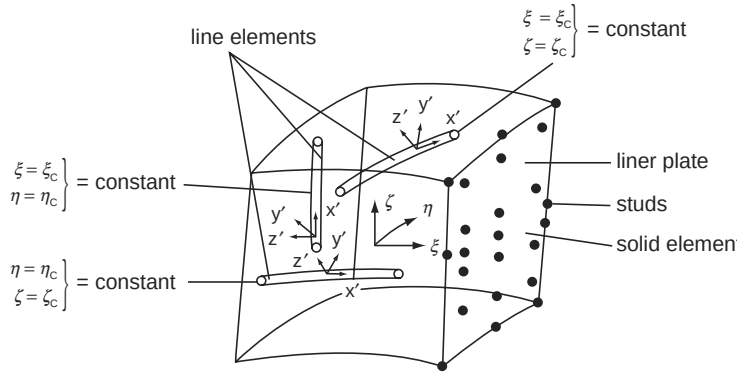

Fig. 7.2. Finite element modeling of linear–stud interaction

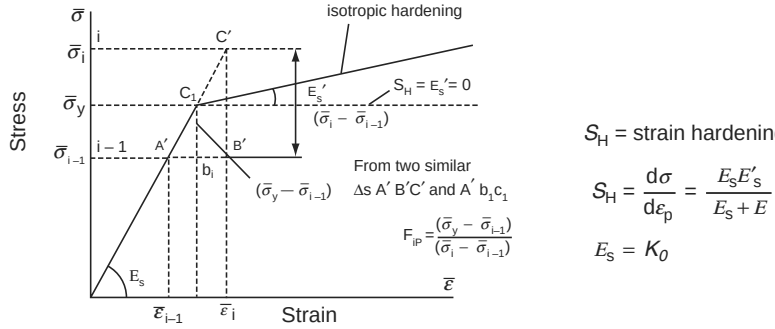

Fig. 7.3. Equivalent stress–strain curve for steel. (E_s = initial yield modulus; E_s = post-yield modulus)

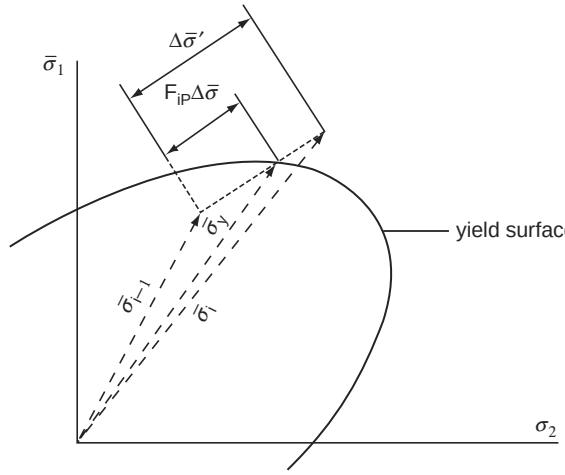

Fig. 7.4. Failure surface

(3) Incremental displacement are now computed as $\{\Delta U_i\} = [K]_{\mathrm{e}}{}^{-1}\{R\}$, where i is the iteration.
(4) Total displacements are now accumulated in the following form:

$$\{U_i\} = \{U_{i-1}\} + \{\Delta U_i\}. \tag{7.78}$$

(5) Strain increments are calculated from step 4 as $\{\Delta \in_i\} = [B]\{\Delta U_i\}$. The accumulated strains at this stage would then be written as

$$\{\in_i\} = \{\in_{i-1}\} + \{\Delta \in_i\}. \tag{7.79}$$

(6) The stress increments are calculated using the current nonlinear constitutive matrices of various models described earlier: $\{\Delta\sigma_i\} = \{f(\sigma)\}\{\Delta \in\}$. The accumulated stresses are computed as $\{\sigma_i\} = \{\sigma_{i-1}\} + \{\Delta\sigma_i\}$. In order to differentiate stresses at elastic and plastic conditions, a stress point indicator I_{p} is introduced.
$I_{\mathrm{p}} = 0$ (elastic point),
$= 1$ (plastic point),
$= 2$ (unloading from plastic state).
(7) The stress increment is calculated using the elastic material matrix as

$$\{\Delta\sigma_i'\} = [D']\{\Delta \in\}.$$

Total stresses are given as

$$\{\sigma_{\mathrm{i}}'\}_T = \{\sigma_{i-1}\} - \{\Delta\sigma_i'\}. \tag{7.80}$$

(8) The stress $\{\sigma_i\}$ is now calculated using step 7:

$$\{\sigma_i'\} = \{f(\sigma'_i)\}, \{\sigma_{i-1}\} = \{f(\sigma_{i-l})\} \tag{7.81}$$

any yield criterion required.
(9) If a plastic point is obtained, step 11 should be considered.
(10) If $\sigma_i \geq \sigma_{\mathrm{y}}$ — plastic point ($I_{\mathrm{p}} = 1$), transition from elastic to plastic, calculate factor F_{TP} using Figs. 7.3 and 7.4

$$F_{\mathrm{TP}} = \left[\frac{\sigma_{\mathrm{y}} - \bar{\sigma}_{i-1}}{\sigma_i - \sigma_{i-1}}\right].$$

The stress at the yield surface $\{\sigma_i\}_{\mathrm{y}}^* = \{\sigma_{\mathrm{i}-1}\} + F_{\mathrm{TP}}^*\{\Delta\sigma_i\}$. Elasto-plastic stress increments are calculated as $\{\Delta\sigma_i\} = [D]_{\mathrm{ep}}\{\sigma_i\}^*(1 - F_{\mathrm{TP}})\{\Delta\in\}$. Total stress $\{\sigma_i\}_{\mathrm{T}} = \{\sigma_i\} + \{\Delta\sigma_i\}$.
(11) Plastic point from steps 9 and 10, check for unloading, i.e. if $\bar{\sigma} \geq \sigma_{\mathrm{y}}$ it is necessary to proceed to step 12. For the unloading case at this point, set $I_{\mathrm{p}} = 2$, total stress $\{\sigma_i\}_{\mathrm{T}}$ then given by $\{\sigma_{\mathrm{i}}\} = \{\sigma_{\mathrm{i}-1}\} + \{\Delta\sigma_{\mathrm{i}}\}$. Set $\{\sigma_{\mathrm{y}}\} = \{\bar{\sigma}_{i-1}\}$, and the procedure is repeated for the additional increments.

(12) Loading at this point $\{\Delta\sigma_i\} = [D]_{\mathrm{ep}}\{\bar{\sigma}_{i-1}\}\{\Delta\mathrm{e}\}$. Total stress $\{\sigma_\mathrm{i}\}_\mathrm{T} = \{\bar{\sigma}_{i-1}\} + \{\Delta \in\}$.

(13) Sometimes it is necessary to correct stresses from the equivalent stress–strain curve: $\sigma_{\mathrm{corr}} = \sigma_{\mathrm{i}-1} + S_H\Delta\in_\mathrm{p}$, where $\Delta\in_\mathrm{p} = \sqrt{2/3\Delta\varepsilon_{ij}^\mathrm{p}\Delta_{ij}^\mathrm{p}} =$ equivalent plastic strain increment. S_H is the strain hardening parameter, such that $\Delta\in_\mathrm{p} = \lambda$. Equivalent stress, calculated from the current stress state, is given by $\{\sigma_\mathrm{i}\} = F_{\mathrm{TP}}\{(\sigma_i)\}$. The correct stress state, which is on the yield surface, will therefore be given as $\{\sigma_i\} = F_{\mathrm{TP}}\{\sigma_\mathrm{i}\}$. The total stresses are converted into equivalent nodal loads from $\int_v[B]^\mathrm{T}\{\sigma_i\}d$ vol, and the residual load vector is calculated from $\{R\} = \{\mathrm{F_n}\} - \int_\mathrm{v}[B]^\mathrm{T}\{\sigma_i\}d$ vol.

(14) Check for convergence. For detailed information see Appendices I and II.

$$(\| R \| / \| F \|) \leq \mathrm{TOL} \quad (\| \Delta U \| / \| U \|) \leq \mathrm{TOL}$$

where "TOL" is chosen from 0.01 to 0.001; $\| R \| = \sqrt{R_i^{T''}R_i}$ is the Euclidean norm of the residuals; $\| F \| \sqrt{P^\mathrm{T}P}$ is the Euclidean norm of the externally applied load; and $\| \Delta U \| = \sqrt{\Delta U_i^{T''}U_i}$ is the Euclidean norm.

If convergence is not achieved, step 3 is invoked and all steps repeated for the next iteration. If convergence is achieved, then proceed with the next load increment.

7.1.14 Computer Program ISOPAR-II: Three-Dimensional Finite Element Analysis

General Introduction

Program ISOPAR-II linked to FEMVIEW and DEXA is a comprehensive nonlinear finite element program which has been a modified version of ISOPAR-I. It is written in Fortran so as to evaluate traumatic injuries in orthopedic area using a partial input provided by medical personnel. In Sect. 6.1 the program is to evaluate the stress-distribution in a human femur with endoprosthesis. Here the objective is to improve the basic knowledge of the load transfer from the implant to the bone and further to arrive at a general basis for the design of the fixation component of the hip endoprostheses. In this analysis geometrical and material data are taken from a real case study with a high degree of accuracy. The FE model has been used to study the influence of design and material parameters on the stresses in implant, cement and surrounding bone. Program ISOPAR-II checks the status of medical parameters such as loads, material properties, etc., the entire prosthesis is checked for reliability. Taking the provided loading conditions, the load is raised in increment and the implant, cement and bone, etc. are checked for undue stresses, strains, implant plasticity, cracking, buckling, and bond loss. Further increasing the load till such time none of the materials in prosthesis exhibit failure as defined in this text. The ultimate load just before failure divided by the design load

shall give a factor of safety. Since wear and tear do affect the material properties, the analysis must take into consideration as a time dependent ones while calculating such a factor of safety. This analysis, hopefully, shall contribute to the validity or non-validity of the medical postulation. In case he results including a safety factor of a typical prosthesis present invalidation, the analytical results will assist the medical profession for a revision in the design of prosthesis prior to the final surgery or transplantation.

Major Input Data for Femur and Hip Prosthesis

FE Modeling

(1) Total no. of 20-sided isoparametric elements: 4,233
(2) Step cross-section 15 elements
(3) Cement layers 2 no: 18 elements each
(4) Two layers of bone: 34 elements

A reference is made to the appendix for the data on isoparametric elements, shape functions and computational aspects of stress, strains, and cracks. Contact elements are used, as stated in the appendix to establish a perfect bond between all elements so as to transfer tensile, compressive and shear stresses at the interface between implant and cement and cement and bone.

(5) Nodal points > 6,000 with degrees of freedom to be 18,000 plus
(6) E-values
    (a) Cancellous bone $= 186\,\mathrm{N\,m^{-2}}$
    (b) Cortical bone $= 1.5\,\mathrm{GN\,m^{-2}}$
    (c) Bone shaft external diameter $= 0.03\,\mathrm{m} = d$ to $0.10\,\mathrm{m}$.

Note: With intermediate values proportional to the square of the radiological density. To each element groups with equal radiological density different elastic moduli have been allocated. The compressive moduli of the bone tissue and the apparent density assumed to have a little influence on cancellous bone and the implant and hence ignored.

(7) The bone material anisotropic see $[D]$ matrix in the appendix
(8) $V =$ Poisson's ratio for bone tissue $= 0.33$
(9) Implant material

Titanium Grade 5

Ti–6%Al–4%V alloy
Chemical composition (wt%)
Al: 5.5–6.75, V: 3.5–4.5, Fe: 0.3 max, H: 0.015 max, O: 0.3 max (0.13 max for ELI grade), C: 0.08 max, N: 0.05 max, Other: 0.40 total (max 0.1 each), bal – Ti

Description. Grade 5 is the most widely used of the titanium alloys and has applications both in the medical and aerospace industry and in general engineering. It has good tensile strength at room temperature and useful creep resistance at up to 350°C.
Implant length = 150 mm
Mechanical properties at room temperatures

	minimum value	typical value
yield strength (MPa)	828	885
tensile strength (MPa)	895	940
elongation (%)	10	15
reduction in area (%)	25	38
hardness		HV 320–350
elastic modulus (GPa)		110
Charpy impact (J)		25
Vst		0.3

Note: To stop having relatively poor wear resistance, the titanium is coated with laser or electron beam surface alloying. Electrode nickel plating can be beneficial particularly if PTFE or ceramics are incorporated into the coating. Any deterioration in fatigue properties can largely be restored by shot peening of the component prior to the plating operation.

(10) Cement $E = 2.3\ \mathrm{KN\,m^{-2}\,m}$
(11) *Loading modes*[1]
  (a) The femur is loaded with a resultant force $F_\mathrm{R} = \sum F_1, F_2, F_3$ at joint = 2.7 KN
  The abductor force $F_\mathrm{M} = 1.98$ KN at stance phase of slow walking.
  The tension banding force F_T acting of the iliotibial = 0–0.95 KN.
  The partial body weight = 0.95 KN ≠ note for mode as suggested by the medical profession.
  The value of F'_T shall be taken as 0.2 KN and $W_\mathrm{B} = 0$ for this mode (a)
  (b) F_R and F_M of mode (a) + $F'_\mathrm{T} = W_\mathrm{B} = 0.95$ KN acting at trochanter.
  (c) Mode (a) + F'_T = mode(a) + 2.5 F_T = mode(a) + 2.375 KN
  (d) $F_\mathrm{R} = 2.7$ KN acting alone on prosthetic ball.
  (e) A vertical resultant $F_{\mathrm{R}2}$ (two-legged stance) = 0.30 KN on femoral head.
  (f) $F_\mathrm{para} = 0.3$ KN acting parallel to the longitudinal axis of the femoral shaft.

[1] The data extracted from medical records and research experimentations from 15 research institutions of repute from UK, USA and European countries such as Germany, France and Sweden.

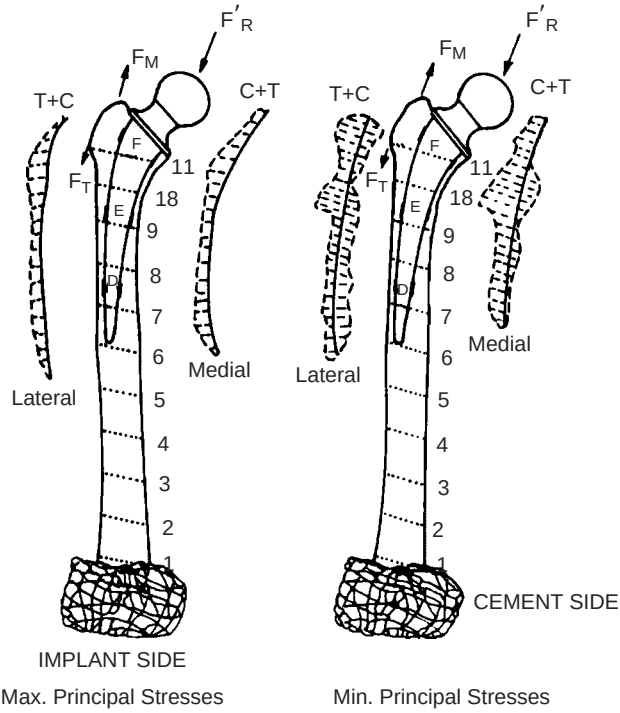

Plate 7.7. Principal stresses at the interface

The loading modes have been decided on the basis of thorough discussions with medical professional establishments.

(12) *Results.* Plate 7.7 is the brief results from appropriate loading cases which include a stance phase of walking with a force $F'T$ in the iliotibial tract of partial body weight of W_B. In the diaphyses three loads are applied around circumference, ventrally, dorsomedially, and dorsolaterally at the level of the shaft. Level f is the height of the lesser trochanter. Finite element analysis indicates the comparison of maximum and minimum principal stresses. The maximum principal stress mostly positive indicating tension T where as the minimum principal stresses are mostly negative, indicating on the plates of compression C. Due to enormous output, the book cannot afford extensive and numerous pages on strains, deflections, etc. under those modes of loading. The maximum and minimum principal strains for the femur with hip endoprosthesis differed by 12.5%. If the femur is intact these differences from the outputs are generally reduced to around 9%. The micromotion and stresses normal to the stem-cement interface occur during loading. In these circumstances, the finite element analysis use a gap or contact element developed by Hallquist et al. given in the appendix

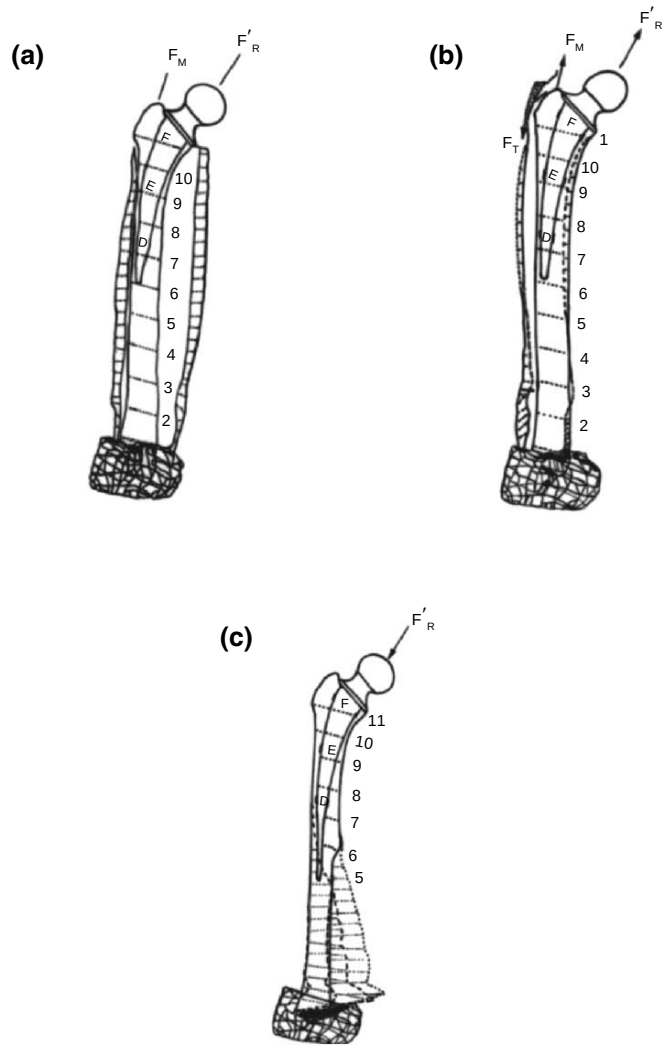

(a) Principal Stresses at this Load Mode At Femur
(b) Principal Stress at three Loads Mode At Femur
(c) Principal Stress at Single Inclined Loading Mode At Femur

Plate 7.7. *Continued*

to represent the interface of stem and the cement. Along the z-axis, the angles of the principal strains on the femoral surface were identical and differences were slight. However, on the latoral/dorsal side the difference was great around 10%.

The principal stresses on the femoral surface were discovered to be dependent on the relative position of the body. However, in this analysis they are computed from normal and shear stresses. In three-dimensional analysis three mutually perpendicular principal stresses and their directions were calculated. The maximum principal and minimum principal stresses are plotted in the plates on the boundary outline of the model. The principal stresses at femoral surface in the central frontal plane for different modes of loading are given here in the lateral and medial limits of the bone form the base line which is a continuous line. Positive values are plotted on the outside of the base line and indicate tensile stresses. The compressive stresses are assumed negative are plotted on the inner side of the base line.

The stress distributions on the femoral surface with and without implanted endoprosthesis show slight difference. The analysis made the assumption that implantation makes the proximal end of the femur stiffness; reducing the magnitude of stresses on the femoral surface in that specific area.

Load transfer from the implant to the bone is different from the normal flow of forces in the neck area of the intact femur, thus giving large differences in stresses in the intertrochanteric region. In the entire analysis is the gap element in the F.E. Analysis of bone and implant showed a good bond. The reduction of stresses in the bone medially under the prosthetic collar became important. The principal stresses at the implant stem-cement interface have been looked at thoroughly. The stresses and strains at the interface in the element side belonging to the implant elements and those of cement elements must come out to be the same. This validates the accuracy of the finite element analysis. It is interested to point out that in the element the stresses are calculated at Gussian points. On medical grounds, the cement thickness varied between 2 and 10 mm. In the stem values and directions of principal stresses were computed. The highest compressive stresses predominate on the medial side and high tensile stresses on the lateral side.

7.2 The Human Skull: An Engineering Analysis

7.2.1 General Introduction to Human Skull Structure

The skull or cranium is the skeleton of the head. The human skull consists of twenty two irregular bones. The cranial bones are bonded together by many sutures and by two synovial joints to form eight important cavities. The largest cavity is the neurocranium which encloses, supports and protects the brain. The other seven cavities support and protect the organs of the special senses and constitute the viscerocranium. For example, the two narrow nasal cavities serve both olfaction and respiration; the two pyramidal orbital cavities serve vision; the two most irregular auditory cavities serve audition and balance, and the large oral cavity serves both gestation and mastication.

7.2.2 The Bones of the Neurocranium

The Neurocranium is made of eight large and irregular bones. Six of these bones also assist in forming the seven cavities of the viscerocranium.

The name of the neurocranial bones underlying the ventral aspect of the brain and their rostrocaudal arrangement at the internal base of the cranium are as follows:

Frontal bone/frontal lobes
Ethmoid bone/olfactory bulbs
Sphenoid bone/brainstem
Temporal bones/temporal lobes
Occipital bone/occipital lobe
Parietal bones/parietal lobes

During fetal development, most neurocranial bones are formed in the cartilage underlying the ventral surface of the brain and then expand toward the vertex to enclose the growing brain.

The frontal bone is single and strong. It envelops most of the frontal lobes of the brain and consists of two major parts. The squamous part forms the forehead and anterior vault of the neurocranium. The orbital part forms a major portion of the anterior cranial fossa and the roof of the orbits. The supraorbital foramina or supraorbital notches which transmit the supraorbital nerve and blood vessels are located at the supraorbital margin. The frontal crest and the frontal grooves are located on the sagittal plane of the internal aspect of the squamous part. The crest gives attachment to the falx cerebri. The grooves are the impression of the superior sagittal dural/venous sinuses. There are two or more frontal cells/sinuses in the frontal bone.

The ethmoid bone is single and consists of very thin parts. It underlies the olfactory bulb and articulates with 13 bone. It forms only a small part of the neurocranium but constitutes a major part of the nasal cavities. The ethmoid bone has four parts: horizontal or cribriform plate, perpendicular or vertical plate, and the orbital/lateral plates or lateral masses.

The horizontal/cribriform plate forms a small part of the anterior crania fossa and the roof of the nasal cavities. It prominent features are the crista galli for the falx cerebri and cribriform foramina for the olfactory nerves (CN I).

The vertical plate together with the vomer forms the bony nasal septum. The two lateral plates form the lateral walls of the nasal cavities and the medial walls of the orbits. They contain many ethmoidal cells/sinuses.

The sphenoid bone is single and consists of very this parts. The bone resembles a bat or a butterfly. It assists in forming six cavities: the neurocranium, two orbital cavities, two nasal cavities and the nasopharynx. The sphenoid bone underlies the frontal and temporal lobes of the brain, the pituitary gland, five cranial nerves (CN II, III, IV, V, VI), the internal carotid arteries, the middle meningeal arteries and the arterial circle/circle of Willis.

The sphenoid bone is very complex. It has seven parts: the body, two lesser wings, two greater wings and two pterygoid processes. These parts articulate with 12 bones.

The body is cuboidal and forms the median part of the middle crania fossa. It contains two or more sphenoidal cells/sinuses. Its anterior surface assists in forming the roof of the nasal cavity; it posterior surface assists in forming the posterior crania fossa. Its lateral surfaces fuse with the greater wings and the pterygoid processes and carry the impressions of the internal carotid arteries. Its inferior surface forms part of the roof of the pharynx; its superior surface is marked by the chiasmatic groove and the sella turcica. The latter includes the tuberculum sellae, dorsum sellae, and posterior clinoid processes which surround a depression, the hypophyseal fossa.

The lesser wings have to connections with the body. The optic canals for the optic nerves and ophthalmic arteries traverse these connectors. Intracranially, the lesser wings form the posterior part of the anterior cranial fossa and provide the anterior clinoid processes for the attachment of the tentorium cerebelli. Extracranially, the lesser wings assist in forming the apex of the orbits.

The greater wings are connected to the lateral surface of the body. Intracranially, they form part of the floor of the middle cranial fossae which underlie the temporal lobes of the brain. Between the greater and lesser wings are the superior orbital fissures through which four cranial nerves (CN III, IV, V^{i}, VI) pass. Near the junction of the greater wings and the body are located the foramen rotundum for V^{2}, foramen ovale for V^{3} and foramen spinosum for the middle meningeal artery.

The pterygoid processes assist in forming the choanae, the nasopharynx and the pterygopalatine fossae. The pterygoid/vidian canals for the passage of the pterygoid/vidian nerves are located at the junction of these processes and the body. The pointed and curved tips of the medial plates of the pterygoid processes are the hamulus.

The temporal bones are twins. They consist of five parts: squamous, petrous, tympanic, mastoid, and styloid. These robust bones fill the two spaces surrounded by the sphenoid, occipital and parietal bones. The temporal bones underlie the temporal lobes of the brain.

The squamous part assists in forming the middle cranial fossa, the temporal fossa and the infratemporal fossa. The articular mandibular fossa for the temporomandibular joint is located in the infratemporal fossa.

The petrous part is the hardest bone in the body. It assists in forming both the middle and posteriors or cranial fossa. It forms the posterior wall of the middle ear and contains the labyrinth of the inner ears, the internal acoustic meatus, the facial canal, the carotid canal, the bony auditory (Eustachian) tube and the canal of the tensor tympani muscle.

The tympanic part is small and thin. It forms the anterior half of the external acoustic meatus and the wall of the middle ear (tympanic) cavity.

The mastoid part is the conical projection of the temporal bone. It has numerous air cells which communicate with the middle ear cavity. It provides attachment for several muscles of the neck.

The styloid process also provides attachment for several muscles and ligaments. Its length varies from one to nine centimeters. The stylomastoid foramen of the facial nerve is located between the styloid process and the mastoid processes.

The occipital bone is single. It is a strong bone consisting of four parts: squamous, laterals, basilar. It underlies and partially envelops the occipital lobes, the pons, the cerebellum and the medulla oblongata.

All four parts of the occipital bone surround the foramen magnum which transmits the spinal cord, the motor roots of the spinal accessory nerves, sympathetic nerves and the vertebral arteries.

The parietal bones are twins. These strong bones overlie the parietal lobes. They articulate with the frontal bone at the coronal suture, with each other at the sagittal suture, with the occipital bone at the lamdoid suture, with the sphenoid bone at the sphenoparietal suture and with the temporal bone at the squamosal suture. On their internal surface are imprints or canals of several branches of the middle meningeal arteries.

The following picture illustrates the rostrocaudal arrangement of the cranial bones at the base of the neurocranium.

7.2.3 The bones of the Viscerocranium

The Viscerocranium consists of 14 bones. Thesebones vary greatly in size, shape, and strength. They form five cavities for the organs of the special senses. The oral cavity is composed of its own bones. The nasal and orbital cavities consist of their own bones as well as bones shared by other cavities. Listed below are the bones specific to the cavities (in italics) as well as the bones shared by other cavities.

The nasal cavities:	*nasal* (2), *inferior conchae* (2), *vomer* (1) + frontal, ethmoid, sphenoid, maxillary, palatine
The orbital cavities:	*Lacrimal* (2) + frontal, ethmoid, sphenoid, maxillary, zygomatic, palatine
The oral cavities:	*Maxillary* (2) *Palatine* (2) *Mandibular* (1)
The cheek:	*Zygomatic* (2)

The *nasal bones* are twins. They are thin, small and rectangular. They are located between the frontal and maxillary bones. They articulate with each other at the *internasal suture* to form the bridge of the nose.

The inferior nasal conchae are a pair of slender bones. They articulate with *the ethmoid*, *maxillary* and *palatine bones*. They separate the middle meatus from the interior.

The nasal bone and the *inferior nasal concha* can be observed in the following illustration.

The vomer is an unpaired, thin, quadrilateral bone. It articulates with the ethmoid bone anteriorly, the sphenoid bone superiorly, and *the maxillary bone inferiorly*. It forms a significant part of the nasal septum.

The lacrimal bones are the smallest bones of the viserocranium. They form a part of the medial walls of the orbits, the lacrimal lake and the nasolacrimal duct. They articulate with the frontal, *ethmoid and maxillary bones*.

The maxillae or maxillary bones are relatively strong. They are the second largest bones of the *viscerocranium*. They form the major part of the face, the mouth and the upper jaw. Each maxilla has a body and four processes.

The body contains the largest *paranasal* sinus and has four surfaces. The anterior/facial surface is marked by the *infraorbital* foremen of the *infraorbital* nerve. *The posterior/infratemporal* surface contains several alveolar canals of the posterior superior alveolar nerves. The orbital surface assists in forming the orbit and the *infraorbital* groove of the *infraorbital* nerve. The nasal surface forms part of the nasal cavity and the maxillary sinus.

The four processes are: the alveolar process of the sockets of the upper teeth; the frontal process of the *lacrimal fossa*; the palatine process or the anterior three-fourth of the hard palate; the *zygomatic* process of the *zygoma*.

The palatine bones are twins. They are very thin and are located between the posterior surface of the maxillae and the *pterygoid processes* of *the sphenoid bone*. Each *palatine bone* resembles the letter L which consists of two plates: horizontal and vertical or perpendicular. Each bone has three important processes: orbital, *sphenoidal* and *pyramidal*.

The horizontal plate forms the posterior one-fourth of the hard palate. The vertical or perpendicular plate assists in forming the lateral wall of the nasal cavity. Its medial surface has small crests for the sutural joints of the middle and *inferior conchae*. Its lateral surface assists in forming the wall of the maxillary sinus, the *pterygopalatine fossa*, and the greater *palatine canal*.

The orbital process contributes to the orbital surface and the inferior orbital fissure. *The sphenoidal process* contributes to the *pterygopalatine fossa* and articulates with the medial pterygoid plates to form a part of *the pterygopalatine fossa*. It is marked by the lesser palatine foramen of the lesser palatine nerve.

The mandible (mandibular bone) is the largest and strongest *bone of the viscerocranium*. It extends from the chin to the *mandibular fossa* of the temporal bones. The mandible consists of a horseshoe-shaped body and two rami.

The body has two surfaces and two parts.

The external surface is marked by the *symphysis menti*, mental protuberance, mental tubercles, *incisive fossae* and *mental foramina*.

The internal surface is marked by the genial tubercle, mylohyoid line, *sublingual fossa* and *submandibular fossa*.

The superior or alveolar part contains sixteen sockets for the lower teeth.

The inferior or basal part is thick and contains *the digastric*, *sublingual* and *submandibular fossae*. *The mandibular canals* of the inferior alveolar nerve are located between these two parts and extend from the *mandibular foramen* to the mental foramen.

The rami of the mandible are quadrilateral plates which meet the body at an angle of about 125°. Each ramus has two surfaces and three borders.

The lateral surface is flat and becomes rough near the angle due to the insertion of the masseter. The medial surface is marked by *the mandibular foramen*, the lingual and the *mylohyoid groove*. *The mandibular foramen* transmits the inferior alveolar nerves and blood vessels into *the mandibular canal*. The lingual protects the neurovascular bundles and gives attachment to the *sphenomandibular ligament*. The *mylohyoid groove* marks the path of the mylohyoid nerve.

The anterior and posterior borders of the ramus are unremarkable but the superior border is marked by the mandibular notch which separates the condyle from *the coronoid process*. The condyle articulates with the mandibular fossa of the temporal bone by means of *synovial joint*. *The coronoid process* is the site of insertion of the *temporalis muscle*.

The zygomatic bones are quadrangular. They are strong and form the prominence of the cheek. Each *zygomatic bone* has three surfaces. The lateral surface is marked by the *zygomatiocofacial foramen*; the orbital surface forms one-third of the orbital border and the lateral wall of the orbit; the temporal surface forms a small part of the temporal and *infratemporal fossae*.

Types of Bones

The early fetal brain is surrounded by the *mesenchymal* "membrane". Subsequently, islets of mesenchymal membrane under the ventral surface of the brain are replaced by cartilage. In later fetal stages and early childhood, the cartilage is, in turn, replaced by bone. The bones that are formed incartilage are *endochondral*. In other parts of the *mesenchyman membrane*, bones are formed directly in it. These bones are membranous.

The endochondral bones include *the ethmoid*, *sphenoid* (body, lesser wings), temporal (petrous, mastoid), occipital, and inferior nasal conchae.

The membranous bones include the *frontal*, *parietal*, *nasal*, *vomer*, *lacrimal*, *maxillary*, *palatine*, *mandible*, *squamous part of temporal*, *squamous* part of occipital, greater wings and pterygoid processes of sphenoid.

The cranial bones are, in most part, flat, complex and very irregular. Regardless of their size, shape and complexity, all cranial bones include three layers: outer, middle, and inner:

The outer layer/lamina/table is made of thin, brittle, compact bone.
The middle layer/lamina/table/diploe is spongy with marrow and veins.
The inner layer/lamina/table is made of thin, strong, compact bone.

Types of Joints

The cranial bones articulate with one another at their borders by means of *synovial* joints or sutures to form the cranium.

The mandible articulates with the two temporal bones by means of *synovial* joints. Each of the other cranial bones articulates with many other cranial bones at their numerous borders by means sutures.

During fetal development, the adjacent border of cranial bones is smooth and widely separated by *fibrocartilage.* This *sutural* articulation not only allows cranial bones to expand their borders in all directions to accommodate the fast growing brain but also provides the flexibility of the cranium during birth. During infancy, the gap between the borders of cranial bones becomes narrower except at the corners of the parietal bones where the sutures remain widely separated. These wide gaps are called *fontanelles.* The anterior *fontanelle* is located at the intersection of the coronal and *sagittal* sutures. The posterior fontanelle is located at the intersection of the *sagittal* and *lamloid* sutures. The *anterolateral* or sphenoid *fontanelles* are located between the parietal bones and the great wings of the sphenoid bone. The *posterolateral* or mastoid *fontannelles* are located between the parietal bone and the mastoid process of temporal bones.

In adulthood, the sutures are marked by serrated border of adjacent bones which are tightly fitter together and inflexibly bonded by *fibrocartilage.* The suture are named after the bones which form them. For example: the suture between the nasal and frontal bones is *nasofrontal* suture. There are three exceptions, however:

The coronal suture is located between posterior borders of the frontal bone and the anterior border of the two parietal bones.
The *sagittal* suture is located between the adjacent border of the parietal bones.
The *lamdoid* suture is located at the posterior border of the parietal bones and the border of the *squamous* part of the occipital bone.

Cavities of the Cranium

The cranium consists of eight important cavities which provide essential support and protection of the brain and the organs of special senses. In addition, the nasal cavities and the oral cavity serve as the entrance of the respiratory and digestive systems, respectively.

The important cavities of the cranium and their contents or their roles are:

The neurocranium (1): for the brain
The nasal cavities (2): for smell and respiration

The orbital cavities (2): for sight
The auditory cavities (2): for sound and balance
The oral cavities (1): for taste and digestion

Major Passageways between Neurocranium and Viscerocranium

The brain communicates with the five organs of special senses through cranial nerves which traverse the *neurocranium* by way of the following passageways: canal, *canaliculus*, fissure, foramen (pl. foramina), hiatus, and meatus (pl. meati or meatuses).

Major Passageways for Cranial Nerves

Cribriform foramina: Olfactory neres (CN I)
Optic canal: Optic nerve (CN II), Ophthalmic artery
Superior orbital fissure:
- Oculomotor nerve (CN III)
- Trochlear nerve (CN IV)
- Ophthalmic division of trigeminal nerve (V^i)
- Abducent nerve (CN VI)
- Sympathetic nerves from superior cervical ganalion
- Ophthalmic veins

Foramen rotundum: Maxillary division of trigeminal nerve (V^2)
Foramen ovale: Mandibular division of trigeminal nerve (V^3)
Internal acoustic meatus:
- Facial nerve (CN VII)
- Vestibulocochlear nerve (CN VIII)

Jugular foramen (between Temporal and Occipital bones):
- Glossopharyngeal nerve (CN IX)
- Vagus nerve (CN X)
- Spinal accessory nerve (CN XI)
- Internal jugular vein

Hypoglossal canal: Hypoglossal nerve (CN)
Foramen magnum: Spinal cord, CN XI, Sympathetic nerves
- Vertebral arteries

Passageways for Branches of Cranial Nerves

Supraorbital foramen/notch: Supraorbital nerve (V^1)
Infraorbital foramen: infraorbital nerve (V^2)
Zygomatico-facial foramen: Zygomaticofacial nerve (V^2)
Pterygoid/Vidian canal: Pterygoid/Vidian nerve
Incisive foramen: Nasopalatine nerve (V^2)
Greater palatine foramen: Greater palatine nerve
Lesser palatine foramen: Lesser palatine nerve

Mental foramen: Mental nerve (V^3)
Stylomastoid foramen: Facial nerve
Petrotympanic fissure: Chorda tympani nerve

Major Passageways for Major Blood Vessels

Carotid Canal (temporal bone): Internal carotid artery
Foramen magnum (occipital bone): Vertebral artery
Foramen spinosum (sphenoid bone): Middle meningeal artery
Jugular foramen (temporal and occipital bones): Internal jugular vein

Major Fossae of Cranium

Intracranial Fossae

Anterior cranial fossa: Frontal lobes of brain
Hypophyseal fossa: Hypophysis/pituitary gland
Middle cranial fossa: Temporal and Occipital lobes of brain
Posterior cranial fossa: Pons, Cerebellum, Medulla oblongata

Extracranial fossae

Temporal fossae: Temporalis muscles
Infratemporal fossae:
- Temporomandibular joint
- Pterygoid muscles
- Mandibular division of CN V (V^3)
- Otic ganglion
- Maxillary arteries and branches
- Pterygoid venous plexus

Pterygopalatine fossae:
- Pterygopalatine ganglion, V^2
- Terminal branches of maxillary artery

Paranasal Sinuses: Frontal, Ethmoidal, Sphenoidal, Maxillary Sinuses

Falx cerebri and cerebelli: points of attachment:
- Crista galli of ethmoid bone
- Sagittal Crests on internal aspect of frontal
- Parietal

Occipital bones
- Internal occipital protuberance of occipital bone

Tentorium cerebelli: points of attachment
- Clinoid processes, dorsum sellae (sphenoid bone)
- Superior petrosal margin (temporal bone)
- Horizontal occipital crest (occipital bone)

7.2.4 International Mechanisms of Brain Injury Due to Impactive Forces

While we often picture the brain being injured as a result of the external force on the head, it is what happens inside the skull, which causes the "closed head injury." The term "closed head injury" means an injury to the brain where the skull is not broken or penetrated. While there are many complex interrelationships which explain the internal injury, the two most significant causes of injury to the brain are the "contact" of the head with a blunt object and the "inertia" which many occur as a result of a rapid acceleration or deceleration of the brain. The term "impact" and "shear" are also often used to differentiate the internal mechanisms of injury between the contact and inertial causes of injury.

In using the term "impact injury" it is not the impact with the head with something that is being described, but the impact of the brain with the hard, often sharp insides of the skull. The term "contact phenomenon" is used to describe the sequence of events which occurs when the energy of the impact of the head with something is transferred to the brain. These "contact phenomenon" include deformation of the skull and shock waves which emanate at the speed of sound from the point of impact throughout the brain.

Coup: Contrecoup Brain Injury

Injury from contact forces often occurs in two places – the site of the initial impact of the brain with the skull and the diametrically opposite part of the brain. This happens because of the rebound of the brain from the initial impact with the skull. To describe this phenomenon, the term coup and contrecoup are used.

These next three graphics were developed by Dr. Mariusz Ziejewksi, North Dakota State University, to illustrate the biomechanical calculations involved in an impact mechanism.

Diffuse vs. Focal Injuries

"Contact phenomenon," typically result in what is called a "focal" brain injury as opposed to a "diffuse" brain injury. The term "focal" is used to describe the situation where the pathology is concentrated or focused in a particular part of the brain. The term "diffuse" is used to describe the situation where the pathology is spread throughout the brain. Focal injuries are typically large enough that they can be identified "mascroscopically" (meaning without the use of a microscope) and diffuse injuries are typically microscopic. As conventional imaging techniques can only see macroscopic damage, only focal injuries can typically be identified by use of CT and MRI scan. Fortunately for acute care management, it is typically only focal injuries for which surgical intervention can make a difference in reducing secondary brain damage.

Unfortunately, difficulty in imaging the precise pathology and the lack of current surgical intervention for diffuse injuries, is far too often taken to mean that focal injuries are worse than diffuse injuries. In fact, the opposite is often the case.

As high as 50% of those in a coma, have diffuse injuries, that cannot be seen on a CT scan. A significant percentage of patients with severe focal injuries, have lucid intervals after their injuries, as opposed to those with severe diffuse injuries who rarely have a lucid interval. The effect of focal injuries while certainly lethal, are often reversible through surgical intervention. Intervention for diffuse injuries is minimal at present.

Diffuse brain injury in its severest forms, is a major cause of death and disability. A large percentage of those patients who are unconscious from the moment of impact, who do not experience a lucid interval and remain unconscious, vegetative, or severely disabled have suffered diffuse as opposed to focal injuries.

"Certainly the potential cascade of events that can follow the localized damage in focal injury is different from the more global changes that may result when the brain damage is diffuse. However, the pathophysiology of the two share many common events..." *Source*: Greenfield's Neuropathology, 1997, Arnold, p. 204.

Focal Injuries

Impact Phenomenon can result in the following focal injuries:

- Contusions on the surface of the brain
- Hematoma (a localized area of blood as a result of vessel leakage or bleeding)
  - Epidural (above the dura – a collection of blood between the dura and the skull)
  - Subdural (below the dura – collection of blood between the dura and the brain);
  - Intracerebral (a collection of blood with in the brain)

  The dura is the protective sheath around the brain, between the brain and the skull.
- Hemorrhage
  - Epidural, subdural or intracerebral.
- Edema – excessive water accumulation resulting in swelling.

Diffuse Brain Injury

Diffuse brain injury can exist in four principal forms, although only three of these forms involve patients who have any chance of survival. The most severe diffuse brain injury is diffuse vascular injury, which almost always proves fatal in a short time after the injury. The other three types of diffuse injury are:

- Diffuse axonal injury
- Diffuse hypoxic/anoxic/ischemic injury
- Diffuse swelling

Of these three, diffuse axonal injury is the one that is gaining the most attention. Part of the reason for the focus on the axonal injury is undoubtedly its relationship in its less severe forms, to the sequelae of subtle brain injury. The consequences of diffuse hypoxic/anoxic/ischemic brain injury are often catastrophic, although the degree to which nonsevere occurrences of these phenomenon result in subtle sequelae is an area that future research may shed light. Likewise, the effects of diffuse brain swelling can span the spectrum of severity, with little being understood about the interplay of subtle changes upon long term symptomatology.

The problem in understanding the nature of the pathology of diffuse injuries, is that as these injuries typically occur on the cellular level, making them far too small to be seen except under a microscopic. A microscope can only be used to examine cells of the brain after death. Thus, it is a long and arduous process to learn about the mechanism of these various types of pathologies. This is particularly true in those that do not result in severe injuries, because conclusion does not result in death.

Advances in functional imaging have increased the speed at which neuropathologists can learn about the subtly injured living brain and it is hoped that in the next ten years, much will be learned about these pathologies and how to prevent their potentially disabling effects.

Injury Assessment via Scanning Techniques Assisting Finite Element Modeling

CT and MRI are volumetric scanning techniques widely used in medicine as well as in many nonmedical settings, such as nondestructive testing and quality control in manufacturing applications.

X-ray computed tomography (CT or CAT for computer assisted tomography) involves an X-ray source and detector deployed on opposite sides of the specimen or patient. This equipment is arranged in such a way that the X-ray beam can be rotated about one axis while the specimen is translated parallel to the axis. In this way, a sequence of transverse cross-sections are obtained with X-ray images of each section digitally recorded from many angles. Subsequently, algorithms derived from a mathematical procedure called tomography are applied to reconstruct a three-dimensional matrix of values representing the X-ray transmission properties in the volume occupied by the specimen.

The following image is a Slicer Dicer rendering derived from the CT sample data. It includes a projected volume (maxima) rendered on the background surfaces and an isosurface delineating the skull. A cutout has been used to cut away a portion of the skull and reveal its interior.

Descriptions. CT scanning – X-ray CT scanning involves passing a narrow beam of traditional X-rays through the brain of a person lying in a scanner 4. This beam of X-rays is sent out by an X-ray tube that rotates around the head, and the X-rays are detected on the opposite side of the person's head by X-ray sensitive detectors. The amount, type and position of substances that are in the scanner, between the tube and the detector are then reconstructed using computers, into an axial image of the brain (hence the name computerized, axial tomography or CAT scan, or CT scan for short). Thus, CT scanning can be thought of as a whole series of chest X-rays taken at every angle around the body and then combined in a computer to form an image of whatever is in the machine (a head or body or even violins or mummies). Thus, CT scanning has associated with it many of the limitations of traditional X-ray imaging. For example, CT's involve radiation equivalent to many traditional X-rays so there are limits to the total number of scans that can be performed safely within an individual. Also, CT scanning displays very prominently those things which most deflect the X-ray, such as bone. While this makes CT scanning the imaging method of choice for examining skull fractures, the presence of lots of bone at the base of the skull make CT scans very difficult to read for the cerebellum and base of the skull. However, CT scanners are very common in the US and this is likely one of the least expensive imaging modalities.

MRI: Basic Principles. In contrast to CT, which involves traditional radiation, magnetic resonance imaging uses an entirely different set of principles to obtain an image, although in the end a computer reconstructs the image just as in CT. In fact all of the imaging advances discussed in this issue of primary psychiatry would not be possible without computers.

To see how any MRI image is made, it is important to understand three fundamental steps: (1) magnetic field, (2) resonance, and (3) relaxation.

Magnetic Field A person is placed with half to two-third of their body lying in a tube inside in a very strong magnet. Magnetic elements in a person's body – ones having an odd number of protons or neutrons such as 1H, 31P, and 23 Na – line up in the direction of the main magnetic field which is usually along the line from the person's foot to head.

These elements spin around their axes like the earth spins around its axis and also rotates or processes around the z-axis like the axis of a spinning top rotates as it starts to wobble. The rate at which an atom rotates around the z-axis is called its precession frequency and it is proportional to the strength of the magnetic field. The precession frequency is specific for each atom and the strength of the magnetic field it experiences which in turn is affected by the atom's particular position in a molecule. Thus, 1H will have a different precession frequency from 23Na, and 1H in water will have a different precession frequency from 1H in lipids. Also, while 1H atoms in water might be spinning at the same precession frequency, they may be doing so out of phase. For instance, 1H atom in water may be like a clock keeping US eastern time whereas another may be like a clock keeping US pacific time, as they both

spin at the same rate, they will always remain 3 h apart in time. This concept will become important later when talking about 12∗ relaxation.

Resonance. Brief magnetic pulses flip only specific magnetic elements in certain molecules onto their sides (into the *xy* plane, for example). In order to be flipped, these elements must have been spinning at frequencies that resonated with the magnetic pulse. This is analogous to singing in a bottle at just the right pitch (frequency) to make bottle vibrate (resonate). Importantly, all the atoms become in keeping with the brief magnetic pulse as they are flipped. This means that they are all keeping eastern time. It is in this state that they produce a signal in an antenna in the scanner tuned to their precession frequency, much as a rotating magnet induces a current in a loop of wire nearby.

Relaxation. After the magnetic pulse has been turned off , the "excited" flipped atoms gradually return (relax) to their original position after the magnetic pulse has been turned off, with the signal decaying exponentially with a rate characterized by two constants, T1 and T2 . Several different ways of measuring image signals are used to take advantage of the different characteristic relaxation rates of different tissue. T1 – weighted images reflect the recovery of the recovery of the original signal as the flipped atoms return to baseline from the excited state. In other words, their appearance is dominated by the signal intensity along the *z*-axis(the direction of the main magnetic field. T2* weighted images reflect the signal remaining in the exited state as the flipped atoms return to baseline and the degree to which spins are still in phase. In other words, T1* measures the net remaining signal intensity in the *xy* plane. Decreases in T2* signal are due to dephasing of the flipped atoms. This means that they again lose their synchrony for keeping time in the same time zone. Dephasing is generally caused by two factors: (1) intrinsic magnetic inhomogeneity of the tissue being imaged and (2) extrinsic magnetic inhomogeneity in the main magnetic field (which is never completely uniform). Part of the intrinsic magnetic inhomogeneity is due to nearby atoms, and atoms with magnetic properties in the imaged tissue like Fe in deoxyhemoglobin. These exert different pulls on flipped atoms depending partly on how close a flipped atom is. These differences in pull cause the flipped atoms to dephase and lose T2* signal. Dephasing caused by the deoxyhemoglobin is the main factor causing signal intensity variations in the BOLD – fMRI techniques.

In conventional structural MRI, the machine is tuned to resonate and thus flip 1H atoms, particularly the 1H atom of water which is the most abundant 1H –containing molecule. The image is created by manipulating the 1H atoms in their excited "flipped" state. Contrast is created because the 1H atoms in grey matter, white matter and cerebrospinal fluid have different relaxation rates, characterize by T1 and T2.

Numerical Modeling of the Human Head

Introduction Head injury is the most frequent severe injury resulting from traffic accidents. Head injury mechanism is difficult to study experimentally

due to the variety of impact conditions involved, as well as the ethical issues, such as the use of human cadavers and animals. Finite element modeling is a comprehensive technique through which human head impact tolerance can be studied. A representative finite element human head model would allow the assessment of the injurious effects of different impact conditions and enable the development of enhanced head injury and protection criteria in the automotive environment.

The section deals with the development of a three-dimensional finite element (FE) model based on the digital data set from the head section. The fresh CT scans were used for the skull model and the MRI images for the brain model. The first approach to validate the model and to investigate different boundary conditions by using experimental data are shown.

Head injuries are related to tissue material failure, characterized in some form of stress, strain or deformation. Finite element analysis can provide stress, strain and/or deformation distributions across and within the different tissues for a given biomechanical input, such as head motion or head impact. By identifying magnitudes and location of these quantities, at which the tolerance level of the tissue is exceeded, provides the link between the external mechanical quantities and the internal injuries. Finite element models are repeatable and reproducible, and simulations can be seen as surrogate experiments without biological variability.

Geometry. The geometry of the human head has initially been determined by CT, MRA and sliced color photos. The geometric data are generally available through the visible Human Database with 0.3 mm incrementation in the coronal plane. It is used to generate a three-dimensional geometry. Points on the boundary of the different tissues are determined and used to determine the lines and surfaces that define the geometry of the scalp, the skull, the dura, the brain tissues, etc. Hereby a realistic skull thickness variation was achieved which is significant. The variations include the extension from the thick and porous frontal bone to thin temporal bones.

Crashes due to accidents have been simulated through the model of the human head in which the brain is affected due to impact.

The size of the human head varies within a large span. The parametrised geometry of the model utilizes a tool for studying the effects of these variations. A study has been conducted on the dependency of the coup and contrecoup pressure the overall size (length, width and height) for a frontal impact to the head. The head length, width and height were scaled to fit the percentiles according to statistical data. It was found that the intracranial pressure at the opposite side of impact (contrecoup), decreases with increasing overall size of the head.

A model is created based on images obtained from Computer Tomography (CT) and Magnetic Resonance Tomography (MR). The biomechanics of the human head can be seen as a brain movement within an externally loaded skull and this gives a complex three dimensional dynamic boundary value problem. These internal biomechanical responses of the brain cannot be completely

measured by experimental techniques. The biomechanics of diffuse axonal injury (DAI) and contusions (coup and contrecoup) can be seen in Plates 7.10 and 7.11.

Finite Element Analysis

The impact dynamic hybrid finite element analysis has been followed for modeling of head of a female as shown in Plate 7.8, Program BANGF-II is used again. The anatomical image data were transformed into a 3D finite element model. It is expected that the model will be able to predict the risk of head injuries in a crash event. It will further help understanding injury mechanisms and quantify mechanical parameters related to a specific impact event so that injury tolerances can be formulated. The same methodology can, with few necessary adjustments, be adopted for other kinds of impact and with different head model conditions. Owing to complex shape of the skull, the FE models were constricted using VHM, the fully automatic voxel based hexahedron meshed creating 20-noded Isoparametric Elements. The grid size may either be adapted to the actual scanning resolution or may be reduced by scaling the digital model. In order to reduce the number of elements in our three-dimensional FE model, we had to scale down the binary volume data by a factor of five resulting in an element size of roughly $4.5 \times 4.5 \times 5.0\,\text{mm}^3$. Since a traditional VHM approach leads to models with edged surfaces an interpolation scheme was incorporated using nodal averaging, which resulted in an FE model of the skull with smooth surfaces as depicted (Plate 7.8). Plate 7.10 shows the actual brain with finite element modeling, The brain enclosing into the skull by using finite element model is shown in Plate 7.11 which indicates the interior of the skull model. The same steps have been taken to generate the FE model of the brain using the X-ray and MRI data (Plates 7.11–7.16).

Criteria for input data

- Material properties for skull bones (Table 7.3)
- CT scaled = 0.9 mm pixel size
- Pixel matrix = 512×512
- Skull three-dimensional mm voxel size = 782,910 triangular elements with 421,420 nodes
- Skull model = 14,960 with 20,900 nodes 20-noded isoparametric elements
- Brain model = 10,280 with 12,152 nodes 20-noded isoparametric elements
- The motion sequence = 10 ms for Impact simulation
- Mass of brain elements = 4,400 grams center 2.10 cm in the region of corpus callosum with sagittal symmetry
- Human brain mass = 1,300 grams

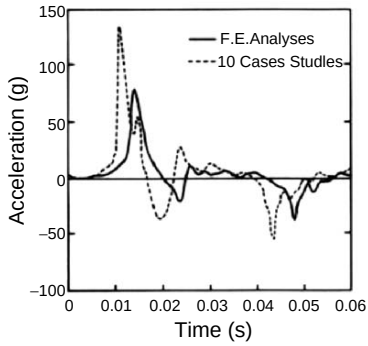

(a) Acceleration Time Curve (3D)

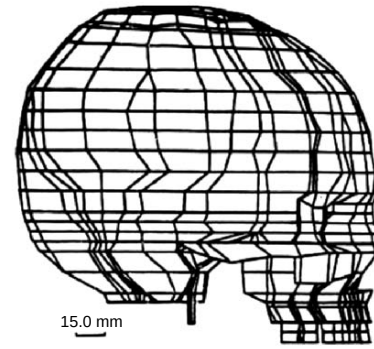

(b) Finite Element Mesh Scheme

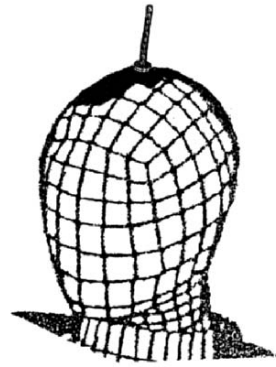

(c) Coarse F.E. Scheme (2D)

Plate 7.8.

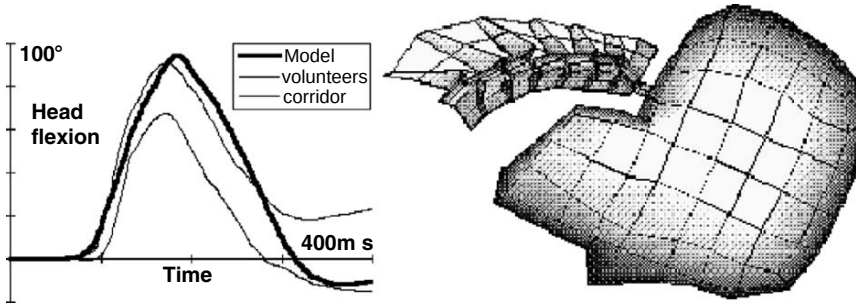

Plate 7.9. Dynamic model of the head-neck complex

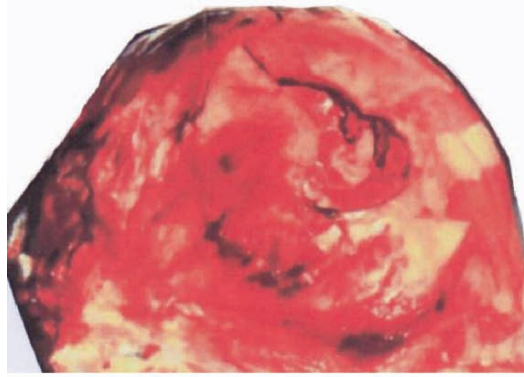

Actual Brain

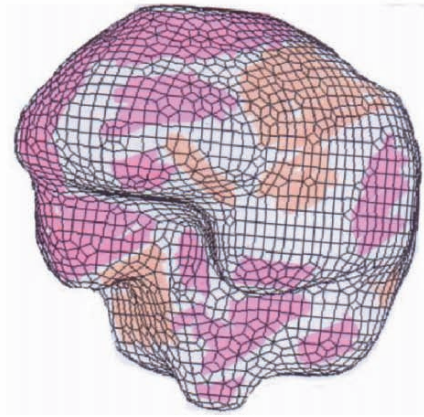

Finite Element Brain Model

Plate 7.10. Brain injury

- Designated CSF space = 158 ml
- Force corresponding

  To occipital = 8,000 N
- Areas of occiput = 26.7 cm^2 (Posterior – Anterior Directions)
- Poisson ratio brain material = 0.499
- Peak pressure (negative) = 100 KN m^{-2} at 1.6 ms (positive) = 95.2 KN m^{-2}
- Impact velocity V_{ij} = 10m/sec
- Loading and rebound phases ≈ 400 ms
- V_{v}, velocity of the vertebra

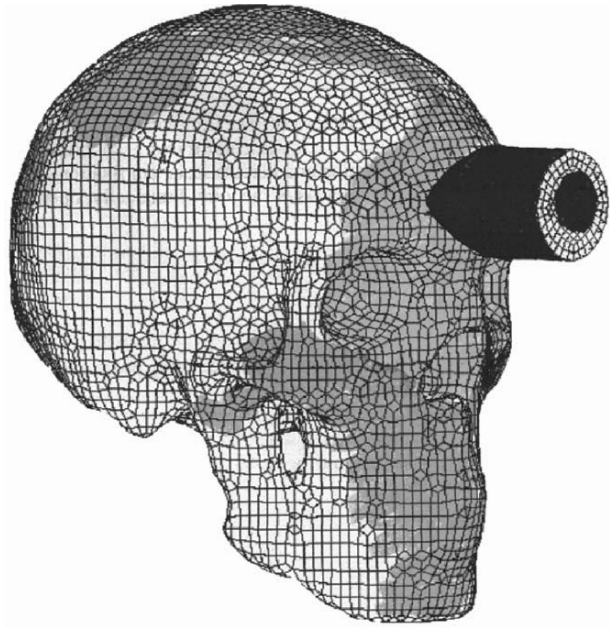

Plate 7.11. Impact with sharp steering arm at the forehead level

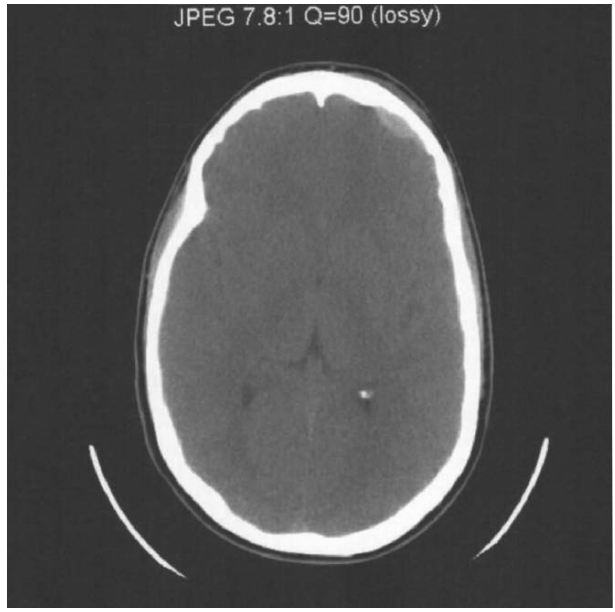

Plate 7.12. Scan focuses on the brain

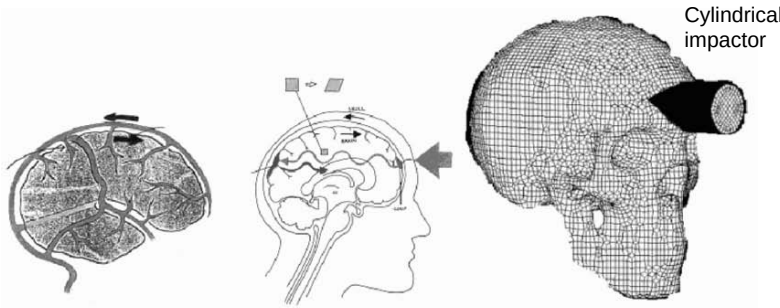

A Finite Element Model of the Head

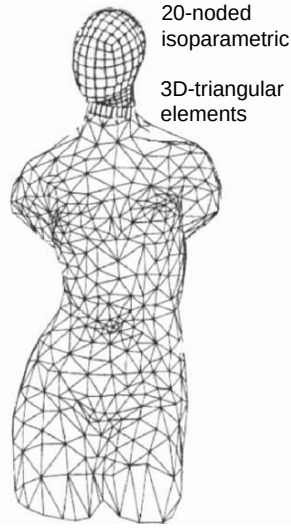

Body Influences

Plate 7.13. Female body

7.2.5 Dynamic Model of the Human Head: Neck Complex

Introduction

This study also includes the development and validation of a numerical three-dimensional (BANGF-II) dynamic model of the head–neck complex. This model is a part of a human body model which may help to better understand the car occupant kinematics during impact and thus improve car design to prevent injuries.

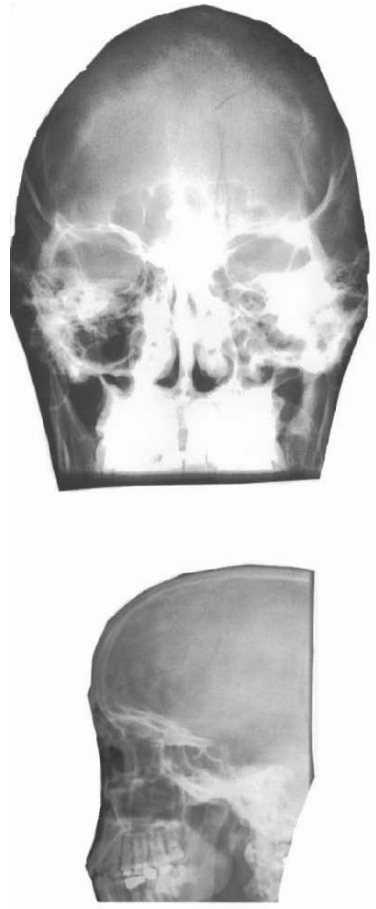

Plate 7.14. X-ray predicted damage due to front impact

Methods

Each vertebra from T1 to C2 and the head were considered as rigid bodies. Only the functional geometry was taken into account (articular facets, vertebral bodies, ligaments insertion). Between the vertebrae, intervertebral discs were modeled as 8-noded isoparametric elements, ligaments and muscles were combined as spring-damper elements and articular facets as contact interfaces. The upper cervical spine was globally modeled using two spherical joints. Mechanical properties were introduced when available from literature or were assessed using a parameter identification process. Mass and inertia characteristics were taken from the literature. A reference is made to the appendix and materials in this chapter.

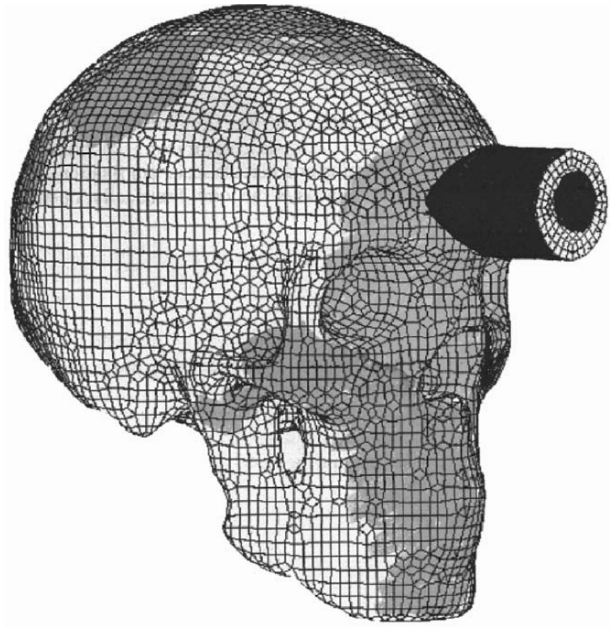

Plate 7.15. Impact with sharp steering arm at the forehead level

(a) **(b)**

(a) Damage due to front and Back impact

(b) Stress Trajectory of skull with high Lights of damage, BANG-F modelling

Plate 7.16. Skull damage scenario

Table 7.3. Material properties of skull bones

material	density (δ,w)	modulus of elasticity ($\mathrm{KN\,m^{-2}}$)	details on Poisson ratio (ν)
dura membrane	1.134	31500	0.45
brain	1.040	66.7	0.499
skull	1.420	4.46×10^6	0.21
vertebra	1.410	4.46×10^6	0.21
cord	1.040	66.7	0.4999
jaw	1.410	4.46×10^6	0.21

Where both head and neck are concerned, frontal, lateral, and oblique impacts were considered. The velocity of the vertebra V_v has been used as an input for the simulation of impacts. Linear acceleration of the head anatomical center, head angular accelerations and rotations. The head displacements relative to head anatomical center also related to the velocity of the vertebra are to be computed.

The model response of frontal, lateral, and oblique impacts was verified using the head–neck responses of human volunteers subjected to sled acceleration impacts performed at the Naval Biodynamics Laboratory. The velocity of vertebra T1 was used as an input to the model to simulate the impacts. The model responses were compared to volunteer response corridors for: linear accelerations of the head anatomical center, head angular accelerations, head rotations, and displacements of the head anatomical center relative to T1 vertebra.

Results and Discussion

A good correlation was obtained between model responses and experimental corridors for all impact directions and throughout the duration of the impact (loading and rebound phases up to 400 ms).

The main parameters, concerning behavior of the head, founded during the identification process were: interspinous ligament and occipitoatlantal joint in flexion extension for frontal impact; facet joints and atlantoaxial joint around odontoide process for lateral impact; and those from frontal and lateral in oblique impact (Plate 7.9).

Conclusion

The model response to frontal, lateral, and oblique impact agreed with volunteer responses. Thus, kinematic response of the head relative to the torso is well simulated and main parameters were identified. Further research work will be focused on experimental testing on cadavers in rear-end impact and modeling of injury mechanisms.

7.3 A Relevant Engineering Analysis of the Traumatic Knee Injuries

General Introduction

The knee joint is the largest and most complex joint in the human body. The joint capsule and ligaments, which provide structural stability to the knee, are particularly vulnerable to injury by large moments that can be created through the forces acting along the long lever arms of the lower limb. Thus, it is not surprising that the knee is one of the most frequently injured joints. An injury to the knee, such as disruption of the anterior cruciate ligament (ACL), can result in an extensive disability because this injury may alter normal knee kinematics and therefore locomotion. An extensive background in biomechanics or mathematics is not required to understand the fundamental mechanical principles governing the knee joint. Knowledge of knee biomechanics provides an essential framework for understanding the consequences of injury and joint disorders; it aids in the intelligent planning of surgical procedures, serves as the basis for developing objective rehabilitation programs, and describes the effects of different types of orthoses on the knee joint.

The knee joint comprises three independent articulations, one between the patella and femur and the remaining two between the lateral and medial tibial and femoral condyles. The patellofemoral articulation consists of the patella, which has a multifaceted dorsal surface that articulates with the femoral trochlear groove. The tibiofemoral articulations consist of femoral condyles with saddle-shaped tibial condyles and interposing menisci. The posterior aspect of the femoral condyles is spherical, whereas the anterior aspect of the femoral condyles is more flat. Thus, in extension, the flat portion of the femoral condyles is in contact with the tibia, and in flexion, the spherical portion of the femoral condyles is in contact with the tibia.

The knee joint may appear to function as a simple pinned hinge (ginglymus) with flexion–extension rotation the only apparent motion between the femur and tibia. The motion characteristics of the knee joint are extremely complex, however, requiring a full six degrees of freedom (three translations and three rotations) to completely describe the coupled, or simultaneous, joint. Finite Element Analysis is required to solve such complex problems.

Experimental Studies of the Entire Knee

ASBM approach for knee joint has recommended the following techniques.

Flexibility Approach

This approach involves observing or measuring the displacement due to an applied joint load; a ligament is then cut, and the procedures is repeated. The relative difference is displacement is then used to establish the importance

of that ligament. This method is analogous to clinical laxity examinations (i.e., Lachman's test), in which the clinician applies a load and estimates the resulting joint displacement. This technique is useful in evaluating the sensitivity of knee laxity tests to injuries created in human cadavers. A drawback of this technique is that the difference in the behavior of a knee joint before and after excision of a ligament does not necessarily indicate hat the cutting of the ligament was responsible.

Stiffness Approach

This approach establishes the role of a particular ligament by applying a predetermined displacement while simultaneously measuring the load applied to the knee joint, cutting the structure under investigation, and repeating the test while documenting the decrease in load that results. This methodology is useful for determining what motions are resisted by each ligament and the relative importance of the structure.

A comparison between methodologies reveals that the stiffness approach produces results independent of the order in which the ligaments are sectioned and therefore is a more direct approach, whereas the results from the flexibility approach are governed by the order of ligament cutting. Thus, the outcomes of these later studies may be difficult to interpret.

7.3.1 Experimental Studies of Individual Ligaments

Anatomic Observation

The clinical approach is to infer a ligament's function from its anatomy. The important information that can be obtained is anatomic location of the ligament attachment points, orientations of major fiber bundles, and size (length and cross-sectional area). Important early observations were made by Hughston and coworkers, Slocum and colleagues, and Kennedy and associates. Careful dissection techniques have been employed by a number of workers to improve our qualitative understanding of the knee ligaments. More recently, the cross-sectional areas of the ACL, the posterior cruciate ligament (PCL), and the meniscofemoral ligaments were reported at four flexion angles.

7.3.2 Force Measurement of Ligaments

Measurement of ligament or tendon force continues to be one of the biggest challenges in orthopaedic biomechanics. To meet this challenge, Salmons introduced the buckle transducer. The buckle transducer is a structure containing a beam over which the ligament is looped to create bending of the buckle frame. The beam is attached separately, and therefore transverse cutting of the ligament is not required. Lengthwise incisions are required, however, disrupting many ligament fibers and altering the normal function of the ligament

by dissociating one group of fiber bundles from another. Salmons and other investigators have applied this technique to various knee ligaments. This approach is limited to in vitro applications in which a knee ligament is instrumented with the transducer and the knee joint is loaded. The output from the buckle transducer is then directly recorded. After the tissue is tested in situ, it is dissected free from one of its bony attachments so that a known load can be applied to the tissue–buckle system and a calibration of the gauge–soft tissue system can be made. By use of this approach, the load can be determined for the tissue in situ. This technique cannot be used for in vivo testing.

7.3.3 Strain Measurement of Ligaments

Several investigators have measured ligament displacement, enabling the calculation of strain pattern, to understand the effect of knee joint position and muscle activity on ligament biomechanics. Most of this work has been carried out in vitro, and the results are conflicting.

Validation of the Ottawa Knee Rule in Children

Study objective: The main objective of this study was to determine the sensitivity and specificity of the Ottawa Knee Rules when they were applied to children. The secondary objective was to determine post hoc whether use of the rules would reduce the number of knee radiographs ordered.

Methods

This prospective, multicenter validation study included children aged 2 to 16 years who presented to the emergency department with a knee injury sustained in the preceding 7 days. Children were assessed for the variables comprising the Ottawa Knee Rules, and physicians ordered radiographs at their discretion. A positive outcome was defined as any fracture. A negative outcome was defined as children who did not have a fracture on radiograph or, if no radiograph was obtained, were asymptomatic after 14 days.

Results

A total of 750 children were enrolled. The mean age was 11.8 ± 3.1 years, and 443 (58.7%) were male patients. Seventy children had fractures. Radiography was performed for 670 children, whereas 80 children had only a structured telephone interview. The Ottawa Knee Rules were 100% sensitive (95% confidence interval [CI] 94.9–100%). Only 460 children would have required a radiograph if radiographs had been performed according to the Ottawa Knee Rules, which would have resulted in an absolute reduction of 209 (31.2%) radiographs (Plate 7.17).

Plate 7.17. Knee injuries-X-ray

Conclusion

The Ottawa Knee Rules are valid in children and have the potential to decrease the use of radiography in children with knee injury. [Ann Emerg Med 2003; 42:48–55]. The knee was defined broadly as the patella, the head and neck of the fibula, the proximal 8 cm of the tibia, and the distal 8 cm of the femur. This study was approved by the institutional review board at each of the participating centers. Informed written consent was obtained from all parents or legal guardians.

7.3.4 Finite Element Model of the Knee Joint

A complete detailed procedures are given about the FE technique and solution methodologies. The finite model includes:

- Biphasic behavior of the articular cartilage and the meniscus
- Transverse isotropic behavior of the meniscus realistic stiffness distribution in the articular cartilage void ratio dependent permeability
- Contact between the meniscus and the two articular cartilage layers
- Large deformations

Three-dimensional FE modeling is a useful tool for understanding of the stress distributions within articular cartilage in response to external loads

and investigating both the prevention of injury and the pathological degeneration of the joints. Various computational models of the human knee have been constructed. However, more accurate cartilage models are required to enable reliable predictions of stress–strain distributions within the cartilage. MR imaging provides multiplanar and three-dimensional image data with high spatial resolution. It is therefore feasible to construct three-dimensional FE models using MR images of the knee joint. However, the processing of MR images, either by manual digitization or by the threshold method, might cause certain variations in cartilage thickness. This paper investigated the effect of thickness variation of the cartilage on contact stress analysis when the knee is subjected to axial compressive loads.

Procedures

Magnetic resonance images of a human cadaveric knee specimen in the sagittal plane were obtained with the knee at full extension position. The scan consisted of 128 parallel digital images with a resolution of 512×512 pixels. The contours of the femoral and tibial cartilage were manually digitized data was then used to construct the inner and outer surfaces of the cartilage. The 3D cartilage thickness was defined as the shortest distance from one point of the outer surface of the cartilage to the inner surface. Solid models of the cartilage were then constructed from the inner and outer surfaces of the cartilage.

Data Input

Program BANGF-II results have been tested with MSC/Patran software and they are in good agreement. A three-dimensional cartilage model of the knee has been constructed using the mean digitized contours. All other data give per materials properties are still valid for the knee analysis, in addition the following are included in the input data both for the femoral and tibial cartilage for short- and long-term response to functional loads

F = axial compressive load = 400 N
$E = 5\,\mathrm{MN\,m^{-2}}$
$\nu = 0.45$
U = frictional coefficient = 0.02

material property	value
elastic modulus of cortical bone	15,000 MPa
elastic modulus of cancellous bone	456 MPa
elastic modulus of disc	1.8 MPa
Poisson's ratio of cortical bone	0.81
Poisson's ratio of cancellous bone	0.21
Poisson's ratio of disc	0.40

solid elements: isoparametric and nodded elements = 990 disc for artificial, implant = 750.

Results

Results are shown in Plates 7.18–7.27.

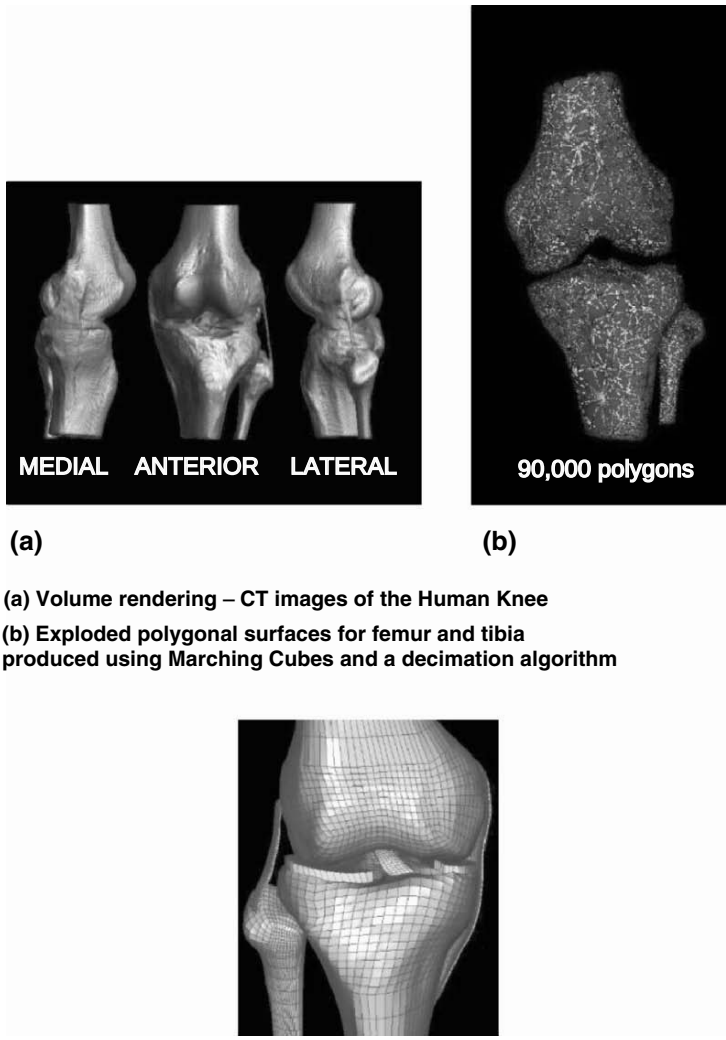

Plate 7.18. Three-dimensional simulation of the human knee finite element modeling

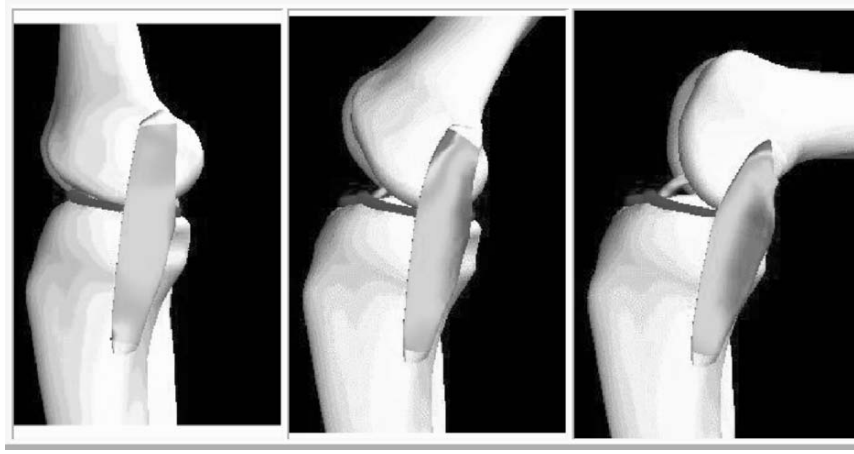

Finite Element Simulation of Knee Flexion

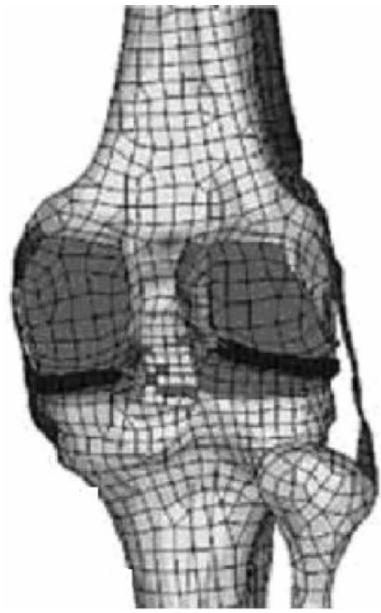

View of ligamentous LLMS knee joint, whole model overview
Finite Element – cum – Patran Modelling

Plate 7.19.

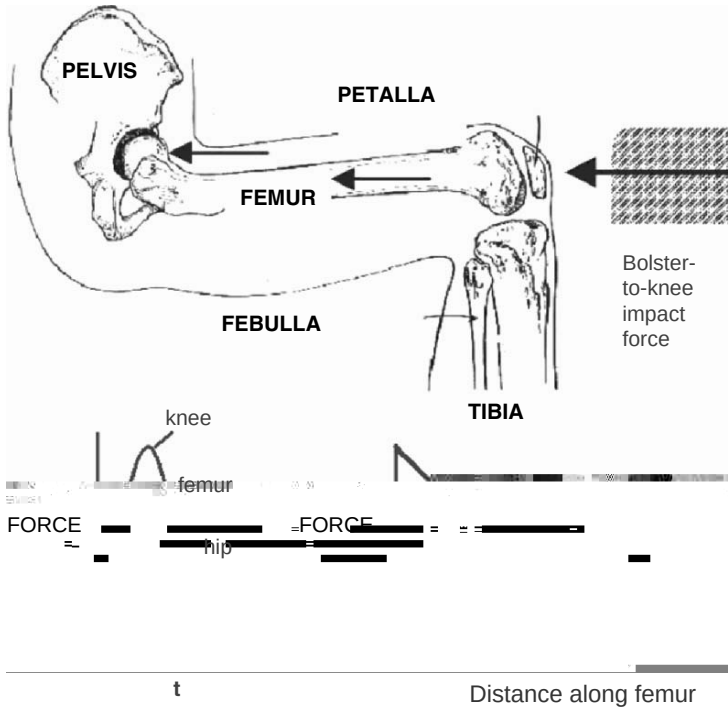

Forces applied at the knee is transmitted through the thigh and to the hip

Plate 7.20. Frontal crashes

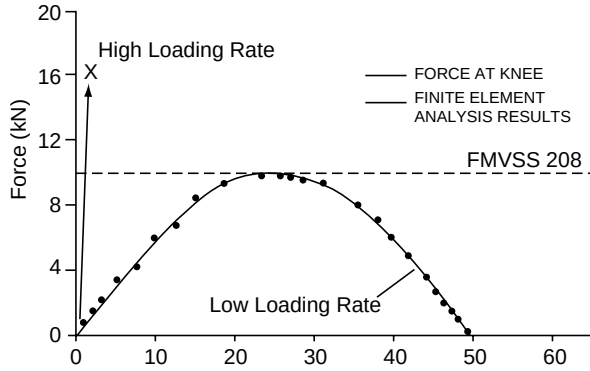

Effect of join compliances on short-and long-duration loads (Knee Impact Test)

Plate 7.21.

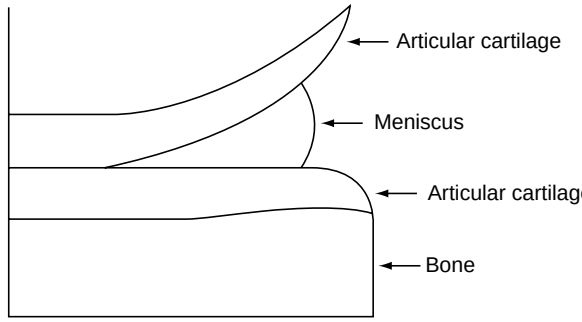

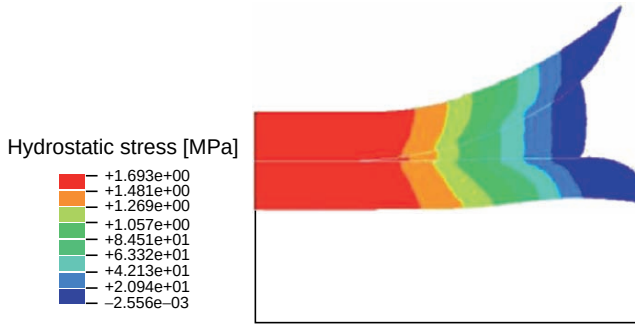

Hydostatic stress in articluar cartilage during heel-strike of the 14th gait cycle

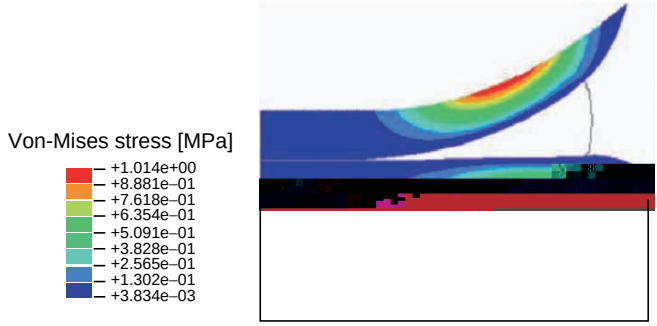

Von-Mises stress in articluar cartilage during heel-strike of the 14th gait cycle

Plate 7.22.

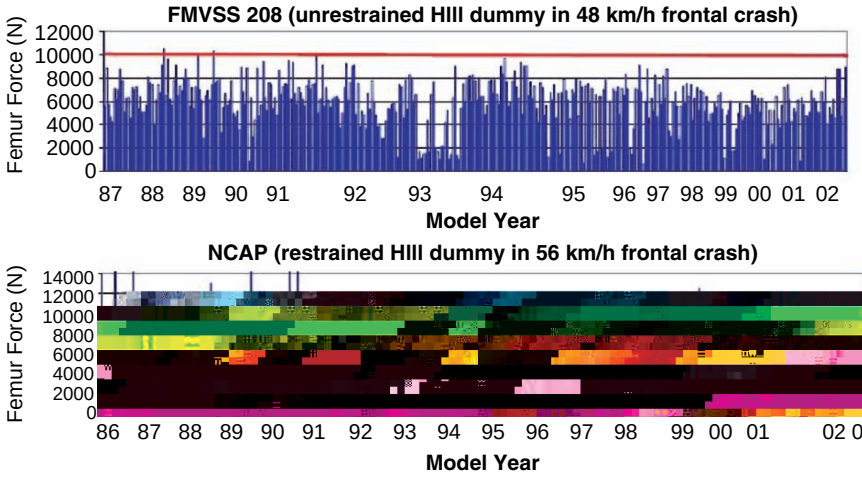

Plate 7.23.

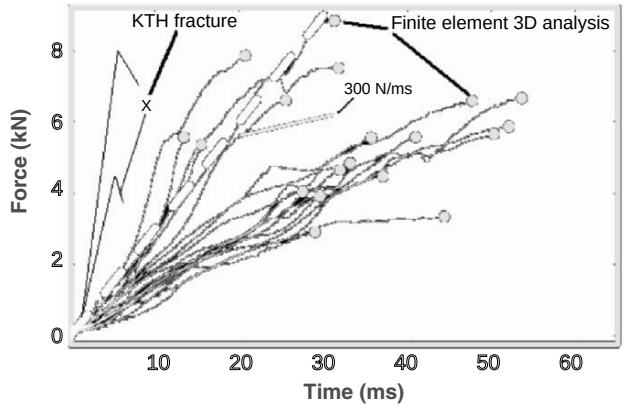

Stiffness of Human Cadaver Knee/Femur complex at Loading Rates in Previous Studies

Plate 7.24.

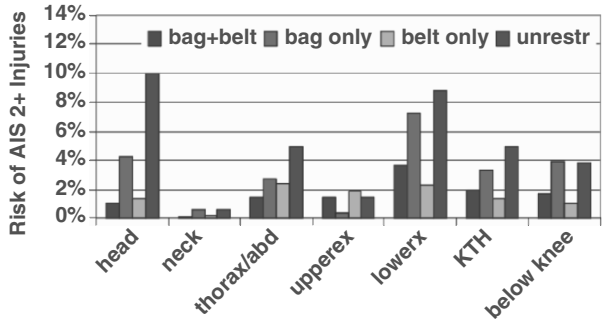

Plate 7.25. Risk of AIS 2+ injury in different restraint environment

7.4.2 Extraction of the Curve Parameters

Reconstruction of the Back Surface

Through a method based on structured light we obtain a reconstruction of the back surface by means of the deformation of a known structured pattern that is projected over the objects in the scene (object grid). So, we can obtain the three-dimensional position points of the object surface and make the correspondence between points or regions in smooth surfaces as it is the case of human backs.

In order to establish the deformation, and in addition to the object grid, the utilized procedure requires the digitization of the images of the grid projected on a flat surface (screen) placed, respectively, behind the object (back grid), and in the front of the object (front grid). This method allows to achieve the correspondence of the grid nodes on the three images (back grid, front grid and object grid) and to obtain the values of z (depths) for the nodes in the object grid. This procedure needs to be made just once for each setup for calibration purposes.

In the surface reconstruction phase, we analyse the list of the nodes in the object grid and calculate the co-ordinates of the intersection points of the straight pattern lines for the front grid and back grid images. This way, we get the positions (x, y, z) of the grid nodes as they are projected on the object and we can build a depth map for he grid nodes on the surface of the human back. The rest of points on the surface are reconstructed by a parametric approximation. The evaluation of the errors during the measurement process have been estimated in less than 4%.

Spine Curve Positioning on the Surface

Once we have the back surface depth map, the objective is to obtain the curve that passes over the vertebrae beneath the skin. Two data sources are utilized to obtain this spine curve.

1. Locate on the back surface the verebral spinous processes, from C7, also named the prominent vertebra, to the last lumbar vertebra L5.[2]
2. The study of the shape of the spine curve in X-ray images. In this case, we have a real knowledge about the displacements of the vertebrae and their rotations through the projection of the vertebral pedicles. Also, we can locate a center point for each vertebra in the radiograph and, by means of an alignment process, a transformation of scale, rotation, and translation

[2] The vertebrae are enumerated from the head to the hip with the following sequence: Cervical (C1...C7), thoracic or dorsal (D1...D12) and lumbar (L1...L5). The vertebrae C7 and L5 are the extremes of the spine curve considered. Thus, only thoracic and lumbar zones are considered in this work can be positioned with an accuracy of ± 5 mm.

is made to put the points of the spine shape in the X-ray image over our depth map.

7.4.3 Study of the Spine Curve in Three Dimensions

The parameters of the curve are essentially to be found considering both the front and sagittal planes. Generally the cobb angle is of 24° and the lumbar cobb is 12°. The curvature K and the torsion T must have peaks values. If the two peaks that appear in torsion, imply a high rotation in the region of the curve. A curve fitting technique is applied to determine accurately the curvature in three-dimensional which is needed for the finite element analysis.

$$K = \frac{\partial \eta}{\partial s}; \quad \tau = \frac{\partial p}{\partial s},$$

where s is the length, η and ρ the angle variations of the vector t, the tangent vector, and b is the binormal. The representation of t, g, b, and η are the controlling points of the spinal curve. The reader must be aware of vector algebra and is not repeated here in. However, the true geometry is necessary for the correct evaluation finite element results.

Finite Element Analysis

Background

Increases in fracture incidence are generally accepted as the consequence of the decrease in overall vertebral strength that occurs with aging. Since the overall strength of the vertebral body undoubtedly depends on the structural contribution of all of its components, understanding their relative roles and relevance to age-related changes is helpful in assessing the effect of any medical intervention on fracture risk. Despite its importance, results from several studies, both by experimental and analytical means, have supported no consensus.

The objective of this study is to investigate, using an anatomically accurate finite element model of a vertebrae unit, the relative roles of the cortex and centrum in vertebral load carrying capacity and how those are influenced by such parameters as loading conditions and vertebral material and geometric properties.

Methodology

Finite Element (FE) Model Description. The model consisted of three lumbar vertebral bodies, through and the two inter-vertebral discs that connect them. Since the focus of this study was on the load sharing within the vertebral body, the posterior elements and their effects were neither included in the model nor

accounted for. Also the vertebral ligaments are included in FE model with the participation of pure compressive loading.

The vertebral endplates and cortex were modeled using three-dimensional isoparametric four-noded shell elements. The trabecular centrum, annulus fibrosus, and nucleus pulposus were modeled using three-dimensional isoparametric eight-noded solid elements. The entire model was represented by about 44,000 nodes and 5,000 elements. All vertebral regions, except the centrum, were assigned isotropic material properties. The centrum was modeled using transversely isotropic material properties. The finite element mesh generation of hand-wrist/fingers is shown in Plate 7.29. The finite element model and baseline material properties are shown in Plate 7.30 and Table 7.4.

All simulations were performed using ANSYS and Patran software's including pre- and postprocessing.

Parametric Studies

Loading Conditions. Two idealized load cases were analyzed. The first was a physiologic condition simulating a person lifting a 4 kg mass. The second was

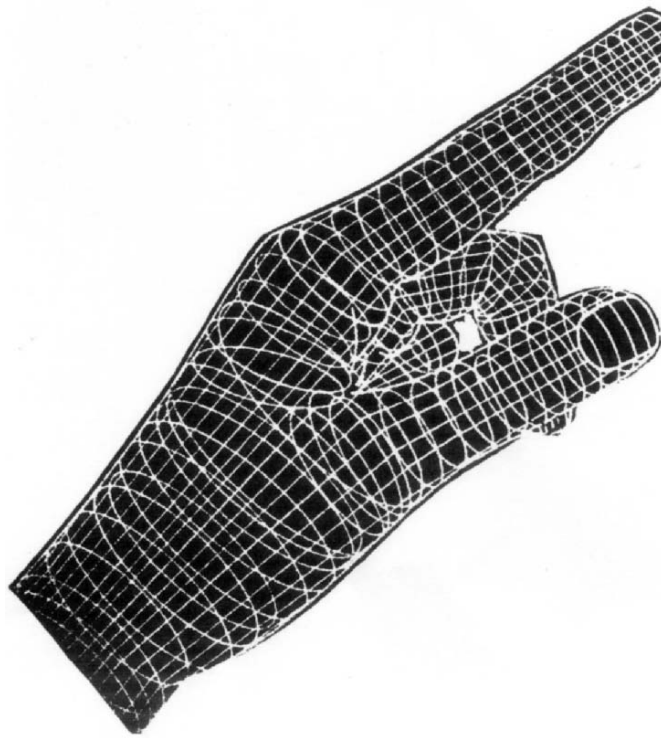

Plate 7.29. Finite element mesh generation for the trauma analysis of hand-wrist fingers

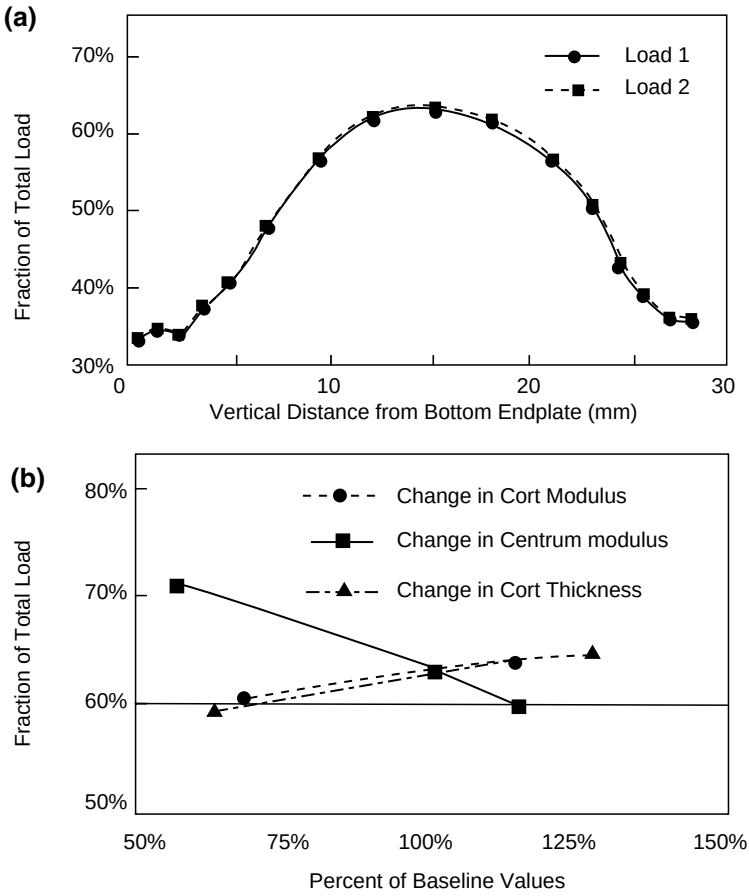

Plate 7.30. The finite element analysis and baseline material properties

a non-physiologic load case simulating an experimental condition in which the load was applied to the vertebral body directly through rigid platens. In both cases, the loads were applied uniformly to the superior endplate of the vertebral body.

Material Properties. Three material parameters were studied, centrum modulus, cortical modulus and cortical thickness. Besides the baseline values listed in Table 7.4 each of these parameters was assigned two additional values, 50 and 100 MPa (centrum modulus), 7,500 and 12,500 MPa (cortical modulus), and 0.40 and 0.80 mm (cortical thickness).

Geometric Properties. Four configurations incorporating two variations of the cortical and endplate curvatures were simulated. The two values assigned to the cortical and endplate curvatures were zero and 1.98 deg. mm^{-1}, and

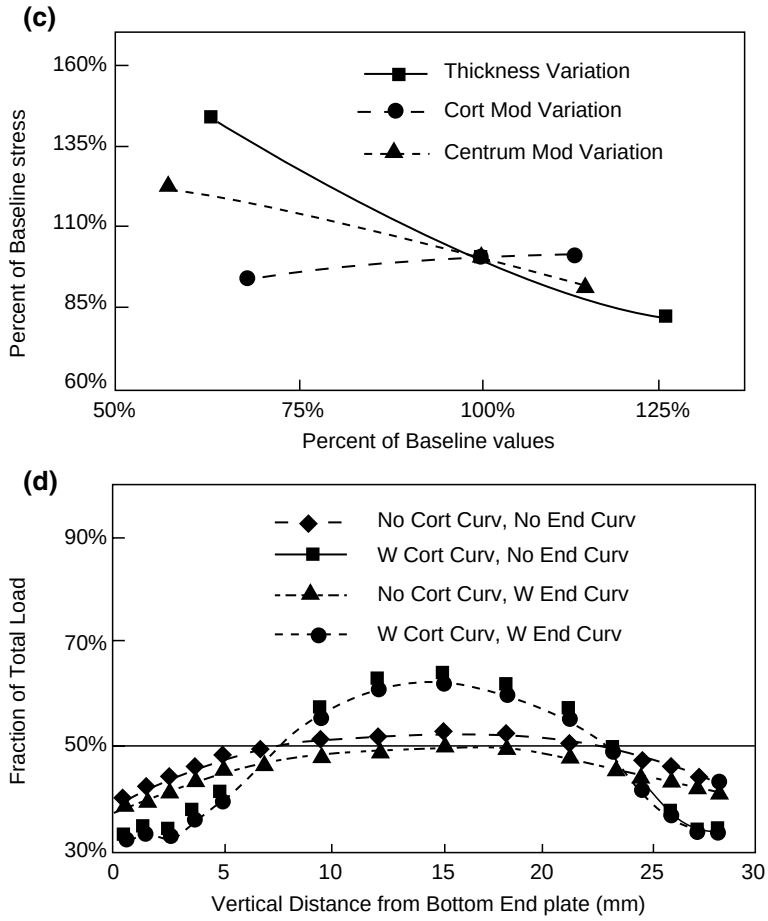

(a) Influences of load conditons

(b) Influences of material properties

(c) Influences of material properties

(d) Influences of geometrical properties

Plate 7.30. *Continued*

zero and 1.28 deg. mm^{-1} respectively. These values were recorded at the mid-lateral plane.

Results

BANGF-II Three-dimensinal finite element program was used. The results are shown in Plate 7.30.

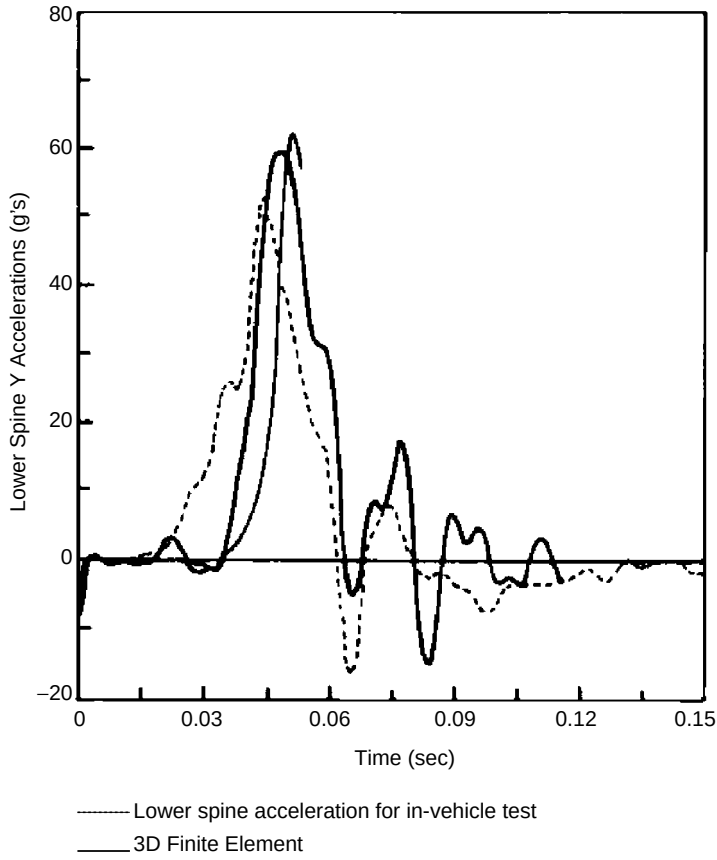

Plate 7.30. *Continued*

Table 7.4. Material properties, baseline values

vertebral region	Young's modulus (MPa)	Poisson's ratio	thickness (MM)
cortex	11,032	0.30	0.635
centrum	$F_z = 87.44$	$U_{yx} = 0.30$	
	$F_x = F_y = (1/3)F_z$	$U_{zx} = 0.30$	
endplate			
center	12,480	0.28	0.512
peripheral	12,480	0.28	0.812
annulus fibrosus	40	0.45	
nucleus pulposus	2,225		

7.5 Hand and Wrist Trauma Under Impact Loading Using Three-Dimensional Finite Element Analysis

7.5.1 Introduction

Hand surgery is a recognized surgical sub-specialty and the hand receives the severe nature of upper extremity trauma. Although many acute and chronic hand conditions are initially seen and evaluated, the management prefers to have a condition for a surgeon a certificate of added qualifications. The biggest problem in the muscle-tendon units of the hand. It is necessary to explain the classifications. They are classified as extrinsic and intrinsic.

7.5.2 Extrinsic Muscles

The extrinsic muscles originate proximal to the wrist (Plate 7.31). The extensor muscles are located dorsally and divide into three subgroups. The lateral subgroup is termed the mobile wad and consists of the brachioradialis, the extensor carpi radialis longus, and the extensor carpi radialis brevis (ECRB). The extensor carpi radialis longus and the extensor carpi radialis brevis extend and radially deviate the wrist. The second subgroup forms a superficial layers and consists of three muscles. The extensor carpi ulnaris extends and

Plate 7.31. X-ray on wrist

ulnarly deviates the wrist. The extensor digiti quinti and extensor digitorum communis act primarily to extend metacarpophalangeal (MCP) joints of small and remaining fingers, respectively. The third subgroup is deep and consists of four muscles, all of which act on the thumb and index finger. The abductor pollicis longus, extensor pollicis brevis, and extensor pollicis longus act on the thumb, and the extensor indicis proprius act on the index finger.

The extensor tendons pass through six compartments under the extensor retinaculum. From radial to ulnar, they are as follows. The first compartment contains the abductor pollicis longus and the extensor pollicis brevis, the first two tendons of the anatomic "snuff box." The second compartment contains the radial wrist extensors, the extensor carpi radialis longus and the extensor carpi radialis brevis. The third compartment contains the extensor pollicis longus, the third tendon of the anatomic snuff box. The finger extensors, the extensor digitorum communis, and the extensor indicis proprius, pass through the fourth compartment. The small finger extensor, the extensor digiti quinti, passes through the fifth compartment, and the extensor carpi ulnaris passes through the sixth compartment.

The flexor muscles are located volarly and are arranged in three layers. The superficial group consists of four muscles: pronator teres, flexor carpi ulnaris, and palmaris longus, which is absent in 30% of patients. The intermediate group consists of the flexor digitorum superficialis (FDS), which independently flexes the proximal interphalangeal (PIP) joints. The deep group contains three muscles: flexor pollicis longus, which flexes the interphalangeal (IP) joint of the thumb; flexor digitorum profundus (FDP), which flexes the distal interphalangeal (DIP) joints of the fingers; and pronator quadratus, which lies between the radius and ulna.

Intrinsic Muscles

The intrinsic muscles originate at or distal to the wrist. Those in the thenar eminence activate the thumb, and those in the hypothenar eminence activate the small finger. Four dorsal interossei and three palmar interossei provide abduction and adduction, flexion of the MCP joints, and extension of the IP joints. Four lumbricals originate on the FDP tendons in the palm and insert on the radial side of the extensor mechanism; they assist the interossei.

Vascular Supply

The ulnar artery enters the palm through Guyon's canal and forms the superficial palmar arch. The digital arteries arise from this arch, which is deep to the palmar fascia but superficial to the nerves and flexor tendons. The radial artery branches at the wrist into superficial and deep branches. The superficial branch crosses the thenar eminence and can anastomose with the superficial arch. The deep branch forms the deep palmar arch, which crosses the palm proximal to the superficial arch and beneath the flexor tendons. The deep arch provides the dominant blood supply to the thumb. Of the general population, 0.5% have a persistent median artery.

7.5.3 Innervation

The radial nerve provides motor innervation to the extrinsic extensors of the hand, the wrist extensors, and the supinator. The superficial branch provides sensation to the dorsum of the thumb, the proximal radial three digits, and a portion of the dorsum of the hand. The median nerve innervates the FDS, the flexor pollicis longus, the two radial FDP, the two radial lumbricals, and most of the thenar musculature. The median nerve provides sensation to the radial palm, the palmar skin of the radial $3\frac{1}{2}$ digits, and the dorsal skin distal to the PIP joints of the radial $3\frac{1}{2}$ digits. The ulnar nerve provides motor innervation to the flexor carpi ulnaris, the two ulnar FDP and lumbricals, the hypothenar musculature and interossei, the abbuctor pollicis, and the deep portion of the flexor pollicis brevis. The ulnar nerve provides sensibility to the ulnar side of the hand, both dorsal and palmar, and the ulnar $1\frac{1}{2}$ digits.

7.5.4 Wrist Injuries from Impact Loading

One of the most common injuries observed by orthopedic surgeons is the distal radius fracture. The typical injury mechanism is a fall on the outstretched hand, thereby producing an axial compressive force across the wrist on the distal forearm. There are many names for fractures of the distal radius, such as Colles, Smith, Barton and Pouteau. Unfortunately, there is limited published data on the dynamic loading required to cause these injuries. Research is being performed currently to quantify the risk of wrist injuries subject to impact loading. This injury criteria will have applications in automobile safety and elderly wrist injuries from falls.

Plate 7.31 shows a typical wrist having finger tips. Based on the impact loud of 10 Newton (10 N) falling at 1.5 m high. If the wrist deformation is assumed to be $\delta_{\max}(\mathrm{t})$, the energy dissipated by the wrist shall be $R_{\mathrm{T}}\delta_{\max}(t)$ where R_{T} is the resistance prior to bone cracking. Assuming the height h is 1.5 m, the potential energy lost during the load is 10 $[h = 1.5\,\mathrm{m} + \delta_{\max}(\mathrm{t})] = 15 + 10\,\delta_{\max}(\mathrm{t})$. In ultimate case, the value of R_{T} is computed as

$$R_{\mathrm{T}}8_{\max}(\mathrm{t})] = 15 + 10\,\delta_{\max}(\mathrm{t}).$$

If the bone prior to cracking is deflected at the wrist level = 0.001 m then

$$R_{\mathrm{T}} = 0.015\,\mathrm{N}; \quad M_{\mathrm{u}} = \text{ultimate cracking moment}$$

$$\text{Hand dimension from wrist} = 0.175\,\mathrm{m} = 10\%0.175\left[1 + \frac{1.5}{0.001}\right] = 2626.75\,\mathrm{N\,m}$$

Using finite element, this value of M_{u} would indicate cracking of fingers and the wrist.

The finite element mesh scheme is given in Plates 7.29 and 7.32.

The bone and muscle properties are given in the text.

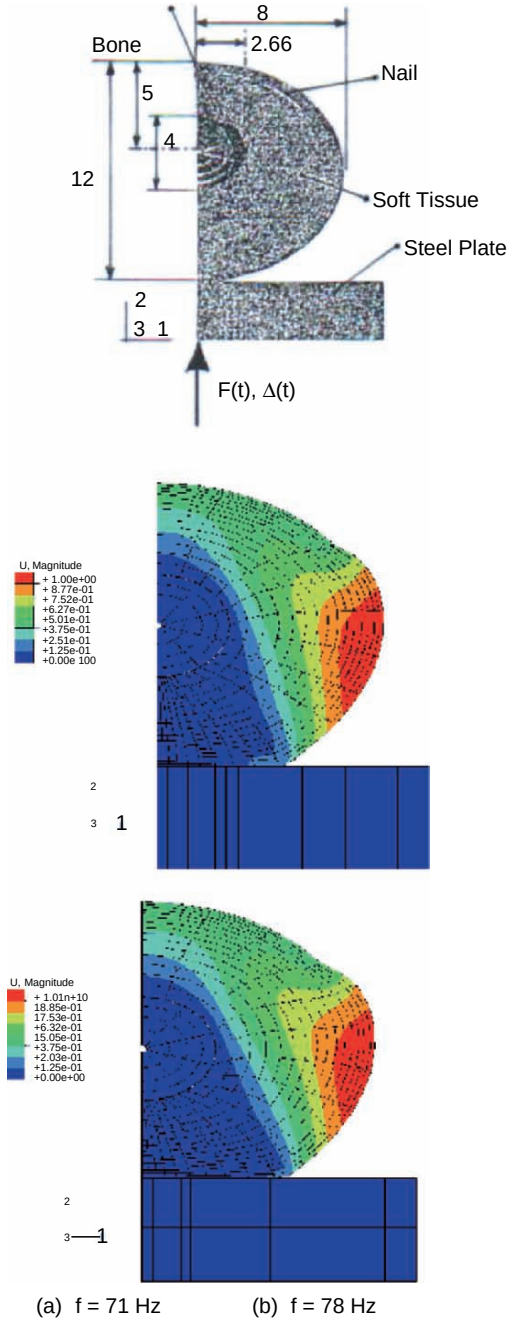

Plate 7.32. Finite element model of a fingertip

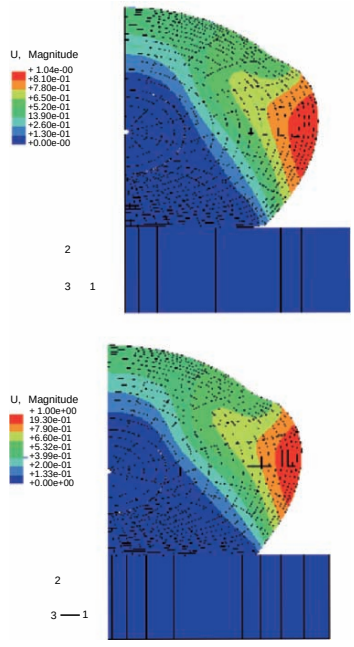

(c) f = 88 Hz (d) f = 101 Hz

Influence of static deformation on the deflection pattern corresponding to the first mode : (a) Δ = 1.5; (b) Δ = 2.0; (c) Δ = 2.5; and (d) Δ = 3.0 mm

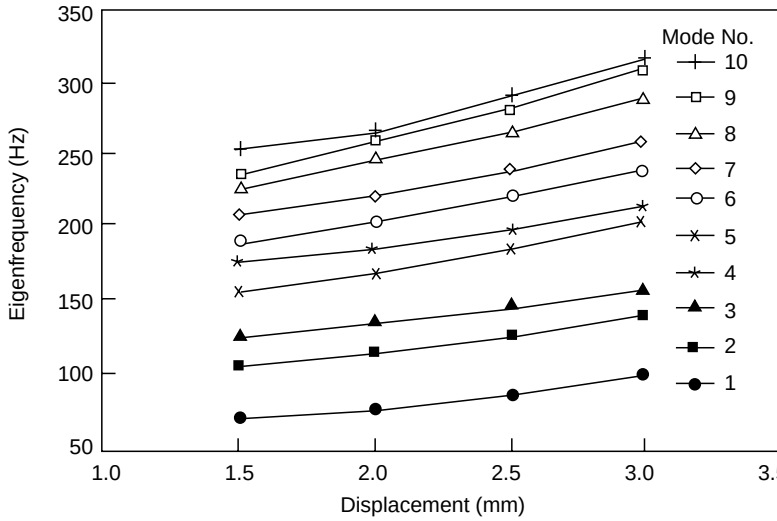

Static deformation dependence of the modal frequencies

Plate 7.32. *Continued*

7.5.5 Free Vibration of a Finger Tip: Finite Element Analysis

John Z. Wu, Subhash Rakheja, Ren G. Dong, Aaron W. Schopper, and W. Paul Smutz, National Institute for Occupational Safety and Health, Morgantown, WV, USA.

Introduction

This fascinating paper gives an extended occupation exposure to hand transmitted vibration, arising from the operation of hand-held power tools, has been associated with the development of an array of vascular, sensorineural and musculoskeletal disorders. The vibrotactile perception threshold (VPT) measurement technique is widely used to diagnose the sensory neuropathy of the hand-induced by an extended exposure to vibrations. The measured values of VPT have been reported to depend on the contact force, vibration frequency and magnitude, and the temperature of the finger skin. Although the measured values of VPT responses of fingertips have been widely spread, no attempts have been made to develop adequate analytical models to study the mechanics of tactile sensation. This study proposes a finite element model of a human fingertip to study its responses to impinged vibration.

A two-dimensional finite element (FE) model of a fingertip is developed to study its deformation-dependent vibration responses. The model is composed of linearly elastic bone and nail, and nonlinearly elastic and viscoelastic soft tissue. The fingertip was assumed to be symmetric (Plate 7.32). The skin tissue is assumed to be in contact with a linearly elastic, smooth steel plate, representing the vibrotactile probe. The dimensions of the fingertip model are assumed to be representative of the index finger of a male subject. The material parameters of the soft tissues, bone and nail are taken from the published experimental data. The fingertip tissue is subjected to varying levels of static deformations and contact force by displacing the contact plate vertically, at $t = 0$, the plate is considered to be in contact with the fingertip skin surface with negligible resultant contact force.

Results

The model analysis of the fingertip model was performing using the tangential stiffness of the tissue corresponding to the maximum deformation at $t = T_c$. The free vibration ($T_c = 1\,s$) analysis of the fingertip model, as expected, resulted in a large number of natural modes. Considering that most power tools generate dominant vibration in the frequency range of 25–320 Hz , the first ten eigenfrequencies of the fingertip model were extracted corresponding to each static deformation. Plate 7.32 illustrates the variations in the modal frequencies as a function of the static tissue deformation. The natural frequencies corresponding to the extracted modes lie in the 40–320 Hz frequency range.

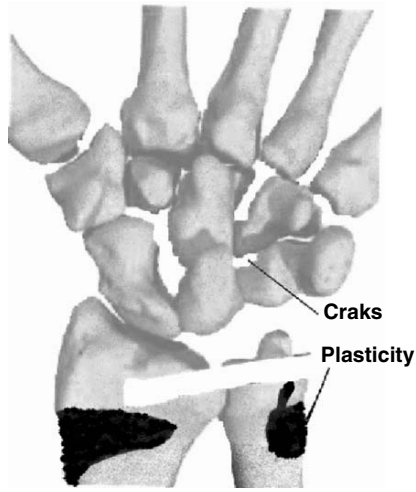

Plate 7.33. Wrist and finger fracture under impact load of 20 N

The eigenfrequencies corresponding to the selected modes increase considerably with increase in the magnitude of the tissue compression or pre-load. The eigenfrequency corresponding to a specific mode tends to increase almost linearly with the magnitude of the static deformation, irrespective of the mode of vibration. The variations in the static deformation also affect the deformation patterns of the fingertip corresponding to the selected modes.

7.5.6 Three-Dimensional Dynamic Analysis of Impacted Fingers

Program BANGF-II has been applied to wrist-cum-fingers using eight nodded isoparametric elements for the stated loads, the results obtained for the parameters adopted by Wu J.Z. et al., are now compared in Plates 7.32 and 7.33.

7.6 Simulation of Lower Extremity Traumatic Injuries in Sport

7.6.1 Introduction

Injuries resulting from repetitive and acute musculoskeletal loading are common during recreational and competitive sport activities (e.g., Mummery et al. 1998; Sandelin and Santavirta 1991). Musculoskeletal loads are influenced by factors such as the task being performed, anatomy, muscle coordination and equipment selection (e.g., footwear). For a given movement or task,

muscle coordination and equipment selection are factors that can be altered within limitations to help reduce musculoskeletal loading. However, it is not clear a priority how these factors will affect the loading because of the highly nonlinear dynamics and complex lower extremity movement kinematics.

The objective of this case study was to develop a 3D musculoskeletal model of the lower extremity with individual muscle actuators and ground contact elements and to generate subject-specific forward dynamic simulations that can be applied to studies of lower extremity loading dying dynamic activities. As an example application of the model, two commonly used treatments for patellofemoral pain were examined along with functional significance of muscle activation timing deficits between the vastus medialis oblique and vastus laterlis on patellofemoral loads. A 3D model developed keeping in mind muscle actuator and ground contact elements to examine the musculoskeletal loading during human movement.

Methods

Musculoskeletal Model

A forward dynamic musculoskeleal model was developed using *ABACUS* and *BANGF-II* (Plate 7.34) software and consisted of rigid segments representing the foot, talus, shank, patella, and thigh of the support leg and a rest of the body segment. Musculoskeletal geometry and joint models were based on three-dimensional movements at the knee. Fourteen functionally independent muscle groups were used to drive the model . The vasti muscle group consisted of four individual muscles all receiving the same muscle excitation; the vastus lateralis, intermedius, medialis-longus and medialis oblique. The force length velocity characteristics of the muscles were represented by a lumped parameter model.

The contact between the foot and the ground was modeled by 66 discrete independent viscoelastic elements, each attached to one of the tree foot segments in locations that describe the three-dimensional exterior surface of a shoe when the foot joints are in neutral position. Each element permitted deformation perpendicular to the floor and represented the mechanical properties of the shoe sole and underlying soft tissue. The anterior–posterior and media-lateral forces were modeled as a Coulomb friction force resisting slipping of the foot relative to the ground.

Data were collected from a group of nine healthy male subjects (height = $177.0 \pm 10.4\,\mathrm{cm}$; weight = $73.3 \pm 12\,\mathrm{kg}$) during heel–toe running at $4.0 \pm 0.4\,\mathrm{m\,s^{-1}}$ to provide initial conditions for the simulation (positions and velocities of the body segments at heel strike) and tracking data for the optimization algorithm. All trials were normalized to the durations from heel strike to toe-off, and the forces and joint angles were sampled at 100th of the stance durations. A typical orthotic was modeled in the shoe by increasing the stiffness of the individual shoe elements in the arch area in the pattern

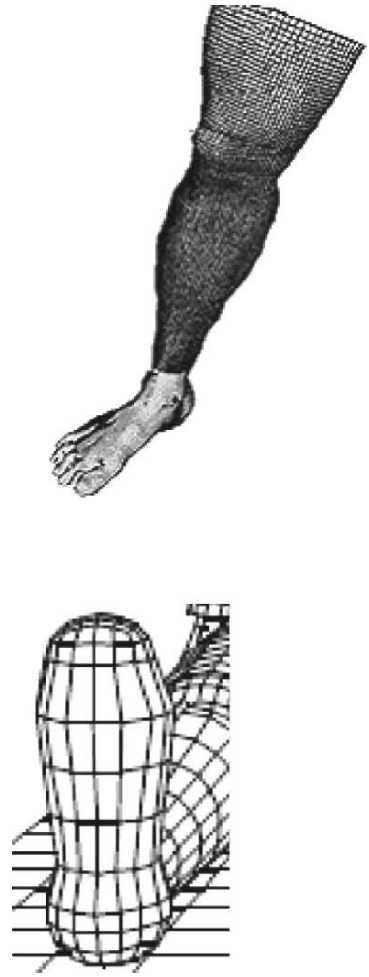

Vertical ground reaction force comparison between a typical subject (mean ±1SD) and their corresponding simulation data.

Plate 7.34. Musculoskeletal simulation model

of the orthotic. The patellafemoral load was defined as the lateral constraint force between the patella and the femoral groove.

To assess the effect of these treatments on lateral patellofemoral loads, a one-way (treatment) repeated measures analysis of variance was performed on the absolute differences from the normal loads in the peak and average loads ($p < 0.05$). When significant treatment effects were detected, a paid t-test was used to identify which treatments were significantly different ($p < 0.05$).

Results

The optimization was able to find the muscle controls (excitation onset, offset, and magnitude) to reproduce the salient feature of the experimentally connected data for each subject. The major joint angles ground reaction forces and muscle stimulation patters compared well with the subject data.

7.6.2 Car Impact and Explosion Analysis

General Data

Principles of impulse and momentum are frequently adopted in the study of various vehicle collisions. Rational velocity changes are included in the overall analysis. The energy loss ranges from 32% to 90% for nonzero moment impulse with a range of restitution coefficients between -0.001 and 0.810. For a zero moment impulse with the same range of energy loss the restitution coefficients will be between 0 and 0.4. The friction coefficients along the impact range are between -0.07 and 0.90.

Finite-Element Analysis and Results

A typical finite-element mesh scheme for car is shown in Fig. 7.7 (damaged car). Where the analysis includes a human body, a seat-belted dummy is added. Bovine materials (given in the text) and steel material properties are included in the analysis of bone and the car. Empty body and body with packing, as dampers, for difference position in the car have been examined. A force–time function, given in Fig. 7.5 is considered for the finite-element analysis.

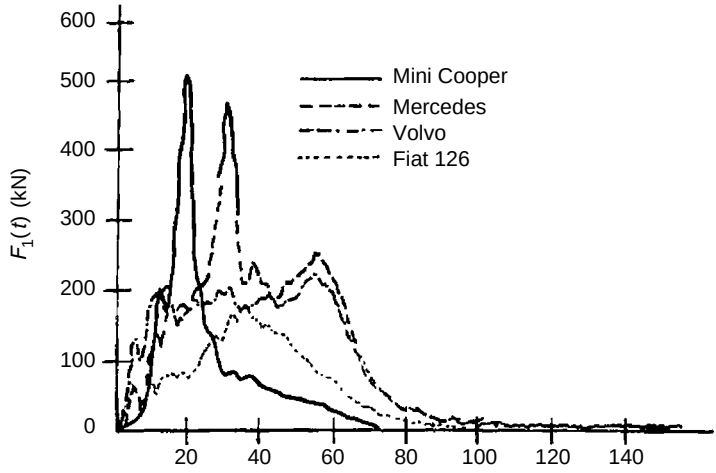

Fig. 7.5. Force–time relationship

The vehicles impacted the steel and aluminum barriers at velocities ranging from 30 to 50 mph. Additional input data:

cars	
solid isoparameteric elements (20-noded type, quadratic)	2,700
prism isoparametric elements (20-noded type)	298
gap elements, mixed dashpots	735
Total nodes	17,805
Barriers	
solid isoparametric elements (20-noded type, single layer)	235
Total increments	10
Total time for impact analysis	140 s case^{-1}
T (time interval)	14 s
Maximum impact load F1 (t)	500 kN

An IBM 4381 computer with Cray-2 front ended was used for analysis.

Figure 7.6 shows the deceleration- time relationship for two types of car. The damaged car is shown in Fig. 7.7. The force–deflection and the car crash with time results are show in Fig. 7.8 the barriers were examined for several impacts and various car velocities. Fig. 7.9 illustrates the results for flat steel and aluminum barrier braced and belted to vertical posts.

During the car crash investigation the entire dummy body was examined. The seat belts were assumed to be tension elements, each carrying 20

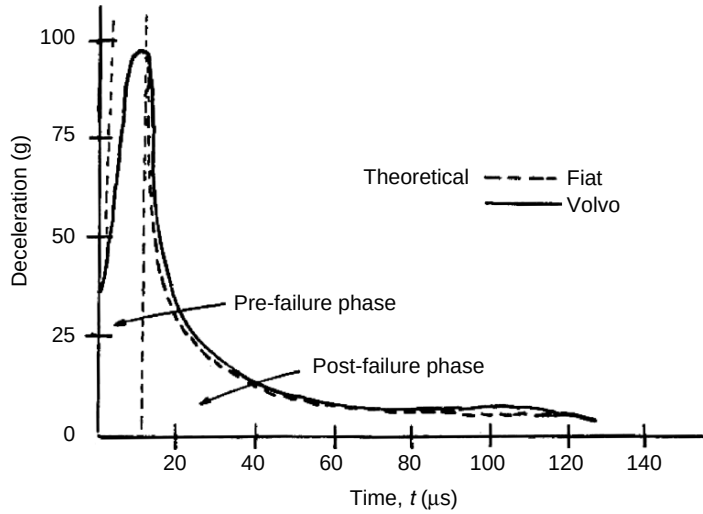

Fig. 7.6. Deceleration–time relationship

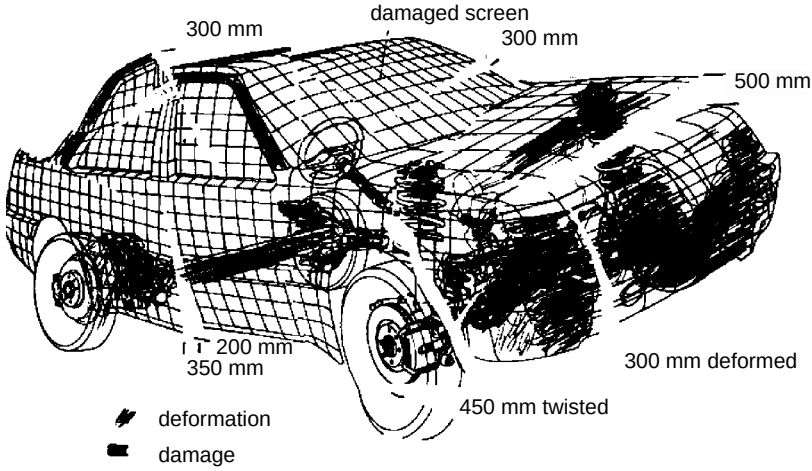

Fig. 7.7. Car: postmortem

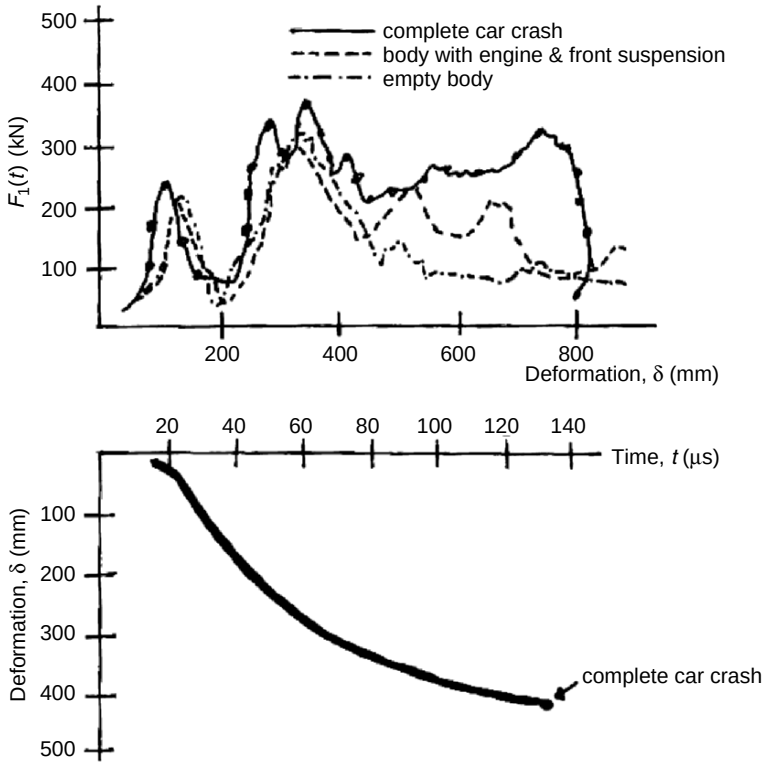

Fig. 7.8. Deformation–time and car crash results

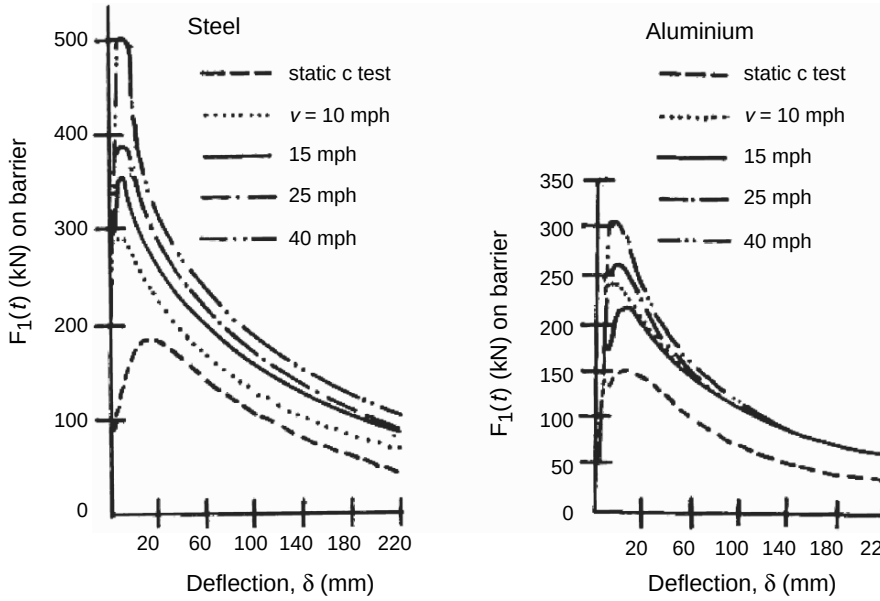

Fig. 7.9. Analytical results for steel and aluminium barriers

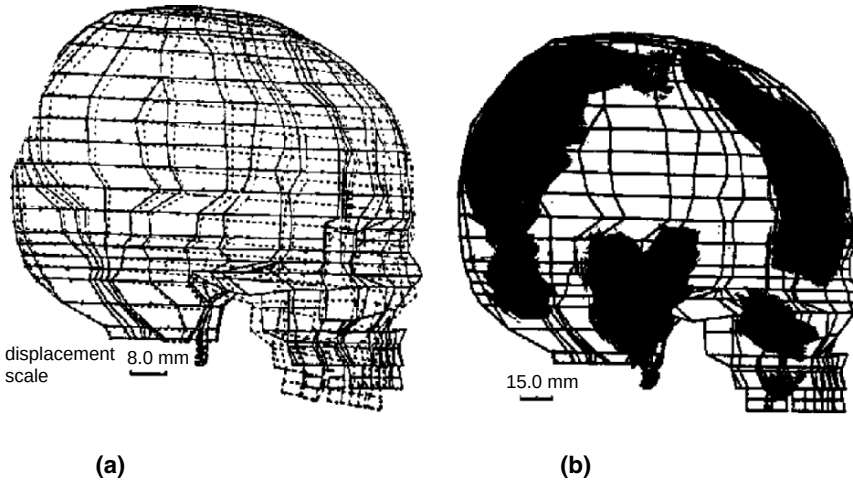

Plate 7.35. Typical damaged skull: (**a**) finite-element mesh and displacement due to impact and (**b**) final skull damage(Program ISOPAR)

line nodes in total, subdivided into three divided into 3-noded isoparametric elements. A typical damaged skull is shown in Plate 7.35. The number of finite elements representing the skull part is 350 and 210 for bones and tissues, respectively. The brain elements numbered 105. All were 20-node isoparametric elements.

7.7 The Solid Modeling of the Human Leg in a Car Accident

James J. Dowling and Jennifer Durkin, Department of Kinesiology, McMaster University, Hamilton, CANADA has carried out solid modeling of a human leg using DXA scanner.

7.7.1 Introduction

The use of dual photon absorptiometry (DXA) has recently been shown to be an accurate method of calculating the mass, moment of inertia and location of the center of mass of human limb segments (Durkin, 1998a). Briefly, living subjects were scanned via DXA which sent a beam consisting of photons at two energy levels through the body. The attenuation of the high energy photon as measured by the detector was proportional to the quantity of matter (mass) that the beam passed through. The beam has the dimensions of 2.6 mm by 1.8 mm which creates a file of 336 by 730 scanned elements. (Plate 7.36 for a graphical representation of this file). A computer program was written to digitally section this file using the density plot to locate joint centers such that the mass of human limb segments could be calculated by summing the mass elements within the segment. The center of mass was also calculated from the weighted centroid of those elements and the moment of inertia about this centroid was also calculated from the sum of the elements multiplied by the square of their radial distances from the centroid.

Access to a DXA scanner and the process of determining the inertial characteristics of each subject may not be practical in many biomechanical

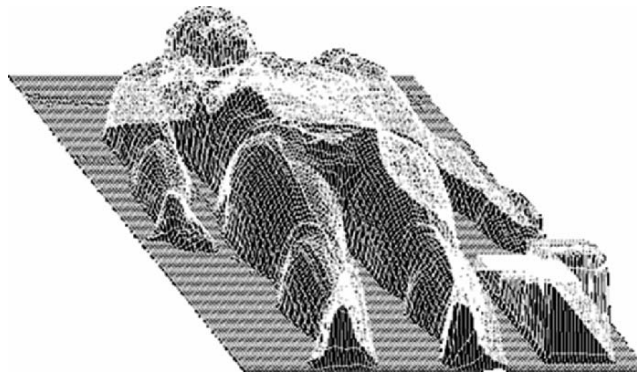

Mass map of the 336 x 730 scanned elements of a human subject. The height of the surface is proportional to the mass of each scanned element.

Plate 7.36. Geometric solid modeling of the internal characteristics of the human subject

investigations. It would be useful if a geometric solid could be constructed mathematically from a few easily measured anthropometric variables that would allow the accurate and reliable calculation of the inertial variables. Previous attempts to develop geometric shapes of the leg include the use of a cylinder (Zatsiorsky et al. 1990a) and a frustum (Hanavan 1964a). To our knowledge no study has validated the use of geometric shapes on measured inertial characteristics of living human subjects from various populations.

The purpose of this study was to examine the characteristics of the mass distributions along human leg segments of male and female subjects of different ages to determine the degree of geometric similarity between these populations. If a high degree of geometric similarity was found, the second purpose of the study was to define that shape and present an accurate and reliable method of predicting the inertial characteristics from a small set of easily measured anthropometric variables.

Methods

Twenty subjects were randomly selected from a pool of 100 subjects that were DXA scanned by Durkin (1998a). Five subjects were taken from each of four subpopulations (males and females between 19 and 30 years of age and males and females over 55 years of age). A computer program was written to normalize the scanned mass data for each percentage of the segment length from the proximal to the distal ends. The amplitudes of the scanned masses were normalized to 100% of the total mass. The five subjects in each of the subpopulations were ensemble averaged and plotted. Each variance about the ensemble averages was analyzed for geometric similarity. If the variance within a population was greater than the difference between the populations, the segments were deemed to be geometrically similar. A geometric solid was created that captured the salient features of the ensemble average. The accuracy of the model was evaluated by calculating the errors between the geometric solids and the actual masses and moments of inertia of the segments of 20 different subjects that were also randomly selected from the original pool of 100 subjects. The additional subjects included five subjects from each of the four sub-populations. These errors were also compared to those using the method of Hanavan (1964a) and to those using the table values reported in Winter (1990a).

Results

Plate 7.37 shows the ensemble averages for the four populations. It can be seen that there was a similar shape for each sub-population. This indicated that a geometric solid could be defined that would estimate the inertial characteristics of human legs regardless of age or gender. The shape of the mass distribution revealed that it was unlikely that a constant density cylinder would be a very good representation. Even if an average radius could be found

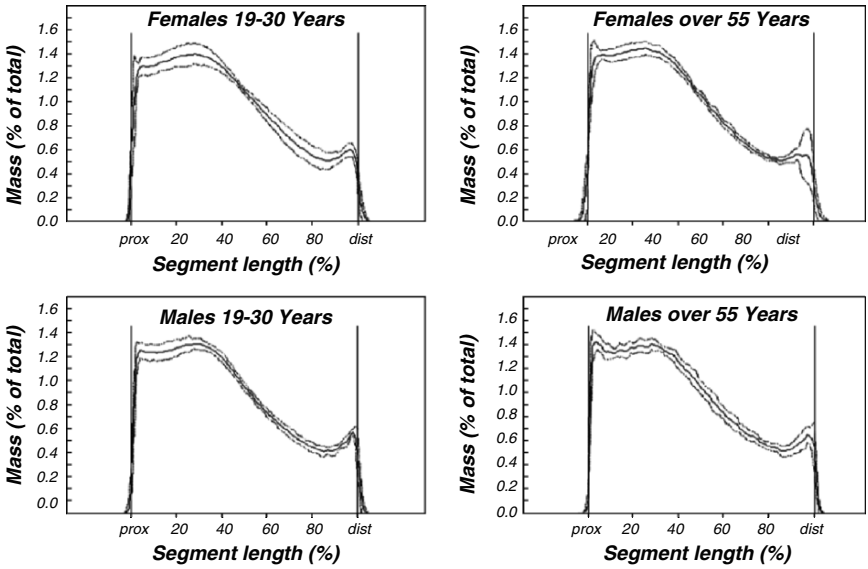

Plate 7.37. Ensemble averages (*solid lines*) and standard deviations (*dashed lines*) for the mass distributions of the four subpopulations. The area under each curve represents 100% of the total mass of each leg

that predicted mass well, the location of the center of mass and moment of inertia would have large errors. A simple frustum with a decreasing radius would account for the greater mass located near the proximal end but would not account for the increased mass near the distal end. The method will give a valuable information on plotting mesh generation of 8-noded isoparametric elements in order to evaluate the traumatic injury on legs.

The geometric shape chosen in this study was one that was a composite of a cylinder and two frusta. The cylinder accounted for 39% of the leg mass and extended for 28% of the segment's length from the proximal end toward the distal end. A frustum with a decreasing radius comprised 52% of the mass of the leg and was located from 28% to 86% of the segment length from proximal to distal. The remaining 9% of the mass was accounted for by a frustum of increasing radius from 86% to 100% (Plate 7.38).

The use of the composite geometric solid required the length of the segment to be measured as well as the radius of the proximal end. The circumference of the knee joint was selected as the measured anthropometric variable to predict τ_1. The length was initially measured as the distance between the knee at the tibial plateau and the distal end of the lateral malleolus but it was found that this most often overestimated the actual segment length as determined from the DXA scan. It was found that 22% of whole body height was a more reliable measure of segment length than surface palpation of the knee and ankle joint centers. Once the length and proximal radius had been

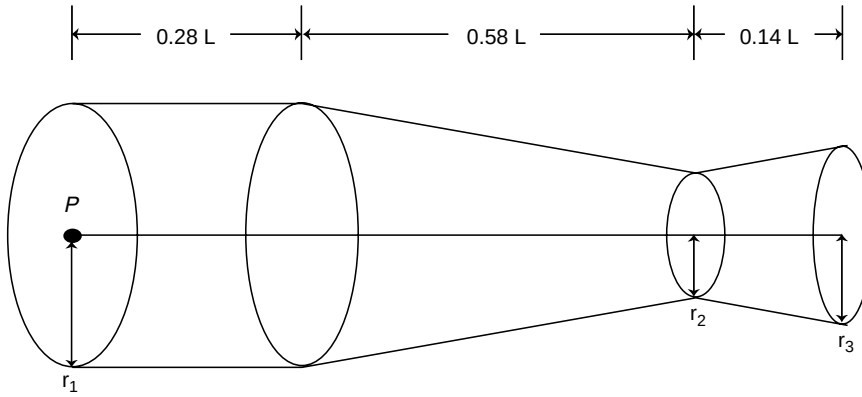

Plate 7.38. Geometric solid that captures the main features of the mass distributions of the ensemble average

established, the volume and the remaining two radii could be calculated by ensuring that the above criteria of the geometric solid were satisfied. A value of 1,090 $\mathrm{kg\,m^{-3}}$ was used for the density to convert the volume to mass.

7.8 Traumatic Damages to Achilles Tendon

7.8.1 Introduction

Traumatic damages of Achilles tendon constitute an important and serious problem in clinical practice. Many theories are applied in order to explain the pathomechanism of traumatic damages of Achilles tendon. Among them, there is a mechanical theory which claims that sudden and not coordinated contraction of the calf triceps muscle with plantarly bent foot and extended limb causes rupture of the tendon continuity. In clinical practice, Achilles tendon appeared more susceptible to rupture in persons over 35 when elasticity degree is reduced due to the tendon deformative lesions (fragmentation and collagen fibres homogenization).

Achilles tendon is the strongest one in the human organism. It is 10–12 cm long, with 0.5–1 cm diameter and it is composed by the common attachment of the calf triceps muscle to calcanea bone tuber.

Finite Element Analysis of Traumatic Rupture

The analysis carried out of an Achilles tendon under tension with and without temperature effects. The length = 105 mm with a breaking velocity $\nu = 20\,\mathrm{mm\,min^{-1}}$. Left lower limb and right lower limb, both have been taken into consideration. Human body surface thermal processes range between

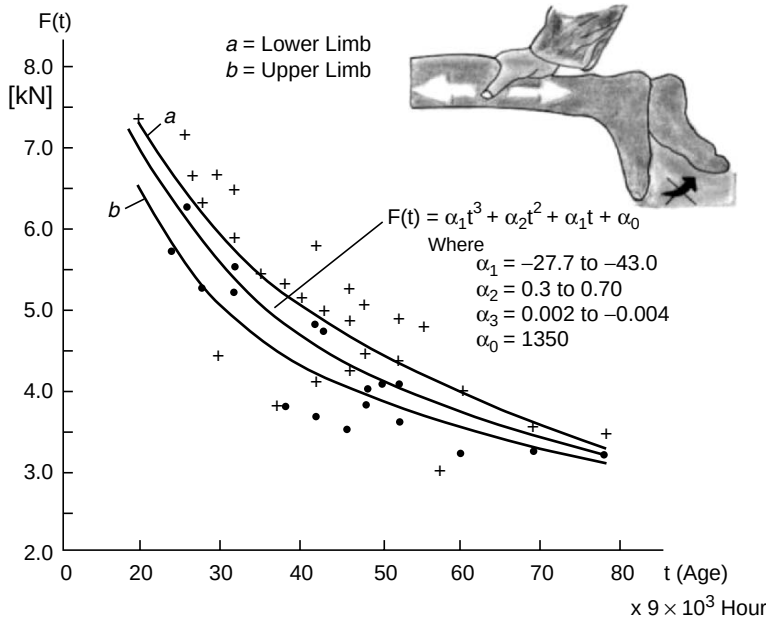

Plate 7.39. Load–age time curve

23°C (foot level) and 32°C maximum Achilles tendon level. The material properties are examined elsewhere in the text. The rupture analysis and criterion are given also in Plate 7.39 indicates the tendon fracture scenario. Plate 7.39 shows Load–time relation after carrying out. FE dynamic analysis for 100 Achilles tendons. Based on a curve fitting technique, curves are drawn. The empirical formulae have been established for other tendon lengths and loading time. The temperature aspect time Δt is equal to 0.62°C. The initial force varies from 0 to 8 KN. The best possible curve obtained will give fracture for age changes.

7.8.2 Finite Element Analysis of a Foot with Traumatic Injuries

Introduction

The understanding of the impact mechanics during human motion is important for research within the fields of motion analysis and foot injuries. Many fundamental and applied human motions are influenced by complex deformations, internal stresses, and the shock wave of the foot skeletal system. It is difficult to directly measure the internal stresses and shock wave. However, these stresses and shock wave can be predicted using a mathematical or numerical model of the foot skeleton. The purpose of this study is the development a foot joint skeletal model using the finite element method for the analysis of physical exercise, sports injury.

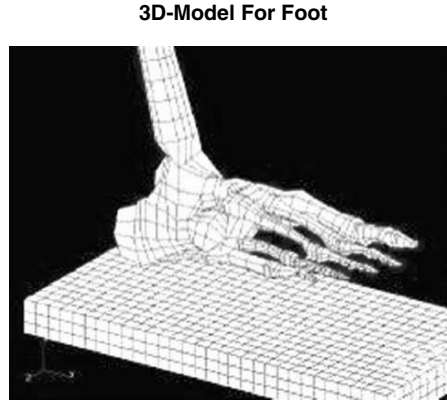

Plate 7.40.

Basic Analysis

The basic shape of the finite element foot joint model is described using a commercial foot skeletal model for computer graphics and anatomical data, and the solid model is defined after simplifying that model. The axis system of the model is chosen such that, with respect to the foot. It is a three-dimensional model as shown in Plate 7.40 involving 8-noded isoparametric elements. The horizontal dimensions of the foot (external and internal direction) are on the X-axis. The direction of Y-axis is upward along the tibia. The right-handed coordinate system is completed by the Z-axis. The finite element mesh scheme is from solid modeling with PATRAN. Linear and nonlinear static analysis has been carried out using BANGF-II Implicit finite element code. The dynamic transient analysis has been performed using explicit FEM code version of BANGF-II. Complete details of such analysis are given in Appendices I and II.

Input Data

(a) Hard tissue modeling of the foot: 28 bone models (calcaneus, metatarsal)
(b) Soft tissue parts: 20 joint models (talocalcanean, calcaneocuboid joints)
(c) Ligaments and retina cula are geometrically represented
(d) Mesh: 550 no. 8-noded elements hard tissues 110 no. 8-noded elements soft tissues
(e) material properties
E (hard tissue) foot joint model = 7.4 $\mathrm{KN\,m^{-2}}$
ν (Poisson's ratio) = 0.3
E (soft tissue) = 1–5 $\mathrm{N\,m^{-2}}$
(f) F = impact load on Trochlear
Surface of the talus = 310 N

(g) For dynamic transient analysis
E (soft tissue) = 6 $N\,m^{-2}$
Added mass (muscles, etc. with skin)
(h) ν_i = initial velocity at impact = $-1.1\,m\,s^{-1}$
θ_i = initial rotational velocity = $8.8\,rad\,s^{-1}$

Results and Discussion

The displacement of the inside arch height by a vertical load (310 N) in the analysis using a cadaver foot was reported to be 2.98 mm, while the same result for other case of this study was 280 mm. The plantar flexion angle of the calcaneus in the experiment was 1.8 deg. And that in this study was 3.0 deg. It seems that the stiffness of the soft tissue in this simulation model was slightly lower than that of a real human fort.

In the vertical drop test simulation, the contact time of the foot model and the floor model was about 20 ms, and the vertical peak force was about 9,400 N for the model weight of 65 kg. It seems that a good approximation is acquired when comparing the actual ones with that values in the experiment (Plate 7.41). The vertical peak force for this boundary condition was much higher than that reported for real human running (Nigg 1986; Lafortune and Lake 1995). It was observed that the highly stressed regions were the metatarsals in both the linear static analysis and dynamic transient analysis.

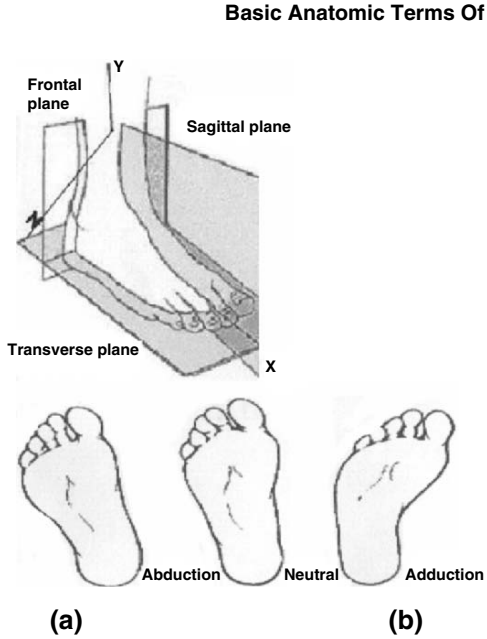

Plate 7.41.

(Contd.)

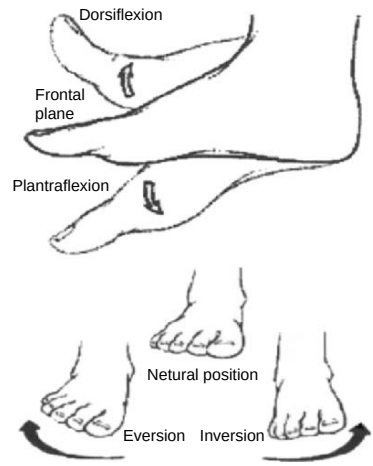

(a) Anatomical planes of the foot
(b) Abduction and Adduction
(c) Dorsiflexion and plantarflexion
(d) Inversion and Eversion

Plate 7.41. *Continued*

7.9 Fractures about Shoulder, Arm and Elbow Joint Fracture

7.9.1 Fractures of Scapula

Open reduction with or without fixation rarely is required for fractures of the scapula. Computed tomography (CT) often is necessary for accurate assessment of these injuries. Most can be treated by supporting the upper extremity in a sling and instituting early active motion. The following fractures may require open reduction and internal fixation.

1. *Significantly displaced fractures of the acromion and lateral scapular spine with retraction of the fragment and encroachment on the subacromial space.* These are extremely rare. If deltoid function is impaired or if the subacromial space is significantly compromised, causing impingement of the tuberosities during abduction, open reduction, and internal fixation using Kirschner wires or plate and screws may be indicated.
2. Fractures of the coracoid with *acromioclavicular separation.* If fracture of the coracoid occurs with dislocation of the outer end of the clavicle, open

reduction with internal fixation of the coracoid with a screw or heavy suture and repair of the acromioclavicular ligament should be carried out.

3. *Glenoid rim fractures.* Fractures of the glenoid rim associated with traumatic dislocations of the shoulder are probably more common than recognized. If a glenoid rim fracture involves as much as one fourth of the articulating surface, primary open reduction and internal fixation are required to prevent recurrent dislocation or subluxation. Small glenoid rim fractures following dislocation should be treated by the nonoperative measures used in treating the dislocation.

Other fractures of the glenoid and scapular neck usually can be treated by sling support of the extremity and early active motion. If the glenoid is markedly angulated or displaced, lateral traction through an olecranon pin for 3–4 weeks may be carried out. Rarely can fractures of the scapular neck be satisfactorily reduced and internally fixed. Fortunately, despite severe displacement, functional results usually are quite satisfactory.

7.9.2 Fractures and Fracture-Dislocations of Shoulder

Fractures and fracture-dislocations of the shoulder are common injuries and occur in all age groups. Fractures in children generally involve the proximal humeral epiphysis, and although most are successfully managed by closed reduction and conservative measures, open reduction occasionally may be required.

Impacted fractures occur almost exclusively in older people. Rarely should impacted fractures be manipulated or subjected to surgery to improve position, since restoration of function would probably be made more difficult. Because people with such fractures tend to develop periarthritis about the shoulder, these fractures should be treated by methods that allow early motion and early restoration of function. Even if significant angulation is present, the results usually are much better than one might expect from the appearance on roentgenograms.

Numerous classifications for displaced fractures and fracture-dislocations are based on the mechanism of injury or on the displacement. The four-part classification proposed by Neer in 1970 is used in the following discussions:

1. *Fractures without displacement.* Regardless of the number of fracture lines or the anatomical structures involved, nondisplaced fractures essentially are one-part fractures and can be treated with sling support and gradual exercises. Nondisplaced fractures of the anatomical neck with shoulder dislocation should be stabilized prophylactically before attempting to reduce the dislocation to prevent iatrogenic displacement of the anatomical neck fracture. Hersche and Gerber found that careful closed reduction of the dislocation with the patient under general anesthesia did not prevent displacement of the anatomical neck fracture and that prophylactic fixation

of the anatomical neck fracture before reduction did not always prevent avascular necrosis.

2. *Two-part fractures.* Displaced two-part fractures involving the tuberosities are treated as described under avulsion fractures. Two-part fractures involving the anatomical neck render the articular fragment avascular and may require prosthetic replacement. If reduction can be obtained.
3. *Three-part fractures.* Three-part fractures are best treated by open reduction and internal fixation. In a three-part fracture one of the tuberosities remains with the articular head fragment, thereby retaining its vascularity. With accurate reduction and fixation and intensive rehabilitation, good results can be obtained. Methods of internal fixation are similar to those used for two-part fractures. Screws, heavy sutures, or wire tension bands combined with some form of intramedullary device or plate provide stable fixation in osteopenic bone.
4. *Four-part fractures.* In four-part fractures the articular head segment has lost its blood supply, and prosthetic replacement will give the best result, provided the patient is a low operative risk and is active enough to require a well-functioning shoulder. Esser, as well as Darder et al., believes that prosthetic replacement for four-part fractures should be reserved for elderly patients with osteoporosis and patients with irreparable fracture-dislocations. This view is supported by, who achieved only 22% excellent results after open reduction and internal fixation of four-part fractures and recommended primary hemiarthroplasty. Jakob et al., described a four-part valgus impacted fracture of the humeral head and recommended closed reduction or limited open reduction to reduce the risk of avascular necrosis. Zyto et al. reviewed 27 patients who had undergone hemiarthroplasty for displaced three- and four-part proximal humeral fractures and found that 30% had moderate or severe disability. The treatment of four-part fractures remains controversial. Hemiarthroplasty probably should be reserved for older patients with osteoporosis and patients with irreparable injuries. Osteosynthesis should be attempted in younger patients. Zyto et al. found acceptable results in one third of 11 patients treated conservatively for four-part fractures. For a more extensive discussion of treatment options, the reader is referred to the works of Cofield, Hawkins, and Schlegel, and Hawkins.

7.9.3 Arm and Elbow Joint Fracture

Frontal Airbag Induced Forearm Fractures

Although airbags have reduced the number of fatalities in automobile crashes, they have increased the number of minor injuries, and in particular, the incidence of upper extremity fractures. Research has been performed to investigate the vulnerability of the forearm to frontal airbag loading. Experiments

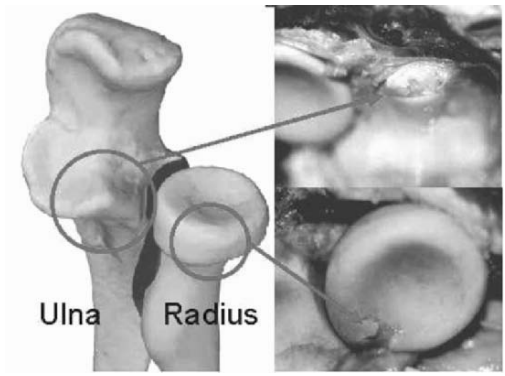

Osteochondral and Chondral Fracture of the chomoid on the ulna and proximal head of the radius as a result of side air bag loading.

Plate 7.42. Elbow joint injuries

with the small female instrumented upper extremity and human cadaver subjects have helped to elucidate the injury mechanisms and injury criteria of the male and female forearm. Additional work is being performed to develop validated finite element models of the upper extremity that may be used in the prediction of airbag induced upper extremity injuries (Plate 7.42).

Elbow Joint Injuries from Side Airbags

In order to characterize the interaction between a small female upper extremity and a deploying side air bag, a study was performed that utilized 12 tests with small female cadavers and 15 tests with the instrumented SAE fifth percentile female upper extremity attached to the fifth percentile Hybrid III female dummy. The upper extremity was loaded by a deploying seat mounted thoracic side bag in a static test environment. Chondral and osteochondral fracture in the elbow joint were recorded for seven of the twelve cadaver tests, While a simple fracture of the distal humerus head was observed in one test. Linear regression was performed to correlate occurrence of observe injury and the test parameters. Injury risk function was constructed for age, forearm acceleration, elbow moment, and air bag inflator level.

Forearm and Humerus Fracture Tolerance

The dynamic injury tolerances for the female humerus and forearm were derived from dynamic three-point bending tests using 22 female cadaver upper extremities. The strain rates were chosen to be representative of those observed during upper extremity interaction with frontal and side airbags. The average moment to failure when mass scaled for the 5% female was

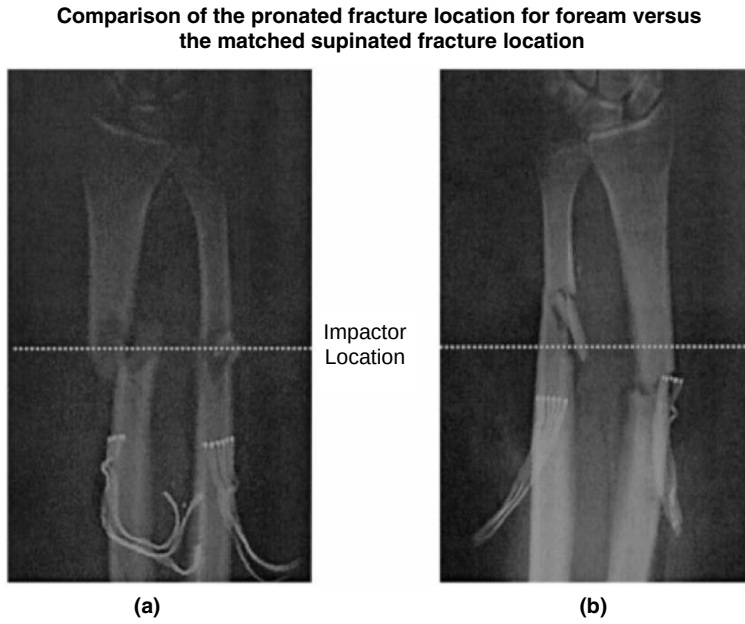

(a) Versus the matched supinated fracture location for test
(b) The strain guage and wiring can be seen proximal to the impactor location on both bones for both tests.

Plate 7.43. Forearm and humerus fracture tolerance

$128 \pm 19\,\mathrm{N\,m}$. Using three matched forearm pairs, it was determined that the forearm is 21% stronger in the supinated position, $92 \pm 5\,\mathrm{N\,m}$, vs. the pronated position, 75 ± 7. Two distinct fracture patterns were seen for the pronated and supinated groups. To produce a conservative injury criterion, a total of 7 female forearms were tested in the pronated position, which resulted in the forearm injury criterion of $58 \pm 12\,\mathrm{N\,m}$ when scaled for the 5% female. It is anticipated that this data will provide injury reference values for he female forearm during side air bag loading (Plate 7.43).

7.10 Trauma of a Female Bladder Due to Dynamic Loads Caused by a Short Cough and Other Impacts

7.10.1 Introduction

This model is related to functional study of the main organs of the female pelvic floor and the phenomenon under investigation is the dynamic response of the bladder subjected to a particular load, in this case a short cough. From a clinical point of view and in particular in urology, a specific test is available

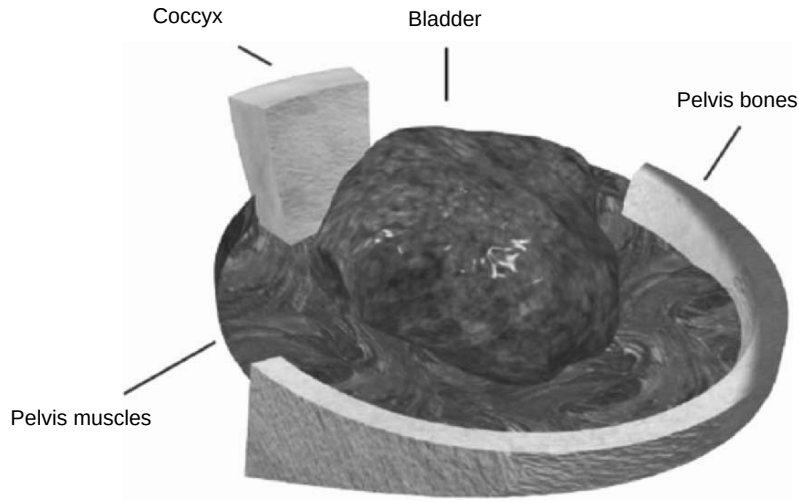

Fig. 7.10. The bladder placed on the muscles of the pelvic floor between the pelvic bones

in order to establish the degree of functionality of the bladder. This test and the related measurements are more properly defined as "urodynamics." The researchers will here look at the displacement and stresses that the bladder can be subjected to during such a test.

The aim of this analysis is to reproduce the dynamics of the bladder, placed in the pelvic floor, when subjected to the movement caused by a short cough. The pelvic floor is characterized by the present of numerous organs, bone, and muscles. In order to simplify the analysis, four principal components are considered: the bladder itself (full of fluid), the muscles of the pelvic floor, and the two pelvis bone shown in Fig. 7.10. One of the main difficulties of the model is the generation of the geometry of the various components from CAT (Computed Axial Tomography) scan images; here COMSOL Multiphysics' interface with COMSOL Script comes very handy.

Figure 7.10 above shows the main components considered in the finite element model: the bladder, the pelvis muscles and a portion of the bones of a pelvis to which the muscles are attached.

7.10.2 The Geometry

The geometry of the bladder is derived entirely from CAT scan images, illuminated on a diaphanoscope, in order to get the profiles of the bladder in various sections. The distance between the cross-sections give in each of the scan is 1 cm.

The bladder can be considered as a little bag with variable thickness that at rest is 5 mm on average. For this particular case, a CAT scan was executed

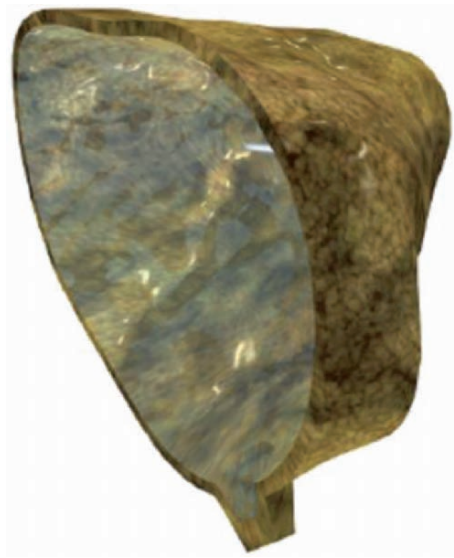

Fig. 7.11. Cross-section of the bladder including the junction with the urethra

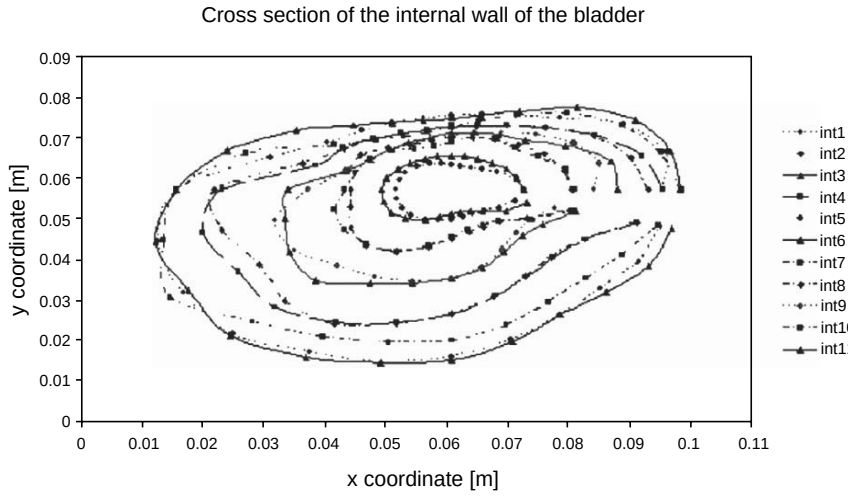

Fig. 7.12. Contours of the internal walls of the bladder. The geometry is define by 11 contour curves along the depth of the bladder

on a patient placed in a vertical position, with the bladder filled with fluid so that the thickness is 2 mm. Fig. 7.11 shows a section of the bladder including the junction with the urethra. The thin three-dimensional structure is built up using contours of the cross-sections of the internal and external walls of the bladder Fig. 7.12 shows an example of such a set of cross-sections obtained from a CAT scan.

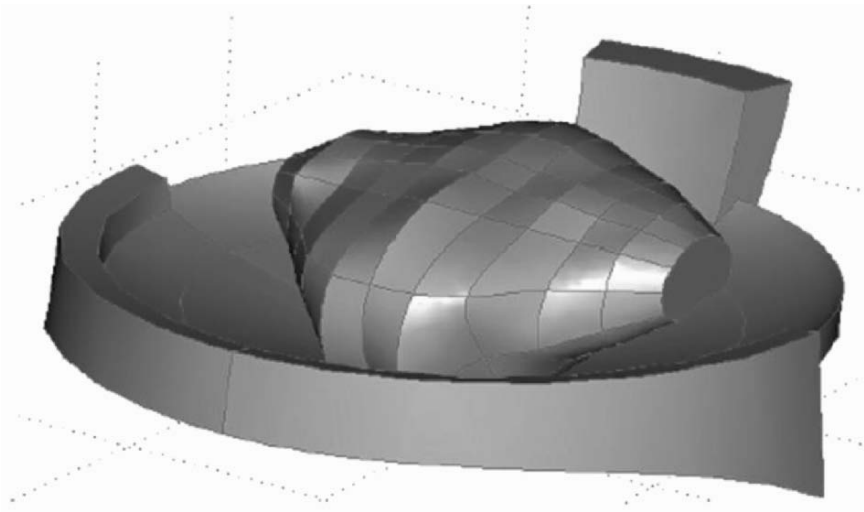

Fig. 7.13. Bladder geometry used in the COMSOL Multiphysics model

Each section is defined by 24 points taken with 15 degrees angles around the central axis of the structure. 22 sections (11 external and 11 internal) are collected in 22 spline curves and two groups of 11 splines are then joined to create two three-dimensional geometries using the "loft" function. Two COMSOL Script files automatize this process.

The created geometry object are exported to COMSOL Multiphysics from the COMSOL Script workspace. The remaining part of the model is created using COMSOL Multiphysics's CAD tool. Fig. 7.13 shows the resulting geometry as seen in the COMSOL Multiphysics GUI.

The resulting mesh consists of about 49,000 elements, which gives about 66,000 degrees of freedom. Fig. 7.14 shows the mesh as generated by COMSOL Multiphysics.

7.10.3 Input Data

Biological tissues have in general peculiar constitutive properties and can in general also show time-dependent behavior. It is very difficult to find literature data for such materials, but in the last few years a lot of research has been dedicated to the mechanical properties of biological tissue. One possible way of treating these materials is through the use of hyperelastic models. However, in this model where the mechanical loads are comparably small, linear elastic behavior is used for all materials. Also the fluid that fills the bladder is treated as an elastic material with a very small value of the Young's modulus. This is acceptable in this case, because we are only interested in the mass contribution of the fluid during the dynamic analysis. Material properties are defined as follows:

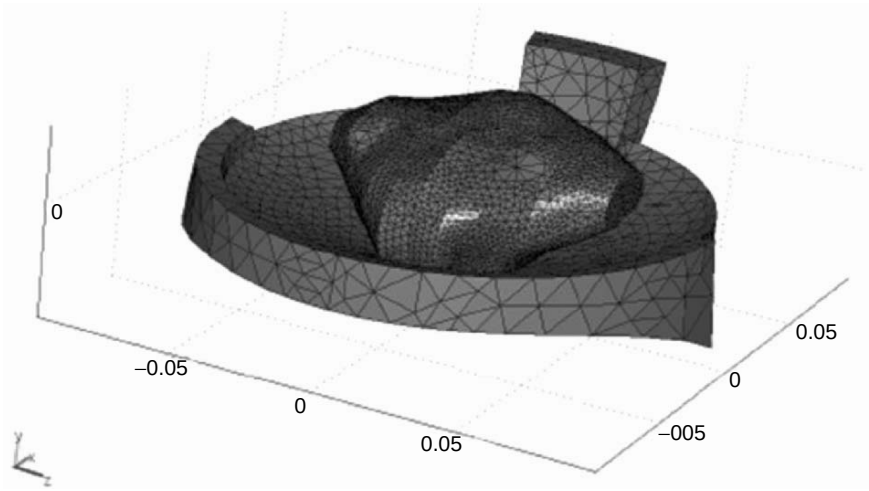

Fig. 7.14. Finite element mesh created by COMSOL Multiphysics

Bladder
- Density = $956\,\mathrm{kg\,m^{-3}}$
- Young's modulus = $3.5\mathrm{E}5\,\mathrm{N\,m^{-2}}$
- Poisson's ratio $\nu = 0.45$

Pelvis muscles
- Density = $1,200\,\mathrm{kg\,m^{-3}}$
- Young's modulus = $1.162\mathrm{E}6\,\mathrm{N\,m^{-2}}$
- Poisson's ratio $\nu = 0.4$

Pelvis bones
- Density = $2570\,\mathrm{kg\,m^{-3}}$
- Young's modulus = $1.0E9\,\mathrm{N\,m^{-2}}$
- Poisson's ratio $\nu = 0.3$

Fluid
- Density = $1,000\,\mathrm{kg\,m^{-3}}$
- Young's modulus = $1.0\mathrm{E}3\,\mathrm{N\,m^{-2}}$
- Poisson's ratio $\nu = 0.495$

Curves and two groups of 11 splines are then joined to create two three-dimensional geometries using the "loft" function. Two COMSOL Script files automatize this process.

7.10.4 Dynamic Analysis

The aim is to simulate the effect of two short coughs and the relaxation of the modeled components after such an excitation. The coughs are applied by

imposing a displacement to the pelvis bones, since these are almost rigid. The time duration of each single cough is 0.5 s and a sinusoidal amplitude has been assumed for the applied displacements. A vertical and a rotational motion is applied for 1 s. During the remaining part of the time interval the imposed displacements are set to zero.

Results

Figure 7.15 shows the vertical displacement after 0.125 s of the analysis, corresponding to the positive peak value of the displacement during the first cough.

It is also of interest to determine the stresses in the bladder and their variation during the process. Figure 7.17 shows the distribution of the von Mises stress after 0.125 s along the vertical cross-section corresponding to the displacements in Fig. 7.16.

Model Library path: Structural_Mechanics_Module/
Bioengineering/bladder
Modeling Using the Graphical User Interface

1. Click on the *COMSOL Multiphysics* icon to open the *Model Navigator.*
2. Select *3D* in the *Space dimension* list.

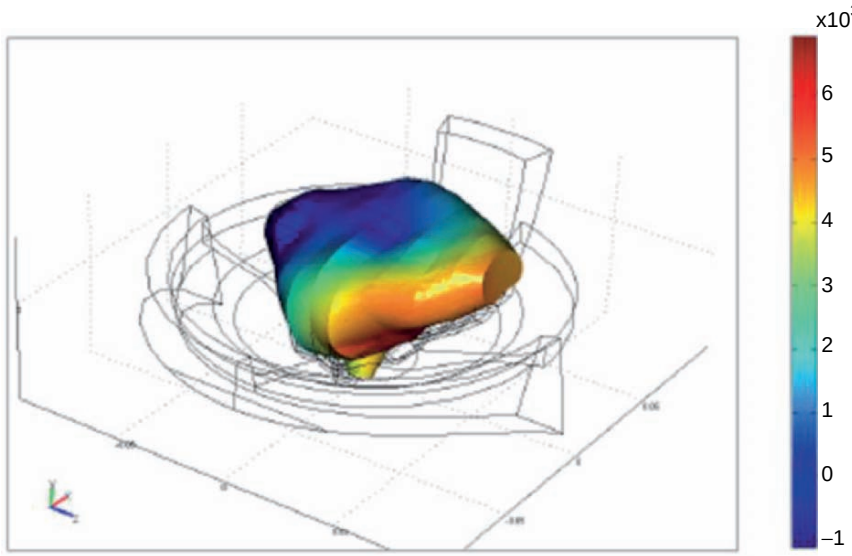

Fig. 7.15. *Y*-displacement of the bladder taken as a snap shot after 0.125 s of the analysis

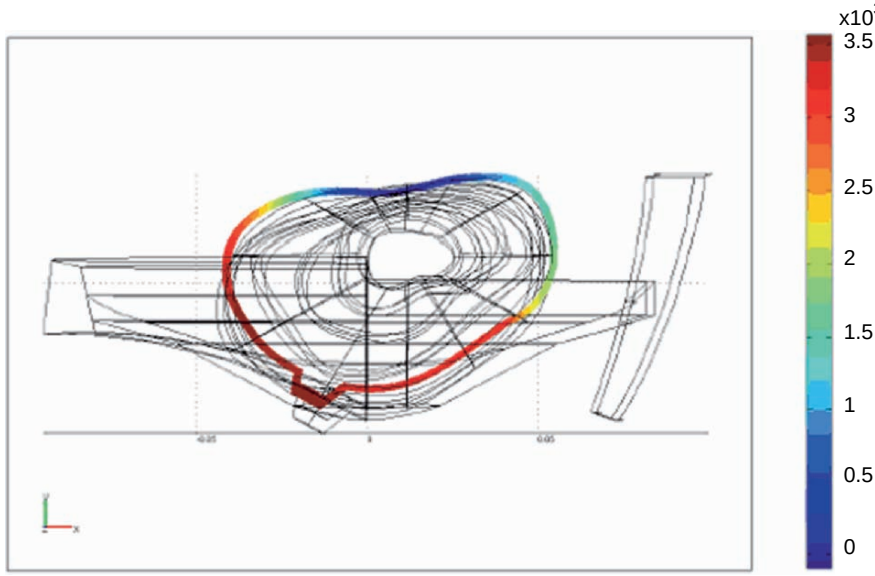

Fig. 7.16. Vertical cross-section of the displacement of the bladder after 0.125 s

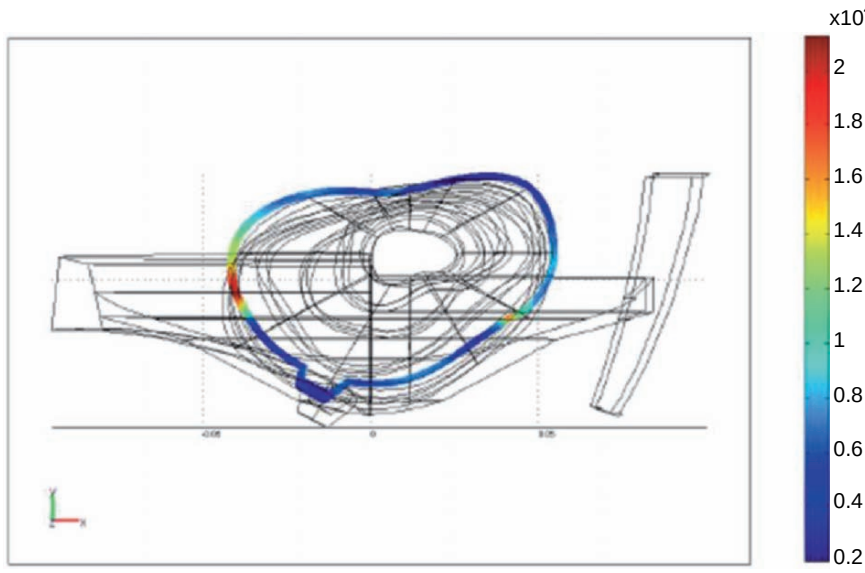

Fig. 7.17. von Mises stresses along a vertical cross-section of the bladder after 0.125 s

3. In the list of application modes, select the *Structural Mechanics Module > Solid, Stress-Strain > Transient analysis* application mode.
4. Click *OK*.

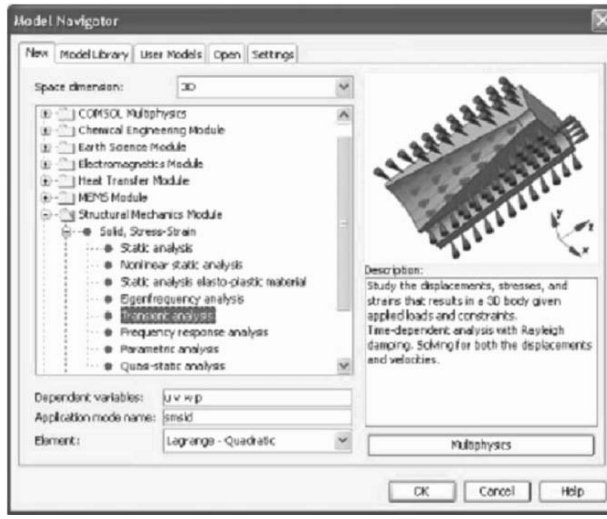

This problem will be solved using SI units (meters, seconds, Newtons, etc.).

Options and Settings

Define the following constants in *Constants* dialog box, which you can open from the *Options* menu.

1. Define a variable with *Name* E_bone and *Expression* 1.0e9.
2. Define a variable with *Name* v_bone and *Expression* 0.3.
3. Define a variable with *Name* rho_bone and *Expression* 2570.
4. Define a variable with *Name* E_bladder and *Expression* 3.5e5.
5. Define a variable with *Name* v_bladder and *Expression* 0.45.
6. Define a variable with *Name* rho_bladder and *Expression* 956.
7. Define a variable with *Name* E_fluid and *Expression* 1.0e3.
8. Define a variable with *Name* v_fluid and *Expression* 0.495.
9. Define a variable with *Name* rho_fluid and *Expression* 1,000.
10. Define a variable with *Name* E_muscle and *Expression* 1.162e6.
11. Define a variable with *Name* v_muscle and *Expression* 0.4.
12. Define a variable with *Name* rho_muscle and *Expression* 1.200.
13. Define a variable with *Name* gravity and *Expression* 9.81.
14. Click *OK*.

Geometry Modeling

1. Select *Import* and *Cad Data From File* from the *File* menu.
2. Select *All files* in the *Files of type* list.
3. Select the file bladder.mphbin in the Structural Mechanics Model Library folder and click *Import*.
4. Click the *Zoom Extents* button.
5. Click the *Headlight* button and rotate the geometry to get a proper view according to the figure.

Physics Settings

Subdomain Settings

1. Select *Subdomain Settings* From the *Physics* menu.
2. Select subdomain 1 and set *Young's modulus* to E_bone, *Poisson's ratio* to v_bone and *Density* to rho_bone.
3. Click the *Constraint* tab and set *Rx* to 0 and
4. Type (t<=1)*(0.2*z+0.005)* sin(4*pi*t)+(t>1)*(0) in the *Ry* edit field.
5. Click the *Load* tab and set *Fy* to –rho_bone*gravity.
6. Click the *Element* tab and select *Lagrange-Linear* elements.
7. Select subdomain 2 and set *Young's modulus* to E_muscle, *Poisson's ratio* to v_muscle and *Density* to rho_muscle.
8. Click the *Load* tab and set *Fy* to –rho_muscle*gravity.
9. Click the *Element* tab and select *Lagrange-Linear* elements.
10. Select subdomain 3 and set *Young's modulus* to E_bladder, *Poisson's ratio* to v_bladder and *Density* to rho_bladder.
11. Click the *Load* tab and set *Fy* to –rho_bladder*gravity.
12. Click the *Element* tab and select *Lagrange-Linear* elements.
13. Select subdomain 4 and set *Young's modulus* to E_fluid, *Poisson's ratio* to v_fluid and *Density* to rho_fluid.
14. Click the *Load* tab and set *Fy* to –rho_fluid *gravity.
15. Click the *Element* tab and select *Lagrange-Linear* elements.
16. Select subdomain 5 and set *Young's modulus* to E_bone, *Poisson's ratio* to v_bone and *Density* to rho_bone.
17. Click the *Constraint* tab and set *Rx* to 0.
18. Type (t<=1)*(0.005* sin(4*pi*t))+(t>1)*(0) in the *Ry* edit field.
19. Click the *Load* tab and set *Fy* to –rho_bone*gravity.
20. Click the *Element* tab and select *Lagrange-Linear* elements.
21. Click *OK*.
22. Select *Properties* in the *Physics* menu and select *on* in the *Large Deformation* list.

Mesh Generator

1. Click the *Initialize Mesh* button.

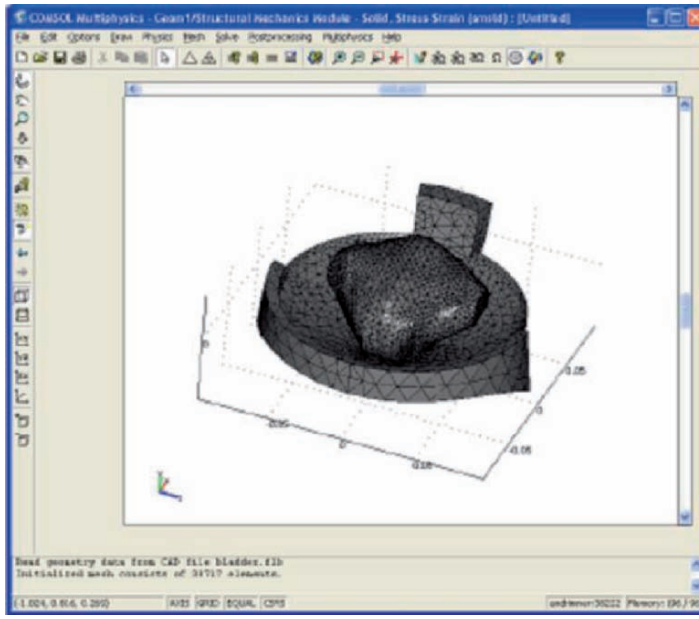

Solving the Model

1. Click the *Solve Parameters* button.
2. Select *Time dependent* analysis in the *Solver* list.
3. Type 0:0.02:2 in the *Times* field.
4. Click *OK*.
5. Click the *Solve* button.

7.10.5 Traumatic Injuries in a Network of Blood Vessels

Introduction

Based on Structural fluid interaction, the model is created using FEM LAB-3 – a multiphysics Modeling. This work has been carried out by Dr. Tamer Elnady and is being included in the text with this compliments and permission.

This model studies a portion of the vascular system of a young child, in particular the upper part of the aorta (Fig. 7.18). The aorta and its ramified blood vessels are embedded in biological tissue, specifically the cardiac muscle. The flowing blood applies pressure to the artery's internal surfaces and its branches, thereby deforming the tissue. The analysis consists of two distinct

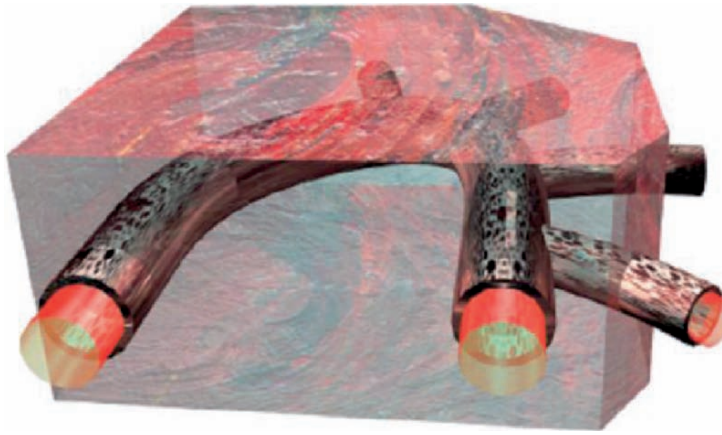

Fig. 7.18. The model domain consists of part of the aorta, its branches, and the surrounding tissue

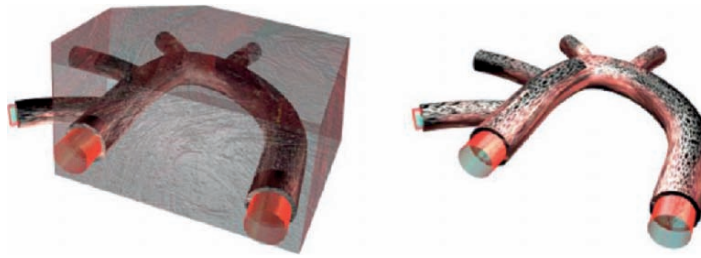

Fig. 7.19. A view of the aorta and its ramification (branching vessels) with blood contained, shown both with (**a**) and without (**b**) the cardiac muscle

but coupled procedures: first, a fluid-dynamics analysis including a calculation of the velocity field and pressure distribution in the blood (variable in time and in space); second, a mechanical analysis of the deformation of the tissue and artery. In this model, any change in the shape of the vessel walls does not influence the fluid domain, which implies that there is only a:

1. Way fluid–structural coupling using FEMLAB
2. Way coupling using the software's ALE methods

Model Definition

Figure 7.19 shows two views of the problem domain, one with and without the cardiac muscle. The model's mechanical analysis must consider the cardiac muscle because it presents a stiffness that resists artery deformation due to the applied pressure. The modeler created the geometry using FEMLAB's built-in CAD editor using several work planes. In doing so, the modeler made

extensive use of Boolean operators to join the 3D geometries and also to evaluate their intersections or differences. The file blood_vessel_geo.fl contains the initial geometry for the FEMLAB model, which you can examine with the FEMLAB Multiphysics Viewer, which we distribute at no charge.

The main characteristics of the analyses are:

- *Fluid-dynamics analysis*
  Here the model solves the Navier–Stokes equations. This analysis considers only the subdomains of the blood. At the point where the model brings the vessels to an abrupt end it represents the load with a known pressure distribution.
- *Mechanical analysis*
  This analysis is highly nonlinear due to the assumption of a large displacement and the constitutive behavior of the materials (the model describes the response of the artery and cardiac muscle with a hyperelastic law similar to those for rubber components). Only the subdomains related to the biological tissues are active in this analysis. The model represents the load with the pressure distribution it computes during the fluid-dynamics analysis.

7.10.6 Analysis of Rubber-Like Tissue and Artery Material Model

The analysis of rubber-like elastomers is generally a difficult task for several reasons:

- The material can undergo very large strains (finite deformation).
- The stress–strain relationship is generally nonlinear.
- Many rubber-like materials are almost incompressible. You must revise standard displacement-based finite element formulations in order to arrive at correct results (mixed formulations).

You must pay particular attention to the definition of stress and strain measures. Finite deformations are displacements where standard assumptions about infinitesimal displacements are no longer valid. It is permissible to consider finite deformations in a model when:

- Significant rigid-body rotations occur (finite rotations).
- The strains are no longer small (larger then a few percent).
- The loading of the body depends on the deformation.

Under these assumptions, one of the most commonly used definitions of strain is the Green-strain, E, where

$$E = \frac{1}{2} \cdot \left(F^{\mathrm{T}} F - I \right) \text{ or } E = \frac{1}{2} \cdot (C - I) \,, \tag{7.74}$$

where F is the deformation gradient, and $C = F^{\mathrm{T}}F$ is the right Gauchy–Green tensor. Using the displacements, you can write the Green strain as

$$E_{ij} = \frac{1}{2} \cdot \left(\frac{\partial u_i}{\partial X_j} + \frac{\partial u_j}{\partial X_i} + \frac{\partial u_k}{\partial X_i} \cdot \frac{\partial u_k}{\partial X_j} \right). \tag{7.75}$$

The stress measure conjugate to the Green strain is the Second-Piola–Kirchhoff stress, S, which is related to the Cauchy stress, σ, according to

$$\sigma = J^{-1} F S F^{\mathrm{T}}. \tag{7.76}$$

It is common to model rubber-like materials as hyperelastic materials, where the constitutive law is defined beginning from a strain energy function, W. You compute stresses, S, deriving W with respect to strains E, so that

$$S + \frac{\partial W}{\partial E}. \tag{7.77}$$

There are many choices for the strain energy density, W, resulting in material models, and just a few of the most common ones include Neo-Hookean, Mooney–Rivlin, polynomial, Ogden, and Arruda–Boyce. For an isotropic material, W can only be a function of the strain invariants, and due to the material's incompressibility, it is better to work with modified invariants with no dependency on the volume change. To do so, introduce $J = \det(F)$ as the ratio between the present and the original volume. The following equations illustrate this approach:

$$I_1 = trace(C) = C11 + C22 + C33 \tag{7.78}$$

$$\bar{I}_1 = I_{1.} J^{-\frac{2}{3}}. \tag{7.79}$$

The simplest model is the Neo-Hookean model, defined as

$$\bar{W} = \frac{1}{2}\mu \left(\bar{I}_1 - 3 \right) + \frac{1}{2} K \left(J - 1 \right)^2. \tag{7.80}$$

You obtain the stress tensor, S, from the derivation

$$S = \mu J^{-\frac{2}{3}} \left(I - \frac{1}{3} \bar{I}_1 C^{-1} \right) + \mathrm{K} J \left(J - 1 \right) C^{-1}. \tag{7.81}$$

For highly incompressible hyperelastic materials, one cannot derive the stresses, S, directly from (7.81) because J is close to unity. Instead, a direct dependence on the pressure, p, replaces the contribution from the last term of (7.81) so that

$$S = \mu J^{-\frac{2}{3}} \left(I - \frac{1}{3} \bar{I}_1 C^{-1} \right) - pJC^{-1} \tag{7.82}$$

Note that the pressure enters the stress directly, whereas the displacements contribute through their derivatives. Thus the order of the pressure interpolation should be one lower than that used for the displacements.

Materials

The model in this discussion uses the following material properties:

- Blood
  - Density = $1,060\,\mathrm{Kg/m^3}$
  - Dynamic viscosity = $0.005\,\mathrm{N\,s\,m^{-2}}$
- Artery
  - Density = $960\,\mathrm{kg\,m^{-3}}$
  - Neo-Hookean hyperelastic behavior: the coefficient μ equals $62{,}04{,}106\,\mathrm{N\,m^{-2}}$, while the bulk modulus equals $20\,\mu$ and corresponds to a value for Poisson's ratio, ν, of 0.45. An equivalent elastic modulus equals $1.0\mathrm{E}7\,\mathrm{N\,m^{-2}}$.
- Cardiac muscle
  - Density = $12{,}000\,\mathrm{kg\,m^3}$
  - Neo-Hookean hyperelastic behavior: the coefficient μ equals $7{,}19{,}676\,\mathrm{N\,m^{-2}}$, while the bulk modulus equals $20\,\mu\mathrm{m}$ and corresponds to a value for Poisson's ratio, ν, of 0.45. An equivalent elastic modulus equals $1.16\mathrm{E}6\,\mathrm{N\,m^{-2}}$.

7.10.7 Fluid-Dynamics Analysis

The fluid-dynamics analysis considers the solution of the three-dynamics Navier–Strokes equations. You can do so in both a stationary case or in the time domain. As a first step, consider the nonlinear stationary analysis (see the file *blood_vessel_fluid_stat.fl*). To establish the boundary conditions, the model uses six pressure conditions with the configuration in Fig. 7.20.

For the time dependent analysis, the model uses a simple trigonometric function to vary the pressure distribution over time:

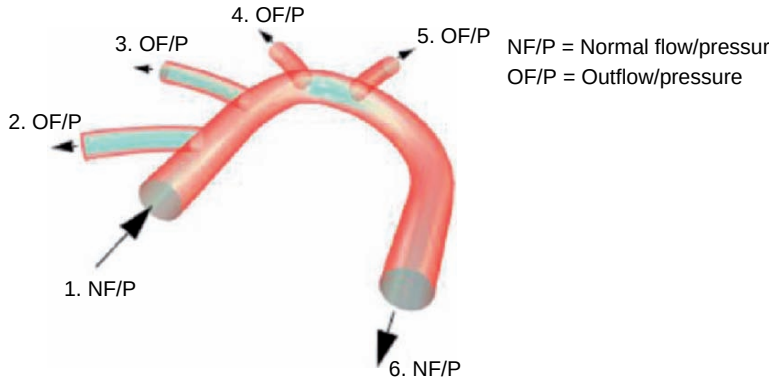

Fig. 7.20. Boundary conditions for the fluid-flow analysis

$$0 \leq t \leq \frac{1}{2}\,\text{sec} \quad \sin \pi t,$$

$$\frac{1}{2} \leq t \leq \frac{3}{2}\,\text{sec} \quad \frac{3}{2} - \frac{1}{2} \cdot \cos\left(2\pi\left(t - \frac{1}{2}\right)\right). \tag{7.83}$$

You can implement this effect in FEMLAB with an expression (in this case with the name amplitude), which you define on the active subdomain.

The pressure conditions are:

- Sect. 1: $11,208\,\text{N}\,\text{m}^{-2}$
- Sect. 2: $11,181\,\text{N}\,\text{m}^{-2}$
- Sect. 3: $11,109\,\text{N}\,\text{m}^{-2}$
- Sect. 4: $11,109\,\text{N}\,\text{m}^{-2}$
- Sect. 5: $11,109\,\text{N}\,\text{m}^{-2}$
- Sect. 6: $11,062\,\text{N}\,\text{m}^{-2}$

Results and Discussion

First examine the steady flow field so as to compare its result to the transient case.

In comparison, the transient analysis (in the file *blood_vessel_fluid_stat.fl*) reveals only a small difference between two pressure distributions (the one computed with the time dependent analysis, and the one from the stationary analysis with pressure defined as in (7.83). In other words, the pressure field reaches its steady-state very quickly when you change the boundary conditions.

Figure 7.21 shows the pressure at a point in center of the vessel as computed with a time dependent model where the boundary conditions change at a show, continuous rate. The small difference implies that you can scale the pressure computed in a steady state condition.

A final model in the file *blood_vessel_fluid_mech_lin_large.fl* accounts for the influence of large displacements, and it accounts for the hyperelastic behavior of the biological tissues. To limit the dimensions of the finite element model, the modeler chose to consider only the artery and to apply a constant pressure ($11,109\,\text{N}\,\text{m}^{-2}$) to the internal surfaces multiplied with an amplitude function defined through parameter time.

Another case includes effects due to the presence of the cardiac muscle (see the file *blood_vessel_fluid_mech_hyper.fl.* Here the model has a foundation load that is simply a stiffness E/l multiplied by the normal displacement $u \cdot n$. The constant l is the depth fluid-dynamics stationary analysis in the subsequent parametric nonlinear mechanical analysis by multiplying the value p with the amplitude function in 7.2.

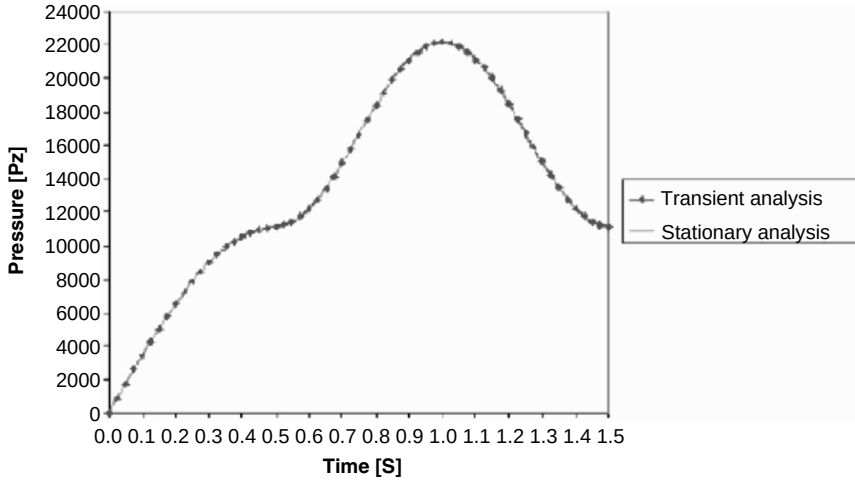

Fig. 7.21. Pressure at a given point in the transient model (datapoints) and the stead-flow model (*solid line*). Both cases take the value of the boundary condition from Equation 7.2, but the steady-flow model varies time using the parametric solver assuming a steady-state condition at every point

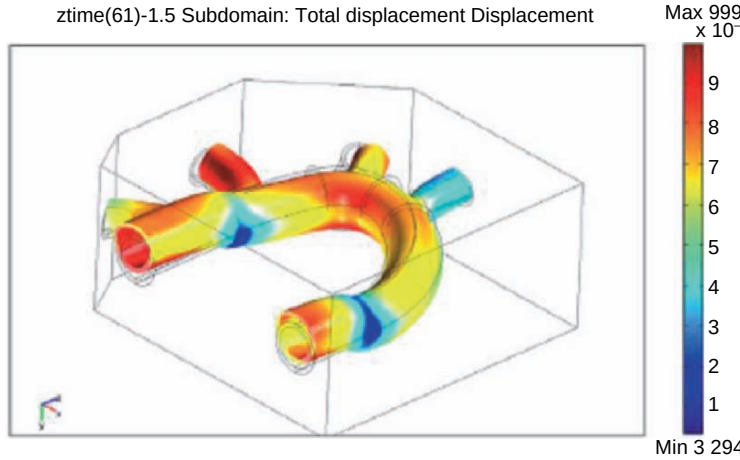

Fig. 7.22. Total displacements in the blood vessel using a linear elastic model

This example performs this scaling in a first approach (in the file *blood_vessel_fluid_mech_lin.fl*) based on a linear elastic constitutive law for the biological tissues. This case does not use large displacement theory due to the low strains. Figs. 7.22 and 7.23 show the distribution of the total displacement (measured in m) and the Tresca stress (in the units $\mathrm{N\,m^{-2}}$) at $t = 1.0\,\mathrm{s}$, corresponding to the peak of the load path. The distribution of

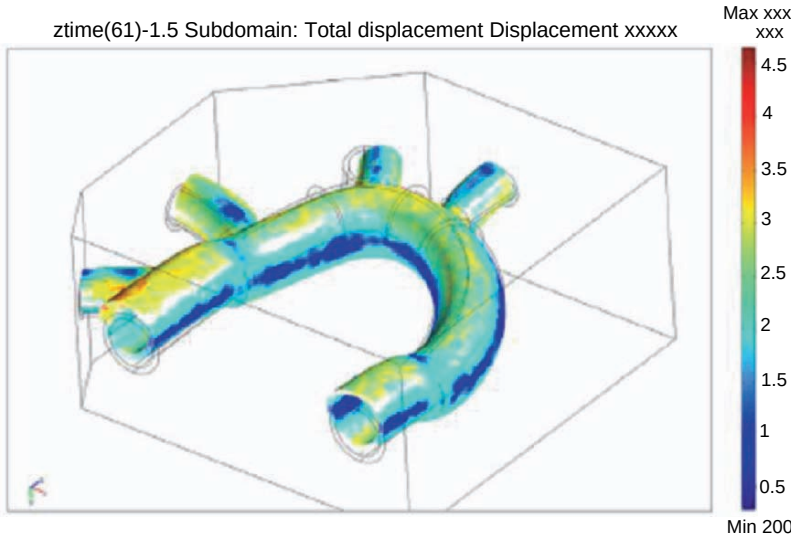

Fig. 7.23. Tresca stress used in the lindear elastic model

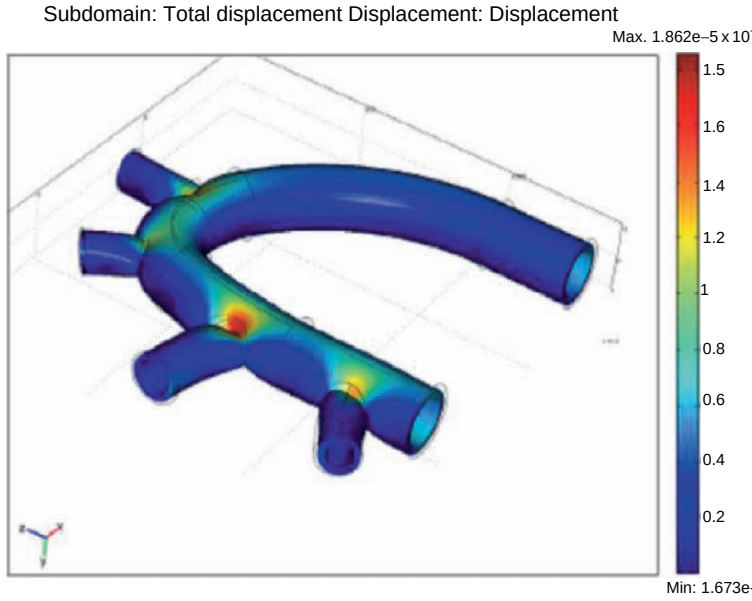

Fig. 7.24. Displacements in the blood vessel using a hyperelastic model

pressure represents the load, and the parameter you vary for the incremental iterative nonlinear analysis is *ztime*. Boundaries of the muscle are fixed in the normal direction (both for the global and the local coordinate systems) of the surrounding muscle, here set to 0.02 m. Modelers often use this numeric trick to limit a model's size, in this case to 67,227 degrees of freedom.

As previously described, for this hyperelastic analysis the modeler selected two application modes: a PDE general form with a variable p that identifies the pressure, and a 3D solid application mode using nonlinear structural analysis driven by parameter *ztime*. The CPU time in this hyperelastic case is larger than in the previous simplified analysis. Fig. 7.24 shows the total displacement in this case at the load peak (after 1 s), and it is interesting to compare these results to Fig. 7.22 for the less-elaborate model.

7.11 Posterior Rib Fractures from Side Airbag Deployment

The deployment of a seat mounted side air bag may contact the posterior and lateral side of the thorax. This contact can result in rib fractures in vulnerable occupant, such as elderly or osteoporitic subject, even in low speed collisions. The National Highway Traffic Safety Administration has investigated a case through their Special Crash Investigation programme that illustrates this phenomenon. The case involved a low speed side impact in which the seat mounted side air bag deployed. The occupant sustained fractures of the eight, ninth, and tenth ribs on the posterior and lateral side. In order to quantify this interaction, research is being performed with instrumental dummies and human cadavers (Table 7.5).

The physical test data from test 95S008 could not be used due to lack of lower spine and pelvic acceleration date (i.e., the test accelerometers failed), therefore, the data from test 95S014 was used for comparison with finite element models. Unfortunately, the camera behind the SID ATD in test 95S014 malfunctioned so the position of the SID at the time of impact could not be precisely determined. The SID ATD had started leaning toward the window at the time of impact. Also, a vehicle roll of 3 degrees was observed in the test films. In the finite element simulations the SIDs were given a rotation of six degrees towards the impact side door (same position of SID in test 95S008) and the vehicle was given a roll angle of 3 degrees. The vehicle impacted the rigid pole laterally with a velocity of 32.8 km h^{-1}. The results of simulation are shown in Table 7.6, Plates 7.44–7.46.

Table 7.5. Impact conditions of the taurus rigid pole tests and simulation

	95S008	95S014	simulations
velocity	36.5 Km h^{-1}	32.8 km h^{-1}	32.8 km h^{-1}
roll	4°	3°	3°

Table 7.6. Peak acceleration for a $32\,\mathrm{km\,h^{-1}}$ side impact of a ford taurus and a rigid pole

	95S014	SRI-SID-V2	PD-SID-V3
T12 peak acceleration	53.00	59.80	62.40
LURY peak acceleration	40.70	100.08	-
LLRY peak acceleration	45.60	90.84	-
peal lateral pelvic acceleration	98.90	105.20	141.80
Thoracic Trauma Index (TTI)	49.30	74.94	-

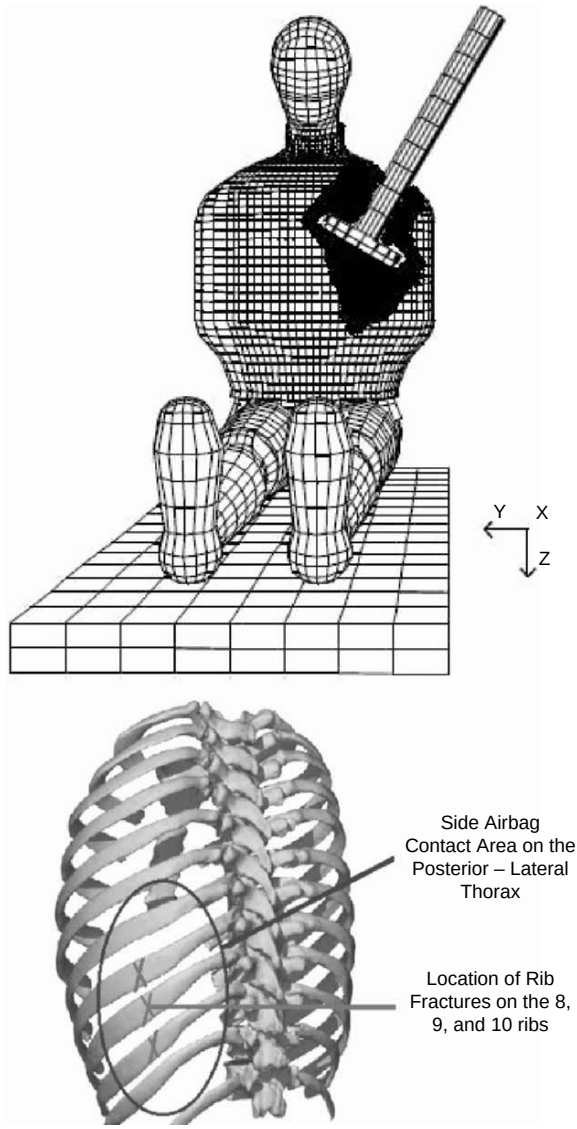

Plate 7.44. Rib fractures on the posterior and lateral thorax corresponding to the contact location of a deploying side air bag

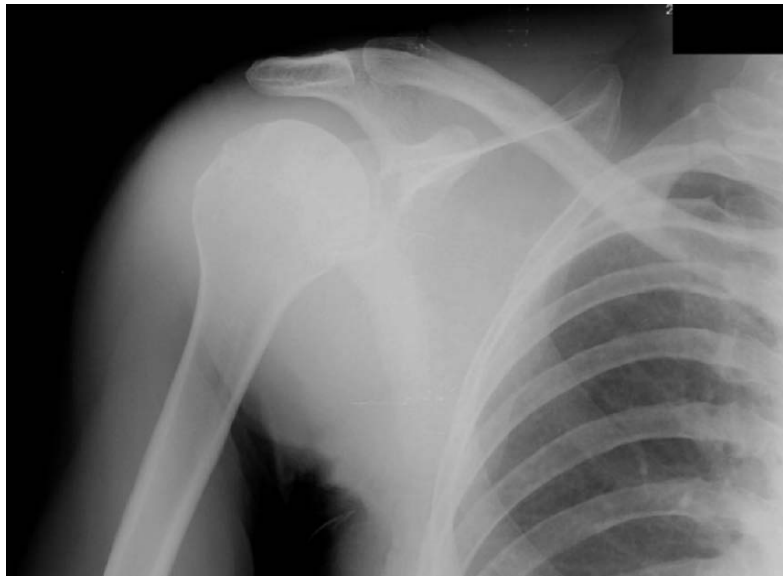

Plate 7.45. Rib fractures-X-ray

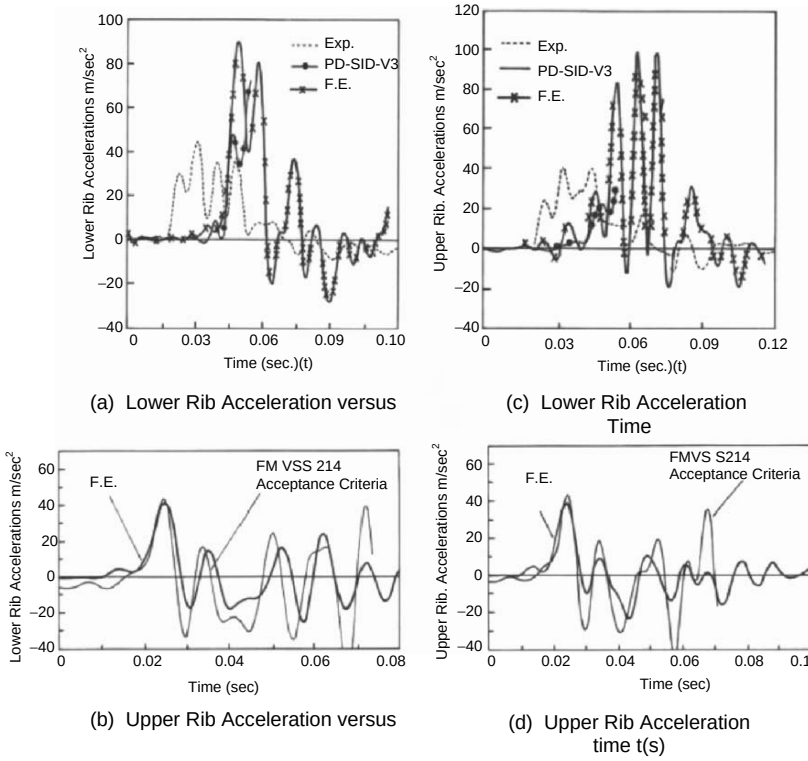

Plate 7.46. Rib fractures–acceleration vs. time

The test simulation with the SIR-SID-V2 terminated at 114 ms due to excess mass scaling in the door trip material in the rear right door. The coarse mesh in the rear door trim opposite to the impact side began hourglassing after 100 ms causing the mass scaling. The head of the SID was pinched between the B pillar and the pole causing the SID to rotate about the neck as the seat was crushed by the pole. This behavior is very similar to that observed in the physical test. The results indicate that the SRI-SID-V2 predicts approximately the same lower spine and pelvic accelerations as the physical test. The rib accelerations are however higher and occur later than in the physical tests. The high rib accelerations could be due to the uncertain SID position at the time of impact.

8

Traumatic Injuries, Complications, and Management

8.1 Head Traumatic Injury Complications and Management

Many patients who have sustained minor head trauma develop a variety of vague persistent symptoms. The postconcussive syndrome (PCS) can be extremely debilitating. Some patients are unable to return to work or other normal activities for weeks to months after what appears to be inconsequential injury. Common complaints are headaches, memory loss, or problems with concentration. PCS in children manifests as mental status changes, including irritability, hyperactivity, decreased attention span, sleep disturbances, and emotional lability. Occasionally the child complains of headaches and dizziness. Examination reveals minimal or no neuralgic abnormalities. Imaging studies done initially at the second visit are usually normal. Neuropsychometric studies of patients with PCS have produced conflicting results, some early studies detect neurobehavioral deficits, whereas others do not, and suggest that symptoms resolve when secondary gain is successfully achieved. The inability to measure organic function in the ED setting has made the evaluation of these patients difficult.

Magnetic resonance imaging (MRI) often detects abnormalities in patients with minor head injury who later have PCS. These abnormalities include contusions not detected on earlier computed tomography (CT) scans, focal edema, and other microscopic lesions. Patients with delayed presentation and persistent problems after seemingly minor head injury require a thorough assessment. CT or MRI may be warranted to rule out delayed complications of head injury. Careful follow-up should be arranged from the ED. An aggressive approach to the long-term facilitated by the EP may promote rapid rehabilitation and reduce the associated morbidity.

Brain abscesses develop infrequently after penetrating missile injuries to the head. Abscesses can also develop after open depressed skull fractures, if bony fragments are not removed, or as a postoperative complication. Posttraumatic cerebrospinal fluid (CSF) fistulas and fractures that disrupt air-filled

sinuses predispose to the formation of brain abscesses. Clinical manifestations include headaches, nausea, vomiting, declining mental status, signs of increased ICP, or new focal neurologic findings in patients who had been improving after trauma. Occasionally, nuchal rigidity, hemiparesis, or seizures may be present. Systemic signs are often subtle, and CSF leukocytosis may be absent.

The diagnosis of brain abscess is made by contrast-enhanced CT scan. A ring pattern with a low-density center is characteristic of a brain abscess. The enhanced ring represents surrounding altered vascular permeability and therefore is also seen in the cerebritis stage early in abscess formation. Lumbar puncture is often not helpful and should not be performed in the patient with sings of increased ICP (e.g., headache, vomiting, papilledema).

The treatment of brain abscess is usually operative drainage. The patient with cerebritis may respond to IV antibiotics but requires close monitoring with repeated CT scans. Common organisms isolated from posttraumatic abscesses are *Staphylococcus aureus* and gram-negative aerobes.

Cranial osteomyelitis can occur after penetrating injury to the skull. The clinical manifestations include pain, tenderness, swelling, and warmth at the infected site. More than 50% of cases will be obvious on plain skull films. Technetium bone scans can help in the diagnosis when the skull radiographs are negative but false-positive bone scans occur in patients with previous trauma or craniotomy. Adding a gallium scan will help to differentiate infection from other causes of a positive technetium scan. Patients with posttraumatic cranial osteomyelitis require surgical debridement and removal of the infected bone.

The injured brain is a source of tissue thromboplastin that activates the extrinsic clotting system. Disseminated intravascular coagulation (DIC) can develop within hours after any injury disrupting brain tissue. It has been detected in as many as 90% of all patients with severe brain injury. DIC increases morbidity and mortality after severe head trauma, as well as the risks of delayed intracranial hemorrhage. If a stable patient with DIC suddenly deteriorates, a repeat CT scan should be obtained to rule out hemorrhage.

The extent of tissue destruction determines the degree of DIC that develops. The diagnosis is based on abnormalities in prothrombin and partial thromboplastin times (PT, PTT), platelets, plasma fibrinogen levels, and fibrin degradation products.

Neurogenic pulmonary edema can develop from minutes to days after head trauma. This noncardiac pulmonary edema probably results from altered hydrostatic forces and microvascular permeability directly caused by brain injury. Lowering the ICP appears to reverse the neurogenic stimulation that causes this edema.

Head trauma is the leading cause of death among injured children and is responsible for 80% of all trauma deaths. Each year, 29,000 children younger than 19 years of age suffer permanent disability.

What are the etiologies of pediatric head trauma? Falls account for 37% of head injuries. MCVs are responsible for 18% of pediatric head trauma. In addition, pedestrian injuries account for 17% and falls from bicycles 10%. On an age-related basis, infants and toddlers are more prone to falls from their own height, school-age children are involved in sports injuries and MCCs, and all ages are subject to the sequelae of abuse.

An important anatomic difference of the pediatric patient, compared to the adult, is that the cranial vault of a child is larger and heavier in proportion to its total body mass. This predisposes children, specifically toddlers and infants, to high degrees of torque that are generated by any forces along the cervical spin axis. Sutures within the pediatric skull are both protective and detrimental to the outcome of head injury in these patients. While the cranium may be more pliable relative to traumatic insult, forces are generated internally that predispose the pediatric patient to parenchymal injury in the absence of skull fractures. The pediatric brain is less myelinated, predisposing it to shearing forces and further injury.

The clinician must obtain as many details surrounding the traumatic even as possible the height of the fall or injury is particularly important with regard to the development of associated injury. Most children fall from their own height. Children involved in MVCs are best evaluated by the degree of restraint that was present during the time of the accident. An infant in a properly installed car seat favors a benign outcome in most cases. Unrestrained children involved in high-speed crashes are prone to serious injury. It is important to consider the quality of the surface at the point of impact, specifically the presence or absence of carpeting within the home or location of injury.

In most cases it is important to establish whether there was loss of consciousness at the time of the injury event. With playground trauma, the history may be vague and the interpretation of any change in consciousness of the child may be regarded as an actual loss of consciousness. The behavior of the child after the even should include questions related to the presence or absence of irritability, lethargy, abnormal gait, or alterations in behavior. Most importantly, establishment of a timeline from the point of insult is helpful in determining whether there have been changes in the mental status of the patient.

The prognostic significance of vomiting after pediatric head trauma presents the clinician with many challenges. There is an adequate study defining an acceptable time frame in which vomiting after head injury is benign in nature. The development of seizures after head trauma, in contrast to vomiting, has been well studied. A brief seizure that occurs immediately after the insult (with rapid return of normal level of consciousness) is commonly called "an impact seizure" and is usually unassociated with intracranial parenchymal injury and in no way mandates the institution of anticonvulsant therapy. Seizures that occur later (longer than 20 min after the insult) portend the greater possibility of both internal injury and the development of seizures at a later date. Patients who experience seizures later in the course of the

posttraumatic event are best evaluated by the neurosurgical service. As in all instances of trauma, a careful history related to the possibility of substance abuse must be obtained.

The physical examination of the head-injured child must include strict attention to the "ABCs" of emergency care. While internal injuries are certainly important in the outcome of these patients, the maintenance of oxygenation and perfusion is paramount in eliminating further insult. Because the pediatric brain is sensitive to decreases in glucose, oxygen, and perfusion, their maintenance optimizes the chances of good recovery. Strict attention must be paid toward the maintenance of euvolemia because cerebral perfusion pressure (CPP) is adequate only in the face of a normal mean arterial pressure (MAP). CPP is equal to the MAP minus the ICP or, more simply, CPP = MAP − ICP. As the blood pressure is reduced, so is the CPP.

Pediatric Patients

There are several methods for evaluating head-injured patients. These include AVPU and GCS. The GCS has been modified for pediatric patients.

Studies involving reliability of the GCS in predicting the outcome in children with traumatic brain injury are optimistic with regard to actual outcome. In a study involving 80 children with traumatic brain injuries admitted to a intensive care unit (ICU), initial GCS scores were compared with eventual outcome. Both ICU lengths of stay and time to cognition relative to GCS scores indicated that scores greater than or equal to 6 were associated with favorable outcomes and neurologic status. While the numbers in this study are small, the important message for the clinician is that no matter how the patient presents neurologically, all efforts should be generated to ensure survival and maintain stable neurologic status within the ED.

Examining the brain-injured child involves cranial nerve testing and motor and sensory testing. The evaluation of cranial nerve function is essentially not different from that of the adult. The most important aspect of both motor and cranial nerve evaluation involves ruling out the presence of increased ICP. Common symptoms and signs of increased ICP in infants and children are outlined in Tables 8.1 and 8.2.

Minor injury to the scalp of infants and children involves the development of three possible injury complexes: caput succedaneum, injury to the

Table 8.1. Common symptoms and signs of increased intracranial pressure in infants

full fontanelle
split sutures
altered state of consciousness
paradoxical irritability
persistent emesis
the "setting sun" sign (inability to fully open eyes)

Table 8.2. Common symptoms and signs of increased intracranial pressure in children

headache
stiff neck
photophobia
altered state of consciousness
persistent emesis (vomiting)
cranial nerve involvement
papilloedema
hypertension, bradycardia, and hypoventilation
decorticate of decerebrate posturing

connective tissue itself; subgaleal hematoma, injury to the tissue surrounding the skull; and cephalohematoma, a collection of blood under the periosteum.

Skull fractures in children occur in many different configurations. Linear fractures, the most common type of *skull fracture*, rarely require therapy and are often associated with good outcomes. Factors favoring a poor outcome include the presence of the fracture overlying a vascular channel, a diastatic fracture, or a fracture that extends over the area of the middle meningeal artery. Diastatic fractures, or defects extending through suture lines, are unlike linear fractures, in that leptomeningeal cysts (growing fractures) may develop at these sites. Fractures of the basilar portions of the occipital, temporal, sphenoid, or ethmoid bones commonly occur in children. The presence of CSF, rhinorrhea, and otorrhea have been associated with these injuries. Signs of basilar *skull fractures* in children are similar to adults and include posterior auricular ecchymoses, or Battle's sign and raccoon eyes, or the presence of periorbital subcutaneous bleeding.

Strictly speaking concussion is defined as a brain insult with transient impairment of consciousness. Amnesia is often involved. Patients who suffer from concussive insults demonstrate anorexia, vomiting, or pallor soon after the insult. This transitional period is followed by rapid recovery to baseline and if a CT scan of the head is obtained, it is most often normal. In contrast, contusions are often the results of coup and contrecoup forces at work. They may not be associated with any loss of consciousness at the time of insult. Patients often present with associated symptoms such as altered level of consciousness, severe headache, vomiting, or focal deficits on neurologic assessment. These injuries are clearly demonstrable on CT.

Posttraumatic meningitis is caused by a variety of microbes depending on the portal of bacterial entry. Patients present with typical signs and symptoms of meningitis, including fever, altered mental status, and occasional focal neurologic signs. In patients with a CSF leak after basilar fracture, early meningitis (i.e., within 3 days of injury) is usually caused by pneumococci. Ceftriaxone or cefotaxime is a reasonable antibiotic choice, but sensitivities must be performed because pneumococcal resistance has been increasing.

If a high pneumococcal resistance is known, vancomycin should be added to the above regimen. Meningitis that develops more than 3 days after trauma is often caused by gram-negative organisms. A third-generation cephalosporin, with nafcillin or vancomycin added to ensure coverage of *S. aureus*, should be started. In children, posttraumatic meningitis may be caused by Haemophilus influenzae. Prophylactic antibiotics are not currently recommended in the acute setting in patients with CSF leaks caused by basilar *skull fractures*.

8.2 Diagnostic Strategies and Management

As a basic rule, serial examinations are the most reliable indicators of clinical deterioration. The presence of focality is a reliable indicator of a localized insult, whereas the absence of focality may be misleading. Infants are classically late in developing the signs of increased ICP. As in the adult, papilledema may require days to develop. Unfortunately, the classic Cushing's response (bradycardia and hypertension) is also unreliable in children.

Most clinicians favor early and controlled intubation in pediatric patients with GCS scores that are deteriorating. Always obey basic advance trauma life support protocols because isolated head injuries are uncommon in the multiply traumatized child.

If ICP elevation is suspected, the clinician has many therapeutic options that may be exercised within the ED setting. These interventions are summarized.

It is important to recognize the presence of herniation syndromes in the pediatric patient. Uncal herniation involves the presence of a unilaterally dilated pupil, contralateral hemiplegia, and the presence of spontaneous hyperventilation. Brainstem herniation is characterized by small, sluggish pupils, decorticate posturing, and Cheyne–Strokes respirations. The final common pathway, brainstem herniation, presents with fixed and dilated pupils, flaccid muscle tone, and slow or apneic breathing. Management of suspected herniation is controlled hyperventilation. Clinical endpoints of hyperventilation are improved patient status or constriction of dilated pupil(s). Arterial blood gas determination is used to assess adequacy of hyperventilation with a target Pco2 of 30–35 mm Hg.

Excessive hyperventilation can result in excessive cerebral vasoconstriction and secondary brain injury, therefore begin ventilation at an age-appropriate rate and then increase ventilation rates until papillary constriction occurs.

8.3 Radiology

8.3.1 Skull Films

The role of skull films in the evaluation of pediatric patients involves studies that were done before the advent of CT. As mentioned previously, the presence of a *skull fracture* on plain film in no way guaranteesthe presence or absence

of underlying tissue damage. Studies that have been done in the past have attempted to establish low- and moderate-risk groups on the basis of clinical presentations.

The low-risk group involves patients who are asymptomatic neurologically, with headache, dizziness, scalp lacerations, and the absence of neurologic anomaly. Moderate-risk groups for *skull fractures* include a history of loss of consciousness or amnesia, progressively worsening headache, an age younger than 2 years, seizures, or the presence of protracted vomiting. Most clinicians agree that at present, firm indications for skull films alone include the skeletal survey involved with the evaluation of child abuse, establishment of a functioning ventricular peritoneal shunt, penetrating wounds of the scalp or the suspicion of foreign bodies underlying scalp lacerations.

8.3.2 Computed Tomography of the Head

There has been considerable research surrounding the indications and relative value of CT scanning in the pediatric head-injured patient. A study was performed on 185 children between the ages of 2 and 17 years with loss of consciousness and GCS scores of 15 after mild head injury. The authors partitioned these children into further categories according to physical examination findings, neurologic status, and whether the head injury was part of an isolated or nonisolated trauma presentation. Of the 185 patients in the study, 17 patients were excluded on the basis of obvious *skull fractures* on physical examination. The remaining 168 patients demonstrated two variables that were highly associated with the presence of intracranial hemorrhage, namely neurologic status and presence of multiple injuries. None of the 49 neurologically normal children with isolated head injury had intracranial hemorrhages. All patients with intracranial hemorrhages were noted to have other traumatic insults on physical examination. The authors conclude that after isolated head injury with loss of consciousness, children older than 2 years of age who were neurologically normal may be discharged without a CT scan after careful physical examination alone.

8.4 Trauma Types vs. Management

8.4.1 Severe Head Trauma

The neurosurgical literature defines severe head injury as TBI manifested by a postresuscitation GCS of 8 or less within 48 h. In the emergency setting, however, this definition is not practical because the outcome for the patient beyond the initial resuscitation is not known. Most emergency medicine research defines severe head injury as that presenting with a GCS score of 8 or less at the acute presentation after injury. The presence of any intracranial contusion, hematoma, or laceration is also considered as severe injury.

Head trauma can cause profound effects on the cardiovascular system if compression of the brainstem and medulla occurs. Any cardiac dysrhythmia can occur and produce cardiac instability. All head inured patients should therefore be placed on a cardiac monitor as they are transported from the accident scene.

The secondary survey of the head-injured patient should include the search for external signs of head trauma. Scalp lacerations may bleed a large volume into a bulky dressing. A less bulky dressing should be used with firm constant pressure applied to avoid excessive blood loss.

8.4.2 Out-of-Hospital Care

The goals of the out-of-hospital management are the establishment of an efficient and adequate airway to prevent hypoxia and intravenous access to treat hypotension. An accurate neurologic assessment provides a means to determine the subsequent effectiveness of treatment and should focus on the GCS, papillary responsiveness and size, level of consciousness, and motor strength and symmetry.

Many severely head-injured patients are initially combative or agitated. Transporting an agitated patient who is fighting against physical restraints may exacerbate physical injury, cause a rise in ICP, and interfere with appropriate stabilization and management. It may be necessary to use out-of-hospital sedation or paralysis for control. It should be recognized that the use of sedatives or neuromuscular blockade may influence the initial ED evaluation of the neurotrauma patient. The risks and benefits of this acute intervention must be carefully considered and decisions made on a case-by-case basis. Out-of-hospital protocols allowing the use of sedative agents for selected agitated head-injured patients should be established. Currently used agents include lorazepam (Ativan), diazepam (Valium), midazolam (Versed), or droperidol (Inapsine).

Severe head injury is the most common reason for helicopter transfer in trauma care. Although the decision to transport by helicopter should be made on a case-by-case basis as well, considerations for helicopter use at a scene include a long extrication time, ground transport of longer than 30 min to appropriate ED and trauma care facility, two or more severely injured patients at a scene, and assistance in performing expedient lifesaving procedures, especially airway management. Field intubation in patients with severe head injuries has been shown to improve survival to the hospital.

8.4.3 Emergency Department

Airway

Rapid sequence intubation (RSI) is an effective and the preferred method for securing the airway in combative or agitated patients. If possible, a

brief neurologic examination should be performed before the patient is given any sedative or paralytic agents. In general the agents used for RSI in the head-injured patient are the same as those for other patients, although attention must be given to the increased ICP that can occur with any physical stimulation of the respiratory tract. Lidocaine (1.5–2 mg kg^{-1} IV push) effectively attenuates the cough reflex, hypertensive response, and increased ICP associated with intubation. Thiopental may also be effective but should not be used in hypotensive patients. If succinylcholine is used, premedication with a subparalytic dose of a nondepolarizing agent should be considered if time permits, since fasciculations produced by succinylcholine may increase ICP. The degree of ICP elevation and its clinical significance are unclear, however, and must be balanced against the need for rapidly establishing an airway. Etomidate (0.3 mg kg^{-1} IV), a short-acting sedative-hypnotic agent, has beneficial effects on ICP by reducing cerebral blood flow and metabolism.

8.4.4 Hypotension

If hypotension is detected at any time in the emergent management of a head-injured patient, a cause other than the head injury should be sought. Hypotension is rarely caused by head injury except as a terminal event, but important exceptions occur. Profound blood loss from scalp lacerations can cause hypovolemic hypotension. In small children, hemorrhage into an epidural or subgaleal hematoma can produce profound hypovolemic shock. In the presence of concomitant spinal cord injury, neurogenic hypotension may occur. This is rare and can be differentiated from hypovolemic hypotension by its nonresponsiveness to fluid administration.

System hypotension cannot be tolerated in the head-injured patient without profound worsening of neurologic outcome, fluids should therefore be delivered to maintain a systolic blood pressure of at least 90 mm Hg. The delivery of large amounts of fluid to severely head-injured patients who are hypotensive from other injuries does not produce clinically significant increases in ICP; fluids should never be withheld in the head trauma patient with hypovolemic hypotension for fear of increasing cerebral edema and ICP. Hypotension may interfere with the accurate neurologic assessment of the brain-injured patient. Often, when blood pressure is restored, an improved neurologic status is observed.

Traditionally, normal saline or lactated Ringer's solution has been used for resuscitation of trauma patients with hypovolemic hypotension. Although not yet included in practice guidelines on the management of head-injured patients, recent research suggests that fluid resuscitation with hypertonic saline rather than normal saline may improve neurologic outcome after TBI.

As many as 60% of patients with severe head injury are victims of multiple trauma. The dramatic presentation of the head injury should not distract the clinician from a thorough search for other life threats.

The ED neurological assessment should be compared with the initial out-of-hospital examination, focusing on evidence of neurologic, deterioration or signs of increasing ICP. If the patient is deteriorating or has signs of increased ICP, active intervention must be initiated in the ED.

8.4.5 Hyperventilation

Hyperventilation to produce an arterial Pco2 of 30–35 mm Hg will temporarily reduce ICP by promoting cerebral vasoconstriction and subsequent reduction of CBF. The onset of action is within 30 s and probably peaks within 8 min after the Pco2 drops to the desired range. In most patients, hyperventilation lowers the ICP by 25%; if the patient does not rapidly respond, the prognosis for survival is generally poor. Pco2 should not fall below 25 mm Hg because this may cause profound vasoconstriction and ischemia in normal and injured areas of the brain. As previously described hyperventilation is recommended for brief periods during the acute resuscitation and only in patients demonstrating neurologic deterioration.

8.4.6 Osmotic Agents: Mannitol

Additional therapy for increased ICP includes the use of osmotic diuretics, such as mannitol. With deepening coma, pupil inequality, or other deterioration of the neurologic examination, mannitol may be lifesaving. Mannitol ($0.25–1\,g\,kg^{-1}$) can effectively reduce cerebral edema by producing an osmotic gradient that prevents the movement of water from the vascular space into the cells during membrane pump failure and draws tissue water into the vascular space. This reduces brain volume and provides increased space for an expanding hematoma or brain swelling. The osmotic effects of mannitol occur within minutes and peak about 60 min after bolus administration. The ICP-lowering effects of a single bolus may last for 6–8 h.

Mannitol has many other neuroprotective properties. It is an effective volume expander in the presence of hypovolemic hypotension and therefore may maintain systemic blood pressure required for adequate cerebral perfusion. It also promotes CBF by reducing blood viscosity and microcirculatory resistance. It is an effective free radical scavenger, reducing the concentration of oxygen free radicals that may promote cell membrane lipid peroxidation. Mannitol can produce renal failure or hypotension if given in large doses. It may also induce a paradoxical effect of increased bleeding into a traumatic lesion by decompressing the tamponade effect of a hematoma. Because of these and other potential problems, use of mannitol should be reserved for head-injured patients with evidence of increasing ICP.

8.4.7 Barbiturates

Barbiturate therapy is occasionally used in severely head-injured patients to reduce cerebral metabolic demands of the injured brain tissue. Barbiturates

also affect vascular tone, and inhibit free radical-mediated cell membrane lipid peroxidation. The effects of barbiturates are delayed relative to other acute interventions for reducing ICP and therefore are rarely initiated in the ED. If other methods of reducing ICP have been unsuccessful, barbiturates may be added in the hemodynamically stable patient. Pentobarbital, loaded at $10\,\mathrm{mg\,kg^{-1}}$ over 30 min, is the barbiturate most often used.

8.4.8 Steroids

Despite their popularity in the past, no evidence indicates that steroids are of benefit in head injury. They do not lower ICP or improve outcome and are therefore no longer recommended.

Computed Tomography

In the acute phase the most useful imaging technique is a noncontrast-enhanced head CT scan. This will delineate acute intra- and extraaxial bleeding, subarachnoid blood, cerebral swelling, ischemic infarction caused by hypoxia after trauma, evidence of increased ICP, and pneumocephalus. Emergency management decisions are strongly influenced by these acute CT scan findings. The bony windows of the CT scan can detect *skull fractures* (including basilar fractures); plain skull radiographs should not be obtained in patients who undergo CT scanning. A CT scan can be rapidly performed and is available at most institutions, and patients generally can be monitored during the scan.

Magnetic Resonance Imaging

MRI has limited applications in the immediate posttraumatic period. MRI is better than CT in detecting posttraumatic ischemic infarctions, subacute nonhemorrhagic lesions and contusions, axonal shear injury, and lesions in the brainstem or posterior fossa. MRI is not as useful as CT in detecting bony injuries or hyperacute bleeding. Furthermore, magnetic resonance (MR) scanning takes longer than CT scanning, and patients are relatively inaccessible for longer periods.

Angiography

Angiography should be considered when CT scanning is unavailable. It demonstrates the vascular tree and characteristic patterns can suggest the location but not always the nature of traumatic lesions. Mass effect, vascular disruptions or dissections, and venous sinus thromboses can be detected, although angiography is not sensitive for the detection of infratentorial masses.

Consultation

All patients with severe head trauma will require an imaging modality to determine the extent and nature of their brain injury and the necessity of neurosurgical intervention. Early neurosurgical consultation should be obtained as soon as possible to help direct subsequent patient management.

Transfer

Severely head-injured patients require admission to an institution capable of intensive neurosurgical care and acute neurosurgical intervention. If this is not available at the receiving hospital, the patient should be transferred to an appropriate institution by the most expedient transport method available.

Priority Management

The hemodynamically unstable patient with multiple trauma that includes head injury presents difficult emergency management decisions. The EP must decide on the sequence that best addresses the most life-threatening pathologic conditions, while still preventing morbidity and mortality from other serious injury. If the patient requires immediate surgical intervention of a life-threatening chest or abdominal injury, complete evaluation of the head injury may be curtailed; moreover, these patients will be anesthetized for surgery, and any neurologic deterioration will not be detected. If the patient has responded to fluid and blood administration, it may be possible to obtain a sing-cut CT scan of the head through the level of the lateral ventricles. This is a high-yield view for traumatic hematomas that can expand during surgery. Some patients may be too unstable to obtain even this abbreviated head CT scan before emergent surgical intervention for other life threats. In this circumstance, early neurosurgical and general surgical consultation should be coordinated by the EP. Intraoperative ventriculostomies or bilateral trephinations may provide some temporary protection from increasing ICP while the patient undergoes surgical correction of the life-threatening injury. A CT scan can be performed later, after the primary life threats have been corrected method. Neurosurgical literature often advocated CT scanning of all minor head trauma patients with a history of loss of consciousness (LOC; duration not clearly defined) or with amnesia for the traumatic event. When interpreting this recommendation, however, EPs must recognize that ED patients with minor head trauma requiring neurosurgical consultation probably represent a select, more injured population. Others advocate only hospital observation because the yield of initial abnormal scans requiring acute neurosurgical intervention is low, but those patients who do deteriorate after minor head trauma have substantial morbidity and mortality. If resources allow, prolonged ED observation may be practical in some circumstances. For example, intoxicated patients with minor head injury who otherwise fulfill low-risk criteria

should undergo meticulous serial evaluations in the ED until clinical sobriety is achieved. In these patients CT scan may be unnecessary, and observation is beneficial. Some studies advocate both CT scanning and observation of all minor head trauma patients, to allow early detection of delayed complications or deterioration when the initial scan is normal. Other studies do not show a benefit of additional hospital observations of all minor head trauma patients, to allow early detection of delayed complications or deterioration when the initial scan is normal. Other studies do not show a benefit of additional hospital observation after an initial normal CT scan. About 3% of all patients with minor head trauma will deteriorate unexpectedly; fewer than 1% will have surgically significant lesions. The risk of intracranial lesions and delayed complications is minimal in low-risk patients with minor head trauma.

The most practical approach regarding CT scanning of ED patient is probably selective scanning or observation, based on risk stratification of the minor head trauma patient. If the low-risk patient is fully awake and not intoxicated, has no focal neurologic findings and no clinical evidence of *skull fracture* and can be kept under competent observation for 12–24 h, neuroimaging is usually not indicted. A recent study prospectively identified and validated high-risk criteria for adult minor head trauma patients that correlate with increased likelihood of intracranial lesions. These include the presence of a headache, vomiting, age over 60, drug or alcohol intoxication, short-term memory deficits, external signs of trauma above the clavicles, and posttraumatic seizures. A CT scan should therefore be considered in patients with these high-risk findings, as well as the other criteria.

Skull radiography after head trauma in adults had been largely replaced by more sophisticated imaging, when imaging is performed. On rare occasions, minor head trauma patients who are deemed to be at indeterminate- or moderate-risk for intracranial injury and who cannot undergo a head CT scan (e.g., CT not immediately available) might be screened by plain skull radiographs to determine the need for a subsequent scan. Skull radiographs may reveal the presence of a *skull fracture*, and penetrating foreign bodies. Most fractures that are detected in minor head trauma patients are linear fractures with limited clinical significance in adults. Patients with clinical signs of a basilar *skull fracture* have a 50–90% increased incidence of intracranial lesions associated with their minor head trauma. When the clinical examinations show evidence of *skull fractures*, CT scanning should be considered, forgoing plain radiographs. Facial scalp or external signs of head trauma by themselves do not predict TBI in minor head trauma patients, but a *skull fracture* substantially increases the risk. The *skull fracture* is therefore helpful to determine an increased risk for TBI, but its absence does not rule out TBI. Unless a specific skull lesion is suspected by physical examination, the yield of skull radiographs in minor head trauma patients is very low, and CT scanning is the preferred imaging study, when imaging is done.

MRI is more sensitive than CT for detecting diffuse axonal injury and some hemorrhagic lesions, especially those located at the base of the skull or

in the posterior fossa. Many studies suggest that significant long-term neuropsychiatric sequelae after minor head trauma can occur despite an initial negative head CT scan, and these may be related to lesions seen initially only by MRI.

No routine laboratory tests are needed for patients with isolated minor head trauma. A urine toxicology screen and blood alcohol level may be useful in interpreting the patient's mental status. Alcohol can affect the GCS, but this effect is not observed until the blood alcohol concentration is greater than $200\,\mathrm{mg\,dl^{-1}}$; until that level, changes in mental status cannot be explained solely by acute alcohol intoxication.

8.4.9 Disposition

Most patients with low-risk minor head trauma can be discharged from the ED after a normal examination and observation of 4–6 h. If the EP decides that the patient with high-risk minor head trauma can be sent home, an appropriate early follow-up should be arranged. Patients should be discharged with instructions describing the signs and symptoms of delayed complications of head injury, should have access to a telephone, and should be monitored in the acute posttrauma period by a responsible sober adult. The physician should recognize that home monitoring of adult head-injured patients may not actually occur despite agreement by friends or family to do so. If any doubt exists regarding the safety of the discharged patient with minor head injury, a brief inpatient observation period (i.e., 12–24 h) is advisable.

If a patient with minor head trauma returns to the ED because of persistent symptoms, delayed complications of minor head injury should be sought.

Concussion

A concussion is a temporary and brief interruption of neurologic function after minor head trauma, which may involve LOC. Often, concussions occur during sports, resulting from direct impact or rotational forces. Many theories exist regarding the pathophysiology of concussion: shearing or stretching of white matter fibers at the time of impact, temporary neuronal dysfunction, transient alterations in levels of neurotransmitters, and temporary changes in CBF and oxygen use. Acute CT or MRI abnormalities are usually found after concussions, but levels of some neurotransmitters remain elevated, and a hypermetabolic state may persist in the brain for several days after the initial injury. One recent study found that more than 25% of patients with concussion demonstrated abnormal absent cerebrovascular autoregulation for several days after injury. During this time the brain appears to be particularly vulnerable to additional minor head injury, which may result in severe sequelae, including greatly increased cerebral edema and death. This has been termed the second impact syndrome. Although its existence and frequency are

debated, its serious implications affect subsequent management decisions regarding head-injured athletes and others with concussion.

Clinical features suggest the severity of the sustained injury. Adults may complain of seeing stars or feeling nauseated, dizzy, or disoriented for a brief period. A brief LOC may last of seconds up to several minutes, but many patients report no LOC. In children, acute symptoms of concussion differ from adults and may include restlessness, lethargy, confusion, or irritability. On presentation, they may be vomiting, be tachycardic, or appear pale. These signs and symptoms usually are completely resolved by 6 h.

Disposition

The management decisions faced by the EP are the same as those addressed when evaluating all patients with apparently minor head trauma: extent of workup to initiate in the ED and whether the patient can be safely discharged home. In addition, patients who sustain concussions while involved in organized sports, such as football or boxing, may require a physician's statement to return to their previous level of involvement. Severe organizations have developed guidelines to assist in making this determination.

8.4.10 Cranial Decompression

Under extreme circumstances when all other attempts at reducing ICP have failed, emergency cranial decompression must be considered in the deteriorating patient. Patients with signs of herniation who have not responded to other means of ICP reduction and who are rapidly deteriorating in the ED should be considered for placement of emergency burr holes. Emergency trephination is a blind invasive procedure, and the chances of localizing the expanding lesions are uncertain. In carefully considered patients, however, emergency cranial decompression may temporarily reverse or arrest the herniation syndrome, providing the time needed to prepare the patient for formal craniotomy.

Most patients who have been unconscious since the accident, with erratic or absent respiratory effort, bilateral fixed and dilated pupils, no spontaneous eye movements, and decerebrate posturing, have sustained diffuse massive brain injury with no focal lesion amenable to emergency decompression; these patients will probably not benefit from emergent burr holes. Instead, these patients should undergo rapid CT scanning or formal surgical decompression. The rapidity of obtaining CT scans in most institutions has reduced the frequency of the need for emergency cranial decompression in the ED.

Seizure Prophylaxis

Up to 9% of all patients who sustain blunt head trauma and 42% of those with penetrating head injury develop early posttraumatic seizures. Although the occurrence of seizures in the immediate posttrauma period has no predictive value for future epilepsy, early seizures can cause hypoxia, hypercarbia,

Table 8.3. Comparison of head imaging modalities

	computed tomography scans	magnetic resonance imaging	angiography	skull radiography
advantages	fast patient accessible for monitoring defines acute hemorrhages, mass effects, bony injuries, hydrocephalus, intraventricular blood, edema	defines contusions and pericontusion edema, posttraumatic ischemic infraction, brainstem injuries	helps localize acute traumatic lesions defines vascular injuries, injuries to venous sinuses detects mass effects	readily available may help screen some patients for further imaging studies
disadvantages	artifacts arise from patient movement, foreign bodies streak artifacts may obscure brainstem or posterior fossa	slow patients not easily accessible for monitoring does not define most acute hemorrhagic lesions not useful for bony injuries	does not define nature of acute lesion does not detect infratentorial masses	does not indicate presence or absence of intracranial injury
indications	acute severe head trauma acute moderate head trauma high-risk minor head trauma deteriorating neurologic status	persistent symptoms with postconcussive syndrome suspected contusions not seen on CT scan	CT scan not available	CT scan may not be done penetrating head trauma suspected depressed *skull fracture* suspected child abuse in minor head trauma

release of excitory neurotransmitters, and increased ICP, which can worsen secondary brain injury. Constantly firing neurons are soon depleted of their energy sources, and in the head trauma patient with compromised cerebral metabolism, uncontrolled seizures exacerbate the neurologic deficit.

Table 8.3 shows a comparison of head imaging modalities.

Lists accepted indications for early anticonvulsant therapy after head trauma. If the patient is in active seizure, benzodiazepines are effective rapid-acting first-line anticonvulsants. Lorazepam (0.05–0.15 mg kg^{-1}, 1 or 2 mg IV,

every 5 min up to a total of 4 mg) has recently been found to be most effective at aborting status epilepticus. Diazepam (0.1 mg kg^{-1}, up to 5 mg IV, every 5 min up to a total of 20 mg) is an alternative. For long-term anticonvulsant activity, phenytoin (13–18 mg kg^{-1} IV) or fosphenytoin (13–18 phenytoin equivalents kg^{-1}) can be given. Early seizure prophylaxis does not prevent late posttraumatic seizures.

If the patient has been paralyzed to facilitate management, clinical manifestations of generalized seizures will be obscured. Therefore all paralyzed head-injured patients should have prophylactic anticonvulsant therapy in the acute phase. Continuous electroencephalographic (EEG) monitoring is necessary for the ongoing assessment of seizure activity in paralyzed patients and, if available, should be initiated in the ED or the ICU.

Antibiotic Prophylaxis

Infection may occur as a complication of penetrating head injury, open *skull fractures*, and complicated scalp lacerations. Prophylactic antibiotics may be used in these circumstances but are not recommended in patients with otorrhea or rhinorrhea from a basilar *skull fracture*.

Ancillary Evaluation: Laboratory Tests

The acute management of the severely head-injured patient is directed by physical examination and diagnostic imaging. Ancillary laboratory tests that may provide useful information in the subsequent management of the patient include a urine toxicology screen, blood alcohol level, complete blood count (CBC), electrolytes, glucose, and coagulation studies.

8.4.11 Moderate Head Trauma

Approximately 10% of all patients with head injury have sustained moderate head trauma, defined as a postresuscitation GCS of 9–13. Moderate head trauma is often caused by motor vehicle crashes. Most patients with moderate head trauma do not die at the scene from their initial head injury and present to the ED for stabilization and evaluation.

Moderate head trauma produces a number of physiologic abnormalities, including neuronal cell membrane dysfunction and a mild, brief acidosis with no concurrent depletion of adenosine triphosphate (ATP). These changes are probably reversible and therefore may be amenable to acute intervention to correct or prevent progression. The neuropathology of moderate brain injury likely represents the front-end of the spectrum of pathophysiology seen with severe head trauma. Because of this, patients must be vigilantly monitored to avoid hypoxia and hypotension and other secondary systemic insults that could worsen neurologic outcome.

Clinical Features and Acute Management

A wide variety of clinical presentations occur with moderate head injury. Patients often have experienced a change in consciousness at the time of injury, a progressive headache, posttraumatic seizures, vomiting, and posttraumatic amnesia. On ED presentation, patients are often confused or somnolent, but most can still follow commands. Focal neurologic deficits may be present. Many patients with moderate head trauma have concurrent serious facial injuries that may interfere with attempts at securing their airway. Other trauma must also be ruled out.

An important clinical scenario in the spectrum of moderate head injury is the "talk and deteriorate" patient. "Talk and deteriorate" patients speak after their head injury but deteriorate to a status of a severe head injury within 48 h. Approximately 75% of these patients have sustained subdural or epidural hematomas. Patients with an initial GCS of 9 or greater who later deteriorate to a GCS of 8 or less have a poorer outcome than those who originally presented with a GCS less than 8. Successful management of moderately head-injured patients involves close clinical observation for changing mental status or focal neurologic findings, early CT scanning, and aggressive neurosurgical intervention. When no neurosurgeon is available and the patient develops symptoms consistent with herniation syndrome not reversed by acute hyperventilation and mannitol, ED trephination and hematoma evacuation should be considered.

Because of the varied presentation of the patient with moderate head trauma, the initial clinical examination alone cannot accurately predict who will have surgically correctable intracranial lesions. Approximately 40% of moderately head-injured patients have an abnormal CT scan, and 10% lapse into coma. A CT scan is essential in patients with moderate head trauma to avoid delayed diagnosis of traumatic mass lesions or diffuse injury. Skull radiographs may be useful if the patient has sustained a depressed *skull fracture* or a penetrating injury but are otherwise rarely helpful.

Disposition

All patients with moderate head injury should be admitted for observation, even with an apparently normal CT scan. Ninety percent of patients will improve over the first few days after injury. Frequent neurologic checks should be initiated, and a repeat CT scan is indicated if the patient's condition deteriorates or fails to improve over the first 48 h after trauma.

Complications

The overall mortality of patients with isolated moderate head trauma is about 20%, but the morbidity is substantial. Most moderate head trauma patients remain symptomatic for extended periods after head injury. At 3 months after

trauma, up to 70% are unable to return to work, 90% have memory difficulties, and more than 90% complain of persistent headaches. Almost 50% are left with a permanent disability that interferes with their previous daily activities. In patients with persistent symptoms of headache, confusion, or memory difficulties, delayed MRI may define lesions in the regions related to cognition that cannot be seen on CT. Although not useful in the acute setting, MRI has prognostic value during subsequent care and assists in directing the future rehabilitation of these patients.

8.4.12 Minor Head Trauma

Minor head trauma has classically been defined as isolated head injury producing a GCS of 13–15.

Nevertheless, the clinical presentation and outcome of patients with a GCS of 13 frequently resemble those of patients usually classified as having moderate head injuries. These patients also have a significantly higher incidence of abnormal CT scans than minor head trauma patients with GCS of 14–15. Therefore the definition of minor head trauma is now usually accepted as that producing a GCS of 14–15. From 75% to 80% of all head injuries presenting for emergency medical evaluation are minor.

Clinical and Historical Features

The most common complaint after minor head trauma is headache, but most patients will have no complaints by the time they reach the ED and present with a GCS of 14 or 15. Other common problems are nausea and emesis.

Occasionally, patients may complain of disorientation, confusion, or amnesia after the injury, but these symptoms are usually transient. There has been little research to correlate these symptoms with the presence of intracranial lesions in patients with minor head injury, but most investigators believe these symptoms suggest potential TBI in adult patients.

A careful and complete neurologic examination is essential to detect subtle neurologic abnormalities after minor head trauma. Studies, but because of inconsistent methodology and reporting, have limitations. For example, LOC in minor head trauma has historically been considered as a sign of significant injury, but its negative predictive value has never been determined, and therefore it is not prognostic indicator of potentially serious TBI. However, in minor head trauma patients with a GCS of 15 and a history of a LOC, the incidence of intracranial lesions is 6–9%; therefore patients with a history of LOC are probably high-risk minor head trauma patients. Conversely, many patients who have TBI may have sustained only brief or no LOC. Current data suggest that the longer the duration of LOC, the more likely that an intracranial exists, but the actual correlation between the duration of the LOC and the incidence of intracranial lesions has not been determined. Other high-risk minor head trauma criteria have also been proposed. The key for

the EP, however, is to determine the low-risk patient, and these criteria are less controversial.

Imaging Studies

A major and controversial decision regarding the ED management of minor head trauma is whether imaging studies should be performed. Several approaches have been described in the literature, but the research behind these suggestions remains confusing primarily due to differences in study populations, definitions and indications for the use of the various diagnostic modalities.

8.4.13 Pathological Appearances

Fractures of the Skull

The following descriptions apply to plain films and CT. Like fractures elsewhere, these may be simple or comminuted. When they are frequently depressed toward the brain; in this context, a compound fracture is one in which the cranial cavity is in real or potential communication with the exterior.

Simple fractures of the vault are characteristically linear, although they might be irregular, particularly if due to a sharp direct blow. When acute, they are typically well defined, and appear as fine lines of decreased density. They sometimes branch, and must be distinguished from vascular markings, including the groove in the squamous temporal bone caused by a deep temporal artery.

Acute fractures are usually straighter, more angulated, more radiolucent, and do not have corticated margins. A fracture passing through a sinus or air cell is effectively compound, and of much greater potential significance than a simple fracture.

Fractures may be associated with widening (diastasis) of one or more sutures, particularly the lambdoid.

A direct blow may depress a fragment of bone. On plain skull film, one border of the fragment appears dense where it overlaps the adjacent bone, and a projection at right angles shows a dense bony flake lying beneath the cranial vault. Unlike demonstration of simple linear fractures, this observation has importance therapeutic consequences, and should not be overlooked. CT is particularly effective at demonstrating depressed fractures provided bone windows are used. Usually there is a focal contusion in the underlying cerebral cortex (a coup contusion). In penetrating trauma, a bony and metallic fragments may be driven deep into the brain.

Fractures of the skull base often are manifested on plain and fluid levels representing bleeding or leakage of CSF, particularly in the sphenoid sinus and petromastoid air cells. Air may also be seen within the cranium. If sharply defined, lying superficially, adjacent to the midline or the expected position

of the fractured sinus, it is usually extradural; it may be very extensive when subdural. Diffuse air, in bubblesm or outlining the brain, is more likely to be subarachnoid, in which case the leptomeninges have been torn. Purely intraventricular air is uncommon but can be severe, with acute hydrocephalus. CT can also be extremely helpful in assessment of fractures of the skull base, including the petrous bone, where it may also reveal ossicular dislocation, a treatable cause of traumatic hearing loss. This section CTs (1–3 mm) are recommended. *Traumatic aeroceles*, although visible on plain film or MRI, are best assessed by CT. It may be evident that sub- or extradural air is under pressure, displacing the brain. In severe injuries, air can be seen within the damaged brain itself.

Skull radiographs and CT may also indicate the presence of associated injuries to the facial skeleton or upper cervical spine, and foreign bodies.

8.4.14 Temporal Bone Fractures

Children are particular prone to basilar skull fractures, which usually involve the temporal bone. Seventy to eighty percent of the temporal bone fractures are longitudinal and are commonly manifested by bleeding from a laceration of the external canal or tympanic membrane; hemotympanum (blood accumulating behind an intact eardrum); conductive hearing loss resulting from laceration of the tympanic membrane, hemotympanum, or ossicular injury; delayed onset of facial paralysis (which usually improves spontaneously); and temporary CSF otorrhea (from CSF running down the Eustachian tube). Transverse fractures of the temporal bone have a graver prognosis than longitudinal fractures are often associated with immediate facial paralysis. Facial paralysis may improve if caused by edema.

8.5 Fractures of Capitellum and Trochlea

8.5.1 Introduction

Although Cooper (1841) reported to cases of capitellar fracture, it was not until 1853 that the characteristic of this fracture was described by Hahn. After an autopsy on one of his former patients Hahn found a capitellar fracture with anterior displacement and bony union with the humerus. Steinthal (1898) reported a similar case of capitellar fracture that he had treated by excision, and thereafter the most common type of capitellar fracture became known as the Hahn–Steinthal fracture. Kocher, Mouchet, and Lorenz reported a less common type of capitellar osteochondral fracture, which is known as Kocher–Lorenz or Mouchet fracture. Excision of the capitellum was considered the standard treatment for these fractures, but after introduction of small fragments sets and better fixation methods, open reduction and internal fixation (ORIF) has replaced excision in Hahn–Steinthal fractures. The trochlear

fracture first was described by Laugier in 1853 and later credited by Stimson, and so the trochlear fracture is known as Laugier fracture.

8.6 Epidemiology

Fractures of the capitellum account for 60% of the fracture of the distal humerus as reported in a number of literary references.

These fractures are seen almost exclusively in individual older than age 12. Because of the largely cartilaginous composition of the capitellum in childhood, a similar injury in children usually results in a supracondylar or late condyle fracture, although rare reports.

Concerning capitellar fractures in this age group are cited in the literature. Fractures of capitellum are more common in women, which has been attributed to the increased carrying angle of the elbows and increase metabolic susceptibility from osteoporosis in women.

Few cases of isolated trochlear fractures have been reported. The trochlea, having no muscular or ligamentous attachment, rarely fracture in isolation and usually is accompanied by other injuries to the elbow. Trochlear fracture may be seen with elbow dislocation or as extension of capitellar fracture into the trochlear.

8.7 Functional Anatomy

The condyles of the distal humerus are made of articular and nonarticular surface. The articular surface is divided into two areas, the capitellum and the trochlea. The lateral colopum of the distal humerus ends in the capitellum, whereas the trochlea is centrally located between the medial and lateral columns, helping to form the distal humeral triangle.

The capitellum which is the first epiphyseal center of the elbow to ossify is directed distally and anteriorly, at an angle of 30° to the long axis of the humerus. Anteriorly and inferiorly, the capitellum is covered with articular cartilage but is devoid of articular cartilage posteriorly. The head of the radius rotates on the anterior surface of the capitellum in elbow flexion and articulates with its inferior surface in elbow extension. The lateral ligament, which has an important role in elbow stability, is situated next to the lateral margin of the capitellum.

The trochlea which is similar to a spool functions as the articulating axis of the distal humerus. The trochlear axis with respect to the longitudinal axis of the humerus is approximately 94° in valgus in males and 98° in females, creating the carrying angle of the elbow. The trochlea has medial and lateral ridges with an intervening trochlear groove. The lateral ridge is separated from the medial border of the capitellum by the capitellotrochlear sulcus and is essential in maintaining elbow stability. The rotation center of

the capitellum is displaced 12–15 mm forward of the humeral shaft axis and is aligned with the trochlear axis, enabling the radius and ulna to flex and extend coaxially.

The radial and coronoid fossae are located superior to the capitellum and trochlea and are separated by a ridge of bone that continues distally with the lateral lip of the trochlea. In full flexion, the margin of the radial head approximates the radial fossa.

The blood supply of the distal humerus has been investigated thoroughly. Because the major nutrient artery of the humerus terminates proximal to the distal humerus, the elbow appears to be relatively dependent on local osseous perforating vessels for it blood supply. Three general arcades (lateral, medial, and posterior) have been described about the elbow. The radial and medial collateral arteries (branches of the profunda brachii) anastomose with the ascending interosseous and radial recurrent arteries to form the lateral arcade, which supplies the capitellum from its posterior aspect. The medial arcade, principally the inferior ulnar collateral artery (a branch of the brachial artery), is responsible for supplying the trochlea. The intraosseous pathway of the vessels show a hypovascular area in the trochlear groove, making this area theoretically more susceptible to nonunion or avascular necrosis. Restoration of elbow anatomy is of paramount importance during reconstruction of elbow trauma, or else motion is restricted and even ankylosis can occur.

8.8 Fracture Classification

The three-part classification is widely accepted and is useful for therapeutic and prognostic reasons:

Type 1 or Hahn–Steinthal fracture. This fracture, which is a coronal shear fracture of the capitellum, involves most of the capitellum with little or no involvement of the trochlea. This is considered to be the most common type of capitellar fracture.

Type 2 or Kocher–Lorenz fracture. The fracture, which is encountered less commonly than type 1, involves a variable amount of articular cartilage of the capitellum with minimal subchondral bone.
Mouchet describes this fracture as uncapping of the capitellum.

Type 3. This is a comminuted or compression fracture of the capitellum. In the compression type, the articular surface is driven proximally and impacted into the osseous portion of the capitellum.

The fourth type has been described that is a shear fracture of the distal end of the humerus extending in the coronal plane across the capitellum to include most of the lateral trochlear ridge and the lateral half of the trochlea. The significance of this fracture is the potential instability of the elbow joint because of the involvement of the lateral trochlear ridge and the difficulty is accurately visualizing and reducing medial extent of the fracture.

Although trochlear fractures have not been classified as their counterpart, they can be considered either as fracture of the whole trochlear process or an osteochondral fracture, which is usually associated with elbow dislocations. This latter type is similar to the Kocher–Lorenz fracture of the capitellum and is seen more commonly than the previous type.

8.9 Clinical Evaluation and Radiography

The anatomic landmarks of the elbow usually are preserved with minimal swelling or gross findings. Pain is present independent of motion, with tenderness on the lateral side of the lateral side of the elbow. Although prosupination is not usually limited, loss of flexion and extension is likely often accompanied by crepitus.

Examination of type 1 fractures shows a mechanical block in elbow flexion, which is due to the anteriorly displaced fragments, whereas type 2 fractures show a mechanical block in extension as a result of the posteriorly displaced osteochondral fragment. If pain is not severe, a fullness may be palpated in the antecubital fossa in type 1 fractures. Diffuse tenderness on the lateral side of the elbow can be a result of a concomitant radial head fracture. The combination of radial head and capitellar fractures is estimated to be 10% by Milch (1931, 1964), 15% by Collert (1977), 20% by Grantham et al. (1981), and 31% by Palmer (1961). Tenderness on the medial side of the elbow can indicate a concomitant medial injury varying from an avulsion fracture of the medial collateral ligament to a rupture of this ligament. Marked elbow instability exists in these associated lesion. Although Johansson (1962) reported a high incidence of 61% of combined medial collateral ligament injuries and capitellar fractures, this has not been confirmed by other authors. Dushuttle et al. (1985) reported this association in 17% and Collert (1977) in 5% of their cases.

The clinical picture is commonly more dramatic in trochlear fractures because of the usual associated injuries to the elbow. Apart from a dislocated elbow, trochlear fractures can be accompanied by ulnar. A careful examination is mandatory in cases of suspected capitellar fracture, looking for associated fractures, ligamentous tears, and nerve injuries. As in any other elbow trauma, the shoulder and wrist should be examined carefully with special attention to the neurovascular status of the extremity. Capitellar fractures are not obvious on anteroposterior radiographs because the outline of the distal humerus is typically unaffected, and the fracture line may not be recognized against the background of the distal humerus. These fractures are best seen on a lateral view, but if this view is somewhat oblique, the fragment is hidden by rotation the humerus, and the diagnosis can be missed. Milch also has emphasized that if a fragment is seen proximal to radial head, a capitellar fracture is most likely because radial head fractures do not migrate proximally. In the lateral view, a type 1 fracture is characterized by a semilunar fragment detached in the coronal plane from the humeral condyle with its articulating surface facing

proximally in most cases. Type 4 fractures are identified by the double arc sign in the lateral view, with one arc representing the subchondral bone of the capitellum and the other the lateral ridge of the trochlea. Type 2 fractures are most difficult to diagnose because of the minimal amount of subchondral bone involved. Positive clinical findings associated with a posterior fat pad sign should alert the physician of a probable fracture in the elbow joint and urge him or her to obtain other accessory views and a CT scan of the joint. Greenspan and Norman (1987) described the radial head–capitellum view, which can be useful in showing capitellar and radial head fractures. In this modified lateral view of the elbow, the patient's arm is abducted 90° at the shoulder and flexed 90° at the elbow, and the radiographic plate is under the elbow. The radiographic beam is centered on the radial head, as for a standard lateral view, but angled 45° dorsoventrally, eliminating the overlap of the humeroradial articulations. This view outlines the radial head and capitellum in profile, enhancing identification of any fracture.

The presence of a fracture fragment medial to the midline of the joint and distal to the epicondyle should alert the clinician of a possible trochlear fracture. In contrast, osteochondral fractures of the trochlear may not be apparent on plain radiographs, similar to their capitellar counterpart. CT scans in the axial or transverse plane provide better details of the different fracture patterns of capitellar and trochlear fractures than does tomography.

8.10 Treatment Approach and Management

Although surgical excision is the preferred treatment for all small and unfixable osteochondral and the comminuted capitellar fractures, the selection of appropriate treatment for displaced large fragments of capitellar fractures is a controversial issue. Options include closed reduction, excision, open reduction with or without internal fixation and prosthetic replacement. Whatever treatment is proposed, apart from resection, if normal function is to be restored, anatomic reduction is imperative.

Few authors recommend closed reduction of capitellar fractures. Most believe that apart from difficulty in achieving reduction as a result of rotation of the fractured fragment, maintaining the reduction is even more difficult, with unsatisfactory functional results after this type of treatment. Although proponents of closed reduction claim avascular necrosis is not seen after nonoperative management, there have been case of avascular necrosis after closed reduction. Another disadvantage of this treatment is long period of immobilization and rehabilitation. Closed reduction is usually not successful in capetillar fractures because of rotation of the displaced fragment. In fact, it is this rotation as the displaced fragment migrates proximally that makes closed reduction of these fractures so difficult.

The simplicity of fragment excision is appealing and is recommended by many authors.

Proponents of this surgery believe that early resection, apart from being a simple procedure, has good functional results and can be considered a definitive treatment with no risk of avascular necrosis or nonunion of the capitellar fragment. This has its own pitfall, however Wilson (1933, 1960, 1982) believes that after resection of the capitellar fragment, the remaining raw bone surface predisposes the elbow to capsular adhesions and results in restricted elbow mobility. Resection performed in type 4 fractures can lead to elbow instability because of removal of lateral trochlear ridge, which is considered a major stabilizer or the elbow joint.

Jackobsson (1957) reported two cases in which the humeral surface was reconstructed with an alloy prothesis made from a cast of the fragment. This procedure required two separate surgeries. First the fragment was resected and an alloy prothesis made from it, then in the second operation, the prosthesis was inserted in the elbow. Because of the poor functional results and the two-stage surgery, this procedure has not been adopted by other authors.

Although open reduction had been proposed since 1933, fear of avascular necrosis and inappropriate fixation devices prevented this method from gaining popularity for a long time. With the evolution of small fragment fixation methodology and the introduction of small cancellous and Herbert screws, ORIF is considered as the preferred method of treatment for these fractures. This type of surgery provides rigid fixation, which, if followed by early mobilization, can lead to good and excellent results.

The surgical approach to the capitellum is through a Kocher (1896) posterolateral approach. If surgical resection is planned for small osteochondral and comminuted fragments of the capitellum, it is preferable to be performed as early as possible before hemorrhage and exudate have begun to organize. Intraoperative radiographs are recommended before capsular closure to ensure that no fragment has been left behind. Feldman (1997) has reported arthroscopic excision of type 2 capitellar fractures with excellent postoperative results. After the introduction of the arthroscope into the joint under tourniquet control, thorough lavage cleans the associated hemarthrosis and intraarticular debris and allows clear visualization of the fracture fragments. If they are too small to allow reduction and fixation, they can be removed in a fashion similar to the technique used to remove loose bodies. A motorized bur or shaver can then be used to smooth any projection or irregularity of the capitellar surface of the distal humerus. Early motion is initiated postoperatively.

In open reduction of capitellar fractures, many techniques of internal fixation have been described in the literature. Catgut suture through fine drill holes, K-wires, Palmers pins, biodegradable pins, fibrin glue or sealant, cancellous screws, and Herbert screws have all been proposed as methods of fixation. The fixation device that compresses the fracture site provides stable fixation for commencement of early range-of-motion, does not require further removal, and creates the least damage to the articular surface is considered ideal for fixation of these fractures. If the subchondral bone is sufficient in the anterior shear fragment to accommodate the threaded portion of a par-

tially threaded small fragments cancellous screws, this device can be inserted posteroanteriorly after provisional fixation of the fracture site with K-wires. Use of the Herbert screw, for fixation of capitellar fractures, was initially described by Simpson and Richards (1986). In the original technique, the screw was inserted anteroposteriorly, and the tip was buried under the articular cartilage, but Liberman (1991) and later Silveri (1994) proposed posteroanterior insertion of the Herbert screw as the most appropriate route to prevent further articular damage to the anterior surface. Although this technique seems appealing, further posterior dissection for insertion of the screw may compromise the vascular supply of the capitellum, which is supplied only from the posterior surface and creates a higher rate of avascular necrosis.

Displaced trochlear fractures are treated by ORIF to prevent any elbow instability or incongruity. Excision may be appropriate for a small fragments. Trochlear fractures generally are approached medially, and fixation can be accomplished by K-wires of screws, of which the latter is more appropriate. Care must be taken not to narrow the dimensions of the trochlea, especially in comminuted fractures, because this may prevent the proper seating of the sigmoid notch of the olecranon.

Postoperative Management

Controlled postoperative mobilization is of a major importance in restoring a functional arc of motion after treatment of intraarticular fractures of the distal humerus. How that is achieved varies, but the author's preference is to remove the postoperative dressing and splint at 24 h; a lightweight, removable thermoplastic orthosis is then applied with the elbow 90° of flexion. This orthosis is worn for the first 4–6 weeks and removed for active motion exercises beginning on the first postoperative day. The patient is instructed to lie supine and to forward flex the involved shoulder to bring the elbow overhead. With the uninjured arm supporting the involved forearm, gravity is used to assist flexion of the elbow. A similar approach is used for elbow-extension exercises except that the patient is instructed to sit, and the uninjured arm assists the forearm into extension. The use of resting splint is tapered, and muscle-strengthening exercises are begun 8–12 weeks after injury. After union, the institution of turnbuckle splinting can increase motion in recalcitrant cases. Morrey has shown that a wearing schedule of bracing can produce clinically significant improvements in elbow flexion and extension, when instituted 9–12 months after injury. As outlined before, the patient should have primary role in the postoperative rehabilitation, and cognitive defects and any lack of motivation especially in older patients, may impair results despite successful fixation.

Although Milch (1931) treated two cases of associated radial head and capitellar fracture by excision of both fractured fragments with no resultant instability, the authors believe it is preferable to fix the capitellar and the radial head, if technically feasible. If the capitellar fragment cannot be fixed, fixation of the radial head should be attempted. As a rule, excision of the

capitellum is not indicated if accompanied by other fractures or elbow dislocation. Excision of the capitellum is contraindicated in the presence of medial collateral ligament injury because it can lead to a cubitus valgus deformity with an unstable elbow.

Trochlear fractures are rarely isolated and are usually seen with elbow dislocations. All elbow dislocations undergoing open reduction for whatever reason should be evaluated for trochlear fractures, which may not be evident on radiographs, and, as outlined before, appropriate therapeutic measures should be taken for these injuries.

8.11 Results: Based on Management cum Surgical Techniques

8.11.1 Two Groups Have Reported Good Results After Immediate Excision of the Capitellar Fracture Fragments

Fowles and Kassab (1974) reported six patients treated by excision of the capitellar fragment. Three of them who had immediate removal of the fragment gained excellent results after surgery. Two of these had full range-of-motion in the operated elbow, and one lacked only 15° in the flexion–extension arc. The other three who had delayed excision of the fragment, despite improvement after surgery, did not achieve good results. Alvarez et al. (1975) reported an average range-of-motion of 15°–140° after excision in nine capitellar fractures. Both groups believe that delayed excision of capitellar fractures 6–8 months after injury, although somewhat helpful, does not usually lead to a good results.

The best results have been reported with ORIF. Lansinger and Mare (1981) reported ten capitellar fractures treated by ORIF mainly with K-wires with an average range-of-motion of 30°–115° postoperatively. Collert reported 12 fractures treated by ORIF. He had five excellent results and no poor results in capitellar fractures fixed by K-wires. Richard et al. (1999) reported four fractures that were internally fixed by Herbert screws, with three excellent results and one poor result because of concomitant extensive elbow injury. Three of six capitellar fractures were reported by Mckee et al. (1992, 1996) to have excellent results (elbow range-of-motion 0°–140°) and the other three good results (elbow range-of-motion 30°–140°) after ORIF. Overall, capitellar fractures fixed with Herbert screws are reported to have good to excellent results with minor complications, further supporting the recommendation in fixing these fractures operatively.

Few reports document the outcome of trochlear fractures. When associated with other elbow injuries, the result has been poor. Richard et al. reported a trochlear fracture that was accompanied by a separate capitellar fracture and forearm fractures with a limited elbow range-of-motion of only 50°–75° postoperatively. Foulke et al. (1995) reported a rare case of an isolated trochlear

fracture that gained full range-of-motion after anatomic reduction and internal fixation.

Capitellar and trochlear fractures are rare injuries that can be easily missed, leading to poor results. Large fragments should undergo ORIF. Similar to all other articular fractures, the goal should be anatomic reduction and stable fixation, so that early range-of-motion can be started in 24–48 h. This treatment has given the best result in the author's hands with the lowest complication rate. Smaller osteochondral fragments that are not amenable to fixation should be excised. Although avascular necrosis of detached capitellar fragments is a potential complication, it is relatively uncommon and should not dissuade the surgeon from proceeding with ORIF of these fractures.

8.12 Cervical Spine Injury

Perspective

In the United States more than 1,100 spine-injured children are reported annually, leading to an annual cost exceeding 4 billion dollars. Cervical injury patterns vary with the age of the patient. Fractures below the C3 level account for only 30% of spinal lesions among children less than 8 years of age, dramatically different from those patterns seen in the adult population. Likewise, spinal cord injury without radiographic abnormality (SCIWORA) has been found in 25–50% of spinal cord injuries in this same age group.

8.12.1 Principles of Disease

Anatomic features of the cervical spine approach adult patterns between the ages of 8 and 10 years. However, the injury patterns of adults are often not fully manifested until the age of 15 years.

The pediatric spine has greater elasticity of the supporting ligamentous structures than the adult spine. The joint capsules of the child have greater elastic properties, and the cartilaginous structures are less calcified than adults. In the spine itself, there is a relatively more horizontal orientation of the facet joints and uncinate processes, and the anterior surfaces of the vertebral bodies have a more wedge-shaped appearance. Compared to adults, the child has relatively underdeveloped neck musculature and a head that is disproportionately large and heavy compared to the body. Both of these differences lead to an "anatomic fulcrum of the spine" in children that is at the level of the C2 and C3 vertebrae vs. the lower cervical vertebrae as found in adults.

8.12.2 Clinical Features

In the evaluation of the pediatric trauma patient, there are several situations in which spinal cord injuries should be suspected. Any severe multiple trauma

patient should be considered to have a spinal cord injury until proven otherwise. Likewise, significant head, neck or back trauma and trauma associated with height, speed, MVAs, and falls from any height (especially those with associated head injury) should be suspected for spinal cord injury and evaluated appropriately. The evaluation of the pediatric patient should begin with a primary survey to assess airway patency, ventilatory status, and perfusion. After initial evaluation and stabilization, the examination of the cervical region can be done. Palpation of the neck for pain and bony deformity should be performed. However, factors such as pain can be elicited only in the child old enough to talk. Similarly, patients with head injury, decreased level of consciousness, intoxication, or distracting injury may not reliably localize pain in the cervical region and spinal precautions should be maintained to avoid injury.

Gross neurologic examination in the pediatric patient can be difficult, but several factors should be evaluated in the physical examination of the suspected cervical spine injury. Pain in the cervical region should raise suspicion of cervical spine injury. Likewise, the presence of paralysis, perceived parenthesias, ptosis, or priapism are neurologic signs highly correlated with spinal cord injuries. Finally, upper extremity positioning and function can help to elucidate the presence and level of a spinal cord injury.

Several characteristic spinal cord syndromes can be diagnosed on initial ED evaluation. Partial-cord syndrome is characterized by flaccid paralysis below the level of the spinal cord lesion, absent reflexes, decreased sympathetic tone, automatic dysfunction with hypotension, and with preservation of sensation. In complete-cord transaction, all characteristics of partial-cord syndrome are present, but sensation is also absent in these patients. Central-cord syndrome (seen commonly in extension injuries to the cervical spine) consists of decreased or absent upper extremity muscles tone with preservation of the lower extremity function at the level of the lesion. Anterior-cord syndrome (associated with flexion injuries to the cervical spine) is characterized by complete motor paralysis with loss of pain and temperature sensation; however, position and vibration sensation is preserved in this disorder. Finally, Brown–Sequard's syndrome represents hemisection of the spinal cord with ipsilateral loss of motor function and proprioception. There is also contralateral loss of pain and temperature sensation. Spinal cord syndromes are rare in children.

8.12.3 Diagnostic Strategies

Radiology

Children with neck pain, involvement in an MVA, or any suspicion of cervical injury should receive radiographic evaluation because when present these factors were 100% sensitive in identifying cervical spine injuries in this patient group. Radiographic evaluation should routinely consist of three views:

a crosstable lateral view, an anteroposterior view, and a Water's view to help visualize the odontoid process of C1. With these three plain film views of the cervical region, the sensitivity for cervical fractures is 93% and the specificity is 91%. The negative predictive value of these three views is 99%. Interpretation of plain cervical spine films in children may be challenging because of the anatomic changes that occur with growth. In addition, pseudosubluxation C2 and C3 is common in children up to adolescence, occurring in approximately 40% of patients. The EP distinguishes between pseudosubluxation and true subluxation by the posterior cervical line of spinolaminar line, also known as the line of Swischuk. A line is drawn from the anterior cortical margin of the spinous process of C1 down through the anterior cortical margin of C3. If this line at C2 crosses the anterior cortical margin of the spinous process at C2 or is off by less than 2 mm and no fractures are visualized, then the patient has pseudosubluxation vs. subluxation of the ligaments at that level.

An important criterion for radiographic clearing of the cervical spine is complete visualization of all seven cervical vertebral bodies down to, and including, the C7–T1 interface. The predental space should not exceed 4–5 mm in children younger than 10 years of age, and the prevertebral soft-tissue space should not be greater than normal. The four cervical radiographic lines should be evaluated, and the atlantooccipital alignment should be assessed for dislocation in this region.

Other imaging modalities that can be used to delineate cervical fractures include thin-section CT and MRI.

8.12.4 Management

There are two phases of spinal cord injury. Direct injury (initial phase) results in largely irreversible injury to the spinal cord. Indirect injury results from preventable or reversible injury to the spinal cord secondary to ischemia, hypoxemia, and tissue toxicity. Resuscitation of the patient with injury to the cervical spine should focus on prevention of minimization of the indirect causes of injury to the cervical spine. Management of the possible cervical injury should begin in the prehospital phase of emergency treatment. Most injured children arrive at the ED with adequate immobilization. However, some recent evaluations of traditional cervical collars and rigid backboards have shown less than adequate neutral positioning of the pediatric patient related to their relatively large cranium in proportion to the rest of their body. Nevertheless, in the absence of modified backboards with cutouts for the occiput of the child, the child should be immobilized with stiff cervical collar, rigid backboard, and external fixation by means of head blocks, cloth tape, or straps to provide adequate precautions.

Breathing should be assessed to determine presence of hypoventilation. Spinal cord-injured patients may hypoventilate because of diminished diaphragmatic activity or intercostals muscle paralysis. It is important to note that otherwise normal children held in a supine position have demonstrated

reduced ventilatory abilities as measured by the forced vital capacity. Head or chest injury or pulmonary compromise related to contusion, aspiration, or other causes may likewise contribute to relatively compromised ventilatory status. Supplemental oxygen should routinely be given, and ventilatory assistance by BVM ventilation or definitive airway management should be considered in the presence of prolonged hypoventilation. Finally, circulatory status must be assessed, as hypotension can be seen early in the traumatic patient and needs to be addressed promptly to prevent end-organ perfusion deficits. Hypotension can result from hypovolemia or secondary to spinal shock. If the patient is hypotensive and is attempting to compensate for a lack of adequate volume, the normal response would be to increase the heart rate. However, hypotension related to neurologic causes can be seen in the presence of a relative bradycardia. In either case, fluid administration, chronotropic agents, such as atropine, and vasopressors, such as dopamine, may be required. Spinal shock remains a diagnosis of exclusion.

Any patient with definite spinal cord injury should be given added precautions to ensure immobilization of the cervical spine. The use of IV steroids has been described in the neurosurgical literature and should be administered to decrease inflammatory infiltration and cord edema. Immediate evaluation by a spinal cord specialist should be sought. In the absence of such a specialist, the patient should be transported to a center with adequate facilities to care for spinal cord-injured patients.

8.13 Abdominal Injury

8.13.1 Perspective

Serious abdominal injury accounts for approximately 8% of admissions to pediatric trauma centers. Abdominal trauma is the third leading cause of traumatic death after head and thoracic injuries. Abdominal trauma is the most common cause of unrecognized fatal injury in children. Pediatric abdominal trauma results from blunt cases in 85% of cases, and penetrating trauma accounts for the remaining 15%. Of patients presenting primarily for other associated injuries, 9% die from abdominal trauma associated with these injuries.

Blunt trauma related to MVCs causes more than 50% of the abdominal injuries in children and is also the most lethal. “Lap-belt” injury including small bowel injury and chance fractures occurs in approximately 5–10% of restrained children involved in MVCs. Another common cause of abdominal injury involves bicycle crashes. Handlebar injuries represent a serious cause of hospitalization for the pediatric population, with those requiring admission having a mean hospital stay exceeding 3 weeks. Often the effects of bicycle injuries may not be seen on initial presentation, with the mean elapsed time to onset of symptoms being nearly 24 h.

Sports-related injuries are another common pediatric cause of abdominal trauma. Sports-related injuries are most commonly associated with isolated organ injury as a result of a blow to the abdomen. At particular risk are the spleen, kidney, and intestinal tract in children. Finally, significant abdominal injury occurs in only about 5% of child abuse cases, but it is the second most common cause of death after head injury in these cases.

8.13.2 Principles of Disease

The anatomy of the child lends special protection from some abdominal injury patterns and predisposes the patient to other types of injuries in both blunt and penetrating abdominal trauma. Children have proportionally large solid organs, less subcutaneous fat, and less protective abdominal musculature than adults and therefore relatively more solid organ injury from both blunt and penetrating mechanisms. Children also have relatively larger kidneys with fetal lobulations that predispose them to renal injury. The child also has a fairly flexible cartilaginous ribcage that allows for significant excursion of the lower chest wall, permitting compression of the internal organs. The combination of these factors provides the basis for the differences in abdominal injury patterns seen between children and adults.

8.13.3 Clinical Features

Blunt abdominal trauma often presents as a part of the multitraumatized pediatric patient. In the child, history is often limited, traditional signs of decompensation seen in adults are often not as evident, and physical examination can be difficult. Therefore subtle, early abdominal findings may be overlooked, leading to significant morbidity and mortality. The history and examination of young children who have suffered trauma are challenging as it may be difficult to know if the child hurts "all over" or has focal findings. The EP may use distraction with toys, lights, or keys in order to get the child's mind off the examiner and onto the distraction; in this way areas of tenderness may be located.

Signs and symptoms of abdominal injury in children include abdominal distention, tachypnea from impaired diaphragmatic excursion, abdominal tenderness, ecchymoses, and signs of shock. Children with hepatic and splenic injuries may have trouble localizing their pain. Thus, any abdominal tenderness on examination should prompt evaluation of the abdomen. Vomiting is usually a late sign or one associated with duodenal hematoma or pancreatitis. Signs of small bowel injury may be delayed and only noted clinically with serial examinations. Pelvic bone stability and a rectal examination looking for signs of urethral injury (rare) in boys or blood in the stool (both girls and boys) needs to be performed in all cases of serious trauma.

Even minor falls can result in significant splenic injury, but with only minimal findings on examination. Repeated examination, prolonged observation,

and close attention to vital signs are warranted. Any child with a clinically suspicious abdominal examination should be evaluated further with additional radiologic and laboratory studies.

8.13.4 Diagnostic Strategies and Management

In patients with suspected abdominal injury or with mechanisms of possible injury, management and resuscitation must be rapid. Children, because of fear and pain, can compound the difficulties in management of serious penetrating or blunt abdominal trauma. Children tend to distend the stomach greatly with ingested air that can greatly decrease the diaphragmatic excursion related to overdistention of the abdomen. This can compromise respiratory efforts, and therefore early decompression via nasogastric or orogastric tube insertion should be considered. Children in whom a stable pelvis has been established and who are not at risk of urethral trauma should have a urinary catheter inserted to decompress the bladder, evaluate for the presence of urinary retention, and examine for the presence of blood in the urine. Also, before any invasive evaluation of the abdomen such as DPA, the bladder should be decompressed to prevent accidental laceration during the procedure.

8.13.5 Diaphragmatic Herniation

Acute diaphragmatic herniation secondary to trauma occurs from sudden compressive forces exerted over the abdomen causing an increase in the intraabdominal pressure and resulting in tearing of the diaphragm. Most commonly, the herniation occurs over the left side and results from the "lap-belt" injury complex from restraint in an MVC. "Lap-belt" injury complex consists of bursting injury of solid or hollow viscera and/or disruption of the diaphragm or lumbar spine. Lap-belt injury is characterized by ecchymosis across the abdomen and flanks.

8.13.6 Splenic Injury

Injuries to the spleen are in the largest proportion of pediatric abdominal trauma. Children involved in MVCs, sudden deceleration injuries, and contact sports-related injuries suffer from splenic trauma. Typical findings include left upper quadrant abdominal pain radiating to the left upper quadrant of the abdomen. Patients may be hemodynamically stable or, after significant splenic rupture or laceration, may be persistently hypotensive or in fulminant cardiovascular collapse. All patients with suspected splenic injury should be evaluated by a surgeon. Stable patients may undergo CT for radiologic evaluation or bedside US. Most often, in minor splenic trauma, bleeding will spontaneously be controlled without operative intervention; however, spontaneous splenic rupture 3–5 days after injury has been described. Patients with splenic injury should be admitted to the hospital, with close observation and repeated examination.

8.13.7 Liver Injury

The liver is the second most commonly injured solid organ in the pediatric patient with abdominal trauma. It is, however, the most common cause of lethal hemorrhage, carrying a mortality of 10–20% in severe liver injury. Similar mechanisms of injury seen in patients suffering from splenic injury also cause liver trauma. Tenderness on palpation of the right upper quadrant of the abdomen along with complaint of abdominal pain in this region or in the right shoulder are signs of possible liver injury. CT scan and bedside US provide useful information in the stable pediatric trauma patient in regards to the extent of liver involvement and amount of bleeding that has occurred. Patients managed conservatively often do well; however, those that are initially treated as such and then go on to require delayed laparotomy often have significantly morbidity and mortality. Therefore close observation in the hospital, serial abdominal examinations, and serial hemoglobin should be performed.

8.13.8 Renal Injury

The other major organ system to consider in the pediatric abdominal injury is the kidney, which is less susceptible to trauma from forces applied to the anterior abdomen, but is often involved in the multitrauma patient. Because this organ is a retroperitoneal organ, abdominal pain complaints are often less obvious and are more diffuse. Often dull back pain, ecchymosis in the costovertebral region, or hematuria are the only clues to renal injury. Renal US and CT may be used in the stable patient to assess the degree of renal involvement. Other organs such as the pancreas and gastrointestinal tract are less frequently injured in the pediatric patient.

8.13.9 Penetrating Injury

Penetrating wounds to the abdomen usually require rapid evaluation by a surgeon and probable operative intervention. DPL provides the most rapid, objective evaluation of possible intraperitoneal injury. The role of DPL in the management of pediatric trauma is controversial. Certainly patients that remain critically injured despite fluid resuscitation may be candidates for DPL if they are too unstable for CT and there are multiple potential sites of blood loss. Finally, DPL may be considered in the operating room for patients undergoing emergent craniotomy and adequate evaluation of the abdomen cannot take place because of the lack of time available prior to the need for surgery.

The organs that can be commonly involved in blunt trauma are also implicated in penetrating abdominal injuries.

8.13.10 Radiology

Because pediatric patients suffer more from injury to the spleen, liver, kidneys, and the gastrointestinal tract, CT of the abdomen can provide high sensitivity

and specificity for identification of these injuries while being relatively non-invasive. The necessity of using oral contrast media in CT has recently come under significant criticism because of delays in evaluation, difficulty with administration, and risk for aspiration.

Another useful procedure in the acutely traumatized pediatric patient is bedside abdominal US. When used by a properly trained EP, US can provide sensitive identification of intraperitoneal hemorrhage without invasive measures. Although radiologic evaluation can provide important diagnostic information in the pediatric patient with possible abdominal trauma, any patient with unstable vital signs should not be delayed in receiving operative intervention. Children with persistent or recurrent hypotension, continued abdominal pain, or persistent abdominal distention should have expedient evaluation by a surgeon.

8.14 Management of Traumatic Injuries: Head, Scalp, Cranium, and Brain

Scalp and Cranium

The scalp consists of five tissue layers. The dermis is the outermost layer and is among the thickest layers of skin on the body. The underlying subcutaneous tissue contains the hair follicles and the rich blood supply of the scalp. The large blood vessels of the scalp do not fully constrict if they are lacerated and can be the source of significant blood loss. The middle scalp layer is the galea, which is made of tough fascial tissue. It contains the occipitofrontalis and temporoparietalis muscles, which move the scalp backward and forward, elevate the eyebrows, and wrinkle the forehead. Under the galea is a loose areolar tissue layer. Because the areolar attachments to the rest of the scalp are loose, scalp avulsions frequently occur through this layer. This is also the site for development of subgaleal hematomas, which can become quite large because blood easily dissects through the loose areolar tissue. The deepest layer of the scalp, the pericranium, is firmly adhered to the skull itself.

The skull comprises the frontal, ethmoid, sphenoid, and occipital bones, and two parietal and two temporal bones. The unique layered architecture of the bones of the skull enhances its strength. Each bone consists of solid inner and outer layers, separated by a layer of cancellous bony tissue (the diploe). In adults the bones of the skull average between 2 and 6 mm in thickness; the bones in the temporal region are usually the thinnest of the skull. The cranial bones form a smooth outer surface of the skull, but within the cranial vault are many bony protrusions and ridges. Contrecoup injuries and contusions far from the site of head impact often occur as the accelerating brain strikes against these uneven bony surfaces.

The inner aspect of the skull is lined with the periosteal dura, which is a thick connective tissue layer that adheres closely to the bony surface. The

inner meningeal layer of the dura is the outermost covering of the brain. This dural membrane reflects back on itself to make folds within the cranial space. These folds serve to protect and compartmentalize different components of the brain. The midline falx cerebri separates the two cerebral hemispheres from each other. The tentorium cerebelli partitions the cerebellum and brainstem from the cerebral hemispheres. The U-shaped free margin of this dural fold is important in the pathology of the transtentorial herniation syndromes that can complicate severe head injury. Within the margins of the dural reflections, the two dural layers separate to form large dural venous sinuses. Injury to the dural sinuses carries significant morbidity and mortality because of the potential for uncontrolled hemorrhage and the difficulty in repairing these structures.

The cranial vault is rigid and nonexpendable, with an average volume for adults of about 1,900 ml. Cranial contents exit or enter the skull through many foramina. The largest, the foramen magnum, is the site of exit for the brainstem and spinal cord from the cranium.

8.14.1 Brain and Cerebrospinal Fluid

The brain is a semisolid structure, which weighs about 1,400 g (3 lb) and occupies about 80% of the cranial vault. It is covered by three distinct membranes; the meningeal dura, the arachnoid layer, and the pia. The location of traumatic hematomas relative to these membranes defines the pathologic condition and determines the consequences of the injury.

The major divisions of the brain are the cerebrum, cerebellum, and brainstem. Each lobe of the cerebrum is the source of highly specific neurobehavior, and specific injury to each lobe can disrupt normal behavior patterns. The brain is suspended in the CSF, which provides some buffering for the brain during trauma. CSF is produced by the choroids plexus, located primarily in the lateral ventricles of the brain. CSF passes from the ventricular system into the subarachnoid space that surrounds the brain and spinal cord. CSF provides a fluid pathway for delivery of substances to brain cells, elimination of the products of brain metabolism, and transport of peptide hormones and hormone-stimulating proteins from their site of production within the central nervous system (CNS) to their peripheral sites of action.

8.15 Fractures of Hip

Most proximal femoral fractures occur in elderly individuals as a result of only moderate or minimal trauma. In younger patients these fractures usually result from high-energy trauma. Despite similar locations of the fracture, of the difference in low- and high-velocity injuries in older vs. younger patients outweigh the similarities. Most often than not, high-velocity injuries are more difficult to treat and are associated with more complications than low-velocity

injuries. This chapter discusses inter- and subtrochanteric femoral fractures, fractures of the head and neck of the femur, and dislocation and fracture dislocation of the hip, including classification of fractures and some of the more commonly used methods of surgical management.

8.15.1 Hip Fractures

Fractures of the proximal femur, generally referred to as fractures of the hip, are classified first according to their anatomical location. Isolated fractures of the lesser or greater trochanter are not common and rarely require surgery; they can be associated with pathological disease. Avulsions of the lesser trochanter occur in immature children from the pull of the iliopsoas muscle and can be treated nonoperatively. Fractures of the greater trochanter often result from direct trauma to the trochanter, usually are minimally displaced, and can be treated nonoperatively with protected weight-bearing on crutches until the symptoms subside. If a fracture of the greater trochanter is obvious on routine roentgenograms, then CT or MRI should be performed to rule out an intertrochanteric element before the decision is made for nonoperative treatment. An unsuspected intertrochanteric fracture can drift into varus without open reduction and internal fixation.

Femoral *neck fractures* and intertrochanteric fractures occur with about the same frequency. They are more common in women than in men by a margin of three to one. Other risk factors include Caucasian race, neurological impairment, malnutrition, impaired vision, malignancy, and decreased physical activity. Osteoporosis, although present in the population at risk, has not been shown to be more prevalent in those with fractures than in age-matched controls. Subtrochanteric fractures, which account for 10–15% of proximal femoral fractures, have a bimodal distribution pattern, appearing commonly in patients 20–40 years of age and in those over 60 years of age. Fractures in younger patients usually result from high-energy trauma.

The prognosis for each of the three major categories of hip fractures is entirely different. Intertrochanteric fractures usually unite if reduction and fixation are properly done, and, although malunions may be a problem, late complications are rare. A wide area of bone is involved, most of which is cancellous, and both fragments are well supplied with blood. Fractures of the neck of the femur are intracapsular and involve a constricted area with comparatively little cancellous bone and a periosteum that is thin or absent. Although the blood supply to the distal fragment is sufficient, the blood supply to the femoral head may be impaired or entirely lacking; for this reason, avascular necrosis and later degenerative changes of the femoral head often follow femoral *neck fractures*. Subtrochanteric fractures associated with high rates of nonunion and implant fatigue failure because of the high stresses in this region.

Open reduction and internal fixation of hip fractures should be done with the aim of obtaining rigid and stable internal fixation that will permit patients

to be ambulatory within a short period. Most patients are allowed to sit in a chair the day after surgery. Mobilization is advantageous in preventing pulmonary complications, venous thrombosis, pressure sores, and generalized deconditioning. Protected weight-bearing may be permitted within 24 h after surgery, provided the fracture is well reduced and securely and rigidly fixed with stable internal fixation.

8.15.2 Intertrochanteric Femoral Fractures

Classification

As their institution, Boyd and Griffin (1949) classified fractures in the peritrochanteric area of the femur into four types. Their classification, which follows, included all fractures from the extracapsular part of the neck to a point 5 cm distal to the lesser trochanter:

Type 1. Fractures that extend along the intertrochanteric line from the greater to the lesser trochanter. Reduction usually is simple and is maintained with little difficulty. Results generally are satisfactory.

Type 2. Comminuted fractures, the main fracture being along the intertrochanteric line but with multiple fractures in the cortex. Reduction of these fractures is more difficult because the comminution can vary from light to extreme. A particularly deceptive form is the fracture in which an anteroposterior linear intertrochanteric fracture occurs, as in type 1, but with an additional fracture in the coronal plane, which can be seen on the lateral roentgenogram.

Type 3. Fractures that are basically subtrochanteric with at least one fracture passing across the proximal end of the shaft just distal to or at the lesser trochanter. Varying degrees of comminution are associated. These fractures usually are more difficult to reduce and result in more complications, both at operation and during convalescence.

Type 4. Fractures of the trochanteric region and the proximal shaft, with fracture in at least two planes, one of which usually is the sagittal plane and may be difficult to see on routine anteroposterior roentgenograms. If open reduction and internal fixation are used, two-plane fixation is required because of the spiral, oblique, or butterfly fracture of the shaft. Fortunately, the most difficult types to manages, types 3 and 4, accounted for only about one-third of the trochanteric fractures in Boyd and Griffin's series.

Evans devised a widely used classification system based on the division of fractures into stable and unstable groups (Table 8.4). He divided the unstable fractures further into those in which stability could be restored by anatomical or near anatomical reduction and those in which anatomical reduction would not create stability. In an Evans type I fracture, the fracture line extends upward and outward from the lesser trochanter. In type II, the reversed

obliquity fracture, the major fracture line extends outward and downward from the lesser trochanter. Type II fractures have a tendency toward medial displacement of the femoral shaft because of the pull of the adductor muscles.

The AO group-classified trochanteric fractures have largely been abandoned. Horowitz (1960) reported a mortality rate of 34.6% for trochanteric fractures treated by traction and 17.5% for those treated by internal fixation. Rigid internal fixation of intertrochanteric fractures with early mobilization of the patient should be considered standard treatment. Medical complications after internal fixation are fewer and less serious than those after nonoperative treatment. The rare exception to this is a medically unstable patient who is an extremely poor anesthetic and surgical risk.

Operative Treatment

One goal of operative treatment is strong, stable fixation of the fracture fragments. Kaufer, Matthews, and Sonstegard listed the following variables as those that determine the strength of the fracture fragment–implant assembly (1) bone quality, (2) fragment geometry, (3) reduction, (4) implant design, and (5) implant placement. The surgeon can control only the quality of the reduction and the choice of implant and its placement.

Because most of the patients with intertrochanteric fractures have considerable osteopenia, with the quality of bone for the purchase of fixation within the femoral head and neck less than desirable, it is important that the internal fixation device be placed in that part of the head and neck where the quality of bone is best.

8.15.3 After Treatment

In peritrochanteric fractures with a stable configuration (i.e., where the medial cortical buttress and lesser trochanter remain intact), early full weight-bearing is permitted. Mobilize the patient the first day after surgery and allow full weight-bearing as tolerated.

8.15.4 Prosthetic Arthroplasty

Prosthetic replacement for intertrochanteric fractures has been advocated but has not gained widespread support. Pinder, Durnin, and Cook; Heiman; and Stern and Angerman all reported the use of Leinbach prostheses in selected patients, with good results in 86–94%. Green, Moore, and Proano, and Haentjens et al. reported primary bipolar arthroplasty for unstable intertrochanteric fractures in elderly patients. In patients with severe osteoporosis with significant comminution, prosthetic replacement may be considered; however, the extensive surgery necessary may be unjustified in elderly patients with low activity demands and limited life expectancies.

Table 8.4. Intramedullar hip screw nailing technique

Place the patient supine on a standard fracture table. Rest both feet in a padded foot holder and use a padded perineal post. The pelvis must lie in the horizontal position. Addict the affected femur to allow access to the trochanteric region. Addict the unaffected limb while adducting the trunk and affected extremity. Tilt the trunk away from the fracture and strap the arm on the same side across the chest of the patient. This is particularly important in obese patients. Place the uninjured leg either adjacent to the injure side (in a heel-to-toe position with the uninjured side lower) or flexed and abducted to allow unimpeded access of the image intensifier between the legs.
Before the start of the operative procedure, reduce the fracture. Peritrochanteric fractures are usually reduced with internal rotation of the femur and traction. Most subtrochanteric fractures are reduced by a small degree of external rotation. Avoid excessive traction of the affected limb. It is especially important to ensure that the head fragment of the femur is reduced to the shaft fragment in the lateral position. If closed reduction is impossible, perform a more extensive operative incision to reduce the fracture openly. A successful outcome is unlikely if the implant is inserted into an unreduced fracture. Comminuted peritrochanteric fractures with loss of medial cortical buttress including the lesser trochanter are more likely to result in failure of fixation. In such patients, an intramedullary device may reduce the risk of failure.
Prepare the operative field in the usual manner. Extend the sterile field from just above the iliac crest to the knee and from beyond the midline anteriorly to the midline posteriorly and drape as described in Chap. 1. A vertical "isolation" drape is commonly used because it allows the operative field to be separated from the image intensifier and any unscrubbed personnel.
Make a lateral incision, similar to all intramedullary procedures of the femur. Extend the skin incision from the tip of the trochanter proximally for 3–8 cm, depending on the size or obesity of the patient. Split the aponeurosis of the gluteus maximus in line with it fibers, from the tip of the trochanter proximally for 5 cm. This brings into view a small fat pad that lies between the tip of the trochanter and piriformis fossa. Then, split the gluteus medius in the line of its fibers.
The eventual size of the incision depends on both obesity of the patient and whether the fracture has been reduced adequately. In most patients a satisfactory reduction is achieved before the operative procedure is started. If an open reduction is necessary, extend the surgical approach distally to allow and anterior approach to the hip capsule and fracture. Check the adequacy of the open reduction roentgenographically. It is critical that the head fragment is reduced on the shaft fragment in the lateral plane.
Femoral preparation. Insert the intramedullary hip screw through the tip of the greater trochanter. The 4° bend allows this without encroachment of the femoral neck, which may be fractured. After adequate exposure of the tip of the trochanter with the cured awl. Position the tissue protector on the tip of the trochanter and insert a 3.2-mm tip threaded guide pin through the tissue protector's guide pin centering sleeve.

Table 8.4. *Continued*

Advance the pin down the femoral canal well beyond the subtrochanteric region. Check the position of the pin roentgenographically in the anteroposterior and lateral planes. Remove the guide pin centering sleeve from the tissue protector. Use the proximal reamer to open the proximal portion of the femur to 18 mm to accommodate the proximal portion of the nail (17.5 mm). The minimum length of the femur that requires reaming is 7 cm. The proximal reamer's positive stop has three settings. The "7" setting will ream to 7 cm, the "7.5" setting will ream to 8 cm. Once the positive stop is set, guide the proximal reamer over the guide pin and through the issue protector and ream until the positive stop meets the outer portion of the tissue protector. In elderly patients with peritrochanteric fractures, the bone of the proximal femur and, in particular, the fractured greater trochanter, often are very soft. The tip of the greater trochanter can be opened with the curved awl and checked roentgenographically in the anteroposterior and lateral planes. Then ream the proximal femur to 18 mm using the proximal reamer without the use of a ball-tipped guide pin. Reaming over a 3.2-mm tip threaded guide pin is optional. If the trochanteric region is very osteoporotic, proximal reaming may be unnecessary.
The intramedullary hip screw is available in two angles – 130° and 135°. Using the templates on the preoperative roentgenograph, estimate the appropriate diameter of the nail and the ideal angle and length for the lag screw. The final decision on the lag screw angle is a matter of experience. Most patients require an angle of 130°.
Using the drill guide and the appropriate angle guide attachment, insert a guide pin into the femoral head to verify the angle. Refer to the proximal targeting section for the proper technique. Always remove the guide pin before removing the trial. If the canal is narrow and will not accommodate a 10-mm nail, then standard intramedullary reaming should be carried out over a ball-tipped guide rod. The femur should be reamed to 1 mm larger than the nail's diameter. Special attention should be paid to the anterior bow to ensure that a nail of the correct length and orientation, left or right, is used.

Drill Guide and Nail Assembly

The assembly of the drill guide with the chosen nail and the corresponding angle guide attachment is critical. If the angle guide attachment and nail are incorrectly matched, it will be impossible to insert the lag screw. For this reason, it is recommended that the angle guide attachment be assembled to the drill guide before the insertion of the intramedullary hip screw. First, assemble the drill guide to the drill guide handle. Secure the selected angle guide attachment to the drill guide with the angle guide attachment bolt and tighten using the 11/16-in. universal socket wrench. Next, attach the appropriate nail to the drill guide assembly with the drill guide bolt (tighten the bolt using the 11/16-in. universal socket wrench). Then attach the driver to the drill guide and tighten using the 9/16-in. open-end wrench. Confirm correct assembly by passing the sleeve reamer through the silver drill sleeve and the proximal hole of the intramedullary.

Nail Insertion

In some patients the intramedullary hip screw can be inserted without the use of a guide rod. When using the long screw make sure the bow is anterior. Insert the tip of the nail into the prepared proximal femur and push it down the shaft. Carry this out under fluoroscopic control. Under no circumstances the nail and driver assembly should be hammered down into the femur. If the nail will not pass easily down the canal with simple, gentle twisting movements of the driver assembly, it should be removed and the canal reamed by 1 or 2 mm before reinsertion.

Remove the driver as this part of the assembly is no longer needed. If the driver was tightened during nail insertion, the 9/16-in. open-end wrench can be used to loosen it. The remainder of the insertion apparatus does not obscure the femoral head on the lateral roentgenogram.

Proximal targeting. Correct positioning of the nail is crucial to ensure that the lag screw will be placed in the center of the femoral head in both anteroposterior and lateral planes. Two silver drill sleeves are available for use with the angle guide attachment, with lengths of 14 and 16 cm. When the nail is in the correct position, thread the appropriate drill sleeve into the angle guide attachment. Make a incision in the skin to allow the selected size silver drill sleeve to be screwed in until it is flush with the angle guide attachment. Choose the sleeve that comes closest to the lateral cortex without impeding its ability to be screwed completely into the angle guide attachment. Insert the guide pin sleeve until it rests on the lateral cortex of the femur. It is important that the sleeve fits flush against the femur to reduce the likelihood of the guide pin "walking." Using anteroposterior fluoroscopy, estimate the approximate position of the lag screw.

Insert a 3.2-mm tip threaded guide pin through the guide pin sleeve and into the femoral neck and head. The position of the guide pin, and thus the ultimate position of the lag screw, can now be determined on both the anteroposterior and lateral roentgenographic views. If any fine adjustments in the nail depth need to be made, withdraw the guide pin and insert or withdraw slightly the intramedullary hip screw until the correct final position is achieved.

The perfect position of the guide pin is in the exact center of the femoral neck and head on both the anteroposterior and lateral views. The pin should lie within the central third of the femoral neck and head on both roentgenographic views. Once the correct position of the guide pin is achieved in both planes, advance it to within 5 mm of the articular surface of the femoral head.

Selecting the lag screw. After inserting the guide pin, remove it from the silver drill sleeve so that the lag screw length measurement can be correctly determined. Position the lag screw length gauge so that it rests against the guide pin and is flush with the silver drill sleeve. Read the length of the lag screw directly from the guide pin.

Reaming for the lag screw. Use the lag screw shaft reamer to prepare the femoral neck for the lag screw. The correct depth for reaming is 5 mm less than the length of the guide pin, as previously measured. This reduces the likelihood of the guide pin being removed with the reamer. Set the lag screw shaft reamer

Table 8.4. *Continued*

to the correct length and advance it through the silver drill sleeve and into the femoral head until the positive stop makes contact with the sliver drill sleeve. If the guide pin is removed with the reamer reinsert the guide pin sleeve and reintroduce the guide pin without moving the external jig. Check the position roentgenographically and remove the lag screw shaft reamer. Insert the sleeve reamer to ream the lateral cortex and metaphysic until the positive stop makes contact with the silver drill sleeve. Remove the sleeve reamer.

Tapping for the lag screw. Tapping is unnecessary in an osteoporotic femur. In younger individuals, tapping the femoral neck to prepare for the lag screw is preferred, otherwise, the femoral neck and head fragment may tend to rotate during the insertion of the lag screw. Set the lag screw tap for the same length as the lag screw shaft reamer (5 mm less than the guide pin measurement) and insert it through the silver drill sleeve.

Selection of the lag screw. Use the standard Richard AMBI/Classic lag screw, but not an enlarged or "super" lag screw, because it will not pass through the nail. The tip of the lag screw should like within 5–10 mm of the articular surface of the femoral head, since the bone in this region is denser than in the center of the head. This makes the screw cutout less likely. The length given by the measurement already allows for 5 mm of compression. In most peritrochanteric fractures compression is only temporarily effective and is not considered necessary.

Insertion of lag screw, sleeve, and set screw. Assemble a centering sleeve onto the lag screw insertion wrench. Attach the appropriate lag screw to the wrench and tighten the lag screw retaining rod. Snap the insertion wrench handle over the lag screw retaining rod and onto the shaft of the wrench. Insert the entire assembly over the guide pin and through the silver drill sleeve. Advance the lag screw into the proximal femur to the desired level using roentgenographic control. When the notch on the wrench's shaft is flush with the edge of the silver drill sleeve, the screw is correctly positioned for 5 mm of compression. The handle of the insertion wrench must be perpendicular to the axis of the femoral shaft to ensure maximum strength of the lag screw in situ.

Once the lag screw has been inserted to the correct depth, remove the insertion wrench handle, leaving the wrench shaft and lag screw retaining rod attached to the lag screw. Slide the sleeve inserter over the wrench shaft and up through the silver drill sleeve. Use it to push the centering sleeve through the lateral cortex of the femur and into the nail. The sleeve inserter may be tapped with the slotted hammer until it contracts the silver drill sleeve. An anteroposterior view with the image intensifier will confirm that the centering sleeve is centered within the nail.

Use the universal set-screw driver with the 75 $\mathrm{in.\,lb^{-1}}$ torque wrench to insert a set screw through the drill guide bolt and into the top of the nail. The set screw will lock into a groove of the centering sleeve. When an audible snap is heard while turning the torque wrench, the set screw is secured firmly against the centering sleeve. For optimal results, the torque wrench and the universal set-screw driver should be in line with the nail as closely as possible. Also, a retorque after a 1-min pause ensures maintenance of optimal torque. Once the centering sleeve is secured by the set screw, the lag screw will no longer

rotate, but it will be able to slide. The sleeve inserter, lag screw insertion wrench, and silver drill sleeve can.

Now be Removed

Insertion of the compression screw. Release the traction on the injured leg. If desired, compression of the lag screw can now be carried out. Reinsert the silver drill sleeve and sleeve inserter in the drill guide. Insert the AMBI/Classic compression screw into the lag screw with the hex driver and compress it against the centering sleeve.

Distal locking. Lock the distal end of the long intramedullary hip screw with 4.5-mm cortical screws using a 3.5-mm drill and standard freehand techniques.

Closure. Close the proximal operative wound over a suction drain. The fibers of the gluteus medius can be carefully approximated and the gluteus maximus aponeurosis closed with a continuous suture. The distal wounds require skin closure only. Finally, apply an impermeable dressing.

Prosthetic

It is important before treatment to distinguish by roentgenograms whether the intertrochanteric fracture is stable or unstable based on fracture geometry and whether reduction can restore cortical contact medially and posteriorly. The status of the lesser trochanter is important in evaluating the stability of the reduction. If the lesser trochanter is displaced with a large fragment, a significant cortical defect is present posteromedially and the fracture geometry indicates a potentially unstable reduction. The surgeon should carefully inspect the roentgenograms for this defect or palpate this region to feel for a defect.

Reduction can be carried out by either open or closed means; with either. The objective is a stable reduction, whether anatomical or nonanatomical. Usually, closed reduction by manipulation should be attempted initially. After the anesthetized patient has been placed on the fracture table and the extremity has been secured in the traction foot piece, traction is exerted longitudinally on the abducted extremity.

While traction is maintained, the limb is adducted and internally rotated at the same time. Traction is probably the most important element in reducing intertrochanteric fractures. In most fractures, an anatomical reduction with posteromedial apposition is possible. Fluoroscopy, with good quality anteroposterior and lateral views, is used to evaluate the quality of the reduction, with special attention paid to the cortical contact medially and posteriorly. If good medial cortical contact is seen on the anteroposterior view and good posterior cortical contact is seen on the lateral view, the fracture can be internally fixed in this position. If a gap or overlap exists, either medially or posteriorly, adjustments in the traction or rotation may correct the reduction to a stable anatomical position. Frequently, in comminuted fractures, the distal shaft fragment sags posteriorly and cannot be corrected by closed manipulation.

In such cases, open anatomical reduction should be considered, and the posterior sag may be corrected by lifting up with a hip skid under the fracture by an assistant. This position may need to be maintained during internal fixation to prevent recurrence of the deformity. In rare cases, a nonanatomical means of achieving stability, such as osteotomy or medial displacement of the shaft fragment, may be appropriate.

An open anatomical reduction of the medial and posterior cortical support usually can be accomplished by applying a bone-holding forceps across the fracture in an anteroposterior plane while adjusting the traction and rotation. Once an anatomically stable reduction has been achieved, a compression hip screw or other device can be used to secure the reduction. In rare cases, if the fracture is severely comminuted, anatomical reduction even by open means is difficult, if not impossible. In such circumstances it may be wise to accept the nonanatomical but stable reduction obtained by osteotomy and displacement techniques; however, a reduction that is both nonanatomical and unstable should not be accepted.

Stable fractures are treated by internal fixation after anatomical reduction. Unstable fractures can be usually treated by anatomical reduction with the use of a collapsible fixation device, such as a hip compression screw. Such collapsible internal fixation devices permit the proximal fragment to collapse or settle on the fixation device, seeking its own position of stability, with the shaft usually displacing medially. Very large posteromedial fragments can be stabilized with interfragmentary fixation through the most proximal screw hole of the side plate of a hip compression screw, usually with some difficulty. In extremely unstable fractures, if a standard compression hip screw is used, formal medial displacement osteotomy or nonanatomical reduction with displacement of the shaft beneath the calcar portion of the neck to convert it into a stable fracture pattern may be necessary. Such fractures, however, can be treated with an intramedullary device.

Physical therapy is essential or successful restoration of mobility. The goal of physical therapy is a return to prefracture ambulation and overall function. In a study by Koval et al. (1996), 41% of patients returned to their prefracture ambulatory ability, and 40% remained community and household ambulators. Age younger than 85 years and the absence of multiple comorbid conditions correlated with the resumption of prefracture ambulatory status.

8.15.5 Implant Selection

Two broad categories of internal fixation devices are commonly used for intertrochanteric femoral fractures: sliding compression hip screws with side plate assemblies and intramedullary fixation devices sliding hip screws include traditional compression hip screws that provide compression in the intertrochanteric plane and compression plates that provide additional compression axially. Intramedullary devices include cephalomedullary nails with two screws (Recon type nails) or compression type screws (such as the Gamma

or intramedullary hip screw). The intramedullary compression type screw may be short and end in the diaphyseal femur or long and end in the supracondylar region. Condylocephalic nails, such as those designed by Ender and others, were inserted from the condyles up the medullary canal into the femoral head. This has been abandoned in favor of antegrade cephalomedullary nails owing to associated complications, namely, malunion and back-out of the nails.

The preferred type of device is a matter of debate. Intramedullary nails have a biomechanical advantage over standard compression hip screws because they can be inserted with less exposure of the fracture and less blood loss, although they require more fluoroscopic exposure and have been associated with fracture comminution. In addition, intramedullary nailing is a more technically demanding procedure. Goldhagen et al. compared the Gamma nail to a standard compression hip screw and found no differences in surgical time, blood loss, or fluoroscopy exposure. Clinical rates of healing have been similar for the two devices, but a 3–6% incidence of secondary fracture of the femoral shaft at the tip of the intramedullary device has been reported. Because of this complication, we prefer the longer version of these implants that extend to the supracondylar region of the femur. The Gamma nail appears to have some advantage in certain unstable fractures, especially those with reverse obliquity and subtrochanteric extension that cannot be easily treated with standard hip compression screws.

8.15.6 Fixation with Sliding Compression Hip Screw Devices

In the 1970s, sliding compression screw assemblies were introduced to allow compression of some intertrochanteric fractures. The depth to which the lag screw fixation is inserted into the head is critical for maximal purchase on the proximal fragment; the screw should be inserted to within 1 cm of the subchondral bone. The optimal angle between the barrel and the side plate of a hip compression screw has been the subject of controversy. Many authors have argued that 150° plates are preferable because the angle of the lag screw more closely parallels the compressive forces within the femoral neck. Theoretically, this should lead to less binding of the screw within the barrel of the side plate and less chance of failure of the implant from bending. In clinical studies, however, no difference has been found in the compression ability of 135° hip compressing screws and 150° devices. Plate fracture due to failure in a bending mode has been reported only rarely in true intertrochanteric fractures. More problematic is the placement of 150° lag screws in the center of the femoral head because they tend toward superior placement within the head, leading to a higher chance of screw cutout. Because the 135° devices are easily placed and because their clinical results are similar to those for the 150° plates, the higher angle plates are only rarely indicated for extremely valgus femoral necks and more distal fractures.

In the past, with fixation devices that did not allow collapse, medial displacement osteotomy was performed more frequently. Cheng et al. (1994)

compared the results of sliding compression hip screw fixation with anatomical reduction with those of fixation with medial displacement osteotomy to enhance bony contact, as advocated by Dimon and Hughston. They found that in four-part intertrochanteric fractures, anatomical reduction with the sliding hip screw, regardless of the presence of a postermedial fragment on the side plate than did medial displacement osteotomy. Desjardins et al. compared unstable intertrochanteric fractures treated with anatomical reduction and a hip compression screw to those treated with medial displacement osteotomy and found no significant differences in eventual healing or walking ability, although surgery time and blood loss were higher in the osteotomy group. In a study by Hopkins, Nugent, and Dimon, 97% of anatomically reduced unstable intertrochanteric fractures healed uneventfully, with medial displacement of the distal fragment by controlled collapse in 89%. These researchers concluded that there was no advantage to medial displacement osteotomy in these fractures. With current designs of compression hip screws, we rarely perform medial displacement osteotomies in extensively comminuted fractures.

The techniques for hip screw insertion are similar for all devices.

Biaxial Compression Plate Fixation

Medoff modified the standard compression hip screw, recognizing the need for axial compression until stability is reached. His modification includes the traditional proximal screw in a barrel, a two-part sliding plate, and a distally positioned compression screw in a barrel to compress the proximal femoral fracture fragment to the shaft in the subtrochanteric region. The plate that is applied to the lateral part of the femur is in two parts, with the barrel and proximal part sliding into a slot on the distal part that is fixed to the femur with oblique screws. Lunsjo et al. reported good results and a low rate of complications with this plate. It is usually recommended for unstable intertrochanteric fractures and subtrochanteric fractures.

The Medoff plate comes in two versions: six- and four-hole plates. The six-hole plate has an axial compression screw at the end of the plate and a proximal blocking screw to prevent barrel back-out in highly comminuted fractures and to provide for more axial and anatomical compression. The Medoff plate is designed to accept the compression screws of other hip screw manufacturers (Smith and Nephew Richards, Synthes, Deputy, Zimmer).

Fixation with Intramedullary Devices

Intramedullary devices have at least theoretical advantages over open reduction procedures in that the surgical procedure for insertion is much less extensive, the fracture is not opened, and the operating time and blood loss may be lessened. With the fixation device within the medullary canal, the bending moment on it is considerably less than on standard compression screw and side plate devices.

Cephalomedullary nails, such as the Gamma nail, the intramedullary hip screw, the Russell–Taylor reconstruction nail, and others have used for fixation of unstable intertrochanteric fractures. These devices are centromedullary nails with proximal fixation into the femoral head by nails or screws. The Gamma nail and intramedullary hip screw began as shorter nails than reconstruction nails, with the device ending within the diaphysis of the femur. This allows relatively reliable targeting of the distal interlocking screws through a proximally replacement, a valuable technique for a patient with an intertrochanteric nonunion failure of fixation.

Subtrochanteric Femoral Fractures

Boyd and Griffin (1949) called attention to subtrochanteric fractures as a variant of peritrochanteric fractures and noted their higher incidence of unsatisfactory results after operative treatment. Since that time, subtrochanteric fractures have been variously defined, but most authors limit the term to fractures between the lesser trochanter and the isthmus of the diaphysis. These fractures account for 10–34% of all hip fractures. They have a bimodal age distribution and very different mechanisms of injury. Older patients typically sustain low-velocity trauma, whereas in younger patients these fractures commonly result from high-energy trauma and often are associated with other fractures and injuries. Reported incidences of concomitant injuries requiring surgical treatment range from 21 to 52%, and reported mortality ranges from 8.3 to 20.9%. Restoration of femoral length and rotation and correction of femoral head and neck angulation to restore adequate abductor tension and strength are essential to restoring maximal ambulatory capacity.

Classification

The introduction of various classification systems gives some insight into the evolution of treatment options and also indicates the uncertainty regarding the treatment and prognosis of this complex fracture. Seinsheimer developed the following classification system based on the number of fragments and the location and configuration of the fracture lines:

Type I. Nondisplaced fracture or one with less than 2 mm of displacement
Type II. Two-part fracture
Type IIa. Transverse fracture
Type IIb. Spiral configuration with lesser trochanter attached to proximal fragment
Type IIc. Spiral configuration with lesser trochanter attached to distal fragment
Type III. Three-part fracture
Type IIIa. Three-part spiral configuration with lesser trochanter, a part of the third fragment

Type IIIb. Three-part spiral configuration with the third part a butterfly fragment
Type IV. Comminuted fracture with four or more fragments
Type V. Subtrochanteric–intertrochanteric configuration

With the development of modern reconstruction nails, also known as second-generation intramedullary nails, the classification schemes of Fielding and Seinsheimer have become less useful because they do not separate fractures according to the different treatment methods. At this institution, Russell and Taylor devised a classification scheme based on lesser trochanteric continuity and fracture extension posteriorly on the greater trochanter involving the piriformis fossa, the major two variables influencing treatment. Type I fractures do not extend into the piriformis fossa, whereas type II fractures do involve the piriformis fossa, the most commonly used nail.

In type I fractures closed intramedullary nailing has the advantage of minimizing vascular compromise of the fracture fragments. In type II fractures the extension into the piriformis fossa complicates closed nailing techniques. In type A fractures, the lesser trochanter is intact, thus making medial stability more likely. Plate fixation may be the device of choice.

Treatment and Management

Treatment methods for subtrochanteric fractures have included nonoperative methods, such as traction techniques, which yielded variable results. Velasco, Comfort, and Waddell obtained satisfactory results in only 50 and 36% of patients, respectively, without surgical treatment. However, DeLee, Clanton, and Rockwood reported union of all 15 inoperable or open fractures treated with closed methods.

Plate and screw fixation of subtrochanteric fractures is still advocated by many authors, especially for fractures with intertrochanteric extension, such as Russell–Taylor types IIa and IIb fractures. Kinast et al. reported use of an AO blade-plate for fixation of 24 fractures in which medial dissection was performed in 54%, prophylactic antibiotics were used in 12%, bone grafting was used in 41%, and plate tension was applied in 37%. In this group they found a 21% infection rate and a 32% nonunion rate. In a second group of patients, medial dissection was avoided, prophylactic antibiotics were given 87%, no bone grafts were used, and all plates were tensioned. In this group all fractures united, and there were no deep infections.

Compression hip screws have been a popular method of internal fixation for subtrochanteric fractures. Wile, Panjabi, and Southwick reported no implant failures in 25 fractures. However, Waddell found a 10% failure or nonunion rate in 21 fractures, noting that the device functions as an intramedullary nail in the femoral neck, with no ability to allow fracture site compression. Bergman et al., in a study of 38 fractures fixed with compression screws and side plates, found high union rates in stable configurations, but recommended

intramedullary nailing techniques if the medial cortical buttress cannot be restored. Advantages of intramedullary devices include retained blood supply to bone fragments, less operative blood loss, and less disruption of the fracture environment.

Modern reconstruction nails have greatly improved the outcome and ease of treatment of subtrochanteric fractures. The Russell–Taylor reconstruction nail is a closed section, stainless steel, cephalomedullary nail with proximal interlocking screws that extend into the femoral head and distal interlocking screws similar to standard first-generation interlocking nails. In the original series of patients treated with this device, 59 subtrochanteric fractures all healed uneventfully without the need for bone grafting, auxiliary fixation, immobilization, or nail dynamization (removal of the distal locking screws to allow fracture impaction in cases of delayed union).

Short cephalomedullary nails, principally the Gamma nail and similar devices, including the hip intramedullary hip screw have been used for high subtrochanteric fractures, as well as for intertrochanteric fractures with subtrochanteric extension. A potential complication of these devices is late femoral fracture at the tip of the device; this does not occur with nails that extend well into the distal metaphysic of the femur. We do not use short intramedullary devices.

Before the development of closed section interlocking reconstruction nails, complex subtrochanteric fractures were treated at our institution with compression hip screws and side plates, with bone grafting if the medial cortex was comminuted. Difficulty often was encountered when comminution was extensive. Cephalomedullary interlocking nailing allows length and rotational control, even when the lesser trochanter is not intact. Involvement of the piriformis fossa, the entry portal for the device, does not contraindicate its use but does increase the technical difficulty of placement.

The choice of treatment of subtrochanteric fractures depends on several factors. A hip compression screw with a locking barrel can be used to control rotation of the femoral head in fractures with greater trochanteric comminution; however, accessory screws should not be placed through the plate into the proximal fragment, or the top screw will function as a neutralization plate.

Fixation with Hip Compression Screw and Side Plate

Biomechanical and clinical studies have indicated that Russell–Taylor type II subtrochanteric fractures can be fixed adequately with a hip compression screw and side plate combination. Newer systems have improved fatigue characteristics, and loss of fixation usually occurs from cutout of the screw from the femoral head rather than from fracture of the plate as occurred with older designs. For subtrochanteric fractures, detailed preoperative planning is essential. Lag screw fixation of major fragments should be planned carefully to avoid placing the screws in areas that will be compromised by plate application. We use an AO femoral distractor and the indirect reduction technique

described by Kinast et al. After provisional reduction has been obtained and is held with Kirschner wires, the hip compression screw is inserted in the standard manner. At least four screws should engage both cortices in the distal fragment. Lag screws can be used through the plate, but screw fixation in the proximal fragment prevents the compression screw from obtaining some dynamization. The hip compression screw device used should prevent rotation of the lag screw in the barrel. If medial dissection is necessary autogenous iliac bone grafting should be. In a similar way, the Medoff plate can be used, especially if the comminution does not extend distally down the shaft of the femur.

Indirect Reduction and Fixation with 95° Condylar Plate

Kinast et al. compared their results of open reduction and blade-plate fixation of subtrochanteric fractures with indirect reduction and fixation. They found that delayed union or nonunion resulted in 16.6% of fractures fixed with open reduction and in none fixed with indirect reduction; infection rates were 20.8% and 0%, respectively.

After treatment is similar to that for hip compression screw fixation of intertrochanteric fractures. Generally, the medial buttress is not completely restored, and only touch-down weight-bearing is allowed until signs of early fracture healing are present at 6–8 weeks.

Fractures of Femoral Neck

Fractures of the neck of the femur have always presented great challenges to orthopaedic surgeons and remain in many ways today the unsolved fracture as far as treatment and results are concerned. With life expectancy increasing with each decade, our society is becoming more and more a geriatric society, with significant number of hospitalized and nursing home patients suffering from femoral *neck fractures* and their sequelae. Femoral *neck fractures* in young patients are usually caused by high-energy trauma and often are associated with multiple injuries and high rates of a vascular necrosis and nonunion. Results after this injury apparently depend on (1) the extent of the injury, such as the amount of displacement, the amount of comminution, and whether the circulation has been disturbed, (2) the adequacy of the reduction, and (3) the adequacy of fixation. Even when undisplaced, there is no assurance that a fracture of the femoral neck will attain an excellent result. Between 10% and 15% of these patients develop complications over which the surgeon has little or no control: early anatomical reduction, compression of the fracture, and avascular necrosis because the blood supply to the femoral head after femoral *neck fracture* is quite precarious.

Crock described the blood supply to the proximal end of the femur, dividing it into three major groups (1) an extracapsular arterial ring located

at the base of the femoral neck, (2) ascending cervical branches of the arterial ring on the surface of the femoral neck, and (3) arteries of the ligamentum teres.

The extracapsular arterial ring is formed posteriorly by a large branch of the medial femoral circumflex artery and anteriorly by a branch from the lateral femoral circumflex artery. The ascending cervical branches or retinacular vessels ascend on the surface of the femoral neck in anterior, posterior, medial, and lateral groups; the lateral vessels are the most important. Their proximity to the surface of the femoral neck makes them vulnerable to injury in femoral *neck fracture*. As the articular margin of the femoral head is approached by the ascending cervical vessels, a second less distinct ring of vessels is formed, referred to by Chung at the subsynovial intraarticular arterial ring. It is from this ring of vessels that vessels penetrate the head and are referred to as the epiphyseal arteries, the most important being the lateral epiphyseal arterial group supplying the lateral weight-bearing portion of the femoral head. These epiphyseal vessels are joined by inferior metaphyseal vessels and vessels from the ligamentum teres.

Femoral *neck fractures* are usually entirely intracapsular, and, common to all intracapsular fractures, the synovial fluid bathing the fracture may interfere with the healing process. Because the femoral neck essentially has no periosteal layer, all healing must be endosteal. Angiogenic-inhibiting factors in synovial fluid can also inhibit fracture repair. These factors, a long with the precarious blood supply to the femoral head, make healing unpredictable and nonunions fairly frequent. With anatomical reduction and stable fixation, the incidence of nonunion should be acceptable low. However, in a meta-analysis of 106 reports of displaced femoral *neck fractures* by Yao et al. (1995), nonunion occurred in a cumulative 23–37% of fractures within a 95% confidence interval. Some individual reports, however, claim a nonunion rate as low as 4%, with many around 15%.

As with nonunion, the development of avascular necrosis correlates with the extend of initial trauma and the displacement of the fracture, with some question concerning the tamponading effect of the intracapsular hematoma. In the meta-analysis by Yao et al. (1995), the cumulative rate of avascular necrosis for displaced fractures was 11–19% within a 95% confidence interval. This may understate the true rate of avascular necrosis because segmental collapse does not universally occur, and some cases may not be reported. Urgent, gentle reduction and fixation of these fractures should be carried out. Prompt reduction of the displacement may possibly open some of the retinacular vessels that are temporarily closed by kinking or stretching, and rigid fixation may permit reestablishment of some vascular continuity that otherwise might not be preserved if reduction and fixation are delayed.

Crawfurd et al., Swiontkowski et al., Stromqvist et al., and others demonstrated that intracapsular pressures after femoral *neck fractures* are higher in nondisplaced fractures than in displaced fractures, and Harper, Barnes, and Gregg demonstrated increased intraosseous pressure within the femoral

head after intracapsular femoral *neck fractures*. Joint aspiration lowered the intraosseous pressure and increased the pulse pressure within the femoral head. They and others recommended routine aspiration or capsulotomy or hip aspiration. We do not routinely decompress the hip joint by aspiration or capsulotomy in geriatric patients, but occasionally, we decompress the hip capsule in younger patients.

The method of fracture fixation can have an effect on the rate of avascular necrosis and nonunion with femoral *neck fractures*. The use of a single large compression hip screw for fixation of femoral *neck fractures* was shown by Madsen et al. and Christie et al. to result in lower rates of union for intracapsular fractures. However, in some intracapsular fractures, *neck fractures* at the base of the femoral neck and in severely comminuted femoral *neck fractures*, multiple pin fixation is not ideal because of the lack of an adequate posteromedial buttress. For these fractures, the use of a hip compression screw with side plate is indicated, usually with the addition of a supplemental antirotation screw.

The adequacy of reduction attained with displaced femoral *neck fractures* has been shown to affect the rates of nonunion and avascular necrosis. Garden originally described his alignment index as a guide to adequacy of a given reduction. On the anteroposterior view, the angle between the central compressive trabeculae within the femoral head and the medial cortex of the femur is measured. According to Garden, this angle is normally 160°. On the lateral view in the same axis as the axis of the femoral neck or lie at an angle of 180° higher rates of union and lower rates of a vascular necrosis if the compression head were aligned with the medial cortex of the femur on the anteroposterior 155°–180°, although he strived to correct all of the anteroposterior. He also demonstrated that a vascular necrosis increased from 7 to 65% when less than 155° or more than 180° in either view. He found that a vascular universal when in the anteroposterior view.

Fractures were reduced with an alignment index of less than 150° or more than 185°, the implicating angular and rotational malunion in the incidence avascular necrosis. Other authors, such as Smyth and Shah, reported similar findings.

Multiple methods have been used to preoperatively determine the vascularity of the femoral head in femoral *neck fractures*. To date, bone scans have failed to demonstrate adequate sensitivity or specificity to have useful predictive value. Speer et al. found no evidence of avascular necrosis within the first 48 h after displaced fracture on standard T1- and T2-weighted MRI. They hypothesized that the fatty marrow within the femoral head was relatively resistant to the anoxic insult, with at cell death occurring over 2–5 days, and that this fatty marrow was responsible for the normal signal seen within the femoral head on MRI. Lang et al. demonstrated that gadopentetate dimeglumine-enhanced MRI scanning within 24 h of injury was able to differentiate between femoral heads that were well perfused by digital subtraction angiography and those that were not.

A postoperative bone scan has been demonstrated to correlate with eventual rates of nonunion and avascular necrosis in femoral *neck fractures*. Stromqvist, Kelly, and Lidgren demonstrated that bone scans performed within 2 weeks of operative treatment were able to determine the healing course in 306 fractures (uneventful healing, hardware failure, nonunion, and avascular necrosis) with a prognostic accuracy of 91%. Broeng et al. demonstrated that decreased uptake noted on a bone scan 1–3 weeks postoperatively and 2 months postoperatively was indicative of eventual loss of reduction or segmental collapse in 50% of patients, whereas normal or increased uptake correlated with uncomplicated healing in 90%.

Classification

Various classifications have been described for fractures of the femoral neck. Structurally, there are (1) impacted fractures, (2) undisplaced fractures, and (3) displaced fractures. Causatively, in addition to fractures resulting from trauma without other complicating conditions, there are (1) stress fractures, (2) pathological fractures, and (3) postirradiation fractures. The latter three are discussed separately in this chapter.

The most common classification of displaced femoral *neck fractures* is that of Garden, which is based reconstructive procedure necessary.

Fractures of Femoral Neck with Ipsilateral Femoral Shaft Fractures

This unusual segmental fracture of the femur was initially reported by Delaney and Street as an incidental finding during intramedullary nailing of a femoral fracture. Approximately 19% of femoral *neck fractures* are discovered late or during treatment of femoral shaft fractures. Fractures of the femoral shaft can occur in combination with subtrochanteric fractures, intertrochanteric fractures, nondisplaced femoral *neck fractures*, or displaced femoral *neck fractures*. Shaft fractures, with displaced femoral *neck fractures* as expected, have the worst prognosis. More than 60 different methods have been advocated in the literature for treatment of this rare injury. Swiontkowski, in a review of the literature, estimated a 4.5–15% avascular necrosis rate and a 5% nonunion rate for the femoral *neck fractures* and a 5% nonunion rate for the femoral shaft fractures. This is a better prognosis than is usually seen for femoral *neck fractures*, and it is attributed to the fact that most of the energy causing the fractures is dissipated to the femoral shaft, with less resultant displacement of the femoral *neck fracture*. Any patient sustaining high-energy trauma should be thoroughly examined with a roentgenographic survey of the femoral neck area to rule out this combination of injuries. We routinely reexamine the femoral neck under fluoroscopy after all intramedullary nailings of the femur.

The best treatment of these fractures remains controversial. Swiontkowski, Hansen, and Kellam reported reduction and fixation with lag screws for the

femoral *neck fracture* and a cephalomedullary nail. Some authors now recommend femoral neck fixation with screws and an intercondylar retrograde nail. The use of a hip compression screw and long side plate has also been reported. Cannulated screw fixation into the femoral head, combined with conventional interlocking intramedullary nailing of the shaft fracture, has been advocated by Bucholz and others. The Russell–Taylor reconstruction nail was designed specifically for this injury. It allows fixation by two self-compressing lag screws in the femoral head for control of torsional forces about the femoral neck, in conjunction with a cephalomedullary nail. In a series of 30 consecutive femoral neck and shaft fractures treated with Russell–Taylor reconstruction nails, Azar and Russell reported one femoral neck nonunion and one patient who developed avascular necrosis. Koldenhoven et al. reported one delayed union but no cases of avascular necrosis or nonunion in 11 patients. The one delayed union occurred in a malreduced fracture of 120°. Henry and Seligson also reported successful treatment of ipsilateral femoral neck and shaft fractures with the Russell–Taylor reconstruction nail. It must be emphasized, however, that stabilization of the femoral *neck fracture* takes priority over any type of stabilization of the shaft fracture. We advocate anatomical reduction of the femoral *neck fracture* before stabilization with the implant.

Lambotte's principles of reduction, provisional stabilization, and definitive stabilization can be applied successfully in the treatment of this injury. If the femoral *neck fracture* is displaced, an open reduction through a Watson–Jones approach should be performed first and provisionally fixed with pins, followed by definitive fixation with an interlocking intramedullary nail. Although we have had good results with closed reduction and insertion of a reconstruction nail, the technique requires careful and constant imaging of the femoral *neck fracture* to be sure no displacement occurs during nailing. Two screws must be used for femoral head fixation, and the threads must be well into the head for adequate stability of the femoral neck portion.

When an undetected femoral *neck fracture* is found after conventional intramedullary nailing of a femoral shaft fracture, the nail should be left in place and cannulated screws inserted from the lateral shaft of the femur, anterior to the femoral nail, into the middle of the femoral head to fix the femoral *neck fracture*. The technique for insertion of the Russell–Taylor reconstruction nail is described on p. 2901 and for cannulated femoral neck screws on p. 2913.

Dislocation and Fracture–Dislocation of Hip (Canale: Campbelle Operative Orthopaedics, 10th ed. 2003 Mosh)

Injuries of the hip joint may include pure hip dislocations, dislocations with fracture of the femoral head, and dislocations with fracture of the acetabulum. The position of the femoral head in relation to the acetabulum and the vector of the force at the time of impact determine the type of injury produced. Because of the intrinsic stability and massive bony columns of the

pelvis surrounding the acetabulum, high-energy is usually required to produce these injuries. Hip joint injuries are commonly complicated by injuries to other organ systems or to the pelvis, which can result in hemorrhage and shock. Displacement of the femoral head or acetabulum may injure the sciatic, femoral, or obturator nerve. Associated injuries to the ipsilateral knee are common, especially patellar fracture, open knee laceration, and ligamentous injury. Rupture of the posterior cruciate ligament can be difficult to determine acutely because of difficulty with the initial examination. Late complications include avascular necrosis of the femoral head and posttraumatic arthritis of the joint.

These injuries are orthopaedic emergencies, and the dislocation of the hip should be reduced as quickly as possible. Most hip dislocations can be reduced by closed manipulation, and this procedure should take precedence over the treatment of all other skeletal injuries. Some type of intravenous sedative or analgesic, or even general anesthesia, is usually required. Once the dislocation has been reduced, a thorough roentgenographic examination and a review of the patient's general medical condition and functional demands help to determine appropriate treatment. Operative reduction is indicated if satisfactory closed reduction cannot be obtained promptly, but definitive treatment of femoral head and acetabular fractures can be deferred if the dislocation is reduced by closed means.

Traditionally, this injury complex has been discussed from the point of view of the hip dislocation, the acetabular fracture, or the femoral head fracture. Older classification systems described hip dislocations as posterior, anterior, or central. True central fracture–dislocation is rare. In a few patients with significant metabolic bone disease, a true central dislocation may occur through the floor of the acetabulum without fracture of the anterior or posterior columns. More commonly, a central fracture–dislocation is actually a transverse fracture of the acetabulum, a both-column acetabular fracture, or one of the combined types described by Letournel and Judet. The management of hip dislocations and femoral head fractures is discussed in this section.

Posterior Dislocation and Fracture–Dislocation

Patients with a posterior dislocation of the hip generally represent with a shortened, internally rotated, adducted limb in slight flexion. This position can be altered if the femoral head is impaled upon a fractured posterior acetabular wall. This injury typically occurs from a longitudinally directed force applied through the femur to a flexed hip, often when a patient's knee strikes the dashboard in an automobile head-on collision. If the hip is adducted at the time of injury, a pure dislocation occurs, whereas a neutral position or abduction leads to dislocation associated with a fracture of the femoral head or acetabulum.

8.16 The Dislocated Knee

8.16.1 High-Velocity Knee Dislocation Vascular Injury Treatment: Principles and Management

High-velocity knee dislocations are among the most challenging type of injury that knee surgeons encounter. These injuries usually result in tear of at least three of the four major ligaments of the knee and frequently have severe capsular, neurovascular, integument, meniscal, and tendinous injuries. Patient with high-velocity knee dislocations often have sustained injury to other systems (head, chest and so forth) that may preclude early, aggressive treatment of the torn knee ligaments. Disruption of blood flow through the popliteal artery is common in these injury, and if disruption is not recognized and treated quickly, will result in amputation. The range and complexity of injury patterns in high-velocity knee dislocations requires the use of a variety of treatment options to reduce mortality, prevents amputation, and to maximize the functional outcome of the injured limb. Patients with knee dislocation are at risk for a wide spectrum of long-term problems ranging from severe stiffness to gross instability.

8.16.2 Origins of High-Velocity Knee Dislocation and Injury Mechanism

Separating knee dislocations into high- and low-velocity categories is a somewhat arbitrary division but may be useful in the evaluation and management of these injuries. The exact velocity or energy imparted to the knee joint at the time of injuries is usually unknown. Older literature implicated high-energy mechanisms, such as auto accidents, as the usual cause. More recent studies have reported low-energy sports injuries as a second injuries as a second category. Ultra-low-energy knee dislocations in overweight patients performing activities of daily living have been described as a source of knee *dislocation* injuries. Most high-velocity knee *dislocations* occur as a result of involvement in motor vehicle accidents or of pedestrians who are struck by a motor vehicle. Motorcycle accidents account for a disproportionate number of these injuries because of the lack of a passenger compartment to contain the rider when the accident occurs. Falls from great heights and industrial injuries make up the remainder of causes of high-velocity *dislocations*. One hallmark of high-velocity knee *dislocations* is that the force imparted to the trauma victim is not isolated to the knee joint. Other traumatic injuries can occur in the involved limb, at remote anatomic locations, and in other organ systems. Low-velocity knee *dislocations* usually occur from sports activities or minor falls. The injury force is concentrated about the knee joint, most low-velocity *dislocations* are isolated injuries.

High-velocity knee *dislocations* occur from a variety of applied forces. The mechanism of injury can be a hyperextension force, a severe posterior drawer

force, severe bending, or rotational loads, or combinations of these forces. Kennedy was able to produce an anterior *dislocation* of cadaveric knees with a hyperextension force *Dislocation* of the knee occurred at approximately 30° of hyperextension after rupture of the posterior capsule and the cruciate ligaments. He had a difficult time producing posterior, medial, or lateral *dislocations* with his testing device. Whenever possible, a history of injury mechanisms should be obtained. Approximately 50% of all knee *dislocations* spontaneously reduce, or are reduced in the filed by emergency personnel, and the diagnosis may be delayed or missed altogether. Patients who present with reduced knee *dislocations* have a similar risk of vascular injury and coexisting trauma as those who present with a dislocated knee. The magnitude and direction of the applied force can provide the physician with information about the severity of the knee injury and the anatomic pattern involved. Almost all knee *dislocations* will involve rupture of both cruciate ligaments. Valgus injuries will disrupt the medial ligament and capsule, whereas varus injuries will produce injury to the lateral collateral ligament (LCL) and posterolateral structures. Rotational injuries can disrupt the medial or lateral structures, or both, in addition to the anterior cruciate ligament (ACL) and posterior cruciate ligament (PCL).

The rate of popliteal artery injury with a knee *dislocation* ranges from 14 to 65%. The anatomic location of the popliteal artery places it at significant risk for major injury with a knee *dislocation*. The popliteal artery is held against the femur proximally by the adductor hiatus and distally against the tibia by the fibrinous arch of the soleus muscle. The large displacement that occurs during a knee *dislocation* can easily injure the tethered artery. Most popliteal artery injuries associated with knee *dislocations* are seen in patients who have experienced high-velocity injuries. It is less common for a low-velocity *dislocation* to have an associated arterial or nerve injury. The incidence of vascular injury is the same in knees which present with *dislocation* and those that present reduced. The physician must have a high index of suspicion for a popliteal artery injury in all patients with knee *dislocations*.

8.16.3 Medical Examination

A thorough trauma evaluation needs to be performed in all patients with high-velocity knee *dislocations*. Most patients with this injury will have coexisting major trauma. The physician must not allow a severe knee injury to distract from identifying less obvious but more lethal injuries.

The presence of concomitant trauma occurs with equal frequency in patients with documented knee *dislocations* and those who present with reduced knee *dislocations* with severe ligamentous disruption. Identification of associated injuries may be lifesaving and may alter the eventual management of the knee *dislocation*.

A knee screening examination should be performed in all multiple trauma patients. The presence of other severe injuries should not preclude the

diagnosis of knee *dislocation* in the emergency room. Approximately 50% of knee *dislocations* undergo spontaneous reduction or are reduced in the field before arriving at the emergency room. The rate of arterial injury is the same in reduced knees as it is in knees that present as dislocated. Patients with clinical evidence of combined ACL and PCL injuries should be treated as though they have a dislocated knee. Overlooking a multiple-ligament-injured knee could cause the physician to miss a major popliteal artery injury and put a limb at risk for amputation.

After an initial trauma evaluation, additional attention should be given to the injured leg. The physician should perform a careful neurovascular examination before and after reduction, documenting any evidence of vascular injury. Signs of ischemia should be noted (pain, paralysis, pallor, paresthesia, or diminished limb temperature). More important, the presence and quality of the posterior tibial and dorsalis pedis pulses should be documented and compared with the contralateral limb. Doppler examination is helpful but may be falsely interpreted. A Doppler pulse does not exclude popliteal injury. Some authors have used Doppler pressure measurements as a means to identity arterial injuries. Attention also should be directed to examine for a compartment syndrome. Patients with knee *dislocations* can sustain compartment syndromes from the initial trauma, subsequent hemorrhage, or reperfusion of an ischemic limb. Initially, neurologic deficits should never be attributed only to peripheral nerve injuries. The examiner should have a low threshold for measuring compartment pressures, particularly in patients who cannot cooperate with the physical examination. Serial examinations and measurements are required over the first 48 h because an elevated compartment pressure can be delayed complication of knee *dislocation*.

Finally, a thorough evaluation of the dislocated knee joint should be performed. The skin should be examined for any open injuries or the presence of severe abrasions that might compromise surgical approaches to the injured ligaments. Irreducible posterolateral *dislocations* have a characteristic puckering of the anteromedial skin where the femur has buttonholed through the medial capsule, and the medical collateral ligament (MCL) has invaginated into the joint. Before performing a reduction, the direction of the *dislocation* should be noted. A careful ligament examination should be undertaken. This is best performed immediately after reduction, before gross swelling occurs, or under anesthesia if the patient is going to the operating room emergently for other injuries. The ligament examination should include a Lachman test, a posterior drawer test, varus and valgus stress at 30° and 0°, a spin test, and a varus–recurvatum test. The examiner should also try to determine the position of knee flexion where the joint appears to be most stable. The physician also should search for the present of tendon ruptures about the dislocated knee, most commonly the patellar tendon and the tendon of the biceps femoris. Special care must be taken in severely injured knees not to cause excessive displacement and additional injury. The goal is to diagnose and assess instability, not to cause recurrent *dislocation*.

Radiographs should be obtained for all patients with documented or suspected knee *dislocation*. Anteroposterior and lateral views of the dislocated knee will document the direction of the *dislocation* and to identify bony avulsions. Postreduction radiographs (anteroposterior, lateral, and Merchant views) should be obtained to document the reduced position of the knee joint and to look for any persistent subluxation. These radiographs will help to identify osteochondral fractures and ligament or tendon avulsions that are treated by early surgical repair. Intraarticular and periarticular fractures may be present. "Fracture–dislocation" of the knee may also be present.

MR imaging of the dislocated knee is helpful in planning surgical repair or reconstruction. MR imaging can be performed electively when the patient's overall condition allows, to identify the severity and location of ligament injuries, and to identify meniscal tears and musculotendinous injuries. Studies have shown that MR imaging correlates well with findings at the time of surgery, may be more accurate than the clinical examination findings in multiple trauma patients, and can help to predict the potential for repair of the cruciate ligaments. MR imaging should be used liberally in patients with knee *dislocations*, especially those in whom a thorough physical examination is difficult because of associated injuries. Intraoperative arteriograms are occasionally useful to rule out arterial injury above or below the knee *dislocation* in patients with coexisting ipsilateral extremity trauma.

8.16.4 Initial Treatment

High-velocity knee *dislocations* are orthopedic emergencies. Reduction should be performed as soon as possible; usually this can be achieved in the emergency room with intravenous sedation. Longitudinal traction is applied, and the normal relationship between the tibia and the femur is reestablished. Reduction is usually easy to obtain. If reduction cannot be obtained in the emergency room, the patient should be taken emergently to the operating room where a closed reduction under anesthesia is performed. Occasionally the medial femoral condyle will button hole through the medial capsule, preventing reduction. In this situation, an open reduction is undertaken to prevent skin necrosis. A small anteromedial arthrotomy is made, and the medial capsule is incised to allow the reduction to be performed. Early reduction will help to minimize the neurovascular and skin complications and compartment problems that can occur with high-velocity knee *dislocations*.

Following reduction and a thorough ligament examination, the limb should be splinted. Subluxation or recurrent *dislocation* is common. If the knee is placed in too much extension, the lax posterior capsule can allow subluxation; conversely, these severely injured knees tend to be more unstable in flexion.

Immobilizing the reduced knee in approximately 20° of flexion is preferred. To help prevent compartment syndrome and facilitate serial examination, circumferential casts should be avoided. Access to the dorsalis pedis and posterior tibial pulses is mandatory to monitor the vascular status of the limb.

The author's preferred method is to use a posterior fiberglass splint augmented with medial or lateral struts, as needed. A prefabricated, hinged knee brace locked at 20° can also be used. As soon as possible after the limb is immobilized, radiographs should be obtained to confirm reduction. Additional radiographs should be obtained a few days later because cases of late subluxation can occur. Open Knee dislocations require emergent surgical treatment to minimize the risk of infection. A thorough irrigation and debridement should be undertaken in the operating room. If necessary, the wound can be extended to allow adequate visualization of the entire knee joint. Repair or reconstruction of the knee ligaments should be deferred for a least 7 days to allow overall assessment and to ensure that no infection is present. Following debridement, the capsule should be closed with nonabsorbable suture. The traumatic portion of the skin wound should be left open and a delayed closure performed when the wound is clean. Grossly contaminated wounds should undergo serial debridement every 2–3 days, until the wound is clean. A spanning external fixator should be applied to large open wounds. A spanning external fixator is an excellent means of achieving rigid knee stability while allowing access to the limb for serial examinations and wound care. Two bicortical threaded pins are placed in the midshaft of the femur just to the quadriceps tendon. Two similar pins are also placed in the midshaft of the tibia through the anteromedial surface. The pins are placed far enough away from the knee joint so that they will not interfere with any future surgical approaches. The femoral pins are then attached to one bar, and the tibial pins are attached to a second bar. The two bars are then connected using a universal clamp or by using a third bar to each bar with a swivel clamp. This construct allows adjustments to be made if residual subluxation remains. Normal tibiofemoral alignment and varus–valgus angulation is reproduced, and the fixator is tightened provisionally. Fluoroscopy or radiography in two planes is used to confirm the position of the reduction before the final tightening of the fixator. The use of radiolucent bars enables the surgeon to better assess the reduction radiographically. Radiographs should be obtained approximately 3 days later and approximately every 3 weeks while the fixator is in place, to ensure that no subluxation has occurred. Daily pin site care is mandatory to prevent pin tract on infections. The fixator can be removed when the patient's other injuries allow, usually in 2–6 weeks. The spanning external fixator can be used routinely in case of knee dislocations with vascular repair, open wounds, and associated closed head injuries.

8.16.5 Treatment of Knee Ligaments

Management of ligamentous injuries in the dislocated knee has evolved over the past 20 years. Nonoperative treatment of knee dislocations has resulted in an unacceptably high incidence of knee stiffness or functional instability. Primary repair of all injured ligaments improves the stability of the knee, but prolonged postoperative immobilization frequently leads to a loss of range-of-

motion. Primary repair is still advocated for cruciate ligament avulsion and collateral ligament tears, although in the author's experience, cruciate avulsions are uncommon. Some authors have advocated repair of the collateral ligaments and primary reconstruct of only the PCL; the torn ACL is debrided and not acutely reconstructed. Concern is expressed about the risk of stiffness if both cruciate ligaments are reconstructed acutely; and ACL reconstruction is recommended as a secondary procedure if functional instability develops. More recently, reconstruction of both cruciate ligaments and repair of the collateral ligaments at a single operation have been advocated. The use of allografts for the cruciate reconstructions and early postoperative motion has reduced the complication of stiffness. The author's approach consists of addressing all knee ligament pathology at a single surgery. Cruciate ligament avulsions with bone are primarily repaired; otherwise, reconstruction is carried out for the ACL and PCL using allografts. The collateral ligaments can be usually primarily repaired, but if tissue is found to be adequate in a posterolateral complex injury, the repair can be augmented with allograft or a portion of the biceps femoris tendon.

The timing of surgical repair and reconstruction of the knee ligaments must be individualized. Immediate ligament repair is rarely warranted. Ligament surgeries are extremely complex and should be undertaken by a rested, experienced knee surgeon with an optimal surgical team. MR images are invaluable for planning of ligament surgery in knee dislocations. A vascular surgeon should be readily possible, performing ligament surgery early (within 7 days after injury) will optimize results in the following situations (1) bony avulsions of the cruciate ligaments can be primarily repaired with results that are superior to cruciate ligament reconstruction; (2) periarticular fractures should be addressed early to minimize joint incongruity and late degenerative changes; (3) large, displaced meniscal injuries are amenable to repair if treated early, whereas if they are treated later they will require a subtotal meniscectomy and risk subsequent postmeniscectomy arthritis; and (4) posterolateral ligament injuries are much easier to dissect and repair if treated within 1 week of injury; delayed surgery will require a posterolateral reconstruction with less predictable results.

8.16.6 Emergency Department Evaluation and Treatment of Knee and Leg Injuries

The physical examination should begin by observing the patient ambulate to the bedside, if possible. A history should be obtained, with a focus on mechanism of injury and prior injuries to the knee. It is often difficult to obtained an accurate history on the patient's exact positioning at the time of injury. It is known that a flexed knee can dissipate a force better than an extended knee. The time at which the onset of swelling should be noted, and when any associated pain in the knee was noticed. In children, pain in the hip can be referred to the knee, and so the hip must be specifically examined.

The physical examination includes the leg and knee for swelling, ecchymosis, effusions, masses, patellar location/size, muscular development, erythema, evidence of local trauma, and leg length with the patient supine. The injured knee should always be compared with the uninjured knee. The knee should be examined for a range-of-motion (0°–135° of flexion) and palpated for tenderness. Check for an effusion in the knee by palpating for a ballotable. Palpation should begin in the nontender areas, moving toward the tender areas last. Palpate for temperature (increased warmth), strength, sensation, and character or location of distal pulses. The patella should be examined for location, size, and shape with the knee in flexion. Patella mobility should be checked with the knee in extension. Palpate the popliteal space for masses, swelling, and circulatory status.

Because of patient discomfort, stress testing of the knee should be the final step. Relax the patient as possible and test the uninjured knee as a baseline for normal. The first examination maneuver should be the most valuable diagnostic test to perform as the patient will not be expecting the stress and will have less voluntary guarding.

Radiographic Examination of the Knee

Routine radiographic views of the knee consist of the anteroposterior (AP), lateral, and oblique views (internally and externally rotated knee). Internal and external oblique projection provides a prospective of the femoral condyles, tibial tuberosities, and medial and lateral patellar margins not visible on the standard AP and lateral views. Some authors also advocate a "tunnel" (or notch) view to aid in detecting loose bodies in the joint space. If patellar injury is suspected, an axial (i.e., tangential, "skyline," "sunrise," or Hughstone) projection should be obtained. In children with an epiphyseal growth plate, it is helpful to get comparison views of the uninjured knee.

Radiographs will be detected not only bony injury, but also can confirm a clinical suspicion of a joint effusion. An effusion causes distension of the knee joint capsule that displaces the quadriceps femoris muscle, suprapatellar tendon, and the patella anteriorly.

There is growth support for the reduction of unnecessary knee radiographs. Historically, up to 80% of patient with knee injuries seen US EDs undergo radiography but have a low-yield from knee fracture (6–12%), three recent studies have examined the effects of implementing clinical decision rules for obtaining knee radiographs.

Published in 1995, the Ottawa knee rules have been shown to be highly reliable. A knee radiograph is indicated only in patients with acute knee injuries and one or more of the following five conditions:

1. Blunt knee trauma in a patient greater than 55-years old
2. Tenderness of the head of the fibula on palpation
3. Isolated tenderness of the knee to 90°

4. Inability to bear weight both immediately and inability to take four steps in the ED

Exclusion criteria include:

1. Isolated skin injuries (i.e., superficial abrasions/lacerations)
2. Referred patients from another ED or clinic
3. Injury greater than 7-days old
4. Patient returning for reevaluation
5. Distracting injuries (multiple trauma)
6. Altered mental status
7. Age less than 18-years old
8. Pregnant patients
9. Paraplegia

In a study of 3,907 adult, 100% sensitivity was achieved in detecting 59 fractures with a potential reduction in radiographs of the knee by 26%. Failure to obtain radiographs did not adversely influence patient satisfaction with care.

Weber's clinical decision rule is intended for isolated nonpenetrating knee trauma less than 24-h old. Radiographs are not indicated in a patient with a history of twist injury who can ambulate without limp and have no effusion present. Patients are excluded if they have multitrauma, mental impairments, prosthesis, or known fracture elsewhere. Although still undergoing clinical evaluation, the initial study population had 100% sensitivity, with a potential reduction in knee radiographs by 29%.

The Pittsburgh rules for knee radiographs were found to be more specific (60–80% vs. 27–49%) without loss of sensitivity (99 vs. 97%) when compared with the Ottawa knee rule.

Exclusion criteria from the Pittsburgh rules for knee radiographs include:

1. Injury greater than 6-days old
2. Isolated skin injuries (i.e., superficial abrasions/lacerations)
3. History of knee fracture or surgery
4. Repeat visit for the same injury

A 1998 article compared the Pittsburgh rules with the Ottawa knee rules. Knees radiographs could have been reduced by 52% with one missed fracture with the Pittsburgh rules, whereas the Ottawa knee rules could have decreased knee radiographs by 23% with three missed fracture.

Specific Injuries

Patellar Fractures

The patella is the largest sesamoid bone in the body and helps to increase the mechanical advantages of the quadriceps tendon (i.e., the extensor force of the knee). Approximately 1% of all adults' fractures involve the patella. It

is less common in children awing to patella's being surrounded by thick cartilage. Many patellar fractures (up to 27% in one series) occur during a motor vehicle crash, when the flexed knee strikes the dashboard. The patella can also be fractured after a forceful contraction of the quadriceps muscle (and therefore violent flexion of the knee). There are several types of patella fractures, including transverse, communicated (satellite), vertical, and marginal.

Transverse and comminuted (satellite) fractures of the patella are the commonest and occur usually after a direct blow to knee. Marginal fractures involve the medial and lateral borders of the patella, are relatively uncommon, and occur usually after dislocation or direct blow to the edge of the patella. Displaced patellar fractures are defined as greater than 3 mm of bony separation and greater than 2 mm of AP step-off.

All fractures of the patella (except small avulsion, rim fracture) are intraarticular. Usually the patient is unable to maintain the knee in active extension and may have a palpable defect or crepitus and effusion over the patella. Because most patella fractures occur with the knee in flexion, one must look closely for other injuries, including knee dislocations, femur fractures, acetabular fractures, and hip dislocations.

The patella is best imaged with AP, lateral, and tangential and radiographs, the tangential view radiograph (also known as the "skyline" or sunrise view) is taken across a knee flexed to 45° and helps to show small vertical fractures of the patella. The tangential view is also useful for detecting intraarticular step-off. Bipartite patellas occur where ossification centers have not fused: these are bilateral and be distinguished from a patella fracture by their smooth margin.

Nondisplaced patella fractures are treated nonsurgically with a knee immobilizer and partial weight-bearing for 3 weeks. Radiographs are repeated in 3 weeks and if the patellar fracture is still nondisplaced, the knee immobilizer is worn for three additional week for horizontal (transverse) fractures and a shorter period for vertical fracture. Isometric quadriceps contractions usually are begun early in the treatment. Displaced fracture needs an orthopedical evolution in the ED for probable surgical fixation. Displaced fracture is usually managed with a modified tension band around the patellar fragment and longitudinally directed Kirschner wires. Several comminuted fracture may need a partial or total patellectomy, in which the patella fragments are removed and the quadriceps and patella tendons sutured together. As with any open fracture, it should be irrigated and debrided in the operating room.

Patellar Dislocations

A patellar dislocation occurs after a powerful contraction of the quadriceps in combination with sudden flexion and external rotation of the tibia on the femur. Patellar dislocations are commoner in adolescent females, obesity, and in those with patella alta ("high-riding patella") excessive genu valgum ("knock knee"), weak vastus medialis (quadriceps muscle), or excessive tibial

torsion. The patella is usually disclosed laterally because the medial femoral condyle is larger and more prominent than the lateral femoral condyle. In addition, the slope of the smaller medial facet of the posterior surface of the patella is steeper than that of the larger lateral facet.

The patient often complains of his or her knee having "gone out of place" and then return to normal position, and present with a tender, swollen knee. Often there is a history of a subluxed or dislocated patella, and there is a 15–50% recurrence rate of patella dislocations, especially in patients with anatomic predisposition. Up to 40% of acute patella dislocations are associated with an osteochondral (i.e., thin, curved fragment of cortical bone its covering cartilage) fracture than often is not seen on routine radiographs.

The lateral pressure syndrome can develop after a patellar dislocation; this is an aching anterior knee joint pain with excessive use (especially descending stairs), and after long periods of sitting ("moviegoers" knee).

A patient who has sustained a patellar dislocation often has pain at the medial side of the patella where the attachments have been torn. The patient also may have a positive patellar apprehension test ("Fairbank's test"), which indicates instability of the patellofemoral joint. This test is performed by having the patient flex the knee to 30° while relaxing the quadriceps muscle, and while the examiner supports the foot's attempt to push the patella laterally. If excessive laxity (>1 cm) is present, the patella will be pushed up onto the lateral femoral condyle, producing the sensation of impending subluxation/dislocation, and the patient either grabs the knee or involuntarily contracts the quadriceps muscle and extends the knee. Always check the cruciate ligaments carefully because up to 12% of all patellar dislocations have a concomitant major ligamentous or meniscal injury. Postreduction radiographs should be obtained to look for a marginal or osteochondral fracture of the patella.

Most patella dislocations reduce spontaneously. If the patella is dislocated on the patient's arrival in the ED, extend the leg with the hip flexed (reduce tension of quadriceps tendon) and apply gentle pressure on the patella directed laterally to medially. Once the knee is reduced, a knee immobilizer should be placed in full extension for 3–7, weeks, with progressive weight-bearing as tolerated. Ice should be applied for the first 24 h, and a compressive dressing is advocated by some for the first 4 days to reduce anteromedial effusion than can occur postreduction. A quadriceps strength and stretching program, as well as functional rehabilitation, should be started once the patient can do range-of-motion exercises without discomfort. Even with rehabilitation, one-third of acute patellar dislocations will recur.

Some orthopedic surgeons believe that all first-time patella dislocations (especially in athletes) should be surgically repaired initially. Arthroscopic medial capsular repair with lateral release can reduce the recurrence in the future and reduce the chronic pain risk; however, one study still found that 20–30% of patients will experience symptoms of patellofemoral instability even after surgical realignment of the patellas.

3. Knee Dislocations

Knee dislocations are true orthopedic emergencies because of associated vascular and neurological injuries. Two thirds of all dislocations are the result of motor vehicle crashes, with the remainder usually occurring from falls, sports injuries, and industrial injuries. The peak incidence of knee dislocations is in male subjects (3:1) in their third decade of life. Knee dislocations are classified by the direction of tibial displacement in relation to the femur and can dislocate in any direction (including laterally and medially). Anterior dislocations involve 50–60% of all knee dislocations.

Anterior knee dislocations usually occur after a high-energy (e.g., motor vehicle crash) hyperextension injury (80%), although even stepping into a hole (low-energy) can cause a knee dislocation. The knee hyperextends, causing a posterior capsule tear with possible anterior cruciate ligament (PCL) tears, or stretching of the popliteal artery, or tears of both the ACL and PCL. The collateral ligaments stay intact.

Knee dislocations are often associated with a fracture of the proximal tibia. Because of a high incidence of spontaneous reduction before arrival to the ED, the diagnosis is easy to miss, and a high index of suspicion must be maintained. Some authors have advocated expanding the definition of knee dislocation to include those patients who have bicruciate (ACL and PCL) ligament injury, even when the knee is reduced on initial presentation. This definition is primarily to prevent missing the diagnosis of vascular injuries in spontaneously reduced knee dislocation.

Anterior knee dislocations have a high incidence (5–40%) of associated vascular injuries usually involving the popliteal artery, and these, up to one half (20–50%) can result in amputation of the leg.

The incidence of peroneal nerve injury after an anterior knee dislocation is reported as up to 40% and is permanent in up to 78% of patients.

An accurate neurovascular motor examination must be performed on a patient with a suspected knee dislocation. The patient may have massive swelling of the knee and it should be evaluated for valgus, varus, and instability in 20° flexion. The presence of distal pulses in the foot does not rule out an arterial injury; it is reported that there is a 10% incidence of popliteal artery injury despite present distal pulses. Never attribute diminished pedal pulses to arterial spasm without angiographic evaluation. The amputation rate approaches 86% in legs with vascular compromise on which repairs are begun more than 8 h after injury. The peroneal nerve should be evaluated by determining sensation of the dorsum of the foot and by having the patient dorsiflex the ankle. The tibial nerve is evaluated by plantar sensation and by plantar flexion of the foot.

Historically, an arteriogram was advocated for all anterior knee dislocation, even in the presence of a normal postreduction vascular examination because of reports of normal distal vascular examinations and subsequent significant popliteal artery injuries. Arteriograms are costly, invasive procedures with a

low but well defined risk of complications. Duplex Doppler ultrasonography has been recently advocated by some authors and has been shown to correlate well with arteriography. A downside to the duplex Doppler ultrasonography is that it may miss an intimal tear. The current recommendation is that patients with low-energy knee dislocation and a normal vascular examination do not require arteriography but do require serial examination. Serial examinations or arteriography can follow patients with high-energy knee dislocations and a normal vascular examination. Arteriography should not delay surgical exploration. Many advocate taking a cool, cyanotic ischemic lower extremity directly to the operating room for perioperative angiogram or direct popliteal artery exploration.

Treatment goals are early reduction, immobilization, assessment of distal neurovascular function, and emergent referral. A dislocated knee should be reduced as soon as possible. One should have an assistant to apply longitudinal traction on the leg while the EP keeps one hand on the tibia and one on the femur to lift the femur anteriorly and guide it back into position. The knee should be immobilized with a posterior splint in 15° of flexion to avoid tension on the popliteal artery. The patient should be admitted for observation and arteriography. Best results occur with early surgical treatment of ligamentous injuries. If no vascular injury is detected by arteriography, knee is splinted for 8 weeks of immobilization.

Anterior Cruciate Ligament Injury

There are estimated 90,000 acute ACL injuries in the United State per year and the incidence has been increasing largely because of athletic activity. The ACL is taunt in an extended knee, preventing rotatory motion, and will relax once the knee is in 20° or greater of flexion. The knee ligaments are elastics and can elongate up to 30%. The ACL prevents knee hyperextension, prevents excessive internal rotation, and prevents excessive lateral mobility. Full knee extension causes the ACL to be tight and prevents rotary motion of the knee, known as the "screwing home" mechanism. Injuries to the ACL usually occurs with sudden declaration, hyperextension, and marked internal rotation of the tibia on the femur.

Ligamentous knee injuries in children are rare, and pediatric patients usually present with fracture of the epiphysis (Salter I) instead. Children can also fracture the base of the intercondylar or medial tubercle, which indicates that the ACL has been detached from tibia. These children will usually have a negative anterior drawer test.

Important historical question to ask include:

1. Mechanism of injury
2. Pain
3. Feeling/hearing a "pop"
4. Feeling knee "give out"

5. Ability to continuation playing sport
6. Loss of knee motion
7. History of previous knee injury

Up to 50% of patient with acute knee injury who report feeling or hearing a "cracking" or "popping" sound will be found to have an ACK injury. A complete ligament tear may be immediately painful, then resolve, whereas the pain of a partial ACL tear may persist.

The ACL has a plentiful vascular supply, and hemarthrosis is always present. Immediately after injury there will be no effusion or spasm, and ACL injuries can often be easily to defect. An ACL injury is rarely isolated and often is associated with tears of MCL and medial meniscus.

Always examine the uninjured knee first to determine the motion limits of the normal knee. Compare the laxity encountered in an injured knee. Because ligamentous testing involves vigorous force on the joint, it should be the last part of the physical examination. The Lachman's test is first performed with the knee in 25°–20° of flexion, with the patient lying supine. Using one hand on the anterior aspect of the distal femur and a second hand behind the proximal tibia, the EP should attempt to forwardly displace the tibia from the femur. The Lachman's test is considered positive if there is either more than 5 mm of anterior displacement of the tibia, or a "soft, mushy" endpoint. It is also useful for large knee effusion and hamstring sprains because the knee is not flexed to 90°. The Lachman's test can also identify partial ACL tears.

The anterior drawer (AD) test is another way to detect an ACL tear by attempting to forwardly displace the tibia from the femur in much the same way as the Lachman's test, however, the anterior drawer test is done with the knee in 90° of knee flexion (with the hip flexed to 45°). If there is more than 6 mm of tibial displacement, it indicates an ACL injury. The anterior drawer test is not very sensitive and has been found to be positive in only 77% patient with a complete ACL rupture. There are many other diagnostic tests (e.g., Slocum test, pivot-shift tests) but the above two are the ones most often used. MR imaging also is useful in the diagnosis of an ACL injury because it also detects meniscal tear that can influence the treatment plan.

The goal of treating an ACL is to reduce pain, swelling, and inflammation, and to restore the normal range-of-motion and strength as soon as possible.

The patient should be reexamined in 1 or 2 days by an orthopedist after immobilization, nonweight-bearing (crutches), ice packs application elevation, and analgesics (NSAIDs) have been insulated. If painful tense effusion is present, it should be aspirated. Quadricep- and hamstring-strengthening exercise and physical therapy should also be done in the future. A trial of nonsurgery can be tried if there is a definite endpoint on stressing the joint and no other ligaments are injury. Complete ACL injuries in young active adults need surgical treatment (especially athletically active patients with the secondary ligament tear of the PCL or MCL). Patient with meniscal injuries in addition

to the ACL injury usually requires surgical treatment with meniscal repair, after which the patient will usually need 6 months of rehabilitation.

Marked unstable knees need reconstructive surgery. Remember, a grossly unstable knee is a complete knee dislocation until proven otherwise, and neurovascular injuries cannot be overlooked.

Posterior Cruciate Ligament Injury

The purpose of the PCL is to prevent backward motion of the tibia on the femur. Injuries to the PCL usually result from a direct blow to the pretibial area when the knee is flexed (forcing the knee posteriorly). This "dashboard injury" mechanism often causes other injury to other ligaments, or a fractured patella, femur, or acetabulum. PCL injuries are rarely isolated and typically area associated with severe knee injuries of the ACL and MCL.

The patient usually complains of the pain and having heard an audible "pop" or "snap," or a buckling sound. As with an ACL tear, complete tears of the PCL are usually less painful than partial tears. The pain will be increased with the patient's descending stairs or on the push-off phase of the running cycle. The physical examination of the knee with a PCL injury may show a visible posterior drop-off of the tibia in relation to the femur with the hips and knees both flexed to 90°.

A PCL injury is detected by performing a posterior drawer (PD) test, with the knee in 70°–90° of flexion. The PD test is like the AD test; however, with this the examiner attempts to displace the tibia from the femur posteriorly. Posterior displacement of the tibia more than 5 mm, or a "soft" endpoint, indicates injury. MR imaging is also used for diagnosis, and it is reported to be up to 99% sensitive for documenting a PCL injury.

The quadriceps active is a second test designed to assess the integrity of the PCL. The knee is flexed to 60° while the examiner holds the foot to the table in a flat position. The patient is then asked to extend the knee isometrically. If the PCL is deficient, the tibia translates anteriorly from a subluxed position, and the medial tribal plateau step-off is recreated.

An isolated partial PCL tear is managed surgically. These types of injuries result in no function impairment and there are very few subsequent episodes of instability. The patient with an injured PCL should be placed in a knee immobilize, with crutches, ice, elevation, and orthopedic referral within a few days. Isometric quadriceps exercises are usually begun 1–2 weeks after the initial PCL injury in an isolated PCL injury. Complete tears of the PCL are often treated nonsurgically; however, sometimes surgery is need. If the ACL is also injured, the surgery is necessary. The posterolateral instability of the PCL must be fixed first, then the ACL can be fixed either at the initial surgery or at a later time. Unless the PCL is repaired first, the ACL reconstruction can fail owing to excessive posterolateral instability.

Medical Collateral Ligament Injury

The MCL is the most commonly injured ligament of the knee in the adults and children. The MCL is two-part structure composed of 3–4 layers, with a long superficial ligament overlying a deep capsular structure. The purpose of the MCL is to limit rotation of the knee. The MCL supplies most of the restrain to valgus deformity of the knee final stages of the flexion. The MCL can be injured after a direct blow to the lateral aspect of the knee (i.e., valgus stress). An isolated disruption of the MCL usually occurs after a direct blow to lateral aspect of the knee with the leg fixed:

- Partial MCL tears are usually quite painful, with complete tears being less painless. An MCL tear is often associated with a concomitant ACL injury (e.g., rotational with valgus injury, as in an athlete making an abrupt pivot). Injuries to the cruciate ligaments and menisci must be ruled out with a MCL injury. An MCL tear is diagnosed with a valgus stress flexion. One hand is placed on the lateral aspect of the knee, and the foot and the ankle. The slight external rotation tightness the MCL and allows for detection of laxity. Medial laxity of more than 10 mm without a firm endpoint suggests complete rupture of the MCL. Laxity of less than 10 mm suggests as incomplete or partial tear.
- MR imaging can be used to assist with the diagnosis of a MCL injury and is useful for evaluating associated menisci or ligamentous injury. TI-weighted images causes the ligaments to appear black, whereas the T2 signal is used to produce a bright signal where the actual disruption of the ligament has occurred.
- The treatment of as isolated MCL injury is nonsurgical and consists of ice, elevation, a knee immobilizer, and crutches, with weight-bearing as tolerated. Range-of-motion exercise can begin once the patient is pain free and full activity can usually be resumed in 3–9 weeks, depending on the severity of tear. Sever tear of the MCL are often treated surgically especially if both the ACL and MCL are torn; however this has been debated in the literature.

Lateral Collateral Ligament Injury

- The LCL is the primary knee stabilizer of varus rotation. Unlike the MCL injuries to the LCL are uncommon. The LCL is extracapsular and does not insert on the lateral meniscus. The LCL is injured after an internal rotation (varus) stress to the depended knee; however, if the LCL is injured, lateral instability of the knee is more disabling than medial instability. An isolated LCL injury is the result of a direst varus blow to the medial aspect of the knee with the leg fixed, as occurs with wrestlers who have had a strong varus stress applied. A LCL tear is often associated with an ACL tear (or a PCL tear if a severe enough varus stress is applied).

- Injury to the LCL is tested by applying a varus force to the knee in extension and in 30° of flexion. The knee should be tested with the foot and the leg in a neutral and also in internal rotation lateral laxity of more than 10 mm without a firm endpoint suggests a complete rupture of the LCL. Varus laxity less than 10 mm suggests an incomplete or partial tear.
- An MRI can be obtained to evaluate any associated damage to the menisci or cruciate ligaments. The treatment of an isolated LCL injury is usually nonsurgical and consists of a knee immobilizer, ice, and crutches, with weight-bearing as tolerated. Surgical treatment is for only those LCL injuries associated with some other major ligamentous damage.

Meniscal Knee Injury

- The menisci are two crescent-shaped, fibrocartilaginous, avascular disks important in load-bearing and force transmission across the knee and are interposed between the condyles of the femur and tibia. They serve as the "shock absorbers" of the knee. The periphery of each meniscus is attached to the femur and tibia by the joint capsule. The lateral meniscus is "O" shaped and has only a single attachment, making it more commonly injured. The medial meniscus is anchored firmly to the joint capsule and MCL.
- The menisci are usually injured after a twisting motion to a flexed and can cause the knee to lock in in flexion. This locked knee with the inability to extend fully is a mechanical block from a displaced meniscal tear. In patient with medial meniscal tears, 79% also have an A injury. The pain with a meniscal injury is usually worse with weight-bearing, unlike with injuries to the MCL and LCL. The patient complains of recurring episodes of instability, pain, catching, locking, audible "snap"/"pops," or a history of buckling complaints of the injury knee "giving way." The menisci have a sensory nerve fibers, and any pain is secondary to ligamentous inflammation near the joint line.
- The triad of meniscal tears is joint line pain, swelling, and locking.
- The McMurray test is done with the patient supine and the hip and knee flexed.
- The tibia is rotated, and a valgus stress is applied to a externally rotated foot. Pain can indicate a torn medial meniscal cartilage, especially if a "pop" or grinding is felt along the lateral or medical joint lines when the leg is extended. The McMurray test may not be tolerated well on an acutely injured knee if the patient is in pain or has limited movement of the knee owing to spasm. The Apley distribution (grinding) test is similar to the McMurray test; however, the patient is prone rather then supine. The knee is flexed to 90° angle and then rotated while under traction. Pain and popping in the knee indicate to the knee capsule or a tear in the posterior horn of the medial meniscus. Payr's sign is increased pain with

downward forces of the knee while the patient sits, with the legs crossed ("Indian style"). It is associated with a medial meniscus posterior-horn injury.
- Radiographs of the knee (e.g., AP, lateral, tunnel, and tangential view) should be routed to evaluate for other possible mechanical causes of a locked knee, such as a dislocated patella or a loose calcific body (osteochondritis dessican).
- MR imaging has the gold standard for diagnostic testing of meniscal tears. MR imaging is superior to clinical assessment in the diagnosis of meniscal tear, with the MR having an 80% accuracy for medial meniscal injuries (as determined by lateral arthroscopy). Arthroscopy is valuable for diagnosing unsuspected pathologic condition such as a loose foreign body, chondral fracture, or a torn ACL.
- The definitive treatment of a meniscal injury is not a urgent problem unless the tear is displaced into the intercondylar notch ("locked" knee). The knee should be immobilized, elevated, and the patient sent to an orthopedist in 2–4 days.

8.17 Leg Emergencies

8.17.1 Anatomy of the Leg

- The leg is typically defined as the position of the lower extremity from the knee to the ankle. This portion of the lower extremity can be further subdivided into anterior, lateral, superficial posterior, and deep posterior compartment. The boundaries of these compartments are formed by the tibia, interosseous membrane, and the tibiofibular syndesmosis. The EP should be aware of the content of each of these compartments to better diagnose and treat injuries to the leg.
- The anterior compartment is bounded by the tibia medially, the fibula laterally, the interosseous membrane posteriorly, and the crural fascia anteriorly. Muscles enclosed in the anterior compartment include the tibialis anterior, extensor digitorum longus, extensor hallucis longus, and the peroneus tertius. This group of muscles is primarily responsible for dorsiflexion of the foot, ankle and digit of the foot. The anterior tribal artery and the deep personal nerve traverse this compartment as well but both lie in a relatively well-protected position from direct trauma.
- The lateral compartment is found lateral to the fibula and is bounded by more yielding tissues than the anterior compartment. The peroneus brevis and peroneus longus muscles are contained within this compartment and are responsible for plantar flexion and eversion of the foot. The superficial peroneal nerve is relatively projected, except over the proximal fibula, where it is more susceptible to both direct and indirect trauma.

– The superficial posterior compartment contains no significant arteries, but the sural cutaneous nerve is within its confines. The gastrocnemius, soleus, popliteus, and plantaris muscles are found in the superficial posterior compartment and are responsible for plantar flexion of the ankle and foot. The deep posterior compartment contains several important structure for consideration. Arterial structures of concern include the posterior tribal and peroneal arteries. The posterior tribal nerve is found in proximal to the artery. Muscles in this compartment include the tibialis posterior, flexor digitorum longus, and flexor hallucis longus. These muscles are primarily responsible for plantar flexion of the foot and digits as well as inversion of the foot.

8.17.2 Tibial Diaphyseal Fracture

– The tibia is the major load-bearing structure of the lower leg. Fracture of this bone represents a spectrum of injuries and creates significant disability for the patient. The tibia is just subcutaneous for most of its length; and this relatively exposed location leads to the high frequency of fractures from direct trauma. Complications of these fracture can be significant and include nonunion, neurovascular injury, and compartment syndrome. Tibial fractures can be divided into four basic types based on the degree and type of force applied to create the fracture.
– The first type, stress fracture, occurs by low-energy forces repeatedly applied to the bone over some time. These fractures are typically stable and require little intervention, but they must be recognized to avoid progression to a more unstable and require little intervention, but they must be recognized to avoid progression to a more unstable fracture. The second type, from application of direct force to the tibia, is a common cause of injury and generally produces crushing of the overlying soft-tissue as well as the osseous tissue. Third, torsional injuries of the tibia result in spiral fractures, which are typically produced when the foot is planted and the body rotates around this fixed point. Last, three or four point bending forces result in oblique or transverse fractures. Comminution is common with injury, particularly as the point is spread farther apart.
– From a clinical standpoint, tibial fracture should be suspected with trauma to the lower extremity, pain, and inability to provide unrestricted weight-bearing. The degree and nature of the trauma should be considered, as well as concomitant diseases in the patient likely to have a pathologic fracture. As always the joint above and below the sight of injury should be examined. Particularly in the case of tibial diaphyseal fractures, distal neurovascular status should be documented. These fractures carry a significant risk for compartment syndrome compared with other fractures of long bones. Radiographs are diagnostic, however, in the case of stress fracture, bone scan and MR imaging are occasionally necessary to establish the diagnosis.

- Treatment of tibial diaphyseal fracture is determined by a variety of factors. Any open fracture requires immediate orthopedic referral for surgical acute debridement and reduction of the fragments. The need for immediate or delayed orthopedic referral in closed fractures is determined by the degree of deformity as well as other associated injuries. Isolated nondisplaced tribal fracture can be splinted with outpatient referral. Because of the relative frequency of the development of compartment syndrome, early follow-up is recommended for all tribal fractures.
- Outpatient treatment should include a splint to immobilize the joint above and below the site of the fracture. In addition, the patient should be nonweight-bearing until follow-up. Cold therapy with ice packs during the early stages of the treatment can be quite helpful to slight elevation seems to be most effective in limiting while maintaining blood flow to the distal tissues.

8.17.3 Fibular Fractures

- Fibular fracture may be considered in isolation or with injury of the tribal and connecting structures. Isolated fracture of the fibular is commonly caused by the direct trauma to lateral aspect of the leg. They are easily recognized by symptoms of localized pain and difficult walking, with sign of localized tenderness and swelling.
- Complication arises from isolated fibular fractures are rare. Fibular nonunion may occur and is quite painful. Treatment is dictated by the degree of pain experience by the patient. Short leg casts or braces can be used in the patient having significant pain. In most cases, an ace bandage from the toes to the knee will suffice. All patients with isolated fibular fracture can be allowed to bear weight immediately. The more complicated situation in which the proximal fibula appears to be fractured in isolation is the Maisonneuve fracture, first described by French surgeon Maisonneuve in 1840. He used cadaveric studies to demonstrate that an external rotational force applied to the foot could produce a fracture of the proximal third of the fibula. A common presenting history of this injury is the patient who reports internal rotation of the leg over a planted foot. During the history of the injury is the patient who reports internal rotation of the leg over a planted foot. During the application of this external rotatory force, the foot is momentarily plantar flexed, which creates a greater strain on the medial column of the ankle joint. This increased stain causes failure of the deltoid ligament or the medial malleolus. After failure of the ligaments or osseous tissues of the medial ankle, the force is transmitted up the tibiofibular syndesmosis and interosseous membrane. This syndesmosis is generally ruptured, and the remaining energy is transmitted to the proximal third of the fibula.
- Several cases have been reported in the literature of patients with Maisonneuve fracture who complained only of the ankle pain. For this reason, the

clinician must remain alert to the possibility of a proximal fibular fracture in association with ankle injuries, tenderness to palpation. Of the proximal fibula is a consistent finding of the Maisonneuve fracture. Other physical examination findings include tenderness at the anterior medial ankle joint capsule or at the ankle syndesmosis. The peroneal nerve crosses over the head of the fibula and the fibula is subjected to injury, so that all patient with suspected or established Maisonneuve fracture should have a complete distal neurologic examination. Radiographs of the proximal fibula will establish the diagnosis. Ankle films may show widened medial clean space, isolated posterior tribal fracture, or decreased overlap of the fibula with the anterior tubercle of the tibia. Once the diagnosis is established, orthopedic referral is indicated. Many of these fractures are treated nonsurgically; however, when a significant diastasis or syndesmotic instability occurs, many authors recommend surgical repair. Nonsurgical treatment includes reduction by internal rotation of the food, followed by immobilization for 6–12 weeks.

– Midshaft fibular fractures associated with tribal fractures are fairly easy to manage. Because the fibula is essential a nonweight-bearing structure, little consideration is given to this injury. As long as the tribal fracture receives appropriate care, the fibula is fine.

8.18 Traumatic Fracture of Distal Humerus

8.18.1 General Introduction

Open reduction and internal fixation can be complicated or impossible in elderly patients with marked intraarticular comminution. Joint stiffness, loss of reduction, and early posttraumatic osteoarthrosis are common sequelae. As an alternative to open reduction and internal fixation, patients older than age 65 years with extensive comminution, replacement with a semiconstrained elbow implant is a reasonable consideration. In older patients, because of osteoporosis and comminution, in some, rigid fixation cannot be attained, and nonunited segment and replacement with a prosthetic device have proven to be effective and sometimes the only option under these circumstances.

Posttraumatic osteoarthrosis differs from acute traumatic conditions and nonunion in several aspects and poses more difficulties in the treatment. Elbows with posttraumatic arthrosis are often characterized by a chronic painful stiffness, soft-tissue contracture joint and bone deformity, and instability. The typical circumstances of having undergone numerous previous procedures result in a poor soft-tissue envelope, damaged and hypersensitive nerves, and a predisposition for infection.

Few options exist for operative treatment of severe posttraumatic arthrosis. Arthrodesis reliably relieves pain, and restores a strong extremity. Because it results in great functional impairment, however, arthrodesis of the elbow is rarely considered a viable option. Interposition arthroplasty may be considered

for young patients, particularly who have stiffness. This procedure has an even higher rate of complications than that associated with semiconstrained total elbow replacement. For severe posttraumatic osteoarthrosis, total elbow replacement using the semiconstrained Coonrad–Morrey (Zimmer, Warsaw, IN) prosthesis has proven to be a suitable and reliable option for older patients.

8.18.2 Acute Trauma

The indication for semiconstrained total joint replacement for acute fractures of the distal humerus is limited to a restricted group of patients older than 60–65 years with an extensively comminuted fracture that is not amenable to an adequate and stable osteosynthesis. This usual findings are (1) severe comminution with multiple small fragments, (2) severely osteoporotic bone, and (3) preexisting joint damage in patients with rheumatoid arthritis or inflammatory joint diseases. The fact that at the Mayo Clinic only 22 acute distal humerus fractures (ten of them having associated rheumatoid arthritis) were treated by total joint replacement during a 10-year period emphasizes the strict selection criteria.

8.18.3 Nonunion

If the nonunited fragment is at or distal to the level of the olecranon fossa, replacement is possible without altering extremity length or muscle tension. Patients with nonunited fragments of the distal humerus who are older than 60–65 years old are considered candidates for elbow replacement.

8.18.4 Traumatic Arthrosis

Fracture frequently causes arthrosis requiring treatment by replacement. There is little in the literature about the outcome of the total elbow replacement for posttraumatic problems. Advanced destruction of the glenohumeral joint with marked narrowing or loss of the joint space in patients who are older than age 60 constitutes the basis for semiconstrained elbow joint replacement. Even in this age group, however, participation in heavy physical work and anticipated noncompliance is considered relative contraindications for this procedure. For young patient with sever posttraumatic osteoarthrosis, Interposition arthroplasty may be considered as first choice of treatment rather than total joint replacement. In cases of failed interposition arthroplasty, total joint replacement is a treatment choice for most patients.

8.18.5 Technique

A posterior midline incision is used. The ulnar nerve is transposed in a subcutaneous pocket if that had not been previously performed. For acute fractures

and distal humeral nonunion, preservation of the triceps attachment is possible because in these circumstances the triceps insertion can be left intact. This is because the fracture is treated by excision allowing articulation with humeral component fully seated. Otherwise, the triceps reflection technique of Bryan and Morrey is performed. To preserve the triceps attachment, all soft tissues are released from the bone, a fragment of the distal humerus is then exposed from the lateral margin of the triceps. The ulna is exposed form the medial by rotating the forearm internally. The triceps is partially released to facilitate this maneuver. For condition with an intact distal humerus, the cutting guide is used to prepare the distal humerus and the ulna is prepared with serial rasping. An intramedullary injecting system is used for optimal insertion of the cement to which 1 g of vancomycin is added. An important element is places of a bone graft, harvested from a fracture fragment or the resected trochlea, between the anterior flange and the distal part of the humerus, after in growth, this graft is believed to resist posterior displacement and rotational stresses on the humeral components. The semiconstrained Coonrad–Morrey device is preferred by the author in all instances. Significant bone-stock deficiencies with lack of one or both epicondyles do not change or complicate the implantation of the humeral component because this device requires only the humeral diaphysis to obtain secure fixation. Internal fixation of the condyles is not required. This implant offers three lengths of humeral components: 10, 15, and 20 cm in standard and small sizes. In posttraumatic condition, the 15-cm stem is normally used. If the patient may need a shoulder replacement or if the canal is small, the shorter 10 cm may be used. Variable lengths and diameters of the ulna are also available. At the end of the procedure, if the triceps has been reflected, it is reattached to the olecranon with 2–5.

Nonabsorbable sutures allow immediate use of the joint. Compression dressings and elevation of the extremity are recommended for 1 day, followed by gentle range-of-motion exercises as tolerated. Formal physical therapy is not necessary.

8.18.6 Results

Literature Review

There is little information regarding total replacement for the treatment of elbow trauma. There is one simple report about the treatment of acute fracture with replacement. What little information is available deals with established traumatic arthrosis and shows unfavorable results. Low et al. reported a satisfactory results in only of seven posttrauma patients treated with an unconstrained device. Soni (1984) reported a good and excellent result for three of eight patients who had an unconstrained implant. Kraay et al. (1994) reported the experience with 113 linked semiconstrained implants, of which 18 had been managed for posttraumatic osteoarthrosis, nonunion, or fracture. The results of these patients were disappointing, with a 5-years rate of survival

Table 8.5. Experience with Coonrad/Morry elbow replacement for traumatic conditions

condition	no.	year	objective (satisfaction %)	subjective (satisfaction %)	follow-up
acute	21	1997	90	95	4
arthrosis	41	1997	73	90	6
nonunion	39	1995	88	92	5
total/mean	101		86	92	5

of the implants of 53%. There were five loose humeral components and two infection among 18 patients. Gschwend et al. (1996) reported their experience of 26 patients with posttraumatic osteoarthrosis of the elbow treated with total joint replacement using the semiconstrained Gschwend–Scheier–Bahler (GSB)-III (Zurich, Switzerland) implant. The mean follow-up was 4.3 years (maximum, 14 years). Pain relief was obtained in 82% of cases. The mean arc of flexion was 34–126. The revision rate was 31% because of aseptic loosening in elbows, disassembly in four, and ectopic bone formation in two.

Mayo Experience: Coonrad–Morrey Prosthesis

Experience with 101 semiconstrained replacement used after 1981 for the management of traumatic elbow condition is shown in Table 8.5 in all instances, the Coonrad–Morrey implant was used.

Acute Fractures

The mayo experience of 21 semiconstrained Coonrad–Morrey total elbow replacements in 20 patients was reported by Cobb (1997) and is the only report of the total replacement for acute fracture. The specific indication for the total elbow arthroplasty was an extensively comminuted intraarticular fracture in 11 patients who were older than age 65 and comminuted acute fracture of the distal aspect of the humerus in nine patients (ten elbows), who also had destruction of the article surface secondary to rheumatoid arthritis. The mean age of the patients at the time of injury was 72 year (range 48–92 years). Follow-up averaged 3.3 years. Subjectively, all 20 patients were satisfied on the basis of the Mayo elbow performance sore, 15 elbows had excellent result, and five had a good result. Pain relief was reliably obtained, with 17 patients having no pain and three patients have mild pain, the mean arc of flexion follow-up of 10.5 years, there were no loose implants. Severe osteoporosis was common but did not appear to influence the function result. One patient fell while sailing and fractured the ulnar component. At 8 years after revision, this retired surgeon is without pain and fully functional. Based on this experience, it appears that semiconstrained Coonrad–Morrey total elbow replacement for acute fracture of the distal aspect of the humerus can be a reliable treatment

in specific group of elderly patients, but it is not an alternative procedure to osteosynthesis in younger patients.

Posttraumatic Arthritis

Reviews of the Mayo experiences were presented by Schneeberger (1997) and consist of 41 consecutive patients with posttraumatic osteoarthrosis or dysfunction treated from 1981 to 1993 by semiconstrained Coonrad–Morrey elbow replacement and followed an average of almost 6 years. The average age of the patient was 57 years (range 32–82 years). The indication for joint replacement was pain for 36 patients; reduced painful range-of-motion for two patient, and dysfunction with a flail elbow for three patient. The average time from the original fracture to joint replacement was 16 years (range 36 months–64 years).

This is a difficult group of patients to manage. All but two patients (95%) had previously surgery, the average being 2.3 procedures (range 0–7 procured). Significant bone-stock deficiency with loss of at least one condyle was present in 13 patient, and 14 patient had a significant joint or home deformity. Ten of 41 elbow joint were preoperatively subluxed, and seven were dislocated. Additional complications from prior surgery included mild to moderate ulnar neuropathy in six patient and radial nerve palsy resulting from a complete traumatic laceration in one patient.

At the latest follow-up, objectively, 40% were rated excellent and 43% were considered good for an overall rate of 83% satisfactory objective outcome. Subjectively, 95% of the patients with a functioning implant expressed satisfaction with the operation. Although the incidence of pain relief (76%) was considered to be high, it was not as high as the reported after the treatment of rheumatoid arthritis (93%) at follow-up, the mean arc of flexion extension was 27–131 and the mean arc of pronation–supination was 66–66. An average of 4.8 of 5 activates of daily living could be performed, and strength improvement averaged approximately 30%. The radiologic analysis showed that all grafts behind the flage incorporated. There was no case of aseptic loosening within the 12 years of follow-up.

The follow-up of 41 patients to 12 years is the most comprehensive in the literature and shows that several posttraumatic osteoarthrosis or dysfunction can be reliably and durably treated with a noncustomized semiconstrained device. Patient satisfaction was high. All implants were stable, and function was reliably restored.

Distal Humeral Nonunion

Experience with 39 procedures all employing a triceps attachments preserving exposure, excision of the fragment, and insertion of a noncustom 15-cm Coonrad–Morrey humeral stem was reviewed. Surveillance averaged almost 5 years (range 2–10 years). In this sample, subjective pain relief exceeded 90%, and the mean arc of motion subjectively satisfied with the procedure.

In this report, no patient had mechanical loosening. Infection occurred in two patients and ulnar nerve irritation in one. The bushing became excessively worn in two patients, and one patient had a major wound dehiscence. Considering the nature of the pathology, the frequency of prior surgery, and previous complications, the complication rate of this expensive appears understandable. As greater surveillance is obtained, it is anticipated that the incidence of wear and lysis will increase as well. Considering that few options exist to manage this difficult problem, it appears that all the overall outcome is acceptable with joint replacement.

Complications

The complications from these three report are shown. At least one major postoperative complication occurred in 2 (10%) of 20 patients with an acute fracture and in 13 (27%) of 41 patient in the posttraumatic group. Gschwend et al. (1996) described a complication rate off 43% from a meta-analysis of 22 publication of total elbow replacement, and of these were performed for rheumatoid arthritis which cases usually are associated with fewer complications compared with cases with most complication are of a mechanical nature. In several instances, the C locking ring has become disengaged, but no pin in the author's practice has backed out because of this. Fracture of the ulnar component occurred in one prosthesis in the acute fracture group and in five elbows in the posttraumatic group 2–9 years (average 4.3 years) postoperatively. Before breakage, four patients had an excellent result and two a good result both an asymptomatic elbow and essentially normal function. The causes of failure were severe noncompliance.

9

Trauma Management, Safety, and Health

9.1 General Introduction

This chapter covers the subject of trauma and safe systems of work from the Engineering Science point of view. Subjects such as components and requirements for a safe system of work been highlighted. The HSE approach to risk assessment has been described. Risks are quantified. Supervision and control form the basic theme. Post accident strategies have been devised, for a layman or woman; the principles of accident preventions related to trauma have been adequately explained. Health and safety issues have been fully discussed followed by systematic training and processes. Major and fatal traumatised accidents have been identified.

9.2 Trauma and Safe Systems of Work

A safe system of work is defined as "the integration of personnel, articles and substances in a suitable environment and workplace to produce and maintain as acceptable standard of safety. Due consideration must also be given to foreseeable emergencies and the provisions of adequate rescue facilities." HSWA requires the provision and maintenance of plant and systems of work that are, as far as is reasonably practicable, safe and without risks to health.

9.2.1 Components of Safe System of Work

People

People are human assets of the enterprise. A safe system of work should incorporate safe behavior, sound knowledge, skills, both mental and physical, willingness to conform to the system, motivation, resistance to pressure to behave unsafely and job experience.

Machinery, Plant, and Equipment

Sound design and safety specification of plant, machinery, and equipment, including consideration or ergonomic factors, together with efficient and planned maintenance, are important features of a safe system of work.

Materials

Materials must be safe during processing and as finished products, meet quality assurance standards, and be safe for disposal as waste products and by-products of manufacture.

Environment

The fourth aspect includes control of temperature, lighting and ventilation, dust, fumes, vapors, radiation, chemical and biological hazards and provision of safe access and egress, sound levels of welfare amenity provision and safe levels of noise and vibration.

Place of Work

This may be a factory workshop, construction site or office. The place of work should be safe in terms of its construction, means of fire protection, including means of escape in the event of fire, and layout.

Requirements for a Safe System of Work

The principal requirement is planning the safest way to combine people and plant so that the work can be undertaken in a specific area. This includes:

(a) A layout which allows for safe access to and egress from the working area and plant within, and adequate space between machines and operating plant
(b) A correct sequence of operations with materials and products conveyed mechanically, wherever appropriate, to and from work positions
(c) Analysis of tasks, including job safety analysis and the provision of clear job instructions
(d) Identification of safe procedures, both routine and emergency, including requirement
(e) Provision of safe and healthy working environment, in particular:
    (1) Illumination levels which prevent glare and sharp contrasts between light and shadow.
    (2) Heating and ventilation systems which avoid extremes of temperature and humidity and which allow circulation of fresh air to all parts of working area. The level of risk assessment should be broadly proportionate to the type of risk.

Prevention/Control Risks

The third stage of the risk assessment process is defined as the preventive or control measure to be installed, e.g., prohibition of a particular practice, replacement of a hazardous substance with a safer alternative, machinery guarding, implementation of a safe system of work, enclosing the hazard, provision of information, instruction and training etc.

Managing the Risks

It must be appreciated that risk assessment is not a precise science. What may be a "risky" operation of one person may a "matter of common sense" to another. It is necessary, therefore, to quantify the risks in a way which is understandable and credible to all concerned.

Once the risks have been assessed and the controls installed, then they must be maintained by a number of techniques, including safety monitoring activities, planned maintenance procedures, operation of cleaning schedules, environmental monitoring, testing and examination of certain items of plant and equipment and occupational health surveys.

The HSE Approach to Risk Assessment

In their publication Five Steps to Risk Assessment the HSE recommend the following procedure for undertaking a risk assessment as shown in Table 9.1.

Quantifying the Risks

A quantitative approach to the assessment of risk is commonly used through the use of "risk ratings," taking into account the factors of probability, severity and frequency, each of which can be measured on a scale from 1 to 10. A risk rating is calculated thus:

$$\text{Risk Rating} = \text{Probability (P)} \times \text{Severity (S)} \times \text{Frequency (F)} \qquad (7.1)$$

which gives a range of risk rating between 1 and 1,000. Standard Probability, Severity and Frequency Tables are used.

The urgency or priority of action in respect of a particular risk can be evaluated as shown in Table 9.2. The probability index is shown for risk assessment in Table 9.3.

Inadequate Supervision and Control

The duty of all levels of management to supervise and control safety at work is well established in law. Many accidents are a result of failure of management to do this.

Table 9.1. HSE risk assessment procedure

Assessment of risk for:
Company name
_____
Company address
_____
_____
__
_____ Post code
_____
Assessment undertaken (date)
_____
Signed
_____
Assessment review date
_____

Hazard
Look only for hazards which you could reasonably expect to result in significant harm under the conditions in your workplace. Use the following examples as a guide:

Slipping/tripping hazards	Fire
Electricity	Chemicals
Dust and/or fume	Moving parts of machinery
Work at heights	Manual handling
Ejection of material from machine	Noise
Pressure systems	Poor lighting
Vehicles	Low temperature

List hazards here:
_____
__
_____
__
_____
__
_____
__
_____
__
_____
__

Table 9.2. Priority of action in respect of risk

below 200	no immediate action necessary, but keep under review
200–400	action within next year
400–600	action within next three months
600–800	action within next month
800–1,000	immediate action/possible prohibition of use

Table 9.3. Probability index

probability index	descriptive phase
10	inevitable
9	almost certain
8	very likely
7	probable
6	more than even chance
5	even chance
4	less than even chance
3	improbable
2	very improbable
1	almost impossible

Inadequate Training

Management has duty to train staff in general and specific areas of heal and safety at work. As with supervision and control, the level of training received by workers varies greatly. A clearly defined health and safety training policy should be included in every Statement of Health and Safety Policy, and the training needs of individual groups of workers identified. Poorly trained workers, or workers who have received no health and safety training, are a danger to themselves and others, particularly in high-risk situation. There is a need to establish the principle that a safe worker is an efficient one.

Deficiencies in Personal Protective Systems

Every year many accidents are associated with deficiencies in personal protection. There may be a failure by management to provide protection; alternatively, workers may refuse to wear or use the protection because it is uncomfortable, hinders their working routine or in the case of eye protection, reduces their vision owing to misting. There is a need, therefore, to assess individual requirements by consulting the workers. This approach is established in case law, much of which has concerned the suitability of eye protection. In certain cases, the wrong type of personal protection may be a lot of problem.

Personal Protective Equipment

Personal protective equipment is considered as important personal protective clothing should be selected carefully for reasons of hygiene and workers should be made aware of limitation of such equipment.

Careful Conduct for the Safety of the Individual and Others

Dangerous behaviors and “horseplay” at work have always existed to some extent. Examples of dangerous behavior are the willful removal of machine

guards; fighting; smoking undesignated "no smoking" areas; the dangerous driving of vehicles; abuse of equipment, gases and flammable substances; failure to wear personal protective clothing and equipment, such as eye protection or safety helmets, where the need arises; and the playing of practical jokes which expose workers to risk of injury. HSWA places a duty on every "employee" while at work to take reasonable care for the health and safety of himself and of other persons who may be affected by his acts or omissions at work.

Caution Toward Danger

All workers and management should appreciate the risks in the workplace, and these risks should be clearly identified in the Statement of Health and Safety Policy, together with the precautions to be taken by workers to protect themselves from such risks.

Postaccident Strategies

Accidents are usually unforeseeable (see above). This may be attributable to insufficient research into hazards: the philosophy of "it can't happen to me," which is particularly prominent among skilled workers; human error, failure on the part of management or manufacturers of articles and substances to provide information; or simple mechanical failures in plant and machinery. Thus, while there must be an emphasis on accident prevention through the use of pre-accident strategies, provision must be made, by means of post-accident strategies, to deal with the aftermath of accidents and to learn from mistakes. Postaccident strategies can be classified in the following way.

Disaster/Emergency Planning

It is important, particularly in any large industrial or commercial enterprise, that a disaster or emergency plan be developed. Depending upon the inherent risks, the plan should be tailored to take account of the procedure in the event of a large fire, an explosion, a sudden release of toxic liquids, gases or fumes, building collapse or a major vehicular traffic accident on the premises.

Ameliorative Strategies

These strategies are concerned mainly with minimising the effects of injuries as quickly and effectively as possible following an accident. They will include the provision and maintenance of first aid services, procedure for the rapid hospitalisation of injured persons and possibly, a scheme for rehabilitation following major injury.

Feedback Strategies

There is much to be learned following an accident. Investigation must be directed at identifying the causes of the accident and not just the effects. By the study of past accidents, feedback strategies attempt to prevent their recurrence. The correct use and interpretation of statistical information is vital here.

The Causes of Accidents

No chapter dealing with strategies in accident prevention would be complete without an examination of the causes of accidents. In major injury or multiple accidents, there may be up to twenty factors which contribute to the accident. In disaster such as the Flixborough incident the contributory causes are even greater in number. Whatever the accident situation, almost inevitable there will be some form of human involvement, however. People are unpredictable, they make mistakes, their attitude to safety varies and they forget things. While the "human factor" features strongly in the majority of accidents, it is only part of the process, and many other factors are relevant. A resume of the principal causes of accidents is given later.

Design and/or Layout of the Working Area

Bad design and layout of working areas, in many cases producing congestion and overcrowding, is one principal contributory causes of accidents. Ideally, work process should follow a sequential flow of the raw materials coming in at one end of the building and the finished products going out at the other end. However, most manufacturing tend up in the air, as with construction workers, or several miles below the Earth's surface in the case of miners. Consideration must be given, therefore, to matters such as factory approach roads, yards, work at high level, the use of portable and fixed access equipment – e.g. ladder and lifts – and the shoring of underground workings. The legal requirement relating to access to workplaces are outlined in specific Regulation, e.g. the Construction (Health, Safety, and Welfare Regulations 1996).

Adequate Supervision

In all organisation, there must be adequate safety supervision directed by senior management through supervisory management to the shop floor. The responsibilities of directors, senior managers, departmental manager, supervisors, specialists – such as health and safety practitioners – and shop floor workers must be clearly identified in writing in the Statement of Health and Safety Policy. Moreover, since many workers have a written form of

job description, this should incorporate their various duties and responsibilities related to health and safety. Failure to observe these contractual duties can lead to disciplinary action including, in cases of flagrant abuse, summary dismissal. Supervisory management has a key role in ensuring the maintenance of a safe place of work. They are the "linkmen" between management and shop floor and, therefore have the most immediate contact with the workforce. The duties of supervisors should be clearly identified and they should receive sufficient training and management support to discharge these duties effectively (failure to have properly trained supervisors can have serous legal consequences). First, there will be a criminal liability on the part of the employer for breach of HSWA, S2(2)(c) and, second, there may be a civil liability if injury is suffered by an employee as a result of lack of or inadequacy of supervision (bus vs. Slough Metals Ltd (1974) 1 AER 262).

Competent and Trained Personnel

The duty to train all staff levels in safe systems of work is laid down in HSWA, S2(2)(c). Every employee will need some form of health and safety training. This should be satisfied through induction training, on-the-job training, and training in specialised aspects, such as the operation of permit to work systems or driver training. Moreover, persons who are designated; competent persons; in order to comply with specific requirements – e.g. Electricity at Work Regulations 1989 – will also require specific training, as will the various categories of first aides under the Health and Safety (First Aid Regulations 1981). A well trained labor force is a safe labor force and in organisations which undertake safety training accident cost tend to be lower.

"Safe Person" Strategies

These strategies are concerned with protecting the individual in specific situation where a Safe Place strategy may not be wholly appropriate or possible to implement. They depend upon the individual conforming to certain prescribed standards, e.g., wearing personal protective equipment. Safer person strategy may be classified as follows:

(1) Safe premises
(2) Safe process
(3) Safe system of work
(4) Safe access to work

9.3 Principle of Accident Prevention Related to Trauma

9.3.1 What is an Accident

A number of definitions have been put forward over the last 30 years and they are quoted as:

(a) "An unforeseeable event, often resulting in injury."
(b) "An unplanned and uncontrolled event which has led to or could have caused injury to persons, damage to plant or other loss." (RoSPA)
(c) "An unexpected, unplanned event in a sequence of events that occurs through a combination of causes. It results in physical harm (injury or disease) to an individual, damage to property, business interruption or any combination of these" (Department of Occupational and Environmental Health, University of Aston in Birmingham).
(d) "An accident is an undesired event that results in physical harm to a person or damage to property. It is usually the result of a contact with a source of energy (i.e. kinetic, electrical, chemical, thermal, ionizing radiation, nonionizing radiation, etc.) above the threshold limit of the body or structure" (Frank Bird, Executive Director, American Institute of Loss Control).
(e) "A management error; the result of errors or omissions on the part of management."

A number of significant factors emerge from these definitions. Generally accidents are:

(a) Unforeseeable, as far as the accident victim is concerned
(b) Unplanned
(c) Unintended
(d) Unexpected

9.3.2 Health and Safety: A Multiple Approach Related to Trauma

The reasons for preventing accidents are threefold – legislative, humanitarian and economic.

1. The legislative approach is based on the enforcement of statutory provision contained in Acts, Regulation, order, and approved codes of practice.
2. The humanitarian or social approach is based on the premise that no one likes to think that his error or omission has been the principal cause of an accident. No two people respond identically in their assessment or quantification of hazards. An approach based on subjective criteria of a situation is, therefore, of very little value.

Systematic Training

The term "systematic" immediately distinguishes such training from the traditional apprenticeship consisting of "sitting by Nellie," i.e. learning through listening and observation. Systematic training makes full use of skills available in training staff. It attracts recruits, achieves the target of an experienced operator's skill in one half to one third of the traditional time, and creates confidence in the minds of trainees. It guarantees better safety performance and morale, and results in greater earnings and productivity, ease of mind, a sense of security and contentment at work. Furthermore, it excludes misfits and diminishes unrest, while facilitating the understanding and acceptance of change. Systematic training implies the following:

(a) The presence of a trained and competent instructor working with suitable trainees
(b) Defined training objectives
(c) A content of knowledge broken down in to sequential units which can be readily assimilated
(d) A content of skills analyzed by elements
(e) A clear and orderly training programme
(f) An appropriate place in which to learn
(g) Suitable equipment and visual aids
(h) Sufficient time to attain a desired standard of knowledge and competence, with frequent testing to ensure trainees understand and know what has to be learned

A well-designed training programme can be truly educational. First, it is possible to place the specific job knowledge or skill in a wider context, relating it to affiliated topics, to what is already known by the trainee, and to possible future trends and developments. Second, any programme of technical instruction must be supplemented by other courses which enable an operator to relate to his entire sociopolitical environment, and answer his questions about the structure and meaning of society, the destiny of Man, the meaning of law and the lessons of history.

The Training Process

Any process of systematic training must take place in a number of clearly defined stages. These stages are outlined:

(1) *Identification of training needs.* A training need exists when the optimum solution to an organization's problem is through some form of training. For instance, a training need may exist where there is damage to stored goods and buildings through fork lift truck activity, or where a particular procedure, such a permit to work system, is about to be introduced. For training to be effective, it must be integrated with the selection, placement and promotion policies of the organization. Selection, however,

must ensure that the trainees are capable of learning which is to be taught. Promotion must ensure that the promoted person is fully aware of his responsibilities in terms of health and safety at work.

Training needs should be identified with regard to the retraining, or the reinforcement of training, of existing personnel, and the induction training of new recruits. The identification should show what kind of training is needed, e.g., safety procedure, duties and responsibilities, general safety training for supervisors.

(2) Fatal and major traumatized injury accidents. Given the possibility of the occurrence of a fatal or major injury accident, it is important that organizations have a clearly established procedure, including the allocation of responsibility for specific tasks, following the accident. Generally, this procedure can be subdivided into two aspects, the notification sequence and the postaccident procedures.

(3) Notification sequence. On receipt of a report of a fatal accident or one causing major injury, a senior manager should immediately contact by telephone the ambulance service, the factory doctor where appropriate and, in the case of a fatal accident, the police. In the case of a fatal accident, the manager, in consultation with the police, should arrange to visit the next of kin to advise that person of the accident.

Following this, the senior manager or safety specialist should inform, by telephone, to the following people:

(a) The divisional manager, where appropriate.
(b) HSE or local authority environmental health officer, as appropriate.
(c) the head of the central health and safety department, where appropriate.
(d) The personnel manager for the organisations.
(e) The insurance company.

9.4 Major Incidents and Emergency Procedures Causing Trauma and Traumatic Injuries

Such incidents may be precipitated by a malfunction of the normal operating procedures, by the intervention of some outside agency, such as a crashed aircraft, a severe electrical storm, flooding, a rail disaster, of arson or sabotage or as a result of terrorist activities. Bomb threats and product interference or contamination threats should be classed as major incident situations. Traumatic effects can occur due to seismic incidents and fire hazards and other scenarios.

A major incident could result from a scheduled dangerous occurrence, such as a pressure vessel explosion or collapse of a crane. Alternatively, it could be food poisoning outbreak associated with a food manufacturer's products or a number of cases of food poisoning among staff due to unsound hygiene practices in catering operations. Discovery of asbestos in existing premises could be classed as a major incident.

APPENDICES

APPENDICES I-IV RELATED TO TRAUMA ENGINEERING ANALYSES AND COMPUTATIONS

I

Three-Dimensional Cracking Phenomenon and Crack Calculations

I.1 General Steps of Crack Flow and Crack Calculations

(1) The load increment $\{\Delta P_n\}$ applied where n is the load increment.
(2) The total is accumulated as $\{P_n\} = \{P_{n-1}\} + \{\Delta P_n\}$, and $\{\mathrm{R}\} = \{\Delta P_n\}$, where $\{R\}$ is the residual load vector.
(3) Incremental displacement are now computed as $\{\Delta U_i\} = [K]_{\mathrm{e}}^{-1}\{R\}$, where i is the iteration.

I.1.1 Flow Chart on Cracking Phenomenon

Crack Indicators NCK (1), NCK (2), NCK (3)
NCK (1) – crack normal to the principal stress '1'
NCK (2) – crack normal to the principal stress '2'
NCK (3) – crack normal to the principal stress '3'
NCK (1) = 0
NCK (2) = 0 }no cracks
NCK (3) = 0
NCK (1) = 1
NCK (2) = 1 }no cracks open
NCK (3) = 1
NCK (1) = 2
NCK (2) = 2 }no cracked closed
NCK (3) = 2
$\underline{\sigma}$, $\underline{\varepsilon}$ − stress strain state at integrated point
ε_i − principal strains
σ_i − principal stresses
i = 1,2,3
σ_t − limiting tensile strength of concrete
T_ε, T_σ − transformation matrix

Plate AI.1.

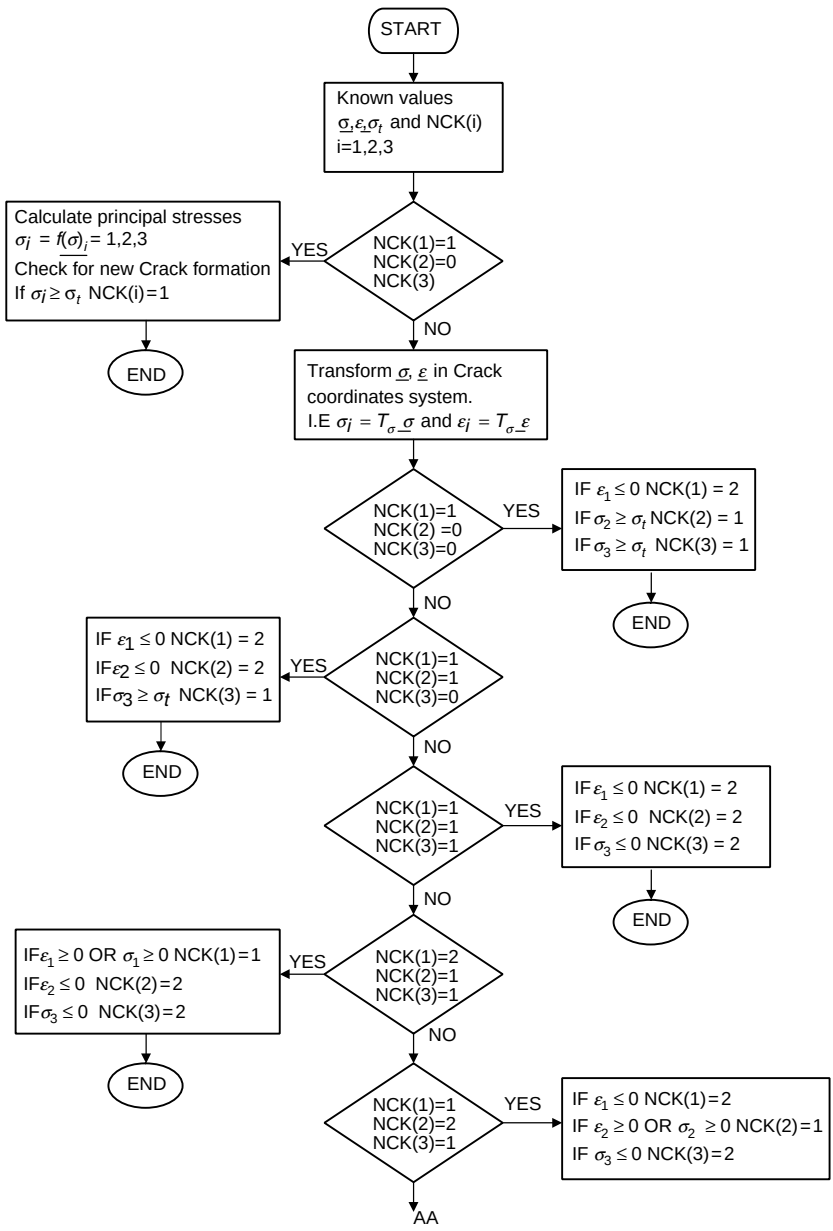
START
Known values
σ,ε,σt and NCK(i)
i=1,2,3
NCK(1)=1
NCK(2)=0
NCK(3)
YES
Calculate principal stresses
σi = f(σ)i = 1,2,3
Check for new Crack formation
If σi ≥ σt NCK(i)=1
END
NO
Transform σ, ε in Crack
coordinates system.
I.E σi = Tσ σ and εi = Tσ ε
NCK(1)=1
NCK(2) =0
NCK(3)=0
YES
IF ε1 ≤ 0 NCK(1) = 2
IF σ2 ≥ σt NCK(2) = 1
IF σ3 ≥ σt NCK(3) = 1
END
NO
NCK(1)=1
NCK(2)=1
NCK(3)=0
YES
IF ε1 ≤ 0 NCK(1) = 2
IF ε2 ≤ 0 NCK(2) = 2
IF σ3 ≥ σt NCK(3) = 1
END
NO
NCK(1)=1
NCK(2)=1
NCK(3)=1
YES
IF ε1 ≤ 0 NCK(1) = 2
IF ε2 ≤ 0 NCK(2) = 2
IF σ3 ≤ 0 NCK(3) = 2
END
NO
NCK(1)=2
NCK(2)=1
NCK(3)=1
YES
IF ε1 ≥ 0 OR σ1 ≥ 0 NCK(1)=1
IF ε2 ≤ 0 NCK(2)=2
IF σ3 ≤ 0 NCK(3)=2
END
NO
NCK(1)=1
NCK(2)=2
NCK(3)=1
YES
IF ε1 ≤ 0 NCK(1)=2
IF ε2 ≥ 0 OR σ2 ≥ 0 NCK(2)=1
IF σ3 ≤ 0 NCK(3)=2
AA

Plate AI.1. (contd)

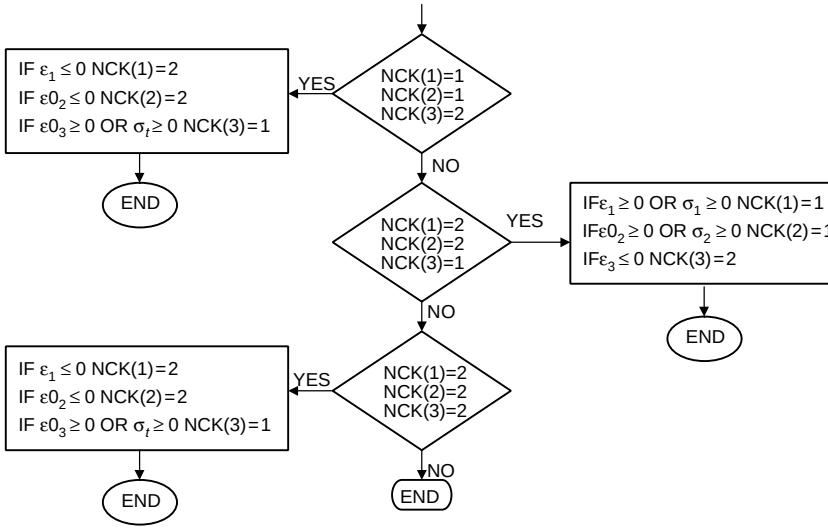

σ_3 σ_2 σ_3 σ_2

σ_1 σ_1

σ_3 σ_2

σ_1

CRACK IN PRINCIPAL THREE AND ONE

$$
\begin{aligned}
D_{11} &= D_{33} = D_{12} = D_{21} = 0 \\
D_{13} &= D_{31} = D_{23} = D_{31} = 0 \\
D_{22} &= D_{22} - D_{12}\frac{D_{12}}{D_{11}} - D_{23}\frac{D_{23}}{D_{33}} \\
D_{44} &= \beta' D_{44} \\
D_{55} &= \beta' D_{55} \\
D_{66} &= \beta' D_{66}
\end{aligned}
$$

CRACKS IN ALL THREE PRINCIPAL DIRECTION

$[\mathrm{D}] = [0]$

(4) Total displacements are now accumulated in the following form: $\{U_i\} = \{U_{i-1}\} + \{\Delta U_i\}$.

(5) Strain increments are calculated from step 4 as $\{\Delta \in_{\mathrm{i}}\} = [B]\{\Delta U_i\}$. The accumulated strains at this stage would then be written as

$$\{\in_{\mathrm{i}}\} = \{\in_{\mathrm{i}-1}\} + \{\Delta \in_{\mathrm{i}}\}$$

(6) The stress increments are calculated using the current nonlinear constitutive matrices of various models described earlier: $\{\Delta\sigma_i\} = \{f(\sigma)\}\{\Delta \in\}$. The accumulated stresses are computed as $\{\sigma_i\} = \{\sigma_{i-1}\} + \{\Delta\sigma_i\}$. In order to differentiate stresses at elastic and plastic conditions, a stress point indicator I_{p} is introduced.
$I_{\mathrm{p}} = 0$ (elastic point)
$= 1$ (plastic point)
$= 2$ (unloading from plastic state)

(7) The stress increment is calculated using the elastic material matrix as $\{\Delta\sigma'_i\} = [D']\{\Delta \in\}$. Total stresses are given as $\{\sigma'_i\}_{\mathrm{T}} = \{\sigma_{i-1}\} - \{\Delta\sigma'_i\}$.

(8) The stress $\{\sigma_i\}$ is now calculated using step 7: $\{f(\sigma'_i)\}$, $\{\sigma_{i-1}\} = \{f(\sigma_{i-1})\}$ – any yield criterion required.

(9) If a plastic point is obtained, step 11 should be considered.

(10) If $\sigma_i \geq \sigma_y$ – plastic point ($I_{\mathrm{p}} = 1$), transition from elastic to plastic, calculate factor F_{TP} using Figs. I.1 and I.2.

$$F_{\mathrm{TP}} = \left[\frac{\sigma_y - \sigma_{i-1}}{\sigma_i - \sigma_{i-1}}\right]$$

The stress at the yield surface $\{\sigma_i\}^*_{\mathrm{y}} = \{\sigma_{\mathrm{i}-1}\} + F^*_{\mathrm{TP}}\{\Delta\sigma_i\}$. Elasto-plastic stress increments are calculated as $\{\Delta\sigma_i\} = [D]_{\mathrm{ep}}\{\sigma_i\}^*(1 - F_{\mathrm{TP}})\{\Delta \in\}$. Total stress $\{\sigma_i\}_{\mathrm{T}} = \{\sigma_i\} + \{\Delta\sigma_i\}$.

(11) Plastic point from steps 9 and 10, check for unloading, i.e., if $\sigma \geq \sigma_y$ it is necessary to proceed to step 12. For the unloading case at this point,

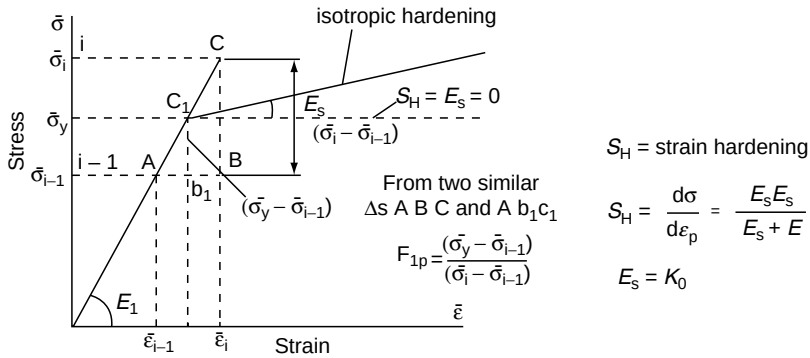

Fig. I.1. Equivalent stress–strain curve for steel (E_{s} = initial yield modulus; $\acute{E}_{\mathrm{s}}$ = postyield modulus)

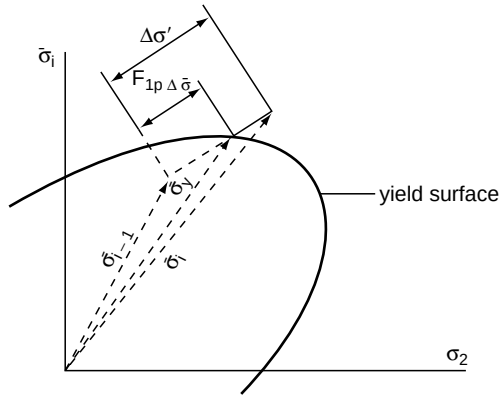

Fig. I.2. Failure surface

set $I_{\mathrm{p}} = 2$, total stress $\{\sigma_i\}_{\mathrm{T}}$ then given by $\{\sigma_i\} = \{\sigma_{i-1}\} + \{\Delta\sigma_i\}$. Set $\{\sigma_y\} = \{\sigma_{i-1}\}$, and the procedure is repeated for the additional increments.

(12) Loading at this point $\{\Delta\sigma_i\} = [D]_{\mathrm{ep}}\{\sigma_{i-1}\}\{\Delta e\}$. Total stress $\{\sigma_i\}_{\mathrm{T}} = \{\sigma_{i-1}\} + \{\Delta\in\}$.

(13) Sometimes it is necessary to correct stresses from the equivalent stress–strain curve: $\sigma_{\mathrm{corr}} = \sigma_{\mathrm{i-1}} + S_{\mathrm{H}}\Delta\in_{\mathrm{p}}$, where $\Delta\in_{\mathrm{p}} = \sqrt{2/3}\Delta\in^{\mathrm{p}}{}_{\mathrm{ij}}\Delta^{\mathrm{p}}{}_{\mathrm{ij}} =$ equivalent plastic strain increment. S_{H} is the strain hardening parameter, such that $\Delta\in_{\mathrm{p}} = \lambda$.

Equivalent stress, calculated from the current stress state, is given by $\{\sigma_i\} = F_{\mathrm{TP}}\{(\sigma_i)\}$. The correct stress state, which is on the yield surface, will therefore be given as $\{\sigma_i\} = F_{\mathrm{TP}}\{\sigma_{\mathrm{i}}\}$. The total stresses are converted into equivalent nodal loads from $\int_{\mathrm{v}}[B]^{\mathrm{T}}\{\sigma_i\}\mathrm{d}$ vol, and the residual load vector is calculated from $\{\mathrm{R}\} = \{\mathrm{F_n}\} - \int_{\mathrm{v}}[B]^{\mathrm{T}}\{\sigma_i\}\mathrm{d}$ vol.

(14) Check for convergence.

$$(||R||/||F||) \leq \mathbf{TOL} \qquad (||\Delta U||/||U||) \leq \mathbf{TOL}$$

where **TOL** is chosen from 0.01 to 0.001; $||R|| = \sqrt{R_i^{\mathrm{T}''}R_i}$ is the Euclidean norm of the residuals; $||F||\sqrt{P^{\mathrm{T}}P}$ is the Euclidean norm of the externally applied load; and $||\Delta U|| = \sqrt{\Delta U_i^{\mathrm{T}''}U_i}$ is the Euclidean norm.

If convergence is not achieved, step 3 is invoked and all steps repeated for the next iteration. If convergence is achieved, then proceed with the next load increment.

II

Finite Element Program ISOPAR-Major Subroutines

(Note: This program has a new version **BANG-FII**)

STATEMENT

Program ISOPAR Mentioned in the Text has been Modified Specifically for Biomedical Engineering.

SAL.l Subroutines for Finite Element Formulation

```
      MASTER MAR1
      DIMENSION A2 (20,12,12), S(20,12,12), X(12), XP (5),
      YP (5)                                                    2
      DIMENSION A (60,60), Y(100), P(150),C (12,12), Z(12,12),
      A1(13,13)
      DIMENSION D (20,3,3), N1 (20), N2 (20), N3 (20)           3
      DIMENSION Y1 (100)                                        3.1
      REAL LOAD
      WRITE (2,911)
911   FORMAT (1H1,55X, 10HINPUT DATA/56X, 10 (1H=) ////////)
      READ (5,100) NN, NDOF, NEL, NTSC                          4
100   FORMAT (410)                                              5
      WRITE (2,912) NN, NDOF, NEL, NTSC
912   FORMAT ( 42X, 24HTOTAL NUMBER OF NODES = , I3/
     1              45X, 21HDEGREES OF FREEDOM = , I3/
     2              39X, 27HTOTAL NUMBER OF ELEMENTS = , I3/
     3              41X, 25HNUMBER OF STRESS CARDS = ,
      I3////////)
      WRITE (2,900)                                             6

C
C       PART 1 (REPEATED FOR EACH ELEMENT)
C       ********
C
C       READ DATA FOR ELEMENT
C

900   FORMAT (13X, 97 (1H-) / 13X, 1H |, 15X 1H |, 31X, 1H | ,
      3 (15X,1H | ) /
     1   13X, 49H | ELEMENT        |        CO-ORDINATES OF |,
```

```
     2    48H THICKNESS|    POISSIONS    |        YOUNGS      | /
     3   13X,1H |, 15X, 1H | , 31X, 1H |, 3 (15X, 1H | ) /
     4    13X, 49H |       NUMBER    |       NODE A       | ,
     5    48H       |       RATIO       |       MODULUS      | /
     6   13X, 1H | , 15X, 1H | , 31X, 1H | , 3(15X,1H | ) / 13X, 1H | ,
          6 (15X, 1H | ) /
     7   13X, 1H | , 15X, 1H | , 31H X | Y,1H | , 3 (15X,
     8    1H | ) / 13X, 1H |) / 13X, 97 (IH-) / 13X, 1H | , 6 (15X, 1H | ))
112  READ (5,101) I, XA, YA, T, PR, E                                  10
101  FORMAT (I0,5F0.0)                                                 11
     WRITE (6,901) I, XA, YA, T, PR, E                                 12
901  FORMAT (13X, 1H | ,I8, 7X, 1H | , 5 (F12.4, 3X, 1H | ) / 13X, IH | ,
     6(15X,1H | ))
       X(1) = XA                                                       14
       X(94) = -XA                                                     15
       X(7) = -XA                                                      16
       X(10) = XA                                                      17
       Y(1) = YA                                                       18
       Y(4) = YA                                                       19
       Y(7) = -YA                                                      20
       Y(10) = -YA                                                     21
       DO 102 J=1, 12                                                  22
       DO102 K=1, 12                                                   23
       C (J,K) = 0.0                                                   24
       A1 (J,K) = 0.0                                                  25
102    A2 (I,J,K,) = 0.0                                               26
C
C                                FORM C MATRIX
C
       DO 103 J=1, 10,3                                                27
       C(J,1) = 1.0                                                    28
       C(J,2) = X(J)                                                   29
       C(J,3) = Y(J)                                                   30
       C(J,4) = X(J)**2                                                31
       C(J,5) = X(J)*Y(J)                                              32
       C(J,6) = X(J)**2                                                33
       C(J,7) = X(J)**3                                                34
       C(J,8) = Y(J)*X(J)**2                                           35
       C(J,9) = X(J)*Y(J)**2                                           36
       C(J,10) = Y(J)**3                                               37
       C(J,11) = Y(J)*X(J)**3                                          38
       C(J,12) = X(J)*Y(J)**3                                          39
       C(J+1,3) = 1.0                                                  40
       C(J+1,5) = X(J)                                                 41
       C(J+1,6) = 2.*Y(J)                                              42
```

```
      C(J+1,8) = X(J)*.*2                                          43
      C(J+1,9) = 2.*X(J)*Y(J)                                      44
      C(J+1,10) = 3.*Y(J)**2                                       45
      C(J+1,11) = X(J)**3                                          46
      C(J+1,12) = 3.*X(J)*Y(J)**2                                  47
      C(J+2,2) = -1.0                                              48
      C(J+2,4) = -2.*X(J)                                          49
      C(J+2,5) = -Y(J)                                             50
      C(J+2,7) = -3.*X(J) **2                                      51
      C(J+2,8) = -2.*X(J) *Y(J)                                    52
      C(J+2,9) = -Y(J) **2                                         53
      C(J+2,11) = -3.*Y(J)*X(J)**2                                 54
103   C(J+2, 12) = -Y(J) **3                                       55
      DO 104 J=1, 12                                               56
      DO 104 K=1, 12                                               57
      A (J,K) = 0.0                                                58
104   Z (J,K,) = C(K,J)                                            59
      DO 105 N=1, 12                                               60
      DO 105 J=1, 12                                               61
      DO 105 K=1, 12                                               62
105   A1 (J,N) = A1 (J,N) + C(J,K) * Z(K, N)                       63
C
C          CALL SUBROUTINE MATRIX TO INVERT (C) MATRIX
C
      CALL MATRIX (A1, Y, 12, 12, 2, 6)
      DO 106 N=1, 12                                               65
      DO 106 J=1, 12                                               67.1
      C(N, J) = 0.0                                                66
      DO 106 K=1, 12                                               67
106   A2 (I, J, N) = A2 (I, J, N) + Z(J, K) * A1(K, N)             68
      HX = -XA                                                     69
      HY = -YA                                                     70

C               FORM (K) MATRIX FOR ELEMENT
C
C
      AREA = 4. *HX*HY                                             71
      Q = (1.0 – PR) /2.0                                          72
      C(4, 4) = 4.0                                                73
      C(4, 6) = 4.*PR                                              74
      C(5, 5) = 4.*Q                                               75
      C(5, 11) = 4.*Q*HX**2                                        76
      C(5, 12) = 4.*Q*HY**2                                        77
      C(6, 6) = 4.0                                                78
```

```
      C(7, 7) = 12.*HX**2                                                79
      C(7, 9) = 4.*PR*HX**2                                              80
      C(8, 8) = 4.*(HY**2 + 4.*Q*HX**2) /3.0                             81
      C(8, 10) = 4.*PR*HY**2                                             82
      C(9, 9) = 4.*(HX**2 + 4.*Q*HY**2) /3.0                             83
      C(10, 10) = 12.*HY**2                                              84
      C(11, 11) = AREA**2/4.0 + 36.*Q*HX**4) /5.0                        85
      C(11, 12) = (PR+Q) *AREA**2 /4.0                                   86
      C(12, 12) = AREA**2/4.0 + 36.*Q*HY**4) /5.0                        87
      DO 107 J=1, 11                                                     88
      NX = J+1                                                           89
      DO 107 K = NX, 12                                                  90
107   C(K, J) = C (J, K)                                                 91
      DO 108 J=1, 12                                                     92
      DO 108 N=1, 12                                                     93
      A1 (N, J) = 0.0                                                    94
      DO 108 K=1, 12                                                     95
108   A(J, N) = A(J, N) + C (J, K)*A2(I, K, N)                           96
      DO 109 N=1, 12                                                     97
      DO 109 J=1, 12                                                     98
      DO 109 K=1, 12                                                     99
109   A1(J, N) = A1 (J, N) + A2(I, K, J)* A(K, N)                        100
      D1 = E*T**3/ (12.*(1.0 – PR**2))                                   101
      AR = AREA*D1                                                       102
      DO 110 J=1, 12                                                     103
C
C             FORM (K) MATRIX FOR ELEMENT
C
  110 S(I, J, K)=AL(J, K) *AR                                            105
      DO 111 J=1,3                                                       106
      DO111 K=1,3                                                        107
C
C             FORM (D) MATRIX FOR ELEMENT
C
  111 D(I, J, K)=0.0                                                     108
      D(I, 1, 1)=D1                                                      109
      D(I, 1, 2)=D1*PR                                                   110
      D(I, 2, 1)=D1*PR                                                   111
      D(I, 2, 2)=D1                                                      112
      D(I, 3,3)=D1*Q                                                     113
      IK=IK+1                                                            114
      IF (IK.LE.NEL)GO TO 112                                            115
      WRITE (2,910)
  910   FORMAT (13X, 97(1H-)       /////////)
```

```
C
C                    PART 2
C                ******************
C
C                FORMA OVERALL (K) MATRUX
C
      WRITE (2,920)                                                    117
  902 FORMT (45X, 15HASSEMBLEY CARDS/ 45X,15(1H-)/////
     1    35X,52(1H-) / 35X, 1H| ,2 (15X, 1H|) , 18X, 1H| /
     2    35X,52H|  ELEMENT  |  NUMBER OF  |  NODES  |/
     3    35XX1H| ,2 (15X, 1H|) , 18X, 1H| /
     4    35X,52H|  NUMBER  | EXTREMITIES  | A B C D |/
     5    35X,1H| ,2 (15X, 1H|) , 18X, 1H| /35X, 52 (1H-) / 35X, 1H| ,
          2(15X, 1H|),
     6    18X, 1H | )
  500 NN1 = NN * NDOF                                                  119
      DO 200 J=1, NN1                                                  120
      P(J) = 0                                                         121
      DO 200 K=1, NN1                                                  122
  200 A(J, K) = 0.0                                                    123
      DO 201 J=1, 12                                                   124
  201 N2 (J) = NDOF * (J-1)                                            125
      NDUMMY = NN1 + 1                                                 126
      IK = 1                                                           127
C
C                INPUT ASSEMBELY DATA
C
  207 READ (5, 202) I, NEI, (N1 (J),J=1 ,NEI)                          128
  202 FORMAT (22I0)                                                    129
      WRITE (2, 903) I ,NEI, (N1 (J),J=1,NEI)                          130
  903 FORMAT ( 35X, 1H|,2(I8, 7X, 1H|), 3X, 4I3, 3X, 1H| /
     1  ( 35X, 1H| ,2(I5X, 1H|), 18X, 1H| )
      DO 203 J=1, NEI                                                  132
      IF (N1 (J) .EQ.0) N1(J) = NDUMMY                                 133
      IF (N1 (J) ,NE.NDUMMY) N1 (J) = NDOF* (N1(J)-1)                  134
  203 CONTINUE                                                         135
      DO 204 J=1, NEI                                                  136
      IF (N1 (J) .EQ.NDUMMY) GO TO 204                                 137
      NJ = N1 (J)                                                      138
      NL = N2 (J)                                                      139
      DO 205 K=1, NEI                                                  140
      IF (N1 (K) .EQ.NDUMMY) GO TO 205                                 141
      NK = N1 (K)                                                      142
      NM = N2 (K)                                                      143
```

```
        DO 206 L=1, NDOF                                                144
        DO 206 M=1, NDOF                                                145
  206  A(NJ+L,NK+M) = A(NJ+L,NK+M) + S(I,NL+L,NM+M)                      146
  203  CONTINUE                                                          147
  203  CONTINUE                                                          148
       IK = IK+1                                                         149
  501  IF (IK.LE.NEL) GO TO 207                                          150
       WRITE (2, 913)
  913  FORMAT (35X, 52 (1H-) /////////)
C
C                    PART 3
C             ******************
C
C             SOLVE TO FIND DISPLACEMENTS
C
C
C             INPUT LOADING AND BOUNDARY CONDITIONS
C
       WRITE (2,918)
  918 FORMT (60X, 5HLOADS / 60X, 5(1H-)/////
      1   44X, 33(1H-) / 44X, 1H| ,2 (15X, 1H|) /
      2   44X, 17H|    LOADING     |, 15X, 1H| / 44X, 1H| ,2 (15X, 1H|) /
      3   44X, 33H|    VECTOR     |, LOAD | / 44X, 1H| ,2 (15X, 1H|) /
      4   44X, 17H|    NUMBER     |, 15X, 1H| / 44X, 1H| ,2 (15X, 1H|) /
      5   44X, 33(1H-) / 44X, 1H| ,2 (15X, 1H|) )
  919 READ (1,916) NNT, LOAD
  916 FORMAT (10, F0 . 0)
       IF(NNT.EQ.0) GO TO 931
       P (NNT) = LOAD
       WRITE (2,917) NNT, LOAD
  917 FORMAT (44X, 1H| , I8,7X,1H| ,F12.4,3X,1H| / 44X, 1H| ,
      2(15X, 1H| ) )
       GO TO 919
  931 WRITE (2,920)
  920 FORMAT (44X, 33(1H-) ////////)
       WRITE (2,921)
  921 FORMAT (55X, 10HRESTRAINTS /55X, 10 (1H-) /////
      1   52X, 18(1H-) / 52X, 1H| ,16x, 1H| /52X, 1H| ,16H
          DISPLACEMENT
      2   ,1H| / 52X,1H| ,16X, 1H| / 52X, 18H| VECTOR |/
      3   52X,1H| ,16X, 1H| / 52X, 18H| NUMBER |/
      4   52X,1H| ,16X, 1H| / 52X, 18(1H-) / 52X,1H| ,16X, 1H| )
     XX = 1.0E+30
  922 READ (1,923) NEST
  923 FORMAT (I0)
```

```
      IF(NEST.EQ.0) GO TO 924
      A (NEST, NEST) = XX
      WRITE (2,925) NEST
  925 FORMAT (52X, 1H| , I8, 8X, 1H| / 52X, 1H| ,16X, 1H| )
      GO TO 922
  924 WRITE (2,926)
  926 FORMAT ( 52X, 18(1H-) ////////)
C
C          CALL SUBROUTINE MATRIX TO SOLVE EQUATIONS
C
        CALL MATRIX (A, P, NN1, 100, 1, 6)
C
C           WRITE RESULTS
C
      WRITE (2,904)                                                    155
  904 FORMAT ( 1H| ,54X, 7HRESULTS / 55X, 7 (1H=) /////
     1   28X, 65(1H-) / 28X, 1H| ,2 /15X, 1H| ,31X, 1H| /
     2   28X, 33H | NODE    |    VERTICAL    |,
     3          32H          ROTATION              |   /
     4   28X,   1H| ,2 /15X, 1H| ,31X, 1H|   /     / 28X, 1H| ,15X,
     5          49H|     DEFLECTION    |
     6   28X,   1H| ,2 (15X, 1H|), 32H X | Y | /
     7   28X,  1H| / ,4 /15X, 1H| 28X, 65(1H-) / 28X, 1H|, 4(15X, 1H| ))
          DO 300 J=1, NM                                               157
          K = NDOF *(J-1) +1                                           158
  300 WRITE (2,905) J,P(K),P(K+1),P(K+2)                               159
  905 FORMAT (28X, 1H| , I8, 7X, 1H |, 3(F15.7,1H| / 28X, 1H| ,
     4(15X, 1H| ))
      WRITE (2,914)
C
C           PART 4
C         **********
C
C       FIND STRESS MOMENTS AT REQUIRED POINTS
C
       WRITE (2,906)                                                   162
  906 FORMAT ( 12X, 97(1H-) / I2X, 1H|, 15X, 1H| ,31X, 1H| ,
     47X, 1H|) /
     1  12X, 49H| ELEMENT     |     CO-ORDINATES OF POINT |,
     2              48H                STRESS MOMENTS | /
     3  12X, 1H| , I5X, 1H|, 31X, 1H| ,47X, 1H| / 12X, 1H| ,
        6(15X, 1H| ) /
        4   12X, 49H|                |         X         |         Y         | ,
```

```
      5 48H          X       |          Y          |        XY | /
      6 12X, 1H| ,6(15X, 1H|) / 12X, 97(1H-) / 12X, 1H| ,6(15X, 1H| ))
        DO 400 J=1, 3                                                    165
        DO 400 K=1, 12                                                   166
  400   A(J, K) =0.0                                                     167
        NDUMMY = NM+1                                                    168
        DO 401 J=1, NDOF                                                 169
  401   P (NDOF + NDUMMY –J+1) = 0.0                                     170
        A(1, 4) = -2.0                                                   171
        A(2, 6) = -2.0                                                   172
        A(3, 5) = -2.0                                                   173
        IK = 1                                                           179
C
C       READ POSITION OF POINT
C
  410   READ (1, 402) I,NEI, NP, (N3 (J) ,J= , NEI), (XP (K), YP (K)
        ,K=1 ,NP)                                                        180
  402   FORMAT (7I0, 2FO.0)                                              181
        L = 0                                                            182
        DO 403 K=1,NEI                                                   183
        N = N3 (K)                                                       184
        IF (N.EQ.0) N = NDUMMY                                           185
        DO 404 J=1, 3                                                    186
  404   Y1 (J+L) = P(3*N-3+J)                                            187
        L = L+3                                                          189
  403   CONTINUE                                                         190
        DO 405 J=1, 12                                                   191
        X(J) = 0.0                                                       192
        DO 405 K=1, 12                                                   193
  405   X(J) = X(J) + A2 (I, J, K) * Y1 (K)                             194
        DO 406 N=1, NP                                                   195
        DO 407 J=1, 3                                                    196
        Y(J) = 0.0                                                       197
  407   Y1(J) = 0.0                                                      198
C
C         FORM (N) MATRIX
C
        A (1, 7) = -6*XP(N)                                              199
        A (1, 8) = -2*YP(N)                                              200
        A (1, 11) = -6*XP(N) *YP(N)                                      201
        A (2, 9) = -2*XP(N)                                              202
        A (2, 10) = -6. *YP(N)                                           203
        A (2, 12) = -6. *XP(N) *YP(N)                                    204
        A (3, 8) = -4. *XP(N)                                            205
        A (3, 9) = -4. *YP(N)                                            206
        A (3, 11) = -6. *XP(N) **2                                       207
        A (3, 12) = -6. *YP(N) **2                                       208
```

```
            DO 408 J=1, 3                                              209
            DO 408 K=1, 12                                             210
      408   Y1(J) = Y1(J) + A (J, K) * X (K)                           210
            DO 409 J=1, 3                                              211
            DO 409 K=1, 3                                              212
      409   Y(J) = Y(J) + D (I, J, K) * Y1 (K)                         213
C
C             WRITE RESULTS
C
      406   WRITE (2, 907) I, XP(N) , YP(N)
            ,(Y(J), J=1, 3)                                            214
      907   FORMAT (12X,1H| , I8, 7X, 1H|,
6(F13 .5,2X, 1H| ) / 12X, 1H| ,6(15X,1H| ))
            IK = IK + 1                                                216
            IF(IK.LE.NTSC) GO TO 410                                   217
            WRITE (2, 930)
      930   FORMAT ( 12X, 97(1H-))
            STOP                                                       218
            END                                                        219

END OF SEGMENT, LENGTH 2284, NAME MARI

            SUBROUTINE MATRIX (A, B, N, IA, KNOT, OUT)
            DIMENSION A (IA, N),B(N) ,C(100),IND(100)
            INTEGER OUT                                                222
            M = N                                                      223
      100   AMAX = 0.0                                                 224
            DO 2 I=1, M                                                225
            IND(I) = I                                                 226
            IF(ABS (A(I,1)) - AMAX) 2, 2, 3                            227
        3   AMAX = ABS (A (I, 1))                                      228
            I4 = I                                                     229
        2   CONTINUE                                                   230
            MM = M-1                                                   231
            DO 111 J=1 , MM                                            232
            IF(14 - J) 6, 6, 4                                         233
        4   ISTO = IND(J)                                              234
            IND(J) = IND (J)                                           235
            IND (14) = ISTO                                            237
            DO 5 K=1, M                                                238
            STO = A(14, K)                                             239
            A(I4, K) = A(J, K)                                         240
            A(J, K) = STO                                              241
        5   CONTINUE                                                   242
            GO TO (7, 6) KNOT                                          243
```

```
  7   STO = B(I4)                                              244
      B(I4) = B(J)                                             245
      B(J) = STO                                               246
  6   AMAX = 0.0                                               247
      J1 = J+1                                                 248
      IF (A(J,J).EQ.0) A(J,J) = 1                              248.1
      DO 11 I=J1,M                                             251
      A(I,J) = A(I,J) /A(J,J)                                  252
      DO 10 K=J1,M                                             253
      A(I,K) = A(I,K) - A(J,J) * A(J, K)                       254
      IF(K-J1) 14, 14, 10                                      255
 14   IF (ABS(A(I,K) ) – AMAX) 10, 10, 17                      256
 17   AMAX = ABS (A(I,K) )                                     257
      I4 = I                                                   258
 10   CONTINUE                                                 259
  9   GO TO (12, 11) KNOT                                      260
 12   B (I) = B (I) - A(I,J) *B(J)                             261
 11   CONTINUE                                                 262
111   CONTINUE                                                 263
       IF (A(M,M) .EQ.0) A(M,M) = 1                            263.1
 94   GO TO (19, 18) KNOT                                      267
 19   DO 127 I1=1,M                                            268
      I = M + 1 - I1                                           269
      IF(M-I) 327, 327, 28                                     270
 28   12 = I + 1                                               271
      DO 32 K=I2=1,M                                           272
      B (I) = B (I) - A(I,K) *B(K)                             273
 32   CONTINUE                                                 274
327   B (I) = B (I) / A(I,I)                                   275
127   CONTINUE                                                 276
 18   GO TO (64, 65) KNOT                                      277
 65   DO 140 I1=1,MM                                           278
      I = M+1 - I1                                             279
      I2 = I-1                                                 280
      DO 41 J1=1, I2                                           281
      J= I2 + 1 - J1                                           282
      J2 = J + 1                                               283
      W1 = -A(I, J)                                            284
      IF(12 – J2) 141, 43, 43                                  285
 43   DO 42 K=J2, I2                                           286
      W1 = W1 - A(K, J) * C(K)                                 287
 42   CONTINUE                                                 289
141   C(J) = W1                                                290
 41   CONTINUE                                                 291
      DO 40 K=1, I2                                            292
```

```
      A(I, K) = C(K)                                          293
 40   CONTINUE                                                294
140   CONTINUE                                                295
      DO 150 I1=1, M                                          296
      I = M+1 - I1                                            297
      I2 = I + 1                                              298
      W = A(I, I)                                             299
      IF(W.EQ.0) W=1                                          299.1
 95   DO 56 J=1, M                                            304
      IF(I – J) 52, 53, 54                                    305
 52   W1 = 0.0                                                306
      GO TO 55                                                307
 53   W1 = 1.0                                                308
      GO TO 55                                                309
 54   W1 = A(I, J)                                            310
 55   IF(I1 – I) 156, 156, 57                                 311
 57   DO 58 K=I2, M                                           312
      W1 = W1 - A(I, K) * A(K, J)                             313
 58   CONTINUE                                                317
156   C(J) = W1                                               318
 56   CONTINUE                                                319
      DO 50 J=1, M                                            320
      A(I, J) = C(J) /W                                       321
 50   CONTINUE                                                322
150   CONTINUE                                                323
      DO 60 I=1, M                                            324
 63   IF(IND(I) – I) 61, 60, 61                               325
 61   J = IND(I)                                              326
      DO 62 K=1, M                                            327
      STO = A(K, I)                                           328
      A (K, I) = A (K, J)                                     329
      A (K, J) = STO                                          331
 62   CONTINUE                                                332
      ISTO = IND(J)                                           333
      IND(J) = J
      IND (I) = ISTO
      GO TO 63
 60   CONTINUE
 64   RETURN
      END
```

END OF SEGMENT, LENGTH 723, NAME MATRIX

SAI
Relevant Computer Programs
For Finite Element Analysis
Abstracts from main program ISOPAR based on finite element analysis

SAI.4 Program: Mesh Generation Associated with Finite Element Program ISOPAR

(With compliments from F.D. Wang, M.C. Sun and J. Wolgamott)
Original Computer Program: U.S. Department of Interior Bureau of Mines, I.C.8510 (1971) (Modified by M.Y.H. Bangash to suit Trauma Structures and their Mesh Generation)

Program Listing.

```
      PROGRAM MESH
C
      COMMON NUMEL, NUMNP, NESTART, NPSTART
      COMMON /COOR / XORD (1000), YORD (1000)
      COMMON / NORF / IX (10000,4 )
      COMMON / HED / HED (10)
C
     READ 1, MTYPE, IPLOT, IPCARD
   1  FORMAT ( 315)
      GO TO (11, 12, 13 ), MTYPE
  11 CALL MESH 1 $          GO TO 15
  12 CALL MESH 2 $          GO TO 15
  13 CALL MESH 3 $          GO TO 15
C
     CALCULATE MAXIMUM BAND WIDTH
C
  15 K=0
     DO 101 I=1,4
     KK=IABS (IX(N,I)-IX(N,J)
     KK=IABS (KK,GT,K)          K=KK
  102 CONTINUE
  101 CONTINUE
      MBAND=2*K+2
      PRINT 23,MBAND

23 FORMAT (///*MAXIMUM BAND WIDTH = * 13)
C
```

```
C     IF PLOT ELEMENT MESH
C
      IF (IPLOT . EQ.0 ) GO TO 201
      CALL PLMESH
C
C     IF PUNCH CARDS
C
      201 IF (IPCARD.EQ.O) GO TO 202
          PUNCH 21, (N,XORD (N), N=NPSTART,NUMNP)
          PUNCH 22,(M,IX (M,J),J=1,4),M=NFSTART, NUMEL)
C
      21 FORMAT (I5,5X,2F10.4)
      22 FORMAT (515)
      202 STOP
          END
      SUBROTINE MESH 2
C
C     FINITE ELEMENT MESH GENERATOR PROGRAM 2
C     FOR INCLINED LAYERS WITH OR WITHOUT OPENING(S)
C
      COMMON NUMFL,NUMNP,NESTART, NPSTART
      COMMON / COOR/ XORD (1000), YORD (1000)
      COMMON/NODE/NPI(1000), NPK (1000)NPL (1000)
      COMMON / HED/ HED (10)
      COMMON / LAYR/XL1 (50),YL1 (50),XL2 (50),YL2(50),NLAYER
      COMMON/ GENE/MEL,M1,M2,NODE2,MTS,NEL
      DIMENSION XTOP (5),YTOP (5) XBOT (5), YBOT (5),
      NOPEN (50)
      DIMENSION XTOP (5), NNPL (50),MT (50)
      DIMENSION XINT(50,YINT (50), YINB (50), Y (50),YT(50)
      DIMENSION NPO (50,3,2) , NPD (50,4,2), NPSD (50, 4 ,2 ),
      MTD 50,4,2)
C
      READ 1, HED
      READ 2, NLYER, NSLICE, NSLICE, NPTOP, NPBOT, NESTART,
      NPSTART
      READ 3, (N, XL1 (N), YL1 (N) ,XL2 (N), N=1, NLAYER_
      NSL=NSLICE+1
      SLOPE = (YL2(1)-YL1(1)/ (XL2(1)- XL1(1))
      READ 4, (XX(N),N=1, NPTOP)
      READ 4, (XTOP (N), YTOP (N), N=1, NPTOP)
      READ 4, (XBOT (N), YBOT (N), N=1, NPBOT)
```

```
      READ 5, (NOPEN (N), N=1, NSLICE

C
      1     FORMAT    (8A10)
      2     FORMAT    (615)
      3     FORMAT    ( I 5,4F10.0 )
      4     FORMAT    ( 8F10.0)
      5     FORMAT    (50I1)

C     PRINT 11,       HED
      PRINT 12,       NLAYER, NSLICE,NPTOP, NPBOT, NESTART,
      NPSTART
      PRINT 13,       (N,XL1 (N), YL1 (N), XL2(N), YL2(N), N=1,
      NLAYER)
      PRINT 14,       (XX (N), N=1,NSL)
      PRINT 15,       (XTOP (N), YTOP (N), N=1,NPTOP
      PRINT 16,       (XBOT (N), YBOT (N), N=1, NPBOT)
      PRINT 17,       (NOPEN (N),N=1, NSLICE)
C
      DO 50 I=1, NSLICE
C     CHECKING COLUMN CONTAINING OPENING (S)
      IF (NO OPEN (I ).EQ.0) GO TO 50
C     IF YES , READ-IN TWO CARDS FOR EACH COLUMN
      NN=NOPEN (I)
      PRINT 21, I NN
      DO 51 L=1, 2
      READ 6, (NPO (I,N,L) YO1 (I,N,L), YO2 (I,N,L), N=1,NN)
6     FORMAT (3 (15,2F10.0) )
      LL= I+L-1
51    PRINT 22, LL, (NPO (I,N,L)YO1 (I,N,L), YO2 (I,N,L),N=1,NN)
50    CONTINUE

C
C     FIND POINT ON THE TOP LIE AND BOTTOM LINE
C
      DO 1001 I=1,NSL
      XI=XX (I)
      IP=0
      DO 101 N=2, NPBOT
      CALL INTLN (XI ,XBOT (N-1), YBOT (N-1), XBOT (N), YINB (I),
      IT)
      IF ( IT.EQ.O ) GO TO 103
      IP=1
      GO TO 102

    101  CONTINUE
```

```
    102  IF (IP.NE.1) GO TO 2001
         IB=0
         DO 103 N=2, NPBOT
         CALL INTLN (XI,XBOT (N-1), YBOT (N), YBOT (N),
         YINB (I), IT)
         IF (IT.EQ.O) GO TO 2002
   1001 CONTINUE
C
C     FINE INTERSECTION POINT OF VERTICAL AND LAYER LINES
C
      NODE = NPSTART-1
      DO 1002 II=1,NSLICE
      I=II
      IF (I.NF.1) I= I+1
500   LAYERS=0
C     CHECKING COLUMN CONTAINING OPENING(S)

      IF (NOPEN (II) . NE. O) GO TO 600
      CALL INTLAY (XX(I), YINB (I), Y,NNPL(I),MT(I),LAYER)
      GO TO 601
600   NN=NOPEN (II)        $ NIV= NN+1
      IF (I . EQ. 1 ) GO TO 502
C
C     CHECK TO SE IF DATA ON LEFT LINE OF THE COLUMN ARE
C     THE SAME AS ON RIGHT LINE OF THE NEXT COLUMN
C     IF YES, STORE NPD,NPSD,MTD.        IF NO, RE-CONT THEM
C
      IF (NO OPEN (II). NE NOPEN (II-1) ) GO TO 515
      DO 121 N=1,NN
      IF (YO1 (II,N,1 .NE.YO1 (II-1,N,2) ) GO TO 515
      IF (NOP (II,N,1 .NE.NOP(II-1,N,2) ) GO TO 515
      IF (YO2 (II,N,1 .NE.YO2 (II-1,N,2) ) GO TO 515

121   CONTINUED
      DO 122 N=1,NDIV
      NPSD (II,N,1)=NPSD (II-1,N,2)
      NPD (II,N,1 )= NPD (II-1,N,2)
      MTD (II,N,1)=MTD (II-1,N,2)

122   CONTINUED

    SUBROTUINE MESH 3

C
C      FINITE ELEMENT MESH GENERATOR PROGRAMM 3
```

```
C     FOR FINE MESH AROUND SINGLE OPENING OR MULTIPLE
      OPENINGS
C
      COMMOM MNUMEL, NUMNP,NESTART, NPSTART
      COMMON/ COOR/ XORD (1000), YORD (1000)
      COMMON / NODE / NPI (1000), NPJ (1000), NPK (1000),
      NPL(1000)
      COMMON / HED /HED (10)
      COMMON / GENP/ IFLG, NOPEN (25), NEXT (50), NPSD (25,5,2,
     1                              IR, NODE, LUROW (25), LINE
      COMMON /POINT/ NPSL (50,2), NPD (25,5,2), NPO (25,5,2),
      NSK(25,5,2),
     1              XO1 (25,5,2), YO1(25,5,2), XO2(25,5,2), YO2 (25,5,2)
      COMMON /ADDI/ IROW,NI(50), IRELIN (50,10), NADD (50,10)
      COMMON/ GENE/ MEL.M1,M2, NODE1,NODE2,MT,NEL
      DIMENSION XX \(50), YY(50),KTYPE(50),NNPL(50), MTD (25,5)

C
      READ 1,          HED
      READ 2,          NX,NY,NESTART, NPSTART
      READ 3,          (XX(I), I=1,NX)
      READ 3,          (YY(I), I=1,NY)
      PRINT 11,        HED
      PRINT 12,        NX, NY, NEWSTART, NPSTART
      PRINT 13,        (XX (I),I=1,NX)
      PRINT 14,        (YY(I),I=1, NY)

C


    NROW=NY-1
    PRINT 15
   DO 15 I=1, NROW
   READ 4, NR, KTYPE (I), NIREL,(IRELN (I,J), J=1, NIREL)
   NI(I)= NIREL
   IF (KTYPE (I).EQ.1) GO TO 51
   PRINT 16, I, KTYPE (I), NIREL, (IRELIN (I,J), J=1, NIREL)
   GO TO 50

51 PRINT 17,I, KTYPE(I)
50 CONTINUE


C
```

```
  1  FORMAT (10A8)
  2  FORMAT (4I5)
  3  FORMAT (8F10.0)
  4  FORMAT (3I5, 20I3)
 11  FORMAT (1H1,10A8/)
 12  FORMAT (*0NUMBER OF POINTS ON BOTTOM LINE—* I3/
    1            (*0NUMBER OF POINTS ON LEFT LINE—* I3/
    2            *ELEMENTS OF STARTING NUMBER—* I3/
    3            *NODAL POINT STARTING NUMBER—*13/)
   13 FORMAT (*OX-ORD OF POINTS ON THE BOTTOM LINE*/
     (8F9.4) )
   14 FORMAT (*OY-ORD OF POINTS ON THE LEFT LINE*/(8F9.4) )
   15 FORMAT ( *OROW NO. TYPE HOOW MANY ———WHERE—-*)
   16 FORMAT (217,I10,4X, 20I3)
   17 FORMAT (217, 9X,*0     *)
C
C      DETERMINE NODE'S NUMBERS OF ELEMENT
C
       NEL =NESTART-1
       DO 1003 I=1, NSLICE
       IF (NOPEN (I).NE.0) GO TO 201
       M1= NNPL (I)       $    M2=NNPL (I+1)
       IF (SLOPE)   212,211,211
211    MTS=MT(I+1)        $    M2=NNPL(I+1)
212    MTS=MT(I)
       IF (MTS.EQ.2)   MTS=3
213    NODE1=NPSL(I+1,1)
       NODE2=NPSL (I+1,1)
       CALL GENELQ
       GO TO 1003
201    NN=NOPEN (I)           $        NDIV=NN+1
       N1=N2=0
       DO 202 N=1, NDIV
       M1=NPD(I,N,1)
       M2=NPD (I,N,2)
       IF (SLOPE)      222,221,221
221    MTS=MTD (I,N,2)         $          GO TO 223
222    MTS= MTD (I,N,1)
       IF (MTS.EQ.2) MTS=3
223    NODE1= NPSD (I,N,1)
       NODE2=NPSD (I,N,2)
       CALL GENELQ
202    CONTINUE
1003   CONTINUE
       NUMEL=NEL
```

```
      PRINT 18, NUMEL,NUMNP
      PRINT 19, (M,NPI(M), NPJ(M), NPK (M), NPL(M), M=NESTART,
      NUMEL)
      PRINT 20, (N,XORD(N), YORD(N), N=NPSTART, NUMNP)
      RETURN
   11 FORMAT (1H1, 8A10)
   12 FORMAT (*0NUMBER OF LAYER LINE————————*15/
      1 *NUMBER OF SLICES————————————*15/
      2 *NUMBER OF POINTS ON TOP LINE——*15/
      3 *NUMBER OF POINTS ON BOTTOM LINE-*15/
      4 *ELEMENT SATRTING NUMBER————*15/
      5 *NODAL POINT STARTING NUMBER—*15/ )

   13 FORMAT (* OLAYER      X1    Y1    X2    Y2*/
      1 (I5, 4F10.4))
   14 FORMAT (/*0X-ORDS      FOR SLICES—*/ (8F9.4))
   15 FORMAT (/*0X- AND Y- ORDS OF POINT ON TOP LINE
      —*/ (8F9.4))
   16 FORMAT (/*0X- AND Y- ORDS OF POINT ON BOTTOM
      LINE—/(8F9.4))
   17 FORMAT (/*0OPENING IDENTIFICATION CODE FOR
      SLICES*/1X, 50I1)
   18 FORMAT (*0NUMBER OF ELEMENT ————————*I5/)
      1          * NUMBER OF NODAL POINTS———*I5/)
   19 FORMAT (*1 EL. I J K L */ (515))
   20 FORMAT (*1NODE X-ORD Y-ORD */ (I5, 5X,
      2F10.4))
   21 FORMAT (*/*0SLIC NO.* 13,* NUMBERING OF OPENING
      =* 13)
   22 FORMAT ( * LINE * 13, *–*, 5 (I5,2F10.4) )
 2001 PRINT 31
   31 FORMAT ( * ERROR IN INPUT DATA ON THE TOP LINE*)
      STOP
 2002 PRINT 32
   32 FORMAT (*ERROR IN INPUT DATA ON BUTTOM LINE*)
      STOP
      END

      SUROUTINE INTLAY (XX, YINTOP, YINBOT, Y, M ,MT,
      LAYER)

C
C     FIND THE INTERSECTIOM POINTS OF VERTICAL LINE AND
      LAYER LINES
```

```
C       DEFINR MESH TYPE AND NUMBER OF POINTS ALONG
        VERTICAL LINE
C
        COMMON/ LAYER / XL1(50),XL2(50), YL2(50),NLAYER
        DIMENSION Y(50)

C
     M=0 $MT=1       $       L1= LAYER +1

     DO 110 L=L1, MALAYER
     LAYER=LAYER+1
     CALL INTLN      (       xx, xl1 (l), yl1(l), yl2 (2), yt, it)
     If (IT. NE . O ) GO TO 111
     IF (M) 112, 110,112
  111        IF (YT.GT. YINTOP. OR .YT.LT.YINBOT) GO TO 117

             M= M+1      $       Y(M)=YT $ GO TO 110
  117        IF (M.GT.0) GO TO 112
  110        CONTINUE
C
  112        DY = ABS (Y(1)-YINTOP)
             IF (DY. GT.0.0001) GO TO 113
             MT2    $       GO TO 114
  113        M=M+1
             DO 115 J=2, M
             JJ=M-J+2
  115        Y(JJ)=Y(JJ-1)
             Y (1)=YINTOP
C
  114        DY=ABS (Y(M)-YINBOT
             IF (DY.LE.0.0001) GO TO 116
             M=M+ 1      $       Y(M)=YINBOT
C
  116        RETURN
             END

             SUBROUTINE INTLN (X,X1,Y1,X2,Y2,YT,IT)
C
C            FIND AN INTERSECTION OF LINE AND A VERTICLE
C            LINE


             IT=0
             IF (X2 .EQ.X1) GO TO 10
             IF(X2.LT.X1.OR.X.GT.X2) GO TO 10
             IT=1
```

```
      S=(Y2-Y1)/(X2-X1)
      YT=Y1+S*(X-X1)
10    RETURN
      END

      SUBROUTINE GENNP (X,Y)
C
C     GENERATING NODAL POINT WHEN ROW CONTAIM
      OPENING(S)
C
      COMMON/ COOR/ XORD(1000), YORD(1000)
      COMMON/ GENP/
      IFLG,NOPEN(25),NOROW(25),NEXT(25),NPSD(25.5.2),
      1          IR,NODE,LUROW(25), LINE
      COMMON/
      PONT/NPSL(50,2),NPD(25,5,2),NPO(25,5,2),NSK(25,5,2)
      1     XO1(25,5,2),YO1(25,5,2),XO2(25,5,2),YO2(25,5,2)
      DINEMSION X(50)
C
C     CHECK LOWER LINE OF ROW
C
111   IF (LUROW (II).LE.1) NP=NPSL(IR,1)
      IF (LUROW (II).EQ.2) NP=NPSL(IR,2)+1
      NPSD(II,1,1)=NP
      DO 101 JJ=1,NO
      NP=NP+NPD(II,JJ,1)-1
      XORD(NP)=XO1(II,JJ,1)
      YORD(NP)=YO1(II,JJ,1)
      IF (NPD(II,JJ+1,1).LT.2) GO TO 121
      NP=NP+NPO(II,JJ,1)+1
      XORD (NP)=X02(II,JJ,1)
      YORD(NP)=YO2(II,JJ,1)

121   NPSD(II,JJ+1,1)=NP
101   CONTINUE
      GO TO 100
C
108   DO 109 JJ=1,ND
109   NPSD (II,JJ,1)=NPSD(II-1,JJ,2)
      GO TO 100
C
C     GET UPPER LINE OF ROW OR LOWER LINE OF IST
C     ROW
C
122   KK=1      $      GO TO 123
```

```
      100   KK=2
      123   NS=1      $      K=0
            DO 102 JJ=1,ND
            N2=NPD(II,JJ,KK)
            NPSD (II,JJ,KK)=NODE-NS+2
            DO 112 N=NS,N2
            K=K+1
            NODE =NODE+1
            XORD(NODE)=X(K)
            YORD(NODE)=Y
      112   CONTINUE
            SUBROUTINE GENELQ
C
C           FOR GENERATING ELEMENTS OF A ROW OR A
            COLOUMN WHICH HAS
C           TRIANGULAR ELEMENT AT END(S) OF THE ROW OR
            COLOUMN
C
            COMMON/ NODE/ NPI(1000), NPK(1000), NPL(1000)
            COMMON/ GENE/ MEL.M1,M2,NODEL, NODE2, MTS,
            NEL


C           GO TO (111,112,113), MTS
      111   IF (M1-M2)   11,12,13
       11   NELS=M2-1  $      MTL=3      $      GO TO 115
       12   NELS=M1-1  $      MTL=1      $      GO TO 115
       13   NELS=M1-1  $      MTL=2      $      GO TO 115
      112   MM1=M1-1
            IF (MM1-M2) 21,22,23
       21   NELS=M2    $      MTL=3      $      GO TO 115
       22   NELS=M1-1  $      MTL=1      $      GO TO 115
       23   NELS=M1-1  $      MTL=2      $      GO TO 115
      113   MM2=M2-1
            IF (M1-MM2) 31,32,33
       31   NELS=M2-1  $      MTL=3      $      GO TO 115
            NELS=M2-1  $      MTL=1      $      GO TO 115
       33   NELS=M2    $      MTL=2      $      GO TO 115
C


      115   DO 200       II=1, NELS
            NEL=NEL+1
            IF (II.EQ.1)    GO TO 201
            IF (II.EQ.NELS) GO TO 202

         GO TO 1
```

```
  201   GO TO (1,2,3), MTS
  202   GO TO (1,2,3), MTL
    1   NPI(NEL)=NODEI
        NPJ(NEL)=NODE1+1
        NPK(NEL)=NODE2+1
        NPI(NEL)=NODE2
        NODE1=NODE1+2
        NODE2=NODE2+1
        GO TO 200
    2   NPI(NEL)=NODEI
        NPJ(NEL)=NODE1+1
        NPK(NEL)=NODE2
        NPL(NEL)=NPK(NEL)
        NODE1=NODE1+1
        GO TO 200
    3   NPI(NEL)=NODEI
        NPJ(NEL)=NODE2+1
        NPK(NEL)=NODE2
        NPL(NEL)=NPK(NEL)
        NODE2=NODE2+1
  200   CONTINUE
        RETURN
        END

        SUBROUTINE GENEL (IEL)
C
        COMMON/ NODE/ NOI(1000, NPK(1000), NPL(1000)
        COMMON/ ADDI/ IROW,NI(50), IRELN (50,10), NADD(50,10)
        COMMON/ GENE/ MEL, M1, M2, NODE2, MT, NEL
C
        GO TO (1,2,3,4) , IEL
C
    1   DO 10 N=1, MEL
        NEL=NEL+1
        NPI(NEL)=NODE1
        NPJ(NEL)=NODE1+1
        NPK(NEL)=NODE2+1
        NPL(NEL)= NODE2
        NODE1=NODE1+1
        NODE2=NODE2+1
   10   CONTINUE
        GO TO 100
C
    2   I=IROW+1    $          M=1       $          NN=NI(I)
        DO 20 N=1, MEL
```

```
      NEL=NEL+1
      NPI(NEL)=NODE1
      NPJ(NEL)=NODE1+1
      NPL(NEL)=NODE2
      NODE1=NODE1+1
      IF (M.GT.NN) GO TO 21
      K=IRELN(I,M)
      IF(N.EQ.K) GO TO 22
   21 NPK (NEL)= NODE2+1
      NODE2=NODE2+1
      GO TO 20
   22 NPK(NEL)=NODE2+2
      NODE2=NODE2+2
      M=M+1
   20 CONTINUE
C     ADD NN-TRIANGULAR ELEMENTS FOR TYPE-2 ROW
      DO 23 N=1,NN
      NEL=NEL+1
      NPI(NEL)=NADD(I,N)-1
      NPJ(NEL)=NADD(I,N)+1
      NPK(NEL)=NADD(I,N)
      NPI(NEL)=NADD(I,N)
   23 CONTINUE
      GO TO 100
C
    3 I=IROW-1 $ M=1 $ NN=NI(I)
C     ADD NN=TRIANGULAR ELEMENTS FOR TYPE-3 ROW
      DO 33 N=1,NN
      NEL=NEL+1
      NPI(NEL)=NADD(I,N)
      NPJ(NEL)=NADD(I,N)+1
      NPK(NEL)=NADD(I,N)-1
      NPI(NEL)=NADD(I,N)-1
   33 CONTINUE
      DO 30 N=1, MEL
      NEL=NEL+1
      NPI(NEL)= NODE2+1
      NPL(NEL)= NODE2
      NODE2=NODE2+1
      IF (M.GT.NN) GO TO 31
      K= IRE;N(I,M)
      IF (N.EQ.K) GO TO 32
   31 NPK (NEL)= NODE1+1
      NODE1=NODE1+1
      GO TO 30
```

```
   32  NPK(NEL)=NODE1+2
       NODE1=NODE1+2
       M=M+1
   30  CONTINUE
       GO TO 100
C
    4  CONTINUE
  100  RETURN
       END


C
C      DETERMINE NODE NUMBERING OF ELEMENTS
C
       NEL=NESTART-1
       DO 200 I=1, NROW
       N1=(I-1)*NP+1+NPS $ L1=N1+NP-1
       N2=L1+2 $ L2=L1+NP
       DO 201 J-1, NP
       NEL=NEL+1
       NPL(NEL)=N1
       IF ((N1+1).GT.L1) N1=(I-I)*NP+NPS
       NPJ(NEL)=N1+1
       NPL(NEL)=N2
       IF ((N2+1) ).GT.L2) N2=I*NP+NPS
       NPK(NEL)=N2+1
       N1+N1+1 $ N2=N2+1
  201  CONTINUE
  202  CONTINUE
       NUMEL=NEL


C
       PRINT 15, NUMEL, NUMNP
      PRINT 16, (M,NPI(M),NPJ (M), NPL (M), M=NESTART, NUMEL)
      PRINT 17, (N, XORD(N), YORD(N), N=NPSTART, NUMNP)
C
   11  FORMAT (1H1,10A8/)
   12  FORMAT (*0NUMBER OF LINE          =    *       14/
    1       *NUMBER OF ROWS              =    *       14/
    2       *ELEMENT STARTING NO.        =    *       14/
    3       * NODE      STARTING NO.     =    *       14/
   13  FORMAT (* LINE X1      Y1      X2      Y2*/
       1          (I5,4F10.4))
   14  FORMAT (// * SCALE FACTORS FOR ROWS - - -    * / (8F9 .4))
   15  FORMAT (*ONUMBER OF ELEMENTS — * I5/
```

```
     1     * NUMBER OF NODEL POINTS— * I5 /)
  16 FORMAT (*1 EL.      I     J     K     L * / (5I5))
  17 FORMAT (*1 NODE      X-ORD      Y-ORD * / (I5, 5X, 2F10.4))
     RETURN
     END
```

Material Models

Subroutine

Material matrix for reinforcement

```
     IMPLICIT REAL*8(A – H,O – Z)
     COMMAN/MTMD3D/D(6,6),STRESS(6),STRAIN(6),IPT,NEL
     DIMENSION PRO(1),DS(6,6),SIG(1),EPS(1),NCK(1),PS1(1),PS2(1),
    1          PS3(1),DC1(1),DC2(1),DC3(1)
     DO 111 II=1,6
     DO 111 JJ=1,6
 111 DS(II,JJ)=0.0
     DS(1,1)=PROP(9)/PROP(6)*PROP(2)
     DS(2,2)=PROP(10)/PROP(7)*PROP(2)
     DS(3,3)=PROP(11)/PROP(8)*PROP(2)
     CALL TESTCK (PROP,SIG,EPS,NCK,PS1,PS2,PS3,DC1,DC2,DC3)
     IF (NCK(1).EQ.1.OR.NCK(2).EQ.1..OR.NCK(3).EQ.1)
    @     GOTO 220
     CALL DMAT(PROP,NCK)
 220 DO 222 III = 1,6
     DO 222 JJJ = 1,6
 222 D(III,JJJ)=D(III,JJJ)+DS(III,JJJ)
     RETURN
END
```

Orthotropic variable-modulus model

```
     IMPLICIT REAL*8(A – H,O – Z)
     DIMENSION E(3),G(3,3),D(6,6),PROP(1)
     DO 222 II = 1,6
     DO 222 JJ = 1,6
 222 D(II,JJ) = 0.0
     AA=(1.0-PROP(S))/(1.0+PROP(5))*(1.0-2.0*PROP(5))
     BB=PROP(5)/(1.0-PROP(5))
     E(1)=PROP(12)/PROP(1)*PROP(6)+PROP(2)*PROP(9)
     E(2)=PROP(12)/PROP(1)*PROP(7)+PROP(2)*PROP(10)
     E(3)=PROP(12)/PROP(1)*PROP(8)+PROP(2)*PROP(11)
     DO 7100 J = 1,3
     DO 7100 K = 1,3
7100 G(J,K) = 0.25*(AA*(E(J)+E(K)))-2.0*AA*BB*DSQRT(E(J)*E(K))
     D(1,1) = AA*E(1)
```

```
      D(1,2) = AA*BB*DSQRT(E(1)*E(2))
      D(1,3) = AA*BB*DSQRT(E(1)*E(3))
      D(2,1) = D(1,2)
      D(2,2) = AA*E(2)
      D(2,3) = BB*DSQRT(E(2)*E(3))
      D(3,1) = D(1,3)
      D(3,2) = D(2,3)
      D(3,3) = AA*E(3)
      D(4,4) = G(1,2)
      D(5,5) = G(1,3)
      D(6,6) = G(2,3)
      RETURN
      END


Ottoson model
      IMPLICIT REAL*8(A – H,O – Z)
      COMMON/MTMD3D/D(6,6),STRESS(6),STRAIN(6),IPT,NEL
      DIMENSION PAR(3,5),FS(6,6),FSTPOS(6,6),PROP(1),SIG(1),
     @                  DVI1DS(6),DVJ2DS(6),DVJ3DS(6),DVTHDS(6)
      OPEN(UNIT=5,FILE='PARAMETERS',STATUS='OLD')
      READ(5,*,END=3700)(PAR(IF,JF),JF=1,5),IF=1,2=3)
 3700 CLOSE(5)
      PK = PROP(3)/PROP(4)
      IP = 0
      JP=0
      IF (PK.LE.0.08)IP = 1
      IF (PK.EQ.0.10)IP = 2
      IF (PK.GE.0.12)IP = 3
      IF (PK.LT.0.10)JP = 1
      IF (PK.LE.0.10)JP = 2
      IF (IP.EQ.0) GOTO 3800
      A = PAR(IP,2)
      B = PAR(IP,3)
      PK1 = PAR(IP,4)
      PK2 = PAR(IP,5)
      GOTO 3900
 3800 SUB1 = PK – PAR(JP,1)
      SUB2 = PAR(JP+1,1) – PAR(JP,1)
      A = SUB1*PAR(JP+1,2)-PAR(JP,2))/SUB2+PAR(JP,2)
      B = SUB1*PAR(JP+1,3)-PAR(JP,3))/SUB2+PAR(JP,3)
      PK1 = SUB1*PAR(JP+1,4)-PAR(JP,4))/SUB2+PAR(JP,4)
      PK2 = SUB1*PAR(JP+1,5)-PAR(JP,5))/SUB2+PAR(JP,5)
 3900 VAR11=SIG(1)+SIG(2)+SIG(3)
      VARJ2=1.0/6.0*((SIG(1)-SIG(2))**2+(SIG(2)-SIG(3)**2+
```

```
     @           (SIG(3)-SIG(1))**2+(SIG(4)**2+SIG(5)**2+SIG(6)**2
       VARI13=VARI1/3.0
       VI131=SIG(1) – VARI13
       VI132=SIG(2) – VARI13
       VI133=SIG(3) – VARI13
       VARJ3=VI131*(VI132*VI133-SIG(5)**2)-SIG(4)*(SIG(4)*VI133
     @          -SIG(5)*SIG(5)+SIG(6)*(SIG(4)*SIG(5)-SIG(6)*VI132)
       VAR3TH=1.5*3.0**(0.5)*VARJ3/VARJ2**1.5
       IF(VAR3TH.GE.0.0) GOTO 4000
       ALAM=22.2/21.0 – 1.0/3.0*ACOS(-PK2*VAR3TH)


       TOTLAM = PK1*COS(ALAM)
       DFD3TH = PK1*PK2*VARJ2**0.5*SIN(ALAM)/(3.0*PROP(4)*
     @              SIN(ACOS(- PK2*VAR3TH)))
       GOTO 4100
  4000 ALAM = 1.0/3.0*ACOS(PK2*VAR3TH)
       TOTLAM = PK1*COS(ALAM)
       DFD3TH = PK1*PK2*VARJ2**0.5*SIN(ALAM)/(3.0*PROP(4)*
     @              SIN(ACOS(- PK2*VAR3TH)))
  4100 DFDI1 = B/PROP(4)
       DFDJ2 = A/PROP(4)**2 + TOTLAM = /(PROP(4)*VARJ2**0.5)
       DVI1DS(1) = 1.0
       DVI1DS(2) = 1.0
       DVI1DS(3) = 1.0
       DVI1DS(4) = 0.0
       DVI1DS(5) = 0.0
       DVI1DS(6) = 0.0
       DVJ2DS(1) = 1.0/3.0*(2.0*SIG(1) – SIG(2) – SIG(3))
       DVJ2DS(2) = 1.0/3.0*(2.0*SIG(2) – SIG(1) – SIG(3))
       DVJ2DS(3) = 1.0/3.0*(2.0*SIG(3) – SIG(1) – SIG(2))
       DVJ2DS(4) = 2.0*SIG(4)
       DVJ2DS(5) = 2.0*SIG(5)
       DVJ2DS(6) = 2.0*SIG(6)
       DVJ3DS(1) = 1.0/3.0*(VI131*(- VI132 - VI133)) + 2.0*VI132*VI131
     @              - 2.0*SIG(5)**2 + SIG(4)**2 + SIG(6)**2
       DVJ3DS(2) = 1.0/3.0*(VI132*(- VI131 - VI133)) + 2.0*VI131*VI133
     @              - 2.0*SIG(6)**2 + SIG(4)**2 + SIG(5)**2
       DVJ3DS(3) = 1.0/3.0*(VI133*(- VI131 - VI132)) + 2.0*VI131*VI132
     @              - 2.0*SIG(4)**2 + SIG(5)**2 + SIG(6)**2
       DVJ3DS(4) = - 2.0 *VI133*SIG(4) + 2.0*SIG(5)*SIG(6)
       DVJ3DS(5) = - 2.0 *VI131*SIG(5) + 2.0*SIG(4)*SIG(6)
       DVJ3DS(6) = - 2.0 *VI132*SIG(6) + 2.0*SIG(4)*SIG(5)
       CONVJ2 = 3.0*3.0**0.5/(2.0*VARJ2*1.2)
       VJ3J2 = VARJ3/VARJ2**0.5
```

```
      DVTHDS(1) = CONVJ2*(- 0.5*VJ3J2*(2.0*SIG(1) – SIG(2) –
                  SIG(3))+DVJ3DS(1))
      DVTHDS(2) = CONVJ2*(- 0.5*VJ3J2*(2.0*SIG(2) – SIG(1) –
                  SIG(3))+DVJ3DS(2))
      DVTHDS(3) = CONVJ2*(- 0.5*VJ3J2*(2.0*SIG(3) – SIG(1) –
                  SIG(2))+DVJ3DS(3))
      DVTHDS(4) = CONVJ2*(- 3.0*VJ3J2*SIG(4) +DVJ3DS(4))
      DVTHDS(5) = CONVJ2*(- 3.0*V33J2*SIG(5) +DVJ3DS(5))
      DVTHDS(6) = CONVJ2*(- 3.0*VJ3J2*SIGA6) +DVJ3DS(6))
      DO 4200 IS = 1,6
      FS(IS,1)=DFDI1*DVI1DS(IS)+DFDJ2*DVJ2DS(IS)
               +DFD3TH*DVTHDS(IS)
4200  FSTPDS(1,IS) = FS(IS,1)
      RETURN
      END
```

Subrouting CRACKD (PROP, NCK, SIG, EPS, PS1, PS2, PS3, DC1, DC2, DC3) IMPLICIT REAL *8(A – H 0 – Z)

```
      SET UP MATERIAL MATRICES FOR CRACKED CONCRETE

      COMMON /MTMD3D/ D(6,6), STRESS(6),STRAIN(6), IPT,NEL
      DIMENSION DD(6,6),PROP(1),NCK(1),SIG(1), EPS(1),
                     PS1(1), PS(1), PS3(1), DC1(1), DC2(1), DC3(1)
      CALL PRINCL (IPT,STRESS, PS1, PS2, PS3,DC1, DC2, DC3)
      CALL RCMOD (PROP,D)
      CALL DMAT (PROP,NCK)
      DO 222 I = 1,6

      DO 222 J = 1,6
222   DD(I,J) = 0.0
      JJJ = 1
      LL = 0
      IF (NCK(1).EQ.1) LL = 1
      IF (NCK(2).EQ.1) LL = 2
      IF (NCK(3).EQ.1) LL = 3
      IF (NCK(1).EQ.1 AND.NCK(2).EQ.1) LL = 4
      IF (NCK(2).EQ.1 AND.NCK(3).EQ.1) LL = 5
      IF (NCK(1).EQ.1 AND.NCK(3).EQ.1) LL = 6
      IF (NCK(1).EQ.1 AND.NCK(2).EQ.1.AND.NCK(3).EQ1) LL = 7
      IF (LL.EQ.7) GOTO 99
      IF (JJJ.EQ.0) GOTO 200
      IF (LL.EQ.0) GOTO 999
```

```
      GOTO (113,114,115,116,117,118),LL
      ONLY ONE DIRECTION CRACKED
  113 CONTINUE
      CRACK IN DIRECTION 1
      DD(1,1) = 0.0
      DD(1,2) = 0.0
      DD(1,3) = 0.0
      DD(2,1) = 0.0
      DD(2,2) = D(2,2) – D(1,2)*D(1,2)/D(1,1)
      DD(2,3) = D(2,3) – D(1,3)*D(1,2)/D(1,1)
      DD(3,1) = 0.0
      DD(3,2) = DD(2,3)
      DD(3,3) = DD(3,3) – D(1,3)*D(1,3)/D(1,1)
      DD(4,4) = PROP(12)*D(4,4)
      DD(5,5) = DD(5,5)
      DD(6,6) = PROP(12)*D(6,6)
      GO TO 121
  114 CONTINUE
      CRACK IN DIRECTION 2
      DD(1,1) = D(1,1) – D(2,1)*D(2,1)/D(2,2)
      DD(1,2) = 0.0
      DD(1,3) = D(1,3) – D(1,2)*D(2,3)/D(2,2)
      DD(2,1) = 0.0
      DD(2,2) = 0.0
      DD(2,3) = 0.0
      DD(3,1) = DD(1,3)
      DD(3,3) = D(3,3) – D(2,3)*D(2,3)/D(2,2)
      DD(4,4) = PROP(12)*D(4,4)
      DD(5,5) = PROP(12)*D(5,5)
      DD(6,6) = D(6,6)
      GO TO 121
  115 CONTINUE
      CRACK IN DIRECTION 3
      DD(1,1) = D(1,1) – D(1,3)*D(1,3)/D(3,3)
      DD(1,2) = D(1,2) – D(1,3)*D(2,3)/D(3,3)
      DD(1,3) = 0.0
      DD(2,1) = DD(1,2)
      DD(2,2) = D(2,2) – D(2,3)*D(2,3)/D(3,3)
      DD(2,3) = 0.0
      DD(3,1) = 0.0
```

```
      DD(3,2) = 0.0
      DD(3,3) = 0.0
      DD(4,4) = D(4,4)
      DD(5,5) = D(5,5)*PROP(12)
      DD(6,6) = D(6,6)*PROP(12)
      GO TO 121
116   CONTINUE
      CRACKS IN TWO DIRECTIONS
      CRACKS IN DIRECTIONS 1 & 2

      DD(1,1) = 0.0
      DENOM=D(1,1)*D(2,2)-D(1,2)*D(2,1)
      DD(1,1) = 0.0
      DD(1,2) = 0.0
      DD(1,3) = 0.0
      DD(2,1) = 0.0
      DD(2,2) = 0.0
      DD(2,3) = 0.0
      DD(3,1) = 0.0
      DD(3,2) = 0.0
      DD(3,3) = D(3,3)
     1            - D(3,1)*(D(2,2)*D(1,3)-D(1,2)*D(2,3))/DENOM
     2            - D(3,2)*(D(1,1)*D(2,3)-D(2,1)*D(3,1))/DENOM
      DD(4,4) = PROP(12)* D(4,4)
      DD(5,5) = PROP(12)* D(5,5)
      DD(6,6) = PROP(12)* D(6,6)
      GO TO 121

117   CONTINUE

      CRACKS IN DIRECTIONS 3 & 2

      DENOM=D(2,2)*D(3,3)-D(2,3)*D(3,2)
      DD(1,1) = D(1,1)
1             - D(1,2)*(D(3,3)*D(2,1)-D(3,1)*D(2,3))/DENOM
2             - D(1,3)*(D(2,2)*D(3,1)-D(2,1)*D(3,2))/DENOM
      DD(1,2) = 0.0
      DD(1,3) = 0.0
      DD(2,1) = 0.0
      DD(2,2) = 0.0
      DD(2,3) = 0.0
      DD(3,1) = 0.0
      DD(3,2) = 0.0
      DD(3,3) = 0.0
```

```
      DD(4,4) = PROP(12)* D(4,4)
      DD(5,5) = PROP(12)* D(5,5)
      DD(6,6) = PROP(12)* D(6,6)
      GO TO 121

118   CONTINUE

      CRACKS IN DIRECTIONS 1 & 3

      DENOM=D(1,1)*D(3,3)-D(3,2)*D(1,3)
      DD(1,1) = 0.0
      DD(1,2) = 0.0
      DD(1,3) = 0.0
      DD(2,1) = 0.0
      DD(2,2) = D(2,2)
     1            - D(2,1)*(D(3,3)*D(1,2)-D(3,2)*D(1,3))/DENOM
     2            - D(2,3)*(D(1,1)*D(3,2)-D(3,1)*D(1,2))/DENOM
      DD(2,3) = 0.0
      DD(3,1) = 0.0
      DD(3,2) = 0.0
      DD(3,3) = 0.0
      DD(4,4) = PROP(12)* D(4,4)
      DD(5,5) = PROP(12)* D(5,5)
      DD(6,6) = PROP(12)* D(6,6)
      DD(2,3) = 0.0
      DD(3,1) = 0.0
      DD(3,2) = 0.0
      DD(3,3) = 0.0
      DD(4,4) = PROP(12)* D(4,4)
      DD(5,5) = PROP(12)* D(5,5)
      DD(6,6) = PROP(12)* D(6,6)
121   CONTINUE
      GOTO 99
200   CONTINUE
      IF (LL. .EQ.0) GOTO 999
      GOTO (1,2,3,4,5,6),LL
1     CONTINUE
      DD(2,2) = D(2,2)
      DD(2,3) = D(2,3)
      DD(3,2) = DD(2,3)
      DD(3,3) = D(3,3)
```

```
      DD(4,4) = PROP(12)* D(4,4)
      DD(5,5) = PROP(12)* D(5,5)
      DD(6,6) = PROP(12)* D(6,6)
      GOTO 99

2     CONTINUE
      DD(1,1) = D(1,1)
      DD(1,3) = D(2,3)
      DD(3,1) = D(1,3)
      DD(3,3) = D(3,3)
      DD(4,4) = PROP(12)* D(4,4)
      DD(5,5) = PROP(12)* D(5,5)
      DD(6,6) = PROP(12)* D(6,6)
      GOTO 99

3     CONTINUE
      DD(1,1) = D(1,1)
      DD(2,2) = D(2,2)
      DD(1,2) = D(1,2)
      DD(3,3) = D(3,3)
      DD(2,1) = DD(1,2)
      DD(4,4) = D(4,4)
      DD(5,5) = PROP(12)* D(5,5)
      DD(6,6) = PROP(12)* D(6,6)
      GOTO 99

4     CONTINUE
      DD(3,3) = D(3,3)
      DD(4,4) = PROP(12)* D(4,4)
      DD(5,5) = PROP(12)* D(5,5)
      DD(6,6) = PROP(12)* D(6,6)
      GOTO 99

5     CONTINUE
      DD(1,1) = D(1,1)
      DD(4,4) = PROP(12)*D(4,4)
      DD(5,5) = PROP(12)* D(5,5)
      DD(6,6) = PROP(12)* D(6,6)
      GOTO 99

6     CONTINUE
      DD(2,2) = D(2,2)
      DD(4,4) = D(4,4)
      DD(5,5) = D(5,5)
      DD(6,6) = D(6,6)
99    CONTINUE
```

```
      CRACKS IN ALL THREE DIRECTIONS TRANSFER DD
      TO D

      DO 101 J=1.6
      DO 101 K=1.6
      D(J,K)=DD(J,K)
101   CONTINUE
999   CONTINUE
      RETURN
      END
```

Program ISOPAR to print displacements and (if ISTAT.NE.0) velocities and accelerations (Jointly developed by J. Tang and the authors.)

```
      IND.EQ.0, PRINT DISPL/VEL./ACC AT ALL NODES
      IND.NE.0, PRINT DISPL/VEL./ACC ONLY AT NODES
           CONTAINED IN PRINTOUT BLOCKS
      COMMON/EL/IND.ICOUNT.NPAR(20),NUMEG,NEGL,NEGNG,
           IMASS,IDAMP,ISTAT,NDOFDM,KLIN,IEIG,IMASSN,IDAMPN
      COMMON /PRCPM/ NPB.IDC,IVC,IAC,IPC,IPNODE(2.8)
      DIMENSION DISP(NEQ),VEL(NEQ).ACC(NEQ),ID(NDOF,I)
      DIMENSION D(6)
      READ ID ARRAY INTO CORE
      REWIND 8
      NDBLK = NUMNP
      READ (8) ((ID(I,J),I=I,NDOF),J = I,NUMNP)
      PRINT DISPLACEMENTS
      IC = 4
      IF (IND.EQ.0) GO TO 10
      IF (IND.EQ.0) GO TO 180
10    WRITE (6,2000)
      WRITE (1,2000)
      IC = IC + 5
      DO 150 IB = I,NPB
      NODE1 = IPNODE(1,IB)
      IF (NODE1.EQ.0) GO TO 150
      NODE2 = IPNODE(2,IB)
      IF (IND.EQ.0) NODE1 = 1
      IF (IND.EQ.0) NODE2 = NUMNP
      DO 100 ii = NODE1,NODE2
      IC = IC + 1
      IF (IC,LT.56) GO TO 105
```

```
      WRITE (6,2045)
      WRITE (1,2045)
      IC = 4
105   DO 110 I = 1,6
110   D(I) = 0.
      DO 120 I = I,NDOF
      KK = ID(I,II)
      IL = 1
      IF (NDOF.EQ.2) IL = 1 + 1
120   IF (KK,NE.0) D(IL) = DISP(KK)
      WRITE (1,2010) II,D
100   WRITE (6,2010) II,D
      IF (IND.EQ.0) GO TO 180
      IF (IC.GE.55) GO TO 150
      IC = IC + 1
      WRITE (6,2050)
      WRITE (1,2050)
150   CONTINUE
180   IF (ISTAT.EQ.0) RETURN
      PRINT VELOCITIES
      IF (IND.EQ.0) GO TO 201
      IF (IVC.EQ.0) GO TO 280
201   IC = IC + 5 + IDC
      IF (IDC.NE.0) WRITE (6,2050)
      IF (IDC.NE.0) WRITE (1,2050)
      IF (IC.GE.54) GO TO 205
      WRITE (6,2020)
      WRITE (1,2020)
      GO TO 206
205   WRITE (6,2022)
      WRITE (1,2022)
      IC = 4
206   DO 250 IB = 1,NPB
      NODE1 = IPNODE(1,IB)
      IF (NODE1.EQ.0) GO TO 250
      NODE2 = IPNODE(2,IB)
      IF (IND.EQ.0) NODE1 = 1
      IF (IND.EQ.0) NODE2 = NUMNP
      DO 200 II = NODE1.NODE2
      IC = IC + 1
      IF (IC.LT.56) GO TO 207
      WRITE (6,2022)
      WRITE (1,2022)
      IC = 4
```

```
207   DO 210 I = 1,6
210   D(I) = 0.
      DO 220 I = 1,NDOF
      KK = 1D(I,II)
      IL = 1
      IF (NDOF.EQ.2) IL = 1 + 1
220   IF (KK.NE.0) D(IL) = VEL(KK)
      WRITE (1,2010) II,D
200   WRITE (6,2010) II,D

      IF (IND.EQ.0) GO TO 280
      IF (IC.GE.55) GO TO 250
      IC = IC + 1
      WRITE (6,2050)
      WRITE (1,2050)

250   CONTINUE

      PRINT ACCELERATIONS

280   IF (IND.EQ.0) GO TO 290
      IF (IAC.EQ.0) RETURN
      IF (IDC.EQ.0 .AND. IVC.EQ.0) GO TO 305
290   IC = IC + 6
      IF (IC.GE.54) GO TO 303
      WRITE (6,2050)
      WRITE (1,2050)
      WRITE (6,2030)
      WRITE (1,2030)
      GO TO 308
303   WRITE (6,2032)
      WRITE (1,2032)
      IC = 4
      GO TO 308
305   IC = IC + 5
      WRITE (6,2030)
      WRITE (1,2030)
308   DO 350 IB = 1,NPB
      NODE1 = IPNODE(1,IB)
      IF (NODE1.EQ.0) GO TO 350
      NODE2 = IPNODE(2,IB)
      IF (IND.EQ.0) NODE1 = 1
      IF (IND.EQ.0) NODE2 = NUMNP

      DO 300 II = NODE1,NODE2
      IC = IC + 1
      IF (IC.LT.56) GO TO 307
      WRITE (6,2032)
```

```
      WRITE (1,2032)
      IC = 4
307   DO 310 I = 1,6
310   D(I) = 0.
      DO 220 I = 1,NDOF
      KK = 1D(I,II)
      IL = 1
      IF (NDOF.EQ.2) IL = 1 + 1
320   IF (KK.NE.0) D(IL) = ACC(KK)
      WRITE (1,2010) II,D
300   WRITE (6,2010) II,D
      IF (IND.EQ.0) RETURN
      IF (IC.GE.55) GO TO 350
      IC = IC + 1
      WRITE (6,2050)
      WRITE (1,2050)
350   CONTINUE
      RETURN
```

Algorithm For Principal Stresses

Principal stresses and direction cosines D1, D2, D3 are the direction cosines of principal stresses PS1, PS2, PS3

```
      IF (X5.GE.X6 .AND. X6 .GE. X7) GOTO 430
      IF (X5.GE.X7 .AND. X7 .GE. X6) GOTO 431
      IF (X6.GE.X5 .AND. X5 .GE. X7) GOTO 432
      IF (X6.GE.X7 .AND. X7 .GE. X5) GOTO 433
      IF (X7.GE.X5 .AND. X5 .GE. X6) GOTO 434
      IF (X7.GE.X5 .AND. X6 .GE. X5) GOTO 435
430   X1 = X5
      X2 = X6
      X3 = X7
      GOTO 438
431   X1 = X5
      X2 = X7
      X3 = X6
      GOTO 438
432   X1 = X6
      X2 = X5
      X3 = X7
      GOTO 438
433   X1 = X6
      X2 = X7
```

```
      X3 = X5
      GOTO 438
434   X1 = X7
      X2 = X5
      X3 = X6
      GOTO 438
435   X1 = X7
      X2 = X6
      X3 = X5
      GOTO 438
438   CONTINUE
      PRINCIPAL STRESSES
      PS1(IPT) = X1
      PS2(IPT) = X2
      PS3(IPT) = X3
      DO 440 IS = 1,3
      GOTO (443,445,447),IS
443   AS1 = G1 - X1
      AS2 = G2 - X1
      AS3 = G3 - X1
      GOTO 444
445   AS1 = G1 – X2
      AS2 = G2 – X2
      AS3 = G3 – X2
      GOTO 444
447   AS1 = G1 – X3
      AS2 = G2 – X3
      AS3 = G3 – X3
444   CONTINUE
      AK = G4
      BK = G5
      CK = G6
      YAP1 = AS2*CK – BK*AK
      YAP2 = AK*AK – AS1*AS2
      IF (YAP1 .EQ. 0.0) YAP1 = 1.0
      IF (YAP2 .EQ. 0.0) YAP2 = 1.0
      BJM1 = (BK*BK – AS2*AS3)/YAP1
      BJM2 = (AS1*BK – AK*CK)/YAP2
      BJ1 = BJM1*BJM1
      BJ2 = BJM2*BJM2
      ZIP = DSQRT(BJ1 + BJ2 + 1.0)
```

ULF Wickstrom Program on Thermal Analysis
SUB-PROGRAM-PART of BANG-FIRE/TEMPERATURE

```
1745      SUBROUTINE PROG2(IX,IY,NN,NE,NA,N,KTOP,NODFL,MNODFL,X,Y,T,TT,TMAX,
1746     1  ELA,EV4,A,MAX,P,W,EN,F,FLOW,AXIAL,NODCPL,NODINT,DTA)
1747 C-----------------------------------------------------------------------
     C-----
1748 C-----
1749 C-----                    *** T A S E F ***
1750 C-----
1751 C-----TEMPERATURE ANALYSIS OF STUCTURES EXPOSED TO FIRE
1752 C-----
1753 C-----FINITE ELEMENT PROGRAM FOR ANALYSIS OF TRANSIENT NONLINEAR
1754 C-----HEAT TRANSFER PROBLEMS
1755 C-----
1756 C-----PROGRAMMED BY
1757 C-----ULF WICKSTROM
1758 C-----LUND INSTITUTE OF TECHNOLOGY
1759 C-----MARCH 1979
1760 C-----
1761 C-----------------------------------------------------------------------
1762 C-----THIS IS THE MAIN CONTROL ROUTINE
1763 C-----
1764 C-----DEFINITIONS OF VARIABLES
1765 C-----IX,IY      NUMBER OF X- AND Y-LINES
1766 C-----NN         NUMBER OF NODES IN BASE STRUCTURE
1767 C-----NE         NUMBER OF ELEMENTS IN BASE STRUCTURE
1768 C-----NR         NUMBER OF REGIONS
1769 C-----N          VECTOR OF REGION NUMBERS
1770 C-----KTOP       NODES ADJACENT TO EACH ELEMENT
1771 C-----NODEL      ELEMENTS ADJACENT TO EACH NODE
1772 C-----MNODEL     NUMBER ELEMENTS ADJACENT TO EACH NODE
1773 C-----X,Y        NODE COORDINATES
1774 C-----T          CURRENT NODAL TEMPERATURES
1775 C-----TT         MAXIMUM NODAL TEMPERATURES
1776 C-----TMAX       TRUE IF MAXIMUM NODAL TEMPERATURE OBTAINED
1777 C-----ELA,EV4    DUMMY GEOMETRICAL CONSTANTS
1778 C-----A          HEAT CONDUCTION MATRIX
1779 C-----P          HEAT CAPACITY VECTOR
1780 C-----W          NODAL VOLUME VECTOR
1781 C-----EN         MODAL ENTHALPY VECTOR
1782 C-----F          INTERNAL NODAL HEAT FLOW VECTOR
1783 C-----FLOW       EXTERNAL NODAL HEAT FLOW VECTOR
1784 C-----AXIAL      TRUE IF AXISYMMETRIC PROBLEM
1785 C-----NODCPL     INDICATES COUPLED NODES
1786 C-----NODINT     INDICATES INTERFACE NODES
1787 C-----DTA        DUMMY VECTOR FOR CRITICAL TIME INCREMENT CALCULATION
1788 C-----
1789 C-----PARAMETER CONSTANTS
1790 C-----
1791 C-----NB         MAXIMUM NUMBER OF NODE GROUPS
  71       SUBROUTINE OUTMA2(IX,IY,NN,NE,X,Y,TIME,KTIME,T,TT,TMAX,FLOW,AXIAL)
  72 C-----THIS ROUTINE PRINTS MAXIMUM CALCULATED NODAL TEMPERATURES
  73       COMMON/FIRE/TIM(5C),TB(50),TITFIR
  74       INTEGER TITFIR(18)
  75       LOGICAL TMAX,AXIAL
  76       DIMENSION X(NN),Y(NN),T(NN),TT(NN),TMAX(NN),FLOW(NN)
  77       PRINT 200,TITFIR,X(NN),Y(NN)
  78       IDUM1=1-IY
  79       DO 10 I=1,IX
  80       IDUM1=IDUM1+IY
  81       IDUM2=IDUM1+IY-1
  82       IF(IY.LE.7) PRINT 210, (J,TT(J),J=IDUM1,IDUM2)
  83       IF(IY.GT.7) PRINT 230, (TT(J),J=IDUM1,IDUM2)
```

```
 84  10   CONTINUE
 85       PRINT 220,TIME,KTIME
 86 200   FORMAT(/////1X,75(1HF)/2HF,F/F*   MAXIMAL TEMPERATURES'/'F*,
 87       1 18A4/' F MAX=',F8.3,1CX,'YMAX=',F8.3/'F')
 88 210   FORMAT('F',13(I5,F5,0))
 89 220   FORMAT(2H F/2H F/'F MAX-TIME',F7.2,10X,'NUMBER OF'
 90       1     'TIME INCREMENTS',I5/2H F/2H F/2H F,75(1HF))
 91 230   FORMAT('F',18F7.C)
 92       RETURN
 93       END
 94
 95       SUBROUTINE OUT2(IX,IY,NN,NE,X,Y,TIME,KTIME,DELTI,T,TT,TMAX,FLOW,
 96       1   TFIRE,NODT,AXIAL)
 97 C-----THIS ROUTINE PRINTS NODAL TEMPERATURES AND VOID AIR TEMPERATURES
 98       DIMENSION X(NN),Y(NN),TT(NN),TMAX(NN),FLOW(NN)
 99       LOGICAL TMAX,AXIAL,LDUM,LEN
 00       COMMON/ENCON/H(50),TAIR(2)
 01       COMMON/ENCLOS/LEN,NENC,NENCNG(2),IGREN(2,4),NNODEN(2)
 02       1  INODEN(100);XSYM(7);YSYM(2)
 03       COMMON/TOUT/II,TOUT(100),TIMMAX,DTMAX,TIMFAC,KTMAX,KUPDA
 04       TIME1=TIME-DELTI
 05       DO 5 IJ=1,NN
 06       IF(TMAX(IJ) GOTO 5
 07 C-----IF THE NODAL TEMPERATURES DECREASES SET TMAX=.TRUE. AND PRINT
 08 C-----MAX TEMPERATURE TT
 09       IF(TT(IJ).GT.1.001*T(IJ))
 10       1     PRINT 200,IJ,TT(IJ),TIME1,DELTI
 11       IF(TT(IJ).GT.1.001*T(IJ))TMAX(IJ)=.TRUE.
 12       TT(IJ)=AMAX1(TT(IJ),T(IJ))
 13   5   CONTINUE
 14 C-----IF TIME=TOUT PRINT ALL TEMPERATURES
 15       IF((TIME-TOUT(II)).LT.-1.E-4) GOTO 70
 16       PRINT 100,TIME,KTIME,TFIRE,NDDT
 17       IF(.NOT.LEN) GOTO 30
 18       PRINT 300
 19       DO 20 I=1,NENC
 20   20  PRINT 310,I,TAIR(I)
 21   30  CONTINUE
 22       II1=II+1
 23       IDUM1=1-IY
 24       LDUM=IY.LT.7
 25       DO 10 I=1,IX
 26       IDUM1=IDUM1+IY
 27       IDUM2=IDUM1 +IY-1
201       SUBROUTINE BRBCA(BR,BC,EPSIG,BET,BAR,NUMI,N3,ING1)
202 C-----FORM BOUNDARY RADIATION AND CONVECTION MATRICES
203       DIMENSION BR(NUM1,2),BC(NUMI,2),BAR(NB,NUMI)
204       BR(1,1)=0.
205       BR(1,2)=.33333333*BAR(ING1,2)
206       NUM1=NUMI-1
207       IF(NUM1.EQ.1) GOTO 20
208       DO 10 I=2,NUM1
209       BR(I,1)=.16666667*BAR(ING1,I)
210       BR(I,2)=.3333333*(BAR(ING1,I)+BAR(ING1,I+1))
211   10  CONTINUE
212   20  CONTINUE
213       BR(NUM1,1)=.16666667*BAR(ING1,NUMI)
214       BR(NUM1,2)=.33333333*BAR(ING1,NUMI)
215 C
216       DO 30 1=1,NUMI
217       DO 30 J=1,2
218       BC(I,J)=BET*BR(I,J)
219       BR(I,J)=EPSIG*BR(I,J)
220   30  CONTINUE
221       RETURN
222       END
223
```

```
      SUBROUTINE BRBCB(BR,BC,TR,TC,TRD,TCD,NUMI,DTA,NN,MAX,FLOW,TG,
     1   T,ING1)
C-----THIS ROUTINE CALCULATES EXTERNAL HEAT FLOW BY RADIATION AND
C-----CONVECTION AND ADDS THE CORRESPONDING CONTRIBUTIONS TO THE
C-----VECTOR DATA FOR CALCULATION OF CRITICAL TIME INCREMENT
      DIMENSION BR(NUMI,2),BC(NUMI,2),DTA(NN),FLOW(NN),T(NN)
     1, TR(NUMI),TC(NUMI),TRD(NUMI),TCD(NUMI)
      PARAMETER NB=10,NNP=30,NNB2=2*NNB
      COMMON/BNOD/NUMB(NB),NBOUND(NB,NNB),BAREA(NB,NNB),
     1  EPSG(NB),BETA(NB),CPG(NB),FA(NB)
      LOGICAL FA
C
C-----FIRST NODE
C
      NODE=NBOUND(ING1,1)
      TR2=TR(1)
      TC2=TC(1)
      TR3=TR(2)
      TC3=TC(2)
      TRCD2=TRD(1)
      TCD2=TCP(1)
      TRD3=TRD(2)
      TCD3=TCD(2)
      BR2=BR(1,2)
      BC2=BC(1,2)
      BR3=BR(2,1)
      BC3=BC(2,1)
      FLW=BR2*TR2+BC2*TC2
      FLW=FLW+BR3*TR3
      FLW=FLW+5C3*TC3
      DA=BR2*TRD2+BC2*TCD2
      DA=DA+BR3*TRD3

      SUBROUTINE PTBNDB(T,TFIRE)
C-----SET PRESCRIBED NODAL BOUNDARY TEMPERATURE
      DIMENSION T(1)
      PARAMETER NB=10,NNB=30,NNB2=2*NNB
      COMMON/PTB/NPTNG,NPTG(NB)
      COMMON/BNOD/NUMB(NP),NBOUND(NB,NNB),BAREA(NB,NNB),TH(NB),
     1  EPSG(NB),BETA(NB),CPG(NB),FA(NB)
      COMMON/UNIT/SIGMA,TABS,TINIT,TAMB,TAMB4
      LOGICAL FA
C-----
      IF(NPTNG.EQ.0) RETURN
C-----EACH PRESCRIBED TEMPERATURE BOUNDARY NODE GROUP
      DO 10 IB=1,NPTNG
      TG=TAMB
      ING1=NPTG(IB)
      IF(FA(ING1)) TG=TFIRE
      NUMI=NUMB(ING1)
      DO 10 I=1,NUMI
      NODE=NBOUND(ING1,1)
      T(NODE)=TG
 10   CONTINUE
      RETURN
      END

      SUBROUTINE RADVEC(F,ETA,N,Q)
C-----THIS ROUTINE FORMS THE LOCAL ENCLOSURE SURFACE RADIATION HEAT
C-----EXCHANGE VECTOR Q=E*ETA
      DIMENSION Q(1),ETA(1),E(N,N)
      QTOT=0.
      DO 20 I=1,N
      QT=0.
      DO 10 J=1,N
 10   QT=QT+E(I,J)*ETA(J)
      QTOT=QTOT+QT
```

```
 20   Q(I)=QT
      RETURN
220   FORMAT(/'TOTAL RADIATION HEAT EXCHANGE',E11.3)
      END

      SUBROUTINE REG2(NN,NE,NR,N,KTOP,X,Y,NODEL,MNODEL)
C-----THIS SUBROUTINE FORMS VECTOR OF REGION NUMBERS N OF EACH ELEMI
      DIMENSION X(NN),Y(NN),N(NE),KTOP(4,NE),NODEL(4,NN),MNODEL(NN)
      PARAMETER MNR=10
      COMMON/RGEO/ELFICT(MNR),ET(MNR),SRDIAC(4,MNR)
      LOGICAL ELFICT
      EPS=1.E-7
      DO 10 I=1,NE

      N(I)=1
      IF(NR.EQ.1) GOTO 10
      ND1=KTOP(1,I)
      ND2=KTOP(4,I)
      DO 5 J=2,NR
      IF((X(ND1)-SRDIAC(3,J)).GT.-EPS) GOTO 5
      IF((Y(NC1)-SRDIAC(4,J)).GT.-EPS) GOTO 5
      IF((X(ND2)-SRDIAC(1,J)).LT.EPS) GOTO 5
      IF((Y(NC2)-SRCIAC(2,J)).LT.EPS) GOTO 5
      N(I)=J
 5    CONTINUE
10    CONTINUE
      DO 40 T=1,NN
      II=0
20    DO 30 IE=1,NE
      N1=N(IE)
      IF(ELFICT(N1)) GOTO 30
      DO 20 J=1,4
      IF(KTOP(J,IF).NF.I) GOTO 20
      II=II+1
      NODEL(II,I)=IE
      IF(II.EQ.4) GOTO 30
20    CONTINUE
30    CONTINUE
      MNODEL(I)=II
40    CONTINUE
      RETURN
      END

589       SUBROUTINE ENCON1
590 C-----THIS ROUTINE FORMS CONVECTION ARRAY H
591       PARAMETER NB=10,NNB=30,NNB2=2*NNB
592       COMMON/BNOD/NUMB(NB),NBOUND(NB,NNB),BAREA(NB,NNB),TH(NB),
593       1  EPSG(NB),BETA(NB),CPG(NB),FA(NB)
594       COMMON/ENCLOS/LEN,NENC, NENCNG(2),IGREN(2,4),NNODEN(2),
595       1  INODEN(100),XSYM(2),YSYM(2)
596       COMMON/ENCON/H(50),TAIR(2)
597       COMMON/DUMMY/HZ(25),DUM 2(25)
598       LOGICAL LEN
599       LOGICAL XSYM,YSYM,SYM
600       INTEGER EN
601       IND=1
602 C-----FORM ZONE CONVECTION ARRAY
603 C-----EACH VOID
604       DO 150 EN=1,NENC
605       SYM=XSYM(EN).OR.YSYM(EN)
606       IN=0
607       NENG=NENCNG(EN)
608 C-----EACH NODE GROUP
609       DO 10 IG=1,NENG
610       I1=IGREN(EN,IG)
611       NUMI=NUMB(I1)
612       BE=BETA(I1)
```

```
613 C-----EACH ZONE
614       DO 10 I=2,NUMI
615       IN=IN+1
616  10   HZ(IN)=BE*BAREA(I1,1)
617 C-----FORM NODE CONVECTION ARRAY
618       CALL HTRANS(HZ,H(IND),IN,SYM)
619       N=IN
620       IF(SYM) N=N+1
621       IND=IND+N
622 150   CONTINUE
623       RETURN
624       END
625
2013      SUBROUTINE TIME
2014 C-----READ TIME INTEGRATION CONTROL DATA
2015      COMMON/TOUT/II,TOUT(100),TIMMAX,DTMAX,TIMEAC,KTMAX,KUPDA
2016      PRINT 200
2017 C-----
2018      READ 100,NT,TIMMAX,DTMAX,TIMFAC,KTMAX,KUPDA
2019 C-----
2020      IF(DTMAX.EQ.0) DTMAX= TIMMAX
2021      IF(TIMFAC.EQ.0) TIMFAC=.8
2022      IF(KTMAX.EQ.0) KTMAX=1000
2023      IF(KUPDA.EQ.0) KUPDA=1
2024 C-----
2025      READ 100,(TOUT(I),1=1,NT)
2026 C-----
2027      PRINT 210,TIMMAX,DTMAX,TIMFAC,KTMAX,KUPDA
2028      PRINT 220,(TOUT(I),1=1,NT)
2029 100   FORMAT()
2030 220   FORMAT('PRINT OUT TIMES',3X,8G7.2/(19X,8G7.2))
2031 200   FORMAT(//'TIME'/' ****'/)
2032 210   FORMAT('MAXIMUM TIME=',G8.3/' MAXIMUM TIME INCREMENT=',G8.3/
2033      1  'CRITICAL TIME INCREMENT FACTOR=',G8.3/
2034      2  'MAXIMUM NUMBER OF TIME INCREMENTS=',I5/
2035      3  'NUMBER OF STEPS BETWEEN UPDATING OF CONDUCTION MATRIX=',I5)
2036      RETURN
2037      END
 708      SUBROUTINE ENRAD1(X,Y)
 709 C-----FORM RADIATION MATRICES FOR EACH VOID AND STORE THEM IN
 710 C-----THE VECTOR E.
 711 C-----CALCULATE VIEW-FACTOR MATRIX VIEW AND ZONE AREA VECTOR D
 712      DIMENSION X(1),Y(1),A(25,25),B(25,25)
 713      PARAMETER NB=10,NNB=30,NNB2=2*NNB
 714      COMMON/BNOD/NUM B(NB),N BOUND(NB,NNB),BAREA(NB, NNB),
 715      1  EPSG(NB),BETA(NB),CPG(NB),FA(NB)
 716      COMMON/ENCLOS/LEN,NENC,NENCNG(2),IGREN(2,4),NNODEN(2),
 717      1  INODEN(100),XSYM(2),YSYM(2)
 718      COMMON/ENRAD/E(1000)
 719      COMMON/UNIT/SIGMA,TABS
 720      COMMON/DIM/MAXNG,MAXNOD
 721      COMMON/DUMMY/D(25),DUM2(25)
 722      DIMENSION VIEW(25,25)
 723      EQUIVALENCE (A(1),VIEW(1))
 724      DATA IND,IE/0,11
 775      LOGICAL LEN
 726      LOGICAL XSYM,YSYM,SYM
 727      INTEGER EN
 728 C-----EACH VOID
 729      DO 150 EN=1,NENC
 730      CALL VIEWFC(X,Y,D,EN,VIEW,MAXNOD)
 731 C-----FORM THE MATRICES A AND B
 732      NENG=NENONG(EN)
 733      IN=0
 734 C-----EACH NODE GROUP
 735      DO 120 IG=1,NENG
 736      I1=IGREN(EN,IG)
```

```
      NUMI=NUMB(I1)
C-----EACH ZONE
      DO 120 I=2,NUMI
      IN=IN+1
      JN=0
      DO 120 JG=1,NENG
      J1=IGREN(EN,JG)
      NUMJ=NUMB(J1)
      EPSJ=EPSG(J1)
      DO 120 J=2,NUMJ
      JN=JN+1
      B(IN,JN)=VIEW(IN,JN)*SIGMA
      A(IN,JN)=-VIEW(tN,JN),(1.-EPSJ)/EPSJ/D(JN)
      IF B(IN.NE.JN) GOTO 120
      B(IN,JN)=-SIGMA+B(IN,JN)
      A(IN,JN)=1./EPSJ/D(JN)+A(IN,JN)
120   CONTINUE
      N=IN
C-----INVERT A AND STORE RESULT IN A
      CALL INVER(A,N,MAXNOD)
C-----MULTIPLY A AND B AND STORE RESULT IN A
      CALL MULT(A,B,N,MAXNOD)
      SYM=.FALSE.
      IF(XSYM(EN).OR.YSYM(EN)) SYM=.TRUE.
      NZ=N
      IF(SYM) N=N+1
C-----TRANSFORM THE LOCAL RADIATION MATRICE A AND STORE THE RESULT IN
C-----VECTOR E
C-----B IS EMPLOYED AS A DUMMY MATRIX
      CALL ETRANS(A,B,E(IE),N,NZ,SYM,MAXNOD)
      IE=IE+N*N
      SUBROUTINE FQBNDB(T,FLOW,DTA,NN,MAX,TFIRE)
C-----THIS ROUTINE PREPARES CALCULATION OF PRESCRIBED BOUNDARY FLOW
      DIMENSION T(NN),DTA(NN),FLOW(NN)
      PARAMETER NB=10,NNB=30,NNB2=2*NNB
      COMMON/FQB/NFQNG,NFQG(NB),TR(NNB),TC(NNB)
      1   ,BR(NNB2),BC(NNB2),TRD(NNB),TCD(NNB)
      COMMON/BNOD/NUMB(NB),NBOUND(NB,NNB),BAREA(NB,NNB),
      1  EPSG(NB),BETA(NB),CPG(NB),FA(NB)
      COMMON/UNIT/SIGMA,TABS,TINIT,TAMB,TAMB4
      LOGICAL FA
C-----NULL FLOW VECTOR
      DO 777 I=1,NN
777   FLOW(I)=0.
C-----RETURN IF NO PRESCRIBED BOUNDARY FLOW
      IF(NFQNG.EQ.0) RETURN
      TF4=(TFIRE+TABS)**4
      IND=1
C-----EACH BOUNDARY FLOW NODE GROUP
      DO 30 IB=1.NFQNG
      TG4=TAMB4
      TG=TAMB
      ING1=NFQG(IB)
      IF(FA(ING1)) TG=TFIRE
      IF(FA(ING1)) TG4=TF4
      NUMI=NUMB(ING1)
      CP=CPG(ING1)
      DO 20 I=1.NUMI
      NODE=NBOUND(ING1,I)
      TNODE=T(NODE)
      TNABS=TNODE+TABS
C-----RADIATION
      TRD(I)=4.*TNABS**3
      TR(I)= TG4-TNABS**4
C-----CONVECTION
      DUM=TG-TNODE
      TCD(I)=CP*ABS(DUM)**(CP-1.)
```

III

Threshold Limits

III.1

The aim of this appendix is to survey the state of the art of the impact biomechanics in car-to-pedestrian collisions. The information will be organized in a way that makes it easy to overview, which provide the updated references and values for use in car crash safety research.

A literature review was carried out with collected scientific publications. He work focused on the biomechanical impact responses, injury mechanisms, tolerance levels, injury criteria for the body segments, and reference values for the whole body in loading conditions that have relevance for the mechanical loading to the human body in pedestrian accidents.

III.2 Pedestrian Injuries

Determination of the cause of injuries to pedestrians is complicated, as the body parts could come into contact with the car and/or the ground. In this report, the emphasis will place on the injury biomechanics in connection with car front impacts.

III.2.1 Injury Distribution by Body Segments

The injury frequency of the pedestrian body segments has been investigated since the 1960s in quite number of studies by researchers from different countries (McLean 1972; Fisher and Hall 1972; Tarriere et al. 1974; Appel et al. 1975; Ashton et al. 1977; Lucchini and Weissner 1978; Fowler and Harris 1983; Niederer and Schlumpf 1984; Pritz 1983; Harris and Grew 1986; Kessler 1988; Ishikawa et al. 1993). The head and lower extremities have been found to be most frequently injured. Table III.1 shows an example of the distribution of injuries by body regions (Otte 2001).

Table III.1. Distribution of injuries by body regions of pedestrians struck by the front of cars (Otte 2001)

body region	293 cases	
	distribution of injured body regions (%) at primary impact (with 933) injuries	distribution of injured body regions (%) at secondary impact (with 463) injuries
head	42.8	35.6
neck	0.8	0.4
thorax	22.2	15.7
upper extremities	33.8	37.7
abdomen	6.9	5.5
pelvis	14.1	10.6
lower extremities	66.1	43.7

III.2.2 Overall Pedestrian Impact Responses

The kinematics of the pedestrians and the distribution of the injuries in vehicle–pedestrian impacts are influenced by the impact speed, type of vehicles, stiffness, and shape of the vehicle front (such as the bumper height, bonnet height and length, windscreen frame), age and size of the pedestrians, and standing position of the pedestrian relation to the vehicle front.

When an adult is struck by a car front, the first contact occurs between the bumper and either the leg or knee-joint area, followed by thigh-to-bonnet edge contact. The lower extremity of the body is accelerated forwards and the upper body is rotated and accelerated relative to the car. Consequently, the pelvis and thorax are impacted by the bonnet edge and top, respectively, Tables III.2 and III.3. The head may hit the bonnet or windscreen at a velocity estimated as ratio of 0.7–0.9 to the car-travel speed for big car–bonnet impacts (Pritz 1983) and 1.1–1.4 for small car head–windscreen impacts (Cavallero et al. 1983). The victims then fall onto the ground. Injuries are usually caused by a direct impact to body segments and a force transmission through body segments. During the course of car–pedestrian contacts, the whole body wraps around the front of the car. The contact location of the upper body segments can be estimated by the wrap-around distance (WAD) along the card front surface, when a pedestrian experiences the most common lateral impact loading.

The representative distribution of the injuries to an adult pedestrian in frontal car–pedestrian collisions, trajectories of the head with respect to small and big cars, changes of the locations of the head impact speeds, and the WAD.

To compare injuries to pedestrian on a standardized basis, a relative position of the bumper and bonnet leading edge to a pedestrian I defined as (Ashton et al. 1977)

$$\lambda_\mathrm{b} = \frac{h_\mathrm{b}}{h_\mathrm{p}} \quad \text{and} \quad \lambda_\mathrm{e} = \frac{h_\mathrm{e}}{h_\mathrm{p}},$$

where λ_b is the relative bumper position, λ_b the bumper height, λ_p the pedestrian height, λ_e the relative leading edge position of the bonnet and λ_e the leading edge height.

III.3 Threshold and Tolerances

III.3.1 Thorax

Table III.2. Thorax lateral impact injury tolerances

force (kN)	deflection (mm)	compression (%)	TTI (g)	VC_{max} ($m\,s^{-1}$)	references
	58–61				Bierman et al. (1946)
7.4 (AISO)		35 (AIS3)			Tarrierre et al. (1979)
10.2 (AIS3)		half thorax			
5.5 (25%		38.4 (AIS4)		1.47	Viano (1989)
AIS4)		whole thorax			
		35 (AIS3)			Stalnaker et al. (1979)
		half thorax			
			85 (adult)		FMVSS 214
			60 (child)		NHTSA (1993)
				1.0	Cavanaugh et al. (1990)

III.3.2 Pelvis

Table III.3. Pelvis injury tolerances in lateral impact

body parts	compression force (kN)	deflection (mm)	acceleration (g)	compression (%)	references
pelvis	10 (50thM)				Cesari et al. (1982)
	4.6 (5thF)				
			50–90		Tarrierre et al. (1979)
	9–12.5			27	Viano (1989)
				32.6	Cavanaugh et al. (1990)

The long bone strength was also presented in Tables III.4, III.5 and III.6 in terms of tensile and compressive stress responses within the bone structures.

The femur fractures were reported at peak impact forces from 3 to 10 kN and the moments at about 320 N m (Kress et al. 1993).

The tibia fracture were reported at peak impact forces from 2.5 to 8 kN (Kramer et al. 1973; Pritz 1978; Bunketorp 1983). Nyquist et al. (1985), determined the strength of the tibia in dynamic three-point bending tests with cadaver leg specimens.

Table III.4. The tolerance of the long bones

body parts	axial compression force (kN)	torque male/fem (Nm)	bending moment (Nm)	transverse shear force (kN)	references
femur	3–10		320		Kress et al. (1993),
	7.7 (M) 7.1 (F)	175/136	310 (M) 180 (F)	3.9(M) 2.6 (F)	Messerer (1880),
tibia				2.5–8	Bunketorp 1983
			317 ± 88 (M) 278 ± 30 (F)	4.7 ± 1.4 (M) 4.1 ± 1.2 (F)	Nyquist et al. (1985),
	10.4 (M) 7.5 (F)	89/56	207 (M) 124 (F)	3.4 (M) 2.3 (F)	Messerer (1880),
			208 (20–29 year) 164 (70–89 year)		Kramer et al. 1973; Pritz (1978),
fibula	0.6 (M) 0.5 (F)	9/10	27 (M) 17 (F)	0.5 (M) 0.3 (F)	Messerer (1880),
humerus	5.0 (M) 3.6 (F)	70/55	151 (M) 85 (F)	2.7 (M) 1.7 (F)	Messerer (1880),
radius	3.3 (M) 2.2 (F)	22/17	48 (M) 23 (F)	1.2 (M) 0.7 (F)	Messerer (1880),
ulna	5.0 (M) 3.6 (F)	14/11	49 (M) 28 (F)	1.2 (M) 0.8 (F)	Messerer (1880),

Remarks:
(1) Messerer carried out the studies in static loading condition

III.3.3 The Knee Joint

Causation and knee injury mechanisms – the knee injuries is usually caused by a bumper impact to the knee region as well as by the forces transferred through the knee joint, including femoral/tibial condyle fractures, patella fracture, ligament tearing and rupture (Fig. III.1).

The knee reaction forces can be considered as a combination of a shear force and a bending moment which consists of a ligament tension force and a joint surface compression force.

Shearing and bending injury mechanisms of the knee joint to lateral impact was proposed by Kajze et al. (1990 and 1993) in their study by using cadaver specimens. Figure III.1 show a proposed model of transmission of a shear force and bending moment through the knee. When the leg is struck from lateral side near the knee level, which is the most common collision configuration, a shearing dislocation between the knee articular interfaces occurs due to the delay of the femur movement. Table III.7 shows the strength of the knee due to the bending and shearing forces.

Table III.5. The tensile strength of the long bones

	elastic modulus (MPa)	yield stress (MPa)	ultimate stress (MPa)	references
femur				
20–29 years	17,000	120	140	Burstein (1976)
30–39 years	17,600	120	136	
40–49 years	17,700	121	139	
50–59 years	16,600	111	131	
60–69 years	17,100	112	129	
70–79 years	16,300	111	129	
80–89 years	15,600	104	120	
wet	13,507–14,609		77–84	Evans (1951)
dry	17,159–19,020		99–111	
wet	17,259		122	Yamada (1970)
dry	20,201		151	
tibia				
20–29 years	18,900	126	161	Burstein (1976)
30–39 years	27,000	129	154	
40–49 years	28,800	140	170	
50–59 years	23,100	133	164	
60–69 years	19,900	124	147	
70–79 years	19,900	120	145	
80–89 years	29,200	131	156	
wet	18,044		140	Yamada (1970)
dry	20,593		170	

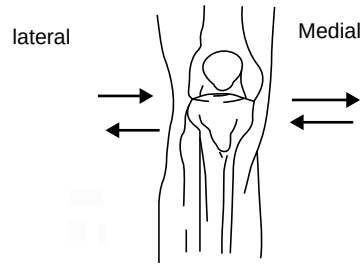

Fig. III.1. The forces acting on the knee joint during a lateral impact and possible injuries

Table III.6. The compressive strength of the long bones

	elastic modulus (MPa)	yield stress (MPa)	ultimate stress (MPa)	references
femur				
20–29 years	18,100		209	Burstein (1976)
30–39 years	18,600		209	
40–49 years	18,700		200	
50–59 years	18,200		192	
60–69 years	15,900		179	
70–79 years	18,000		190	
80–89 years	15,400		180	
20–69 years			145–167	Yamada (1970)
tibia				
30-39 years	35,300		213	Burstein (1976)
40–49 years	30,600		204	
50–59 years	24,500		192	
60–69 years	25,100		183	
70–79 years	26,700		183	
80–89 years	25,900		197	

Table III.7. The strength of the knee

body parts	bending force (kN)	bending moment (Nm)	shearing force (kN)	references
knee		156 (average)		Levine et al. (1984)
		101 ± 21 ($15\,\mathrm{km\,h^{-1}}$)	1.8 ± 0.4 ($15\,\mathrm{km\,h^{-1}}$)	Kajzer et al. (1990)
		123 ± 35 ($20\,\mathrm{km\,h^{-1}}$)	2.6 ± 0.5 ($20\mathrm{km\,h^{-1}}$)	Kajzer et al. (1993)
	0.75–3 kN (quasistatic)	129 (average)		Ramet et al. (1995)
		331 ± 79 ($40\,\mathrm{km\,h^{-1}}$)	2.6 ± 0.5 (20 and $40\,\mathrm{km\,h^{-1}}$)	Kajzer et al. (1997) Kajzer et al. (1999)

Remarks

(1) The lateral shearing responses of the knee joint at impact speeds of 15–20 $\mathrm{km\,h^{-1}}$, the transverse dislocation between articular surfaces as investigated. The peak transverse dislocation was 9–11 mm during the first 10 ms of the impact.

(2) The knee joint to lateral bending load at impact speeds of 15–20 $\mathrm{km\,h^{-1}}$, lateral bending angle was about 8–13° at 20 ms after impact.

(3) The intercondylar eminence fracture and ACL failure are attributed to the lateral shearing force acting on the articular interface and the MCL failure is correlated to the lateral bending moment during the impact by the bumper.

III.3.4 Body Segments: A Summary

The threshold and injury criteria used in research on pedestrian safety are summarized in Table III.8 based on the results from extensive studies in the past three decades. The injury related parameters can be used for evaluation the safety performance of the vehicle front structures.

Table III.8. The thresholds and injury criterion for the body segments

parameters	body segments	tolerance levels
force	tibia	4 kN[a]
	knee	2.5 kN (shear)
	femur	4 kN[a]
	pelvis	4 kN (female)/10 kN (male)
HIC	adult	1,000[a]
	child	1,000[a]
linear acc	head	80 g
	thorax	60 g
	tibia	150[a] g
angular acc	head	3,000 rad s^{-2}
rotation angle	knee	15°[a]
	neck	60°
bending moment	knee	350 N m
	tibia	200 N m
	femur	220[a] N m
searing dislocation	knee	6[a] mm

[a] Acceptance levels of EEVC proposal

IV

Injury and Protection Criteria

STATEMENT

The Analysis and Computational Results Need To be Checked Against the Empirical Formulae and Experimental Test Results. They are Bracketed in this Appendix as a Reference. The Main Idea is to Check the Validity of Computational Results and Their Limits Against these Approved Limits.

IV.1 Neck Injury Criterion NIC

Assuming that pressure gradients caused by a sudden change of the fluid flow inside the fluid compartments of the cervical spine are related to neck injuries, the neck injury criterion NIC was developed by Bostrom et al. (1996). The definition of the NIC as a function of time was validated based on animal experiments. A relation to predict injury cause by pressure gradients (IV.1) was found between the acceleration in the anterior–posterior direction (i.e., x-direction when using SAE J211/2) of the center of gravity of the head relative to the first thoracic vertebra (T1) and the velocity derived thereof.

$$\mathrm{NIC(t)} = 0,2\mathrm{a}_{\mathrm{rel}}^{(\mathrm{t})} + \mathrm{v}_{\mathrm{rel}}^{(\mathrm{t})} \tag{IV.1}$$

The threshold value above which a significant risk of sustaining minor (AISI) neck injury is assumed to be inherent was set to be $15\,\mathrm{m^2\,s^{-2}}$. This value has served well in accidentological studies and is still used. However, it has emerged that reasonable values are only obtained for the retraction phase of a rear-end impact, i.e., when, in a vehicle fixed reference system, both acceleration and velocity are directed backwards. In addition, it tuned out that a considerable error is introduced to the NIC(t)-curve as soon as the head is no longer parallel to T1, i.e., the head extension angle reaches values of about 20–30°. Thus, the $\mathrm{NIC_{max}}$ was introduced, which indicates that the maximum value of the NIC(t)-curve found within the time interval of the first 150 ms has to be used.

A modification of the NIC for low-speed frontal impact – called NIC protraction – has been proposed (Bostrom et al. 2000) and was related to long-term AISI neck injuries, i.e., for AISI injuries with symptoms for more

than 6 months. As a threshold for 50% injury risk, $25\,\mathrm{m^2\,s^{-2}}$ was proposed. Bohmann et al. (2000) reduced this value to $15\,\mathrm{m^2\,s^{-2}}$ extending the injury assessment to short-term and long-term consequences. The following equations are used to determine $\mathrm{NIC_{protraction}}$:

$$\mathrm{NIC_{generic}}(t) = 0,2a_{\mathrm{rel}}(t) + v_{\mathrm{rel}}(t)|v_{\mathrm{rel}}(t)| \tag{IV.2}$$

$$\mathrm{NIC_{protraction}}(t) = |\mathrm{Min}(\mathrm{NIC_{generic}}(t))| \tag{IV.3}$$

IV.2 N_{ij} Neck Injury Criterion

This criterion was proposed by the US National Highway Traffic Safety Administration (NHTSA) (Klinch et al. 1996; Kleinberger et al. 1998) to assess severe neck injuries in frontal impacts, including those with airbag deployment and thus accounting for more severe impact conditions at higher Δv. Recently, the N_{ij} criterion was included as part of FMVSS 208.

The underlying concept for the N_{ij} can be found in a study by (Prasad and Daniel (1984) who performed crash tests using piglets as child surrogates. As a result with respect to neck injuries, they suggested to combine axial forces with moments for a composite neck injury indicator. The N_{ij} criterion developed implies a linear combination of the axial forces and the flexion/extension bending moment, both normalized by critical intercept values:

$$N_{\mathrm{ij}} = \frac{F_z}{F_{\mathrm{int}}} + \frac{M_y}{M_{\mathrm{int}}} \tag{IV.3}$$

where F_z and M_y are the axial force and the sagittal bending moment, respectively, Fint and Mint indicate the according critical intercept values. These intercept values were established and validated for a three-year-old dummy. Scaling techniques were used to obtain the according intercept values for other dummy sizes and thus making the N_{ij} eligible for those shown in Table IV.1. Hence, evaluating the criterion for all possible load cases, four different values are obtained: N_{te} for tension and extension N_{tf} for tension and flexion as well as N_{ce} and N_{cf} giving analogue values for compression. An injury threshold value of 1.0 applies for each load case.

Adopting the N_{ij} to analyze the effect of deploying side airbags, Duma et al. (1999) replaced the sagittal bending moment by the total bending moment.

To assess AISI neck injury, reduced threshold values of 0.2 and 0.16 for long-term and short-term injury, respectively, were proposed (Bostrom et al. 2000; Bohmann et al. 2000).

However, evaluating the N_{ij} in its original form for rear-end collisions (for which it was not designed) produced difficulties in the interpretation of

Table IV.1. Intercept values for calculating N_{ij} as included in FMVSS 208

dummy	M_y (flexion) (N m)	M_y (extension) (N m)	F_z (compression/ tension) (N)
50th%	310	125	4,500
5th%	155	62	3,370
6 year	93	39	2,800
3 year	68	27	2,120

the results obtained (Linder et al. 2000). Therefore a modification of the N_{ij} criterion – called the N_{km} – which is suitable for the assessment of low-speed rear-end collisions was developed.

IV.3 Neck Protection Criterion N_{km}

The neck protection criterion N_{km} was proposed by Schmitt (2001). It is based on the hypothesis that such a criterion should take into account a linear combination of loads and moments. A similar approach led to the definition of the N_{ij} criterion for frontal impact Kleinberger et al. (1998) and thus the newly proposed N_{km} can be regarded as a modification thereof.

However, with respect to possible injury mechanisms in rear-end collisions, sagittal shear forces rather than axial forces are regarded as the critical load case. A combination of shear and the sagittal bending moment accounts for a constellation often found in the cervical spine also during S-shape formation (e.g., Deng et al. 2000). To date, the S-shape formation is mainly associated with the retraction phase, but, looking at the kinematics, an opposite S-shape, i.e., the torso lags behind the head, could result in a similar deformation and therefore also incorporate an injury risk (Bostrom et al. 2000). This opposite S-shape which can for instance be observed during the rebound phase is not assessed by the maximum NIC due to its time limitation.

Furthermore, it is assumed that shear forces could potentially be harmful to the facet joints, in particular in the upper neck region (Yang et al. 1997; Deng et al. 2000; Winkelstein et al. 2000). Although the actual injury mechanism is unknown, the load cases of shear and extension/flexion moment seem to be relevant for neck injuries. Therefore the N_{km} does not address a single injury mechanism but takes into account a potential injury risk caused by the combination of loads and moments.

To combine shear and moment linearly seems straightforward, as for the calculation of a resulting load on a certain structure of the neck a linear combination of the existing forces and moments follows the understanding of simple mechanics. Additionally, the interpretation of the N_{km} results becomes more obvious when implementing a linear combination – a practical consideration which is important for the use of the criterion.

In the human, axial compression/tension forces are considered to influence the amount of shear (Yang et al. 1997) and are as such included. However, difficulties arise when measuring such axial forces. Performing crash tests using an ATD with standard instrumentation and an additional load cell at the upper neck position, the latter will measure the occurring axial forces. Different reasons causing an inaccuracy in such measurements can be identified:

- The centripetal force from rotation of the dummy around the pelvis is measured as an axial force.
- Due to the fact that most dummies of today (except the BioRID dummy) do not represent the thoracic kyphosis, they consequently do not account for compression forces resulting from the straightening (ramping) effect.
- Recent dummy designs do not allow physiological backward movement of the head during the retraction phase, i.e., when the torso is pushed forward by the seat back, the head is expected to lag behind due to its inertia. However, as the neck is connected with joints to the head and to the torso, a rotation of the head is originated which creates axial forces.
- In cases where the head in extension reaches above the head restraint and causes it to be pushed into a lower position ("hammer effect"), axial forces from this extension are also measured.

Due to this inaccuracies concerning the measurement of the axial forces, they were not explicitly included the N_{km} Hence, the N_{km} criterion was defined according to the following equation:

$$N_{\mathrm{km}}(t) = \frac{F_x(t)}{F_{\mathrm{int}}} + \frac{M_y(t)}{M_{\mathrm{int}}}, \tag{IV.4}$$

where $F_x(t)$ and $M_y(t)$ are the shear force and the flexion/extension bending moment, respectively; both values should be obtained from the load cell positioned at the upper neck. F_{int} and M_{int} represent critical intercept values used for normalization.

Distinguishing positive shear, negative shear, flexion, and extension, the N_{km} criterion identifies four different load cases: N_{fa}, N_{ea}, N_{fp} and N_{ep}. The first index represents the bending moment (f: flexion, e: extension) and the second indicates the direction of the shear force (a: anterior, i.e., in positive x-direction, p: posterior, i.e., in negative x-direction). The sign convention according to SAE J211/2 was used. Consequently, positive shear forces measured at the upper neck load cell indicate that the head is moved backwards relative to the uppermost cervical vertebra.

The intercept values used to calculate the criterion are shown in Table IV.2 which exhibits the human tolerance levels for the causation of AIS 1 injuries (Goldsmith and Ommaya 1984). These values were determined on the basis of volunteer experiments. Mertz and Patrick (1993) and suggest tolerance levels up to which no injury is expected. The tests revealed no difference for the maximum shear tolerated in anterior and posterior direction. Sled tests as well as computational simulations have been evaluated (Schmitt et al. 2002a) to validate the proposed criterion.

Table IV.2. Intercept values for calculating N_{km}

load case	value	reference
extension	47.5 N m	Goldsmith and Ommaya (1984) Mertz and Patrick (1993)
flexion	88.1 N m	
negative and positive	845 N	

For computation of the N_{km} values, the load curves measured are divided by the according intercept values, then the bending modes and the load types under investigation are identified. Finally the N_{km} values are obtained by adding the adequate shear force and moment curves, while keeping the time scale unchanged, and determining the maximum of the resulting curve. Hence, the N_{ep} for instance represents the maximum value in time when extension and negative shear occur simultaneously. If a certain combination of loads and moments is not observed within the time interval analyzed, the N_{km} quadruples can be incomplete.

When regard to a critical N_{km} value, 1.0 was used taking into account that either a moment or a shear force exceeding the intercept value produces a risk of sustaining neck injuries.

To date, the N_{km} has shown its usefulness to assess low speed rear-end collisions in various tests (e.g., Muser et al. 2002, Szabo et al. 2002, Kullgren et al. 2003). In particular, it was shown the N_{km} values allow for the characterization of the crash phase of forward movement and as such the N_{km} gives additional information to that gained by the NIC_{max}, which accounts for the earlier phase only. As for the correlation of the N_{km} and the risk of sustaining neck injuries Muser et al. (2003) found the Nea load case to be the strongest predictor. Also Kullgren et al. (2003) report a good correlation of the N_{km} with risk of AISI neck injury and thus recommend to use the N_{km} (and the NIC) in rear-end test evaluation.

Furthermore, it was shown that the N_{km} values are capable to quantify different characteristics of seat design (Muser et al. 2002). With respect to the ongoing discussion about the design principles for the perfect car seat, i.e., the conflict on allowing deformation (plasticity) vs. elasticity (Parkin et al. 1995) the N_{km} was found to be a helpful tool since minimizing both values simultaneously indicates a balanced seat design. Consequently, the criterion was proposed to be included in an ISO standard seat test procedure.

IV.4 Intervertebral Neck Injury Criterion (IV-NIC)

Assuming that neck pain sustained from rear-end collisions is caused by an intervertebral rotation exceeding the limit of physiological intervertrebral motion, Panjabi et al. (1999) proposed the intervertebral neck injury criterion (IV-NIC). The IV-NIC is defined as the ratio of the intervertebral motion

under traumatic loading θ_{trauma} and the physiological range of motion θ_{physio} (IV.6). The criterion is defined for each intervertebral joint i and is calculated separately for flexion and extension.

$$\text{IV} - \text{NIC}_i = \frac{\theta_{\text{trauma},i}}{\theta_{\text{physio},i}}. \tag{IV.5}$$

Hence the maximum IV-NIC value identifies the time, location and bending mode of the maximal intervertebral rotation and for values greater than 1.0, it indicates that the physiological range is exceeded.

IV.5 Lower Neck Load Index (LNL)

Recently a further neck injury criterion to assess the risk of soft tissue neck injuries, called Lower Neck Load Index (LNL) was proposed by Heitplatz et al. (2003). The LNL takes into account three force components and two of the moment components measured at the base of the neck (IV.6). Hence, evaluation of this criterion requires a dummy that is equipped with a lower neck load cell.

$$\text{LNL}(t) = \left| \frac{\sqrt{\left(My_{\text{lower}}\,(t)\right)^2 + \left(Mx_{\text{lower}}(t)\right)^2}}{C_{\text{moment}}} \right| + \left| \frac{\sqrt{\left(Fy_{\text{lower}}(t)\right)^2 + \left(Fx_{\text{lower}}\,(t)\right)^2}}{C_{\text{shear}}} \right| + \left| \frac{Fz_{\text{lower}}\,(t)}{C_{\text{tension}}} \right| \tag{IV.6}$$

where Fi(t) and Mi(t) are the force and moment components, respectively. The denominators represent intercept values which are proposed to be $C_{\text{moment}} = 15$, $C_{\text{shear}} = 250$ and $C_{\text{tension}} = 900$ for a RID dummy (Heitplatz et al. 2003). For other dummies intercept values are not yet proposed.

IV.6 Neck Displacement Criterion (NDC)

The neck displacement criterion (NDC) has been proposed to assess the risk of soft tissue neck injury (Viano and Davidsson 2001b). It addresses the S-shape of the neck by taking into account the extension moment, displacement in z (axial) direction and displacement in X (sagittal) direction. By plotting the head rotation vs. the x-displacement and plotting the z-displacement vs. the x-displacement, the two NDC diagrams are obtained (Fig. IV.1). Sled tests utilizing volunteers, the BioRID and the Hybrid III dummy.

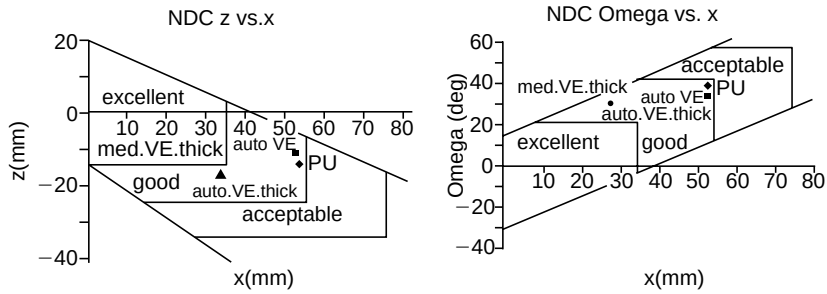

Fig. IV.1. NDC diagrams plotting axial (z) displacement vs. sagittal (x) displacement (left) and head rotation vs. sagittal displacement (right). Furthermore the tolerance corridors for the BioRID dummy are included rating "excellent," "good" and "acceptable." As an example, the NDC diagrams show results of a study investigating the benefit of different head restraint material (Schmitt et al. 2003)

.

IV.7 Compression Criterion (C)

Analyzing blunt impact tests Kroell et al. (1971, 1974) concluded that the maximum thorax compression correlated well with AIS while force and acceleration did not. Defining compression (C) as the chest deformation divided by the thickness of the thorax the following relationship was established:

$$\mathrm{AIS} = -3,78 + 19,56\mathrm{C} \tag{IV.7}$$

Thus measuring 92 mm thorax deflection for the 230 mm chest of the 50th percentile male results in a compression C of 40% and predicts AIS4.30% compression lead to AIS2. Performing statistical analysis of the injury risk shows that in frontal impact a thorax compression of 35% results in a 25% probability of severe injuries rated AIS4 or higher. FMVSS 2008 allows a maximum 76 mm deflection for the 50th percentile Hybrid III dummy in frontal impact.

IV.8 Viscous Criterion (VC)

The viscous criterion (velocity of compression), also called the soft tissue criterion, is an injury criterion for the chest area taking into account that soft tissue injury is compression-dependent and rate-dependent. The VC value ($\mathrm{m\,s^{-1}}$) is the maximum of the momentary product of the thorax deformation speed and the thorax deformation. Both quantities are determined by measuring the rib deflection (side impact) or the chest deflection (frontal impact). Hence:

$$\mathrm{VC} = V\,(t) \times C\,(t) = \frac{\mathrm{d}[D\,(t)]}{\mathrm{d}t} \times \frac{D\,(t)}{b} \tag{IV.8}$$

Where $V(t)$ ($\mathrm{m\,s^{-1}}$) is the velocity of the deformation calculated by differentiation of the deformation $D(t)$, and $C(t)$ denotes for the instantaneous compression function which is defined as the ratio of the deformation $D(t)$ and the initial torso thickness b.

IV.9 Acceleration and Force

Early attempts to quantify thoracic loading focused on acceleration. As of today, the human tolerance for severe thorax injuries is considered as peak spinal acceleration sustained for 3 ms or longer not to exceed 60 g in a frontal impact.

IV.10 Lateral Impact Tolerances of the Thorax

Table IV.3 gives a tolerance level vs. injury level. If the analysis due to lateral impact is to be carried out, then for a specific injury the stated tolerance level for force, velocity, acceleration and compression must be adhered to.

IV.11 Thoracic Trauma Index (TTI)

The Thorax Trauma Index is an injury criterion for the thorax in the case of a side impact. It assumes that the occurrence of injuries is related to the mean of the maximum lateral acceleration experienced by the struck side rib cage and the lower thoracic spine. Furthermore, the TTI takes into account the weight and the age of the test subject and thus combines information on the kinematics with parameters of the subject's individual physique. The TTI (dimension(g)) is defined as follows:

$$\mathrm{TTI} = 1,4\mathrm{AGE} + 0,5\,(\mathrm{RIB}_Y + \mathrm{T12}_Y)\ \ (M/M_{\mathrm{std}}) \tag{IV.9}$$

With AGE being the age of the test subject (in years); RIBy(g) represents the maximum of the absolute value of the lateral acceleration of the 4th and 8th rib on the struck side; $\mathrm{T12_y(g)}$ gives the maximum of the absolute value of the lateral acceleration of the 12th thoracic vertebra; M denotes the subject's mass (kg) and M_{std} refers to a standard mass of 75 kg.

When using a 50th percentile Hybrid III dummy to perform crash tests, a different version of the TTI, called the TTI(d), can be calculated. To obtain TTI(d) values, the age related term in Eq. IV.9 is omitted and the mass ratio becomes 1.0. It is important to note that the acceleration signals needed to determine the TTI and TTI(d), respectively.

Table IV.3. Lateral impact tolerances of the thorax

tolerance level	injury level	reference
force:		
7.4 kN	AISO	Tarriere et al. (1979)
10.2 kN	AIS3	Tarriere et al. (1979)
5.5 kN	25% probability of AIS ≥ 4	Viano (1989)
acceleration:		
T8-Y 45.2 g	25% probability of AIS ≥ 4	Viano (1989)
T12-Y 31.6 g	25% probability of AIS ≥ 4	Viano (1989)
60 g	25% probability of AIS$\geq$ 4	Cavanaugh et al. (1993)
TTI(d):		
TTI(d) 85 g	Max. in SID dummy for 4-door cars	FMVSS 214
TTI(d) 90 g	Max. in SID dummy for 2-door cars	FMVSS 214
TTI 145 g	25% probability of AIS ≥ 4	Cavanaugh et al. (1993)
TTI 151 g	25% probability of AIS ≥ 4	Pintar et al. (1997)
compression to half thorax:		
35%	AIS3	Stalnaker et al. (1979) Tarriere et al. (1979)
33%	25% probability of AIS ≥ 4	Cavanaugh et al. (1993)
compression to whole thorax:		
38.4%	25% probability of AIS ≥ 4	Viano (1989)
VC_{max} to half thorax:		
0.85 m s^{-1}	25% probability of AIS ≥ 4	Cavanaugh et al. (1993)
VC_{max} to half thorax:		
1.0 m s^{-1}	50% probability of AIS ≥ 3	Viano (1989)
1.47 m s^{-1}	25% probability of AIS ≥ 4	Viano (1989)

IV.12 Combined Thoracic Index (CTI)

The Combined Thoracic Index represents an injury criterion for the chest area in case of frontal impact (Kleinberger et al. 1998). Combining compression and acceleration responses, the CTI particularly addresses both airbag and belt loading. The CTI is defined as the evaluated 3 ms value from the resultant acceleration of the spine and the deflection of the chest. The calculation of the CTI value is based on the following equation:

$$\mathrm{CTI} = \frac{A_{\max}}{A_{\mathrm{int}}} + \frac{D_{\max}}{D_{\mathrm{int}}}, \tag{IV.10}$$

where

A_{max} = 3 ms value (single peak) of the resultant acceleration of the spine (g)

A_{int} = critical 3 ms intercept value (g)

D_{max} = deflection of the chest (mm)

D_{int} = critical intercept value for deflection (mm)

Intercept values are defined for different dummy types. For the 50th percent Hybrid III, for example, they read 85 g for A_{int} and 102 mm for D_{int}. The combined compression and acceleration criterion accounts for the differences in loading of the thorax by belt versus airbag systems. It is based on the assumption that, for a given load, a belt system would apply greater pressure along its contact area than an airbag system, which has a larger contact area.

APPENDICES V-X RELATED TO MEDICAL EQUIPMENT USED IN TRAUMATIC SURGERIES AND CASE STUDIES

V

Knee Systems and Instrumentation

Modular Rotating Hinge Knee System – Keel Baseplate

Using Monogram® IM Revision Instruments

stryker Howmedica OSTEONICS

Modular Rotating Hinge Knee System Using Monogram® IM Revision Instruments

Mr C R Howie FRCS
Consultant Orthopaedic Surgeon
Princess Margaret Rose Orthopaedic Hospital
Edinburgh

Mr D J Weir FRCS
Consultant Orthopaedic Surgeon
Freeman Hospital
Newcastle upon Tyne

Mr I M Pinder FRCS
Consultant Orthopaedic Surgeon
Freeman Hospital
Newcastle upon Tyne

Dr Sam Nasser, M.D.
Associate Professor
Department of Orthopaedic Surgery
Wayne State University School of Medicine
Detroit, Michigan

Stryker® Howmedica Osteonics also recognises the contribution of the following surgeons who assisted in the evaluation and development of the Monogram IM Revision Instruments; J V Bono, MD; K A Krackow, MD; L S Borden, MD; E T Habermann, MD; A K Hedley, MD; D S Hungerford, MD.

The Modular Rotating Hinge Knee System

The system has been designed for knees with severe joint destruction and/or ligament instability where a condylar style implant is not thought appropriate. While the hinge mechanism has been designed for those knees in which the soft tissue envelope is compromised, where possible the collateral ligaments should be preserved to enhance the longevity of the device.

In the revision situation, severe bone deficit may be encountered. Where this is symmetrical, the defect may be made up by thicker implants. However, it is not uncommon to require an asymmetrical augment medially or laterally. The Modular Rotating Hinge prosthesis has a selection of femoral and tibial augments which can be attached to the device after suitable bone preparation using intramedullary instrumentation.

This device provides considerable restraint, and it is recommended that a minimum stem length of 80 mm is used. Due to the design modularity, this device can be used with cemented and two styles of press-fit stems in a variety of diameters, lengths and offsets, thus maximizing surgical options.

Surgical Technique

The surgeon should utilize his/her normal technique for mobilizing the knee prior to implant surgery. If necessary, the medial or lateral collateral ligaments and quadriceps mechanism should be mobilized while preserving the soft tissue envelope to maintain tension in the capsule ligament system. Insertion of a rotating hinge does not compensate for inadequate soft tissue release. Tissue tightness may also result in poor access and secondary malalignment.

Prior to definitive implant insertion, trial reduction should be carried out to ensure correction of alignment and stability with estimation of the range of motion.

Occasionally, particularly in staged reconstruction for infection, the femoral component may require down-sizing or placement posteriorly to reduce tension to allow soft tissue closure.

This publication sets forth detailed recommended procedures for using Stryker® Howmedica Osteonics devices and instruments. It offers guidance that you should heed, but, as with any such technical guide, each surgeon must consider the particular needs of each patient and make appropriate adjustment when and as required.

Implant Overview

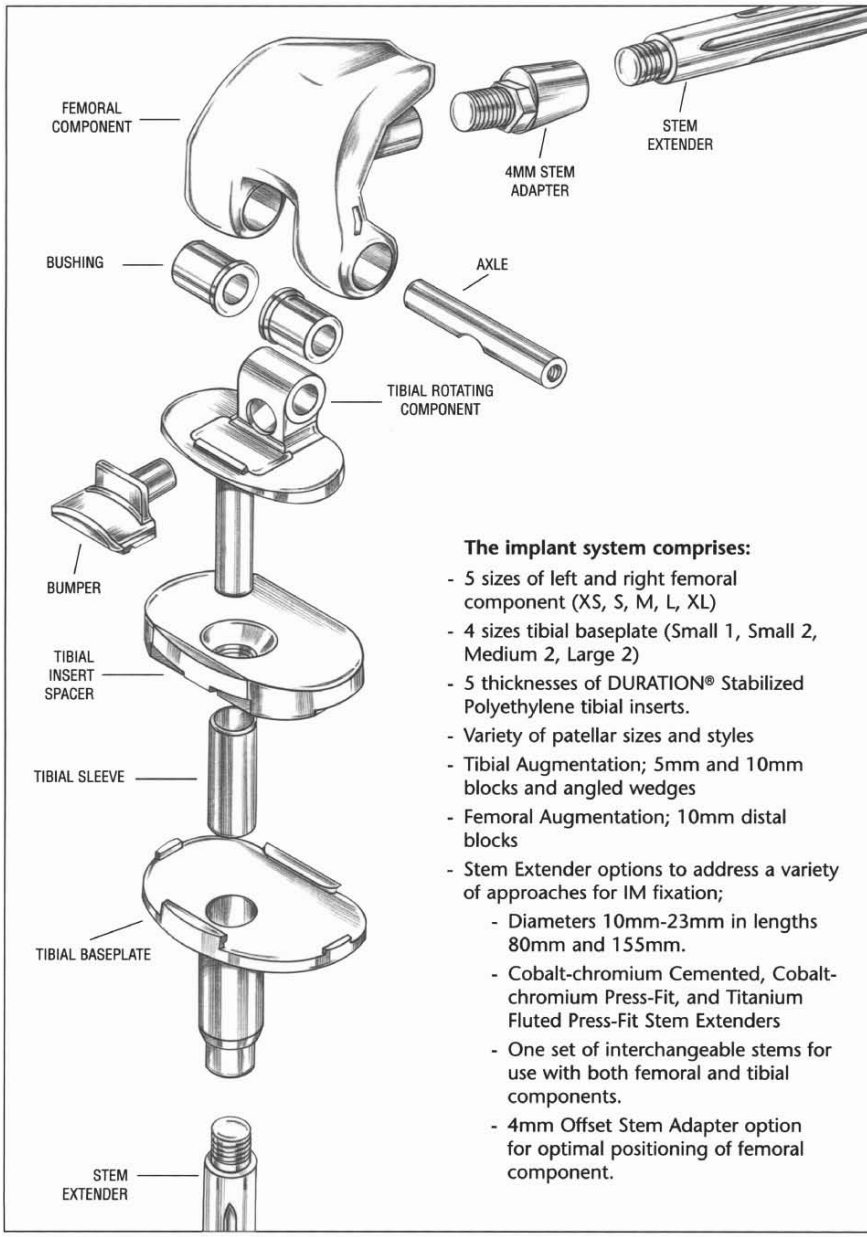

The implant system comprises:

- 5 sizes of left and right femoral component (XS, S, M, L, XL)
- 4 sizes tibial baseplate (Small 1, Small 2, Medium 2, Large 2)
- 5 thicknesses of DURATION® Stabilized Polyethylene tibial inserts.
- Variety of patellar sizes and styles
- Tibial Augmentation; 5mm and 10mm blocks and angled wedges
- Femoral Augmentation; 10mm distal blocks
- Stem Extender options to address a variety of approaches for IM fixation;
  - Diameters 10mm-23mm in lengths 80mm and 155mm.
  - Cobalt-chromium Cemented, Cobalt-chromium Press-Fit, and Titanium Fluted Press-Fit Stem Extenders
  - One set of interchangeable stems for use with both femoral and tibial components.
  - 4mm Offset Stem Adapter option for optimal positioning of femoral component.

Alignment Rationale

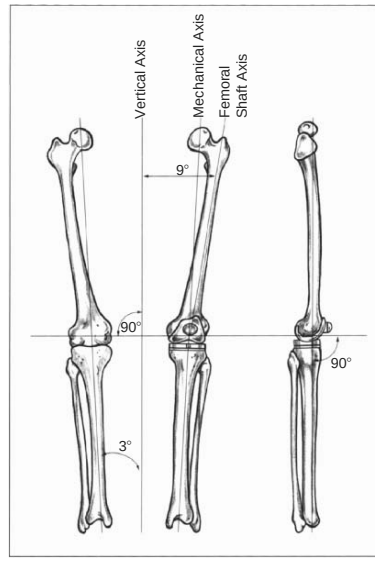

The Modular Rotating Hinge femoral and tibial components are positioned at 90° to the coronal and sagittal planes, with alignment references taken from the intramedullary (IM) canal.

The Monogram® IM Revision Instruments provide for the sizing, alignment and positioning of the bone cuts and preparation for stem extenders and augmentation blocks.

By referencing and maintaining fixation in the IM canal, Monogram IM Revision Instruments provide a stable construct for reliable and accurate bone preparation and implant placement.

Options are also provided for extramedullary alignment to be used where intramedullary referencing is not possible, for example where the canal is severely bowed.

Resection Length

The Modular Rotating Hinge Knee offers a wide range of assembly options with 5 thicknesses of Duration® Stabilized polyethylene tibial inserts and an array of femoral and tibial augmentation blocks.

The minimum resection length is 27 mm, the maximum including full augmentation options is 61 mm.

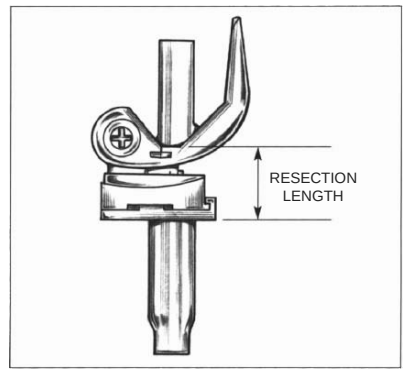

Modular Rotating Hinge

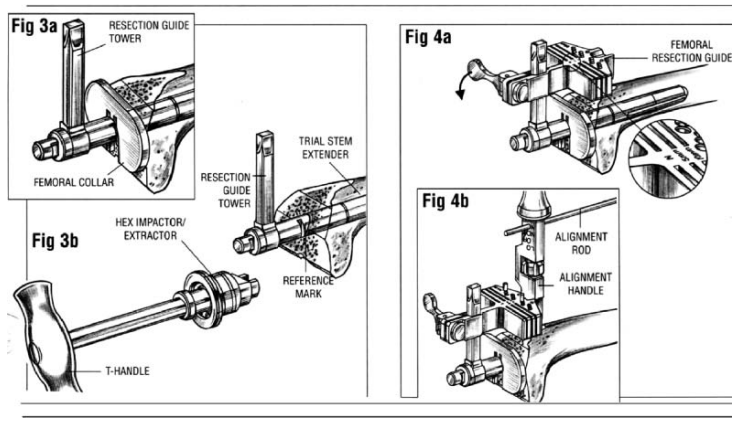

Femoral Canal Preparation

A Stem Extender of at least 80 mm should be used on the Femoral and Tibial Components for Modular Rotating Hinge procedures.

The medullary canal must be reamed in order to accommodate the new implant. Fluted reamers, available in diameters 8–23 mm, are sequentially advanced into the canal until the tip of the appropriate depth gauge reaches the level of the most prominent bony aspect of the distal femur (**Figure 1**).

Note: Reamer Depth Gauges for femoral preparation are available in two lengths for neutral stems and two lengths for offset stems. 80 mm and 155 mm refer to the depth required to properly seat the implant with the respective 80 mm and 155 mm length Stem Extender.

Figure 2 gives an example of depth gauge marking, and how it relates to preparation of the medullary canal for a given combination of implants.

Technical Hint: In situations where Press-Fit Stem diameters of 14 mm or less are being used, it is necessary to ream the medullary canal of the distal femur with a 15 mm reamer to at least 40 mm. This reaming provides the necessary clearance to fully seat the cutting guide tower instrument and the "stem boss" portion of the stemmed femoral component.

It is strongly recommended that intramedullary reaming be performed manually to avoid bone perforation and/or fracture.

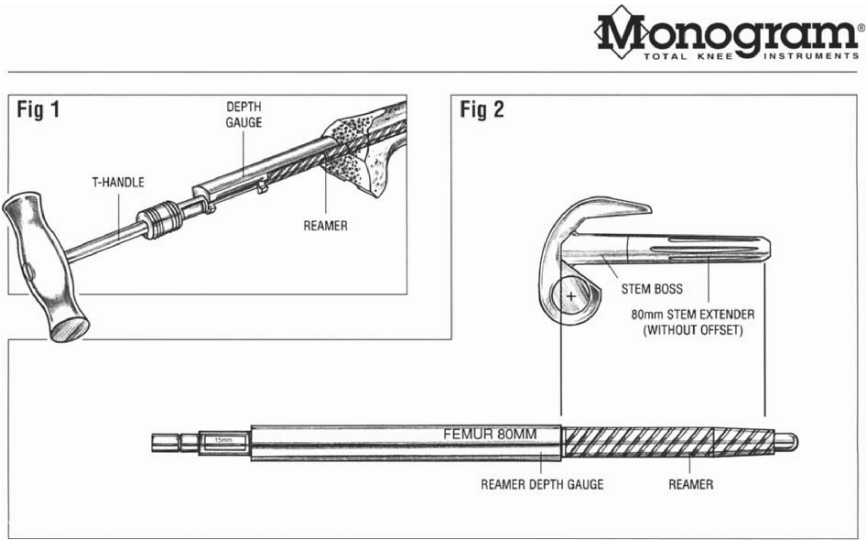

Femoral Distal Resection

After preparing the medullary canal, the corresponding diameter stem trial is selected and attached to the resection guide tower.

The assembly is inserted into the canal until the reference mark on the resection guide tower is aligned with the most prominent bony aspect of the distal femur. This position will allow a 2 mm distal femoral "clean up" cut to be made.

The appropriate left or right femoral collar may be attached to the tower to assist in setting the final depth and rotation of the instrument (**Figure 3a**).

Technical Hint: To impact and extract the assembly in and out of the medullary canal, the T-Handle Impactor Extractor can be utilized (**Figure 3b**).

The 6° Valgus Femoral Resection Guide is assembled onto the tower, slid down to touch the anterior femur and secured using the cam-lock mechanism (**Figure 4a**).

Further fixation to the femur can be achieved by adding 1/8″ (3.2 mm) drills through the guide. A pin may also be inserted obliquely into the "X" drill hole to provide additional stability.

With the Femoral Resection Guide securely fixed to the stem assembly for enhanced stability, the 2 mm "clean up" cut is performed using the slot marked "N" for neutral.

If Distal Femoral Augments are required, the 10 mm cutting guide slots are used.

Note: If a further resection is required, the cutting guide can be re-positioned referencing the pins placed on the distal femur through the 2 mm or 4 mm pin holes on the resection guide. If this is done, the medullary canal should be reamed a further 2 mm or 4 mm in order to ensure the implant will be fully seated.

Technical Hint: Before fixing the resection guide with 1/8″ drills, alignment can be verified by referencing the position of the femoral head with the extramedullary rod inserted through the "NF" hole on the alignment handle, attached to the Femoral Resection Guide (**Figure 4b**). The position of the femoral head is determined from pre-operative X-ray templating.

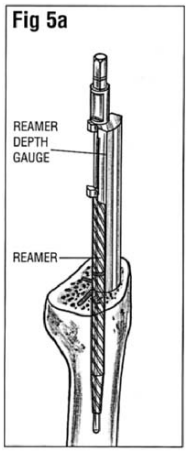

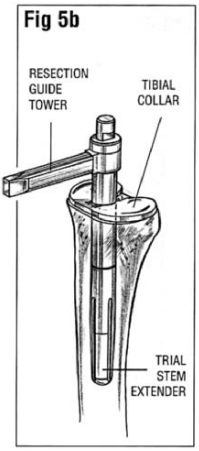

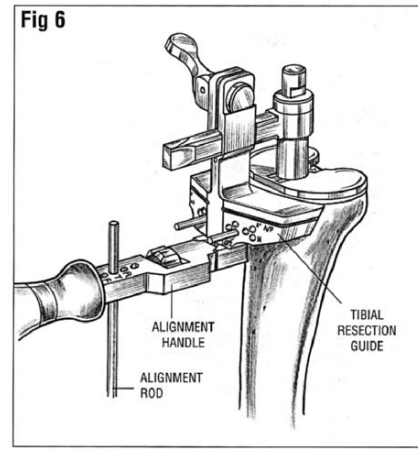

Tibial Preparation

Fluted reamers, available in diameters 8–23 mm are sequentially advanced into the medullary canal until the tip of the Tibial Reamer Depth Gauge reaches the level of the most prominent bony aspect of the proximal tibia (**Figure 5a**).

Note: Reamer Depth Gauges for tibial preparation are available in two lengths. 80 mm and 155 mm refer to the depth required to properly seat the implant with the respective 80 mm and 155 mm length Stem Extender.

After preparing the medullary canal, the corresponding diameter stem trial is selected and attached to the resection guide tower. The tibial collar is attached to the tower to assist in setting the final depth and rotation of the instrument (**Figure 5b**). The assembly is inserted into the canal until the tibial collar contacts the most prominent bony aspect of the proximal tibia. This position should allow a 2 mm proximal tibial "clean up" cut to be made.

Technical Hint: To impact and extract the assembly in and out of the medullary canal, the T-Handle Impactor Extractor can be utilized.

The Tibial Resection Guide (making a Neutral-Neutral cut relative to the mechanical axis) is assembled onto the tower, slid down to touch the anterior tibia and secured using the cam-lock mechanism (**Figure 6**).

Fixation to the tibia can be achieved by adding 1/8″ (3.2 mm) drills through the guide. A pin may also be inserted obliquely into the "X" drill hole to provide additional stability.

With the assembled construct stabilized, the 2 mm "clean up" cut is performed through the slot on the guide while the stem assembly is still in place, providing enhanced stability.

Note: If a further resection is required, the cutting guide can be re-positioned referencing the pins placed on the proximal tibia through the 2 mm or 4 mm pin holes on the resection guide. If this is done, the medullary canal should be reamed a further 2 mm or 4 mm in order to ensure the implant will be fully seated.

Technical Hint: Before fixing the resection guide with 1/8″ (3.2 mm) drills, rotational alignment can be verified by referencing the center of the ankle with the extramedullary rod inserted through the "NT" hole on the alignment handle, attached to the Tibial Resection Guide (**Figure 6**).

Note: A/P alignment should not be referenced by use of the handle, since the handle has a 3° slope.

Modular Rotating Hinge

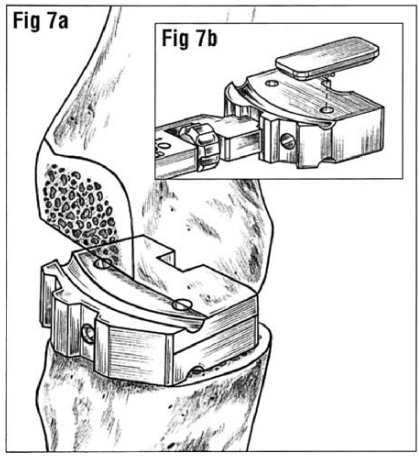

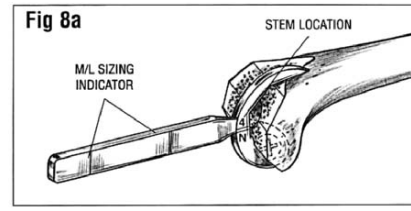

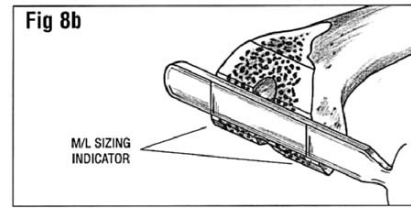

Extension Gap Assessment

A Spacer Block can be used to assess the extension gap, but not the size of the final flexion gap as the posterior cut has not been made.

Select the appropriate thickness Spacer Block and place it into the joint gap with the knee in full extension (**Figure 7a**).

Modular 5 mm and 10 mm Half Spacers can be attached to the appropriate faces of the Spacer block to compensate for bone loss in order to carry out soft tissue evaluation (**Figure 7b**).

Technical Hint: The position of the patella is a helpful indicator in deciding where to locate the position of the femoral and tibial implants. The distal femur can be built up with 10 mm augmentation blocks. The proximal tibia can be built up with the 5 and 10 mm augmentation blocks and/or thicker tibial insert spacers.

Femoral Sizing

In addition to pre-operative templating, femoral sizing can be accomplished using the femoral sizing template, by placing the posterior aspect of the template in the intercondylar notch to enable the internal cuts profile to seat flush against the bone (**Figure 8a**).

The handle of the template also provides markings that correspond to the M/L width of the implant (**Figure 8b**).

To accurately locate the template using the fixed stem position of the implant as the A/P reference point, replace the resection guide tower and trial stem in the femur, and position the sizing template so that the etched line marked "N" ("neutral" stem position) is coincident with the center line of the guide tower and the medullary canal. If an anterior gap is present, reposition the sizing template posteriorly so the engraved line marked "4 mm" is coincident with the center line of the guide tower and reassess the fit of the template in this "4 mm offset stem" position.

Repeat this process with a different size template if necessary to determine the best size femoral component and whether a 4 mm offset stem is required.

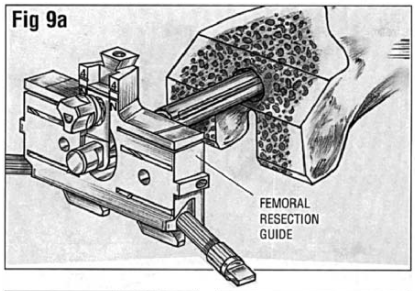

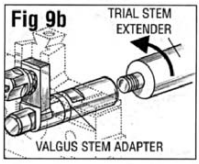

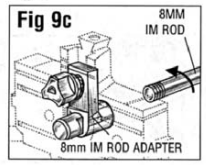

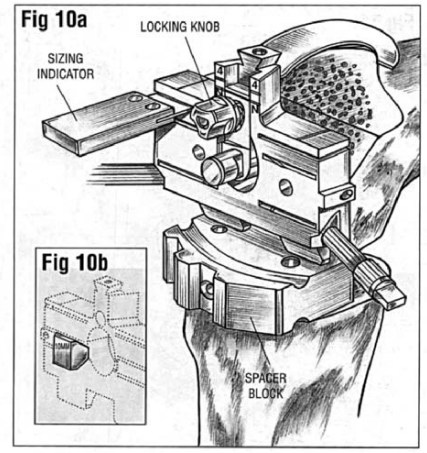

Intramedullary Alignment

The appropriate left or right 6° Valgus Stem Adapter is assembled to the selected size Femoral A/P Chamfer Resection Guide and set to the "N" line on the resection block if no offset is to be used. If the 4 mm posterior offset is to be used, the Valgus Stem Adapter should be locked at the "4" line.

The Trial Stem Extender is then attached (**Figure 9b**), and inserted into the canal until the Resection Guide rests against the cut distal femur (**Figure 9a**).

If a 10 mm distal augment cut has been made on the femur, as detailed in **Figure 4a**, a magnetic 10 mm Resection Guide Spacer should be attached to the Femoral Resection Guide (**Figure 10b**).

Option: An 8 mm IM Rod can be used to reference the medullary canal, if the 8 mm IM Rod Valgus Adapter is attached to the Femoral Resection Guide (**Figure 9c**).

Femoral Sizing and Resection

Femoral sizing can be verified using the Sizing Indicator, referencing the anterior cortex, as indicated (**Figure 10a**).

If it is desirable at this stage to change the position of the Resection Guide to Neutral or 4 mm posterior offset, this can be done by releasing the Locking Knob on the Valgus Adapter one half turn and sliding the Resection Guide to its new position. Then tighten the Locking Knob.

Correct internal/external rotation of the Femoral Resection Guide can be achieved by setting the Resection Guide parallel to the transepicondylar axis. The Resection Guide can then be fixed using 1/8″ (3.2 mm) drills or pins.

The anterior femoral cut may now be made using a .050″ (1.27 mm) oscillating sawblade through the most anterior slot on the guide.

Technical Hint: The tabs on the posterior aspect of the Femoral Resection Guide represent the external profile of the posterior condyles of the Femoral Component. With the knee in flexion, the correct rotation of the Femoral Resection Guide can also be assessed by referencing the spacer block between the resected tibial surface and the posterior condyle tabs on the Resection Guide to ensure a parallel flexion gap (**Figure 10a**).

Modular Rotating Hinge

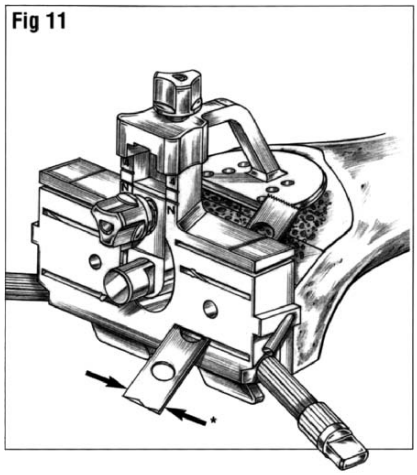

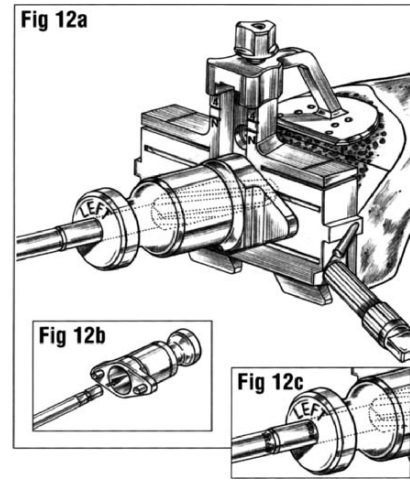

The Anterior Shim Plate can be attached to the Femoral Resection Guide to provide stability for the Resection Guide assembly during the anterior and posterior chamfer resections (**Figure 11**).

Technical Hint: A narrow oscillating sawblade of less than 1″ (25 mm) is recommended for the chamfer cuts.

Option: If IM referencing is not used, the Anterior Shim Plate can be attached to the Femoral Resection Guide to reference the existing anterior cut. Care should be taken in checking that the original anterior cut is not malrotated.

Offset Stem Preparation

If the 4 mm Offset Stem Adapter Implant is being used it is necessary to ream the femur to prepare for the new posterior position of the Femoral Component Stem Boss and Offset Adapter (**Figure 12a**).

Remove the Trial Stem Extender and Valgus Adapter and assemble the Femoral Offset Reamer through the Reamer Bushing (**Figure 12b**). Attach the Bushing to the Femoral Resection Guide and ream to the "Offset" reamer depth marking.

Note: If a straight stem with a diameter of 14 mm or less is used on the Femoral Component, the Offset Reamer and Reamer Bushing should be used to the "Boss" reamer depth marking (**Figure 12c**) to prepare the distal femur for the stem boss of the femoral component.

If the 8 mm IM Rod has been used for IM referencing (shown in **Figure 9c**), stem reaming should be completed at this stage for at least an 80 mm length stem.

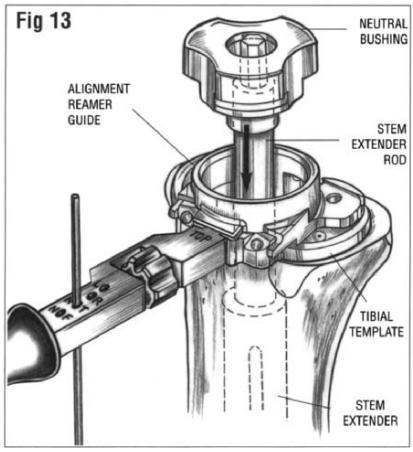

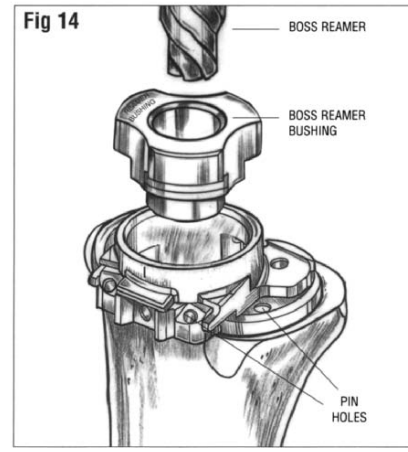

Tibial Preparation

Select the size of Tibial Template which best matches the cut proximal tibia without overhanging the cortex.

Use the Stem Extender Rod, attached to a Trial Stem Extender, through the Alignment Reamer Guide and Neutral Bushing to center the Template with the Stem construct in the canal (**Figure 13**).

With the knee in full flexion, and the Alignment Handle attached to the Template, an Alignment Pin is placed through the "NT" hole position of the Handle to verify alignment. The tibial tubercle will normally be positioned just lateral to the pin which should be centered distally over the center of the ankle.

When alignment is correct, the Template is secured with Headed Nails or pins through holes located anteriorly and posteriorly on the template.

Then ream the Stem Boss using the Stem Boss Bushing and Stem Boss Reamer to the "Boss" depth marking (**Figure 14**).

Modular Rotating Hinge

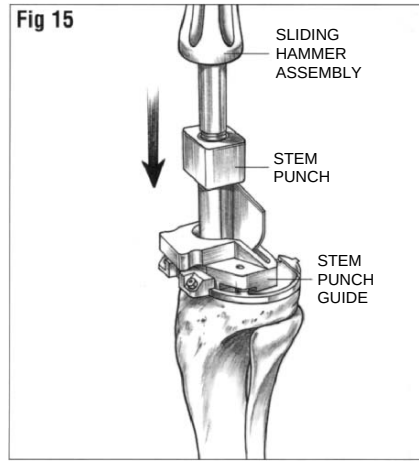

For the Keel Baseplate, the Stem Punch Guide is placed in the corresponding locking holes in the Tibial Template (**Figure 15**). Attach the Stem Punch to the Sliding Hammer Assembly. The Stem Punch fits into the cut out on the guide.

Tibial Bone Augment Preparation

Prior to punching for the tibial baseplate, assess the need for tibial augmentation. Based on the nature of the deformity, attach the appropriate resection guide to the tibial template and secure by tightening the locking knob. Drill pins through the holes located on the augment-cutting guide (**Figure 16**). Remove the tibial template and complete the cut through the appropriate slot.

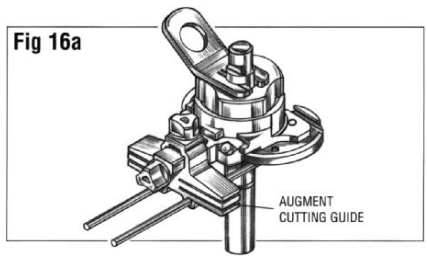

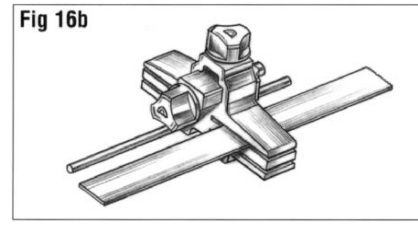

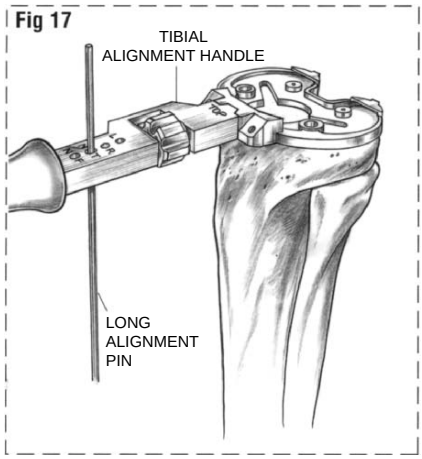

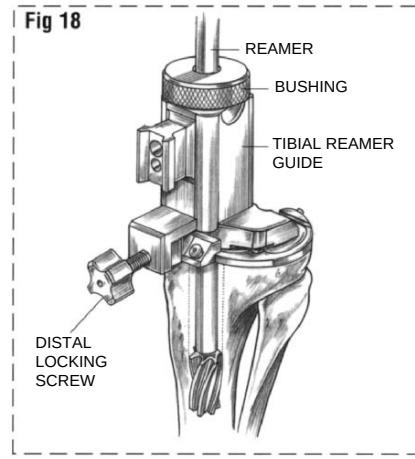

Tibial Preparation: Primary Option

It is possible to prepare the tibia for a Modular Rotating Hinge Tibial Baseplate using the Monogram® primary tibial instruments.

Select the size of Tibial Template which best matches the cut proximal tibia without overhanging the cortex.

With the knee in full extension, and the Alignment Handle attached to the Template, an Alignment Pin is placed through the "NT" hole position of the Handle to verify alignment (**Figure 17**). The tibial tubercle will normally be positioned just lateral to the pin which should be centered distally over the center of the ankle.

When alignment is correct, the Template is secured with Headed Nails or pins through holes located anteriorly and posteriorly on the template.

Tibial Stem Reaming

The Tibial Reamer Guide and Stem Boss Reamer can be used to ream the canal for the Tibial Baseplate "Stem Boss". If the medullary canal has not been prepared for at least an 80 mm Stem Extender as described on page 5, then this should be done at this stage using the appropriate diameter stem extender reamer.

The Tibial Reamer Guide is placed onto the Tibial Template and the distal Locking Knob is tightened, securing the assembly (**Figure 18**).

With the bushing in place, ream to the appropriate depth, indicated by the 80 and 155 mm markings on the Reamer shaft.

Technical Hint: The Alignment Handle can be attached to the Anterior face of the Tibial Reamer Guide to enable an extramedullary alignment check before reaming.

Modular Rotating Hinge

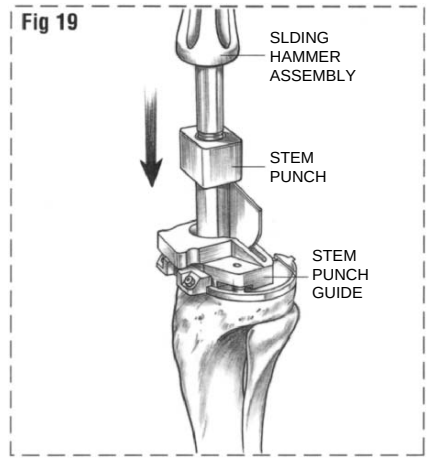

The Stem Punch Guide is placed in the corresponding locking holes in the Tibial Template (**Figure 19**). Attach the Stem Punch to the Sliding Hammer Assembly. The stem punch fits into the cut out on the guide.

Tibial Bone Augment Preparation

Prior to punching, the Augment Drill Guide is attached, by tightening the Locking Knob to the anterior face of the Tibial Template (**Figure 20a**). Two 1/8″ (3.2 mm) drill bits are placed through the guide into the tibia. The drill guide is then removed. After punching the Tibial Template is removed and the Tibial Augment Cutting Jig is then placed on the 1/8″ (3.2 mm) drill bits.

The Tibial Augment Cutting Jig allows accurate defect resection to provide full bony contact for the configured component (**Figure 20b**).

The Jig offers four options: a 12° or 24° angled wedge resection, and a 5 mm or 10 mm flat resection for full or half spacers (**Figure 20c**).

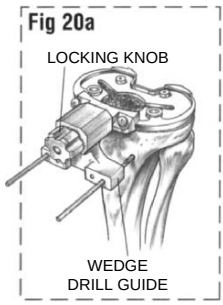

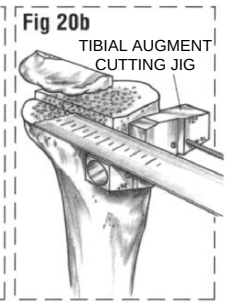

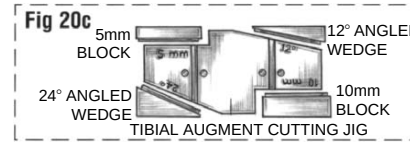

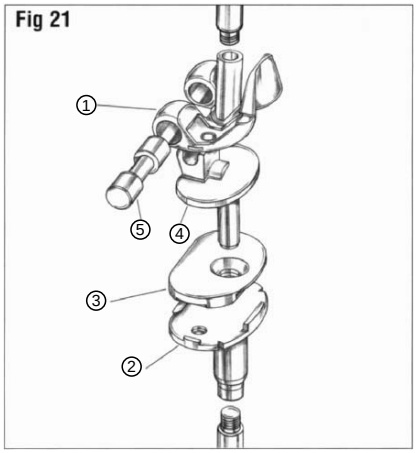

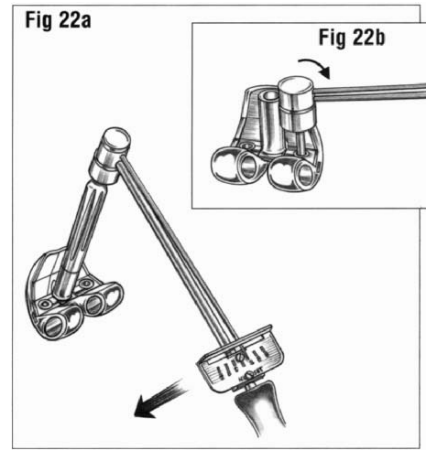

Trialing

On completion of the femoral and tibial bone preparation a trial reduction should then be performed to confirm that appropriate motion, stability and patellar tracking have been achieved.

The Trial Femoral Component (1) and Trial Tibial Baseplate (2) can be fitted with the appropriate Trial Augments and Trial Stem Extenders before being placed onto the prepared bones. If a 4 mm offset adapter is to be used, this can be attached to the femoral component in the same way as the implant, as detailed on pages 16 and 17.

Place the appropriate thickness Trial Tibial Insert (3) onto the Trial Tibial Baseplate and drop in the appropriate Trial Tibial Rotating Component (4).

Insert the Trial Axle (5) into the bore of the Trial Femoral Component until the groove lines up with the intercondylar gap between the condyles. Engage the Trial Axle down into the "snap-fit" hinge on the Trial Rotating Component (4).

Femoral Implant Assembly

The implant Femoral Spacers are attached by screw fixation to the distal condylar area of the femoral component. The Torque Wrench is attached to the Distal Locking Screw Adapter. A locking torque of 60–80 in/lbs is applied to the screw head in order to lock the Spacer and Femoral Component together (**Figure 22b**).

To attach a Press-Fit Stem Extender to the implant, hand tighten the stem into the Femoral Stem Boss as far as possible. Attach the Stem Socket Wrench to the Torque Wrench, insert the male hex tip of the wrench into the hex recess on the Stem Extender and tighten to 120 in/lbs–180 in/lbs (**Figure 22a**).

Option: If using a 155 mm Titanium Fluted Stem Extender, tighten to 120 in/lbs–180 in/lbs with the Tri-Fluted Stem Wrench, illustrated in **Figure 25b**.

If using a Cemented Stem Extender, hand tighten the Stem into the Femoral Stem Boss as far as possible. The Combination Wrench is then used to fully tighten.

Note: A Stem Extender of at least 80 mm should be used on the Femoral Components for Modular Rotating Hinge procedures.

Modular Rotating Hinge

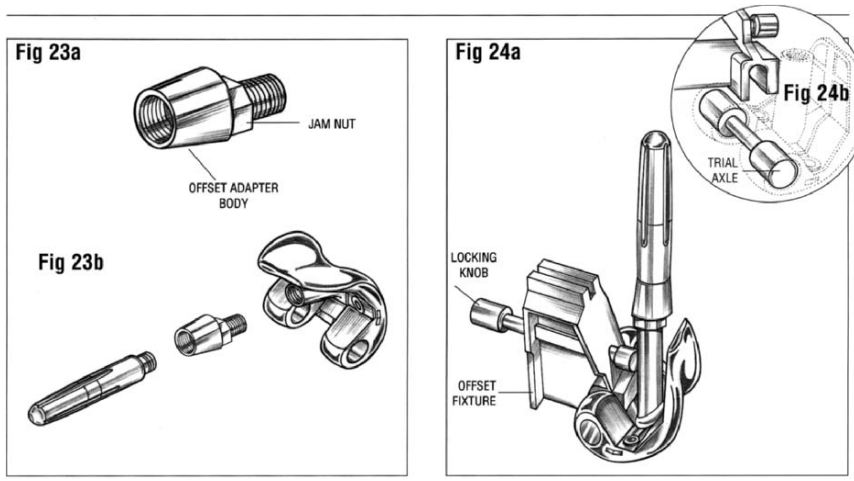

Femoral Offset Stem Assembly

Step 1

Turn the jam nut along the threaded stud until it contacts the offset adapter body (**Figure 23a**). Screw the offset adapter into the boss of the femoral component implant until it is fully seated. Tighten the stem extender into the adapter by hand as far as possible.

Step 2

Slide the Trial Axle into the Femoral Component implant and drop the Offset Fixture onto the axle between the condyles (**Figure 24b**). Tighten the locking knob by hand until it sits firmly against the stem boss of the femoral component implant (**Figure 24a**).

Step 3

Turn the offset adapter body counter-clockwise until the stem is anterior to the boss of the femoral component (**Figure 24a**). **DO NOT EXCEED ONE FULL TURN.**

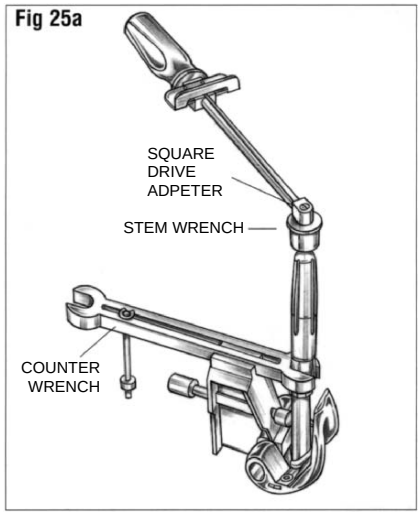

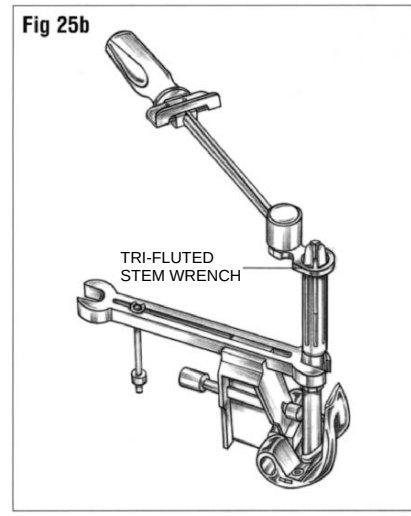

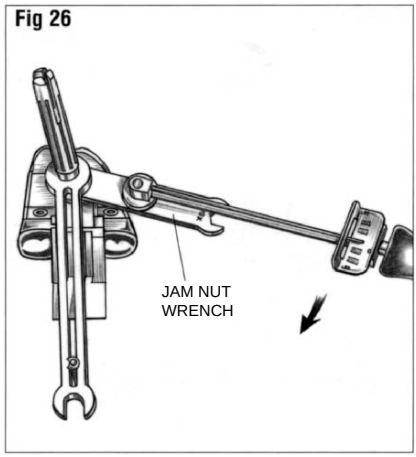

Step 4

Attach the counter wrench to the appropriate left or right positioning rail on the offset locking jig and engage the offset adapter body. Using the stem wrench (hex tip (**Figure 25a**) or tri-fluted (**Figure 25b**)) and torque wrench, tighten the stem extender to the adapter body to a torque value of 120 in/lbs–180 in/lbs (**Figure 25**).

Step 5

Attach the jam nut wrench to the torque wrench. Engage the jam nut with the torque wrench assembly while holding the counter wrench and tighten to 120 in/lbs–180 in/lbs (**Figure 26**).

Note: Orient the square drive adapter, tri-fluted stem wrench and jam nut wrench with the long axis of the torque wrench.

Modular Rotating Hinge

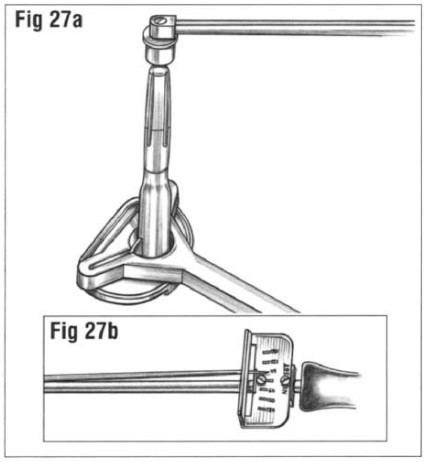

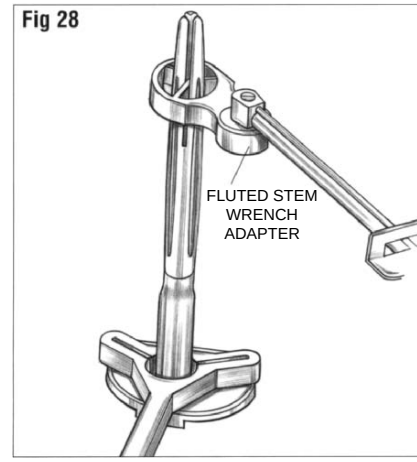

Tibial Stem Implant Assembly

To attach a Press-Fit Stem Extender to the implant, hand tighten the stem into the Tibial Stem Boss as far as possible. Attach the Stem Socket Wrench to the Torque Wrench, insert the male hex tip of the wrench into the hex recess on the Stem Extender and tighten to 120in/lbs–180in/lbs (**Figure 27a** and **27b**).

Note: A Stem Extender of at least 80 mm should be used on the Tibial Components for Modular Rotating Hinge procedures.

Option: If Cemented Stem Extenders are to be used, hand tighten the stem into the Tibial Stem Boss as far as possible. The Combination Wrench and Counter Wrench are then used to fully tighten.

Titanium Tri-Fluted Stem Option:

When using a 155 mm Titanium Fluted Stem Extender, the Tri-Fluted Stem Wrench Adapter must be used to apply the final torque to the implant. This adapter is attached to the Torque Wrench and slid into the slots of the Stem until it has bottomed out on the implant. The Stem must be tightened to the final locking torque of 120in/lbs–180in/lbs (**Figure 28**).

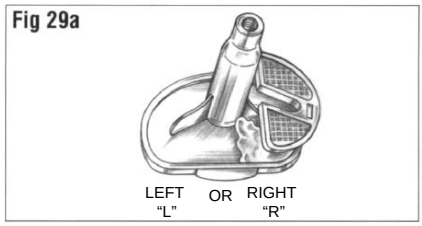

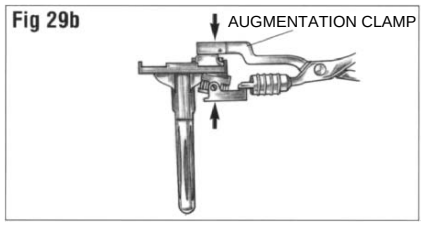

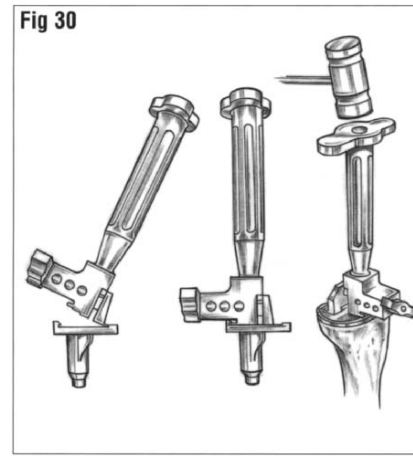

Tibial Spacer Implant Assembly

Cement is placed onto the surface of the Baseplate and the undersurface of the Tibial Spacer. The lip on the Spacer is placed into the rim of the Baseplate (**Figure 29a**), and the Augmentation Clamp is attached to the assembly and left in place until the cement has fully hardened (**Figure 29b**).

The Full or Half Augment Clamp and Clamp Pad should be used when cementing the appropriate Full or Half Augments.

Note: The Trial Spacers are colour coded, by size, to match the appropriate implant package.

Tibial Baseplate Implantation

The Tibial Impactor Extractor (**Figure 30**) is used to impact the Tibial Baseplate to its full depth, ensuring the Keel engages in the prepared bone.

Modular Rotating Hinge

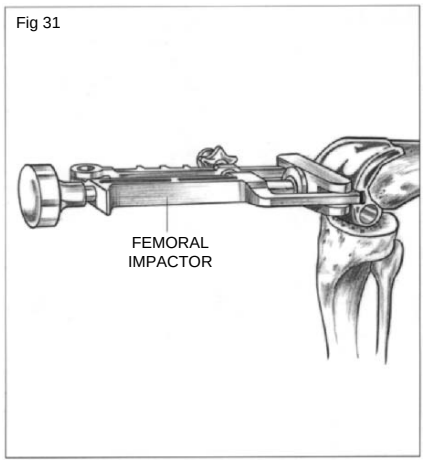

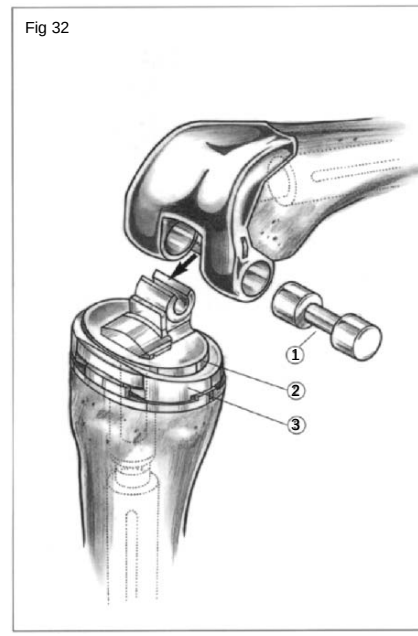

Femoral Implantation

The implant Femoral Component Assembly is attached to the Femoral Impactor Extractor, guided onto the femur and impacted flush (**Figure 31**).

With the Femoral Component and Tibial Baseplate implanted, it is possible to use the Trial Axle (1) with the Trial Rotating Component (2) and Trial Tibial Insert Spacer (3) to verify that the appropriate motion, stability and patellar tracking have been achieved. With the knee in full extension this also assists in loading the femoral and tibial baseplate components while the cement is curing to provide an optimal bond between implant and bone.

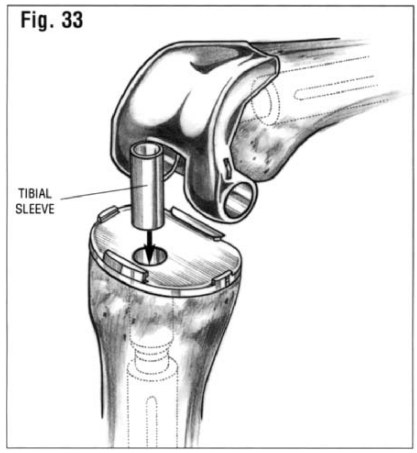

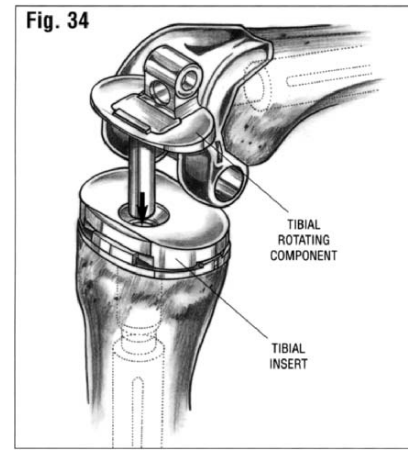

Final Implant Assembly

To complete the assembly of the final implant components, insert the Tibial Sleeve into the Tibial Baseplate until it is flush with the surface.

There are two sizes of Tibial Insert Spacer, Small 1/Small 2 and Medium 1/Large 2, which fit with the corresponding Tibial Baseplates. They both come in 5 different thicknesses of 10 mm, 13 mm, 16 mm, 20 mm and 24 mm.

Snap in the appropriate thickness Tibial Spacer, chosen at the trialing stage and drop in the Tibial Rotating Component.

Option: An additional Tibial Rotating component with 3 mm posterior offset is available for Large and Extra Large Femoral components. This component offsets the Femoral component posteriorly, relative to the tibial stem, a further 3 mm to enable optimal patellar tracking.

Modular Rotating Hinge

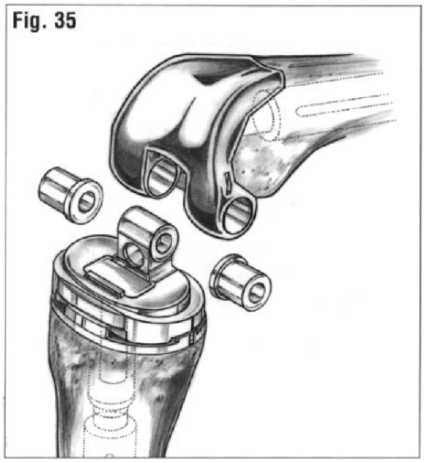

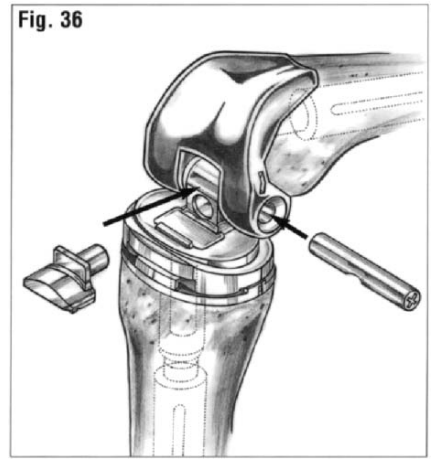

Insert the two Femoral Bushings into the Femoral Component so that the flanges are inside the intercondylar cut out (**Figure 35**).

Line up the Tibial Rotating Component with the holes of the Femoral Component Bushings and slide the implant Axle into the assembly until the "recess" in the Axle can be seen through the Tibial Rotating Component from the front. Twist the Axle so that the "recess" is inferior. The grooves on the end of the axle which engage into the Axle Introducer Handle are a helpful indicator in aligning the Axle.

With the Axle correctly oriented the Bumper can now be inserted. This should be impacted into the Tibial Rotating Component until it is flush with the hinge housing and has cleared the "snap-fit" lip on the Tibial Rotating Component.

Note: With the Bumper inserted the axle should **not be further rotated**.

Option: The Bumper implant is available in two options, neutral and 3° flexion.

Assembly Options

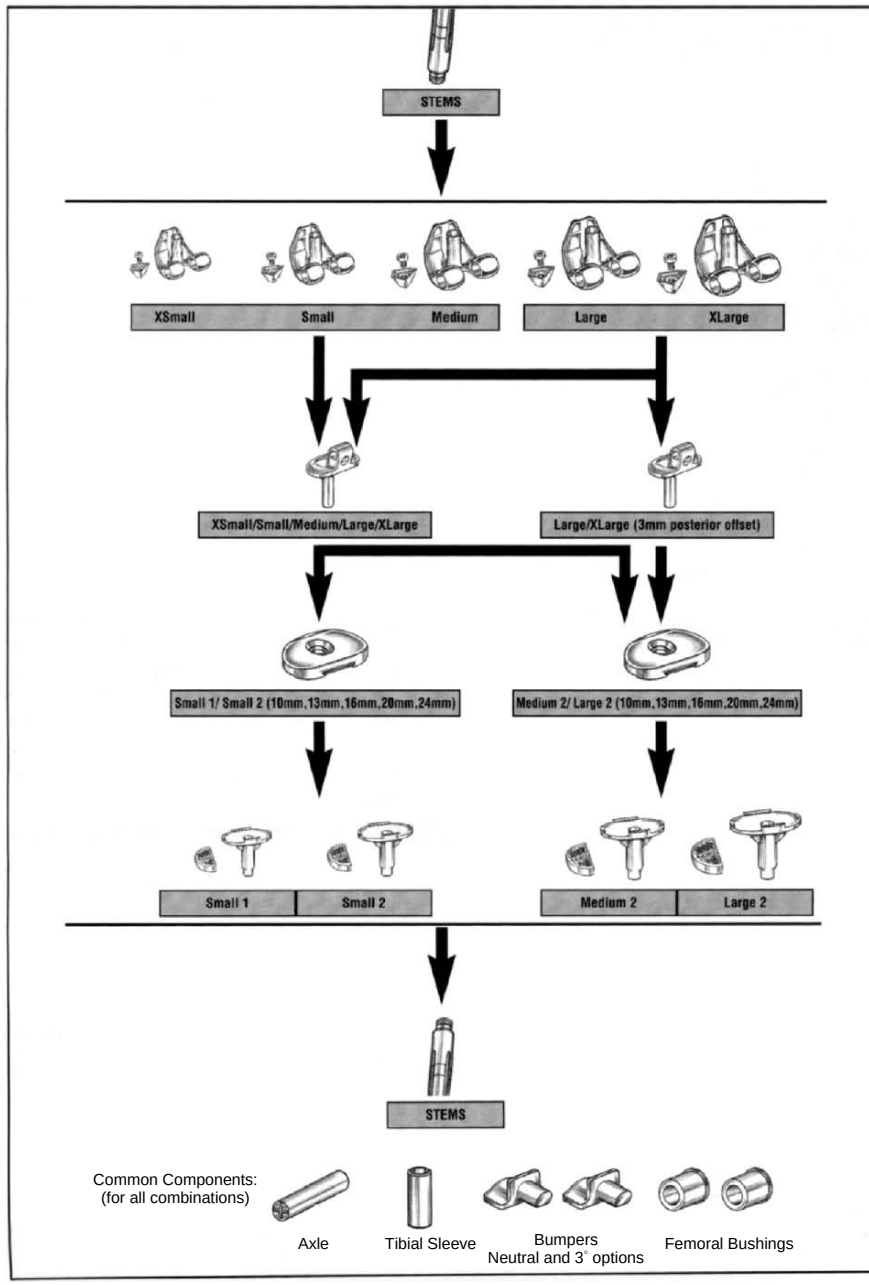

Implant Listing

Description	Size	Implant Cat. No. Left	Implant Cat. No. Right	Trial Cat. No. Left	Trial Cat. No. Right
Femoral Component	Extra-Small	6481-1-100	6481-1-101	6481-1-300	6481-1-301
Femoral Component	Small	6481-1-110	6481-1-111	6481-1-310	6481-1-311
Femoral Component	Medium	6481-1-120	6481-1-121	6481-1-320	6481-1-321
Femoral Component	Large	6481-1-130	6481-1-131	6481-1-330	6481-1-331
Femoral Component	Extra-Large	6481-1-140	6481-1-141	6481-1-340	6481-1-341

Description	Size	Implant Cat. No.	Trial Cat. No.
Tibial Keel Baseplate	Small 1	6481-3-110	6481-3-410
Tibial Keel Baseplate	Small 2	6481-3-111	6481-3-411
Tibial Keel Baseplate	Medium 2	6481-3-112	6481-3-412
Tibial Keel Baseplate	Large 2	6481-3-113	6481-3-413

Description	Size	Implant Cat. No.	Trial Cat. No.
Tibial Insert 10 mm	Small 1/Small 2	6481-3-210	6481-3-510
Tibial Insert 13 mm	Small 1/Small 2	6481-3-213	6481-3-513
Tibial Insert 16 mm	Small 1/Small 2	6481-3-216	6481-3-516
Tibial Insert 20 mm	Small 1/Small 2	6481-3-220	6481-3-520
Tibial Insert 24 mm	Small 1/Small 2	6481-3-224	6481-3-524
Tibial Insert 10 mm	Medium 2/Large 2	6481-3-310	6481-3-610
Tibial Insert 13 mm	Medium 2/Large 2	6481-3-313	6481-3-613
Tibial Insert 16 mm	Medium 2/Large 2	6481-3-316	6481-3-616
Tibial Insert 20 mm	Medium 2/Large 2	6481-3-320	6481-3-620
Tibial Insert 24 mm	Medium 2/Large 2	6481-3-324	6481-3-624

Description	Size	Implant Cat. No.	Trial (All sizes)
Femoral Block, Distal 10 mm	Extra-Small	6481-1-200	
Femoral Block, Distal 10 mm	Small	6481-1-210	
Femoral Block, Distal 10 mm	Medium	6481-1-220	
Femoral Block, Distal 10 mm	Large	6481-1-230	
Femoral Block, Distal 10 mm	Extra-Large	6481-1-240	
Trial Femoral Block, Distal 10 mm	(All sizes)		6481-1-400

Description	Size	Implant Cat. No.	Trial Cat. No.
Tibial Rotating Component	Extra Small-Extra Large	6481-2-100	6481-3-500
Tibial Rotating Component (3 mm posterior offset)	Large – Extra Large	6481-2-101	6481-3-600
Femoral bushing (1 per pack)	All Sizes	6481-2-110	—
Tibial Sleeve	All Sizes	6481-2-140	—
Bumper Insert – Neutral	All Sizes	6481-2-130	—
Bumper Insert, 3 Degrees	All Sizes	6481-2-133	—
Axle	All Sizes	6481-2-120	6481-2-220

Description	Implant Cat. No.	Trial Cat. No.
Offset Adapter 4 mm (including Jam Nut)	6478-6-490	—
Trial Offset Adapter 4 mm (not including Jam Nut)	—	6778-6-490
Jam Nut Trial	—	6778-6-485

Implant Listing

Tibial Augmentation	Size	Left		Right	
		Implant	Trial	Implant	Trial
Hemi Flat Wedge 5 mm	Small 1	6630-6-125	6633-9-505	6630-6-105	6633-9-506
Hemi Flat Wedge 5 mm	Small 2	6630-6-170	6633-9-505	6630-6-150	6633-9-506
Hemi Flat Wedge 5 mm	Medium 2	6630-6-270	6633-9-509	6630-6-250	6633-9-510
Hemi Flat Wedge 5 mm	Large 2	6630-6-370	6633-9-513	6630-6-350	6633-9-514
Hemi Flat Wedge 10 mm	Small 1	6630-6-130	6633-9-523	6630-6-110	6633-9-524
Hemi Flat Wedge 10 mm	Small 2	6630-6-175	6633-9-523	6630-6-155	6633-9-524
Hemi Flat Wedge 10 mm	Medium 2	6630-6-275	6633-9-527	6630-6-255	6633-9-528
Hemi Flat Wedge 10 mm	Large 2	6630-6-375	6633-9-531	6630-6-355	6633-9-532
Hemi Flat Wedge 12°	Small 1	6630-6-135	6633-9-545	6630-6-115	6633-9-546
Hemi Flat Wedge 12°	Small 2	6630-6-180	6633-9-545	6630-6-160	6633-9-546
Hemi Flat Wedge 12°	Medium 2	6630-6-280	6633-9-549	6630-6-260	6633-9-550
Hemi Flat Wedge 12°	Large 2	6630-6-380	6633-9-553	6630-6-360	6633-9-554
Hemi Flat Wedge 24°	Small 1	6630-6-140	6633-9-565	6630-6-120	6633-9-566
Hemi Flat Wedge 24°	Small 2	6630-6-185	6633-9-565	6630-6-165	6633-9-566
Hemi Flat Wedge 24°	Medium 2	6630-6-285	6633-9-569	6630-6-265	6633-9-570
Hemi Flat Wedge 24°	Large 2	6630-6-385	6633-9-573	6630-6-365	6633-9-574

Tibial Augmentation	Size	RM/LL		RM/LL	
		Implant	Trial	Implant	Trial
Full 5° Angled Wedge	Small 1	6630-6-620	6631-6-770	6630-6-625	6631-6-775
Full 5° Angled Wedge	Small 2	6630-6-627	6631-6-770	6630-6-628	6631-6-775
Full 5° Angled Wedge	Medium 2	6630-6-640	6631-6-790	6630-6-645	6631-6-795
Full 5° Angled Wedge	Large 2	6630-6-660	6631-6-815	6630-6-665	6631-6-820

Tibial Augmentation	Size	Left		Right	
		Implant	Trial	Implant	Trial
Full Flat Block 10 mm	Small 1	6630-6-510	6630-6-710	6630-6-510	6630-6-710
Full Flat Block 10 mm	Small 2	6630-6-515	6630-6-710	6630-6-515	6630-6-710
Full Flat Block 10 mm	Medium 2	6630-6-525	6630-6-720	6630-6-525	6630-6-720
Full Flat Block 10 mm	Large 2	6630-6-535	6630-6-730	6630-6-535	6630-6-730

Press Fit Stem Extenders	Vitallium Press Fit Cat. No.	Titanium Press Fit Cat. No.	Trial Fit Cat. No.
10 mm × 80 mm	6478-6-395	6478-6-600	6778-6-395
11 mm × 80 mm	6478-6-396	6478-6-605	6778-6-396
12 mm × 80 mm	6478-6-397	6478-6-610	6778-6-397
13 mm × 80 mm	6478-6-398	6478-6-615	6778-6-398
14 mm × 80 mm	6478-6-399	6478-6-620	6778-6-399
15 mm × 80 mm	6478-6-400	6478-6-625	6778-6-400
16 mm × 80 mm	6478-6-405	6478-6-630	6778-6-405
17 mm × 80 mm	6478-6-410	6478-6-635	6778-6-410
18 mm × 80 mm	6478-6-415	6478-6-640	6778-6-415
19 mm × 80 mm	6478-6-420	6478-6-645	6778-6-420
21 mm × 80 mm	6478-6-425	6478-6-655	6778-6-425
23 mm × 80 mm	6478-6-430	6478-6-665	6778-6-430
10 mm × 155 mm	6478-6-435	6478-6-680	6778-6-435
11 mm × 155 mm	6478-6-436	6478-6-685	6778-6-436
12 mm × 155 mm	6478-6-437	6478-6-690	6778-6-437
13 mm × 155 mm	6478-6-438	6478-6-695	6778-6-438
14 mm × 155 mm	6478-6-439	6478-6-705	6778-6-439
15 mm × 155 mm	6478-6-440	6478-6-710	6778-6-440
16 mm × 155 mm	6478-6-445	6478-6-715	6778-6-445
17 mm × 155 mm	6478-6-450	6478-6-720	6778-6-450
18 mm × 155 mm	6478-6-455	6478-6-725	6778-6-455
19 mm × 155 mm	6478-6-460	6478-6-730	6778-6-460
21 mm × 155 mm	6478-6-465	6478-6-740	6778-6-465
23 mm × 155 mm	6478-6-470	6478-6-750	6778-6-470

Cemented Stem Extenders	Implant Cat. No.	Trial Cat. No.
80 mm	6476-8-260	6778-7-060
155 mm	6476-8-270	6778-7-065

VI

Surgical Technique

VI.1 Meridian® ST Femoral Component* Meridian® PA Femoral Component* Meridian® TMZF® Femoral Component*

Surgical Technique Using the Command® Instrument System*

The Partnership® System, which includes the Meridian® ST, Meridian® PA and Meridian® TMZF® Femoral Components and the Command® Instruments, is a collaboration between Howmedica Osteonics, a group of orthopaedic surgeons and biomedical design engineers. This team has developed an integrated series of implants and instruments designed to address the needs of patients, surgeons, and O.R. staff in today's changing healthcare environment. The design group includes:

Lester S. Borden, MD
Head of Adult Reconstructive Surgery
Cleveland Clinic Foundation, Cleveland, OH

Edward T. Habermann, MD
Professor and Chairman
Department of Orthopaedic Surgery
Albert Einstein College of Medicine
Orthopaedic Surgeon-in-Chief
Montefiore Medical Center
Albert Einstein College of Medicine, Bronx, NY

Anthony K. Hedley, MD, FRCS
Chairman, Department of Orthopaedic Surgery
St. Luke's Medical Center, Phoenix, AZ

David S. Hungerford, MD
Chief, Division of Arthritis Surgery
Professor of Orthopaedic Surgery
Johns Hopkins University, Baltimore, MD
Chief of Orthopaedic Surgery
Good Samaritan Hospital, Baltimore, MD

Kenneth A. Krackow, MD
Professor of Orthopaedic Surgery
State University of New York at Buffalo
Department Head
Department of Orthopaedic Surgery
Buffalo General Hospital, Buffalo, NY

Roger N. Levy, MD
Chief of Arthritis Surgery
Mt. Sinai Medical Center, New York City, NY

Joseph C. McCarthy, MD
The Department of Orthopaedic Surgery
New England Baptist Hospital, Boston, MA
Associate Clinical Professor
Tufts University School of Medicine, Boston, MA

Philip C. Noble, PhD
Dunn Professor of Orthopedic Research
The Methodist Hospital, Houston, TX

Hugh S. Tullos, MD
Wilhelmina Barnhart Chairman
Department of Orthopedic Surgery
Baylor College of Medicine, Houston, TX

Roderick H. Turner, MD
The Department of Orthopaedic Surgery
New England Baptist Hospital, Boston, MA
Tufts University, Boston, MA

Technique Options

The Command® Instrument System is extremely versatile, offering surgeons great flexibility in approaching the implantation of the Meridian® Femoral Components. This publication presents a basic technique, followed by three appendices. Appendix I presents options for ***Starting***; Appendix II presents options for ***Reaming***; and Appendix III presents ***Technique Options at-a-Glance***, an over-view of the system. These options allow surgeons to customize the Command® Instrument System to an approach that suits individual preferences and circumstances.

Preoperative Templating

The Meridian® Hip System offers a complete set of femoral templates. All templates are at 120% magnification.

Acetabular Options

Howmedica Osteonics offers a wide variety of acetabular components that are compatible with the Meridian® Femoral Components. The surgeon should refer to a specific acetabular component's surgical technique for a discussion of acetabular surgical procedures.

Surgical Approach

Each surgeon should use the surgical approach for total hip arthroplasty with which he is most familiar. Patient positioning, prepping and draping, the skin incision, soft tissue dissection, and hip dislocation are performed according to the surgeon's preferred technique, making certain to adequately expose the acetabulum and the proximal femur.

This publication sets forth recommended procedures for using Howmedica Osteonics devices and instruments. It offers guidance that you should heed, but, as with any such technical guide, each surgeon must consider the particular needs of each patient and make appropriate adjustments when and as required.

*__Command®__: US Patent Nos. 5,665,091; 5,810,830; 5,607,431.
__Meridian®__: US Patent Nos. 4,550,448; 4,668,290; 4,714,468; 4,834,756; and 5,441,537

VI.2 STARTING†

Determine and Mark the Osteotomy Level

By using anatomic landmarks identified during templating, the osteotomy guide identifies the location of the osteotomy cut. The osteotomy guide has several features to assist the surgeon:

- [**A**] Long tail of the osteotomy guide for alignment with the femoral shaft axis.
- [**B**] Notch in the proximal portion of the guide for referencing the proximal tip of the greater trochanter.
- [**C**] Location holes for determining the center of rotation for the head position options available for stem size.

Care must be taken to restore proper leg length by referencing the osteotomy level back to the center of rotation of the implanted acetabular component.

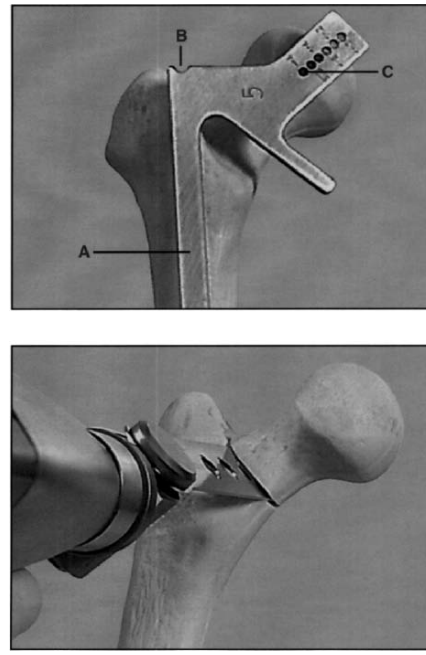

The resection level, relative to the lesser trochanter, should be about a fingerbreadth above. Angled surface provides a plane for marking the level of the cut, or can be used as a cutting surface for the sawblade.

Perform Osteotomy

A 40° osteotomy angle allows single cut across the neck, and generally reduces the need for a second cut to complete the resection.

† Additional options available; see Appendix I.

MERIDIAN®

Open and Size the Canal with Starter Awl

The tapered starter awl is a hand-operated instrument designed to open the femoral canal and indicate distal diameter size. Assemble the ***small*** hex T-handle onto starter/sizer awl, and target piriformis fossa to open canal. Progress the awl distally until some cortical resistance is achieved. Use aggressive cutting teeth of starter awl to achieve lateralization.

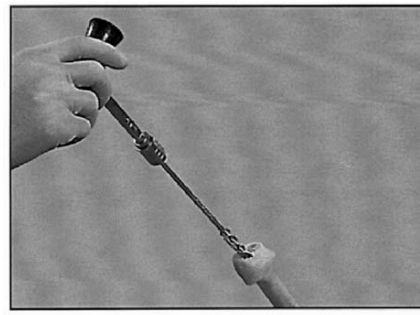

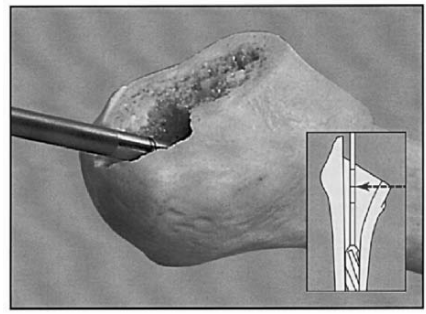

Depth of Starter Awl

Make note of millimeter diameter marking that appears at the medial osteotomy level. These marking grooves on shaft identify distal diameter sizing of femoral canal.

REAMING†

Assemble and Introduce Straight Reamer

Assemble a power adaptor or ***large*** hex T-handle, if preferred, to the straight, cylindrical reamer. Select diameter of reamer based on starter awl diameter reading, starting with a size one or two millimeters smaller.

Caution: Do not exceed diameter of anticipated implant size as indicated on preoperative templates.

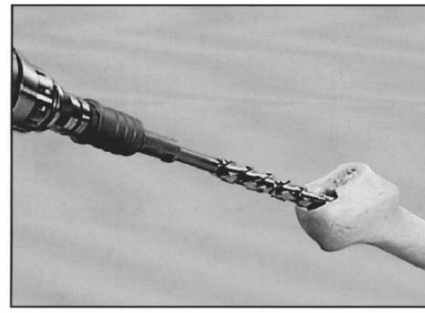

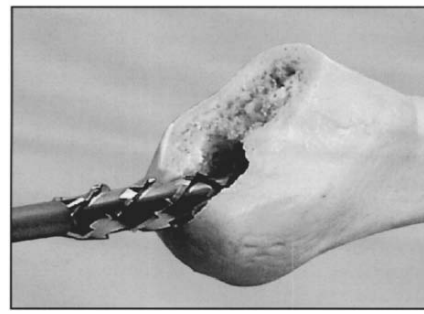

Use of the Straight Reamer and Depth Markings

Ensure the reamer is directed laterally and into a neutral position. Insert reamer until the most proximal depth marking groove is aligned with the medial edge of the osteotomy.

Note: When lateralizing rigid reamers, take care to properly retract/protect the abductor muscle fibers of the gluteus minimus/medius at the superior tip of the greater trochanter.

†Additional options available; see Appendix II.

MERIDIAN®

Select Proximal-Conical/Distal-Bullet Reamer

Select proximal-conical/distal-bullet reamer corresponding to the size of the implant determined by preoperative templating and the preceding cylindrical reaming. Each size implant has a corresponding proximal-conical/distal-bullet reamer. These reamers have the ***large*** hex drive fitting, which can be attached to the power adaptor or used with the large manual T-handle.

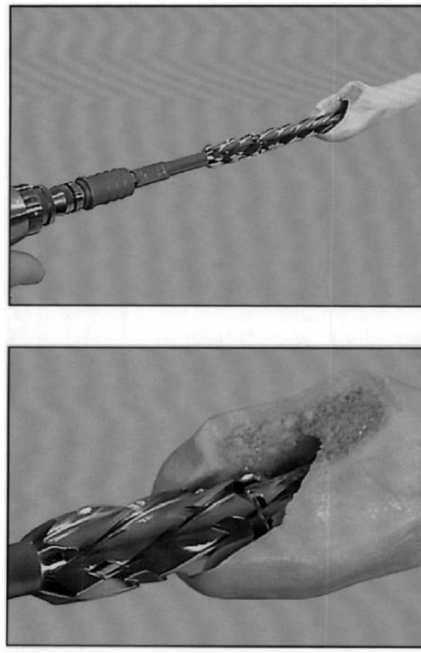

Position Proximal-Conical/Distal-Bullet Reamer and Gauge Depth

Insert proximal-conical/distal-bullet reamer into the canal, maintaining neutral/lateral alignment and achieving lateralization. Insert reamer until the most proximal depth marking groove is aligned with the medial edge of the osteotomy.

VI.3 BROACHING

Assemble Modular Distal Tip to Broach

Select a broach one size smaller than the anticipated implant size. Select modular distal tip that corresponds to the distal-bullet diameter of previous step. Assemble tip to broach by threading tip ***tightly*** onto end of broach; use pin-wrench, if necessary. Accurately sized modular bullet tip engages the axis that you have reamed, providing neutral placement of broach.

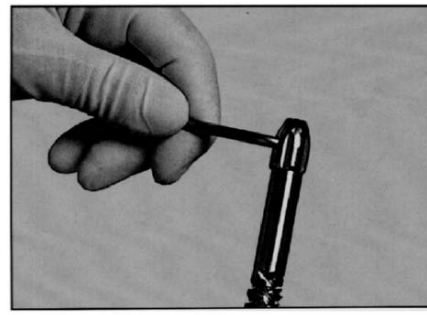

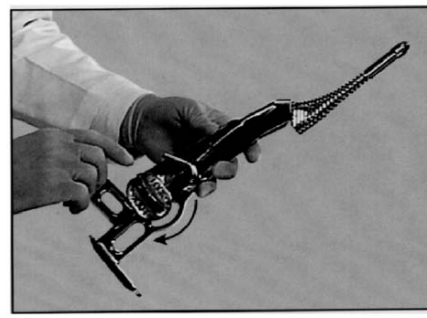

Assemble Broach Handle to Broach

Assemble the broach handle to the broach. Make sure that the tip of the broach handle is correctly mated with the keyway on the broach. For ease of assembly, hold hands as illustrated in the accompanying photograph. Turn cam in "lock" direction until audible clicks are heard, and the broach is securely attached.

MERIDIAN®

Introduce Broach

Introduce broach into proximal femur. Drive the broach down the canal with a mallet, keeping it aligned with the neutral femoral axis. ***Assess fit and resistance to movement***. If a larger size is needed, remove the broach and replace it with the next size.† To facilitate final seating of the broach, partially withdraw the broach to clear cutting teeth of bone; then re-introduce the instrument into the canal.

Note: If a broach larger than the size templated is to be used, it may be necessary to ream the canal up to the appropriate diameter.

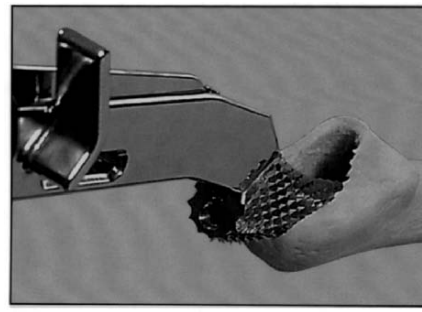

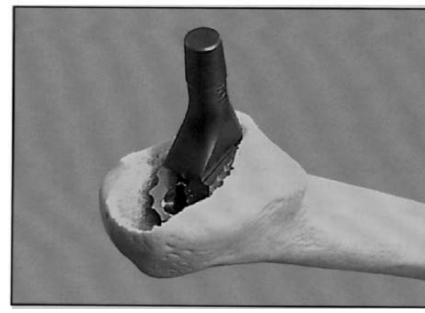

Fit Neck Trial to Broach

Disassemble the broach handle, and select appropriate size neck trial corresponding to broach/implant size, and push the neck trial securely onto the broach.

VI.4 COMPLETION

Attach Head Trial

Select the head diameter [22 mm, 26 mm, 28 mm, or 32 mm] according to surgeon preference. The head trials have a circumferential groove which identifies the level of the center of rotation. Select neck length: −4 mm,† Std., +4 mm, +8 mm, +12 mm, +16 mm† based on preoperative templating. Attach the head trial to the neck trial and perform a trial reduction, assessing the hip for stability, leg length, and overall range of motion. Remove the broach and all trials.

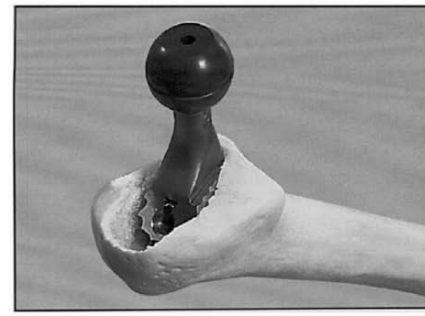

Note: +16 mm is only suitable for stem sizes #2 and above; −4 mm is not available in 22 mm or 26 mm head sizes. Refer to sizing chart on page 24.

Assemble Introducer to Implant

Assemble the insertion tool to the implant. ***Make sure that the distal tip of the instrument is correctly mated to the orientation keyway of the insertion feature of the implant***. For ease of assembly, hold hands as illustrated in the photograph at right, using the thumb to turn the locking knob. Fully and securely attach the instrument to the stem.

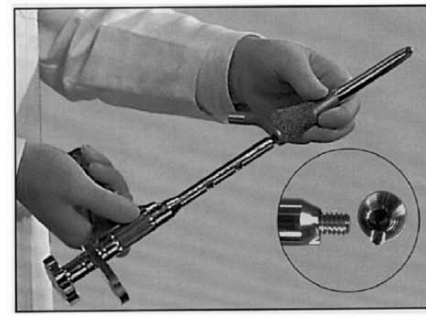

Insert the Implant

Insert the implant. The handle can be used to control anteversion as you implant the prosthesis. Remove the inserter by turning the locking knob on the top of the stem inserter.

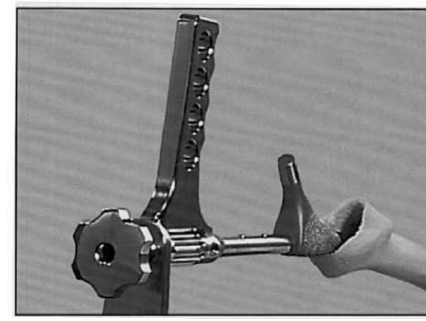

MERIDIAN®

Final Trial Reduction

A head trial can be placed onto the implant and a final trial reduction performed.

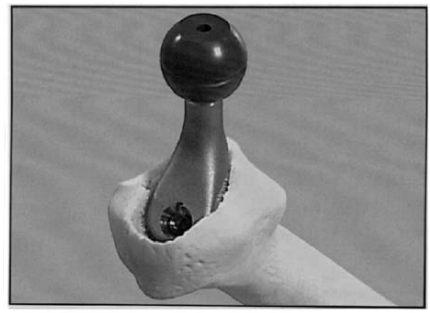

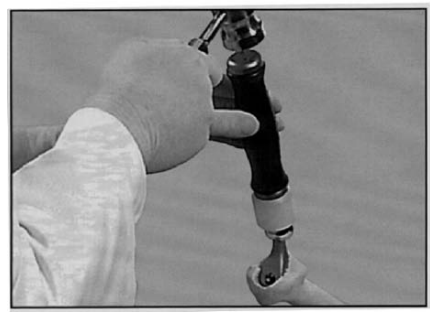

Impact Head onto Stem

Select appropriate size Howmedica Osteonics V40^{TM} femoral head, wipe trunnion clean, and impact head on trunnion with femoral head impactor.

Note: Only Howmedica Osteonics V40^{TM} femoral heads labeled as 5°40′ taper may be used with the stems in this system.

Reduce Joint and Close

Relocate the femoral head into the acetabular cup and check the laxity and range of motion. The surgical site is then closed according to the standard procedure for the surgical approach chosen.

VI.5 Starting Options

The Starter Kit has three technique options for opening and sizing the femoral canal. The options contain both standard and new methods for gaining access to the femoral canal and for providing a neutral/lateral start for each subsequent instrument.

Starting Option 1: Starter Awl (Presented in Basic Technique)

Open and Size the Canal with Starter Awl

The tapered starter awl is a hand-operated instrument designed to open the femoral canal and indicate distal diameter size. Assemble ***small*** hex T-handle onto starter/sizer awl, and target piriformis fossa to open canal. Progress the awl distally until some cortical resistance is achieved. Use aggressive cutting teeth of starter awl to achieve lateralization.

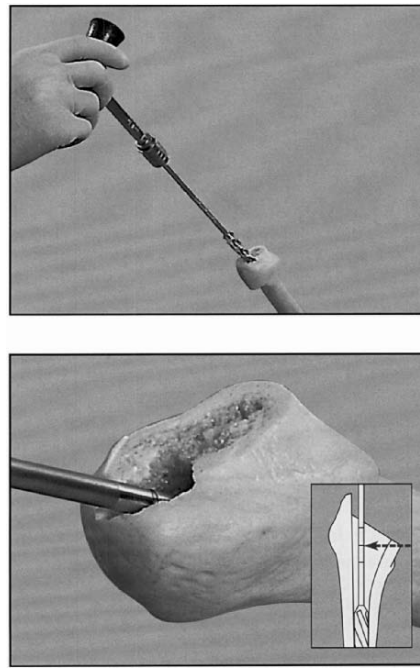

Depth of Starter Awl

Make note of millimeter diameter marking that appears at the medial osteotomy level. These marking grooves on shaft identify distal diameter sizing of femoral canal.

Starting Option 2: Box Chisel

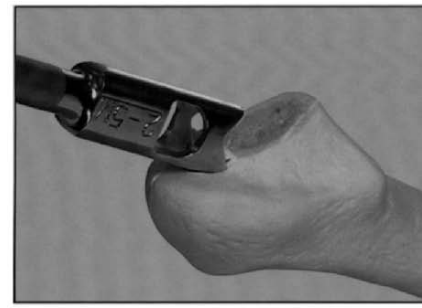

There are three sizes of the box chisels: the ***small*** size corresponds to the #00/9 mm to #1/11 mm Meridian® femoral implants; the ***medium*** to sizes #2/10 mm to #5/15 mm; and the ***large*** to sizes #6/14 mm to #9/19 mm.

Box Chisel Technique Variation A

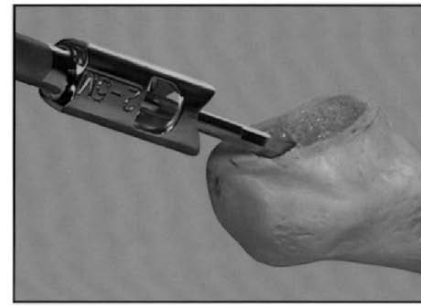

The box chisel may be used to open the proximal femur prior to use of the tapered starter/sizer awl. After the osteotomy has been performed, the appropriate size box chisel is selected and introduced into the axis of the femoral shaft, starting lateral to the cortex of the neck. This will remove a wedge of bone at the medial base of the greater trochanter, helping to achieve neutral/lateral alignment of the tapered starter/sizer awl.

Box Chisel Technique with Box Chisel Guide Variation B

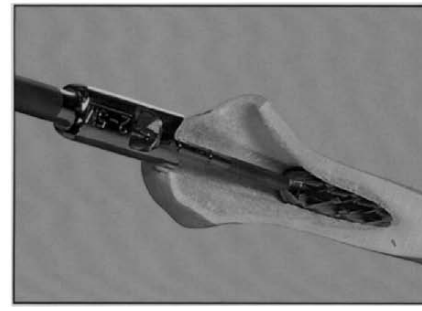

The box chisel may also be used with the sharp trochar point box chisel guide. Assemble the box chisel guide to the box chisel by threaded engagement. The box chisel guide is inserted into the long axis of the femur, targeting the piriformis fossa; the guide will serve to direct/align the box chisel cutting head.

Box Chisel Technique with the Starter Awl Variation C

The box chisel may also be used with the tapered starter/sizer awl. After the awl has been used to open and size the femoral canal, the ***small*** hex T-handle may be removed with the awl engaged in the isthmus of the femoral canal. The shaft of the awl may now be used as an axial guide coinciding with the long axis of the femur. The box chisel is cannulated so that it slides over the shaft of the awl, removing a wedge of bone at the medial base of the greater trochanter.

Starting Option 3: Proximal Reamer Sleeves with the Starter Awl

The System's proximal reamer sleeves come in three sizes. Those applicable to the Meridian® femoral components are: ***small*** (#00–#1), ***medium*** (#2–#5), and ***large*** (#6–#9). After the tapered starter awl has been used to open and size the distal femoral canal, remove it from the femur and assemble the appropriate size proximal reamer sleeve. Re-introduce the assembly of the proximal reamer sleeve and awl distally into the femoral canal. Lateralize the proximal reamer sleeve to manually groove out the medial aspect of the greater trochanter. The depth of insertion has been established in the previous step. The intent of the proximal reamer sleeve is to attain neutral alignment by lateralizing into the greater trochanter.

Note: When lateralizing rigid reamers, take care to properly retract/protect the abductor muscle fibers of the gluteus minimus/medius at the superior tip of the greater trochanter.

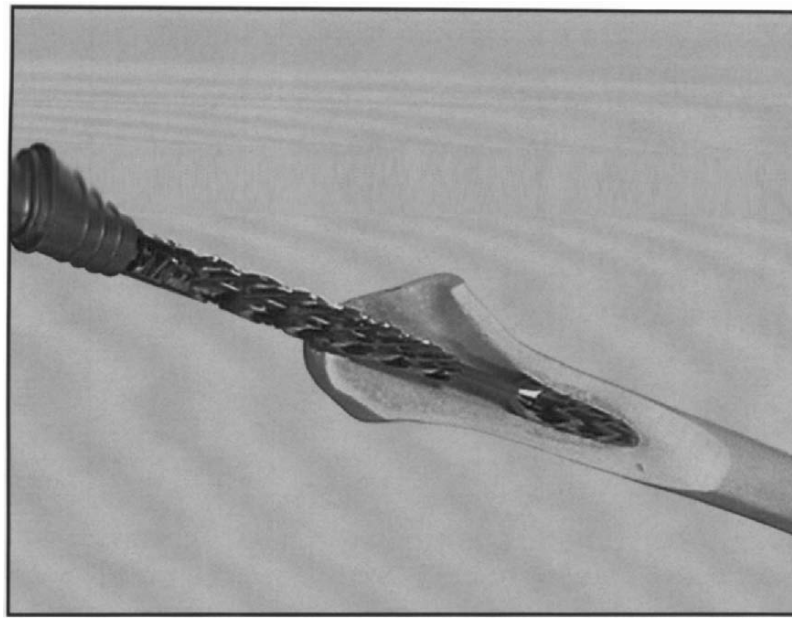

VI.6 Reaming Options

Presented here are six technique options for ***Reaming*** the femoral canal, using the Command® Instrument System:

Option 1: ***Straight Reamer and Proximal-Conical/Distal-Bullet Reamer***
Option 2: ***Proximal-Distal Baton Reamer***
Option 3: ***Gray™ Fixed Head IM Flexible Reamer***
Option 4: ***Gray™ Fixed Head IM Flexible Reamer and Proximal-Conical/Distal-Bullet Reamer***
Option 5: ***Proximal-Conical/Distal-Bullet Reamer and Flexible Proximal Reaming System***
Option 6: ***Proximal-Distal Baton Reamer and Flexible Proximal Reaming System***

Reaming Option 1: Straight Reamer and Proximal-Conical/Distal-Bullet Reamer (Presented in Basic Technique)

Assemble and Introduce Straight Reamer

Assemble a power adaptor or ***large*** hex T-handle, if preferred, to the straight, cylindrical reamer. Select diameter of reamer based on starter awl diameter reading, starting with a size one or two millimeters smaller.

Caution: Do not exceed diameter of anticipated implant size as indicated on preoperative templates.

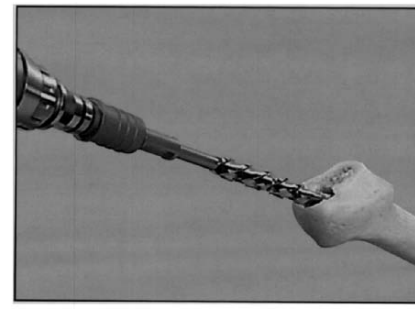

Use of the Straight Reamer and Depth Markings

Ensure the reamer is directed laterally and into a neutral position. Insert reamer until the most proximal depth marking groove is aligned with the medial edge of the osteotomy.

Note: When lateralizing rigid reamers, take care to properly retract/protect the abductor muscle fibers of the gluteus minimus/medius at the superior tip of the greater trochanter.

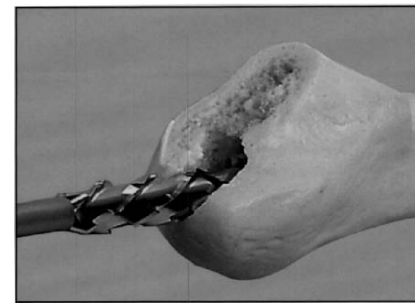

Continued on next page

Reaming Option 1: Straight Reamer and Proximal-Conical/Distal-Bullet Reamer (*Continued*)

Select Proximal-Conical/ Distal-Bullet Reamer

Select proximal-conical/distal-bullet reamer corresponding to the size of the implant determined by preoperative templating and the preceding cylindrical reaming. Each size implant has a corresponding proximal-conical/distal-bullet reamer. These reamers have the ***large*** hex drive fitting, which can be attached to the power adaptor or used with the large manual T-handle.

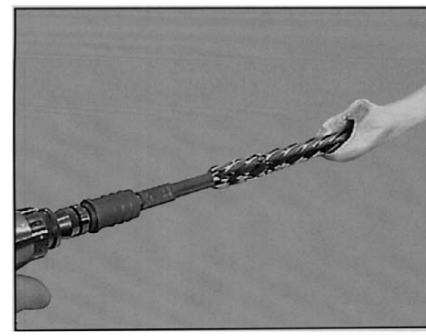

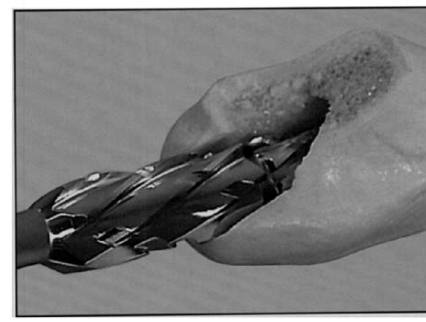

Position Proximal-Conical/Distal-Bullet Reamer and Gauge Depth

Insert proximal-conical/distal-bullet reamer into the canal, maintaining neutral/lateral alignment and achieving lateralization. Insert reamer until the most proximal depth marking groove is aligned with the medial edge of the osteotomy.

Reaming Option 2: Proximal-Distal Baton Reamer

Proximal-Distal Baton Reamer

The proximal-distal baton reamer is designed to combine the distal cutting of the straight IM reamer and the proximal cutting of the proximal-conical/distal-bullet reamer. [This reamer is also known as the ONE-STEP reamer.]

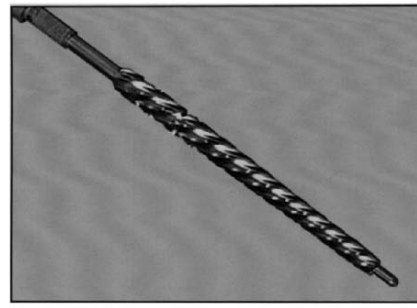

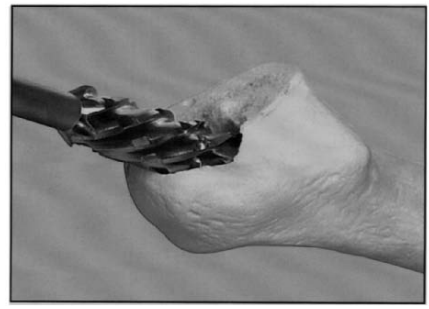

Introduce Proximal-Distal Baton Reamer

Assemble a power adapter or large hex T-handle, if preferred, to the proximal-distal baton reamer. Select the reamer that corresponds to the implant size as determined by preoperative templating and the distal diameter of the femoral canal as determined by the tapered starter/sizer awl. Each size implant has a corresponding proximal-distal baton reamer that will simultaneously prepare the distal diameter and proximal-conical region of the femoral canal. Insert proximal-distal baton reamer into the canal, maintaining neutral/lateral alignment and achieving lateralization. Advance the reamer distally until the depth marking groove is aligned with the medial edge of the osteotomy.

Reaming Option 3: Gray™ Fixed Head IM Flexible Reamer

Gray™ Fixed Head IM Flexible Reamer

To prepare the cylindrical, distal diameter using flexible reamers rather than straight cylindrical reamers, select diameter of reamer based on starter awl diameter reading. Start with a size one or two millimeters smaller.

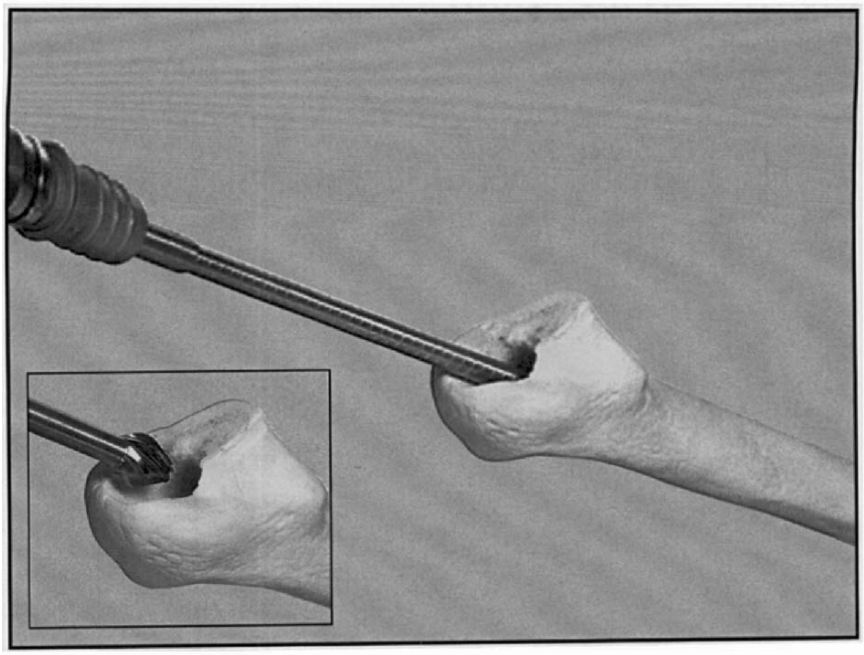

Reaming Option 4: Gray™ Fixed Head IM Flexible Reamer and Proximal-Conical/Distal-Bullet Reamer

Gray™ Fixed Head IM Flexible Reamer

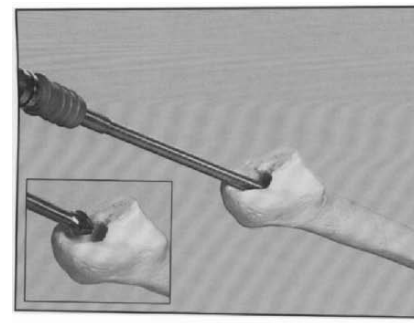

To prepare the cylindrical, distal diameter using flexible reamers rather than straight cylindrical reamers, select diameter of reamer based on starter awl diameter reading. Start with a size one or two millimeters smaller.

Select Proximal-Conical/ Distal-Bullet Reamer

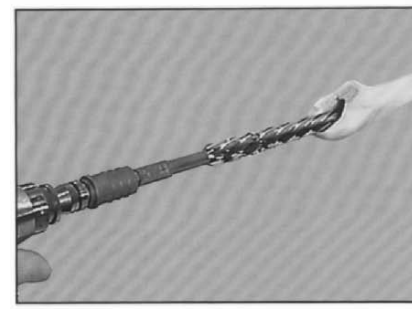

Select proximal-conical/distal-bullet reamer corresponding to the size of the implant determined by preoperative templating and the preceding cylindrical reaming. Each size implant has a corresponding proximal-conical/distal-bullet reamer. These reamers have the ***large*** hex drive fitting, which can be attached to the power adaptor or used with the large manual T-handle.

Position Distal-Bullet Reamer and Gauge Depth

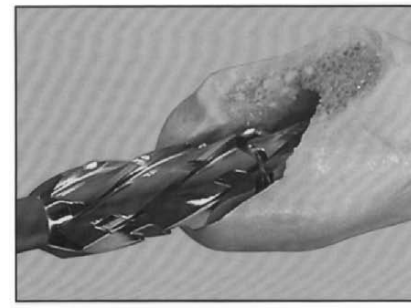

Insert proximal-conical/distal-bullet reamer into the canal, maintaining neutral/lateral alignment and achieving lateralization. Insert reamer until the most proximal depth marking groove is aligned with the medial edge of the osteotomy.

Reaming Option 5: Proximal-Conical/Distal-Bullet Reamer and Flexible Proximal Reaming System

Assemble and Introduce Straight Reamer

Assemble a power adaptor or ***large*** hex T-handle, if preferred, to the straight, cylindrical reamer. Select diameter of reamer based on starter awl diameter reading, starting with a size one or two millimeters smaller.

Caution: Do not exceed diameter of anticipated implant size as indicated on preoperative templates.

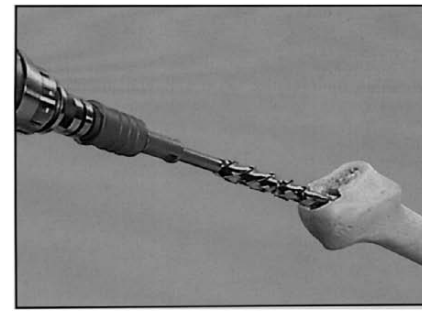

Use of the Straight Reamer and Depth Markings

Ensure the reamer is directed laterally and into a neutral position. Insert reamer until the most proximal depth marking groove is aligned with the medial edge of the osteotomy.

Note: When lateralizing rigid reamers, take care to properly retract/protect the abductor muscle fibers of the gluteus minimus/medius at the superior tip of the greater trochanter.

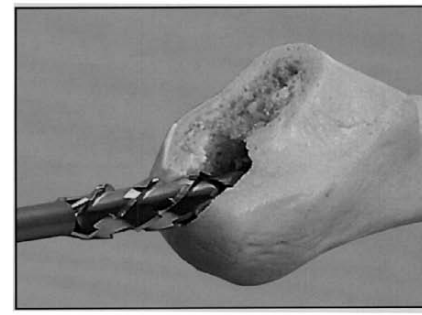

Select Proximal-Conical/ Distal-Bullet Reamer

Select proximal-conical/distal-bullet reamer corresponding to the size of the implant determined by preoperative templating and the preceding cylindrical reaming. Each size implant has a corresponding proximal-conical/distal-bullet reamer. These reamers have the ***large*** hex drive fitting, which can be attached to the power adaptor or used with the large manual T-handle.

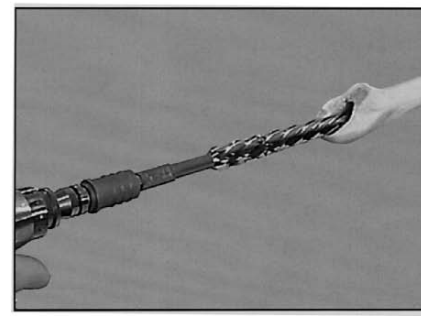

Position Distal-Bullet Reamer and Gauge Depth

Insert proximal-conical/distal-bullet reamer into the canal, maintaining neutral/lateral alignment and achieving lateralization. Insert reamer until the most proximal depth marking groove is aligned with the medial edge of the osteotomy.

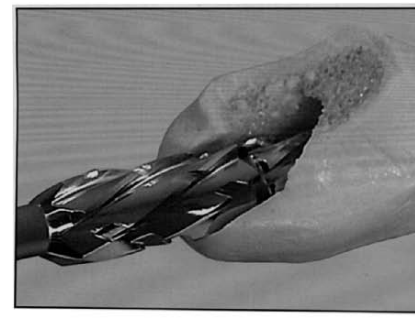

Flexible Proximal Reaming System

The Flexible Proximal Reaming System is designed to machine the medial flare/curve of the metaphysis. Used with the other medullary reamers available in the Command™ Instruments, the flexible proximal reaming system will reduce the amount of effort required during broaching.

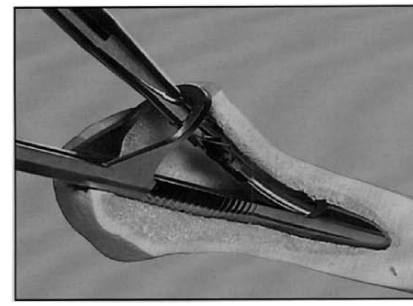

Use of the Flexible Proximal Reaming System

The Flexible Proximal Reaming System is comprised of one handle, two flexible proximal reamers (same size), and 16 templates for flexible proximal reaming. [There are no templates for sizes #00/9 mm and #0/10 mm.] Select the appropriate size template, based on preoperative templating and the last proximal-distal baton reamer used. Attach the template handle with torsion bar directed laterally. Secure by means of threaded engagement. Insert the template into the long axis of the femur until the metaphyseal loop rests on the osteotomy cut.

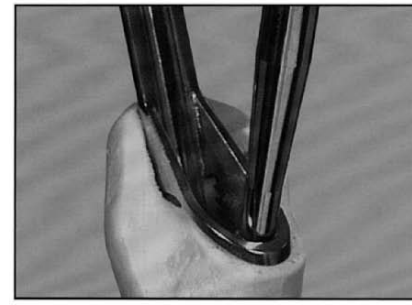

Note: The loop, when resting on the osteotomy cut, will serve as a guide to the size implant that will fill the metaphysis of the femur. The template may be tapped into place, using the lateral cutting teeth to attain neutral alignment and some light fixation. Once the proper template is in place, the flexible proximal reamer may be introduced into the internal track of the template. The medial and anterior/posterior calcar may be reamed by flexing the reamer to the margin of the loop, and "feathering" the reamer proximal to distal until the reamer "bottoms" in the distal template. When reaming is complete, remove the template and introduce the definitive broach into the proximal femur utilizing traditional broaching technique.

Reaming Option 6: Proximal-Distal Baton Reamer and Flexible Proximal Reaming System

Proximal-Distal Baton Reamer

The proximal-distal baton reamer is designed to combine the distal cutting of the straight IM reamer and the proximal cutting of the proximal-conical/distal-bullet reamer. [This reamer is also known as the ONE-STEP reamer.]

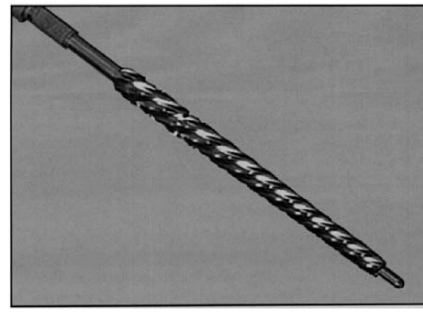

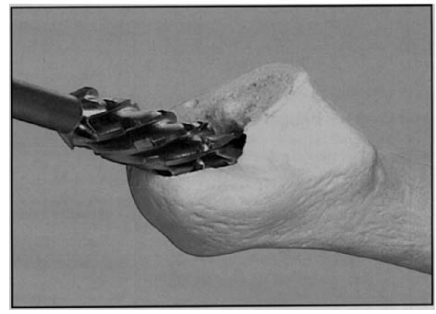

Introduce Proximal-Distal Baton Reamer

Assemble a power adapter or large hex T-handle, if preferred, to the proximal-distal baton reamer. Select the reamer that corresponds to the implant size as determined by preoperative templating and the distal diameter of the femoral canal as determined by the tapered starter/sizer awl. Each size implant has a corresponding proximal-distal baton reamer that will simultaneously prepare the distal diameter and proximal-conical region of the femoral canal. Insert proximal-distal baton reamer into the canal, maintaining neutral/lateral alignment and achieving lateralization. Advance the reamer distally until the depth marking groove is aligned with the medial edge of the osteotomy.

Flexible Proximal Reaming System

The Flexible Proximal Reaming System is designed to machine the medial flare/curve of the metaphysis. Used with the other medullary reamers available in the Command® Instruments, the flexible proximal reaming system will reduce the amount of effort required during broaching.

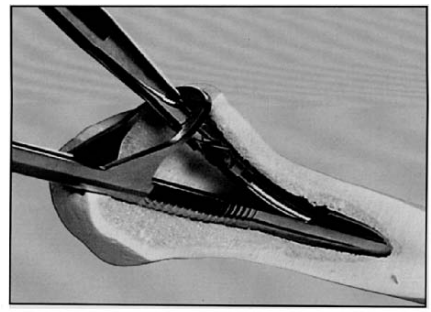

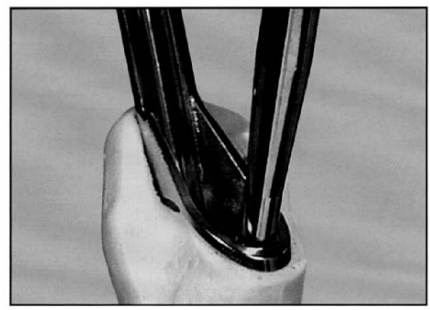

Use of the Flexible Proximal Reaming System

The Flexible Proximal Reaming System is comprised of one handle, two flexible proximal reamers (same size), and 16 templates for flexible proximal reaming. [There are no templates for sizes #00/9 mm and #0/10 mm.] Select the appropriate size template, based on preoperative templating and the last proximal-distal baton reamer used. Attach the template handle with torsion bar directed laterally. Secure by means of threaded engagement. Insert the template into the long axis of the femur until the metaphyseal loop rests on the osteotomy cut.

Note: The loop, when resting on the osteotomy cut, will serve as a guide to the size implant that will fill the metaphysis of the femur. The template may be tapped into place, using the lateral cutting teeth to attain neutral alignment and some light fixation. Once the proper template is in place, the flexible proximal reamer may be introduced into the internal track of the template. The medial and anterior/posterior calcar may be reamed by flexing the reamer to the margin of the loop, and "feathering" the reamer proximal to distal until the reamer "bottoms" in the distal template. When reaming is complete, remove the template and introduce the definitive broach into the proximal femur utilizing traditional broaching technique.

VII

Total Hip System

Exeter™ total hip system V40™

The Exeter™ V40™ stem

The V40™ trunnion has been incorporated onto the Exeter™ stem as part of the standardization of the Stryker® Howmedica Osteonics hip range to a single trunnion design.

No aspect of the stem design that resides within the cement mantle has been modified. The V40™ has been included with minimal change to the neck of the prosthesis as illustrated in **Figure 1**.

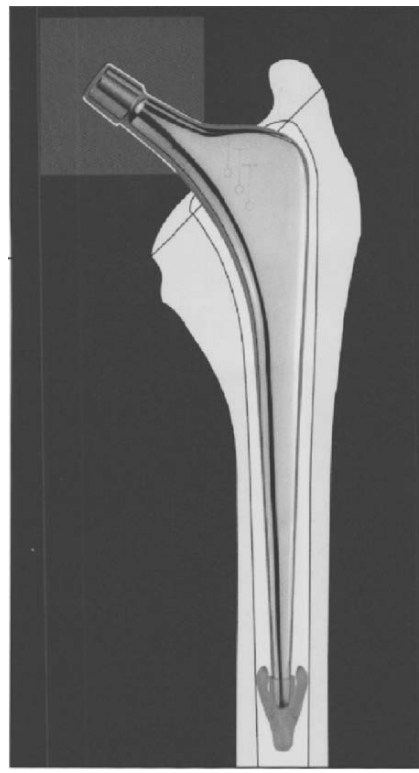

Figure 1. The V40™ trunnion superimposed on the previous Exeter™ trunnion, (indicated in white) showing no change to the stem design residing within the cement mantle.

The Exeter™ V40™ stem introducer

To assist ease of implantation of the Exeter™ V40™ implant, a V40™ stem introducer has been developed. It provides for a positive engagement between the introducer and a dimple in the lateral shoulder of the prosthesis,

see **Figure 2** inset. The dimple has been placed in a region of low tensile stress.

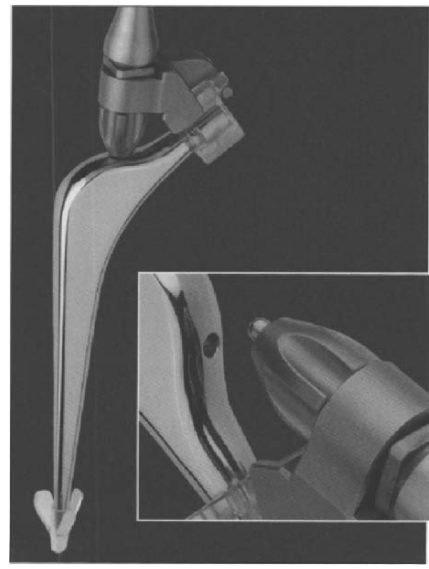

Figure 2. The connection of the V40™ stem introducer with the Exeter™ V40™ stem.

The technical requirement for the stem introducer was not to change the method of releasing the stem. This has been achieved through an evolution of the original stem introducer design, retaining the connection with the trunnion protector so that the Exeter™ V40™ stem can still be implanted with the original stem introducer. A smooth trigger action mechanism, carefully positioned in relation to an ergonomically designed handle, ensures complete control of the V40™ stem introducer while it is being released from the stem, without disturbing the cement mantle.

The Exeter™ V40™ stem increased range of motion

The Exeter™ V40™ stem, with a smaller diameter neck at the base of the trunnion, will afford an increase in range of motion. This increase in ROM will depend on the chosen diameter of the femoral head, as illustrated in *Table 1.*

Table 1.

Diameter of Head	Nominal Range Of Motion (ROM)		
	Previous Exeter™ Stem	Exeter™ V40™ Stem	Increase in ROM
22.2 mm	98°	110°	+12°
26 mm	111°	120°	+9°
28 mm	116°	125°	+9°
30 mm	120°	128°	+8°
32 mm	120°	128°	+8°

The Exeter™ V40™ system provides:

- Increased implant size range
- Increased head offset options
- Increased range of motion
- State-of-the-art stem introducer
- Easy to use modular rasps
- No change to the long established Exeter design principles

The Exeter™ V40™ Modular Rasps:

From pre-operative templating to final implantation, the goal of the Exeter Instrumentation is to provide an easy-to-use instrument system that improves operating room efficiency. For accurate trialing, modular Exeter™ V40™ Trial Necks feature a V40™ trunnion[1] to replicate the Exeter™ V40™ implant. The modular neck trials will allow the operating surgeon to trial different stem offsets without having to remove the rasp from the femoral canal. In addition, it will also enable the operating surgeon to work on the acetabulum while leaving the rasp in place. The modular rasp system is designed to achieve a high level of simplicity and precision while allowing greater intra-operative flexibility. See Figure 3 & 4.

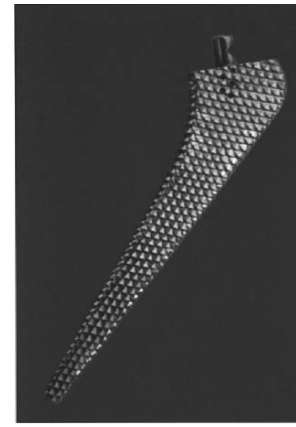

Figure 3. Exeter™ Modular Rasp.

Figure 4. Exeter™ V40™ Neck Trial.

The Exeter™ V40™ enhanced range of options

Three new stem sizes have been added to the Exeter™ V40™ range, bringing the number of stem sizes up to twenty-four, spread over a range of six offsets.

The new sizes are:

- 44 mm offset No.0
- 50 mm offset No.1
- 50 mm offset No.2

The new stems have been subject to rigorous testing to confirm their mechanical performance will meet the standards set by the existing range.

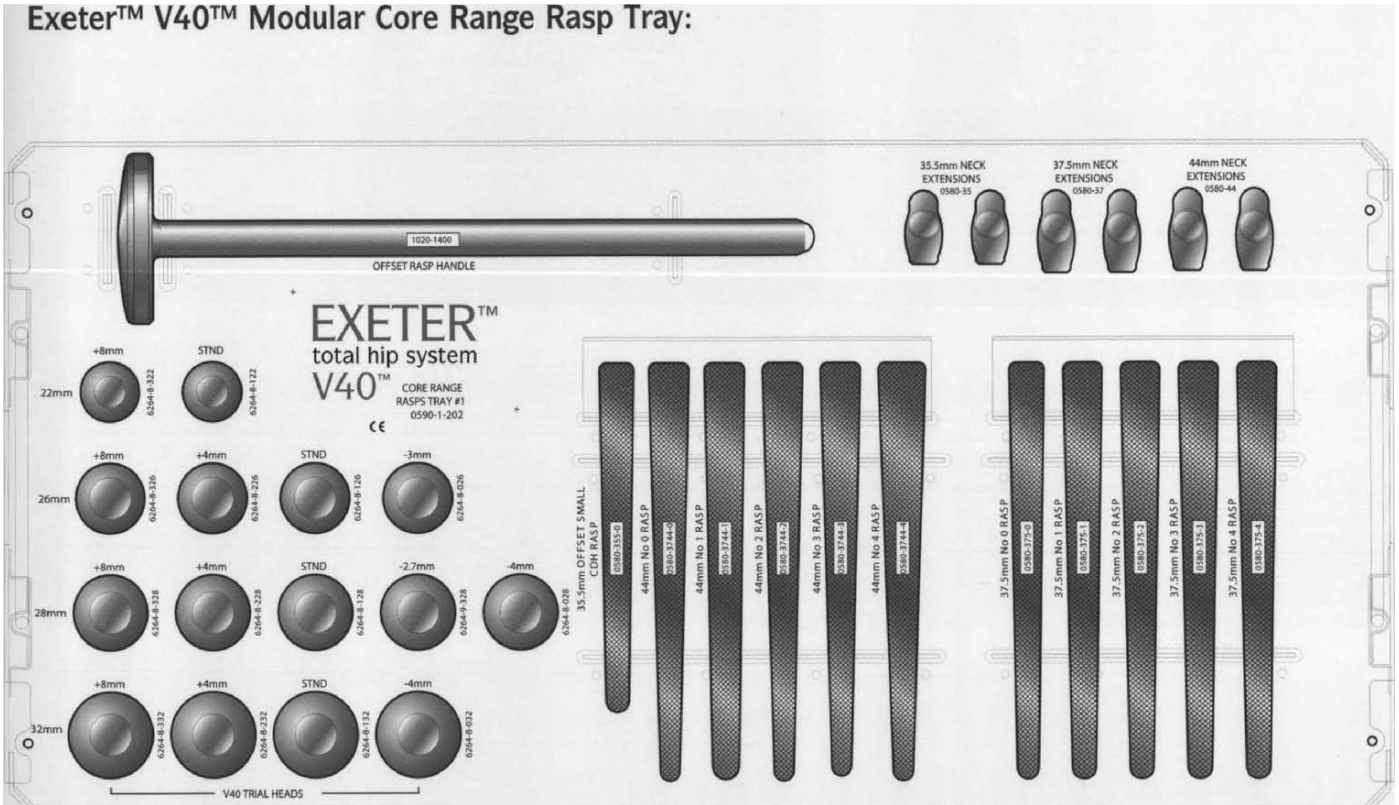
Exeter™ V40™ Modular Core Range Rasp Tray:
1020-1400
OFFSET RASP HANDLE
35.5mm NECK EXTENSIONS 0580-35
37.5mm NECK EXTENSIONS 0580-37
44mm NECK EXTENSIONS 0580-44
EXETER™
total hip system
V40™
CORE RANGE RASPS TRAY #1 0590-1-202
22mm
26mm
28mm
32mm
+8mm
STND
+4mm
-3mm
-2.7mm
-4mm
6264-8-322
6264-8-122
6264-8-326
6264-8-226
6264-8-126
6264-8-026
6264-8-328
6264-8-228
6264-8-128
6264-9-328
6264-8-028
6264-8-332
6264-8-232
6264-8-132
6264-8-032
V40 TRIAL HEADS
35.5mm OFFSET SMALL CDH RASP
0580-355-0
44mm No 0 RASP
0580-3744-0
44mm No 1 RASP
0580-3744-1
44mm No 2 RASP
0580-3744-2
44mm No 3 RASP
0580-3744-3
44mm No 4 RASP
0580-3744-4
37.5mm No 0 RASP
0580-375-0
37.5mm No 1 RASP
0580-375-1
37.5mm No 2 RASP
0580-375-2
37.5mm No 3 RASP
0580-375-3
37.5mm No 4 RASP
0580-375-4

Ordering Information: Exeter™ V40™ Instruments

Core Range Rasp Tray:

#	Catalog No.	Description
1	0580-355-0	35.5 mm Offset Small CDH Rasp
2	0580-375-0	37.5 mm No 0 Rasp
3	0580-375-1	37.5 mm No 1 Rasp
4	0580-375-2	37.5 mm No 2 Rasp
5	0580-375-3	37.5 mm No 3 Rasp
6	0580-375-4	37.5 mm No 4 Rasp
7	0580-3744-0	44 mm No 0 Rasp
8	0580-3744-1	44 mm No 1 Rasp
9	0580-3744-2	44 mm No 2 Rasp
10	0580-3744-3	44 mm No 3 Rasp
11	0580-3744-4	44 mm No 4 Rasp
12	0580-35 (2)	35.5 mm Neck Extension
13	0580-37 (2)	37.5 mm Neck Extension
14	0580-44 (2)	44 mm Neck Extension
15	6264-8-122	22 mm V40 Trial Head 0
16	6264-8-322	22 mm V40 Trial Head +8
17	6264-8-026	26 mm V40 Trial Head −3
18	6264-8-126	26 mm V40 Trial Head 0
19	6264-8-226	26 mm V40 Trial Head +4
20	6264-8-326	26 mm V40 Trial Head +8
21	6264-8-028	28 mm V40 Trial Head −4
22	6264-9-328	28 mm V40 Trial Head −2.7
23	6264-8-128	28 mm V40 Trial Head 0
24	6264-8-228	28 mm V40 Trial Head +4
25	6264-8-328	28 mm V40 Trial Head +8
26	6264-8-032	32 mm V40 Trial Head −4
27	6264-8-132	32 mm V40 Trial Head 0
28	6264-8-232	32 mm V40 Trial Head +4
29	6264-8-332	32 mm V40 Trial Head +8
30	1020-1400	Rasp Handle
31	0590-1-202	Exeter Core Range Rasp Tray
32	6136-0-950	Single Tier Outer Case

Extension 50 mm Rasp Tray: (not shown)

#	P/N	Description
1	0580-30-0	30 mm Offset A/P Rasp
2	0580-33-0	33 mm Offset A/P Rasp
3	0580-4450-1	50 mm No 1 Rasp
4	0580-4450-2	50 mm No 2 Rasp
5	0580-4450-3	50 mm No 3 Rasp
6	0580-4450-4	50 mm No 4 Rasp
7	0580-4450-5	50 mm No 5 Rasp
8	0580-30	30 mm Offset Neck Trial
9	0580-33	33 mm Offset Neck Trial
10	0580-50	50 mm Offset Neck Trial
11	6264-8-122	22 mm V40 Trial Head 0
12	6264-8-322	22 mm V40 Trial Head +8
13	6264-8-026	26 mm V40 Trial Head −3
14	6264-8-126	26 mm V40 Trial Head 0
15	6264-8-226	26 mm V40 Trial Head +4
16	6264-8-326	26 mm V40 Trial Head +8
17	6264-8-028	28 mm V40 Trial Head −4
18	6264-8-128	28 mm V40 Trial Head 0
29	6264-8-228	28 mm V40 Trial Head +4
20	6264-8-328	28 mm V40 Trial Head +8
21	6264-9-328	28 mm V40 Trial Head −2.7
22	6264-8-032	32 mm V40 Trial Head −4
23	6264-8-132	32 mm V40 Trial Head 0
24	6264-8-232	32 mm V40 Trial Head +4
25	6264-8-332	32 mm V40 Trial Head +8
26	1120-1000	Slotted Mallett
27	1020-1400	Rasp Handle
28	0930-5-000	V40 Introducer
29	0930-6-000	V40 Leg Length Gauge
30	0590-2-200	Inner Tray
31	6136-0-950	Single Tier Outer Case

Exeter™ V40™ General Tray:

#	Catalog No.	Description
1.	1120-1000	Slotted Mallet
2.	1020-1400	Rasp Handle
3.	0930-5-000	V40 Introducer
4.	0930-6-000	V40 Leg Length Gauge
5.	0932-0-000	Tapered Pin Reamer
6.	1113-1001	Box Chisel
7.	1020-2700	Calcar Planer
8.	0590-1-201	Inner Tray
9.	6136-0-950	Single Tier Outer Case

Exeter™ V40™ Optional Instruments:

#	Catalog No.	Description
1.	0932-2-000	Tapered Pin Reamer Large
2.	0933-2-000	Gouge Half Crook
3.	0932-4-000	Gouge Double Crook
4.	0929-1-000	Femoral Lever
5.	0929-2-000	Gluteus Medius Retractor
6.	0929-3-000	Capsulotomy Scissors
7.	0937-3-200	Horse Collar Backing Plate
8.	0937-8-100	Proximal Seal Backing Plate

Ordering Information: Exeter™ V40™ Implants

The Complete Range of Exeter™ V40™ Stems

Catalog No.	Description	Rasp non-V40™	Impactor non-V40™	
0580-1-300	Femoral Stem 30 mm offset			
0580-1-330	Femoral Stem 33 mm offset			
0580-1-351	Femoral Stem 35.5 mm offset			
0580-1-352	Femoral Stem 37.5 mm offset No.0			
0580-1-371	Femoral Stem 37.5 mm offset No.1			
0580-1-372	Femoral Stem 37.5 mm offset No.2			
0580-1-373	Femoral Stem 37.5 mm offset No.3			
0580-1-374	Femoral Stem 37.5 mm offset No.4			
0580-1-440	Femoral Stem 44 mm offset No.0	0580-9-440	0943-4-440	NEW
0580-1-441	Femoral Stem 44 mm offset No.1			
0580-1-442	Femoral Stem 44 mm offset No.2			
0580-1-443	Femoral Stem 44 mm offset No.3			
0580-1-444	Femoral Stem 44 mm offset No.4			
0580-1-445	Femoral Stem 44 mm offset No.5			
0580-1-501	Femoral Stem 50 mm offset No.1	0580-9-501	0943-4-501	NEW
0580-1-502	Femoral Stem 50 mm offset No.2	0580-9-502	0943-4-502	NEW
0580-1-503	Femoral Stem 50 mm offset No.3			
0580-1-504	Femoral Stem 50 mm offset No.4			
0580-1-505	Femoral Stem 50 mm offset No.5			
0580-1-200	44 mm offset No.3 Stem 200 mm			
0580-1-220	44 mm offset No.3 Stem 220 mm			
0580-1-240	44 mm offset No.3 Stem 240 mm			
0580-1-260	44 mm offset No.3 Stem 260 mm			
0580-3-422	44 mm offset No.2 Stem 205 mm			

Exeter™ Trial Heads For Monobloc Rasps/ Exchange Impactors

Part Number	Exeter™ Trial Heads For Monobloc Rasps/ Exchange Impactors
6364-8-122	22 mm Standard
6364-8-026	26 mm −3
6364-8-126	26 mm Standard
6364-8-226	26 mm +4
6364-8-028	28 mm −4
6364-8-128	28 mm Standard
6364-8-228	28 mm +4
6364-8-032	32 mm −4
6364-8-132	32 mm Standard
6364-8-232	32 mm +4
0930-6-001	Trial Trunnion Protector

Orthinox™ V40™ Femoral Heads

Catalog No.	Description
6364-2-122	Orthinox V40 Femoral Head 22 mm
6364-2-322	Orthinox V40 Femoral Head 22 mm +8
6364-2-026	Orthinox V40 Femoral Head 26 mm −3 mm Neck
6364-2-126	Orthinox V40 Femoral Head 26 mm
6364-2-226	Orthinox V40 Femoral Head 26 mm +4 mm Neck
6364-2-326	Orthinox V40 Femoral Head 26 mm +8 mm Neck
6364-2-028	Orthinox V40 Femoral Head 28 mm −4 mm Neck
6364-2-128	Orthinox V40 Femoral Head 28 mm
6364-2-228	Orthinox V40 Femoral Head 28 mm +4 mm Neck
6364-2-328	Orthinox V40 Femoral Head 28 mm +8 mm Neck
6364-2-032	Orthinox V40 Femoral Head 32 mm −4 mm Neck
6364-2-132	Orthinox V40 Femoral Head 32 mm
6364-2-232	Orthinox V40 Femoral Head 32 mm +4 mm Neck
6364-2-332	Orthinox V40 Femoral Head 32 mm +8 mm Neck

EXETER™
total hip system
V40™

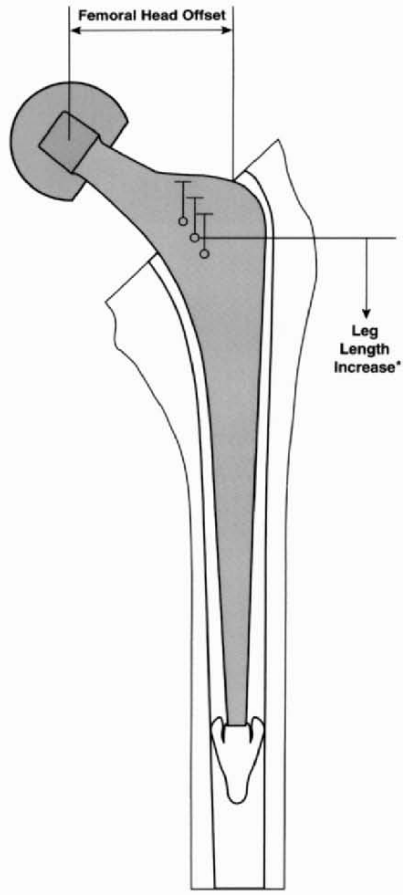

stryker
Howmedica

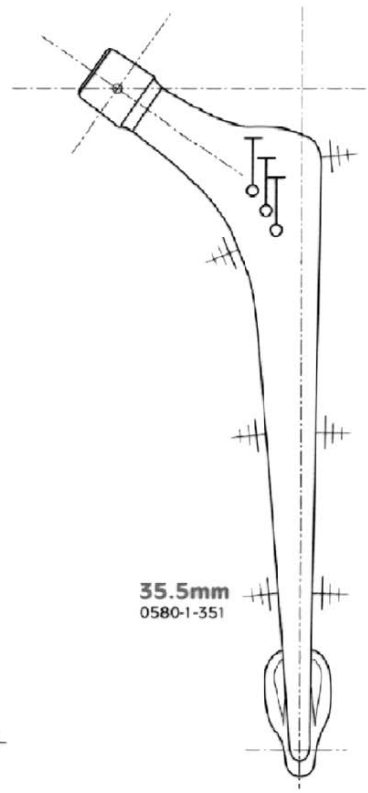

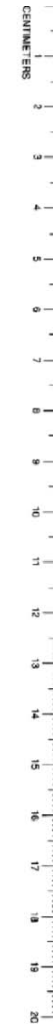

EXETER™
total hip system
V40™
core range

20% oversize to allow for X-Ray magnification

Graduated marker indicating minimum cement mantle 2 mm

Alignment points:
Proximal Stem seal

Neck resection level

The stem centralizer will compress to a minimum of 10 mm. If the femoral canal is less than this, the centralizer wings should be removed.

stryker
Howmedica
OSTEONICS
59 Route 17 South
Allendale, NJ 07401
www.howost.com

Stryker® is a registered trademark of Stryker Corporation.
Exeter™ and V40™ are trademarks of Howmedica Osteonics Corp.
©Howmedica Osteonics 2002 Lit. No. **LTEM68 1M** 03/02 MC/HCG Printed in U.S.A.

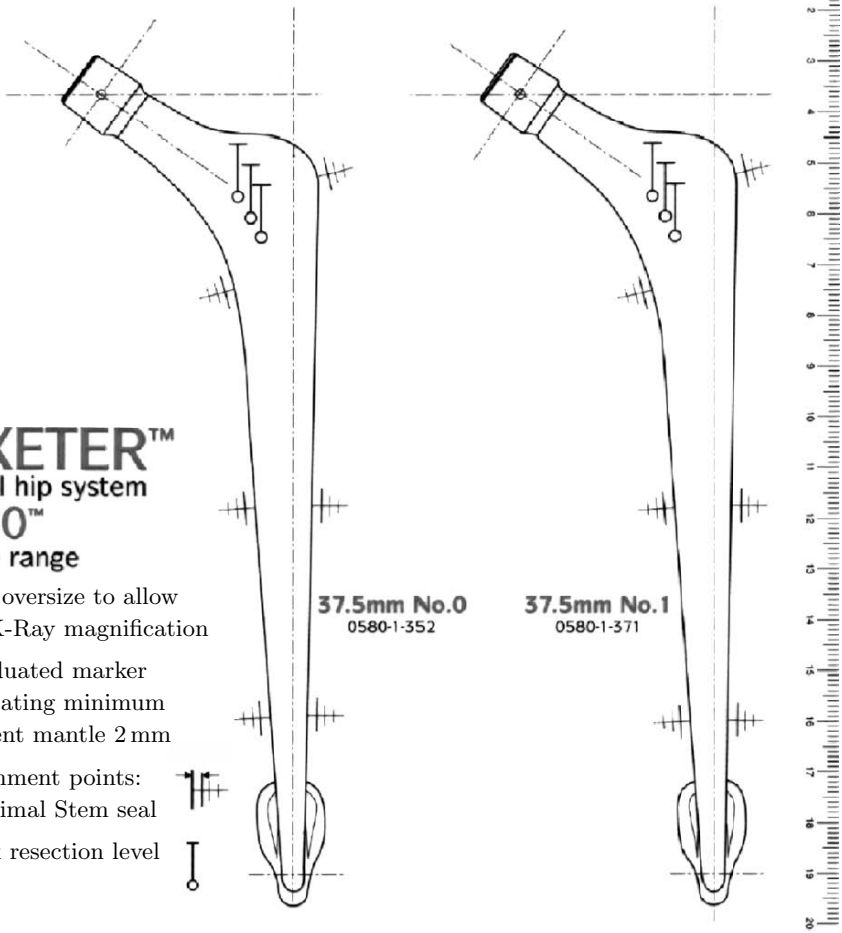

EXETER™
total hip system
V40™
core range

20% oversize to allow for X-Ray magnification

Graduated marker indicating minimum cement mantle 2 mm

Alignment points: Proximal Stem seal

Neck resection level

The stem centralizer will compress to a minimum of 10 mm. If the femoral canal is less than this, the centralizer wings should be removed.

Stryker® is a registered trademark of Stryker Corporation.
Exeter™ and V40™ are trademarks of Howmedica Osteonics Corp.
©Howmedica Osteonics 2002 Lit. No. **LTEM68 1M** 03/02 MC/HCG Printed in U.S.A.

stryker
Howmedica
OSTEONICS
59 Route 17 South
Allendale, NJ 07401
www.howmet.com

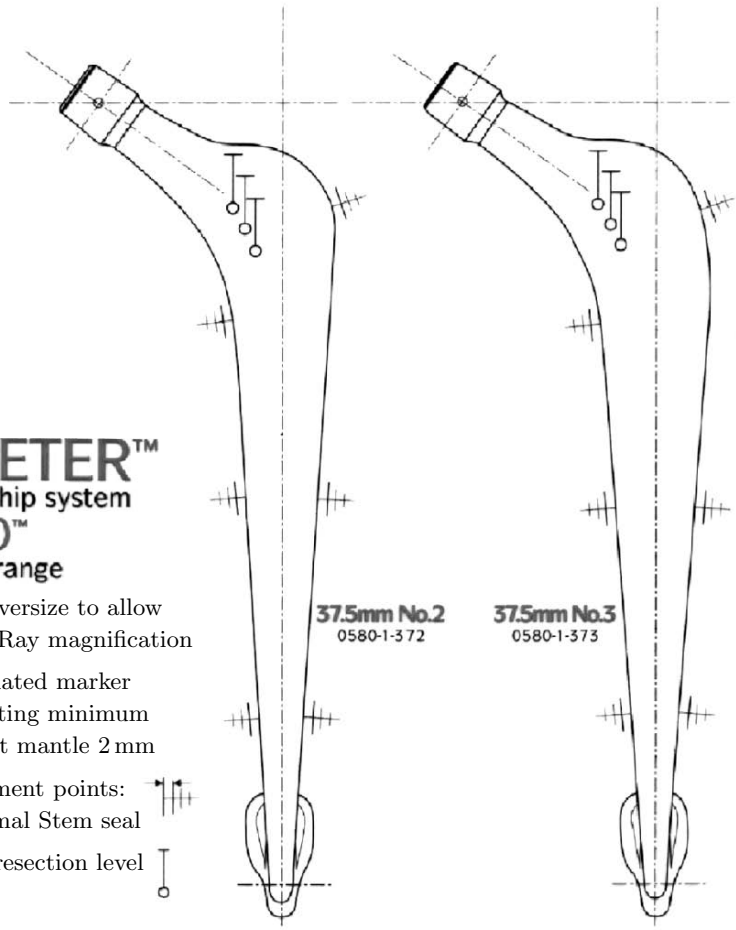

EXETER™
total hip system
V40™
core range

20% oversize to allow for X-Ray magnification

Graduated marker indicating minimum cement mantle 2 mm

Alignment points: Proximal Stem seal

Neck resection level

The stem centralizer will compress to a minimum of 10 mm. If the femoral canal is less than this, the centralizer wings should be removed.

Stryker® is a registered trademark of Stryker Corporation.
Exeter™ and V40™ are trademarks of Howmedica Osteonics Corp.
©Howmedica Osteonics 2002 Lit. No. **LTEM68 1M** 03/02 MC/HCG Printed in U.S.A.

stryker
Howmedica
OSTEONICS
59 Route 17 South
Allendale, NJ 07401
www.howmet.com

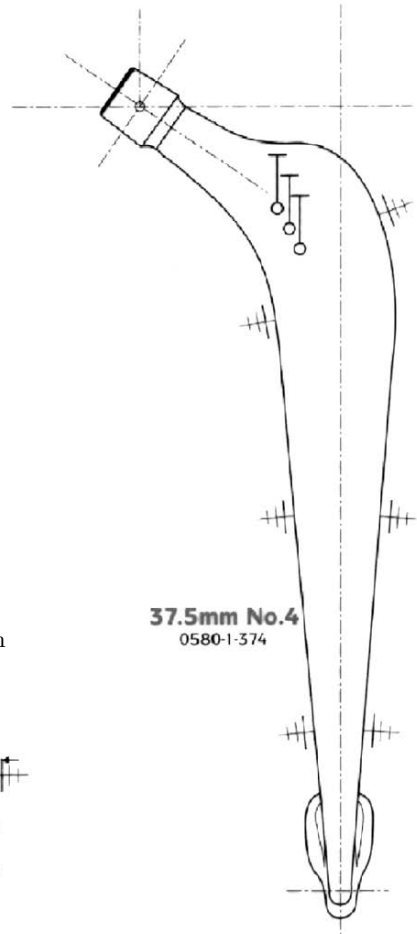

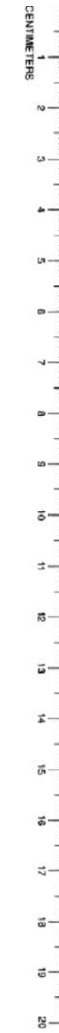

EXETER™
total hip system
V40™
core range

20% oversize to allow for X-Ray magnification

Graduated marker indicating minimum cement mantle 2 mm

Alignment points: Proximal Stem seal

Neck resection level

The stem centralizer will compress to a minimum of 10 mm. If the femoral canal is less than this, the centralizer wings should be removed.

Stryker® is a registered trademark of Stryker Corporation.
Exeter™ and V40™ are trademarks of Howmedica Osteonics Corp.
©Howmedica Osteonics 2002 Lit. No. **LTEM68 1M** 03/02 MC/HCG Printed in U.S.A.

stryker
Howmedica
OSTEONICS
59 Route 17 South
Allendale, NJ 07401
www.howmet.com

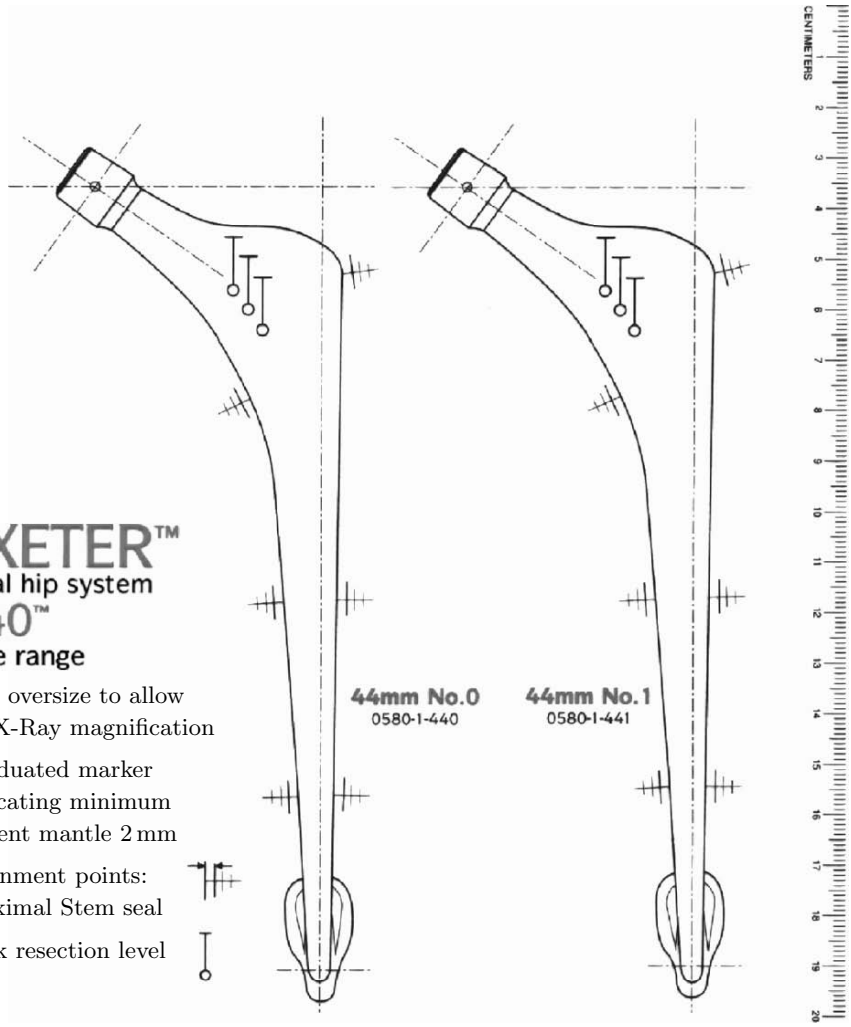

The stem centralizer will compress to a minimum of 10 mm. If the femoral canal is less than this, the centralizer wings should be removed.

Stryker® is a registered trademark of Stryker Corporation.
Exeter™ and V40™ are trademarks of Howmedica Osteonics Corp.
©Howmedica Osteonics 2002 Lit. No. **LTEM68 1M** 03/02 MC/HCG Printed in U.S.A.

stryker
Howmedica
OSTEONICS
59 Route 17 South
Allendale, NJ 07401
www.howmet.com

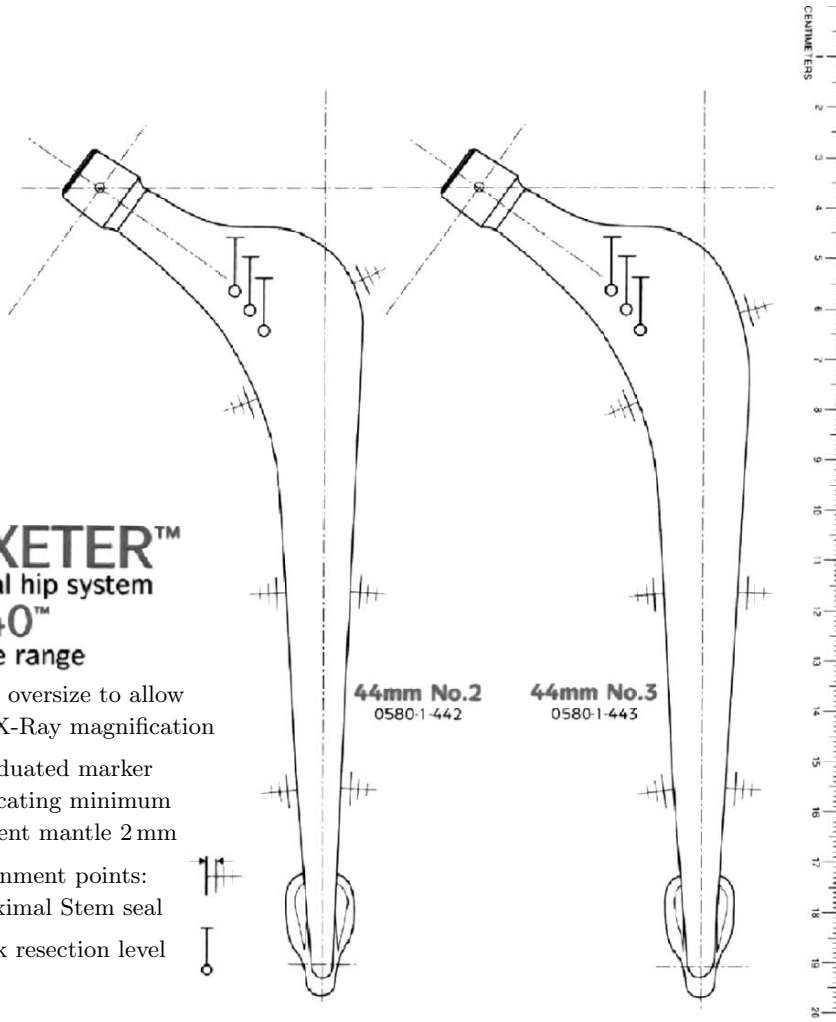

EXETER™
total hip system
V40™
core range

20% oversize to allow for X-Ray magnification

Graduated marker indicating minimum cement mantle 2 mm

Alignment points: Proximal Stem seal

Neck resection level

The stem centralizer will compress to a minimum of 10 mm. If the femoral canal is less than this, the centralizer wings should be removed.

Stryker® is a registered trademark of Stryker Corporation.
Exeter™ and V40™ are trademarks of Howmedica Osteonics Corp.
©Howmedica Osteonics 2002 Lit. No. **LTEM68 1M** 03/02 MC/HCG Printed in U.S.A.

stryker
Howmedica
OSTEONICS
59 Route 17 South
Allendale, NJ 07401
www.howmet.com

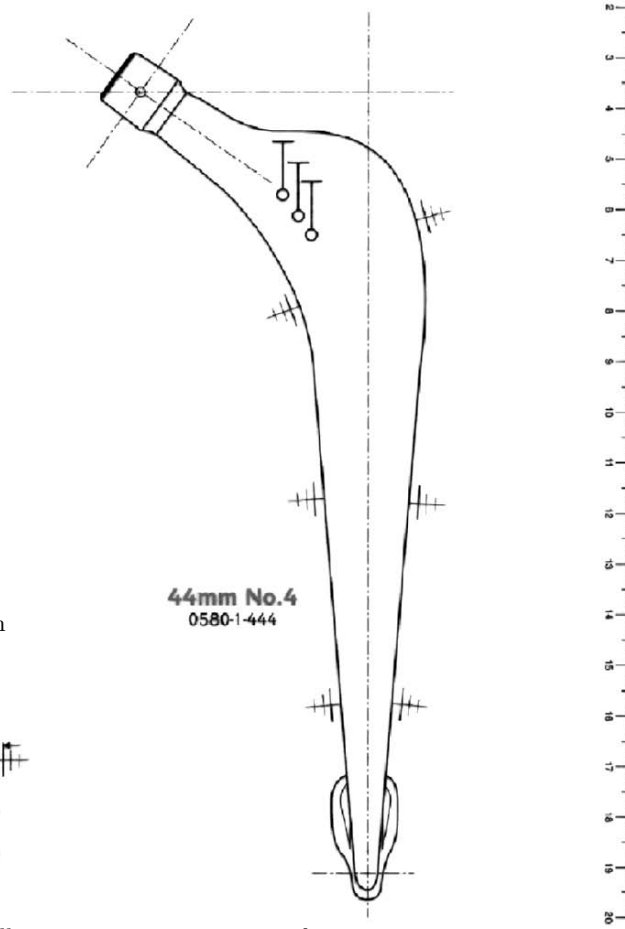

EXETER™
total hip system
V40™
core range

20% oversize to allow for X-Ray magnification

Graduated marker indicating minimum cement mantle 2 mm

Alignment points: Proximal Stem seal

Neck resection level

The stem centralizer will compress to a minimum of 10 mm. If the femoral canal is less than this, the centralizer wings should be removed.

Stryker® is a registered trademark of Stryker Corporation.
Exeter™ and V40™ are trademarks of Howmedica Osteonics Corp.
©Howmedica Osteonics 2002 Lit. No. **LTEM68 1M** 03/02 MC/HCG Printed in U.S.A.

stryker
Howmedica
OSTEONICS
59 Route 17 South
Allendale, NJ 07401
www.howmet.com

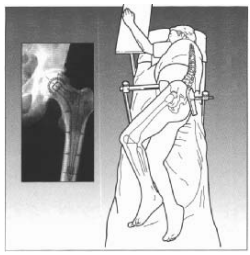

1. Pre-operative Planning:
Pre-operative templating is important to select the correct implant sizes, offset component, position and the minimum cement mantle thickness required. Any surgical approach can be used, and where appropriate, it is important that the patient is firmly and accurately supported in the lateral decubitus position.

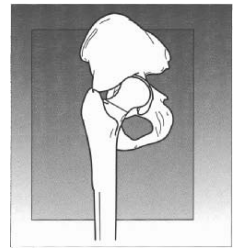

2. Neck Resection
Full exposure of the proximal femur is necessary to prepare, cement and implant the components. The osteotomy is defined medially, as the mid point distance between the inferior border of the articular surface of the femoral head and the superior border of the lesser trochanter. As the Exeter^{TM} stem has no collar, the level and orientation of neck resection are not critical.

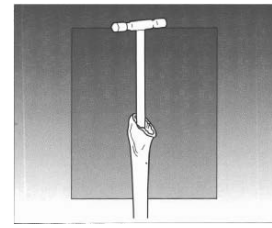

3. Reaming
Using the tapered reamers, and the long-handled bone gouge the surgeon opens up the canal. Opening the medullary can includes "lateralization" of the opening to achieve neutral alignment down the canal with the reamer, the rasp, and ultimately the final prosthesis. The reamer will be driven into the canal to the depth of 19 cm which is indicated on the reamer as the line where the surface changes from all polished to matt finis. This line should be aligned with the tip of the greater trochanter.

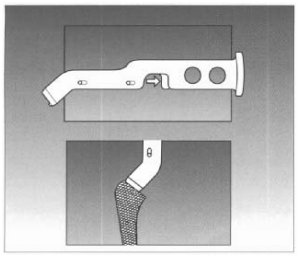

4. Rasping
The Exeter^{TM} V40^{TM} System features modular rasps with improved tooth pattern and an easy to use offset rasp handle. Rasping usually begins with a smaller rasp than that anticipated for final size. The last rasp corresponds to the size templated as appropriate for the femur. Rasping is intended to create a cavity which will hold the stem with a complete cement mantle of at least 2 mm. Care should be taken when rasping the canal to avoid removal of too much cancellous bone. A calcar planer may be used if the rasp is countersunk.

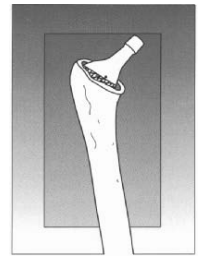

5. Neck trials
There are two sets of neck trials in the core range and extension size rasp instrument trays. The appropriate neck trial is positioned onto the rasp to prepare for trial reduction.
(Please refer to **Table 1**)

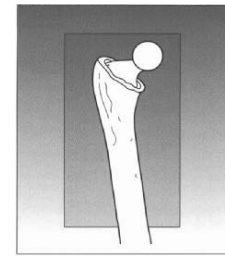

6. Trial Heads
V40^{TM} trial heads offer various head offsets to restore biomechanics of the hip. The appropriate size trial head is placed over the neck trial trunnion and the hip is reduced. For easier handling and to provide better stability during the procedure, the head trials feature an O-ring design.

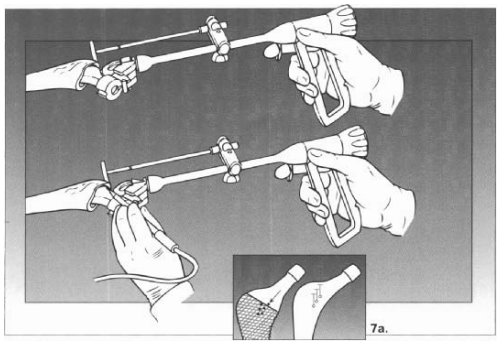

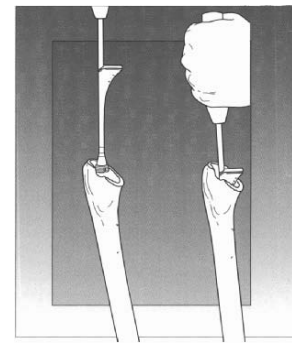

7. Trial Reduction
A trial reduction using the rasp and neck extension will verify the correct stem size, offset and position. When the correct leg length has been achieved the trial femoral head is removed and a trunnion protector is positioned over the neck trial. The V40™ stem introducer is mounted onto the trunnion protector ensuring that it is aligned with the rasp. Using a surgical marker, a straight mark is made on soft tissue or bone along the base plate of the leg length gauge. This mark will aid in proper alignment of the implant during insertion. Care must be taken when removing the introducer to avoid adjusting the position of the gauge. The trunnion protector and neck trial are removed and the rasp handle is reattached. The rasp is removed from the canal.

7a. Reference Points
The rasps and the implants are marked with an identical set of reference points. They will provide guidance during rasping and stem implantation. The 44 mm and 50 mm offset rasps are marked with two sets of reference points with an arrow pointing to the specific offset being used for trialing with the given neck trial.
(Please refer to picture 7a)

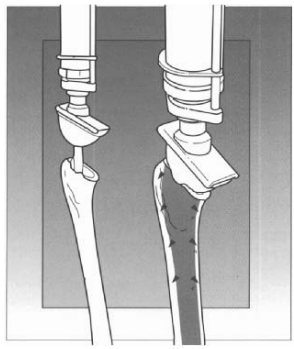

9. Femoral Cementing
After retrograde filling with cement, the nozzle is cut off at the seal, and the seal is then forced onto the end of the femur to form a closed cavity appropriate for pressurization. The remaining cement is injected and the pressure maintained until immediately prior to stem insertion.

8. Plug Introduction
The correct intramedullary plug size is selected by using flexible reamers of increasing size, or Exeter™ plug trials. The corresponding sized plug is implanted to provide a firm seal for pressurizing the cement. The femur is then cleaned with lavage and brush to provide a clean dry surface prior to cement injection. Aggressive reaming of the canal is not recommended.

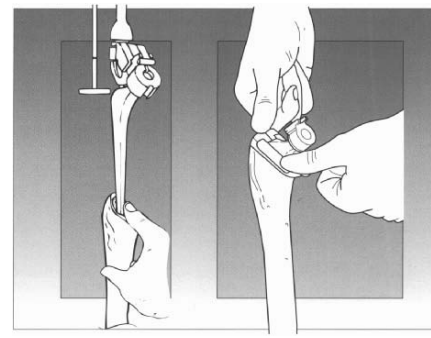

10. Stem Introduction and Reduction
With the hollow distal centralizer in place in the stem, the stem is inserted in one continuous smooth movement down the canal of the femur. The stem is introduced through the proximal femoral opening closer to the posterior femoral cortex than the anterior. During insertion, pressure is maintained by placing the thumb over the medial area of the calcar. The stem can be inserted through the stem seal to its final position, or the seal can be positioned after the stem is inserted and held in place until the cement hardens. In case of a canal 10mm or smaller, the wingless centralizer that is packaged with each implant should be used. The trunnion protector is removed and the trunnion should be cleaned. The appropriate size femoral head is impacted onto the stem and the hip is reduced.

Note: The Exeter™ V40™ Stems Can Only be used with Exeter™ Orthinox™ heads up to +8 mm Offset.

stryker Howmedica
OSTEONICS

SOLAR®

Solar® Humeral Fracture System

Surgical Protocol

stryker
Howmedica
OSTEONICS

Surgical Protocol

Table of Contents

Table of Contents

Step By Step Procedure..... 1
Patient Positioning 3
Surgical Exposure 4
Preparation of Humeral Shaft 7
Trialing of Humeral Components..... 7
Cementing 10
Tuberosity Reattachment..... 10
Post-Operative Rehabilitation 12

This surgical protocol was compiled in conjunction with:

Steven R. Groman, MD
Assistant Clinical Professor of Orthopedics,
Oregon Health Sciences University
Head,
Hand & Upper Extremity Service
Kaiser - Sunnyside Medical Center
Clackamas, Oregon

Step by Step Procedure (At A Glance) Surgical Technique for Three and Four Part Fractures of the Proximal Humerus

Step 1: Position patient in the semi-beach chair upright position.

Step 2: A long deltopectoral approach is utilized, using the corocoid process, palpated glenohumeral joint and the humerus as guides.

Step 3: Identify biceps tendon and its course. Dissect soft tissue until adequate exposure has been reached.

Step 4: Sequentially hand ream the distal canal until desired diameter is reached (***image 1***).

Image 1

Step 5: Tuberosities need to be identified, isolated, tagged and immobilized.

Step 6: Place humeral trial stem into humeral canal (***image 2***).

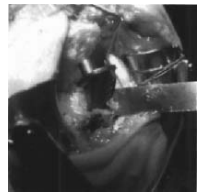

Image 2

Step 7: Position lateral fin approximately 1 cm posterior to bicipital groove (***image 3***).

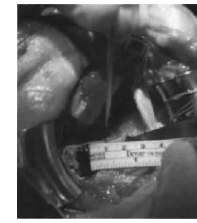

Image 3

Step 8: Place a 1 cm piece of cortico-cancellous wedge-shaped bone under medical collar of humeral component (***image 4***).

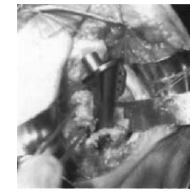

Image 4

Step 9: Select the humeral head trial that approximates the diameter and thickness of the patient's humeral head (***image 5***).

Image 5

Step 10: Place humeral head onto trial and adjust to achieve proper version and height of prosthesis (***image 6***).

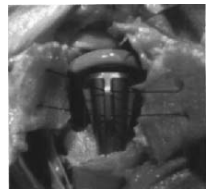

Image 6

Step 11: Pull tuberosities around the humeral head, on either side of the humeral component, to assure full closure of tuberosities. Assess for ROM (***image 7***).

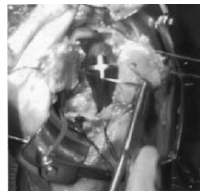

Image 7

Step 12: Drill holes in humeral shaft cortex for insertion of anchoring sutures for eventual attachment of tuberosities (***image 8***).

Image 8

Step 13: Inject methyl methacrylate cement into the distal canal.

Step 14: Insert humeral component into canal using bone wedge to achieve proper height (***image 9***).

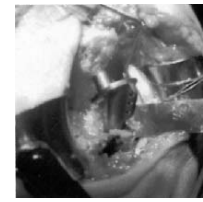

Image 9

Step 15: Remove excess cement from incision. Reattach tuberosities to humeral shaft and close incision as required (***image 10***).

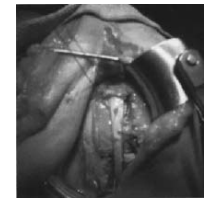

Image 10

The Solar® Shoulder Fracture System is designed to permit accurate and reproducible implantation of a humeral head replacement for indicated proximal humeral fractures. Proper soft tissue tensioning and humeral component positioning can be achieved to facilitate postoperative mobility and improved function, with the use of this streamlined instrumentation system.

Patient Positioning

The patient should be placed in the semi-upright beach chair position with the operative shoulder off the side of the table so that the arm can be freely moved about (***image 1***). This will permit the shoulder to be brought into full adduction and extension, aligned perpendicularly to the operating room floor, in order to gain full access to the humeral diaphysis. The patient's head should be secured to a headrest. Perform pre-operative preparation of arm, including the shoulder, axilla, and adjacent chest wall anteriorly and posteriorly.

Surgical Exposure:

A long deltopectoral approach is utilized, using the coracoid process, palpated glenohumeral joint and the humerus as the guides (***image 2***). Care should be taken in identifying the bony anatomy, as these landmarks can be particularly difficult to find in swollen shoulders or in obese patients.

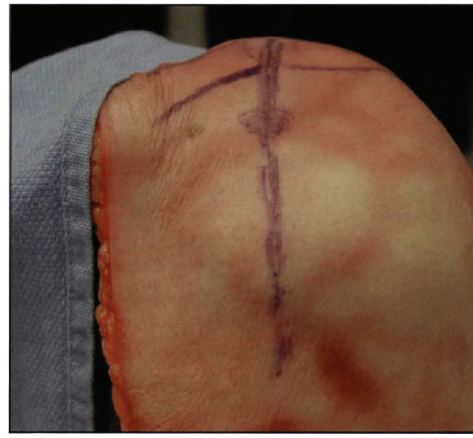

Image 2

The cephalic vein is identified and retracted laterally with the deltoid, as the deltopectoral interval is then developed (***image 3***). The upper fibers of the tendon of the pectoralis major should be released from the proximal humeral shaft to improve the exposure of the shaft. Retractors are then placed as the dissection is carried deeper.

Image 3

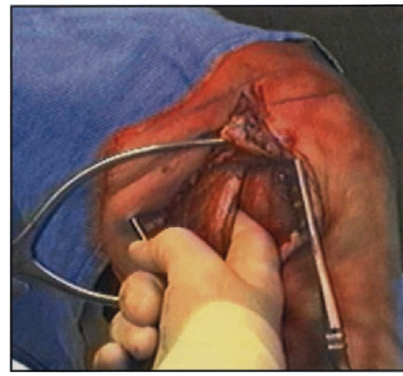

Image 4

The greater and lesser tuberosities are identified and the, often-hemorrhagic, subdeltoid bursa is debrided off the humeral head. The axillary nerve is palpated along the anterior border of the subscapularis (***image 4***), and followed in its course beneath the axillary pouch. Its position should be noted and care should be taken to protect the nerve from injury. The biceps tendon should be identified (***image 5***) and the overlying tissue incised to release it from its groove. It is then followed proximally over the superior portion of the humeral head and then the rotator interval. A division is made in the tissues overlying the humeral head in line with this interval. The tuberosities are then separated and grasped with tissue-holding forceps.

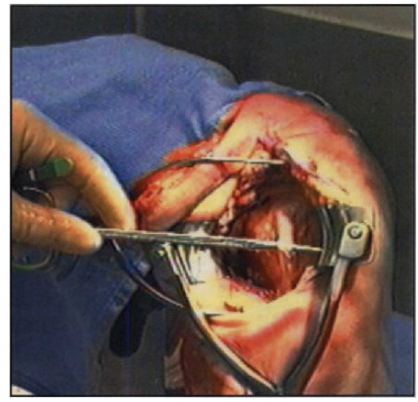

Image 5

Sutures are passed into the soft tissue and bone (***image 6***) at the attachment of the subscapularis and infraspinatus to the lesser and greater tuberosities, respectively. Heavy non-absorbable #2 or #5 cottony dacron should be used. Occasionally, the humeral head may have remnants attached either to the greater, or more commonly, the lesser tuberosity. These remnants must be carefully osteotomized at the anatomic neck to free the tuberosity. Save the humeral head for later use both as a sizing template and a source of cancellous bone graft (***image 7***).

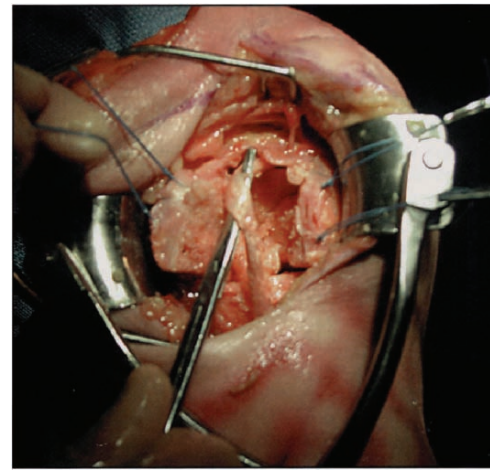

Image 6

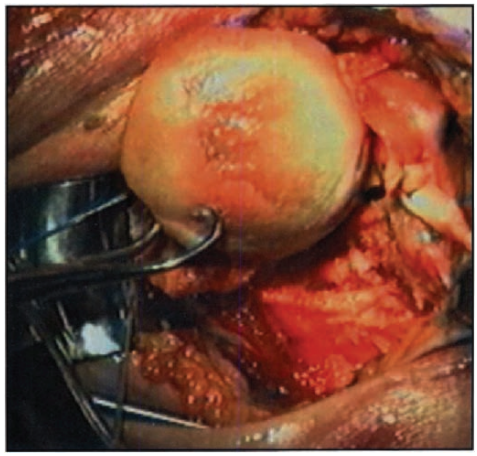

Image 7

Release any capsular attachments at the bases of the tuberosities that remain to free them from the shaft. No dissection of the bony fragments of the tuberosities is needed nor desired, and care should be taken to maintain their soft-tissue attachments. The biceps tendon should be temporarily rerouted, lateral to the greater tuberosity, to gain a clear view of the glenoid. The glenoid cavity should be cleaned well of bony fragments and hematoma, and thoroughly irrigated.

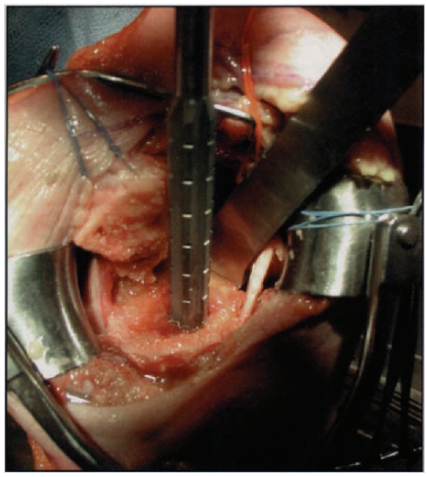

Image 8

Preparation of the Humeral Shaft:

The humeral shaft is now delivered into the wound, as the arm is extended and adducted. Medial soft tissue attachments at the proximal end may need to be released to allow the shaft to be delivered anteriorly. The proximal 1/3 of the pectoralis major insertion may be released.

Two retractors are placed behind the shaft and the intramedullary canal is debrided of hematoma and any bony debris. It is not desirable to actually ream out the contents of the intramedullary canal and no attempt should be made to ream to cortical bone, which is frequently thin. Often, the fatty marrow and lack of cancellous bone in the humeri of the elderly allow "sizing" the humeral canal by simply placing the reamer or a prosthetic trial stem down the canal and making an assessment from this (***image 8***). One should allow for an approximately 1 mm circumferential cement mantle when sizing the prosthetic stem.

If there is metaphyseal comminution, such as butterfly fragments, they should be cerclaged together before proceeding.

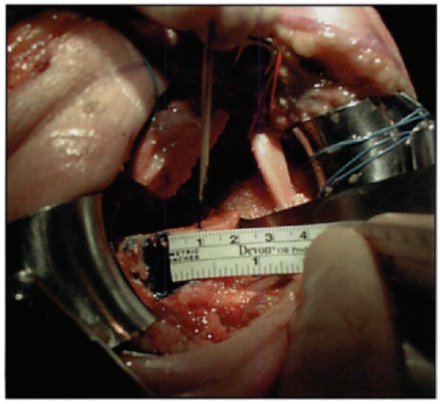

Image 9

Trialing the Humeral Components and Soft-tissue Balancing:

Proper soft tissue tension to provide for stability, mobility and optimal biomechanical advantage, requires proper height and version adjustments of the stem, and proper head diameter and thickness. The Solar® Fracture system provides excellent flexibility in choosing the appropriate combination of implant components and heads due to the wide array of sizes.

The humeral stem trial is inserted down the intramedullary canal. Since the natural position of the humeral head is in retroversion to the humeral shaft, some reference point to re-establish this relationship must be defined. To position the prosthetic stem in the appropriate retroversion, **place the lateral fin of the humeral component approximately 1 cm posterior to the bicipital groove**, at the proximal end of the canal (***image 9***).

Furthermore, with the arm placed so that the hand and forearm align perpendicular to the plane of the operating table, the trunnion should point toward the glenoid (***image 10***).

The humeral implant should sit slightly "proud" to the medial edge of the fracture (the calcar), to position the base of the collar at the level of the anatomic neck of the native shoulder when trialing. (This position is noted and will need to be reproduced upon implantation).

The tuberosities must be brought around the stem, under the prosthetic collar, without undo tension, and must permit adequate ROM in all planes. If necessary, choose a slightly smaller or thinner head. To achieve these requirements, debulk the tuberosity bone, and if necessary, release the capsule as described earlier.

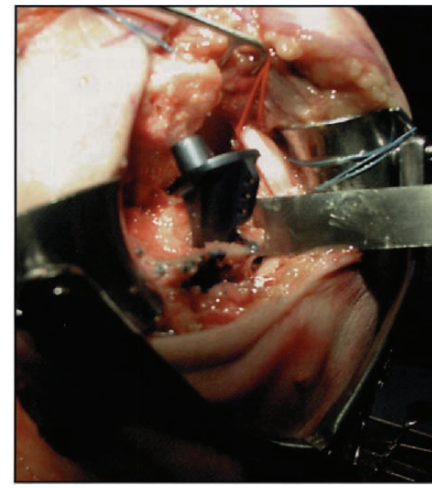

Image 10

The trial humeral head is chosen to be approximately the same diameter and thickness as (or slightly smaller than) the patient's native humeral head (***image 11A & 11B***).

Image 11A

Image 11B

A cortico-cancellous wedge-shaped piece of bone can now be shaped from the humeral head. This piece of bone should be placed under the medial collar of the prosthesis to fill and support the gap medially, between the collar and the end of the "calcar" area of the shaft fracture. This will give additional support post-implantation, as well as aid to reduce "settling" of the implant while the cement is hardening (***image 12***).

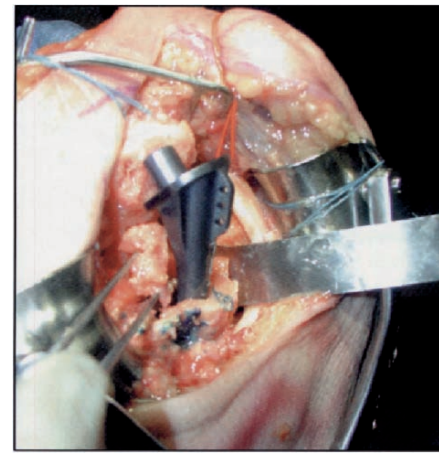

Image 12

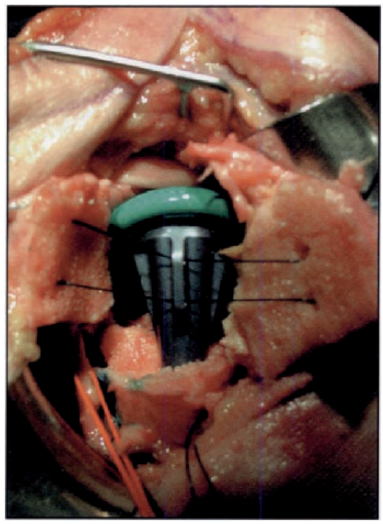

Image 13

Both tuberosities can now be brought around the humeral head, on either side of the humeral component to ensure that closure of the tuberosities and adequate ROM can be attained (***image 13***). Internal and external rotation can now be checked, as well as stability, while maintaining the tuberosities in position and ranging the shoulder. Elevation of 150° is desirable. At least 45° of external rotation, and internal rotation to the posterior axillary line should be achieved.

The hand should be placed across the chest and touch the opposite shoulder and axilla. If there is limitation of motion in rotation, check to be sure that sufficient tuberosity and any remnant of the humeral head have been trimmed (best accomplished from the intra-articular side of the joint), and that the head size is not too thick. Make adjustments as necessary. The trial component may now be removed.

Drill holes must be made in the humeral shaft cortex for insertion of anchoring sutures that will eventually pull the tuberosities down to the shaft. Four drill holes, just large enough to pass the needle of a double-armed #5 cottony Dacron suture through them, are made in the shaft at about 1 cm below the fracture line, and centered about the bicipital groove on the shaft (***image 14***). The free ends of the suture are brought out external to the shaft. The drill holes may be placed 2 cm distal to the fracture line if bone is very soft. The humeral canal is then irrigated and dried, and debris removed.

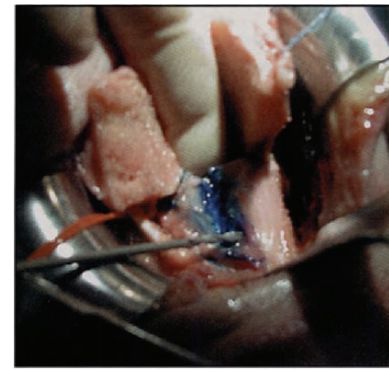

Image 14

Cementing: Simplex® P Bone Cement (Methyl methacrylate cement), of slightly doughy consistency, is now injected into the canal. It is not necessary to insert a bone plug or cement restrictor into the canal since the cement should not be injected very far distally or in a very liquid form. The cement's primary purpose is to provide proximal rotational control of the Solar humeral component.

Excessive cement should be removed from around the stem, especially in the two lateral quadrants. Bare metallic implant should show so that there is plenty of room to reattach the tuberosities. Medially, the previously designed cortico-cancellous wedge should be impacted into position as an additional calcar support. While the cement is hardening, cancellous bone from the humeral head should be harvested and saved for placement under the tuberosities prior to their full reattachment.

Tuberosity re-attachment: Once the cement fully cures, irrigate the joint and wound to remove any debris. The sutures in the tuberosities can now be brought through the holes in the lateral fin in order to close the interval between the greater and lesser tuberosities aligned with bicipital groove (***image 15***). Aligning the closure with the biciptal groove may require readjusting the suture placement so that more of the greater tuberosity and less of the lesser tuberosity is grasped with the sutures.

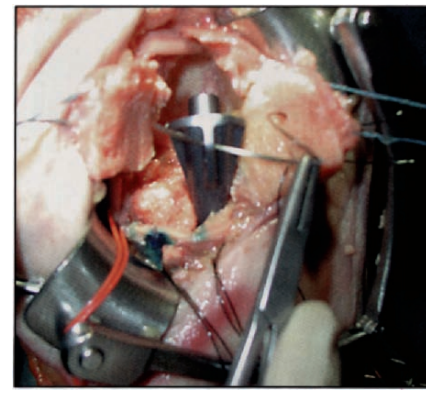

Image 15

Placing the lesser tuberosity too far laterally will result in loss of external rotation. The sutures should be brought through the opposite tuberosity after passing through the fin holes, so that transversely tying the sutures now brings the tuberosities together. Do not tie these sutures yet. Using the previously placed sutures in the shaft with their needles attached, place them into the soft tissues (the rotator cuff tissue) just superior and lateral to the tuberosities, in a figure-of-eight fashion, incorporating both tuberosities in each set of sutures (***image 16***). Do not place these sutures through the holes in the prosthetic stem.

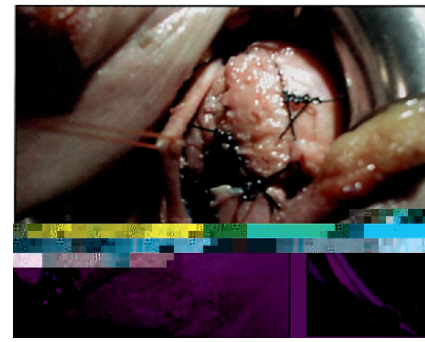

Image 16

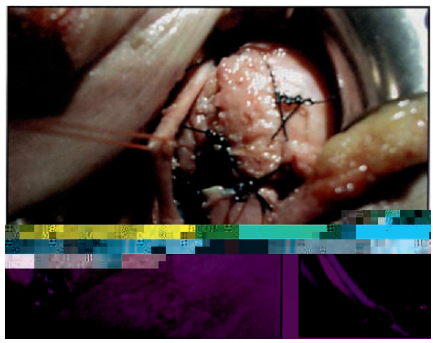

Image 17

Tie the first set of transversely placed inter-tubercular sutures first. Then, prior to pulling the tuberosities distally with the other set of figure-of-eight-sutures, place as much of the cancellous pieces of bone graft under the lateral portion of the Solar humeral component collar (anteriorly and posteriorly) as possible. Bone graft should also be placed down to the upper part of the shaft to enhance bony union of the tuberosities. Finally, the sutures can be pulled taught and tied down. The tuberosities should now be horizontally approximated, as well as closely applied to the shaft, adjacent to the implant and slightly overlapping the bony humeral shaft. Allow the biceps tendon to fall back in to place. The rotator interval may be re-approximated at this point with non-absorbable suture (***image 17***).

The resulting construct can now be tested for range-of-motion and stability. The entire construct should move as a unit, permitting 150° of elevation, 45°–60° of external rotation, and internal rotation to the posterior axillary line and the opposite axilla. Routine closure of the delto-pectoral interval, subcutaneous tissue and skin is then performed. Light dressings and a sling are then applied.

Post-Operative Rehabilitation (as suggested by Steven R. Groman, MD)

Immediately Postop:

Sufficient analgesics are required to allow the patient to begin ROM exercises immediately post-operatively. Motions are passive, and can generally be done by the patient with monitoring. Self-assisted passive range of motion (PROM) using the opposite arm as the motor with relaxation of the operative arm, can be taught, and should be done in a supine position. Additional devices such as pulleys, sticks, etc., may be of benefit, but caution should be maintained to not force the shoulder too aggressively. Substituting motions, such as shoulder shrugging, should be discouraged as well. Most patients can achieve at least 2/3 of the motion achieved on the operating room table within 2 days. Encouragement and monitoring is imperative, however, to achieve maximal results.

First 6 Weeks:

The same self-assisted PROM techniques are practiced several times per day by the patient. Active use of the hand and forearm may be permitted, and elbow ROM should not be neglected. By the end of 6 weeks, generally there is sufficient healing of the tuberosities so that active motions can be initiated. X-rays of the shoulder in AP-Internal and external rotation and an axillary view can aid in this determination.

After 6 Weeks:

Generally, all external support can be discarded and gentle active motions are allowed. Rotator rehabilitation is begun and patients are not permitted to lift until good strength and good active ROM is achieved. It can take many months, often up to a year, to achieve maximum results.

(Steven R. Groman, MD)

stryker
Navigation
Hip Navigation
Operative Outline

Anchor Pelvic Tracker and Digitize Both ASIS and Pubic Symphysis

Prior to placing in lateral position, affix the pelvic tracker to the iliac crest(1). Make sure that the pelvic tracker is facing anterior lateral as depicted. Use the pointer to digitize the left and right anterior superior iliac spines and the pubic symphysis.

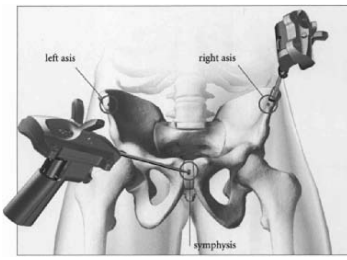

Anchor Femoral Tracker and Record Neutral Leg Position and Landmarks

2

After draping, affix the femoral tracker to the distal lateral femur. Make sure that the femoral tracker is visible to the camera also after dislocation of the hip joint. Record the leg in a neutral position. With the knee flexed to 90 degrees, digitize the piriformis fossa, popliteal fossa and achilles tendon midpoint with the pointer.

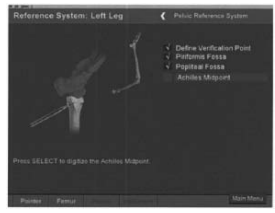

Digitize Foveal Surface

3

Following femoral neck resection, map the surface of the fovea with the pointer(2).

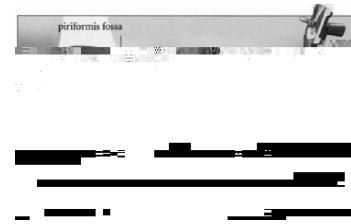

Acetabular Reaming

4

Attach the instrument tracker to the navigated reamer handle to monitor anteversion, indination and depth to fovea.

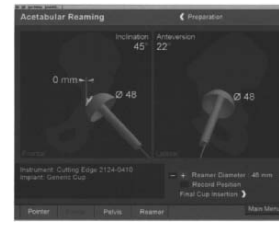

Cup Insertion

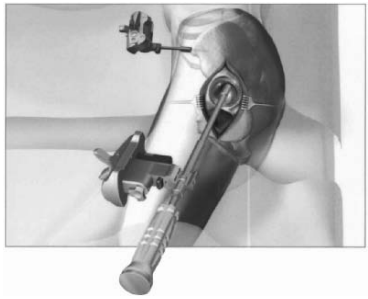

5

Attach the instrument tracker to the navigated cup insertion handle to monitor position during cup impaction.

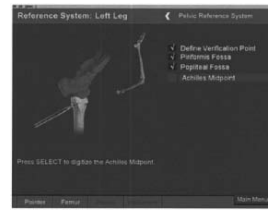

Analyze Leg Length, Offset, Range of Motion and Lift-Off

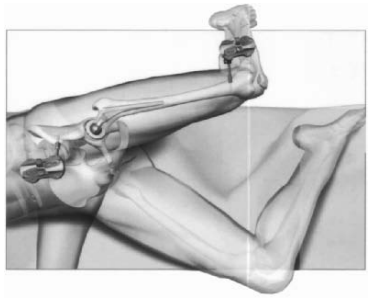

6

With trials or final implants in place, motion analysis determines the hip center and leg length, femoral offset, range of motion and lift-off can be demonstrated.

(1) Alternatively, the patient may be positioned, prepped and draped before placing the pelvic anchoring pin. The anatomy survey can be conducted through the drapes with extreme care.

(2) This hip navigation operative outline is intended to address acetabular preparation and implantation only. For femoral stem navigation please reference the User Manual.

VIII

Recon Nailing System

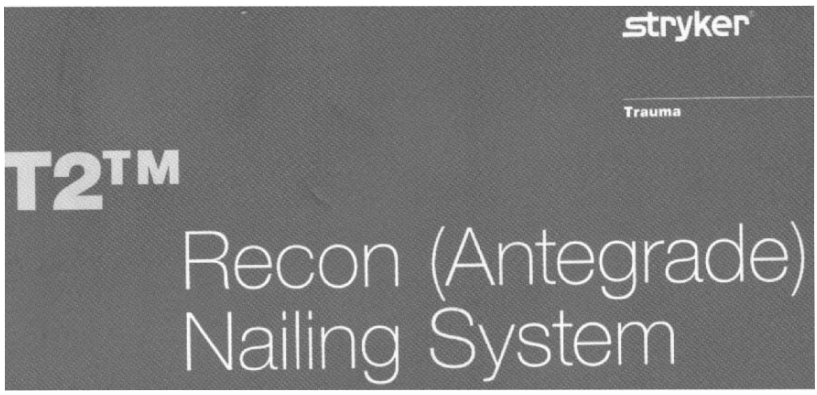

Contributing Surgeons

1. Kyle F. Dickson M.D.
Director Orthopedic Trauma
Charity Hospital
New Orleans, Louisiana, U.S.A.

2. Srino B. Huram M.D.
St Vincent Medical Center Trauma
New York, U.S.A.

3. Robert M. Harris M.D.
Orthopedic Trauma,
Atlanta, Georgia, U.S.A.

4. Anthony T. Sorkin M.D.
Rockford Orthopedic Associates
Rockford Memorial Hospital
Rockford, Illinois, U.S.A.

5. Steven Touliopoulos M.D.
University Orthopedic of New York.
New York, U.S.A.

6. Ariaan D.P. van Walsum M.D.
Trauma Surgeon Medical Spectrum, Twente, Netherland.

7. Walter W. Virkus M.D.
Rush University Medical Center
Cook Country Hospital
Chicago, Illinois, U.S.A.

8. Don Weber M.D.
University of Alberta Hospital
Edmonton, Alberta, Canada

Introduction

1. Introduction

Over the past decades **antegrade femoral nailing** has become the treatment of choice for most femoral fractures.

As an addition to the **T2™ Nailing System**, Stryker Trauma has created a new generation femoral implant: the **T2™ Recon Nail** for the treatment of complex, as well as more common fractures.

The advantages of using intramedullary fixation for the treatment of proximal femur fractures include less soft tissue dissection and stable fracture fixation with a load sharing device.

Through the development of a common, streamlined instrument system and intuitive surgical approach, both in principle and in detail, the **T2™ Recon Nail** offers **the opportunity for significantly increased speed and functionality** for the treatment of fractures and simplifies the training requirements for all personnel involved.

Furthermore, the **T2™ Recon Nail** offers the following competitive advantages:

- **Versatility to switch from antegrade femoral nailing to a recon option without changing the nail**
- **An optional Set Screw* (Recon Mode) can be tightened down onto the superior Lag Screw, thus minimizing the potential sliding of the proximal Lag Screw**
- **Static or dynamic distal locking options for the antegrade femoral mode**
- **Trochanteric entry point**
- **Minimized proximal nail diameter allowing freehand placement of accessory K-Wires around the nail (anterior and posterior) for precise femoral neck fracture reduction**

1.1. Implant Features

The **T2™ Recon Nail** is the realization of superior biomechanical intramedullary stabilization using strong, cannulated implants for the internal fixation of the Femur.

As with all other T2™ Nails, the **T2™ Recon Nail** is made of **Type II anodized Titanium Alloy (Ti6Al4V) for enhanced biomechanical and biomedical performance**.

The **T2™ Recon Nail** features a **125° CCD angle and a 10° anteversion angle for the two proximal holes that utilize 6.5 mm Cannulated Lag Screws**. With this **CCD angle**, easy insertion of two screws into the femoral head can be achieved.

No system currently on the market allows better visualization at the femoral head in the lateral view for ease of placement of the reconstruction screws.

Alternatively **a proximal 70° Oblique hole with 7° retroversion** for a 5 mm Fully Threaded Screw can target the Lesser Trochanter in the Femoral Antegrade mode.

The 6.5 mm Cannulated Lag Screws have a unique thread design providing a better grip, and improved front cutting flutes.

Secure placement of the Lag Screws within even very small neck diameters can be achieved due to the optimal design of a 10.5 mm inner, therefore 17 mm outer distance between the two 6.5 mm Lag Screws.

Two Set Srews are available:

- **Recon Set Screw*** to tighten down on the proximal Lag Screw (for the Recon Mode) and
- **Antegrade Set Screw** to tighten down on the oblique Fully Threaded Screw (for the Femoral Antegrade Mode).

Available as **left** and **right versions**, the **T2™ Recon Nail** incorporates an antecurvature radius of **2000 mm**, as well as a **4° lateral valgus bend** for trochanteric insertion.

The **distal locking configuration** features a round and an oblong hole to allow for **static or dynamic distal locking**.

Low profile 5 mm cortical screws, common to the T2™ Nailing System, are designed to simplify the surgical procedure and promote a minimally invasive approach.

- Fully Threaded Locking Screws are available for distal locking (Recon or Femoral Antegrade Mode) and for the proximal locking in Femoral Antegrade Mode.

End Caps are available in various lengths to provide a **"best fit"** for every indication.

See the **detailed chart on the next page** for the design specifications and size offerings of the implants.

*Not available for sale in U.S. at time of printing.

Features

T2™ Recon Nail

Diameter	9, 11, 13 and 15mm (Left and Right)
Sizes	340–480mm (in 20mm increments)

Note:
Proximal diameter is 13mm for the 9 and 11mm Nails and 15mm for the 13 and 15mm Nails.

Note:
Screw length is measured from top of head to tip.

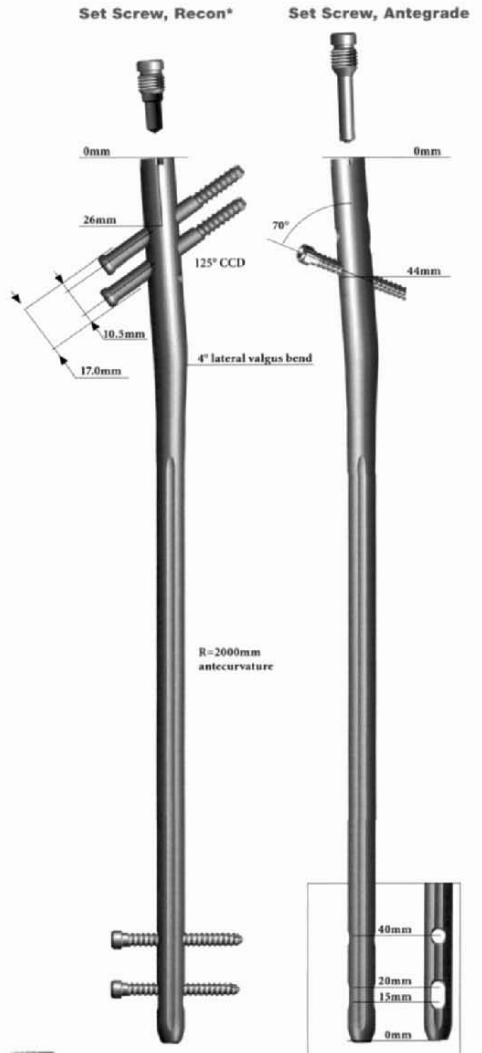

5.0mm Fully Threaded Locking Screws
L = 25–120mm

6.5mm Cannulated Lag Screws
L = 65–130mm

End Caps

Standard +5mm +10mm +15mm

* Not available for sale in U.S. at time of printing.

Features

1.2. Instrument Features

A major advantage of the instrument system is a break-through in the integration **of a core instrument platform** that can be used not only for the complete **T2™ Nailing System**, but represents the platform for all future Stryker Trauma nailing systems, reducing complexity and inventory. **The T2™ Instrument Platform** offers advanced precision and usability, and features ergonomically styled targeting devices.

Except for the addition of a small number of dedicated instruments, the T2™ Femoral Instrument Platform is used for the **T2™ Recon Nail**.

Dedicated instruments for the **T2™ Recon Nail** include the **Recon Targeting Device**, which has one **Nail Adapter** and two Targeting Arms:

- **Recon Targeting Arm** (1806–3002) used for the placement of two 6.5 mm Cannulated Lag Screws into the femoral head in the Recon mode,
- **Antegrade Targeting Arm** (1806–3003) used for insertion of the oblique screw in the Antegrade mode.

In addition to the advanced precision and usability, the instruments are number and color coded to indicate their usage during the surgical procedure. The number coding indicates the step during the procedure in which the instrument is used.

With the exception of the carbon fiber targeting device, all dedicated instruments for the recon mode have a "bronze" color code.

This makes it easy to differentiate them from the core platform instruments.

Drills

Drills feature color coded rings:
4.2 mm = Green
(Consistant with the T2™ Instrument Platform, this drill features a green color ring.)
The 4.2 mm drills are used for 5.0 mm Fully Threaded Locking Screws (either for distal locking or for proximal oblique locking).
6.5 mm = Bronze
Stepdrill for Lag Screw has the "bronze" color coding indicating Recon Mode.

Indications

2. Indications

The **T2™ Recon Nail** is indicated for:

- Open and closed femoral fractures
- Pseudathrosis and correction osteotomy
- Pathologic fractures and impending pathologic fractures
- Subtrochanteric fractures
- Combination femoral neck, intertrochanteric and subtrochanteric fractures
- Ipsilateral neck/shaft fractures

3. Pre-operative Planning

A Recon X-Ray Template (1806–3080) is available for pre-operative planning. Thorough evaluation of pre-operative radiographs of the affected extremity is critical. Careful radiographic examination of the trochanteric region and neck regions can reduce the potential for intra-operative complications.

According to the fracture type, either Recon or Antegrade Femoral Mode can be chosen.

Evaluation of the femoral neck angle on the pre-operative X-Rays is mandatory as the **T2™ Recon Nail** has a fixed 125° neck angle for the two Lag Screws and proper placement of both Lag Screws in the femoral head is essential.

If possible, X-Rays of the contralateral side (taken with similar rotation) should be used to determine the normal neck angle and length of the femur.

The proper nail length should extend from the Tip of the Greater Trochanter to the Epiphyseal Scar of the distal femur.

Note: Check with local representative regarding availability of nail sizes.

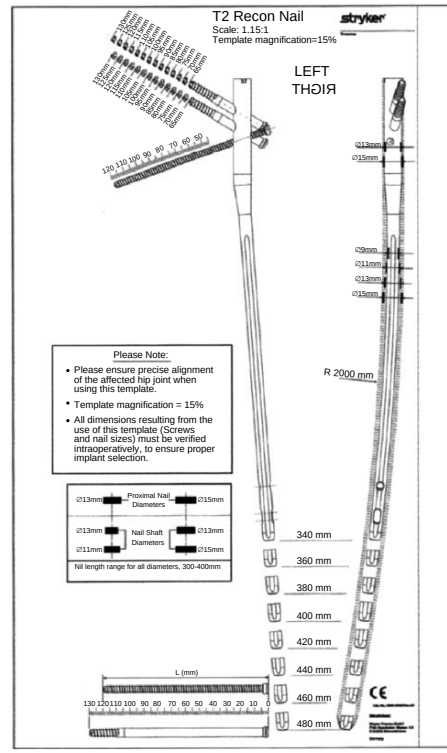

Operative Technique

4. Locking Options

The T2™ **Recon Nail** can be locked proximally either with two Lag Screws (Recon Mode, **Fig. 1**) or with one Fully Threaded Screw (Antegrade Femur Mode, **Fig. 2**).

For both Recon and Antegrade Femur applications, depending on fracture pattern, either static or dynamic distal locking can be used.

Recon Mode **Fig. 1**

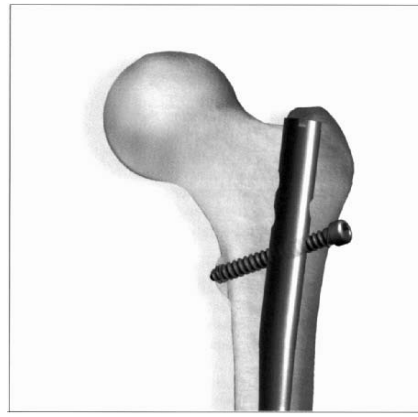

Antegrade Femoral Mode **Fig. 2**

Operative Technique

5. Operative Technique

5.1. Patient Positioning

Patient positioning for **T2™ Recon Nail** insertion is surgeon dependent. However, it is recommended to position the patient in supine or lateral position on a fracture table, to allow closed reduction of the fracture (Fig. 3).

Manipulate and reduce the fracture in the usual fashion, according to the fracture type. Reduction should be achieved as anatomically as possible. If this is not possible, reduction in one plane should be complete, leaving reduction in the other plane to be achieved prior to reaming and nail insertion.

The unaffected leg is maneuvered or manipulated so that appropriate images can be obtained. This will also allow easier entry point access.

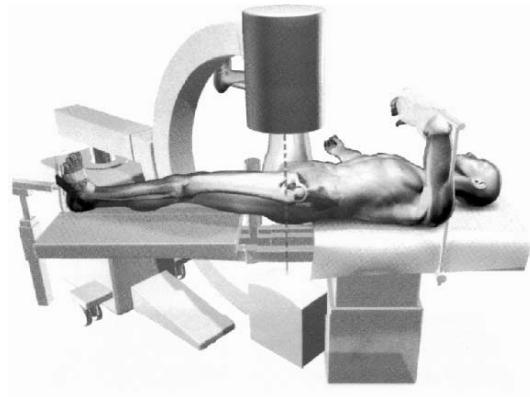

Fig. 3

5.2. Incision

The design of the **T2™ Recon Nail**, with a **4° lateral valgus bend**, will **only** allow for insertion through the **Tip of the Greater Trochanter**.

With experience, the Tip of the Greater Trochanter can be identified by palpation (Fig. 4).

A 3–5 cm longitudinal incision is made just proximal to the Greater Trochanter (Fig. 5). The incision is then deepened to expose the Tip of Greater Trochanter.

Smaller or larger incisions may be used based on individual patient's anatomy and at the surgeon's discretion.

Note: The targeting instruments of the **T2™ Recon Nail** have been designed to allow for a more percutaneous approach.

Fig. 4

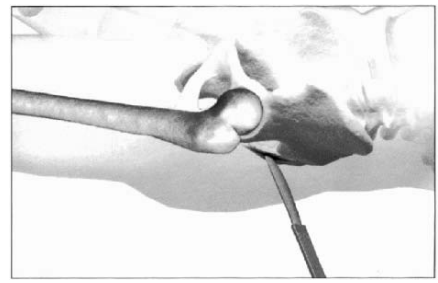

Fig. 5

Operative Technique

5.3. Entry Point

• **The Tip of the Greater Trochanter**

The entry point is located at the junction of the anterior third and posterior two-thirds of the Greater Trochanter, on the medial edge of the tip itself (Fig. 6).

Note: Before opening the Tip of Greater Trochanter, use image intensifier views (A/P and M/L) to confirm correct identification of the entry point and direction down the shaft.

The medullary canal can be opened with the

- **Curved Awl** (1806–0040)/**Curved Awl**, **90° Handle** (1806–0041) or
- **One Step Conical Reamer** (1806–3010 or 1806–3015).

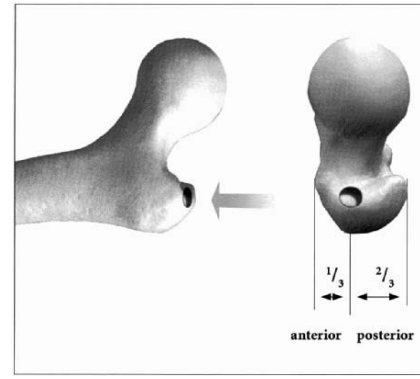

Fig. 6

Note: During opening of the entry portal with the Awl, dense cortex may block the tip of the Awl. An optional Awl Plug (1806–0032) can first be inserted through the Awl to avoid penetration of bone debris into the cannulation of the Awl shaft, and then removed for Guide Wire insertion.

•**Entry point with Curved Awl**

Once the Tip of the Greater Trochanter has been penetrated, the Ø3 × 1000 mm Ball Tip Guide Wire (1806–0085S) may be advanced through the cannulation of the **Curved Awl** with the Guide Wire Handle and Chuck (1806–0095 and 1806–0096) (Fig. 7).

Fig. 7

- The proximal femur may then be prepared with the One Step Conical Reamer.

Operative Technique

• Entry point with One Step Conical Reamer

Alternatively, the 13 mm diameter One-Step Conical Reamer (1806–3010) for the 9 and 11 mm nails or the 15 mm diameter Reamer (1806–3015) for the 13 and 15 mm nails may be used for opening the medullary canal and reaming of the trochanteric region.

Under image intensification control, the entry point is made with a Ø3.2 × 400 mm Recon K-Wire (1806–3031S) attached to the Guide Wire Handle and advanced into the medullary canal. Confirm its placement within the center of the medullary canal on A/P and lateral image intensifier views.

Note: The Recon K-Wire used for the entry point should not be used again for the Lag Screw insertion. It is recommended to utilize a new K-Wire.

The Recon Protection Sleeve (1806–3057) and Multi-hole Trocar (1806–3055) are positioned with the central hole over the K-Wire.

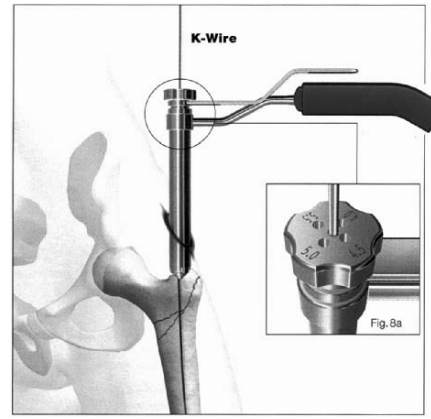

Fig. 8

Note: The Multi-hole Trocar has a special design for more precise insertion of the Ø3.2 mm Recon K-Wire (Fig. 8). Besides the central hole, four other holes are located eccentrically at different distances from the center (Fig. 8a) to easily revise insertion of the guiding K-Wire in the proper position (Entry Point).

When correct placement of the guiding K-Wire is confirmed on image intensifier views (A/P and lateral), keep the Tissue Protection Sleeve in place and remove the Multi-hole Trocar.

The T-Handle (702628) is attached to the One-Step Conical Reamer and **hand reaming is** performed over the K-Wire through the Tissue Protection Sleeve (Fig. 9).

The K-Wire is then removed and replaced with the Ø3×1000 mm Ball Tip Guide Wire.

Fig. 9

Operative Technique

5.4. Reaming

The Ø3 × 1000 mm Ball Tip Guide Wire is inserted with the Guide Wire Handle through the fracture site to the level of the Epiphyseal Scar.

The Ø9 mm Universal Rod (1806–0110) with Reduction Spoon (1806–0125) may be used as a fracture reduction tool to facilitate Guide Wire insertion through the fracture site (Fig. 10).

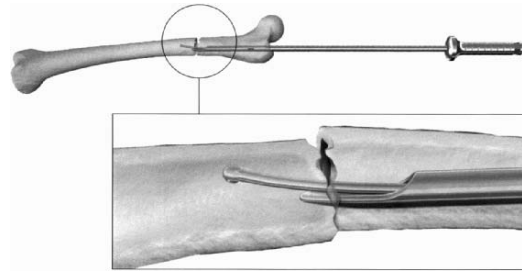

Fig. 10

Note: The Ball Tip at the end of the Guide Wire will stop the Bixcut® Reamer* head (**Fig. 11**).

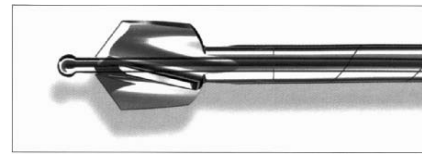

Fig. 11

Note: Prior to reaming, it is important to check the intramedullary position of the Guide Wire with the image intensifier to make sure that it is centered. Lateral displacement of the Guide Wire could lead to resection of more bone on the lateral side of the wire, which in turn could lead to a malunion and increased risk of fracturing the shaft.

Note: Make sure that the reduction is maintained throughout the reaming process.

Reaming is commenced in 0.5 mm increments until cortical contact occurs (**Fig. 12**).

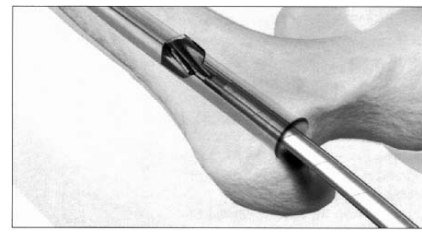

Fig. 12

For easier nail insertion, the medullary canal should be reamed 2 mm more than the diameter of selected nail.

Note: The **T2™ Recon Nail** may be inserted without reaming of the subtrochanteric and dyaphyseal region of the femur, particularly in eldery patients with wide medullary canals. If appropriate, after the trochanteric region is prepared with the One-Step Conical Reamer, the nail can be inserted without further reaming of the medullary canal. Reaming of the trochanteric region is needed (Fig. 13) as the proximal nail diameter (driving end) is larger than the nail diameter (13 mm for the 9 and 11 mm diameter nails and 15 mm for the 13 and 15 mm diameter nails).

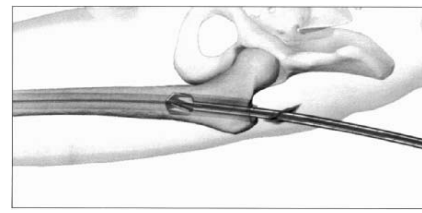

Fig. 13

For both reamed or unreamed applications, the proximal 5 cm of the trochanteric region must be opened to at least 13 mm or 15 mm, (depending on the proximal diameter of the nail).

*see pages 28–29 for additional Bixcut® Reamer system details

Operative Technique

5.5. Nail Selection

Diameter

The diameter of the selected nail should be 1.5–2.0 mm smaller than that of the last reamer used.

Note: The proximal femur should be over-reamed by 2 mm.

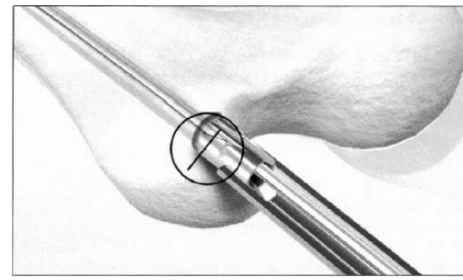

End of Guide Wire Ruler equals Measurement Reference

Fig. 14

Length

Nail length may be determined by measuring the remaining length of the Guide Wire. The Guide Wire Ruler (1806–0020) may be used by placing it on the Guide Wire and reading the correct nail length at the end of the Guide Wire on the Guide Wire Ruler (**Fig. 14** and **15**).

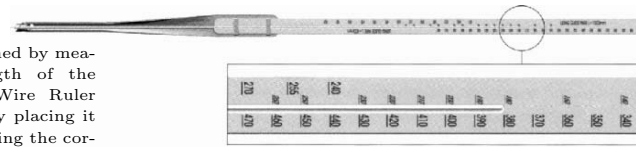

Fig. 15

5.6. Nail Insertion

Upon completion of reaming, the appropriate size nail is ready for insertion. A unique design feature of the T2^{TM} Recon Nail is that the Ø3 × 1000 mm Ball Tip Guide Wire does not need to be exchanged.

The selected nail is assembled onto the Nail Adapter (1806–3001) with the Nail Holding Screw (1806–3005) (**Fig. 16a**). Securely tighten the Nail Holding Screw with the Ball-Tip Screwdriver Shaft (1806–3090) and T-Handle (702628) so that it does not loosen during nail insertion. Maintain reduction of the fracture during nail insertion.

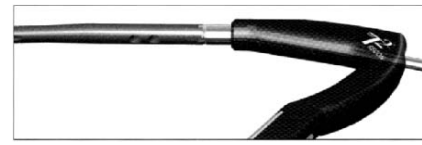

Fig. 16a

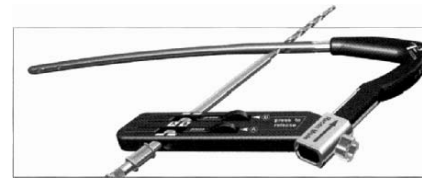

Fig. 16b

Note: Check the correct assembly by passing the Stepdrill for the Lag Screw through the Recon Tissue Protection Sleeve and/or the Recon Drill Sleeve placed in the corresponding hole of the Recon Targeting Arm into the holes of the nail (**Fig. 16b**). For the Femoral Antegrade Mode, use the Antegrade Targeting Arm with the Tissue Protection Sleeve and Drill Sleeve assembly to pass the Ø4.2 × 340 mm Drill through the oblique hole of the nail.

The nail is advanced through the entry point past the fracture site to the appropriate level.

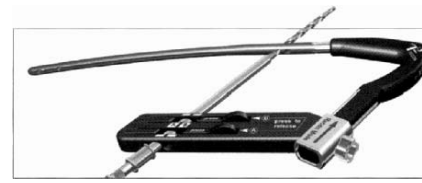

Fig. 17

If dense bone is encountered, first re-evaluate that sufficient reaming has been achieved, then, if necessary, the Recon Strike Plate (1806–3096) can be attached to the Nail Adapter and the Slotted Hammer (1806–0170) may be used to further insert the nail (**Fig. 17**).

Note: The nail must progress smoothly, without excessive force. If too much resistance is encountered, removal of the nail and additional reaming may be necessary.

Note: Remove the Guide Wire prior to drilling or K-Wire insertion.

Operative Technique

5.7. Guided Locking for Recon Mode (via Target Device)
(A) Nail/Lag Screws Positioning

Drive the T2™ Recon Nail to the depth that correctly aligns the proximal screw holes coaxial with the femoral head and neck under fluoroscopic visualization.

Two aspects regarding the Nail/Lag Screws position must be carefully checked with the image intensifier before drilling into the femoral head:

- Alignment of the anteversion (lateral view)
- Depth of Nail insertion (A/P view)

The distal Lag Screw should run along the calcar region (on the A/P view) and centered into the femoral neck and head (on Lateral view) (**Fig. 18**).

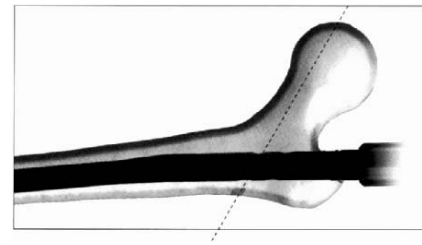

Fig. 18

Note: Correct placement of the Nail/Lag Screws can be achieved with or without the optional **One Shot™ Device** (1213–3010).

- **Nail/Lag Screws Positioning without the One Shot™ Device**

Slide the Recon Targeting Arm (1806–3002) onto the Nail Adapter (1806–3001) to the desired position and then securely tighten the Fixation Screw (1806–1007) (**Fig. 19**).

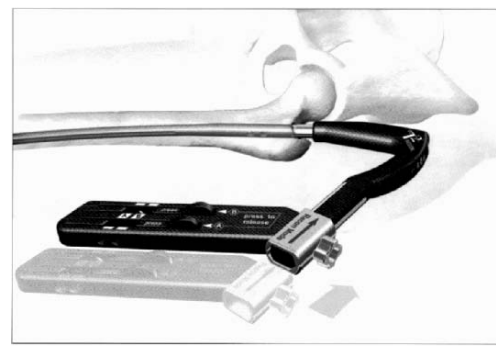

Fig. 19

Note: Make sure that no pressure is applied on the Recon Targeting Arm while securely tightening the Fixation Screw or while inserting the drill sleeves in order to avoid possible malalignment.

Slide the first Recon Tissue Protection Sleeve (1806–3045) together with the Recon K-Wire Sleeve (1806–3040) into the distal hole (A) on the Recon Targeting Arm by pressing the distal safety clip. A small skin incision is made and the assembly is pushed through until it is in contact with the lateral cortex and then release the distal safety clip. The mechanism will keep the sleeve in place and prevent it from sliding out. (**Fig. 20**)

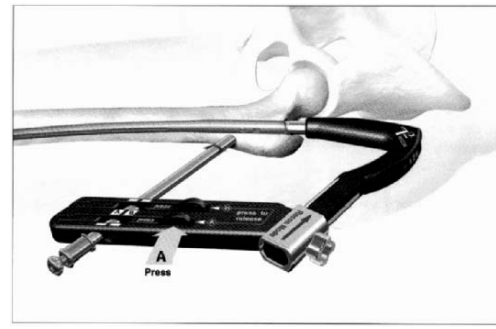

Fig. 20

Note: Avoid using a mallet to insert the Drill Sleeves as this can lead to the K-Wire/Stepdrill not passing through the center of the hole in the nail.

Operative Technique

Place a Recon K-Wire (1806–3030S) into the K-Wire Inserter(1806–3070) and attach it to the T-Handle (702628). The K-Wire is then, manually advanced through the K-Wire Sleeve until it reaches the subchondral bone of the femoral head, but not through the lateral cortex (**Fig. 21**). Alternatively, the K-Wire Inserter can be attached to a Power Tool and the Recon K-Wire inserted to the same depth.

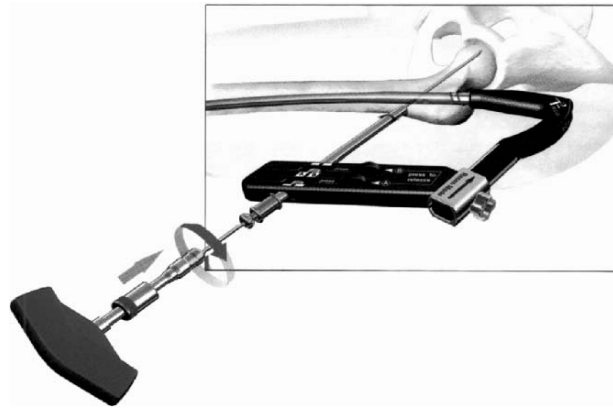

Fig. 21

Note: With the image intensifier, verify if the tip of the K-Wire is placed along the calcar region in the A/P view (depth of nail insertion), and central on the lateral view (correct anteversion) (**Fig. 22**).

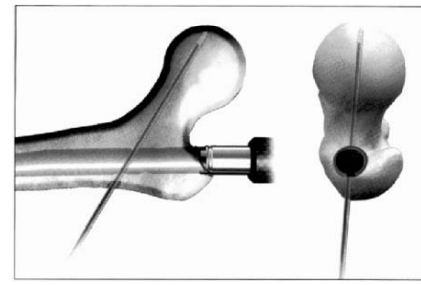

Fig. 22

If the K-Wire is incorrectly positioned, the first step is to remove it and then to reposition the nail.

More commonly, the nail is positioned too high and repositioning should be carried out either by hand or by using the Recon Strike Plate (1806–3096) placed into the Nail Adapter, inserting the nail further. If a higher position is required, the Universal Rod (1806–0110) and Slotted Hammer (1806–0170) may then be attached to the Recon Strike Plate to carefully and smoothly extract the assembly (**Fig. 23**).

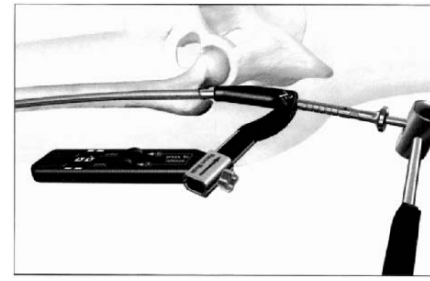

Fig. 23

The new position is checked again with the image intensifier as described above.

Note: In case of very dense femoral neck bone, the Recon K-Wire might deflect during insertion. If any deflection of the first K-wire is noticed, it is recommended to use the solid Stepdrill technique.

Operative Technique

• Nail/Lag Screws Positioning with the One Shot™ Device

Alternatively, the **One Shot™ Device** (1213–3010) can be used to determine the correct K-Wire, lag screws and nail placement (**Fig. 24**). The **One Shot™ Device** is made of carbon fiber and works by providing a target to indicate the position of the K-Wire on the fluoroscope screen. The target contains three radio-opaque wires embedded in the arm – a dashed inner wire and two solid outer wires. These wires work like a gun sight to indicate the position of the K-Wire.

Fig. 24

The **One Shot™ Device** is attached by slightly pressing the grip and releasing it when positioned onto the Tissue Protection Sleeve. To reposition or remove the device, the grip must be depressed.

Note: The use of the **One Shot™ Device** should not interfere with or replace any steps in the **T2™ Recon Nail** Operative Technique.

While depressing the attachment grip, the device is positioned between the anterior aspect of the patient's hip and the fluoroscope screen positioned for an A/P view of the hip (**Fig. 24** and **25**).

Note: It is important to drape the patient such that the **One Shot™ Device** does not interfere with any drapes anterior to the patient's hip.

When positioned correctly, the target will appear in the fluoroscopic image (A/P view), with the dashed inner wire in the middle of the two solid outer wires (**Fig. 25**).

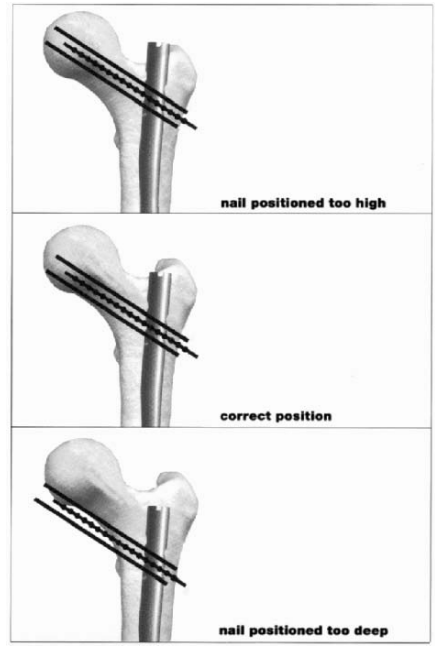

A/p View **Fig. 25**

If it does not, the **One Shot™ Device** should be moved towards or away from the patient by depressing the grip slightly until the target is seen as described above.

Operative Technique

Note: The **One Shot™ Device** cannot be rotated 90° with the Tissue Protection Sleeve because it will be stopped by the Nail Adapter. Therefore, **the C-Arm must be turned more than 90°, in order to get a lateral view** of the **One Shot™ Device**.

To identify the position of the K-Wire accurately, the dashed wire of the target must appear between the two solid wires at the desired position. **If the position is incorrect, the T2™ Recon Nail may be repositioned by rotating the target device to attain the appropriate anteversion.** The K-Wire can then either be placed into the femur or, the targeting arm is held in place until the K-Wire's position in the lateral view has been determined (**Fig. 26**). When positioned correctly, the target will appear in the fluoroscopic lateral views (**Fig. 27**).

Fig. 26

If the dashed wire of the target appears between the two solid wires, insert the K-Wire (**Fig. 28**) and continue following the **T2™ Recon Nail** Operative Technique.

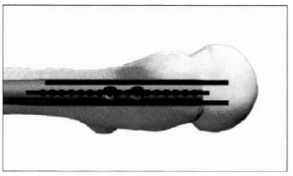

Lateral view **Fig. 27**

Note: Prior to advancing the K-Wire, check the correct guidance through the K-Wire Sleeve. Do not use bent K-Wires.

Note: The K-Wire inserted into the most distal Lag Screw hole of the nail helps in achieving the correct positioning of the nail (depth & rotation) with minimal resection of bone in case repositioning is needed.

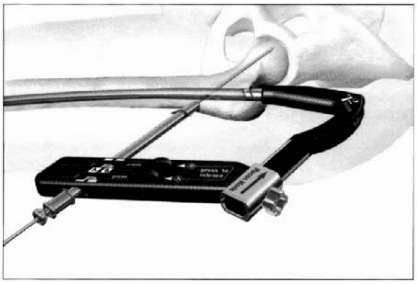

Fig. 28

After this is achieved, the surgeon can choose to use either

- the cannulated Stepdrill to perform insertion of the Lag Screws over the K-Wire or,
- the solid Stepdrill to perform insertion of the Lag Screws without the K-Wire guidance.

Note: If any deflection of the first K-Wire is noticed, it is recommended to use the solid Stepdrill technique.

Operative Technique

(B) Lag Screw Selection and insertion
Option 1:
Cannulated Stepdrill Technique

After achieving a satisfactory position of the first Recon K-Wire, slide the second Recon Tissue Protection Sleeve together with the Recon K-Wire Sleeve into the proximal hole (B) on the Recon Targeting Arm by pressing the proximal safety clip (B) (**Fig. 30**). A small skin incision is made and the assembly is pushed through until it is in contact with the lateral cortex and then release the safety clip (**Fig. 29**).

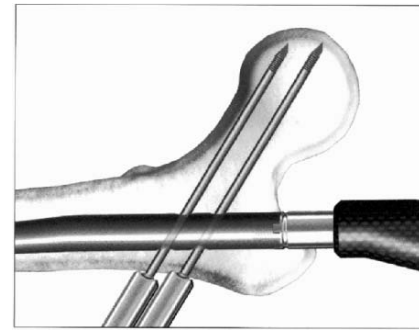

Fig. 29

Place a second Recon K-Wire into the K-Wire Inserter and attach it to the T-Handle or power tool. The K-Wire is then advanced through the K-Wire Sleeve until it penetrates the subchondral bone of the femoral head, but not through the medial cortex (**Fig. 29**).

Note: Correct placement of the K-Wire tip in subchondral bone must be checked with image intensifier in both A/P and Lateral views.

Note: Accuracy of K-Wire/Solid Stepdrill penetration and lag screw measurement is directly dependent on both sleeves being in contact with the lateral cortex.

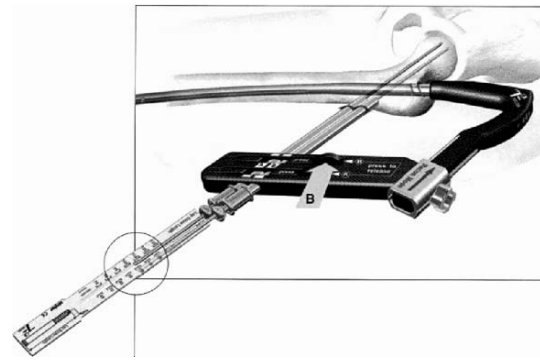

Fig. 30

The required length of the Lag Screw is measured using the Recon Lag Screw Gauge (1806–3035). Before starting to measure, ensure that the Tissue Protection Sleeve and K-Wire Sleeve assembly is firmly pressed against the lateral cortex of the femur (**Fig. 30**).

Take the Recon Lag Screw Gauge and place it directly under the distal K-Wire and against the K-Wire Sleeve (**Fig. 30**). The correct Lag Screw length corresponds to the measurement indicated at the end of the K-Wire on the Lag Screw Gauge.

This length will then be set on the cannulated Stepdrill for Recon Lag Screw (1806–3025) (**Fig. 31**).

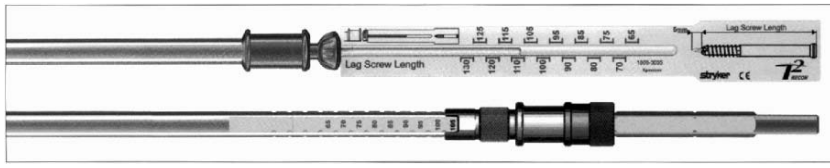

Fig. 31

Operative Technique

Note: Before proceeding with drilling for the selected Lag Screw, check the A/P fluoroscopic views to see if the two Recon K-Wires are parallel.

The distal K-Wire Sleeve is removed while the Tissue Protection Sleeve remains in position (**Fig. 32a**). The cannulated Ø6.5mm Stepdrill for Recon Lag Screw (1806–3025) is forwarded over the K-Wire through the Tissue Protection Sleeve and pushed onto the lateral cortex. The stop on the drill will only allow drilling up to 5mm before the K-Wire ends (**Fig. 32b**).

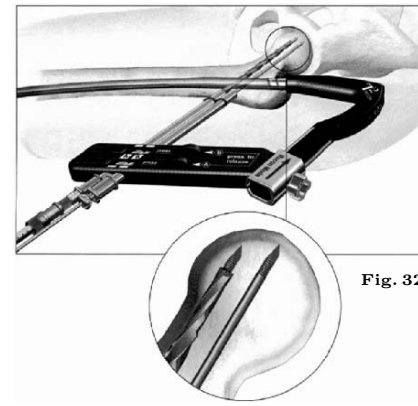

Fig. 32a

Fig. 32b

Note: Do not use the cannulated Stepdrill for Recon Lag Screw over a deflected K-Wire.

Using the Recon Screwdriver (1806–3060), the correct Lag Screw is inserted through the Tissue Protection Sleeve and threaded up to the subchondral bone of the femoral head. The screw is near its proper seating position when the groove around the shaft of the screwdriver is approaching the end of the Tissue Protection Sleeve (**Fig. 33**).

Alternatively, the Recon Screwdriver Shaft (1806–3050) assembled into the T-Handle (702628) can be used for the Lag Screw insertion.

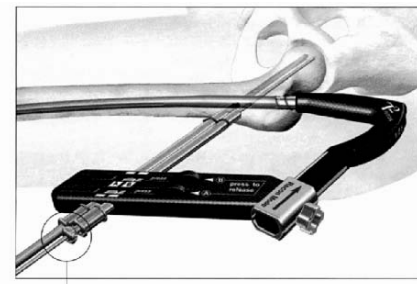

Fig. 33

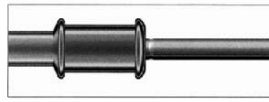

The required length of the second Lag Screw is measured using the Recon Lag Screw Gauge. Repeat the same surgical steps for drilling and insertion of the proximal Lag Screw (**Fig. 34**).

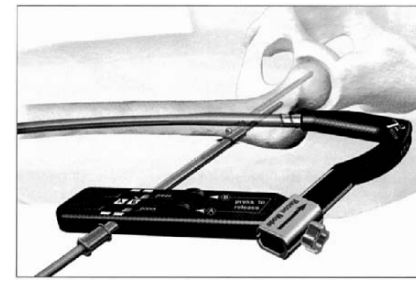

Fig. 34

Operative Technique

Option 2:
Solid Stepdrill Technique
If any deviation of the distal K-Wire is noticed, reaming and Lag Screw insertion should be done without K-Wire guidance.

The distal Recon K-Wire and K-Wire Sleeve are left in place and another Tissue Protection Sleeve, assembled with the Drill Sleeve for the Solid Recon Stepdrill (1806–3041) is inserted through the proximal hole of the Recon Target Arm. The Ø6.5 mm Solid Stepdrill for Recon Lag Screw (1806–3026S) is forwarded through the Tissue Protection Sleeve and Drill Sleeve assembly and pushed onto the lateral cortex.

Reaming is performed under fluoroscopic control until the tip of the Solid Stepdrill for Lag Screw is just before the subchondral bone. The required length of the Lag Screw can be read directly off the Solid Stepdrill for Recon Lag Screw at the end of the Drill Sleeve (**Fig. 35a** & **35b**).

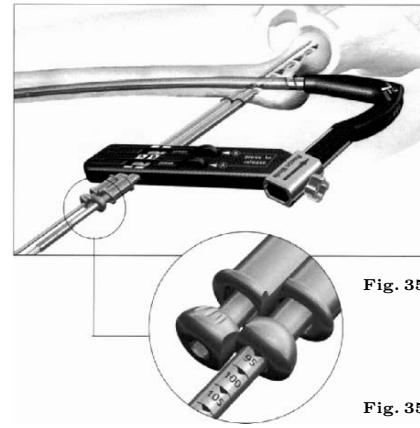

Fig. 35a

Fig. 35b

Using the Recon Screwdriver (1806–3060), the correct Lag Screw is inserted through the Tissue Protection Sleeve and threaded up to the subchondral part of the femoral head. The screw is near its' proper seating position when the groove around the shaft of the screwdriver is approaching the end of the Tissue Protection Sleeve (**Fig. 36** & **37**). The required length of the second Lag Screw can be measured using the Recon Lag Screw Gauge.

Remove the distal Recon K-Wire and K-Wire Sleeve and insert the Sleeve for the solid Stepdrill into the distal Tissue Protection Sleeve.

Repeat the same surgical steps for drilling and insertion of the distal Lag Screw without K-Wire guidance.

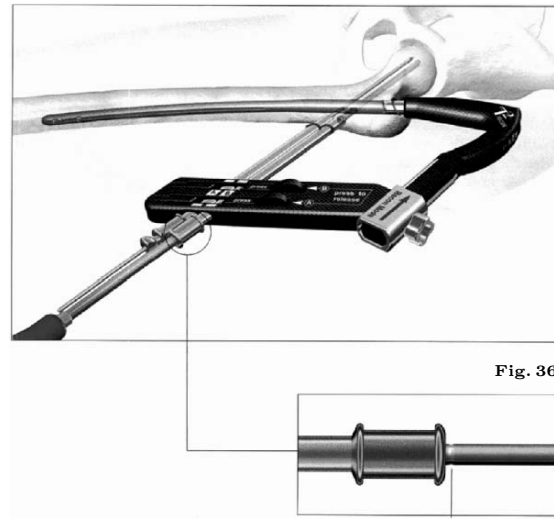

Fig. 36a

Groove on screwdriver shaft **Fig. 37**

Operative Technique

5.7.1. Guided Locking Mode for Antegrade Femoral Mode (via Target Device)

For standard Antegrade Femoral Mode, slide the Antegrade Targeting Arm (1806–3003) onto the Recon Nail Adapter (1806–3001). The Targeting Arm will sit in the groove positioned on the upper surface of the Nail Adapter because of an integrated spring locking mechanism, which prevents sliding. A "click" will confirm correct positioning of the Targeting Arm. Tighten the Locking Knob to ensure precise proximal locking (**Fig. 38**).

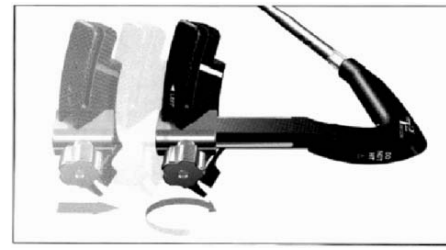

Fig. 38

Note: Avoid using a mallet to insert the Drill Sleeve as this can lead to the Locking Knob of the Antegrade Targeting Arm loosening and the Drill missing the hole in the nail.

Slide the Long Tissue Protection Sleeve (1806–0185) together with the Long Drill Sleeve (1806–0215) and the Long Trocar (1806–0315) into the corresponding hole of the Antegrade Targeting Arm (for Left or Right) by pressing the Safety Clip. A small skin incision is made and the assembly is pushed through until the Tissue Protection Sleeve is in contact with the lateral cortex. Release the safety clip when the sleeves hit the lateral cortex. The mechanism will keep the sleeve in place and prevent it from falling out. It will also prevent the sleeve from sliding during screw measurement. To release the Tissue Protection Sleeve, the Safety Clip must be pressed again. (**Fig. 39**).

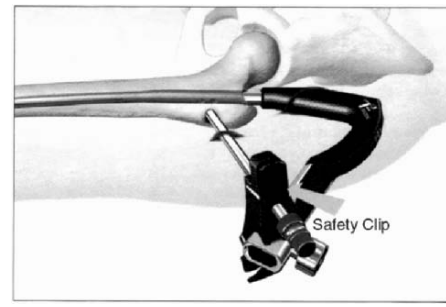

Fig. 39

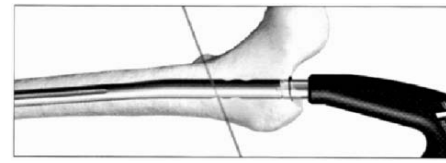

Fig. 40

Note: For optimal stability, the tip of the oblique screw should be positioned at the level of the Lesser Trochanter (**Fig. 40**).

Use the center-tipped, calibrated Ø4.2 × 340 mm Drill (1806–4260S) and drill through both cortices (**Fig. 41**) so that the tip of the bit is where you want the end of the screw.

The screw length may be read directly from the Calibrated Drill, at the end of the Drill Sleeve (**Fig. 42**).

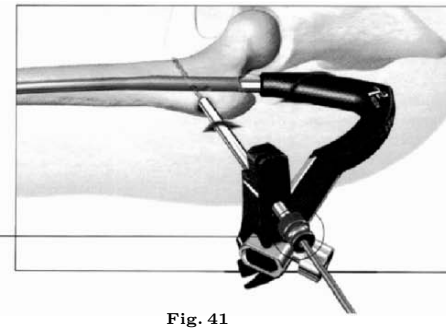

Fig. 41

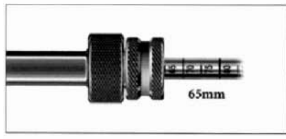

Fig. 42

Operative Technique

Note: Start the drill before touching the bone and then keep gentle pressure on the first cortex to ensure accurate drilling.

Alternatively, to help ensure accurate drilling for the oblique screw, use the Ø4.2 × 250 mm Drill (1806–8018S) to open the first cortex. The Drill is forwarded through the Drill Sleeve and pushed onto the cortex. After opening the first cortex, use the center-tipped, calibrated Ø4.2 × 340 mm Drill (1806–4260S) and drill through both cortices (**Fig. 38** and **39**).

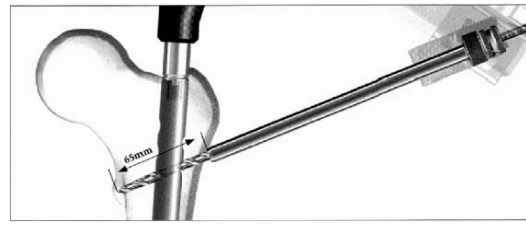

Fig. 43

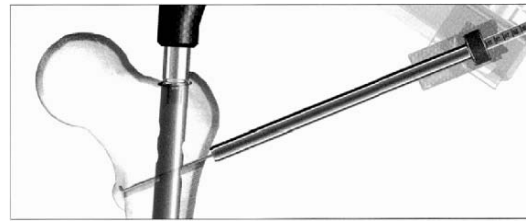

Fig. 44

Note: The position of the end of the Drill, as it relates to the far cortex, is the same as where the end of the screw will be.

Therefore, if the end of the Drill is 3mm beyond the far cortex, the end of the screw will also be 3mm beyond (**Fig. 43**). **Check the position of the end of Drill with image intensification before measuring the screw length**. If Screw measurement with the Long Screw Gauge (1806–0325) is preferred, first remove the Long Drill Sleeve and read the screw length directly at the end of the Long Tissue Protection Sleeve.

Note: The Long Screw Gauge is calibrated so that with the hook at the end pulled back to engage the far cortex, the screw tip will end 3mm beyond the far cortex (**Fig. 44**).

When the Drill Sleeve is removed, the correct Locking Screw is inserted through the Tissue Protection Sleeve using the Long Screwdriver Shaft (1806–0227) with Teardrop Handle (702429) (**Fig. 45**). The screw is advanced through both cortices. The screw is near its proper seating position when the groove around the shaft of the screw-driver is approaching the end of the Tissue Protection Sleeve (**Fig. 46**).

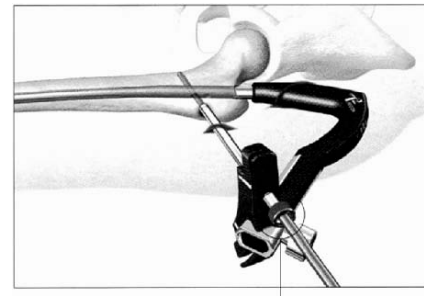

Fig. 45

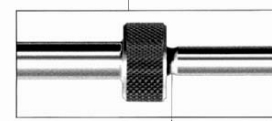

Groove on Screwdriver shaft

Fig. 46

Operative Technique

5.8. Freehand Distal Locking

The freehand technique is used to insert Fully Threaded Locking Screws into both distal transverse holes in the nail.

Rotational alignment must be checked prior to locking the nail. This is performed by checking a lateral view at the hip and a lateral view at the knee. The anteversion should be the same as on the contralateral side.

Multiple locking techniques and radiolucent drill devices are available for freehand locking. The critical step with any freehand locking technique, proximal or distal, is to visualize a perfectly round locking hole with the C-Arm.

The center-tipped Ø4.2 × 180 mm Drill (1806–4270S) or the Ø4.2 × 230 mm Drill (1806–4290S) is held at an oblique angle to the center of the locking hole (**Fig. 47**). I X-Ray verification, the Drill is placed pe dicular to the nail and drilled throug lateral and medial cortex (**Fig. 48**). Co in both the A/P and lateral views by X that the Drill passes through the hole i nail.

After drilling both cortices, the screw length may be read directly off of the Long Screw Scale (1806–0365) at the green ring on the center-tipped Ø4.2 × 180 mm Drill (**Fig. 49**).

Alternatively, the Screw Gauge (1806–0480) for Freehand technique can be used instead of the Long Screw Scale to determine the screw length.

Routine Locking Screw insertion is employed with the assembled Long Screwdriver Shaft and Teardrop Handle.

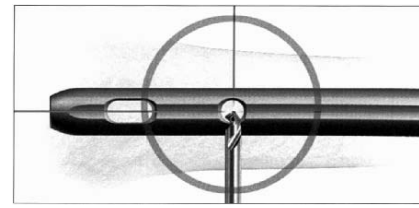

Fig. 47

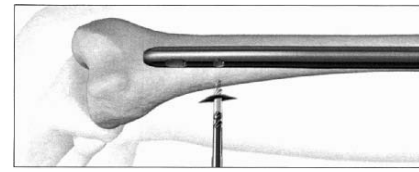

Fig. 48

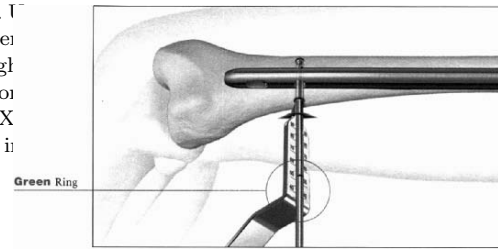

Fig. 49

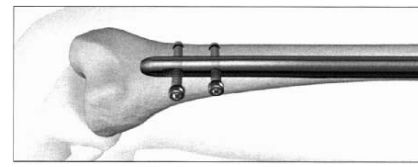

Fig. 50

Note: The Screwdriver Shaft can be used in conjunction with the Long Screw Capture Sleeve (1806–0240).

Repeat the locking procedure for the insertion of the second 5mm Fully Threaded Locking Screw into the oblong hole, in a static position (**Fig. 50**).

The T2^{TM} **Recon Nail** may only be used in the **dynamic locking mode** for transverse, stable fractures. Dynamic locking can only be performed at the end of the nail, requiring freehand distal targeting of the oblong hole in the dynamic position. This allows the nail to move and the fracture to dynamize while torsional stability is maintained.

Operative Technique

5.9. Set Screw or End Cap Insertion

After removal of the Target Device, a Set Screw or End Cap can be used.

Two different Set Srews are available (**Fig. 51a**):

- **Recon Set Screw*** to tighten down on the proximal Lag Screw (for the Recon Mode) and
- **Antegrade Set Screw** to tighten down on the oblique Fully Threaded Screw (for the Femoral Antegrade Mode).

Note: If a Set Screw is used, an End Cap can no longer be inserted.

Four different sizes of End Caps are available to adjust nail length and to reduce the potential for bony ingrowth into the proximal thread of the nail (**Fig. 51b**).

Note: Only the Standard End Cap is the same as used with the T2™ Femoral and Tibial Nails. The +5 mm, +10 mm, and +15 mm End Caps are unique to the T2™ Recon Nail due to the larger diameter of the end of the nails.

The Set Screw or End Cap is inserted with the Long Screwdriver Shaft and Teardrop Handle after intra-operative radiographs confirm satisfactory reduction and hardware implantation (**Fig. 52**). Fully seat the End Cap or Set Screw to minimize the potential for loosening.

Fig. 51a

Fig. 51b

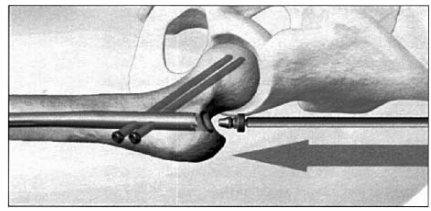

Fig. 52

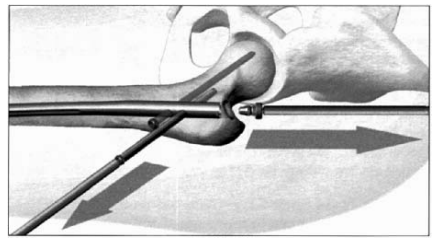

Fig. 53

5.10. Nail Removal

Nail removal is an elective procedure. The Set Screw or End Cap is removed with Long Screwdriver Shaft and Teardrop Handle (**Fig. 53**).

The Universal Rod is inserted into the driving end of the nail. Alternatively, the Conical Extraction Rod (1806–0350) can be attached to the Universal Rod to facilitate extraction of the nail. All Locking Screws are removed with the Long Screwdriver Shaft and Teardrop Handle. The optional Long Screw Capture Sleeve (1806–0240) may be used on the Screwdriver Shaft. For removal of the Recon Lag Screws, the Recon Screwdriver or the Recon Screwdriver Shaft and T-Handle are to be used.

The Slotted Hammer is used to extract the nail in a controlled manner. An optional (captured) Sliding Hammer (1806–0175) is available to add to the dedicated instrument set (**Fig. 54**).

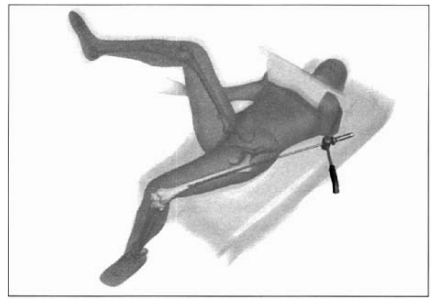

Fig. 54

*Not available for sale in U.S. at time of printing.

Ordering Information – Implants

T2™ Recon Nail, Left

Titanium Cat.#	Diameter mm	Length mm
1846–0934S	9.0	340
1846–0936S	9.0	360
1846–0938S	9.0	380
1846–0940S	9.0	400
1846–0942S	9.0	420
1846–0944S	9.0	440
1846–0946S	9.0	460
1846–0948S	9.0	480
1846–1134S	11.0	340
1846–1136S	11.0	360
1846–1138S	11.0	380
1846–1140S	11.0	400
1846–1142S	11.0	420
1846–1144S	11.0	440
1846–1146S	11.0	460
1846–1148S	11.0	480
1846–1334S	13.0	340
1846–1336S	13.0	360
1846–1338S	13.0	380
1846–1340S	13.0	400
1846–1342S	13.0	420
1846–1344S	13.0	440
1846–1346S	13.0	460
1846–1348S	13.0	480
1846–1534S	15.0	340
1846–1536S	15.0	360
1846–1538S	15.0	380
1846–1540S	15.0	400
1846–1542S	15.0	420
1846–1544S	15.0	440
1846–1546S	15.0	460
1846–1548S	15.0	480

T2™ Recon Nail, Right

Titanium Cat.#	Diameter mm	Length mm
1847–0934S	9.0	340
1847–0936S	9.0	360
1847–0938S	9.0	380
1847–0940S	9.0	400
1847–0942S	9.0	420
1847–0944S	9.0	440
1847–0946S	9.0	460
1847–0948S	9.0	480
1847–1134S	11.0	340
1847–1136S	11.0	360
1847–1138S	11.0	380
1847–1140S	11.0	400
1847–1142S	11.0	420
1847–1144S	11.0	440
1847–1146S	11.0	460
1847–1148S	11.0	480
1847–1334S	13.0	340
1847–1336S	13.0	360
1847–1338S	13.0	380
1847–1340S	13.0	400
1847–1342S	13.0	420
1847–1344S	13.0	440
1847–1346S	13.0	460
1847–1348S	13.0	480
1847–1534S	15.0	340
1847–1536S	15.0	360
1847–1538S	15.0	380
1847–1540S	15.0	400
1847–1542S	15.0	420
1847–1544S	15.0	440
1847–1546S	15.0	460
1847–1548S	15.0	480

6.5 mm Lag Screws

Titanium Cat.#	Diameter mm	Length mm
1897–6065S	6.5	65
1897–6070S	6.5	70
1897–6075S	6.5	75
1897–6080S	6.5	80
1897–6085S	6.5	85
1897–6090S	6.5	90
1897–6095S	6.5	95
1897–6100S	6.5	100
1897–6105S	6.5	105
1897–6110S	6.5	110
1897–6115S	6.5	115
1897–6120S	6.5	120
1897–6125S	6.5	125
1897–6130S	6.5	130

5 mm Fully Threaded Locking Screws*

Titanium Cat.#	Diameter mm	Length mm
1896–5025S	5.0	25.0
1896–5030S	5.0	30.0
1896–5035S	5.0	35.0
1896–5040S	5.0	40.0
1896–5045S	5.0	45.0
1896–5050S	5.0	50.0
1896–5055S	5.0	55.0
1896–5060S	5.0	60.0
1896–5065S	5.0	65.0
1896–5070S	5.0	70.0
1896–5075S	5.0	75.0
1896–5080S	5.0	80.0
1896–5085S	5.0	85.0
1896–5090S	5.0	90.0
1896–5095S	5.0	95.0
1896–5100S	5.0	100.0
1896–5105S	5.0	105.0
1896–5110S	5.0	110.0
1896–5115S	5.0	115.0
1896–5120S	5.0	120.0

End Caps

Titanium Cat. #	Diameter mm	Length mm
1822–0003S	8.0	Standard
1847–0005S	13.0	+5 mm
1847–0010S	13.0	+10 mm
1847–0015S	13.0	+15 mm

Set Screws

Titanium Cat.#	Diameter mm	
1847–0002S	8.0	Set Screw, Recon**
1847–0003S	8.0	Set Screw, Antegrade

Implants are packed sterile

*Not available for sale in U.S. at time of printing.

Ordering Information - Instruments

	Cat. #	Description
	Standard (Core) Instruments	
	1806-0020	Guide Wire Ruler (2 pieces)
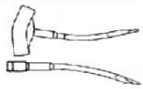	1806-0040	Awl, Curved, Ø10mm
	1806-0041	Awl, Curved, Ø10mm, 90° Handle (optional, not stored on tray)
	1806-0032	Awl Plug (optional; not stored on tray)
	1806-0095	Guide Wire Handle
	1806-0096	Guide Wire Handle Chuck
	1806-0110	Universal Rod
	1806-0125	Reduction Spoon
	1806-0130	Wrench
	1806-0170	Slotted Hammer
	1806-0185	Tissue Protection Sleeve, Long
	1806-0215	Drill Sleeve, Long
	1806-0227	Screwdriver Shaft AO, Long
	1806-0232	Screwdriver, Long
	1806-0315	Trocar, Long
	1806-0325	Screw Gauge, Long
	1806-0292	Screwdriver Shaft, 3.5 x 85mm
	1806-0350	Extraction Rod, conical
	1806-0480	Screw Gauge, Femur
	1806-4260S	Drill Ø4.2×340mm, AO
	1806-4290S	Drill Ø4.2×230mm, AO
	1806-4270S	Drill Ø4.2×180mm, AO
	702429	Teardrop Handle, AO Coupling
	702628	T-Handle, AO Medium Coupling
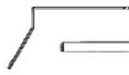	1806-0365	Screw Scale, Long
	1806-0240	Screw Capture Sleeve, Long

Ordering Information - Instruments

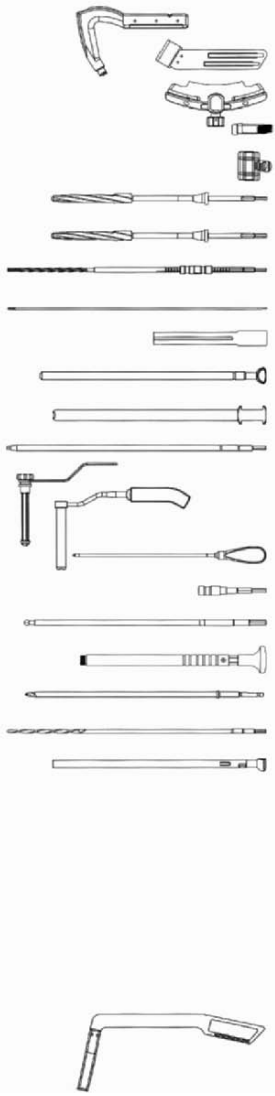

Cat. #	Description
Dedicated (Recon Only) Instruments	
1806-3001	Nail Adapter, Recon
1806-3002	Targeting Arm, Recon
1806-3003	Targeting Arm, Antegrade
1806-3005	Nail Holding Screw, Recon (2 of each)
1806-1007	Fixation Screw (2 of each)
1806-3010	One Step Conical Reamer Ø13, Recon
1806-3015	One Step Conical Reamer Ø15, Recon
1806-3025	Cannulated Stepdrill for Lag Screw, Recon
1806-3031S	K-Wire, Recon (2 of each)
1806-3035	Lag Screw Gauge, Recon
1806-3040	K-Wire Sleeve, Recon (2 of each)
1806-3045	Tissue Protection Sleeve, Recon (2 of each)
1806-3050	Screwdriver Shaft, Recon
1806-3055	Multi-hole Trocar
1806-3057	Protection Sleeve, Antegrade
1806-3060	Screwdriver, Recon
1806-3070	K-Wire Inserter
1806-3090	Screwdriver Shaft, AO, Ball Tip
1806-3096	Strike Plate, Recon
1806-8018S	Drill Ø4.2×250mm, oblique, AO
1806-3026S	Solid Stepdrill for Lag Screw, Recon
1806-3041	Drill Sleeve for Solid Stepdrill
Instrument Sets	
1806-9400	Dedicated Instrument Tray, empty
1806-9401	Dedicated Instrument Set (contains all Standard and Dedicated Instruments)
1806-9410	Add-On Instrument Tray, empty
1806-9411	Add-On Instrument Set (contains only Dedicated Instruments)
Optional Instruments	
1806-3080	X-Ray Template, Recon
1213-3010	One Shot Device (optional, not stored within tray)

Ordering Information – Instruments

Bixcut®

Complete range of modular and fixed-head reamers to match surgeon preference and optimize O.R. efficiency, presented in fully sterilizable cases.

Large clearance rate resulting from reduced number of reamer blades coupled with reduced length of reamer head to give effective relief of pressure and efficient removal of material.*

Cutting flute geometry optimized to lower pressure generation.*

Forward- and side-cutting face combination produces efficient material removal and rapid clearance.*

Double-wound shaft transmits torque effectively and with high reliability. Low-friction surface finish aids rapid debris clearance.*

Smaller, 6 and 8 mm shaft diameters significantly reduce 1M pressure.*

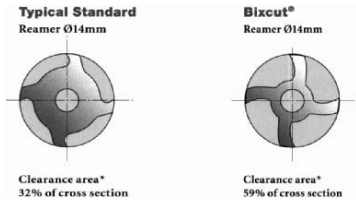

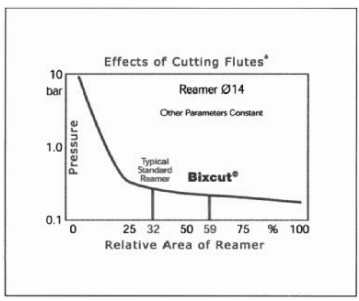

Recent studies[1] have demonstrated that the pressures developed within the medullary cavity through the introduction of unreamed IM nails can be far greater than those developed during reaming – but this depends very much upon the design of the reamer.

After a three year development study[2] involving several universities, the factors that determine the pressures and temperatures developed during reaming were clearly established. These factors were applied to the development of advanced reamers that demonstrate significantly better performance than the best of previous designs.

[1] Jan Paul M. Frolke, et al.; Intramedullary Pressure in Reamed Femoral Nailing with Two Different Reamer Designs., Eut. J. of Trauma, 2001 #5

[2] Mehdi Mousavi, et al.; Pressure Changes During Reaming with Different Parameters and Reamer Designs, Clinical Orthopaedics and Related Research Number 373, pp.295–303, 2000

* Data on file at Stryker

Ordering Information – Instruments

Bixcut® Modular Head

Cat.#	Description	Diameter mm
0226–3090	Bixcut Head	9.0
0226–3095	Bixcut Head	9.5
0226–3100	Bixcut Head	10.0
0226–3105	Bixcut Head	10.5
0226–3110	Bixcut Head	11.0
0226–3115	Bixcut Head	11.5
0226–3120	Bixcut Head	12.0
0226–3125	Bixcut Head	12.5
0226–3130	Bixcut Head	13.0
0226–3135	Bixcut Head	13.5
0226–3140	Bixcut Head	14.0
0226–3145	Bixcut Head	14.5
0226–3150	Bixcut Head	15.0
0226–3155	Bixcut Head	15.5
0226–3160	Bixcut Head	16.0
0226–3165	Bixcut Head	16.5
0226–3170	Bixcut Head	17.0
0226–3175	Bixcut Head	17.5
0226–3180	Bixcut Head	18.0
0226–4185	Bixcut Head	18.5
0226–4190	Bixcut Head	19.0
0226–4195	Bixcut Head	19.5
0226–4200	Bixcut Head	20.0
0226–4205	Bixcut Head	20.5
0226–4210	Bixcut Head	21.0
0226–4215	Bixcut Head	21.5
0226–4220	Bixcut Head	22.0
0226–4225	Bixcut Head	22.5
0226–4230	Bixcut Head	23.0
0226–4235	Bixcut Head	23.5
0226–4240	Bixcut Head	24.0
0226–4245	Bixcut Head	24.5
0226–4250	Bixcut Head	25.0
0226–4255	Bixcut Head	25.5
0226–4260	Bixcut Head	26.0
0226–4265	Bixcut Head	26.5
0226–4270	Bixcut Head	27.0
0226–4275	Bixcut Head	27.5
0226–4280	Bixcut Head	28.0

Bixcut® Shaft – Modified Trinkle fitting (sterile)+

Cat.#	Description	Length mm
0227–3000(S)	Shaft, Mod. Trinkle	450
0227–8240(S)	Shaft, Mod. Trinkle	240

Bixcut® Shaft – AO fitting (sterile)

Cat.#	Description	Length mm
0226–3000(S)	Shaft, AO	450
0226–8240(S)	Shaft, AO	240

Bixcut® Trays

Cat.#	Description
0225–6000	Tray, Modular Head (up to size 22.0 mm)
0225–6001	Tray, Modular Head (up to size 28.0 mm)
0225–8000	Tray, Fixed Head (up to size 18.0 mm)

Bixcut® Fixed Head – Modified Trinkle fitting+

Cat.#	Diameter mm	Length mm
0227–5060	6.0*	400
0227–5065	6.5*	400
0227–5070	7.0*	400
0227–6075	7.5	480
0227–6080	8.0	480
0227–6085	8.5	480
0227–6090	9.0	480
0227–6095	9.5	480
0227–6100	10.0	480
0227–6105	10.5	480
0227–6110	11.0	480
0227–8115	11.5	480
0227–8120	12.0	480
0227–8125	12.5	480
0227–8130	13.0	480
0227–8135	13.5	480
0227–8140	14.0	480
0227–8145	14.5	480
0227–8150	15.0	480
0227–8155	15.5	480
0227–8160	16.0	480
0227–8165	16.5	480
0227–8170	17.0	480
0227–8175	17.5	480
0227–8180	18.0	480

Bixcut® Fixed Head – AO fitting

Cat.#	Diameter mm	Length mm
0225–5060	6.0*	400
0225–5065	6.5*	400
0225–5070	7.0*	400
0225–6075	7.5	480
0225–6080	8.0	480
0225–6085	8.5	480
0225–6090	9.0	480
0225–6095	9.5	480
0225–6100	10.0	480
0225–6105	10.5	480
0225–6110	11.0	480
0225–8115	11.5	480
0225–8120	12.0	480
0225–8125	12.5	480
0225–8130	13.0	480
0225–8135	13.5	480
0225–8140	14.0	480
0225–8145	14.5	480
0225–8150	15.0	480
0225–8155	15.5	480
0225–8160	16.0	480
0225–8165	16.5	480
0225–8170	17.0	480
0225–8175	17.5	480
0225–8180	18.0	480

+ Use with Stryker Power Equipment

* Use with 2.2 mm × 800 mm Smooth Tip and 2.5 mm × 800 mm Ball Tip Guide wires only.

IX

Small Bone External Fixation System

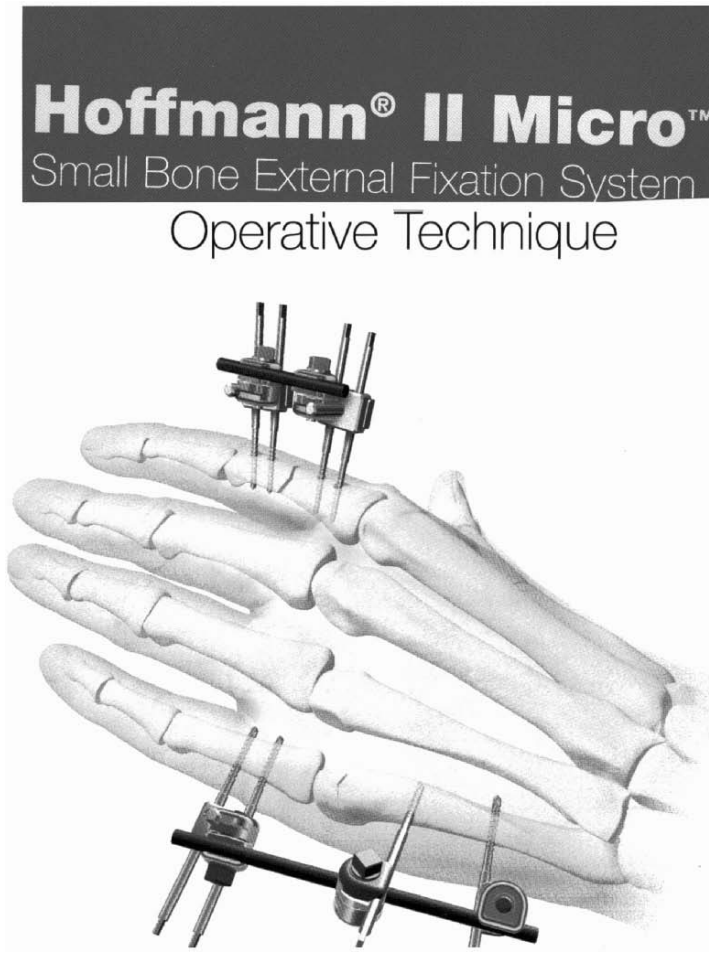

Components

1. Standard Instruments
2. Hoffmann®II Micro™ Rod-to-Rod Coupling
3. Hoffmann®II Micro™ Pin-to-Rod Coupling
4. Hoffmann®II Micro™ to Hoffmann®II Compact™ Rod-to-Rod Coupling
5. Hoffmann®II Micro™ Multi-Pin Clamp
6. Hoffmann®II Micro™ 90° Multi-Pin Clamp
7. Blunt or Self-Drilling/Self-Tapping Half-Pins (1.65 - 2mm)
8. Carbon and Stainless Steel Rods (3mm)

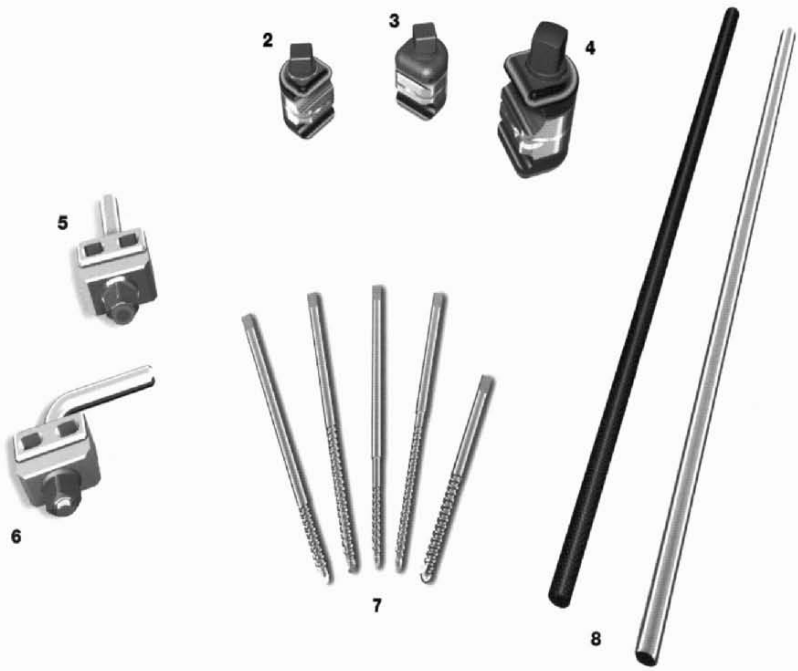

Indications & Contraindications

Indications

The Hoffmann®II Micro™ System is ideal for small bone fractures. It is particularly suited for the following indications:

- Small bone fracture fixation
- Osteotomy
- Arthrodesis
- Correction of deformity
- Revision procedures where other treatments or devices have been unsuccessful
- Bone reconstruction procedures
- Non-unions and delayed unions

The Hoffmann®II Micro™ System is also approved for use in children and in the maxillofacial area.

Contraindications

Since external fixation devices are often used in emergency situations to treat patients with acute injuries, there are no absolute contraindications for use. The surgeon's education, training and professional judgement must be relied upon to choose the most appropriate device and treatment for each individual patient. Whenever possible, the device chosen should be of a type indicated for the fracture being treated and/or for the procedure being utilized.

Conditions presenting an increased risk of failure include:

1. Insufficient quantity or quality of bone that would inhibit appropriate fixation of the device.
2. Compromised vascularity that would inhibit adequate blood supply to the fracture or operative site.
3. Previous history of infections.
4. Any neuromuscular deficit that would interfere with the patient's ability to limit weight bearing.
5. Any neuromuscular deficit that places an unusually heavy load on the device, during the healing period.
6. Malignancy in the fracture area.
7. Mental, physical or neurological conditions that may impair the patient's ability to cooperate with the postoperative regimen.

Operative Technique

Due to the versatility of the Hoffmann®II Micro™ System, an unlimited number of frame configurations may be constructed, providing surgeons ease of use while treating a variety of conditions.

This Technical Guide provides a step-by-step surgical technique for three basic frame assemblies. These constructs may then be adapted to other indications.

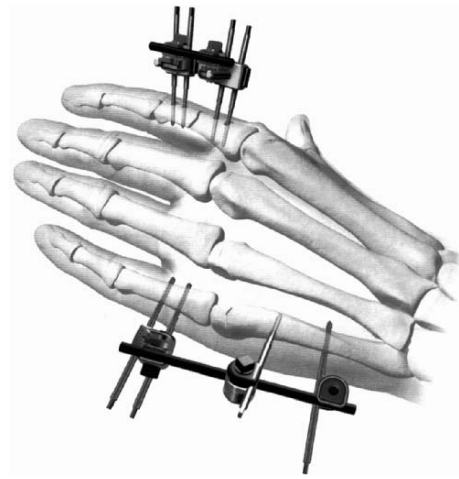

General Half Pin Insertion and Frame Building Guidelines

Frame Building Guidelines

The Hoffmann®II Micro™ Multi-Pin Clamp is designed for ease-of-use and precise pin insertion. The Clamp has oval pin slots that allow the Half Pins to be inserted in one plane in a variety of angles. (Figure 1)

The Hoffmann®II Micro™ Pin-to-Rod Coupling with patented "snap fit" clamp design, offers independent pin placement, which is needed to address the most complex cases. (Figure 2)

Multi-Pin Clamps and Couplings should be placed at least 5 mm to 10 mm away from the skin to allow for post-operative swelling and proper pin site care.

To reduce forces on the bone, it is recommended to hold the Half Pins with standard surgical pliers while tightening the Clamps and Couplings.

The Hoffmann® II Micro™ System is compatible with the larger Hoffmann® II Compact™ System (accepts 3–4 mm pins) allowing easy bridging between systems. The 3 mm/5 mm clamp is used to connect the systems and can be tightened with the 5 mm Wrench 3 mm/4 mm Pin Driver. (Figure 3)

Figure 1

Figure 2

Figure 3

Insertion Guidelines

Blunt or Self-Drilling/Self-Tapping Half Pins are offered in the system. Pre-drilling is necessary when using Blunt/Self-Tapping Half Pins. Half Pins have a 2.0 mm shaft diameter.

Note: Use a 1.5 mm drill bit to pre-drill a Blunt 2.0 mm Half Pin

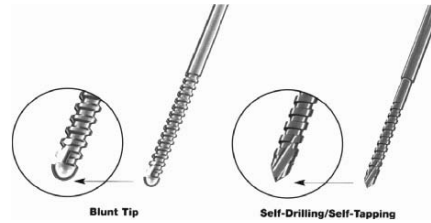

A (mini) open insertion technique is recommended to avoid unnecessary damage to the soft tissues. A Drill/Insertion Guide is provided in the system to facilitate this technique.

Hand

Placement in the Phalanges

I: Insert Half Pins from the radial side in the frontal plane.
II: Insert 0° to 45° from the frontal plane on the dorsal-radial side.
III: Insert 40° to 60° from the frontal plane on the dorsal-radial side.
IV: Insert 40° to 60° from the frontal plane on the dorsal-ulnar side.
V: Insert from the ulnar side in the frontal plane.

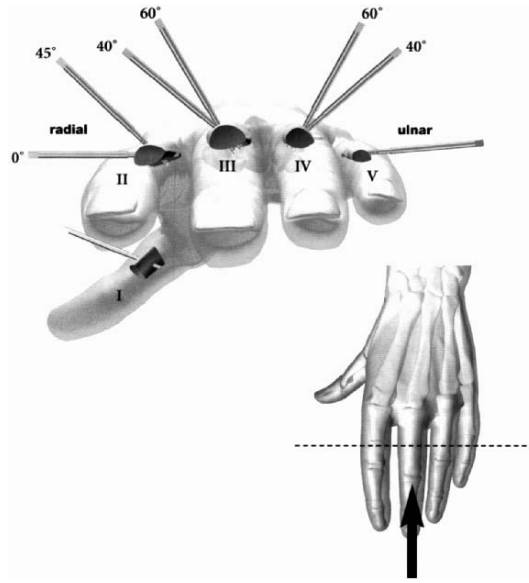

Placement in the Metacarpals

I: Insert Half Pins from the radial side in the frontal plane.
II: Insert 20° to 60° from the frontal plane on the dorsal-radial side.
III: Insert 40° to 60° from the frontal plane on the dorsal-ulnar side.
IV: Insert 40° to 60° from the frontal plane on the dorsal-ulnar side.
V: Insert from the ulnar side in the frontal plane.

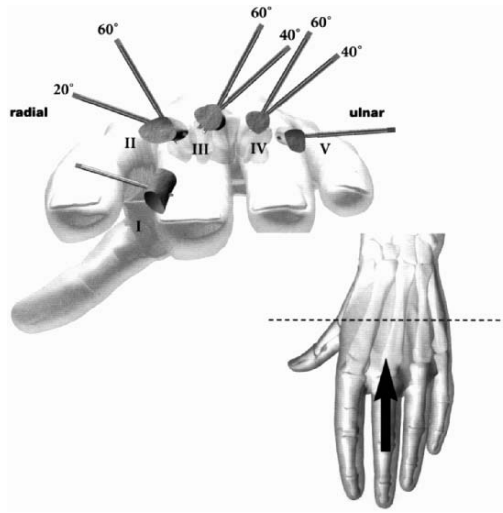

Note: When inserting pins, ensure bicortical purchase.

Frame 1

Mid-shaft fracture of the proximal phalanx of the index finger (Digit II).

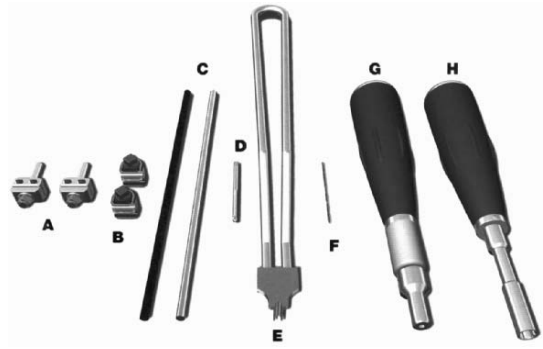

Material used:

A) 2 – Multi-Pin Clamps
B) 2 – Rod-to-Rod Couplings
C) 1 – Connecting Rod (Carbon or Stainless Steel)
D) 4 – 1.65 mm or 2 mm Apex® Half-Pins
E) 1 – Drill/Pin Insertion Guide
F) 1 – 1.5 mm Drill Bit for Blunt Pins
G) 1 – 2 mm Pin Driver
H) 1 – 4 mm Nut Wrench

Step 1:
Drill the first proximal hole at least 5 mm from the fracture site using the Drill/Pin Insertion Guide and the 1.5 mm drill bit. If Self-Drilling/Self-Tapping Half Pins are used, it is possible to insert the Half Pins without pre-drilling as described in this step.

Note: The drill/pin insertion angle is 0° to 45° from the frontal plane radially. Use image intensification to determine proper pin placement and to ensure bi-cortical purchase.

Step 2:
Manually insert the Half Pin using the 2 mm Pin Driver and Drill/Pin Insertion Guide.

Frame 1

Step 3:
Place one Multi-Pin Clamp over the Half Pin at least 5 mm to 10 mm away from the skin.

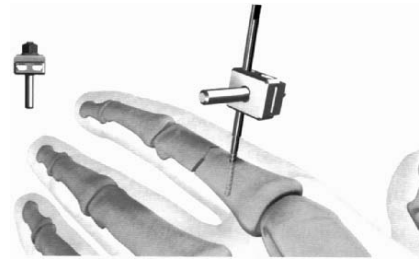

Step 4:
Using the Multi-Pin Clamp as a guide and the Drill/Pin Insertion Guide to protect soft tissue, drill the second proximal hole with the 1.5 mm drill bit. If Self-Drilling/Self-Tapping Half Pins are used, it is possible to insert the Half Pins without pre-drilling as described in this step.

Step 5:
Manually insert the second 2 mm Half Pin through the Multi-Pin Clamp using the 2 mm Pin Driver and the Drill/Pin Insertion Guide.

Step 6:
Tighten the Multi-Pin Clamp to the Half Pins at the desired position using the 4 mm Nut Wrench.

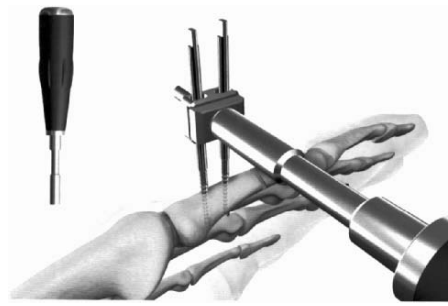

Frame 1

Step 7:
Build the same Pin/Clamp construct on the distal side of the fracture following steps 1 through 6.

Note: Insert the distal Half Pin closest to the fracture first.

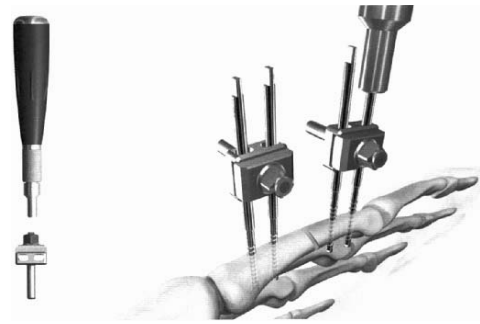

Step 8:
Two Rod-to-Rod Couplings are "snapped" on the clamp posts. The Connecting Rod (carbon or stainless steel) is then "snapped" into the two Rod-to-Rod Couplings and the fracture is reduced manually.

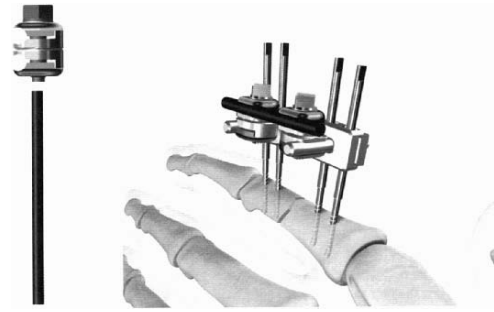

Step 9:
With the fracture reduced, tighten the Rod-to-Rod Couplings with the 4 mm Nut Wrench. The frame is now complete.

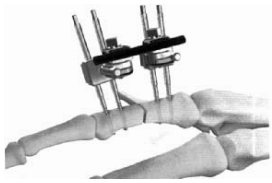

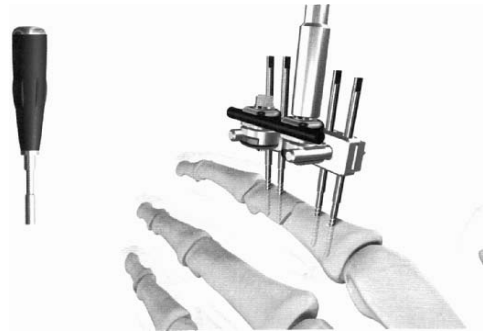

Frame 2

Metaphyseal fracture of the proximal phalanx of the index finger (Digit II).

Material used:

A) 2 – Multi-Pin Clamps
B) 2 – Rod-to-Rod Couplings
C) 1 – Connecting Rod (Carbon or Stainless Steel)
D) 4 – 1.65 mm or 2 mm Apex® Half-Pins
E) 1 – Drill/Pin Insertion Guide
F) 1 – 1.5 mm Drill Bit for Blunt Pins
G) 1 – 2 mm Pin Driver
H) 1 – 4 mm Nut Wrench

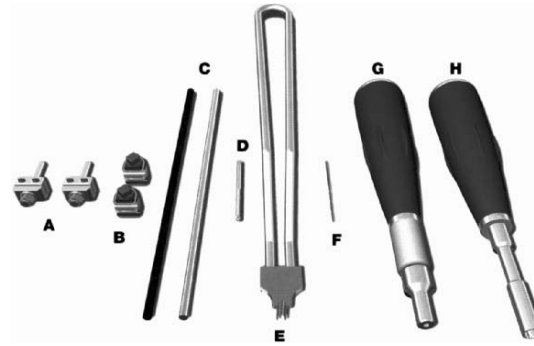

Step 1:

The proximal Half Pins are manually inserted parallel to the joint using the 2 mm Pin Driver and Drill/Pin Insertion Guide. Due to the design of the Clamp, the Half Pins can be placed parallel or convergent within the Clamp.

Use the Drill/Pin Insertion Guide and a 1.5 mm drill bit to pre-drill the blunt Half Pins.

Note: The drill/insertion angle is 0° to 45° from the frontal plane radially. Use image intensification to determine proper pin placement and to ensure bi-cortical purchase.

Step 2:

Tighten the Multi-Pin Clamp to the Half Pins at the desired position using the 4 mm Nut Wrench.

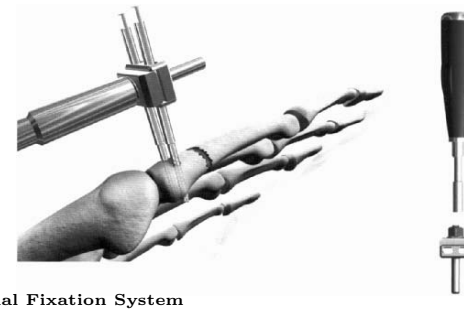

Frame 2

Step 3:
Construct a Half Pin/ Multi-Pin Clamp assembly distal to the fracture as shown in the figure. Securely tighten the Clamp onto the Half Pins.

Step 4:
Two Rod-to-Rod Couplings are "snapped" onto each of the clamp posts. The Connecting Rod (carbon or stainless steel) is then "snapped" into the two Rod-to-Rod Couplings and the fracture is reduced manually.

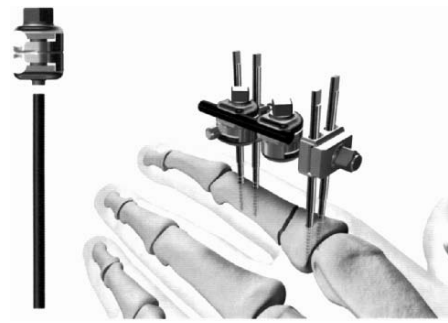

Step 5:
With the fracture reduced, tighten the Rod-to-Rod Couplings with the 4 mm Nut Wrench. The frame is now complete.

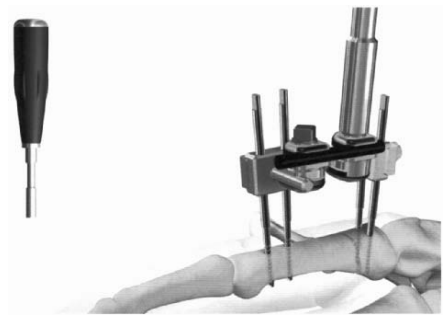

Frame 3

Intra-Articular fracture of the fifth metacarpal with severe soft-tissue damage.

Note: This frame offers additional freedom of independent pin placement, which is dictated by the soft-tissue damage and the fracture. This frame also allows for more accessible wound treatment while the frame is in place.

Material used:

A) 2 – Pin-to-Rod Couplings
B) 1 – Multi-Pin Clamps
C) 1 – Rod-to-Rod Couplings
D) 1 – Connecting Rod (Carbon or Stainless Steel)
E) 4 – 1.65 mm or 2 mm Apex® Half-Pins
F) 1 – Drill/Pin Insertion Guide
G) 1 – 1.5 mm drill bit for Blunt Pins
H) 1 – 2 mm Pin Driver
I) 1 – 4 mm Nut Wrench

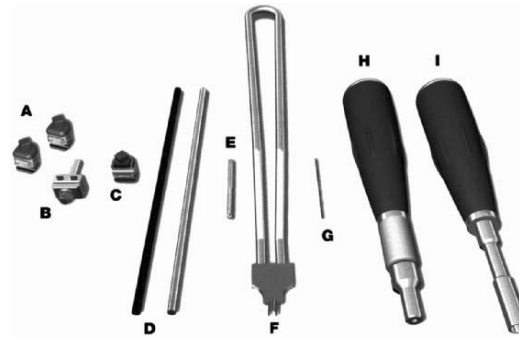

Step 1:

Manually insert the distal Half Pins into the fifth proximal phalanx using the 2 mm Pin Driver and the Drill/Pin Insertion Guide.

Place the Half Pins and Clamp parallel to the long axis of the bone. Use the Drill/Pin Insertion Guide and the 1.5 mm drill bit to pre-drill for the Blunt Half Pins. Insert the Half Pins from the ulnar side in the frontal plane. Use image intensification to determine proper pin placement and to ensure bi-cortical purchase.

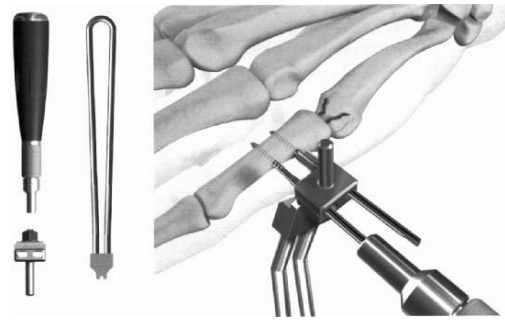

Step 2:

Tighten the Multi-Pin Clamp to the Half Pins at the desired position using the 4 mm Nut Wrench.

Frame 3

Step 3:
Attach a Rod-to-Rod Coupling to the Clamp.

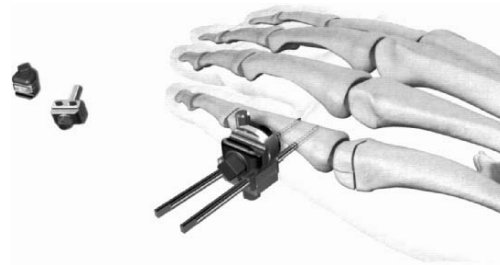

Step 4:
Insert one Half Pin in the fifth metacarpal proximal to the fracture, careful of any soft-tissue injuries. Attach a Pin-to-Rod Coupling to the Half Pin. "Snap" a 3 mm Connecting Rod (carbon or stainless steel) into the Rod-to-Rod Coupling and into the Pin-to-Rod Coupling.

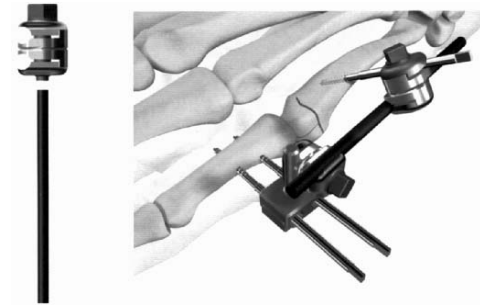

Step 5:
Attach the second Pin-to-Rod Coupling to the proximal end of the Connecting Rod.

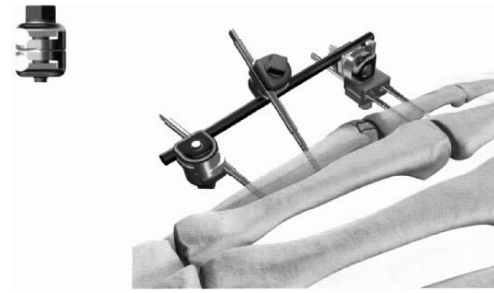

Frame 3

Step 6:
Insert the Half Pin into the shaft of the metacarpal using the Drill/Pin Insertion Guide and the Pin-to-Rod Coupling as guides. Then, manually reduce the fracture.

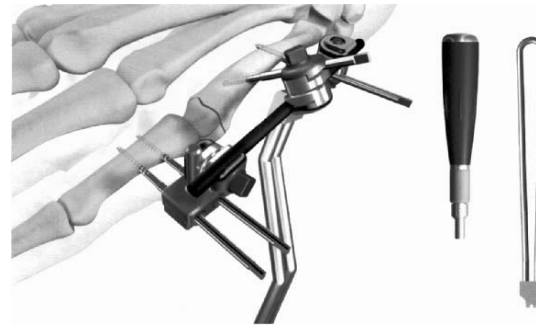

Step 7:
With the fracture reduced, tighten the Rod-to-Rod Coupling and Pin-to-Rod Couplings using the 4 mm Nut Wrench.

The frame is now complete.

Foot

A small, limited, open surgical approach allows central pin placement and may help avoid injury to or impingement of important soft tissue structures (tendons, ligaments, nerves and arteries). Half Pin placement should not interfere with soft tissue excursion during range of motion.

Consideration should also be given to any anatomical changes due to the current injury and to planning for any secondary surgeries that may be needed.

A general recommendation is for the pin size to be 1/3 the diameter of the bone treated. The Hoffmann® II Micro™ System is compatible with the larger Hoffmann® II Compact™ System (accepts 3–4 mm pins) allowing easy bridging between systems.

Note: Accurate pin size and placement must be determined by the surgeon on a case by case basis.

Pin Placement in the Phalanges

I: Insert Half Pins from the medial or dorsomedial side 0–115° from the frontal plane
II: Insert Half Pins medially or laterally 15–45° from the frontal plane
III: Insert Half Pins medially or laterally 15–45° from the frontal plane
IV: Insert Half Pins medially or laterally 15–45° from the frontal plane
V: Insert Half Pins from the lateral to dorsolateral side 0–110° from the frontal plane

Note: Caution must be taken to avoid all neurovascular or tendonous structures.

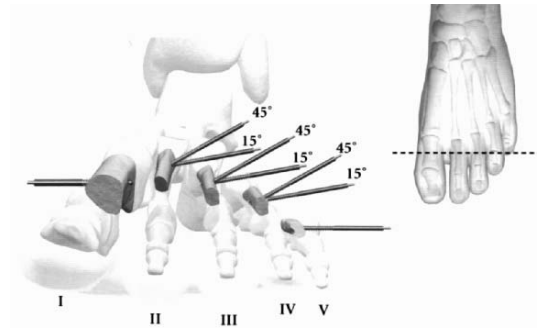

Pin Placement in the Metarsals

I: Insert Half Pins from the medial or dorsomedial side 0–115° from the frontal plane
II: Insert Half Pins medially or laterally 15–45° from the frontal plane
III: Insert Half Pins medially or laterally 15–45° from the frontal plane
IV: Insert Half Pins medially or laterally 15–45° from the frontal plane
V: Insert Half Pins from the lateral to dorsolateral side 0–110° from the frontal plane

Note: Caution must be taken to avoid all neurovascular or tendonous structures.

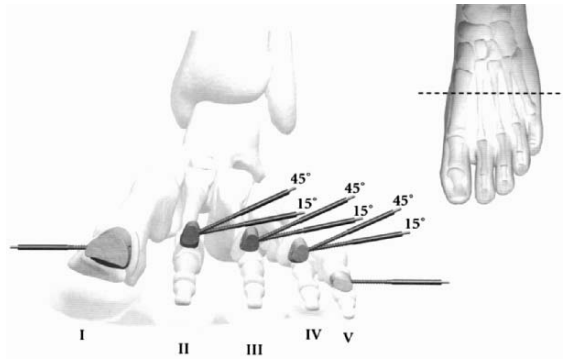

Ordering Infromation - Implants

Couplings and Clamps

	Catalog No.	Description	Diameter mm
	4960-1-010	Rod-to-Rod Coupling	3/3 mm
	4960-1-020	Pin-to-Rod Coupling	1.65-2 mm/3mm
	4960-1-060	Rod-to-Rod Coupling	5 mm/3mm
	4960-2-020	Multi-Pin Clamp	
	4960-2-030	90° Multi-Pin Clamp	

Warning: Bone Screws referenced in this material are not approved for screw attachment or fixation to the posterior elements (pedicles) of the cervical, thoracic or lumbar spine.

Ordering Infromation - Implants

Connecting Rods

Catalog No.	Description	Diameter	Total Length
5079-6-030	Carbon Connecting Rod	3 mm	30 mm
5079-6-040	Carbon Connecting Rod	3 mm	40 mm
5079-6-050	Carbon Connecting Rod	3 mm	50 mm
5079-6-060	Carbon Connecting Rod	3 mm	60 mm
5079-6-090	Carbon Connecting Rod	3 mm	90 mm
5079-6-120	Carbon Connecting Rod	3 mm	120 mm
5079-6-150	Carbon Connecting Rod	3 mm	150 mm

5079-5-030	Stainless Steel Connecting Rod	3 mm	30 mm
5079-5-040	Stainless Steel Connecting Rod	3 mm	40 mm
5079-5-050	Stainless Steel Connecting Rod	3 mm	50 mm
5079-5-060	Stainless Steel Connecting Rod	3 mm	60 mm
5079-5-090	Stainless Steel Connecting Rod	3 mm	90 mm
5079-5-120	Stainless Steel Connecting Rod	3 mm	120 mm
5079-5-150	Stainless Steel Connecting Rod	3 mm	150 mm

Blunt Self-Tapping Apex® Half Pins

Catalog No.	Diameter	Total Length	Thread Length
5065-3-615	2 mm, Stainless Steel	36 mm	15 mm
5065-4-520	2 mm, Stainless Steel	45 mm	20 mm
5065-9-015	2mm, Stainless Steel	90 mm	15 mm

Self-Drilling/Self-Tapping Apex® Half Pins

Catalog No.	Diameter	Total Length	Thread Length
5080-2-012	2 mm, Stainless Steel	45 mm	12 mm
5080-2-020	2 mm, Stainless Steel	45 mm	20 mm
5080-1-612	1.65 mm, Stainless Steel	45 mm	12 mm
5080-1-620	1.65 mm, Stainless Steel	45 mm	20 mm

K-Wires

Catalog No.	Description	Diameter	Thread Length
390142	K-Wire	1.0 mm	150 mm
390152	K-Wire	1.2 mm	150 mm
390162	K-Wire	1.4 mm	150 mm
390164	K-Wire	1.6 mm	150 mm

Ordering Infromation - Instruments

	Standard Instruments Catalog No.	Description
	4960-9-040	Drill/Pin Insertion Guide
	4960-9-030	4 mm Nut Wrench
	4960-9-020	2 mm Pin Driver
	4940-9-030	5 mm Wrench/3mm–4mm Pin Driver
	5084-4-044	4 mm Spanner Wrench
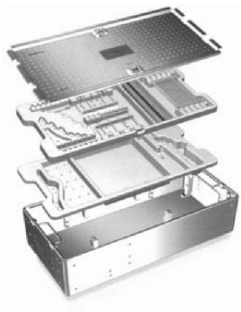	4960-9-901	Storage Case Base
	4960-9-902	Storage Case Lower Insert
	4960-9-903	Storage Case Upper Insert
	4960-9-904	Storage Case Lid
	4960-9-905	Drill Bit Holder Insert

Stryker®
Trauma

Hoffmann® II Micro™
Small Bone External Fixation System

Frame 3

Intra-articular fracture of the fifth metacarpal with severe soft-tissue damage

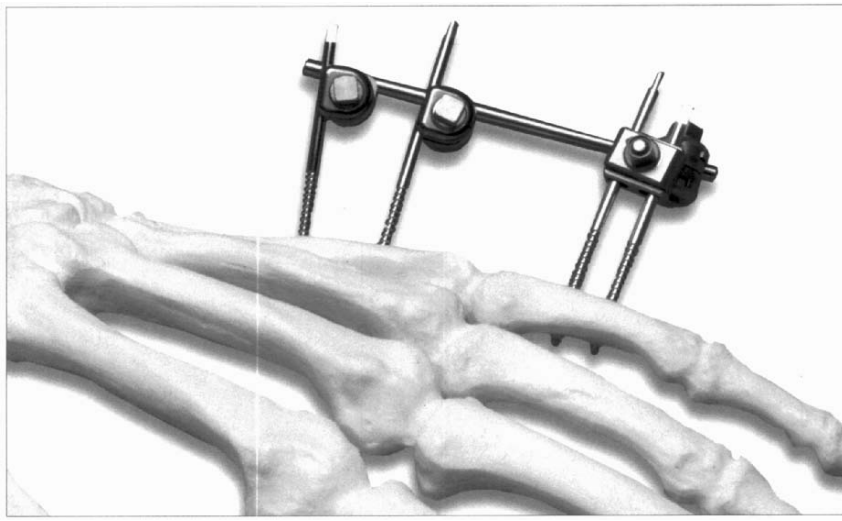

Components

Cat. No.	Description	Quantity
4960-2-020	Multi-Pin Clamp	1
4960-1-010	Rod-to-Rod Coupling 3/3 mm	1
4960-1-020	Pin-to-Rod Couplings 2/3 mm	2
5079-6-Series	Carbon Connecting Rod	
OR		1
5079-5-Series	Stainless Steel Connecting Rod	
5065-3-615	Blunt Half Pins 2 mm (36 mm length)	
OR		4
5065-4-520	Blunt Half Pins 2 mm (45 mm length)	

Hoffmann® II Micro™

Small Bone External Fixation System Features

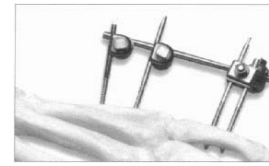

- **Only Patented Snap-Fit** external fixation clamp system used in fracture fixation of the digits.
- **Modular components** allow for true independent pin placement and virtually unlimited frame configurations.
- **Oblong holes** in multi-pin clamps allow convergent and divergent pin placement within clamps.
- **System cross-over** provides compatibility with the Hoffmann® II Compact™ System and creates a complete external fixation system for treatment of polytrauma patients.
- **New Ø3 mm carbon fiber rods** provide unrestricted fracture visualization.
- **Limited Inventory** – only 5 components in system: Rod-to-Rod Clamp (3 mm/3 mm), Pin-to-Rod Clamp, 0° Multi-Pin Clamp, 90° Multi-Pin Clamp and Rod-to-Rod Clamp (5 mm/3 mm).

The information presented is intended to demonstrate a Stryker product. Always refer to the package insert, product label and/or user instructions before using any Stryker product. Products may not be available in all markets. Product availability is subject to the regulatory or medical practices that govern individual markets. Please contact your Stryker representative if you have questions about the availability of Stryker products in your area.

Products referenced with™ designation are trademarks of Stryker.
Products referenced with® designation are registered trademarks of Stryker.

Literature Number: LH2MSS-F3
GC/GS 5c 05/04

Copyright © 2004 Stryker
Printed in USA

325 Corporate Drive
Mahwah NJ 07430
t: 201-831-5000 t: 800-447-7836

www.stryker.com

Stryker®
Trauma

Hoffmann® II Micro™
Small Bone External Fixation System

Frame 5

Fracture dislocation (Digit IV or V)

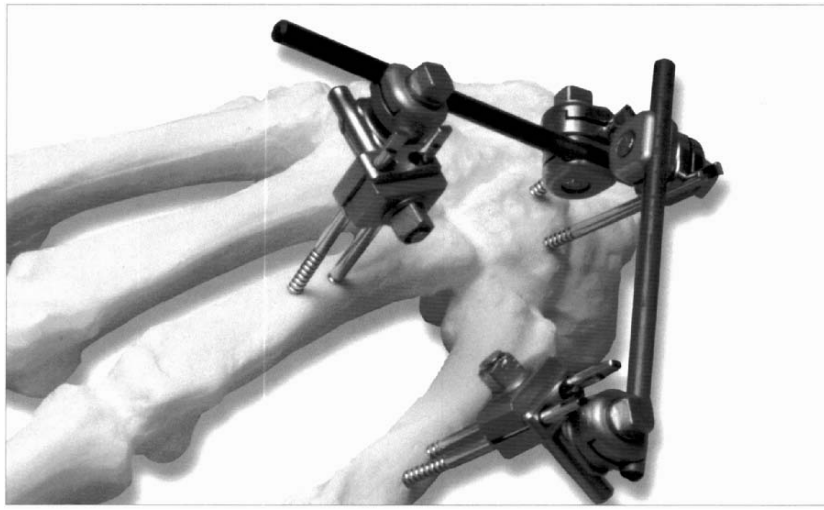

Components

Cat. No.	Description	Quantity
4960-2-020	Multi-Pin Clamps	2
4960-1-010	Rod-to-Rod Couplings 3/3 mm	2
4960-1-020	Pin-to-Rod Couplings 2/3 mm	2
5079-6-Series	Carbon Connecting Rods	
OR		2
5079-5-Series	Stainless Steel Connecting Rods	
5065-3-615	Blunt Half Pins 2 mm (36 mm length)	
OR		6
5065-4-520	Blunt Half Pins 2 mm (45 mm length)	

Hoffmann® II Micro™

Small Bone External Fixation System Features

- **Only Patented Snap-Fit** external fixation clamp system used in fracture fixation of the digits.
- **Modular components** allow for true independent pin placement and virtually unlimited frame configurations.
- **Oblong holes** in multi-pin clamps allow convergent and divergent pin placement within clamps.
- **System cross-over** provides compatibility with the Hoffmann® II Compact™ System and creates a complete external fixation system for treatment of polytrauma patients.
- **New Ø3 mm carbon fiber rods** provide unrestricted fracture visualization.
- **Limited inventory** – only 5 components in system: Rod-to-Rod Clamp (3 mm/3 mm), Pin-to-Rod Clamp, 0° Multi-Pin Clamp, 90° Multi-Pin Clamp and Rod-to-Rod Clamp (5 mm/3 mm).

The information presented is intended to demonstrate a Stryker product. Always refer to the package insert, product label and/or user instructions before using any Stryker product. Products may not be available in all markets. Product availability is subject to the regulatory or medical practices that govern individual markets. Please contact your Stryker representative if you have questions about the availability of Stryker products in your area.

Products referenced with™ designation are trademarks of Stryker.

Products referenced with® designation are registered trademarks of Stryker.

Literature Number: LH2MSS-F5
GC/GS 5c 05/04

Copyright © 2004 Stryker
Printed in USA

325 Corporate Drive
Mahwah NJ 07430
t: 201-831-5000 t: 800-447-7836

www.stryker.com

Stryker®
Trauma

Hoffmann® II Micro™
Small Bone External Fixation System

Frame 4
Fracture dislocation (Digit IV or V)

Components

Cat. No.	Description	Quantity
4960-2-020	Multi-Pin Clamps	2
4960-1-010	Rod-to-Rod Couplings 3/3 mm	2
4960-1-020	Pin-to-Rod Couplings 2/3 mm	3
5079-6-Series	Carbon Connecting Rod	
OR		1
5079-5-Series	Stainless Steel Connecting Rod	
5065-3-615	Blunt Half Pins 2 mm (36 mm length)	
OR		6
5065-4-520	Blunt Half Pins 2 mm (45 mm length)	

Hoffmann® II Micro™

Small Bone External Fixation System Features

- **Only Patented Snap-Fit** external fixation clamp system used in fracture fixation of the digits.
- **Modular components** allow for true independent pin placement and virtually unlimited frame configurations.
- **Oblong holes** in multi-pin clamps allow convergent and divergent pin placement within clamps.
- **System cross-over** provides compatibility with the Hoffmann® II Compact™ System and creates a complete external fixation system for treatment of polytrauma patients.
- **New Ø3 mm carbon fiber rods** provide unrestricted fracture visualization.
- **Limited Inventory** – only 5 components in system: Rod-to-Rod Clamp (3 mm/3 mm), Pin-to-Rod Clamp, 0° Multi-Pin Clamp, 90° Multi-Pin Clamp and Rod-to-Rod Clamp (5 mm/3 mm).

The information presented is intended to demonstrate a Stryker product. Always refer to the package insert, product label and/or user instructions before using any Stryker product. Products may not be available in all markets. Product availability is subject to the regulatory or medical practices that govern individual markets. Please contact your Stryker representative if you have questions about the availability of Stryker products in your area.

Products referenced with™ designation are trademarks of Stryker.

Products referenced with® designation are registered trademarks of Stryker.

Literature Number: LH2MSS-F4
GC/GS 5c 05/04

Copyright © 2004 Stryker
Printed in USA

325 Corporate Drive
Mahwah NJ 07430
t: 201-831-5000 t: 800-447-7836

www.stryker.com

Stryker®
Trauma

Hoffmann® II Micro™
Small Bone External Fixation System

Frame 1
Mid-shaft fracture of the proximal phalanx of the index finger (Digit II)

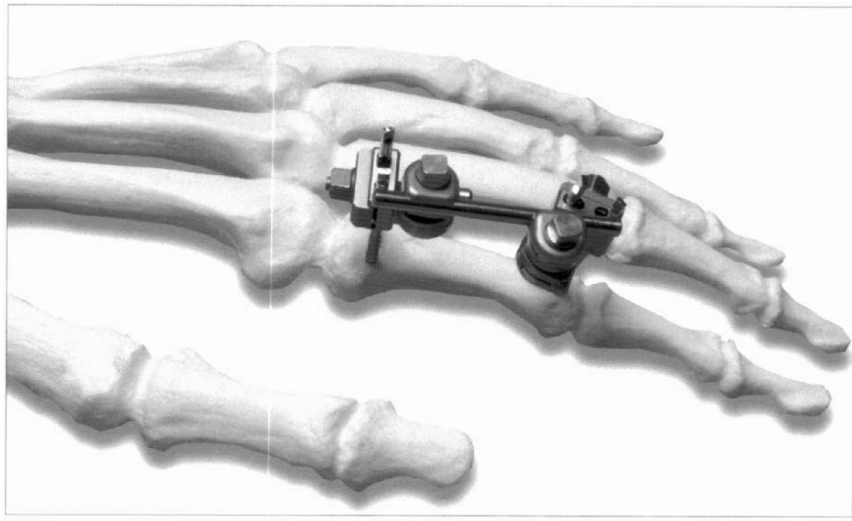

Components

Cat. No.	Description	Quantity
4960-2-020	Multi-Pin Clamps	2
4960-1-010	Rod-to-Rod Couplings 3/3 mm	2
5079-6-Series	Carbon Connecting Rod	
OR		1
5079-5-Series	Stainless Steel Connecting Rod	
5065-3-615	Blunt Half Pins 2 mm (36 mm length)	
OR		4
5065-4-520	Blunt Half Pins 2 mm (45 mm length)	

Hoffmann® II Micro™

Small Bone External Fixation System Features

- **Only Patented Snap-Fit** external fixation clamp system used in fracture fixation of the digits.
- **Modular components** allow for true independent pin placement and virtually unlimited frame configurations.
- **Oblong holes** in multi-pin clamps allow convergent and divergent pin placement within clamps.
- **System cross-over** provides compatibility with the Hoffmann® II Compact™ System and creates a complete external fixation system for treatment of polytrauma patients.
- **New Ø3 mm carbon fiber rods** provide unrestricted fracture visualization.
- **Limited inventory** – only 5 components in system: Rod-to-Rod Clamp (3 mm/3 mm), Pin-to-Rod Clamp, 0° Multi-Pin Clamp, 90° Multi-Pin Clamp and Rod-to-Rod Clamp (5 mm/3 mm).

The information presented is intended to demonstrate a Stryker product. Always refer to the package insert, product label and/or user instructions before using any Stryker product. Products may not be available in all markets. Product availability is subject to the regulatory or medical practices that govern individual markets. Please contact your Stryker representative if you have questions about the availability of Stryker products in your area.

Products referenced with™ designation are trademarks of Stryker.

Products referenced with® designation are registered trademarks of Stryker.

Literature Number: LH2MSS-F1
GC/GS 5c 05/04

Copyright © 2004 Stryker
Printed in USA

325 Corporate Drive
Mahwah NJ 07430
t: 201-831-5000 t: 800-447-7836

www.stryker.com

Hoffmann® II Micro™
Small Bone External Fixation System

Frame 6
Mid-shaft metacarpal fracture (Digit 1)

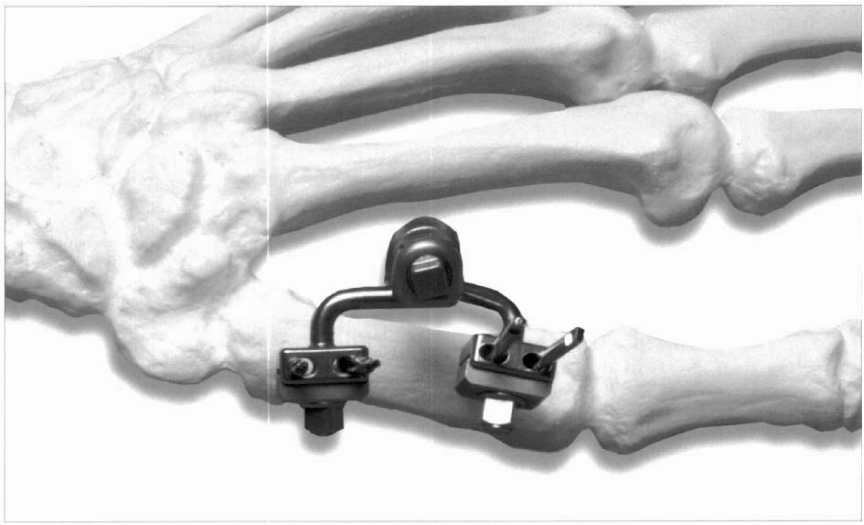

Components

Cat. No.	Description	Quantity
4960-2-030	90° Multi-Pin Clamps	2
4960-1-010	Rod-to-Rod Coupling 3/3 mm	1
5065-3-615	Blunt Half Pins 2 mm (36 mm length)	
OR		4
5065-4-520	Blunt Half Pins 2 mm (45 mm length)	

Hoffmann® II Micro™

Small Bone External Fixation System Features

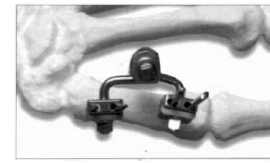

- **Only Patented Snap-Fit** external fixation clamp system used in fracture fixation of the digits.
- **Modular components** allow for true independent pin placement and virtually unlimited frame configurations.
- **Oblong holes** in multi-pin clamps allow convergent and divergent pin placement within clamps.
- **System cross-over** provides compatibility with the Hoffmann® II Compact™ System and creates a complete external fixation system for treatment of polytrauma patients.
- **New** Ø3 mm **carbon fiber rods** provide unrestricted fracture visualization.
- **Limited inventory** – only 5 components in system: Rod-to-Rod Clamp (3 mm/3 mm), Pin-to-Rod Clamp, 0° Multi-Pin Clamp, 90° Multi-Pin Clamp and Rod-to-Rod Clamp (5 mm/3 mm).

The information presented is intended to demonstrate a Stryker product. Always refer to the package insert, product label and/or user instructions before using any Stryker product. Products may not be available in all markets. Product availability is subject to the regulatory or medical practices that govern individual markets. Please contact your Stryker representative if you have questions about the availability of Stryker products in your area.

Products referenced with™ designation are trademarks of Stryker.

Products referenced with® designation are registered trademarks of Stryker.

Literature Number: LH2MSS-F6
GC/GS 5c 05/04

Copyright © 2004 Stryker
Printed in USA

325 Corporate Drive
Mahwah NJ 07430
t: 201-831-5000 t: 800-447-7836

www.stryker.com

X

Polyethylene Products, Usage and Surgical Protocol

For X3™ Polyethylene and Trident® Alumina Ceramic Inserts With PSL® HA and Hemispherical Acetabular Shells.

Trident® PSL® HA Acetabular Shell

Trident® Hemispherical Acetabular Shell

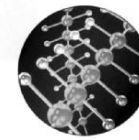

Acknowledgements

Stryker® Orthopaedics thanks the following principal investigators for their clinical expertise in the development of the Stryker® Orthopaedics Ceramic Acetabular System.

Study Co-Chairs:

William N. Capello, MD
Indiana University Medical Center
Indianapolis, IN
James A. D'Antonio, MD
Greater Pittsburgh Orthopaedics Assoc.
Moon Township, PA

Benjamin E. Bierbaum, MD
New England Baptist Hospital
Boston, MA
Clifford W. Colwell, MD
Scripps Clinic
LaJolla, CA
Joseph H. Dimon, III, MD
Peachtree Orthopaedic Clinic
Atlanta, GA
William Hozack, MD
Rothman Institute
Philadelphia, PA
William L. Jaffe, MD
Hospital for Joint Diseases
New York, NY
Ormonde Mahoney, MD
Athens Orthopedic Clinic, PA
Athens, GA
Kenneth E. Marks, MD
Cleveland Clinic Foundation
Cleveland, OH
J. Wesley Mesko, MD
Ingham Medical Center
Lansing, MI
James R. Roberson, MD
Emory Sports Medicine & Spine Center
Decatur, GA
Sean P. Scully, MD, PhD
Duke University
Durham, NC
Scott Siverhus, MD
Flower Hospital
Sylvania, OH
Robert Zann, MD
Orthopaedic Surgery Associates
Boca Raton, FL

Stryker® Orthopaedics extends thanks to the following independent radiographic reviewers for this study:
Daniel J. Berry, MD
Mayo Clinic
Rochester, MN
Peter Bonutti, MD
Bonutti Clinic
Effingham, IL
Special Thanks to:
John Andronaco, MD
for instrumentation evaluation

This publication sets forth detailed recommended procedures for using Stryker® Orthopaedics devices and instruments. It offers guidance that you should heed, but, as with any such technical guide, each surgeon must consider the particular needs of each patient and make appropriate adjustments when and as required.

Trident® Acetabular System Surgical Protocol

Introduction

The Trident® Acetabular System utilizes the Cutting*Edge*™ Total Hip Acetabular Instrumentation. This surgical technique is a guide to preparing the acetabulum for the Trident® Acetabular System Implants utilizing a single set of acetabular instruments.

The Trident® Acetabular System is a two-piece component design that is assembled during surgery. Trident® PSL® HA Acetabular Shells provide a 1.8 mm peripheral press-fit. Reaming is done line-to-line, as the press-fit is built into the sizing (e.g, 52 mm shell = 53.8 mm periphery at the bottom of the shell). Trident® Hemispherical Acetabular Shells are a true hemispherical shape designed to achieve a 1–2 mm press-fit by under-reaming the acetabulum. It is sized true to dimension (e.g, 52 mm shell = 52 mm).

Reference the Trident® Acetabular System Compatibility Table for sizing options (**Table 1**).

The Trident® Acetabular System utilizes the patented Innerchange™ Locking Mechanism. This unique locking mechanism helps provides a secure interface between the ceramic or polyethylene insert and the shell.

Trident® Alumina Ceramic Inserts gain fixation within the shell by means of mating tapers. Rotational stability between the components is achieved when the shell's anti-rotational barbs interlock with the insert scallops. **The Trident® Alumina Ceramic Inserts must be used with Stryker® Orthopaedics Alumina Heads.**

The Trident® Polyethylene Inserts lock into the shell by means of a circumferential ring that engages the shell's mating groove. Rotational stability is achieved when the shell's anti-rotational barbs interlock with the insert scallops.

Table 1. Compatibility Table

	Trident® PSL® HA Acetabular Shell			Trident® Hemispherical Acetabular Shell			
Alpha Code	Trident® PSL® HA Shell Size	Trident® Hemispherical Shell Size	X3™ 0°, 10° Inserts (mm)	X3™ Eccentric 0°, 10° Inserts (mm)	Trident® Alumina 0° Inserts I.D. (mm)	X3™ Elevated Rim Inserts (mm)	Constrained Inserts (mm)
A	40	42	22	–	–	–	–
B	42	44	22	28*	–	–	–
C	44	46	22, 26, 28	28	–	28	–
D	46, 48	48, 50	22, 26, 28, 32	28, 32	28	28	–
E	50, 52	52, 54	22, 26, 28, 32, 36	28, 32	32	28, 32, 36	22
F	54, 56	56, 58	22, 26, 28, 32, 36	28, 32	32	28, 32, 36	22
G	58, 60	60, 62	22, 26, 28, 32, 36	28, 32	36	28, 32, 36	28
H	62, 64	64, 66	22, 26, 28, 32, 36	28, 32	36	28, 32, 36	28
I	66, 68	68, 70	22, 26, 28, 32, 36	28, 32	36	28, 32, 36	28
J	70, 72	72, 74	22, 26, 28, 32, 36	28, 32	–	28, 32, 36	28

* Available in 0° only.

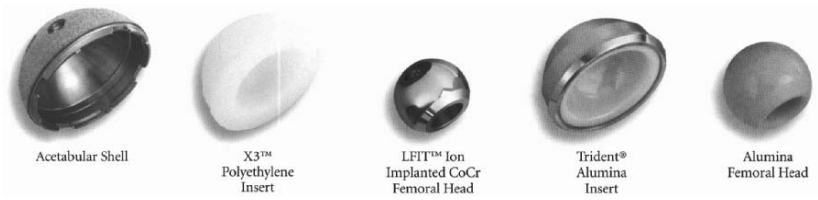

Step 1: Preoperative Planning and X-ray Evaluation

Preoperative planning and X-ray evaluation aids in the selection of the most favorable implant style and optimal size for the patient's hip pathology. Selecting potential implant styles and sizes can facilitate operating room preparation and assure availability of an appropriate size selection. X-ray evaluation may also help detect anatomic anomalies that could prevent the intraoperative achievement of the established preoperative goals.

Step 2: Acetabular Preparation

The acetabulum is prepared by the release and removal of soft tissue using the surgeon's preferred technique to gain adequate exposure for reaming. Excision of the labrum and osteophytes allows for proper visualization of the bony anatomy, and improves ease of reaming.

Stryker® Orthopaedics' Femoral and Wing Retractors can be utilized to gain acetabular exposure (**Figure 1**).

With the acetabulum exposed, bony defects, can be identified. If necessary, bone grafting options may be considered prior to reaming.

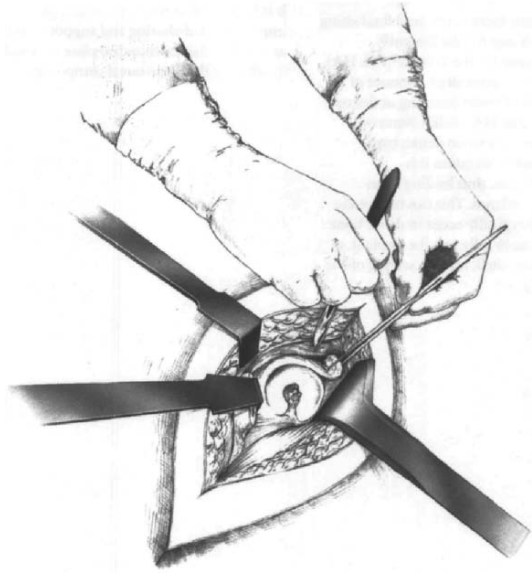

Trident® Acetabular System Surgical Protocol

Step 3: Spherical Reaming

To obtain congruity in the reaming process, an optional 45/20° Abduction/Anteversion Alignment Guide can be attached to the Cutting*Edge*™ Reamer Handle (**Figure 2**). The alignment guide, when perpendicular to the long axis of the patient, will orient the reamer handle at 45° of abduction, thereby placing the axis of the spherical reamer at 45° of inclination (**Figure 3**). The reamer handle may be positioned at 20° of anteversion by aligning the left/right anteversion rod on the alignment guide so that it is parallel to the long axis of the patient.

It is recommended that the initial reaming begin with a Cutting*Edge*™ Spherical Reamer that is 4 mm smaller than the templated or gauged size. The reamer is attached to the reamer handle by pushing down and applying a quarter-turn to lock in place. Reaming progresses in 1 mm increments until final sizing is achieved (1–2 mm under size of cup for the Trident® Hemispherical; line-to-line reaming for the Trident® PSL HA). Surgical judgement is used to assess bone stock, amount of interference, and proper amount of underreaming as desired. When implanting the Trident® PSL HA shell, 1.8 mm of interference fit is not always necessary when dense, hard, sclerotic bone is encountered. In this situation it is recommended to over-ream by 1 mm, thus leading to an interference fit of slightly less than 1 mm. This can reduce the potential for problems that may typically occur in dense bone such as acetabular fracture, failure to fully seat the implant, or slight deformation of the titanium shell, making seating of the insert more difficult.

The low profile of the Cutting*Edge*™ Spherical Reamer necessitates reaming to the full depth. The reamer head should be driven to the point where the rim/cross bar contacts the acetabular wall at the peripheral lunate region. Removal of the reamer from the handle is performed by pulling back on the locking sleeve and rotating the reamer head a quarter-turn in a clockwise direction (**Figure 4**).

Care should be taken so as not to enlarge or distort the acetabulum by eccentric reaming. Final acetabular reaming ideally shows the hemispherical acetabulum denuded of cartilage, with the subchondral plate preferably intact, and the anterior acetabular wall preserved.

It is believed that the subchondral plate functions as an important load-sharing and support mechanism. Preserving as much of the subchondral plate as possible may improve the qualities of the bone/metal composite.

Trident® PSL® HA | **Trident® Hemispherical**

Trident® PSL® HA – Note: Trident® PSL® Acetabular Shells contain a 1.8 mm peripheral press-fit built into the shell as marked (e.g. 52 mm = 53.8 mm).

Trident® Hemispherical – Note: Trident® Hemispherical Shells are sized true to dimension indicated (e.g. 52 mm = 52 mm).

Note: The Cutting*Edge*™ Spherical Reamers are very aggressive and perform best when sharp. Care should be taken to protect the reamer from unnecessary handling, as dull or damaged cutting teeth may cause improper reaming. Dull cutting teeth will deflect to cut softer bone and resist hard bone. This situation may result in an irregularly shaped or enlarged acetabulum preparation.

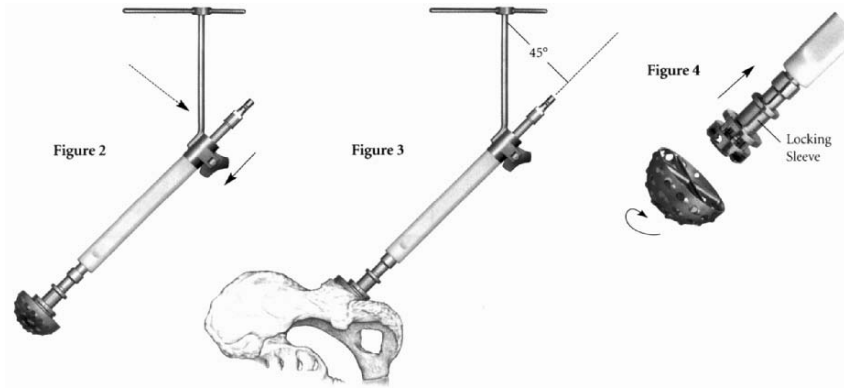

Trident® PSL® HA

"1.8 mm of interference fit is not always necessary when dense hard bone is encountered. Over reaming by 1 mm will lead to an interference of slightly less then 1 mm, while still achieving a secure fit."

James A. D'Antonio, M.D.

Trident® Acetabular System Surgical Protocol

Step 4: Trial Evaluation

Following the reaming procedure, the appropriate Trident® Universal Window Trial (**Table 2**), of the same diameter as the last spherical reamer used, is threaded onto the Cutting*Edge*™ Shell Positioner/Impactor and placed in the acetabulum to evaluate the size and congruity of the preparation (**Figure 5**). Use the trial that has the same diameter as that of the last spherical reamer used. The trial is "windowed" for visualization and assessment of fit, contact and congruency of the trial within the acetabulum. By inserting the Trident® Trial Insert into the Universal Window Trial (**Figures 6** & **7**), joint mechanics can be evaluated. To ensure that the Trial Insert is well fixed to the Universal Window Trial during the trial evaluation, an Acetabular Trial Insert Containment Screw can be used. The Containment Screw Kit (2230–0010) is optional (**Figure 6**).

Table 2. Trident® Universal Window Trial/Trial Insert Sizing

Trial Insert Compatibility Class	Reamer Size (mm)	Trident® Universal Window Trial (mm)
A	40	40
B	42	42
C	44	44
D	46	46
D	48	48
E	50	50
E	52	52
F	54	54
F	56	56
G	58	58
G	60	60
H	62	62
H	64	64
I	66	66
I	68	68
J	70	70
J	72	72

To facilitate insertion/removal of the Trial Insert, Holding Forceps may be placed into the two holes in the plastic face.

Figure 5

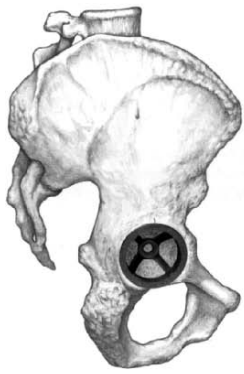

Figure 6

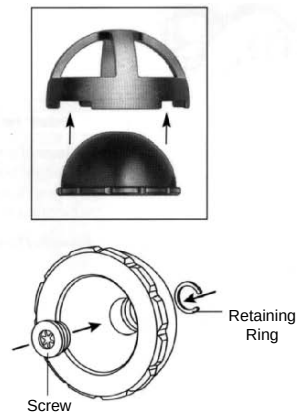

Figure 7

Step 5: Trident® PSL® HA Acetabular and Hemispherical Shell Implantation

After completing the trial reduction, select the appropriately sized implant component.

If desired, the Cutting*Edge*™ Abduction/Anteversion Alignment Guide can be attached to the Cutting*Edge*™ Shell Positioner/Impactor to help establish the recommended 45° of abduction inclination and 20° of anteversion (**Figures 8** & **9**).

Caution: Proper pelvic orientation is critical if relying upon the CuttingEdge™ Alignment Guide to achieve the desired abduction/anteversion angles for shell positioning.

The metal shell is threaded onto the impactor at the threaded hole in the dome of the metal shell. It is important to fully engage the threads and seat the impactor against the shell. Otherwise, the threads on the metal shell could become damaged, resulting in difficulty with the removal of the impactor from the shell.

If the cluster screw hole pattern shell is utilized, the holes are intended to be oriented superiorly (**Figure 10**).

Note: Shell positioning must be carefully considered when selecting a ceramic insert as no hooded option is available to adjust joint stability. Proper positioning of the Trident® Acetabular Shell will minimize potential impingement and provide optimal stability and articulation between the Alumina insert and Head. Excessive vertical orientation of the Shell should be avoided as this may lead to premature wear of the ceramic material.

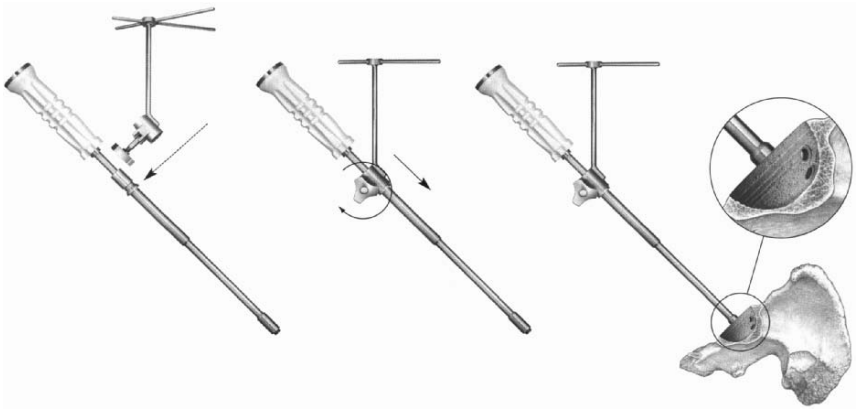

Trident® Acetabular System Surgical Protocol

Step 5: Trident® PSL® HA Acetabular and Hemispherical Shell Implantation (cont.)

The recommended metal shell abduction angle of 45° is determined by positioning the alignment guide perpendicular to the long axis of the patient (**Figure 11**).

Metal shell anteversion is set at approximately 20° by moving the cup impactor so that the left/right anteversion rod is parallel to the long axis of the patient (**Figure 12**).

The metal shell is impacted into the acetabulum using a mallet until a tight, stable press-fit is achieved. The thumbscrew on the alignment guide is then loosened to remove the guide. After removing the guide, the impactor handle is carefully unthreaded from the shell.

The depth of the shell seating may now be determined by viewing through the threaded hole in the dome. If it is determined that the shell is not fully seated, the Cutting*Edge*™ Final Cup Impactor may then be required to assist in impacting the shell until it is completely seated in the prepared acetabulum.

"While the alignment guides are of some assistance, it is important to critically evaluate anatomic landmarks before placement of the acetabular component. These anatomic landmarks include the anterior and posterior walls of the acetabulum, the sciatic notch, the floor and/or acetabular fossa of the acetabulum."
James A. D'Antonio, M.D.

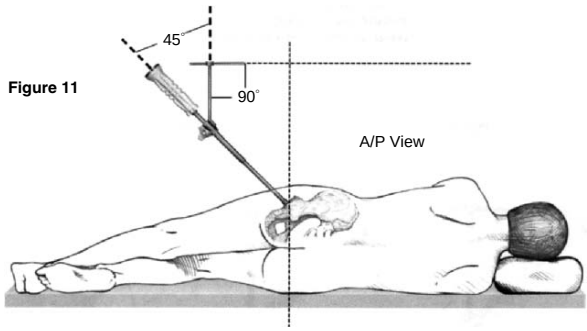

Figure 11

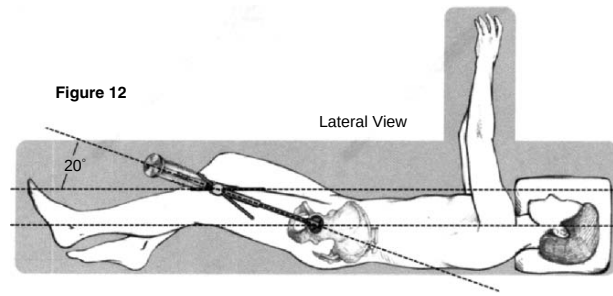

Figure 12

Step 5A: Optional Screw Utilization

If the option to use screws is selected, then only Stryker® Orthopaedics Torx® Bone Screws can be used. Stryker® Orthopaedics offers 6.5 mm diameter cancellous bone screws for use in the shell dome, which are available in a variety of lengths (**Table 3**). Stryker® Orthopaedics Cancellous Bone Screws are designed to be inserted or removed only with the assistance of Stryker® Orthopaedics screw instruments.

After determination of the proper site for screw placement, a 3.3 mm diameter drill is passed through a drill guide to the desired depth (**Figure 13**). The screw hole is then sounded to determine the hole's depth. The properly sized screw is then selected and implanted into the bone using Stryker® Orthopaedics Screw Drivers with a high torque configuration driver head (**Figure 14**).

Note: In hard bone, the use of 6.5 mm dome screws prepared in the usual fashion may be difficult. The use of a 4.0 mm drill bit can make the utilization easier, without substantial compromise of screw purchase.

Caution: Do not pass a drill, screw or any other instrumentation beyond the inner table of the pelvis. Malposition of either the shell screw hole orientation, screw hole preparation or improper use of the screws themselves may contribute to detrimental clinical consequences.

Step 6: Trial Insert Reduction

After metal shell implantation, the Trident® Trial Insert will provide a final check of hip mechanics.

TABLE 3: Stryker® Orthopaedics Cancellous 6.5 mm Bone Screws

Screw Lengths (mm)	Catalog Number
16	2030-6516-1
20	2030-6520-1
25	2030-6525-1
30	2030-6530-1
35	2030-6535-1
40	2030-6540-1
45	2030-6545-1
50	2030-6550-1
55	2030-6555-1
60	2030-6560-1

Figure 13

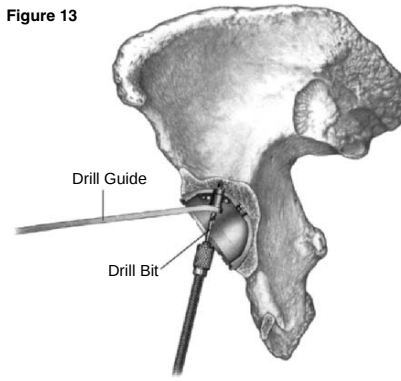

Figure 14

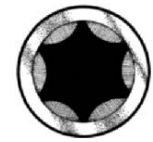

Top view of a high torque configuration driver head

Trident® Acetabular System Surgical Protocol

Step 7: Insert Implantation

1. Select the appropriate size Silicone Insert Positioner Tip.
2. Load Silicone Insert Positioner Tip to Insert Positioner/Impactor Handle (**Figure 15**).
3. Load either the polyethylene or ceramic insert to Insert Positioner Tip. Press firmly to ensure insert is being securely held (**Figure 16**).

Note: Use caution handling ceramic components during assembly because of brittle nature of the ceramic material. Ceramic components are presterilized and cannot be sterilized after opening.

4. Ensure that the inside of the shell is clean and free of soft tissue or any other debris, which could prevent the insert from properly sitting in the shell.

Figure 15

Figure 16

Step 7: Insert Implantation (cont.)

5. Gently introduce the ceramic or polyethylene insert making sure that the insert flange scallops are aligned with the slot at the rim of the shell (this allows seating the insert at the initial position supported by four indexing barbs). Once the insert is seated at the initial position, slowly turn and drop the insert into the final pre-locking position (**Figure 17**).

Note: Having a clear view of the rim of the acetabulum will allow easier visualization of the shell's slot and indexing barbs for proper positioning of the insert.

6. Remove Silicone Insert Positioner Tip from the Insert Positioner/Impactor Handle.
7. Select appropriate size Plastic Insert Impactor Tip.
8. Load Plastic Insert Impactor Tip to Insert Positioner/Impactor Handle.
9. Position Insert Positioner/Impactor Handle into ID of insert. Take care to align handle with axis of shell. Strike handle with approximately four firm mallet blows to fully seat insert.

Note: In order to obtain a secure lock it is recommended to use only the hard plastic Insert Impactor Tips to impact the ceramic and polyethylene inserts.

10. Verify insert is fully seated and properly aligned into the acetabular shell. Check the taper lock by running a small osteotome around the periphery of the shell/insert interface.

As with any modular interface under load, there is a potential for micromotion and associated fretting and/or corrosion. However, the Trident® design minimizes the amount of motion at the taper interface and should reduce the corrosion potential.

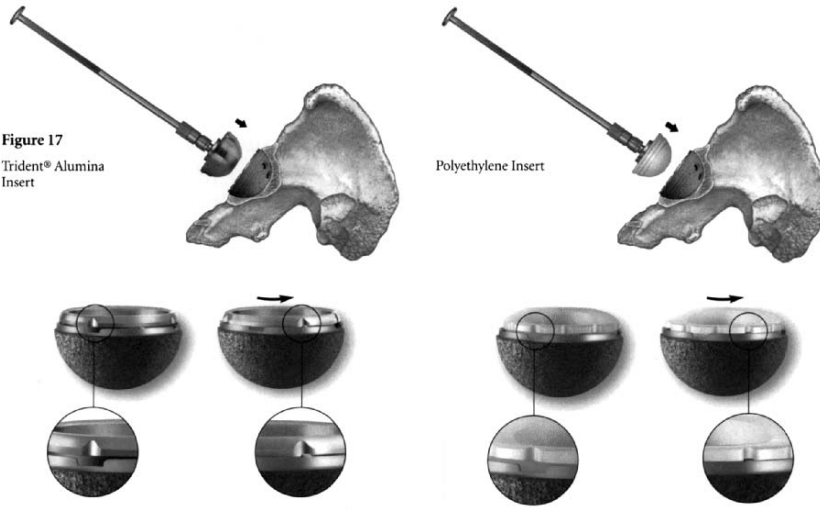

Figure 17
Trident® Alumina Insert

Trident® Acetabular System Surgical Protocol

Removal of the Cup Insert and Shell

Ceramic Insert Removal

The Trident® Alumina Insert Removal Tool is designed to provide the surgeon with two options for extracting the ceramic insert from the Trident® shell.

Option 1: "Flat Head"

Connect the "T" handle to the L-shaped end of the removal tool. Insert the flat end of the removal tool between the shell and ceramic insert at one of the four notches at the shell rim. While applying continuous force toward the center of the shell, twist the "T" handle (like a screwdriver), to dislodge the ceramic insert (**Figure 18**). It may be required to repeat this procedure at the other notches in order to successfully disengage the taper.

Figure 18

Option 2: "L-Shaped"

Insert the L-shaped end of the removal tool between the shell and ceramic insert at one of the four notches at the shell rim. Apply continuous force toward the center of the shell, and lever the tool in a plane tangent to the shell's outside edge, to dislodge the ceramic insert (**Figure 19**). It may be required to repeat this procedure at the other notches in order to successfully disengage the taper.

Figure 19

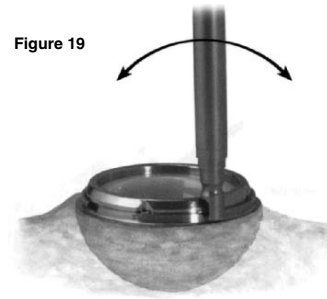

The removal tool may be attached to the Insert Positioner/Impactor Handle to increase leverage and length for larger patients.

Removal of the Cup Insert and Shell (cont.)

Polyethylene Insert Removal

Utilize a 3/16″ (5 mm) drill bit to create an off-center hole in the polyethylene insert. Use the "T" handle to thread the Polyethylene Insert Removal Tool into the insert, and advance the tool to the medial wall of the shell to dislodge the insert (**Figures 20** & **21**).

Figure 20

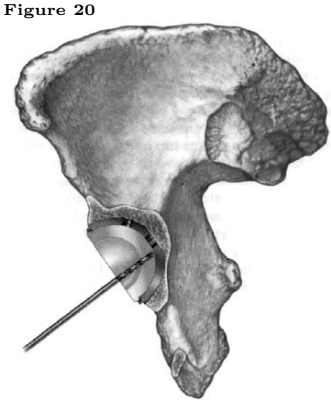

Revising the Trident® Acetabular Shell with a Trident® Polyethylene Insert

Should it become necessary to remove the ceramic insert, a Trident® Polyethylene Insert can be inserted into the Trident® Acetabular Shell.

1. Carefully remove the Trident® Alumina insert
2. The Trident® Insert Trials are used to evaluate the shell face position and provide a final check of hip biomechanics. The polyethylene inserts provide 12 different insert orientations within the shell to provide optimal joint stability.
3. Follow **Step 7: Implantation Technique**, to insert the polyethylene insert.

Figure 21

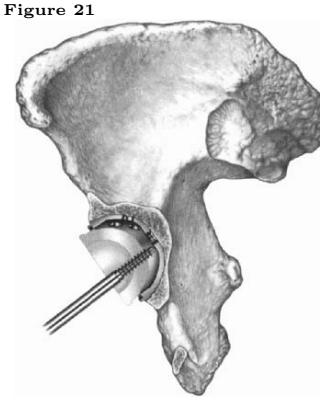

Shell

Should removal of the metal shell ever become necessary, an osteotome or small burr can be passed around the cup periphery to loosen the fixation interface. The Cutting*Edge*™ Universal Shell Positioner can be threaded into the dome hole of the cup. A Slotted Mallet is slid over the positioner shaft to assist with the shell removal.

Trident® Acetabular System Surgical Protocol

Head Disassembly

The Head Disassembly Instrument is used to remove an impacted head. Inspect the stem neck taper to verify that no damage has occurred prior to impacting a replacement head. A replacement head may then be attached to the stem neck taper and secured using the Stem Head Impactor.

Note: Revision of Ceramic Components – If the ceramic head needs to be revised for any reason, a new ceramic head must not be affixed to the existing stem taper because the taper will have been deformed through assembly with the first ceramic head component. If the surgeon wishes to revise with a ceramic head, the entire hip stem must be replaced as well. If the surgeon wishes to revise with a metal head, either the ceramic insert must be replaced with an Stryker® Orthopaedics Trident® Polyethylene Insert or the entire acetabular component must be replaced with a metal/polyethylene alternative. However, in the case of revision to a metal head, if the original stem and its trunnion appear intact, the original hip stem need not be replaced.

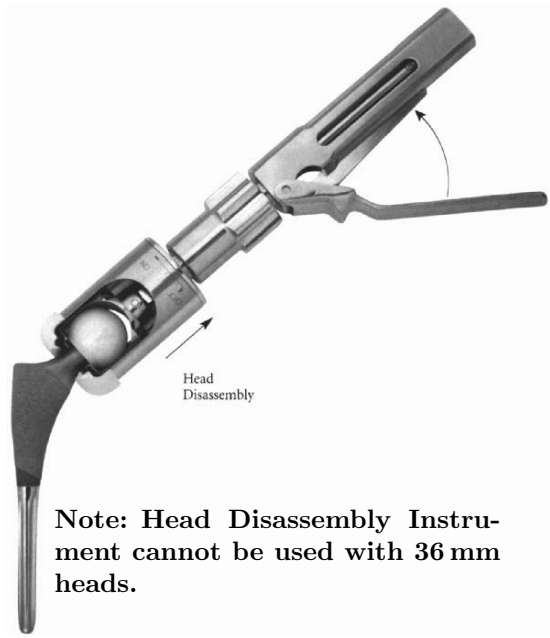

Note: Head Disassembly Instrument cannot be used with 36 mm heads.

Trident® PSL® HA | Trident® Hemispherical

Instrument Information

Trident® Insert Trials

●=0° (2200-XXX) and 10° (2210-XXX)
o= Elevated Rim (2260-XXX)

Alpha Code	22mm	26mm	28mm	32mm	36mm
A	●				
B	●				
C	●	●	●o		
D	●	●	●o	●	
E	●	●	●o	●o	●o
F	●	●	●o	●o	●o
G	●	●	●o	●o	●o
H	●	●	●o	●o	●o
I	●	●	●o	●o	●o
J	●	●	●o	●o	●o

Trident® Eccentric Trials

Alpha Code	0° (2240-XXX) 28mm	0° (2240-XXX) 32mm	10° (2250-XXX) 28mm	10° (2250-XXX) 32mm
B	●*			
C	●			
D	●		●	
E	●		●	
F	●		●	
G	●		●	
H	●		●	
I	●		●	
J	●		●	

*Note: 10° B Trial N/A

C-Taper Femoral Head Trials

1204-62200	22mm +0mm
1204-62225	22mm +2.5mm
1204-62205	22mm +5mm
1204-62210	22mm +10mm
1204-62600	26mm +0mm
1204-62625	26mm +2.5mm
1204-62605	26mm +5mm
1204-62675	26mm +7.5mm
1204-62610	26mm +10mm
1204-62897	28mm -2.5mm
1204-62800	28mm +0mm
1204-62805	28mm +5mm
1204-62875	28mm +7.5mm
1204-62810	28mm +10mm
1204-63297	32mm -2.5mm
1204-63200	32mm +0mm
1204-63205	32mm +5mm
1204-63275	32mm +7.5mm
1204-63210	32mm +10mm
1204-63699	36mm -5mm
1204-63600	36mm +0mm
1204-63605	36mm +5mm
1204-63610	36mm +10mm

V40™ Femoral Head Trials

6264-8-122	22mm +0mm
6264-8-222	22mm +3mm
6264-8-322	22mm +8mm
6264-8-026	26mm -3mm
6264-8-126	26mm +0mm
6264-8-226	26mm +4mm
6264-8-326	26mm +8mm
6264-8-426	26mm +12mm
6264-8-526	26mm +16mm
6264-8-328	28mm +8mm
6264-8-428	28mm +12mm
6264-8-528	28mm +16mm
6264-8-332	32mm +8mm
6264-8-432	32mm +12mm
6264-8-532	32mm +16mm
6264-8-036	36mm -5mm
6264-8-136	36mm +0mm
6264-8-236	36mm +5mm
6264-8-336	36mm +10mm

Trident® Universal Window Trials

2208-2040	40mm
2208-2042	42mm
2208-2044	44mm
2208-2046	46mm
2208-2048	48mm
2208-2050	50mm
2208-2052	52mm
2208-2054	54mm
2208-2056	56mm
2208-2058	58mm
2208-2060	60mm
2208-2062	62mm
2208-2064	64mm
2208-2066	66mm
2208-2068	68mm
2208-2070	70mm
2208-2072	72mm
2208-2074	74mm

2101-0200
Cutting*Edge*™
Shell Positioner/Impactor Handle

2101-0210
Cutting*Edge*™
Abduction/Anteversion Alignment Guide

2111-0000B
Insert Positioner/Impactor Handle

Silicone Insert Positioner Tips

2111-0022	22mm
2111-0026	26mm
2111-0028	28mm
2111-0032	32mm
2111-0036	36mm

Plastic Insert Impactor Tips

2111-3022	22mm
2111-3026	26mm
2111-3028	28mm
2111-3032	32mm
2111-3036	36mm

1118-6000
Head Disassembly Instrument

1118-1005
Ceramic Head Sleeve Disassembly Adapter

1101-2100
T-Handle

2102-0003
Hudson to Stryker® Adapter

2102-0410
Acetabular Reamer Handle

2112-0000
Ceramic Removal Tool

2112-0010
Polyethylene Removal Tool

Trident® Acetabular System Surgical Protocol

Instrument Information

2402-0020
Case (not including lid and trays)

2402-0090
Lid

2402-0040
Top Tray: Insert Trials (0° & 10°)

2402-0060
Middle Tray: Universal Window Trials

2402-0080
Bottom Tray: Preparation Tray

Stryker® Orthopaedics Bone Screw Instrumentation Kit
Hip-Bone Screw

Templates:

LTEM59B 1-2 Trident® PSL®

LTEM60B 1-2 Trident® Hemispherical

2230-0010
Acetabular Trial Insert Containment Screw - Kit

Contains 5 screws and retaining rings. (Containment Screw Kit is optional - screws come pre-assembled with the Eccentric and Constrained trial inserts.)

Eccentric/Constrained Cases and Trays (for trials only)

The system provides the option of either a Single Tier or Double Tier case. The Double Tier Case accommodates both the Constrained Insert Trial Tray and the Eccentric Trial Tray.

8000-0200
Double Tier Case

8000-0100
Single Tier Case

2402-1100
Trident® Constrained Insert Trial Tray

CuttingEdge™ Acetabular Reamers

2102-0438	38mm
2102-0439	39mm
2102-0440	40mm
2102-0441	41mm
2102-0442	42mm
2102-0443	43mm
2102-0444	44mm
2102-0445	45mm
2102-0446	46mm
2102-0447	47mm
2102-0448	48mm
2102-0449	49mm
2102-0450	50mm
2102-0451	51mm
2102-0452	52mm
2102-0453	53mm
2102-0454	54mm
2102-0455	55mm
2102-0456	56mm
2102-0457	57mm
2102-0458	58mm
2102-0459	59mm
2102-0460	60mm
2102-0461	61mm
2102-0462	62mm
2102-0463	63mm
2102-0464	64mm
2102-0465	65mm
2102-0466	66mm
2102-0467	67mm
2102-0468	68mm
2102-0469	69mm
2102-0470	70mm
2102-0471	71mm
2102-0472	72mm

Innerchange™ Locking Mechanism

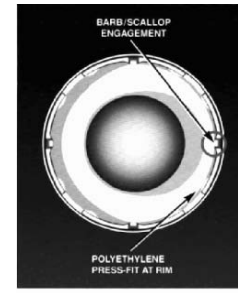

The Innerchange™ Locking Mechanism allows for independent locking of polyethylene and ceramic inserts into the shell. This provides superior locking of both inserts without compromise.

The Trident® polyethylene insert allows for proper rotational alignment using 12 indexable scallops. Polyethylene inserts lock into the shell in three ways:

- Four alignment studs on the shell provide proper rotational and axial alignment
- Unique bead and groove mechanism
- Additional rim locking provides for exceptional insert stability

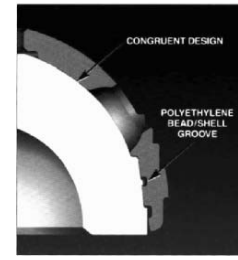

Extensively Tested Locking Mechanism

- Fully congruent design
- Independent testing by Alan Litsky, MD, PhD at Ohio State University[1]
- Robust push-out and lever-out resistance[2]
- Hip simulation testing with Crossfire® polyethylene has demonstrated improved wear performance[3]

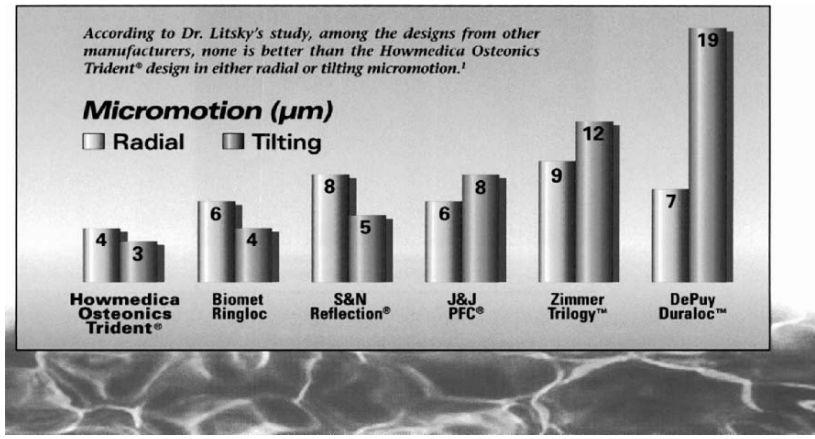

Polyethylene

Polyethylene

Trident® polyethylene inserts are:

- Fully congruent to the shell
- Supported by extensive research on range of motion and head stability[10]
- Available in neutral, hooded and eccentric designs

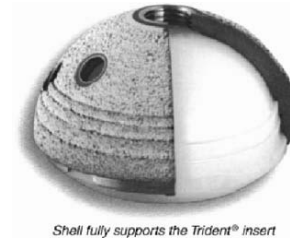

Shell fully supports the Trident® insert

Polyethylene Thickness

Polyethylene thickness plays an important role in the wear performance.[4] Size for size, the Trident® polyethylene inserts are the thickest in the industry.

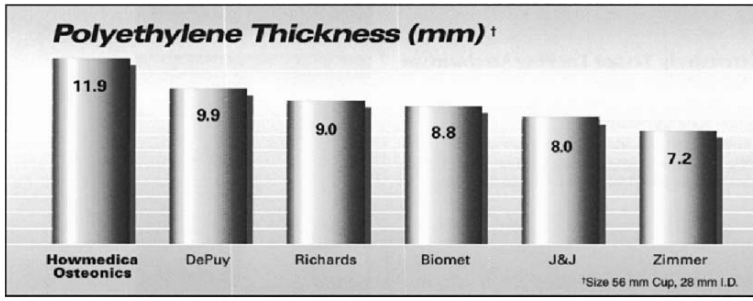

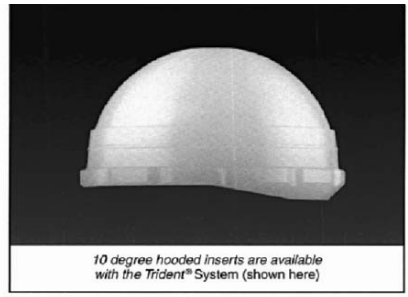

10 degree hooded inserts are available with the Trident® System (shown here)

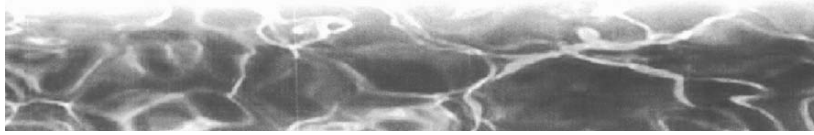

Crossfire® Highly Crosslinked Polyethylene

Crossfire® Highly Crosslinked polyethylene has demonstrated significant wear reduction compared to standard polyethylene. Howmedica Osteonics' technology and conservative process have allowed increased crosslinking while maintaining the material properties of the polyethylene.

- ***90% reduction in wear***[5]
  Crossfire® polyethylene demonstrates 90% reduction in wear over nitrogen sterilized polyethylene in joint simulation testing, thereby reducing the potential for osteolysis.
- ***Material properties are retained***
  The material properties of Crossfire® polyethylene are similar to those of standard polyethylene, as shown in **Figure 1**.
- ***Preserves the polymer structure of UHMWPE***
  The crystalline and amorphous regions of Crossfire® are similar to standard polyethylene which suggests predictable clinical performance[6] (**Figure 2**).
- ***N_2/Vac^{TM} packaging provides resistance to oxidation***
  Packaging polyethylene in an oxygen-free environment improves material toughness and strength on shelf-stored polyethylene up to 10 years.[7]
- ***Same particle size and shape as standard polyethylene***
  The biological response to Crossfire® particles is not expected to be different from standard polyethylene.

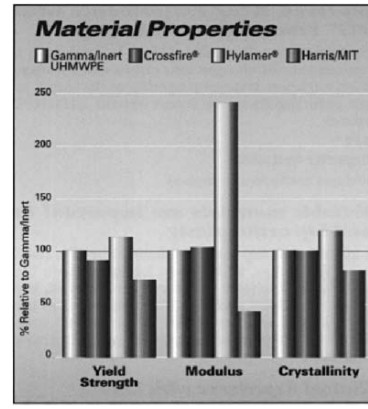

Figure 1 Crossfire® polyethylene maintains similar yield strength, modulus and crystallinity as standard polyethylene. When these properties change significantly, the clinical wear performance cannot be predicted.

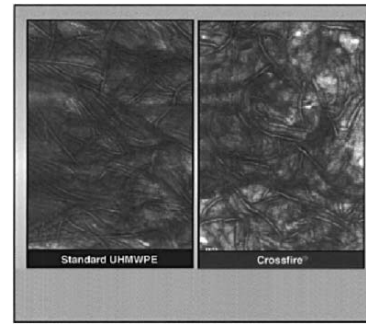

Figure 2 Crossfire® exhibits a morphology that is very similar to that of standard UHMWPE

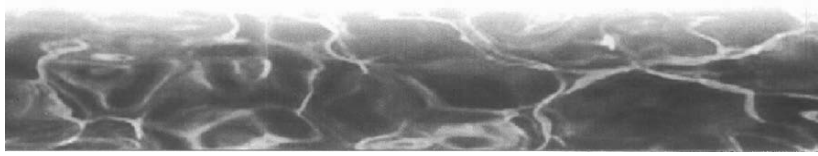

LFIT™ Technology

Improved Wear Performance with LFIT™ Femoral Head Technology

Low Friction Ion Treatment (LFIT™) technology is a bombardment of nitrogen ions onto a CoCr surface, which enhances material properties of the metal, in turn reducing frictional forces against UHMWPE surfaces.

LFIT™:

- Improves wettability
- Reduces coefficient of friction

Wettable materials are important in total hip arthroplasty

In an anatomic hip joint, the femoral head is cushioned by cartilage, which seeps lubrication into the joint. When the joint is diseased or removed, the natural lubrication surface is also removed, and the femoral head and acetabular insert contact each other. LFIT™ femoral heads are designed to increase lubrication.

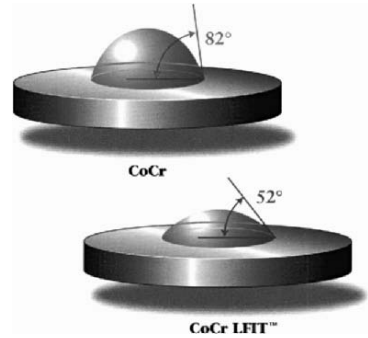

Wettable materials have a lower boundary angle between a liquid and a solid.

Clinical Experience with LFIT™

The LFIT™ heads demonstrated a 28% reduction in linear wear over CoCr heads in 110 patients at minimum 3-year follow up[9] (**Figure 3**). This data coincides with hip simulation testing.[8]

"These results are encouraging... Nitrogen ion implanted femoral heads may be an effective way to decrease UHMWPE wear and increase implant longevity in THA."[9]

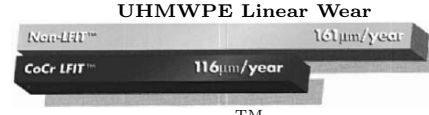

Figure 3 LFIT™ heads demonstrated a 28% reduction in linear wear over CoCr heads

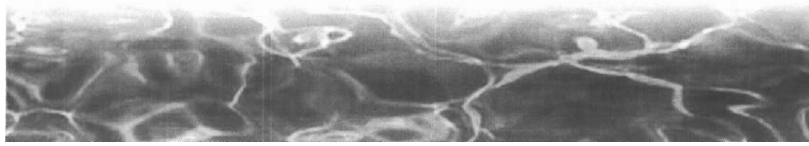

Revision Options

- A Trident® Hemispherical Multi-Hole Acetabular Shell with Purefix™ HA is available providing increased screw hole options (**Figure 4**).
- Eccentric and Constrained Inserts augment the Trident® System with revision options to increase surgeon flexibility in complex primary or revision surgery.
- The Trident® Eccentric Inserts feature Crossfire® Highly Crosslinked Polyethylene for improved wear performance.[5] The head center is lateralized 6 mm from the center of the acetabular shell allowing increased polyethylene thickness and joint stability (**Figure 5**).
- Trident® Constrained Inserts are available for total hip patients who exhibit a high risk of hip dislocation. Constrained Inserts feature Howmedica Osteonics uniquely designed pre-assembled inserts with the UHR® bipolar (**Figure 6**).

Figure 4. Trident® Hemispherical Multi-Hole Acetabular Shell

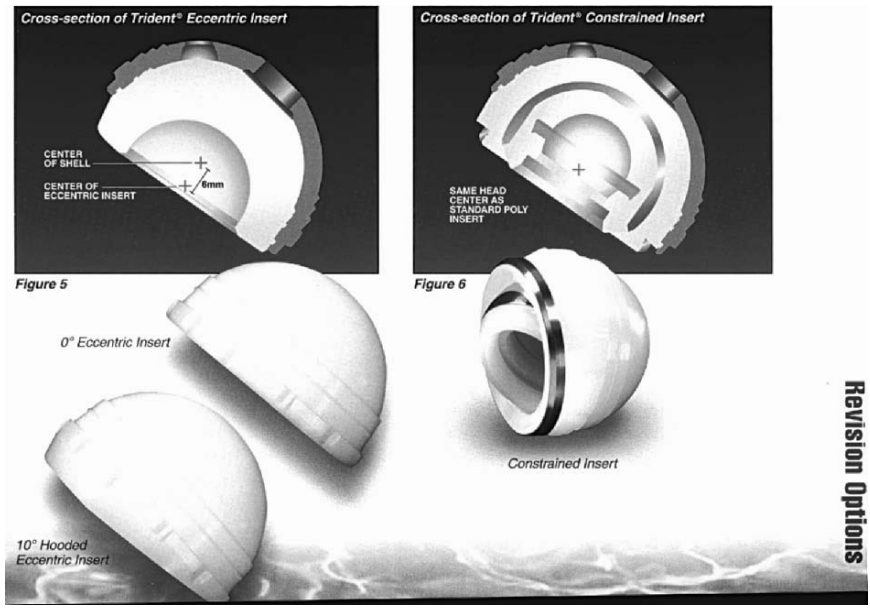

Compatibility

Trident® polyethylene inserts may be used with V40™ or C-taper femoral heads.
The alphabetical letter at the end of all Trident® catalog numbers identifies compatibility among all Trident® acetabular components. Matching the shell and insert Alpha Codes will ensure proper compatibility.

Trident® Compatibility Chart

Alpha Code	Trident® PSL® HA Shell Size (mm)	Trident® Hemispherical Shell Size (mm)	Crossfire® 0° and 10° Inserts (mm)	N_2/Vac™ 0° and 10° Inserts (mm)
A	40	42	22	N/A
B	42	44	22	N/A
C	44	46	22, 26	N/A
D	46, 48	48, 50	22, 26, 28	28
E	50, 52	52, 54	22, 26, 28, 32	28
F	54, 56	56, 58	22, 26, 28, 32	28
G	58, 60	60, 62	22, 26, 28, 32	28
H	62, 64	64, 66	22, 26, 28, 32	28
I	66, 68	68, 70	22, 26, 28, 32	28
J	70, 72	72, 74	22, 26, 28, 32	28

N/A=not available

References

1 Litsky, AS, et al, "Micromotion Between the cup and the Liner in Modular Acetabular Prostheses," 1999 Society for Biomaterials, 25th Annual Meeting Transactions.
2 Data on file at Howmedica Osteonics.
3 Schmidig G, et al, "Trident® Polyethylene Acetabular Insert Performance Characteristics", Howmedica Osteonics Literature #LTAP/TM.
4 Jasty, M, et al, "Wear of Polyethylene Acetabular Components in Total Hip Arthroplasty," JBJS, 70A, March 1997.
5 Taylor, S, "Advances in Polyethylene: Crossfire®," Howmedica Osteonics Literature #LSA23.
6 Dumbleton, JH, Edidin, AA, "A Highly Crosslinked Oxidation-Resistant Polyethylene: Crossfire®," Howmedica Osteonics Literature #LSA29.
7 Edidin, AA, et al, "Gamma Sterilization in Nitrogen Prevents Degradation for More Than 10 Years," Trans. ORS, p. 1, 2000.
8 Taylor, S, "Reduction in Polyethylene Wear through Ion-Implantation into CoCr Alloy," Surface Modification Technologies VI, The Minerals, Metals & Materials Society, 1993.
9 Maruyama, M, et al, "Effect of Low Friction Ion Treated Femoral Heads on Polyethylene Wear Rates," CORR, Number 370, pp. 183–191.
10 Dong, et al, "Hip Joint Stability Determined by Acetabular Bearing Insert Design, An in-vitro Simulated Study," ORS, 1999.

Stryker® is a registered trademark of Stryker Corporation.
Crossfire®, PSL®, Trident® and UHR® are registered trademarks of Howmedica Osteonics Corp.
Innerchange™, LFIT™, N_2/Vac™, Purefix™, and V40™ are trademarks of Howmedica Osteonics Corp.
Hylamer®, PFC®, and Reflection® are not registered trademarks of Stryker Corporation. Duraloc™ and Trilogy™ are not trademarks of Stryker Corporation.
U.S. Patent No.: 4,798,610 Patent Pending for Innerchange™.

stryker Howmedica OSTEONICS

359 Veterans Boulevard
Rutherford, NJ 07070

59 Route 17 South
Allendale, NJ 07401

Strength Matters

X3™ Polyethylene is the first highly crosslinked polyethylene without trade-offs.

- Maintains Structural Fatigue Strength[5,6]
- Greater Wear Reduction than first generation highly crosslinked polyethylene[7]
- Oxidation Resistance[8,9]

Remelting following irradiation of polyethylene significantly alters the crystallinity and crystalline morphology, with up to a 35% drop in ultimate tensile strength and 15% drop in yield stress (Figure 1)[10].

In contrast, annealing following irradiation has been shown to maintain those morphologies leading to preserved structural strength (Figure 2).

Clinical relevance is demonstrated in designs that are available on the market today (Figure 3).

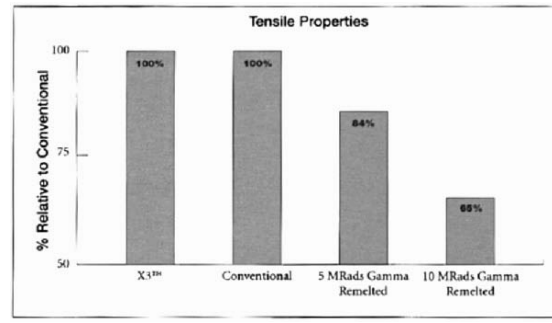

Figure 1: The higher the irradiation dose, the more remelting compromises the strength of the polyethlyene.

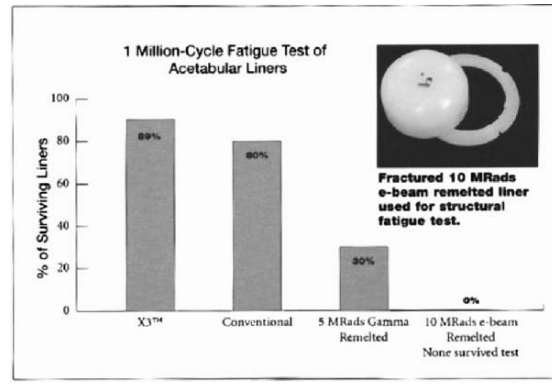

Figure 2: In laboratory studies of rim loaded thin acetabular liners made from different crosslinked polyethylene materials, highly crosslinked (10 MRads of irradiation) remelted liners fractured 100% of the time before 1 Million cycles, while 70% of the moderately crosslinked (5 MRads of irradiation) remelted polyethylene liners fractured.

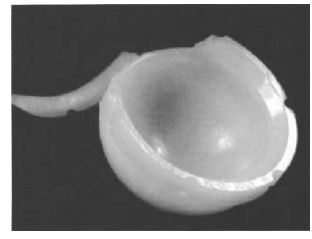

Figure 3: This picture shows a highly crosslinked remelted liner that was retrieved from a patient 10 months after surgery.

Wear Matters

Hip simulator testing demonstrates a 97% reduction in wear over conventional polyethylene[11], compared with a 90% reduction in wear for first generation highly crosslinked polyethylene (**Figure 4**)[12-17].

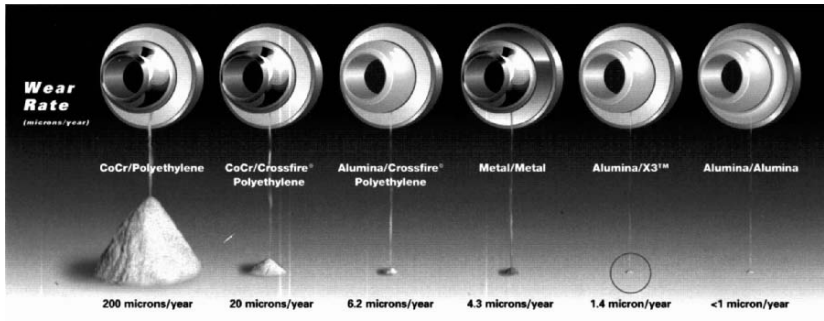

Figure 4

Further hip simulator testing revealed that for X3™ polyethylene; wear did not vary significantly with head size or polyethylene thickness in the range shown[18] (**Figure 5**).

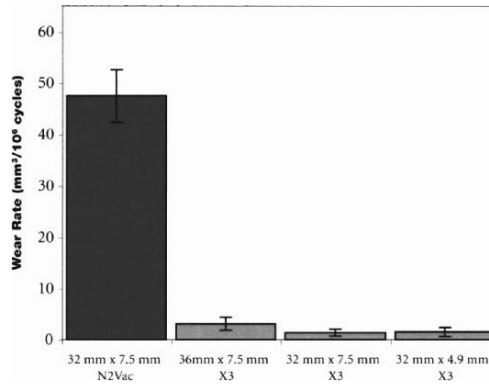

Figure 5

Oxidation Resistance

X3™ polyethylene demonstrates high oxidation resistance under extreme laboratory conditions (immersion in 5 atmospheres of oxygen at 70-degrees C for 14 days)[8,9] (**Figure 6**).

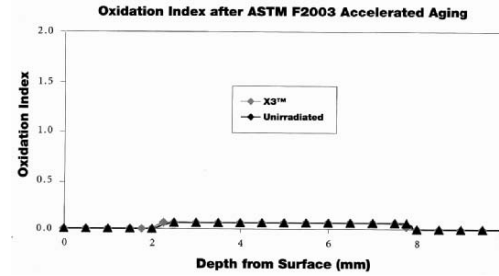

Figure 6: Oxidation resistance is shown to be similar to virgin, unirradlated polyehtylene.

X3™ polyethylene maintains mechanical properties after accelerated oxidative age laboratory testing. No statistical difference was found for tensile-yield strength, ultimate tensile strength, and elongation[19] (**Figure 7**)[8,9].

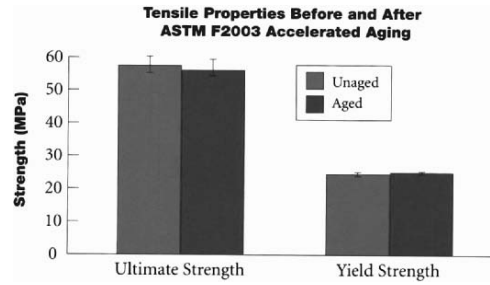

Figure 7:

X3™ is THE next generation in polyethylene performance improvements.

The first highly crosslinked polyethylene to offer:

- Structural fatigue strength better than conventional polyethylene.[3,8]
- 97% wear reduction; greater than first generation highly crosslinked polyethylene[11]
- Oxidation resistance similar to virgin polyethylene<??>

REFERENCES/BIBLIOGRAPHY

References/Bibliography

References on Trauma-Engineering Analysis (Investigation of Medical Case Studies)

1. General

AAAM (2001): The abbreviated injury scale, 1990 version/update 98. Association of Advancement of Automotive Medicine, Barrington, IL

AAAM (2004): AIS 2005: the injury scale (Eds. Gennarelli T, Wodzon E). Association of Advancement of Automotive Medicine, Barrington, IL

Appel H, Krabbel G, vetter D (2002): Unfallforschung, Unfallmechanik and Unfallrekonstrucktion. Verlag Information Ambs GmbH, Kippenheim, Germany

Baker S, O'Neil B (1976): The injury severity score: an update. J Trauma 11:882–885

Bathe K (1996): Finite element procedures. Prentice-Hall, Upper Saddle River, NJ, p 07458

Begley JA and Landes JD (1971): Fracture Toughness, Nuclear Engineering and Design 17, 91–102

Boyd HB, Griffin LL (1949): Classification and treatment of trochanteric fractures. Arch Surg 58: 853–863

Broughton WR, Hull D (1987): Measurement of mode II strain energy release rates using the ENF test. A VAMAS group project on delamination tests of composite materials, Department of Material Science and Metallurgy, University of Cambridge, Pembroke Street, Cambridge CB2 3QZ, 1987/1988

Bullinger H, Solf J (1979): Ergonomische Arbeitmittergestaltung I. Systematic. Bundesanstalt fur Arbeitsschutz and Unfallforschung, Dortmund (In German)

Campbell F, Woodford M, Yates D (1994): A comparison of injury impairment scale scores and physician's estimates of impairment following injury to the head abdomen and lower limbs. In: Proceedings of 38th AAAM Conference

Carsten O, Day J (1988): Injury priority analysis. NHTSA Technical Report DOT HS 807 224

Chow W, Odell E (1978): Deformations and stresses in soft body tissues of a sitting person. J Biomed Eng 100:79–87

Comptom C (2002): The use of public crash data in biomechanical research. In: Accidental Injury – Biomechanics and Prevention (Eds. Nahum A, Melvin J). Springer, Berlin Heidelberg New York

Davidson BD, Kruger R, Konig M (1995): 2-Dimensional analysis and resulting design recommendation for unidirectional and multidirectional end-notched-flexure tests. J Compos Mater 29:2108–2133

Davidson BD, Kruger R, Konig M (1996): Effects of stacking sequence on energy release rate distribution in multilayer DCB and ENF specimens. Engineering Fracture Mechanics. Syracuse University Department of Mechanical, Aerospace and Manufacturing Engineering Technical Report Number 95-101

Davidson BD, Altonen CS, Polaha JJ (1996): Effects of stacking sequence delamaination toughness and delamination growth behavior in composite end-notched-flexure specimens. In: Composite Materials: Testing and Design (Eds. Saff CR, Deo RB) (Vol. 12), ASTM STP 1274 ASTM, pp. 393–413

Daridon L, Cochelin B, Ferry M (1995): Delamination and fiber bridging modeling in composite samples. University de Metz-IIe du Sauley 57045 Metz-Cedex 01, France, 1995

Denton ATD, Inc., Milan, USA

DSD (2000): PC-Crash, Dr. Steffan Datentechnik, Linz, Austria

Dugdale DS (1960): Yielding of steel sheets containing slits. Spie Milestone Series MS, Vol. 137, pp. 280–284

ESI (1998): Engineering Systems International S.A.; 20 rue Saarinen, 94578

Griffith AA (1921): The phenomena of rupture and flow in solids. Phil. Trans. Roy. Soc. London, A, V. 221, 163–198

Horvath I, Vergeest J (1998): Theoretical fundamentals of natural representation of shapes generated with gestural devices. In: Proceeding of the 2nd International Symposium On TMCE (Eds. Horvath I, Taleb-Bendiab A), Manchester, UK, pp. 393–409

IBB (2002): Carat 4.0, Ibb-Informatik, Mulheim/Mosel, Germany

Inglis CE (1913): Stresses in a plate due to the presence of cracks and sharp corners. Trans. Inst. Naval Arch., London, V. LV, 219–230

ISO WorldSID Task Group, `http://www.worldsid.org`

Iwamoto M, Kisanuki Y, Watanabe I, Furusu K, Miki K, Hasegawa J (2002): Development of a finite element model of the total human model for safety (THUMS) and application to injury reconstruction. In: Proceedings of IRCOBI Conference, pp. 31–42

Kramer F (1998): Passive Sicherheit von Kraftfahrzeugen. Vieweg Verlag, Braunschweig, Germany

Livermore (1999): Livermore Software Technology Corporation, http://www.lstc.com

Malliaris A (1985): Harm causation and ranking in car crashes. SAE paper No. 85090

Manschot J, Brakkee A (1987a): Characterization of in vivo mechanical skin properties independent of measuring configuration. Bioengineering and the Skin 3:1–10

Manschot J, Brakkee A (1987b): Seasonal variations in the mechanical properties of the human skin. Bioeng Skin 3:25–33

Mecalog (2000): Radioss, Mecalog Sarl, France, http://www.radioss.com

Moes C (1998): Measuring the tilt of the pelvis. Ergonomics 41(12):1821–1831

Moes C (2000a): Distance between the points of maximum pressure for sitting subjects. In: Proceedings of the 6th International Design Conference DESIGN2000 (Ed. D. Marjanovic), University of Zagreb, Zagreb, pp. 227–232

Moes C (2000b): Geometric model of the human body. In: Third International Symposium on Tools and Methods of Competitive Engineering (Eds. Horvath I, Medland AJ, Netherlands JS). Delft University Press, Delft, pp. 79–92

Moes C (2000c): Pressure distribution and ergonomics shape conceptualization. In: Proceedings of the 6th International Design Conference DESIGN2000 (Ed. Marjanovic D), University of Zagreb, Zagreb, pp. 233–240

Moes C (2001a): Generation of shape instances for FE modelling of the human body. In: Design Methods for Performance and Sustainability (Eds. Culley S, Duffy A, McMahon C, Wallace K). Proceedings of the 13th International Conference on Engineering Design, ICED01 Glassgow: Professional Engineering Publishing, Bury St Edmunds, UK, pp. 131–138

Moes C (2001b): Mathematics and algorithms for pressure distribution controlled shape design. In: Design Methods for Performance and Sustainability (Eds. Culley S, Duffy A, McMahon C, Wallace K). Proceedings of the 13th International Conference on Engineering Design, ICED01 Glasgow: Professional Engineering Publishing, Bury St Edmunds, UK, pp. 99–106

Moes C, Rusak Z, Horvath I (2001): Application of vague geometric representation for shape instance generation of the human body. In: Proceedings of DETC'01, Computers and Information in Engineering Conference (Eds. Mook D, Balachandran B), Pittsburgh, Pennsylvania, ASME 2001, pp. (CDROM: DET2001/CIE-21298)

Money MW (1989): Measurement of mode I and mode II strain energy release rates. National Physical Laboratory, NPL Report DMA(A) 178, March, 1989

Moody D, Lozanoff S (1999): Surf Driver, Rapid and Reliable 3-D Reconstruction. Version 3.5.5, http://www.surfdriver.com

Muser M, Zellmer H, Walz F, Hell W, Langwieder K (1999): Test procedure for the evaluation of the injury risk to the cervical spine in a low speed rear

end impact. Proposal for the ISO/TC22 N 2071/ISO/TC22/SC10 (collision test procedures), http://www.agu.ch

Ono K, Kaneoka K (1997): Motion analysis of human cervical vertebrae during low speed rear impacts by the simulated sled. In: Proceedings of IRCOBI Conference, pp. 223–237

Reinhart TJ (1987): Engineering materials handbook. ASM International 1:788

Rice JR et al. (1968): Plane-strain deformation near a crack tip in a power-law hardening material. J Mech Phys. solid, 16:13, 1–12

Rolhauser H (1950): Die Sugfestigkeit der Menschlichen Haut. Unknown Journal, pp. 249–261. Aus dem Anatomischen Institut der Universitat Marburg/ Lahn

Sandedrs M, McCornick E (1993): Human Factors in Engineering and Design, Pyschology Series, 7th edition. Mcgraw-Hill, London

Schmitt K-U, Muser M, Walz F, Niederer P (2002): On the role of fluid–structure interaction in the biomechanics of soft tissue neck injuries. Traffic Injury Prev 3(1):65–73

Schmitt K-U, Muser M, Vetter D, Walz F (2004): Whiplash injuries: cases with a long period of sick leave need biomechanical assessment. European Spine, on-line publication at Springer, Berlin, Heidelberg, New York

Schmitt K-U, Beyeler F, Muser M, Niederer P (2003b): A visco-elastic foam as head restraint material – experiments and numerical simulations using a BioRID mode. Traffic Injury (Private Communications)

Sih GC (1976): Fracture toughness concept. ASTM special technical publication 605, 3–15

Spitzer W, Skovron M, Salmi L, Cassiy J, Duranceau J, Suissa S, Zeiss E (1995): Scientific monograph of the Quebec task force on Whiplash associated disorders: redefining Whiplash and its management. Spine 20(8S):3–73

Stephen T, Hahn W, Thomas H (1980): Introduction to composite materials, Sect. 7.2. Technomic Publishing Company, Lancaster

TNO (2001): Madymo V6.0, TNO Automotive, Delft, The Netherlands

Todd B, Tacker J (1994): Three-dimensional computer model of the human buttocks, in vivo. J Rehabil Res Dev 31(2):111–119

VHP (1997): The Visible Human Project TM, URL: http://www.nlm.nih.gov/research/visible/visible_human.html

Wells AA and Post D (1958): The dynamic stress distribution surrounding a running crack - a Photoelastic analysis. Spie Milestone Series MS, Vol. 138 461–484.

Williams ML (1957): On the stress distribution at the base of a stationary crack. Journal of Applied Mechanics, pp. 101–106

Williams P, Warvick R, Dyson M, Bannister L (Eds.) (1989): Gray's Anatomy, 37th edition. Churchill Livingstone, Edinburgh

Wismans J (1994): Injury biomechanics, course notes. Eindhoven University of Technology, The Netherlands

Zeidler F, Pletschen B, Mattern R, Alt B, Miksch T, Eichendorf W, Reiss S (1989): Development of a new injury cost scale. Proceedings of 33rd Annual conferences AAAM

Zienkiewicz O, Taylor R (1994): The finite element method. McGraw-Hill, London, ISBN 0-07-084175-6

2. Head Injuries and Trauma

AAAM (2004): AIS 2005: The injury scale (Eds. Gennarelli T, Wodzin E). Association of Advancement of Automotive Medicine, Barrington, IL

Advani S, Powell W, Huston J, Ojala S (1975): Human head impact response experimental data and analytical simulations. In: Proceedings of International Conference on Biomechanics and Prevention (Eds. Nahum A, Melvin J), Springer, Berlin Heidelberg New York

Advani S, Ommaya A, Yang W (1982): Head injury mechanisms. In: Human Body Dynamics (Ed. Ghista). Oxford University Press, Oxford

Allsop D, Kennett K (2002): Skull and facial bone trauma. In: Accidental Injury – Biomechanics and Prevention (Eds. Nahum A, Melvin J). Springer, Berlin Heidelberg New York

Allsop D, Warner C, Wille M, Schneider D, Nahum A (1988): Facial impact response – a comparison of the Hybrid III dummy and human cadaver. In: Proceedings of 32nd Stapp Car Crash Conference, SAE 881719

Allsop D, Perl T, Warner C (1991): Force/deflection and fracture characteristics of the temporoparietal region of the human head. In: Proceedings of 35th Stapp Car Crash Conference, SAE 912907, pp. 139–155

Beier G, Schuller E, Schuck M, Ewing C, Becker E, Thomas D (1980): Center of gravity and moments of inertia of human head. In: Proceedings of 5th Internernational Conference on the Biokinetics of Impacts, pp. 218–228

Gennarelli T, Thibault L, Ommaya A (1972): Pathophysiologic responses to rotational and translational accelerations of the head. In: Proceedings of 16th Stapp Car Crash Conference, SAE 720970, pp. 269–308

Gladd C (1961): Criteria for injury potential. In: Impact Acceleration Stress Symposium, National Academy of Science, Washington, National Research Council Publication No. 977:141–144

Got C, Patel A, Fayon A, Tarriere C, Walfisch G (1978): Results of experimental head impacts on cadavers: the various data obtained and their relation to some measured physical parameters. In: Proceedings of 22nd Stapp Car Crash Conference, SAE 780887, pp. 57–99

Gurdjian E, Lissner H, Latimer R, Haddad B, Webster J (1953): Quantitative determination of acceleration and intercranial pressure in experimental head injury. Neurology 3:417–423

Gurdjian E, Robert V, Thomas L (1996): Tolerance curves of acceleration and intercranial pressure and protective index in experimental head injury. J Trauma 6(5):600–604

Hertz (1993): A note on the head injury criterion (HIC) as a predictor of the risk of skull fracture. In: Proceedings of 37th Annual Proceedings of the AAAM

Hirsch A, Ommaya A, Mahone R (1968): Tolerance of subhuman primate brain to cerebral concussion. Report 2876, Department of the Navy, Washington

Hodgson V, Thomas L (1971): Breaking strength of the human skull vs. impact surface curvature. Department of Neuroscience, Wayne State University School of Medicine, Detroit

Kleinberger M, Sun E, Eppinger R, Kuppa S, Saul R (1998): Development of improved injury criteria for the assessment of advanced automotive restraint systems. NHTSA report, September 1998

Krabbel G (1997): Ein rechnerisches Schaedel–Hirn–Modell zur Untersuchung dynamischer Bellastungen des Kopfes. Dissertation, TU Berlin

Kramer F (1998): Passive Sicherheit von Kraftfahrzeugen. Vieweg Verlag, Braunschweig, Germany

Lissber H, Lebow M, Evans F (1960): Experimental studies on the relation between acceleration and intracranial pressure changes in man. Surg Gynecol Obstet 111:320–338

Lowenhielm (1975): Mathematical simulation of gliding contusions. J Biomech 8:351–356

Melvin J, Lighthall J (2002): Brain injury biomechanics. In: Accidental Injury – Biomechanics and Prevention (Eds. Nahum A, Melvin J). Springer, Berlin Heidelberg New York

Nahum A, Gatts J, Gadd C, Danforth J (1968): Impact tolerance of the skull and face. In: Proceedings of 2nd Stapp Car Crash Conference, SAE 680785

Newman J (1986): A generalized acceleration model for brain injury threshold (GAMBIT). In: Proceedings of IRCOBI Conference, pp. 121–131

Ommaya (1984): Biomechanics of head injury. In: Biomechanics of Trauma (Eds. Nahum A, Melvis J). Appleton–Century–Crofts, Norwalk

Ommaya A, Yarnell P, Hirsch A, Harris Z (1967): Scaling of experimental data on cerebral concussion on sub-human primates to concussion threshold for men. In: Proceedings of 11th Stapp Car Crash Conference, SAE 670906, pp. 47–52

Ono I, Kikuchi A, Nakamura M, Kobayashi H, Nakamura N (1980): Human head tolerance to sagittal impact reliable estimation deduced from experimental head injury using subhuman primates and human cadaver skulls. In: Proceedings of 24th Stapp Car Crash Conference, SAE 801303

Padgaonks A, Krieger K, King A (1975): Measurement of angular acceleration of a rigid body using linear accelerometers. J Appl Mech 42:552–556

Schneider D, Nahum A (1972): Impact studies of facial bones and skull. In: Proceedings of 16th Stapp Car Crash Conference, SAE 720965, pp. 186–203

Sobotta J (1997): Atlas der Anatomie des Menschen. Band 1 and 2, Urban und Schwarzenbberg, Munchen

Tarriere C (1987): Relationship between experimental measuring techniques and real world accidents. In: Head Injury Symposium, New Orleans, AAAM Report

Versace J (1971): A review of the severity index. In: Proceedings of 15th Stapp Car Crash Conference, SAE 710881

Vetter D (2000): Seminar: Biomechanik und Dummy-Technik, TU-Berlin

Viano D (2001): Crashworthiness and Biomechanics. Euromotor Course, June 11–13, Goteborg, Sweden

3. Spinal Injuries and Trauma

AAAM (2004): AIS 2005: The injury scale (Eds. Gennarelli T, Wodzin E). Association of Advancement of Automotive Medicine, Barrington, IL

Aldman B (1986): An analyatical approach to the impact biomechanics of head and neck injury. In: Proceedings of 30th Annual AAAM Conference, Montreal, pp. 439–454

Begeman P, King A, Prasad P (1973): Spinal loads resulting from − Gx acceleration. In: Proceedings of 17th Stapp Car Crash Conference, SAE 730977, pp. 33–360

Bohmann K, Bostrom O, Haland Y, Kullgren A (2000): A study of AISI neck injury parameters in 168 frontal collisions using a restraint Hybrid III dummy. In: Proceedings of 44th Stapp Car Crash Conference, pp. 103–116

Bortenschlager K, Kramberger D, Barnsteiner K, Hartlieb M, Ferdinand L, Leyer H, Muser M, Schmitt K-U (2003): Comparison tests of BioRID II and RID-2 with regard to repeatability, preproducibility and sensitivity for assessment of car seat protection potential in rear-end impacts. Stapp Car Crash J 47:473–488

Bostrom O, Svensson M, Aldman B, Hansson H, Haland Y, Locsund P, Seeman T, Suneson A, Saljo A, Ortengren T (1996): A new neck injury criterion candidate based on injury findings in the cervical spinal ganglia after experimental neck extension trauma. In: Proceedings of IRCOBI Conference, pp. 123–136

Bostrom O, Bohman K, Haland Y, Kullgren A, Krafft M (2000): New AISI long-term neck injury criteria candidates based on real frontal crash analysis. In: Proceedings of IRCOBI Conference, pp. 249–264

Byland P, Bjornstig U (1998): Sick leave and disability pension among passenger car occupants injured in urban traffic. Spine, 23:1023–1028

Deng B, Luan F, Begeman P, Yang K, King A (2000): Testing shear hypothesis of whiplash injury using experimental and analytical approaches. In: Frontiers in Whiplash Trauma (Eds. Yoganandan N, Pintar FA). IOS Press, Amsterdam

Doherty B, Esses S, Heggeness M (1993): A biomechanical study of odontoid fractures and fracture fixation. Spine 18(2):178–184

Duma S, Crandell J, Rudd R, Funk J, Pilkey W (1999): Small female head and neck interaction with a deploying side air bag. In: Proceedings of IRCOBI Conference, pp. 191–199

Eichberger A, Steffan H, Geigl B, Svensson M, Bostrom O, Leinzinger P, Darok M (1998): Evaluation of the applicability of the neck injury criterion (NIC) in rear end impacts on the basis of human subject tests. In: Proceedings of IRCOBI Conference, pp. 153–161

Ferrari R (1999): The whiplash encyclopedia. Aspen, Gaithersburg

Fielding J, Cochran G, Lawsing J, Hohl M (1974): Tears of the transverse ligament of the atlas. J Bone Joint Surg 56A(8):1683–1691

Goldsmith W, Ommaya AK (1984): Head and neck injury criteria and tolerance levels. In: The biomechanics of impact trauma (Eds. Aldman B, Chapon A). Elsevier Science Publishers, Amsterdam, pp. 149–187

Grauer J, Panjabi M, Cholewicki J, Nibu K, Dvorak J (1997): Whiplash produces an S-shaped curvature on the neck with hyperextension at lower levels. Spine 22(21):2489–2494

Heitplatz F, Sferco R, Fay P, Reim J, Kim A, Prasad P (2003): An evaluation of existing and proposed injury criteria with various dummies to determine their ability to predict the levels of soft tissue neck injury seen in real world accidents. In: Proceedings of 18th ESV Conference

King A (2002): Injuries to the thoracolumbar spine and pelvis. In: Accidental Injury – Biomechanics and Prevention (Eds. Nahum A, Melvin J). Springer, Berlin Heidelberg New York

Kleinberger M, Sun E, Eppinger R, Kuppa S, Saul R (1998): Development of improved injury criteria for the assessment of advanced automotive restraint systems. NHTSA report, September 1998

Klinch K et al. (1996): NHTSA Child Injury Protection Team. Techniques for developing child dummy protection reference values, NHTSA Docket No. 74-14

Kornhauser M (1996): Delta-v thresholds for cervical spine injury. Technologies for occupant protection assessment, SAE 960093

Kullgren A, Thomson R, Krafft M (2000): Neck injuries in frontal impacts: influence of crash pulse characteristics on injury risk. Accident Anal Prev 32(2):197–205

Kullgren A, Eriksson L, Krafft M, Bostrom O (2003): Validation of neck injury criteria using reconstructed real-life rear-end crashes with recorded crash pulses. In: Proceedings of 18th ESV Conference

Linder A, Schmitt K-U, Walz F, Ono K (2000): Neck modelling for rear-end impact simulations – a comparison between a multibody system (MBS) and a finite element (FE) model. In: Proceedings of IRCOBI Conference, pp. 491–494

Maiman D, Sances A, Myclebust J, Larson S, Houterman C, Chilbert M, El-Ghatit A (1983): Compression injuries of the cervical spine: a biomechanical analysis. Neurosurgery 13(3):254–260

McElhaney J. Nightingale R, Winkelstein B, Chancey V, Myers B (2002): Biomechanical aspects of cervical trauma. In: Accidental Injury – Biomechanics and Prevention (Eds. Nahum A, Melvin J). Springer, Berlin Heidelberg New York

Mertz H, Patrick L (1967): Investigation of the kinematics and kinetics of whiplash. In: Proceedings of 11th Stapp Car Crash Conference, SAE 670919, pp. 2952–2980

Mertz H, Patrick L (1971): Strength and response of the human neck. In: Proceedings of 15th Stapp Car Crash Conference, SAE 710855, pp. 207–255

Mertz H, Patrick L (1993): Strength and response of the human neck. In Biomechanics of Impact Injury and Injury Tolerance of the Head–Neck Complex (Ed. Backaitis S). SAE 710855, pp. 821–846

Moffat E, Siegel A, Huelke D (1978): The biomechanics of automotive cervical fractures. In: Proceedings of 22nd AAAM Conference, pp. 151–168

Morris A, Thomas P (1996): Neck injuries in the UK co-operative crash injury study, SAE 962433

Murer E, Niederer P, Radanov B, Rumo-Jungo A, Sturzinegger M, Walz F (Eds) (2002): Whiplash Associated Disorders – Medical, Biomechanical and Legal Aspects. Staempfli, Berne

Muser M, Walz F, Zellmer H (2000): Biomechanical significance of the rebound phase in low speed rear end impacts. In: Proceedings of IRCOBI Conference, pp. 411–424

Muser M, Walz F, Schmitt K-U (2002): Injury criteria applied to seat comparison tests. Traffic Injury Prev 3(3):224–232

Muser M, Hell W, Schmitt K-U (2003): How injury criteria correlate with the injury risk – a study analysing different parameters with respect to whiplash injury. In: Proceedings of 18th ESV Conference, paper no. 68

Myers B, McElhaney J, Richardson W, Nightingale R, Doherty B (1991): The influence of end conditions on human cervical spinal injury mechanisms. In: Proceedings of 35th Stapp Car Crash Conference, SAE 912915, pp. 391–400

Nightingale R, McElhaney J, Camacho D, Winkelstein B, Myers B (1997): The dynamic responses of the cervical spine: the role of buckling, end conditions, and tolerances in compression impacts. In: Proceedings of 41st Stapp Car Crash Conference, SAE 973344, pp. 451–471

Nightingale R, Winkelstein B, Van EE C, Myers B (1998): Injury mechanisms in the pediatric cervical spine during out-of-position airbag deployments. In: 42nd Annual Proceedings, AAAM, pp. 153–164

Ono K, Janeoka K (1997): Motion analysis of human cervical vertebrae during low speed rear impacts by the simulated sled. In: Proceedings of IRCOBI Conference, pp. 223–237

Ono K, Kaneoka K (2001): Human cervical vertebra motions and whiplash injury mechanism in low speed rear collision. In: Proceedings of IIWPG/IRCOBI Symposium on Dynamic Testing for Whiplash Injury Risk

Ono K, Kaneoka K, Imami S (1998): Influence of seat properties on human vertebral motion and head/neck/torso kinematics during rear end impacts. In: Proceedings of IRCOBI Conference, pp. 303–321

Panjabi M, Wang J. Delson N (1999): Neck injury criterion based on intervertebral motions and its evaluation using an instrumented neck dummy. In: Proceedings of IRCOBI Conference, pp. 179–190

Parkin S, Machay G, Hassan A, Graham R (1995): Rear end collisions and seat performance – to yield or not to yield. In: Proceedings of 39th Annual AAAM Conference, pp. 231–244

Pintar F, Yoganandan N, Voo L, Cusick J, Maiman D, Sances A (1995): Dynamic characteristics of the human cervical spine. In: Proceedings of 39th Stapp Car Crash Conference, SAE 952722, pp. 195–202

Prasad P, Daniel R (1984): A biomechanical analysis of head, neck, and torso injuries to child surrogates due to sudden torso acceleration. In: Proceedings of 28th Stapp Car Crash Conference, SAE 841656, pp. 25–40

Sances A, Myklebust J, Maiman D, Larson S, Cusick J (1984): The biomechanics of spinal injuries, CRC Crit Rev Biomed Eng 11(1):1–76

Schmitt K-U (2001): A Contribution to the Trauma-Biomechanics of the Cervical Spine – Pressure Phenomena Observed Under Conditions of Low Speed Rear-End Collisions. ISBN 3-18-321117-3, VDI Verlag, Dusseldorf, Germany

Schmitt K-U, Muser M, Walz F, Niederer P (2002a): N_{km} – a proposal for a neck protection criterion for low speed rear-end impacts. Traffic Injury Prev 3(2):117–126

Schmitt K-U, Muser M, Vetter D, Walz F (2002b): Biomechanical assessment of soft tissue neck injuries in cases with long sick leave times. In: Proceedings of IRCOBI Conference, pp. 193–201

Schmitt K-U, Muser M, Vetter D, Walz F (2003a): Whiplash injuries: cases with a long period of sick leave need biomechanical assessment. Eur Spine 12:247–257

Schmitt K-U, Muser M, Niederer P (2003b): Evaluation of a new visco-elastic foam for automotive applications. J Crashworthiness 8(2):71–80

Schuller E (2001): Grenzen der Beurteilung der Insassenverletzungen nach leichtem Verkehrsunfall aus technischer und medizinischer Sicht. In: Proceedings of 11th Symposium der Munchner Forschungsgemeinschaft fur Unfallrekonstruktion

Shea M, Edwards W, White A, Hayes W (1991): Variations of stiffness and strength along the human cervical spine. J Biomech 24(2):95–107

Sobotta J (1997): Atlas der Anatomie des Menschen. Bank 1 and 2, Urban and Schwarzenberg, Munchen

Spitzer W, Skovron M, Salmi L, Cassiy J, Duranceau J, Suissa S, Zeiss E (1995): Scientific monograph of the Quebec task force on whiplash associated and its management. Spine 20(8S):1S–73S

Svensson M, Aldman B, Hansson H, Lovsund P, Seeman T, Suneson A, Ortengren T (1993): Pressure effects in the spinal canal during whiplash

extension motion: a possible cause of injury to the cervical spine ganglia. In: Proceedings of IRCOBI Conference, pp. 189–200
Szabo T, Voss D, Welcher J (2002): Influence of seat foam and geometrical properties on BioRID P3 kinematic response to rear impacts. In: Proceedings of IRCOBI Conference, pp. 87–101
Vetter D (2000): Seminar: Biomechanik und Dummy-Technik, TU-Berlin
Viano D (2001a): Crashworthiness and Biomechanics. Euromotor Course, June 11–13, Goteborg, Sweden
Viano D, Davidsson J (2001b): Neck displacements of volunteers, BioRID P3 and Hybrid III in rear impacts: implications to whiplash assessment by a neck displacement criterion (NDC). In: Proceedings of IIWPG/IRCOBI Symposium, Isle of Man
Walz F, Muser M (2000): Practical biomechanical aspects of cervical spine injuries. In: SAE International Congress and Exhibition, Detroit, Michigan, SAE 950658 in SP-1077
Watts A, Atkinson D, Hennessy M (1996): Low Speed Automobile Accidents. Lawyers & Judges, Tuscon
Wheeler J, Smith T, Siegmund G, Brault J, King D (1998): Validation of the neck injury criterion (NIC) using kinematic and clinical results from human subjects in rear end collisions. In: Proceedings of IRCOBI Conference, pp. 335–348
Winkelstein B, Nightingale R, Richardson W, Myers B (2000): The cervical facet capsule and its role in whiplash injury: a biomechanical investigation. Spine 25(10):1238–1246
Yang K, Begeman P, Muser M, Biederer P, Walz F (1997): On the role of cervical facet joints in rear end impact neck injury mechanisms, SP-1226, SAE 970497, pp. 127–129
Yoganandan N, Pintar F (Eds.) (2000): Frontiers in Whiplash Trauma: Clinical and Biomechanical. IOS, Amsterdam
Yoganandan N, Kumaresan S, Pintar F, Gennarelli T (2002): Pediatric biomechanics. In: Accidental Injury – Biomechanics and Prevention (Eds. Nahum A, Melvin J). Springer, Berlin Heidelberg New York

4. Thoracic Injuries and Trauma

AAAM (2004): AIS 2005: The injury scale (Eds. Gennarelli T, Wodzon E). Association of Advancement of Automotive Medicine, Barrington, IL
Bendjellal F, Walfisch G, Steyer C, Ventre P, Foret-Bruno J (1997): The programmed restraint system – a lesson from accidentology. In: Proceedings of 41st Stapp Car Crash Conference, pp. 249–264
Cavanaugh JM (2002): The biomechanics of thoracic trauma. In: Accidental Injury – Biomechanics and Prevention (Eds. Nahum A, Melvin J). Springer, Berlin Heidelberg New York

Cavanaugh JM, Zhu Y, Huang Y, King AI (1993): Injury and response of the thorax in side impact cadaveric tests. In: Proceedings of 37th Stapp Car Crash Conference, pp. 271–297

Creasy JD, Chiles C, Routh WD, Dyer R (1997): Overview of traumatic injury of the thoracic aorta. Radiographics, 17(1):27–45

Eppinger RH, Marcus JH, Morgan RM (1984): Development of dummy and injury index for NHTSA's thoracic side impact protection research program, SAE 840885

Foret-Bruno J, Trosseille X, Le Coz J, Bendjellal F, Steyer C, Phalempin T, Villeforceix D, Dandres P (1998): Thoracic injury risk in frontal car crashes with occupant restrained with belt load limiter, SAE 983166, pp. 331–352

Fung YC, Yen MR (1984): Experimental investigation of lung injury mechanisms. Topical report, U.S. Army, DAMD17-828C-2062

Kallieris D, Rizzetti A, Mattern R, Morgan R, Eppinger R, Keenan L (1995): On the synergism of the driver airbag and the three-point belt in frontal collisions. In: Proceedings of 39th Stapp Car Crash Conference, pp. 389–402

Kallieris D, Mattern R, Schmidt G, Eppinger R (1981): Quantification of side impact responses and injuries. In: Proceedings of 25th Stapp Car Crash Conference, pp. 329–366

Kleinberger M, Sun E, Eppinger R, Kuppa S, Saul R (1998): Development of improved injury criteria for the assessment of advanced automotive restraint systems. NHTSA report, September 1998

Kramer F (1998): Passive Sicherheit von Kraftfahzeugen. Vieweg Verlag, Braunschweig, Germany

Kroell CK, Schneider DC, Nahum AM (1971): Impact tolerance and response to the human thorax. In: Proceedings of 15th Stapp Car Crash Conference, pp. 84–134

Kroell CK, Schneider DC, Nahum AM (1974): Impact tolerance and response to the human thorax II. In: Proceedings of 18th Stapp Car Crash Conference, pp. 383–457

Lobdell T (1973): Impact response of the human thorax. In: Human Impact Response: Measurement and Simulation. Plenum, New York, pp. 201–245

McElhaney J, Nightingale R, Winkelstein B, Chancey V, Myers B (2002): Biomechanical aspects of cervical trauma. In: Accidental Injury – Biomechanics and Prevention (Eds. Nahum A, Melvin J). Springer, Berlin Heidelberg New York

Melvin JW, Mertz H (2002): Airbag inflation-induced injury biomechanics. In: Accidental Injury – Biomechanics and Prevention (Eds. Nahum A, Melvin J). Springer, Berlin Heidelberg New York

Melvin JW, Mohan D, Stalnaker RL (1975): Occupant injury assessment criteria, SAE 750914

Melvin JW, King AI, alem NM (1985): AATD system technical characteristics, design concepts, and trauma assessment criteria. NHTSA report, DOT-HS-807–224

Netter F (2003): Atlas der Anatomie des Menschen. Georg Thieme Verlag, Stuttgart, Germany, ISBN 3131090235

Oschsner MG, Champion HR, Chambers RJ, Harviel J (1989): Pelvic fracture as an indicator or increased risk of thoracic aortic rupture. J Trauma 29(10):1376–1379

Otte D (1995): Review of airbag effectiveness in real life accidents demands – for positioning and optimal deployment of airbag systems. In: Proceedings of 39th Stapp Car Crash Conference, pp. 1–10

Patrick LM, Mertz HJ, Kroell CK (1969): Cadaver knee, chest and head impact loads. In: Proceedings of 9th Stapp Car Crash Conference, pp. 168–182

Pintar F, Yoganandan N, Hines M, Maltese M, McFAdden J, Saul R, Eppinger R, Khaewpong N, Kleinberger M (1997): Chestband analysis of human tolerance to side impact. In: Proceedings of 41st Stapp Car Crash Conference, SAE 973320, pp. 63–74

Smith RS, Chang FC (1986): Traumatic rupture of the aorta: still a lethal injury. Am J Surg 152:660–663

Sobotta J (1997): Atlas der Anatomie des Menschen. Bank 1 and 2, Urban and Schwarzenberg, Munchen

Stalnaker RL, Mohan D (1974): Human chest impact protection. In: Proceedings of 3rd International Conference on Occupant Protection, SAE, pp. 384–393

Stalnaker RL, Tarriere C, Fayon A, Walfisch G, Balthazard M, Masset J, Got C, Patel A (1979): Modification of part 572 dummy for lateral impact according to biomechanical data. In: Proceedings of 23rd Stapp Car Crash Conference, pp. 843–872

Tarriere C, Walfisch G, Fayon A (1979): Synthesis of human tolerance obtained from lateral impact simulations. In: Proceedings of 7th International Technical Conference on Experimental Safety Vehicles, pp. 359–373

Viano D (1983): Biomechanics of non-penetrating aortic trauma: a review. In: Proceedings of 27th Stapp Car Crash Conference, pp. 109–114

Viano D (1989): Biomechanical responses and injuries in blunt lateral impact. In: Proceedings of 33rd Stapp Car Crash Conference, pp. 113–142

Viano D (1990): Chest anatomy, types and mechanisms of injury, tolerance criteria and limits and injury factors. In: Seminar at AAAM Conference, Orlando

Viano D, Lau IV (1985): Thoracic impact: a viscous tolerance criterion. In: Proceedings of 10th International Technical Conference on Experimental Safety Vehicles, pp. 104–114

5. Abdominal Injuries and Trauma

AAAM (2004): AIS 2005: The injury scale (Eds. Gennarelli T, Wodzin E). Association of Advancement of Automotive Medicine, Barrington, IL

Cavanaugh JM, Nyquist G, Goldberg S, King A (1986): Lower abdominal tolerance and response. In: Proceedings of 30th Stapp Car Crash Conference, SAE 861878, pp. 41–63

Eppinger RH, Morgan RM, Marcus JH (1982): Side impact data analysis . In: Proceedings of 9th International ESV Conference, pp. 244–250

Harms P, Renouf M, Thomas P, Bradford M (1978): Injuries to restrained car occupants. What are the outstanding problems? In: Proceedings of 11th International ESV Conference, SAE 876029, pp. 183–201

Khaewpong N, Nguyen T, Bents F, Eichelberger M, Gotschall C, Morrissey R (1995): Injury severity in restrained children in motor vehicle crashes, SAE 952711

Lane JC (1994): The seat belt syndrome in children. Accident Anal Prev 26(6):813–820

Langwieder K, Hummel T, Felsch R, Klanner W (1990): Injury risks of children in cars – epidemiology and effect of child restraint systems. SAE 905119, pp. 905–919

Mertz H, Weber D (1982): Interpretations of impact responses of a 3-year-old child dummy relative to child injury potential. In: Proceedings of 9th International ESV Conference, SAE 826048, pp. 368–176

Miller MA (1989): The biomechanical response to the lower abdomen to belt restraint loading. J Trauma 29(11):1571–1584

Nusholtz G, Kaiker P, Lehman R (1988): Steering system abdominal impact trauma. University of Michigan Transportation, Research Report no. 88–19

Rouhana SW (1987): Abdominal injury prediction in lateral impact: an analysis of the biofedility of the Euro-SID abdomen. In: Proceedings of 31st Stapp Car Crash Conference, SAE 872203, pp. 95–104

Rouhana SW (2002): Biomechanics of abdominal trauma. In: Accidental Injury – Biomechanics and Prevention (Eds. Nahum A, Melvin J). Springer, Berlin Heidelberg New York

Rouhana SW, Foster ME (1985): Lateral impact – an analysis of the statistics in the NCSS. In: Proceedings of 29th Stapp Car Crash Conference, SAE 851727, pp. 79–98

Rouhana SW, Lau IV, Ridella SA (1984): Influence of velocity and forced compression on the severity of abdominal injury in blunt, nonpenetrating lateral impact. GMR research publication no. 4763

Rouhana SW, Ridella SA, Viano D (1986): The effect of limiting impact force on abdominal injury: a preliminary study. In: Proceedings of 30th Stapp Car Crash Conference, SAE 861879, pp. 65–79

Sobotta J (1997): Atlas der Anatomie des Menschen. Band 1 and 2, Urban und Schwarzenberg, Munchen, Germany

Stalnaker R, Ulman M (1985): Abdominal trauma – review, response, and criteria. In: Proceedings of 29th Stapp Car Crash Conference, SAE 851720, pp. 1–16

Talantikite Y, Brun-Cassan F, Lecoz J, Tarriere C (1993): Abdominal injury protection in side impact – injury mechanisms and protection criteria. In: Proceedings of IRCOBI Conference, pp. 131–144

Walfisch G, Fayon A, Tarriere C, Rosey J, Guillon F, Got C, Patel A, Stalnaker R (1980): Designing of a dummy's abdomen for detecting injuries in side impact collisions. In: Proceedings of IRCOBI Conference, pp. 149–164

6. Injuries and Trauma of the Pelvis and the Lower Extremities

AAAM (2004): AIS 2005: The injury scale (Eds. Gennarelli T, Wodzon E). Association of Advancement of Automotive Medicine, Barrington, IL

Abelseth G, Buckley RE, Pineo GE et al. (1996): Incidence of deep-vein thrombosis in patients with fractures of the lower extremity distal to the hip. J Orthop Trauma 10:230

Begekaj P, Prasad P (1990): Human ankle impact response in dorsiflexion. In: Proceedings of 34th Stapp Car Crash Conference, pp. 39–54

Brown TD, Anderson DD, Nepola JV et al. (1988): Contact stress aberrations following imprecise reductions of simple tibial plateau fracture. J Orthop Res 6:851

Brun-Cassan F, Leung YC, Tarriere C, Fayon A, Patel A, Got C, Hureau J (1982): Determination of knee–femur–pelvis tolerance from the simulation of car frontal impacts. In: Proceedings of IRCOBI Conference, pp. 101–115

Buchko GM, Johnson DH (1996): Arthroscopy assisted operative management of tibial plateau fractures. Clin Orthop 332:29–36

Butler DA, Kay MD, Stouffer DC (1986): Comparison of material properties in fascicle-bone units from human patellar tendon and knee ligaments. J Biomech 19:425–432

Cappon H, van den Krooenberg A, Happee R, Wismans J (1999): An improved lower leg multibody model. In: Proceedings of IRCOBI Conference, pp. 499–509

Cavanaugh J, Walilko T, Malhotra A, Zhu Y, King A (1990): Biomechanical response and injury tolerance of the pelvis in twelve sled side impact tests. In: Proceedings of 34th Stapp Car Crash Conference, SAE 902307

Cohn SL, Sotta RP, Bergfeld JA (1990): Fractures about the knee in sports. Clin Sports Med 9:121–37

Crandall J, Martin P, Sieveka E, Klopp G, Kuhlmann T, Pilkey W, Dischinger P, Burgess A, O'Quinn T, Schnidhauser C (1995): The influence of footwell intrusion on lower extremity response and injury in frontal crashes. In: Proceedings of 39th AAAM Conference, pp. 269–286

Crandall J, Portier L, Petit P, Hall G, Bass C, Klopp G, Hurtwitz S, Pilkey W, Trosseille X, Tarriere C, Lassau J (1996): Biomechanical response and physical properties of the leg, foot and ankle, SAE 962424

Delamarter RB, Hohl M, Hopp E, Jr (1990): Ligament injuries associated with tibial plateau fractures. Clin Orthop 250:226

Gill TJ, Moezzi DM, Oates KM et al. (2001): Arthroscopic reduction and internal fixation of tibial plateau fractures in skiing. Clin Orthop 383:243

Haland Y, Hjerpe E, Lovsund P (1998): An inflatable carpet to reduce the loading of the lower extremities – evaluation by a new sled test method with toepan intrusion. In: Proceedings of ESV Conference, paper no. 98-S1-P-18E

Hirsch A, Whitel L (1965): Mechanical stiffness of man's lower limbs. In: In: Proceedings of ASME Winter Congress

Holt MD, Williams LA, Dent CM (1995): MRI in the management of tibial plateau fractures. Injury 26:595

Hubacher M, Wettstein A (2000): Die Wirksamkeit des Huft-Protektors zur Vermeiiiidung von sturzbedingten Schenkelhalsfrakaturen. Schweizerische Beratungsstelle fur Unnfallverhutung, Berne, Switzerland

ISO (1997): Passenger Cars and Light Commercial Vehicles – Pedestrian Protection – Impact Test Method for Pedestrian Lower Leg And Knee, ISO/TC22/SC10/WG2 Document N540

ISO (2001): Injury Risk Curves for Pedestrian Legs, ISO/TC22/SC12/WG6 Document N552

Kajzer J (1991): Impact biomechanics of knee injuries. Doctoral Thesis, Department of Injury Prevention, Chalmers University of Technology, Goteborg, Sweden

Kajzer J, Cavallero C, Ghanouchi S, Bonnoit J, Ghorbel A (1990): Response of the knee joint in lateral impact: effect of shearing loads. In: Proceedings of the IRCOBI Conference, 12–14 September 1990, Bron, France, pp. 293–304

Kajzer J, Cavallero C, Bonnoit J, Morjane A, Ghanouchi S (1993): Response of the knee Joint in Lateral Impact: effect of bending moment. In: Proceedings of the IRCOBI Conference, 12–14 September 1993, Eindhoven, The Netherlands, pp. 105–116

Kajzer J, Schroeder G, Ishikawa H, Matsui Y, Bosch U (1997): Shearing and bending effects at the knee at high speed lateral loading, STAPP 1997, SAE 973326

Kajzer J, Matsui Y, Ishikawa H, Schroeder G, and Bosch U (1999): Shearing and bending effects at the knee joint at low-speed lateral loading. Detroit, Michigan, SAE 1999–01-0712, SP1432

Kannus P, Parkkari J, Poutala J (1999): Comparison of force attenuation properties of four different hip protectors under simulated falling conditions in the elderly: an in vitro biomechanical study. Bone 25:229–235

King A (2002): Injuries of the thoracolumbar spine and pelvis. In: Accidental Injury – Biomechanics and Prevention (Eds. Nahum A, Melvin J). Springer, Berlin Heidelberg New York

Kitagawa Y, Ichikawa H, King A, Levine R (1998a): A severe ankle and foot injury in frontal crashes and its mechanism, SAE 983145

Kitagawa Y, Ichikawa H, Pal C, King A, Levine R (1998b): Lower leg injuries caused by dynamic axial loading and muscle tensing. In: Proceedings of ESV Conference, Paper no. 98-S7-O-09

Kramer F (1998): Passive Sicherheit von Kraftfahrzeugen. Viewegg Verlag, Braunschweig, Germany

Kress TA, Snider JN, Porta DJ, Fuller PM, Wasserman JF, Tucker GV (1993): Human femur response to impact loading. In: Proceedings of the International IRCOBI Conference on the Biomechanics of Trauma, September 8–10, Eindhoven, The Netherlands. IRCOBI Secretariat, Bron, France, pp. 93–104

Levine R (2002): Injuries to the extremities. In: Accidental Injury – Biomechanics and Prevention (Eds. Nahum A, Melvin J). Springer, Berlin Heidelberg New York

Levine RS, Begeman PC, King AI (1984): An Analysis of the Protection of Lateral Knee Bracing in Full Extension Using a Cadaver Simulation of Lateral Knee Impact. American Academic of Orthopedica Surgerical, 17 August 1984

Marder RA, Chapman MW (1990): Principles of fracture management. Clin Sports Med 9:1–11

McConkey JP, Meeuwisse W (1979): Tibial plateau fractures in alpine skiing. Am J Sports Med 16:159

McMaster J, Parry M, Wallace W, Wheeler L, Own C, Lowne R, Oakley C, Roberts A (2000): Biomechanics of ankel and hindfoot injuries in dynamic axial loading. In: Proceedings of 44th Stapp Car Crash Conference, paper no. 2000-01-SC23

Noyes FR, Grood ES (1976): The strength of the anterior cruciate ligament in humans and rhesus monkeys. J Bone Joint Surg 58-A:1074–1082

Nusholtz G, Alem N, Melvin J (1982): Impact response and injury to the pelvis. In: Proceedings of 26th Stapp Car Crash Conference, SAE 821160

Nyquist GW (1986): Injury tolerance characteristics of the adult human lower extremities under static and dynamic loading. In: Proceedings of the Symposium on Biomechanics and Medical Aspects of Lower Limb Injuries, San Diego, CA, October 29–30, p. 186. SAE, Warrendale, USA, pp. 79–90

Nyquist GW, Cheng R, El-Bohy AAR, King AI (1985): Tibia bending: strength and response. In: Proceedings of 29th STAPP Car Crash Conference, SAE paper 851728, Warrendale, PA, pp. 167, 99–112

Otte D (2002): Unpublished evaluation of the MHH database

Parenteau C, Viano D, Petit P (1998): Biomechanical properties of human cadaveric ankle–subtalar joints in quasi-static loading. J Biomech Eng 120:105–111

Peterson RH, Woo SL-Y (1986): A New Methodology to Determine the Mechanical Properties of Ligaments at High Strain Rate. J Biomech Eng 108:365–367

Petit P, Portier L, Foret-Bruno J, Trosseille X, Parenteau C, Coltat J, Tarriere C, Lassau J (1996): Quasistatic characterization of the human foot–ankle

joints in a simulated tensed state and updated accidentological data. In: Proceedings of IRCOBI Conference, pp. 363–376

Powell WR, Ojala SJ, Advani SH, Martin RB (1975): Cadaver femur responses to longitudinal impacts. In: Proceedings of the 19th STAPP Car Crash Conference, Society of Automative Engineers, Warrendale, PA, pp. 561–579

Pritz HB (1978): Comparison of the dynamic responses of anthropomorphic test devices and human anatomic specimens in experimental pedestrian impacts. In: Proceedings of 22nd STAPP Car Crash Conference, October 24–26, Ann Arbor Michigan, SAE Warrendale, PA, pp. 341–357

Ramet M, Bouquet R, Bermond F, Caire Y, Bouallegue M (1995): Shering and bending human knee joint tests in quasi-static lateral load. In: Proceedings of the International IRCOBBI Conference on the Biomechanics of Trauma, 13–15 September 1995, Brunnen, Switzerland. IRCOBI Secretariat, Bron, France, pp. 93–105

Schatzker J, McBroom R, Bruce D (1911): The tibial plateau fractures: the Toronto experience 1968–1975. Clin Orthop 138:94

Sobotta J (1997): Atlas der Anatomie des Menschen. Band 1 and 2, Urban and Schwarzenberg, Munchen, Germany

States JD (1986): Adult occupant injuries to the lower limb. In: Proceedings of the Symposium on Biomechanics and Medical Aspects of Lower Limb Injuries, San Diego, CA, October 29–30, p. 186. Society of Automotive Engineers, Warrendale, PA, pp. 97–108

Trent PS, Walker PS, Wolf B (1976): Ligament length patterns, strength and rotational axes of the knee joint. Clin Orthop Rel Res 117:263–270

Vetter D (2000): Seminar: Biomechanik und Dummy-Technik, TU Berlin

Viano D, Lau I, Asbury C, King A, Begeman P (1989): Biomechanics of the human chest, abdomen, and pelvis in lateral impact. In: Proceedings of 33rd AAAM Conference, pp. 367–382

Virkus WW, Helfet DL (2001): Tibia plateau fractures. In: Surgery of the Knee (Eds. Insall JN, Scott WN). Churchill Livingstong, Philadelphia, 1265–1289

Wiss DA, Watson JT, Johnson EE (1996): Fractures of the knee. In: Fractures in Adults (Eds. Rockwood CA, Green DP, Bucholz RW). Lippincott-Raven, Philadelphia, p. 1919

Woods GW, Stanley RF, Tulos HS (1979): Lateral capsular sign: x-ray clue to a significant knee instability. Am J Sports Med 7:27

Yamada H (1970): Strength of Biological Materials. R.E. Krieger, New York

Yang JK, Kajzer J, Cavallero C, Bonnoit J (1995): Computer simulation of shearing and bending response of the knee joint to a lateral impact. In: Proceedings of the 39th Stapp Car Crash Conference, Coronado, CA, pp. 251–264

Yoganandan N, Pintar F, Boynton M, Begeman P, Prasad D, Kuppa S, Morgan R, Eppinger R (1996): Dynamic axial tolerance of the human foot–ankle complex, SAE 962426

7. Injuries and Trauma of the Upper Extremities

Atkinson P, Hariharan P, Mari-Gowda S, Teehowski P, Martin S, van Hoof J, Bir C, Atkinson C (2002): An under-hand steering wheel grasp produces significant injury risk to the upper extremity during airbag deployment. In: Proceedings of 46th Annual Association for the Advancement of Automotive Medicine, pp. 45–62

Bass C, Duma S, Crandall J, Morris R, Martin P, Pilkey W, Hurwitz S, Kaewpong N, Eppinger R, Sun E (1997): The interaction of air bags with upper extremities. In: Proceedings of 41st Stapp Car Crash Conference, SAE 973324, pp. 111–129

Begeman P, Pratima K, Prasad P (1999): Bending strength of the human cadaveric forearm due to lateral loads. In: Proceedings of 43rd Stapp Car Crash Conference, SAE 99SC24

Duma S, Crandall J, Hurwitz S, Pilkey W (1998a): Small female upper extremity interaction with a deploying side air bag. In: Proceedings of 42nd Stapp Car Crash Conference, SAE 983148

Duma S, Schreiber R, McMaster J, Crandall J, Bass C, Pilkey W (1998b): Dynamic injury tolerances for long bones of the female upper extremity. In: Proceedings of IRCOBI Conference, pp. 189–201

Duma S, Boggess B, Crandall J, Hurtwitz S, Seki K, Aoki T (2001): Analysis of upper extremity response under side air bag loading. In: Proceedings of 17th ESV Conference, Amsterdam, Paper No. 195

Duma S, Boggess B, Crandall J, Mac Mohan C (2002): Fracture tolerance of the small female elbow joint in compression: the effect of load angle relative to the long axis of the forearm. Stapp Car Crash J 46:195–210

Duma S, Cormier J, Hurst W, Stitzel J, Herring I (2003): The effects of seam design on airbag induced skin abrasions from high-rate shear loading. In: Proceedings of IRCOBI Conference, pp. 95–107

Frampton R, Morris A, Thomas P, Bodiwala G (1997): An overview of upper extremity injuries to car occupants in UK vehicle crashes. In: Proceedings of IRCOBI Conference, pp. 37–51

Hardy W, Schneider L, Reed M, Ricci L (1997): Biomechanical investigation of airbag-induced upper-extremity injuries. In: Proceedings of 41st Stapp Car Crash Conference, SAE 973325, pp. 131–149

Hardy W, Schneider L, Rouhana S (2001): Prediction of airbag-induced forearm fractures and airbag aggressivity. Stapp Car Crash J 45:511–534

Huelke D, Gilbert R, Schneider L (1997): Upper-extremity injuries from steering wheel air bag deployments, SAE 970493

Kallieris D, Rizzetti A, Mattern R, Jost S, Priemer P, Unger M (1997): Response and vulnerability of the upper arm through side air bag deployment. In: Proceedings of 41st Stapp Car Crash Conference, SAE 973323, pp. 101–110

Kirkish S, Begeman P, Paravasthu N (1996): Proposed provisional reference values for the humerus for evaluation of injury potential, SAE 962416

Kuppa S, Olson M, Yeiser C, Taylor L, Morgan R, Eppinger R (1997): RAID – an investigative tool to study air bag/upper extremity interactions, SAE 970399

Levine R (2002): Injuries to the extremities. In: Accidental Injury – Biomechanics and Prevention (Eds. Nahum A, Melvin J). Springer, Berlin Heidelberg New York

Messerer O (1880): Uber Elasitzitat and Festigkeit der menschlichen Hnochen. Verlag der J.G. Cotta'schen Buchhandlung, Stuttgart

Otte D (1998): Biomechnics of upper limb injuries of belted car drivers and assessment of avoidance. In: Proceedings of IRCOBI Conference, pp. 203–216

Pintar F, Yoganandan N, Eppinger R (1998): Response and tolerance of the human forearm to impact loading. In: Proceedings of 42nd Stapp Car Crash Conference, SAE 983149

Saul R, Backaitis H, Beebe M, Ore L (1996): Hybrid III dummy instrumentation and assessment of arm injuries during air bag deployment. In: Proceedings of 40th Stapp Car Crash Conference, SAE 962417, pp. 85–94

Schneider L, Hardy W, Reed M (1998): Biomechanical investigation of airbag-induced forearm fractures. In: Proceedings of 3rd World Congress of Biomechanics, Sapporo, Japan

Schoenau E, Neu C, Rauch F, Manz F (2001): The development of bone strength at the proximal radius during childhood and adolescence. J Clin Endocr Metab 86(2):613–619

Schroeder G, Kallieris, Tschaschke U, Scheunert D, Schutz J, Zobel R (1998): Are sidebags dangerous in certain seating positions? In: Proceedings of IRCOBI Conference, pp. 477–483

Segui-Gomez M, Baker S (2002): Changes in injury patterns in frontal crashes: preliminary comparisons of drivers of vehicles model years 1993–1997 to drivers of vehicles 1998–2001. In: Proceedings of 46th Annual Association for the Advancement of Automotive Medicine, pp. 1–14

Sobotta J (1997): Atlas der Anatomie des Menschen. Band 1 and 2, Urban and Schwarzenberg, Munchen, Germany

Sokol Jafredo A, Potier P, Robin S, Le Coz J, Lassau J (1998): Upper extremity interaction with side impact airbag. In: Proceedings of IRCOBI Conference, pp. 485–495

Weber C (1859): Chirugische Erfahrungen und Untersuchungen, Berlin

8. Injury/Trauma Prevention

AGU(1997): Sicherheit von Leichtfahrzeugen. Bericht Sum Forschungsprojekt, Zurich

AGU (2002): Working Group of Accident Mechanics at ETH Zurich, `http://www.agu.ch`

ASTRA (2002): Verordnung uber die technische Anforderungen an Strassenfahrzeuge (VTS). Bundesamt fur Strassen, Berlin

Autoliv (2003): Autoliv, http://www.autoliv.com

Chapline J, Ferguson S, Lillis R, Lund A, Williams A (2000): Neck pain and head restraint position relative to the driver's head in rear-end collisions. Accident Anal Prev 32:287–297

Eichberger A, Geigl B, Fachbbach B, Steffan H, Hell W, Langwieder K (1996): Comparison of different car seats regarding head-neck kinematics of volunteers during rear-end impact. In: Proceedings of IRCOBI Conference, pp. 153–164

Ferrari R (1999): The whiplash encyclopedia. Aspen, Gaithersburg

Ford (2003): Ford Motor Company, http://www.ford.com

Haland Y, Hjerpe E, Lovsund P (1998): An inflatable carpet to reduce the loading of the lower extremities – evaluation by a new sled test method with toepan intrusion. In: Proceedings of ESV Conference, paper no. 98-S1-P-18E

Hell W, Langwider K, Walz F (1998): Reported soft tissue neck injuries after rear-end car collision. In: Proceedings of IRCOBI Conference, pp. 261–274

Hell W, Langwider K, Walz F, Muser M, Kramer H, Hartwig E (1999): Consequences for seat design due to rear-end accident analysis, sled tests and possible test criteria for reducing cervical spine injuries after rear-end collision. In: Proceedings of IRCOBI Conference, pp. 243–259

Hofinger M, Mayrhofer E, Geigl B, Moser A, Steffan H (1999): Reduction of neck injuries by improving the occupant interaction with the seat back cushion. In: Proceedings of IRCOBI Conference, pp. 201–212

IIHS – Insurance Institute for Highway Safety (2001): Head restraints can protect your neck. Status Rep 36(9)

Kessler JW, Hoyt TA, Monk MW (1988): Pedestrian head injury reduction concepts, National Technical Information Service, Springsfield, VA, DOT HS 807 432

Langwieder K, Hell W, Schick S, Muser M, Walz F, Zellmer Z (2000): Evolution of a dynamic seat test standard proposal for a better protection after rear-end impact. In: Proceedings of IRCOBI Conference, pp. 393–409

Lundell B, Jakobsson L, Alfredsson B, Lindstrom M, Simonsson L (1998): The WHIPS seat – a car seat for improved protection against neck injuries in rear-end impacts. In: Proceedings of 16th ESV Conference, Paper No. 98-S7-O-08

Mazda (2003): Mazda Motor Corporation Japan, http://www.mazda.com

Melvin J, Mertz H (2002): Airbag inflation-induced injury biomechanics. In Accidental Injury – Biomechanics and Prevention (Eds. Nahum A, Melvin J). Springer, Berlin Heidelberg New York

Muser M, Waltz F, Zellmer H (2000): Biomechanical significance of the rebound phase in low speed rear end impacts. In: Proceedings of IRCOBI Conference, pp. 411–424

Muser M, Waltz F, Schmitt K-U (2002): Injury criteria applied to seat comparison tests. Traffic Injury Prev 3(3):224–232

Newman J (2002): Biomechanics of head trauma: head protection. In: Accidental Injury – Biomechanics and Prevention (Eds. Nahum A, Melvin J). Springer, Berlin Heidelberg New York

Otte D (2002a): Severity and mechanism of head impacts in car to pedestrian accidents. In: Proceedings of IRCOBI Conference, pp. 329–341

Otte D (2002b): Personal Communication

Schmitt K-U, Muser M (2002): Seat component to prevent whiplash injury. Patent, European Patent Office, EP 02 405 537.9

Schmitt K-U, Muser M, Niederer P (2003): Evaluation of a new visco-elastic foam for automotive applications. J Crashworthiness 8(2):71–80

Schmitt K-U, Beyeler F, Muser M, Niederer P (2003): Visco-elastic foams as head restraint material – experiments and numerical simulations using a BioRID model. Traffic Injury (Private Communication)

Schmitt K-U, Muser M, Heggendorn M, Niederer P, Walz F (2004): Seat component to prevent whiplash injury. In: Proceedings of 18th ESV Conference, paper no. 224

Schmitt K-U, Muser M, Heggendorn M, Niederer P, Walz F (2004): Development of a damping seat slide to prevent whiplash injury. J Automot Eng. In: Proceedings of Institution Mechanical Engineering, 217 Part D, pp. 949–955

Snedeker J. Muser M, Walz F (2003): Assessment of pelvis and upper leg injury risk in car–pedestrian collisions: comparison of accident statistics, impactor tests and a human body finite element model. Stapp Car Crash J 47:437–457

Sturtz G (1986): Experimental simulation of the pedestrian impact. In: Proceedings of 10th ESV Conference, DOT HS 806916

Szabo T, Voss D, Welcher J (2002): Influence of seat foam and geometrical properties on BioRID P3 kinematic response to rear impacts. In: Proceedings of IRCOBI Conference, pp. 87–101

Walz F, Muser M (1995): Biomechanical aspects of cervical spine injuries. In: SAE International Congress and Exhibition, Detroit, Michigan, SAE 950658 in SP-1077

Wiklund C, Lesson H (1998): Saab active head restraint (SAHR) – seat design to reduce the risk of neck injuries in rear impacts, SAE paper 980297

Viano D, Olsen S (2001): The effectiveness of active head restraint in preventing whiplash. J Trauma 51(5):959–969

Zellmer H, Stamm M, Seidenschwang A, Brunner A (2001): Benefit from a neck protection system for aftermarket fitting. In: Proceedings of IRCOBI Conference, pp. 337–338

9. Fractures in Ankle and Foot

Beaugonin M, Haug E (1996): A numerical model of the human ankle/foot under impact loading in inversion and eversion, SAE 962428, pp. 239–249

Beaugonin M, Haug E, Munck G, Cesari D (1995): A preliminary numerical model of the human ankle under impact loading. In: PLEI Conference, Washington, DC

Beaugonin M, Haug E, Munck G, Cesari D (1996): The influence of some critical parameters on the simulation of the dynamic human ankle dorsiflexion response. In: Proceedings of 15th ESV Conference, Melbourne, Australia, May 13–17, SAE 96-S10-W-31

Begeman P (1995): Direct Communication. Wayne State University, Detroit

Begeman PC, Prasad P (1990): Human ankle impact response in dorsiflexion. In: Proceedings of the 34th Stapp Car Crash Conference, SAE, pp. 39–54

Begeman P, Balakrishnan P, Levine R, King A (1993): Dynamic human ankle response to inversion and eversion. In: Proceedings of 37th Stapp Car Crash Conference, SAE 933115

Bharadwaj K, Hollander KW, Mathis C, Sugar TG (2004): Spring over muscle (SOM) actuator for rehabil devices. In: IEEE International Conference on Engineering in Medicine and Biology Society (EMBS)

Blaya JA, Herr H (2004): Adaptive control of a variable-impedance ankle–foot orthosis to assist drop-foot gait. IEEE Trans Neural Syst Rehabil Eng 12(1):24–31

Caldwell DG, Medrano-Cerda G, Bowler C (1997): Investigation of bipedal Robot locomotion using pneumatic muscle actuators. In: IEEE International Conference on Robotics and Automation (ICRA)

Daerden F, Lefeber D (2002): Pneumatic artificial muscles: actuators for robotics and automation. Eur J Mech Environ Eng 47(1):10–21

Deutsch JED, Latonio J, Burdea G, Boian R (2001): Post stroke rehabilitation with the rutgers ankle system: a case study. J Neuroeng Rehabil 10(4): 416–430

Ferris DP, C zerniecki JM, Hannaford B (2001): An ankle–foot orthosis powered by artificial muscles. In: Proceedings of 25th Annual meeting of the American Society of Biomechanics

Hesse S (2004): Development of a robotized walking simulator for gait rehabilitation HapticWalker, URL: `www:biofuture-wettbewerb.de/index.php?index=102/`

Homma K, Fukuda O, Sugawars J, Nagata Y, Usuba M (2003): A wire-driven leg rehabilitation system: development of a 4-dof experimental system. In: Proceedings of IEEE International Conference of Intelligent Advances Mechatronics

Jacob S et al. (1996): Stress in a 3D two arch model of a normal human foot. Mech Res Commun 23(4):387–393

Kinetic Muscles, Inc., URL: `http://www.kineticmuscles.com/`

Koeneman EJ, Schultz R, Wolf SL, Herring DE, Koeneman JB (2004): A pneumatic muscle hand therapy device. In: IEEE International Conference on Engineering in Medicine and Biology Conference (EMBS), pp. 2711–2713

Krebs HL, Hogan N, Aisen ML, Volpe BT (1998): Robot-aided neurorehabilitation. IEEE Tran Rehabil Eng 6(1):2080–2085

Kumar V, Sugar TG, Pfreundschuh G (1992): A three degree-of-freedom in-parallel actuated manipulator. In: RoManSy 9, 9th CISM-IFToMM Symposium on the Theory and Practice of Robot Manipulators

Lafortune MA, Lake MJ (1995): Human pendulum approach to simulate and quantify locomotor impact loading. J Biomech 28–29:1111–1114

Lestina DC, Kuhlmann TP, Keats TE, Maxwell Alley R (1992): Mechanism of fracture in ankle and foot injuries to drivers in motor vehicle. In: Proceedings of 36th Strapp Car Crash Conference, SAE 922515

Lnenburger L, Colombo G, Riener R, Dietz V (2004): Biofeedback in gait training with the robotic orthosis lokomat. In: IEEE Engineering in Medicine and Biology Conference (EMBS), pp. 4888–4891

Mathiowetz V, Kashman N, Volland G, Weber K, Dowe M, Rogers S (1985): Grip and pinch strength: normative data for adults. Arch Phys Med Rehabil 66(2):69–74

Morgan RM, Eppinger RH, Hennessey B (1991): Ankle joint injury mechanism for adults in frontal automotive impact. In: Proceedings of 35th Stapp Car Crash Conference, SAE 912902

Nair P, Jadhav C, Krovi V (2003): Development and testing of a low-cost diagnostic tool for upper limb dysfunction. In: Proceedings of 2003 IEEE International Conference on Intelligent Robots and Systems

Nigg BM (1986): Experimental techniques used in running shoes research. In: Biomechanics of Running Shoes (Ed. Nigg BM). Human Kinetics, Champaign, p. 29

Nishiwaki T, Nasako M (1998): Cushioning simulation of shoes soles at the heel impact. In: Proceedings of Symposium on Sports Engineering, JSME 98-31, pp. 9–12

Pfreundschuh G, Kumar V, Sugar TG (1994): Design and control of a three degree of freedom in-parallel actuated manipulator. J Robotic Syst 11(2):103–115

Portier L, Troseille X, Le Coz JY, Lavaste F, Coltat JC (1993): Lower leg injuries in real world frontal accidents. In: Proceeding of the 28th International IRCOBI Conference on the Biomechanics of Trauma, pp. 57–78

Schenkman M, Bliss ST, Day DL, Kemppainen S, Pratt J (1999): Multisystem model for management of neurologically impaired adults: an update and illustrative case. NeuroReport 24(4):145–157

Su CY, Lin JH, Chien TH, Cheng KF, Sung YT (1994): Grip strength in different positions of elbow and shoulder. Arch Phys Med Rehabil 75(7):812–815

Taub E, Miller NE, Novack TA (1993): Technique to improve motor deficit after stroke. Arch Phys Med Rehabil 74:347–354

Taub E, Crago JE, Burgio LD, Groomes TE, Cook EWR, DeLuca SC, Miller NE (1994): An operant approach to rehabilitation medicine: overcoming learned nonuse by shaping. J Exp Anal Behav 61:281–293

Taub E, Uswatte G, Pidikiti R (1999): Constraint-induced movement therapy: a new family of techniques with broad application to physical rehabilitation – a clinical review. J Rehabil Res Dev 36:237–251

Taub E, Uswatte G, Elber T (2002): New treatments in neurorehabilitation founded on basic research. Nat Rev Neurosci 3:228–236

The Wise Consumer: Understanding Insurance Coverage. URL: `http://www.azapta.org/consumer/inscovg.asp/`

Verrelst B, Van Ham R, Daerden F, Lefeber D (2002): Design of a biped actuated by pleated pneumatic artificial muscles. In: Proceedings of 5th International Conference on Climbing and Walking Robots and the Support Technologies for Mobile Machines

Wandel A, Jorgensen HS, Nakayama H, Raaschou HO, Olsent TS (2000): Prediction of walking function in Stroke patients with initial lower extremity paralysis: the Copenhagen stroke. Arch Phys Med Rehabil 81(6):736–738

Whittle MW (1994): Gait Analysis: An Introduction, 2nd edition. Williams and Wilkins, Baltimore

Yamada H (1970): Strength of Biological Materials (Ed. Evans FG). Williams & Wilkins, Baltimore

Young VL, Pin P, Kramer BA, Gould RB, Nemergt L, Pellowski M (1989): Fluctuation in grip and pinch strength among normal subjects. J Hand Surg (Am) 14(1):125–129

10. Knee Joints and Knee Ligaments

Andriacchi TP, Mikosz RP, Hamption SJ, Galante JO (1983): Model studies of the stiffness characteristics of the human knee joint. J Biomech 16:23–29

Benvenuti JF, Vallotton JA, Meystre JL, Leyvraz PF (1997): Objective assessment of the anterior tibial translation in Lachman test position: comparison between three types of measurement. In: Revision for Knee Surg Sports Trauma Arthro

Blomstrom GL, Livesay GA, Fujle H, Smith BA, Kashiwaguchi S, Woo SLY (1993): Distribution of in situ forces within the human anterior cruciate ligament. In: ASME Bioengineering Conference, pp. 359–362

Brandser EA, Riley MA, Berbaum KS, el-Khoury GY, Bennett DL (1996): MR imaging of anterior cruciate ligament injury: independent value of primary and secondary signs. Am J Roentgenol 167:121–126

Brown TR, Quinn SF, Wensel JP, Kim JH, Demlow T (1995): Diagnosis of popliteus injuries with MR imaging. Skeletal Radiol 24:511–514

Buckwalter KA, Pennes DR (1990): Anterior cruciate ligament: oblique sagittal MR imaging. Radiology 175:276–277

Buckwalter KS, Braunstein EM, Janizek DB, Vahey TN (1993): MR imaging of meniscal tears: narrow versus conventional window width photography. Radiology 187:827–830

Burke BJ, Escobedo DM, Wilson AJ, Hunter JC (1989): Chondrocalcinosis mimicking a meniscal tear on MR imaging: a case report. Am J Roentgenol 170:69–70

Campbell SE, Sanders TG, Morrison WB (2001): Magnetic resonance imaging of meniscal cysts: incidence, location and associated findings [abstract]. Am J Roentgenol 176(Suppl 3):85–86

Campos JC, Chung CB, Lektrakul N, Pedowitz R, Trudell D, Yu J et al. (2001): Pathogenesiss of the Second fracture: anatomic and MR imaging evidence of an iliotibial tract or anterior oblique band avulsion. Radiology 219:381–386

Cobby MJ, Schweitzer ME, Resnick D (1992): The deep lateral femoral notch: an indirect sign of a torn anterior cruciate ligament. Radiology 184:855–858

Cotton A, Delfaut E, Demondion X, Lapegue F, Boukhhelifa M, Boutry N et al. (2000): MR imaging of the knee at 0.2 and 1.5 T: correlation with surgery. Am J Roentgenol 174:1093–1097

Cowins SC (1989): Bone Mechanics. CRC, Boca Raton

Crues JV, Mikn J, Levy TL, Lotysch M, Stoller DW (1987): Meniscal tears of the knee: accuracy of magnetic resonance imaging. Radiology 164:445–448

De Smet AA, Graf BK (1994): Meniscal tears missed on MR imaging: relationship to meniscal tear patterns and anterior cruciate ligament tears. Am J Roentgenol 162:905–911

De Smet AA, Norris MA, Yandow DR, Quintana FA, Graf BK, Keene LS (1993): MR diagnosis of meniscal tears of the knee: importance of high signal in the meniscus that extends to the surface. Am J Roentgenol 161:101–107

De Smet AA, Asinger DA, Johnson RL (2001): Abnormal superior popliteomeniscal fascicle and posterior pericapsular edema: indirect MR imaging signs of a lateral meniscal tear. Am J Roentgenol 176:63–66

Dietz GW, Wilcox DM, Montgomery JB (1986): Segond tibial condyle fracture: lateral capsular ligament avulsion. Radiology 159:467–469

Dillon EH, Pope CF, Jok1 P, Lynch JK (1991): Follow-up of grade 2 meniscal abnormalities in the stable knee. Radiology 181:849–852

Duncan JB, Hunter R, Purnell M, Freeman J (1995): Mensical injuries associated with actue anterior cruciate ligament tears in alpine skiers. Am J Sports Med 23:170–172

Durselen L, Claes L, Kiefer H (1996): The influence of muscle forces and external loads on cruciate ligament strain. Am J Sports Med 23:129–136

Fruensgaard S, Johannsen HV (1989): Incomplete ruptures of the anterior cruciate ligament. J Bone Joint Surg 71-B:526–530

Graf BK, Cook DA, DeSmet AA, Keene JS (1993): Bone bruises on magnetic resonance imaging evaluation of anterior cruciate ligament injuries. AM J Sports Med 21:220–223

Grover JS, Bassett LW, Gross ML, Seeger LL, Finerman GA (1990): Posterior cruciate ligament MR imaging. Radiology 174:527–530

Ha TP, Li KC, Beaulieu CF, Bergman G, Chen IY, Eller DJ et al. (1998): Anterior cruciate ligament injury: fast spin-echo MR imaging with arthroscopic correlation in 217 examinations. Am J Roentgenol 170:1215–1219

Haramati N, Staron RB, Rubin S et al. (1993): The flipped meniscus sign. Skeletal Radio1 22:273–277

Harper KA, Grood ES (1993): A three dimensional finite element model of an ACL reconstruction. In: ASME Bioengineering Conference, pp. 592–595

Heegard JH, Leyvraz PF, van Kampen A, Takotomanana L, Rubin PJ, Blankevoort L (1994): Influence of soft structures on patellar three-dimensional tracking. Clin Orthop 229:235–243

Helms CA, Fritz RC, Garvin GJ (1995): Plantaris muscle injury: evaluation with MR imaging. Radiology 195:201–203

Hodler J, Haghighii P, Pathria MN, Trudell D, Resnick D (1992): Menisci changes in the elderly: correlation of MR imaging and histologic findings. Radiology 184:221–225

Jee WH, Choe BY, Kim JM, Song HH, Choi KH (1998): The plica syndrome: diagnostic value of MRI with arthroscopic correlation. J Comput Assist Tomogr 22:814–818

Johnson DL, Urban WP Jr, Caborn DN, Vanarthos WJ, Carlson CS (1998): Articular cartilage changes seen with magnetic resonance imaging-detected bone bruises associated with acute anterior cruciate ligament rupture. AM J Sports Med 26:409–414

Justice WW, Quinn SF (1995): Error patterns in the MR imaging evaluation of menisci of the knee. Radiology 196:617–621

Kaplan PA, Walker CW, Kilcoyne RF, Brown DE, Tusek D, Dussault RG (1992): Occult fracture patterns of the knee associated with anterior cruciate ligament tears: assessment with MR imaging. Radiology 183:835–838

Khan KM, Bonar F, Desmond PM, Cook JL, Young DA, Visentini PJ et al (1996): Patellar tendinosis (jumper's knee): findings at histopathologic examination, US and MR imaging. Victorian Institute of Sport Tendon Study Group. Radiology 200:821–827

Kornick J, Trefelner E, McCarthy S, Lange R, Lynch K, Joki P (1990): Meniscal abnormalities in the asymptomatic population at MR imaging. Radiology 177:463–465

LaPride RF, Burnett QM II, Veenstra MA, Hodgman CG (1994): The prevalence of abnormal magnetic resonance imaging findings in asymptomatic knees: with correlation of magnetic resonance imaging to arthroscopic findings in symptomatic knees. Am J Sports Med 22:739–745

Lecas LK, Helms CA, Kosarek FJ, Garret WE (2000): Inferiorly displaced flap tears of the medial meniscus: MR appearance and clinical significance. Am J Roentgenol 174:161–164

Lee K, Siegel MJ, Lau DM, Hildebolt CF, Matava MJ (1999): Anterior cruciate ligament tears: MR imaging-based diagnosis in a pediatric population. Radiology 213:697–704

Lee W, McCauley TR, Galloway MT, Lynch K, Joki P (2000): RSNA grade 2C signal of the meniscus at MR imaging: clinical significance [Abstract]. Radiology 217(Suppl 1):190

Lerman JE, Gray DS, Shweitzer ME, Bartolozzi A (1995): MR evaluation of the anterior cruciate ligament: value of axial images. J Comput Assist Tomogr 19:604–607

Magee TH, Hinson GW (1998): MRI of meniscal bucket-handle tears. Skeletal Radio1 27:495–499

Maurer EJ, Kaplan PA, Dussault RG, Diduch DR, Schuett A, McCue FC et al (1997): Acutely injured knee: effect of MR imaging on diagnostic and therapeutic decisions. Radiology 204:799–805

McLoughlin RF, Raber El, Vellet AD, Wiley JP, Bray RC (1995): Patellar tendonitis: MR imaging features, with suggested pathogenesis and proposed classification. Radiology 197:843–848

Miller TT, Gladden P, Staron RB, Henry JH, Feldman F (1997): Posterolateral stabilizers of the knee: anatomy and injuries assessed with MR imaging. Am J Roentgenol 169:1641–1647

Miller MD, Osborne JR, Gordon WT, Hinkin DT, Brinker MR (1998): The natural history of bone bruises: a prospective study of magnetic resonance imaging detected trabecular microfractures in patients with isolated medial collateral ligament injuries. Am J Sports Med 26:15–19

Mink JH, Deutsch AL (1989): Occult cartilage and bone injuries of the knee: detection, classification and assessment with MR imaging. Radiology 170:823–829

Mommersteeg TJA, Blankevoort L, Huiskes R, Kooloos JGM, Kauer JMG (1996): Characterization of the mechanical behavior of human knee ligaments: a numerical–experimental approach. J Biomech 29:151–160

Muhlle C, Ahn JM, Yeh L, Bergman GA, Boutin RD, Schweitzer M et al. (1999): Iliotibial band friction syndrome: MR imaging findings in 16 patients and MR arthographic study of six cadaveric knees. Radiology 212:103–110

Munshi M, Davidson M, MacDonald PB, Froese W, Sutherland K (2000): The efficacy of magnetic resonance imaging in acute knee injuries. Clin J Sports Med 10:34–39

Murphy BJ, Smith RL, Uribe JW, Janecki CJ, Hechtman KS, Mangasarian RA (1992): Bone signal abnormalities in the posterolateral tibia and lateral femoral condyle in complete tears of the anterior cruciate ligament: a specific sign? Radiology 182:221–224

Pioletti DP (1997): Viscoelastic properties of soft tissues: application to knee ligaments and tendons. PhD Thesis, EPFL

Pioletti DP, Heegaard JH, Rakotomanana RL, Leyvraz PE, Blankevoort L (1995): Experimental and mathematical methods for representing relative surface elongation of the ACL. J Biomech 28:1123–1126

Popp JE, Yu JS, Kaeding CC (1997): Recalcitrant patellar tendonitis: magnetic resonance imaging, histologic evaluation and surgical treatment. Am J Sports Med 25:218–222

Roberts CS, Cummings JF, Grood ES, Noyes FR (1994): In vivo measurement of human anterior cruciate ligament forces during knee extension exercises. In: 40th ORS, New Orleans, 84-15

Robertson PL, Schweitzer ME, Bartolozzi AR, Ugoni A (1994): Anterior cruciate ligament tears: evaluation of multiple signs with MR imaging. Radiology 193:829–834

Rubin DA, Britton CA, Towers JD, Harner CD (1996): Are MR imaging signs of meniscocapsular separation valid? Radiology 201:829–836

Rubin DS, Kettering JM, Towers JD, Britton CA (1998): MR imaging of knees having isolated and combined ligament injuries. Am J Roentgenol 170:1207–1213

Ruff C, Weingardt JJP, Russ PD et al. (1998): MR imaging patterns of displaced meniscus injuries of the knee. Am J Roentgenol 170:63–67

Ryu KN, Kim IS, Kim EJ, Ahn JW, Bae DK, Sartoris DJ et al. (1998): MR imaging of tears of discoid lateral menisci. Am J Roentgenol 171:963–967

Sanders TG, Linares RC, Lawhorn KW et al. (1999): Oblique meniscomeniscal ligament: another potential pitfall for a meniscal tear–anatomic description and appearance at MR imaging in three cases. Radiology 213:213–216

Sanders TG, Medynski MA, Feller JF, Lawhorn KW et al. (2000): Bone contusion patterns of the knee at MR imaging: footprint of the mechanism of injury. Radiographics 20(S):135–151

Schnarkowski P, Tirman PF, Fuchigami KD, Crues JV, Butler MG, Genant HK (1995): Meniscal ossicle: radiographic and MR imaging findings. Radiology 196:47–50

Schweitzer MS, Tran D, Deely DM, Hume EL (1995): Medial collateral ligament injuries: evaluation of multiple signs, prevalence and location of associated bone bruises and assessment with MR imaging. Radiology 194:825–859

Simonian PT, Sussmann PS, Wickiewicz TL, Potter HG, van Trommel M, Weiland-Holland S et al. (1997): Popliteomeniscal fasciculi and the unstable lateral meniscus: clinical correlation and magnetic resonance diagnosis. Arthroscopy 13:590–596

Smith DK, May DA, Phillips P (1996): MR imaging of the anterior cruciate ligament: frequency of discordant findings on sagittal–oblique images and correlation with arthoscopic findings. Am J Roentgenol 166:411–413

Snearly WN, Kaplan PA, Dussault RG (1996): Lateral-compartment bone contusions in adolescents with intact anterior cruciate ligaments. Radiology 198:205–208

Sonin AH, Fitzgerald SW, Friedman H, Hoff FL, Hendrix RW, Rogers LF (1994): Posterior cruciate ligament injury: MR imaging diagnosis and patterns of injury. Radiology 190:455–458

Stark JE, Siegel MJ, Weinberger E, Shaw DW (1995): Discoid menisci in children: MR features. J Comput Assist Tomogr 19:608–611

Suarez-Almazor ME, Kaul P, Kendall CJ, Saunders LD, Johnston DW (1999): The cost-effectiveness of magnetic resonance imaging for patients with internal derangement of the knee. Int J Technol Assess Health Care 15:392–405

Takai S, Woo SLY, Livesay GA, Adams DJ, Fu FH (1993): Determination of the in situ loads on the human anterior cruciate ligament. J Orthop Res 11:686–695

Takeda Y, Ikata T, Yoshida S, Takai H, Kashiwaguchi S (1998): MRI high-signal intensity in the menisci of asymptomatic children. J Bone Joint Surg (Br) 80:463–467

Tuite MJ, DeSmet AA, Swan JS, Keene JS (1995): MR imaging of a meniscal ossicle. Skeletal Radio1 24:543–545

Tyson LL, Daughters TC Jr, Ryu RK, Crues JV III (1995): MRI appearance of meniscal cysts. Skeletal Radio1 24:421–424

Umans H, Wimpfheimer O, Haramati N, Applbaum YH, Adller M, Bosco J (1995): Diagnosis of partial tears of the anterior cruciate ligament of the knee: value of MR imaging. Am J Roentgenol 165:893–897

Vahey TN, Broome DR, Kayes KJ, Shelbourne KD (1991): Acute and chronic tears of the anterior cruciate ligament: differential features at MR imaging. Radiology 181:251–253

Vande Berg BC, Poilvache P, Duchateau F, Lecouvet FE, Dubue JE, Maldague B et al. (2001): Lesions of the menisci of the knee: value of MR imaging criteria for recognition of unstable lesions. Am J Roentgenol 176:771–776

Vellet AD, Marks PH, Fowler PJ, Munro TG (1991): Occult posttraumatic osteochondral lesions of the knee: prevalence, classification and short term sequelae evaluated with MR imaging. Radiology 178:271–276

Virolainen H, Visuri T, Kuusela T (1993): Acute dislocation of the patella: MR findings. Radiology 189:243–246

Wascher DC, Markolf KT, Shapiro MS, Finerman GA (1993): Direct in vitro measurement of forces in the cruciate ligaments. Part 1. The effect of multiplane loading in the intact knee. J Bone Joint Surg 75(3):377–386

Weiss JA (1994): A constitutive model and finite element representation for transversely isotropic soft tissues. PhD Thesis, University of Utah

Wright DH, De Smet AA, Norris M (1995): Bucket-handle tears of the medial and lateral menisci of the knee: value of MR imaging in detecting displaced fragments. AM J Roentgenol 165:621–625

Yao L, Gentili A, Petrus L, Lee JK (1995): Partial ACL rupture: an MR diagnosis? Skeletal Radiol 24:247–251

Yu JS, Cosgarea AJ, Kaeding CC, Wilson D (1997): Meniscal flounce MR imaging. Radiology 203:513–515

11. Trauma of Sports Injuries: Computerized Approach

Albright J, Torl P, Shaw R et al. (1978): Clinical study of baseball pitchers: correlation of injury to the throwing arm with method of delivery. Am J Sports Med 6:15–21

Altchek D, Hyman J, Williams R et al. (2000): Management of medial collateral ligament injuries of the elbow in throwers. Tech Shoulder Elbow Surg 1:73–81

Altman R, Latta L, Keer R et al. (1995): Effect of nonsteroidal anti inflammatory drugs on fracture healing: a laboratory study in rats. J Orthop Trauma 9:392–400

American Academy of Pediatrics (1988): Recommendations for participation in competitive sports. Physician Sportsmed 16:165–167

Anderson B, Perry C, Obergefell L, Rizer A, Ziejewski M (1997): Modeling of human neck response to vertical impact. In: SAFE Symposium, Phoenix, Arizona

Andrews J (1978): Bony injuries about the elbow in the young throwing athlete. Instr Course Lect 34:323–331

Andrews J, Fleisig G (1996): How many pitches should I allow my child to throw? USA Baseball News 4:5

Atkin DM, Fithian DC, Marangi KS et al. (2000): Characteristics of patients with primary acute lateral patella dislocation and their recovery within the first 6 months. Am J Sports Med 28:472

Barnes BC, Cooper L, Kirkendall DT, McDermott PT, Jordan BD, Garrett WE (1998): Concussion history in elite male and female soccer players. Am J Sports Med 26:433–438

Benjamin J, Bried J, Dohm M et al. (1987): Biomechanical evaluation of various forms of fixation of transverse patella fractures. J Orthop Trauma 1:219

Binnet MS, Yilmaz C, Karakas A et al. (2001): Arthroscopic fixation of intercondylar eminence fractures using a 4-portal techbnique. Arthroscopy 17:450

Boden BP, Kirkendall DT, Garrett WE (1998): Concussion incidence in elite college to soccer players. Am J Sports Med 26:238–241

Bostman OM (1990): Refractures after removal of a condylar plate from the distal third of the femur. J Bone Joint Surg 72:1013

Bostrom A (1972): Fractures of the patella: a study of 422 patellar fractures. Acta Orthop Scand 143(Suppl):1

Bradley J (1994): Upper Extremity: Elbow Injuries in Children and Adolescents (Eds. Stanitski CL, Drez D Jr, DeLee J). W.B. Saunders, Philadelphia

Brogdon B, Crow N (1960): Little Leaguer's elbow. Am J Roentgenol 83:671–675

Bro-Nielsen M (1996): Mvox: interactive 2–4D medical image and graphics visualization software. In: Proceedings of Computer Assisted Radiology (CAR'96). See also: `http://www.imm.dtu.dk/mvox/`

Bro-Nielsen M (1996): Mvox: interactive 2–4D medical image and graphics visualization software. In: Proceedings of Computer Assisted Raiology (CAR'96)

Bro-Nielsen M, Cotin S (1996): Real-time volumetric deformable models for surgery simulation using finite elements and condensation. Comput Graph Forum 15(3):57–66 (Eurographics'96)

Bro-Nielsen M, Cotin S (1996): Real-time volumetric deformable models for surgery simulation using finite elements and condensation. Comput Graph Forum 15(3):57–66 (Eurographics'96)

Budoff J, Nirschl M (2001): Resection and repair of lateral tennis elbow. Oper Tech Sports Med 9(4):211–216

Burkhart SS, Peterson HA (1979): Fractures of the proximal tibial epiphysis. J Bone Joint Surg 61A:996

Cash JC, Hughston JC (1988): Treatment of acute patellar dislocation. Am J Sports Med 16:244

Cheng H, Obergefell L, Rizer A (1994): Generator of Body Data (GEBOD) Manual. Armstrong Laboratory Technical Report AL/CF-TR-1994-0051, Wright-Patterson Air Force Base, OH

Conway J, Lowe W (2001): Elbow medial ulnar collateral ligament reconstruction. Oper Tech Sports Med 9(4):196–204

Conway J, Jobe F, Glousman R et al. (1992): Medial instability of the elbow in throwing athletes. Treatment by repair or reconstruction of the ulnar collateral ligament. J Bone Joint Surg Am 74:67–83

Cotin S, Delingette H, Clement JM, Tassetti V, Marescaux J, Ayache N (1996a): Volumetric deformable models for simulation of laparascopic surgery. In: Proceedings of Computer Assisted Radiology (CAR'96), pp. 793–798

Cotin S, Delingette H, Clement JM, Bro-Nielsen M, Ayache N, Marescaux J (1996b): Geometrical and physical representations for a simulator of hepatic surgery. In: Proceedings of MMVR-4'96

Cotin S, Delingette H, Clement MJ, Tassetti V, Marescaux J, Ayache N (1996c) Volumetric deformable models for simulation of laparascopic surgery. In: Proceedings of Computer Assisted Radiology (CAR'96), pp. 793–798

Cotin S, Delingette H, Cl'ement JM, Bro-Nielsen M, Ayache N, Marescaux J (1996d): Geometrical and physical representations for a simulator of hepatic surgery. In: Proceedings of MMVR-4'96

Cover SA, Ezquerra NF, O'Brien JF, Rowe R, Gadacz T, Palm E (1993a): Interactively deformable models for surgery simulation. IEEE Comput Graph Appl 13(6):68–75

Cover SA, Ezquerra NF, O'Brien JF, Rowe R, Gadacz T, Palm E (1993b) Interactively deformable models for surgery simulation. IEEE Comput Graph Appl 13(6):68–75

Dainer RD, Barrack RL, Buckley SL et al. (1988): Arthroscopic treatment of acute patella dislocation. Arthroscopy 4:267

Delp SL (1990): A computer graphics system to analyze and design musculoskeletal reconstructions of the lower limp. PhD Dissertation, Stanford University, Stanford, CA

Desio SM, Burks RT, Bachus KN (1998): Soft tissue restraints to lateral patellar translation in the human knee. Am J Sports Med 26:59

DiGiovane M, Jobe F, Pink M et al. (1992): An electromyographic analysis of the upper extremity in pitching. J Shoulder Elbow Surg 1:15–25

Durkin JL (1998a): The prediction of body segment parameters using geometric modelling and dual photon absorptiometry. Master's Thesis, McMaster University, Hamilton, Ontario

Durkin JL (1998b): The prediction of body segment parameters using geometric modeling and dual photon absorptiometry. Master's Thesis, McMaster University, Hamilton, Ontario

Estep C, Schneck DJ (1992): Modelling of the Human Head/Neck System Using Rigid Body Dynamics. Technical Report VPI-E-92–18, Virginia Polytechnic Institute and State University, College of Engineering, Virginia

Fleisig G, Andrews JR, Dillman C et al. (1995): Kinetics of baseball pitching with implications about injury mechanisms. Am J Sports Med 23:233–239

Geiger B (1993a): Three-dimensional modeling of human organs and its application to diagnosis and surgical planning. INRIA Technical Report, p. 2105

Geiger B (1993b): Three-dimensional modeling of human organs and its application to diagnosis and surgical planning. INRIA Technical Report 2105, December 1993

Geoffe WL, Ferrier GD, Rogers J (1994): Global optimization of statistical functions with simulated annealing. J Econometrics 60:65–99

Gerbino P II, Waters P (1998): Elbow Injuries in the Young Athlete (Eds. Drez D Jr, Delee J). W.B. Saunders, Philadelphia, pp. 259–267

Glassman S, Rose S, Dimar J, Puno RM, Campbell MJ, Johnson JR (1998): The effect of postoperative nonsteroidal anti-inflammatory drug administration on spinal fusion. Spine 23:834–838

Grana WA (1995): Physeal fractures about the knee. J Am Acad Orthop Surg 3:63–69

Halbrecht JL, Jackson DW (1993): Acute dislocation of the patella. In: The Patellofemoral Joint (Eds. Fox JM, Del Pizzo W). McGraw-Hill, New York, p. 123

Hanavan EP (1964a): A mathematical model of the human body. AMRL-TR-64–102, Aerospace medical research Laboratories, Wright-Patterson Air Force Base, Ohio

Hanavan EP (1964b): A mathematical model of the human body. AMRL-TR-64–102. Aerospace Medical Research Laboratories, Wright-Patterson Air Force Base, Ohio

Hanel DP, Burdge RE (1981): Consecutive indirect patella fractures in an adolescent basket ball player. Am J Sports Med 9:215

Harilainen A, Myllynen P (1988): Operative treatment in acute patella dislocation: radiologic predisposing factors, diagnosis and results. Am J Knee Surg 1:178

Hawkins RJ, Bell RH, Anisette G (1986): Acute patella dislocations. The natural history. Am J Sports Med 14:117

Hoffman A (1985): Radiography of the Pediatric Elbow. W.B. Saunders, Philadelphia

Jennings JE (1985): Arthroscopic management of tibial plateau fractures. Arthroscopy 1:160

Jordan SE, Green GA, Galanty HL, Mandelbaum BR, Jabour BA (1996): Acute and chronic brain injury in United States national team soccer players. Am J Sports Med 24:205–210

Kardestuncer H (1987a): Finite Element Handbook. McGraw-Hill, London, ISBN 0-07-033305-X

Kardestuncer H (1987b): Finite Element Handbook. McGraw-Hill, New York, ISBN 0–07-033305-X

Kasser J, Richards K, Millis M (1990): The triceps dividing approach to open reduction of complex distal humerus fractures in adolescents: a cybex evaluation of triceps function and motion. J Pediatr Orthop 10:93–96

Kendall NS, Hsu SC, Chan KM (1992): Fracture of the tibial spine in adults and children. A review of 31 cases. J Bone Joint Sug 74B:848

Kocher MS, Michel LJ (2001): The pediatric knee: evaluation and treatment. In: Surgery of the Knee (Eds. Install JN, Scott WN). Churchill Livingstone, Philadelphia, 1356–1397

Koval JJ, Kummer FJ, Bharam S et al. (1996): Distal femoral fixation: a laboratory comparison of the 95 degrees plate, antegrade and retrograde inserted reamed intramedullary nails. J Orthop Trauma 10:378

Kuhn Ch, Kuhnapfel U, Krumm H-G, Neisius B (1996a): A virtual reality based training system for minimally invasive surgery. In: Proceedings of Computer Assisted Radiology (CAR'96), pp. 764–769

Kuhn Ch, Kuhnapfel U, Krumm H-G, Neisius B (1996b): A virtual reality based training system for minimally invasive surgery. In: Proceedings of Computer Assisted Radiology (CAR'96), pp. 764–769

Kulick MI, Smith S, Hadler K (1986): Oral ibuprofen: evaluation of its effect on peritendinous adhesions and breaking strength of a tenorrhaphy. J Hand Surg 11A:110–120

Laurent L, Lindstrom B (1956): Osteochondrosis of the capitellum of the humeri (Panner's disease). Acta Orthop Scand 26:111–119

Lindholm I, Osterman K, Vankka E (1980): Osteochondritis dissecans of the elbow, ankle and hip: a comparison study. Clin Orthop 148:245–253

Lyman S, Fleisig G, Waterbor J et al. (2001): Longitudinal study of elbow and shoulder pain in youth baseball pitchers. Med Sci Sports Exer 33(1):1803–1810

MacEwen G, Kasser J, Heinrich S (1993): Pediatric fractures: a practical approach to assessment and treatment. Williams and Wilkins, Baltimore, MD

Maffulli N, Chan D, Aldridge M (1992): Overuse injuries of the olecranon in young gymnasts. J Bone Joint Surg (Br) 74:305–309

Mazou CG, Guanche CA, Vrahas MS (1999): Arthroscopic management of tibial plateau fractures: an unselected series. Am J Orthop 28:508

McCaroll JR (1993): Fracture of the patella during a golf swing following reconstruction of the anterior cruciate ligament. Am J Sports Med 11:26

McLenan JG (1982): The role of arthroscopic surgery in the treatment of fracture of intercondylar eminence of the tibia. J Bone Joint Surg 64B:477

Merril JR, Preminger GM, Babayan R, Roy RT, Merril GL (1994a): Surgical simulation using virtually reality technology: design, implementation and implications. In: Surgical Technology III, pp. 53–60

Merril JR, Preminger GM, Babayan R, Roy RT, Merril GL (1994b) Surgical simulation using virtual reality technology: design, implementation, and implications. In: Surgical Technology III, pp. 53–60

Meyers MH, McKeever FM (1978): Fracture of the intercondylar eminence of the tibia. J Bone Joint Surg 41A:209

Miller HL, Schneck DJ (1993): Biodynamic Responses to Emergency Ejections Under Conditions of Added Head Mass. Technical Report VPI-E-93–08, Virginia Polytechnic Institute and State University, College of Engineering, Virginia

Mishra D, Friden J, Schmitz M et al. (1995): Anti-inflammatory medication after muscle injury. J Bone Joint Surg (Am) 77:1510–1519

Morrey B, An K, Stormont T (1988): Force transmission through the radial head. J Bone Joint Surg Am 70:250–256

Mummery WK, Spence JC, Vincenten JA, Voaklander DC (1998): A descriptive epidemiology of sport and recreation injuries in a population-based sample: results from the Alberta Sport and Recreation Injury Survey (ASRIS). Can J Public Health 89:53–56

Obergefell LA, Gardner TR, Kaleps I, Fleck JT (1988): Articulated Total Body Model Enhancements, Vol. 2: Users' Guide. Armstrong Laboratory Technical Report AAMRL-TR-88–043, Wright-Patterson Air Force Base, OH

Panner H (1929): A peculiar affection of the carpitulum humri, resembling Calve Perthis' disease of the hip. Acta Radiol 10:234–242

Pappas A (1982): Elbow problems associated with baseball during childhood and adolescence. Clin Orthop 164:30–41

Perry CE, Rizer A, Smith J, Anderson B (1997): Biodynamic modeling of human neck response during vertical impact. (Private Communication)

Pimpalnerker A, Balasubramaniam G, Young S et al. (1998): Type four fractures of the medial epicondyle: a true indication for surgical intervention. Injury 29:751–756

Powell JW, Barber-Foss KD (1999): Traumatic injury in high school athletes. JAMA 10:958–963

Sallay PI, Poggi J, Speer KP (1996): Acute dislocation of the patella. A correlative pathoanatomic study. Am J Sports Med 24:52

Sandelin J, Santavirta S (1991): Occurrence and epidemiology of sports injuries in Finland. Ann Chir Gynaecol 80:95–99

See also: `http://www.imm.dtu.dk/mvox/`

Shelton WR, Canale TS (1979): Fractures of the tibia through the proximal tibial epiphyseal cartilage. J Bone Joint Surg 61A:169

Simonian PT, Mann FA, Mandt PR (1995): Indirect forces ad patella fractures after anterior cruciate ligament reconstruction with the patellar ligament: case report. Am J Knee Surgery 8:60–64

Smith S, Cramer K, Kargus D et al. (1997): Early complications in the operative treatment of patella fracture. J Orthop Trauma 11:183

van Soest AJ, Bobbert MF (1993): The contribution of muscle properties in the control of explosive movements. Biol Cybern 69:195–204
Thomson NL (1993): Fractures including traumatic, stress and bipartite patella. In: The Patellofemoral Joint (Eds. Fox JM, Del Pizzo W). McGraw-Hill, New York, p. 217
Tibone JE, Stephan JL (1981): Bilateral fractures of the inferior poles of the patellae in a basketball player. Am J Sports Med 9:215
Vaaainionpaa S, Laasonen E, Sivennoinen T et al. (1990): Acute dislocation of the patella. A prospective review of operative treatment. J Bone Joint Surg 72B:366
Viola R, Vianello MD (1999): Three cases of patella fracture in 1320 anterior cruciate ligament reconstructions with bone–patella tendon–bone autograft. Arthroscopy 15:93
Weaver JK (1977): Bipartite patella as a cause of disability in the athlete. Am J Sports Med 5:137
Werner S, Fleisig G, Dillman C et al. (1993): Biomechanics of the elbow during baseball pitching. J Orthop Sports Phys Ther 17:274–278
Willis RB, Blokker C, Stoll TM et al. (1993): Long-term follow-up of anterior tibial eminence. J Pediatr Orthop 13:361
Wilson J (1960): The treatment of fractures of the medial epicondyle of the humerus. J Bone Joint Surg (Br) 42:778–781
Winter DA (1990a): Biomechanics and Motor Control of Human Movement. Wiley, New York, pp. 51–64
Winter DA (1990b): Biomechanics and Motor Control of Human Movement. Wiley, New York, pp. 51–64
Wright IC, Neptune RR, van den Bogert AJ, Nigg BM (1998a): Passive regulation of impact forces in heel-toe running. Clin Biomech 13:521–531
Wright IC, Neptune RR, van den Bogert AJ, Nigg BM (1998b): The effects of ankle compliance and flexibility on ankle sprains. Med Sci Sports Exer (Private Communication)
Zaltz I, Waters P, Kasser J (1996): Ulnar nerve instability in children. J Pediatr Orthop 16(5):567–569
Zatsiorsky V, Seluyanov V, Chugunova L (1990a): Methods of determining mass-inertial characteristics of human body segments. In: Contemporary Problems of Biomechanics (Eds. Chernyi GG, Regirer A). Mir, Moscow, pp. 273–291
Zatsiorsky V, Seluyanov V, Chugunova L (1990b): Methods of determining mass-inertial characteristics of human body segments. In: Contemporary Problems of Biomechanics (Eds. Chernyi GG, Regirer A). Mir, Moscow, pp. 273–291

12. Soft Tissues and Argonomics

Ascenzi A et al. (1977): Initial studies on the crystallinity of the mineral fraction and Ash content of isolated human and bovine osteons differing in their degree of calcification. Calcified Tissue Int. 23, 7–11. Springer-Verlag

Ascenzi A et al. (1978): X-ray diffraction and electron microscope study of Osteons during Calcification. Calcified Tissue International, 9:2–134. Springer-Verlag

Boyde A, Hobdel MH, (1969): Scanning electron microscopy of primary membrane bone. Cell and Tissue Research, Springer-Verlag

Boyde A (1972): Scanning electron microscope studies of bone. The Biochemistry and Physiology of bone

Boyde A (1980): Evidence against "Osteocytic osteolysis". Bone 25:239–255

Boyde A, Jones S (1998): Aspects of anatomy and development of bone the nm, um, and mm hierarchy. Advances in Organ Biology, JAI press Inc. pp. 3–44

Bullinger H, Solf J (1979): Ergonomische Arbeitsmittelgestaltung I, Systematik. Bundersanstalt Fur Arbeitsschutz und Unfallforschung, Dortmund (in German)

Chow W, Odell E (1978): Deformations and stresses in soft body tissues of a sitting person. J Biomed Eng 100:79–87

Enlow DH (1969): The bone of reptiles. Biology of the reptilia. Academic Press, New York

Frasca P et al. (1977): Collagen fiber orientations in human secondary osteons. Acta Anat 98:1–13

Horvath I, Vergeest J (1998): Theoretical fundamentals of natural representation of shapes generated with gestural devices. In: Proceeding of the 2nd International Symposium on TMCE (Eds. Horvath I, Taleb-Bendiab A), Manchester, UK, pp. 393–409

Kim E et al. (1995): Clustering of Shaker-type K channels by interaction with a family membrane-associated guanylate, Nature 286, 836–844

Kingsmill VJ et al. (1998): Mineralisation density of human mandibular bone: quantitative back scattered electron image analysis. J. Anat. 192, No. 2, pp. 245–256

Manschot J, Brakkee A (1987a): Characterization of in vivo mechanical skin properties independent of measuring configuration. Bioeng Skin 3:1–10

Manschot J, Brakkee A (1987b): Seasonal variations in the mechanical properties of the human skin. Bioeng Skin 3:25–33

Martin RB, Burr DB (1989): Structure function and adaptation of compact bone. Raven Press, New York

Moes C (2000a): Distance between the points of maximum pressure for sitting subjects. In: Proceedings of the 6th International Design Conference DESIGN2000 (Ed. D. Marjanovic), University of Zagreb, Zagreb, pp. 227–232

Moes C (2000b): Geometric model of the human body. In: Proceedings of the TMCE2000 (Eds. Horvath I, Medland AJ, Vergeest JS), Third International Symposium on Tools and Methods of Competitive Engineering, Delft University Press, Delft, the Netherlands, pp. 79–92

Moes C (2000c): Pressure distribution and ergonomics shape conceptualization. In: Proceedings of the 6th International Design Conference DESIGN2000 (Ed. Marjanovic D), University of Zagreb, Zagreb, pp. 233–240

Moes C (2001): Generation of shape instances for FE modelling of the human body. In: Design Methods for Performance and Sustainability (Eds. Culley S, Duffy A, McMahon C, Wallace K). Proceeding of the 13th International Conference on Engineering Design, ICED01, Professional Engineering Publishing, Bury St Edmunds, Glasgow, pp. 131–138

Mullender et al. (1996): Osteocytes and bone lining cells. Bone 18:109–113

Neville AC (1993): Biology of Fibrous Composites: Development Beyond the Cell membrane. Cambridge University Press

Salo M et al. (1997): Effects of propofol emulsion and thiopentone on T helper cell type-1/type-2 balance in vitro. Anaesthesia, 52, pp. 341–344

Singh H (1978): Embryology of Gymnosperms. Gebruder Bomtraeger, Berlin

Stein GS et al. (1996): Transcriptional control of osteoblast growth and differentiation. Physerv. Physiology Org. Vol. 76, No. 2, pp. 593–629, Physiological Reviews

Weiner S, Price PA (1986): Disaggregation of bone into crystals. Calcif Tissue Int. 39(6):365–75

13. Fracture and Dislocation of Human Parts

Andersen K, Jensen PO, Lauritzen J (1987): Treatment of clavicular fractures. Figure-of-eight bandage versus a simple sling. Acta Orthop Scand 58:71–74

Bigliani LU, Flatow EL, Pollock RG (1996): Fractures of the proximal humerus. Fractures in Adults (Eds. Rockwood CA Jr, Green DP), 4th edition. Lippincott-Raven, Philadelphia

Butters KP (1996): Fractures and dislocations of the scapula. In: Fractures in Adults (Eds. Rockwood CA Jr, Green DP), 4th edition. Lippincott-Raven, Philadelphia

Capo JT, Hastings H II (1999): Metacarpal and phalangeal fractures in athletes. Clin Sports Med 17:491–511

Cooney WP III, Linscheid RL, Dobyns JH (1996): Fractures and dislocation of the wrist. In: Fractures in Adults (Eds. Rockwood CA Jr, Green DP), 4th edition. Lippincott-Raven, Philadelphia

Craig EV (1996): Fractures of the clavicle. In: Fractures in Adults (Eds. Rockwood CA Jr, Green DP), 4th edition. Lippincott-Raven, Philadelphia

Eliff MP (1997): Management of clavicle fractures. Am Fam Physician 55:121–128

Eliff MP, Saultz JW (1993): Fracture care by family physicians. J Am Board Fam Pract 6:179–181

Eliff MP, Hatch RL, Calmbach WL (1998): Fracture Management for Primary care, 1st edition. W.B. Saunders, Philadelphia

Geyman JP, Rosenblatt RA (1982): The content of family practice: current status and future trends. J Fam Pract 15:677–737

Geymann JP, Gordon MJ (1979): Orthopedic problems in family practice: incidence, distribution and curricular implications. J Fam Pract 8:759–765
Green DP, Butler TE (1996): Fractures and dislocations in the hand. In: Fractures in Adults (Eds. Rockwood CA Jr, Green DP), 4th edition. Lippincott-Raven, Philadelphia
Hatch RL, Rosenbaum CI (1994): Fracture care by family physicians. A review of 295 cases. J Fam Pract 38:238–244
Hintermann B, Holzach PJ, Schutz M et al. (1993): Skier's thumb – the significance of bony injuries. Am J Sports Med 21:800–804
Hotchkiss RN (1996): Fractures and dislocation of the elbow. In: Fractures in Adults (Eds. Rockwood CA Jr, Green DP), 4th edition. Lippincott-Raven, Philadelphia
Hutchinson MR, Ahuja GS (1996): Diagnosing and treating clavicle injuries. Physician Sports Med 24:26–36
Jahss S (1938): Fractures of the metacarpals: a new method of reduction and immobilization. J Bone Joint Surg 20:178–186
Kirkwood CR, Clure HR, Brodsky R et al. (1982): The diagnostic content of family practice: 50 most common diagnoses recorded in the WAMI community practices. J Fam Pract 15:485–492
Langford SA, Whitaker JH, Toby EB (1998): Thumb injuries in the athlete. Clin Sports Med 17:553–566
Louis DS, Huebner JJ, Hankin FM (1986): Rupture and displacement of the ulnar collateral ligament of the metacarpophalangeal joint of the thumb: preoperative diagnosis. J Bone Joint Surg 68:1320–1326
McCown I (1959): Boxing injuries. Am J Surg 98:501
Morgan RL, Linder MM (1997): Common wrist injuries. Am Fam Physician 55:857–868
O'Brien ET (1984): Acute fractures and dislocations of the carpus. Orthop Clin North Am 15:237–258
Ogden JA, Ganey TM, Ogden DA (1996): The biological aspects of children's fractures. In: Fractures in Children (Eds. Rockwood CA Jr, Wilkins KE, Beaty JH), 4th edition. Lippincott-Raven, Philadelphia
Posner MA (1977): Injuries to the hand and wrist in athletes. Orthop Clin North Am 8:593–618
Raby N, Berman L, de Lacey G (1995): Accident and Emergency Radiology, 5th edition. W.B. Saunders, Philadelphia
Recht MP, Burk DL Jr, Dalinka MK (1987): Radiology of wrist and hand injuries in athletes. Clin Sports Med 6:811–828
Rettig ME, Dassa GL, Raskin KBB et al. (1998): Wrist fractures in the athlete. Clin Sports Med 17:469–489
Richards RR, Corley FG Jr (1996): Fractures of the shafts of the radius and ulna. In: Fractures in Adults (Eds. Rockwood CA Jr, Green DP), 4th edition. Lippincott-Raven, Philadelphia

Rosenblatt RA, Hart LG, Gamliel S et al. (1995): Identifying primary care disciplines by analyzing the diagnostic content of ambulatory care. J Am Board Fam Pract 8:34–45

Rosenthall L, Hill RO, Chuang S (1976): Observation of the use of 99m Tc-phosphate imaging in peripheral bone trauma. Radiology 119:637

Simon RR, Wolgin M (1987): Subungual hematoma: association with occult laceration requiring repair. Am J Emerg Med 5:302–304

Stanley D, Norris SH (1998): Recovery following fractures of the clavicle treated conservatively. Injury 19:162–164

Stanley D, Trowbridge EA, Norris SH (1988): The mechanism of clavicular fracture. A clinical and biomechanical analysis. J Bone Joint Surg (Br) 70:461–464

Zemel NP, Stark HH (1986): Fractures and dislocations of the carpal bones. Clin Sports Med 5:709–724

14. Soft Tissues and Trauma: Computer Modelling

Ascenzi et al., X-Ray Diffraction on Cyclically Loaded Osteons, Calcified Tissue International, 1998 – Springer

Azar FS, Metazas DN, Millr RT, Schnall MD (2000): Methods for predicting mechanical deformations in the breast during clinical breast biopsy. In: Proceedings of the 26th IEEE Northeast Bioengineering Conference, pp. 63–64

Bogen DK (1987): Strain energy descriptions of biological swelling. I. Single fluid compartment models. J Biomech Eng 109:252–256

Barnes GL, Kostenuik PJ, Gerstenfield LC, Perspective, growth factor regulation of fracture repair, Bone J. Mineral Research, 1999

Castanet M, Lyonnet S, Bonaiti-Pellie C, Polak M, Familial Forms of Thyroid Dysgenesis among Infants with Congenital Hypothyroidism, content.nejm.org, Volume 343:441–442

Chow WW, Odell EI (1978): Deformations and stresses in soft body tissues of a sitting person. J Biomed Eng 100:79–87

Dusty Miller A, Tom Curran, and Inder M. Verma, *c-fos* protein can induce cellular transformation: A novel mechanism of activation of a cellular oncogene, Cell, Vol. 36, 51–60, January 1984

Enlow DH, Principles of bone remodeling, 1963 – Thomas Springfield

Enlow DH, Brown SO, A comparative histological study of fossil and recent bone tissues, part III, Tex J Sc, 1958

Fagan AM, Zhang, Landis S, Smeyne RJ, Silos I, TrkA, But Not TrkC, Receptors are essential for Survival of Sympathetic Neurons In Vivo, Journal of Neuroscience, 1996

Frasca P, Scanning-electron microscopy studies of 'ground substance' in the cement lines, resting lines, hypercalcified rings and reversal lines of human cortical bone, Acta Anat (Basel). 1981; 109(2):115–21

Ganss B, Kim RH and Sodek J, Bone sialoprotein, Critical Reviews in Oral Biology & Medicine, vol 10, 79–98, Copyright © 1999 by International & American Associations for Dental Research

Gibson LJ, The mechanical behaviour of cancellous bone, J Biomech. 1985; 18(5):317–28

Gorski DH, Potentiation of the antitumor effect of ionizing radiation by brief concomitant exposures, Cancer Research, Vol58, Issue 24 5686-5689, 1998

Horvith I (1998): Shifting Paradigms of Computer Aided Design. Delft University of Technology. Faculty of Industrial Design Engineering. Inaugural Speech

Huiskes R et al. (2000): Effects of mechanical forces on maintenance and adaptation of form in trabecular bone. Nature, 405(6787)

Hulmes et al. Microfibrillar structure of type I collagen in situ, 1995) Structure (London) 3, 541–549

Lowenstam HA, Weiner S, On biomineralization, 1989 - Oxford University Press New York

Lozupone E, Favia A, The structure of the trabeculae of cancellous bone. 2. Long bones and mastoid, Calcif Tissue Int, 1990 Jun;46(6):367–72

MARC (2000): MSC Marc Advanced Course. Course Material, MSC Software, Munchen, Germany

Mainwaring, Cosgrove R, Blume H, Ives J, Landis T, vidence for rapid face recognition from human scalp and intracranial electrodes. Neurophysiol 70, 640–654(1993)

McKee MD, Nanci A, Osteopontin at mineralized tissue interfaces in bone, teeth, and osseointegrated implants, Microscopy Research and Technique, 1996

Moes CCM (2000a): Distance between the points of maximum pressure for sitting subjects. In: Proceeding of the 6th International Design Conference DESIGN2000, pp. 227–232

Moes CCM (2000b): Geometric model of the human body. In: Proceedings of the TMCE2000, pp. 79–92

Moes CCM (2000c): Pressure distribution and ergonomics shape conceptualization. In: Proceeding of the 6th International Design Conference DESIGN2000, pp. 233–240

Moes CCM (2002): Estimation of the nonlinear material properties for a finite elements model of the human body. In: Proceedings of the TMCE2002 (in press)

Moes CCM (2003): Modelling the sitting pressure distribution and the location of the points of maximum pressure for body characteristics and rotation of the pelvis. Ergonomics

Moes CCM, Rusak Z, Horvith I (2002): Application of vague geometric representation for shape instance generation of the human body. In: Proceedings of DETC'01, Computers and Information in Engineering Conference, pp. (CDROM:DETC2001/CIE-21298)

Nakamura S, Crowninshield RD, Cooper RR (1981): An analysis of soft tissue loading in the foot – a preliminary report. Bull Prosthet Res 18(BPR 10–35)(1):27–34

Nanci A, Content and distribution of noncollagenous matrix proteins in bone and cementum: relationship to speed of formation and collagen packing density, J Struct Biol, 126, 256–269, 1999

Olsen BJ, Ninomiya Y (1993) In 'Collagens' Guidebook to the Extracellular Matrix and Adhesion Proteins (eds Kreis T., Vale R), pp. 32–44

Prockop DJ, Kivirikko KL. Collagens: molecular biology, diseases, and potentials for therapy. Annu Rev Biochem. 1995; 64:403–434

Prockop DJ, and Fertala A 1998. The collagen fibril: the almost crystalline structure. J. Struct. Biol. 122:111–118.

Roach HI, Why does bone matrix contain non-collagenous proteins? The possible roles of osteocalcin, Cell Biol Int. 1994 Jun;18(6):617–28

Robling AG, Stout SD, Morphology of the drifting osteon, Cells Tissues Organs. 1999;164(4):192–204

Schäffler, Ludeke R, Taleb-Ibrahimi A, Hughes G, and Rieger D, Sb/GaAs(110) interface: A reevaluation, Phys. Rev. B 36, 1328–1331(1987)

Steege JW, Childress DS (1988): Finite element modeling of the below-knee socket and limb: phase II. In: ASME Modelling and Control Issues in Biomechanical Systems, Vol. BED-4, pp. 121–129

Stein GS, Lian JB, Stein JL, Van Wijnen AJ, M, Transcriptional control of osteoblast growth and differentiation, Physiol. Rev. 76:593–629,1996

Terai M, Hashimoto K, Yoda K, Sata T. High prevalence of human papillomaviruses in the normal oral cavity of adults, Oral Microbilogy and Immunology Volume 14 Issue 4 Page201 – August 1999

Todd BA, Tacker JG (1994): Three-dimensional computer model of the human buttocks, in vivo. J Rehabil Res Dev 31(2):111–119

Vannah WM, Childress DS (1996): Indentor tests and finite element modeling of bulk muscular tissue in vivo. J Rehabil Res Dev 33(3):239–252

VHP (1997): The Visible Human Project. URL: `http://www.nlm.nih.gov/research/visible/visible_human.html`

Wess TJ, Purslow PP, Sherratt MJ, Ashworth JL, Shuttleworth CA and Kielty CM (1998a). Calcium determines the supramolecular organization of fibrillin-rich microfibrils. *J. Cell Biol.* 141, 829–837.

Wess TJ, Purslow PP and Kielty CM (1998b). X-ray diffraction studies of fibrillin-rich microfibrils: effects of tissue extension on axial and lateral packing. *J. Struct. Biol.* 122, 123–127.

Whitehouse WJ, Dyson ED, Scanning electron microscope studies of trabecular bone in the proximal end of the human femur, J Anat. 1974 Dec;118(3):417–44

Zhou XD, Yang ZY, Yu YQ, Yang BH, Lu JZ, Lin ZY, Recurrence after resection of-fetoprotein-positive hepatocellular carcinoma, Journal of Cancer Research and Clinical Oncology, 1994 – Springer

15. Elbow and Fracture – Numerical Modeling

Alvarez E, Patel MR, Nimberg G, et al. (1975): Fracture of the capitulum humeri. J Bone Joint Surg Am 57:1093–1096

Archarya S, Kneife F, Mackinnon JG (1996): Bilateral fractures of the capitulum: a case report. Int Orthop 20:337–338

Blook H, Coyle M (1997): Coronal shear fractures of the distal end of the humerus (letter to editor). J Bone Joint Surg Am 79:1271

Bohler L (1956): The Treatment of Fractures, 5th edition. Grune & Stratton, New York, pp. 664–665

Brumfield RH Fr, Kuschner SH, Gelloman H, et al. (1990): Total elbow arthroplasty. J Arthroplasty 5:359–363

Bryan RS, Morrey B (1982): Extensive posterior exposure of the elbow: a triceps-sparing approach. Clin Orthop 166:188–192

Bryan RS, Morrey BF (1985): Fractures of the distal humerus. In Morrey BF (Ed.): The Elbow and its Disorders, 1st edition. WB Saunders, Philadelphia, pp. 325–333

Christopher F, Bushnell LF (1935): Conservative treatment of fractures of the capitellum. J Bone Joint Surg Am 17:489–492

Cobb T, Morrey B (1997): Total elbow replacement as primary treatment for distal humeral fractures in elderly patients. J Bone Joint Surg Am 79:826–832

Collert S (1977): Surgical management of fracture of the capitulum humeri. Acta Orthop Scand 48:603–606

Cooper AP (1841): Fracture of the external condyle of the humerus. In Cooper LA (Ed.): A Treatise on Dislocations and Fractures of the Joints. Joseph Butler, London, p. 508

Davis RF, Weiland AJ, Hungerford DS, et al. (1982): Nonconstrained total elbow arthroplasty. Clin Orthop 171:156–160

Dee R (1972): Total replacement arthroplasty of the elbow for rheumatoid arthritis. J Bone Joint Surg Br 54:88–95

Dee R (1993): Nonimplantation salvage of failed reconstructive procedures of the elbow. In Morrey BF (Ed.): The Elbow and Its Disorders, 2nd edition. Philadelphia, WB Saunders, pp. 690–695

DeLee JC (1996): Fractures and dislocations of the hip. In Rockwood CA Green DP Jr, Bucholz RW, et al. (Eds.): Rockwood and Green's Fractures in Adults, 4th edition. Philadelphia, Lippincott-Raven, p. 1687

DiShino M, Allizard M, Dran G (1991): Les fractures du capitellum humeral de decouverte tardive. Rev Chir Orthop Reparatriee Appar Mot 77:432–434

Dushuttle RP, Coyle MP, Zawadsky JP, et al. (1985): Fractures of the capitellum. J Trauma 25:317-321

Ewald FC, Jacobs M (1984): Total elbow arthroplasty. Clin Orthop 182:137–142

Feldman MD (1997): Arthroscopic excision of Type II capitellar fractures. Arthroscopy 13:743–748

Fenech CM, Keaveny TM (1999): A Celular Solid Criterion for Predicting the Axial-Shear Failure Properties of Bovine Trabecular Bone. J Biomech Eng 121:414–422

FiggieE III, Inglis AE, Ranawat CS, et al. (1987): Results of total elbow arthroplasty as a salvage procedure for failed elbow reconstructive operations. Clin Orthop 219:185–193

Foulke DA, Robertson PA, Timmerman LA (1995): Fracture of the trochlea. J Orthop Trauma 9:530–532

Fowles JV, KassabMT (1974): Fracture of the capitulum humeri: treatment by excision. J Bone Joint Surg Am 56:794–798

Froimson AI, Silva JE, Richey M (1976): Cutis arthroplasty of the elbow joint. J Bone Surg Am 58:863–865

Garrett JC, Ewald FC, Thomas WH, et al. (1977): Loosening associated with GSB hinge total elbow replacement in patients with rheumatoid arthritis. Clin Orthop 127:170–174

Grant IR, Miller JH (1975): Osteochondral fracture of the trochlea associated with fracture-dislocation of the elbow. Injury 6:257–260

Grantham SA, Norris TR, Bush DC (1981): Isolated fracture of the humeral capitellum. Clin Orthop 161:262–269

Greenspan A, Norman A (1987): Radial head-capitellum view: an expanded imaging approach to elbow injury. Radiology 164:272–274

Gschwend N, Loehr J, Ivosevic-Radovanovic D, et al. (1988): Semiconstrained elbow prosthesis with special references to the GSB III prosthesis, Clin Orthop 232:104–111

Gschwend N, Scheier H, Bahler A, et al. (1996): GSBIII elbow. In Ruth W (Ed.): The Elbow, Endoprosthetic Replacement and Non-endoprosthetic Procedures, Springer, Berling Heidelberg New York, pp. 83–98

Gschwend N, Simmen BR, Matejovsky Z (1996): Late complications in elbow arthroplasty. J. Shoulder Elbow Surg 5:86–96

Hahn NF (1853): Fall von eine besonderes varietat der fracturen des ellen bogens. Zeit schrift Wundarzte und Geburtshelfe 6:185–189

Helfet DL, Schmerling GJ (1993): Bicondylar intra-articular fractures of the distal humerus in adults. Clin Orthop 292:26–36

Hendel D, Halperin N (1982): Fracture of the radial head and capitulum humeri with rupture of the medial collateral ligament of the elbow. Injury 14:98–99

Hirvensallo E, Bostman O, Partio E, et al. (1993): Fracture of the humeral capitellum fixed with absorbable glycolide pins. Acta Orthop Scand 64: 85–86

Holdsworth J, Mossad MM (1990): Fractures of the adult distal humerus. J Bone Joint Surg Br 72:362–365

Hotchkiss RN, Green DP (1991): Fractures and dislocations of the elbow. In Rockwood CA, Green DP, Bucholz RW (Eds.): Rockwood and Green's Fractures in Adults, 3rd edition. Philadelphia, JB Lippincott, pp. 739–841

Hughes RE, Schneeberger AG, An K-N, et al. (1997): Reduction of triceps muscle force after shortening of the distal humerus: a computational model. J Shoulder Elbow Surg 6:444–448

Horowitz NH, On the Evolution of Biochemical Syntheses, Science, July 22, 1960; 132(3421): 200–208

Inglis AE, Pellicci P (1980): Total elbow replacement. J Bone Joint Surg Am 62:1252–1258

Inoue G, Horii E (1992): Case report: combined shear fractures of the trochlea and capitellum associated with anterior fracture dislocation of the elbow. J Orthop Trauma 6:373–375

Jackobsson A (1957): Fracture of the capitellum of the humerus in adults: Treatment with intra-articular chrom-cobalt-molybdenum prosthesis. Acta Orthop Scand 26:184–190

Johansson O (1962): Capsular and ligamentous injuries of the elbow joint. Acta Orthop Scand Suppl 287:50–65

John H, Rosso R, Neff U, et al. (1994): Operative treatment of distal humeral fractures in the elderly. J Bone Joint Surg Br 76:793–796

Judet J, Raynal L (1957): Les fractures du capitellum ou decalottement de l'eminentia capitata. Acta Orthop Belg 23:5–22

Jupiter JB, Neff U, Ragazzoni P, et al.(1988): Unicondylar fractures of the distal humerus: an operative approach. J Orthop Trauma 2:102–109

Jupiter J, Morrey B (1993): Fractures of the distal humerus in the adult. In Morrey BF (Ed.): The Elbow and Its Disorders, 2nd edition. Philadelphia, WB Saunders, p. 351

Jupiter J.B, Neff U, Holzach P, et al. (1985): Intercondylar fractures of the humerus. J Bone Joint Surg Am 67:226

Kasten MD, Skinner HB (1993): Total elbow arthroplasty. Clin Orthop 290:177–188

Knight RA, Zandt L (1952): Arthroplasty of the elbow. J Bone Joint Surg Am 36:610–618

Knirk JL, Jupiter JB (1986): Intraarticular fractures of the distal end of the radius in young adults. J Bone Surg Am 68:647–659

Kocher T (1896): Beitrae zue Kenntniss einiger practisch wichtiger fracturformen, Basel, Carl Sallman, pp. 585–591

Kraay MJ, Figgie MP, Inglis AE, et al. (1994): Primary semi-constrained total elbow arthroplasty. J Bone Joint Surg Br 76:636–640

Lansinger O, Mare K (1981): Fracture of the capitulum humeri. Acta Orthop Scand 52:39–44

Lecestre R (1980): Round table on fracture of the lower end of the humerus. Societe Francaise de Chirurgie Orthopedique et Traumatologie Orthop Trans 4:123

Letts M, Rumball K, Bauermeister S, et al.(1997): Fractures of the capitellum in adolescents. J Pediatr Orthop 17:315–320

Liberman N, Katz T, Howard CB, et al.: Fixation of capitellar fractures with the herbert screw. Arch Orthop Trauma Surg 110:155–157

London JT (1981): Kinematics of the elbow. J Bone Joint Surg Am 63:529–536
Lorenz H (1905): Zur kenntnis der fractura humeri (eminentiae capitatae). Deutsche Zeitschr F Chir 78:531–545
Lowe LW, Miller AJ, Allum RL, et al. (1984): The development of an unconstrained elbow arthroplasty. J Bone Joint Surg Br 66:243–247
Ma YZ, Zheng CB, Zhou TL, et al.(1984): Percutaneous probe reduction of frontal fractures of the humeral capitellum. Clin Orthop 183:17–21
Makela EA, Bostman O, Kekomake M (1992): Biodegradable fixation of distal humeral physeal fractures. Clin Orthop 283:237–243
Maisonneuve JG, Recherches sur la fracture du péroné, 1840 - F. Loquin & Cie
Mckee MD, Jupiter JB (1994): A contemporary approach to the management of complex fractures of the distal humerus and their sequelae. Han Clin 10:479–494
Mckee MD, Jupiter JB, Bamberger HB (1996): Coronal shear fractures of the distal end of the humerus. J Bone Joint Surg Am 78:49–54
Mckee MD, Mehne DK, Jupiter JB (1992): Trauma to the adult elbow and fractures of the distal humerus. In Browner B, Jupiter JB, Levine A, et al. (Eds.): Skeletal Trauma, Fractures, Dislocations, Ligamentous Injuries, 2nd edition. WB Saunders, Philadelphia, pp. 1483–1522
Milch H (1931): Unusuala fractures of the capitulum humeri and the capitulum radii. J Bone Joint Surg Am 13:882–886
Milch H (1964): Fractures and fracture dislocations of the humeral condyles. J Trauma 4:592–607
Morrey BF (1990): Posttraumatic contracture of the elbow: operative treatment including distraction arthroplasty. J Bone Joint Surg Am 72:601–618
Morrey BF, Chao EYS (1985): Functional evaluation of the elbow. In Morrey BF (Ed.): The Elbow and its Disorders, 1st edition. WB Saunders, Philadelphia, pp. 73–91
Mosheiff R, Liebergall M, Elyashuv O, et al.(1991): Surgical treatment of fractures of the capitellum in adults: a modified technique. J Orthop Trauma 5:297–300
Mouchel MA (1898): Fractures de l'extremite inferieure de l'humerus Paris. G Steinheil p. 282
Muller ME, Allgower M, Schneider R, et al. (1979): Fractures fo the distal humerus. In Muller ME (Ed.): Manual of Internal Fixation: Techniques Recommended by The AO Group, 2nd edition. Springer, Berling Heidelberg New York, pp. 176–181
McAuliffe JA, Burkhalter WE, Ouellette EA, et al. (1992): Compression plate arthrodesis of the elbow. J Bone Joint Surg Br 74:300–304
Morrey BF (1990): Post-traumatic contracture of the elbow: operative treatment including distraction arthroplasty. J Bone Joint Surg Am 72:601–618
Morrey BF, Adams RA (1992a): Semi-constrained arthroplasty for the treatment of rheumatoid arthritis of the elbow. J Bone Joint Surg Am 74:479–490

Morrey BF, Adams RA (1992b): Semi-constrained elbow replacement arthroplasty: Rational, technique, and results. In Morrey BF (Ed.): The Elbow and Its Disorders, 2nd edition. WB Saunders, Philadelphia, pp. 648–664

Morrey F, Adams RA (1995): Semi-constrained elbow replacement for distal humeral nonunion. J Bone Joint Surg Br 77:67–72

Morrey BF, Adams RA, Bryan RA (1991): Total replacement for post-traumatic arthritis of the elbow. J Bone Joint Surg Br 73:607–612

Morrey BF, Askew LJ, An K-N (1998): Strength function after elbow arthroplasty. Clin Orthop 234:43–50

Morrey BF, Askew LJ, An K-N, et al. (1981): A biomechanical study of normal functional elbow motion. J Bone Joint Surg Am 63:872–877

Morrey BF, Bryan RS, Dobyns JH, et al. (1981): Total elbow arthroplasty: a five-year experience at the Mayo Clinic. J Bone Joint Surg Am 63:1050–1063

Ochner RS, Bloom H, Palumbo RC, et al. (1996): Closed reduction of coronal fractures of the capitellum. J Trauma 40:199–203

O'Driscoll SW, An K-N, Horinek S, et al. (1992): Kinematics of semi-constrained total elbow arthroplasty. J Bone Joint Surg Br 74:297–299

O'Neill OR, Morrey BF, Tanaka S, et al. (1992): Compensatory motion in the upper extremity after elbow arthrodesis. Clin Orthop 281:89–96

Oppenheim W, Davlin LB, Leipzig JM (1989): Case report: concomitant fractures of the capitellum and trochlea. J Orthop Trauma 3:260–262

Palmer I (1961): Open treatment of transcondylar T-fracture of the humerus. Acta Chir Scand 121:486–490

Perry CR, Gibson CT, Kowalski MF (1989): Transcondylar fractures of the distal humerus. J Orthop Trauma 3:98–106

Pitt MJ, Speer DP (1990): Imaging of the elbow with an emphasis on trauma. Radiol Clin North Am 28:293–305

Poynton Ar, Kelly IP, O'Rourke SK (1998): Fractures of the capitellum: a comparison of two methods. Injury 29:341–343

Pritschard RW (1979):Anatomic surface elbow arthroplasty: a preliminary report. Clin Orthop 179:223–230

Richards RR, Khoury GW, Burke FD et al.(1987): Internal fixation of capitellar fractures using Herbert screw: a report of four cases. Can J Surg 30:188–191

Robertson RC, Bogart FB (1933): Fracture of the capitellum and trochlea, combined with fracture of the external humeral condyle. J Bone Joint Surg Am 15:206–213

Scapinelli R (1990): Treatment of fractures of the humeral capitellum using fibrin sealant. Arch Orthop Trauma Surg 109:235–237

Schneeberger AG, Adams R, Morrey B (1997): Semiconstrained total elbow replacement for the treatment of post-traumatic osteoarthrosis. J Bone Joint Surg Am 79:1211–1222

Silberstein MJ, Brodeur AE, Graviss ER, et al. (1979): Some vagaries of the capitellum. J Bone Joint Surg Am 61:244–247

Silveri CP, Corso SJ, Roofeh J (1994): Herbert screw fixation of a capitellum fracture: a case report and review. Clin Orthop 300:123–126
Simpson LA, Richards RR (1986): Internal fixation of capitellar fractures using Herbert screws: a case report. Clin Orthop 209:166–168
Smith FM (1972): Fractures of lower extremity of humerus . In Surgery of the Elbow, 2nd edition. WB Saunders, Philadelphia, pp. 114–119
Speed JS, Macey HB (1933): Fractures of the humeral condyles in children. J Bone Joint Surg AM 15:903–919
Steinthal D (1898): Die isolierte fraktur de eminentia capitata in ellenbogengelenk. Centrallbl f Chirurgi 15:17–20
Stricker SJ, Thomson JD, Kelly RA (1993): Coronal plane transcondy lar fracture of the humerus in a child. Clin Orthop 294:308–311
Soni RK, Cavendish ME (1984): A review of the Liverpool elbow prosthesis from 1974 to 1982. J Bone Joint Surg Br 66:248–253
Souter WA, Nicol AC, Paul J (1985): Anatomical trochlear stirrup arthroplasty of the rheumatoid elbow. J Bone Joint Surg Br 67:676
Tsuge K, Murakami T, Yasunaga Y, et al. (1987): Arthroplasty of the elbow. J Bone Joint Surg Br 69:116–120
Urbaniak JR, Black KE Jr (1985): Cadaveric elbow allografts: a six year experience. Clin Orthop 197:131–140
Wilson JN (1982): Injuries of the elbow. In Watson-Jones R (Ed.): Fractures and Joint Injuries, 6th edition. Churchill Livingstone, Edinburgh, pp. 587–590
Wilson PD (1933): Fractures and dislocations in the region of the elbow. Surg Gynecol Obstet 56:335–339
Yamaguchi K, Sweet FA, Bindra R, et al. (1997): The extraosseous and intraosseous arterial anatomy of the adult elbow. J Bone Joint Surg Am 79:1653–1662
Zuckerman JD, Lubliner JA (1990): Arm, elbow and forearm injuries. In Zuckerman JD (Ed.): Orthopaedic Injuries in the Elderly. Baltimore, Urban & Schwarzenberg, pp. 345–407

16. Finite Element Analysis to Human Body Parts Affected by Trauma

Ahmadi N, Keer LM, Mura T (1983): Non-Hertzian Contact Stress Analysis for an Elastic HalfSpace-Normal and Sliding Contact. Int J Solid Struct 19(4):357–373
Alvine FG, (1999): Agility Total Ankle System, Surgical Technique, DePuy a Johnson & Johnson, Warsaw, Indiana, p. 10
Balasubramanian V, et al. (1997): Effect of Flexion on Stresses in UHMWPE Tibial Liners in Transactions of the 43rd Annual Meeting, Orthopaedic Research Society, San Fransisco, California p. 793

Baldini T, et al. (1999): Wear Damage is Affected by Conformity in Knee Joint Geometries in Transaction of the Society of Biomaterials, p. 25

Bandak FA, Tannous RE, Toridis T (2001): On the Development of an Osseo-Ligamentous Finite Element Model of the Human Ankle Joint. Int J Solids Struct 38:1681–1697

Barbour PSM, Barton DC, Fisher J (1995): The Influence of Contact Stress on the Wear of UHMWPE for Total Hip Replacement Hip Prosthesis. Wear 181–183:250–257

Barnett C, Napier J (1952): The Axis of Rotation at the Ankle Joint in Man, its Influence Upon the Form of the Talus and Mobility of the Fibula. J Anat 86:1–9

Bartel DL, et al. (1985): The Effect of Conformity and Plastic Thickness on Contact Stresses in Metal Backed Plastic Implants. J Biomech Eng, 107:193–199

Bartel DL, Bickness VL, Wright TM (1986): The Effect of Conformity, Thickness and Material on Stresses in Ultra-High Molecular Weight Components for Total Joint Replacement. Clin Orthop Relat Res, 68A(7):1041–1051

Bartel DL, et al. (1995): Stresses in Polyethylene Components of Contemporary Total Knee Replacement. Clin Orthop Relat Res, 317:76–82

Bauer G, et al. (1996): Total Ankle Replacement. Review and Critical Analysis of the Current Status. Foot Ankle Surg (European), 2:119–126

Bergstrom JS, et al. (2002): Constitutive Modeling of Ultra High Molecular Weight Polyethylene under Large-Deformation and Cyclic Loading Conditions. Biomaterials 23:2329–2343 `www.uhmwpe.org`

Bernakiewicz M, Viceconti M (2002): The Role of Parameter Identification in Finite Element Contact Analysis with Reference to Orthopaedic Biomechanics Applications. J Biomech 35:61–67

Boresi AP, Schmidt RJ, Sidebottom OM (1993): Advanced Mechanics of Materials, 5th edition. Wiley, New York, pp. 716–718

Bottlang M, Marsh JL, Brown TD (1999): Articulated External Fixation of the Ankle: minimizing Motion Resistance by Accurate Axis Alignment. J Biomech 32:63–70

Brosn TD, Fergusson AB (1978): The Development of a Computational Stress Analysis of the Femoral Head. J Bone Joint Surg, 60A:619–629

Buckwalter JA, et al. (1995): Bone Biology. The Journal of Bone and Joint Surgery 77A(8):1256–1289

Buechel FF, Pappas MJ, Iorio LJ (1988): New Jersey Low Contact Stress Total Ankle Replacement: biomechanical Rationale and Review of 23 Cementless Cases. Foot Ankle 8(6):279–290

Calderale PM, et al.(1983): Biomechanical Design of the Total Ankle Prosthesis. Engineering in Medicine 12(2):69–80

Caler WE, Carter DR (1989): Bone Creep-Fatigue Damage Accumulation. J Biomech 22:625–638

Canale ST, (Ed.) (1998): Campbell's Opperative Orthopedics. 9th edition. Mosby-Year Book Inc, St Louis, Missouri, pp. 233–234

Carter DR, Hayes WC (1976): The Compresive Behaviour of Bone as a Two-Phase Porous Structure. J Bone Joint Surg 59:954–962

Carter DR, Schwab GH, Spengler DM (1980): Tensile Fracture of Cancellous Bone. Acta Orthop Scand 51:733–741

Cheal EJ, et al. (1985): Stress Analysis of a Condylar Tibial Component: Influence of Metaphyseal Shell Properties and Cement Injection Depth. J Orthop Res 3:424–434

Chiu YP, Hartnett MJ (1987): A Numerical Solution for the Contact Problem Involving Bodies with Cylindrical Surface Considering Cylinder Effect. J Tribol 109:479–485

Choi K, Goldstein SA (1992): A Comparison of the Fatigue Behaviour of Human Trabecular and Cortical Bone Tissue. J Biomech 25(12):1371–1381

Chu TM, Reddy NP, Padovan J (1995): Three Dimensional Finite Element Stress Analysis of the Polypropylene, Ankle-Foot Orthosis: statis Analysis. Med Eng Phys 17(5):372–379

Conti SF, Wong YS (2001): Complications of Total Ankle Replacement. Clin Orthop Relat Res 391:105–114

Coventry MB (1996): The Histroy of Joint Replacement Arthroplasty. In: Reconstructive Surgery of the Joints, Morrey BF, (Ed.), Churchill Livingstone, New York, pp. 3–5

Cowin SC (1989): Bone Mechanics, 1st edition. Boca Raton, CRC, Florida, pp. 97–155

Crowell HP III (1991): Three Dimensional Finite Element Analysis of an Ankle Prosthesis. Innov Technol Biol Med 12:2–12

Dean DD, et al. (1999): Ultra High Molecular Weight Polyethylene Particles Have Different Effects on Proliferation, Differentiation and Local Factor Production of MG63 Osteoblast-like Cells. J Orthop Res, 17:9–17

DeHeer DC, Hillberry BM (1992): The Effect of Thickness and Nonlinear Material Behaviour on Contact Stress in Polyethylene Tibial Components in 38th Annual Meeting of the ORS p. 327

Demetriades L, Strauss E, Gallina J (1998): Osteoarthitis of the Ankle. Clin Orthop Relat Res 349:28–42 (Private Communications)

Digges KH, et al.: Determination and Modeling of Ankle Injury Causation, `hhtp:/www.ncac.gwu.edu/archives/papers/ankle/ankle.html`. IMechE, 2004 Archives, London

DiGioia AM (1992): A Structural Model of the Ankle: an Examination of Normal Joint Mechanics,In: 38th Annual Meeting, Orthopedic Research Society. Februrary 17–20, Washington, DC. p. 263

Edidin AA, Kurtz SM (2000): The Evolution of Paradigms for Wear in Total Joint Arthroplasty: The Role of Design, Mater Mech

Edidin AA, et al. (2000): Degradation of Mechanical Behaviour in UHMWPE after Natural and Accelerated Aging. Biomater 21:1451–1460

Ellis H, (1972): Clinical Anatomy. 5th edition. Blackwell Scientific, Oxford, p. 224

Estupinan JA, Bartel DL, Wright TM (1998): Residual Stresses in Ultra-High Molecular Weight Polyethylene Loaded Cyclically by a Rigid Moving Indentenr in Nonconforming Geometries. J Biomed Mater Res 16(1):80–88

Flsig J, Hvid I, Jensen NC (1986): Finite Element Stress Analysis of Some Ankle Prosthesis. Clin Biomech 1:71–76

Ford CM, Keaveny TM, Hayes WC (1996): The Effect of Impact Direction on the Structural Capacity of the Proximal Femur During Falls. J Bone Miner Res 11(3):377–383

Ford CM, Keaveny TM (1996): The Dependence of Shear Failure Properties of Trabecular Bone on Apparent Density and Trabecular Orientation. J Biomech 29(10):1309–1317

Fung YC (1993): Biomechanics, Mechanical Properties of Living Tissues. 2nd edition. Springer, Berling Heidelberg New York, p. 500

Fyhrie DP, Vashishth D (2000): Bone Stiffness Predicts Strength Similarly for Human Verterbal Cancellous Bone in Compression and for Cortical Bone in Tension, Bone 26(2):169–173

Genda E, et al.(1999): Three Dimensional Stress Analysis of Ankle and Foot Joints. In: 45th Annual Meeting, Orthopaedic Research Society. February, 1999. Aneheim, California. p. 390

Giannini S, Leardini A, O'Connor JJ (2000): Total Ankle Replacement: Review of the Designs and of Current Status. Foot Ankle Surg, 6:77–88

Giddings VL, et al.(2000): Calcaneal Loading During Walking and Running. Med Sci Sports Exerc 32(2):627–634

Goh JCH, et al. (1992): Biomechanical Study on the Load-Bearing Characteristics of the Fibula and the Effects of Fibular Resection. Clin Orthop Relat Res, (279):223–228

Goldstein GA (1987): The Mechanical Properties of Trabecular Bone: Dependence on Anatomic Location and Function. J Biomech 20(11):1055–1061

Goldstein G.A, et al. (1983): The Mechanical Properties of Human Tibial Trabecular Bone as a Function of Metaphysical Location. J Biomech 16(12):965–969

Goodman GA, et al. (1990): The Histological Effects of the Implantation of Different Sizes of Polyethylene Particles in the Rabbit Tibia. J Biomed Mater Res 24:517–524

Greening DR (1998): Automated Selection and Entry of Computed Tomography Data in Finite Element Modeling of the Human Femur. In: Faculty of Engineering and Applied Science, Memorial University of Newfoundland, Canada

Hertz H (1896): Uber die Beruhrung Fester Elastischer Korper. J Reine Angewandte Mathematik 92:156–171

Hicks JH (1953): The Mechanics of Foot I: the Joints. J Anat, 87:345

Huiskes R, Chao EYS (1983): A survey of finite element analysis in orthopedic biomechanics: the first decade, J Biomech 16(6):385–409

Hvid I, et al. (1985): Trabecular Bone Strength Profiles at the Ankle Joint. Clinical Orthopedics 199:306–312

Inman VT (1976): The Joints of the Ankle, Williams & Wilkins, Baltimore
Ishikawa H, Fujiki H, Yasuda K (1996): Contact Analysis of Ultrahigh Molecular Weight Polyethylene Articular Plate in Artificial Knee Joint During Gait Movement. J Biomech Eng 118:377–386
Jacques G, (1981): Atlas of Human Limb Joints. Springer, Berling Heidelberg New York, p. 93
Jensen NC, Kroner K (1992): Total ankle joint replacement: a clinical follow up. Orthopedics 15:236–239
Jensen NC, Hvid I, Kroner K (1988): Strength Pattern of Cancellous Bone at the Ankle Joint. Eng Med 17(2):71–76
Johnson KL (1985): Contact Mechanics, Cambridge University Press, New York, pp. 84–135
Kalker JJ (1972): On Elastic Line Contact. J Appl Mech 39:1125–1132
Kaplan SJ, et al. (1985): Tensile Strength of Bovine Trabecular Bone. J Biomech 18:723–727
Keaveny TM, Hayes WC (1993a): A 20-Year Perspective on the Mechanical Properties of Trabacular Bone. J Biomech Eng 115:534–542
Keaveny TM, et al. (1993b): Trabecular Bone Yields Like a Damaging Material. Adv Bioeng 26:187–189
Keaveny TM, et al. (1994): Differencies between the Tensile and Compressive Strengths of Bovine Tibial Trabecular Bone Depend on Modulus. J Biomech 27(9):1137–1146
Keaveny TM, et al. (1994a): Trabecular Bone Exhibits Fully Linear Elastic Behaviour and Yields at Low Strains. J Biomech 27(9):1127–1136
Keaveny TM, et al. (1994b): Yield Strains for Bovine Trabecular Bone are Isotropic but Asymmetric. In: Transactions of 40th Orthopaedic Research Society, p. 428
Keaveny TM, et al. (1995): Author's Response. J Biomech 28(6):765
Keaveny TM, et al. (1999): Application of the Tsai-Wu Quadratic Multiaxial Failure Criterion to Bovine Trabecular Bone. J Biomech Eng, 121:99–107
Kempson GE, Freeman MAR, Tuke MA (1975): Engineering Considerations in the Design of an Ankle Joint. Biomed Eng 10:166–180
Kennedy FE, et al. (2000): Contact Fatigue Failure of Ultra-High Molecular Weight Polyethylene Bearing Components of Knee Prostheses. J Tribol 122:332–339
Keyak JH, Rossi SA (2000): Prediction of femoral fracture load using finite element models: an examination of stress- and strain based failure theories. J Biomech 33:209–214
Kitagawa M, Onoda T, Mizutani K (1992): Stress-Strain Behaviour at Finite Strains for Various Strain Paths in Polyethylene. J Mater Sci 27:13–23
Kitaoka HB (1991): Salvage of Nonunion Following Ankle Arthrodesis for failed Total Ankle Arthroplasty. Clin Orthop Relat Res 268:37–43
Kitaoka HB, et al.(1994): Survivorship Analysis of the Mayo Total Ankle Arthroplasty. J Bone Joint Surg 76A(7):974–979

Komistek RD, et al. (1998): Mathematical Model of the Lower Extremity Joint Reaction Forces Using Kane's Method of Dynamics. J Biomech 31:185–189

Komvopoulus K, Saka N, Suh NP (1987): The Role of Hard Layers in Lubricated and Dry Sliding. J Tribol 109

Kopperdahl DL, Keaveny TM (1998): Yield Strain Behaviour of Trabecular Bone. J Biomech 31:601–608

Kuster MS, et al. (2000): The Effects of Conformity and Load in Total Knee Replacement. Clin Orthop Clin Res, (375):302–312

Kurtz SM, et al. (1996): Exponential Model for the Tensile True Stress–Strain Behaviour of As-Irradiated and Oxidatively Degraded Ultrahigh Molecular Weight Polyethylene. J Orthop Res, 14(5):755–761

Kurtz SM, et al. (1998): The Yielding, Plastic Flow and Fracture Behaviour of Ultra-High Molecular Weight Polyethylene Used in Total Joint Replacements. Biomaterials 19:1989–2003

Lachiewicz PF, et al. (1984): Total Ankle Replacement in Rheumatoid Arthritis. J Bone Joint Surg 66A(3):340–343

Lambert KL (1971): The Weight-Bearing Function of the Fibula. J Bone Joint Surg 53A(3):507–513

Leardini A, et al. (1999): A Geometric Model of the Human Ankle Joint. J Biomech 32:585–591

Leardini A, et al. (2000): The role of the passive structures in the mobility and stability of the human ankle joint: a literature review. Foot Ankle Int 21(7):602–614

Leardini A, et al. (2001): computer Asssted Design of the Sagittal Shapes of a Ligament-compatible Total Ankle Replacement. Med Biol Eng Comput 39:168–175

Ledoux WR et al.: Finite Element Foot Modeling, `hhtp:/www.truegrid.com/gallery/show{\_}foot.html` (2004) I. Mech. E Archives, London

Lewis G (1994): The ankle joint prosthetic replacement: clinical performance and research challenges. Foot Ankle Int, 15(9):471–476

Lewis G, (1997): Polyethylene Wear in Total Hip and Knee Arthroplasties. Wear of UHMWPE, pp. 55–75

Lewis G, Austin GE (1994): A Finite Element Analysis Study of Static Stresses in a Biomaterial Implant. Innov Technol Biol Med 15(5):634–644

Li G, Sakamoto M, Chao EYS (1997): A Comparison of Different Methods in Prediting Static Pressure Distribution in Articular Joints. J Biomech 30(6):635–638

Lin L, Argon AS (1994): Review: structure and plastic deformation of polyethylene. J Mater Sci 29:294–323

Linde F, Hvid I, Madsen F (1992): The Effects of Specimen Geometry on the Mechanical Behaviour of Trabecular Bone Specimens. J Biomech 25(4):359–368

Lotz JC, Cheal EJ, Hayes WC (1991): Fracture Prediction of the Proximal Femur Using Finite Element Models Part II–Nonlinear Analysis. J Biomech Eng, Trans ASME 113:361–365

Lotz JC, Gerhart TN, Hayes WC (1991): Mechanical Properties of Metaphyseal Bone in the Proximal Femur. J Biomech 24(5):317–329

Lundberg A, et al.(1989a): The Axis of Rotation of the Ankle Joint. J Bone Joint Surg 71B(1):94–99

Lundberg A, et al.(1989b): Kinematics of the Ankle/Foot Complex-Part 1: Plantarflexion and Dorsiflexion, Foot Ankle 9(4):194–200

Lundberg A, et al.(1989c): Kinematics of the Ankle/Foot Complex-Part 2: Pronation and Supination. Foot Ankle 9(5):248–253

Lundberg A, et al.(1989d): Kinematics of the Ankle/Foot Complex-Part 3: Influence of Leg Rotation, Foot Ankle 9(5):304–309

Mammone JF, Hudson SM (1993): Micromechanics of Bone Strength and Fracture. J Biomech 26(4/5):439–446

Mann RA (1985): Biomechanics of the Foot. In: Atlas of Orthotics/American Academy of Orthopaedic Surgeons, CV Mosby, St Louis, Missouri, pp. 112–125

Martin RB, Burr DB (1982): A Hypothetical Mechanism for the Stimulation of Osteonal Bone Remodeling by Fatigue Damage. J Biomech 15:137–139

McIff TI (2001): Contact and Internal Stress Distribution in Two Types of Contemporary "Unconstrained" Total Ankle Designs. J Biomech 34:S23–S28

Michelson JD, Schmidt GR, Mizel MS (2000): Kinematics of a Total Arthroplasty of the ankle: comparison to normal ankle motion. Foot Ankle Int 21(4):278–284

Michel MC, et al. (1993): Compressive Fatique Behaviour of Bovine Trabecular Bone. J Biomech 26(4/5):453–463

Morgan EF, Keaveny TM (2001): Dependence of Yield Strain of Human Trabecular Bone on Anatomic Site. J Biomech 2001. 34:569–577

Morrissy RT, (Ed.) (1990): Dynamics of the Foot and Gait. 3rd edition. Lovell and Winter's Pediatric Orthopedics, Vol. 1, Lippincott, Philadelphia

Muller R, Ruegsegger P (1996): Analysis of Mechanical Properties of Cancellous Bone Under Conditions of Simulated Bone Atrophy. J Biomech 29(8):1053–1060

Neil JL, et al. (1983): Tensile and Compressive Properties of Vertebral Trabecular Bone. In: Transactions of 29th Orthopeadic Research Society, p. 334

Niebur GL, et al. (2000): High-Resolution Finite Element Models with Tissue Strength Asymmetry Accurately Predict Failure of Trabecular Bone. J Biomech 33:1575–1583

Oonishi H, (1984): Cementless Alumina Ceramic Artificial Ankle Joint. In: Biomaterials and Biomechanics, Ducheyne P, (Ed.), Elsevier Science, Amsterdam, pp. 85–90

Pal GP, Routal RV (1998): Architecture of the Cancellous Bone of the Human Talus. Anat Rec 252:185–193

Pappas M, Buechel FF, DePalma AF (1976): Cylindrical total ankle joint replacement: surgical and biomechanical rationale. Clin Orthop Relat Res 118:82–92

Perillo-Marcone A, Barrett DS, Taylor M (2000): The Importance of Tibial Alignment. J Arthroplasty 15(8):1020–1026

Persson A (1964): On the Stress Distribution of Cylindrical Elastic Bodies in Contact. In: Chalmers Tekniska Hogskola, Goteborg

Petty W (1991): Total Joint Replacement, WB Saunders, Philadelphia, pp. 7–10

Pidaparti RMV, Turner CH (1997): Cancellous Bone Architecture: Advantages of Nonorthogonal Trabecular Alignment Under Multidirectional Joint Loading. J Biomech 30(9):979–983

Procter P and Paul JP (1982): Ankle Joint Biomechanics. J Biomech 15(9):627–634

Pruitt L, et al. (1995): Cyclic Copressive Loading Results in Fatigue Cracks in Ultra-High Molecular Weight Polyethylene. J Orthop Surg, 13:143–146

Psychoyios A, et al. (1998): Wear of Congruent Meniscal Bearings in Unicompartmental Knee Arthroplasty. J Bone Joint Surg, 80B(6):976–982

Pyevich MT, et al. (1998): Total ankle arthroplasty: unique design, two to eleven year follow-up. J Bone Joint Surg 80A(10):1410–1420

Rawlinson JJ, Bartel DL (2002): Flat Medial-Lateral Conformity in Total Knee Replacements does not Minimize Contact Stress. J Biomech 35:27–34

Reeves EA, et al. (1998): A Two-Dimensional Model of Cyclic Strain Accumulation in Ultrahigh Molecular Weight Polyethylene Knee Replacements. In: Proceedings of the Institution of Mechanical Engineers, 212, pp. 189–198

Reilly DT, Burstein AH (1975): The Elastic and Ultimate Properties of Compact Bone Tissue. J Biomech 8:393–405

Ritchie SJK (2000): A Model for the Large-Strain Deformation of Polyethylene. J Mater Sci 35:5829–5837

Rho JY, Ashram RB, Turner CH (1993): Young's Modulus of trabecular and cortical bone material: ultrasonic and microtensile measurements. J Biomech 26(2):111–119

Rho, JY, Kuhn-Spearing L, Zioupos P (1998): Mechanical Properties and the Hierarchical Structure of Bone. Med Eng Phys 20:92–102

Rice JC, Cowin SC, Nowman JA (1988): On the Dependence of the Elasticity and Strength of Cancellous Bone on Apparent Density. J Biomech 21:122–168

Ricos V, et al. (1996): Effects of Anisotropy and Material Axis Registration on Computed Stress and Strain Distributions in the Turkey Ulna. J Biomech 29(2):261–267

Rietbergen BV, et al. (1995): A New Method to Determine Trabecular Bone Elastic Properties and Loading Using Micromechanical Finite-Element Models. J Biomech 28(1):69–81

Rohl L, et al. (1991): Tensile and Compressive Properties of Cancellous Bone. J Biomech 24:1143–1149

Rohlman A, et al. (1988): A Nonlinear Finite Element Analysis of Interface Conditions in Porous Coated Hip Endoprostheses. J Biomech 21(7):1988

Rosse C, Gaddum-Rosse O (1997): Textbook of Anatomy, 5th edition. Lippincott-Raven, Philadelphia, p. 342

Sabry FF, et al. (2000): Internal Architecture of the Calcaneus: Implications for Calcaneus Fractures. Foot Ankle Int, 21(2):114–118

Sarrafian SK (1993): Anatomy of the Foot and Ankle: descriptive, Topographic, Functional, 2nd edition. JB Lippincott, Philadelphia, pp. 474–509

Schroeder U, et al. (1997): The Influence of Tractive Force on the Shear Stresses in UHMWPE of a TKR Component. In: Transcations of the 43rd Annual Meeting, Orthopaedic Research Society, San Fransisco, California p. 794

Seireg A, Arkivar RJ (1975): The Prediction of Muscular Load Sharing and Joint Forces in the Lower Extremities During Walking. J Biomech 8:89–102

Siegler S, Chen J, Schneck CD (1988): The Three-Dimensional Kinematics and Flexibility Characteristic of the Human Ankle and Subtalar Joints. Part 1: Kinematics. J Biomech Eng 110:364–373

Silva MJ, Keaveny TM, Hayes WC (1998): Computed Tomography-Based Finite Element Analysis Predicts Failure Loads and Fracture Patterns for Verterbal Sections. J Orthop Res 16:300–308

Staltzman CL, et al.(2000): Total Ankle Replacement Revistited. J Orthop Sports Phys Ther 30(2):56–57

Stauffer RN, Chao EYS, Brewster RC (1977): Force and Motion Analysis of the Normal. Diseased and Prostetic Ankle Joint. Clin Orthop 127:189–196

Stiehl JB, (1991): Inman's Joints of the Ankle. 2nd edition. Williams & Wilkins, Baltimore, pp. 1–84

Takebe K, (1984): Role of the Fibula in Weight-Bearing. Clin Orthop Relat Res 189:289–292

Tannous RE et al.(1996): A Three-Dimensional Finite Element Model of Human Ankle: Development and Preliminary Application to Axial Impulsive Loading. In: Proceedings of the 40th Stapp Car Crash Conference, Nov. 1996. Albuquerque, NM: Warrendale, PA: Society of Automotive Engineers, pp. 219–238

Taylor M, Tanner KE, Freeman MAR, Yettrman AL (1995): Cancellous Bone stresses surrounding the femoral component of a hip prosthesis: an elastic-plastic finite element analysis. Med Eng Phys 17(7):544–550

Taylor M, Tanner KE, Freeman MAR (1998): Finite element analysis of the implanted proximal tibia: a relationship between the initial cancellous bone stress and implant migration. J Biomech 31:303–310

Taylor M, Tanner KE (1995): Finite element modeling – predictor of implant survival? J Mater Sci: Mater Med 6:808–812

Taylor M, Tanner KE (1997): Fatigue failure of cancellous bone: a possible cause of implant migration and loosening. J Bone Joint Surg 79B(2):181–182

Teoh SH, Chan WH, Thampuran R (2002): An Elasto-Plastic Finite Element Model for Polyethylene Wear in Total Hip Arthroplasty. J Biomech 35:323–330

Tooms RE (1987): Arthroplasty of Ankle and Knee. In: Campbell's Operative Orthopedics, Crenshaw HH (Ed.), Mosby, St Lois, pp. 1145–1150
Turner CH (1989): Is Yield Strain in Cancellous Bone Isotropic? J Biomech 28(6):763
Turner CH, et al. (1999): The elastic properties of trabecular and cortical bone tissues are similar: results from two microscopic measurement techniques. J Biomech 32:437–441
Uchiyama E, Yamakoshi K, Sasaki T (1998): Measurement of Mechanical Characteristics of Tibial Periosteum and Evaluation of Local Differencies. J Biomech Eng 120:85–91
Wang A (2001): A Unified Theory for Ultra-High Molecular Weight Polyethylene in Multi-Directional Sliding. Wear 248:38–47
Wang Q, et al. (1992): Fibula and Its Ligaments in Load Transmission and Ankle Joint Stability. Clin Orthop Relat Res, (330):261–270
Wang A, Stark C, Dimbleton JH (1996): Mechanistic and Morphological Origins of Ultra-High Molecular Weight Polyethylene Wear Debris in Total Joint Replacement Prostheses. In: Proceedings of the Institution of Mechanical Engineers, 210, pp. 141–155
Wang A, et al. (1998): Lubrication and Wear of Ultra-High Molecular Weight Polyethylene in Total Joint Replacements. Tribol Int, 31(1–3):17–33
Waugh TR, Evanski P, McMaster WC (1976): Irvin Ankle Arthroplasty, Prostehetic Design and Surgical technique. Clin Orthop Relat Res 114:181–184
William P (1991): Total Ankle Arthroplasty. In: Total Joint Replacement. Philadelphia, WB Saunders, pp. 749–759
Williams PI, Warwick R (1980): Grays Anatomy. 36th edition. W.B. Saunders, New York, pp. 397–410
Wolff J (1892): Das Gesetz der Transformation der knochen, A Hirchwild, Berlin
Zysset PK, et al. (1999): Elastic Modulus and Hardness of Cortical Bone and Trabecular Bone Lamellae Measured by Nanoindentation in the Human Femur. J Biomech 32:1005–1012

17. Computer Mesh Generation

Bajaj C, Xu G (2002): Anisotropic diffusion of subdivision surfaces and functions on surfaces. To appear in ACM Transactions on Graphics
Bajaj C, Coyle E, Lin K-N (1996): Arbitrary topology shape reconstruction from planar cross-sections. Graph Model Image Process 58(6):524–543
Bajaj CL, Pascucci V, Schikore D (1996): Fast isocontouring for improved interactivity. In: Proceeding of the IEEE Symposium on Volume Visualization, ACM, pp. 39–46
Bajaj C, Pascucci V, Schikore D (1997): The contour spectrum. In: Proceeding of IEEE Visualization, pp. 167–174

Bajaj C, Coyle E, Lin K-N (1999): Tetrshedral meshes from planar cross sections. Comput Method Appl M 179:31–52

Bajaj C, Warren J, Xu G (2001): A smooth subdivision scheme for hexahedral meshes. In: The Visual Computer, the special issue on subdivision (Private Communications)

Bajaj C, Wu Q, Xu G (2002): Level set based volume anisotropic diffusion. In: TICAM Technical Report, The University of Texas, Austin

Bern MW, Eppstein D, Gilbert JR (1990): Provably good mesh generation. In: IEEE Symposium on Foundatins of Computer Science, 231–241

Carr H, Snoeyink J, Axen U (2003): Computing contour trees in all dimensions. Comput Geometry: Theory Appl 24(2):75–94

Cheng SW, Dey TK (2002): Quality meshing with weighted delaunay refinement. In: Proceedings of 13th ACM-SIAM Sympos. Discrete Algorithms (SODA 2002), pp. 137–146

Cheng S-W, Dey TK, Edelsbrunner H, Facello MA, Teng S (2000): Silver exudation, JACM 47:883–904

Clarenz U, Diewald U, Rumpf M (2000): Nonlinear anisotropic diffusion in surface processing. In: Proceedings of the 11th IEEE Visualization Conference (Vis) 2000, pp. 397–405

Eppstein D (1996): Linear complexity hexahedral mesh generation: In: Symposium on Computational Geometry, pp. 58–67

Folwell N, Mitchell S (1998): Reliable whisker weaving via curve contraction. In: Proceedings of 7th International Meshing Roundtable, Sandia National Lab, pp. 365–378

Fujishiro I, Maeda Y, Sato H, Takeshima Y (1996): Volumetric data exploration using interval volume. In: IEEE Transcations on Visualization and Computer Graphics 2(2):144–155

Garland M, Heckbert PS (1998): Simpligying surfaces with color and texture using quadric error metrics. In: IEEE Visualization 1998, Ebert D, Hagen H, Rushmeier H (Eds.) pp. 263–270

Gibson SF (1998): Using distance maps for accurate surface representation in sampled volumes. In: IEEE Visualization 1998, pp. 23–30

Ju T, Losasso F, Schaefer S, Warren J (2002): Dual contouring of hermite data. In: Proceedings of SIGGRAPH 2002, ACM Press/ACM SIGGRAPH, Computer Graphics Proceedings, Annual Conference Series, ACM

Kallieris D, Rizzetti A, Mattern R (1994): Verhalten der Kopt-Hals-Einheit bei der dynamischen Belastung-Vergleich zwischen Dummy und Leiche. Zentralblatt Rechtsmedizin, 42. Band, Heft 6

Keyak JH, Meagher JM, Skinner HB, Mote CD (1990): Automated three-dimensional finite element modelling of bone: a new method J Biomed Eng 12:389–397

Kobbelt L, Botsch M, Schwanicke U, Seidel H (2001): Feature sensitive surface extraction from volume data. In: Proceedings of SIGGRAPH 2001, Computer Graphics Proceedings, pp. 57–66

Laramee R, Bergeron T (2002): An isosurface continuity algorithm for super adaptive resolution data. Computer Graphics International Bradford, UK, July 1–5 2002, Computer Graphics Society 5

Lopes A, Brodlie K (2000): Improving the robustness and accuracy of the marching cubes algorithm for isosurfacing. In: IEEE Transactions on Visualization and Computer Graphics, pp. 16–29

Lorensen WE, Cline HE (1987): Marching cubes: a high resolution 3D surface construction algorithm. In: Proceedings of SIGGRAph 1987, Computer Graphics Proceedings, pp. 163–169

Lorensen WE, Cline HE (1987): Marching cubes: A high resolution 3D surface reconstruction algorithm. Comput Graphics 21:163–169

Meyers D (1994): Multiresolution tiling. In: Proceedings of Graphics Interface, pp. 25–32

Mitchell SA, Vavasis SA (2000): Quality mesh generation in higher dimensions. SIAM J Comput 29(4):1334–1370

Moore D (1992): Compact isocontours from sampled data. Graphics Gems III, pp. 23–28

Muller R, Ruegsegger P (1995): Three-dimensional finite element modelling of non-invasively assessed Trabecular hone structures. Med Eng Phys 17:126–133

Muller R, Hildebrand T, Ruegsegger P (1994): Non-invasive bone biopsy: a new method to analyse and display the three-dimensional structure of trabecular bone, Phys Med Biol 39:145–164

Nielson GM, Hamann B (1991): The asymptotic decider: resolving the ambiguity in marching cubes. In: Proceedings of Visualization 1991, pp. 83–90

Nielson GM, Sung K (1997): Interval volume tetrahedrization. In: IEEE Visualization 1997, pp. 221–228

Pascucci V, Bajaj C (2000): Time critical adaptive refinement and smoothing. In: Proceedings of the ACM/IEEE Volume Visualization and Graphics Symposium 2000, Salt lake City, Utah, pp. 33–42

Ruegsegger P, Munch B, Felder M (1993): Early detection of osteoarthritis by 3D computed tomography, Technol Health Care 1:53–66

Shewchuk JR (1998): Tetrahedral mesh generation by delaunay refinement. In: Proceedings of the 4th Annual Symposium on Computational Geometry (Minneapolis, Minnesota), Association for Computational Machinery, pp. 86–95

Shewchuk JR (2002): Constrained delaunay tetrahedrizations and probably good boundary recovery. In: The 11th International Meshing Roundtable

Shewchuk JR (2002): Two discrete optimization algorithms for the topological improvement of tetrahedral meshes. In: Unpublished manuscript, received in 2002

Shewchuk JR (2002): What is a good linear element? Interpolation, conditioning, and quality measures. In: The 11th International Meshing Roundtable

Tomasi C, Manduchi R (1998): Bilateral filtering for gray and color images. In: Proceedings of the 1998 IEEE International Conference on Computer Vision, Bombay, India, pp. 839–846

Weickert J (1998): Anisotropic diffusion in image processing. BG Teubner Stuttagart, Germany

Westermann R, Kobbelt L, Erti T (1999): Real-time exploration of regular volume data by adaptive reconstruction of isosurfaces. Visual Comput 15(2)100–111

Wood Z, Desbrun M, Schroder P, Breen D (2000): Semi-regular mesh extraction from volumes. In: Visualization 2000 Conference Proceedings, pp. 275–282

Zhou Y, Chen B, Kaufman A (1997): Multiresolution tetrahedral framework for visualizing regular volume data. In: Proceedings of the 8th IEEE Visualization 1997 Conference, pp. 135–142

18. Radiography and Injury Results of Human Parts

Bauer SI, Hollander JE, Fuchs SH, et al. (1995): A clinical decision rule in the evaluation of acute knee injuries. J Emerg Med 13:611–615

Cameron C, Naylor CD (1999): No impact from active dissemination of the Ottawa Ankle Rules: further evidence of the need for local implementation of practice guidelines. CMAJ 160:1165–1168

Diercks DB, Hall KN, Hamilton CA (1997): Validation of the Ottawa Knee Rules in an American urban teaching emergency department. Acad Emerg Med 4:408–409

Feinstein AR (1987): Clinimetrics. Yale University Press, New Haven, CT

Green NE, Allen BL (1977): Vascular injuries associated with dislocation of the knee. J Bone Joint Surg Am 59:236–239

Hill JA, Rana NA (1981): Complications of posterolateral dislocation of the knee: case report and literature review. Clin Orthop 154:212–215

Hoover NW (1961): Injuries of the popliteal artery associated with fractures and dislocations. Surg Clin North Am 41:1099–1112

Jones RE, Smith EC, Bone GE (1979): Vascular and orthopedic complications of knee dislocation. Surg, Gynecol Obstet 149:554–558

Kendall RW, Taylor DC, Salvian AJ, et al. (1993): The role of arteriography in assessing vascular injuries associated with dislocations of the knee. J Trauma 35:875–879

Kennedy JC (1963): Complete dislocation of the knee joint. J Bone Joint Surg Am 45:889–904

Laupacis A, Sekar N, stiell IG (1997): Clinical prediction rules. A review and suggested modifications of methodological standards. JAMA 277:488–494

Lefrak EA (1976): Knee dislocation: an illusive cause of critical arterial occlusion. Arch Surg 11:1021–1024

L'Insalata JC, Harner CD (1996): The dislocated knee: approach to treatment. Pittsburgh Orthop J 7:32–36

McCoy GF, Hannon DG, Barr RJ, et al. (1987): Vascular injury associated with low-velocity dislocations of the knee. J Bone Joint Surg Br 69:285–287

McCutchan JD, Gillham NR (1989): Injury to the popliteal artery associated with dislocation of the knee: palpable distal pulses do not negate the requirement for arteriography. Injury 20:307–310

Meyers MH, Moore TM, Harvey JP Jr, (1975): Follow-up notes on articles previously published in The Journal: traumatic dislocation of the knee joint. J Bone Joint Surg Am 57:430–433

Moore TM (1981): Fracture-dislocation of the knee. Clin Orthop 156:128–140

Nichol G, Stiell IG, Wells GA, et al. (1985): Clinical predition rules: application and methodological standards. N Engl J Med 313:793–797

Noyes FR, Barber-Westin SD (1997): Reconstruction of the anterior and posterior cruciate ligaments after knee dislocation. Am J Sports Med 25:769–778

O'Donnell TF Jr, Brewster DC, Darling RC, et al. (1977): Arterial injuries associated with fractures and/or dislocations of the knee. J Trauma 17:775–784

Quinlan AG, Sharrard WJW (1958): Posterolateral dislocation of the knee with capsular interposition. J Bone Joint Surg Br 40:660–663

Reckling FW, Peltier LF (1969): Acute knee dislocations and their complications. J Trauma 9:181–191

Reddy PK, Posteraro R, Schenk RC (1996): The role of magnetic resonance imaging in evaluation of the cruciate ligaments in knee dislocations. Orthopaedics 19:165–169

Roman PD, Hopson CN, Zenni EJ Jr (1987): Traumatic dislocation of the knee: a report of 30 cases and literature review. Orthop Rev 16:917–924

Savage R (1980): Popliteal artery injury associated with knee dislocation: improved outlook? Am Surg 46:627–632

Sawchuk AP, Eldrup-Jorgenssen J, Tober C, et al. (1990): The natural history of intimal flaps in a canine model. Arch Surg 125:1614–1616

Schenck RC Jr (1994): The dislocated knee. Instruct Course Lect Am Acad Orthop Surg 43:127–136

Seaberg DC, Jackson R (1994): Clinical decision rule for knee radiographs. Am J Emerg Med 12:541–543

Seaberg DC, Yealy DM, Lukens T, et al. (1998): Multicenter comparison of two clinical decision rules for the use of radiography in acute, high-risk knee injuries. Ann Emerg Med 32:8–13

Sedel L, Nizard Rs (1993): Nerve grafting for traction injuries of the common peroneal nerve. J Bone Joint Surg Br 75:772–774

Shapiro MS, Freedman EL (1995): Allograft reconstruction of the anterior and posterior cruciate ligaments after tranmatic knee dislocation. Am J Sports Med 23:580–587

Shelbourne KD, Porter DA, Clingman JA, et al. (1991): Low-velocity knee dislocation. Orthop Rev 20:995–1004

Shields L, Mital M, Cave EF (1969): Complete dislocation of the knee: experience at the Massachusetts General Hospital. J Trauma 9:192–215

Sisto DJ, Warren RF (1985): Complete knee dislocation: a follow-up study of operative treatment. Clin Orthop 198:94–101

Stain SC, Yellin AE, Weaver FA, et al. (1989): Selective management of nonoccclusive arterial injuries. Arch Surg 124:1136–1141

Stiell IG, Wells GA (1999): Methodologic standards for the development of clinical decision rules in emergency medicine. Ann Emerg Med 33:437–447

Stiell IG, Greenberg GH, Wells GA, et al. (1995): Derivation of a decision rule for the use of radiography in acute knee injuries. Ann Emerg Med 26:405–412

Stiell IG, Wells GA, McDowell I, et al. (1995): Use of radiography in acute knee injuries: need for clinical decision rules. Acad Emerg Med 2:966–973

Stiell IG, Greenberg G, Wells GA, et al. (1996): Prospective validation of a decision rule for the use of radiography in acute knee injuries JAMA 275:611–615

Taylor Ar, Arden GP, Rainey HA (1972): Traumatic dislocation of the knee: a report of forty-three cases with special reference to conservative treatment. J Bone Joint Surg Br 54:96–101

Tigges S, Pitts S, Mukundan S, et al. (1999): External validation of the Ottawa Knee Rules in an Urban trauma center in the United States. AJR Am J Roentgenol 172:1069–1071

Treiman GS, Yellin AE, Weaver FA (1992): Examination of the patient with a knee dislocation: the case for selective arteriography. Arch Surg 127:1056–1063

Twaddle BC, Hunter JC, Chapman JR, et al. (1996): MRI in acute knee dislocation: a prospective study of clinical, MRI and surgical findings. J Bone Joint Surg Br 78:573–579

Varnell RM, Coldwell DM, Sangeorzabn BJ, et al. (1989): Arterial injury complicating knee disruption. Am Surg 55:668–704

Verbeek PR, Stiell IG, Herbert G, et al. (1997): Ankle radiograph utilization after learning a decision rule: a 12-month follow-up. Acad Emerg Med 4:776–779

Wagner WH, Calkins ER, Weaver FA, et al. (1988): Blunt popliteal artery trauma: 100 consecutive cases. J Vasc Surg 7:736–748

Walker DN, Hardison RR, Schenck RC Jr (1994): A baker's dozen of knee dislocations. Am J Knee Surg 7:117–124

Wascher DC, Dvirnak PC, DeCoster TA (1997): Knee dislocation: initial assessment and implacations for treatment. J Orthop Trauma 11:525–529

Waschcer DC, Becker JR, Dexter JG, et al. (1999): Reconstruction of the anterior and posterior cruciate ligaments after knee dislocation. Am J Sports Med 27:189–196

Weber JE, Jackson RE, Peacock WF (1995): Clinical decision rules discriminate between fractures and nonfractures in acute isolated knee trauma. Ann Emerg Med 26:429–433
Welling RE, Kakkasseril J, Cranley JJ (1981): Complete dislocations of the knee with popliteal vascular injury. J Trauma 21:450–453
Wigder HN, Cohan Ballis SF, Lazar L, et al. (1999): Successful implementation of a guideline by peer comparisons, education and positive physician feedback. J Emerg Med 17:807–810
Winkelaar GB, Taylor DC (1998): Vascular trauma associated with fractures and dislocations. Semin Vasc Surg 1(4):261–273
Yeh WL, Tu YK, Su JY, et al. (1999): Knee dislocation: treatment of high-velocity knee dislocation. J Trauma 46:693–701
Yu JS, Goodwin D, Salonen D, et al. (1995): Complete dislocation of the knee: spectrum of associated soft tisssue injuries depicted by MR imaging: impression and plan. AJR Am J Roentgenol 164:135–139

19. Advances in Numerical/Finite Element Method Applied Trauma

Andriacchi TP, Alexander EJ (2000): Studies of human locomotion: past, present, future. J Biomech 33:1217–1224
Anglic A, et al. (1999): Mathematical modeling of stress on hip during gait. J Biomech 32:1229–1235
Arruda E, et al. (2000): Finite element modeling of human skin using an isotropic, nonlinear elastic constitute model. J Biomech 33:645–652
Bagge A (2000): A model of bone adaptation of an optimization process. J Biomech 33:1349–1357
Beek M (2000): Three-dimensional finite element analysis of the human temporomandibular joint disc. J Biomech 33:307–316
Berger R, et al. (1997): Normal kinematics of corpal bones: a 3-D analysis of corpal bone motion relative to the radius. J Biomech 30(8):787–793
Biryokva EV, et al. (2000): Kinematics of human reconstructed from spatial tracking system recordings. J Biomech 33:985–995
Boroni G, et al. (1999): Methodological + technological implications of quantitative human movement analysis in long term space flights. J Biomech 32:431–436
Boyd FT (1997): Pedel and knee loads using a multidegree of freedom pedel platform in cycling. J Biomech 30:505–507
Brand RA, et al. (1997): The Jaw area close movements protected by biomechanical modeling. Pelvic muscles + acetabular contact forces during gait. J Biomech 30(9):959–965
Chadwick EKJ (2000): Elbow and wrist joint contact forces during occupational pick + place activities. J Biomech 33:591–600

Charles et al. (1997): A uniform strain criterion for trabecular bone adaption: do continuum level strain gradients drive adaptation? J Biomech 30(6):555–563

Claes LE, Heigele CA (1999): Magnitudes of local stress and strain along bony surfaces predict the causes + type of fracture healing. J Biomech 32:255–266

Covteau B, et al. (2000): The mesh-matching algorithm: an automatic 3D mesh generator for finite element structures. J Biomech 33:1005–1009

Cowin SC (1999): Bone poroelasticity. J Biomech 32:217–238

Cowin SC, et al. (1999): The effect of surface roughness on the stress adaptation of vascular architecture around a cylindrical implant. J Biomech 32:275–284

Daggfeldt K, Therstensson A (1997): The intra-abdominal pressure in spinal unloading. J Biomech 30(11/12):1149–1155

deLooze HP, et al. (1999): Abdominal muscles contribute in a minor way to peak spinal compression in lifting. J Biomech 32:655–662

Evarsson J, et al. (2000): Strain relief from the cerebral ventricles during head impact – experimental studies on natural protection of the brain. J Biomech 33:181–189

Fritz M (2000): Stimulating the response of a standing operator to vibration stress by means of a biomechanical model. J Biomech 33:795–802

Gardiner TN, et al. (2000): The influence of mechanical stimulus on the pattern of tissues differentiation in a long bone fracture on F.E.M study. J Biomech 33:415–425

Glitsch U, Baumann W (1997): The 3-D determination of internal loads in the lower extremity. J Biomech 30(11/12):1123–1131

Golhofer A, et al. (1999): A multi-phase optimal control technique for the stimulation of a human vertical jump. J Biomech 32:87–91

Gradine MD, et al. (2000): Foot displacement but not velocity predicts the outcome of a slip induced in young subjects while walking. J Biomech 33:803–808 `gradiner@bone.ri.ccf.org` Dept of Biomedical Engineering, NDZ, The Institute, The Cleveland Clinic Foundation, 9500 Evclid Avne, Cleveland, OH 44195, USA

Grmarn WS (1997): Geometric and inertial data of the trunk in adult males. J Biomech 30(7):679–688

Guillaume A, et al. (1997): Effects of perfusion on the mechanical behaviour of the brain exposed to hyper gravity. J Biomech 30:383–389

Hansson S. (2000): The relationship between surface roughness and interfacial shear strength of a bone anchored implants. A mathematical model. J Biomech 33:824–836

Hirokawa S, Tsoumo R (2000): Three dimensional deformation and stress distribution in an analytical / computational model of the anterior carciate ligament. J Biomech 33:1069–1077

Hofe CP, Amest CH (2000): A fuzzy logic model by fracture healing. J Biomech 33:961–968

Huis kes R, et al. (1999): Correlation between pre-operative preprosthetic bone density and post operative bone loss in THA can be explained by strain adaptive remodeling. J Biomech 32:695–703

Ilo K, et al. (2000): The influence of the acetabular labrum on hip joint cartilage consolidation, a poroelastic finite element model. J Biomech 33:953–960

Jacobs R, et al. (1996): Mechanical output from individual muscles during Finland explosive leg extensions. The role of biarticular muscles. J Biomech 29(4):513–523

Jacobs CR, et al. (1997): Adaptive bone remodeling incorporating simultaneous density and anisotropy considerations. J Biomech 30(6):603–613

Jensen KJ, et al. (1999): The role of the lemallar interface during torsional yielding of human artral bone. J Biomech 32:303–310

Kellis E, Baltzopoulous V (1999): The effects of the antagonist muscle force in intesegmental loading during isolinetic efforts of the knee exteriors. J Biomech 32:19–25

Keyak JH (2000): Prediction of femoral fracture load using finite element models: an examination of stress strain based fracture theories. J Biomech 33:209–214

Koni PV (2000): Stretch-shortening cycle: a powerful model to study normal + fatigue muscle. J Biomech 33:1197–1206

Koolstra JH (1999): Three-dimensional dynamical capabilities of the human masticatory muscles. J Biomech 32:145–152

Leardini A, et al. (1999): A geometric model of the human angle joint. J Biomech 32:585–597

Li G, et al. (1999): The importance of quadriceps + hamstring muscle loading on knee kinematics + in situ forces in the NCL. J Biomech 32:395–400

Lowet et al. (1996): The study of the vibational behaviour of a healing tibia using finite element modeling. J Biomech 29(8):1003–1010

Marag E, Cavanagh PC (1999): Structural + functional predictors of regional peak pressures under the foot during walking. J Biomech 32:359–370

Marras WS, Granara KP (1997): Spine loading during trunk lateral bending motions. J Biomech 30(7):697–703

Maurel N, et al. (1997): A 3-D parameterized finite element model of the lower cervical spine. Study of the influence of the posterior artricular faces. J Biomech 30(9):921–931

McCarmacc A, et al. (1999): Micro damage accumulation in the cement layer of hip replacements under flexural loadings. J Biomech(32):467–475

Mcwomara B, et al. (1997): The relationship with bone prothesis bonding + load transfer in total hip reconstruction. J Biomech 30(6):621–630

Merz B, et al. (1997): Mechanical implication of humerus incongruity finite element analysis + experiment. J Biomech 30(7):713–721

Miller K, Chinzei K (1997): Constitute modeling of brain tissue: experiment + Theory. J Biomech 30(11/12):1115–1121

Myers BS, et al. (1999): Surface friction in rear vertex head and neck impact increases risk of injury. J Biomech 32:293–309

Napadow VJ, Chen Q, Weedes vas J, Gilbert RJ (1999): Tramural mechanics of the human tongue in association with physiological deformations. J Biomech 32:1–12

Nightingale RW, et al. (2000): Inertial properties and loading rates affect backing modes and injury mechanisms in crucial spine. J Biomech 33:199–197

Patrick CW Jr, Pergman (1998): Frontier tissue engineering. Elsevier Science, P.O. Box 882, New York NY 10159–0882, USA

Pierdegast PJ, Ferris P (2000): Middle ear dynamics before and after vascular replacement. J Biomech 33:581–590

Prefrusze Z (1999): A fabric-dependent fracture criterion for bone. J Biomech 32:934–943

Rally GL, Curry JD (2000): The effects of damage and micro cracking on the impact strength bone. J Biomech 33:337–343

Rednelli A, et al. (1999): Poroelastic finite element analysis of a bone specimen under cyclic loading. J Biomech 32:135–140

Reich J, Daunic WJ (2000): A rigid body model of the forearm. J Biomech 33:1159–1168

Robert R, et al. (1999): Identification of passive elastic joint moments in the lower extremities. J Biomech 32: 515–525

Rohlmern A, et al. (2000): Influence of load carrying on loads in internal spinal fractures. J Biomech 33:1099–1104

Sarron JC, et al. (2000): Identification of linear viscoelastic constitute models. J Biomech 33:685–686

Sasaki N, et al. (1999): Early stage-stress relaxation in compact bone. J Biomech 32:93–97

Schechtmai H (1997): Invitro fatigue of human tendons. J Biomech 30(8):821–835

Scot LD, et al. (1999): Variations of relation moment arms with hip flexion. J Biomech 32:1005–1016

Sevostianov et al. Impact of the porous microstructure on the overall elastic properties of the osteonal vertical bone

Shipkowitz T, et al. (2000): Numerical study on the effect of secondary flow in the human aorta in local shear stresses in abdominal branches. J Biomech 33:717–728

Slates IAC (1999): Quantitative anatomy of the lumbar musclature. J Biomech 32:311–316

Stein RB, et al. (1999): Biomechanics of human quadriceps muscles during electrical stimulation. J Biomech 32:347–357

Steinmar D (2000): Stimulated pathline visualization of computed periodic blood flow patterns. J Biomech 33:623–628

Sumner DR, et al. (1998): Functional adaptation and in growth of bone vary as a function of hip implant stiffness. J Biomech 31:909–917

Van Dijke GH, et al. (1999): A biomedical model on muscle forces in the transfer of spinal load to the pelvis and legs. J Biomech 32:927–933

Von Deursen DL, et al. (2000): Mechanical effects of continuous passive motion on the lunar spine in seating. J Biomech 33:695–699
Weinans H, et al. (2000): Sensitivity of periposthetic stress-shielding to load and the bone density modulus relationship in subject specific finite element models. J Biomech 33:809–817
Wen L, et al. (2000): A mechanical model to determine the influence of masses and mass distribution on the impact force during running. J Biomech 33:219–224
Woo SL-Y (2000): The effect of the point of application of anterior tibial loads on human knee kinematics. J Biomech 33:1147–1152
Wright IC et al. (2000): The influence of foot positioning on ankle sprains. J Biomech 33:513–519
Zhao SZ, et al. (2000): Blood flow and vessel mechanics is a physiologically realistic model of a human control. J Biomech 33:975–984

20. General-Biomedical References

Askew LJ, An K-N, Morrey B, et al. (1987): Isometric elbow strength in normal individuals. Clin Orthop 222:261–265
Brumfield RH Jr, Kuschner SH, Gellman H, et al. (1990): Total elbow arthroplasty. J Arthroplasty 5:359–363, Abstract
Bryan RS, Morrey B (1982): Extensive posterior exposure of the elbow: a triceps-sparing approach. Clin Orthop 166:188–192, Abstract
Cobb T, Morrey B (1997): Total elbow replacement as primary treatment for distal humeral fractures in elderly patients. J Bone Joint Surg Am 79:826–832, Abstract
Davis RF, Weiland AJ, Hungerford DS, et al.(1982): Nonconstrained total elbow arthroplasty. Clin Orthop 171:156–160, Abstract
Dee R (1972): Total replacement arthroplasty of the elbow for rheumatoid arthritis. J Bone Joint Surg Br 54:88–95,Citation
Dee R (1993): Nonimplantation salvage of failed reconstructive procedures of the elbow. In Morrey BF (Ed.): The Elbow and its Disorders, 2nd edition. WB Saunders, Philadelphia, pp. 690–695
DeLee JC (1996): Fractures and dislocations of the hip. In Rockwood CA Jr, Green Dp, Bucholz RW, et al.(Eds.): Rockwood and Green's Fractures in Adults, 4th edition. Lippincott-Raven, Philadelphia, p. 1687
Ewald FC, Jacobs M (1984): Total elbow arthroplasty. Clin Orthop 182:137–142, Abstract
Figgie E III, Ingliszz AE, Ranawat CS, et al. (1987): Results of total elbow arthroplasty as a salvage procedure for failed elbow reconstructive operations. Clin Orthop 219:185–193, Abstract
Froimson AI, Silva JE, Richey M (1976): Cutis arthroplasty of the elbow joint. J Bone Surg Am 58:863–865, Abstract

Garrett JC, Ewald FC, Thomas WH, et al. (1977): Loosening associated with GSB hinge total elbow replacement in patients with rheumatoid arthritis. Clin Orthop 127:170–174, Abstract

Gschwend N. Loehr J, Ivosevic-Radovanovic D, et al. (1988): Semiconstrained elbow prosthesis with special reference to the GSB III prosthesis. Clin Orthop 232:104–111

Gschwend N, Scheier H, Bahler A, et al.(1996): GSB III elbow. In: The Elbow, Endoprosthetic Replacement and Non-endoprosthetic Procedures, Ruther W (Ed.) Springer, Berling Heidelberg New York, pp. 83–98

Gschwend N, Simmen BR, Maejovsky Z (1996): Late complications in elbow arthroplasty. J Shoulder Elbow Surg 5:86–96, Abstract

Helfet DL, Schmerling GJ (1993): Bicondylar intra-articular fractures of the distal humerus in adults. Clin Orthop 292:26–36, Abstract

Hughes RE, Schneeberger AG, An K-N, et al. (1997): Reduction of triceps muscle force after shortening of the distal humerus: a computational model. J Shoulder Elbow Surg 6:444–448, Abstract

Inglis E, Pellicci P (1980): Total elbow replacement. J Bone Joint Surg Am 62:1252–1258, Abstract

John H, Rosso R, Neff U, et al. (1994): Operative treatment of distal humeral fractures in the elderly. J Bone Joint Surg Br 76:793–796, Abstract

Jupiter J, Morrey B (1993): Fractures of the distal humerus in the adult. In Morrey BF (Ed.): The Elbow and its Disorders, 2nd edition. WB Saunders, Philadelphia, p. 351

Jupiter JB, Neff U, Holzach P, et al. (1985): Intercondylar fractures of the humerus. J Bone Joint Surg Am 67:226, Abstract

Kasten MD, Skinner HB (1993): Total elbow arthroplasty. Clin Orthop 290:177–188, Abstract

Knight RA, Zandt L (1952): Arthroplasty of the elbow. J Bone Joint Surg Am 34:610–618

Kraay MJ, Figgie MP, Inglis AE, et al. (1994): Primary semi-constrained total elbow arthroplasty. J Bone Joint Surg Br 76:636–640, Abstract

Lowe LW, Miller AJ, Allum RL, et al.(1984): The development of an unconstrained elbow arthroplasty. J Bone Joint Surg Br 66:243–247, Abstract

McAuliffe JA, Burkhalter WE, Oullette EA, et al. (1992): Compression plate arthrodesis of the elbow. J Bone Joint Surg Br 74:300–304, Abstract

Morrey BF (1990): Post-traumatic contracture of the elbow: operative treatment including distraction arthroplasty. J Bone Joint Surg Am 72:601–618, Abstract

Morrey BF, Adams RA (1992): Semi-constrained arthroplasty for the treatment of rheumatoid arthritis of the elbow. J Bone Joint Surg Am 74:479–490, Abstract

Morrey BF, Adams R (1993): Semi-constrained elbow replacement arthroplasty: Rational, technique, and results. In Morrey BF (Ed.): The Elbow and its Disorders, 2nd edition. WB Saunders, Philadelphia, pp. 648–664

Morrey F, Adams RA (1995): Semi-constrained elbow replacement for distal humeral nonunion. J Bone Joint Surg Br 77:67–72, Abstract

Morrey BF, Askew LJ, An K-N, et al. (1981): A biomechanical study of normal functional elbow motion. J Bone Joint Surg Am 63:872–877, Abstract

Morrey BF, Bryan RS, Dobyns JH, et al. (1981): Total elbow arthroplasty: a five-year experience at the Mayo Clinic. J Bone Joint Surg Am 63:1050–1063, Abstract

Morrey BF, Askew LJ, An K-N (1988): Strength function after elbow arthroplasty. Clin Orthop 234:43–50, Abstract

Morrey F, Adams RA, Bryan RS (1991): Total replacement for post-traumatic arthritis of the elbow. J Bone Joint Surg Br 73:607–612, Abstract

O'Driscoll SW, An K-N, Korinek S, et al. (1992): Kinematics of semi-constrained total elbow arthroplasty. J Bone Joint Surg Br 74:297–299, Abstract

O'Neill OR, Morrey BF, Tanaka S, et al. (1992): Compensatory motion in the upper extremity after elbow arthrodesis. Clin Orthop 281:89–96

Pritschard RW (1979): Anatomic surface elbow arthroplasty: a preliminary report. Clin Orthop 179:223–230

Schneeberger AG, Adams R, Morrey B (1997): Semiconstrained total elbow replacement for the treatment of post-traumatic osteoarthrosis. J Bone Joint Surg Am 79:1211–1222, Abstract

Soni RK, Cavendish ME (1984): A review of the Liverpool elbow prosthesis from 1974 to 1982. J Bone Joint Surg Br 66:248–253, Abstract

Souter WA, Nicol AC, Paul J (1985): Anatomical trochlear stirrup arthroplasty of the rheumatoid elbow. J Bone Joint Surg Br 67:676

Tsuge K, Murakami T, Yasunaga Y, et al. (1987): Arthroplasty of the elbow. J Bone Joint Surg Br 69:116–120, Abstract

Urbaniak JR, Black KE Jr (1985): Cadaveric elbow allografts: a six year experience. Clin Orthop 197:131–140, Abstract

Zuckerman JD, Lubliner JA (1990): Arm, elbow and forearm injuries.In: Orthopaedic Injuries in the Elderly, Zuckerman JD (Ed.) Urban & Schwarzenberg, Baltimore, pp. 345–407

Specialised Experimental and Medical-cum-Analytical References

Anne C. Brower: Arthritis in Black and White. W.B. Saunders, Philadelphia, 1997

Allen L. Carl, Division of Orthopedic Surgery, Albany Medical College, Albany, NY 12208

Andrew Cragg, Department of Radiology, University of Minnesota, Minneapolis, MN 55424

Armstrong P, et al: Imaging of Diseases of the Chest, 3rd edition. Mosby, Baltimore, 2000

Barnard M (Ed.): "Health and Safety for Engineer" 1998 p 198, Thomas Telford, London

Baixauli EL. Avascular necrosis of the femoral head after intratrochanteric fractures. J Orthop Trauma – 01-Feb-1999; 13(2): 134–137

Bass CR, Duma SM, Crandall JR, Pilkey WD, Khaewpong N, Eppinger RH: "The Interaction of Airbags with cadaveric Upper extremities," Proceedings of the 41st International Stapp Car Crash Conference, Orlando, FL, November 1997

Bernard F. Morrey: The Elbow and Its Disorder, 2nd edition. W.B. Saunders, Philadelphia, 1993, Chap. 17 by John H. Wedge

Boutin RD, et al: Update on imaging of orthopedic infections. Orthop Clin North Am 29:41–64, 1998

Canale ST (Ed.): Campbell's Operative Orthopaedics, 9th Edition. Mosby, Philadelphia, 1998

Chew F, Maldjian C: Enchondroma and enchondromatosis. E-Medicine, 2002

Dauvilliers et al, Development of a Finite Element Model of the Neck. 38th Stapp Car Crash Conference, pp. 77–91, 1994

Dias LMA and Coble RJ (Eds.): Proceedings of first International Conference of CIB Working Commission, Portugal 1996, p 416, A.A. Balema, Rotterdam

Duma SM, Crandall JR, Hurwitz SR, Pilkey WD: "Small Female Upper Extremity Interaction with a Deploying Side Air Bag," Proceeding of the 42nd Stapp car Crash Conference, Tampa, AZ, November 1998

Duma SM, Rudd RW, Crandall JR: "The automobile Airbag System," Professional Safety: Journal of the American Society of Safety Engineers, 43(10) 24–27, 1999

Duma SM, Schreiber PH, McMaster JD, Crandall JR, Bass CR, Pilkey WD: "Dynamic Injury Tolerance for Long Bones in the Female Upper Extremity," Journal of Anatomy, 194, Par 3, 463-71, 1999

Eggli KD, et al: Ewing's Sarcoma. Radiol Clin North Am 31(2):325–337, 1993

Eric H. Ledet, Division of Orthopedic Surgery, Albany Medical College, Albany, NY 12208 and Department of Biomedical Engineering, Rensselaer Polytechnic Institute, Troy, NY 12180

Fuchs HA, Kaye JJ, Callahan LF, et al: Evidence of significant radiographic damage in rheumatoid arthritis within the first 2 years of disease. J Rheumatol 16:585, 1989

Grainger RG, Allison D: A Textbook of Medical Imaging, Volume II, 3rd edition. Churchill Livingstone, New York, 1997, pp 1679–1682

Green and Swiontkowski: Skeletal Trauma in Children, Volume 3, 2nd edition. W.B. Saunders, Philadelphia, 1998, Chap. 9 by Neil E. Green

Greenspan A: Bone island (enostosis): current concept – a review. Skeletal Radiol 24(2):111–115, 1995

Greenspan A: Orthopedic Radiology: A Practical Approach, 3rd edition. Lippincott, Philadelphia, 2000, p 60

Greenspan A: Orthopedic Radiology: A Practical Approach, 3rd edition, 2000

Greenspan A: Orthopedic Radiology: A Practical Approach, 3rd edition, Lippincott, Williams & Wilkins, Philadelphia, 2000, pp 371–379

Greenspan A: Orthopedic Radiology, 3rd edition. Lippincott, Philadelphia, 2000, p 248

Greenspan, Orthopedic Radiology: A Practical Approach. Williams & Wilkins, Philadelphia, 2004

Greenspan A: Orthopedic Radiology, 3rd edition. Lippincott, Williams & Wilkins, 2004, pp 283, 306–307

Griffin MJ (1997): Occupational & Environmental Medicine, 54, 73–89

Gurram R et al. (1994): Advances in Industrial Ergonomics & Safety VI, 239–246. Taylor & Francis

Hall FM, Hochman MG: Medial Segond-type fracture: cortical avulsion off the medial tibial plateau associated with tears of the posterior cruciate ligament and medial meniscus. Skeletal Radiol 26:553–555, 1997

Harada N, Griffi MJ (1991). Br J Ind Med, 48, 185–192

HMSO: "Safety and Health at Work" 1972, HMSO London

Huges Phil and Ferrett (Ed.): "Introduction to Health and Safety in Constructions" Elsevier, Amsterdam, 2005 p 440

Jerrold H. Mink, et al: Magnetic Resonance Imaging of the Knee. Raven Press, New York, 1993

Juhl: Paul and Juhl's Essentials of Radiologic Imaging, 7th edition. Lippincott, Williams & Wilkins, Baltimore, 1998

Klarlund M, Ostergaard M, Jensen KE, et al: Magnetic resonance imaging, radiography, and scintigraphy of the finger joints: one year follow up of patients with early arthritis. Ann Rheum Dis 59:521, 2000

Kuntz DG, Baratzs ME: Elbow trauma and reconstruction. Orthop Clin North Am 30:37–58, 1999

Kuper IH, van Leeuwen MA, van Riel PL, et al: Influence of a ceiling effect on the assessment of radiographic progression in rheumatoid arthritis during the first 6 years of disease. J Rheumatol 26:268, 1999

Lafortune MA, and Lake MJ: Human pendulum approach to simulate and quantify locomotor impact loading, J. Biomechanics, Vol. 28-9, 1111–1114, 1995

Lindsell DRM, et al: Fractures on the chest. radiograph in detection of alcoholic liver disease. Br Med J 285:597–599, 1982
Marx JA: Rosen's Emergency Medicine: Concepts and Clinical Practice, 5th edition. Copyright 2002 Mosby, Inc., pp 691–692
McQueen FM, Stewart N, Crabbe J, et al: Magnetic resonance imaging of the wrist in early rheumatoid arthritis reveals a high prevalence of erosions at four months after symptom onset. Ann Rheum Dis 57:350, 1998
McQueen FM, Stewart N, Crabbe J, et al: Magnetic resonance imaging of the wrist in early rheumatoid arthritis reveals progression of erosions despite clinical improvement. Ann Rheum Dis 58:156, 1999
Michael P. Tymeson, Division of Orthopedic Surgery, Albany Medical College, Albany, NY 12208
Moeller JL, et al: Anterior cruciate ligament injuries in female athletes: why are women more susceptible? Physician Sportsmed 25:4, 1997
Nguyen VD, London J, Cone RO 3d. Ring sequestrum: radiographic characteristics of skeletal fixation pin-tract osteomyelitis. Radiology 1986;158: 129–131
Nigg BM: Experimental techniques used in running shoes research, In Biomechanics of Running Shoes (Edited by Nigg, B.M.), Human Kinetics, Champaign, 29, 1986
Nishiwaki T, and Nasako M: Cushioning simulation of shoes sole at the heel impact, Proceedings of Symposium on Sports Engineering, JSME, 98–31, 9–12, 1998
Peterfy CG, Roberts T, Genant HK: Dedicated extremity MR imaging. An emerging technology. Radiol Clin North Am 35:1, 1997
Ramsey RG: Teaching Atlas of Spine Imaging. George Thieme, Stuttgart, 1999, p 275
Regaldo S, Stacy G: Bone island. E-Medicine, 2001
Resnic D: Diagnosis of Bone and Joint Disorders, 4th edition. W.B. Saunders, Philadelphia, 2002
Resnick D, Niwayama G: Diagnosis of Bone and Joint Disorders, Volume 6, 2nd edition. W.B. Saunders, Philadelphia, 1988, pp 3845–3955
Resnick D: Bone and Joint Imaging, 2nd edition, W.B. Saunders, Philadelphia, 1996, pp 1007–1011
Resnik, D: Diagnosis of Bone and Joint Disorders, 3rd ed. Philadelphia, W.B. Saunders. 1995, pp. 4380–4383
Resnick D. Diagnosis of Bone and Joint Disorders, 4th ed., Philadelphia, W.B. Saunders. 2003
Resnik WB: Internal Derangements of Joints. W.B. Saunders, Philadelphia, 1997, pp 679–680
Schmidt AH. Femoral neck fractures. Orthop Clin North Am – 01-Jan-2002; 33(1): 97–111, viii
Ridley J and Channing J: "Safety at Work" 2003 p 1096, Elsevier Amsterdam
Shetty AK, Gedalia A: Septic arthritis in children. Rheum Dis Clin North Am 24:287–304, 1998

Simon Salerno, Division of Neurosurgery, Albany Medical College, Albany, NY 12208

Skiba K, Rutowski R: The method of microsurgical reconstruction of ruptured Achilles tendon [in Polish], 4th Conference of Microsurgery, October 15–17, 1997, Abstracts 60, Wroclaw

Skiba K, Dudek K, Wiczkowski E, Rutowski R, Szumarska M: Application of the thermography in estimating limb fitness following surgical treatment of the Achilles tendon, Acta of Bioengineering and Biomechanics, 2, Suppl. 1, 483–488, 2000

Skiba K, Wiczkowski E, Rutowski R, Zuchowski R: Determination of tensile forces breaking of Achilles tendon, 32nd Solid Mechanics Conference Polish Academy of Sciences, Institute of Fundamental Technological Research, Zakopane, September 1–5, 1998, Abstracts, 339–340

Skinner HD (Ed.): Current Diagnosis and Treatment in Orthopedics, 2nd edition. Appleton & Lange, New York, 2000

Soslowsky LJ: et al: Many unknowns in ACL repair. Am. Acad Orthop Surg Bull 43:4, 1995

Spector TD: Rheumatoid arthritis. Rheum Dis Clin North Am 16, 513, 1990

Swischuk LE: Emergency Imaging of the Acutely Ill or Injured Child, 4th edition. Lippincott, Williams & Wilkins, Philadelphia, 2000, pp 431–433

Thunnissen et al., Human Volunteer Head–Neck Response in frontal Flexion: A New Analysis, 39th Stapp Car Crash Conference, pp. 439–460, 1995

Van der Heijde DM, van Leeuwen MA, van Riel PL, et al: Biannual radiographic assessments of hands and feet in a three-year prospective followup of patients with early rheumatoid arthritis. Arthritis Rheum 35:26, 1992

Weissleder RW, et al: Primer of Diagnostic Imaging, 2nd edition. Mosby, St. Louis, 1997, p 392

William E. Brant, Clyde A. Helms: Fundamentals of Diagnostic Radiology. Williams & Wilkins, Philadelphia, 1999

Wing P. Chan, et al: MRI of the Musculoskeletal System. W.B. Saunders, Philadelphia, 1994

Yamada H (1970): Strength of biological materials, Williams and Wilkins Co., Baltimore

Zenel JA: A febrile infant who has hand edema and erythema. Pediatr Rev 21, 2000

Zhen YP, Mak AF (1994). IEEE Trans Biomed Eng., 43, 912–918

Index

A
Abdominal trauma, 460–464
Abrasion, 5, 33, 35, 311, 488, 493
Acaromion, 5, 91–92, 404
Acetasulum, 5
Acomioclaviclar joint, 5
Acoustic trauma, 5
Acute trauma, 444, 505–506
Adduction, 5, 91, 259, 309, 385, 403–404
Adrenal glands, 5, 48
Alveolus, 41
Ameliorative strategies, 516
Amnesia, 5–6, 41
Anatomy, 5, 29, 32, 34, 37–38, 47, 49–50, 53, 367, 390, 450–451, 461
Aneurysm, 5
Ankle, 2, 11, 16, 43, 50–51, 53, 55, 221, 223, 240–242, 399, 496, 500, 502–505
Anterior, 5, 34, 36, 40, 47, 53, 88–89, 91–92, 187, 205, 208, 211, 213–214, 217, 233, 240–241, 249–251, 344–345, 347, 455, 457, 469, 497–498, 502
Anterior cruciate ligament injury, 250, 251
Anthropomorphic, 3, 53, 56
Aorta, 5, 8, 25, 35, 42, 48–49, 417–418
Apex, 5, 80, 83, 87–88, 317, 345
Aphasia, 6
Appendix, 6
Apraxia, 6
Arachnoid, 6, 14, 29, 99, 465
Arm, 6, 10, 13
Arrythmia, 6
Ataxia, 6
Atrial fibrillation, 6
Atrium, 6, 15
Auditory, 6, 8, 24, 31, 343, 345, 350
Avascular, 6, 406, 501
Avascular necrosis, 6, 85, 90, 308, 406, 453–455, 466, 480–485
Axial skeleton, 6, 228
Axilla, 6, 197, 199, 200

B
Barbiturates, 438–439
Basilar fractures, 34, 97, 439
Bile, 6, 10
Bile duct, 6
Biomechanical engineering, 6
Biomedical engineering, 6, 166, 189
Bionic, 6
Bladder, 6, 10, 13, 24, 26, 48, 408–416, 462
Blood circulation, 49
Bone, 6–9
Bone-fracture, 34, 55, 80, 107, 449
Bowel, 6, 217, 460–461
Boxer's fracture, 83–84
Bradycardia, 6, 433–434, 460
Brain injury, 34, 95–97, 190, 352–354, 360, 430, 432, 434, 440, 443–445
Brain stem, 27–28
Brain structure, 20
Bronchiole, 6
Bronchus, 6, 36, 248

Burns, 6
Bursa, 6

C
Caecum, 6–7
Calcaneus, 7, 50–51, 53, 402–403
Callus, 7, 139–140, 145, 287, 295
Cancellous bone, 93, 138, 142–150, 169–170, 184–189, 252–253, 313, 339, 370, 466
Cannulated, 257, 278–279, 282, 484
Capitellum/capitulum, 7, 89, 211, 449–456
Carbon fibers, 153–156, 158–161, 164
Carpal, 7, 11, 43, 84–86, 278
Carpal fractures, 84–85
Cartilage, 7, 14, 45, 135–136, 187–189, 220–221, 224, 227, 309, 344, 348–349, 369–370, 374, 450–451, 455, 494–495, 501
Cauda equina, 7, 35
Caudal, 7, 175
Cemented enchondroma, 252
Cephalad, 7, 276
Cephalic, 7, 25, 91
Cerebellum, 7, 11, 23, 25, 27–30, 33, 46, 346, 351, 355, 465
Cerebral cortex, 6–7, 448
Cerebrospinal fluid, 7, 29, 35, 38, 356, 429, 465
Cerebrum, 7, 23, 25, 27–30, 46, 465
Cervical, 7, 18, 32–35, 37–38, 192–193, 275, 285, 350, 363, 431, 449, 457–460, 481
Cervix, 7
Choroid, 7, 465
Ciliary body, 7
Clavicle, 7, 17–18, 42, 45, 54, 91, 404, 441
Clot, 7, 98–99
Coccyx, 7, 12, 18, 33, 50
Cochlea, 7
Coeliac, 7
Colles' fracture, 86–87, 201
Colon, 7, 14
Comminuted femur fracture, 307–308
Composite, 148, 155–158, 161, 163, 165–167, 256, 310, 399
Composition – brain, 20–27
Concussion, 7, 34, 190, 433, 442–443
Confusion, 7, 30, 98, 443, 447
Conjunctiva, 7
Connective tissue, 7, 9, 29, 136, 433, 464
Constitutive properties, 168–171, 411
Contralateral, 7, 36, 434, 458, 488
Contrecoup, 7, 98, 352, 357–358, 433, 464
Contusions, 30–31, 34–36, 41–42, 48, 51, 91, 98–99, 101, 353, 358, 429, 433, 435, 439, 444, 448, 460, 464
Convulsion, 7
Cornea, 7
Coronal, 8, 32, 93, 96, 235, 255, 346, 349, 357, 451–452, 467
Coronal plane, 8, 93, 255, 267, 357, 451–452
Coronary arteries, 8
Cortical bone, 145–146, 149–151, 185, 187–188, 252–253, 277, 279, 309, 312, 318, 339, 370, 495
Cracking phenomenon, 107, 527–531
Cranial bones, 343, 346, 348–349, 464
Cranial nerves, 97, 344–345, 350
Cranium, 8, 28–29, 33, 96, 343–344, 349, 351, 431, 448, 459, 464–465
Cricoid, 8
CT scanning, 8, 175, 355, 435, 439, 440–441, 443, 446
Cuboid, 8, 345
Cuneiform, 8
Cutaneous, 8, 503
Cuticle, 8, 140

D
Decerebellate, 8
Decerebrate, 8, 443
Deformity, 8, 52, 80, 83, 87, 90–91, 99, 201, 220, 306, 376, 456, 458, 474, 504–505, 509
Deltoid muscle, 8
Dental, 8, 459
Dentine, 8, 135
Depressed fractures, 96–97, 448
Dermis, 8, 177, 464
Diaphragm, 8, 35, 40, 47, 248, 459, 461–462

Dislocations, 37, 80, 88, 100–102, 213–214, 405, 452, 456, 485–491, 494–497
Disposition, 442–443, 495, 505
Doppler effect, 8
Duodenum, 8, 10, 12, 45
Dura mater, 8–9, 14, 29

E
Ear drum, 8–9, 11
Ecchymosis, 8, 87, 90–91, 235, 462–463, 492
Elasto-plastic finite element, 320–325
Elbow fractures, 88, 208, 211
Electrocardiography, 8
Embolism, 8
Enamel, 8, 135, 139
Enchondroma, 225–227, 243, 252–253
Endochondral bones, 348
Endocrine system, 8, 13
Enzyme, 8, 12
Epicardium, 8
Epidemiology, 2, 37, 228, 450
Epidermis, 8–9
Epididymis, 9, 15
Epigastrium, 9
Epiglottis, 9
Epiphysis, 9, 85–86, 92, 211, 221, 283, 405, 497
Ethmoid bone, 9, 306, 344, 347, 351, 433
Euryon, 9
Eustachian tube, 9, 345, 449
Exsanguination, 9
External carotid artery, 9, 25
Extracellular, 9
Extradural haemorrhage, 9

F
Facet, 9, 34, 38–39, 101, 186, 189, 193–194, 275, 363, 365, 457, 495
Facial index, 9
Fallopian tube, 9
Fascia, 9, 20–22, 312, 385, 464, 502
Female muscular system, 15, 494
Femur, 9, 13, 15, 17, 50–53, 55, 57, 92–93, 100–102, 168, 170, 175, 182, 227, 229, 249–250, 253, 269–272, 279, 284, 288, 292, 305, 307–310, 313–315, 317, 319, 338–343, 366, 369, 371, 373, 375, 466–467, 469–472, 475–477, 479–480, 482–485, 487–490, 494, 496–499, 501
Fetal distress, 9
Fever, 9, 97, 223, 423
Fibrolamellar-Haversian, 140–142
Fibrous dysplasia, 305–308
Fibula, 9, 17, 50–51, 53, 185, 200, 240–242, 262, 265, 369, 492, 502, 504–505
Fixation system, 294–295, 701–727
Flexion, 9, 38, 40, 81, 83, 87–90, 186, 191, 193–194, 200–201, 234–235, 257–259, 269, 309, 359, 365–367, 385, 403, 450–452, 455–456, 458, 485, 488–489, 492, 494, 496–503, 508–509
Flexor, 9, 80, 90, 260, 385–386, 503
Flexure, 9, 193
Focal injuries, 352–353
Fontanelles, 9, 349
Foot-dorsal, 44
Forea, 9
Forearm, 6, 12, 15, 46, 49, 50, 88–90, 195, 199–200, 204, 208, 259, 286, 406–408, 455–457
Fourth ventricle, 9
Frontal lobe, 9, 22, 24, 344, 351
Frozen shoulder, 10

G
Gait, 10, 271, 308, 311, 431
Gall bladder, 6, 10
Gastronemius, 10
Glanuloma, 10, 209
Glass fiber, 165–167
Glomerulus, 10
Gonads, 10, 12
Gracilis, 10
Granulation tissue, 10
Graphite layer, 154

H
Haematoma, 10, 14, 31
Haemoptysis, 10

Haemptysis, 10
Hallux, 10
Hamate fracture, 85–86
Hamstrings, 10, 250
Hand-dorsal, 44
Hand fracture, 221–222
Head injuries, 30, 34, 51, 357–358, 431, 434, 436, 447, 490
Head–neck, 55, 362–365
Head-neck complex, 362
Head trauma, 49, 96, 99–100, 429–431, 435–437, 440, 442–448
Hemiplegia, 10, 434
Hernia, 10
Hip system, 255, 270–273
Human tibia, 148, 185, 188
Humerus, 10, 14, 42–43, 46–47, 89–90, 195–196, 199, 208, 211, 227, 229, 253, 266, 407, 449, 450–452, 454–455, 505–508
Hypertension, 10, 433–434
Hypotension, 10, 235, 436–438, 445, 458, 460, 464
Hypotonia, 10
Hypoxaemia, 10, 41
Hypoxia, 10, 436, 439, 443, 445

I
Ileum, 10
Iliopsoas, 10, 92, 466
Ilium, 10, 17, 50
Impact loading, 4, 48, 53–55, 305, 384, 386
Innervation, 386
Interlobar, 10
Intra-osseous ganglion, 243
Intrinsic muscles, 385
Iris, 7, 10
Ischium, 10, 50, 174

J
Jejunum, 10
Joints, 6–7, 28, 34, 37–38, 46, 53–54, 80, 83–84, 102, 174, 177–178, 182, 184–185, 194, 197, 207, 220–221, 258, 260, 298, 310–311, 343, 347, 349, 363, 365–366, 370, 385–386, 391, 402, 457

K
Knee, 2, 50–53, 100–101, 187, 200–201, 244–245, 249–250, 267–269, 366–373, 399, 485–502, 504
Knee dislocation, 51, 486–491, 496–497, 499
Knee ligaments, 53, 367–368, 486, 490–491, 497
Knee system, 255, 267–269
Knee system-instrumentation, 598
Kyphosis, 10, 33, 194

L
Labyrinth, 11, 345
Lacrimal, 11, 346–348
Lacrimal gland, 11
Larynx, 9, 11
Lateral, 11
Lateral ventricles, 11, 440, 465
Latissimus dorsi, 11
Leg, 9, 12, 14, 50–52, 102, 173, 200–201, 228–233, 262, 273, 308, 312, 391, 397–399 469, 473, 488, 491–492, 495–497, 500–504
Ligaments, 11, 34, 38, 40, 42, 50, 53, 84, 102, 135, 174, 187, 189, 249, 251, 279, 309, 346, 363, 366–368, 380, 402, 459, 486–491, 495–501, 504
Limb, 12, 24, 43, 49–51, 53, 55, 197, 204, 259, 261, 263, 276, 366, 397, 400–401, 469, 473, 485–486, 488–490
Linear fractures, 95–97, 433, 441, 448
Lobe collapse, 248
Lordosis, 11, 33
Lunate bone, 11
Lymph, 19
Lymph nodes, 19
Lymphatic system, 15

M
Malleolus, 11, 240–241, 399, 504
Mallet finger, 80–82
Malleus, 11
Mandible, 11, 33, 187, 347–349
Manubrium, 11
Massetes, 11
Mastoid bone, 11
Matrix porous coating, 269–270

Maxilla, 11, 17, 33
Maxillary sinus, 11, 347, 351
Mechanism of injury, 16, 36, 86, 88–91, 102, 235, 405, 486, 491, 497
Medial, 11, 91, 94, 101, 175, 240–241, 248, 250–251, 267, 272, 283, 343–345, 347–348, 366, 450–451, 453, 458, 469, 473–474, 476, 478–482, 487–490, 492, 494–495, 497–502, 504–505, 507
Medulla oblongata, 11, 30, 35, 346, 351
Meninges, 6, 8, 13–14, 28–29
Meningitis, 11, 97, 433–434
Metacarpal bone, 11, 44
Metacarpal fractures, 82–84
Metatarsal, 11, 51, 53, 402–403
Middle ear, 8–9, 11–12, 14, 97–98, 345–346
Modulus fibers, 153–165
Molar, 11
Moore's fracture, 221–222
Mucous membrane, 8, 11–12
Mucus, 12
Muscle, 6–14, 24–25, 34–35, 38, 40, 42, 47, 50–51, 53, 83, 91–92, 94, 142, 174, 242, 255, 260, 275, 277, 292, 308, 312, 319, 345–346, 348, 351, 363, 368, 384–386, 390, 393, 400, 403, 409, 412, 415–419, 421–422, 425, 434, 455, 458–459, 464, 466, 468, 487, 492, 494–495, 502–503, 506
Muscular system, 20–22
Musculoskeletal model, 391

N

Nail, 12, 15, 80, 90, 277, 288, 292–293, 389, 470–472, 474–475, 477–479, 483–484, 607, 609, 680, 682–685, 481–487, 491–494, 498
Nasal, 12, 22, 30, 97–98, 343–349
Neck fractures, 87, 208, 292, 308, 466, 480–483
Neck injury, 31–32, 38, 192, 585–586, 589–590
Needle penetration, 171
Nervous system, 12, 24, 28, 30, 37, 42, 465
Neuralgia, 12
Neuron, 12, 442, 444–445

O

Occipital lobe, 12, 27, 344, 346, 351
Oesophagus, 12
Olecranon, 12, 208, 292, 405, 455, 506–507
Olfactory, 12, 22, 344, 350
Open fractures, 40, 53, 80, 97, 478
Opthalm-, Opthalma-, 12
Optic chiasma, 12
Optic disc, 12
Orbit, 12, 344, 347–348
Orthopedic devices, 255, 276
Orthopedic fixation, 276–277
Osmotic agents, 428
Osseous ligamentous fracture, 234
Ossicle, 12
Ossification, 12, 220, 253, 494
Osteochrondritis, 252
Osteoporosis, 12, 90, 718, 220, 308, 316, 406, 450, 466, 468
Ovary, 12

P

Pancreas, 8, 12, 48, 463
Paraplegia, 12, 493
Parathyroid glands, 12
Patella, 12, 50–51, 53, 100–101, 250, 269, 292, 366, 369, 391, 399, 485, 492–495, 502, 580, 604, 611, 616–617
Pediatric fractures, 85, 211
Pelvis, 5, 10, 12, 14–15, 18, 47–52, 55, 175, 194, 228–230, 253, 277, 409, 412–413, 462, 469, 485, 578–579, 479, 484, 744
Periosteum, 12, 93, 138, 433, 466
Peritoneum, 12
Phalangeal-fractures, 80
Phalanges (S. phalanx), 12, 43
Pharynx, 13, 345
Pia mater, 13, 29
Pineal gland, 13
Pinna, 13
Pituitary gland, 13, 344, 351
Plantar, 13, 403, 496, 502–503
Plaster management, 197

Pleura, 13, 41–42
Polar dummy, 56
Polyethylene products, 735
Pons, 11, 13, 30, 346
Porotid gland, 12
Posttraumatic arthritis, 485, 509
Prostate gland, 13, 15
Prosthetic sockets, 255, 261
Protection criteria, 357, 381
Psoriatic arthritis, 217
Pulmonary, 13, 91, 94, 248, 430, 460, 467
Pylorus, 13

Q
Quadriceps muscles, 13
Quadriplegia, 13

R
Radial, 13, 83–90, 102, 142, 201, 205–206, 211, 295–296, 314, 384–386, 397, 451–453, 455, 509
Radius, 10, 13, 17, 43, 74, 77, 86–88, 92, 106, 199, 201, 205, 211, 221, 277, 288, 317, 385–386, 398–399, 450
Recon nailing system, 679
Rectum, 13–15
Rectus, 13
Reflex, 13, 306, 437, 458
Relaxation, 355–356, 412, 675
Renal injury, 461, 463
Renal, 13, 438, 461, 463
Resonance, 19, 93, 185, 221, 355–357, 370, 429, 439
Retina, 7, 12–13, 402
Rib fracture, 36, 40–41, 245–247, 425–427
Rib, 13, 36, 40–41, 47, 54, 194–195, 207, 245, 425, 428, 591–592
Risk assessment, 513–517
Rods-nails, 293–294
Rolando's fracture, 84

S
Sacral, 13, 50, 52
Sagittal plane, 13, 94, 194, 344, 370, 377, 379, 403, 467, 600
Sagittal, 13, 41, 94, 175, 192–194, 256, 344, 346, 349, 351, 358, 370, 377, 379, 467, 586–587, 590, 598
Scaphoid fractures, 84–86, 279
Scapula, 10, 13, 42, 54, 91–92, 213, 404–405
Scapular fractures, 91–92
Sclera, 13, 15
Screws, 277
  cancellous, 277, 454–455
  cannulated, 278, 282, 293, 484
  cortica, 277, 290, 473, 680
Segond fracture, 233, 244, 250
Seizure prophylaxis, 443, 445
Seizure, 7, 13, 96–98, 430–431, 435, 441, 443–446
Shoulder, 5, 8, 10, 13–14, 16, 38, 40–43, 46, 50, 54–55, 90–92, 195, 197, 207, 213–214, 217, 223, 228, 234, 255, 265–266, 404–406, 452–453, 455, 463, 507, 646, 666–667, 671–672, 675
Shoulder replacements, 266
Sigmoid colon, 14
Skeletal system, 17, 401
Skull fracture, 95, 235, 238, 429, 431, 433–434, 439, 441, 445–446, 449
Skull structure, 30, 343
Spasm, 14–15, 496, 498, 501
Spinal cord, 6–7, 11, 14, 22, 28–29, 34–36, 38, 50, 346, 437, 457–460, 465
Spinal fixation, 277, 294
Spine, 5–6, 10–11, 14, 18, 32, 34, 36–38, 40, 50, 54, 56, 91, 192–194, 207, 220, 234, 248, 256, 285, 294, 363, 377–379, 388, 404, 425, 428, 449, 457–460, 462, 481, 483, 593–594, 677, 721
Spiral slot, 263
Spleen, 14, 48, 461–463
Splenic, 461–463
Stapes, 14
Sternum, 14, 36, 40, 54, 195
Steroids, 439, 460
Subarachnoid hemorrhage, 14, 99
Subdural haematoma, 14
Sublingual, 14, 348
Supine, 14, 177, 455, 459, 469, 492, 498, 501, 675, 685
Surgical technique, 623–644
Symphysis, 14, 175, 347, 677

T
Talus, 14, 50, 53, 145, 391, 402
Tarsal, 14, 50
Tendon, 6, 9–10, 14, 50–51, 80, 82, 84, 100, 135–137, 174, 250–251, 367, 384–385, 400, 488, 492–495, 664, 667–669, 674, 677, 720
Testis, 14
Thalamus, 14, 22
Thorax, 14, 40–41, 47, 49, 55–56, 194, 425, 578, 588, 592, 594
Threshold limits, 577
Thymus, 14
Thyroid gland, 12, 14
Tibia, 9, 14, 50–51
Tissues, 3, 6, 10, 12, 15, 32, 38, 52, 107, 135, 174–175, 177, 235, 278, 357, 389, 396, 402, 411, 419, 422–423, 502, 504, 507, 668, 674
Toddler's fracture, 242
Tolerance thresholds, 153, 189
Tonsil, 14
Trachea, 6, 14–15
Tragus, 14
Transient osteoporosis, 308
Transverse colon, 14
Trapezius muscle, 14
Trauma, 1, 86, 91, 93, 99–101, 194, 208–209, 225, 229, 251, 278, 292, 308, 384, 408, 430–431, 436–437, 439–447, 460–465, 468, 486–490, 493, 502–503, 506–507, 511, 519–520, 522, 544, 592, 679, 682, 704
Traumatic arthrosis, 506–507
Traumatic injuries, 43–47, 51–53, 124–131, 189–194, 223–233, 276–294, 366–383, 390–393, 401–404, 417–419, 429–507
Traumatic management, 1, 429–522
Triceps muscle, 14, 292, 400
Triquetral fractures, 86
Trochanter, 15, 92–94, 143, 288, 292–294, 308, 312, 340–341, 466–467, 469–470, 473, 477, 479, 625, 627, 634–636, 641, 680, 685, 686, 688, 697

U
Ulna, 12, 14–15, 88, 195, 199, 212, 385, 407, 451, 507
Ulnar fractures, 86
Umbilicus, 15
Uncus, 15
Ungual, 15
Unilateral, 15, 221, 271, 434
Urea, 15
Ureter, 15
Urethra, 13, 15, 410, 461–462
Urinary bladder, 15
Uterus, 7, 15, 48

V
Vagina, 15
Valgus, 15, 88, 100, 102, 211, 245, 406, 450, 456, 475, 487–488, 490, 496, 500–501, 602, 605–606, 680, 685
Valve, 15, 65, 182
Varum/varus, 15
Vas deferens, 9, 15
Vascular system and viscera, 25
Vasospasm, 15, 99
Vena cavae, 15
Ventral, 15, 235, 341, 344, 348
Ventricle, 6–7, 9, 11, 15, 29, 440, 465
Vertebra, 15, 148, 195, 235, 363, 365, 376, 378, 585, 588
Vertebral column, 15, 40, 47–48
Viscerocranium, 343–344, 346–347, 350
Vitreous body, 15
Volar, 15, 83–84, 87, 90, 92
Vulva, 15

W
Wind pipe, 6, 13–15
Wires, 82, 100, 276–278, 292, 404, 454, 692–693, 695
Woven – Lamellar, 139

X
X-ray, 2, 15, 18, 95, 207–208, 228, 254, 305, 308, 314, 316, 354–355, 358, 377–379, 602, 675, 683, 699, 738

Z
Zygoma, 15
Zygomatic arch, 16
Zygomatic arch fracture, 222–223